Handbook of

5

THEORETICAL and COMPUTATIONAL NANOTECHNOLOGY

Transport Phenomena and Nanoscale Processes

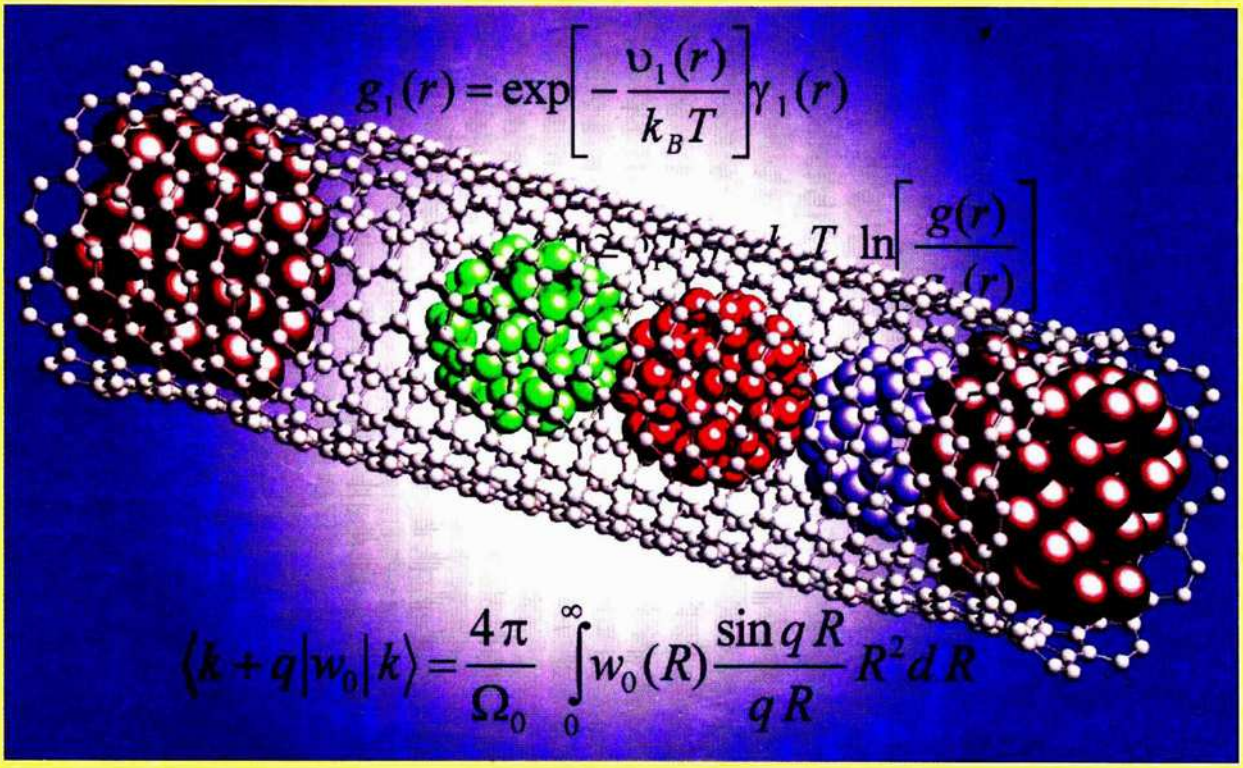

Edited by

M[illegible] Wolfram Schommers

Fo[illegible]

Pierre-Gilles de Gennes, Nobel Prize Laureate

ASP
AMERICAN SCIENTIFIC PUBLISHERS

Handbook of

THEORETICAL and COMPUTATIONAL NANOTECHNOLOGY

Titles in Nanotechnology Book Series

Founding Editor

Dr. Hari Singh Nalwa

1. **Encyclopedia of Nanoscience and Nanotechnology, 10-Volume Set**
   Edited by Hari Singh Nalwa
2. **Handbook of Theoretical and Computational Nanotechnology, 10-Volume Set**
   Edited by Michael Rieth and Wolfram Schommers
3. **Bottom-up Nanofabrication: Supramolecules, Self-Assemblies, and Organized Films, 6-Volume Set**
   Edited by Katsuhiko Ariga and Hari Singh Nalwa
4. **Handbook of Semiconductor Nanostructures and Nanodevices, 5-Volume Set**
   Edited by A. A. Balandin and K. L. Wang
5. **Handbook of Organic-Inorganic Hybrid Materials and Nanocomposites, 2-Volume Set**
   Edited by Hari Singh Nalwa
6. **Handbook of Nanostructured Biomaterials and Their Applications in Nanobiotechnology, 2-Volume Set**
   Edited by Hari Singh Nalwa
7. **Handbook of Electrochemical Nanotechnology, 2-Volume Set**
   Edited by Yuehe Lin and Hari Singh Nalwa
8. **Polymeric Nanostructures and Their Applications, 2-Volume Set**
   Edited by Hari Singh Nalwa
9. **Soft Nanomaterials, 2-Volume Set**
   Edited by Hari Singh Nalwa
10. **Functional Nanomaterials**
    Edited by Kurt E. Geckeler and Edward Rosenberg
11. **Synthesis, Functionalization and Surface Treatment of Nanoparticles**
    Edited by I. M. Baraton
12. **Quantum Dots and Nanowires**
    Edited by S. Bandyopadhyay and Hari Singh Nalwa
13. **Nanoclusters and Nanocrystals**
    Edited by Hari Singh Nalwa
14. **Molecular Nanoelectronics**
    Edited by Mark A. Reed and T. Lee
15. **Magnetic Nanostructures**
    Edited by Hari Singh Nalwa
16. **Nanoparticles for Pharmaceutical Applications**
    Edited by J. Domb, Y. Tabata, M. N. V. Ravi Kumar, and S. Farber
17. **Cancer Nanotechnology**
    Edited by Hari Singh Nalwa and Thomas Webster
18. **Biochips Nanotechnology**
    Edited by Nongyue He and Hari Singh Nalwa
19. **Nanotoxicology**
    Edited by Yuliang Zhao and Hari Singh Nalwa
20. **Polymer Nanocomposites and Their Applications**
    Written by Suprakas Sinha Ray and Mosto Bousmina
21. **Nanoscale Science and Engineering Education**
    Edited by Aldrin E. Sweeney and Sudipta Seal
22. **Hard Nanomaterials**
    Edited by Hari Singh Nalwa

Additional Volumes in Preparation

Visit: www.aspbs.com

Handbook of THEORETICAL and COMPUTATIONAL NANOTECHNOLOGY

Volume 5

Transport Phenomena and Nanoscale Processes

Edited by

Michael Rieth and **Wolfram Schommers**

Forschungszentrum Karlsruhe, Karlsruhe, Germany

AMERICAN SCIENTIFIC PUBLISHERS

25650 North Lewis Way

Stevenson Ranch, California 91381-1439, USA

AMERICAN SCIENTIFIC PUBLISHERS
25650 North Lewis Way, Stevenson Ranch, California 91381-1439, USA
Tel.: (661) 254-0807
Fax: (661) 254-1207
E-mail: order@aspbs.com
WEB: www.aspbs.com

Handbook of Theoretical and Computational Nanotechnology
edited by Michael Rieth and Wolfram Schommers.

The image on the cover of this handbook was provided by Professor Jeong Won Kang, Chung-Ang University, Seoul, Korea. See Jeong Won Kang, Won Young Choi, and Ho Jung Hwang, *Journal of Computational and Theoretical Nanoscience*, Vol. 1(2), pp. 199–203 (2004). Copyright © 2004, American Scientific Publishers.

This book is printed on acid-free paper. ♾

Library of Congress Control Number: 2003111818

International Standard Book Number: 1-58883-042-X (Set)
International Standard Book Number: 1-58883-043-8 (Volume 1)
International Standard Book Number: 1-58883-044-6 (Volume 2)
International Standard Book Number: 1-58883-045-4 (Volume 3)
International Standard Book Number: 1-58883-046-2 (Volume 4)
International Standard Book Number: 1-58883-047-0 (Volume 5)
International Standard Book Number: 1-58883-048-9 (Volume 6)
International Standard Book Number: 1-58883-049-7 (Volume 7)
International Standard Book Number: 1-58883-050-0 (Volume 8)
International Standard Book Number: 1-58883-051-9 (Volume 9)
International Standard Book Number: 1-58883-052-7 (Volume 10)

Dr. Michael Rieth
Forschungszentrum Karlsruhe
Institute of Materials Research I
D-76021 Karlsruhe, GERMANY

Prof. Dr. Wolfram Schommers
Forschungszentrum Karlsruhe
Institute for Scientific Computing
D-76021 Karlsruhe, GERMANY

PRINTED IN THE UNITED STATES OF AMERICA
10 9 8 7 6 5 4 3 2 1

Foreword

Nanoscience is fashionable. All administrations in the Western world have stressed their interest in nanoobjects and nanotechnologies. As usual, this type of large scientific movement has its pluses and minuses. Many scientists join the crowd without necessarily changing anything in their actual work. Most chemists, for instance, build new molecules that may be called nanoobjects; but again, as usual, the movement does generate significant new content.

Let us, for instance, follow the role of nanostructures in *chemistry*. On one side, nature has provided us with beautiful, robust objects such as fullerenes and carbon tubes, which have some admirable properties. The current challenge is to obtain them in large amounts and at a reasonable price. Here is the real problem.

A completely different sector is obtained from *chemical nanomachines*, for which a molecular unit of nanometric size moves with respect to another one through a change in redox potential or pH. Some of these machines have been built. At the moment, I feel rather skeptical about them because they are extremely costly, extremely fragile (sensitive to poisons), and not easy to protect with a suitable coating—or by a local "antipoison" center. But, here again, there is a challenge.

Let us now turn to *biology*. Here we find an immense group of working nanomachines, enzymes, ionic channels, sensor proteins, adhesion molecules, and so on. They are extremely impressive, but of course they represent progressive construction by trial and error over more than a billion years. Should we try to mimic these machines or, rather, use them for technological purposes, *as they are*, for instance, to grow plants or create proteins at an industrial level according to the techniques of molecular genetics? This is a major question.

A third, open side is *quantum physics* and the (remote) possibility of quantum computers. In my youth, I had hopes for digital storage via quantized flux quanta: The corresponding technology, based on Josephson functions, was patiently built by IBM, but they ultimately dropped out. This shows the hardship of nanotechnologies even when they are handled by a large, competent group. But the cause is not lost, and it may well be that our children use some unexpected form of quantum computers.

Thus, we are facing real challenges, not just the vague recommendations of some anonymous boards. And, we need the tools. We need to know the behavior of materials at the nanolevel, the clever tricks of physical chemistry required to produce nanoparticles or nanopores, the special properties of small cooperative systems (nanomagnets, nanosuperconductors, nanoferroelectrics, etc.), the ability for assembling functional units, and so on.

The aim of the present handbook is to help us with the tools by suitable modelizations. It is written by leading experts, starting from general theoretical principles and progressing to detailed recipes.

In the second half of the 18th century, all the knowledge (fundamental and practical) of the Western world was condensed into an outstanding encyclopedia constructed energetically by Denis Diderot just after the industrial revolution started. Here, at a more modest level, we can hope for something similar. Soon after the first wave, including this handbook, a certain form of nanoindustry may be born.

The discussions started in this handbook will continue in a journal (*Journal of Computational and Theoretical Nanoscience*) launched by the present editors. I wish them the best.

Professor Pierre-Gilles de Gennes

Nobel Prize Laureate, Physics
Collège de France
Paris, France

Preface

This is the first handbook that deals with theoretical and computational developments in nanotechnology. The 10-volume compendium is an unprecedented single reference source that provides ideal introduction and overview of the most recent advances and emerging new aspects of nanotechnology spanning from science and engineering to neurogenetics. Many works in the field of theoretical and computational nanotechnology have been published to date, but no book or handbook has focused on all aspects in this field that deal with nanomachines, electronics, devices, quantum computing, nanostructured materials, nanorobotics, medicine, biology, biotechnology, and more.

There is no doubt that nanoscience will be the dominant direction for technology in this new century, and this science will influence our lives to an extent impossible in years past: Specific manipulations of matter at its ultimate level will open completely new perspectives on all scientific and technological disciplines. To be able to produce optimal nanosystems with tailor-made properties, it is necessary to analyze and construct such systems in advance by adequate theoretical and computational methods. The handbook gives a complete overview of the essential methods, models, and basic pictures.

But, as is well known, there are also threats connected with nanotechnology, specifically with respect to biological systems: Self-assembly can be an uncontrolled process, and the final state of a developing system is in general uncertain in such cases. To avoid undesirable developments, the theoretical (computational) analysis of such processes is not only desirable but also absolutely necessary. Thus, the computational and theoretical methods of nanoscience are essential for the prediction of new and custom nanosystems and can help keep nanoscience under control. There is basically no alternative. Therefore, one possible answer to the question, "Why a book on theoretical and computational nanotechnology?" is *to give nanotechnology a direction!*

In the design of macroscopic and microscopic systems, engineering is essentially based on *intuitive concepts*, which are tailored to observations in everyday life. Classical mechanics is also based on these macroscopic observations, and its notions have been chosen with respect to our intuitive demands for *visualizability*. However, when we approach the nanolevel, the tools used for the design of macroscopic and microscopic systems become more and more useless. At the nanolevel, *quantum phenomena* are dominant, and the main features in connection with quantum effects are not accessible to our intuitive concepts, which are merely useful at the macroscopic level; the framework of quantum theory is in striking conflict with our intuitive demands for visualizability, and we are forced to use abstract physical laws expressed by mathematical equations. In other words, effects at the nanolevel are (almost) not accessible to our usual engineering concepts. Therefore, here we rely on the abstract mathematical relations of theoretical physics. In nanotechnology functional systems, machines and the like cannot be adequately designed without the use of these abstract theoretical laws and the application of suitable computational methods. Therefore, in nanotechnology, theoretical and computational methods are centrally important: This makes the present handbook an indispensable compendium.

Nanometer-scale units are by definition very small atomic structures and functional systems; it is the smallest level at which functional matter can exist. We already learned to manipulate matter at this ultimate level: Atoms can be moved experimentally in a controlled manner from one position to another. This is astonishing because one nanometer only corresponds to one millionth of a millimeter. For example, an electrical nanogenerator could be designed consisting of various parts that included a very fast revolving rotator. One million of these generators could be arranged side by side on a length of two centimeters; it is remarkable that not only *static* nanostructures could in principle be produced and significantly manipulated but also artificial *dynamical* nanosystems. But, the downscaling of functional structures from the macroscopic to the nanometer scale is only one of the essential

points in connection with nanotechnology. In addition—and maybe much more important—nanosystems provide unique properties in comparison to those we observe at the macroscopic level. For example, a metal nanocluster shows a melting temperature that strongly deviates from that of a macroscopic piece of metal; its melting point is significantly lower. A decrease down to a fraction of only 20% is typical, depending, however, on the material and particle number.

A professional treatment of the various problems in nanoscience and nanotechnology makes the application and development of theoretical and computational methods in this field absolutely necessary. In other words, the discipline of theoretical and computational nanotechnology has to be considered as a key topic to be able to treat nanotechnology adequately and to reach optimal solutions for certain tasks. It is therefore desirable to get a timely overview about the specific topics presently relevant in this field. In this respect, the handbook gives a complete overview of the specific topics so far established in nanotechnology. Each chapter gives a certain overview of actual activities of the envisaged topic and in most cases an adequate description of the basics, so advanced students also can benefit from the handbook. It was our strategy to provide consistent and complete representations so the reader would be able to study each chapter without consulting other works. This of course leads to certain overlaps, which was also part of our strategy to enable an approach to the same topic from various points of view.

The handbook reflects the spectrum of questions and facts that are and could be relevant in the field of nanotechnology. Not only formal developments and methods are outlined, but also descriptions of a broad variety of applications in particular are typical for the handbook. All relevant topics have been taken into account, from functional structures—like an electrical nanogenerator—or quantum computing to questions that deal directly with basic physics. Almost all fields related to theoretical and computational nanotechnology could be covered, including *multiscale modeling*, which is important for the transition from microscale to nanoscale and vice versa.

All theoretical and computational methods used in connection with the various topics in nanoscience are directly based on the *same* theoretical physical laws. At the nanolevel, all properties of our world emerge at the level of the *basic* theoretical laws. In traditional technologies, engineers do not work at the ultimate level. They use more or less phenomenological descriptions that generally cannot be deduced from the basic physical theoretical laws. We have as many phenomenological descriptions as there are technological disciplines, and each is tailor-made to a specific topic. An exchange of concepts is either not possible or rather difficult. In contrast, at the ultimate nanolevel the world is based on only one theory for all disciplines, and this is expressed by basic theoretical physics. This situation opens the possibility for interconnections between the various topics in nanotechnology to bring about new effects and chances for further applications. In other words, nanotechnology and nanoscience can be considered interdisciplinary. Clearly, the handbook reflects the interdisciplinary character of this new science and technology.

The *Handbook of Theoretical and Computational Nanotechnology* includes 138 chapters written by hundreds of the world's leading scientists. Topics cover mainly the following areas:

(i) Computational biology: DNA, enzymes, proteins, biomechanisms, neurogenetic information processing, and nanomedicine
(ii) Computational chemistry: quantum chemistry, molecular design, chemical reactions, drugs, and design
(iii) Computational methods and simulation techniques from *ab initio* to multiscale modeling
(iv) Materials behavior at the nanolevel, such as mechanics, defects, diffusion, and dynamics
(v) Nanoscale processes: membranes, pores, diffusion, growth, friction, wear, catalysis
(vi) Nanostructured materials: metals, composites, polymers, liquid crystals, photonic crystals, colloids, and nanotubes
(vii) Nanostructures: fullerenes, nanotubes, clusters, layers, quantum dots, thin films, surfaces, and interfaces
(viii) Nanoengineering and nanodesign: nanomachines, nano-CAD, nanodevices, and logic circuits

(ix) Nanoelectronics: molecular electronics, nanodevices, electronic states, and nanowires
(x) Nanomagnetism: magnetic properties of nanostructures and nanostructured materials
(xi) Nanooptics: optical response theory, quantum dots, luminescence, and photonic crystals
(xii) Quantum computers: theoretical aspects, devices, and computational methods for simulating quantum computers and algorithms

The handbook provides broad information on all basic and applied aspects of theoretical and computational nanotechnology by considering more than two decades of pioneering research. It is the only scientific work of its kind since the beginning of nanotechnology, bringing together core knowledge and the very latest advances. The handbook is written for audiences of various levels while providing the latest up-to-date information to active scientists and experts in the field. This handbook is an indispensable source for research professionals and developers seeking the most up-to-date information on theoretical and computational nanotechnology among a wide range of disciplines, from science and engineering to medicine.

This handbook was written by leading experts, and we are highly grateful to all contributing authors for their tremendous efforts in writing these outstanding state-of-the-art chapters that altogether form a unified whole. K. Eric Drexler (designer of nanomachines, founder of the Foresight Institute, coiner of the term *nanotechnology*) gives an excellent introductory chapter about possible trends of future nanotechnology. We especially express our sincere gratitude to Dr. Drexler for his instructive and basic representation.

We cordially extend our special thanks to Professor Pierre-Gilles de Gennes for his valuable and insightful Foreword.

The editors are particularly thankful to Dr. Hari Singh Nalwa, President and CEO of American Scientific Publishers, for his continuous support of the project and the enthusiastic cooperation in connection with all questions concerning the development of the handbook. Furthermore, we are grateful to the entire team at Bytheway Publishing and especially to Kate Brown for copyediting.

Dr. Michael Rieth
Prof. Dr. Wolfram Schommers
Karlsruhe, Germany

Contents

CHAPTER 2. Dynamics of Condensed Phase Proton and Electron Transfer Processes

Raymond Kapral, Alessandro Sergi

CHAPTER 3. Computer Simulation of Nanofiltration Membranes and Processes

Horst Chmiel, Xavier Lefebvre, Valko Mavrov, Mohan Noronha, John Palmeri

CHAPTER 8. Diffusion in Elastically Strained Solids

Vladimir A. Borodin, Maria G. Ganchenkova

CHAPTER 9. Adsorption at Nanostructured Surfaces

Axel Groß

CHAPTER 10. Computational Methods for Atomistic Modeling of Nanoporous Materials and Their Properties

Muhammad Sahimi, Theodore T. Tsotsis

CHAPTER 11. Modeling of Electrocatalytic Surface Reactions

S. J. Mitchell, M. T. M. Koper

CHAPTER 12. Radiation-Induced Modifications in Nanomaterials

M. Chipara, D. Hui

About the Editors

Dr. Michael Rieth has been a research scientist at the Institute of Materials Research I (IMF-I) in the Forschungszentrum Karlsruhe, Germany, since 2002. He has been head of the consulting company AIFT, Karlsruhe, since 1987. He worked as a researcher at the Institute of Materials Research II (IMF-II), Forschungszentrum Karlsruhe, from 1995 to 1999 and at the Engineering Science Department of the University of Patras (Greece) from 1999 to 2000. He was product manager at AMA Systems, Pforzheim, Germany, from 2000 to 2001. He received his master of science (German Dipl. Ing.) degree in electrical engineering from the University of Karlsruhe in 1991 and his doctoral degree in physics from the University of Patras (Greece) in 2001. Dr. Rieth published 23 research articles in refereed journals, 2 book chapters, and four patents. He is the author of *Nano-Engineering in Science and Technology* (World Scientific, Singapore, 2003) and was the editor-in-chief of the *Journal of Computational and Theoretical Nanoscience* (2004–2005). His main scientific interests are in atomistic modeling of metallic nanosystems and materials development for advanced fusion reactor applications.

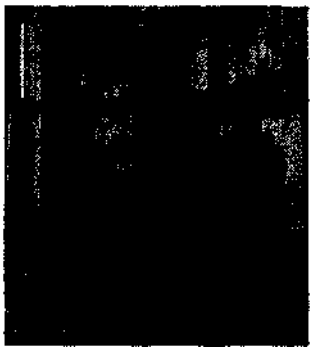

Prof. Dr. Wolfram Schommers is a theoretical physicist and is presently at the Research Center of Karlsruhe in Germany. He is also professor of theoretical physics, professor of physics and materials sciences, and distinguished professor in Europe, China, and the United States. He began his studies of theoretical physics at the Technical University of Munich and continued his course work at the University of Münster, receiving a diploma in physics. After a brief intermezzo in the industry, Professor Schommers joined the Research Center of Karlsruhe. He received his doctoral degree (Dr. rer. nat.) in theoretical physics from the University of Karlsruhe.

Professor Schommers concentrates his scientific activities on computational and theoretical physics. His main fields of interest include foundations of physics, liquids, solids, and gases; superionic conductors; surface science; and nanophysics as the basis for the investigation of properties of nanometer-scale atomic devices, junctions, quantum dots, and nanomachines. He has published the results of his research and thoughts in various scientific journals (214 articles and book chapters).

Some topics concerning liquids, solids, and gases concern interaction potentials, single-particle motion, diffusion, generalized phonon density of states, collective motion, and liquid-solid phase transition. Selected articles include "The Effect of van der Waals-Type Interactions in Metals: A Pseudopotential Model" (*Zeitschrift für Physik B* 121, 1976); "Liquid Argon: The Influence of Three-Body Interactions on Atomic Correlations" (*Physical Review A* 16, 327, 1977); "Theoretical Investigation of the Liquid Solid Transition. A Study for Gallium" (*Solid State Communications* 21, 65, 1977); "Pair Potentials in Disordered Many-Particle Systems: A Study for Liquid Gallium" (*Physical Review A* 28, 3599, 1983); "Many-Body Polarization and Overlap Effects in the Dynamic Structure Factor of Dense Krypton Gas" (with P. A. Egelstaff, J. J. Salacuse, and J. Ram; *Physical Review A* 34, 1516, 1986); and "Comment on 'Pair Interaction from Structural Data for Dense Classical Liquids'" (*Physical Review Letters* 58, 427, 1987).

Topics in connection with superionic conductors involve structure and dynamics, correlated motions, and collective behavior. Selected articles include "Correlations in the Motions of Particles in AgI: A Molecular-Dynamics Study" (*Physical Review Letters* 38, 1536, 1977);

"Current–Current Correlations in AgI" (*Physical Review B* 16, 327, 1977); "Structure and Dynamics of Superionic Conductors" (*Physical Review B* 21, 847, 1979); "Triplet Correlations in Solid Electrolytes" (*Solid State Ionics* 1, 473, 1980).

Topics concerning surface physics touch on temperature effects, structure, dynamics, and interaction. Selected works are as follows: "Structural and Dynamical Behaviour of Noble-Gas Surfaces" (*Physical Review A* 32, 6845, 1985); "Statistical Mechanics of the Liquid Surface and the Effect of Premelting," in *Structure and Dynamics of Surfaces II* (Springer-Verlag, Heidelberg, 1987); "The Effect of Non-Linear Interactions at the Surface of Solids" (*Surface Science* 269/270, 180, 1992); and "Steps, Point Defects and Thermal Expansion at the Au(100) Surface" (with H. Zimmermann, M. Nold, U. Romahn, and P. von Blanckenhagen; *Surface Science* 287/288, 76, 1993).

Some details regarding the work of Professor Schommers on nanophysics include study of nanoclusters, nanostructures, and nanomachines; temperature effects; and electronic states. Selected works include "Phonons and Structure in Nano-Clusters: A Molecular Dynamics Study for Al" (*Nanostructured Materials* 9, 621, 1997); "Excited Nano-Clusters" (*Applied Physics A* 68, 187, 1999); "Thermal Stability and Specific Properties of Nanosystems" (with S. Baskoutas and M. Rieth; *Modern Physics Letters B* 14, 621, 2000); "Computational Atomic Nanodesign," in *Encyclopedia of Nanoscience and Nanotechnology* (with M. Rieth; American Scientific Publishers, Stevenson Ranch, CA, 2004); "Computational Engineering of Metallic Nanostructures and Nanomachines" (with M. Rieth; *Journal of Nanoscience and Nanotechnology* 2, 679, 2002); and "Electron in an Interaction Potential of General Shape" (with M. Rieth; *Journal of Computational and Theoretical Nanoscience* 2, 362, 2005).

Concerning the foundations of physics, Professor Schommers has discussed new aspects in connection with reality, and his basic ideas can be summarized as follows: Information about reality outside flows via sense organs into the body of the observer, and the brain forms a picture of reality. On the basis of many facts, Schommers concluded that the symbols in this picture of reality should have in general no similarity with the objects in the outside world; that is, the reality outside is transformed. On the one hand, we have the reality; on the other hand, we have a picture of reality. The reality is projected on space and time, and we obtain a picture of reality; the structures in the pictures are different from those in the reality outside. This conception is discussed mathematically by Professor Schommers in connection with quantum phenomena leading to new aspects in connection with relevant basic topics. Like both Whitehead and Bergson, Schommers argues for the primacy of processes and shows that space and time are closely tied to real processes. Selected work in this regard are "Inertial Frames of Reference: Mass Coupling to Space and Time" (*International Journal of Theoretical Physics* 20, 411, 1981); "Raum-Zeit, Quantentheorie und Bilder von der Wirklichkeit" (*Philosophia Naturalis* 23, 238, 1986); "Being and Becoming at the Microscopic Level" (*International Journal of Modern Physics B* 3, 1, 1989); "Space-Time and Quantum Phenomena," in *Quantum Theory and Pictures of Reality* (Springer-Verlag, Heidelberg, 1989); and "Truth and Knowledge," in *What Is Life?* (World Scientific, Singapore, 2002).

Professor Schommers is author and editor of the following books: *Fundamentals of Nanometer Structuring; Structure and Dynamics of Surfaces I and II; Quantum Theory and Pictures of Reality; The Visible and the Invisible; Das Sichtbare und das Unsichtbare; Elemente des Lebens; What is Life?; Formen des Kosmos; Space and Time, Matter and Mind; Symbols, Pictures and Quantum Reality*.

Professor Schommers is the editor-in-chief of the *Journal of Computational and Theoretical Nanoscience*. He is also an editorial board member of various scientific journals, and he is principal editor-in-charge of the book series *Foundations of Natural Science and Technology*. He is an invited member of the Humboldt Academy, an invited member of the Academic Board of the Humboldt Society, and an invited member of the Advisory Board of Medical Ethics of the 21st Century. Professor Schommers is also deputy governor of the American Biographical Institute (inauguration 2000).

Professor Schommers has been honored by various awards, medals, and appointments. He has been cited in *Who's Who in the World, Who's Who in Science and Technology, Living Science, The Europe 500, The Barons 500, 2000 Outstanding Intellectuals of the 21st Century, Leading Intellectuals of the World, 500 Leaders of Influence, and International Register of Profiles* (no. 123 of 200), and elsewhere.

List of Contributors

Number in parentheses indicates the page on which the author's contribution begins.

Eduard Arzt (215)
Max Planck Institute for Metals Research, Stuttgart, Germany

T. John Balk (215)
Max Planck Institute for Metals Research, Stuttgart, Germany

Vladimir A. Borodin (437)
RRC Kurchatov Institute, Moscow, Russia

Markus J. Buehler (215)
Max Planck Institute for Metals Research, Stuttgart, Germany and California Institute of Technology, Pasadena, California, USA

M. Chipara (717)
Radiation Effects Research Program, Indiana University Cyclotron Facility, Bloomington, Indiana, USA

Horst Chmiel (93)
Department of Process Technology, Saarland University and Institute for Environmentally Compatible Process Technology, Saarbrücken, Germany

Samir Farhat (251)
Laboratoire d'Ingéniérie des Matériaux et des Hautes Pressions, Villetaneuse, France

Annalisa Fasolino (379)
Theoretical Physics, IMM, Radboud University Nijmegen, Nijmegen, The Netherlands; van 't Hoff Institute for Molecular Sciences (HIMS), and Van der Waals-Zeeman Institute, Universiteit van Amsterdam, Amsterdam, The Netherlands

Y. M. Galperin (1)
Department of Physics, University of Oslo, Oslo, Norway; A. F. Ioffe Physico-Technical Institute of Russian Academy of Sciences, St. Petersburg, Russia; and Argonne National Laboratory, Argonne, Illinois, USA

Maria G. Ganchenkova (437)
Helsinki University of Technology, Espoo, Finland

Huajian Gao (215)
Max Planck Institute for Metals Research, Stuttgart, Germany

L. Y. Gorelik (1)
Department of Applied Physics, Chalmers University of Technology, Göteborg, Sweden

Robert B. Greendyke (251)
Department of Mechanical Engineering, University of Texas at Tyler, Tyler, Texas, USA

Axel Groß (557)
Physik-Department T30, Technische Universität München, Garching, Germany

D. Hui (717)
University of New Orleans, Department of Mechanical Engineering, New Orleans, Louisiana, USA

M. Jonson (1)
Department of Physics, Göteborg University, Göteborg, Sweden

Raymond Kapral (61)
Chemical Physics Theory Group, Department of Chemistry, University of Toronto, Toronto, Canada

M. T. M. Koper (691)
Schuit Institute for Catalysis and Department of Chemical Engineering, Eindhoven University of Technology, Eindhoven, The Netherlands

Xavier Lefebvre (93)
European Membrane Institute (EMI), CNRS ENSCM UMR 5635, University of Montpellier II, CC 047, Montpellier Cedex 5, France

Valko Mavrov (93)
Department of Process Technology, Saarland University and Institute for Environmentally Compatible Process Technology, Saarbrücken, Germany

S. J. Mitchell (691)
Schuit Institute for Catalysis and Department of Chemical Engineering, Eindhoven University of Technology, Eindhoven, The Netherlands

Mohan Noronha (93)
Institute for Environmentally Compatible Process Technology, Saarbrücken, Germany

John Palmeri (93)
European Membrane Institute (EMI), CNRS ENSCM UMR 5635, University of Montpellier II, CC 047, Montpellier Cedex 5, France

N. Quirke (329)
Department of Chemistry, Imperial College, South Kensington, London, United Kingdom

Muhammad Sahimi (603)
Department of Chemical Engineering, University of Southern California, Los Angeles, California, USA

Carl D. Scott (251)
NASA Johnson Space Center, Houston, Texas, USA

Alessandro Sergi (61)
Chemical Physics Theory Group, Department of Chemistry, University of Toronto, Toronto, Canada

R. I. Shekhter (1)
Department of Physics, Göteborg University, Göteborg, Sweden

M. B. Sweatman (329)
Department of Chemical and Process Engineering, University of Strathclyde, Glasgow, United Kingdom

Theodore T. Tsotsis (603)
Department of Chemical Engineering, University of Southern California, Los Angeles, California, USA

V. M. Vinokur (1)
Argonne National Laboratory, Argonne, Illinois, USA

Handbook of Theoretical and Computational Nanotechnology

Edited by

Michael Rieth and Wolfram Schommers

Volume 1. BASIC CONCEPTS, NANOMACHINES, AND MEDICAL NANODEVICES

Volume 2. ATOMISTIC SIMULATIONS—ALGORITHMS AND METHODS

Volume 3. QUANTUM AND MOLECULAR COMPUTING, QUANTUM SIMULATIONS

Volume 4. NANOMECHANICS AND MULTISCALE MODELING

Volume 5. TRANSPORT PHENOMENA AND NANOSCALE PROCESSES

Volume 6. BIOINFORMATICS, NANOMEDICINE, AND DRUG DESIGN

Volume 7. MAGNETIC NANOSTRUCTURES AND NANO-OPTICS

Volume 8. FUNCTIONAL NANOMATERIALS, NANOPARTICLES, AND POLYMER DESIGN

Volume 9. NANOCOMPOSITES, NANO-ASSEMBLIES, AND NANOSURFACES

Volume 10. NANODEVICE MODELING AND NANOELECTRONICS

CHAPTER 1

Shuttle Transport in Nanostructures

R. I. Shekhter,[1] L. Y. Gorelik,[2] M. Jonson,[1]
Y. M. Galperin,[3,4,5] V. M. Vinokur[5]

[1]*Department of Physics, Göteborg University, Göteborg, Sweden*
[2]*Department of Applied Physics, Chalmers University of Technology, Göteborg, Sweden*
[3]*Department of Physics, University of Oslo, Oslo, Norway*
[4]*A. F. Ioffe Physico-Technical Institute of Russian Academy of Sciences, St. Petersburg, Russia*
[5]*Argonne National Laboratory, Argonne, Illinois, USA*

CONTENTS

ISBN: 1-58883-047-0

Handbook of Theoretical and Computational Nanotechnology
Edited by Michael Rieth and Wolfram Schommers
Volume 5: Pages (1–59)

1. INTRODUCTION

Electron transport through conducting matter can be significantly modified compared with ordinary metals and semiconductors if the dimensions of a conductor are reduced to the nanometer scale or if one designs a composite material containing nanoscale components. For example, if electrons can be trapped in small conducting regions within an insulating matrix, quantum-mechanical tunneling and Coulomb interactions turn out to be the main mechanisms controlling electron transport. In particular, this can be the case in granular materials, where the Coulomb blockade phenomenon reduces charge fluctuations and leads to single-electronic tunneling.

Mechanical deformability plays a special role in nanomaterials. On the one hand, it originates from the electronic contribution to the elastic constants of the material, and on the other hand, it has tremendous impact on the electron tunneling. The interplay between electronic and mechanical degrees of freedom is especially important in nanocomposites consisting of materials with very different elastic properties. Liquid nanocomposites or electrolytes represent an extreme case of such systems. There the charges are localized on ions, and it is the mechanical, convective motion of these "nanocarriers" that is responsible for the charge transfer (the ionic transport mechanism).

In solid-state composite materials, the higher density of "carriers" together with a significant "freezing" of their mechanical motion increases the importance of interparticle electron tunneling and makes this charge transport mechanism competitive with mechanical convection. Hence we arrive at the very interesting situation when electrical and mechanical degrees of freedom cannot be separated. One has to consider a new—nanoelectromechanical—type of transport.

This is the situation occurring in many metal-organic nanocomposites, where small conducting nanoparticles or "dots" are embedded in a soft organic molecular matrix. There, on-dot discrete charge fluctuations caused by electrostatically induced mechanical distortions play an essential role providing a feedback to the mechanical motion. Both the response to external perturbations and the noise properties of such materials are qualitatively different from those known for bulk homogeneous conductors.

During the past decade or so, nanotechnology has advanced the ability to fabricate systems in which chemical self-assembly defines the functional and structural units of nanoelectronic devices [1]. Because the elastic parameters of many compounds and devices currently used can be much "softer" than those of semiconductors and metals, mechanical degrees of

freedom may play an important role in charge transfer. In particular, charge transfer via tunneling through a device can be dramatically enhanced by the mechanical motion of some part of the device.

Recently, nanomechanical oscillators [2] have been combined with single-electron tunneling [3] devices, resulting in a new class of nanoelectromechanical systems (NEMS). Experiments measuring electron transport through single, oscillating molecules [4–7], suspended semiconductor systems [8, 9], and suspended carbon nanotubes [10] clearly demonstrate the influence of mechanical degrees of freedom on the current in the single-electron tunneling regime.

As a simple example of a device of this type, consider a metallic grain elastically suspended between a source and a drain electrode as in Fig. 1 [11]. Since the central conducting grain can move, we will refer to this device as a nanoelectromechanical single-electron transistor (NEM-SET) rather than just a single-electron transistor (SET). If, because of a fluctuation in its position, the grain were to come close to the source (or drain) electrode the tunneling coupling between them would increase significantly and the grain would be negatively (positively) charged. Then, accelerated by elastic and Coulomb electrostatic forces, the grain would move back and approach the drain (source) electrode, thus transferring the acquired charge. The described process is usually referred to as "shuttling" of electrons. In general, the shuttle mechanism can be defined as a charge transfer through a mechanical subsystem facilitated by its oscillatory center-of-mass motion. The key factor here is that, in shuttling, the charge of the grain, $q(t)$, is correlated with the grain velocity, $\dot{x}(t)$, in such a way that the time average $\overline{q(t)\dot{x}(t)} \neq 0$. It follows that the average work performed by the electrostatic force is nonzero even if $\overline{\dot{x}(t)} = 0$, and as a result, the mechanical motion and charge transfer can be unstable with respect to the formation of periodic or quasi periodic mechanical motion and electrical signal.

Being induced by the coupling between tunneling electrons and vibrational degrees of freedom, shuttle transport should be discriminated from the conventionally discussed vibron-assisted inelastic tunneling. The difference is that shuttling results from an *electromechanical instability*. If the mechanical motion is strongly damped, the device is mechanically stable, and the number of generated vibrons is close to the equilibrium value. In this situation the notion of vibron-assisted tunneling is adequate. As the damping in the mechanical system decreases, or the driving voltage increases, one may reach a point where the mechanical stability of the device is lost. At this point, the number of generated vibrons increases and reaches a large value. Moreover, a special type of coherence in the mechanical system is maintained due to the coupling to tunneling electrons. This coherence can be characterized by nonzero off-diagonal elements of the density matrix in the vibron-number representation. As a result, the vibrational degrees of freedom can be described by a classical field representing the mechanical displacement of the shuttle. In this (shuttle) regime, the electron-vibron interaction develops into a mechanical transportation of electrons.

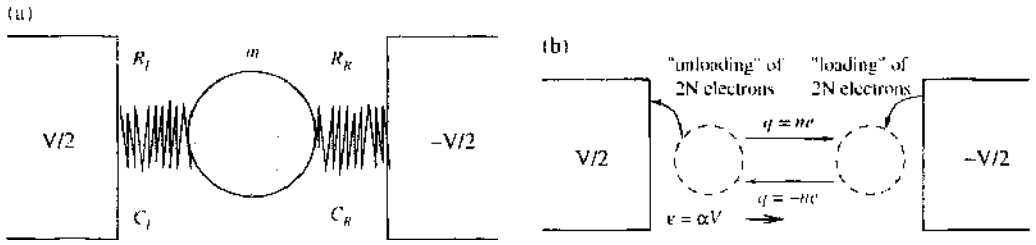

Figure 1. (a) Simple model of a soft Coulomb blockade system in which a metallic grain (center) is linked to two electrodes by elastically deformable organic molecular links. (b) A dynamic instability occurs since, in the presence of a sufficiently large bias voltage V, the grain is accelerated by the corresponding electrostatic force toward first one, then the other electrode. A cyclic change in direction is caused by the repeated "loading" of electrons near the negatively biased electrode and the subsequent "unloading" of the same at the positively biased electrode. As a result the sign of the net grain charge alternates leading to an oscillatory grain motion and a novel "electron shuttle" mechanism for charge transport. Reprinted with permission from [11]. L. Y. Gorelik et al., *Phys. Rev. Lett.* 80, 4526 (1998). © 1998, American Physical Society.

Another important feature of nanosystems is the *Coulomb blockade* [12] phenomenon. A small, initially neutral system that has accepted an extra electron, becomes negatively charged, and under certain conditions another electron cannot, due to Coulomb repulsion, reach the grain. As a result, it has to wait until the first electron has escaped. Until then further transport is blocked. Thus, under Coulomb blockade conditions the electrons can be transferred only *one by one* (or, more generally, in integer numbers). The smaller the system capacitance, the bigger the charging energy. Consequently, Coulomb blockade is an intrinsic property of small devices, and its importance increases with the progress in nanoscience and nanotechnology. Hence, because of Coulomb blockade, shuttling of *single electrons* or single Cooper pairs can take place. We give a very brief review of the Coulomb blockade of tunneling in Appendix A.

During the past seven years, shuttles of different types have been studied theoretically and experimentally. We have just emphasized that shuttling as opposed to vibron-assisted tunneling is due to an intrinsic instability. However, it can also be due to an externally driven grain motion using (e.g., an AC electric or mechanical force). Another point of interest is that electron transport through a NEM-SET device can occur in regimes where either a classical or a quantum mechanical theory is called for. The mechanical degrees of freedom may also require either a classical or a quantum-mechanical description. Hence, shuttle charge transfer in soft nanostructures involves rich and interesting physics.

Presently, many researchers are interested in shuttling in nanoelectromechanical systems aiming to determine fundamental properties of electromechanical coupling in nanostructures and electron, and phonon transport. This knowledge will definitely give renewed impetus to the design of new applications such as, for example, nanogenerators, nanoswitches, and current standards.

Shuttle electron transfer can take place not only through a metallic grain but also through a relatively soft nanocluster. In this connection, it is important to study vibrational modes of electromechanical systems with several degrees of freedom. If the center-of-mass motion can be clearly separated from other modes, then the shuttle electron transfer through the system is similar to that in the case of a rigid grain. Otherwise, it is more appropriate to speak of *vibron-assisted tunneling* rather than shuttling.

Further, electromechanical coupling and shuttle transport is not only a feature of heteroelastic nanocomposites. It also has relevance for other nanoelectromechanical systems intentionally designed to work at the nanometer scale [13–15]. Early work on shuttle transport of electrons were reviewed in Ref. [16].

Our aim is here to discuss the aforementioned issues in more detail. We will start from the simplest case of a particle with one mechanical degree of freedom located between

Table 1. Classification of shuttle transport. Shuttle transport of charge can be categorized according to what type of physical description is needed for the mechanical and electronic subsystems.

Electron transport \ Mechanical motion	Classical	Quantum
Incoherent	Classical shuttling of particles Sec. II A, Appendix B	Quantum shuttling of particles Sec. II D
Coherent	Classical shuttling of waves Sec. II C, Sec. IV	Quantum shuttling of waves Sec. II D, Appendix C

two electrodes and elastically coupled either to the substrate or to the leads. This situation is relevant to several experiments, for example, to electron shuttling through an artificial structure [17], and to shuttling through an oscillating C_{60} molecule [4]. Both classical and quantum electron transport will be considered in Sections 2.1 and 2.3, respectively (see Table 1). It will be shown that in both cases an electromechanical instability occurs which leads to a periodic mechanical motion of the elastically suspended particle [11, 18, 19]. In Section 2.4, our aim is to review theoretical work regarding systems where the mechanical degrees of freedom need to be treated quantum mechanically. A review of the available experimental results is given in Section 3. Finally, the possibility of coherent shuttling of Cooper pairs between two superconductors through a movable superconducting grain will be considered in Section 4, and noise in different types of shuttle systems in Section 5.

2. SINGLE-ELECTRON TRANSFER BY A NANOSHUTTLE

Shuttle charge transfer involves two distinct charge transfer processes: the tunneling of charge between the leads and a (moving) cluster as well as the mechanical, "convective" motion of the charged cluster. The mechanical motion of the shuttle can obey either classical or quantum mechanics. A classical description is sufficient if the force that acts on the shuttle depends only weakly on its spatial position. In general, this requirement can be formulated as

$$\frac{d\lambda\!\!\!^{-}(x)}{dx} \ll 1 \tag{1}$$

where $\lambda\!\!\!^{-}(x) = \hbar/p(x)$ is the effective de Broglie wavelength of the shuttle and $p(x)$ is its classical momentum at a position x on its classical trajectory.

Now, even if the criterion (1) for the shuttle motion to be classical is fulfilled, the tunneling of electrons through the grain can be either sequential or coherent. In the first case, the relevant physical picture is fully classical—the electrons can be regarded as classical particles and their transport properties can be described by a master equation. We will refer to this situation as *classical shuttling of particles*. In the case of coherent tunneling, the electrons should be treated as wave packets while keeping track of the properties of their wave functions. In this situation, we will talk about *classical shuttling of waves*. The word "classical" serves as a reminder that the mechanical motion is still classical. All recent experiments can be interpreted as classical shuttling satisfying the condition (1). If the dissipation is low enough, see the discussion in Section 2.4, this is true also for the experiment of Park et al. [4] involving a C_{60} molecule. However, in principle, the condition (1) may not be fulfilled. If so, the mechanical motion has to be described by quantum mechanics. We refer to this case as *quantum shuttling* of either particles or waves, depending on the nature of the electron tunneling process. In the following Sections all four regimes will be considered (see Table 1). Before we proceed, however, a small digression about the condition (1) is in order.

Whether the criterion (1) for the shuttle motion to be classical is fulfilled or not depends on how quickly the shuttle momentum $p(x)$ varies with position x. This in turn is determined by the forces acting upon the cluster. The character of the shuttle transport is somewhat complicated by the fact that the electron is not necessarily localized at the moving shuttle cluster, it can also be extended between the cluster and the leads as a result of quantum delocalization. Because the forces that act on the cluster are different in the different situations, the concrete forms of the criterion (1) can also be different. If the electron is localized at the cluster, the forces are due to the direct Coulomb interaction between the leads and the excess cluster charge, and the criterion (1) can be cast into the form $x_0 \ll \lambda$. Here $x_0 = \sqrt{\hbar/m\omega_0}$ is the quantum-mechanical zero-point vibration amplitude, ω_0 is the angular eigenfrequency of cluster vibrations, while λ, to be defined in Section 2.1.2, is the characteristic (decay) length of the tunneling coupling. Even if this condition is not met, many properties of shuttle transport can be understood classically, provided the oscillation amplitude, A, is so large that $A \gg x_0$. In this situation, the region where quantum effects are important is relatively narrow compared with the whole trajectory.

Quantum delocalization of electron states between cluster and leads gives rise to what one may call cohesive forces and makes the situation more complicated. In Section 2.4, we will show that for sufficiently small bias voltages (and hence for sufficiently weak electric fields) a specific quantum regime appears, where even relatively large cluster vibration amplitudes, $A \gtrsim \lambda \gg x_0$, do not allow a classical description of the shuttle transport.

2.1. Classical Shuttling of Particles

We begin this section by considering the classical shuttling of electrons and by specifying the conditions, which have to be met for shuttling to fall into this category (Section 2.1.1). We then proceed to considering the classical shuttling of electrons by a harmonically bound cluster between two leads in Section 2.1.2. After that, having seen that low damping is necessary for shuttle transport in this case, we turn to studying a system dominated by viscous forces in Section 2.1.3. We will find that classical shuttling of particles can take place also in this case.

The prospects for finding applications of the shuttle transport mechanism strongly depend on resolving several issues. Among them are (i) what are the conditions for ideal shuttling—crucially important for applications such as standards of electric current or for sensors; (ii) is it possible to achieve gate-controlled shuttling, which is important for single-electron transistor applications; (iii) what is the role of other mechanical degrees of freedom than those associated with the center-of-mass motion. These issues will be discussed later in this section, in Subsections 2.1.4, 2.1.5, and 2.1.6.

2.1.1. Requirements for Incoherent Transport

A schematic picture of a single-electron tunneling device with a movable metallic cluster as its central element is presented in Fig. 1. In this case, center-of-mass mechanical vibrations of the grain are allowed (consider the elastic springs that connect the central electrode to the leads in Fig. 1). Since electronic transport through the device requires electrons to tunnel between the leads and the central small-size conducting grain, it is strongly affected by any vibration-induced displacements of the grain.

A number of characteristic times determine the dynamical evolution of the system. Electronic degrees of freedom are represented by frequencies corresponding to the Fermi energies in each of the conductors and to the applied voltage V. In addition, one has an inverse relaxation time, an inverse phase-breaking time for electrons in the conductors, and a charge relaxation time, $\omega_R^{-1} = RC$, due to tunneling. Here R and C are the resistance and capacitance of the tunnel junction, respectively. Mechanical degrees of freedom are characterized by a vibration frequency ω_0. The condition that $\hbar\omega_R$ should be much smaller than the Fermi energy is the standard condition for a weak tunneling coupling and holds very well in typical tunnel structures. Since a finite voltage is supposed to be applied, causing a nonequilibrium evolution of the system, the question of how fast is the electronic relaxation becomes relevant. Two possible scenarios for the transfer of electrons through the metallic cluster can be identified depending on the ratio between the tunneling relaxation time ω_R^{-1} and the relaxation time τ_0 of electrons on the grain. In the case where τ_0 is much shorter than ω_R^{-1}, the two sequential tunneling events that are necessary to transfer an electron from one lead to the other through the grain cannot be considered to be a quantum mechanically coherent process. This is because relaxation and phase-breaking processes occur in between these events, which are separated by a time delay of order ω_R^{-1}. On the contrary, all tunneling events between either lead and the grain are incoherent (i.e., independent events). Fast relaxation of electrons in all three conductors is supposed to be responsible for the formation of a local equilibrium distribution of electrons in each conductor. This is the approach, which we will use in the present section. In the opposite limit (i.e., when τ_0 is much larger than ω_R^{-1}), quantum coherence plays a dominating role in the electronic charge transfer process and all relaxation takes place in the leads faraway from the central part of the device. This case will be considered in Section 2.3.

2.1.2. Shuttling of Electrical Charge by a Movable Coulomb Dot

The tunnel junctions between the leads and the grain in Fig. 1 are modeled by tunneling resistances $R_L(x)$ and $R_R(x)$, which are assumed to be exponential functions of the grain coordinate x. To avoid unimportant technical complications, we study the symmetric case for which $R_{L,R} = R(0)e^{\pm x/\lambda}$, where we will refer to λ as the tunneling length. When the position of the grain is fixed, the electrical potential of the grain and its charge q_{st} follow from balancing the current between the grain and the leads [12]. As a consequence, at a given bias voltage V, the charge $q_{st}(x)$ is completely controlled by the ratio $R_L(x)/R_R(x)$ and $dq_{st}(x)/dx < 0$. In addition, the bias voltage generates an electrostatic field $\mathscr{E} = \alpha V$ in the space between the leads and, hence, a charged grain will be subjected to an electrostatic force $F_q = \alpha V q$.

The central point of our considerations is that the grain, because of the "softness" of the links connecting it to the leads, may move and change its position. The grain motion disturbs the current balance, and as a result, the grain charge will vary in time together with the grain displacement. This variation affects the work $W = \alpha V \int \dot{x} q(t)\, dt$ performed on the grain during, say, one period of its oscillatory motion.

It is significant that the work is nonzero and positive, that is, the electrostatic force, on the average, accelerates the grain. The nature of this acceleration is best understood by considering a grain oscillating with a frequency that is much lower than the typical charge fluctuation frequency $\omega_R = 1/RC$. Here C is the capacitance of the metallic cluster, which, for room temperature Coulomb-blockade systems, is of the order $10^{-18} - 10^{-19}$ F. In this limit, the charge deviation $\delta q \equiv (q - q_{st}(x))$ connected with retardation effects is given by the expression $\delta q = -\omega_R^{-1} \dot{x} dq_{st}(x)/dx$. Hence the extra charge δq depends on the value and direction of the grain velocity and as a consequence, the grain acts as a shuttle that carries positive extra charge on its way from the positive to the negative electrode and negative extra charge on its return trip. The electrostatic force $\delta F_q = \alpha V \delta q$ is thus at all times directed along the line of motion causing the grain to accelerate. To be more precise, it has been shown [11, 18] that for small deviations from equilibrium ($x = 0$, $q = 0$) and provided $q(t)$ is defined as the linear response to the grain displacement, $q(t) = \int \chi(t - t')x(t')dt'$, the work done on the grain is positive for any relation between the charge fluctuation frequency ω_R and the frequency of the grain vibration.

In any real system, a certain amount Q of energy is dissipated due to viscous damping, which always exist. To get to the self-excitation regime, more energy must be pumped into the system from the electrostatic field than can be dissipated; W must exceed Q. Because the electrostatic force increases with the bias voltage, this condition can be fulfilled if V exceeds some critical value V_c.

If the electrostatic and damping forces are much smaller than the elastic restoring force, self-excitation of vibrations with a frequency equal to the eigenfrequency of the elastic oscillations arise. In this case, V_c can be implicitly defined by the relation $\omega_0 \gamma = \alpha V_c \mathrm{Im}\chi(\omega)$, where $\omega_0 \gamma$ is the imaginary part of the complex dynamic modulus. In the general case, when the charge response is determined by Coulomb-blockade phenomena, χ is an increasing but rather complicated function of V, and there is no way to solve for V_c analytically. However, one can show [18] that the minimal value of V_c corresponds to the situation when the charge exchange frequency ω_R is of the same order as the eigenfrequency ω_0 of the grain vibrations.

Above the threshold voltage, the oscillation amplitude will increase exponentially until a balance between dissipated and absorbed energy is achieved and the system reaches a stable self-oscillating regime. The amplitude A of the self-oscillations will therefore be determined by the criterion $W(A) = Q(A)$.

The transition from the *static regime* to the *self-oscillating* can be associated with either *soft* or *hard* excitation of self-oscillations depending on the relation between the charge exchange frequency ω_R and the grain oscillation eigenfrequency ω_0 [18]. Soft excitation takes place if $\omega_R/\omega_0 > 2\sqrt{3}$. In this case, the amplitude of the stable self-oscillation regime increases smoothly (with voltage increase) from zero at the transition voltage. In a case of hard excitation ($\omega_R/\omega_0 < 2\sqrt{3}$), the oscillation amplitude jumps to a finite value when voltage exceeds V_c. It was also found [18] that the hard excitation is accompanied by a hysteretic behavior of the current-voltage characteristics.

In the fully developed self-oscillating regime the oscillating grain, sequentially moving electrons from one lead to the other, provides a "shuttle mechanism" for charge as shown in Fig. 1b. In each cycle, $2n$ electrons are transferred, so the average contribution to the current from this shuttle mechanism is

$$I = 2enf, \quad n = \left[\frac{CV}{e} + \frac{1}{2}\right] \tag{2}$$

where $f \equiv \omega_0/2\pi$ is the self-oscillation frequency. This current does not depend on the tunneling rate ω_R. The reason is that when the charge jumps to or from a lead, the grain is so close that the tunneling rate is large compared with the elastic vibration frequency. Hence the shuttle frequency—not the tunneling rate—provides the "bottle neck" for this process. We emphasize that the current due to this shuttle mechanism can be substantially larger than the conventional current via a fixed grain. This is the case when $\omega_0 \gg \omega_R$.

To support these qualitative arguments, we have performed analytical and numerical analyses based on the simultaneous solution of Newton's equation for the motion of the grain's center-of-mass and a master equation for the charge redistribution.

Two different approaches were developed. The first, presented in Ref. [11], gives a quantitative description of the shuttle instability for low tunnel-barrier resistances, that is, when the rate of charge redistribution is so large (in comparison with the vibration frequency) that the stochastic fluctuations in the grain charge during a single-vibration period are unimportant. The second approach, describing the opposite limit of low-charge redistribution frequencies characteristic of high-resistance tunnel barriers, was presented in Ref. [18].

In both cases, it was shown that the electromechanical instability has dramatic consequences for the current-voltage characteristics of a single-electron transistor configuration as shown in Fig. 2. Even for a symmetric double junction, where no Coulomb staircase appears in conventional designs, we predict that the shuttle mechanism for charge transport manifests itself as a current jump at $V = V_c$ and as a Coulomb staircase as the voltage is further increased. A more precise calculation along the line l sketched in Fig. 2 is shown in Fig. 3. The nonmonotonic behavior of the current along this line is due to competition between the two charge transfer mechanisms present in the system, the ordinary tunnel current, and the mechanically mediated current $I_{\text{mech}}(x_0, t) = \delta(x(t) - x_0)\dot{x}(t)q(t)$ through some cross section at x_0. We define the shuttle current as the time averaged mechanical current through the plane located at $x_0 = 0$. This current together with the tunnel current for the same cross section is shown in Fig. 3. As the damping in the system is reduced, the oscillation amplitude

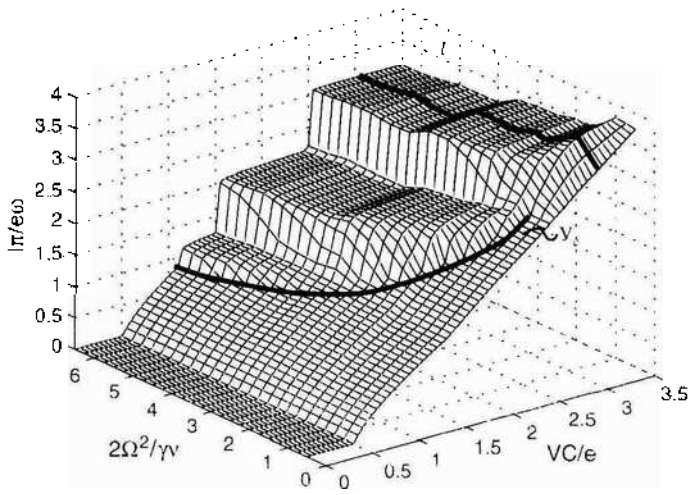

Figure 2. Current due to the shuttle mechanism through the composite Coulomb blockade system of Fig. 1. The current is normalized to the eigenfrequency ω (in the text denoted by ω_0) of elastic grain vibrations and plotted as a function of normalized bias voltage V and inverse damping rate γ^{-1}. With infinite damping no grain oscillations occur and no Coulomb staircase can be seen. The critical voltage V_c required for the grain to start vibrating is indicated by a line. Reprinted with permission from [11], L. Y. Gorelik et al., *Phys. Rev. Lett.* 80, 4526 (1998). © 1998, American Physical Society.

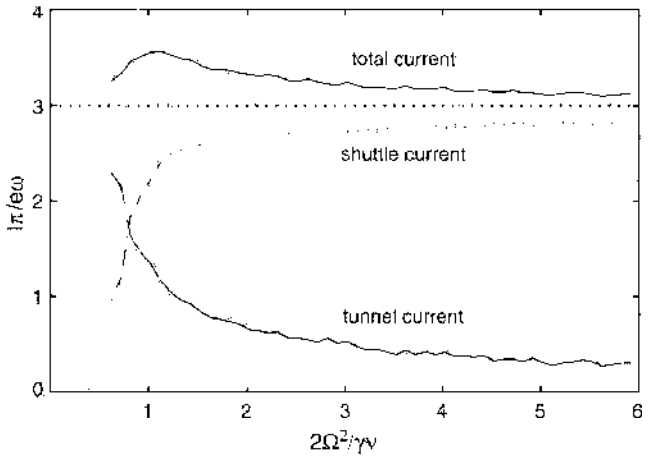

Figure 3. Cross section along the line *l* in Fig. 2. The total time-averaged current consists of two parts, the shuttle current and the tunneling current. The time-averaged shuttle current is the mechanically transferred current through the center of the system $\langle \delta(x(t))\dot{x}(t)q(t)\rangle$, the remaining part comes from ordinary tunneling. As the inverse damping γ^{-1} increases, the shuttle current approaches the quantized value $I\pi/e\omega = 3$. The tunnel current is proportional to the fraction of the oscillation period spent in the middle region, $|x| < \lambda$. This fraction is inversely proportional to the oscillation amplitude and hence the tunnel current decreases as γ^{-1} increases. The fine structure in the results is due to numerical noise. Reprinted with permission from [11], L. Y. Gorelik et al., *Phys. Rev. Lett.* 80, 4526 (1998). © 1998, American Physical Society.

grows and the shuttle current is enhanced while the ordinary tunneling current is suppressed. In the limit of low damping, this leads to a quantization of the total current in terms of $2ef$. The calculation procedure leading to these conclusions are briefly described in Appendix B.

2.1.3. Shuttling in Dissipative Nanostructures

It is clear from this analysis that a large damping is detrimental for the development of the shuttle instability, and in the limit where $\gamma \gtrsim \omega_0$, elastic shuttling of the charge becomes impossible. The mechanical lability of the system, however, is still a dominating feature of the charge transport even in the limit of strong dissipation. The consequences of such a lability are addressed in Ref. [20]. There the elastic restoring force is assumed absent or much weaker than viscous damping forces. According to that model, charge transport through the NEM-SET is affected both by the Coulomb blockade phenomenon and the mechanical motion of the cluster. These two phenomena are coupled since the threshold voltage for electron tunneling depends on the junction capacitances that, in turn, depend on the cluster position with respect to the leads. In general, the threshold voltage increases when the distance between the cluster and an electrode decreases.

To be specific, if a neutral cluster is located in its equilibrium position between the electrodes, no tunneling takes place for a bias voltage V lower than some threshold value V_0. At $V > V_0$, the cluster can be charged due to tunneling onto the cluster. At the same time, the electrical forces produce a mechanical displacement directed *from* the lead that has supplied the extra charge. After some time, the extra charge will leak to the nearest electrode, and the cluster becomes neutral again. An important question at this stage is whether an *extra* tunneling event to the nearest electrode can take place. The answer is not evident because the electrostatic tunneling threshold in the last position is different from that at the initial point in system's center. Consequently, tunneling to the nearest electrode, in principle, could be suppressed due to the Coulomb blockade. The analysis made in Ref. [20] has shown that at zero temperature there is an upper threshold voltage V_t below which the extra tunneling event is not possible. In this case, the cluster is almost trapped near the electrode and the conductance is not assisted by significant cluster displacements between the electrodes.

For voltages above the threshold, $V > V_t$, there is a possibility for another tunneling event between the grain and the nearest lead to happen after the extra charge has tunneled off the cluster. This event changes the sign of the net charge on the grain. In this case, the cluster can be pushed by the Coulomb force toward the more distant electrode where the process

repeats itself. The conductance is now assisted by significant displacements of the grain and this scenario is qualitatively similar to the shuttle vibrations in fully elastic electromechanical structures [11]. This process is also accompanied by a marked rise in the current through the system as shown in Fig. 4.

2.1.4. Accuracy of a Mechanical Single-Electron Shuttle

Several mechanisms contribute to a deviation of the average current from the ideal shuttle value nef_0:

1. Sequential electron tunneling and co-tunneling through the grain, which leads to a "shunting" DC current unrelated to any grain motion.
2. Insufficient contact time t_0 at the trajectory turning point compared with the charge relaxation time ω_R^{-1}. The relation between these characteristic times determines whether the grain can be fully loaded during a single contact event.
3. Thermal fluctuations, which lift the Coulomb blockade limitation for the transferred charge to be an integer number of electron charges.

The contribution of the shunting tunneling seems to be much smaller than the current conveyed by a shuttling grain. Indeed, the former is limited by the *maximum* tunnel resistance, which is *exponentially large*. The second and third limitations to the accuracy of the shuttling current were considered by Weiss and Zwerger [21] where a master equation for the charge of the moving grain was analyzed. In this approach, the shuttling was mapped on a sequence of contact events when charge transfer takes place. The results of an analytical treatment of a simple model and of a numerical treatment are shown in Figs. 5 and 6 taken from Ref. [21]. In Fig. 5, the average number of electrons transferred per period, as well as the root mean square fluctuations, are shown for $T = 0$. In this figure, t_0 represents the effective time the grain spends in contact with the leads, while τ denotes the RC-time at the point of closest approach to the leads. Assuming that the grain is closest to the leads at a time t_{max}, one has $\tau = R(t_{max})C(t_{max})$. Thermal smearing of the single-electron shuttling is demonstrated in Fig. 6. It is clear that for $t_0 \gg \tau$ and $T = 0$ the Coulomb staircase is perfect. For increasing temperatures, the Coulomb staircase is washed out leading to an Ohmic behavior at high temperatures.

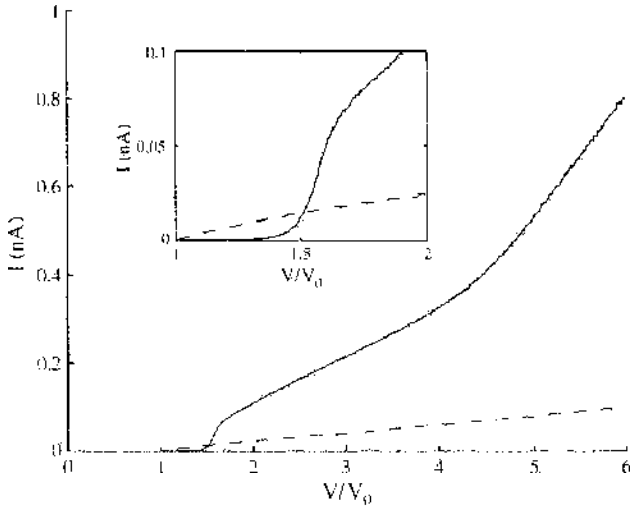

Figure 4. The solid line shows the current-voltage characteristics obtained by a Monte Carlo simulation of the charge transport through a dissipation dominated system. The calculated DC current is plotted as a function of the bias voltage V scaled by the Coulomb blockade threshold voltage V_0 that applies if the movable grain is equally far from both electrodes. The dashed line displays the current through a static symmetric double junction for the same parameters. For voltages above the threshold voltage V_0, the current through the system increases drastically due to grain motion. The inset shows a magnification of the voltage interval around V_0. Reprinted with permission from [20], T. Nord et al., *Phys. Rev. B* 65, 165312 (2002). © 2002, American Physical Society.

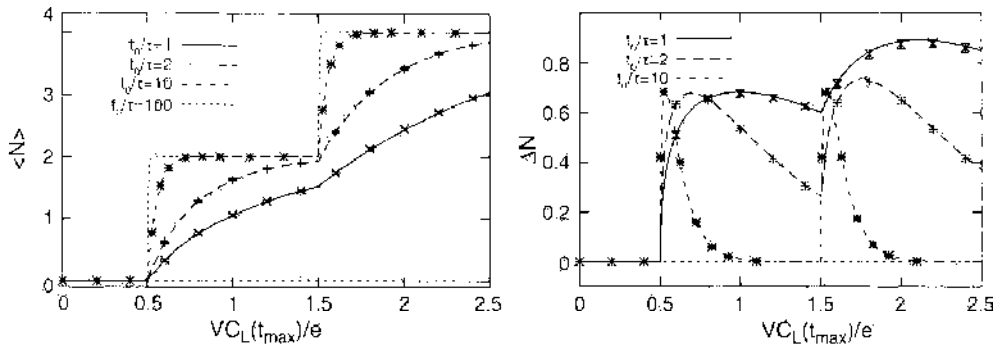

Figure 5. Average number of electrons transferred per period (upper panel) and the root mean fluctuations (lower panel) for $T = 0$. A Coulomb blockade is clearly visible: up to a critical voltage, $VC_L(t_{max})/e = 1/2$, no electrons are transferred. Reprinted with permission from [21], C. Weiss and W. Zwerger, *Europhys. Lett.* 47, 97 (1999). © 1999, EDP Sciences.

2.1.5. Gate Voltage Control of Shuttle Mechanics

The electromechanical coupling also dramatically changes the transistor effect in a NEM-SET as compared with an ordinary SET. We will discuss this problem following Nishiguchi [22]. Let us assume that the tunneling can take place only between the grain and the leads, while there is no tunneling exchange with the gate. The gate voltage controls the equilibrium position of the grain with respect to the leads since it determines the extra charge of the grain. Schematic configuration of a relevant NEM-SET is sketched in Fig. 7. The picture describes a situation when the grain has a net negative charge. The net negative charging of the grain occurs for a certain relation between the bias, V_b, and the gate, V_g, voltages. The positively charged gate electrostatically induces a negative charge on the grain, which tends to be compensated by the tunneling of positive charge from the right lead. Here we assume that the tunneling from the negatively charged remote electrode is exponentially suppressed. Since the grain is shifted from the central position, the current through the device is exponentially small. An increase in the bias voltage decreases the total negative charge. When the compensation is complete, the grain returns to the central position restoring the tunneling transport through the device. The "phase diagram" in the $V_g - V_b$ plane obtained in Ref. [22] is shown in Fig. 8. It is worth mentioning that there is a *qualitative* difference between this "butterfly" phase diagram and the "diamond" phase diagram in conventional SET devices [15], where the mechanically blocked SET operation is absent.

2.1.6. Nanoparticle Chains

We conclude this section on classical shuttling of electrons by considering theoretical work by Nishiguchi [23] regarding nanoparticle chains. Nanoparticle chains consist of small metal grains stabilized by ligands, with electronic transport occurring via tunneling between the

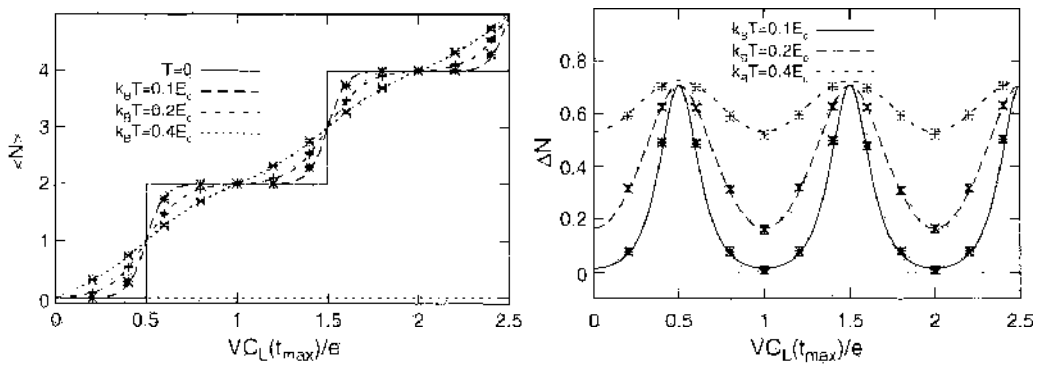

Figure 6. Thermal smearing of single-electron shuttling. The energy scale is given by $E_c = e^2/2C$. t_{max} is the instant when a particle is located at a turning point. Reprinted with permission from [21], C. Weiss and W. Zwerger, *Europhys. Lett.* 47, 97 (1999). © 1999, EDP Sciences.

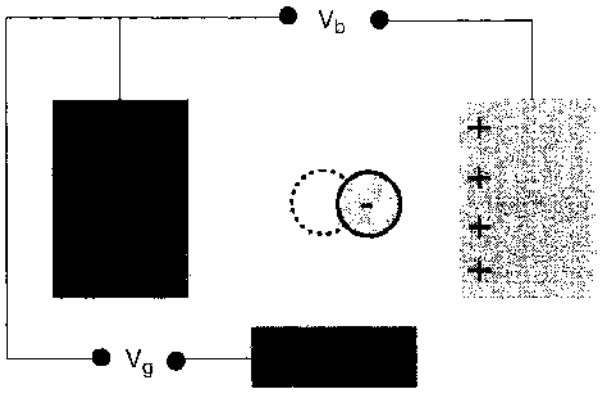

Figure 7. Schematic configuration of a NEM-SET. Reprinted with permission from [16], R. I. Shekhter et al., *J. Phys: Condens. Matter* 15, R441 (2003). © 2003, Institute of Physics and IOP Publishing Limited.

metal particles. Because of the relative softness of the ligand matrix, vibrations of the metal grains can significantly modify the electronic tunneling rates. In systems with several degrees of freedom, the electromechanical instability at special values of system parameters can lead to excitation of more than one mode. As result, the mechanical motion becomes in general nonperiodic with a possibility of a telegraph-like switching between the modes. A crossover from a periodic to a quasi-periodic motion, as well as telegraph-like switching between these regimes was demonstrated in Refs. [23, 24], where electron shuttling through a system of two elastically and electrically coupled particles was numerically simulated. A telegraph-like switching was observed at some value of bias voltage.

2.2. The Charge Shuttle as a Nanomechanical Ratchet

One advantage of the self-oscillating shuttle structures is that it is possible to use a static bias voltage to generate mechanical oscillations of a very high frequency. The fact that the system has an intrinsic and stable oscillating mode suggests that the application of an oscillating voltage may lead to new interesting effects related to the interplay between the external AC

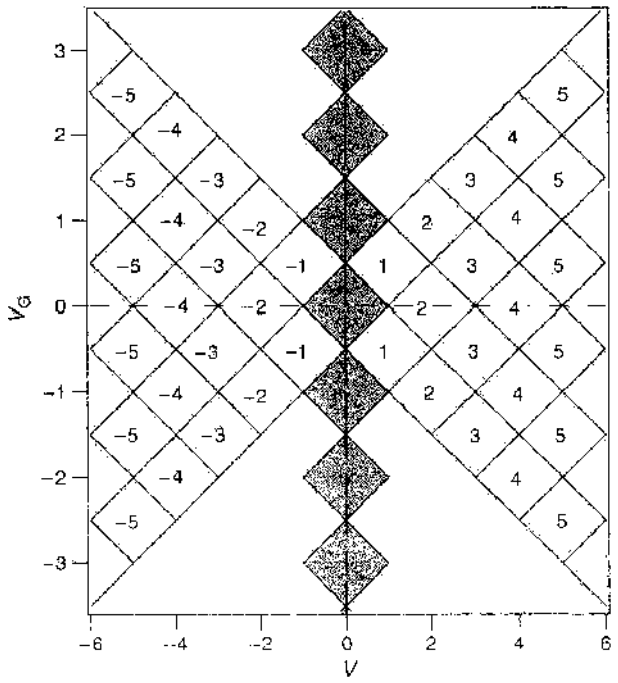

Figure 8. Diagram of the current I in the bias voltage–gate voltage plane (V and V_G, respectively) for symmetrically applied source-drain voltage. The shaded diamonds denote the voltage regions where electron tunneling is prohibited at $T = 0$. The white areas correspond to *mechanically suppressed* SET operation. Reprinted with permission from [22], N. Nishiguchi, *Phys. Rev. B* 65, 035403 (2001). © 2001, American Physical Society.

drive and the internal frequency of the device. Moreover, as the dynamics of shuttle systems is essentially nonlinear, this interplay should emerge in a wide interval of the ratio of the two frequencies.

A shuttle driven by a time-dependent applied bias was considered by Pistolesi and Fazio [25]. They showed that an asymmetric structure can act as a ratchet (see, e.g., Ref. [26]) in which the forcing potential is generated in a self-consistent way. A sizable ratchet effect is present down to bias frequencies much smaller than the mechanical resonance frequency ω_0, due to the adiabatic change of the equilibrium position of the grain. In a recent experiment [27], some results similar to the predictions of Ref. [25] were observed. However, in this experiment, the single-electron tunneling limit was not reached.

Assuming a harmonic bias voltage, $V = V_0 \sin \omega t$, the authors of Ref. [25] simulate the grain dynamics and stochastic electron transfer for an asymmetric system characterized by the resistances $R_L(0) \neq R_R(0)$. The asymmetry is essential, because no DC current can be generated in a symmetric device. Because the electron transition rates are proportional to $|V(t)|$, they turn out to be time dependent. According to the simulation, the system reaches a stationary behavior after a transient time. Figure 9 shows the stationary DC current as a function of the external bias frequency ω.

The rich structure shown in the figure is generic; qualitatively identical behavior was observed for a wide range of parameters. The existence of a direct current as a result of an applied periodic modulation shows that the charge shuttle behaves as a ratchet [26]. Because the system is nonlinear, the external driving force affects the dynamics also for values of ω very different from the intrinsic frequency ω_0. Note that in this model the nonlinearities are intrinsic to the shuttle mechanism. They are due to the specific time dependence of the grain charge, $en(t)$, rather than to a nonlinear mechanical force. As is evident from Fig. 9, the ratchet behavior is present also in the adiabatic limit, $\omega/\omega_0 \ll 1$. In addition, a series of resonances appear. These are due to frequency locking when $\omega/\omega_0 = q/p$ and q and p are integers (see, e.g., Ref. [28]). In this case, the motion of the shuttle and the oscillating source become synchronized in such a way that during q periods of the oscillating field the shuttle performs p oscillations.

2.3. Classical Shuttling of Electron Waves

In this section, we follow the considerations of Fedorets et al. [19]. Here it is assumed that a vibrating grain has a single resonant level, both the position $x(t)$ of this level and the

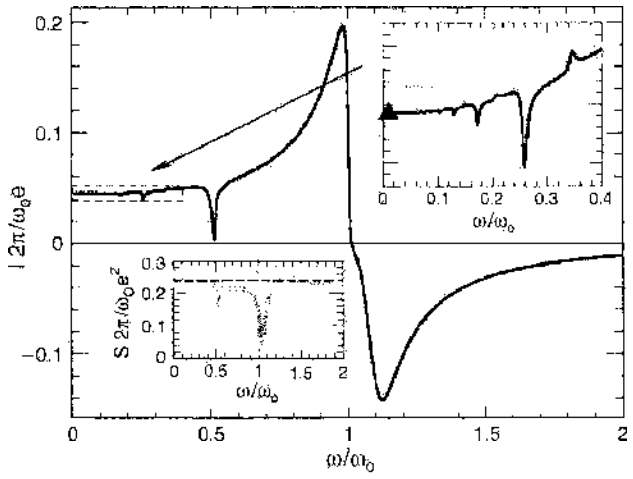

Figure 9. Current through a shuttle system as a function of bias voltage frequency for given bias voltage amplitude and device parameters ($\epsilon = 0.5$, $\gamma/\omega_0 = 0.05$, and $\Gamma/\omega_0 = 1$; see text and Ref. [25]. The result of the simulation of the stochastic dynamics (points) is compared with an approximate analytical solution for the current (full line). In the small frequency region, enlarged in the upper inset, several resonances at fractional values of ω/ω_0 appear. The dotted line is an analytical result in the adiabatic limit. Lower inset: current noise from the simulation (points) and analytical result (dashed) for the static SET. Reprinted with permission from [25], F. Pistolesi and R. Fazio, cond-mat/0408056 (unpublished).

coupling of the grain to the leads, $T_{L,R}(t)$, are oscillatory functions of time (see Fig. 10). The effective Hamiltonian of the problem is defined as

$$H = \sum_{\alpha,k}(\epsilon_{\alpha k} - \mu_\alpha)a^\dagger_{\alpha k}a_{\alpha k} + \epsilon_d(t)c^\dagger c + \sum_{\alpha,k} T_\alpha(t)(a^\dagger_{\alpha k}c + c^\dagger a_{\alpha k}) \tag{3}$$

Here $T_{L,R} = \tau_{L,R}\exp\{\mp x(t)/2\lambda\}$ is the position-dependent tunneling matrix element, $\epsilon_d(t) = \epsilon_0 - e\mathscr{E}x(t)$ is the energy level in the dot shifted due to the voltage-induced electric field $\mathscr{E}$, $a^\dagger_{\alpha k}$ creates an electron with momentum k in the corresponding lead, $\alpha = L, R$ is the lead index, and $c^\dagger$ creates an electron in the dot. The first term in the Hamiltonian describes the electrons in the leads, the second corresponds to the movable quantum dot, and the last term describes tunneling between the leads and the dot.

The evolution of the electronic subsystem is determined by the Liouville–von Neumann equation for the statistical operator $\hat{\rho}(t)$,

$$i\partial_t\hat{\rho}(t) = \hbar^{-1}[\hat{H}, \hat{\rho}(t)]_- \tag{4}$$

while the center-of-mass motion of the dot is governed by Newton's equation,

$$\ddot{x} + w_0^2 x = \frac{F}{m} \tag{5}$$

Here $\omega_0 = \sqrt{k_0/m}$, m is the mass of the grain, k_0 is a constant characterizing the strength of the harmonic potential, and $F(t) = -\mathrm{Tr}[\hat{\rho}(t)\partial\hat{H}/\partial x]$. The force F is computed from an exact solution of the tunneling problem, which exists for arbitrary $T_\alpha(t)$ and $\epsilon_d(t)$. Using the Keldysh Green's function approach [29] in the so-called wide-band approximation and following Ref. [30], one obtains the force F as

$$F(t) = \sum_\alpha g_\alpha \int \mathrm{d}\epsilon f_\alpha(\epsilon)\{e\mathscr{E}|B_\alpha(\epsilon,t)|^2 + (-1)^\alpha\lambda^{-1}T_\alpha(t)\mathrm{Re}[B_\alpha(\epsilon,t)]\} \tag{6}$$

where

$$B_\alpha(\epsilon,t) = -\mathrm{i}\hbar^{-1}\int_{-\infty}^{t}\mathrm{d}t_1 T_\alpha(t_1)\times\exp\left\{\mathrm{i}\hbar^{-1}\int_{t_1}^{t}\mathrm{d}t_2\left[\epsilon - \epsilon_d(t_2) + \mathrm{i}\frac{\Gamma(t_2)}{2}\right]\right\}$$

and $\Gamma(t) = 2\pi\sum_\alpha g_\alpha|T_\alpha(t)|^2$, g_α is the density of states in the corresponding lead while $f_\alpha(\epsilon) = \{\exp[\beta(\epsilon - \mu_\alpha)] + 1\}^{-1}$. The first item in expression (6) for $F(t)$ is the electric force due to accumulated charge; the second item is the "cohesive" force due to position-dependent hybridization of the electronic states of the grain and the leads. Equations (5) and (6) can be used to study the stability of the equilibrium position of the cluster. By linearizing

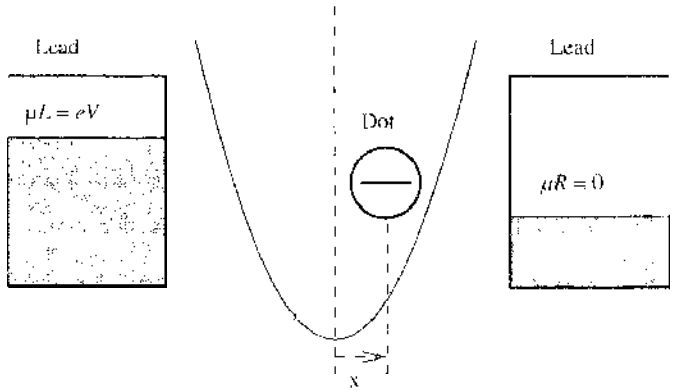

Figure 10. Model system consisting of a movable quantum dot placed between two leads. An effective elastic force acting on the dot from the leads is described by the parabolic potential. Only one single electron state is available in the dot and the noninteracting electrons in each have a constant density of states. Reprinted with permission from [19], D. Fedorets et al., *Europhys. Lett.* 58, 99 (2002), © 2002, EDP Sciences.

Eq. (5) with respect to the small displacement $\propto e^{-i\omega t}$ and solving the proper equations of motion, one can obtain a *complex* vibration frequency. The mechanical instability can then be determined from the inequality $\mathrm{Im}\,\omega \geq 0$. As shown in Ref. [19], the instability occurs if the driving bias voltage exceeds some critical value, which for a symmetrically applied voltage is $eV_c = 2(\epsilon_0 + \hbar\omega_0)$. It was also shown that in the limit of weak electromechanical coupling, when $\Gamma/(4m\omega_0^2\lambda^2)$ and $2e^2\lambda/(\sqrt{\hbar^2\omega_0^2 + \Gamma^2}) \ll 1$, the instability develops into a limit cycle. This is in contrast with a classical shuttle, where stability of the system could be achieved only at finite mechanical dissipation. The reason for the difference is that here dissipation is provided by an explicit coupling to the electronic degrees of freedom in the Hamiltonian (3). In the classical treatment, dissipation was only described phenomenologically by a damping constant in Newton's equation. One can see a qualitative agreement between the experimentally observed $I(V)$ curve for a fullerene-based NEM-SET shown in Fig. 17 and the results of the above calculation displayed in Fig. 11. However, there are alternative interpretations of the experiment by Park et al. [4] (see pp. 31–35) which are based on quantum mechanical treatments of the mechanical motion. Some of these will be discussed next.

2.4. Charge Transfer Through a Quantum Oscillator

In the previous discussion, we assumed, that the mechanical degree of freedom was classical. As discussed in the beginning of Section 2, this assumption is not always correct. For an oscillator with a small enough mass (e.g., the quantum mechanical zero-point vibration amplitude, x_0), can be comparable with the the center-of-mass displacement. In this case, electronic and mechanical degrees of freedom behave as coupled parts of a quantum system, which, in its entirety, should be described by quantum mechanics. The coupling between the subsystems is provided by (i) the dependence of electronic levels, charges, their images, and, consequently, electric forces on the mechanical degrees of freedom, and by (ii) the dependence of tunneling barriers on the spatial configuration of the system.

In general, charge transfer in the systems under consideration is assisted by excitation of vibrational degrees of freedom, which is similar to phonon-assisted tunneling through nanostructures. However, in some cases, the center-of-mass mechanical mode turns out to be more strongly coupled to the charge transfer than other modes. In this case, one can interpret the center-of-mass mode-assisted charge transfer as *quantum shuttle* transport, provided that the center-of-mass motion is correlated in time with the charge on the dot (see the definition of shuttle transport in Section 1). Several authors have addressed the charge transport through a quantum oscillator, and several models have been discussed, some of which will be reviewed next.

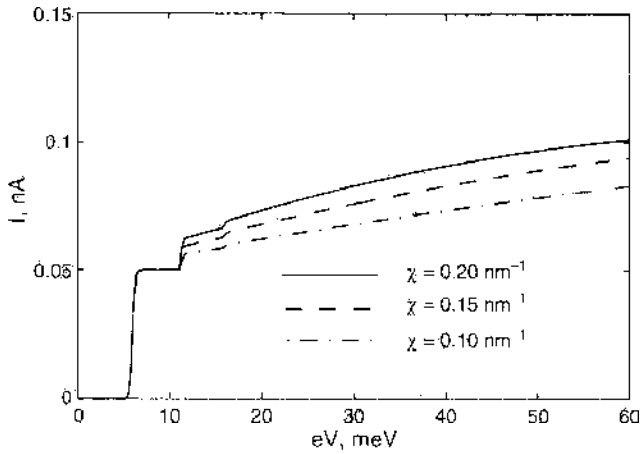

Figure 11. I-V curves for different values of the parameter $\chi = \mathcal{E}/V$, which characterizes the strength of the electric field $\mathcal{E}$ between the leads for a given bias voltage V: $\hbar\omega_0 = 5$ meV, $T = 0.13$ meV, $\epsilon_0 = 6$ meV, and $\Gamma = \Gamma_R + \Gamma_L = 2.3$ μeV. Best fit to Ref. [4] is obtained for an asymmetric coupling to the leads; here we use $\Gamma_R/\Gamma_L = 9$. Reprinted with permission from [19], D. Fedorets et al., *Europhys. Lett.* 58, 99 (2002). © 2002, EDP Sciences.

Single-electron tunneling through molecular structures under the influence of nanomechanical excitations has been considered by Boese and Schoeller [31]. The authors developed a quantum mechanical model of electron tunneling through a vibrating molecule and used it to model the experiment described in Ref. [4]. In contrast to what was done in Sections. 2.1 and 2.3 and Refs. [11, 19], they assumed the vibrational frequency to be several orders of magnitude larger than the electron-tunneling rates. Their system is described by an effective Hamiltonian involving local bosonic degrees of freedom of the molecule. One of the local modes can be interpreted as describing center-of-mass motion. The quantum mechanical calculation leads to a set of horizontal plateaus in the I–V curve due to excitation of different vibrational modes. It is shown that in some regions of parameter space a negative differential resistance occurs. A similar calculation, but with a more detailed account of the dependence of the charge-transfer matrix elements on the shuttle coordinate, has been published by McCarthy et al. [32].

References [31] and [32] provide a qualitative explanation of the experiment by Park et al. [4]. Other fully quantum-mechanical efforts to model this experiment involving vibron-assisted tunneling rather than the shuttle mechanism can be found in Refs. [33–35]. These are actually alternative explanations to that given in Ref. [19], where the center-of-mass motion was treated classically. Vibron-assisted tunneling is the appropriate picture for high damping rates (low Q-factor) and classical shuttling for low damping (high Q-factor). To determine the Q-factor relevant for the experiment of Park et al. [4] requires additional information (e.g., from noise measurements; see Section 5). It is worth mentioning that the shuttle model predicts a finite slope of the I–V curve at large voltages, which is more similar to the experimental result.

A quantum oscillator consisting of a dot coupled by springs to two flanking stationary dots attached to semi-infinite leads was considered by Armour and MacKinnon [36]. These authors concentrate on the quantum aspects of the dot and electron motion. It is shown that the I–V characteristics of the model shuttle can largely be understood by analyzing the eigenspectrum of the isolated system of three dots and the quantum oscillator. Tunneling coupling of the dot states, to each other and to the position of the oscillator, leads to repulsion of the eigenvalues and mixing of the eigenstates associated with states localized on individual dots. The mixed states consist of superpositions of the states associated with the individual dots and hence lead to delocalization of the electronic states between the dots. Analysis of the current flows when the shuttle is weakly coupled to leads, reveals strong resonances corresponding to the occurrence of the delocalized states. The current through the shuttle is found to depend sensitively on the amount by which the oscillator is damped, the strength of the couplings between the dots, and the background temperature. When the electron tunneling length λ is of order x_0, current far from the electronic resonance is dominated by electrons hopping on and off the central dot sequentially. As the authors state, then the oscillator can be regarded as shuttling electrons across the system as has been discussed in Section 2.1.

In the already mentioned work described in Refs. [31–36], as well as in some other papers [33–35, 37–39] that deal with various aspects of the NEM-SET device in the regime of quantized mechanical grain motion, no shuttle instability was found. The reason is that either the coupling between electron tunneling and mechanical vibrations is ignored [31], or that strong dephasing of the mechanical dynamics was assumed [33–35, 37–39]. However, the analysis of the shuttle instability of a NEM-SET structure in the quantum regime is important. Indeed, at the initial stage of the instability the oscillation amplitude, A, can be of the same order as the zero-point oscillation amplitude, x_0. Therefore quantum fluctuations can be important. The necessary analysis of this issue has been performed by Fedorets et al. [40] and, in more detail, by Novotny et al. [41] and Fedorets et al. [42]. In these papers, it was assumed that the shuttling grain has only one electron level, which can be either empty or occupied. The interaction Hamiltonian included linear coupling to the electrical field $\tilde{\mathcal{E}}$ ($e\tilde{\mathcal{E}}\hat{x}\hat{n}$, where $\hat{n}$ is the electron number operator for electrons on the grain), as well as a tunneling coupling to the leads that is exponentially dependent on the displacement operator $\hat{x}$. In addition, an interaction of the oscillator with an external thermal bath was included and treated to lowest order of perturbation theory. By projecting out the leads

and the thermal bath, a so-called *generalized master equation* for the density matrix of the system involving electron states and oscillator variables is obtained under the condition that $eV \gg \hbar\omega_0, |\epsilon_0 - \mu|, k_B T$. In Ref. [41], this equation is numerically analyzed for the case $x_0 \sim \lambda$. The authors suggest to visualize the quantum features expressing the results through the Wigner distribution functions,

$$W_{ii}(x, p) = \int_{-\infty}^{\infty} \frac{dy}{2\pi\hbar} \left\langle x - \frac{y}{2} \middle| \rho_{ii}^{\infty} \middle| x + \frac{y}{2} \right\rangle e^{ipy/\hbar} \tag{7}$$

Here ρ_{ii}^{∞} is the stationary density matrix, $\rho_{ii}(t \to \infty)$, which is diagonal in the electron states $i = 0, 1$. The classical motion of the oscillator can be characterized by its *phase trajectory*, which is a sharp line in the $\{x, p\}$-plane, given by the relation $p^2/2m + kx^2/2 = \text{const}$. Smearing of this line by quantum fluctuations shows the importance of quantum effects. The results of the numerical analysis of $W_{ii}(x, p)$ for $\lambda = x_0$ and different frictions (γ) are shown in Fig. 12. For large friction ($\gamma = 0.25$), the Wigner functions are smeared around the origin (or around a shifted origin when charged) to an extent that depends on the zero-point vibration amplitudes with no particular correlations between its charge state and momentum. This means that the state of the grain is very close to the oscillator ground state (i.e., charge transfer excites the mechanical degree of freedom to a very small extent). This is consistent with the vibrationally assisted charge-transfer mode. For small friction ($\gamma = 0.05$), however, the Wigner functions are smeared around the classical phase trajectory $p^2/2m + kx^2 = \hbar\omega_0$ (ringlike shape of W_{tot} with a hole around the origin), and the correlation between the charge state and the mechanical motion is very strong (half-moon shapes of W_{00}, W_{11}). Thus one can see a quantum *precursor* of the electronic shuttle (see also Ref. [40]). The classical shuttle picture is expected to emerge in the quasiclassical limit $d, \lambda \gg x_0$, where $d \equiv e\mathcal{E}/m\omega_0^2$ is a measure of the electric-field strength.

Interestingly, there exist a region where both vibronic-assisted charge transfer and shuttle features are present. In the crossover region (intermediate friction, $\gamma = 0.1$), we can see that both regimes of transport are contributing additively (ringlike shape plus an incoherent peak around the origin of W_{tot}).

In Ref. [42], an *analytical* treatment of the case $x_0 \sim d \ll \lambda$ is reported, and an intermediate regime between vibronic-assisted charge transfer and shuttling was found. The condition $x_0 \ll \lambda$ allows one to linearize the problem in the displacement x for low levels of excitation of the mechanical degree of freedom. By doing so, one finds a closed set of equations

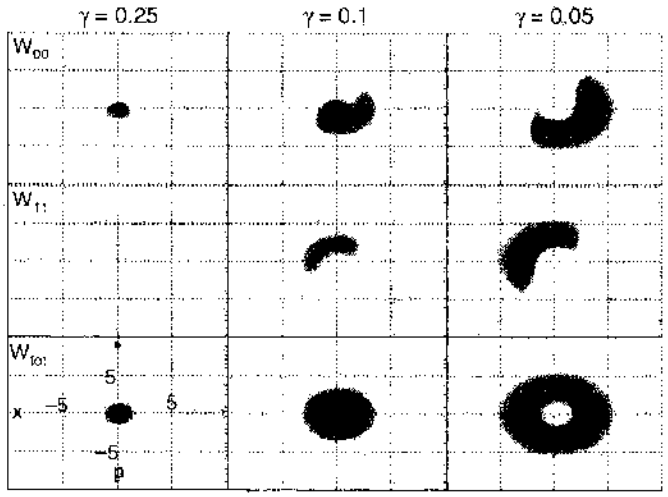

Figure 12. Phase-space picture of the tunneling-to-shuttling crossover. The respective rows show the Wigner distribution functions for the uncharged (W_{00}) and charged (W_{11}) states of the oscillator as well as the sum of these states (W_{tot}) in phase space (horizontal axis: spatial coordinate in units of x_0; vertical axis: momentum in units of $\hbar/x_0$). Parameter values used are $\lambda = x_0$, $d \equiv e\mathcal{E}/m\omega_0^2 = 0.5x_0$, $\Gamma = 0.05\ \hbar\omega_0$. The values of γ are in units of $\hbar\omega_0$. The Wigner functions are normalized within each column. Reprinted with permission from [41], T. Novotny et al., *Phys. Rev. Lett.* 90, 256801 (2003). © 2003, American Physical Society.

describing the time evolution of $\langle x \rangle$ and $\langle p \rangle$. It is found that $\langle x \rangle$ and $\langle p \rangle$ increase exponentially with time, that is, the vibrational ground state is unstable above a threshold value of the electric field,

$$\mathcal{E} > \mathcal{E}_{\text{th}} = \frac{\gamma}{\Gamma}\frac{\omega_0^2 \lambda}{e}$$

In this way the development of the shuttle instability from quantum fluctuations is understood.

The exponential increase of the vibration amplitude leads the system into a nonlinear regime, where the system reaches a stable shuttling state. This state was studied using the Wigner density as suggested in Ref. [41].

The global behavior of the Wigner density in the shuttling state depends on the electric field, $\mathcal{E}$. What is particularly interesting is that there are two shuttling regimes—a classical regime and a quantum regime. The boundary between these regimes is given by the crossover field $\mathcal{E}_q = ce^{-1} m\omega_0^2 \lambda (x_0/\lambda)^4$, where c is a numerical constant. For typical parameters, $c \sim 10^{-2}$. For weak mechanical dissipation, $\gamma/m \lesssim \Gamma c (x_0/\lambda)^4$, the crossover field $\mathcal{E}_q$ is larger than the threshold field $\mathcal{E}_{\text{th}}$, so there is the region of electrical field ($\mathcal{E}_q > \mathcal{E} > \mathcal{E}_{\text{th}}$), where the shuttle regime has a specific quantum character. This regime is described by a Wigner function similar to the one obtained numerically in Ref. [41] for $x_0 = \lambda$ (see Fig. 12) but scaled by the large parameter λ/x_0. It is characterized by pronounced quantum fluctuations and can be interpreted as a quantum regime.

For strong electrical fields, $\mathcal{E} \gg \mathcal{E}_q$, the steady-state Wigner functions are only slightly smeared over the classical trajectory $p^2/2m + k_0 x^2/2 = k_0 A_{\text{cl}}^2(\mathcal{E})$ and demonstrate pronounced shuttle features (here $A_{\text{cl}} \sim \lambda$ is the amplitude of the classical shuttle oscillations, and k_0 is the effective spring constant). This regime can therefore be interpreted as a classical regime.

The results of Ref. [42], demonstrate that the condition $\lambda \gg x_0$, although a necessary condition for the shuttling regime to be classical is not a sufficient condition. This is because the appearance of shuttle vibrations is a nonequilibrium phenomenon that comes from a nanomechanical instability induced by an applied bias voltage. As a nonequilibrium phenomenon, the nature of the vibrations do not only depend on the parameters of the device (such as x_0 and λ), but also on the applied voltage V and the resulting electric field $\mathcal{E}$ that acts on the shuttle. There are two "channels" through which the shuttle vibrations can be excited (corresponding to two types of forces on the shuttle). The first channel is electrical in nature and is caused by the electric charge carried by tunneling electrons. This channel has a classical analog—it corresponds to the work done by the electric force on the charge accumulated on the shuttle. The second channel is not connected with the electric charge but originates from energy corrections caused by quantum delocalization of shuttle electrons onto the leads. The nature of this channel, which is active when the shuttle is in tunneling contact with either lead, can be said to be cohesive. It has no classical analog at large voltages V applied to the system. The reason is that the classical cohesive force acting on the shuttling grain becomes zero in the limit when all electronic states on the leads are either completely empty or completely filled. Hence it is only quantum fluctuations that contribute a vibron-assisted pumping of cohesive energy into the shuttle. For small enough electric fields, $\mathcal{E} \ll \mathcal{E}_q$, quantum cohesive pumping dominates and leads to the formation of nonclassical, quantum shuttle vibrations with large amplitude of order λ.

The temperature dependence of electron transport through a quantum shuttle was recently studied in Ref. [43], assuming that the electric field is below the instability threshold. At low temperatures, the calculated I–V curve shows pronounced steps. It is shown that in the classical limit, $x_0/\lambda \lesssim 0.3$, the temperature dependence of the I–V curve is weak. However, for a quantum shuttle, $x_0/\lambda \gtrsim 0.6$, a variety of behaviors is predicted. The behaviors depend on how deep the shuttle is in the quantum regime and can vary from a $1/T$ decrease to an exponential growth. It is stated that the results can explain a variety of temperature dependencies that have been observed for electron transport through long molecules.

2.5. Spin-Dependent Transport of Electrons in a Shuttle Structure

2.5.1. Nanomechanical Manipulation of Nanomagnets

The possibility to place transition-metal atoms or ions inside organic molecules introduces a new "magnetic" degree of freedom that allows the electronic spins to be coupled to mechanical and charge degrees of freedom [44]. By manipulating the interaction between the spin and external magnetic fields and/or the internal interaction in magnetic materials, spin-controlled nanoelectromechanics may be achieved. An inverse phenomenon—nanomechanical manipulation of nanomagnets—was suggested earlier by Gorelik et al. [45]. A magnetic field, by inducing the spin of electrons to rotate (precess) at a certain frequency, provides a clock for studying the shuttle dynamics and a basis for a DC spectroscopy of the corresponding nanomechanical vibrations. Since spin effects are sensitive to an external magnetic field the electron transport through a shuttle structure becomes *spin dependent*.

A particularly interesting situation arises when electrons are shuttled between electrodes that are so-called half-metals where all the electrons are in the same spin state—the material is fully spin polarized. Examples of such materials can be found among the perovskite manganese oxides, a class of materials that show an intrinsic, so called "colossal magnetoresistance" effect at high magnetic fields (of order 10–100 kOe) [46].

A large magnetoresistance effect at lower magnetic fields has been observed in layered tunnel structures where two thin perovskite manganese oxide films are separated by a tunnel barrier [46–50]. Here the spin polarization of electronic states crucially affects the tunneling between the magnetic electrodes. Indeed, electrons extracted from the source electrode have a certain spin polarization, while to be injected into a drain electrode, they have to be polarized in a generally different direction. Clearly, the tunneling probability and hence the resistance must be strongly dependent on the relative orientation of the magnetization of the two electrodes. The relative magnetization can be tuned by an external magnetic field. A change in the resistance of trilayer devices by factors of order 2–5 have in this way been induced by magnetic fields of order 200 Oe [47–49]. The required field strength is determined by the coercitivities of the magnetic layers. This makes it difficult to use a tunneling device of the described type for sensing very low magnetic fields.

A new functional principle—spin-dependent shuttling of electrons—for low-magnetic field-sensing purposes was proposed by Gorelik et al. in Ref. [51]. This principle may lead to a giant magnetoresistance effect in external fields as low as 1–10 Oe. The key idea is to use the external magnetic field to manipulate the *spin of shuttled electrons* rather than the magnetization of the leads. Since an electron spends a relatively long time on a shuttle, where it is decoupled from the environment, even a weak magnetic field can rotate its spin by a significant angle. Such a rotation allows the spin of an electron that has been loaded onto the shuttle from the spin-polarized source electrode to be reoriented in order to allow the electron finally to tunnel from the shuttle to the spin-polarized drain lead. In this way the shuttle serves as a very sensitive magnetoresistance (GMR) device.

The model employed in Ref. [51] assumes that the source and drain are fully polarized in opposite directions. A mechanically movable quantum dot (described by a time-dependent displacement $x(t)$), where a *single* energy level is available for electrons, performs driven harmonic oscillations between the leads. The external magnetic field, **H**, is perpendicular both to the orientations of the magnetization in both leads and direction of mechanical motion.

The spin-dependent part of the Hamiltonian is specified as

$$\hat{\mathcal{H}}_s(t) = J(t)(a_\uparrow^\dagger a_\uparrow - a_\downarrow^\dagger a_\downarrow) - \frac{g\mu H}{2}(a_\uparrow^\dagger a_\downarrow + a_\downarrow^\dagger a_\uparrow)$$

where $J(t) = J_R(t) - J_L(t)$, $a_{\uparrow(\downarrow)}^\dagger (a_{\uparrow(\downarrow)})$ are the creation (annihilation) operators on the dot, $J_{L(R)}(t) \equiv J_{L(R)}[x(t)]$ are the exchange interactions between the on-grain electron and the left (right) lead, g is the gyromagnetic ratio, and μ is the Bohr magneton. The proper Liouville–von Neumann equation for the density matrix is analyzed, and an average electrical current is calculated for the case of large-bias voltage.

The behavior of the current depends on an interplay between three frequency scales: (i) the frequency of spin rotation, determined by the tunnel exchange interaction, $J_{L(R)}$, with the magnetic leads; (ii) the frequency of spin rotation in the external magnetic field, $g\mu H/\hbar$; and (iii) the frequency of shuttle vibrations, ω_0 .

In the limit of *weak* exchange interaction, $J_{\max} \ll \mu H$, one may neglect the influence of the magnetic leads on the on-dot electron spin dynamics. The resulting current is

$$I = \frac{\omega_0 e}{\pi} \frac{\sin^2(\vartheta/2)\tanh(w/4)}{\sin^2(\vartheta/2) + \tanh^2(w/4)} \tag{8}$$

where w is the total tunneling probability during the contact time t_0, while

$$\vartheta = \hbar^{-1} g\mu H \left(\frac{\pi}{\omega - t_0} \right) \sim \frac{\pi g \mu H}{\hbar \omega_0}$$

is the rotation angle of the spin during the "free-motion" time. The H-dependence of magnetotransmittance in this limit is characterized by two different scales. The first one is associated with resonant magnetic field dependence through the angle ϑ in the denominator of Eq. (8). This scale is

$$\delta H = \frac{w\hbar\omega_0}{g\mu} \tag{9}$$

The second scale,

$$\Delta H = \frac{\hbar\omega_0}{g\mu} \tag{10}$$

comes from the periodic function $\sin^2(\vartheta/2)$ in the numerator of Eq. (8). The magnetic-field dependence of the current is presented in Fig. 13(a). Dips in the transmittance of width δH appear periodically as the magnetic field is varied, the period being ΔH. This amounts to a giant magnetotransmittance effect. It is interesting to notice that by measuring the period of the variations in $I(H)$ one can in principle determine the shuttle vibration frequency. This amounts to a DC method for spectroscopy of the nanomechanical vibrations. Equation (10) gives a simple relation between the vibration frequency and the period of the current variations. The physical meaning of this relation is very simple: every time when $\omega/\Omega = n + 1/2$ ($\Omega = g\mu H/\hbar$ is the spin precession frequency in a magnetic field) the shuttled electron is able to flip fully its spin to remove the "spin-blockade" of tunneling between spin polarized leads having their magnetization in opposite directions.

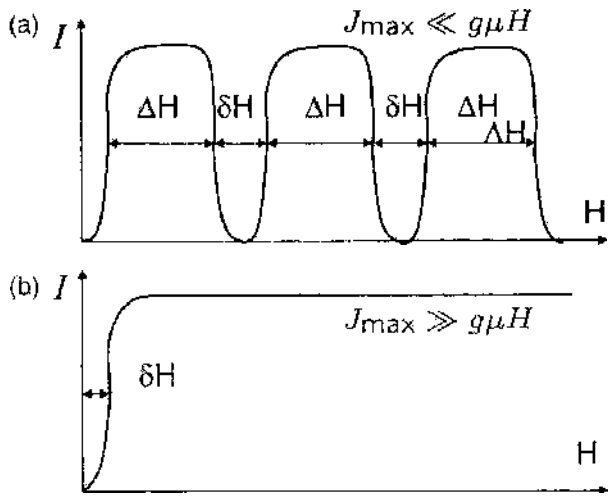

Figure 13. Magnetic-field dependence of the transmittance of the shuttle device for the limiting cases of (a) weak and (b) strong exchange coupling between dot and leads. The period ΔH and the width δH of the "dips" are given by Eqs. (9) and (10) for case (a) and δH is given by Eq. (11) for the case (b). Adapted with permission from [51], I. Y. Gorelik et al., *Phys. Rev. B* 71, 035237 (2005). © 2005, American Physical Society.

A *strong* magnetic coupling to the leads, $J_{max} \gg g\mu H$, preserves the electron spin polarization, preventing spin-flips of shuttled electrons due to an external magnetic field. However, if the magnetization of the two leads point in opposite directions, the signs of the exchange coupling to the leads are different. Therefore, the exchange couplings to the two leads tend to cancel out when the dot is in the middle of the junction. Hence, the effective exchange Hamiltonian affecting a dot electron periodically changes sign—because it is small—close to the time of sign reversal (see Fig. 14). Thus the effect of an external magnetic field is negligible almost everywhere, except in the vicinity of the level crossing, where the external magnetic field removes the degeneracy forming a gap in the spectrum (dashed curve).

The electronic spin-flip in this case occurs via a Landau-Zener [52] reflection from the gap. Note that in this case a Landau-Zener transition across the gap is a mechanism for backscattering of the electron because this is the channel where the electronic spin is preserved. The schematic $I(H)$ dependence for this case is shown in Fig. 13. The width δH of the minimum in the $I(H)$ dependence is

$$\delta H = \frac{\sqrt{J_{\min}\hbar\omega}}{\pi g\mu} \tag{11}$$

where $J_{\min} = \min(J_{L(R)}(t))$.

Thus the shuttling of spin-polarized electrons can facilitate a giant magnetotransmittance effect caused by shuttling of spin-polarized electrons between magnetic source and drain. A typical estimate for the magnetic field leading to a pronounced effect is $\delta H \simeq 1 \div 10$ Oe.

2.5.2. Spintronics of a Nanoelectromechanical Shuttle

In Section 2.5.1, we showed that the charge transfer through a nanomagnetic shuttle structure can be very sensitive to an external magnetic field. This sensitivity brings a possibility to trigger the shuttle instability by relatively weak magnetic fields. Here we discuss the magnetic-field-induced shuttle instability [53], which can occur in structures with spin-polarized electrons. The source of the effect is an influence of the magnetic field on the spin-dependent electron transfer mediated by mechanical vibration of a movable grain.

Let us consider the same system as discussed in the previous section. This system resembles the experimental setup of Ref. [54]. A movable grain having two electronic states with opposite spin directions is placed between magnetic leads having equal and oppositely directed magnetizations able to provide full spin polarizations of electrons. An external magnetic field is assumed to be oriented perpendicularly to the magnetizations of the leads.

The shuttle instability was studied in Section 2.4 by combining the vibrational dynamics of the oscillating grain with the quantum dynamics of the transferred electron. The generalization of the procedure outlined in Section 2.4 amounts to introducing a *spin-dependent* Wigner distribution, $W_{\sigma\sigma'}(x, p)$, defined as

$$W_{\sigma\sigma'}(x, p) = \int_{-\infty}^{\infty} \frac{dy}{2\pi\hbar} \left\langle x - \frac{y}{2} \middle| \rho_{\sigma\sigma'} \middle| x + \frac{y}{2} \right\rangle e^{ipy/\hbar},$$

$$\hat{\rho}_{\sigma\sigma'} = \left(\frac{1}{2}\right)(\hat{\rho}_0\delta_{n,0} + \hat{\rho}_2\delta_{n,2})\delta_{\sigma\sigma'} + \hat{\rho}_1^{\sigma\sigma'}\delta_{n,1}\,.$$

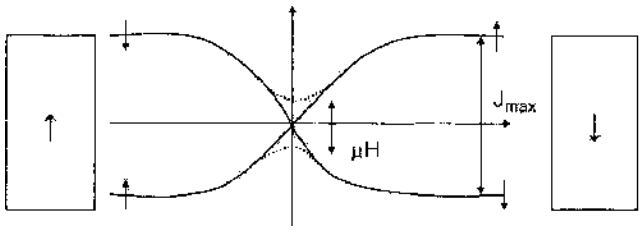

Figure 14. On-dot energy levels for spin-up and spin-down electron states as a function of the position of the dot. Level crossing in the middle of the device is removed by an external magnetic field. Reprinted with permission from [51]. L. Y. Gorelik et al., *Phys. Rev. B* 71, 035237 (2005). © 2005, American Physical Society.

Here $\hat{\rho}_{0,2}$ are operators in vibrational space while $\hat{\rho}_1^{\sigma\sigma'}$ works in both vibrational and spin spaces. In Ref. [53], equations for the time evolution of $W_{\sigma\sigma'}(x, p)$ were derived and their stationary solutions were analyzed in the limit of weak electromechanical coupling and for the quasiclassical regime, that is, when the tunneling length λ is much larger than the zero-point oscillation amplitude x_0. This analysis is presented in some detail in Appendix C. Various stationary regimes can be identified by a "phase diagram" in the $(\mathcal{E}, H)$-plane (Fig. 15). The three domains in this picture correspond to three different types of behavior of the nanomechanical oscillator.

In the "vibronic" domain (v) the system is stable with respect to mechanical displacements from the equilibrium position. The "shuttle" domain (s) corresponds to developed mechanical vibrations behaving classically. The third stationary regime is a "mixed" domain (m). This domain appears because the v- and s-regimes become unstable at *different* values of $\mathcal{E}$ and H, provided H exceeds some value $H_c = (\sqrt{3}/2)\hbar\Gamma/\mu$. While the shuttle regime becomes *unstable* below the line v, the "vibronic" state becomes unstable *above* the line s. Between these lines (m-domain), both states are stable, and the oscillator "bounces" between the v and s type of behavior. This bouncing is due to random electric forces caused by stochastic variations of the grain charge occurring in the course of tunneling events. The transition time between the two locally stable regimes, $\tau_{v\to s}$, depends on the electromechanical coupling parameter $\varepsilon = d/\lambda \ll 1$ and can be expressed as

$$\tau_{v\to s} = \omega_0^{-1} \exp\left(\frac{S_{v\to s}}{\varepsilon}\right)$$

Here $S_{v\to s}(\mathcal{E}, H) \sim 1$ is a function of the external fields. Since $\varepsilon \ll 1$, at $S_{v\to s} \neq S_{s\to v}$, the switching rates corresponding to the reverse transitions differ *exponentially* leading to an exponential difference in realization probability for the two regimes. The line p is determined by the equality $S_{v\to s} = S_{s\to v}$; that is, it corresponds to equal rates of the $v \to s$ and reverse transitions. Below this line, the probability of the v-regime is exponentially larger comparing to the s-regime, while above this line the s-regime exponentially dominates. Because of the smallness of the electromechanical coupling, $\varepsilon \ll 1$, the transition between the two regimes is very sharp. Hence the change of vibration regimes can be regarded as a "phase transition." Such a transition will manifest itself if the external fields are changed adiabatically on the time scale $\max\{\tau_{s\to v}\}$. One can expect enhanced low-frequency noise, $\omega \lesssim \tau_{s\to v}^{-1}$, around the line p as a hallmark of the transition.

In the opposite limit, either s- or v-regimes can be "frozen" in the mixed domain while crossing the line p. If one starts in the v-regime, it preserves until the system crosses the line s, and if one starts from the s-regime, it preserves until the system crosses the line v. Hence, one should observe a hysteretic behavior of the nonadiabatic shuttle transition.

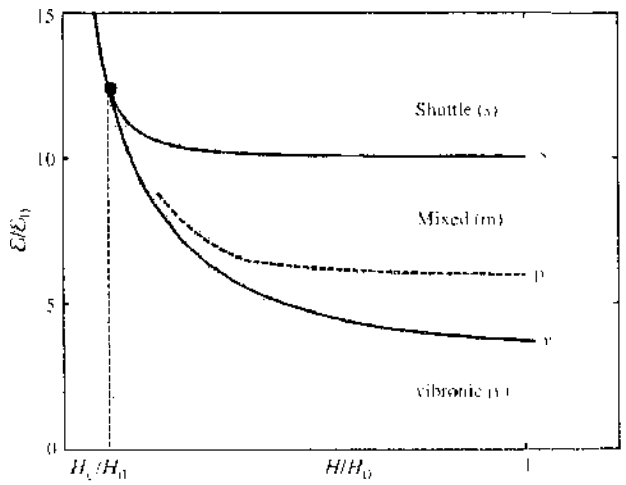

Figure 15. Regimes of a quantum oscillator depending on electrical and magnetic fields for $\Gamma/\omega_0 = 0.1$, $\mathcal{E}_0 = \gamma\lambda\omega_0/e$, $H_0 = \hbar\omega_0/\mu$, $H_c = (\sqrt{3}/2)\hbar\Gamma/\mu$.

Two different scenarios for the onset of shuttle vibrations were demonstrated in Ref. [53]. If one crosses over from the v- to the s-region when $H < H_c$ (i.e., avoiding the mixed phase), the onset is *soft*. In this regime, after crossing the border, the vibration amplitude grows gradually from zero to some finite value. For $H > H_c$, the onset is *hard*. In this case, the vibration amplitude has a step at the transition point, which corresponds to crossing either the p or the s line, depending on whether the transition is adiabatic or not.

Thus, following Fedorets et al. [53], we have demonstrated that magnetic-field-controlled spin effects lead to a very rich behavior of nanomechanical systems.

3. EXPERIMENTS ON ELECTRON SHUTTLING

A recent experimental realization of the shuttle instability resulting in a classical shuttle-electron transfer was reported by Tuominen et al. [17]. The experimental setup is shown in Fig. 16. The measured current-voltage characteristics display distinctive jumps and hysteresis, which reflect the influence of the vibrational environment (the metal beam the figure) on the shuttle dynamics.

Systems in which electron transport between two contacts is mediated by a vibrational mode of a self-assembled structure have also been investigated [4, 55]. The most striking example of such a system is the C_{60} single-electron transistor, fabricated by Park et al. [4]. In this device, a single C_{60} molecule was deposited in a narrow gap between gold electrodes. The current flowing through the device was found to increase sharply whenever the applied voltage was sufficient to excite vibrations of the molecule about the minima of the van der Waals potential in which the molecule resides or an internal mode of the molecule itself.

These transport measurements provided clear evidence for coupling between the center-of-mass motion of the C_{60} molecules and single-electron hopping. This new conduction mechanism had not been observed previously in quantum dot studies. The coupling is manifested as quantized nanomechanical oscillations of the C_{60} molecule against the gold surface, with a frequency of about 1.2 THz. This value is in good agreement with a simple theoretical estimate based on van der Waals and electrostatic interactions between C_{60} molecules and gold electrodes. The observed current-voltage curves are shown in Fig. 17. The device fabricated by Park et al. is an example of a molecular electronic device [56] in which electrical conduction occurs through single molecules connected to conventional leads. The junctions between molecular components and leads will be much more flexible than those in conventional solid-state nanostructures and fluctuations in their width may modify their current characteristics significantly. Furthermore, vibrational modes of the molecular components themselves may play an important role in determining the transport properties [57].

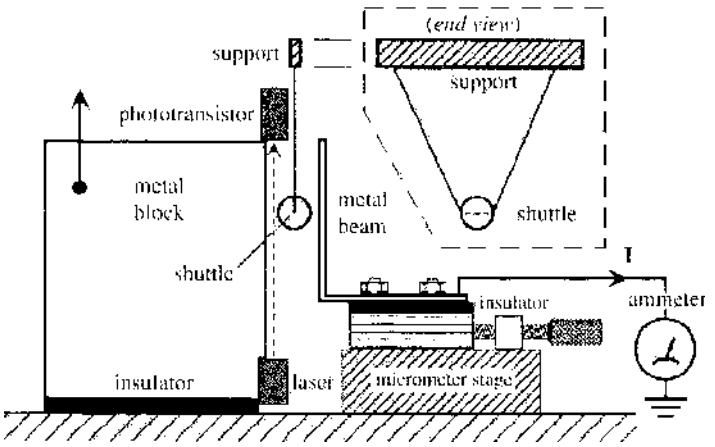

Figure 16. Experimental setup. The block, shuttle, and beam are made of brass. The dimensions of the beam are 40 mm × 22 mm × 1.6 mm. The shuttle mass is 0.157 g; its radius 2.06 mm. The effective mass of the bending beam is 30 g, its fundamental vibrational frequency 210 Hz, and its quality factor 37. Measurements indicate the influence of another vibrational mode at 340 Hz. The micrometer is used to adjust the shuttle gap d. The natural pendulum frequency of the suspended shuttle is 2.5 Hz. Reprinted with permission from [17], M. T. Tuominen et al., *Phys. Rev. Lett.* 83, 3025 (1999). © 1999, American Physical Society.

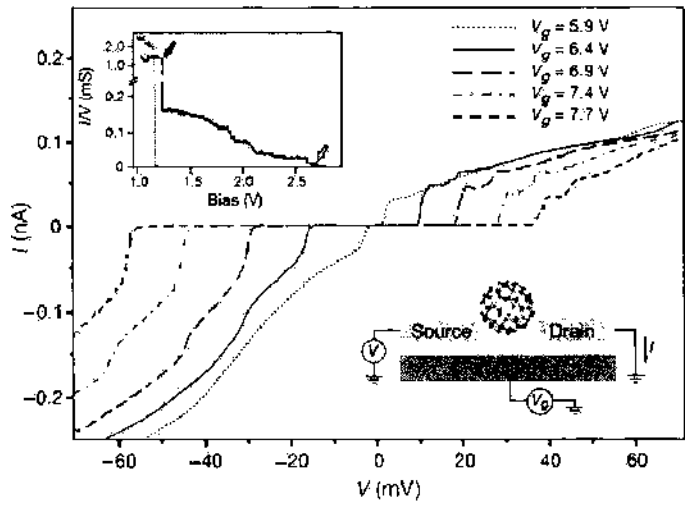

Figure 17. Current-voltage (I–V) curves obtained from a single-C_{60} transistor at $T = 1.5$ K. Five I–V curves taken at different gate voltages (V_g) are shown. Single-C_{60} transistors were prepared by first depositing a dilute toluene solution of C_{60} onto a pair of connected gold electrodes. A gap of 1 nm was then created using electromigration-induced breaking of the electrodes. Upper inset, A large bias was applied between the electrodes while the current through the connected electrode was monitored (black solid curve). After the initial rapid decrease (solid arrow), the conductance stayed above ~0.05 mS up to ~2.0 V. This behavior was observed in most single-C_{60} transistors, but it was not observed when no C_{60} solution was deposited (dotted curve). The bias voltage was increased until the conductance fell low enough to ensure that the current through the junction was in the tunneling regime (open arrow). The low-bias measurements shown in the main panel were taken after the breaking procedure. Lower inset, An idealized diagram of a single C_{60}-transistor formed by this method. Reprinted with permission from [4], H. Park et al., *Nature* 407, 57 (2000). © 2000. Macmillan Publishers Limited.

An interesting possibility of a nanomechanical double-barrier tunneling structure involving shuttling has been realized by Majima et al. [58] and Nagano et al. [59]. The system consists of scanning vibrating probe/colloidal Au particles/vacuum/PtPd substrate see (Fig. 18). The colloidal particles act as Coulomb islands, and because of probe vibration they are brought to motion. What is important is the phase shift between the probe vibrations and the AC current in the system, which allows the singling of out the displacement current. The latter shows clear features of the Coulomb blockade. Comparison of the experimental results with theoretical calculation caused the authors to conclude that about 280 Au particles vibrate in accordance with each other.

An *externally driven* nanomechanical shuttle has been designed by Erbe et al. [13, 14]. In these experiments a nanomechanical pendulum was fabricated on Si-on-insulator substrate using electron and optical lithography, and a metallic island was placed on the clapper, which could vibrate between source and drain electrodes (see Fig. 19). The pendulum was excited by applying an AC voltage between two gates on the left- and right-hand sides of the clapper. The observed tunneling source-drain current was strongly dependent on the frequency of the exciting signal having pronounced maxima at the eigenfrequencies of the mechanical modes. This fact signalizes a shuttling mechanism of electron transfer at typical shuttle frequencies of about 100 MHz. The measured average DC current at 4.2 K corresponded to 0.11 ± 0.001 electrons per cycle of mechanical motion. Both a theoretical analysis [21] and numerical simulations showed that a large portion of the voltage also acts on the island. The authors of Refs. [13, 14] expect that the resolution of the transport through the shuttle can be improved to also resolve Coulomb blockade effects by minimizing the parasitic effects of the driving AC voltage. According to their estimates, a Coulomb blockade should be observable below 600 mK. A very important modification of the setup in Fig. 19 was recently presented by Scheible et al. in Ref. [15]. There a silicon cantilever is part of a mechanical system of coupled resonators—a construction that makes it possible to drive the shuttle mechanically with a minimal destructive influence from the actuation dynamics on the shuttle itself. This is achieved by a clever design that minimizes the electrical coupling between the driving part of the device (either a magnetomotively driven, doubly clamped beam resonator, or a capacitively coupled remote cantilever) and the driven part (the cantilever that carries

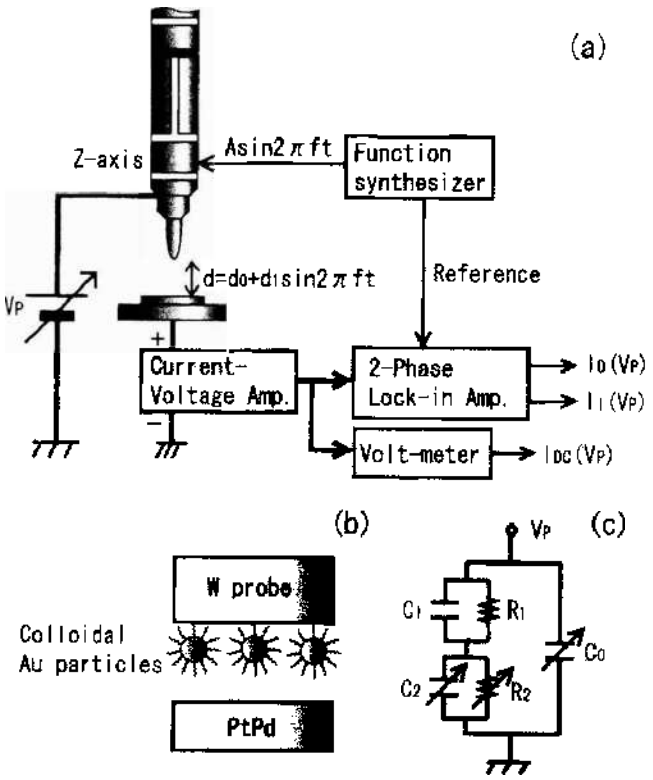

Figure 18. (a) The experimental arrangement of the tunneling current and displacement current simultaneous measuring system. (b) A schematic image of nanomechanical double barrier tunneling structures with vibrating probe (W)/colloidal Au particles (diameter 8 nm)/vacuum/PtPd substrates. (c) The equivalent circuit of a two-junction system. C_1 and R_1 mean capacitance and tunneling resistance between a Au particle and a PtPd substrate, and C_2 and R_2 are those between a Au particle and a tungsten probe, respectively. C_0 is the capacitance between the tungsten probe and PtPd substrate. Reprinted with permission from [59], K. Nagano et al., *Appl. Phys. Lett.* 81, 544 (2002). © 2002, American Institute of Physics.

the shuttle on its tip). Systems of this type in principle, can be used for studies of shuttle transport through superconducting and magnetic systems.

Interesting results on mechanically assisted charge transfer were obtained by Scheible et al. [27] in a device fabricated as a silicon nanopillar located between source and drain contacts (see Fig. 20). The device is manufactured in a two-step process: (1) nanoscale lithography using a scanning electron microscope (SEM) and (2) dry etching in a fluorine reactive ion etcher (RIE). The lithographically defined gold structure acts as both electrical current leads

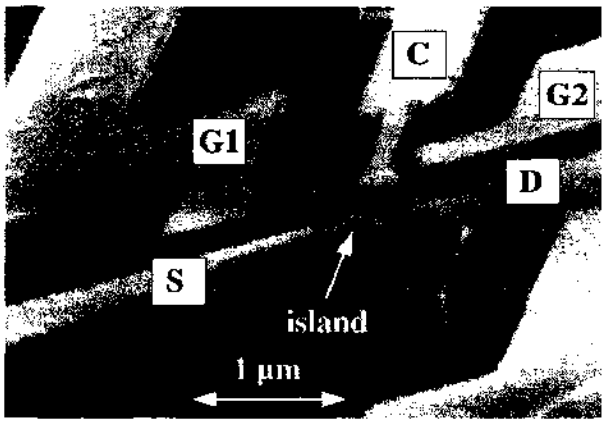

Figure 19. Electron micrograph of the quantum bell: The pendulum is clamped on the upper side of the structure. It can be set into motion by an AC-power, which is applied to the gates on the left- and right-hand side (G1 and G2) of the clapper (C). Electron transport is then observed from source (S) to drain (D) through the island on top of the clapper. The island is electrically isolated from the rest of the clapper, which is grounded. Reprinted with permission from [13], A. Erbe et al., *Appl. Phys. Lett.* 73, 3751 (1998). © 1998, American Institute of Physics.

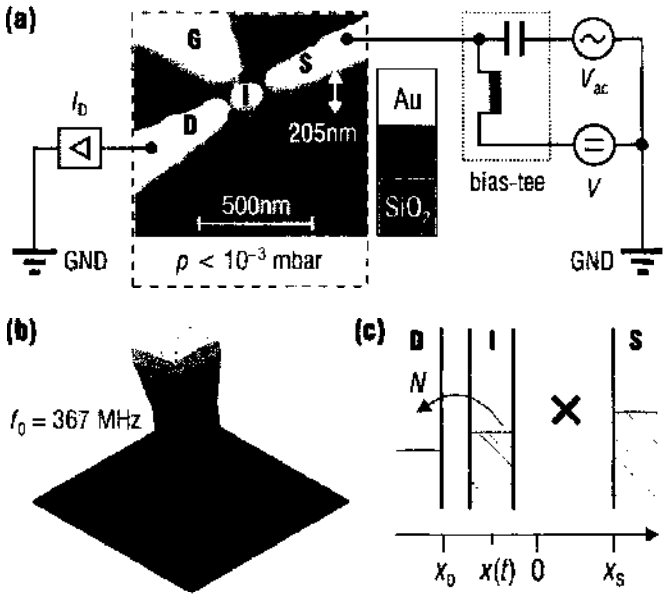

Figure 20. (a) SEM micrograph and experimental circuitry of the silicon nanopillar: At source S, an AC signal, V_{ac}, is applied with a superimposed DC bias V. The net current, I_D is detected at drain D with a current amplifier. The third electrode, G, is floating. (b) Finite element simulation of the base oscillation mode that compiles for the nanopillar to $f_0 = 5367$ MHz. (c) When the island is deflected toward one electrode, the instantaneous voltage bias determines the preferred tunneling direction. Co-tunneling is absent in this case due to an increased distance to the opposite electrode. Reprinted with permission from [27], D. V. Scheible and R. H. Blick, *Appl. Phys. Lett.* 84, 4632 (2004). © 2004, American Institute of Physics.

and etch mask for the RIE. A simple geometry defined by the SEM consequently results in the freestanding isolating nanopillar of intrinsic silicon with a conducting metal (Au) island at its top (see Fig. 20[a]). This island serves as the charge shuttle. The metal island and the nanopillar are placed in the center of two facing electrodes, denoted by source S and drain D. The system is biased by an AC voltage at source, rather than a sole DC bias, to avoid the dc-self excitation. Moreover, application of an ac-signal allows excitation of the nanopillar resonantly in one of its eigenmodes. The device itself is mounted in a probe station, providing vacuum condition for a reproducible and controlled environment of the pillar. This also removes water and solvents that may have condensed at the surface of the NEMS. The devices operated at room temperature and the capacitance was not sufficiently small to realize the single-electron regime.

Experimentally, dependencies of the current through the system on bias frequency, as well as on additional DC bias allowing to tune resonances, were measured. The results are qualitatively explained on the basis of numerical simulations.

Coupling of electron transport to mechanical degrees of freedom can lead to other interesting phenomena. In particular, Kubatkin et al. [60] have observed a current-induced Jahn-Teller deformation of a Bi nanocluster. They have shown that such a transformation influences the electron transport through a change in the geometrical shape of the cluster. We do not review here in detail other experiments (e.g., Ref. [4–10] involving nanoelectromechanical phenomena since they are not directly connected to shuttle charge transport).

4. COHERENT TRANSFER OF COOPER PAIRS BY A MOVABLE GRAIN

In this section, we study a superconducting weak link where the coupling between two bulk superconductors is due to Cooper pairs tunneling through a small movable superconducting grain. The system is depicted in Fig. 21. We begin by looking at the requirements one has to put on the system for the analysis to be valid. Then we briefly review the parity effect and the single-Cooper-pair box in Section 4.2. Following this, in Section 4.3, we consider the two basic processes involved in shuttling of Cooper pairs: (i) scattering of a single grain with a

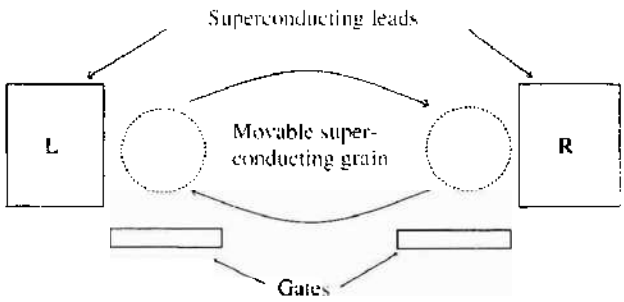

Figure 21. Superconducting shuttle junction. Two superconducting leads are placed too faraway from each other to allow for direct tunneling between them. Using a movable grain, they may still exchange Cooper pairs indirectly via lead-grain tunneling. If the gates are appropriately biased, a single-Cooper-pair box situation occurs close to either lead allowing for a coherent superposition of two different charge states on the grain. Hence, for a grain making repeated alternate contacts with the leads, a coherent exchange of Cooper pairs between them is possible. Reprinted with permission from [16], R. I. Shekhter et al., *J. Phys: Condens. Matter* 15, R441 (2003). © 2003. Institute of Physics and IOP Publishing Limited.

lead, thereby creating entanglement, and (ii) free motion of a grain whose charge state is a quantum mechanical superposition.

Two possible experimental configurations can be imagined for the system in Fig. 21;

1. The pair of remote superconductors might be coupled by an external superconducting circuit, forming a loop. In this case, the superconducting phase difference is given (and is, e.g., determined by a magnetic flux through the loop). Shuttling of Cooper pairs is, in this case, a mechanism allowing for supercurrent flow through the loop. This scenario is analyzed in Section 4.4.
2. A qualitatively different situation is when the two leads are disconnected from each other. Cooper pair exchange between two remote and isolated superconductors (leads) is then allowed only through tunneling via the single-Cooper-pair box, performing oscillatory motion between leads. In this case, the relevant question is whether phase coherence between the leads can be established. This situation is considered in Section 4.5.

4.1. Requirements for Shuttling of Cooper Pairs

The main question we will focus on is how mechanical vibration of the cluster affects coherent tunneling of Cooper pairs. To put the question in a more dramatic way: Could one have coupling between remote superconductors mediated mechanically through inter-lead transportation of Cooper pairs, performed by a small movable superconductor? The analysis given here, leading to a positive answer to this question, has in part been presented in Refs. [61] and [62]. This result follows from the possibility to preserve phase coherence of Cooper pairs despite the nonstationary and nonequilibrium dynamics of the electronic system originating from a time-dependent displacement of the small superconducting mediator. It is necessary, though, that only a few electronic degrees of freedom are involved in the quantum dynamics. The latter criterion is guaranteed to be fulfilled if two conditions are fulfilled:

1. The energy quantum $\hbar\omega_0$ associated with the vibrations is much smaller than the superconducting gap Δ.
2. The charging energy E_C is much larger than the superconducting coupling energy E_J and the thermal energy $k_B T$.

Here E_J is the maximal Josephson energy characterizing the superconducting coupling between grain and leads. Condition (i) prevents the grain motion from creating elementary electronic excitations and therefore guarantees that the quantum evolution of the system is disconnected from any influence of the continuous spectrum of quasiparticles in the superconductors. Condition (ii) guarantees a Coulomb blockade for Cooper pair tunneling and hence prevents significant charge fluctuations on the dot. Such fluctuations imply the existence of a large number of channels for Cooper pair transport and result in strong decoherence due to destructive interference between the different channels. In what follows we will consider the conditions (i) and (ii) to be fulfilled.

4.2. Parity Effect and the Single-Cooper-Pair Box

The ground state energy of a superconducting grain depends in an essential way on the number N of electrons on it. Two important N-dependent contributions are the electrostatic Coulomb energy $E_C(N)$, connected with the extra charge accumulated on the superconducting grain, and the so-called parity term Δ_N [63–65]. The latter originates from the fact that only an even number of electrons can form the Bardeen-Cooper-Schrieffer (BCS) ground state of a superconductor (which is a condensate of paired electrons). Therefore, if the number of electrons N is odd, one unpaired electron has to occupy one of the quasiparticles states. The energy cost for occupying a quasiparticle state, which is equal to the superconducting gap Δ, brings a new energy scale to bear on how many electrons can be accommodated by a small superconducting grain. In view of this discussion, the ground state energy $E_0(N)$ can be expressed as (see Ref. [65])

$$E_0(N) = E_C(N - \alpha V_g)^2 + \begin{cases} 0 \text{ even } N \\ \Delta \text{ odd } N \end{cases} \tag{12}$$

One can see from Eq. (12) that if $\Delta > E_C$ only an even numbers of electrons can be accumulated in the ground state of the superconducting grain. Moreover, for special values of the gate voltage V_g, such that $\alpha V_g = 2N + 1$, the ground state is degenerate with respect to a change of the total number of electrons by one single Cooper pair. An energy diagram illustrating this case is presented in Fig. 22. The occurrence of such a degeneracy brings about an important possibility to create a quantum hybrid state at low temperatures, which will be a coherent mixture of two ground states, differing by a single Cooper pair:

$$|\Psi\rangle = \gamma_1|n\rangle + \gamma_2|n+1\rangle \tag{13}$$

This coherent superposition state has been realized experimentally in so-called single-Cooper-pair boxes [66]. Coherent control of the state (13) was first demonstrated by Nakamura et al. [67] and then confirmed and improved by Vion et al. [68] and others. The idea of the experiment is presented in Fig. 23, where the superconducting dot is shown to be in tunneling contact with a bulk superconductor. A gate electrode is responsible for lifting the Coulomb blockade of Cooper pair tunneling, thereby creating the ground state degeneracy. This allows for delocalization of a single Cooper pair between two superconductors. Such a hybridization results in a certain charge transfer between the bulk superconductor and the grain.

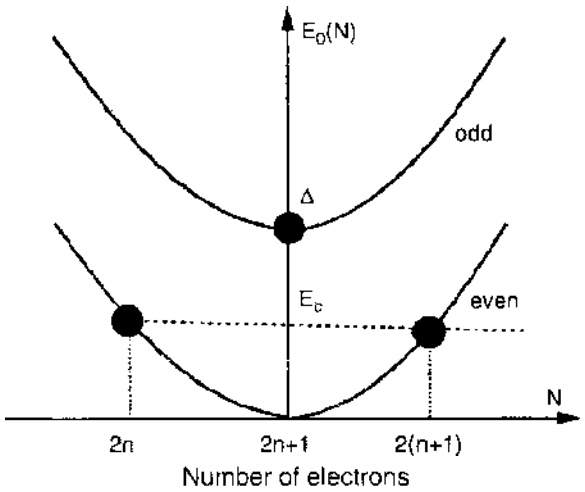

Figure 22. Energy diagram for the ground state of a superconducting grain with respect to charge for the case $\Delta > E_C$. For a certain bias voltage $\alpha V_g = 2n + 1$ [see Eq. (12)] ground states differing by only one single Cooper pair becomes degenerate. Reprinted with permission from [16]. R. I. Shekhter et al., *J. Phys: Condens. Matter* 15, R441 (2003). © 2003. Institute of Physics and IOP Publishing Limited.

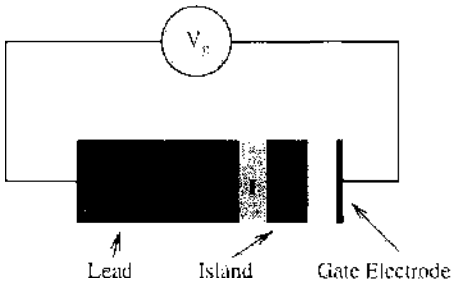

Figure 23. A schematic diagram of a single-Cooper-pair box. An island of superconducting material is connected to a larger superconducting lead via a weak link. This allows for coherent tunneling of Cooper pairs between them. For a nanoscale system, such quantum fluctuations of the charge on the island are generally suppressed due to the strong charging energy associated with a small grain capacitance. However, by appropriate biasing of the gate electrode it is possible to make the two states $|n\rangle$ and $|n+1\rangle$, differing by one Cooper pair, have the same energy (degeneracy of ground state). This allows for the creation of a hybrid state $|\Psi\rangle = \gamma_1|n\rangle + \gamma_2|n+1\rangle$. Reprinted with permission from [16], R. I. Shekhter et al., *J. Phys: Condens. Matter* 15, R441 (2003). © 2003, Institute of Physics and IOP Publishing Limited.

4.3. Basic Principles

To realize the idea of Cooper pair shuttling, a rather straightforward extension of the single-Cooper-pair box experiments mentioned in the previous section is required. Essentially, to shuttle Cooper pairs, one uses the hybridization for coherent loading (unloading) of electric charge to (from) a movable single-Cooper-pair box that transports the loaded charge between the remote superconductors. The necessary setup should contain a movable Cooper pair box capable of performing forced oscillations between two gated superconducting leads as shown in Fig. 21. The two gate electrodes ensure the lifting of the Coulomb blockade of Cooper pair tunneling at the turning points in the vicinity of each of the superconducting electrodes.

4.3.1. Scattering and Free Motion

To illustrate the shuttling process, consider first the simple case when an initially uncharged grain, $n = 0$, gets into contact with the left lead. Before contact the state of the system is

$$|\Psi(t_0)\rangle = |0\rangle \otimes |\psi_{\text{Leads}}\rangle$$

where $|\psi_{\text{Leads}}\rangle$ is the state of the leads. During the time spent in tunneling contact with the lead, the Cooper pair number on the grain may change. When the grain ceases to have contact with the lead, the general state of the system is therefore

$$|\Psi(t_1)\rangle = \alpha|0\rangle \otimes |\psi'_{\text{Leads}}(t_1)\rangle + \beta|1\rangle \otimes |\psi''_{\text{Leads}}(t_1)\rangle$$

This process is depicted in Fig. 24. The coefficients α and β are complex numbers and will depend both on the time spent in contact with the lead and on the initial state $|\psi_{\text{Leads}}\rangle$. We note here that in general the grain will become entangled with the leads.

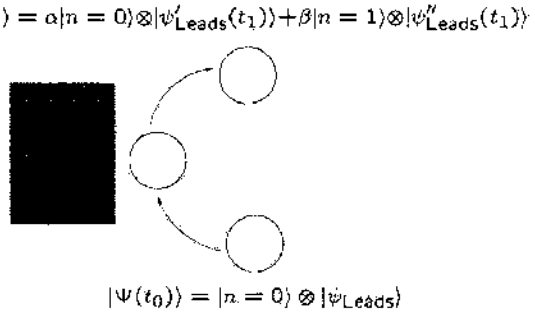

Figure 24. A grain initially carrying zero excess Cooper pairs scatters with the left lead. After the scattering, the state of the grain will be a superposition of zero and one extra Cooper pairs. In the process, the grain becomes entangled with the leads. Reprinted with permission from [16], R. I. Shekhter et al., *J. Phys: Condens. Matter* 15, R441 (2003). © 2003, Institute of Physics and IOP Publishing Limited.

As the grain traverses the region between the leads, there is no tunneling and the magnitudes $|\alpha|$ and $|\beta|$ will remain constant. However, the relative phase between them may change. Thus, when the grain arrives at the right lead at a time t_2 the state of the system will have acquired an additional phase labeled χ_+

$$|\Psi(t_2)\rangle = \alpha|0\rangle \otimes |\psi'_{\text{Leads}}(t_2)\rangle + e^{-i\chi_+}\beta|1\rangle \otimes |\psi''_{\text{Leads}}(t_2)\rangle.$$

As the grain comes into contact with the right lead charge exchange is again possible and the coefficients α and β will change. Then, in the same fashion as during the motion from left to right, the only effect on the state as the grain moves toward the left lead again is that another relative phase denoted by χ_- is acquired. The whole process is schematically illustrated in Fig. 25.

Both the "scattering events" and the "free motion" are thus characterized by quantum phases accumulated by the system. Here we refer to them as the Josephson phase, ϑ, and the electrostatic phase, $\chi_\pm$:

$$\vartheta = \hbar^{-1} \int dt\, E_J(t) \tag{14}$$

$$\chi_\pm = \left(\frac{i}{\hbar}\right) \int dt\, \delta E_c[x(t)] \tag{15}$$

4.3.2. Hamiltonian

Under the condition that the variation of the grain position x is adiabatically slow, no quasiparticle degrees of freedom are involved and one only has to consider the quantum dynamics of the coupled ground states on each of the superconductors. The corresponding Hamiltonian is expressed in terms of the Cooper pair number operator $\hat{n}$ for the grain and the phase operators for the leads, $\hat{\Phi}_{L,R}$,

$$H(x(t)) = -\frac{1}{2} \sum_{s=L,R} E_J^s(x(t))(e^{i\hat{\Phi}_s}|1\rangle\langle 0| + \text{h.c.}) + \delta E_c(x(t))\hat{n} \tag{16}$$

The operator $|0\rangle\langle 1|$ changes the charge on the grain from zero to one extra Cooper pair. The Hamiltonian (16) represents a standard approach to the description of superconducting weak links [69]. However, an essential specific feature here is the dependence of the charging

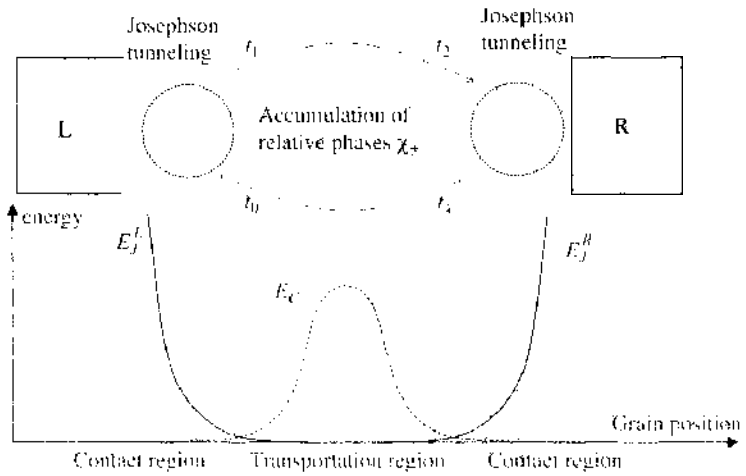

Figure 25. Illustration of the charge transport process. The island moves periodically between the leads. Close to each turning point lead-grain tunneling takes place. At these points the states with net charge 0 and $2e$ are degenerate. As the grain is moved out of contact, the tunneling is exponentially suppressed while the degeneracy may be lifted. This leads to the accumulation of electrostatic phases $\chi_\pm$. Reprinted with permission from [16], R. I. Shekhter et al., *J. Phys: Condens. Matter* 15, R441 (2003), © 2003, Institute of Physics and IOP Publishing Limited.

energy difference δE_C and the coupling energies E_J on the position of the superconducting grain x,

$$E_J^{L,R}(x) = E_0 \exp\left(\frac{-\delta x_{L,R}}{\lambda}\right)$$

Here $\delta x_{L,R}$ is the distance between the grain and the respective lead. Since the displacement x is a given function of time we are dealing with a nonstationary quantum problem.

4.4. Transferring Cooper Pairs Between Coupled Leads

When the leads are completely connected, i.e., they are simply different parts of the same superconductor, there is, because of charge conservation, a one-to-one correspondence between the number of pairs on the conductor and the number of pairs n on the island. One may in this case assume the leads to be in states with definite phases,

$$|\psi_{\text{Leads}}\rangle = |\Phi_L\rangle \otimes |\Phi_R\rangle$$

The effect of this is to replace the operators $e^{\pm i\hat{\Phi}_{L,R}}$ in the Hamiltonian above with c-numbers making it a two-level system. This leaves us with a reduced Hamiltonian where the phases $\Phi_{L,R}$ enter only as parameters,

$$H_{\text{red}}(x(t), \Phi_L, \Phi_R) \equiv \langle \Phi_L | \langle \Phi_R | H(x(t)) | \Phi_R \rangle | \Phi_L \rangle \tag{17}$$

The dynamics of the system is described by the Liouville–von Neumann equation for the density matrix $\hat{\rho}$ [61],

$$\frac{\mathrm{d}\hat{\rho}}{\mathrm{d}t} = -i\hbar^{-1}[H_{\text{red}}, \hat{\rho}] - \nu(t)[\hat{\rho} - \hat{\rho}_0(t)] \tag{18}$$

Since we are not interested here in transient processes, connected with the initial switching on of the mechanical motion, solutions that do not depend on any initial conditions will be in the focus of our analysis. To prevent any memory of initial conditions, one needs to include a dissipation term (the last term on the right-hand side of Eq. (18)) into the dynamics. If this dissipation is weak enough, it does not affect the system dynamics on a time scale comparable to the period of vibrations. However, in a time scale longer than the period of rotation, such relaxation causes solutions to Eq. (18) to be independent of any initial conditions. We use the simplest possible relaxation time approximation (τ-approximation), with ρ_0 being an equilibrium density matrix, for the system described by Hamiltonian H. Relaxation is due to quasiparticle exchange with the leads and depends on the tunneling transparencies

$$\nu(x) = \nu_0 \exp\left(\frac{-\delta x}{\lambda}\right) \tag{19}$$

The Cooper pair exchange, being an exponential function of the grain position, is mainly localized in the vicinity of the turning points. In this region, the Coulomb blockade of Cooper pair tunneling is suppressed and can be neglected while considering the dynamics of the formation (or transformation) of the single-Cooper-pair hybrid (13). In contrast, the dynamics of the system during the time intervals when the grain is faraway from the superconducting leads, is not significantly affected by Cooper pair tunneling and essentially depends on the electrostatic energy $\delta E_C = E_C(n+1) - E_C(n)$ that appears as the Coulomb degeneracy is lifted away from the turning points. This circumstance allows us to simplify the analysis and consider the quantum evolution of the system as a sequence of scattering events and "free motion." Scattering takes place due to tunneling of Cooper pairs in the vicinity of the turning points, and these events are separated by intervals of free evolution of the system, where any tunneling coupling between grain and leads is neglected. A schematic picture of the described sequence is presented in Fig. 25.

Direct calculations [61] give a simple expression for the average current,

$$\bar{I} = 2ef \frac{\cos\vartheta \sin^3\vartheta \sin\Phi(\cos\chi + \cos\Phi)}{1 - (\cos^2\vartheta\cos\chi - \sin^2\vartheta\cos\Phi)^2} \tag{20}$$

where $\Phi = (\Phi_R - \Phi_L) + (\chi_+ - \chi_-)$ and $\chi = \chi_+ + \chi_-$ (for details of the derivation see also [70, 71]). The following features of Eq. (20) should be mentioned:

1. The mechanically assisted supercurrent is an oscillatory function of the phase differences of the superconducting leads similarly to other types of superconducting weak links.
2. The current can be electrostatically controlled if an asymmetrical (χ_+ is not equal to χ_-) phase accumulation is provided by an external electric field varying together with the grain rotation. The same effect appears if the grain trajectory embeds a finite magnetic flux. Then χ is proportional to the flux given in units of the superconducting flux quantum.
3. Depending on the value of the electrostatic phase χ, one can have any direction of the supercurrent flow at a given superconducting phase difference. Also a nonzero supercurrent at $\Phi_L - \Phi_R = 0$ is possible in contrast to ordinary superconducting weak links.
4. The supercurrent is a nonmonotonic function of the Josephson coupling strength ϑ. This fact reflects the well-known Rabi oscillations in the population of quantum states with different numbers of Cooper pairs when a single-Cooper-pair box is formed due to sudden switching of pairs tunneling at the turning points of the trajectory.

In the weak coupling limit, the current is proportional to the third power of the maximal Josephson coupling strength. One needs to stress that this strength might be several orders of magnitude bigger than what a direct coupling between the superconducting leads would give. Cooper pair transportation serves as an alternative to direct Cooper pair tunneling between the leads, thereby providing a mechanism for supercurrent flow between the remote superconductors. In Fig. 26, a diagram of the supercurrent as a function of both superconducting and electrostatic phases is presented.

4.5. Shuttling Cooper Pairs Between Disconnected Leads

We now turn to the question of whether or not a superconducting coupling between remote and isolated superconductors can be mediated by mechanically shuttling Cooper pairs between them [62]. Here we are interested in the situation when up to a time t_0, the

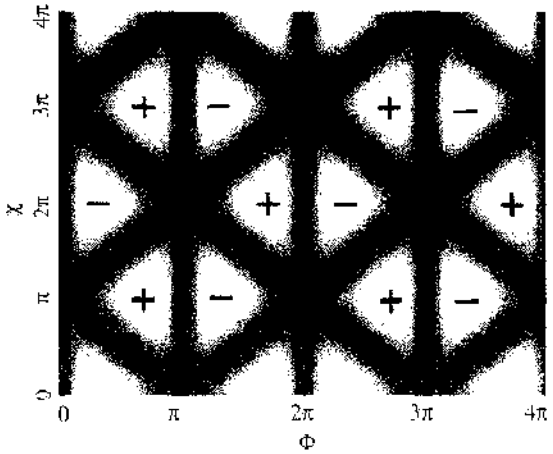

Figure 26. The magnitude of the current $\bar{I}$ in Eq. (20) in units of $I_0 = 2ef$ as a function of the phases Φ and χ. Regions of black correspond to no current and regions of white to $|\bar{I}/I_0| = 0.5$. The direction of the current is indicated in the figure by signs ±. To best see the triangular structure of the current, the contact time has been chosen to $\vartheta = \pi/3$. I_0 contains only the fundamental frequency of the grain's motion and the Cooper pair charge. Reprinted with permission from [16], R. I. Shekhter et al., *J. Phys: Condens. Matter* 15, R441 (2003). © 2003, Institute of Physics and IOP Publishing Limited.

shuttle is absent and no well-defined superconducting phases can be introduced for the leads. This is because of the large quantum fluctuations of the phases on the conductors, which each contain a fixed number of Cooper pairs. At times t larger than t_0, a superconducting grain starts to swing between the leads, and the number of Cooper pairs on each lead is no longer conserved separately. The moving single-Cooper-pair box provides a mechanism for exchange of Cooper pairs between the leads. We are interested to know whether this exchange is able to establish superconducting phase coherence between the leads.

In the case with strongly coupled leads, the limitation that the grain could carry only zero or one excess Cooper pair reduced the problem to a two-state problem. Because the problem was essentially a two-conductor problem (grain + one lead), only this variable was needed to determine the state of the system. For the case with decoupled leads, one has to keep the operator nature of $\hat{\Phi}_{L,R}$ in the Hamiltonian (16). The dimensionality of the Hilbert space depends on the maximum number of Cooper pairs that can be accommodated on the leads. The factors that put a limit to this number are the capacitances of the leads that are not present in the Hamiltonian (16). Instead of including these charging energy terms, another approach was used in Ref. [62]. The Hilbert space was there reduced in such a way that each lead can only accommodate a maximum (minimum) of $\pm N$ extra Cooper pairs.

The time evolution of the system is determined by the Liouville–von Neumann equation for the density matrix. If the total number of particles in the system is conserved and one assumes the whole system to be charge neutral, the state of the system can be written in terms of the state of the grain and one of the leads. The density matrix can, for example, be written as

$$\rho(t) = \sum_{\eta,\sigma=0,1} \sum_{N_L,N_L'=-N}^{N} \rho_{N_L N_L'}^{\eta\sigma}(t) \underbrace{|\eta\rangle\langle\sigma|}_{\text{grain}} \otimes \underbrace{|N_L\rangle\langle N_L'|}_{\text{left lead}} \otimes \underbrace{|-N_L-\eta\rangle\langle -N_L'-\sigma|}_{\text{right lead}} \qquad (21)$$

Here it has been explicitly indicated to which part of the system the various operators belong. The simple relaxation time approximation used for the case with connected leads is not possible to use in this case. That approximation assumed the leads to be in BCS states with definite phases toward which the phase of the grain relaxed. Instead, to account for loss of initial conditions, the influence of the fluctuations of the gate potential on the island charge has been accounted for. The fluctuations are modeled by a harmonic oscillator bath with a spectral density determined by the impedance of the gate circuit. Hence, the density matrix in Eq. (21) is the reduced density matrix obtained after tracing out the bath degrees of freedom.

Denoting the phase difference between the leads by $\Delta\Phi \equiv \Phi_R - \Phi_L$ and the phase difference between the right lead and the grain $\Delta\phi \equiv \Phi_R - \phi_{\text{grain}}$, phase difference states

$$|\Delta\Phi, \Delta\phi\rangle \equiv \frac{1}{2\pi} \sum_n \sum_{N_L} e^{iN_L\Delta\Phi} e^{in\Delta\phi} |n\rangle |N_L\rangle |-(N_L+n)\rangle$$

are introduced. The probability for finding a certain phase difference between the leads is then obtained from the reduced distribution function

$$f(\Delta\Phi) \int_0^{2\pi} d(\Delta\phi) \langle \Delta\Phi, \Delta\phi | \rho | \Delta\Phi, \Delta\phi \rangle = \frac{1}{2\pi} \sum_{N_L,N_L'} \sum_{\eta} e^{i(N_L'-N_L)\Delta\Phi} \rho_{N_L N_L'}^{\eta\eta}$$

This is the function that has been plotted on the z-axis in Fig. 27. At the initial stage of the simulation, the system was in a state with a definite amount of charge in each conductor. This means that the phase distribution is initially completely flat. However, as the grain rotates, the distribution is altered and eventually becomes peaked around a definite value of $\Delta\Phi$ uniquely determined by the system parameters. The width of the final peak depends on the maximum number of excess Cooper pairs that can be accommodated on the leads.

The phase difference mediated by shuttling Cooper pairs will give rise to a current if the two conductors are connected by an ordinary weak junction. In Fig. 28, this current is shown

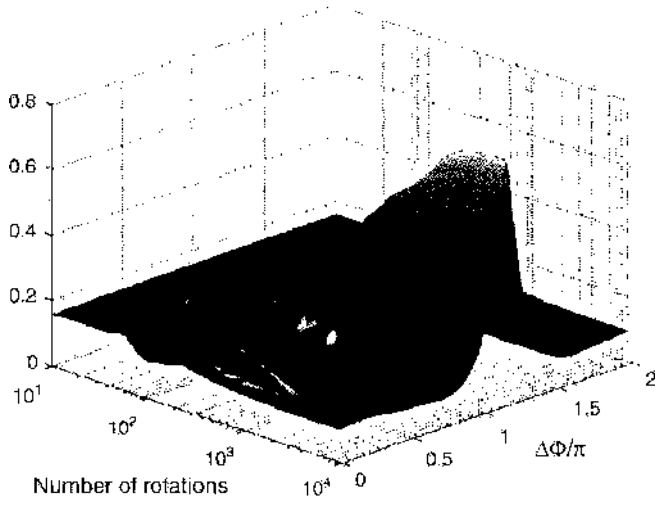

Figure 27. Probability for finding a phase difference $\Delta\Phi$ between the leads as a function of the number of grain rotations. Reprinted with permission from [62], A. Isacsson et al., *Phys. Rev. Lett.* 89, 277002 (2002). © 2002, American Physical Society.

as a function of the dynamical phases for fixed ϑ (contact time). Here an auxiliary, weak probe Josephson junction is assumed to be connected after a large number of rotations. The current is given by the usual Josephson relation weighted over the phase distribution $f(\Delta\Phi)$:

$$I = I_c \int_0^{2\pi} d(\Delta\Phi) \sin(\Delta\Phi) f(\Delta\Phi)$$

where I_c is the critical current of the probe junction.

We conclude that phase coherence can be established by a mechanical transfer of Cooper pairs and that this mechanism can also give rise to a nondissipative current.

The role of an environment-induced decoherence in the shuttling of Cooper pairs was considered by Romito et al. [72]. To allow for decoherence, a finite model damping of the *off-diagonal* part of the density matrix is introduced in the Liouville–von Neumann Eq. (18). The damping is assumed to be different in the contact regions (γ_J) and in the region between the contacts (γ_C) and computed in the Born-Markov approximation. Strong decoherence exponentially suppresses the supercurrent, the leading term being proportional to

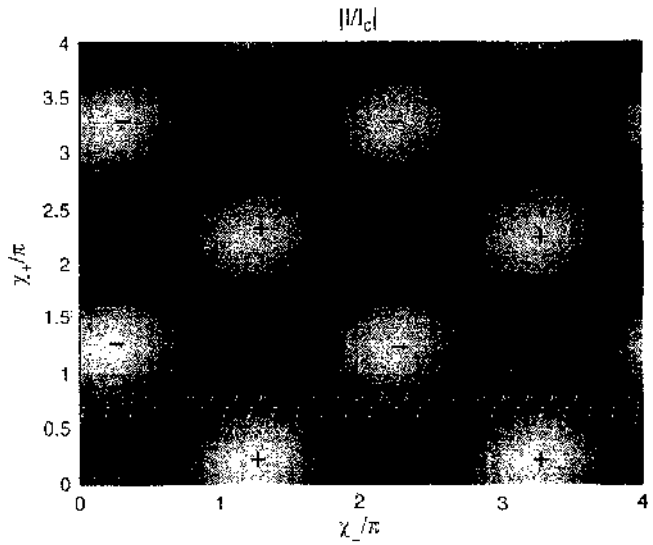

Figure 28. Current through a probe Josephson junction connected between the leads after many rotations. Bright areas correspond to large current, while black ones correspond to zero current. The signs indicate the direction of the current. Reprinted with permission from [62], A. Isacsson et al., *Phys. Rev. Lett.* 89, 277002 (2002). © 2002, American Physical Society.

$\exp(-\gamma_J t_{\parallel} - \gamma_C t_C)$, where $t_C = t - t_{\parallel}$. The supercurrent is also suppressed in the case of weak coupling and $\gamma_J t_{\parallel} \ll \gamma_C t_C$. Consequently, there exists an intermediate region where the decoherence leads to an *enhancement* of the supercurrent. In addition, the decoherence may result in a sign change (π junction). It remains to be seen whether these conclusions are sensitive to damping of the *diagonal* elements of the density matrix.

5. NOISE IN SHUTTLE TRANSPORT

Noise properties are crucial for the performance of nanomechanical systems and have been extensively studied both experimentally and theoretically. In this review, we address only work related to shuttle electron transport.

While many papers were aiming at studies of the conditions for the realization of the shuttle instability or at the dependence of the current on external parameters, at the initial stage only a few papers investigated current fluctuations. However, during the last several years, the interest in current fluctuations have significantly increased and has been shown that the current noise contains much more information about the nature of the shuttle instability then the average current. Indeed, even near equilibrium the noise spectrum allows one to study the AC response of the system *without AC excitation*. Out of equilibrium, the noise spectrum is specifically sensitive to coherence properties of the electron transport, as well as to electron-electron correlations. These two issues lead to several interesting works aimed at various aspects of noise in electron shuttling. We will discuss these works following the scheme of Table 1.

5.1. General Concepts

Before we proceed, let us introduce some basic definitions. The instant current through a device, $I(t)$, differs from its time-averaged value, $\bar{I} \equiv \overline{I(t)}$, and the difference $\Delta I(t) \equiv I(t) - \bar{I}$ is called the *current fluctuation*. The nature of fluctuations is naturally studied by evaluating the correlation function

$$\overline{\Delta I(t)\Delta I(t')} = \overline{I(t)I(t')} - \bar{I}^2$$

In the absence of external time-dependent fields, this correlation function depends only on the time difference, $t - t'$. In addition, for the ergodic systems we are interested in, the time average does not differ from the ensemble average, which we will denote as $\langle \cdots \rangle$. The ensemble average is just the average over the realizations of the random quantity $I(t)$. As a result, the correlation function is conventionally defined as

$$S(\tau) \equiv \langle \Delta I(\tau)\Delta I(0) \rangle \tag{22}$$

The *noise spectrum* is then defined as twice the Fourier transform of the correlation function (see Ref. [73] for a review):

$$S(\omega) \equiv 2\int_{-\infty}^{\infty} d\tau e^{\,i\omega\tau} S(\tau) \tag{23}$$

This is a purely classical definition, which assumes that the current operators commute at different times. In the case of quantum transport, the current is an operator, and in general $\hat{I}(t)$ and $\hat{I}(t')$ do not commute. Then the definition of the correlation function is generalized as

$$S(\tau) = \frac{1}{2}\left\langle \left[\hat{I}(\tau), \hat{I}(0)\right]_+ \right\rangle - \langle I \rangle^2 \tag{24}$$

where $[\hat{A}, \hat{B}]_{\pm} \equiv \hat{A}\hat{B} \pm \hat{B}\hat{A}$. For a small applied voltage, $V \to 0$, the current is proportional to the applied electric field. This implies that $I(\omega) = G(\omega)E(\omega)$, where $G(\omega)$ is the complex conductance of the structure. In this regime, the noise spectrum can be expressed through the real part of the conductance as

$$S(\omega) = \hbar\omega \operatorname{Re} G(\omega) \coth \frac{\hbar\omega}{2k_B T} \approx 2k_B T \operatorname{Re} G(\omega) \tag{25}$$

where the approximate result holds if $\hbar\omega \ll k_B T$; k_B is the Boltzmann constant. The relation (25) is the well-known *fluctuation-dissipation theorem* [74]. In the linear response regime, it follows from Eq. (25) that the noise spectrum provides exactly the same information as the linear conductance. Even in this case, studies of noise can be informative because the noise spectrum allows one to determine the frequency dependence of the conductance without a direct AC excitation.

Nonequilibrium noise ($V \neq 0$) is more interesting because it gives information about temporal correlations of the electrons that cannot be obtained from the conductance. The contribution proportional to the first power of the applied bias voltage is often called the *shot noise*. Such noise has been thoroughly studied in many systems. In devices such as tunnel junctions, Schottky barrier diodes, $p-n$ junctions, and thermionic vacuum diodes [75], the electrons are transmitted randomly and independently of each other. Hence, the transfer of electrons can be described by Poisson statistics, which is used to analyze events that are uncorrelated in time. For these devices, the shot noise has its maximum value at zero frequency,

$$S(0) = 2e\langle I\rangle \equiv S_{\text{Poisson}} \tag{26}$$

and is proportional to the time-averaged current $\langle I\rangle$. This expression is valid for $\omega \ll \tau^{-1}$, where τ is the effective width of a one-electron current pulse, which is determined by the device parameters. For higher frequencies the shot noise vanishes. To characterize the shot noise, the so-called *Fano factor*, $\mathcal{F} \equiv S(0)/2e\langle I\rangle$, is introduced. Correlations suppress the low-frequency shot noise below the Poisson limit, leading to $\mathcal{F} \leq 1$. This suppression is efficiently used to study correlations in the electron transport through mesoscopic devices (see the excellent review articles of Refs. [73, 76]).

Even more interesting information can be extracted by using so-called *full counting statistics* [77], which deals with the probability distribution, $P_t(n)$, of the number of electrons, n, transferred through the system during the measurement time, t. The first and the second moments of this distribution correspond to the average current and the shot-noise correlations, respectively. The probability distribution also contains fundamental information about large current fluctuations in the system.

In the following section, we review work on the noise spectrum and on the full counting (FC) statistics of shuttle transport.

5.2. Incoherent Electron Transport and Classical Mechanical Motion

The case of incoherent electron shuttling involving classical mechanical motion was first addressed by Isacsson and Nord [78]. They considered a model one-dimensional shuttle structure similar to the one shown in Fig. 1(a) and described in detail in Ref. [79]. Accordingly, it was assumed that a metallic grain of mass M and radius r is suspended between two leads by elastic, insulating springs. Applying a bias voltage $V = V_L - V_R$, electron transport occurs by sequential, incoherent tunneling between the leads and the grain. The tunneling rates, $\Gamma^{\mp}_{L,R}(x, q)$, depend on grain position x and charge q through the tunneling matrix elements and the differences in (Gibbs) free energy, $\Delta\mathcal{G}^{\pm}_{L,R}(x, q)$, between the charge configurations $\{q, q_{L,R}\}$ and $\{q \pm e, q_{L,R} \mp e\}$. The electric potentials and charges are determined by using a conventional electric circuit, where the voltage sources V_L and V_R are connected in series with the leads, and the grain as shown in Fig. 29. As a result, the quantities $\Delta\mathcal{G}^{\pm}_{L,R}(x, q)$ are expressed through position-dependent capacitances specified as $C_{L,R}(x) = C^{(0)}_{L,R}/(1 \pm x/a_{L,R})$, where $a_{L,R}$ are characteristic length scales. The tunneling matrix elements are expressed through the position-dependent resistances specified as $R_{L,R}(x) = R^{(0)}_{L,R}e^{\mp x/\lambda}$. In this way, the motion-induced feedback to the stochastic electron hopping is taken into account. Another relationship between the grain charge and displacement is given by Newton's equation of motion, $m\ddot{x} = F(x, \dot{x}, q)$. The force F in this equation contains both elastic and electric components as well as the friction force $\propto \dot{x}$. A new feature is an additional account of the van der Waals force, which turns out to be important [79]. In general, $F(x, \dot{x}, q)$ is a nonlinear function of x and q.

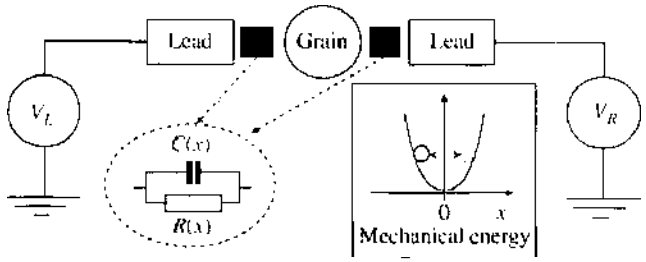

Figure 29. Model one-dimensional shuttle structure and corresponding electric circuit. The inset illustrates how the mechanical energy stored in the grain motion depends on the grain oscillation amplitude.

The results for noise were obtained by direct numerical integration of a set of equations, including the master equation for the grain population with $\{x, q\}$-dependent hopping rates and anharmonic mechanical equation of motion. A typical noise spectrum is shown in Fig. 30. The spectrum in this figure can be divided in four regions marked as I–IV. At the high frequencies of region, IV, the Fano factor is close to 0.5, which is the value one obtains for a static double junction [73]. In region III, two strong peaks are located at the vibration frequency and its harmonic. This is a result of the periodic charging and decharging of the oscillating grain. Directly below the peaks, in region II, the noise is suppressed below the shot noise level of a static double junction because of the additional time correlations between successive tunnel events induced by the oscillating grain. This is a clear hallmark of classical shuttling.

The most interesting part of the spectrum, however, is the low-frequency part in region I, where the Fano factor increases as the frequency decreases. The authors attribute this increase to low-frequency fluctuations in the mechanical energy, which, in turn, lead to low-frequency fluctuations in the current.

The authors have also performed an analytical stability analysis valid in the case of weak electromechanical coupling (i.e., for $\epsilon \equiv F(x = 0, q = e)/m\omega_0^2\lambda \ll 1$). The instability increment, $p(E) = \mathcal{W}(E) - \mathcal{D}(E)$, is determined by the difference between the energy, $\mathcal{W}(E)$, pumped into the mechanical motion during one period and the average energy dissipated per period, $\mathcal{D}(E)$. Hence, the stationary oscillation amplitude is determined by the equation $p(E_0) = 0$. Since $p(E)$ depends both on the bias voltage and the damping of the mechanical motion, this equation actually determines the dependence of the oscillation amplitude on the bias voltage. It has a finite solution only above the instability threshold.

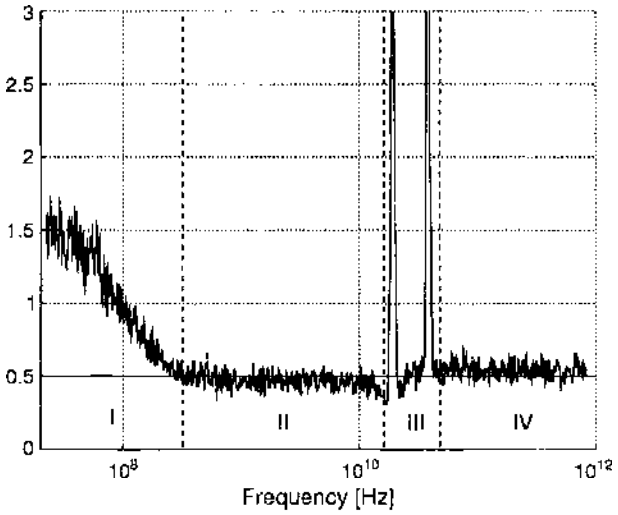

Figure 30. Power spectrum $S(\omega)$ in the shuttle regime. For frequencies above the vibrational frequency, the Fano factor is close to 0.5 as for a static Coulomb-blockade junction. The peaks are located at the frequency of vibration and at the first harmonic. For frequencies below the vibrational frequency, the temporal correlation due to the periodic grain motion leads to a slight suppression of the noise level. At still lower frequencies, the noise is increased due to slow fluctuations in mechanical energy. Reprinted with permission from [78], A. Isacsson and T. Nord, *Europhys. Lett.* 66, 708 (2004), © 2004, EDP Sciences.

The analysis, following the conventional procedure [80], takes into account the fluctuations in the mechanical energy around, say $E = E_0$. These fluctuations induce electrical noise with a Lorentzian spectrum, $S(\omega) \propto (\nu^2 + \omega^2)^{-1}$. The width ν of the spectrum is proportional to $|p'(E_0)|$, where $p'(E_0) \equiv \partial p/\partial E|_{E=E_0}$. Since at the instability threshold $p'(E_0) \to 0$ [18], the noise spectrum diverges while approaching the instability threshold from the "shuttling" side.

The results of numerical studies corresponding to a nanometer-sized Au grain commonly used in experiments with self-assembled Coulomb-blockade double junctions are shown in Fig. 31. Although, as explained in Ref. [79], the non-parabolic confining potential smears any step-structure in the current-voltage characteristics, the transition between static and shuttle operation is clearly visible in the noise spectrum. In accordance with the analytical result, on approaching the threshold from above (going from higher to lower voltages), the noise spectrum $S(\omega)$ shows a divergent behavior. Below the threshold voltage the Fano factor is of the order 1/2.

A rather unusual prediction is that in the shuttle regime, well above the threshold voltage, the Fano factor is increased. This fact is attributed to the anharmonicity of the potential. For the harmonic potential used in the analytical treatment the lowered noise level in region II is continued into region I.

5.3. Noise in a Quantum Shuttle

We will review a theory by Novotny et al. [81] for shot noise in a quantum shuttle. The theory extends previous work of the authors [41] in which they considered the average current. It is assumed that the shuttling grain has two electron charge states, $|0\rangle$, and $|1\rangle$, and that only the diagonal elements of the density matrix in the $|i\rangle$-representation are important. To calculate the noise, the *number-resolved* diagonal density matrices, $\rho_{ii}^{(n)}(t)\,\delta_{ik}$, are introduced. Here n is the number of electrons which have tunneled to the right electrode by time t. These matrices obey a generalized master equation where tunneling into the leads is described by position-dependent transition rates $\Gamma_{L,R}$. In addition, damping of the oscillator motion due to interacting with a thermal bath is taken into account.

Knowing $\rho_{ii}^{(n)}(t)$, one finds the probability for n electrons to be shuttled as

$$P_n(t) = \mathrm{Tr}_{\mathrm{osc}} \sum_{i=0,1} \rho_{ii}^{(n)}(t)$$

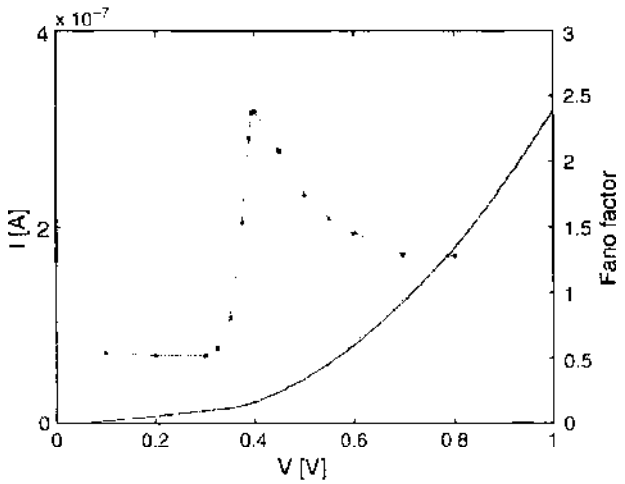

Figure 31. Current-voltage characteristics plotted together with the Fano factor characterizing the noise spectrum in the static limit ($\omega \to 0$). The current is the solid line with the scale on the left ordinate, while the Fano factor is shown for a discrete set of points with the scale on the right ordinate (lines connecting the points are a guide to the eye). Below the critical voltage where there is no sustained grain motion, the Fano factor is that of a Coulomb-blockade double junction. Above the critical voltage, the grain is oscillating and the Fano factor is increased and shows a divergent behavior at the critical voltage. Reprinted with permission from [78], A. Isacsson and T. Nord, *Europhys. Lett.* 66, 708 (2004). © 2004, EDP Sciences.

The calculation of the average current and noise is then straightforward:

$$I = e \lim_{t\to\infty} \sum_n n\dot{P}_n(t)$$

$$S(0) = 2e^2 \lim_{t\to\infty} \frac{\mathrm{d}}{\mathrm{d}t}\left[\sum_n n^2 P_n(t) - \left(\sum_n nP_n(t)\right)^2\right]$$

The relevant elements of the density matrix were found using the generating functional concept, and both the average current and the Fano factor were calculated for different relationships between the characteristic tunneling length, λ, and the amplitude of quantum zero-point oscillations, x_0, as well as for different ratios γ/ω_0. The numerical results agree with an analytical treatment valid for small injection rates. The results are summarized in Fig. 32.

The plot of I versus γ in Fig. 32 shows a crossover from tunneling to shuttling as damping is decreased, in agreement with previous results. The crossover spans a narrower range of γ-values in the case of $\lambda/x_0 = 2$ compared with the $\lambda/x_0 = 1$ case. Thus, already for $\lambda/x_0 = 2$, the shuttle behaves almost semiclassically, where a relatively sharp transition between the two regimes is expected. There is no abrupt transition from tunneling to shuttling, however, and near the transition these regimes can coexist. To demonstrate this phenomenon, the Wigner distribution functions (7) were calculated following Ref. [41]. The results are shown in Fig. 33, where a pure classical motion would correspond to a sharp classical phase trajectory for W_{tot}, which for an oscillator is a circle. The radial smearing of the circle that can be seen corresponds to quantum fluctuations. In addition, one clearly sees a spot in the center that corresponds to tunneling through a static grain. Thus the motion has a complex character showing features corresponding to both the classical and the quantum regimes. The semiclassical transition is accompanied by the nearly singular behavior of the Fano factor reaching the value ≈ 600 at the peak. This is in agreement with the classical study [78] discussed previously.

A result that is different in the quantum-mechanical analysis compared with the classical study is that the predicted enhancement of the Fano factor in the classical shuttling regime compared with the tunneling regime [78] is not reproduced. It remains to be clarified whether this discrepancy is due to the different models for the confining mechanical potential used: it was assumed to be anharmonic in Ref. [78] but harmonic in Ref. [81].

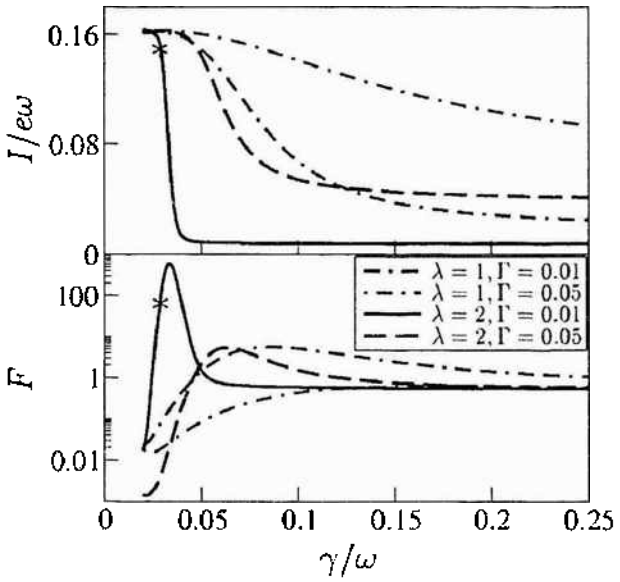

Figure 32. Current I (upper panel) and Fano factor F (lower panel; log scale) versus damping γ for different transfer rates $\Gamma = \Gamma_L = \Gamma_R$ and tunneling lengths λ. γ and Γ are measured in units of ω_0; λ is measured in units of x_0. Other parameters are $eE = m/\omega_0^2 = 0.5x_0$ and $T = 0$. The asterisk defines the parameters of Wigner distributions in Fig. 33. Reprinted with permission from [81], T. Novotny et al., *Phys. Rev. Lett.* 92, 248302 (2004). © 2004. American Physical Society.

Figure 33. Phase-space picture of the shuttle around the transition where the shuttling and tunneling regimes coexist. From left to right, we show the Wigner distribution functions for the discharged, W_{00}, charged W_{11}, and both states, $W_{tot} = \sum_{n=0,1} W_{nn}$, of the oscillator in the phase space. The values of the parameters correspond to the asterisk in Fig. 32. Reprinted with permission from [81], T. Novotny et al., *Phys. Rev. Lett.* 92, 248302 (2004). © 2004, American Physical Society.

5.4. Driven Charge Shuttle

The noise properties of a *driven* charge shuttle [14] are much simpler to account for than those of a self-oscillating shuttle. Here the mechanical energy is conserved and does not fluctuate, so the only source of noise is random electron transfer.

The average number of electrons transferred by a driven shuttle *per one cycle* as as well as its variance were considered by Weiss and Zwerger [21] in connection with a discussion of the accuracy of a mechanical single-electron shuttle (see Section 2.1.4). The variance $\overline{\Delta n} \equiv \langle n^2 - \overline{n}^2 \rangle^{1/2}$ was found using a conventional master equation approach with the tunneling probabilities given by the "orthodox theory" (see Ref. [82] for a review). A typical plot of $\overline{\Delta N}$ versus V is shown in Fig. 5 (lower panel), and the main conclusion is that the variance is small at low temperatures, $k_B T \ll e^2/2C$, and for relatively long contact times, $t_0 \gg RC$.

However, the variance $\overline{\Delta n}$ differs from the noise actually measured because typical measurement times are much longer than one period of oscillation. This case was addressed by Pistolesi in Ref. [83], where both the zero-frequency noise and the FC statistics of the transferred charge were considered.

To find the statistics of the transferred charge, one needs the probabilities for n electron to be transferred, $P_n(t)$, for *all* n. They can be calculated using an elegant formalism involving a generating functional [77]. The generating functional is defined as

$$e^{-\mathcal{G}_t(\chi)} = \sum_{n=0}^{\infty} P_t(n)\, e^{in\chi} \tag{27}$$

where χ is *the counting field*. Then all cumulants of the transferred charge can be calculated as

$$\overline{n} = \langle n \rangle = i \frac{\partial \mathcal{G}}{\partial \chi}\bigg|_{\chi=0}, \quad \langle n^2 - \overline{n}^2 \rangle = \frac{\partial^2 \mathcal{G}}{\partial \chi^2}\bigg|_{\chi=0} \tag{28}$$

and so on. The explicit calculation uses the method developed in Ref. [84] with a proper generalization to the dynamic case. It is assumed that the shuttle has two states with 0 or 1 excess electron. The probability to find the shuttle in one of these states can be expressed as a vector $|p\rangle$ with components $\{p_0, p_1\}$. The dynamics of $|p(t)\rangle$ is governed by the Liouville equation

$$\frac{\partial}{\partial t}|p(t)\rangle = \hat{L}\,|p(t)\rangle\,, \quad \hat{L} = \begin{pmatrix} \Gamma_L(t) & -\Gamma_R(t) \\ -\Gamma_L(t) & \Gamma_R(t) \end{pmatrix} \tag{29}$$

The generating functional can be expressed as

$$e^{-\mathcal{G}_t(\chi)} = \left\langle q \middle| T \exp\left\{ -\int_0^t \hat{L}_\chi(t')\, dt' \right\} \middle| p(0) \right\rangle \tag{30}$$

where $|p(0)\rangle$ is the probability at time $t = 0$, $|q\rangle \equiv \{1, 1\}$, and Texp is the time ordered exponential. The matrix $\hat{L}_\chi(t)$ is constructed from the matrix $\hat{L}(t)$ by multiplying the lower

off-diagonal matrix element by the factor $e^{i\chi}$. Time ordering is very important because the matrices $\hat{L}_\chi(t)$ do not commute for different times.

The generating functional (30) was analyzed numerically as well as analytically for the limiting cases of small and large oscillation amplitude a. In the static case, $a = 0$, and for a symmetric shuttle with $\Gamma_L = \Gamma_R = \Gamma^{(0)} \exp(\mp a \sin \omega_0 t)$, the known result [85] for a static tunneling system is reproduced:

$$\ln_t(\chi) = -\Gamma^{(0)} t(e^{i\chi/2} - 1) \tag{31}$$

In this case, $I = S(0) = \pi\omega_0\Gamma^{(0)}$, and the Fano factor $F = 1/2$.

In the opposite limit of large shuttle oscillation amplitude the ratio Γ_L/Γ_R is most of the time either very large or very small. This is why it was assumed that (i) for $0 < \omega_0 t < \pi$ the quantity Γ_L vanishes identically and (ii) for $\pi < \omega_0 t < 2\pi$ the opposite holds: $\Gamma_R = 0$. The approximation becomes exact for $\Gamma \ll \omega_0$ because, in that case, electrons can tunnel only when the shuttle is near one of the two leads. Under this assumption, the problem can be treated analytically, the result being

$$I = e\frac{1-\alpha}{1+\alpha} \quad S(0) = 4e^2\alpha\frac{1-\alpha}{(1+\alpha)^3} \;\rightarrow\; F = \frac{2\alpha}{(1+\alpha)^2}$$

Here the quantity $1 - \alpha$ with

$$\alpha = \exp\left(-\frac{\Gamma^{(0)}}{\omega_0}\int_0^\pi d\phi\, e^{a\sin\phi}\right)$$

is the probability of transferring one electron during half a cycle. For $a \ll 1$, this probability is nearly 1, and the generating function

$$e^{-\ln_t(\chi)} = [2\alpha + (1-2\alpha)\, e^{i\chi}]^{\omega_0 t/2\pi} \tag{32}$$

corresponds to a binomial distribution

$$P_n(N) = \binom{N}{n}(1-2\alpha)^n(2\alpha)^{N-n}$$

where $N(t) = [\omega_0 t/2\pi]$ is the number of oscillation cycles during the measurement time t. This is a very clear result because during each cycle one electron is transmitted with probability $1 - 2\alpha$ and because $\alpha \ll 1$ the cycles are independent. Indeed, after each cycle, the system is reset to the stationary state within accuracy α^2, regardless of the initial state. This limiting case agrees with the results of Ref. [21], where the variance of the charge transfer during one cycle was analyzed.

For $\alpha \to 1$, the probability for one electron to tunnel during a cycle is very small. The result for this case reads as

$$e^{-\ln_t(\chi)} = [\alpha + (1-\alpha)e^{i\chi/2}]^{\omega_0 t/2\pi} \tag{33}$$

One can notice that the periodicity of the generating function has changed. Equation (33) describes a system of $e/2$ charges that in each cycle are transmitted with probability $1 - \alpha$. Thus the system can be mapped on a fictitious system of charges $e/2$ such that every time one electron succeeds in jumping on or off the central island, one charge $e/2$ is transmitted in the fictitious system. This is possible because it is extremely unlikely that one electron can perform the full shuttling in one cycle. Thus after many cycles ($N \gg 1$), the counting statistics of these two systems coincide. The cycles are no more independent as in the case when $\alpha \ll 1$, but the problem can be mapped onto an independent tunneling problem. For intermediate values of α it is more difficult to give a simple interpretation of the charge transfer statistics because, different cycles are correlated in a nontrivial way.

The FC statistics of nanoelectromechanical systems was recently addressed by Flindt et al. [86]. The authors have developed a generalized theory applicable to a broad class of nanoelectromechanical systems that can be described by a generalized Markovian Master equation. Concrete calculations are made for the models of Refs. [32] and [41, 42, 81]. The three first cumulants are evaluated numerically. For the quantum shuttle [41, 42, 81], the behavior of the third cumulant is shown to be compatible with the concept of slow switching between the tunneling and the shuttling regime. This concept was earlier [81] used to predict n-enhanced noise spectrum at the shuttling transition.

Generally, both the noise and the FC statistics demonstrate a very rich and interesting behavior. This permits us to understand more deeply the charge transfer dynamics and to characterize the threshold for the shuttle instability with greater accuracy.

5.5. Noise in Cooper Pair Shuttling

Noise in Cooper pair shuttling between two superconductors is particularly interesting because it allows one to better understand the coherent properties of superconductor devices. At present, only driven superconducting shuttle systems have been considered. Their noise properties were first considered by Romito et al. [72].

The main purpose of Ref. [72] was to analyze environmentally induced decoherence, the noise being a by-product of a general analysis of the Cooper pair shuttling dynamics. The basic model is similar to that of Refs. [61, 62]. In addition, a finite coupling to a thermal bath was taken into account along the lines of the Caldeira-Legget model (for a review, see Ref. [87]). In the Born-Markov approximation, the coupling to the heat bath results in a damping of the density matrix, which is assumed to be different in the tunneling region and in the region of free motion and characterized by the damping coefficients γ_J and γ_C, respectively.

The results for both the average current and the noise are strongly dependent on the products $\gamma_J t_0$ and $\gamma_C t_C$, where t_C is the time of free motion between the leads. Strong decoherence occurs if $\gamma_J t_0 \gg 1$ or $\gamma_C t_C \gg 1$, whereby the details are dependent on the ratio $\gamma_J t_0/\gamma_C t_C$. Naturally, with strong decoherence, the phase-dependent contribution to $S(0)$ is exponentially suppressed because it comes from correlations over times larger than one oscillation period. At $\gamma_J t_0 \gg 1$, the zero-frequency noise is given by the expression

$$S(0) = \frac{\omega_0 e^2}{\pi} \frac{2\gamma_J E_J}{E_J^2 + \gamma_J^2}$$

This contribution is due to the damped oscillations in the contact regions (L, R).

In the case of weak damping, $\gamma_J t_0 \ll \gamma_C t_C \ll 1$, one finds

$$\begin{aligned} I &= \frac{e\omega_0}{\pi} \tanh\left(\frac{E_J}{k_B T}\right) \frac{(\cos\Phi + \cos 2\chi)\tanh\vartheta \sin\Phi}{1 + \cos\Phi\cos 2\chi} \\ S &= \frac{e^2\omega_0}{\pi} \frac{1}{\gamma_C t_C} \frac{\tanh^2\vartheta \sin^2\Phi}{1 + \cos\Phi\cos 2\chi} \end{aligned} \tag{34}$$

which shows a rich structure as a function of the phases ϑ and χ.

The FC statistics of Cooper pair transfer was considered by Romito and Nazarov [88]. The authors focus on the *incoherent* regime, where coherence is suppressed by classical fluctuations in the gate voltage, and no net supercurrent is shuttled. However, charge transfers occur, and the current is zero only in average. Thus the FC statistics provides a convenient method to reveal this circumstance.

The basic model for the superconducting shuttle in Ref. [88] is similar to that of Refs. [61, 62]. Fluctuations of the gate voltage are allowed for by assuming stochastic "white noise" fluctuations,

$$\langle V_g(t)\rangle = V_g, \quad \langle V_g(t)V_g(t') - V_g^2\rangle = \frac{\gamma\hbar^2}{4e^2}\delta(t - t')$$

Thus defined, γ has the meaning of a decoherence rate for the two charge states. It leads to a damping of the *off-diagonal* elements of the density matrix, while diagonal elements are assumed to be undamped. The FC statistics is computed using the generating function method.

The physics of charge transfer could be clearly understood for the limiting cases of long and short cycles comparing to the decoherence time. If the shuttling period is sufficiently long for decoherence to be accomplished,

$$t_C^{-1}, t_0^{-1} \ll \gamma \ll \frac{E_J}{\hbar}$$

the FC statistics can be interpreted in terms of classical elementary events: Cooper pair transfers. During the shuttling cycle, either no transfer takes place or one pair is transferred in either direction. There is an apparent similarity with the FC statistics of the pumping in normal systems studied in Refs. [77, 89, 90]. In this case

$$p_0 = \frac{1}{2} \quad p_{+2} = \frac{1}{4}$$

so that each shuttling between the superconductors transfers either one Cooper pair or none, this occurs with equal probability. The pair is transferred with equal probabilities in either direction. This simple result is quite general and relies neither on the periodicity of shuttling nor the concrete time dependence of $E_J(t)$, provided adiabaticity is preserved. Leading corrections to the adiabatic FC statistics are exponentially small, $\sim e^{-2\gamma t_0}$.

Adiabaticity is also preserved for small Josephson couplings, where $E_J \ll \hbar\gamma$ provided

$$t_C^{-1}, t_0^{-1} \ll \gamma$$

In this case, the factor $f \equiv e^{t_0 E_J^2/\hbar^2\gamma}$ can be arbitrary, and the FC statistics becomes more complicated [88]. For finite f, all $p_n \neq 0$ but remain positive definite. In the adiabatic limit, the FC statistics does not depend on the superconducting phase Φ or the dynamical phases ϑ and χ.

Beyond the adiabatic limit, the FC statistics does depend on Φ, and a classical interpretation in this case can fail since p_n can be negative or even complex. A relatively simple treatment is possible in the case of very short shuttling periods, $\gamma/\omega_0 \ll 2\pi$. The FC statistics in this case corresponds to a supercurrent that randomly switches between the values $\pm I_s$ on the time scale $1/\tilde{\gamma}$. The quantities $\tilde{\gamma}$ and I_s depend on the phases Φ, ϑ, and χ, the detailed form of these dependencies being given in Ref. [88], (see also Ref. [91]).

To summarize, in the limiting cases of long and short shuttling periods, the FC statistics allows for relative simple classical interpretations. In an intermediate situation, the FC statistics cannot be interpreted in classical terms because the charge transfer probabilities per cycle may be negative or complex. This is a clear signature of the fact that superconducting coherence survives strong dephasing although this coherence does not manifest itself in a net superconducting current.

One can conclude that both the noise spectrum (second cumulant) and the FC statistics provide valuable information about shuttle transport, which is complimentary to the information that can be extracted from the average current. It is a combination of the features of the average current and the noise that can assure that shuttling can be identified as the underlying transport mechanism.

6. DISCUSSION AND CONCLUSION

While designing nanometer-sized devices one inevitably has to face the effects of Coulomb correlations on the electron transport properties. The most peculiar feature of such correlations is known as single-electron tunneling, which determines the transport properties of many interesting nanodevices. Furthermore, in nanosystems, electric charges produce not only large potential differences but also large mechanical forces that can be comparable with interatomic forces in solids. These forces tend to produce mechanical displacements

that, in turn, lead to a feedback to the distribution of electric charges. As a result, coupling of electrical and mechanical degrees of freedom is a hallmark of nanodevices. The aim of this review is to demonstrate one fundamental manifestation of such coupled motion—the *shuttle* transfer of charge due to the conveying of electrons by a movable part of the nanosystem. Shuttling of charge can occur either because of an intrinsic instability or an external AC source. From an "applied" point of view, the role of shuttling can be either positive or negative. Indeed, it can hinder a proper operation of a single-electron transistor at the nanometer scale. However, an intentionally periodic mechanical motion resulting from a designed instability can be used to create building blocks for new applications. In particular, new principal possibilities for generators and sensors at nanometer scale appear.

As we have tried to show, the research area centered around the shuttle instability involves several new principles and possibilities. Thus, there is a wealth of interesting physics to be explored containing both coherent and incoherent electron transport facilitated by either classical or quantum mechanical motion. In particular, one can expect very interesting physics regarding the coherent shuttling of Cooper pairs over relatively large distances as well as the creation of quantum coherence between remote objects by movable superconducting grains. This system, if realized experimentally, would allow for a determination of the decoherence rate of superconducting devices due to their interaction with environment.

One can imagine several concrete systems where electromechanical coupling is very important. Among them are nanoclusters or single molecules that can vibrate between leads they bind to, metal-organic composites showing pronounced heteroelastic properties, colloidal particles, and so on. The likelihood that a similar physical picture is relevant for the coupling of *magnetic* and mechanical degrees of freedom will certainly lead to new phenomena and devices. In the latter case, the coupling is due to exchange forces, and it can lead to shuttling of magnetization.

There are a few experiments where electromechanical coupling has been observed and some evidence in favor of single-electron shuttling was presented. The complete experimental proof of the single-electron shuttle instability remains still a challenging problem. To solve this problem in a convincing way, it seems to be a good idea to study the anomalous structure of the Coulomb blockade in nanomechanical structures with and without gates, as well as to detect periodic AC currents.

Both experimental and theoretical studies of shuttle charge transfer are under development, and new works regularly emerge. In particular, a general approach to shuttling based on an analysis of Breit-Wigner resonances in an electronic circuit was developed in a recent preprint [92].

To summarize, movable nanoclusters can serve as new weak links between various normal, superconducting, and magnetic systems, leading to new functionalities of nanostructures.

ACKNOWLEDGMENTS

This work was supported in part by the European Commission through project FP6-003673 CANEL of the IST Priority. The views expressed in this publication are those of the authors and do not necessarily reflect the official European Commission's view on the subject. Financial support from the Swedish Foundation for Strategic Research, from the Swedish Research Council, and from the U.S. Department of Energy's Office of Science through contract no. W-31-109-ENG-38 is also gratefully acknowledged. Discussions with V. I. Kozub have been greatly appreciated.

APPENDIX A: COULOMB BLOCKADE: REVIEW OF THE "ORTHODOX" THEORY

Here we give a brief review of the so-called *orthodox* theory of Coulomb blockade [12]. Consider a dot coupled to two leads via tunnel barriers. If one transfers the charge q from the source to the grain, the change in the energy of the system is

$$\Delta U = qV_x + \frac{q^2}{2C}$$

Here the first item is the work by the source of the gate voltage, while the second one is the energy of Coulomb repulsion at the grain. We describe it by the effective capacitance C to take into account polarization of the electrodes. The graph of this function is the parabola with the minimum at

$$q = q_0 = -CV_g$$

So it can be tuned by the gate voltage V_G. Now let us remember that the charge is transferred by the electrons with the charge e. Then, the energy as a function of the number n of electrons at the grain is

$$\Delta U(n) = neV_g + \frac{n^2e^2}{2C}$$

Now let us estimate the difference

$$\Delta U(n+1) - \Delta U(n) = eV_g + n\frac{e^2}{C} + \frac{e^2}{2C}$$

We observe that at certain values of V_g,

$$V_{gn} = -(2n+1)\frac{e}{2C} \tag{A1}$$

the difference vanishes. It means that only at that values of the gate voltage resonant transfer is possible. Otherwise one has to pay for the transfer that means that only inelastic processes can contribute. As a result, at

$$k_BT \leq \frac{e^2}{2C}$$

the linear conductance is exponentially small if the condition (A1) is met. This phenomenon is called the *Coulomb blockade of tunneling*. As a result of the Coulomb blockade, electrons tunnel *one-by-one*, and the conductance versus gate voltage dependence is a set of sharp peaks. That fact allows one to create a so-called *single-electron transistor* (SET), which is now the *most sensitive* electrometer. Such a device (as was recently demonstrated) can work at room temperature provided the capacitance (size!) is sufficiently small. Below we shall review the simplest variant of the theory, so-called the *orthodox model*.

For simplicity, let us ignore the discrete character of the energy spectrum of the grain and assume that its state is fully characterized by the number n of excess electrons with respect to an electrically neutral situation. To calculate the energy of the systems let us employ the equivalent circuit shown in Fig. 34. The left (emitter) and right (collector) tunnel junctions are modeled by resistances and capacitances in parallel.

Charge conservation requires that

$$-ne = q_e + q_c + q_g = C_e(V_e - V) + C_c(V_c - V) + C_g(V_g - V) \tag{A2}$$

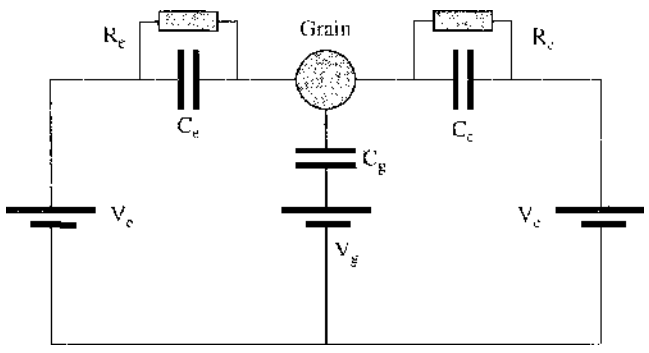

Figure 34. Equivalent circuit for a single-electron transistor. The gate voltage, V_g, is coupled to the grain via the gate capacitance, C_g. The voltages V_e and V_c of emitter and collector are counted from the ground.

where V is the potential of the grain. The effective charge of the grain is hence

$$q_n = CV = ne + \sum_{i=e,c,g} C_i V_i, \quad C \equiv \sum_i C_i$$

This charge consists of four contributions, the charge of excess electrons and the charges induced by the electrodes. The electrostatic energy of the grain is then $U_n = q_n^2/2C$. To organize a transport of one electron, one has to transfer it first from emitter to grain and then from grain to collector. The energy cost for the first transition,

$$U_{n+1} - U_n = \frac{(2n+1)e^2}{2C} + \frac{e}{C}\sum_i C_i V_i \tag{A3}$$

must be less than the voltage drop eV_e. In this way, we come to the criterion

$$U_n - U_{n+1} + eV_e \geq 0 \tag{A4}$$

Similarly, to organize the transport from grain to collector we need

$$U_{n+1} - U_n - eV_c \geq 0 \tag{A5}$$

The inequalities (A5) and (A4) provide the relations between V_e, V_c, and V_g to make the current possible. For simplicity, let us consider a symmetric system. Here

$$G_e = G_c = G, \; C_e = C_c \approx \frac{C}{2}, \; V_e = -V_c = \frac{V_b}{2}$$

where V_b is bias voltage. We have taken into account that $C_g \ll C_e, C_c$. Then we get the criterion

$$V_b \geq (2n+1)\frac{e}{C} - V_g\frac{2C_g}{C}$$

We observe that there is a threshold voltage that is necessary to exceed to organize transport. This is a manifestation of *Coulomb blockade*. It is important that the threshold linearly depends on the gate voltage that makes it possible to create a transistor. Of course, the above considerations are applicable at zero temperature.

The current through the emitter-grain transition can be expressed through the probability, p_n, to find n excess electrons at the grain and transition rates, $\Gamma_{g\leftrightarrow e}$. We have

$$I = e\sum_n p_n(\Gamma_{e\to g} - \Gamma_{g\to e}) \tag{A6}$$

The tunneling rates can be calculated from the golden rule expressions using tunneling transmittance as perturbations. For a symmetric case, the expressions for these rates are given in Appendix B, Eq. (B7). At low temperatures and low bias voltages, $V_b C/e < 1$, only two charge states play a role. At larger bias voltage, more charge states are involved. As a result, the current-voltage curve shows steps called the *Coulomb staircase*.

APPENDIX B: SHUTTLE INSTABILITY FOR WEAK ELECTROMECHANICAL COUPLING

1. Model and Basic Equations

Consider a simple model particle with charge $q = en$ and mass m placed in an one-dimensional harmonic confining potential $k_0 x^2/2$. Assuming that the particle motion is damped by a viscous friction described by the force $-m\gamma\dot{x}$ one arrives at the following equation of motion:

$$m\ddot{x} = -k_0 x - m\gamma\dot{x} + e\mathcal{E}n \tag{B1}$$

For small oscillations the electrical field $\mathscr{E}$ can be considered as position-independent and proportional to the bias voltage V. We put $\mathscr{E} = V/L$, and in this way define the effective length, L, of the system. In the absence of electromechanical coupling, this equation describes harmonic oscillations with the frequency $\omega_0 = \sqrt{k_0/m}$ and amplitude damping $\gamma/2$. Hereby we assume that the damping is weak, $\gamma \ll \omega_0$.

Let us multiply Eq. (B1) by $\dot{x}$ and average over a long time Θ equal to a large integer number of periods, $\Theta = 2\pi N/\omega_0$, which is also much greater than the electron transfer time $t_R = RC$. In this way, one obtains the energy balance for the *mechanical* energy $U = m\overline{\dot{x}^2}/2 + k_0\overline{x^2}/2$ as

$$\dot{U} = e\mathscr{E}\overline{n\dot{x}} - m\gamma\overline{\dot{x}^2} \tag{B2}$$

The first item in the right-hand side, $W \equiv e\mathscr{E}\overline{n\dot{x}}$, is the work produced by the electric field, while the second one is the viscous dissipation. This is actually a *stochastic* equation since the electron transfer occurs via *random* electron hops.

Obviously, an instability would correspond to $\dot{U} > 0$. The analysis can be substantially simplified for a *weak* electromechanical coupling. Then, one can assume that the mechanical energy grows much *slower* that both the grain and the electron move. In this case, the averages in the right-hand side can be calculated assuming that the grain performs small harmonic oscillations that conserved the mechanical energy. This assumption is valid if the averaging time is still less that the typical instability growth time, $t_g \equiv U/\dot{U}$, which we will estimate later. Thus we chose

$$1, \omega_0 RC \ll N \ll \omega_0 t_g \tag{B3}$$

There are two consequences of the coupling weakness. First, the average kinetic and potential energies are equal, $m\langle\dot{x}^2\rangle/2 = k_0\langle x^2\rangle = U/2$. Second, one can split the time average $\overline{n(t)\dot{x}(t)}$ into an average over a period of oscillating motion and a subsequent average over different periods:

$$\begin{aligned}\overline{n(t)\dot{x}(t)} &= \frac{\omega_0}{2\pi N}\int_t^{t+2\pi N/\omega_0} \mathrm{d}t' n(t')\dot{x}(t') \\ &= \frac{1}{N}\sum_{k=1}^{N}\frac{\omega_0}{2\pi}\int_{t+2\pi(k-1)/\omega_0}^{t+2\pi k/\omega_0} \mathrm{d}t' n(t')x(t')\end{aligned}$$

This expression only weakly depends on t through a weak time dependence of the oscillation amplitude, and under conditions of Eq. (B3) this dependence can be ignored.

Since $n(t)$ is a random quantity and $N \gg 1$, one can replace the average over the periods by an *ensemble* average, $\langle n\rangle_t$, introducing a probability $p_n(t)$ to find n excess electrons at the grain at time t. Thus,

$$\begin{aligned}&\overline{n(t)\dot{x}(t)} = \langle\langle n\rangle_t \dot{x}(t)\rangle_{\mathrm{osc}} \\ &\langle n\rangle_t \equiv \textstyle\sum_n n p_n(t), \quad \langle b\rangle_{\mathrm{osc}} \equiv \frac{\omega_0}{2\pi}\int_0^{2\pi/\omega_0}\mathrm{d}t'\, b(t')\end{aligned} \tag{B4}$$

As a result, we arrive at the following energy balance equation:

$$\dot{U} = e\mathscr{E}a\,\langle\langle n\rangle_t \cos\omega_0 t\rangle_{\mathrm{osc}} - \gamma U \tag{B5}$$

where it is assumed that $x(t) = a\sin\omega_0 t$ and the amplitude a is essentially time independent at the scale of ω_0^{-1}.

To calculate the distribution function $p_n(t)$, one has to specify the transition rates $\Gamma^{\pm}(n, x)$ for the processes $\{n \to n \pm 1\}$ occurring at a position x. Knowing these probabilities one can find $p_n(t)$ from the master equation

$$\frac{\partial p_n}{\partial t} = \Big[\Gamma^{-}(n+1, x)p_{n+1} + \Gamma^{+}(n-1, x)p_{n-1} - p_n\sum_{\pm}\Gamma^{\pm}(n, x)\Big]_{x=a\sin\omega_0 t} \tag{B6}$$

To specify the probability, one has to take into account that an electron can arrive from and escape to any of the electrodes. Thus

$$\Gamma^{\pm}(n, x) = \Gamma_L^{\pm}(n, x) + \Gamma_R^{\pm}(n, x)$$

where $\Gamma_L^{+}(n, x)$ is the probability for an electron to hop on the grain *from the left* electrode while $\Gamma_R^{-}(n, x)$ is the probability to hop *from the right* electrode. These partial probabilities are strongly influenced to the Coulomb blockade and can be expressed as

$$\begin{aligned}
\Gamma_L^{(\pm)} &= \frac{1}{RC} e^{-x/\lambda} f\left(\pm\frac{v}{2} \mp n - \frac{1}{2}\right) \\
\Gamma_R^{(\pm)} &= \frac{1}{RC} e^{-x/\lambda} f\left(\pm\frac{v}{2} \pm n - \frac{1}{2}\right) \\
f(z) &\equiv \frac{z}{1 - \exp(-\beta E_C z)}
\end{aligned} \tag{B7}$$

Here we assume that the system is symmetric; the capacitances between the grain and both leads are position-independent, $C_R = C_L = C$, while tunneling resistances depend on x exponentially, $R_{L,R}(x) = R e^{\mp x/\lambda}$. The dimensionless voltage v is defined as VC/e, while β^{-1} is the temperature. At low temperatures, $\beta E_C \gg 1$, the function $f(z) \approx z\Theta(z)$ where $\Theta(z)$ is the Heaviside unit step function. This implies quantization of the grain charge [12].

Here will discuss the simplest case of low temperature, and when the voltage is chosen at the point where a new channel is about to switch on, $v_n = 2n + 1$. In this case, one can directly calculate the ensemble average $\langle n \rangle_t \equiv \sum_n n p_n(t)$ from the differential equation [93]:

$$RC\frac{\partial \langle n \rangle_t}{\partial t} = -2\langle n \rangle_t \cosh\left(\sqrt{\frac{U}{U_0}} \sin\omega_0 t\right) + (1 - v)\sinh\left(\sqrt{\frac{U}{U_0}} \sin\omega_0 t\right) \tag{B8}$$

Here $U_0 \equiv m\omega_0^2\lambda^2/2$ is a typical scale for the mechanical energy. Thus, the produced work depends on the mechanical energy itself and on the bias voltage, v. To estimate a typical scale of this work, let us recall that the transition probabilities (B7) introduce a natural scale, e/C for the bias voltage and a typical scale, λ, for the displacement x. Thus, a typical scale for the quantity $e\mathcal{E}$ can be written as ve^2/CL. Since both v and n are of the order of 1, one has to compare $e\mathcal{E}$ with the mechanical force $m\omega_0^2 x \sim m\omega_0^2\lambda$. As a result, one arrives at the following expression for the dimensionless electromechanical coupling constant:

$$\varepsilon = \frac{e^2}{mCL\lambda\omega_0^2} \tag{B9}$$

For a nanoscale grain and typical organic junctions, $\epsilon \sim 10^{-2}$. We conclude that the mechanical energy should indeed vary slowly in time, the characteristic scale being $t_g = (\epsilon\omega_0)^{-1} \gg \omega_0^{-1}$. This justifies the separation between fast and slow motion. Thus, the produced work can be specified as

$$W(U) = v\varepsilon\omega_0 U_0 \mathcal{W}\left(\frac{U}{U_0}\right)$$

where $\mathcal{W}(U/U_0)$ is the dimensionless energy pumping,

$$\mathcal{W}\left(\frac{U}{U_0}\right) = \frac{\omega_0}{2\pi}\int_0^{2\pi} \mathrm{dt}\,\langle \mathrm{n}\rangle_t \cos\omega_0 \mathrm{t}$$

As a result, at low temperatures and for the threshold values of the voltage one has to analyze the set of equations

$$\dot{E} = v\varepsilon\omega_0 \mathcal{W}(E) - \gamma E \tag{B10}$$

$$\mathcal{W}(E) = \frac{1}{2\pi}\int_0^{2\pi} \mathrm{d}\varphi\,\langle n \rangle_\varphi \cos\varphi \tag{B11}$$

$$\tau_R \frac{\partial \langle n \rangle_\varphi}{\partial \varphi} = -2\langle n \rangle_\varphi \cosh(\sqrt{E}\sin\varphi) + (1 - v)\sinh(\sqrt{E}\sin\varphi) \tag{B12}$$

Here $E \equiv U/U_0$, $\varphi \equiv \omega_0 t$, $\langle n \rangle_\varphi = \langle n \rangle\, t = \varphi$. $\tau_R = \omega_0 RC$.

2. Analysis of the Shuttle Instability

The stationary regime of the system is obviously given by the equation

$$v\varepsilon\omega_0 \mathscr{W}(E) - \gamma E = 0 \tag{B13}$$

This equation has a trivial solution $E = 0$, and when it is stable, the system resides in the equilibrium position. Let us call this state the *stationary regime*. For our symmetric system, the current-voltage curve in this regime shows no pronounced Coulomb blockade structure even though there are peaks in the differential conductance due to the switching on of new channels at voltages $v_n = 2n + 1$ [12].

To analyze the stability of the stationary regime, it is convenient to expand the work $\mathscr{W}(E)$ in powers of the dimensionless mechanical energy, E,

$$\mathscr{W}(E) = \alpha(v)E + \beta(v)E^2 + \ldots \tag{B14}$$

It can be shown that $\alpha(v) = (\partial \mathscr{W}/\partial E)_{E=0} > 0$ [93], while the sign of $\beta = (1/2)(\partial^2 \mathscr{W}/\partial E^2)_{E=0}$ depends on the parameters of the system, see Eq. (B18). Using Eq. (B13) we can define the dimensionless *critical voltage* v_c from the equation

$$v_c\alpha(v_c) = \tilde{\gamma}, \quad \tilde{\gamma} \equiv \frac{\gamma}{\varepsilon\omega_0} \tag{B15}$$

Near the critical voltage, $|v - v_c| \ll v_c$, one can expand the mechanical energy as

$$\mathscr{W}(E) = [\alpha(v_c) + \alpha'(v_c)(v - v_c)]E + \beta E^2 \tag{B16}$$

The energy of mechanical vibrations at a given voltage v is then determined by the equation

$$v[\alpha(v) + \beta E] = \tilde{\gamma} \tag{B17}$$

Using Eq. (B15) we find for the energy

$$E = -\frac{1}{\beta}\frac{v - v_c}{v_c}[\alpha(v_c) + v_c\alpha'(v_c)]$$

This result is meaningful at $\beta < 0$. It shows that at $v > v_c$ the stationary regime is unstable and the stationary amplitude of mechanical oscillations grows as $\sqrt{E} \sim \sqrt{v - v_c}$. Adopting nomenclature from the theory of oscillations [94] we are dealing here with *soft* excitation of self-oscillation where the amplitude is a smooth function of the difference $v - v_c$. The *hard* excitation is associated with a hysteretic behavior of the amplitude versus $v - v_c$. In the language of phase transitions—taking the oscillation amplitude to be the order parameter—the "soft" case corresponds to a second-order transition and the "hard" case to a first-order transition.

When $\beta > 0$, the shuttle instability develops in a completely different way. Consider the graphs in Fig. 35 showing $\mathscr{W}(E)$ for a fixed set of parameters for four different voltages along with the line $\tilde{\gamma}E$. Consider now the system located in O at a voltage $v < v_{c1}$. In this case the system is in the *static regime* and exhibits the same behavior as an ordinary double junction. As the voltage is increased above v_{c1}, a second stable stationary point B appears, but the system cannot reach this point since O is still stable. At $v = v_{c2}$, O becomes unstable and the system "jumps" from O to C. This instability we refer to as *hard* since the amplitude changes abruptly from $E = 0$ to $E = E_2$ as the voltage is raised above v_{c2}. Now consider the case of $v > v_{c2}$ when the system is originally at some stationary point and the voltage is lowered. At $v < v_{c2}$, O becomes stable but cannot be reached by the system until v has dropped to $v = v_{c1}$. At v_{c1}, the point A becomes unstable and the system will "jump" to O. This transition is characterized by an abrupt drop in amplitude from E_1 to $E = 0$ at $v = v_{c1}$. Since $v_{c1} < v_{c2}$, the system will obviously exhibit a hysteretic behavior in the transition region.

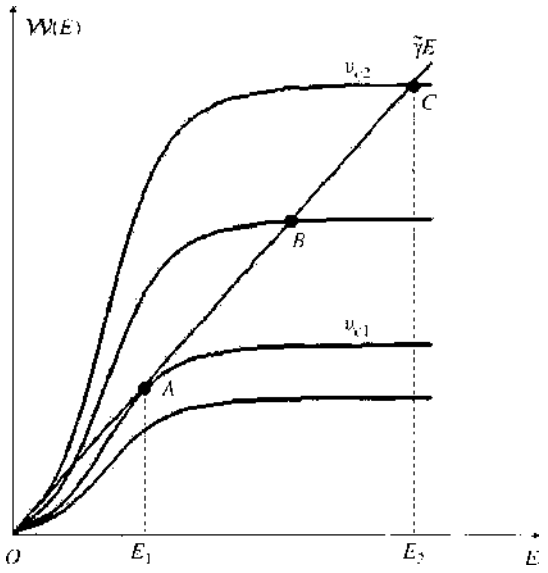

Figure 35. Schematic energy diagram for the case $\beta > 0$. The graph shows $\mathcal{W}(E)$ for a fixed set of parameters for four different voltages along with the line $\tilde{\gamma}E$. When $v < v_{c1}$, only O will be a stable stationary point. At $v = v_{c1}$, a second *unstable* stationary point A appears. For $v_{c1} < v = v' < v_{c2}$, we have two coexisting stable points O and B leading to the hysteretic behavior of the system discussed in the text. At $v = v_{c2}$, A will become unstable and the system is determined to be in the limit cycle with amplitude corresponding to energy E_2 at the intersection C. As v is increased above v_{c2}, the only stable stationary point left is C corresponding to a limit cycle with amplitude $\propto \sqrt{E}$. Adapted with permission from [93], A. Isacsson et al., *Physica B* 255, 150 (1998). © 1998, Elsevier B. V.

For a simplified case of low temperatures and $v = v_n$, one can solve Eq. (B12) approximately for small E, then substitute the solution in Eq. (B11) and compute β. One obtains [93]

$$\beta = \frac{v-1}{16}\,\frac{\tau_R(\tau_R^2 - 12)}{(\tau_R + 4)^2} \tag{B18}$$

Thus the border between the soft and hard excitation corresponds to $\tau_R = 2\sqrt{3}$.

It is worth mentioning that numerical analysis [93] predicts significant difference in the I–V curve in the static and shuttling regime (see Fig. 36).

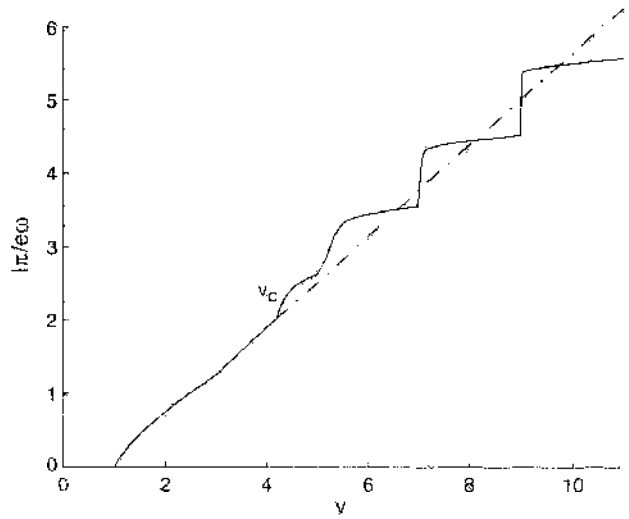

Figure 36. Current through the Coulomb blockade system in the static regime ($v < v_c$) and in the shuttle regime ($v > v_c$). As the system enters the shuttle regime the current (solid line) deviates from the current for a static double junction (dashed line). After the transition to the shuttle regime distinct steps can be seen in the current. The current is normalized to the frequency of harmonic oscillations, ω_0, to demonstrate that the step height in the shuttle regime is proportional to ω_0. In order to make a comparison with the current in the static regime, this current has been scaled by the same factor. Reprinted with permission from [93], A. Isacsson et al., *Physica B* 255, 150 (1998). © 1998, Elsevier B. V.

APPENDIX C: QUANTUM DYNAMICS OF A SHUTTLE

Here, following Fedorets [95], we briefly review the dynamics of a quantum shuttle.

1. Model

The system Hamiltonian reads

$$H = H_{\text{leads}} + \Omega + H_{\text{dot}} + H_{\text{bath}} + H_{\text{bath-osc}}$$

Here the term

$$H_{\text{leads}} \equiv \sum_{\alpha,k} \epsilon_{\alpha k} a^{\dagger}_{\alpha k} a_{\alpha k}$$

describes noninteracting electrons in the leads ($\alpha = L, R$) with constant density of states. The operator $a^{\dagger}_{\alpha k}(a_{\alpha k})$ creates (destroys) an electron with momentum k in the lead α. The electrons in each lead are held at a constant electrochemical potentials $\mu_{L,R} = \mp eV/2$, where $e < 0$ is the electron charge and $V > 0$ is the bias voltage. The term

$$\Omega = \sum_{\alpha} T_{\alpha}(x)[A^{\dagger}_{\alpha} c + c^{\dagger} A_{\alpha}] T_{L,R}(x) = T_0 e^{\mp x/\lambda}$$

represents tunneling of electrons between the island and the leads. For simplicity, it is assumed that the tunneling amplitudes do not depend on the electronic quantum numbers, which allows us to introduce the operators $A_{\alpha} \equiv \sum_k a_{\alpha k}$ in Eq. (C1). The term

$$H_{\text{dot}} \equiv [\epsilon_0 - e\mathcal{E}x]c^{\dagger}c + \frac{p^2}{2m} + \frac{m\omega_0^2 x^2}{2}$$

describes the electronic and vibrational degree of freedom of the central island, that is, the single electronic level and the quantum oscillator associated with the center of mass motion of the island. The operator $c^{\dagger}(c)$ creates (destroys) an electron on the level in the island. To describe damping of the center-of-mass motion, we have coupled the oscillator to a bosonic heat bath H_{bath}. The term $H_{\text{bath-osc}}$ represents the coupling between the oscillator and the heat bath. We assume that this coupling is linear in x and treat it in the weak-coupling limit. The damping is characterized by a dissipation rate γ. For simplicity, only the zero temperature case is considered.

For convenience, later in this section we will use dimensionless variables. All lengths will be measured in units of x_0, p (in units of $\hbar/x_0$), energies (in units of $\hbar\omega_0$), time (in units of ω_0^{-1}), and magnetic field (in units of $\hbar\omega_0/\mu$). Then the Hamiltonian for the island can be written in the simple form

$$H_{\text{dot}} \equiv [\epsilon_0 - dx]c^{\dagger}c + H_{\text{osc}}, \quad H_{\text{osc}} \equiv \frac{1}{2}[p^2 + x^2]$$

where $d \equiv e\mathcal{E}/(M\omega_0^2 x_0)$ is the shift in the equilibrium position of the oscillator caused by the electric field $\mathcal{E}$ after an electron is placed in the dot.

We will study the system analytically in the high voltage limit, assuming that the following conditions are satisfied:

$$\frac{d}{\lambda} \ll 1, \quad \lambda^{-2} \ll 1, \quad \gamma \ll 1 \tag{C1}$$

We assume that the dissipation rate γ is small because we are interested in nontrivial dynamics of the mechanical degree of freedom.

2. Generalized Master Equation

In the Schrödinger representation, the time evolution of the system is determined by the Liouville–von Neumann equation for the total density operator $\sigma(t)$:

$$i\partial_t\sigma[H,\sigma] = [H_{\text{leads}} + H_{\text{dot}}, \sigma] + [\Omega, \sigma]$$

where $[A, B]$ denotes the commutator of the operators A and B.

Since we are interested in the evolution of the dot variables, we need to know only the evolution of the reduced density operator ρ, which describes the vibrational degree of freedom coupled to the single electronic state in the island. This reduced density operator is obtained from the total density operator σ by tracing over the electronic degrees of freedom of the leads:

$$\rho(t) \equiv \text{Tr}_{\text{leads}}\{\sigma(t)\}$$

To derive the equation of motion (EOM) for the reduced density operator (a so-called generalized master equation), we transform Eq. (C2) into the interaction picture with respect to $H_0 \equiv H_{\text{leads}} + H_{\text{dot}}$:

$$i\partial_t\tilde{\sigma}(t) = [\tilde{\Omega}(t), \tilde{\sigma}(t)]$$

where

$$\tilde{\sigma}(t) \equiv e^{iH_0t}\sigma(t)e^{-iH_0t}$$
$$\tilde{\Omega}(t) \equiv e^{iH_0t}\Omega(t)e^{-iH_0t}$$

We treat the electrons in the leads as a fermionic bath whose equilibrium state is virtually unaffected by the coupling to the dot. Therefore, the following approximation can be made

$$\tilde{\sigma}(t) \approx \tilde{\rho}(t) \otimes \sigma_{\text{leads}} \tag{C2}$$

where $\tilde{\rho}(t) \equiv \text{Tr}_{\text{leads}}\{\tilde{\sigma}(t)\}$ is the reduced density operator in the interaction representation. To use the factorization approximation given by Eq. (C2), we transform Eq. (C2) into its equivalent form before tracing over the leads:

$$\partial_t\tilde{\sigma}(t) = -i[\tilde{\Omega}(t), \tilde{\sigma}(0)] - \int_0^t dt_1\,[\tilde{\Omega}(t), [\tilde{\Omega}(t_1), \tilde{\sigma}(t_1)]] \tag{C3}$$

Tracing out from Eq. (C3) the lead variables and assuming large-voltage limit, $eV \gg \hbar\omega_0$, one can transform this equation into a form local in time,

$$\dot{\rho} = -i[H_{\text{dot}}, \rho] + \mathscr{L}_T\rho + \mathscr{L}_\gamma\rho \tag{C4}$$

where the first term in the right-hand side describes the free evolution of the oscillator; the second term

$$\mathscr{L}_T\rho \equiv \sqrt{\hat{\Gamma}_L}c^\dagger\rho c\sqrt{\hat{\Gamma}_L} - \frac{1}{2}\{\hat{\Gamma}_L cc^\dagger, \rho\} + \sqrt{\hat{\Gamma}_R}c\rho c^\dagger\sqrt{\hat{\Gamma}_R} - \frac{1}{2}\{\hat{\Gamma}_R c^\dagger c, \rho t\}$$

describes tunneling of electrons on and off the dot; $\hat{\Gamma}_\alpha \equiv \Gamma_\alpha(\hat{x}) \equiv 2\pi\mathscr{D}_\alpha T_\alpha^2(\hat{x})/\hbar\omega_0$;

$$\mathscr{L}_\gamma\rho \equiv -\frac{i\gamma}{2}[x, \{p, \rho\}] - \frac{\gamma}{2}[x, [x, \rho]]$$

is the dissipation term, and γ is a dissipation rate; $\{A, B\}$ denotes anticommutator of the operators A and B.

It follows from Eq. (C4) that the time evolution of the electronic diagonal elements $\rho_0 \equiv \langle 0|\rho|0\rangle$ and $\rho_1 \equiv \langle 1|\rho|1\rangle$, $|1\rangle \equiv c^\dagger|0\rangle$ is decoupled from the evolution of the off-diagonal

elements. After shifting the origin of the x-axis to the point $x = d/2$, we get the system of EOMs for the diagonal elements ρ_0 and ρ_1:

$$\dot{\rho}_0 = \frac{1}{i}\left[H_{\rm osc} + \frac{d}{2}x, \rho_0\right] - \frac{1}{2}\{\widetilde{\Gamma}_L(x), \rho_0\} + \sqrt{\widetilde{\Gamma}_R(x)}\rho_1\sqrt{\widetilde{\Gamma}_R(x)} + \mathscr{L}_\gamma\rho_0 \tag{C5}$$

$$\dot{\rho}_1 = \frac{1}{i}\left[H_{\rm osc} - \frac{d}{2}x, \rho_1\right] - \frac{1}{2}\{\widetilde{\Gamma}_R(x), \rho_1\} + \sqrt{\widetilde{\Gamma}_L(x)}\rho_0\sqrt{\widetilde{\Gamma}_L(x)} + \mathscr{L}_\gamma\rho_1 \tag{C6}$$

where $\widetilde{\Gamma}_\alpha(x) \equiv \Gamma_\alpha(x + d/2)$. Henceforth, we drop the tilde symbol and write $\widetilde{\Gamma}_\alpha(x)$ as $\Gamma_\alpha(x)$.

The expectation value of an observable $A(x, p)$ in the vibrational space is given by

$$\begin{aligned}\langle A(x, p)\rangle(t) &\equiv {\rm Tr}\{A(x, p)\rho(t)\}\\ &= {\rm Tr}_{\rm osc}\{A(x, p)[\rho_0(t) + \rho_1(t)]\}\end{aligned}$$

and completely determined by the reduced density operator $\rho_+ \equiv \rho_0 + \rho_1$ for the oscillator.

Therefore, instead of working with the density operators ρ_0 and ρ_1, it is convenient to introduce a new set ρ_+ and $\rho_- \equiv \rho_0 - \rho_1$. The operator ρ_- describes the correlations between the vibrational degree of freedom and the electronic degree of freedom of the dot.

3. Shuttle Instability

In this section, we will study nonequilibrium dynamics of the oscillator in the vicinity of its ground state. If the state of the oscillator evolves in the direction away from its ground state then the ground state is unstable.

Let us look at the time evolution of the first vibrational moments $x_\pm \equiv {\rm Tr}\{x\rho_\pm\}$ and $p_\pm \equiv {\rm Tr}\{p\rho_\pm\}$. The EOMs for the first moments are

$$\begin{aligned}\dot{x}_+ &= p_+\\ \dot{p}_+ &= -\gamma p_+ - x_- - \frac{d}{2}n_-\\ \dot{n}_- &= -\langle\Gamma_-(x)\rangle_- + \langle\Gamma_-(x)\rangle_+\\ \dot{x}_- &= p_- - 2\langle x\Gamma_+(x)\rangle_- + 2\langle x\Gamma_-(x)\rangle_+\\ \dot{p}_- &= -\gamma p_- - x_- - \frac{d}{2} - \langle\{p, \Gamma_+(x)\}\rangle_- + \langle\{p, \Gamma_-(x)\}\rangle_+\end{aligned}$$

where $\langle A\rangle_\pm \equiv {\rm Tr}\{\rho_\pm A\}$ and $\Gamma_+(x) \equiv \Gamma_R(x) \pm \Gamma_L(x)$. One can see from this system that the dynamics of the first moments is coupled to the dynamics of the higher moments of all orders.

The problem significantly simplifies if $\Gamma_L(0) = \Gamma_R(0) \equiv \Gamma$. In the first order in λ^{-1}, the system of EOMs for x_+, p_+, and n_- becomes closed:

$$\begin{aligned}\dot{x}_+ &\approx p_+\\ \dot{p}_+ &\approx -\gamma p_+ - x_+ - \frac{d}{2}n_-\\ \dot{n}_- &\approx -\Gamma n_- + \frac{2\Gamma}{\lambda}x_-\end{aligned}$$

The corresponding characteristic equation,

$$(\alpha + \Gamma)(\alpha^2 + \alpha\gamma + 1) + \Gamma\frac{d}{\lambda} = 0$$

has three roots

$$\alpha_1 \approx -\Gamma - \Gamma\frac{d}{\lambda}\frac{1}{\Gamma^2 + 1}, \quad \alpha_2 \approx i - \frac{\gamma}{2} + \Gamma\frac{d}{2\lambda}\frac{1}{1 - i\Gamma}, \quad \alpha_3 = \alpha_2^*$$

where we have assumed, for simplicity, that $\gamma \ll \Gamma$. Thus

$$x_+(t) = Ce^{\alpha t} + Ae^{rt}\cos(t) \tag{C7}$$

$$r = \frac{1}{2}(\gamma_{\text{thr}} - \gamma), \quad \gamma_{\text{thr}} = \frac{d}{\lambda}\frac{\Gamma}{\Gamma^2 + 1} \tag{C8}$$

The first term in Eq. (C7) decays with time, and we can neglect it. If the dissipation rate γ is below its threshold value γ_{thr}, then the expectation value of the displacement x_+ exponentially grows in time and the vibrational ground state becomes unstable.

4. Steady State in the Wigner Function Representation

In order to find the stable regime, it is convenient to work with the Wigner function representation of the density operators $\rho_\pm$:

$$W_\pm(x, p) \equiv \frac{1}{2\pi}\int_{-\infty}^{+\infty} d\xi e^{-ip\xi}\left\langle x + \frac{\xi}{2}|\rho_\pm|x - \frac{\xi}{2}\right\rangle$$

Equations for $W_\perp(x, p)$ can be derived from Eqs. (C5) and (C6). Stationary solutions of these equations can be obtained analytically in the limit given by Eq. (C1). In the leading order of all small parameters, one obtains the distribution function for the vibration amplitude A as

$$W_-(A) = \mathcal{Z}^{-1}\exp\left\{-\int_0^A \frac{dA}{\lambda}\frac{f(A)}{D(A)}\right\}$$

where $\mathcal{Z}$ is a normalization constant determined by the condition

$$2\pi\int_0^\infty dA\, AW_-(A) = 1$$

while the functions $f(A)$ and $D(A)$ are defined by some analytical expressions that we do not show here.

One can show that the function $W_-(A)$ has maxima at the points A_M, which are defined by the conditions

$$f(A_M) = \frac{A_M}{2\lambda}\left[\gamma - \frac{d}{\lambda}\alpha_0(A_M) - \frac{1}{2\lambda^4}\alpha_1(A_M)\right] = 0 \tag{C9}$$

and $f'(A_M) > 0$. The functions $\alpha_0(A)$ and $\alpha_1(A)$ are shown in Figs. 37 and 38. Thus, the expression (C9) is actually an *equation* to find the most probable A_M. In the vicinity of these points, W_+ is bell shaped and can be approximated by a Gaussian distribution function

$$W_+(A) \approx \mathcal{Z}^{-1}\exp\left\{-\int_0^{A_M}\frac{dA}{\lambda}\frac{f(A)}{D(A)}\right\}\exp\left\{-\frac{(A - A_M)^2}{2\sigma_M^2}\right\}$$

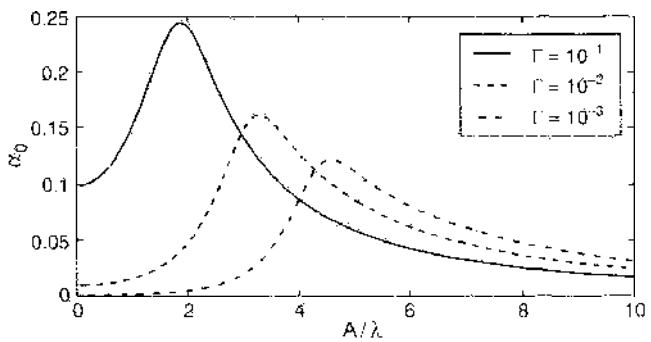

Figure 37. The function $\alpha_0(A)$ in Eq. (C9) for $\Gamma = 10^{-1}$, 10^{-2}, 10^{-3}. Reprinted with permission from [42], Fedorets et al., *Phys. Rev. Lett.* 92, 166801 (2004). © 2004, American Physical Society.

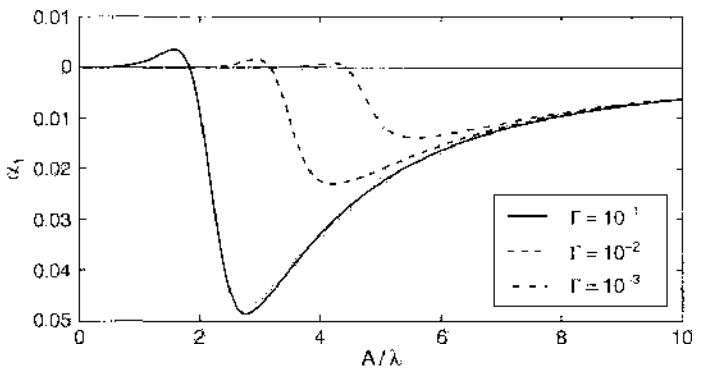

Figure 38. The function $\alpha_1(A)$ in Eq. (C9) for $\Gamma = 10^{-1}$, 10^{-2}, 10^{-3}. Reprinted with permission from [42], Fedorets et al., *Phys. Rev. Lett.* 92, 166801 (2004). © 2004, American Physical Society.

with variance $\sigma_M^2 \equiv \lambda D(A_M)/f'(A_M)$. Expanding $f(A)$ around $A = 0$, we find that

$$f = \frac{A}{2\lambda}(\gamma - \gamma_{\text{thr}}) + \mathcal{O}(A^3), \quad A \to 0$$

Thus, $W_+(A)$ always has an extremum at $A = 0$: a maximum if $\gamma > \gamma_{\text{thr}}$ and a minimum if $\gamma < \gamma_{\text{thr}}$. This reflects the fact that the vibrational ground state is unstable when the dissipation is below the threshold value.

The function $W_+(A)$ has a maximum at a nonzero point A_C if

$$\alpha(A_C) \equiv \frac{d}{\lambda}\alpha_0(A_C) + \frac{1}{2\lambda^4}\alpha_1(A_C) = \gamma, \quad \alpha'(A_C) < 0 \tag{C10}$$

In order to find the points of maxima (stable points), we have to look at the functions $\alpha_0(A)$ and $\alpha_1(A)$, which are shown in Figs. 37 and 38. The positive bounded function $\alpha_0(A)$ behaves as $\Gamma(1 + A^2/2\lambda^2)$ in the vicinity of $A = 0$ and for large A, it decreases as $(\pi A^2/\lambda^2)\ln(2A/\lambda\Gamma)$. The bounded function $\alpha_1(A)$ grows as $4A^2\Gamma^3/9\lambda^2$ for small A. For large A, it is negative and goes to zero as $-2\lambda^2/(\pi A^2)$.

From the analysis of the functions $\alpha_0(A)$ and $\alpha_1(A)$, one can conclude that

- If $\gamma > \gamma_{\max} \equiv \max \alpha(A)$, then there is only one stable point $A = 0$.
- If $\gamma_{\text{thr}} < \gamma < \gamma_{\max}$, then the point $A = 0$ is stable, but there is another stable point $A_C \neq 0$.
- If $\gamma < \gamma_{\text{thr}}$, then the point $A = 0$ becomes unstable.

One can separate two qualitatively different regimes: a "quasiclassical" regime, defined by the condition $d/\lambda \gg \lambda^{-4}$ and a "quantum" regime, where $d/\lambda \ll \lambda^{-4}$. The names for the regimes stem from the fact that the Gaussian "bell" of $W_+(A)$ around the stable point is narrow in the quasiclassical regime and has a width of the order of $\lambda \gg 1$ in the quantum regime.

In the quasiclassical regime, the role of $\alpha_1(A)$ is negligible and $Af(A)$ is equal to the average rate of the energy pumped into the vibrational degree of freedom of the island that oscillates classically with a constant amplitude A. Thus, the stable points A_C determined by Eq. (C10) are exactly the same as the limit-cycle amplitudes obtained in the high-voltage limit of the semiclassical treatment, where the motion of the island was treated classically. In this regime, an external dissipation is required to stabilize the system. In contrast, in the quantum regime, there is a finite stable point even in the absence of external dissipation.

5. Shuttling of Spin-Polarized Electrons

The previous approach can be generalized to allow for transport of spin-polarized electrons between oppositely magnetized leads (see Section 2.5). In this case, the density matrix has a spin structure $\rho \to \rho_{\sigma\sigma'}$. The local in-time equation for $\rho_{\sigma\sigma'}$ can be found similarly to

Eqs. (C5) and (C6). The condition for the shuttling instability is similar to Eq. (C8), however, with magnetic field dependent $\gamma_{\rm thr}$,

$$\gamma_{\rm thr}(H) = \Gamma \frac{d}{\lambda} \frac{2H^2}{H^2 + \Gamma^2}$$

Introducing spin-dependent Wigner function (see Section 2.5.2), one can find in the case (C1) the stationary distribution function of the vibration amplitude. In the quasiclassical limit,

$$\frac{d}{\lambda} \gg \lambda^{-4}$$

the distribution $W_+(A)$ is sharply peaked around stable points A_M determined by the equation

$$A_M \left[\gamma - \frac{d}{\lambda} \beta_0(A_M) \right] = 0, \quad f'(A_M) > 0$$

with

$$\beta_0(A) = \Gamma \frac{2H^2}{H^2 + \Gamma^2} + \mathcal{O}(A^2)$$

and

$$f = \frac{A}{2\lambda}(\gamma - \gamma_{\rm thr}) + \mathcal{O}(A^3)$$

Thus, for the dissipation rates above the threshold value $\gamma_{\rm thr}$, the function $W_+(A)$ has a maximum at $A = 0$ (i.e., the point $A = 0$ is stable). If $\gamma < \gamma_{\rm thr}$, then $W_+(A)$ has a minimum at $A = 0$ (i.e., the vibrational ground state is unstable when the dissipation is below the threshold value).

The positive-bounded function $\beta_0(A, H)$ has only one maximum and monotonically decreases for large A (Fig. 39). One can show that if $H < \sqrt{3}\Gamma$, the function $\beta_0(A)$ has a maximum at $A = 0$, while if $H > \sqrt{3}\Gamma$, the function $\beta_0(A)$ has a minimum at $A = 0$.

The above structure of the function $\beta_0(A, H)$ determines the behavior of the system in the two-dimensional parametric space $d - H$ (or $\gamma - H$), which is summarized in Fig. 15 in the form of a "phase diagram."

- If $d/(\gamma\lambda) > 1/[\max \beta_0(A)](H)$, the only stable point is $A = 0$ ("the ground state phase").
- If $1/[\max \beta_0(A)](H) < d/(\gamma\lambda) < (H^2 + \Gamma^2)/(2H^2\Gamma)$, there are two stable points: $A = 0$ and $A = A_C$ ("the bistable phase").
- If $d/(\gamma\lambda) > (H^2 + \Gamma^2)/(2H^2\Gamma)$, there is only one stable point: $A = A_C \neq 0$ ("the shuttle phase").

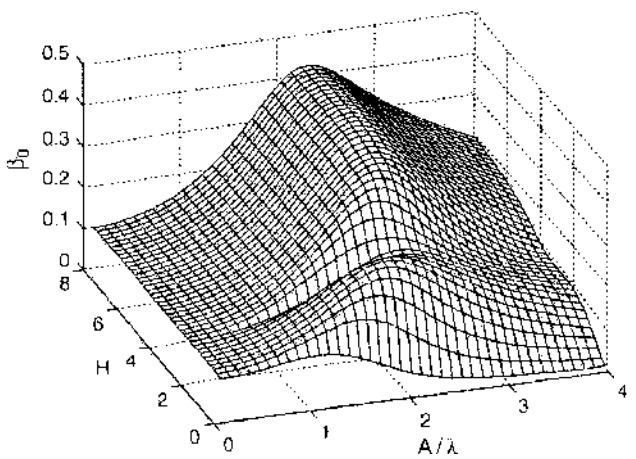

Figure 39. The function $\beta_0(A, H)$ for $\Gamma = 0.05$. Reprinted with permission from [53], Fedorets et al., cond-mat/0408591 (unpublished).

APPENDIX D: ABBREVIATIONS

AC	(alternating current) nonstationary
DC	(direct current) stationary
EOM	equation of motion
FC	full counting (statistics)
GMR	giant magnetoresistance
NEM-SET	nanoelectromechanical SET
NEMS	nanoelectromechanical system
RIE	reactive ion etching
SEM	scanning electron microscope
SET	single-electron transistor

APPENDIX E: NOTATIONS

e	elementary (electron) charge
n	number of electrons on island
x	oscillator displacement from its equilibrium position
$x_0 = \sqrt{\hbar/m\omega_0}$	de Broglie wavelength of the oscillator
$q = en$	oscillator charge
m	oscillator mass
k_0	effective spring constant
$\omega_0 = \sqrt{k_0/m}$	natural angular vibration frequency
a	amplitude of mechanical oscillations
γ	damping constant for mechanical motion
Γ	typical tunneling rate
$\mathcal{E}$	electric field
$d = e\mathcal{E}/m\omega_0^2$	displacement of the single-change oscillator in the electric field
t_0	contact time
$f_0 = \omega_0/2\pi$	natural vibration frequency [Hz]
$T_0 = 1/f$	period of vibration
λ	characteristic tunneling length
$R_{L,R}(x)$	position dependent tunnel resistances between island and (left/right) lead
$C_{L,R}(x)$	position dependent capacitances between island and (left/right) lead
$\omega_R^{-1} = RC$	charge relaxation rate
V	applied DC bias voltage
V_0	coulomb blockade threshold voltage
I	direct current
T	temperature
$P_t(n)$	probability for n electrons to be transferred during time t
$p_n(t)$	probability to find n excess electrons on the shuttle

REFERENCES

1. R. P. Andres, T. Bein, M. Dorogi, S. Feng, J. I. Henderson, C. P. Kubiak, W. Mahoney, R. G. Osifchin, and R. Reifenberger, *Science* 272, 1323 (1996).
2. A. N. Cleland, "Foundations of Nanomechanics," Springer, Heidelberg, 2002.
3. M. H. Devoret and H. Grabert, (Eds.), "Single Charge Tunnelling," NATO ASI Series B29, Plenum, New York, 1992; G.-L. Ingold and Yu. V. Nazarov, *ibid.*
4. H. Park, J. Park, A. K. L. Lim, E. H. Anderson, A. P. Alivisatos, and P. L. McEuen, *Nature* 407, 57 (2000).
5. E. S. Soldatov, V. V. Khanin, A. S. Trifonov, D. E. Presnov, S. A. Yakovenko, G. B. Khomutov, C. P. Gubin, and V. V. Kolesov, *JETP Lett.* 64, 556 (1996).
6. S. Kubatkin, A. Danilov, M. Hjort, J. Corni, J.-L. Brédas, and N. Stuhr-Hansen, Per Hedegård, and T. Bjørnholm, *Nature* 425, 698 (2003).
7. R. H. M. Smit, Y. Noat, C. Untiedt, N. D. Lang, M. C. van Hemert, and J. M. van Ruitenbeek, *Nature* 419, 906 (2002).
8. R. G. Knobel and A. N. Cleland, *Nature* 424, 291 (2003).
9. E. M. Weig, R. H. Blick, T. Brandes, J. Kirschbaum, W. Wegscheider, M. Bichler, and J. P. Kotthaus, *Phys. Rev. Lett.* 92, 046804 (2004).

10. B. J. LeRoy, S. G. Lemay, J. Kong, and C. Dekker, cond-mat/0403316 (unpublished).
11. L. Y. Gorelik, A. Isacsson, M. V. Voinova, B. Kasemo, R. I. Shekhter, and M. Jonson, *Phys. Rev. Lett.* 80, 4526 (1998).
12. I. Giaver and H. R. Zeller, *Phys. Rev. Lett.* 20, 1504 (1968); R. I. Shekhter, *Sov. Phys.—JETP* 36, 747 (1973); I. O. Kulik and R. I. Shekhter, *Sov. Phys.—JETP* 41, 308 (1975); D. V. Averin and K. K. Likharev, *J. Low Temp. Phys.* 62, 345 (1986).
13. A. Erbe, R. H. Blick, A. Tilke, A. Kriele, and J. P. Kotthaus, *Appl. Phys. Lett.* 73, 3751 (1998).
14. A. Erbe, C. Weiss, W. Zwerger, and R. H. Blick, *Phys. Rev. Lett.* 87, 096106-1 (2001).
15. D. V. Scheible, A. Erbe, and R. H. Blick, *New J. Phys.* 4, 86 (2002).
16. R. I. Shekhter, Yu. Galperin, L. Y. Gorelik, A. Isacsson, and M. Jonson, *J. Phys: Condens. Matter* 15, R441 (2003).
17. M. T. Tuominen, R. V. Krotkov, and M. L. Breuer, *Phys. Rev. Lett.* 83, 3025 (1999).
18. A. Isacsson, L. Y. Gorelik, M. V. Voinova, B. Kasemo, R. I. Shekhter, and M. Jonson, *Physica B*, 255, 150 (1998).
19. D. Fedorets, L. Y. Gorelik, R. I. Shekhter, and M. Jonson, *Europhys. Lett.* 58, 99 (2002).
20. T. Nord, L. Y. Gorelik, R. I. Shekhter, and M. Jonson, *Phys. Rev. B* 65, 165312 (2002).
21. C. Weiss and W. Zwerger, *Europhys. Lett.* 47, 97 (1999).
22. N. Nishiguchi, *Phys. Rev. B* 65, 035403 (2001).
23. N. Nishiguchi, *Japan. J. Appl. Phys.* 40, 1 (2001).
24. N. Nishiguchi, *Phys. Rev. Lett.* 89, 066802-1 (2002).
25. F. Pistolesi and R. Fazio, cond-mat/040856 (unpublished).
26. P. Hänggi and R. Bartussek, *Lecture Notes Phys.* 476, 294 (1996).
27. D. V. Scheible and R. H. Blick, *Appl. Phys. Lett.* 84, 4632 (2004).
28. R. C. Hilborn, "Chaos and Nonlinear Dynamics." Oxford University Press, New York, 2000.
29. L. V. Keldysh, *Sov. Phys.—JETP* 20, 1018 (1965).
30. A. P. Jauho, N. S. Wingreen, and Y. Meir, *Phys. Rev. B* 50, 5528 (1994).
31. D. Boesse and H. Schoeller, *Europhys. Lett.* 54, 668 (2001).
32. K. D. McCarthy, N. Prokof'ev, and M. Tuominen, *Phys. Rev. B* 67, 245415 (2003).
33. A. Mitra, I. Aleiner, and A. J. Millis, *Phys. Rev. B* 69, 245302 (2004).
34. V. Aji, J. E. Moore, and C. M. Varma, cond-mat/0302222 (unpublished).
35. K. Flensberg, *Phys. Rev. B* 68, 205323 (2003); S. Braig and K. Flensberg, *Phys. Rev. B* 68, 205324 (2003).
36. A. D. Armour and A. MacKinnon, *Phys. Rev. B* 66, 035333 (2002); A. D. Armour and A. MacKinnon, *Physica* 316, 403 (2002).
37. A. S. Alexandrov and A. M. Bratkovsky, *Phys. Rev. B* 67, 235312 (2003).
38. Jian-Xin Zhu and A. V. Balatsky, *Phys. Rev. B* 67, 165326 (2003).
39. R. Lü, cond-mat/0303338 (unpublished).
40. D. Fedorets, L. Y. Gorelik, R. I. Shekhter, and M. Jonson, in "Fundamental Problems of Mesoscopic Physics" (I. V. Lerner, B. L. Altshuler, and Y. Gefen, Eds.), p. 65. Kluwer Academic Publishers, Dordrecht, 2004.
41. T. Novotny, A. Donarini, and A.-P. Jauho, *Phys. Rev. Lett.* 90, 256801 (2003).
42. D. Fedorets, L. Y. Gorelik, R. I. Shekhter, and M. Jonson, *Phys. Rev. Lett.* 92, 166801 (2004).
43. A. Y. Smirnov, L. G. Mourokh, and N. J. M. Horing, *Phys. Rev. B* 69, 155310 (2004).
44. J. Park, A. Pasupathy, J. I. Goldsmith, C. Chang, Y. Yaish, J. R. Petta, M. Rinkoski, J. P. Sethna, H. D. Abruña, P. L. McEuen, and D. C. Ralph, *Nature* 417, 722 (2002).
45. L. Y. Gorelik, R. I. Shekhter, V. M. Vinokur, D. Feldman, V. Kozub, and M. Jonson, *Phys. Rev. Lett.* 91, 088301 (2003).
46. Y. Tokura, "Collosal Magnetoresistive Oxides." Gordon and Breach Science Publishers, Amsterdam, 2000.
47. J. Z. Sun, W. J. Gallagher, P. R. Duncombe, L. Krusin-Elbaum, R. A. Altman, A. Gupta, Yu. Lu, G. Q. Gong, and Gang Xiao, *Appl. Phys. Lett.* 69, 3266 (1996).
48. J. Z. Sun, L. Krusin-Elbaum, P. R. Duncombe, A. Gupta, and R. B. Laibowitz, *Appl. Phys. Lett.* 70, 1769 (1997).
49. Yu, Lu, X. W. Li, G. Q. Gong, Gang Xiao, A. Gupta, P. Lecoeur, J. Z. Sun, Y. Y. Wang, and V. P. Dravid, *Phys. Rev. B* 54, R8357 (1996).
50. T. Kimura, Y. Tomioka, H. Kuwahara, A. Asamitsu, M. Tamura, and Y. Tokura, *Science* 274, 1698 (1996).
51. L. Y. Gorelik, S. I. Kulinich, R. I. Shekhter, M. Jonson, and V. M. Vinokur, *Phys. Rev. B* 71, 035237 (2005).
52. L. D. Landau, *Phys. Z. Sowjetunion* 2, 46 (1932); C. Zener, *Proc. R. Soc. London. A* 137, 696 (1932).
53. D. Fedorets, L. Y. Gorelik, R. I. Shekhter, and M. Jonson, *Phys. Rev. Lett.* 95, 057203 (2005).
54. A. N. Pasupathy, R. C. Bialczak, J. Martinek, J. E. Grose, L. A. K. Donev, P. L. McEuen, and D. C. Ralph, *Science* 306, 86 (2004).
55. S. H. M. Persson and L. Olofsson, *Appl. Phys. Lett.* 74, 2546 (1996).
56. C. Jaochim, J. K. Gimzewski, and A. Aviram, *Nature* 408, 541 (2000).
57. J. Gaudioso, L. J. Lauhon, and W. Ho, *Phys. Rev. Lett.* 85, 1918 (2000).
58. Y. Majima, K. Nagano, and A. Okuda, *Japan. J. Appl. Phys.* 41, 5381 (2002).
59. K. Nagano, A. Okuda, and Y. Majima, *Appl. Phys. Lett.* 81, 544 (2002).
60. S. E. Kubatkin, A. V. Danilov, H. Olin, and T. Claeson, *Phys. Rev. Lett.* 84, 5836 (2000).
61. L. Y. Gorelik, A. Isacsson, Y. M. Galperin, R. I. Shekhter, and M. Jonson, *Nature* 411, 454 (2001).
62. A. Isacsson, L. Y. Gorelik, R. I. Shekhter, Y. M. Galperin, and M. Jonson, *Phys. Rev. Lett.* 89, 277002 (2002).

63. M. T. Tuominen, J. M. Hergenrother, T. S. Tighe, and M. Tinkham, *Phys. Rev. Lett.* 69, 1997 (1992); *Phys. Rev. B* 47, 11599 (1993); J. M. Hergenrother, M. T. Tuominen, and M. Tinkham, *Phys. Rev. Lett.* 72, 1742 (1994).
64. P. Lafarge, P. Joyez, D. Esteve, C. Urbina, and M. H. Devoret, *Phys. Rev. Lett.* 70, 994 (1993); T. M. Eiles, J. M. Martinis, and M. H. Devoret, *Phys. Rev. Lett.* 70 1862 (1993); P. Joyez, P. Lafarge, A. Filipe, D. Esteve, and M. H. Devoret, *Phys. Rev. Lett.* 72, 2458 (1994).
65. K. Matveev, M. Gisselfält, L. I. Glazman, M. Jonson, and R. I. Shekhter, *Phys. Rev. Lett.* 70, 2940 (1993); F. W. J. Hekking, L. I. Glazman, K. Matveev, and R. I. Shekhter, *Phys. Rev. Lett.* 70, 4138 (1993); K. A. Matveev, L. I. Glazman, and R. I. Shekhter, *Mod. Phys. Lett.* B8, 1007 (1994); L. I. Glazman, F. W. Hekking, K. A. Matveev, and R. I. Shekhter, *Physica* B203, 316 (1994).
66. V. Bouchiat, D. Vion, P. Joyez, D. Esteve, and M. Devoret, *Phys. Scr.* T 76, 165 (1998).
67. Y. Nakamura, Yu. A. Pashkin, and J. S. Tsai, *Nature* 398, 786 (1999).
68. D. Vion, A. Aassime, A. Cottet, P. Joyez, H. Pothier, C. Urbina, D. Esteve, and M. H. Devoret, *Science* 296, 886 (2002).
69. Y. Makhlin, G. Schön, and A. Shnirman, *Rev. Mod. Phys.* 73, 357 (2001).
70. R. I. Shekhter, L. Y. Gorelik, A. Isacsson, Y. M. Galperin, and M. Jonson, *Phys. Scr.* T 102, 13 (2001).
71. L. Y. Gorelik, A. Isacsson, Y. M. Galperin, R. I. Shekhter, and M. Jonson, cond-mat/0012201 (unpublished).
72. A. Romito, F. Plastina, and R. Fazio, *Phys. Rev. B* **68**, 140502(R) (2003).
73. M. J. M. de Jong and C. W. J. Beenakker, in "Mesoscopic Electron Transport" (L. L. Sohn, G. Schön, and L. P. Kouwenhoven, Eds.) Kluwer Academic Publishers, Dordrecht, 1997.
74. H. B. Callen and T. W. Welton, *Phys. Rev.* 83, 34 (1951).
75. A. van der Ziel, "Noise in Solid State Devices and Circuits." Wiley, New York, 1986.
76. Y. Blanter and M. Büttiker, *Phys. Rep.* 336, 1 (2000).
77. L. S. Levitov and G. B. Lesovik, *Pis'ma Zh. Eksp. Teor. Fiz.* 58, 225 (1993); *JETP Lett.* 58, 230 (1993); L. S. Levitov, H.-W. Lee, and G. B. Lesovik, *J. Math. Phys.* 37, 4845 (1996).
78. A. Isacsson and T. Nord, *Europhys. Lett.* 66, 708 (2004).
79. T. Nord and A. Isacsson, *Phys. Rev. B* 69, 035309 (2004).
80. C. W. Gardiner, "Handbook of Stochastic Methods," 2nd Edn. Springer, Berlin, 1997.
81. T. Novotny, A. Donarini, C. Flindt, and A.-P. Jauho, *Phys. Rev. Lett.* 92, 248302 (2004).
82. H. Grabert and M. H. Devoret, (Eds.), "Single Charge Tunnelling," Vol. 294, NATO ASI Ser. B, Plenum, New York, 1992.
83. F. Pistolesi, *Phys. Rev. B* 69, 245409 (2004).
84. D. A. Bagrets and Yu. V. Nazarov, *Phys. Rev. B* 67, 085316 (2003).
85. M. J. M. de Jong, *Phys. Rev. B* 54, 8144 (1996).
86. C. Flindt, T. Novotný, and A. P. Jauho, *Europhys. Lett.* 69, 475 (2005).
87. U. Weiss, "Quantum Dissipative Systems," World Scientific, Singapore, 1999.
88. A. Romito and Yu. V. Nazarov, *Phys. Rev.* 70, 212509 (2004).
89. L. S. Levitov, cond-mat/0103617 (2001).
90. A. Andreev and A. Kamenev, *Phys. Rev. Lett.* 85, 1294 (2000).
91. W. Belzig and Yu. V. Nazarov, *Phys. Rev. Lett.* 87, 197006 (2001).
92. A. Dykhne and A. G. Rudavets, cond-mat/0409658 (unpublished).
93. A. Isacsson, L. Y. Gorelik, M. V. Voinova, B. Kasemo, R. I. Shekhter, and M. Jonson, *Physica B* 255, 150 (1998).
94. A. A. Andronov, A. A. Vitt, and S. E. Khaikin, "Theory of Oscillators." Pergamon, Oxford, 1966, Chap. 9, Sec. 9.
95. D. Fedorets, Ph.D. Thesis, Göteborg University (2004), ISBN 91-628-6228-6 (unpublished).

CHAPTER 2

Dynamics of Condensed Phase Proton and Electron Transfer Processes

Raymond Kapral, Alessandro Sergi

Chemical Physics Theory Group, Department of Chemistry, University of Toronto, Toronto, Canada

CONTENTS

ISBN: 1-58883-047-0

Handbook of Theoretical and Computational Nanotechnology
Edited by Michael Rieth and Wolfram Schommers
Volume 5: Pages (61–92)

1. INTRODUCTION

Proton and electron transfer reactions are ubiquitous in chemistry and govern many important physical and biological functions [1–3]. In order to understand the mechanisms through which such reactions take place and to determine their rates, one must account for the quantum nature of these transferring particles. This feature provides challenges for theory and simulation because quantum dynamics in many-body environments is difficult to carry out.

The rate constants that characterize the interconversion of chemical species can be computed from a knowledge of reactive flux correlation functions. In this chapter, we sketch the derivation of these microscopic formulas for rate constants that can be used to compute electron and proton transfer rates. For activated chemical rate processes, where chemical reactions take place on timescales that are long compared to typical microscopic relaxation times accessible in computer simulation methods, one must devise schemes for sampling rare reactive events. We discuss one such method, the blue moon ensemble, which can be used to obtain the rate from short time simulations of the dynamics. The reactive flux formalism provides a natural decomposition of the rate constant expression into a transition state theory contribution and a transmission coefficient that accounts for dynamical recrossing events. Because the transition state theory rate depends on the free energy along the reaction coordinate, this quantity is an important ingredient in estimating the reaction rate. We give examples of the computation of the free energy for reactions occurring in bulk condensed phases as well as in materials with nanoscale dimensions such as clusters and micelles.

The main focus of this chapter is on quantum mechanical rate processes, such as those associated with electron and proton transfer processes, and we describe methods for computing rates of these reactions. The methods will be illustrated by considering again simple models for such processes in bulk and cluster environments. The emphasis of this presentation is on the theoretical methods and the basic elements of the physical mechanisms that underlie and govern such processes.

2. CHEMICAL REACTION RATES

A phenomenological description of the dynamics of a chemical reaction $A \rightleftharpoons B$ can be given in terms of the mass action rate law,

$$\frac{d\bar{n}_A(t)}{dt} = -k_f \bar{n}_A(t) + k_r \bar{n}_B(t) \tag{1}$$

where $\bar{n}_A(t)$ and $\bar{n}_B(t)$ are the mean number densities of species A and B, respectively. If we let $\bar{\chi} = \delta\bar{n}_A = \bar{n}_A - n_A^{eq} = -\delta\bar{n}_B = -(\bar{n}_B - n_B^{eq})$ be the deviations of the species densities from their equilibrium values, the rate law takes the form,

$$\frac{d\bar{\chi}}{dt} = -(k_f + k_r)\bar{\chi} \tag{2}$$

Our goals are to determine microscopic expressions for the rate constants and to construct algorithms to compute the forward k_f and reverse $k_r = k_f K_{eq}^{-1}$ (K_{eq} is the equilibrium constant) rate constants by molecular dynamics simulation.

2.1. Microscopic Expressions for Rate Constants

We present a quantum mechanical formulation of reaction rates because our primary interest is in proton and electron transfer processes. However, as we shall see below, the classical limit results can be used in some circumstances to obtain approximations to quantum rates. The rate at which the A and B species interconvert can be determined from the reactive

flux correlation expression for the rate constant [4–6]. To derive the chemical rate law [7, 8], we start from the Heisenberg equation of motion for $\hat{\chi}$, an operator that characterizes the deviation of species A from its equilibrium value,

$$\frac{d\hat{\chi}(t)}{dt} = \frac{i}{\hbar}[\hat{H}, \hat{\chi}(t)] \equiv i\hat{\mathcal{L}}_q\hat{\chi}(t) \tag{3}$$

Here the last equality defines the quantum Liouville operator, $\hat{\mathcal{L}}_q$. We shall discuss suitable choices for such species operators in later sections. We may extract the evolution proportional to $\hat{\chi}(t)$ using projection operator methods [9, 10]. An appropriate projection operator is $\hat{\mathcal{P}}\hat{C} = \langle\hat{C}; \hat{\chi}\rangle\langle\hat{\chi}; \hat{\chi}\rangle^{-1}\hat{\chi}$, as $\hat{\mathcal{P}}$ just projects $\hat{C}$ onto $\hat{\chi}$. The Kubo transformed correlation function is defined as [11]

$$\langle\hat{A}; \hat{B}^\dagger\rangle = \beta^{-1}\int_0^\beta d\lambda\, \hat{A}e^{-\lambda\hat{H}}\hat{B}^\dagger e^{\lambda\hat{H}}\hat{\rho}_e \tag{4}$$

Here $\hat{\rho}_e$ is the quantum canonical equilibrium density matrix, $\hat{\rho}_e = e^{-\beta\hat{H}}/\mathrm{Tr}e^{-\beta\hat{H}}$. Using the operator identity

$$e^{i\hat{\mathcal{L}}_q t} = \int_0^t d\tau e^{i\hat{\mathcal{L}}_q(t-\tau)}\hat{\mathcal{P}}i\hat{\mathcal{L}}_q e^{i\hat{\mathcal{L}}_q\tau} + e^{i\hat{\mathcal{L}}_q t} \tag{5}$$

where $\hat{\mathcal{Q}} = 1 - \hat{\mathcal{P}}$, we obtain the generalized Langevin equation for $\hat{\chi}(t)$,

$$\frac{d\hat{\chi}(t)}{dt} = -\int_0^t \tilde{k}(\tau)\hat{\chi}(t-\tau) + \hat{R}(t) \tag{6}$$

where the rate kernel is defined as

$$\tilde{k}(t) = \langle e^{i\hat{\mathcal{Q}}\hat{\mathcal{L}}_q t}i\hat{\mathcal{L}}_q\hat{\chi}; i\hat{\mathcal{L}}_q\hat{\chi}\rangle\langle\hat{\chi}; \hat{\chi}\rangle^{-1} \tag{7}$$

The random reactive flux is $\hat{R}(t) = e^{i\hat{\mathcal{Q}}\hat{\mathcal{L}}_q t}i\hat{\mathcal{L}}_q\hat{\chi}$. If we average the generalized Langevin equation over an initial nonequilibrium ensemble where $\hat{\chi}$ is fixed, we find the generalized chemical rate law.

$$\frac{d\bar{\chi}(t)}{dt} = -\int_0^t d\tau\tilde{k}(\tau)\bar{\chi}(t-\tau) \tag{8}$$

If the rate kernel decays on a timescale τ_m that is much more rapid than the chemical relaxation time $\tau_{chem} = (k_f + k_r)^{-1}$, then the generalized rate law takes the form of the mass action rate law with

$$k = k_f + k_r = \int_0^\infty d\tau\tilde{k}(\tau) \tag{9}$$

If the projected dynamics in this equation is replaced by ordinary dynamics [6] and the above inequalities on the microscopic and chemical relaxation times apply, the rate coefficient may be written as

$$k = \int_0^{t^*} d\tau k(\tau) = \int_0^{t^*} d\tau\langle e^{i\hat{\mathcal{L}}_q t}i\hat{\mathcal{L}}_q\hat{\chi}; i\hat{\mathcal{L}}_q\hat{\chi}\rangle\langle\hat{\chi}; \hat{\chi}\rangle^{-1} \tag{10}$$

where t^* is a time such that $\tau_m \ll t^* \ll \tau_{chem}$. It is convenient to define the time-dependent rate coefficient as

$$K(t) = k_f(t)(1 + K_{eq}^{-1}) = \int_0^t d\tau k(\tau) = \frac{-1}{i\hbar\beta}\mathrm{Tr}[\hat{\chi}, \hat{\chi}(t)]\hat{\rho}_e\langle\hat{\chi}; \hat{\chi}\rangle^{-1} \tag{11}$$

where we have used the fact that $\hat{\chi}(t) = e^{i\hat{\mathcal{L}}_q t}\hat{\chi}$. We shall consider the calculation of this expression in later sections.

2.2. Classical Mechanical Rate Expression

To formulate the classical statistical mechanical description of chemical reactions, consider a molecular system containing N atoms with Hamiltonian $H = K(p) + V(r)$, where $K(p)$ is the kinetic energy, $V(r)$ is the potential energy, and (p, r) denotes the $6N$ momenta and coordinates defining the phase space of the system.

We suppose that the progress of the reaction can be characterized on a microscopic level by a scalar reaction coordinate $\xi(r)$ that is a function of the positions of the particles in the system. For the reaction $A \rightleftharpoons B$, we assume that a dividing surface at $\xi^\ddagger$ serves to partition the configuration space of the system into two A and B domains that contain the metastable A and B species. (In general, it is not always clear what a suitable choice of a reaction coordinate is for any given problem. There is an active area of research devoted to the development of schemes for the determination of reaction paths and suitable coordinates to describe the reaction [12–16]. Here we assume that such microscopic coordinates are known and show how to compute the rate.) The microscopic variable determining the fraction of systems in the A domain is $\chi(r) = n_A(r) - \langle n_A(r)\rangle = \theta[\xi^\ddagger - \xi(r)] - n_A^{eq}$, where θ is the Heaviside function. The angular brackets denote an equilibrium canonical average, $\langle \cdots \rangle = Q^{-1} \int dr\, dr \exp\{-\beta H\} \cdots$, where Q is the partition function and n_A^{eq} is the equilibrium density of species A. Likewise, the fraction of systems in the B domain is $n_B(r) = \theta(\xi(r) - \xi^\ddagger)$. The time rate of change of $n_A(r)$ is

$$\dot{n}_A(r) = -\dot{\xi}(r)\delta[\xi(r) - \xi^\ddagger] \tag{12}$$

The time-dependent forward rate coefficient can be expressed in terms of the equilibrium correlation function of the initial flux of A with the B species density at time t as [4]

$$k_f(t) = \frac{1}{n_A^{eq}}\langle \dot{n}_A(r) n_A(r, t)\rangle = \frac{1}{n_A^{eq}}\langle \{\dot{\xi}\delta[\xi(r) - \xi^\ddagger]\}\theta\{\xi[r(t)] - \xi^\ddagger\}\rangle \tag{13}$$

For an activated rate process, the reactive flux correlation function will decay rapidly initially, followed by a much slower decay that occurs on the timescale of the slow chemical interconversion process. The rate constant can be determined from the "plateau" value established during the slow decay of this time-dependent rate coefficient [6, 7].

Static and dynamic contributions to the rate coefficient can be defined by multiplying and dividing each term on the right-hand side of Eq. (13) by $\langle \delta[\xi(r) - \xi^\ddagger]\rangle$ to obtain

$$\begin{aligned} k_f(t) &= \left\{ \frac{\langle \dot{\xi}\delta[\xi(r) - \xi^\ddagger]\theta[\xi(r(t)) - \xi^\ddagger]\rangle}{\langle \delta(\xi(r) - \xi^\ddagger)\rangle} \right\} \left\{ \frac{\langle \delta[\xi(r) - \xi^\ddagger]\rangle}{n_A^{eq}} \right\} \\ &= \langle \dot{\xi}\theta\{\xi[r(t)] - \xi^\ddagger\}\rangle_{\xi^\ddagger}^{cd} \left\{ \frac{e^{-\beta W(\xi^\ddagger)}}{\int_{\xi' < \xi^\ddagger} d\xi'\, e^{-\beta W(\xi')}} \right\} \end{aligned} \tag{14}$$

where $\langle \cdots \rangle_{\xi^\ddagger}^{cd}$ defines an average conditional on $\xi(r) = \xi^\ddagger$,

$$\langle \cdots \rangle_{\xi'}^{cd} = \frac{\langle \cdots \delta[\xi(r) - \xi']\rangle}{\langle \delta[\xi(r) - \xi']\rangle} \tag{15}$$

In writing the second factor in Eq. (14), we used the fact that the equilibrium average $\langle \delta[\xi(r) - \xi^\ddagger]\rangle = P(\xi^\ddagger)$ is the probability density of finding the value $\xi(r) = \xi^\ddagger$ of the reaction coordinate. The free energy $W(\xi')$ associated with the reaction coordinate is defined by $W(\xi') = -\beta^{-1} \ln[P(\xi')/P_u]$, where P_u is a uniform probability density of ξ'. Typically, the free energy will have the form shown schematically in Fig. 1. A high free energy barrier at $\xi = \xi^\ddagger$ separates the metastable reactant and product states. The equilibrium density of species A is

$$n_A^{eq} = \langle \theta[\xi^\ddagger - \xi(r)]\rangle = \int_{\xi' < \xi^\ddagger} d\xi'\, P(\xi') \tag{16}$$

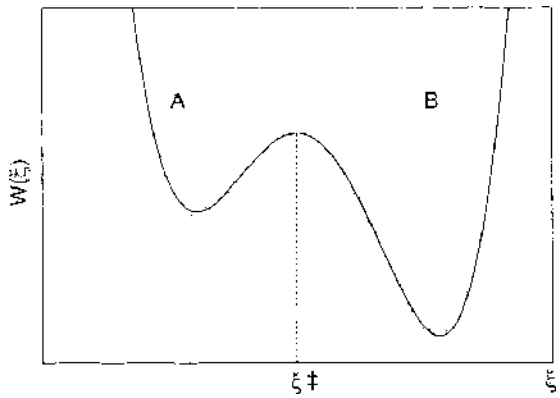

Figure 1. Schematic representation of the free energy versus ξ showing the free energy maximum at $\xi = \xi^{\ddagger}$ and specification of the A and B domains.

The time-dependent transmission coefficient $\kappa(t)$ is defined as $\kappa(t) = k_f(t)/k_f^{\mathrm{TST}}$, where the transition state theory value of the rate constant is given by the limit $t \to 0_+$ of Eq. (13) as [5]

$$k_f^{\mathrm{TST}} = \frac{1}{n_A^{eq}} \langle \dot{\xi} \delta(\xi(r) - \xi^{\ddagger}) \theta(\dot{\xi}) \rangle \tag{17}$$

The transmission coefficient $\kappa(t)$ measures the deviations from k_f^{TST} due to dynamical barrier recrossing events.

2.3. Blue Moon Ensemble

From this discussion, we see that the calculation of the rate coefficient requires the determination of conditional averages depending on specific values of the reaction coordinate. The ensemble of such configurations, which are visited "once in a blue moon," is termed the blue moon ensemble [17]. In the blue moon ensemble method, conditional averages of observables depending only on configuration space variables can be computed by applying holonomic constraints to the equations of motion. For the rate problem, while the value $\xi^{\ddagger}$ we wish to sample is rare in the original ensemble, only configurations with $\xi = \xi^{\ddagger}$ are sampled in the ξ-constrained ensemble. This is illustrated schematically in Fig. 2. In the blue moon ensemble, conditional averages are related to constrained averages by (here we consider the case of a single constraint but generalization to other situations is straightforward [17])

$$\langle A(r) \rangle_{\xi'}^{cd} = \frac{\langle A(r) \delta[\xi(r) - \xi'] \rangle}{\langle \delta[\xi(\mathbf{r}) - \xi'] \rangle} = \frac{\langle |Z|^{-1/2} A(r) \rangle_{\xi'}}{\langle |Z|^{-1/2} \rangle_{\xi'}} \tag{18}$$

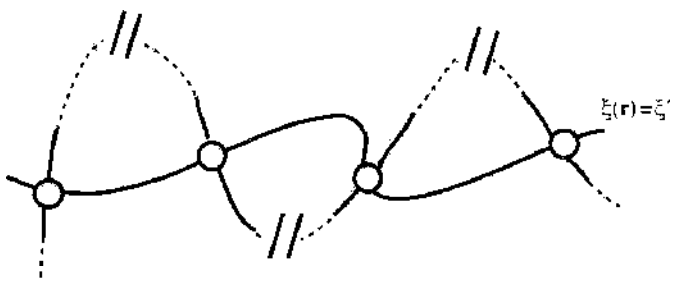

Figure 2. Schematic representation of the sampling procedure in the blue moon ensemble. The bold line depicts the constrained $[\xi(r) = \xi']$ dynamical evolution in phase space. The unconstrained natural evolution of the system is shown as a dashed line. The open circles represent common points in configuration space, which are the initial conditions of the activated trajectory sampling. These points are not real crossings in phase space, as the two trajectories differ in momentum space. Breaks in the dashed line denote long segments in the natural trajectory and indicate that "crossings" are rare events. The dynamics represented by the solid line segments of the unconstrained trajectory close to the crossing points yields the information needed to compute averages.

where the observable $A(r)$ is any function of the configuration space coordinates,

$$Z = \sum_{i=1}^{N} \frac{1}{m_i} \frac{\partial \sigma}{\partial r_i} \cdot \frac{\partial \sigma}{\partial r_i} \tag{19}$$

with $\sigma = \xi(r) - \xi'$ and $\langle \cdots \rangle_{\xi'}$ denotes an average over the constrained ensemble with $\xi = \xi'$. Equation (18) allows one to estimate the *conditional* average on the left-hand side in terms of averages in the *constrained* ensemble, which is statistically advantageous.

In a similar manner, any time correlation function of conditional averages may be written in terms of constrained averages as

$$\frac{\langle A(r, p)B[r(t), p(t)]\delta[\xi(r) - \xi']\rangle}{\langle \delta(\xi(r) - \xi')\rangle} = \frac{\langle |Z|^{-1/2} A(r, p)B[r(t), p(t)]\rangle_{\xi'}}{\langle |Z|^{-1/2}\rangle_{\xi'}} \tag{20}$$

The $|Z|$ factors [18, 19] in these equations arise from the need to unbias the momentum distribution, which is obtained from the constrained dynamics. When Newton's equations of motion are integrated with holonomic constraints [20], both σ and $\dot{\sigma}$ are constrained and this distorts the momentum distribution.

3. FREE ENERGY ALONG THE REACTION COORDINATE

Knowledge of the free energy along the reaction coordinate is important for understanding the mechanisms of condensed phase reactions. From the previous section, we saw that it enters the reactive flux formula for the rate coefficient; it also is an important factor in the transition state theory approximation to the rate constant.

The free energy $W(\xi')$ is the reversible work needed to bring the system from a given reference state to $\xi = \xi'$. The thermodynamic force,

$$F(\xi') = -\frac{dW(\xi')}{d\xi'} \tag{21}$$

can be expressed as the conditional average of $\partial H/\partial \xi$. If we perform the derivative in Eq. (21), we find

$$\begin{aligned} F(\xi') &= -\frac{\langle \frac{\partial H}{\partial \xi} \delta[\xi(r) - \xi']\rangle}{\langle \delta(\xi(r) - \xi')\rangle} = \frac{\left\langle \left(\beta^{-1} \frac{\partial}{\partial \xi} \ln |J| - \frac{\partial V}{\partial \xi}\right) \delta[\xi(r) - \xi'] \right\rangle}{\langle \delta(\xi(r) - \xi')\rangle} \\ &\equiv \frac{\langle \hat{F} \delta[\xi(r) - \xi']\rangle}{\langle \delta[\xi(r) - \xi']\rangle} = \frac{\langle Z^{-1/2} \hat{F}\rangle_{\xi'}}{\langle Z^{-1/2}\rangle_{\xi'}} \end{aligned} \tag{22}$$

where $|J|$ is the Jacobian of the transformation $r \leftrightarrow u = (\sigma, q)$ from coordinates r to the constraint $\sigma = \xi(r) - \xi'$ and a set of remaining coordinates q. The quantity $\hat{F}$ whose conditional average determines the mean force is the sum of two terms: the first term, $\beta^{-1} \frac{\partial}{\partial \xi} \ln |J|$, represents the apparent forces acting on the system due to the use of generalized (noninertial) coordinates, and the second term, $-\partial V/\partial \xi$, corresponds to the force coming from the potential V. Thus, the thermodynamic force can be determined from a conditional average, which can be computed numerically using the blue moon ensemble [see the last equality of Eq. (22)]. Another expression that does not require the computation of the Jacobian and the ξ derivative of the potential has been derived [21]. The thermodynamic integration of $F(\xi')$ over ξ' will yield the potential of mean force.

3.1. Imaginary Time Path Integral Molecular Dynamics

In proton and electron transfer processes, the quantum character of the transferring particle cannot be neglected although, in many circumstances, the environment in which the reaction occurs can be treated classically. Equilibrium properties such as the free energy along the

reaction coordinate for quantum activated processes can be computed using Feynman's path integral approach to quantum mechanics in imaginary time [22]. In this representation of quantum mechanics, quantum particles are mapped onto closed paths $r(t)$ in imaginary time t, $0 \le t \le \beta\hbar$. To see this isomorphism, consider a single quantum particle of mass m with coordinate and momentum operators $\hat{r}$ and $\hat{p}$, respectively. The Hamiltonian operator is

$$\hat{H} = \frac{\hat{p}^2}{2m} + \hat{V}(\hat{r}) \tag{23}$$

where $\hat{V}$ is the potential energy operator. The path integral formalism is derived by evaluating the trace in the definition of the quantum canonical partition function $Z_Q = \mathrm{Tr}\exp[-\beta\hat{H}]$ in the coordinate representation,

$$Z_Q = \int dr \left\langle r|e^{-\beta\left(\frac{\hat{p}^2}{2m}+\hat{V}(\hat{r})\right)}|r\right\rangle \tag{24}$$

Using the Trotter formula, this can be rewritten as

$$Z_Q = \lim_{P\to\infty} \int dr \left\langle r|\left[e^{-\frac{\beta}{2P}\hat{V}(\hat{r})}e^{-\frac{\beta}{P}\frac{\hat{p}^2}{2m}}e^{-\frac{\beta}{2P}\hat{V}(\hat{r})}\right]^P|r\right\rangle \tag{25}$$

This equation involves the product of P operators. One can insert $P-1$ identity operators in the coordinate basis $\hat{I} = \int dr|r\rangle\langle r|$ to obtain

$$Z_Q = \int \prod_{i=1}^{P} dr_i \left[\prod_{i=1}^{P}\langle r_i|e^{-\frac{\beta}{2P}\hat{V}(\hat{r})}e^{-\frac{\beta}{P}\frac{\hat{p}^2}{2m}}e^{-\frac{\beta}{2P}\hat{V}(\hat{r})}|r_{i+1}\rangle\right] \tag{26}$$

where, because of the trace, the condition $r_{P+1} = r_P$ must be imposed. The matrix element has the form,

$$\langle r_i|e^{-\frac{\beta}{2P}\hat{V}(\hat{r})}e^{-\frac{\beta}{P}\frac{\hat{p}^2}{2m}}e^{-\frac{\beta}{2P}\hat{V}(\hat{r})}|r_{i+1}\rangle = e^{-\frac{\beta}{2P}V(r_i)}\langle r_i|e^{-\frac{\beta}{P}\frac{\hat{p}^2}{2m}}|r_{i+1}\rangle e^{-\frac{\beta}{2P}V(r_{i+1})} \tag{27}$$

The coordinate matrix elements of the kinetic energy operator $\hat{p}^2/(2m)$ can be evaluated by inserting the identity operator in terms of momentum eigenstates, $\hat{I} = \int dp\,|p\rangle\langle p|$, using the scalar product between coordinate and momentum eigenstates $\langle r|p\rangle = (2\pi\hbar)^{-1/2}\exp[ipr/\hbar]$, and performing the resulting gaussian momentum integral. One obtains

$$\langle r_i|e^{-\frac{\beta}{P}\frac{\hat{p}^2}{2m}}|r_{i-1}\rangle = \left(\frac{mP}{2\pi\beta\hbar^2}\right)^{1/2}\exp\left[-\frac{mP}{2\beta\hbar^2}(r_{i+1}-r_i)^2\right] \tag{28}$$

With this result, the path integral expression for the canonical partition function becomes

$$Z_Q = \lim_{P\to\infty}\left(\frac{mP}{2\pi\beta\hbar^2}\right)^{1/2}\int\prod_{i=1}^{P} dr_i e^{-\sum_{i=1}^{P}\left[\frac{mP}{2\beta\hbar^2}(r_{i+1}-r_i)^2+\frac{\beta}{P}V(r_i)\right]} \tag{29}$$

In simulations, a finite number P of beads is chosen. Equation (29) is the starting point for a classical isomorphism: the single quantum particle with coordinate r is mapped to a closed or *ring polymer* with P beads with coordinates r_i [23]. The configurational statistics of the polymer is governed by the effective potential,

$$V_{\mathrm{eff}}(r) = \frac{Pm}{2(\beta\hbar)^2}\sum_{i=1}^{P}(r_{i+1}-r_i)^2 + \frac{1}{P}\sum_{i=1}^{P}V(r_i) \tag{30}$$

The problem is then reduced to sampling from a classical canonical distribution involving V_{eff}. In molecular dynamics, this can be achieved by defining the Hamiltonian $H_{\mathrm{eff}} = \sum_{i=1}^{P}(1/2)m_{\mathrm{eff}}\dot{r}_i^2 + V_{\mathrm{eff}}(r_i)$, where m_{eff} is an arbitrary mass assigned to the polymer beads. The number of polymer beads P enters into the definition of the effective potential V_{eff} in two different ways: it scales the magnitude of the interaction potential acting on the quantum particle (the higher P the smaller this effect); and it determines the harmonic spring constant

$k_{eff} = Pm/[2(\beta\hbar)^2]$, which represents quantum dispersion effects; it is stiffer for higher P. This stiffness makes it difficult to obtain an ergodic sampling of the dynamics. Moreover, the larger P, the larger the number of degrees of freedom one must integrate numerically. Thus, although a very large P is desirable to represent quantum effects accurately and calculate averages correctly, in practice a compromise is needed.

This formulation can be generalized easily to a single quantum particle interacting with a bath of classical particles. In this case, the bath particles are simply described by a single polymer bead, and the potential operator $\widehat{V}_{eff}(r, R)$ is

$$\widehat{V}_{eff}(r, R) = V_{eff}(r) + V_c(r, R) + V_b(R) \tag{31}$$

where $V_b(R)$ describes the energy of the bath of classical particles with coordinates R and $V_c(r, R)$ the interaction between the quantum particle (polymer beads) and the classical bath particles. Again, the Hamiltonian H_{eff} used for molecular dynamics sampling must be augmented by the kinetic energy of the classical particles: $\sum_{j=1}^{N}(1/2)M_j\dot{R}_j^2$, where N is the number of classical particles and M_j are their masses. Extension to a bath of distinguishable quantum particles is straightforward. If the bath particles are indistinguishable, then sampling is more difficult.

The path integral approach has been used by Gillan [24] to study rates of quantum activated processes with the centroid density as a reaction coordinate. This approach has been developed extensively by Voth [25]. In this scheme, the reaction coordinate is identified with the position of the centroid of the quantum path $\bar{r}_c$

$$\xi(r) \equiv \bar{r}_c = \frac{1}{P}\sum_{i=1}^{P} r_i \tag{32}$$

With this definition of the reaction coordinate and the isomorphism to a classical ring polymer, the classical blue moon ensemble can be applied straightforwardly to compute the free energy, $W(\xi)$, using the relations given earlier specialized to the centroid reaction coordinate,

$$e^{-\beta W(\xi^{\ddagger})} \propto \langle \delta[\xi(r) - \xi^{\ddagger}] \rangle \propto \int dR \prod_{i=1}^{P} dr_i \delta[\xi(r) - \xi^{\ddagger}] e^{-\beta V_{eff}(r,R)} \tag{33}$$

These equations form the basis for the calculation of free energy in transfer processes of a quantum particle embedded in a bath of classical degrees of freedom.

3.2. Electron Solvation in Reverse Micelles

As the first example of the computation of the free energy along a reaction coordinate, we consider the solvation of an electron in aqueous reverse micelle [26]. Reverse micelles are formed when surfactants are dissolved in neat organic solvents or in organic phases containing small amounts of water. In the latter case, the reverse micelles are roughly spherical pools of water surrounded by the polar head groups of the surfactant molecules. The water/surfactant ratio determines the micellar size and properties. Reverse micelles are useful as microreactors for chemical and biochemical reactions [27, 28]. Chemical reactions can be carried out in confined environments where the encounter rates between species are rapid compared to those in the bulk phases and, because polar and nonpolar environments are in close proximity, reactions that are difficult to achieve in bulk homogeneous environments may be carried out efficiently.

Many of the unusual properties of reverse micelles have their origin in the nature of the water phase within the micelle. Micellar water is often partitioned into two zones corresponding to *surface* water, that is, water tightly bound to the surfactant head groups and associated counterions, and *bulk* water in the center of the micelle. The size of the reverse micelle and the relative amounts of these two water phases can be tuned by changing the ratio w_0 = [water]/[surfactant]. The water structure within the micelles is often studied through its interactions with probe species and solvated electrons, produced by radiolysis or other means. Such studies have provided insight into the nature of the reverse micellar

structure. Chemical and biochemical reactions in reverse micelles often involve electron transfer processes.

Molecular-level studies of electron solvation in reverse micelles are difficult. The micellar structure is complex because it involves the formation of the micelle by arrangement of the surfactant head groups around the water pool. The configurational degrees of freedom of the tail groups play an important part in the stabilization of the micelle. Microscopic studies of micelles in which the full structure of the surfactant molecules has been taken into account have been carried out [29]. Faeder and Ladanyi [30] constructed a simple model for the surfactant molecules to study micellar structure. The tail groups were neglected by supposing that the interior of the micelle was confined by a spherical potential. The surfactant head groups extended into the water pool and were free to move on the micellar surface. This model mimics micelles formed using the sodium bis(2-ethylhexyl)sulfosuccinate (AOT) surfactant in dilute mixtures of water in nonpolar solvents. For this model, the effects of the hydrophobic portions of the amphiphiles and the nonpolar phase are taken into account through a confining potential that gives the micelle a spherical structure with radius R. The SO_3^- head groups and Na^+ counter ions of the surfactant molecules are taken into account explicitly.

Electron solvation in reverse micelles was studied by treating the electron by an imaginary time path integral representation [22]. The model of Faeder and Ladanyi was used for the micelle. Figure 3 shows a molecular configuration for the $w_0 = 7.5$ micelle with a solvated electron–polymer in the interior of the aqueous pool.

The coupling of the electron to the other molecules in the micelle was described by the potential V_{es}, which has three main contributions, $V_{es} = V_{e-w} + V_{e-SO_3} + V_{e-Na^+}$. Here V_{e-w} is the electron–water potential, which was taken from the pseudopotential model of Schnitker and Rossky [31]. Assuming a united atom model for SO_3^- groups, the electron-SO_3^- interaction V_{e-SO_3} was taken to consist of pairwise additive Coulombic terms. For the electron-counter ion contribution V_{e-Na^+}, the local pseudopotential form given in Bachelet et al. [32] was adopted. The potential energy among the classical particles V_{cl} was taken from Faeder and Ladanyi [30], except for the water–water interactions where the SPC model

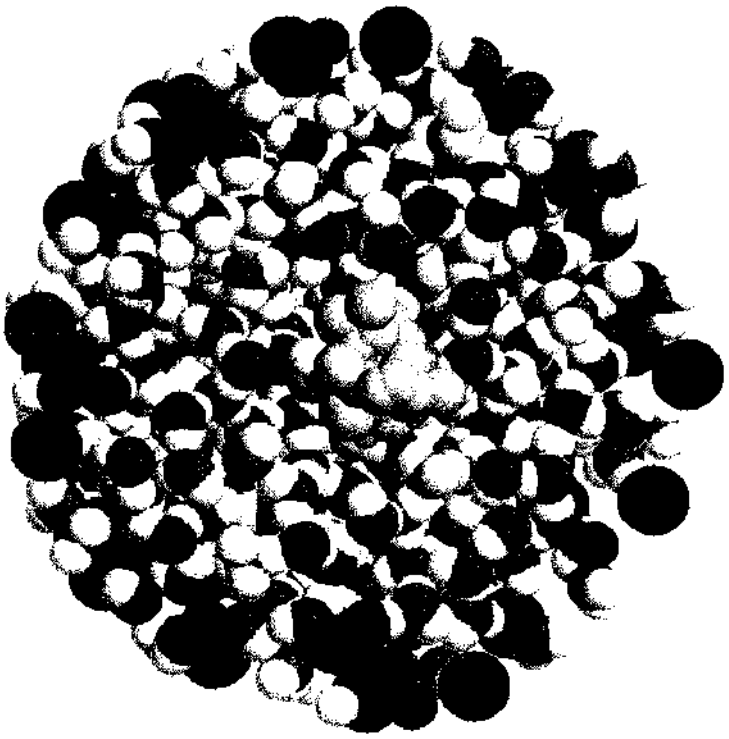

Figure 3. Cross section of the micelle showing a molecular configuration of the internal structure of a $w_0 = 7.5$ aqueous reverse micelle with the electron–polymer (light gray) solvated in the central (bulk water) part of the aggregate. The counter ion and surfactant head groups at the micelle boundary are rendered in black and dark gray shading, respectively.

was employed [33]. To sample the phase space of this system governed by an effective potential V_{eff} of the form in Eq. (31), the multiple time step integration of Newton's equation of motion [34] and the staging algorithm [35] were implemented. A chain [36] of Nosé-Hoover thermostats was used to simulate canonical dynamics. Chains consisting of three Nosé-Hoover thermostats set at $T = 298$ K were coupled to each Cartesian coordinate of the polymer–electron; an additional chain was also attached to the rest of the classical particles.

We now describe the results of simulations of electron solvation on micelles whose sizes lie in the nanometer range and were characterized by the ratios $w_0 = 3$ ($R = 13.2$ Å) and 7.5 ($R = 19.4$ Å). To investigate the solvation of the electron in the micelle, the electron centroid,

$$r_C = \frac{1}{\beta\hbar}\int_0^{\beta\hbar} r(t)\,dt = \frac{1}{P}\sum_{i=1}^{P} r_i \tag{34}$$

was fixed at a given distance from the micelle center by a holonomic constraint. The free energy was computed as a function of this distance from the micelle center from MD simulations of the constrained equations of motion using the SHAKE algorithm [37]. The centroid free energies $W_C(r)$ for two micelle sizes are presented in Fig. 4. One can see that the most favorable radial positions for the electron solvation in $w_0 = 3$ and $w_0 = 7.5$ micelles correspond to $r_C \approx 2$ and ≈ 5.5 Å, respectively. A rough estimate of the actual radial domain within which the electron centroid is likely to be found can be obtained by considering regions where $W_C(r)$ remains comparable to normal thermal energies. For $w_0 = 3.5$, this region is a spherical shell defined by $0.5 \leq r \leq 3$ Å, whereas for $w_0 = 7.5$ the corresponding shell is shifted and is defined by $3.5 \leq r \leq 7$ Å. These calculations show that the electron is preferentially solvated in the interior of the micelle. Additional, more detailed, information on the electron solvation structure has been obtained from such path integral simulation studies [26].

3.3. Proton Transfer in Nanoscale Molecular Clusters

Clusters are an interesting environment for the study of solvent influenced reactions. The competition between bulk and surface solvation forces influences the reaction dynamics and modifies the reaction rate. We present results for the proton transfer free energy in large liquid clusters whose linear dimensions are in the nanometer range [38]. Such clusters lie between the microscopic and macroscopic domains and possess unusual properties. We examine the mechanism for proton transfer in a strongly hydrogen bonded proton–ion complex in a cluster that consists of a classical solvent of polar diatomic molecules. The activation free energy in strongly hydrogen bonded systems arises almost exclusively from solvent effects and proton transfer provides a sensitive probe of cluster solvent structure and dynamics.

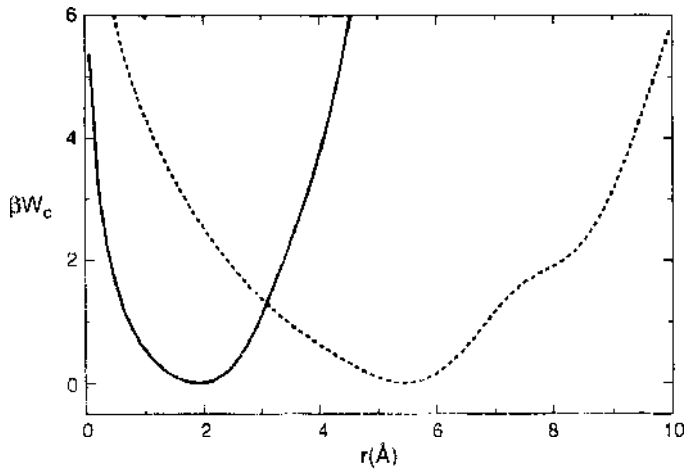

Figure 4. Free energy as a function of the position of the electron centroid for different micelle sizes: $w_0 = 3$ (solid line); $w_0 = 7.5$ (dot-dashed line). The zeros of the mean potential were arbitrarily set at the curve minima.

The proton transfer is assumed to take place between two A^- ions in a proton–ion complex,

$$A - H \cdots A^- \rightleftharpoons A^- \cdots H - A$$

embedded in a cluster of N diatomic molecules composing the solvent. The two ions are fixed at $R_{1,2} = (0, 0, \pm 1.3)$ Å. The solvent diatomic molecules have a dipole moment of $\mu = 5.0$ D. The interactions among the cluster solvent molecules, as well as those between the A^- ions and the solvent, arise from Lennard-Jones and Coulomb forces. The proton interacts with the solvent via Coulomb forces. The proton–ion potential was constructed to model strongly hydrogen bonded systems and has a negligibly small intrinsic barrier. Simulations were carried out for clusters with $N = 40$ solvent molecules at a temperature of 220 K, where the cluster (solvent plus proton–ion complex) is in the liquid state.

The calculations of the proton free energy along the reaction coordinate were performed by treating the proton quantum mechanically and the solvent ions classically as discussed earlier for electron solvation. The equilibrium averages involved in the computation of the free energy were estimated from time averages over trajectories of a system with the Hamiltonian obtained by using fictitious masses for the polymer beads representing the quantum proton. Sampling from a canonical distribution was carried out using Nosé-Hoover dynamics [39, 40]. In order to achieve a proper thermalization of the proton degrees of freedom, a second thermostat, acting exclusively on the proton–polymer degrees of freedom, was included [41].

The free energy was computed using the formulas given earlier, again choosing the z coordinate of the centroid of the proton quantum path in imaginary time, $\bar{z} = \xi(\langle t \rangle)$ [24, 42, 43] as the reaction coordinate. The free energy as a function of z is shown in Fig. 5. The calculations were carried out using the constrained dynamics method described above, namely, the mean force was calculated by constraining $\bar{z}$ and the free energy was obtained by integration of the average force acting on $\bar{z}$. The activation energy (barrier height) is estimated to be $W(0) = 4.94$ kT (2.15 K cal/mol) and the minima of the free energy profile are located at $z_{min} = \pm 0.68$ Å. Because the intrinsic (bare) barrier is negligibly small (0.2 K cal/mol), essentially all of the activation free energy arises from solvent effects. Figure 5 also shows the free energy determined from a histogram of $P(\xi)$ obtained in a 2 ns unconstrained MD run.

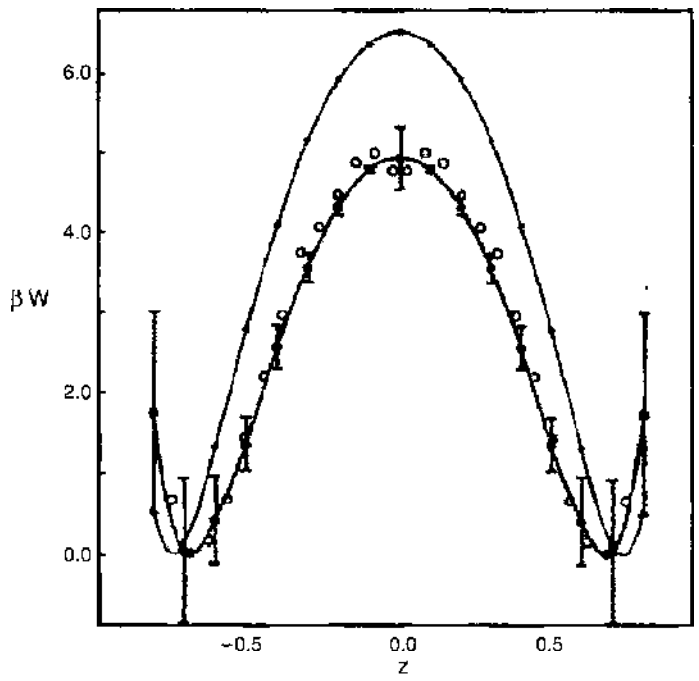

Figure 5. Free energy profiles for the proton transfer reaction. The large dots correspond to the results obtained by integration of the mean force for the quantum proton. The heavy solid line is the interpolation curve to the above results. The open circles are the results from the unconstrained calculation for the quantum proton. The smaller dots and thin line correspond to the results obtained by integration of the mean force for the classical proton.

For comparison, the free energy treating the proton as a classical particle was also computed. These classical results, obtained from a series of constrained MD runs, are shown in Fig. 5 as a thin solid line. The activation energy is 6.56 kT (2.79 K cal/mol), and the minima are located at ±0.74 Å. These differences can be attributed to the delocalization of the proton charge density in the quantum system, which influences how the proton interacts with the solvent [41], and not to tunneling through the bare barrier as in the case of weakly hydrogen bonded systems [42, 43].

One may contrast these cluster results with the analogous results obtained for bulk phase systems with similar potential models [41, 44]. Although the temperatures are different (250 K for the bulk phase simulations and 220 K for the cluster) (the temperature range in which a liquid cluster shows no evaporation over the timescale of the simulation dynamics is restricted), we can compare the barrier heights in units of kT. For the same solvent with a molecular dipole moment of $\mu = 5.0$ D, the bulk phase free energy barrier height was 2.63 kT, much smaller than that found in the cluster. In both cases, the intrinsic barrier in the strongly bonded proton–ion complex is negligible. This model did not include vibrations of the complex, which can lead to substantial changes in the proton transfer dynamics [45].

The solvent polarization reaction coordinate provides another view of the proton transfer activation free energy. The solvent polarization is given by [44, 46–48],

$$\xi(R) = \Delta E(R) = \sum_{i,a} z_a e \left(\frac{1}{|r_i^a - u|} - \frac{1}{|r_i^a - u'|} \right) \tag{35}$$

The points u and u' are chosen at $(0, 0, \pm 0.3)$ Å, which are the minima of the bare potential [44]. The free energy as a function of ΔE was computed by monitoring ΔE in a 2 ns, unconstrained MD run. The proton was treated quantum mechanically as well as classically. The results are shown in Fig. 6, where the heavy line is the quantum result and the thin line is the classical result. The barrier height for the quantum calculation is 4.35 kT and the minima are located at $\pm 2.98 \times 10^{-21}$ C/Å. For this choice of reaction coordinate, the free energy profiles are quadratic over much larger distance ranges about the potential minima and the barrier is sharper. The choice of reaction coordinate should not influence the computation of the full rate constant provided the barrier is sufficiently high to make transitions rare events. As we shall show in the next section, the solvent polarization is a convenient choice for the reaction coordinate in studies of the dynamics of proton transfer in condensed phases.

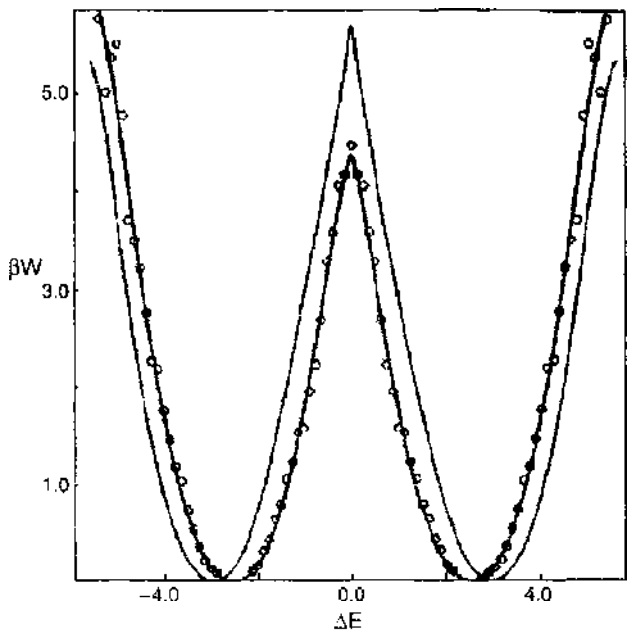

Figure 6. Free energy profiles using the solvent polarization as the reaction coordinate. The heavy and thin solid lines correspond to the least squares fitting of the unconstrained calculations for the quantum and classical protons, respectively. The open circles are the simulation results for the quantum proton. The units for ΔE are 10^{21} C/Å.

4. ADIABATIC REACTION DYNAMICS

Thus far, we have focused on the free energy along the reaction coordinate. In this section, we consider dynamics and the computation of the reaction rate constant. Instead of treating the most general situation of nonadiabatic dynamics, which is the topic of the next section, we begin with a study of the adiabatic dynamics of a quantum reactive system in bath or environment of classical particles. Adiabatic dynamics has been used to compute proton transfer rates [44, 49].

From a theoretical perspective, the treatment of adiabatic dynamics is conceptually simple; one needs to solve the Schrödinger equation for the relevant quantum degrees of freedom in the fixed field field of the classical particles to determine the ground state energy as a function of the positions of the classical particles. The motions of the classical particles are, in turn, governed by Newton's equations of motion with Hellmann-Feynman forces derived from the ground state potential energy function. Here we outline how such a description follows from an approximation to the full quantum correlation function expression for the rate coefficient and present examples to illustrate adiabatic reaction dynamics.

4.1. Quantum-Classical Adiabatic Dynamics

We begin by sketching a derivation of the expression for the rate of a chemical reaction for quantum-classical adiabatic dynamics [6]. The starting point of the analysis is the quantum mechanical expression for the reaction rate given earlier [see Eq. (11)].

We suppose that the quantum system is described by the Hamiltonian

$$\hat{H} = \frac{\hat{P}^2}{2M} + \frac{\hat{p}^2}{2m} + \hat{V}(\hat{q}, \hat{Q}) \tag{36}$$

where $\hat{q}$ and $\hat{Q}$ are the coordinate operators of the quantum subsystem and bath, respectively, and the potential energy operator is $\hat{V}(\hat{q}, \hat{Q})$. Also, we denote the corresponding momentum operators and masses by lower and upper case letters, respectively. We shall consider the limit where the masses M of the bath particles are much larger than those of the quantum subsystem particles, $M \gg m$.

To begin, we rewrite the trace in the quantum expression for the rate kernel $K(t)$ in Eq. (11) in the $\{Q\}$ representation for the bath degrees of freedom and retain the abstract notation for the quantum subsystem degrees of freedom,

$$K(t) = \frac{-1}{i\hbar\beta}\langle\hat{\chi};\hat{\chi}\rangle^{-1}\mathrm{Tr}'\int dQ\ \langle Q|[\hat{\chi}, \hat{\chi}(t)]\hat{\rho}_e|Q\rangle \tag{37}$$

The prime on the trace indicates that only the subsystem degrees of freedom are traced over. Next, we introduce a partial Wigner representation [50] of the bath degrees of freedom. The partial Wigner transform of any operator $\hat{A}$ is

$$\hat{A}_W(R, P) = \int dZ\ e^{-iP\cdot Z/\hbar}\left\langle R + \frac{Z}{2}|\hat{A}|R - \frac{Z}{2}\right\rangle \tag{38}$$

and the partial Wigner transform of the equilibrium density matrix is

$$(\hat{\rho}_e)_W(R, P) = (2\pi\hbar)^{3N}\int dZ\ e^{iP\cdot Z/\hbar}\left\langle R - \frac{Z}{2}|\hat{\rho}_e|R + \frac{Z}{2}\right\rangle \tag{39}$$

These quantities are still operators in the subsystem degrees of freedom.

The evaluation of the rate kernel requires the computation of the matrix elements of triple operator products whose partial Wigner transform is [51]

$$\int dQ\langle Q|\hat{A}\hat{B}\hat{\rho}_e|Q\rangle = \int dR dP\left[\hat{A}_W(R, P)e^{\hbar\Lambda/2i}\hat{B}_W(R, P)\right](\hat{\rho}_e)_W(R, P) \tag{40}$$

where

$$\Lambda = \overleftarrow{\nabla}_P\cdot\overrightarrow{\nabla}_R - \overleftarrow{\nabla}_R\cdot\overrightarrow{\nabla}_P \tag{41}$$

and the directions of the arrows on the gradient operators indicate the directions in which these operators should be applied. Using these results the rate kernel takes the form,

$$K(t) = \langle\hat{\chi};\hat{\chi}\rangle^{-1}\frac{1}{-i\hbar\beta}\mathrm{Tr}'\int dRdP\,[\hat{\chi}_W(R,P)e^{\hbar\Lambda/2i}\hat{\chi}_W(R,P,t) - \hat{\chi}_W(R,P,t)e^{\hbar\Lambda/2i}\hat{\chi}_W(R,P)](\hat{\rho}_e)_W(R,P) \quad (42)$$

where $\hat{\chi}_W(R,P,t) \equiv \hat{\chi}_W(t)$ is the solution of the equation of motion

$$\frac{d\hat{\chi}_W(t)}{dt} = \frac{i}{\hbar}[\hat{H}_W e^{\hbar\Lambda/2i}\hat{\chi}_W(t) - \hat{\chi}_W(t)e^{\hbar\Lambda/2i}\hat{H}_W] \quad (43)$$

Here the partial Wigner representation of the Hamiltonian is

$$\hat{H}_W(R,P) = \frac{P^2}{2M} + \frac{\hat{p}^2}{2m} + \hat{V}_W(\hat{q},R) \quad (44)$$

Next, we take the limit where the bath particles are massive compared to those of the quantum subsystem. It is convenient to introduce scaled variables such that the momenta of the heavy particles have the same order of magnitude as the momenta of the light particles. Consequently, we scale distances by the characteristic wavelength of the light particles, $\lambda_m = (\hbar^2/m\epsilon_0)^{1/2}$, time in units of $t_0 = \hbar/\epsilon_0$. Here ϵ_0 is an energy unit, typically $\epsilon_0 = \beta^{-1}$. In these units the light particle momenta are scaled by $p_m = m\lambda_m/t_0 = (m/\epsilon_0)^{1/2}$ and the heavy particle momenta by $P_M = (M\epsilon_0)^{1/2}$. In scaled units $\hbar\Lambda/(2i) \to \mu\Lambda/(2i)$, and we may expand the equation of motion in the small parameter $\mu = (m/M)^{1/2}$. Expanding to linear order in μ and then returning to unscaled units, the equation of motion, Eq. (43), becomes [6],

$$\frac{d\hat{\chi}_W(t)}{dt} = \frac{i}{\hbar}[\hat{H}_W,\hat{\chi}_W(t)] - \frac{1}{2}(\{\hat{H}_W,\hat{\chi}_W(t)\} - \{\hat{\chi}_W(t),\hat{H}_W\}) \quad (45)$$

This is a quantum-classical Liouville equation for a dynamical variable [6, 52]. Carrying out a similar μ expansion, the rate kernel, Eq. (42), takes the form,

$$K(t) = \frac{1}{\beta}\langle\hat{\chi};\hat{\chi}\rangle^{-1}\mathrm{Tr}'\int dRdP\left(\frac{i}{\hbar}[\hat{\chi}_W,\hat{\chi}_W(t)] - \frac{1}{2}(\{\hat{\chi}_W,\hat{\chi}_W(t)\} - \{\hat{\chi}_W(t),\hat{\chi}_W\})\right)(\hat{\rho}_e)_W \quad (46)$$

We may evaluate this expression (45) in any convenient representation and for this purpose we choose the basis of adiabatic eigenstates of the Hamiltonian operator $\hat{h}_W(R) = \hat{p}^2/2m + \hat{V}_W(q,R)$:

$$\hat{h}_W(R)|\alpha;R\rangle = E_\alpha(R)|\alpha;R\rangle \quad (47)$$

Equation (46) can also be represented in this basis. This analysis is the starting point for a systematic approach to nonadiabatic dynamics which will be presented in some detail in the next section. Here we will be concerned solely with the adiabatic limit where the dynamics is assumed to take place on a single adiabatic surface. In this case, the adiabatic representation of Eq. (45) takes an especially simple form,

$$\frac{d\chi_W^\alpha(t)}{dt} = \{\chi_W^\alpha(t), H_W^\alpha\} \quad (48)$$

where $\chi_W^\alpha = \langle\alpha;R|\hat{\chi}_W(t)|\alpha;R\rangle$ and $H_W^\alpha = P^2/2M + E_\alpha(R)$. This is just a classical evolution equation but with Hellmann-Feynman forces,

$$F_W^\alpha = -\langle\alpha;R|\nabla\hat{h}_W(R)|\alpha;R\rangle = -\frac{\partial E_\alpha(R)}{\partial R} \quad (49)$$

determined by the potential $E_\alpha(R)$ obtained from the solution of the Schrödinger equation for the α adiabatic eigenstate. The rate kernel may be written in the adiabatic limit as

$$K^\alpha(t) = \langle\chi_W^\alpha\chi_W^\alpha\rangle^{-1}\frac{1}{\beta}\int dRdP\,\{\chi_W^\alpha(t),\chi_W^\alpha\}\rho_W^\alpha \quad (50)$$

with $\rho_{0\alpha}^{n}(R,P) = e^{-\beta H_{0\alpha}^{n}} / \int dR dP\ e^{-\beta H_{0\alpha}^{n}}$. The algorithm for adiabatic mixed quantum-classical dynamics is simple. The dynamical variables depend on the classical coordinates (R, P) and the adiabatic state $|\alpha; R\rangle$. The classical coordinates evolve by Newton's equations of motion but with Hellmann-Feynman forces corresponding to the α adiabatic state determined as a function of the instantaneous position R.

4.2. Adiabatic Proton-Transfer Reactions in Solution

We now return to the study of proton transfer reactions in strongly hydrogen bonded complexes but now embedded in a bulk solvent of dipolar molecules with dipole moment 5.0 D. The molecular dynamics calculations we describe were carried out for a system of $N = 342$ solvent molecules, two ions, and a proton in a cubic box with periodic boundary conditions [44]. The simulations of the dynamics of the quantum proton coupled to the classical solvent were carried out as follows. Given a configuration of the solvent, the Schrödinger equation,

$$H(r; R)\Psi(r; R) = E(R)\Psi(r; R) \tag{51}$$

where $H(r; R)$ is the Hamiltonian for the proton with coordinate r in the fixed field of the classical particles with coordinates R, was solved by expanding the proton wave function in a set of $n = 156$ localized Gaussian functions $\phi_i(r)$ as

$$\Psi(r; R) = \sum_{i=1}^{n} c_i(R)\phi_i(r) \tag{52}$$

yielding a standard (nonorthogonal) eigenvalue problem from which the energies and eigenfunctions were obtained. After calculating the proton ground state wave function $\Psi_0(r; R)$ and energy $E_0(R)$, the proton contribution to the force acting on every site of the solvent was calculated. Given these forces, the solvent equations of motion,

$$M_i \ddot{R}_i = -\nabla_{R_i} E_0(R) \tag{53}$$

were integrated.

Solution of the eigenvalue problem in the absence of the solvent yields an energy spacing between the ground and first excited states which is somewhat greater than $k_B T$, just within the region of validity of the adiabatic approximation. In the presence of solvent, the energy gap is large when the proton is hydrogen bonded to one of the ions (reactant or product configurations) but is comparable to that in the absence of solvent when the proton is in the vicinity of the activated region. Proton transfer events are triggered by solvent fluctuations that provide no preferential solvation for either ion, making this an interesting reaction in which to study solvent effects on quantum reactive events.

The choice of the reaction coordinate depends on the nature of the transition process, and there are a number of possible ways to construct a function of the solvent coordinates that can be used to monitor the proton transfer. A possible choice of the reaction coordinate is the mean value of the z component of the position of the proton,

$$\xi(R) = \bar{z}(R) = \langle \Psi_0(R)|\hat{z}|\Psi_0(R)\rangle \tag{54}$$

If the reaction involves the passage of the proton from a region near one ion to the other, configurations with negative and positive values for ξ would correspond to reactant and product states, respectively. By symmetry, the activated state is located at $\xi = \xi^{\ddagger} = 0$.

The solvent polarization $\Delta E(R)$ [see Eq. (35)] is another, more convenient, choice for the reaction coordinate because it reflects the participation of the solvent in the proton transfer process. Furthermore, because $\Delta E(R)$ is an analytical function of the solvent coordinates, it is easy to generate trajectories in which the initial states are located at the transition state using blue moon sampling.

The expression (17) for the TST rate constant, specialized to the polarization reaction coordinate is

$$k^{TST} = (2\pi\beta)^{1/2} \frac{\langle D^{1/2}\delta(\Delta E - \Delta E^{\ddagger})\rangle}{\langle \theta(\Delta E - \Delta E^{\ddagger})\rangle} \tag{55}$$

where

$$D = \frac{1}{2m}\sum_i \left(\sum_\alpha \nabla_{i,\alpha}\Delta E\right)^2 \tag{56}$$

assuming all solvent masses are equal. The reaction coordinate ΔE and its time derivative are not statistically independent, and the expected value in the expression for k^{TST} does not factor into coordinate and velocity contributions [17].

Equation (55) can be calculated in the blue moon ensemble as discussed earlier [see Eq. (18)] using the expression,

$$k^{TST} = (2\pi\beta)^{-1/2}\frac{\langle\delta(\Delta E - \Delta E^{\ddagger})\rangle}{\langle D^{-1/2}\rangle_{\Delta E=0}\langle\theta(\Delta E - \Delta E^{\ddagger})\rangle} \tag{57}$$

Using this formula, the TST value for the rate coefficient was found to be $k^{TST} = (4.03 \pm 0.29) \times 10^9\ s^{-1}$ [44].

Deviations from transition-state theory are accounted for by the transmission coefficient $\kappa = \kappa(t^*)$, where $\tau_{mic} \ll t^* \ll \tau_p$, with τ_{mic} a time that characterizes the relaxation of the microscopic degrees of freedom and τ_p the proton transfer time. The transmission coefficient takes the form,

$$\kappa(t) = \frac{\langle D^{-1/2}\dot{\Delta E}\theta[\Delta E(t)]\rangle_{\Delta E=0}}{\langle D^{-1/2}\dot{\Delta E}\theta(\Delta E)\rangle_{\Delta E=0}} \tag{58}$$

Figure 7 shows the time-dependent transmission coefficient. Initial state configurations were generated using the blue moon ensemble. At $t = 0$, the constraint on the reaction coordinate was released, and particle velocities were assigned according to the generalization of Boltzmann statistics for rigid diatomic molecules. From these simulations, the transmission coefficient is estimated to be $\kappa = 0.57 \pm 0.11$. There is a non-negligible deviation from TST for this proton transfer process.

4.3. Proton Transfer Dynamics in Nanoclusters

We next consider the same proton–ion complex but now embedded in a mesoscopic molecular cluster [53] instead of a bulk condensed phase. Again we treat the proton dynamics adiabatically. Calculations were performed for clusters of $N = 20$ and $N = 67$ solvent molecules at temperatures of 200 and 260 K, respectively. Under these conditions, the clusters were in the liquid state. Evaporation did not occur on the timescale of the simulations, typically several nanoseconds. As discussed earlier, both the average proton position and the solvent polarization can be used to track the hops of the proton between the reactant and product configurations.

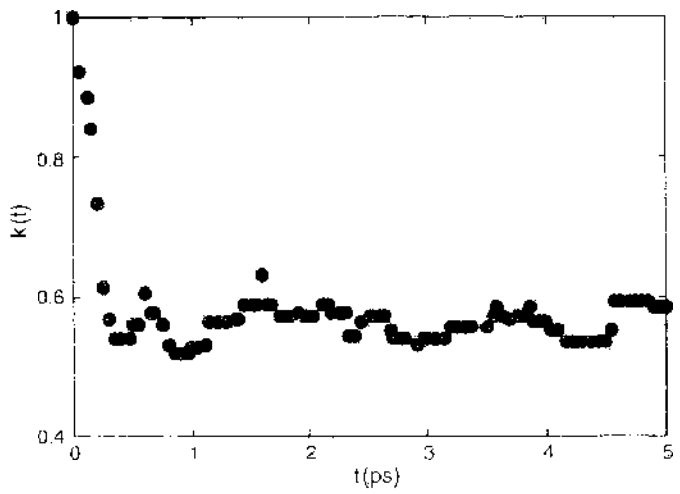

Figure 7. The time-dependent transmission coefficient for adiabatic dynamics.

The cluster solvent molecules tended to strongly solvate the part of the proton–ion complex with the more exposed negative charge: that is, the end of the complex that is less strongly bonded to the H^+ ion. This suggests that the complex tends to "float" on the surface of the cluster. When the H^+ ion is strongly bound to one A^- ion, this $A^- \cdots H$ dipole has a smaller dipole moment than that of a solvent molecule. Consequently, the solvent–solvent interactions are stronger than the interactions between a solvent molecule and this part of the proton–ion complex. These energetic arguments suggest that it may be favorable for this end of the proton–ion complex to reside on the surface of the cluster, a fact supported by the simulation results. Of course, both entropic as well as energetic factors come into play in determining the structure of mixed clusters [54] but, in the cases studied, energetic factors played a dominant role.

The position of the proton–ion complex in the cluster has a strong influence on the nature of the proton transfer dynamics. In the case of a 20 molecule cluster the complex resides for long portions of time on the surface of the cluster and long portions of time in the interior of the cluster. If the complex is on the surface of the cluster, then transitions rarely occur; however, if the complex makes an excursion into the interior, then this excursion correlates with a proton transfer. The picture is somewhat different for the 67 molecule cluster. The proton–ion complex rarely penetrates deeply into the cluster. Some of the proton transfer events correlate with excursions of the complex into the cluster, but only one solvent layer deep and never far from the surface. However, even when the complex floats on the surface of the cluster, there are frequent proton transfer events. Figure 8 shows such a proton transfer event. Initially, the proton (gray) is strongly bound to the one of the ions (black) in the complex. The complex resides on the surface of the cluster with one end, to which the proton is weakly bound, solvated in the cluster, and the other end extending out of the cluster. In the course of time, a fluctuation occurs that causes the complex to assume a configuration parallel to the surface so that there is a more nearly equal solvation of the two ends of the complex. This is a favorable configuration for the proton transfer so that it takes place in frame (a) of this figure. Once the proton transfer is complete, then the favorable complex configuration is for the now strongly hydrogen bonded end to protrude from the cluster and the weakly bound end to lie within the cluster [frame (b)].

Thus, the mechanism of the proton transfer depends on the size of the cluster. For smaller clusters, fluctuations lead to penetration of the complex into the interior of the cluster where proton transfer is likely. For larger clusters, transitions occur primarily by orientational motion of the complex on the surface of the cluster or when the complex makes shallow penetrations into the cluster. Deep penetrations of the complex into the cluster are rare. For the smaller 20 molecule cluster, presumably the orientational motion of the complex is restricted on the surface due to the larger surface forces.

Figure 9 shows the transmission coefficient as a function of time for the 67 molecule cluster. The results in this figure show a rapid decay on a timescale that is less than a picosecond followed by a somewhat longer decay, of the order of a few picoseconds, to a plateau value. From this graph, the transmission coefficient may be determined from the plateau values and one finds $\kappa = 0.4$. The timescale for the establishment of a plateau in $\kappa(t)$ is longer in the

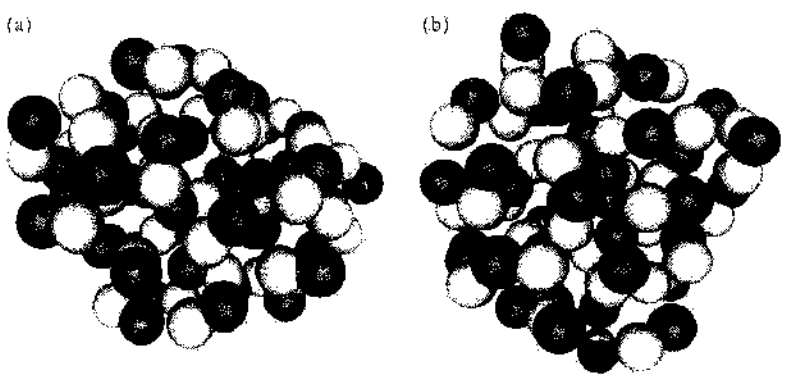

Figure 8. Cluster configurations during (a) and after (b) a proton transfer event for a 67 molecule cluster.

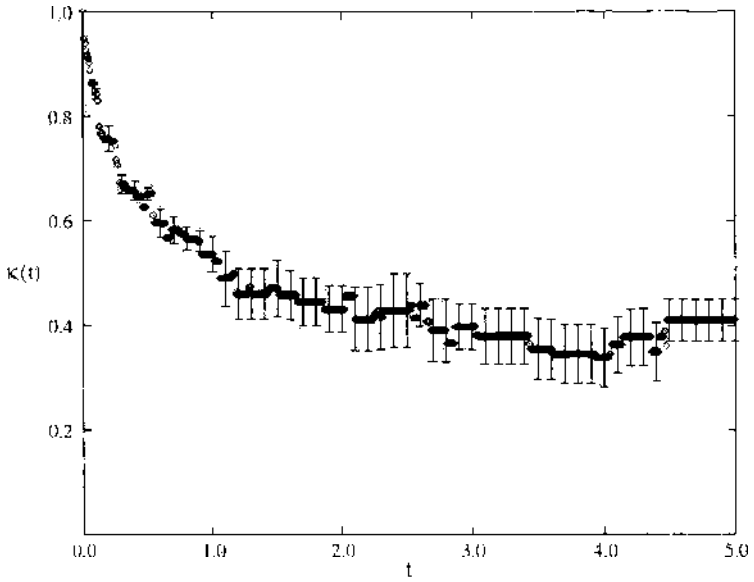

Figure 9. Transmission coefficient as a function of time for a 67 solvent molecule cluster.

cluster environment than in the bulk for a similar but not identical intrinsic potential. This again signals different dynamics in the cluster compared to the bulk.

5. MEAN FIELD AND SURFACE HOPPING DYNAMICS

There are many instances where the dynamics can take place on more than one potential energy surface and transitions between different quantum states must be taken into account. In such cases, the adiabatic approximation is inadequate. Charge transfer in molecules is one example; nonradiative relaxation in molecular or condensed phase systems and the field of photochemistry provide other good examples.

In order to see how nonadiabatic effects enter the dynamics, we consider the total Hamiltonian for a system composed of light (mass m) particles with coordinates r and heavy (mass M) particles with coordinates R,

$$H(r, R) = -\frac{\hbar^2}{2M}\frac{\partial^2}{\partial R^2} + h(r; R) \tag{59}$$

where $h(r; R) = -\frac{\hbar^2}{2m}\frac{\partial^2}{\partial r^2} + V(r, R)$ is the Hamiltonian for the light particles in the field of the fixed heavy particles. The adiabatic basis is given by the solution of the eigenvalue problem $\hat{h}|\alpha; R\rangle = E_\alpha(R)|\alpha; R\rangle$. We let $\langle r|\alpha; R\rangle = \phi_\alpha(r; R)$ be the adiabatic wave function for state α and make the ansatz

$$\Psi(r, R, t) = \sum_\alpha \psi_\alpha(R, t)\phi_\alpha(r; R) \tag{60}$$

for the wave function of the entire system. Substitution into the time-dependent Schrödinger equation

$$i\hbar\frac{\partial}{\partial t}\Psi(r, R, t) = H\Psi(r, R, t) \tag{61}$$

yields the following equation for the wave function for the heavy mass degrees of freedom:

$$i\hbar\frac{\partial}{\partial t}\psi_\alpha(R, t) = \left[-\frac{\hbar^2}{2M}\frac{\partial^2}{\partial R^2} + E_\alpha(R)\right]\psi_\alpha(R, t) + \sum_{\alpha'} C_{\alpha\beta}\psi_{\alpha'}(R, t) \tag{62}$$

where we have introduced the coupling operator

$$C_{\alpha\alpha'} = \left\langle \alpha; R\left|\frac{\hat{P}^2}{2M}\right|\alpha'; R\right\rangle - \frac{\hbar^2}{M}\langle\alpha; R|\nabla_R|\alpha'; R\rangle \cdot \nabla_R \tag{63}$$

where $\hat{P}^2/2M$ is the kinetic energy operator. The diagonal elements $C_{\alpha\alpha}$ give corrections to the adiabatic eigenvalues E_{α}, and the off-diagonal terms describe the coupling between the different quantum states. When $C_{\alpha\beta} \approx 0$ (Born-Oppenheimer approximation), we recover adiabatic dynamics.

We next consider various schemes for constructing mixed quantum-classical dynamics that allow for nonadiabatic effects. The quantum and classical degrees of freedom interact and their dynamics must be treated in a consistent fashion. Time-dependent variations of the classical degrees of freedom induce transitions between quantum states of the light mass subsystem and these transitions, in turn, modify the forces that govern the motion of the classical particles. Ehrenfest (or mean-field) and surface-hopping schemes are two approximate mixed quantum-classical methods to describe nonadiabatic dynamics [55]. Quantum-classical Liouville dynamics provides a more rigorous approach to nonadiabatic dynamics.

5.1. Mean-Field Method

The mean field approach is based on Ehrenfest's equations of motion for the evolution of the position and momentum operators of the heavy mass particles. Assuming that the expectation value of a function can be approximated by the function of the expectation value, we obtain the following mean field equations,

$$\begin{aligned} \frac{dR(t)}{dt} &= \frac{P(t)}{M} \\ \frac{dP(t)}{dt} &= -\nabla\langle\psi[R(t),t]|\hat{h}[R(t)]|\psi[R(t),t]\rangle \end{aligned} \tag{64}$$

where the wave function evolves through the time-dependent Schrödinger equation,

$$i\hbar\frac{\partial}{\partial t}|\psi[R(t),t]\rangle = \hat{h}[R(t)]|\psi[R(t),t]\rangle \tag{65}$$

According to these equations, the heavy mass degrees of freedom evolve classically along a single *mean* trajectory determined by the effective potential energy surface $E_{ef}[R(t)] = \langle\psi[R(t),t]|\hat{h}[R(t)]|\psi[R(t),t]\rangle$. Mean-field methods have been used to compute proton transfer rates. [56, 57] Outside strong interaction regions, the quantum system will typically collapse onto a given state, and the mean field equations will likely be a poor approximation to the dynamics. Surface-hopping algorithms have been devised to account for this difficulty.

5.2. Surface-Hopping Dynamics

In surface-hopping dynamics, the system evolves on specified adiabatic energy surfaces interspersed by quantum transitions that occur probabilistically and change the state of the system. Observables are computed from an average over an ensemble of such surface-hopping trajectories. A variety of such schemes have been proposed. One of the most popular is Tully's fewest switches algorithm [55, 58]. In this method, the time-dependent Schrödinger equation (65) is solved by expanding the wave function in the instantaneous adiabatic eigenstates of the Hamiltonian $\hat{h}[R(t)]$, $\hat{h}[R(t)]|\alpha; R(t)\rangle = E_{\alpha}[R(t)]|\alpha; R(t)\rangle$,

$$|\Psi(R(t),t)\rangle = \sum_{\alpha} c_{\alpha}(t)|\alpha; R(t)\rangle \tag{66}$$

yielding the evolution equation for the coefficients

$$i\hbar\frac{dC_{\alpha}(t)}{dt} = (E_{\alpha} - E_0)C_{\alpha}(t) - i\hbar\sum_{\alpha'}\frac{P}{M}\cdot d_{\alpha\alpha'}C_{\alpha'}(t) \tag{67}$$

where $d_{\alpha\alpha'} = \langle\alpha; R(t)|\nabla_{R(t)}|\alpha; R(t)\rangle$ is the nonadiabatic coupling matrix element and

$$C_{\alpha}(t) = c_{\alpha}(t)\exp\left\{i\int_0^t dt' E_0[R(t')]/\hbar\right\} \tag{68}$$

During each molecular dynamics time step Δ, the classical degrees of freedom evolve by Newton's equation of motion subject to Hellmann-Feynman forces that depend on

instantaneous adiabatic eigenstates. The probability of a hop from state α to α' is given by

$$w_{\alpha\alpha'} = \gamma_{\alpha\alpha'}\theta(\gamma_{\alpha\alpha'}) \tag{69}$$

where $\theta(x)$ is the Heaviside function and

$$\gamma_{\alpha\alpha'} = \frac{-2\Re\{\rho^*_{\alpha'\alpha}(t+\Delta)[P(t)/M]\cdot d_{\alpha\alpha'}[R(t)]\Delta\}}{\rho_{\alpha\alpha}(t+\Delta)} \tag{70}$$

Here $\rho^{\alpha\alpha'}(t)$ is a matrix element of the density matrix in the adiabatic basis, $\rho^{\alpha\alpha'}(t) = \langle\alpha; R(t)|\hat{\rho}(t)|\alpha'; R(t)\rangle = \langle\alpha; R(t)|\Psi[R(t), t]\rangle\langle\Psi[R(t), t]|\alpha'; R(t)\rangle = c^*_\alpha(t)c_{\alpha'}(t)$.

Pechukas [59] presented a description of nonadiabatic dynamics based on an analysis of the Feynman path integral expression for the propagator. The equations of motion for the bath degrees of freedom involve a nonlocal quantum force. Surface-hopping schemes that use approximations to this nonlocal force have been constructed by Rossky et al. [60] and Coker et al. [61]. In particular, Coker and Xiao [61] have shown that a short time approximation that localizes the Pechukas force leads to Tully's algorithm.

5.3. Nonadiabatic Proton Transfer in Nanoclusters

Surface-hopping schemes have been used to study proton and hydrogen atom transfer rates in the condensed phase [62] and in biosystems [63]. We begin with an investigation of nonadiabatic effects on proton transfer rates in nanoclusters using Tully's surface-hopping dynamics [53].

The model system is the same as that described in Section 4.3, namely, a proton–ion complex embedded in a cluster of polar diatomic molecules. The average position of the proton $\bar{z}(R) = \langle\alpha; R(t) \mid \hat{z} \mid \alpha; R(t)\rangle$ is shown in Fig. 10 (bottom panel) as a function of time for a nonadiabatic reactive trajectory. The upper panel of the figure shows the protonic

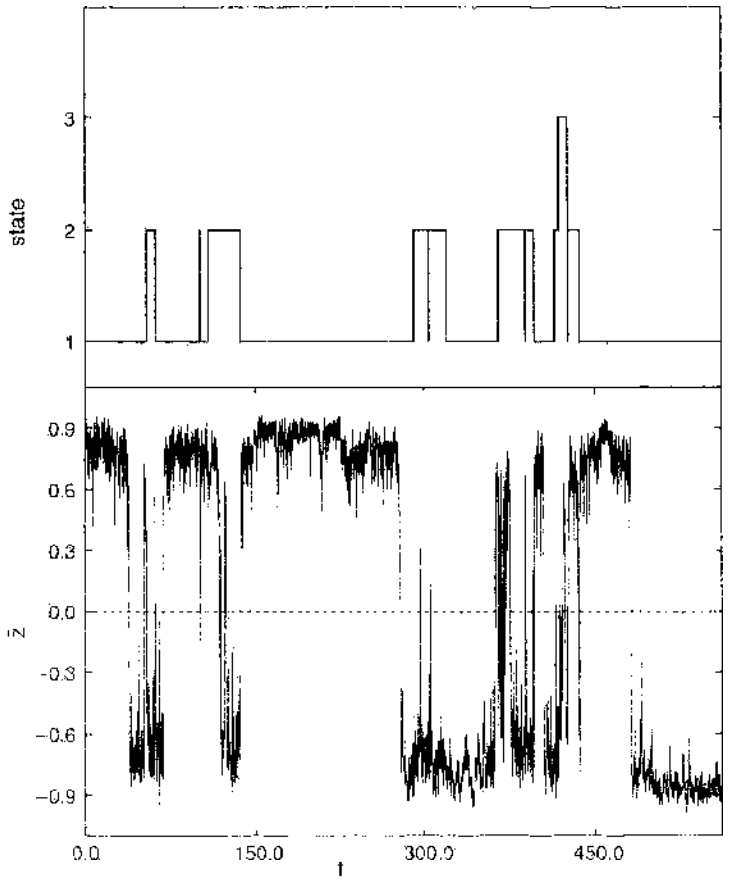

Figure 10. (top) Protonic state. (bottom) expectation value of the position of the proton $\bar{z}$ as a function of time for a 67-molecule cluster.

state determined by the stochastic algorithm that is used to compute the Hellmann-Feynman forces for the classical particles. Nonadiabatic transitions frequently occur when the proton transfers to and from reactant and product configurations. This breakdown of the adiabatic approximation occurs because the transition state configurations correspond to a nearly symmetrical solvation of the proton–ion complex, and the energy gap between the lowest adiabatic states is small for such configurations. The three lowest adiabatic energies for a short time interval close to the transition state regime are shown in Fig. 11. The black dots denote the path of the proton in the proton state space. The three lowest eigenvalues show similar time variations. Proton hops between the different states occur by jump transitions when the difference between the energy states is close to 1–2 kT.

Nonadiabatic transitions influence the mechanism and rate of the reaction. When the proton is in an excited state, the proton density is diffuse and symmetric, and solvent configurations that favor the transition state are favored. As a result, the number of quantum transitions and proton recrossing attempts increase. This changes the transfer rate. The rate constant for the reaction was computed by counting the number of proton transfers in the nonadiabatic dynamics trajectories and was found to be $\kappa = 0.011$ ps^{-1}. The dynamics is dominated by the ground state, and the change in the rate due to surface hopping is not great for this model system. In systems where the nonadiabatic character is more pronounced, effects due to proton hops to the excited states will have important implications for the mechanisms and rates of the reaction.

6. QUANTUM-CLASSICAL LIOUVILLE EQUATION

Both mean-field and surface-hopping dynamics make assumptions about the nature of the time evolution of the system. Mean-field equations assume that the Hellmann-Feynman forces that govern the classical degrees of freedom can be computed from the time-evolving wave function. Surface-hopping dynamics assumes that the classical degrees of freedom evolve on adiabatic potential energy surfaces with quantum transitions determining switches among different potential surfaces. We now show how quantum-classical dynamics can be derived from quantum Liouville equation by carrying out an expansion of the evolution operator in the small parameter $\mu = (m/M)^{1/2}$ introduced in Section 4.1 [52]. We again consider a quantum system with Hamiltonian given by Eq. (36) whose time evolution is described by the quantum Liouville or von Neumann equation,

$$\frac{\partial \hat{\rho}}{\partial t} = -\frac{i}{\hbar}[\hat{H}, \hat{\rho}] \tag{71}$$

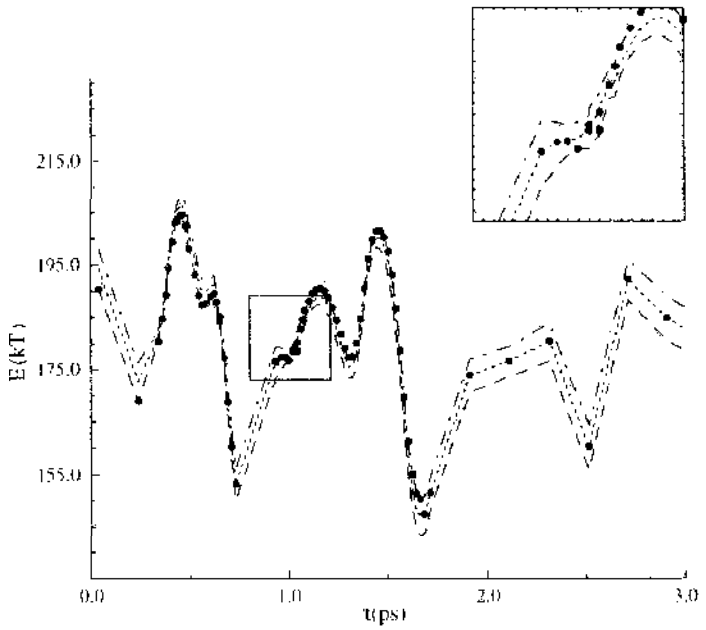

Figure 11. Instantaneous protonic adiabatic eigenstates as a function of time.

If we take the partial Wigner transform [defined in Eqs. (38) and (39)] of this equation we obtain,

$$\frac{\partial \hat{\rho}_W(R,P,t)}{\partial t} = -\frac{i}{\hbar}\Big[(\widehat{H}\hat{\rho})_W - (\hat{\rho}\widehat{H})_W\Big]$$
$$= -\frac{i}{\hbar}\Big[\widehat{H}_W(R,P)e^{\hbar\Lambda/2i}\hat{\rho}_W(R,P,t) - \hat{\rho}_W(R,P,t)e^{\hbar\Lambda/2i}\widehat{H}_W(R,P)\Big] \quad (72)$$

which is the analog of Eq. (45) for a dynamical variable. The operator Λ is defined in Eq. (41) and is the negative of the Poisson bracket operator. Scaling variables as discussed earlier for adiabatic dynamics, expanding in μ and finally returning to unscaled variables we obtain the quantum-classical Liouville equation [52, 64–68],

$$\frac{\partial \hat{\rho}_W(R,P,t)}{\partial t} = -\frac{i}{\hbar}[\widehat{H}_W(R,P), \hat{\rho}_W(R,P,t)]$$
$$+\frac{1}{2}\Big(\Big\{\widehat{H}_W(R,P), \hat{\rho}_W(R,P,t)\Big\} - \Big\{\hat{\rho}_W(R,P,t), \widehat{H}_W(R,P)\Big\}\Big)$$
$$\equiv -i\widehat{\mathcal{L}}\hat{\rho}_W(R,P,t) = -\big(\widehat{H}_W, \hat{\rho}_W(R,P,t)\big) \quad (73)$$

where the last line defines the quantum-classical Liouville operator, $\mathcal{L}$, and the quantum-classical bracket, $(\cdot,\cdot)$ [69, 70].

To construct a surface-hopping picture of the dynamics we consider the representation of this equation in a basis of adiabatic eigenstates defined in Eq. (47). Taking matrix elements of Eq. (73) and letting $\rho_W^{\alpha\alpha'}(R,P) = \langle\alpha; R|\hat{\rho}_W(R,P)|\alpha'; R\rangle$, we obtain

$$\frac{\partial \rho_W^{\alpha\alpha'}(R,P,t)}{\partial t} = \sum_{\beta\beta'} -i\mathcal{L}_{\alpha\alpha',\beta\beta'}\rho_W^{\beta\beta'}(R,P,t) \quad (74)$$

where

$$-i\mathcal{L}_{\alpha\alpha',\beta\beta'} = (-i\omega_{\alpha\alpha'} - iL_{\alpha\alpha'})\delta_{\alpha\beta}\delta_{\alpha'\beta'} + J_{\alpha\alpha',\beta\beta'} \equiv -i\mathcal{L}^0_{\alpha\alpha'} + J_{\alpha\alpha',\beta\beta'} \quad (75)$$

where $\omega_{\alpha\alpha'}(R) = [E_\alpha(R) - E_{\alpha'}(R)]/\hbar = \Delta E_{\alpha\alpha'}/\hbar$ and J is defined by

$$J_{\alpha\alpha',\beta\beta'} = -\frac{P}{M}\cdot d_{\alpha\beta}\left(1 + \frac{1}{2}S_{\alpha\beta}\cdot\frac{\partial}{\partial P}\right)\delta_{\alpha'\beta'} - \frac{P}{M}\cdot d^*_{\alpha'\beta'}\left(1 + \frac{1}{2}S^*_{\alpha'\beta'}\cdot\frac{\partial}{\partial P}\right)\delta_{\alpha\beta} \quad (76)$$

and the nonadiabatic coupling matrix element is $d_{\alpha\alpha'} = \langle\alpha; R|\partial/\partial R|\alpha'; R_0\rangle$, and

$$S_{\alpha\beta} = \Delta E_{\alpha\alpha'}d_{\alpha\beta}\left(\frac{P}{M}\cdot d_{\alpha\beta}\right)^{-1} \quad (77)$$

The classical Liouville operator involving the mean of the Hellmann-Feynman forces for states α and α' is

$$iL_{\alpha\alpha'} = \frac{P}{M}\cdot\frac{\partial}{\partial R} + \frac{1}{2}(F^\alpha_W + F^{\alpha'}_W)\cdot\frac{\partial}{\partial P} \quad (78)$$

The quantum-classical Liouville equation may be integrated and solved by iteration to yield a representation of the dynamics as a sequence of terms involving increasing numbers of nonadiabatic transitions [52],

$$\rho_W^{\alpha_0\alpha'_0}(R,P,t) = e^{-i\mathcal{L}^0_{\alpha_0\alpha'_0}t}\rho_W^{\alpha_0\alpha'_0}(R,P) + \sum_{n=1}^{\infty}\sum_{(\alpha_1\alpha'_1)\cdots(\alpha_n\alpha'_n)}\int_0^{t_0}dt_1\int_0^{t_1}dt_2\cdots\int_0^{t_{n-1}}dt_n$$
$$\times\prod_{k=1}^{n}\Big[e^{-i\mathcal{L}^0_{\alpha_{k-1}\alpha'_{k-1}}(t_{k-1}-t_k)}J_{\alpha_{k-1}\alpha'_{k-1},\alpha_k\alpha'_k}\Big]e^{-i\mathcal{L}^0_{\alpha_n\alpha'_n}t_n}\rho_W^{\alpha_n\alpha'_n}(R,P) \quad (79)$$

Here $\rho_W^{\alpha\alpha'}(R, P)$ is the initial value of the density matrix element. In this equation, the diagonal part of the quantum-classical evolution operator, $\exp\{iL_{\alpha\alpha'}^0 t\}$, may be written in terms of classical evolution on the $(\alpha\alpha')$ surface and a phase factor as,

$$e^{iL_{\alpha\alpha'}^0(t-t')} = e^{-i\int_t^{t'} d\tau\, w_{\alpha\alpha'}(R_{\alpha\alpha'},\tau)} e^{-iL_{\alpha\alpha'}(t-t')} \equiv W_{\alpha\alpha'}(t,t')e^{-iL_{\alpha\alpha'}(t-t')} \tag{80}$$

The successive terms in the series correspond to increasing numbers of nonadiabatic transitions, starting with the first term that describes simple adiabatic dynamics. As an example, consider the calculation of the diagonal element of the density matrix, $\rho_W^{\alpha\alpha}(R, P, t)$. The contributions to this matrix element are determined by backward evolution from time t to time 0. The first term in the series corresponds to adiabatic evolution on state α. The next term accounts for single nonadiabatic transitions to states β ($\beta \neq \alpha$), which occur at times t' intermediate between t and 0. These transitions are accompanied by continuous momentum changes in the environment specified by the term in J involving a momentum derivative. Because a single quantum transition takes place, this contribution must come from an off-diagonal density matrix element, $\rho_W^{\alpha\beta}$ at time 0. During the portion of the evolution segment from t' to 0, the classical bath phase space coordinates are propagated on the mean of the two α and β adiabatic surfaces and a phase factor $W_{\alpha\beta}$ contributes to the population in state α.

The terms involving the bath momentum derivative in J are difficult to evaluate exactly. Consequently, we make a "momentum-jump" approximation that gives J the structure of a momentum translation operator whose effect on any function of the momentum is to shift the momentum by some value [52, 70]. To derive this approximation, we first consider the operator identity, $(S_{\alpha\beta}/2)\cdot\frac{\partial}{\partial P} = \Delta E_{\alpha\beta} M \frac{\partial}{\partial (P\cdot\hat{d}_{\alpha\beta})^2}$. The action of the operator on any function $f(P)$ of the momentum may be written approximately as

$$\begin{aligned}\left[1 + \Delta E_{\alpha\beta} M \frac{\partial}{\partial (P\cdot\hat{d}_{\alpha\beta})^2}\right] f(P) &\approx e^{\Delta E_{\alpha\beta} M \partial/\partial (P\cdot\hat{d}_{\alpha\beta})^2} f(P) \\ &= f\left[\hat{d}_{\alpha\beta}^{\perp}(P\cdot\hat{d}_{\alpha\beta}^{\perp}) + \hat{d}_{\alpha\beta}\,\mathrm{sgn}(P\cdot\hat{d}_{\alpha\beta})\sqrt{(P\cdot\hat{d}_{\alpha\beta})^2 + \Delta E_{\alpha\beta} M}\right] \\ &= f(P + \hat{d}_{\alpha\beta}\Delta P)\end{aligned} \tag{81}$$

where $\Delta P = -(\hat{d}_{\alpha\beta}\cdot P) + \mathrm{sgn}(P\cdot\hat{d}_{\alpha\beta})\sqrt{(P\cdot\hat{d}_{\alpha\beta})^2 + \Delta E_{\alpha\beta} M}$. In the second approximate equality on the right-hand side of this equation, we have replaced the sum by an exponential. The momentum vector may be written in terms of its components along $\hat{d}_{\alpha\beta}$ and a perpendicular vector $\hat{d}_{\alpha\beta}^{\perp}$, $P = \hat{d}_{\alpha\beta}(\hat{d}_{\alpha\beta}\cdot P) + \hat{d}_{\alpha\beta}^{\perp}(\hat{d}_{\alpha\beta}^{\perp}\cdot P)$. In the last line, we used the fact that the exponential operator is a translation operator in the variable $(P\cdot\hat{d}_{\alpha\beta})^2$. Using this momentum jump approximation, a member of the ensemble of trajectories that is used to compute the density matrix elements is shown schematically in Fig. 12.

A similar set of equations with similar interpretations can be written for an operator $\hat{A}_W(R, P)$. We have,

$$\begin{aligned}A_W^{\alpha_0\alpha_0'}(R,P,t) = e^{(iL_{\alpha_0\alpha_0'}^B)t} A_W^{\alpha_0\alpha_0'}(R,P) + \sum_{n=1}^{\infty}(-1)^n \sum_{(\alpha_1\alpha_1')\cdots(\alpha_n\alpha_n')} \int_0^t dt_1 \int_{t_1}^t dt_2 \cdots \int_{t_{n-1}}^t dt_n \\ \times \prod_{k=1}^{n}\left[e^{iL_{\alpha_{k-1}\alpha_{k-1}'}^0 (t_k - t_{k-1})} J_{\alpha_{k-1}\alpha_{k-1}',\alpha_k\alpha_k'}\right] e^{iL_{\alpha_n\alpha_n'}^B (t-t_n)} A_W^{\alpha_n\alpha_n'}(R,P)\end{aligned} \tag{82}$$

In order to compute correlation functions, we require the quantum-classical time evolution of operators as we shall see when we consider the calculation of rate constants using this formalism.

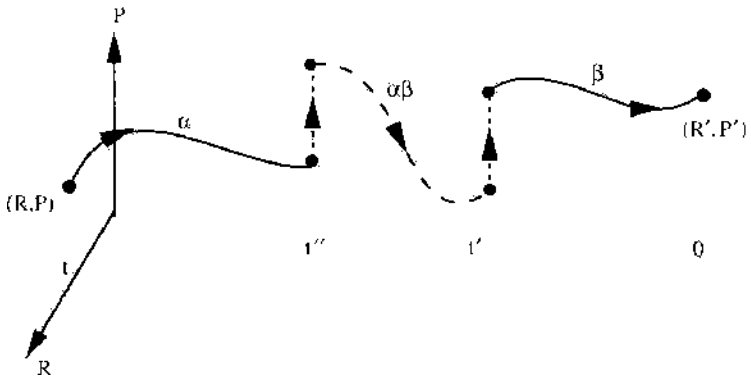

Figure 12. A trajectory segment with two nonadiabatic transitions that contributes to the diagonal element $\rho_W^{\alpha\alpha}(R, P, t)$ coming from $\rho_W^{\beta\beta}(R, P, t = 0)$. In the time segment between t'' and t', the system evolves coherently and the contains the phase factor $W_{\alpha\beta}$.

6.1. Simulation Algorithm

As we shall see below, in order to evaluate the time-dependent rate coefficient, the quantum-classical time evolution of the matrix elements of species operators must be computed. This evolution may be simulated using the sequential short-time algorithm [71, 72]. When the quantum-classical Liouville operator is time-independent, the evolution equation for the matrix elements of an operator or dynamical variable may be written as

$$\frac{d}{dt}A_W^{\alpha\alpha'}(R, P, t) = \sum_{\beta\beta'} i\mathcal{L}_{\alpha\alpha',\beta\beta'}A_W^{\beta\beta'}(R, P, t) \tag{83}$$

whose formal solution is

$$A_W^{\alpha\alpha'}(R, P, t) = \sum_{\beta\beta'}(e^{i\mathcal{L}t})_{\alpha\alpha',\beta\beta'}A_W^{\beta\beta'}(R, P, t) \tag{84}$$

Consequently, to compute the evolution we must be able to simulate the action of the quantum-classical propagator.

The propagator can be written simply as a composition of propagators in time segments of arbitrary length. For example, divide the time interval t into N segments of lengths $\Delta t_j = t_j - t_{j-1}$ so that

$$(e^{i\mathcal{L}t})_{\alpha_0\alpha'_0,\alpha_N\alpha'_N} = \sum_{\{\alpha_1\alpha'_1\},\ldots,\{\alpha_{N-1}\alpha'_{N-1}\}} \prod_{j=1}^{N}(e^{i\mathcal{L}(t_j-t_{j-1})})_{\alpha_{j-1}\alpha'_{j-1},\alpha_j\alpha'_j} \tag{85}$$

In any of these time intervals, the propagator satisfies the Dyson equation, starting from

$$(e^{-i\mathcal{L}t})_{\alpha\alpha',\beta\beta'} = e^{-i\mathcal{L}^0_{\alpha\alpha'}t}\delta_{\alpha\beta}\delta_{\alpha'\beta'} + \sum_{\nu\nu'}\int_0^t dt' e^{-i\mathcal{L}^0_{\alpha\alpha'}(t-t')}J_{\alpha\alpha',\nu\nu'}(e^{-i\mathcal{L}t'})_{\nu\nu',\beta\beta'} \tag{86}$$

If Δt is sufficiently small, one can make a one-point approximation to the time integral in Eq. (86) by choosing a point t'' in Δt. Letting $t'' = t_j$, one obtains

$$\begin{aligned}(e^{i\mathcal{L}(t_j-t_{j-1})})_{\alpha_{j-1}\alpha'_{j-1},\alpha_j\alpha'_j} &\approx e^{i\mathcal{L}^0_{\alpha_{j-1}\alpha'_{j-1}}(t_j-t_{j-1})}(\delta_{\alpha_{j-1}\alpha_j}\delta_{\alpha'_{j-1}\alpha'_j} - \Delta t J_{\alpha_{j-1}\alpha'_{j-1},\alpha_j\alpha'_j}) \\ &= W_{\alpha_{j-1}\alpha'_{j-1}}(t_{j-1}, t_j)e^{i\mathcal{L}_{\alpha_{j-1}\alpha'_{j-1}}(t_j-t_{j-1})}(\delta_{\alpha_{j-1}\alpha_j}\delta_{\alpha'_{j-1}\alpha'_j} - \Delta t J_{\alpha_{j-1}\alpha'_{j-1},\alpha_j\alpha'_j})\end{aligned} \tag{87}$$

At the end of each segment, the system may either stay on the same energy surface or make a transition to a new state.

The sequential short-time algorithm is easily implemented. The total time of the calculation is divided into a fixed number of time slices, the most natural choice being to take the molecular dynamics integration time step Δt as the length of the slice. The phase space

coordinates are propagated adiabatically in a time step, and the phase factor W is computed if the evolution is on the mean of two adiabatic surfaces. At the end of each time step, the probabilities $\Pi = |(P/M) \cdot d|\Delta t\,(1 + |(P/M) \cdot d|\Delta t)^{-1}$ and $\Sigma = 1 - \Pi$ are respectively used for acceptance or rejection of a quantum transition.

7. NONADIABATIC REACTION DYNAMICS

In this section we sketch a general formulation of the statistical mechanics of nonadiabatic chemical rate processes and give reactive flux correlation function expressions for the rate constant. We then illustrate the formalism with calculations on a two-level model system that captures the essential features of many transfer rate processes.

7.1. Quantum-Classical Reactive Flux Correlation Functions

The reactive-flux correlation functions that may be used to determine the rate constant for activated quantum processes can be derived using linear response theory [73]. We consider a multicomponent system where r independent chemical reactions take place. We may associate progress variables, $\bar{\chi}_i$ and affinities $\mathcal{A}_i$, $(i = 1, \ldots, r)$, with each independent reaction step. From linear irreversible thermodynamics, the chemical rate law describing the time evolution of the reaction rates $\mathcal{J}_i$ takes the form [74],

$$\mathcal{J}_i \equiv \frac{d\bar{\chi}_i}{dt} = -\sum_{j=1}^{r} L_{ij}\beta\mathcal{A}_j \tag{88}$$

where L_{ij} is an Onsager coefficient.

To derive this rate law using linear response theory, we suppose the system is subject to external time-dependent forces (affinities) that couple to microscopic species variables $\hat{\chi}_{Wi}$. The time-dependent Hamiltonian in the presence of the external forces is

$$\hat{\mathcal{H}}_W(t) = \hat{H}_W - \sum_{i=1}^{r} \hat{\chi}_{Wi}^{\dagger}\mathcal{A}_i(t) \tag{89}$$

where the dagger stands for the adjoint. The species variables are in general operators in Hilbert space and functions of the classical phase space variables, $\hat{\chi}_{Wi}(R, P)$.

The chemical rate law can be derived by calculating the nonequilibrium average of $\hat{\chi}_{W,i}$

$$\mathcal{J}_i \equiv \frac{d\overline{\hat{\chi}_{Wi}}(t)}{dt} = \mathrm{Tr}' \int dR dP\, \hat{\chi}_{Wi}\hat{\rho}_W(R, P, t) \tag{90}$$

to linear order in the affinities. Assuming the time dependence of the affinities can be represented by a single Fourier component $\mathcal{A}_i(t) = \exp(i\omega t)\mathcal{A}_i(\omega)$, linear response theory gives

$$\frac{d\bar{\chi}_{Wi}(t)}{dt} = \sum_{j=1}^{r} \Phi_{ij}(\omega)\mathcal{A}_j(t) \tag{91}$$

where the one-sided Fourier transform of the matrix response function is given by

$$\Phi_{ij}(\omega) = \int_0^{\infty} dt\, \langle(\hat{\chi}_{Wi}(t), \hat{\chi}_{Wj}^{\dagger})\rangle e^{-i\omega t} \tag{92}$$

Although the zero frequency limit of Eq. (91) has the same form as the phenomenological rate law (88), the zero frequency limit of Eq. (92) may be shown to be identically zero. This is the well-known plateau value problem, which is solved by using a projection operator formalism to project out the time variations that occur on the timescale of the chemical relaxation processes [6, 7]. Provided the timescales of the chemical relaxation processes, τ_r,

are much slower than those for other microscopic relaxation processes in the system, τ_m, the phenomenological coefficients may be obtained through the correlation function expression,

$$\beta L_{ij} = -\int_0^{t^*} dt' \,\mathrm{Tr}' \int dR dP\, \hat{\dot{\chi}}_{Wi}(t')\left(\hat{\chi}^{\dagger}_{Wj}, \hat{\rho}_{We}\right) \tag{93}$$

where $\tau_m \ll t^* \ll \tau_c$. In writing this expression, we have moved the quantum-classical bracket to act on the equilibrium density and the initial value of the species operator. It is also convenient to define the time-dependent Onsager coefficients by

$$\begin{aligned}\beta L_{ij}(t) &= -\int_0^{t} dt' \,\mathrm{Tr}' \int dR dP\, \hat{\dot{\chi}}_{Wi}(t')\left(\hat{\chi}^{\dagger}_{Wj}, \hat{\rho}_{We}\right) \\ &= -\mathrm{Tr}' \int dR dP\, \hat{\chi}_{Wi}(t)\left(\hat{\chi}^{\dagger}_{Wj}, \hat{\rho}_{We}\right)\end{aligned} \tag{94}$$

where the time integral has been performed to obtain the second line of this equation. The true phenomenological coefficients, appearing in Eq. (88), may be determined from the plateau value of this expression, should such a plateau exist. In quantum-classical dynamics the Onsager reciprocal relations are valid to $O(\mu^2)$. This is a consequence of the fact that the quantum-classical bracket satisfies the Jacobi identity only to $O(\mu^2)$ [73].

7.2. Two-Level Model for Transfer Reactions

Often many features of proton and electron transfer processes can be captured by simple two-level models. In this section, we show how the general reactive flux formalism may be specialized to a transfer reaction $A \rightleftharpoons B$ where excited states participate in the reaction.

To this end, we consider a two-level system coupled to a classical bath. In accord with the standard picture of reaction rates for such systems, the Hamiltonian operator, expressed in a diabatic basis $\{|\uparrow\rangle, |\downarrow\rangle\}$, is taken to have the form [73].

$$\mathbf{H} = \begin{bmatrix} V_a(R_0) + \hbar\gamma_0 R_0 & -\hbar\Omega \\ -\hbar\Omega & V_a(R_0) - \hbar\gamma_0 R_0 \end{bmatrix} + \left[\sum_{j=0}^{N} \frac{P_j^2}{2M_j} + \sum_{j=1}^{N} \frac{M_j}{2}\omega_j^2\left(R_j^2 - \frac{c_j}{M_j\omega_j^2}R_0\right)^2\right]\mathbf{I} \tag{95}$$

In this model, a two-level system is coupled to a classical nonlinear oscillator with mass M_0 and phase space coordinates (R_0, P_0). The coupling to the two-level system is given by $-\hbar\gamma_0 R_0 = \hbar\gamma(R_0)$. The nonlinear quartic oscillator, $V_a(R_0) = aR_0^4/4 - bR_0^2/2$, is bilinearly coupled to a harmonic bath with Ohmic spectral density. From the structure of the first 2×2 matrix in Eq. (95), the diabatic energies are given by $E^d_{1,2}(R_0) = V_a(R_0) \pm \hbar\gamma_0 R_0$ and the coupling between the diabatic states is $-\hbar\Omega$. The N independent harmonic oscillators labeled $j = 1, \ldots, N$ have masses M_j and frequencies ω_j. The bilinear coupling is characterized by a spectral density, $J(\omega) = \pi\sum_{j=1}^{N}(c_j^2/(2M_j\omega_j^2))\delta(\omega - \omega_j)$, of Ohmic type where [75, 76] $c_j = (\xi\hbar\omega_0 M_j)^{1/2}\omega_j$, $\omega_j = -\omega_c \ln(1 - j\omega_0/\omega_c)$ and $\omega_0 = \frac{\omega_c}{N}(1 - e^{-\omega_{\max}/\omega_c})$.

The adiabatic states are obtained by diagonalization of the two-level system hamiltonian (95) and are given by,

$$|1; R_0\rangle = \frac{1}{\mathcal{N}}[(1+G)|\uparrow\rangle + (1-G)|\downarrow\rangle] \tag{96}$$

$$|2; R_0\rangle = \frac{1}{\mathcal{N}}[-(1-G)|\uparrow\rangle + (1+G)|\downarrow\rangle] \tag{97}$$

where $\mathcal{N}(R_0) = \sqrt{2(1+G^2(R_0))}$ with $G(R_0) = \gamma(R_0)^{-1}[-\Omega + \sqrt{\Omega^2 + \gamma^2(R_0)}]$. In the following, we use the notation $(R, P) = (R_0, R_1, \ldots, R_N, P_0, P_1, \ldots, P_N)$ for the point in the $2(N+1)$ dimensional phase space of the model. The corresponding adiabatic energies are $E_{1,2}(R) = V_b(R) \mp \sqrt{\Omega^2 + \gamma^2(R_0)}$, where

$$V_b(R) = V_a(R_0) + \sum_{j=0}^{N} \frac{P_j^2}{2M_j} + \sum_{j=1}^{N} \frac{M_j}{2}\omega_j^2\left(R_j^2 - \frac{c_j}{M_j\omega_j^2}R_0\right)^2 \tag{98}$$

Insight into the nature of the reaction dynamics can be gained by considering the adiabatic free energies along the R_0 coordinate, $W_{1,2}(R_0)$, defined by

$$W_{1,2}(R_0) = -\beta^{-1}\ln\left(\int\prod_{j=1}^{N} dR_j\, Z_{1,2}^{-1} e^{-\beta E_{1,2}(R)}\right)$$
$$= \beta^{-1}\ln Z_{1,2} + V_n(R_0) \mp \sqrt{\Omega^2 + \gamma_0^2 R_0^2} \tag{99}$$

where $Z_{1,2} = \int dR \exp[-\beta E_{1,2}(R)]$.

These free energy functions are plotted in Fig. 13. The ground state free energy profile has two minima corresponding to two stable states separated by a barrier at $R_0 = 0$.

We define the positive and negative values of R_0 with species A and B, respectively. Thus, we take for the species variables, $\hat{N}_A = \Theta(R_0)$ and $\hat{N}_B = \Theta(-R_0)$. The chemical reactions,

$$A \underset{k_{BA}}{\overset{k_{AB}}{\rightleftharpoons}} B \tag{100}$$

are described by the mass action rate law,

$$\frac{d\bar{n}_A(t)}{dt} = -k_{AB}\bar{n}_A(t) + k_{BA}\bar{n}_B(t) \tag{101}$$

which may also be written in the form

$$\frac{d\bar{n}_A(t)}{dt} = -k_{AB}\bar{n}_A(t)(1 - e^{-\beta\mathcal{A}(t)}) \tag{102}$$

by using the fact that the chemical potential of species α is $\mu_\alpha = \mu_\alpha^{(0)} + \beta^{-1}\ln\bar{n}_\alpha$ where $\alpha = A, B$. This form makes evident the fact that the driving force of the reaction is the chemical affinity $\mathcal{A}(t) = \mu_A(t) - \mu_B(t)$. If we linearize this rate law close to equilibrium, we obtain

$$\frac{d\bar{n}_A(t)}{dt} = -k_{AB}\bar{n}_A^{eq}\beta\mathcal{A}(t) \tag{103}$$

We may now read off the relation between the Onsager coefficient and the rate constant. We have,

$$L_{BA} = k_{AB}\bar{n}_A^{eq} \tag{104}$$

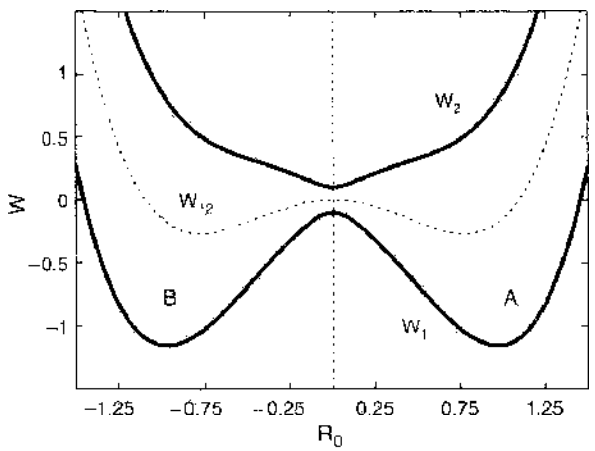

Figure 13. Free energy curves versus R_0 for the two-state model. The heavy solid lines are the ground and excited state free energy curves, and the light line depicts the mean of these curves.

Consider the calculation of $L_{BA}(\bar{n}_A^{eq})^{-1} = k_{AB}$. Using Eq. (94) and the definition (104), we have

$$k_{AB}(t) = -(\beta \bar{n}_A^{eq})^{-1} \mathrm{Tr}' \int dR dP\, \hat{\chi}_B(t)(\hat{\chi}_A, \hat{\rho}_{We}),$$
$$= -(\beta \bar{n}_A^{eq})^{-1} \sum_{\alpha\alpha'} \int dR dP\, \chi_B^{\alpha'\alpha}(t)(\hat{\chi}_A, \hat{\rho}_{We})_{\alpha\alpha'} \tag{105}$$

In the second line of this equation, we expressed the trace in terms of the adiabatic basis. This correlation function expression can be used to compute k_{AB}.

An expression for the time-dependent rate coefficient $k_{AB}(t)$ can be found by evaluating the matrix elements of the quantum-classical bracket in the adiabatic basis and using $\hat{N}_A^{\alpha\alpha'} = \delta_{\alpha\alpha'}\Theta(R_0)$ and $\hat{N}_B^{\alpha\alpha'} = \delta_{\alpha\alpha'}\Theta(-R_0)$. If we make use of the fact that the quantum-classical equilibrium density has the form,

$$\rho_{We}^{\alpha\alpha'} \approx \rho_{We}^{(0)\alpha}\delta_{\alpha\alpha'} - i\hbar f_{We}^{\alpha\alpha'}(1 - \delta_{\alpha\alpha'}) \tag{106}$$

where

$$\rho_{We}^{(0)\alpha} = Z_0^{-1} e^{-\beta H_0^\alpha}, \quad Z_0 = \sum_\alpha \int dR dP\, e^{-\beta H_0^\alpha} \tag{107}$$

and

$$f_{We}^{\alpha\alpha'} = \frac{P_0}{M_0} \cdot d_{\alpha\alpha'}\rho_{We}^{(0)\alpha}\left[\frac{\beta}{2}\left(1 + e^{-\beta E_{\alpha'\alpha}}\right) + \frac{1 - e^{-\beta E_{\alpha'\alpha}}}{E_{\alpha\alpha'}}\right] \tag{108}$$

the time-dependent rate coefficient in Eq. (105) can be decomposed into the sum of two contributions:

$$k_{AB}(t) = k_{AB}^d(t) + k_{AB}^o(t) \tag{109}$$

The diagonal part of the density matrix gives rise to the contribution

$$k_{AB}^d(t) = -\frac{1}{n_A^{eq}} \sum_{\alpha=1}^{2} \int dR dP\, N_B^{\alpha\alpha}(R, P, t)\delta(R_0)\frac{P_0}{M}\rho_{We}^{\alpha\alpha} \tag{110}$$

and the off-diagonal part of the density matrix yields

$$k_{AB}^o(t) = -\frac{2\hbar}{\beta \bar{n}_A^{eq}} \int dR dP\, \mathrm{Im}\{N_B^{12}(R, P, t)\}\delta(R_0)\frac{\partial f_{We}^{12}}{\partial P_0} \tag{111}$$

The rate coefficient can be calculated from the plateau value of $k_{AB}(t)$.

7.3. Two-Level Reaction Simulation Results

In this section, we present the results of simulations of the two-level reaction model to show how the nonadiabatic rate constant can be calculated in the context of quantum-classical Liouville dynamics. In presenting the results, we use a set of dimensionless coordinates $\tilde{R}_0 = (M_0\omega_c/\hbar)^{1/2}R_0$, $\tilde{P}_0 = (\hbar M_0\omega_c)^{-1/2}P_0$, $\tilde{R}_j = (M_j\omega_c/\hbar)^{1/2}R_j$ and $\tilde{P}_j = (\hbar M_j\omega_c)^{-1/2}P_j$, so that $\tilde{\hat{H}} = \hat{H}/(\hbar\omega_c)$, and the dimensionless parameters of the model are $\tilde{\Omega} = \Omega/\omega_c$, $\tilde{\omega}_j = \omega_j/\omega_c$, $\tilde{c}_j = (\xi\omega_0/\omega_c)^{1/2}\omega_j$, $\tilde{a} = (\hbar/(M_0^2\omega_c^3))a$, $\tilde{b} = b/(M_0\omega_c^2)$, $\tilde{\gamma}_0 = (\hbar/M_0\omega_c^3)^{1/2}\gamma_0$, and $\tilde{\gamma}_b = (\hbar/M_0\omega_c)^{1/2}\gamma_b$. The dimensionless reciprocal temperature and time are $\tilde{\beta} = \hbar\omega_c\beta = \hbar\omega_c/k_BT$ and $\tilde{t} = t\omega_c$, respectively. In the following, the tilde will be omitted to avoid cluttering the notation, but the use of dimensionless units should be understood. Our calculations were carried out for a bath of $N = 100$ harmonic oscillators with the following values for the parameters: $\omega_{max} = 3$, $\xi = 4$, $\Omega = 0.1$, $\gamma_0 = 1$, $a = 3$, $b = 1.8008$, and $\beta = 6$.

If the dynamics is restricted to the adiabatic ground state, the time evolution of $R_0(t)$ shown in Fig. 14 exhibits the features of an activated rate process between two metastable

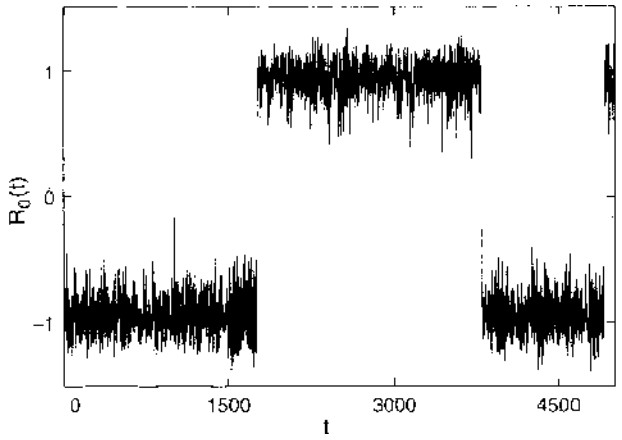

Figure 14. Time series of the coordinate $R_0(t)$ along a trajectory evolving on the ground state surface, typical of classical activated barrier crossing dynamics.

states. In the adiabatic limit, only the first term in Eq. (87) contributes, and the time-dependent rate coefficient in Eqs. (109) and (110) reduces to

$$k_{AB}^{ad}(t) = \frac{1}{\bar{n}_A^{eq}} \int dR dP \, (e^{iL_0 t}\Theta(R_0))\delta(R_0)\frac{P_0}{M_0}\rho_W^0 \tag{112}$$

the standard reactive flux autocorrelation expression for a classical activated rate process. This adiabatic time-dependent rate coefficient is plotted in Fig. 15. It has an initial rapid decay followed by a much slower decay, which takes place on the timescale of the chemical rate process. The adiabatic rate constant can be determined from the extrapolation of this slowly decaying portion of the dynamics to $t = 0$.

In order to compute the nonadiabatic rate constant, we must calculate the contributions coming from the two terms in Eq. (109). The term $k_{AB}^{d}(t)$ in Eq. (110) involves even numbers of quantum transitions, whereas k_{AB}^{o} in Eq. (111) requires an odd number of transitions. Figure 16 shows the nonadiabatic transmission coefficient including both terms in Eq. (109) for up to two quantum transitions per trajectory. For this contribution, the trajectory starts at $t = 0$ from the ground state at the top of the barrier and evolves on the ground state surface until time τ_1 where a quantum transition occurs. Between the times τ_1 and τ_2, evolution occurs on the mean surface. The jump at time τ_2 must bring the trajectory back either to the ground or to the excited state surface after which the evolution proceeds adiabatically until time t. Thus, one has three trajectory segments: the first and the last have no quantum phase factor but the middle trajectory segment has a nonzero phase factor arising from the coherent evolution on the mean surface $[E_1(R) + E_2(R)]/2$.

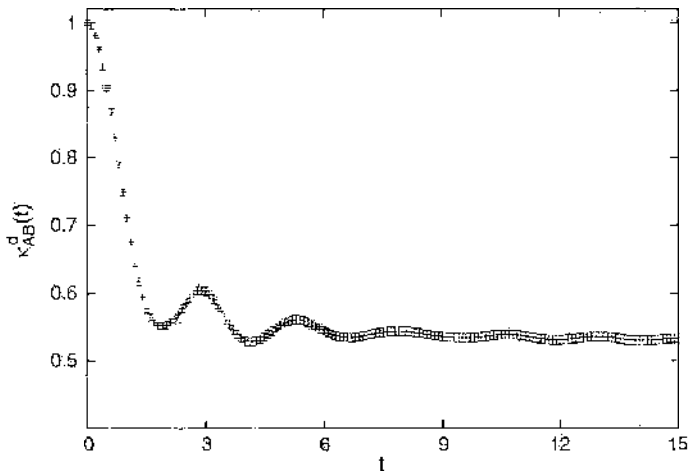

Figure 15. Transmission coefficient $\kappa_{AB}^{d}(t) = k_{AB}^{ad}(t)/k_{AB}^{TST}$ versus time for adiabatic dynamics.

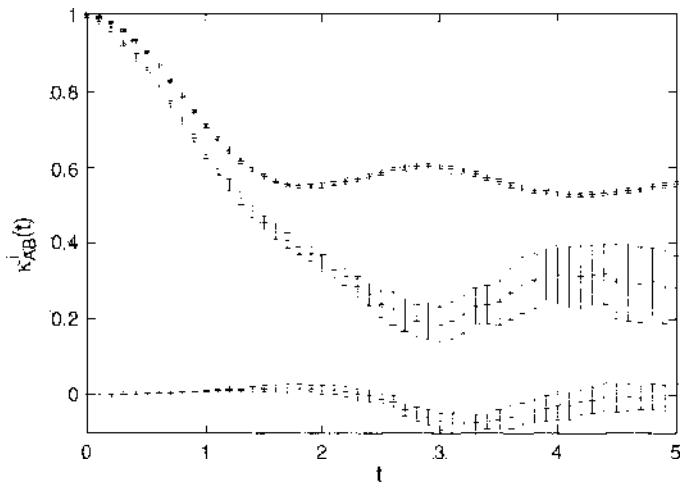

Figure 16. Time-dependent transmission coefficients $\kappa^{i}_{AB}(t) = k_{AB}(t)/k^{TST}_{AB}$. The lower curve shows the off-diagonal contribution (κ^{o}_{AB}). The middle curve arises from the sum of all the nonadiabatic corrections $[\kappa^{d}_{AB}(t) + \kappa^{o}_{AB}(t)]$ considering up to two quantum transitions. For comparison, the upper curve shows the adiabatic result $\kappa^{ad}_{AB}(t)$.

Figure 16 shows also the nonadiabatic term $\kappa^{o}_{AB}(t) = k^{o}_{AB}/k^{TST}_{AB}$ versus time. Only odd numbers of nonadiabatic transitions contribute to this term. The contribution $k^{o}_{AB}(t)$ in Eq. (111) depends on the off-diagonal part of bracket $(\widehat{N}_A, \widehat{\rho}_{W_c})_{\alpha\alpha'}$ and the off-diagonal part of the species variable $N^{\alpha'\alpha}_{B}(t)$, $(\alpha \neq \alpha')$. One can see that this off-diagonal term gives a negligible contribution so that the main physics is contained in $k^{d}_{AB}(t)$. Finally, the full time-dependent rate constant in Fig. 16 shows that the inclusion of nonadiabatic transitions significantly reduces the rate constant below that obtained using adiabatic dynamics.

8. CONCLUSIONS

The rates of proton and electron transfer reactions in condensed phase environments are difficult to determine because the quantum nature of the transferring particle must be taken into account. In most circumstances, we can use a mixed quantum-classical approach to study such reactions because solvent molecules are typically much heavier than the proton or electron being transferred in the reaction. Equilibrium properties such as the free energy along the reaction coordinate may be computed using Feynman path integral methods. The free energy provides information on the reaction mechanism and is an important ingredient in the transition state theory approximation to the rate constant. Dynamical properties, such as the full rate constant, are much more difficult to compute. Mixed quantum-classical dynamical schemes may be used to determine transport properties. Adiabatic dynamics, where the motion of the classical degrees of freedom takes place on a single potential energy surface, is the simplest such scheme. However, this approach breaks down when transitions among the quantum states take place. In this case, nonadiabatic dynamics must be used. The quantum-classical Liouville equation and the associated statistical mechanical derivation of the nonadiabatic reactive flux formula for the rate of the reaction provide a way to study nonadiabatic proton and electron transfer rates.

If charge transfer reactions take place in domains with nanometer dimensions, then the competition between bulk and surface forces leads to interesting effects on reaction mechanisms and rates. Our examples of electron solvation in reverse micelles and proton transfer in polar molecule clusters served to illustrate such effects.

ACKNOWLEDGMENTS

This work was supported in part by a grant from the Natural Sciences and Engineering Research Council of Canada.

REFERENCES

1. M. D. Joesten and L. J. Schaad, "Hydrogen Bonding," Marcel-Deckker, New York, 1974.
2. R. P. Bell, "The Proton in Chemistry," Chapmann & Hall, London, 1973.
3. J. Ulstrup, "Charge Transfer Processes," Springer, New York, 1979.
4. T. Yamamoto, *J. Chem. Phys.* 33, 281 (1960).
5. D. Chandler, *J. Chem. Phys.* 68, 472 (1978).
6. S. Constas, R. Kapral, and L. McWhirter, in "Classical and Quantum Dynamics in the Condensed Phase" (G. Ciccotti, B. Berne, and D. Coker, Eds.), p. 583, World Scientific, Singapore, 1998.
7. R. Kapral, *J. Chem. Phys.* 56, 1842 (1972).
8. F. Garisto and R. Kapral, *J. Chem. Phys.* 58, 3129 (1973).
9. H. Mori, *Prog. Theor. Phys.* 33, 423 (1965).
10. R. Zwanzig, *Phys. Rev.* 124, 983 (1961).
11. R. Kubo, *J. Phys. Soc. (Japan)* 12, 570 (1957); *Repts. Prog. Phys.* 29, 255 (1966).
12. W. E and E. Vanden-Eijnden, "Metastability, Conformational Dynamics, and Transition Pathways in Complex Systems, in Multiscale Modelling and Simulation" (S. Attinger and P. Koumoutsakos, Eds.), Lecture Notes in Computational Science and Engineering, Vol. 39, Springer, Berlin, 2004.
13. W. E, W. Ren, and E. Vanden-Eijnden, "Finite Temperature String Method for the Study of Rare Events," *J. Phys. Chem. B* 109, 6688 (2005).
14. H. Jónsson, G. Mills, and K. W. Jacobsen, in "Classical and Quantum Dynamics in Condensed Phase Simulations" (B. J. Berne, G. Ciccotti, and D. F. Coker, Eds.), World Scientific, Singapore, 1998.
15. R. Elber, A. Ghosh, and A. Cardenas, *Acc. Chem. Res.* 35, 396 (2002).
16. C. Dellago, P. G. Bolhuis, and P. L. Geissler, *Adv. Chem. Phys.* 123, 1 (2002).
17. E. Carter, G. Ciccotti, J. T. Hynes, and R. Kapral, *Chem. Phys. Lett.* 156, 472 (1989).
18. M. Fixman, *Proc. Natl. Acad. Sci. U.S.A.* 71, 3050 (1974).
19. N. G. van Kampen, *Am. J. Phys.* 52, 419 (1984).
20. H. Goldstein, "Classical Mechanics," Addison-Wesley Reading, MA, 1980.
21. M. Sprik and G. Ciccotti, *J. Chem. Phys.* 109, 7737 (1998).
22. R. P. Feynman, "Statistical Mechanics," Addison-Wesley, Reading MA, 1972.
23. D. Chandler and P. G. Wolynes, *J. Chem. Phys.* 74, 4078 (1981).
24. M. Gillan, *J. Phys. C* 20, 3621 (1987).
25. G. A. Voth, *Adv. Chem. Phys.* 93, 135 (1996).
26. D. Laria and R. Kapral, *J. Chem. Phys.* 117, 7712 (2002).
27. P. L. Luisi and B. E. Straub, Eds., "Reverse Micelles," Plenum, New York, 1984.
28. M. P. Pelini, Ed., "Structure and Reactivity in Reverse Micelles," Elsevier, Amsterdam, 1989.
29. B. Derecskei, A. Derecskei-Kovacs, and Z. A. Schelly, *Langmuir* 15, 1981 (1999).
30. J. Faeder and B. Ladanyi, *J. Phys. Chem. B* 104, 1033 (2000); *J. Phys. Chem. B* 105, 11148 (2001).
31. J. Schnitker and P. J. Rossky, *J. Chem. Phys.* 86, 3462 (1987).
32. G. B. Bachelet, D. R. Hamann, and M. Schlüter, *Phys. Rev. B* 26, 4199 (1982).
33. H. J. C. Berendsen, J. R. Grigera, and T. P. Straatsma, *J. Phys. Chem.* 91, 6269 (1987).
34. M. Tuckerman, G. J. Martyna, and B. J. Berne, *J. Chem. Phys.* 97, 1990 (1992).
35. G. J. Martyna, M. E. Tuckerman, D. J. Tobias, and M. L. Klein, *Mol. Phys.* 87, 1117 (1996).
36. G. J. Martyna, M. L. Klein, and M. Tuckerman, *J. Chem. Phys.* 97, 2635 (1992).
37. J. P. Ryckaert, G. Ciccotti, and H. J. C. Berendsen, *J. Comp. Phys.* 23, 327 (1977); G. Ciccotti and J. P. Ryckaert, *Comp. Phys. Rep.* 4, 345 (1986).
38. S. Consta and R. Kapral, *J. Chem. Phys.* 101, 10908 (1994).
39. S. Nosé, *Mol. Phys.* 52, 255 (1984); *J. Chem. Phys.* 81, 511 (1984); *Mol. Phys.* 57, 187 (1986); *Prog. Theor. Phys. Suppl.* 103, 1 (1991).
40. W. Hoover, *Phys. Rev. A* 31, 1695 (1985).
41. D. Laria, G. Ciccotti, M. Ferrario, and R. Kapral, *Chem. Phys.* 180, 181 (1994).
42. D. Li and G. Voth, *J. Phys. Chem.* 95, 10425 (1991).
43. J. Lobaugh and G. Voth, *Chem. Phys. Lett.* 198, 311 (1992); *J. Chem. Phys.* 100, 3039 (1994).
44. D. Laria, G. Ciccotti, M. Ferrario, and R. Kapral, *J. Chem. Phys.* 97, 378 (1992).
45. D. C. Borgis, S. Lee, and J. T. Hynes, *Chem. Phys. Lett.* 19, 162 (1989); D. C. Borgis and J. T. Hynes, *J. Chem. Phys.* 94, 3619 (1991).
46. R. A. Marcus and N. Sutin, *Biochim. Biophys. Acta* 811, 265 (1985).
47. A. Warshel, *J. Am. Chem. Soc.* 86, 2218 (1982).
48. D. A. Zichi, G. Ciccotti, J. T. Hynes, and M. Ferrario, *J. Phys. Chem.* 93, 6261 (1989).
49. H. Azzouz and D. C. Borgis, *J. Chem. Phys.* 98, 7361 (1993).
50. E. Wigner, *Phys. Rev.* 40, 749 (1932).
51. K. Imre, E. Özizmir, M. Rosenbaum, and P. F. Zwiefel, *J. Math. Phys.* 5, 1097 (1967)
52. R. Kapral and G. Ciccotti, *J. Chem. Phys.* 110, 8919 (1999).
53. S. Consta and R. Kapral, *J. Chem. Phys.* 104, 4581 (1996).
54. A. S. Clarke, R. Kapral, B. Moore, G. Patey, and X.-G. Wu, *Phys. Rev. Lett.* 70, 3283 (1993); A. S. Clarke, R. Kapral, and G. N. Patey, *J. Chem. Phys.* 101, 2432 (1994).
55. J. C. Tully, "Modern Methods for Multidimensional Dynamics Computations in Chemistry" (D. L. Thompson, Ed.), p. 34, World Scientific, NY, 1998.

56. H. J. Berendsen and J. Mavri, *J. Phys. Chem.* 97, 13464 (1993).
57. P. Bala, B. Lesyng, and J. A. McCammon, *Chem. Phys. Lett.* 219, 259 (1994).
58. J. C. Tully, *J. Chem. Phys.* 93, 1061 (1990); J. C. Tully, *Int. J. Quantum Chem.* 25, 299 (1991); S. Hammes-Schiffer and J. C. Tully, *J. Chem. Phys.* 101, 4657 (1994).
59. P. Pechukas, *Phys. Rev.* 181, 166, 174 (1969).
60. F. Webster, P. J. Rossky, and P. A. Friesner, *Comp. Phys. Comm.* 63, 494 (1991); F. Webster, E. T. Wang, P. J. Rossky, and P. A. Friesner, *J. Chem. Phys.* 100, 483 (1994).
61. L. Xiao and D. F. Coker, *J. Chem. Phys.* 100, 8646 (1994); D. F. Coker and L. Xiao, *J. Chem. Phys.* 102, 496 (1995); H. S. Mei and D. F. Coker, *J. Chem. Phys.* 104, 4755 (1996).
62. S. Hammes-Schiffer and J. C. Tully, *J. Chem. Phys.* 103, 8528 (1995).
63. S. R. Billeter, S. P. Webb, T. Iordanov, P. K. Agarwal, and S. Hammes-Schiffer, *J. Chem. Phys.* 114, 6925 (2001).
64. V. I. Gerasimenko, *Repts. Ukranian Acad. Sci.* 10, 65 (1981); V. I. Gerasimenko: *Theor. Math. Phys.* 50, 77 (1982); D. Ya. Petrina, V. I. Gerasimenko, and V. Z. Enolskii, *Sov. Phys. Dokl.* 35, 925 (1990).
65. I. V. Aleksandrov, *Z. Naturforsch.* 36a, 902 (1981).
66. W. Boucher and J. Traschen, *Phys. Rev. D* 37, 3522 (1988).
67. W. Y. Zhang and R. Balescu, *J. Plasma Phys.* 40, 199 (1988); R. Balescu and W. Y. Zhang, *J. Plasma Phys.* 40, 215 (1988).
68. C. C. Martens and J.-Y. Fang, *J. Chem. Phys.* 106, 4918 (1996); A. Donoso and C. C. Martens, *J. Phys. Chem.* 102, 4291 (1998).
69. S. Nielsen, R. Kapral, and G. Ciccotti, *J. Chem. Phys.* 115, 5805 (2001).
70. R. Kapral and G. Ciccotti, "A Statistical Mechanical Theory of Quantum Dynamics in Classical Environments, in Bridging Time Scales: Molecular Simulations for the Next Decade" (P. Nielaba, M. Mareschal, and G. Ciccotti, Eds.), SIMU Conference, 2001. Springer, Berlin, 2003.
71. D. Mac Kernan, G. Ciccotti, and R. Kapral, *J. Phys.: Condens. Matt.* 14, 9069 (2002).
72. A. Sergi, D. Mac Kernan, G. Ciccotti, and R. Kapral, *Theor. Chem. Acc.* 110, 49 (2003).
73. A. Sergi and R. Kapral, *J. Chem. Phys.* 118, 8566 (2003).
74. S. R. de Groot and P. Mazur, "Non-Equilibrium Thermodynamics." North-Holland, Amsterdam, 1962.
75. N. Makri and K. Thompson, *Chem. Phys. Lett.* 291, 101 (1998); K. Thompson and N. Makri, *J. Chem. Phys.* 110, 1343 (1999); N. Makri, *J. Phys. Chem. B* 103, 2823 (1999).
76. D. Mac Kernan, R. Kapral, and G. Ciccotti, *J. Chem. Phys.* 116, 2346 (2002).

CHAPTER 3

Computer Simulation of Nanofiltration Membranes and Processes

Horst Chmiel,[1] Xavier Lefebvre,[2] Valko Mavrov,[1]
Mohan Noronha,[3] John Palmeri[2]

[1]*Department of Process Technology, Saarland University and Institute for Environmentally Compatible Process Technology, Saarbrücken, Germany*
[2]*European Membrane Institute (EMI), CNRS ENSCM UMR 5635, University of Montpellier II, CC 047, Montpellier Cedex 5, France*
[3]*Institute for Environmentally Compatible Process Technology, Saarbrücken, Germany*

CONTENTS

ISBN: 1-58883-047-0

Handbook of Theoretical and Computational Nanotechnology
Edited by Michael Rieth and Wolfram Schommers
Volume 5: Pages (93–214)

1. INTRODUCTION TO NANOFILTRATION

Biological membranes are ubiquitous. Their capacity for selective mass transfer, for example, to ensure the inflow of nutrients and the outflow of end products in metabolic processes, is a prerequisite not only for cell activity but also life as we know it itself. Biological membranes are even capable of transporting substances against a gradient (more precisely, against an electrochemical potential) by means of energy that is produced in the cell.

However, this latter feature is not characteristic of synthetic membranes, which are defined as being thin-walled structures that allow the individual components of a fluid mixture (solution or suspension) to pass selectively. This means that the composition of the fluid entering (feed) and exiting (permeate) the membrane is different. The objective of membrane technology is to make the best possible use of selective transport mechanisms.

During the last 40 years, astonishing progress has been made in the development of synthetic membranes used for the separation of fluid mixtures.

Before the 1960, the application of these membranes was mostly limited to hemodialysis, a blood purification process in which the blood flows on the one side of a membrane and an aqueous solution (dialysate), which aborbs the toxic molecules of the blood, flows on the other side of the membrane. Because of the principle that molecules differ in their solubility and diffusion rates in the matrix of polymer films, there is a direct correlation between the size of the molecule and its transport velocity through the membrane, with the small molecules permeating more quickly than the large ones. This is true for both toxic and nontoxic molecules. The dialysate must contain all substances vital to healthy human blood and in the same concentrations to prevent these substances from passing into the dialysate. However, these membranes cannot hinder toxic medium molecules, because of their lower diffusion velocity, from accumulating in the blood.

This fact led to the development of hemofiltration membranes, which let all molecules with sizes ranging up to the size of the membrane pores permeate at almost the same rate. Again, one disadvantage of these membranes, whose pore diameter is approximately 10–50 nm, is that they allow both toxic and nontoxic molecules whose diameter is smaller than that of the membrane to permeate. Therefore, detoxification will sometimes be conducted using hemofiltration membranes, also called high-flux dialysis membranes, combined with dialysate.

Finally, very porous membranes with pore diameters of roughly 0.2 μm were developed to separate blood corpuscles from plasma, a process termed plasmapheresis and based solely on a sieving mechanism. However, it was observed that as operating time increased, a decrease in membrane flux occurred, obviously caused by deposits on the membranes [1]. This phenomenon has been defined in literature as "membrane fouling."

It was soon realized that each of these three processes could be put to good use in other technological fields to solve separation problems. For example, the solution/diffusion

principle of hemodialysis was adopted in seawater desalination as "reverse osmosis." For this purpose, very high transmembrane pressures were needed, and no dialysate was used.

Hemofiltration, now called "ultrafiltration," is applied in industrial processes to separate macromolecular from low-molecular components.

The plasmapheresis membrane, being more commonly known as "microfiltration membrane," is widely applied in technological processes to remove corpuscles from suspensions.

The following facts give an insight into the major achievements in membrane development in recent years:

1. Because pore structure is no longer symmetrical but mainly asymmetrical (Fig. 1), the actual selective layer is extremely thin and hence flow resistance is very low.
2. There has been a continuous increase in porosity, which is the ratio of the free pore area to the total membrane area.
3. At the beginning, membranes were produced from cellulose or cellulose derivatives, whereas nowadays, an increasing variety of materials (including inorganic) is used.
4. Selectivity, that is, the ability to differentiate between permeating substances with different molecular weight, is being improved continually.
5. Attempts at closing the gaps between the three pressure-driven membrane processes—reverse osmosis, ultrafiltration, and microfiltration—have been increasingly successful.
6. Electrical charges could be fixed on the surface of the membrane, providing an additional separation mechanism.

Particularly the aspects mentioned in points 5 and 6 led to the discovery of a new membrane process, called "nanofiltration."

A nanofiltration membrane is defined as having pores from 0.5 up to 10 nm as well as an electric surface charge.

Table 1 shows the so-called pressure-driven membrane processes and examples of their industrial applications.

While in the past, focus centered on the development and optimization of membranes and membrane elements/modules (the apparatus into which the membrane is integrated) [2–4], nowadays models are needed for describing mass transport in the membrane as well as computer programs for designing membrane processes. Until now, only programs for designing reverse osmosis processes and apparatuses have been available.

Although there is a close relationship between reverse osmosis and nanofiltration in terms of the structure of the membrane elements, plant engineering, and mass transport, there are also differences concerning the separation principles.

This chapter will deal with the computer simulation of nanofiltration membranes and processes.

The first section will focus on the application of nanofiltration, definition of the main membrane parameters and membrane phenomena, nanofiltration membranes and modules,

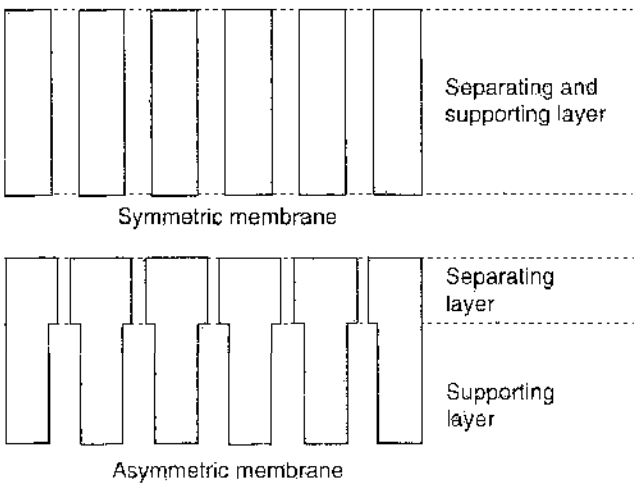

Figure 1. Schematic representation of symmetric and asymmetric membrane structures.

Table 1. Pressure-driven membrane process.

Membrane separation process	Separation principle	Transmembrane pressure [bar]	Pore diameter/ cut-off	Application
Microfiltration	Sieving effect	0.1–2	100–2000 nm	Separation of suspended matter
Ultrafiltration	Sieving effect	1.0–5.0	5–100 nm 10^3–10^6D cut-off	Concentration, fractionation, and purification of macromolecular solutions
Nanofiltration	Sieving effect, solution/diffusion and membrane charge	5.0–20.0	0.5–10 nm 10^2–10^3D cut-off	Separation of organic and inorganic components (organic components in aqueous solutions, ions of higher valence)
Reverse osmosis	Solution/diffusion	10.0–200.0	$<$100 D cut-off salt retention 90%	Desalination of aqueous solutions

and their characterization. In the second section, the modeling of neutral solid and ion transport in charged nanofiltration membranes using computer simulation programs will be presented. Finally, the third section will deal with computer-aided simulation and design of nanofiltration processes that are conducive to the optimization of industrial nanofiltration processes.

1.1. Application of Nanofiltration

Synthetic nanofiltration membranes have reached a high state of development. Today, they are available in nearly every type of material, and their prices are continually falling, making them attractive for numerous fields of application (Table 1). For example, nanofiltration membranes have been applied for selectively removing multivalent salts for the purpose of water softening [5, 6]. Drinking water can be produced by eliminating the organics (particularly humic acid) from surface water [6]. Ceramic nanofiltration membranes have been used successfully for decolorizing textile wastewater, while in the food industry, the acids and bases (particularly caustic soda) used for cleaning in place, can be recycled [7].

In downstream processing in biotechnology, charged metabolites can be separated from low-molecular weight uncharged metabolites [8], and natural active substances can be concentrated via nanofiltration membranes [9].

In our own experiments with nanofiltration membranes, we produced a permeate from the treatment of oil/water emulsions that was of such high quality that it could be reused as process water.

These are only a selection of examples from the multitude of possible applications for nanofiltration membranes.

1.2. Definitions of Main Membrane Parameters and Membrane Phenomena

The pressure-driven membrane processes including nanofiltration operate in cross-flow mode to avoid the disadvantages of membrane fouling occurring in dead-end filtration. The schematic principle of the two different filtration modes are shown in Figure 2.

The most important terms of pressure-driven membrane processes in the cross-flow mode can be seen in Figure 3 which is a schematic representation of a membrane separation element, called a membrane module.

1.2.1. Feed, Permeate, and Retentate Flows: Membrane Flux and Permeability

The feed volume flow $\dot{Q}^f$ [m^3/h] containing the solute concentration in the feed c_i^f [mg/m^3, mol/m^3] of the dissolved components enters the module, where it is divided into two partial streams by the membrane: the retentate volume flow $\dot{Q}^r$, containing the solute concentration in the retentate c_i^r, which is retained by the membrane, and the permeate volume

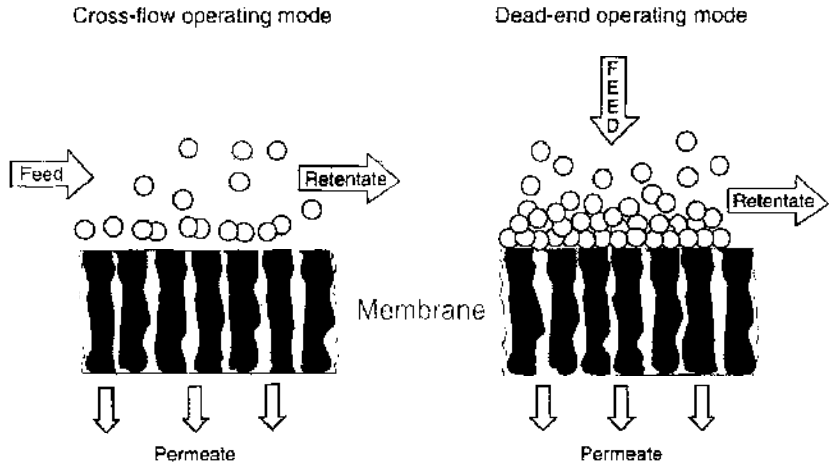

Figure 2. Comparison of dead-end and cross-flow filtration. Adapted from [20].

flow $\dot{Q}^p$, containing the solute concentration in the permeate c_i^p, which passes through the membrane.

Then the membrane volume flux density j_v is:

$$j_v = \frac{\dot{Q}^p}{A_m}\left[\frac{m^3}{m^2 h}\right] \tag{1}$$

where A_m is the membrane area in [m^2].

To obtain the membrane solution hydraulic permeability $\bar{L}_p$ [m^3/m^2h.bar], the permeate volume flow is divided by the membrane area A_m and the transmembrane pressure difference

$$\begin{aligned} \Delta P &= \frac{(P^f + P^r)}{2} - P^p \,[\text{bar}] \\ \bar{L}_p &= \frac{\dot{Q}^p}{A_m \cdot \Delta P} = \frac{j_v}{\Delta P} \end{aligned} \tag{2}$$

1.2.2. Rejection and Selectivity

The separation efficiency of membranes is characterized by rejection and the selectivity for different components in the feed solution. Rejection R_i [-] for a component i is defined by:

$$R_i = 1 - \frac{c_i^p}{c_i^f} \tag{3}$$

where c_i^p and c_i^f are the concentrations of the component i in the permeate and in the feed.

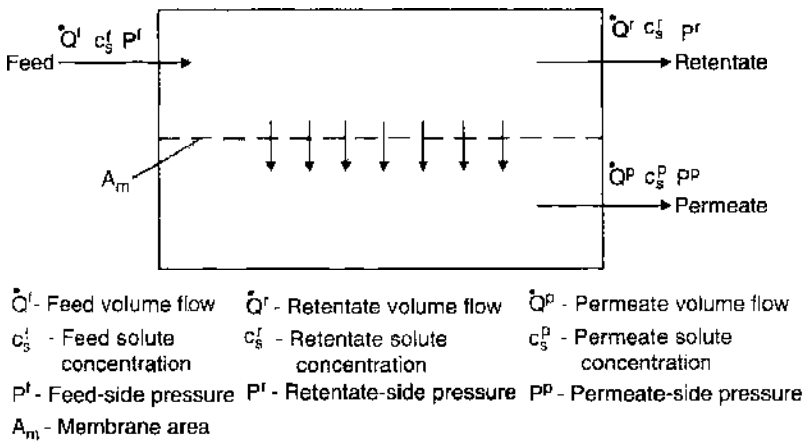

Figure 3. Schematic representation of a membrane module with input and output streams.

However, this equation should be extended by adding the definition for the concentration in the feed c_i^f to allow clear information to be deduced. The concentration in the feed c_i^f can refer to either the concentration in the bulk flow c_i^b or the concentration at the membrane surface c_i^w. As a result of concentration polarization (see following), the rejection value calculated can differ considerably. For this reason, we differentiate between real rejection of the component $iR_{i,\,\mathrm{Real}}$ and apparent rejection R_i. Real rejection can be expressed as

$$R_{i,\,\mathrm{Real}} = 1 - \frac{c_i^p}{c_i^w} \tag{4}$$

where c_i^p and c_i^w are the concentration of the component i in the permeate and at the membrane surface (wall).

The concentration in the bulk flow is a measurable parameter, whereas the concentration at the membrane surface can only be estimated. Therefore, the rejection specified usually refers to the feed concentration at the system inlet. However, it is a fact that real membrane rejection $R_{i,\,\mathrm{Real}}$ is usually greater than the rejection R_i according to Eq. (3).

$$R_{i,\,\mathrm{Real}} > R_i \tag{5}$$

Equations (3) and (4) refer to local concentrations. However, as far as industrial membrane elements (membrane modules) with a large membrane area are concerned, concentration in the feed c_i^f increases continuously along the length of the element and cannot be considered as constant. Because the feed-side measurement values can only be determined at the inlet and outlet of the element, the mixed concentration of the total permeate c_i^p and the average arithmetical value of the feed-side concentrations at the inlet and outlet of the element c_i^f are used to calculate membrane rejection.

Membrane selectivity $S_{i,j}$ describes the ability of the membrane to differentiate between two components i and j in a mixed solution:

$$S_{i,j} = \frac{c_i^p / c_j^p}{c_i^f / c_j^f} = \frac{T_i}{T_j} \tag{6}$$

where c_i^f, c_j^f are the concentration of the components i and j in the feed [mol/m^3; mg/m^3], c_i^p c_j^p are the concentration of the components i and j in the permeate [mol/m^3; mg/m^3], and T_i, T_j are the passage of the component i, j, through the membrane [-].

1.2.3. Membrane Yield

The ratio between permeate and feed volume flow in the membrane module is referred to as membrane yield (recovery) Y [-]:

$$Y = \frac{\dot{Q}^p}{\dot{Q}^f} \tag{7}$$

1.2.4. Concentration Polarization

As a result of the transmembrane flux during filtration, dissolved substances are transported via convection to the membrane surface. The rejection of dissolved substances by the membrane results in an increase in concentration near the membrane surface, which is defined as concentration polarization [10–12]. An equilibrium with a final constant value for profile concentration on the membrane is established for steady-state operations. This increased concentration on the membrane surface results in a reversed transport of dissolved substances, because of diffusion, back into the bulk flow, which passes in a crossflow direction along the membrane surface. Rediffusion into the bulk flow occurs as a result of the concentration gradient (Fick's diffusion). Figure 4 is a schematic representation of the concentration profile of dissolved substances as a function of distance from the membrane surface.

Concentration polarization has a considerable influence on the industrial application of membrane separation processes. In nanofiltration and reverse osmosis processes, it results

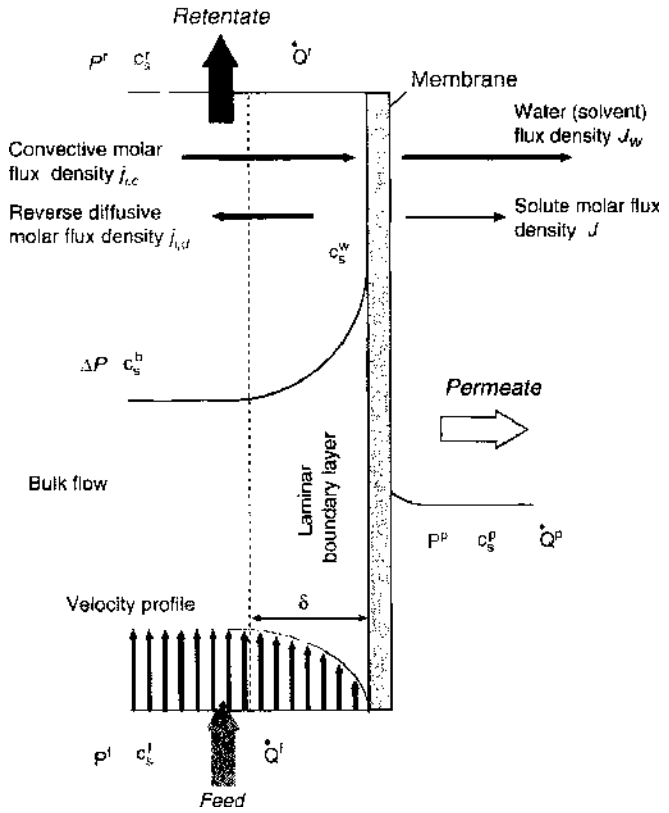

Figure 4. Schematic representation of concentration polarization in cross-flow filtration. Adapted from [20].

in an increase in the concentration of the dissolved substances, which are retained on the membrane, and generally results in an increase in osmotic differential pressure. As a result, an apparent decrease in membrane separation efficiency can occur as well as the formation of a coating layer that can be caused by colloidal (organic/inorganic), organic, microbiological, and crystallizing components present in the solution to be filtered.

The mass balance for a component i can be expressed as

$$j_i = j_{i,d} + j_{i,c} \tag{8}$$

where j_i is the total molar flux density of component i/ion i [mol/m^{2}h], $j_{i,d}$ is the diffusive molar flux density of component i/ion i [mol/m^{2}h], and $j_{i,c}$ is the convective molar flux density of component i/ion i [mol/m^{2}h].

The diffusive molar flux density $j_{i,d}$ induced by diffusion into the bulk flow can be expressed as

$$j_{i,d} = -D_i \cdot \frac{\partial c_i}{\partial x} \tag{9}$$

where D_i is the diffusion coefficient for a component i/ion i [m^2/s], and $\partial c_i/\partial x$ is the space derivative of the concentration of component i/ion i, c_i.

The convective molar flux density $j_{i,c}$ of a component i can be expressed as

$$j_{i,c} = J_w \cdot c_i \tag{10}$$

where J_W is the transmembrane volume water (solvent) flux density [m^3/m^{2}h].

The mass balance in the steady state leads to constant water and solute flux densities across the system:

$$j_i = J_w \cdot c_i^p \tag{11}$$

From Eq. (8), this leads to

$$j_i = J_W \cdot c_i^p = -D_i \cdot \frac{\partial c_i}{\partial x} + J_W \cdot c_i \tag{12}$$

Integration of the Eq. (12) via c_i into boundaries c_i^b (concentration of the component i in the bulk flow) and c_i^w (concentration of the component i at the membrane surface) and via x into the boundaries from 0 to δ of the laminar boundary layer results in

$$J_W \cdot \frac{\delta}{D} = \ln\left(\frac{c_i^w - c_i^p}{c_i^b - c_i^p}\right) \tag{13}$$

In literature, the feed-side mass transport coefficient k_F [m/s] is often also used for the term D_i/δ for the mass transport between the laminar boundary layer and the bulk, so that Eq. (13) can also be expressed as

$$\frac{c_i^w - c_i^p}{c_i^b - c_i^p} = \exp\left(\frac{J_W}{k_F}\right) \tag{14}$$

According to Eq. (13), concentration polarization can be influenced essentially by three factors:

1. Membrane volume flux density j_v: An increase in the membrane volume flux density (resulting in an increase in convective mass transport towards the membrane) generates a greater degree of concentration polarization.
2. The diffusion coefficient D_i for the retained components: A greater degree of concentration polarization occurs by reducing the reverse diffusive molar flux density $j_{i,d}$ for retained substances with smaller diffusion coefficients D_i.
3. Feed-side flow velocity u(cross-flow): High flow velocities along the membrane reduce the thickness δ of the laminar boundary layer and thus concentration polarization as well (see velocity profile in Fig. 4).

Generating turbulence can also be a constructive means of counteracting concentration polarization to obtain a more intensive flow across the membrane surface. In spiral wound elements (see following), for example, the direction of a solution can be diverted several times by using specially developed spacers in the feed channel. However, one disadvantage of fine-meshed spacers is that pressure loss increases in the feed.

The feed-side mass transport coefficient k_F can be correlated to other flow parameters by introducing the dimensionless numbers, Sherwood *Sh*, Schmidt *Sc*, and Reynolds *Re*, for which the following relations apply:

$$Sh = \frac{k_F \cdot d_H}{D_i}, \quad Sc = \frac{\nu}{D_i}, \quad \mathrm{Re} = \frac{u \cdot d_H}{\nu} \tag{15}$$

where d_H is the feed flow channel hydraulic diameter [m], u is the flow velocity of the feed solution along the membrane [m/s], and ν is the kinematic viscosity of the feed solution [m²/s].

Different correlations have been determined as a result of membrane geometry. The following correlation was determined by Schock and Miquel [13] for spiral wound elements based on experimental data:

$$Sh = 0.065 \cdot Re^{0.875} \cdot Sc^{0.25} \tag{16}$$

Thus, the feed-side mass transport coefficient k_F depends on the diffusion coefficient D_i, the hydraulic diameter d_H, the kinematic viscosity ν, as well as the flow velocity u of the solution along the membrane:

$$k_F = 0.065 \cdot D_i^{0.75} \cdot d_H^{-0.125} \cdot \nu^{-0.625} \cdot u^{0.875} \tag{17}$$

1.2.5. Membrane Fouling

Membrane fouling [14] always leads to a more or less pronounced decrease in membrane permeability and can result in complete blockage of the membrane, causing a breakdown

in the membrane unit. This incurs an increase in operating costs because of the additional cleaning measures and, possibly, the need to install a greater membrane area. This rise in costs can render membrane processes uneconomical.

It is only evidence of cost-effectiveness and operational reliability that will convince operators to apply membrane separation processes, and this can only be achieved by effectively preventing uncontrolled membrane fouling. One requirement for controlling or preventing fouling is information on fouling mechanisms.

Basically, membrane fouling can be divided into two categories (Fig. 5):

1. Fouling outside the membrane (gel-like layer)
2. Fouling inside the membrane (pore blocking)

Depending on the compounds causing the fouling, it is possible to divide fouling into the following types:

1. Scaling (precipitation of inorganic salts resulting from the solubility limit being reached)
2. Organic fouling (caused by the insoluble or dissolved organic materials)
3. Biofouling (caused by microorganisms)

The causes of fouling are concentration polarization and adsorption on or in the membrane (Fig. 5)

Fouling phenomena generally do not occur separately but, rather, frequently in a combined form during filtration of real media.

Particularly the roughness of a membrane surface as well as hydrodynamic conditions during filtration are decisive for the development of fouling outside the membrane. Because surface roughness cannot usually be changed, the following measures can be implemented to prevent this type of fouling:

- Increasing shear rate by increasing turbulence via
  - — An increase in feed flow rate
  - — Implementation of inserts with different configurations
- Reducing the specific permeate flux

Membrane fouling caused by pore blocking can only be prevented by pretreatment of the feed solution or by changing the membrane pore size. Fouling by adsorption can, for example, be reduced or prevented by changing the membrane material, feed composition, or process conditions (temperature, pH value).

1.2.6. Donnan Equilibrium

Negative rejection can occur for monovalent anions, particularly chloride, during the filtration of electrolytic solutions using nanofiltration membranes. This effect, which is characterized by a higher concentration of anions on the permeate side than on the feed side,

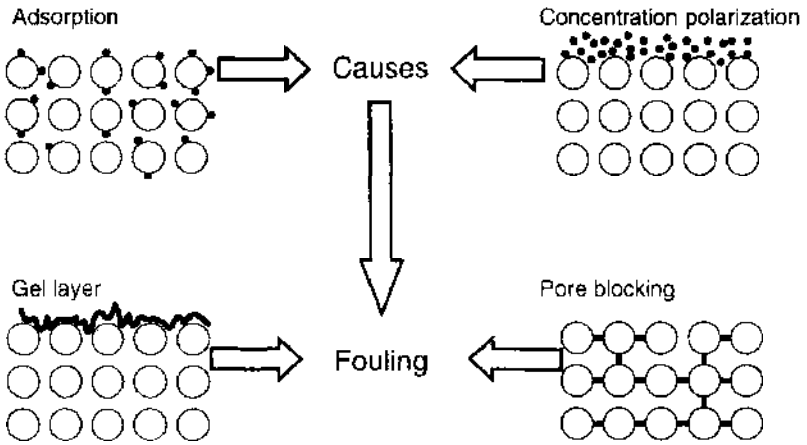

Figure 5. Membrane fouling and its causes.

is caused by a fixed negative charge on the membrane and is called the "Donnan Effect" [15–17].

When a NaCl solution (feed side) is separated from fully desalinated water (permeate side) by a nanofiltration membrane without applying pressure, the monovalent ions migrate to the permeate side because no selectivity exists as a result of the concentration gradient. After a certain period of time, an equilibrium is established, resulting in a fairly equal concentration on both sides (Fig. 6a).

This equilibrium is disturbed by adding Na_2SO_4 on the feed side (Fig. 6b). The increase in Na^+ concentration results in a further relatively unimpeded permeation of cations. Because of the bivalent charge, the sulfate SO_4^{2-} is retained, to a great extent (on condition that the membrane is perfectly impermeable to the sulfate ions), by the membrane via electrostatic repulsion. As the SO_4^{2-} concentration increases on the feed side, Cl^- is forced to pass to the permeate side against the concentration gradient via electroneutrality (Fig. 6c).

1.3. Nanofiltration Membranes and Modules

1.3.1. Transport Mechanisms in Nanofiltration Membranes

In nanofiltration processes, several separation mechanisms operate in parallel and can also have a reciprocal effect on each other. The transport of dissolved components in the membrane is governed by the following mechanisms (Fig. 7):

- Convection: Dissolved components pass through the membrane pores via convection in the permeate flow. An increase in permeate flow intensifies the transport of dissolved components to the permeate side.
- Solution-diffusion: The concentration gradient between the feed and permeate side is a major driving force that causes the dissolved substances to diffuse through the nanofiltration membrane.
- Sieve mechanism (or steric hindrance): Components, which are larger than the pore diameter, are retained. Steric hindrance may occur when the size of the components is similar to pore diameter.
- Membrane charge (electrostatic interaction): The surface charge of a nanofiltration membrane either attracts or rejects charged components (co-ions or counter-ions) that can have a reciprocal effect on each other.

1.3.2. Organic Nanofiltration Membranes and Modules

Nanofiltration membranes were developed from reverse osmosis membranes. In literature, "loose reverse osmosis membrane" can often be found as a synonym for nanofiltration membranes. Whereas reverse osmosis membranes have a cut-off of less than 100 Dalton, nanofiltration membranes are characterized by 200 ≤ cut-off < 1000 Dalton.

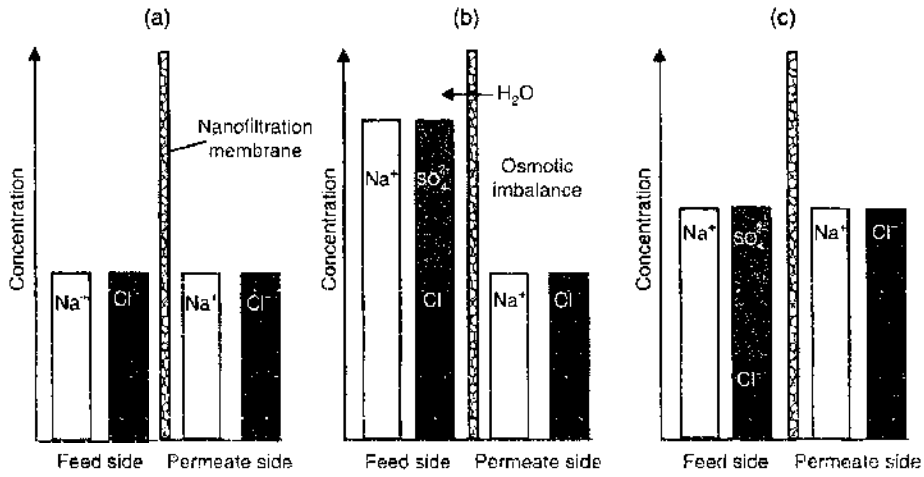

Figure 6. Establishment of Donnan equilibrium: (a) equilibrium; (b) addition of Na_2SO_4; (c) transport of Cl^- from feed to permeate side.

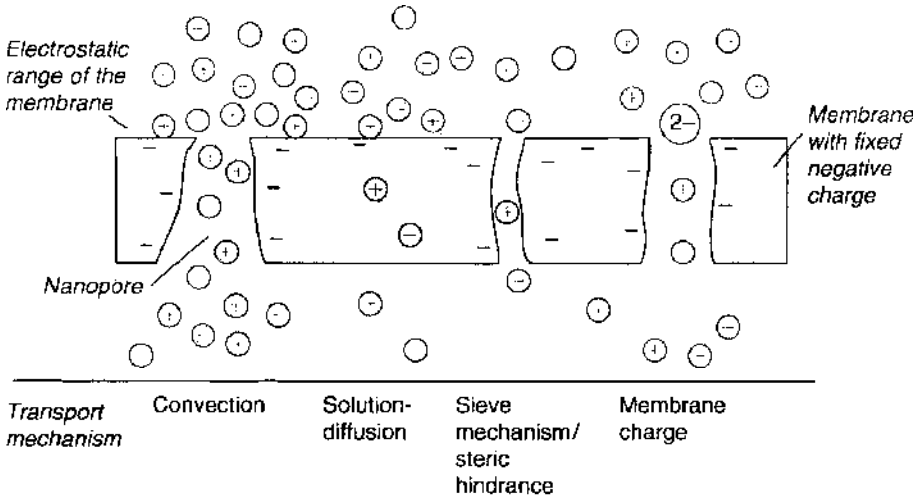

Figure 7. Transport mechanisms of nanofiltration (simplified).

Most reverse osmosis and nanofiltration membranes are asymmetric composite membranes, the construction of which is based on the same principle: a very thin active layer is supported by several microporous layers, the last of which can be made of cloth or fleece (Fig. 8).

Different polymers are used as an active layer (e.g., cellulose acetates [CA], polyamide [PA], polyethersulfone [PES], polypropylene amide [PPA], etc). CA has a high water permeability and is resistant to chlorine but not to solvents, and the polyamides are resistant to numerous solvents but not to chlorine.

An informative survey on commercially available polymer nanofiltration membranes can be found in Ref. [18].

The technical arrangement of membranes is called a "module." Depending on the application in question, optimum conditions for the membrane separation process should prevail in the module. A compromise is usually made in optimizing the development of modules because some of the requirements, listed below, are contradictory:

- A good, uniform flow across the membrane
- Low pressure losses
- Large packing density
- Mechanical, chemical and thermal resistance
- Cheap to produce
- Easy to clean.

The module types with polymeric membranes, currently available, are fitted with tubular (including hollow fiber membranes) as well as flat-sheet membranes (pads [19] and spiral wound membranes). The most frequently used configuration of the spiral wound module with polymeric nanofiltration membranes is shown in Figure 9.

Figure 8. Asymmetric composite polymer membrane.

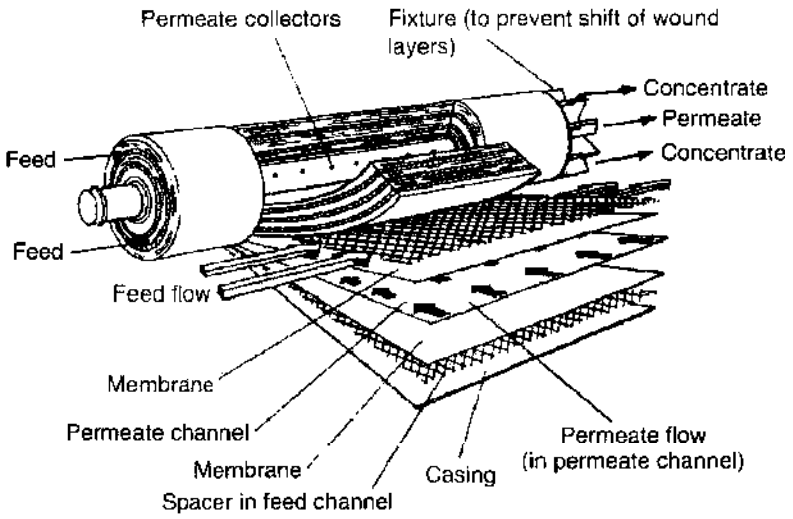

Figure 9. Spiral wound module with polymeric nanofiltration membranes.

1.3.3. Inorganic Nanofiltration Membranes and Modules

The inorganic membranes, particularly ceramic membranes, have the following advantages compared to organic membranes:

- High temperature resistance (can be sterilized by steam)
- High chemical resistance, particularly to
  - — oxidants (chlorine, ozone, H_2O_2)
  - — solvents
  - — acids and bases
- Longer service life
- High durability
- Better backflushing properties
- Narrow pore size distribution (Fig. 10).

However, vis-a-vis these advantages, are the following disadvantages:

- High degree of brittleness and therefore sensitivity to impact
- Unfavorable ratio: area/volume and area/weight
- Complex membrane production (several layers, at high temperatures)
- Expensive module construction (because of sealing problems in particular).

The last two factors incur considerably higher investment costs compared to polymer membrane modules.

Inorganic membranes are by far not as new as is generally thought. The first polymer membranes were used in artificial kidneys at roughly the same time as the first inorganic membranes were applied for enriching the uranium 235 isotope. The significance of this

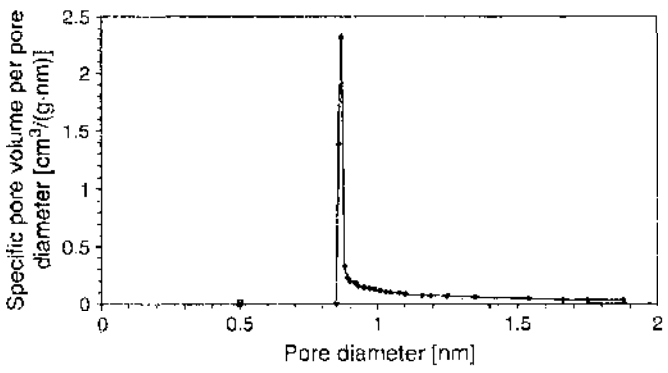

Figure 10. Narrow pore size distribution of a ceramic membrane.

for nuclear weapons and atomic energy production led to an enormous effort being put into research in the United States, Russia, and Europe (particularly France), thus bringing inorganic membrane technology forward. However, microporous (microfiltration and ultrafiltration) membranes only became commercially available in the 1980s, and nanoporous (NF) membranes after the year 2000.

Nanoporous ceramic membranes are always constructed in several layers. This is highlighted in Figure 11a by a schematic representation and by an electron micrograph in Figure 11b. One or more microfiltration layers (0.05–0.8 μm) or one or more ultrafiltration layers (5–50 nm) are arranged on a support (pore diameter 1–10 μm), and finally, a very thin, selective nanofiltration layer 4 nm or less is placed on top.

The individual layers can be made from different materials (e.g., Al_2O_3, TiO_3, ZrO_2, SiO_2, and SiC). The support, which is several millimeters thick, is formed by pressing the powdered substances by extrusion or by slip casting. A high degree of roughness, inhomogeneity, and defects in the support can cause imperfections in the layers above and should therefore be prevented.

The process most commonly applied to produce microporous and nanoporous layers is the "Sol–Gel-Technique" whereby a colloidal suspension (inorganic polymer) is brought onto the support by immersion, spraying, or rotation. This coating layer becomes gel-like during the drying process and is then calcinated at high temperatures. Finally, the layer is sintered at temperatures above 1000°C. The narrow pore size distribution and the resulting sharp cut-off that can be achieved by this process are shown later.

Recently, attempts have been successful in bringing zeolites, which are crystalline aluminium silicates with a strictly defined structure, onto inorganic nanofiltration membranes, thus producing inorganic membranes with a molecular sieve character [20]. However, because the development process is still at the prototype stage, this topic will not be dealt with in any great detail at this point.

The most common ceramic membrane configuration is the tubular membrane, which can be a single tube or multichannel structure (Fig. 12).

Although ceramic flat-sheet membranes (Fig. 13), through which flow passes from the outside to the inside, are gaining in significance, they are still not commercially available as nanofiltration membranes.

If the membrane module with ceramic membranes or, more precisely, the casing were made of polymer material, some of the above-mentioned advantages of ceramic membranes would be lost. Ideally, the casings should also be made of ceramic material. Although this type of casing is now commercially available, they are still too expensive and are sensitive to impact. Most inorganic membrane modules consist of a stainless steel casing, an example of which is shown in Figure 14.

Because the thermal expansion coefficient of membranes and their casings varies to a great extent, particular significance is given to the sealing between the membrane and the

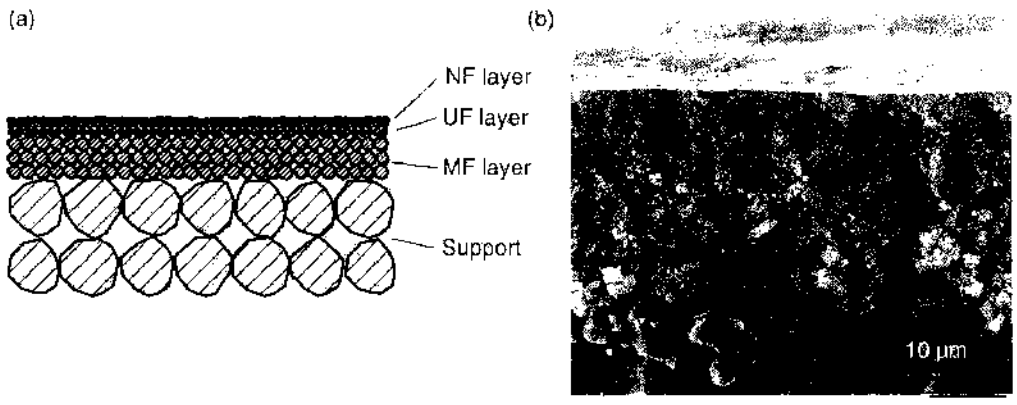

Figure 11. Schematic representation (a) and electron micrograph (b) of a nanoporous ceramic membrane. Reprinted with permission from [21], R. Weber, Ph.D. Thesis on Charakterisierung, Stofftransport und Einsatz keramischer Nanofiltrationsmembranen, Saarland University, Saarbrücken, 2001. © 2001.

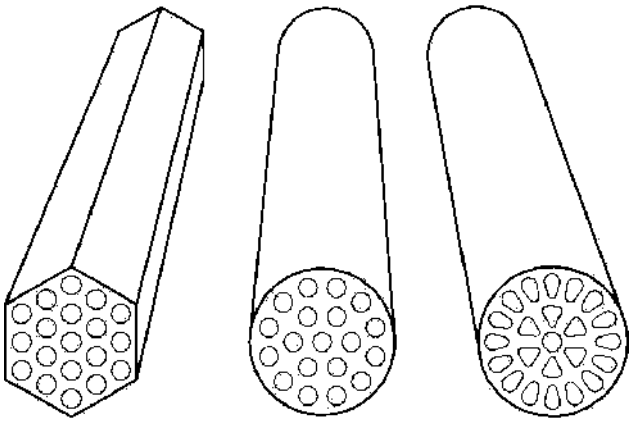

Figure 12. Various multi channel tubular modules (19-or 23-channel ceramic membranes). Reprinted with permission from [21]. R. Weber, Ph.D. Thesis on Charakterisierung, Stofftransport und Einsatz keramischer Nanofiltrationsmembranen, Saarland University, Saarbrücken, (2001), © 2001.

casing. O-ring seals, which are thermally and chemically resistant, have proven successful in this respect.

1.4. Characterization of Nanofiltration Membranes

A test stand, as shown in Figure 15 [21], is a suitable apparatus for determining the efficiency of nanofiltration membranes and modules under various process conditions.

This test set-up allows the transmembrane flux density (and thus the membrane hydraulic permeability) and rejection characteristics of the membranes to be determined as a function of transmembrane pressure at varying operating parameters such as flow velocity, temperature, pH value, yield, and so on.

1.4.1. Determination of Pure Water Hydraulic Permeability

By filtering demineralized water (pure water quality, electric conductivity = 0.055 μS/cm) pure water membrane hydraulic permeability $\tilde{L}_p^0$ [m^3/m^{2}hbar] can be determined according to Eq. (2).

Plotting these experimental results $\tilde{L}_p^0 = f(\Delta P)$ in graphic form produces a trend typical for organic nanofiltration membranes, as shown in Figure 16.

Initially, pure water membrane hydraulic permeability, $\tilde{L}_p^0$ decreases considerably, but the expected constant permeability rate becomes established at a certain level of pressure difference ΔP, which is characteristic of each membrane/module. The reason for this is the compressibility of the polymer membrane. Therefore, module manufacturers define a

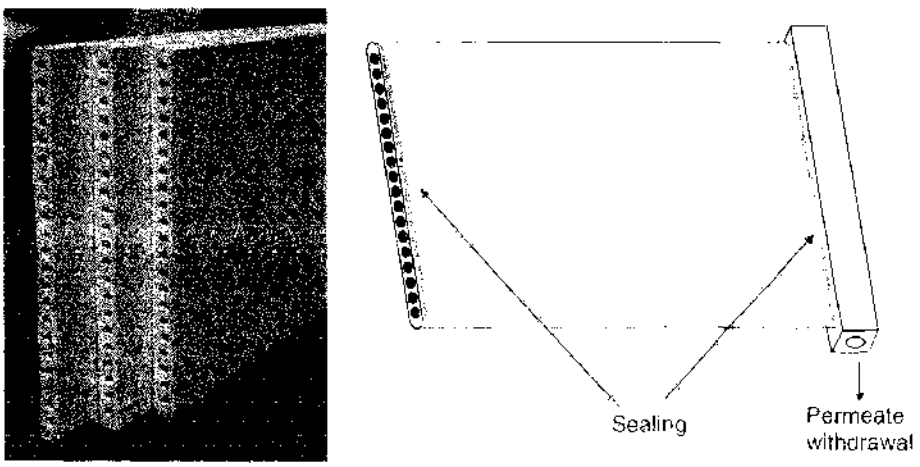

Figure 13. Ceramic flat-sheet membrane.

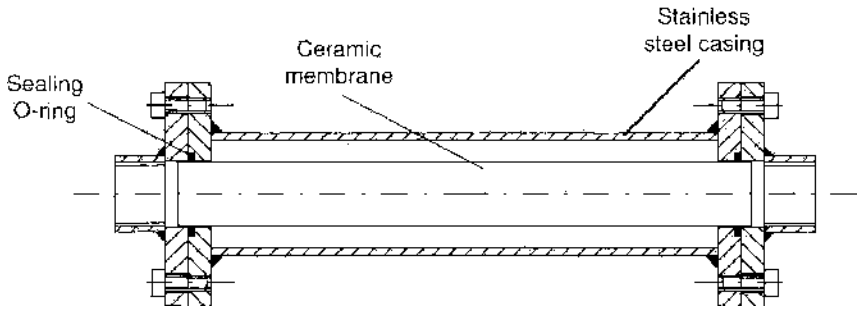

Figure 14. Membrane module with a stainless steel casing for a ceramic membrane. Reprinted with permission from [21], R. Weber, Ph.D. Thesis on Charakterisierung, Stofftransport und Einsatz keramischer Nanofiltrationsmembranen, Saarland University, Saarbrücken, 2001. © 2001.

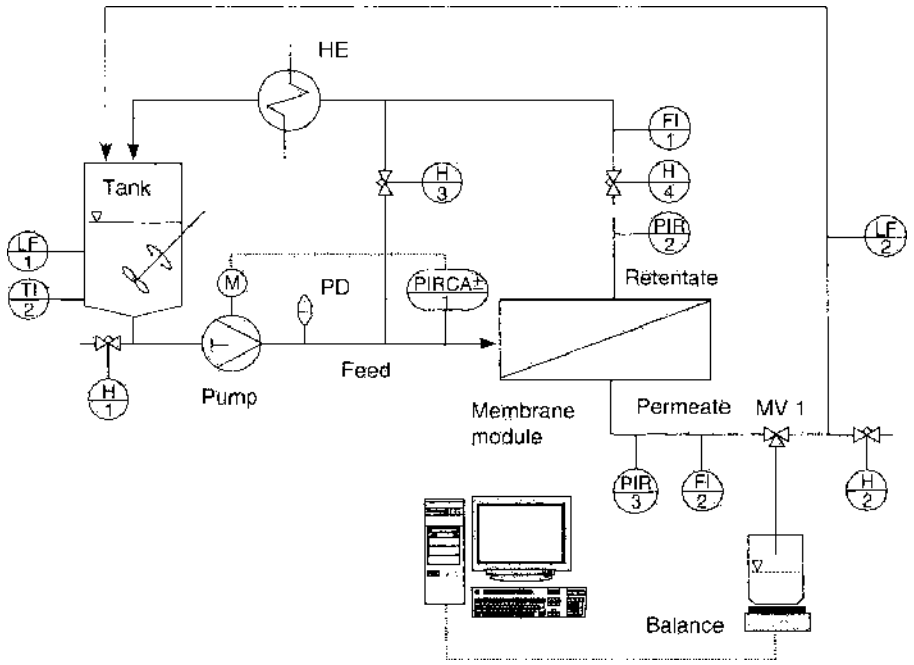

Figure 15. A test stand for the characterization of nanofiltration membranes and modules. Reprinted with permission from [21], R. Weber, Ph.D. Thesis on Charakterisierung, Stofftransport und Einsatz keramischer Nanofiltrationsmembranen, Saarland University, Saarbrücken, 2001. © 2001.

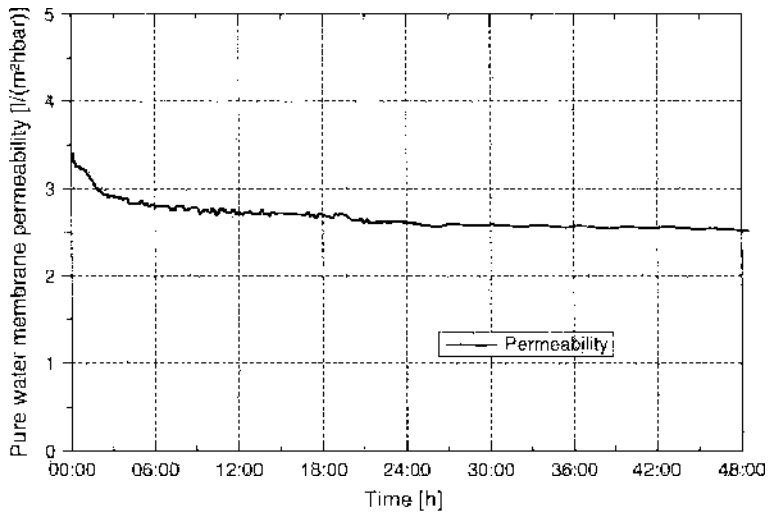

Figure 16. Typical pure water hydraulic permeability trends of a polymer nanofiltration membrane during the compacting phase (T = 293 K, $P^{\prime}$ = 6 bar). Reprinted with permission from [21], R. Weber, Ph.D. Thesis on Charakterisierung, Stofftransport und Einsatz keramischer Nanofiltrationsmembranen, R. Weber, Saarland University, Saarbrücken, 2001. © 2001

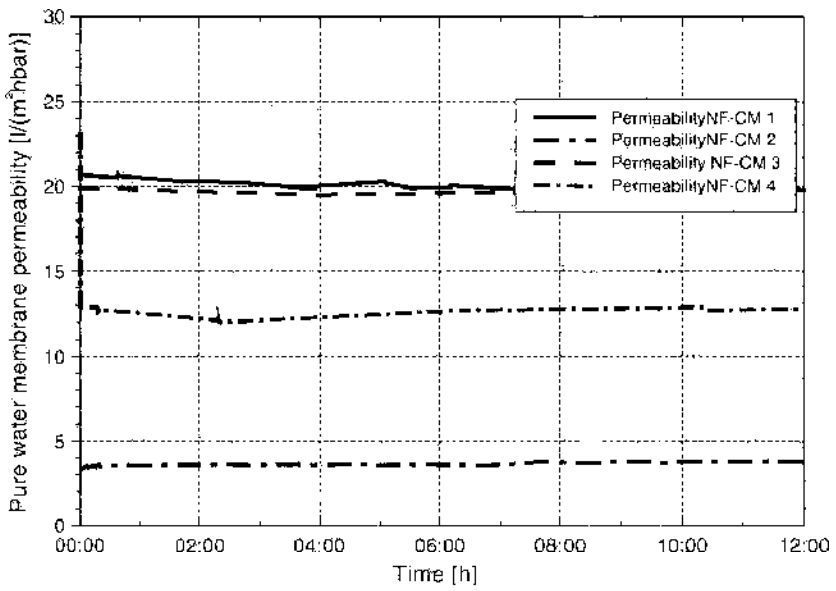

Figure 17. Pure water hydraulic permeability rates of the ceramic membranes (T = 293 K, P' = 6 bar). Reprinted with permission from [7], R. Weber et al., *Desalination* 157, 113 (2003). © 2003, Elsevier.

transmembrane pressure level at which a new module can be compacted for a specific period of time before it reaches the guaranteed separation efficiency.

Typical pure water membrane hydraulic permeabilities for nanofiltration polymer membranes are between 2 and 6 [l/m^{2}h.bar] (Fig. 16).

As can be seen from Figure 17, defect-free, inorganic nanofiltration membranes show a constant pure water permeability rate from the start in the range between 5 and 20 [l/m^{2}h.bar].

1.4.2. Rejection and Cut-off Characteristics

In general, the rejection and cut-off characteristics of a nanofiltration membrane can be defined by performing numerous filtration tests, using inorganic salts and single uncharged organic substances of a defined molecular weight. The respective rejection values are then calculated according to Eq. (3). The typical inorganic salt rejection characteristics of ceramic nanofiltration membranes are shown in Figures 18 and 19 [7, 21].

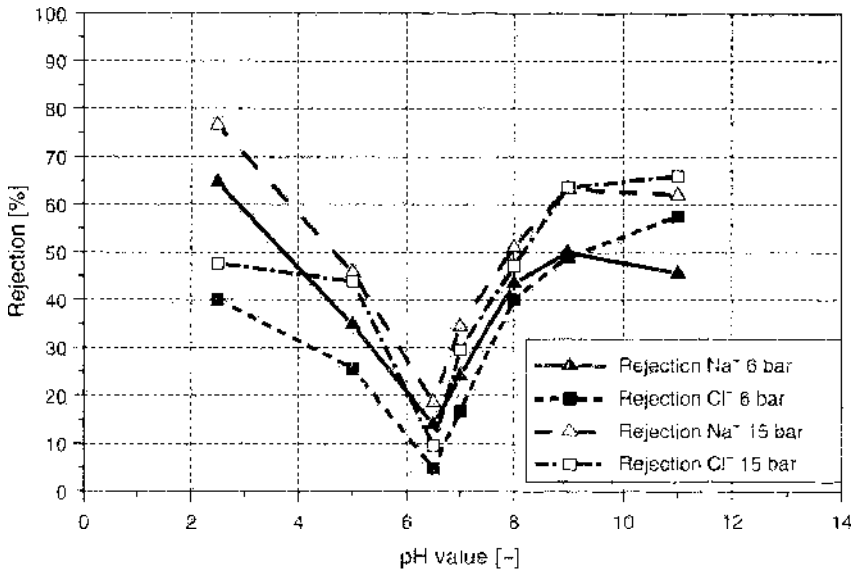

Figure 18. NaCl rejection for the ceramic membrane NF-CM 1 at different pH values. c(NaCl) = 0.01 mol/l. Reprinted with permission from [7], R. Weber et al., *Desalination* 157, 113 (2003), © 2003, Elsevier.

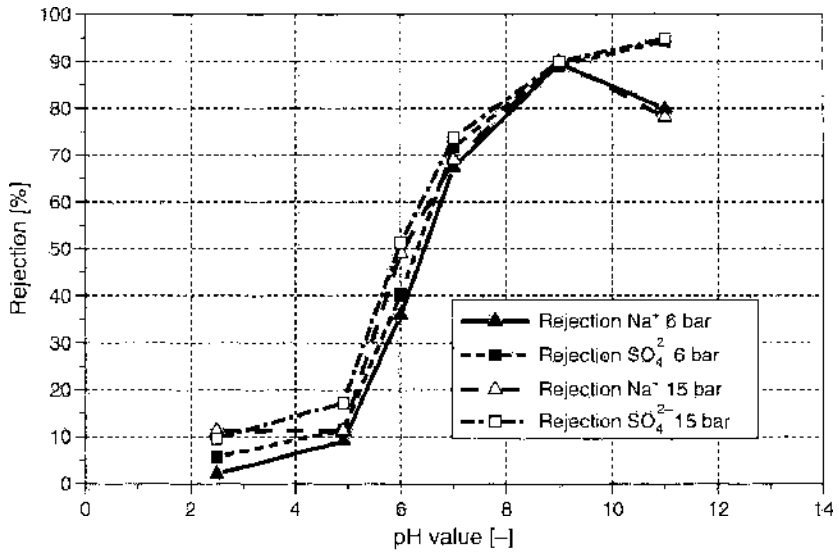

Figure 19. $CaCl_2$ rejection for NF-CM 1 at different pH values $c(CaCl_2) = 0.01$ mol/l. Reprinted with permission from [7]. R. Weber et al., *Desalination* 157, 113 (2003). © 2003, Elsevier.

The dependence of rejection on the molecular weight of rejected organic substances is defined as the cut-off characteristic of a membrane, and the molecular weight of rejected organic substances at 90% rejection is defined as the cut-off value of the membranes.

Compared with the French AFNOR standard NF X 45-103, Weber et al. [7, 21, 22] proposed a modified procedure in which a mixture of various uncharged macromolecules were dissolved in water for filtration tests. For nanofiltration membranes, polyethylene glycols, which are commercially available in the range between 100 and 3000 Da in relatively narrow molecular-weight distribution, were used.

The composition of the feed and permeate solutions were determined via size exclusion chromatography. Desalinated water with high purity was used as an elution agent. Detection was carried out via the RI detector.

The cut-off characteristics of some commercially available organic nanofiltration membranes are shown in Figure 20.

Figure 21 shows the PEG rejection for commercial ceramic membranes, available as nanofiltration membranes. From this figure, it can be said that only one of them fulfills the definition for nanofiltration membranes (i.e., cut-off below 1000 g/mol molecular weight).

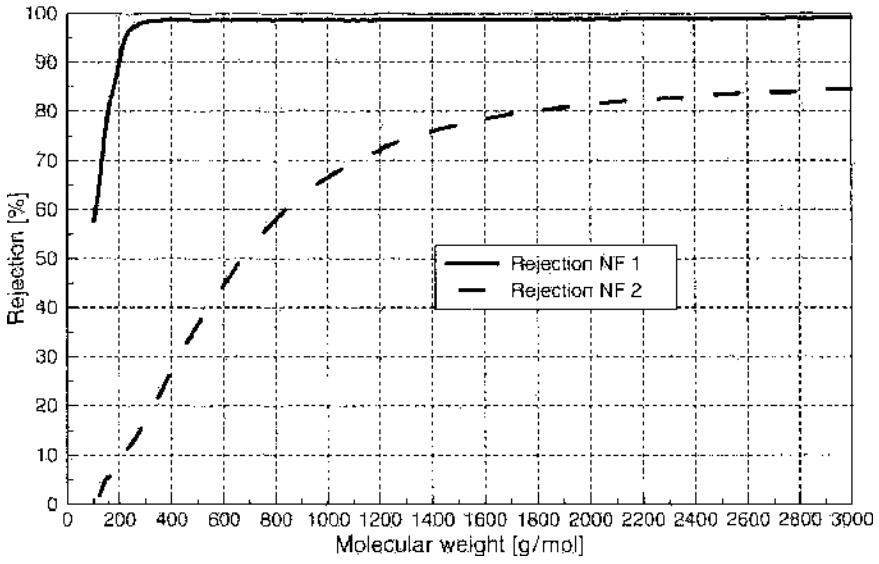

Figure 20. PEG rejection for the polymer membranes NF 1 and NF 2. Reprinted with permission from [21], R. Weber, Ph.D. Thesis on Charakterisierung, Stofftransport und Einsatz keramischer Nanofiltrationsmembranen, Saarland University, Saarbrücken, 2001. © 2001.

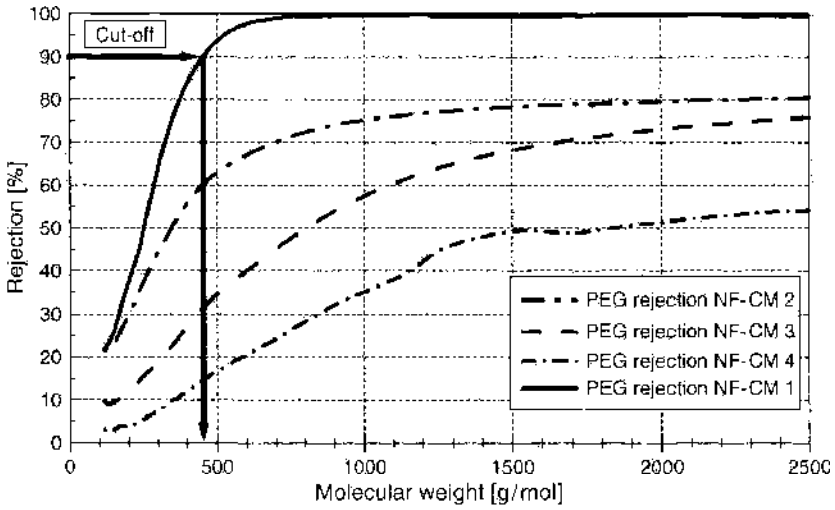

Figure 21. PEG rejection for some commercial ceramic membranes. Reprinted with permission from [7]. R. Weber et al., *Desalination* 157, 113 (2003). © 2003, Elsevier.

2. MODELING OF NEUTRAL SOLUTE AND ION TRANSPORT IN CHARGED NANOFILTRATION MEMBRANES, USING COMPUTER SIMULATION PROGRAMS

2.1. Introduction

Nanoscale solute transport is controlled by the primary interactions operating in the condensed state of matter: electrostatic, electrodynamic (Lifshitz-Van der Waals), polar (acid–base), and chemical (covalent) [23, 24]. The detailed way in which these primary interactions manifest themselves in water-saturated nanoporous media containing solvated ions and molecules is a difficult and still open problem [25–27]. A solution to this problem, however, could potentially provide the key to the development of tailor-made membrane materials perfectly adapted to a given industrial filtration problem. It is likely that biological and artificial nanofiltration (NF) transport mechanisms share many properties, and therefore an understanding of one will probably go hand in hand with the other, opening up the exciting possibility of discovering new separation methods at the bio–nano interface and perfecting the elaboration of nano-engineered membranes [28].

Although at this time it is thought that the transport of ions in NF membranes is determined mainly by the effective electrostatic and steric/hydrodynamic interactions (charge and size exclusion, respectively [29–31]) between the ions and the membrane matrix, there may very well be other important physicochemical interactions operating. These other interactions include the Born exclusion mechanism, based on the difference in ion hydration (self) energy inside the pore and in the bulk solution, and the Dielectric exclusion, based on the loss in electrostatic energy experienced by an ion partitioning into the pores of a membrane with low dielectric constant [25–27, 32]. Untangling the contributions of the various effective interactions is still an open problem: It is still not clear how the effective electrostatic, Born, and Dielectric interactions are related to the primary ones alluded to earlier, nor is it easy to tell whether or not other important interactions have inadvertently been left out of the theory. It should clearly be kept in mind that even today there is still no definitive NF theory, and therefore ion transport cannot yet be predicted from first principles, even at dilute salt concentrations. Incorporating in a consistent way all the important physical interactions into NF theory, to improve its predictive powers, is an ongoing endeavor, as witnessed by the enormous increase in literature publications in this research area.

Given the industrial importance of the current and potential applications, the extension of NF theory to both complex mixtures and highly concentrated brines [>50 g/L of NaCl (1 M)] is now considered to be a major open problem in this extremely active field of research and development. It is also essential to incorporate the most up-to-date NF models into software

for simulating multimodule/multistage plants to put the full power of these models at the fingertips of plant design engineers (see section 3). Because in NF plants many membrane modules may be linked in series, it is important for performing reliable plant simulations to be able to account for the changing feed that is injected into each successive stage, as well as the concomitant change in membrane performance (typically as the feed gets more and more concentrated in proceeding from one stage to the next, the membrane rejection performance gets degraded).

Given this situation, our objective here will be to first provide an overview of current NF theory and modeling at the one membrane element level and then, for illustration, apply this theory in a simplified form to the rejection of ions and neutral molecules by selected polymer and ceramic nanofilters: NTR-7450 [33], Desal5DK, NTR-729 (HN PVD1) [32, 34], NF200, Desal5DL, Membralox commercial nanofilters [35, 36], and homemade hafnia [37, 38] and titania ceramic nanofilters [7, 22].

2.2. Nanofiltration Transport Theory

We present here a concise summary of the current state of the art in NF theory and modeling. Despite the extensive work on the modeling of solute transfer in membranes over the last 40 years, we still do not have a complete understanding of the basic mechanisms involved in nanofiltration. The current models have, however, been developed to the point at which membrane/single salt pairs can be characterized in terms of a few physical parameters, such as effective pore radius, membrane charge density, and thickness [30, 31, 39–49]. Such models could profitably be used to predict the performance of membranes, vis-à-vis complicated electrolyte mixtures, and incorporated into NF plant simulation tools. A more fundamental understanding, currently lacking, would involve predicting the physical parameters listed above from the basic chemistry and nanoporous structure of the membrane material, the latter depending on the preparation methods used.

In simple terms, the objective of any NF modeling study is to relate the incoming solute feed concentration c_s^f and imposed transmembrane pressure difference ΔP to the outgoing solute permeate concentration c_s^p and membrane volume flux density of the solution j_v. The feed and permeate solute concentrations can be used to calculate the solute rejection R_s. The primary goal of the model is to predict R_s given the membrane volume flux density j_v, the composition of the feed (ionic concentrations), and the properties of the membrane (such as its effective pore size r_p, effective membrane charge density X_m, and effective active membrane layer thickness, l_{eff}). A further goal of NF modeling is to predict j_v as a function of ΔP. Here we are only interested in steady-state NF processes for which all quantities studied are independent of time and all fluxes are independent of position in the membrane. An approximate, but useful and sufficiently accurate, understanding of ion transport across a membrane can be developed in three distinct steps [39–41]:

(1) Ion (quasi-equilibrium) partitioning from the feed into the membrane,
(2) Ion transport by diffusion, electrical migration, and convection across the membrane, and
(3) Ion (quasi-equilibrium) partitioning from the membrane into the permeate.

The composition of the feed can be either fixed by directly listing the concentration of each ion present or determined indirectly by the concentration c_s^f of each salt in the mixture. In the latter case, each salt is taken to be completely dissociated into a cation (C) of valence $z_{c,s} > 0$ and stoichiometric coefficient $\nu_{c,s}$ and an anion (A) of valence $z_{a,s} < 0$ and stoichiometric coefficient $\nu_{a,s}$:

$$C_{\nu_{c,s}} A_{\nu_{a,s}} \rightarrow \nu_{c,s} C^{|z_{c,s}|+} + \nu_{a,s} A^{|z_{a,s}|-} \tag{18}$$

The total salt concentration in the feed (f) is given by

$$c_{tot}^f = \sum_{s=1}^{N_s} c_s^f \tag{19}$$

The mole fraction of salt s in the feed mixture is defined by

$$x_s^f = \frac{c_s^f}{c_{tot}^f} \tag{20}$$

A mixture of N_S salts in the feed gives rise to a mixture of N distinct ionic species, each with a concentration $c_i^f (i = 1, \ldots, N)$. The ions can be divided into two groups: counter-ions, with charges opposite that of the membrane, and co-ions, having charges of the same sign.

2.2.1. Macroscopic Approach

Using the basic tenets of nonequilibrium irreversible thermodynamics and treating the membrane as a black box, it is possible to establish a set of macroscopic equations describing membrane transfer as a function of the relevant driving forces:

- Brownian force depending on the gradient of the chemical potential $\mu_s = RT \ln[c_s]$,
- Mechanical force, induced by the gradient of the effective pressure (ΔP_0), and
- Electrical force, created by a gradient of electrical potential ($\Delta\phi$).

The flux densities crossing the membrane can then be related to the driving forces [50–52]:

$$I_e = -\bar{L}_{11}(\Delta\phi) - \bar{L}_{12}(RT\Delta \ln c_s) - \bar{L}_{13}(\Delta P_0) \tag{21}$$

$$J = -\bar{L}_{21}(\Delta\phi) - \bar{L}_{22}(RT\Delta \ln c_s) - \bar{L}_{23}(\Delta P_0) \tag{22}$$

$$j_v = -\bar{L}_{31}(\Delta\phi) - \bar{L}_{32}(RT\Delta \ln c_s) - \bar{L}_{33}(\Delta P_0) \tag{23}$$

where $P_0 = P - \Pi$ is the effective pressure, P is the pressure, and Π the osmotic pressure, [bar]; $\Pi = RT(\nu_1 + \nu_2)c_s$ for a simple salt and $\Pi = RTc_s$ for a neutral solute, where c_s is the solute/salt concentration [mol/m^3]. The phenomenological transport coefficients (macroscopic) representing the contribution of each type of force (the Onsager relations lead to $\bar{L}_{i,j} = \bar{L}_{j,i}$) are $\bar{L}_{i,j}$. The variable J is the solute molar flux density [mol/m^{2}h], j_v is the membrane volume flux density [m^3/m^{2}h], and I_e is the electrical current density [C/m^{2}s], zero in NF, which implies that Eqs. (21–23) can be put in the standard form [50]:

$$J = -\bar{P}_s \Delta c_s + (1 - \bar{\sigma}_f)c_s j_v \tag{24}$$

$$j_v = -\bar{L}_p(\Delta P - \bar{\sigma}_d \Delta\Pi) \tag{25}$$

with $\bar{P}_s$ being the solute permeability in macroscopic irreversible thermodynamics [m/h], $\bar{\sigma}_f$, $\bar{\sigma}_d$ being the global filtration and osmotic reflection coefficients [-], and $\bar{L}_p$ being solution membrane hydraulic permeability [m^3/m^{2}hbar].

It is usually assumed that for neutral solutes, $\bar{\sigma}_f = \bar{\sigma}_d$.

2.2.2. Mesoscopic Approach

To obtain a more detailed description of the transport process, it is also possible to write Eqs. (21–23) in a local mesoscopic form:

$$I_e = -L_{11}\left(\frac{\partial\phi}{\partial x}\right) - L_{12}\left(RT\frac{\partial(\ln c_s)}{\partial x}\right) - L_{13}\left(\frac{\partial P_0}{\partial x}\right) \tag{26}$$

$$J = -L_{21}\left(\frac{\partial\phi}{\partial x}\right) - L_{22}\left(RT\frac{\partial(\ln c_s)}{\partial x}\right) - L_{23}\left(\frac{\partial P_0}{\partial x}\right) \tag{27}$$

$$j_v = -L_{31}\left(\frac{\partial\phi}{\partial x}\right) - L_{32}\left(RT\frac{\partial(\ln c_s)}{\partial x}\right) - L_{33}\left(\frac{\partial P_0}{\partial x}\right) \tag{28}$$

which leads in the case of NF to [43]

$$J = -P_s\frac{\partial c_s}{\partial x} + (1 - \sigma)c_s j_v \tag{29}$$

$$j_v = -L_p\left(\frac{\partial P}{\partial x} - \sigma\frac{\partial\Pi}{\partial x}\right) \tag{30}$$

where σ is the local reflection coefficient [-], $L_{v,s}$ is the phenomenological transport coefficient (mesoscopic), P_s is the solute permeability in mesoscopic irreversible thermodynamics [m²/h], and L_p is the specific solution membrane hydraulic permeability (mesoscopic) [m³/mh.bar].

When the transport coefficients are assumed to be independent of solute concentration and the filtration condition ($c_s^p = J/j_v$) is applied, we obtain the solute rejection (according to Eq. 3):

$$R_s = 1 - \frac{c_s^p}{c_s^f} = \frac{(1-G)\sigma}{1-\sigma G} \tag{31}$$

where $G = \exp(-Pe)$, with

$$Pe = j_v l_m \frac{1-\sigma}{P_s} \tag{32}$$

the Péclet number, where l_m is the active membrane layer thickness [m].

At low flux the rejection increases linearly with membrane volume flux density j_v,

$$R_s \approx \frac{\sigma_s l_m j_v}{P_s}. \tag{33}$$

At high flux the rejection tends toward its limiting value:

$$R_s^{\infty} = \sigma \tag{34}$$

This approach has been used to model neutral solute (macromolecular) transport through cylindrical pores by calculating the relevant transport coefficients within the framework of the Hindered Transport (HT) Theory. For cylindrical pores, this theory predicts that the reflection coefficient σ and specific solute permeability P_s depend on $\lambda_s = r_s/r_p$, the ratio of solute to membrane pore radius:

$$\sigma = 1 - \Phi' K_{s,c} \tag{35}$$

and

$$P_s = \frac{D_s \varphi_p K_{s,d} \Phi^s}{\tau} \tag{36}$$

where D_s is the bulk diffusion coefficient [m²/s], φ_p the membrane porosity [-], τ the membrane pore tortuosity [-], $\Phi_s = (1-\lambda_s)^2$ the steric partitioning coefficient [-], and $K_{s,c}(\lambda_s)$ and $K_{s,d}(\lambda_s)$ the convective and diffusive hindered transport coefficients [-] (see Appendix 1) [45, 53]. This model has also been applied to molecular transport in reverse osmosis (RO), NF, and ultrafiltration (UF) membranes [48, 49, 54].

Unfortunately, the concentration dependence of the transport coefficients in the case of salts makes solving the above transport equations very difficult. These equations are also difficult to generalize to multielectrolyte mixtures. Nevertheless, this approach has been used in RO, NF, and UF to perform simple modeling for single salts [43] and to explain the NF behavior of mixtures possessing a simple salt (NaCl) and one large organic ion rejected at 100% (e.g., dye-salt separation) [55, 56]. In applying this model to NF, the transport coefficients (reflection coefficient σ and specific solute permeability P_s) were simply taken as adjustable parameters, which leads to a useful approach for correlating data, but in this case it cannot lead to a truly predictive model. In this early work on NF modeling, it was correctly pointed out that because the salt reflection coefficient σ was less than unity, the classic solution-diffusion model developed previously for RO cannot be used reliably in NF (because convective transport is far from being negligible).

2.2.3. Microscopic Approach: Pore-Level Space Charge Model

The pore-level Space Charge model was developed by Osterle and collaborators in the 1960s [57–59], as well as by Dresner [60, 61]. This model is based on a mechanistic continuum approach within a cylindrical pore and only takes into account the electrostatic interactions, but it does include the radial variations of ion concentration and electric potential [62–65].

In this model the molar flux densities are described by local extended Nernst-Planck (ENP) equations:

$$j_i = -D_i \nabla c_i - \frac{F}{RT} z_i D_i c_i \nabla \psi + c_i v \tag{37}$$

where j_i is the local molar flux density of ion i [mol/m^{2}h], D_i is the diffusion coefficient of ion i [m^2/s], c_i is the local concentration of ion i [mol/m^3], z_i is the valence of ion i [-], ψ is the local electric potential [mV], and v is the local solution flow velocity [m/h], which obeys the creeping flow Stokes equation:

$$-\nabla p + \eta \nabla^2 v - \rho \nabla \psi = 0 \tag{38}$$

with p being the local fluid pressure [bar], η the fluid dynamic viscosity [Pa.s], $\rho = F \sum_{i=1}^{N} z_i c_i$ the ion charge density [C/m^3], N the total number of ions, and F the Faraday constant [C/mol].

(We list in Table 2 the relevant ion properties that will be used in the NF modeling studies presented in section 2.7). The local electric potential is governed by the Poisson equation:

$$\nabla^2 \psi = -\frac{F}{\varepsilon} \sum_{i=1}^{N} z_i c_i \tag{39}$$

where ε is the dielectric constant of the solution [C^2/J.m].

The boundary conditions on Eq. (37) are

$$\left.\frac{\partial c_i}{\partial r}\right|_{r=r_p} + c_i \frac{z_i F}{RT} \left.\frac{\partial \psi}{\partial r}\right|_{r=r_p} = 0 \quad \text{(no flux at pore wall)} \tag{40}$$

and

$$\left.\frac{\partial c_i}{\partial r}\right|_{r=0} = 0 \quad \text{(by symmetry)} \tag{41}$$

$$\left.\frac{\partial \psi}{\partial r}\right|_{r=0} = 0 \quad \text{(by symmetry)} \tag{42}$$

The pore wall surface charge density σ_i is related to the potential gradient at the pore wall by Gauss' law:

$$\left.\frac{\partial \psi}{\partial r}\right|_{r=r_p} = \frac{\sigma_i}{\varepsilon} \tag{43}$$

One conventionally assumes that the local electric potential can be decomposed into two parts, $\psi(x, r) = \Psi(x, r) + \varphi(x)$, where the first contribution controls the electric double layer structure and the second controls the macroscopic streaming potential. One also makes the reasonable approximation that the "no radial flux" condition that applies at $r = 0$ and $r = r_p$ can be extended over the whole pore cross-section

$$\frac{\partial c_i}{\partial r} - \frac{z_i}{z_1} c_i \frac{\partial \tilde{\Psi}}{\partial r} \approx 0 \quad \text{(all } r\text{)} \tag{44}$$

Table 2. Bulk diffusion coefficients, Stokes-Einstein ($T = 25°$) and Crystal (Pauling) radii of the selected ions.

Ion	Bulk diffusion coefficient (10^{-9} m^2 · s^{-1})	Stokes-Einstein radius (nm)	Crystal (Pauling) radius (nm)
Na^+	1.334	0.184	0.095
K^+	1.957	0.125	0.133
Ca^{2+}	0.792	0.309	0.099
Mg^{2+}	0.706	0.347	0.065
Cl^-	2.032	0.121	0.181
NO_3^-	1.902	0.129	0.264
HCO_3^-	1.185	0.207	0.207
SO_4^{2-}	1.065	0.231	0.290

where $\tilde{\Psi} = -z_1 F\Psi/(RT)$ is the dimensionless local potential. If we limit ourselves to a single salt (one cation and one anion), then upon integration, Eq. (44) leads to approximate radial ion equilibrium (Boltzmann distribution)

$$c_i(x, r) \approx \nu_i C(x) \exp\left[\frac{z_i}{z_1}\tilde{\Psi}(x, r)\right] \tag{45}$$

where $C(x)$ is the concentration of a virtual salt in local equilibrium with the pore at axial position x. When the Boltzmann distribution is inserted into the Poisson equation, one obtains the (approximate) Poisson-Boltzmann equation

$$\frac{2}{\tilde{r}}\frac{\partial}{\partial\tilde{r}}(\tilde{r}\tilde{\Psi}) \approx \left(\frac{r_p}{\lambda_e}\right)^2 \sum_{i=1}^{2} \exp\left[\frac{z_i}{z_1}\tilde{\Psi}\right] \tag{46}$$

with

$$\lambda_e(x) = \left(\frac{\varepsilon RT}{2F^2 z_1^2 C(x)}\right)^{1/2} \tag{47}$$

a local Debye length [in arriving at Eq. (46), the $\partial^2\psi/\partial x^2$ term in the Poisson equation has been neglected, because it is smaller than the retained terms by a factor $\sim \max\{(\lambda_m/l_m)^2, (\lambda_e/l_m)^2\} \ll 1$ [66], where l_m is the active membrane layer thickness; this inequality is always true for NF]. Gauss's law can also be put into dimensionless form,

$$\left.\frac{\partial\tilde{\Psi}}{\partial\tilde{r}}\right|_{\tilde{r}=1} = 4\sigma^* \equiv \left(\frac{r_p}{\lambda_m}\right)^2 \tag{48}$$

where

$$\lambda_m = \left(\frac{2\varepsilon RT}{|z_1|F^2|X_m|}\right)^{1/2} \tag{49}$$

is a Debye length associated with the effective membrane charge density, measured in moles per unit pore volume of the membrane:

$$X_m = \frac{\sigma_f}{Fr_H} \tag{50}$$

with r_H = (pore volume)/(pore surface area) the hydraulic radius (for cylindrical pores $r_H = r_p/2$). The qualitative properties of the solution to the Poisson-Boltzmann equation depend critically on the values of the three important length scales: the pore radius r_p and the two Debye lengths λ_e and λ_m.

Solving the Space Charge system of equations is generally difficult, even numerically. The equations can be simplified, however, by noting that in the NF range, there is a strong overlap of electrical double layers within the pores, which allows the pore-level equations to be spatially averaged in a simple way [46]. This homogeneous approximation, which allows the model to be reduced to a simpler one-dimensional system of mesoscopic equations, is valid when the gradient of the dimensionless potential $\tilde{\Psi}$ at the pore wall is less than four (i.e., $\sigma^* < 1$) or

$$\frac{r_p}{\lambda_m} < 2 \tag{51}$$

This is equivalent to the following inequality:

$$|X_m| < \frac{1.5}{|z_1| r_p^2} \tag{52}$$

with the pore radius $r_p \sim r_H$ in *nm* and X_m in mol/lt of pore volume. The range of validity of this approximation covers the separation range from tight UF, through NF, to loose RO

(the concept of a porous membrane probably breaks down for conventional RO membranes). Within the range of validity of the homogeneous approximation, the Debye length λ_c controls only the strength of the electrostatic interaction between the ions and the charged membrane (and not the thickness of the electric double layer, as it would in the thin double-layer approximation, which is valid only when $\lambda_c \ll r_p$ and $r_p \gg \lambda_m$, inequalities that are not satisfied in the NF range). Within the NF range ($r_p < \lambda_m$), if $\lambda_c \gg \lambda_m$, or $|X_m| \ll C$, the electrostatic interaction is weak, the ions easily enter the pores, and ion rejection by electrostatic exclusion is low; if, however, $\lambda_c \ll \lambda_m$, or $|X_m| \gg C$, this interaction is strong, the coions are repelled from the pores, and ion rejection by electrostatic exclusion is high.

An upper bound on the effective membrane charge density can be obtained on physical grounds. Intrinsic material limitations for membrane materials lead to a maximum charge density of potentially ionizable groups of about 1–5 e/nm^2, which is equivalent to a pore surface charge density $\sigma_i \sim 16$–80 μC/cm^2. Although this is the maximum surface charge density that a surface can develop, the actual charge will in general be (much) less, as, depending on the pH and electrolyte environment at the pore surface, not all groups will be charged (NF membranes are similar in this respect to weak ion exchange ones, for which the effective ion exchange capacity depends on pH and feed salt concentration and the maximum ion exchange capacity is usually not observed in practice). Using Eq. (50), we find a maximum physical effective membrane charge density of

$$|X_m^{\max}| \approx \frac{1.65 \text{ to } 8.25}{[r_p]} \tag{53}$$

with $r_p \sim r_H$ in *nm*. In the nanometric pore range, we obtain maximum physical effective membrane charge densities of about 2–10 [mol/l], which is on the order of those found for strong ion exchange membranes [39, 67], with the value of 10 [mol/l], being a generous upper bound corresponding to no known membrane. It should be firmly kept in mind that because NF membranes are similar to weak ion exchange ones, only a small percentage of the surface groups will be ionized or unscreened and therefore the actual effective membrane charge densities expected for real NF membranes are usually below this maximum upper limit (cf. Ref. [67]).

2.3. Homogeneous Theory of Nanofiltration Transport

Using the spatial averaging method [44, 46], the Space Charge Model can be extended to the mesoscopic scale, leading to the classic extended Nernst-Planck (ENP) and Stokes equations that form the basis of the Electro-transport (ET) theory (in Table 3 we present an inventory of the homogeneous transport models commonly used in nanofiltration modeling). In a more general form, this type of mesoscopic model was proposed earlier in various more or less complete forms on semiphenomenological grounds [39–42, 68]. In a typical NF transport problem, the feed (permeate) is characterized by the ion concentrations $\{c_i^{f(p)}\}$, the electric potential $\Phi^{f(p)}$, and the pressure $P^{f(p)}$; the fluxes crossing the membrane are the ionic molar fluxes $j_i = c_i^p j_v$ (filtration condition) and the solution volume flux density j_v. The ionic feed concentrations and the volume flux density are considered known. Given these quantities, we would like to calculate the ion permeate concentrations, the electric filtration potential gradient $\underline{\Delta}\Phi^F = \Phi^f - \Phi^p$, and the applied pressure gradient $\underline{\Delta}P = P^f - P^p$. Conversely, we would also like to solve the inverse problem of calculating the membrane volume flux density j_v, given the transmembrane pressure difference $\underline{\Delta}P$.

There are two distinct types of solutions to the homogeneous NF transport model, based on the asymptotic behavior at high membrane volume flux density j_v of the ionic concentration profiles in the membrane. The Dresner type 1 solutions have concentration profiles that become flat starting at the feed–membrane interface (except for a thin "diffusion boundary layer" near the permeate–membrane interface), and the limiting rejection behavior can be found by solving the algebraic system of equations obtained by neglecting the diffusion term in the ENP equations. Dresner type 2 solutions have some concentration profiles that do not become flat in the membrane, and the limiting rejection behavior can only be found by solving the ENP equations with the diffusion term [41, 68, 69]. Type 2 solutions can be found

Table 3. Inventory of homogeneous transport models commonly used in nanofiltration modeling.

Transport model	Species	Transport modes	Partitioning modes	Model parameters
Hindered Transport (HT)	neutral solutes	Hindered convection, diffusion.	steric	pore radius, effective membrane thickness, solute radius, solute diffusivity
Electro-Transport (ET)	charged solutes (point ions)	convection, diffusion, and electrical migration [extended Nernst-Planck (ENP) equations]	Electrostatic (Donnan)	effective membrane charge density and thickness, ion valence and diffusivity
Hindered Electro-Transport (HET) [Electrostatic-Steric (ES) or Donnan-steric-pore-model (DSPM)]	charged solutes (finite size ions)	Hindered convection, diffusion, and electrical migration [Hindered extended Nernst-Planck (ENP) equations]	Electrostatic (Donnan), steric	pore radius; effective membrane charge density and thickness; ion valence, diffusivity, and radius
Extended Hindered Electro-Transport HET) [Extended ES/DSPM]	charged solutes (finite size ions)	Hindered convection, diffusion, and electrical migration (plus possible additional forces)	Electrostatic (Donnan), steric, Dielectric, Born, ion activity, etc.	same as HET model, plus membrane and confined water dielectric constants, etc.
Extended Maxwell Stefan	neutral and charged solutes (finite size ions)	same as Extended HET model, plus solute-solute frictional cross-coupling	same as Extended HET model	same as Extended HET model, plus solute-solute frictional cross-coupling coefficients

only for ion mixtures with more than one counter-ion, and both counter and co-ions in a type 2 mixture can be divided into either normal or anomalous ions, depending on whether or not their concentration profiles become asymptotically flat in the membrane. A typical behavior for a type 2 mixture is one for which the rejection of the most mobile counter-ions tends exponentially to zero and the rejection of the least mobile counter-ions becomes negative with increasing j_v (it should be kept in mind, however, that a clear experimental indication of this anomalous asymptotic behavior might not be attainable at physically realistic applied pressures).

2.3.1. Extended Nernst-Planck Ion Flux and Stokes Flow Equations

A generalized expression for the spatially averaged ion molar flux density j_i, incorporating ionic diffusion, electrical migration, and convection, is the ENP equation:

$$j_i = -\bar{D}_i \partial_x \bar{c}_i - z_i \bar{c}_i \bar{D}_i \frac{F}{RT} \partial_x \phi + K_{i,c} \bar{c}_i j_v - \bar{c}_i \bar{D}_i \partial_x \ln(\bar{\gamma}_i) \tag{54}$$

where $\partial_x Q = \partial Q / \partial x$ [as is usually done, we have neglected in Eq. (54) a small term proportional to the pressure gradient and the specific ion volume] The averaged (creeping flow) Stokes equation for the flux of a charged fluid takes the form

$$\frac{1}{\bar{L}_p^0} j_v = -\partial_x P - \rho \partial_x \phi - RT \sum_i \bar{c}_i \partial_x (\ln \bar{\gamma}_i) \tag{55}$$

where $0 \le x \le l_m$ is the membrane thickness, $\rho(x) = F \sum_i z_i \bar{c}_i(x)$ is the local ion charge density, and $j_v \approx \langle v \rangle$, where $\langle v \rangle$ is the average solution velocity in the pore of the membrane (approximately equal to the volume flux density j_v). In the homogeneous theory, we use the following quantities:

$\bar{D}_i = \langle D_i \rangle$: effective diffusion coefficient of ion i in the membrane [m^2/s],
$\bar{c}_i = \langle c_i \rangle$: average concentration of ion i in the membrane [mol/m^3]

$\phi = \langle\psi\rangle$: average intramembrane electric potential (Diffusion + Streaming potential) [mV]
$P = \langle p\rangle$: average pressure [bar]
$\bar{L}_p^0$: pure water hydraulic permeability [$m^3/m^2h.bar$]
$K_{i,c}$: convective ion hindrance factor [-]

The term $\bar{\gamma}_i$ is the effective intramembrane ion activity coefficient, and the brackets denote spatial averaging of pore level quantities. The diffusion coefficient in the pore

$$\bar{D}_i = \frac{K_{i,d} D_i \varphi_p}{\tau} = \frac{K_{i,d} D_i l_m}{l_{eff}} \tag{56}$$

can be related to D_i, the bulk ion diffusion coefficient, and $K_{i,d}$, the diffusive ion hindrance factor. The convective and diffusive hindrance factors $K_{i,c}$ and $K_{i,d}$ depend on $\lambda_i = r_i/r_p$, the ratio of the ionic radius r_i, to the effective pore radius r_p (see Appendix 1). Within the approximation adopted here, we see in Eqs. (54) and (55) that the ion molar flux density j_i depends directly on the volume flux density crossing the membrane j_v and only indirectly on the transmembrane pressure difference ΔP [via the j_v versus ΔP relation obtained by solving the averaged Stokes equation (Eq. 55)]. This is why in most NF modeling investigations, one studies ion rejection R_i versus membrane flux density j_v and j_v versus transmembrane pressure difference ΔP separately, instead of R_i versus ΔP directly (the effective membrane thickness is $l_{eff} = l_m \tau/\varphi_p$, cf. [33].)

In the feed (f) and permeate (p), the electroneutrality condition is

$$\sum_{i=1}^{N} z_i c_i^{f(p)} = 0 \tag{57}$$

and the ion rejection [according to Eq. (3)] is given by

$$R_i = 1 - \frac{c_i^p}{c_i^f} \tag{58}$$

The filtration condition is

$$c_i^p = \frac{j_i}{j_v} \tag{59}$$

which simply means that the permeate solute concentration is determined in the steady-state by the molar and volume flux densities crossing the membrane. The ion transmission [according to Eq. (6)], or passage, is the complement of the rejection $T_i = 1 - R_i = c_i^p/c_i^f$.

The selectivity of two ions is defined as the ratio of their passages $S_{i,j} = T_i/T_j$. Generally speaking, for single salts the magnitude of salt rejection is high when the absolute value of the normalized membrane charge density $\xi = X_m/c_s^f$ is greater than one and low if ξ is less than one. The rejection of single salt increases monotonically from zero at zero-volume flux density to a limiting plateau value (limiting rejection) at high-volume flux density. The rate at which the salt rejection approaches this limiting value, as the volume flux density increases, depends critically on the effective membrane thickness and salt diffusion coefficient via the Péclet number [Eq. (32)]: When the Péclet number is greater than one, the salt rejection changes slowly and is close to its limiting value; in contrast, in the Péclet number range between zero and one, the salt rejection is a strongly increasing function of volume flux density. From this we can conclude that, as a function of volume flux density, the salt rejection approaches its limiting value faster for large effective membrane thickness and small salt diffusivity (see section 2.7 for concrete examples).

Spatial averaging of the Poisson equation leads to the approximate electroneutrality condition in the membrane,

$$\sum_{i=1}^{N} z_i \bar{c}_i + X_m \approx 0 \tag{60}$$

valid when $(\lambda_{in}/l_m)^2, (\lambda_e/l_m)^2 \ll 1$, which is always true for NF membranes [44, 46, 66]. The zero net electrical current condition, valid for the open electrical circuit conditions employed in NF, is

$$I_e = F\sum_{i=1}^{N} z_i j_i = 0 \tag{61}$$

By combining charge electroneutrality in the permeate [Eq. (57)] and the filtration condition [Eq. (59)], we see that the zero net electrical current condition is not an independent assumption but, rather, follows from the first two. When the ENP equations are inserted into the zero net electrical current condition, we obtain the following relation between the (dimensionless) electric potential and the ionic concentrations:

$$\tilde{\phi}(x) = \frac{F\phi(x)}{RT} = \tilde{\phi}_d(x) + \tilde{\phi}_s(x) \tag{62}$$

where

$$\partial_x \tilde{\phi}_d(x) = -\frac{\sum_{i=1}^{N} z_i \bar{D}_i \partial_x \bar{c}_i(x)}{\sum_{i=1}^{N} z_i^2 \bar{D}_i \bar{c}_i(x)} \tag{63}$$

is the gradient of the (dimensionless) diffusion potential and

$$\partial_x \tilde{\phi}_s(x) = j_v \left(\frac{\sum_{i=1}^{N} z_i K_{i,c} \bar{c}_i(x)}{\sum_{i=1}^{N} z_i^2 \bar{D}_i \bar{c}_i(x)} \right) \tag{64}$$

is the gradient of the (dimensionless) streaming potential. This form for $\partial_x \tilde{\phi}(x)$ is useful for identifying the two contributions to the electric potential in the membrane: the diffusion potential $\tilde{\phi}_d$, which is proportional to the ionic concentration gradients, and the streaming potential $\tilde{\phi}_s$, which is manifestly proportional to the volume flux density.

Although the above decomposition of $\partial_x \tilde{\phi}(x)$ in terms of the diffusion and streaming potentials is convenient for identifying the two contributions (and also for finding analytical solutions to the NF transport problem for a single salt [one anion and one cation]), the presence of the ionic concentration gradients in the diffusion potential complicates numerical methods of solution. In this case, it is more convenient to divide the ENP Eq. (54) for ion i by $\bar{D}_i$ and then sum over all ions. The sum of the concentration gradient terms vanishes thanks to the electroneutrality condition in the membrane, leading to

$$\partial_x \tilde{\phi} = \frac{\sum_{i=1}^{N} \{[z_i(K_{i,c}\bar{c}_i(x) - c_i^p)]\bar{D}_i^{-1}\}}{\sum_{i=1}^{N} z_i^2 \bar{c}_i(x)} j_v \tag{65}$$

Although this form for $\partial_x \tilde{\phi}(x)$ mixes in a nontrivial way the two contributions to the electric potential, the absence of gradient terms simplifies the implementation of numerical methods of solution.

By inserting the filtration condition and one of the above expressions for $\partial_x \tilde{\phi}(x)$ back into the ENP equations and eliminating the Nth ionic species via the electroneutrality condition, we obtain $N - 1$ equations for the $N - 1$ independent ionic concentrations, $\{\bar{c}_i(x), i = 1, \ldots, N-1\}$ [33, 41, 68, 70]. This system of $N - 1$ nonlinear first-order ordinary differential equations (ODEs) for the ion concentrations describes transport in the membrane itself ($0^+ \le x \le l_m^-$). To solve the complete transport problem, we must establish the appropriate boundary conditions at the feed ($x = 0^+$) and permeate ($x = l_m$) interfaces. In a composite system with several membrane layers, the model must be solved across the whole system (see Fig. 22). The so-called active NF layer is adjacent to the feed, and the other layers can be tight UF supports, (larger pore microfiltration [MF] supports do not contribute to ion rejection). The first layer can also be a laminar concentration polarization layer (see section 1) if the effective membrane charge density $X_m = 0$ and $1/\bar{L}_p^0 = 0$—in this case the active NF layer is the second one. We now turn to this boundary condition problem by studying the ion partitioning and pressure jumps at the external solution—membrane interfaces.

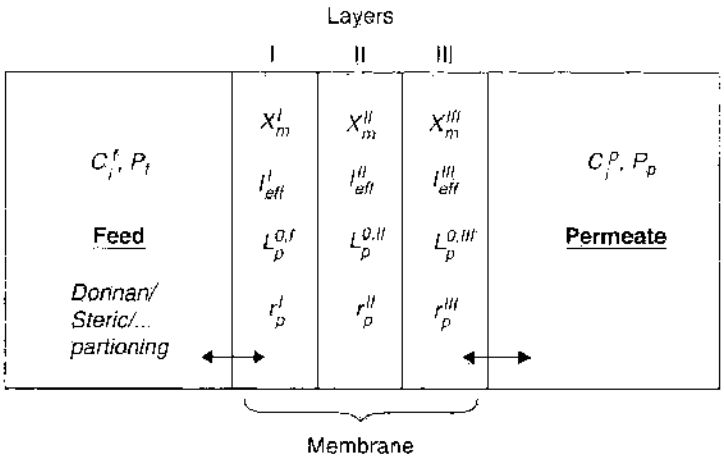

Figure 22. Schematic diagram showing the different membrane layers of a three-layer composite system. In the four-parameter HET model, each layer is characterized by an effective membrane charge density X_m, thickness l_{eff}, pore radius r_p, and pure water hydraulic permeability L_p^0. The feed (permeate) is characterized by the pressure $P^{f(p)}$ and the ionic concentrations $C_i^{f(p)}$. Donnan/steric partitioning holds across all the system interfaces, including between the different membrane layers.

2.3.2. Interfacial Thermodynamic and Mechanical Equilibria

As stated earlier, an important simplification in the treatment of membrane transport arises thanks to the large thickness of the NF membrane compared with the other relevant length scales in the problem ($\lambda_m, \lambda_c, r_p$). In this case, there is approximate thermodynamic and mechanical equilibrium across the external solution–membrane interfaces [26, 44, 66].

2.3.2.1. Ion Partitioning The ion transfer from the external solutions (feed and permeate) into the membrane is determined by Donnan (quasi-equilibrium) partitioning at the membrane-external solution interfaces. This is a valid approximation because the effective ionic electro-chemical potentials remain practically constant across these interfaces because of the large transport impedance of the membrane itself. This can be demonstrated formally by starting with the ENP ion flux equations and showing that when $\lambda_m/l_m, \lambda_c/l_m, r_p/l_m \ll 1$ (always true in NF), the flux density terms (proportional to j_i and j_v) are negligible (for physically reasonable trans-membrane flux densities), compared with the gradient terms in the interfacial regions, leading to

$$-\bar{D}_i \partial_x \bar{c}_i - z_i \bar{c}_i \bar{D}_i \frac{F}{RT} \partial_x \phi - \bar{c}_i \bar{D}_i \partial_x \ln(\bar{\gamma}_i) \approx 0 \quad \text{(interfacial regions)} \tag{66}$$

The ion partitioning equations do not therefore require further assumptions, as they follow directly as a limiting form of the ENP equations themselves, valid in the interfacial regions. As Eq. (66) shows, ion partitioning arises from a balance between diffusion (first term) and the forces caused by interactions (second and third terms).

The ionic electrochemical potentials in the bulk feed (f) and permeate (p) solutions are defined by

$$\mu_i^{f(p)} = RT \ln(c_i^{f(p)}) + z_i F \Phi^{f(p)} + RT \ln(\gamma_i^{f(p)}) \tag{67}$$

where $\Phi^{f(p)}$ is the electric potential and $\gamma_i^{f(p)}$ is the bulk activity coefficient that arises as a result of ion–ion interactions. Integration of Eq. (66) across the interfacial regions leads to approximate thermodynamic equilibrium (i.e., electrochemical potentials that are nearly constant across the interfaces) [39–42, 44, 66, 68]:

$$\mu_i^f \approx \bar{\mu}_i(0^-) \equiv \bar{\mu}_i^f \tag{68}$$

$$\mu_i^p \approx \bar{\mu}_i(l_m) \equiv \bar{\mu}_i^p \tag{69}$$

The ion electrochemical potential in the membrane takes into account all the forces of interaction [23, 24] between the ion and the membrane, as well as the ion–ion interactions:

$$\bar{\mu}_i(x) = RT \ln[\bar{c}_i(x)] + z_i F\phi(x) + RT \ln(\bar{\gamma}_i) \tag{70}$$

where the effective intramembrane activity coefficient $\bar{\gamma}_i$ accounts for all but mean field electrostatic effects [26, 39–42, 44, 68] (such as steric, dielectric, ion–ion interactions, etc.; for compactness, and without loss of generality, we have also incorporated the so-called "standard chemical potentials" directly into $\bar{\gamma}_i$). The above (thermodynamic equilibrium) equations lead to the ionic partition coefficients at the feed and permeate interfaces

$$k_i^{f(p)} = \frac{\bar{c}_i^{f(p)}}{c_i^{f(p)}} = \left(\frac{\gamma_i^{f(p)}}{\bar{\gamma}_i^{f(p)}}\right) \exp[-z_i \Delta\tilde{\phi}_D^{f(p)}] \tag{71}$$

where

$$\Delta\phi_D^f = \phi(0^+) - \Phi^f$$

is the (interfacial) feed-side Donnan potential [71],

$$\Delta\phi_D^p = \phi(l_m^-) - \Phi^p \tag{72}$$

is the permeate-side Donnan potential, and $\Delta\tilde{\phi}_D^{f(p)} = F\Delta\phi_D^{f(p)}/(RT)$. Because the sign of the Donnan potential is (usually) opposite that of the counter-ion, it acts to bring these ions into the membrane while at the same time excluding co-ions. We note that in the approximation of interfacial thermodynamic equilibrium, there exist concentration jumps across the external solution–membrane interfaces. In reality there are smooth, but rapid, concentration variations on a length scale $\sim \max\{\lambda_m, \lambda_c, r_p\}$ much less than the membrane thickness. Conveniently, the quasi-equilibrium approximation described above allows all the complicated phenomena taking place in the strongly heterogeneous regions near the pore entrances and exits to be skirted [66].

If the feed (permeate) and intramembrane activity coefficients are known, then $\Delta\phi_D^{f(p)}$ can be calculated as a function of the ion feed (permeate) concentrations and the membrane charge density X_m by using the electroneutrality condition in the membrane (60); along with the definition of the ion partition coefficient (71), this provides an algebraic equation,

$$\sum_{i=1}^{N} z_i c_i^{f(p)} k_i^{f(p)} + X_m = \sum_{i=1}^{N} z_i c_i^{f(p)} \left(\frac{\gamma_i^{f(p)}}{\bar{\gamma}_i^{f(p)}}\right) [\Gamma_D^{f(p)}]^{-z_i} + X_m = 0 \tag{73}$$

that can be transformed into a polynomial equation for $\Gamma_D^{f(p)} \equiv \exp[-\Delta\tilde{\phi}_D^{f(p)}]$. Once $\Gamma_D^{f(p)}$ is found, the Donnan potential $\Delta\tilde{\phi}_D^{f(p)}$ and the ionic partition coefficients $k_i^{f(p)}$ can be also be obtained.

2.3.2.2. Pressure Jumps The interfacial concentration jumps that arise as a result of quasi-equilibrium ion partitioning lead to interfacial osmotic pressure jumps. Because of approximate interfacial mechanical equilibrium, these osmotic pressure jumps lead in turn to identical interfacial pressure jumps [44]. This can also be demonstrated formally without any further assumptions by starting with the averaged Stokes equation and neglecting the flux term, proportional to the membrane flux density j_v, in the interfacial regions

$$-\partial_x P(x) - \rho(x)\partial_x\phi(x) - RT\sum_i \bar{c}_i(x)\partial_x(\ln\bar{\gamma}_i(x)) \approx 0 \quad \text{(interfacial regions)} \tag{74}$$

(this is justified in NF for physically reasonable fluxes, because the characteristic length scale of interfacial variations $[\lambda_m, \lambda_c, r_p]$ is always small compared with the membrane thickness, l_m, itself). Combining Eq. (74) with the quasi-continuity of the electrochemical potentials [Eqs. (68) and (69)] leads to

$$\underline{\Delta}P^{f(p)} = \underline{\Delta}\pi^{f(p)} \tag{75}$$

where

$$\underline{\Delta}P^f = P^f - P(0^+) \tag{76}$$

and

$$\underline{\Delta}P^p = P(l_m^-) - P^p \tag{77}$$

are the interfacial pressure jumps, and

$$\underline{\Delta}\pi^f = \Pi^f - \Pi(0^+) \tag{78}$$

and

$$\underline{\Delta}\pi^p = \Pi(l_m^-) - \Pi^p \tag{79}$$

are the interfacial osmotic pressure jumps with $\Pi^{f(p)} = RT\sum_i c_i^{f(p)}$ the bulk feed (permeate) osmotic pressure and $\Pi(x) = RT\sum_i \tilde{c}_i(x)$ the local (intramembrane) osmotic pressure. We have used the notation, $\underline{\Delta}Q = -\Delta Q$ for any quantity Q. By using the definition of the ion partition and transmission coefficients (passages), $\Pi(0^+) = RT\sum_i \tilde{c}_i(0^+)$ and $\Pi(l_m^-) = RT\sum_i \tilde{c}_i(l_m^-)$ can be written as

$$\Pi(0^+) = RT\sum_i k_i^f c_i^f \tag{80}$$

and

$$\Pi(l_m^-) = RT\sum_i k_i^p c_i^p = RT\sum_i k_i^p c_i^f T_i \tag{81}$$

Using the above results, the sum of the interfacial pressure jumps can be expressed in terms of the osmotic pressure differences

$$\underline{\Delta}P^f + \underline{\Delta}P^p = \underline{\Delta}\Pi - \underline{\Delta}\Pi_m \tag{82}$$

where we have used the total osmotic pressure difference across the membrane

$$\underline{\Delta}\Pi = \Pi^f - \Pi^p = RT\sum_i c_i^f R_i \tag{83}$$

and the intramembrane osmotic pressure difference

$$\underline{\Delta}\Pi_m = \Pi(0^+) - \Pi(l_m^-) = RT\sum_i c_i^f (k_i^f - k_i^p T_i) \tag{84}$$

2.3.3. Physical Nanofiltration Parameters

The three main experimentally measurable physical NF parameters that we would like to obtain as solutions to the model transport equations are the ionic rejections R_i and the electric filtration potential $\Delta\Phi^F$, as a function of the transmembrane volume flux density j_v, and the latter as a function of the trans-membrane pressure gradient ΔP.

2.3.3.1. Ionic Rejection The ionic feed concentrations c_i^f and volume flux density j_v are considered known, and we must solve the partitioning/transport equations for the $N-1$ unknown ionic permeate concentrations c_i^p. The unknown permeate concentrations are found by solving a system of coupled nonlinear algebraic/differential equations that we summarize here: The feed and permeate ion partition equations

$$\sum_{i=1}^{N} z_i c_i^{f(p)} k_i^{f(p)} + X_m = 0, \tag{85}$$

and the $N-1$ independent ion flux (ENP) equations

$$\partial_x \tilde{c}_i = -z_i \tilde{c}_i(\partial_x \tilde{\phi}) + (K_{i,r}\tilde{c}_i - c_i^p)\bar{D}_i^{-1} j_v \tag{86}$$

where we have used the permeate filtration condition (59). The ion partition coefficients (71) depend on the activity coefficients and the interfacial Donnan potentials, and electroneutrality is respected in the external solutions (57). The gradient of the (dimensionless) electric

potential is given either by the sum of the gradients of the diffusion and streaming potentials [Eqs. (62–64)] or, alternatively, by Eq. (65).

The solution to the above system of equations is composed of the ionic permeate concentrations c_i^p, the Donnan potentials $\Delta\tilde{\phi}_D^{f(p)}$, and the intramembrane ionic concentration profiles $\bar{c}_i(x)(0^+ \le x \le l_m)$. Once the permeate concentrations are found, the ionic rejections R_i can then be obtained.

2.3.3.2. Electric Filtration Potential Once the Donnan potentials and the intramembrane ionic concentration profiles $\bar{c}_i(x)$, are known, it is possible to obtain the electric filtration potential $\underline{\Delta}\Phi^f$, which can be measured by inserting electrodes in the feed and permeate (care should be taken to subtract the electrode potential from the measured EMF before comparing theory with experiment).

During the separation of salt solutions in NF, the counter-ions are pulled into the pore, whereas the co-ions are repelled. If a pressure gradient is imposed, charge build-up occurs on the scale of the (small) Debye length, near the external solution–membrane interfaces during a short transient period. To reestablish macroscopic electroneutrality in the steady state, this weak charge build-up engenders an electric field E_x in the membrane whose direction is determined by the sign of the membrane charge. This electric field creates a force on the counter-ions that opposes their convective transport. As a consequence, this force makes the co-ions transfer faster, while retarding the counter-ions [42]. Along with the interfacial Donnan potentials, this (dimensionless) intramembrane potential difference $\Delta\tilde{\phi} = \tilde{\phi}(l_m^-) - \tilde{\phi}(0^+)$ will contribute to the (dimensionless) electric filtration potential $\underline{\Delta}\tilde{\Phi}^f$.

Equations (62–65), which give the gradient of the intramembrane electric potential as a function of the position in the membrane, can be integrated to obtain

$$\Delta\tilde{\phi} = \Delta\tilde{\phi}_d + \Delta\tilde{\phi}_s \tag{87}$$

When this result is combined with the interfacial Donnan potentials $\Delta\tilde{\phi}_D^{f(p)}$, we obtain

$$\underline{\Delta}\tilde{\Phi}^f = -\Delta\tilde{\phi}_D^f - \Delta\tilde{\phi} + \Delta\tilde{\phi}_D^p. \tag{88}$$

The electric filtration potential $\underline{\Delta}\tilde{\Phi}^f$ so defined is useful because it (usually) has the same sign as the membrane charge.

Because the sum of the diffusion and Donnan potentials is usually denoted as the membrane potential

$$\Delta\tilde{\phi}_m = \Delta\tilde{\phi}_D^f + \Delta\tilde{\phi}_d - \Delta\tilde{\phi}_D^p \tag{89}$$

the electric filtration potential can also be written as $\underline{\Delta}\tilde{\Phi}^f = -\Delta\tilde{\phi}_m - \Delta\tilde{\phi}_s$. Although the dimensionless electric filtration potential $\underline{\Delta}\tilde{\Phi}^f$ versus membrane flux density j_v curve is in general nonlinear, at high Péclet number, $Pe = j_v l_m/\bar{D}_{\max}$, it becomes asymptotically tangent to a straight line described by

$$\underline{\Delta}\tilde{\Phi}^f_{\lim} = -\Delta\tilde{\phi}^f_{\lim} + \tilde{\nu}_j j_v \tag{90}$$

where $-\Delta\tilde{\phi}^f_{\lim}$ is the y-intercept and $\tilde{\nu}_j$ the slope ($\bar{D}_{\max} = \max\{\bar{D}_i\}$). Both of these quantities provide information on the membrane properties. The slope $\tilde{\nu}_j$ is a reduced streaming potential

$$\tilde{\nu}_j = \lim_{Pe\to\infty} \frac{d(\underline{\Delta}\tilde{\Phi}^f)}{dj_v} = -\lim_{Pe\to\infty} \frac{d(\Delta\tilde{\phi}_s)}{dj_v} \tag{91}$$

that depends only on the asymptotic behavior of the streaming potential $\Delta\tilde{\phi}_s$. The y-intercept $-\Delta\tilde{\phi}_{\lim}$, however, generally combines contributions from the limiting (high flux) forms of the membrane (diffusion and Donnan) and streaming potentials.

For Dresner type 1 solutions, the reduced streaming potential $\tilde{\nu}_j$ is simply related to the gradient of the streaming potential evaluated at $x = 0^+$:

$$\tilde{\nu}_j = -(\partial_x\tilde{\phi}_s)_{0^+} j_v^{-1} l_m = -l_m\left(\frac{\sum_{i=1}^N z_i K_{i,c} c_i^f k_i^f}{\sum_{i=1}^N z_i^2 \bar{D}_i c_i^f k_i^f}\right) \quad \text{(type 1)} \tag{92}$$

(always true for single salts, $N = 2$, and mixtures with a single counter-ion). In general, for Dresner type 2 solutions, the exact expression [Eq. (91)] must be employed.

By using $\bar{D}_i = K_{i,d} D_i l_m / l_{eff}$ in Eqs. (91) or (92), we see that the reduced streaming potential $\tilde{v}_j$ increases with increasing effective membrane thickness (by an increase in the real active layer thickness l_m or tortuosity τ, or decrease of porosity, φ_p). Furthermore, as $K_{i,c}/K_{i,d}$ increases rapidly with increasing λ_i, at fixed $X_m \tilde{v}_j$ also increases rapidly with decreasing pore size (see Appendix 1).

We conclude that because both charge and hindered transport effects can play an important role in determining the asymptotic behavior of the electric filtration potential, its experimental measurement can provide valuable information concerning membrane properties.

For several reasons, the reduced streaming potential $v_j = RT\tilde{v}_j/F$ appears to be a better choice than the usual definition

$$\nu_p = \frac{\lim_{\Delta P \to \infty} d(\Delta \Phi^F)}{d(\Delta P)} \tag{93}$$

for characterizing the streaming potential. First, because electroviscous and osmotic effects complicate the relationship between j_v and ΔP (see following), and second, although thicker and larger pore supporting layers in composite systems may contribute to the total pressure drop across the system (in a way that is often difficult to quantify), j_v, on the contrary, is constant across composite systems in the steady state. Thus, in principle, the use of the reduced streaming potential v_j allows one to obtain a more direct grasp on membrane charge and structural parameters via the measured electric filtration potential, provided that the potential differences across the supporting layers are negligible (which may not always be true) [47].

2.3.3.3. Volume Flux Density (Osmotic and Electroviscous Effects) Both the dimensionless intramembrane potential difference $\Delta\tilde{\phi}$ and the interfacial pressure jumps $\underline{\Delta}P^{f(p)}$ influence the flow of a charged fluid through a charged membrane and determine how the transmembrane volume flux density responds to an applied pressure gradient ΔP (electroviscous and osmotic effects). The volume-averaged Stokes equation becomes in the core of the membrane ($0^+ < x < l_m^-$), sufficiently far away from the interfacial regions [40, 44],

$$\frac{1}{L_p^0} j_v \approx -\partial_x P + RTX_m \partial_x \tilde{\phi} \tag{94}$$

where L_p^0 is the specific pure water membrane hydraulic permeability [m^3/m^2h.bar].

The intramembrane electric potential couples to the solution flow via the electric body force [second term on the right of Eq. (94)]. For simplicity, we have once again supposed that supplementary body forces acting on the fluid in the membrane as a result of nonideality (last term in the averaged Stokes equation) are only important in the external solution–membrane interfacial regions (and are thus negligible within the core of the membrane). For this reason, a small, hindered transport contribution to (Eq. 94) caused by the finite ion size has been left out. Equation (94) can be integrated to obtain the intra-membrane pressure difference:

$$\Delta P_m = P(l_m^-) - P(0^+) = -\frac{j_v l_m}{L_p^0} + RTX_m \Delta\tilde{\phi} \tag{95}$$

where the intramembrane potential difference $\Delta\tilde{\phi}$ [-], as well as the ionic rejections, are now considered known functions of j_v (see earlier).

At the membrane–external solutions interfaces, we must account for osmotic pressure differences that arise as a result of ionic partitioning into the membrane. The total pressure difference across the membrane is given by

$$\underline{\Delta}P = P^l - P^u = \underline{\Delta}P^f + \underline{\Delta}P_m + \underline{\Delta}P^p \tag{96}$$

When the pressure jumps at the interfaces Eq. (82) are inserted into this last expression, it can be transformed into

$$\underline{\Delta}P = \underline{\Delta}\Pi - \underline{\Delta}\Pi_m + \underline{\Delta}P_m \tag{97}$$

where we have used the total osmotic pressure difference across the membrane [Eq. (83)] and the intramembrane osmotic pressure difference [Eq. (84)]. Combining the above results, we obtain an equation relating the transmembrane pressure difference $\underline{\Delta}P$ to the volume flux density j_v,

$$\underline{\Delta}P = \frac{l_m}{L_p^0} j_v + \underline{\Delta}\Pi - \underline{\Delta}\Pi_m - RTX_m\Delta\tilde{\phi}. \tag{98}$$

where all quantities on the right of Eq. (98) are (implicitly or explicitly) functions of j_v. This expression can also be written in standard form,

$$j_v = \frac{L_p^s}{l_m}(\underline{\Delta}P - \Sigma\underline{\Delta}\Pi) \tag{99}$$

using the specific salt solution membrane hydraulic permeability L_p^s [m³/mhbar]

$$L_p^s = \frac{L_p^0}{1+\kappa} \tag{100}$$

and the following operational definitions for electroviscosity coefficient κ [-]

$$\kappa = RTL_p^0 X_m l_m^{-1}\tilde{\nu}_j \tag{101}$$

(independent of j_v) and the global osmotic reflection coefficient Σ [-] [cf. $\bar{\sigma}_d$; Eq. (25)]

$$\Sigma = 1 - \frac{\underline{\Delta}\Pi_m}{\underline{\Delta}\Pi} - \frac{RTX_m}{\underline{\Delta}\Pi}\left[\underline{\Delta}\tilde{\phi} + j_v\tilde{\nu}_j\right] \tag{102}$$

which, although j_v dependent, tends to a constant (finite) value $\Sigma_{\lim}$ at high volume flux density. Thus, in the limit of high transmembrane pressure, j_v asymptotically becomes a linear function of $\underline{\Delta}P$,

$$j_v \approx \frac{L_p^s}{l_m}(\underline{\Delta}P - \Sigma_{\lim}\underline{\Delta}\Pi_{\lim}) \tag{103}$$

with slope L_p^s/l_m and x-intercept $\Sigma_{\lim}\underline{\Delta}\Pi_{\lim}$. Thus, by measuring the slope and x-intercept of the straight line asymptotic to the j_v versus $\underline{\Delta}P$ curve, we can obtain information concerning membrane properties. We note that although only the asymptotic behavior of the reduced streaming potential $\tilde{\nu}_j$ contributes to the electroviscosity coefficient κ, the diffusion potential, subasymptotic streaming potential, and interfacial pressure jumps all contribute to the global osmotic coefficient Σ.

The asymptotic slope of the j_v versus $\underline{\Delta}P$ curve can be put in the form

$$\frac{L_p^0}{(1+\kappa)l_m} = \frac{K_D^0}{\eta^{eff}}\frac{1}{l_m} \tag{104}$$

with

$$\eta^{eff} = \eta(1+\kappa) \geq \eta \tag{105}$$

and K_D^0 the pure water Darcy hydraulic permeability ($L_p^0 = K_D^0/\eta$). The volume flux density for pure water

$$j_v^w = L_p^0\frac{\underline{\Delta}P}{l_m} = \frac{K_D^0}{\eta}\frac{\underline{\Delta}P}{l_m} \tag{106}$$

has a slope

$$\frac{j_v^w}{\underline{\Delta}P} = \frac{K_D^0}{\eta l_m} \geq \frac{dj_v}{d\underline{\Delta}P} \tag{107}$$

The quantity η^{eff} thus represents an effective electroviscosity, for the salt-membrane system responds as if the viscosity of the fluid were greater than the pure water value.

The electroviscosity coefficient κ is proportional to the reduced streaming potential $\tilde{\nu}_j$ and the effective membrane charge density X_m. Although, because of hindered transport effects,

it is possible for $\bar{v}_j$ to be nonzero, even in the absence of membrane charge ($X_m = 0$), electroviscous effects ($\kappa > 0$) arise in this model only in the presence of nonzero membrane charge ($X_m \neq 0$). The reason for this is simply that electroviscous effects can be traced back to the electric body force term in the averaged Stokes Eq. (55). These effects are engendered by the asymptotic streaming potential ($\propto j_v$). Because it couples directly to the total intramembrane ionic concentration, this term of course vanishes in the absence of membrane charge (because of intramembrane charge electroneutrality).

Similar to the reduced streaming potential, the electroviscosity coefficient κ increases with increasing tortuosity τ and decreasing porosity φ_p or pore size r_p. If, as is usually found for ions in charged NF membranes, $l_{eff}/l_m \gg 1$, then electroviscous effects can be important and much larger than would be predicted by simple capillary pore models that assume $l_{eff} = l_m$.

2.3.4. Nanofiltration Model Development

A basic simplifying assumption in the above approach is that within the core of the membrane, the ions interact with each other and the membrane solely via the direct mean field electrostatic interactions. This assumption implies *inter alia* that the cross-coupling terms that appear in more general theoretical frameworks (such as the Maxwell-Stefan approach) are negligible [41] and that the last term in the ENP equation [Eq. (54)], involving gradients of the effective activity coefficient, is also negligible within the membrane. Note that this approximation does not require that all other ion–ion and ion–membrane interactions be weak within the membrane but, rather, that these interaction potentials be quasi-uniform there, which leads to negligible supplementary forces in the transport equations. The simplifying assumption of quasi-equilibrium at the feed and permeate/membrane interfaces, which can be justified by the high transport resistance found within the membrane, compared with the interfacial regions, allows the ionic concentrations within the membrane to be approximately related to the external concentrations via a quasi-equilibrium partition coefficient.

Although more detailed methods, like the Maxwell-Stefan approach, of modeling transport in nanofilters are potentially interesting, a large number of unknown supplementary parameters enter into the problem [72]. Given the relative paucity of the data necessary to assess the importance of these extra parameters, it is in our opinion premature to consider such complex theories until it is possible to discriminate clearly between the Maxwell-Stefan approach and the simpler, but already complicated, ENP system of transport equations (the approach that will be used exclusively here).

In general, the ionic partition coefficient for ion i in a mixture k_i can be factored into various contributions originating from the primary physicochemical interactions operating between the ions in solution (bulk and intrapore) and between the ions in the pores and the membrane matrix:

$$k_i = [\text{electrostatic}] \times [\text{electrodynamic(Lifshitz-VanderWaals)}] \times [\text{polar(acid-base)}] \times [\text{chemical(covalent)}]. \tag{108}$$

As stated earlier, the way in which these primary interactions manifest themselves in nanopores has not yet been clearly elucidated, and therefore state-of-the-art NF modeling is based on hybrid theories that include the following effective contributions to the ion partition coefficients [26, 27, 30, 33, 39, 41, 47–49, 68, 73, 74]:

$$k_i \cong [\text{electrostatic(Donnan)}] \times [\text{steric}] \times [\text{dielectric}] \times [\text{hydration(Born)}] \times [\text{ion–ion}] \times \ldots \tag{109}$$

These extended theories reduce to the ET model when all but the Donnan exclusion term are neglected, reduce to the HT model when the ion charge tends to zero, and reduce to the HET model when all but the Donnan and steric terms are neglected (see Table 3).

The last term in Eq. (109) is nothing but the generalization of the Debye-Huckel contribution to ion activity as a result of ion–ion interactions in nondilute solutions. Indeed, the last three terms can be shown to arise naturally by generalizing the bulk Debye-Huckel approach to ions in a nanoporous membrane with material and confined pore water dielectric constants both different from the bulk solution value [27].

Although the Hindered Electro-transport (HET) model [29], which accounts for only the electrostatic and hindered transport effects [the first two terms in Eq. (109)], was first extended in an approximate way to NF in 1995 to account for the hindered transport of large trace organic ions [30], it was not applied to the NF of mixtures of the smaller inorganic ions until 1996 [31]. In the first applications of this model to inorganic ions, the steric contribution to ionic partitioning was neglected, because it seemingly led to anomalous results (effectively reducing the partitioning part of the model to Donnan partitioning) [31, 32, 34]. In later publications the full HET model, including Donnan/steric partitioning, was used for inorganic ions (see e.g., Refs. [35, 36, 76, 77]).

We note that in parallel to these developments, other models were developed for RO based on various approaches. In Ref. [26], charged and uncharged RO membranes were studied by developing a generalized ENP approach that accounts for electrostatic (Donnan) and hydration (Born) contributions to ion partitioning (but not steric ones). The Kimura-Sourirajan model [78] and the Surface Force-Pore Flow model [79, 80] were also developed for modeling RO processes and were extended to NF [81]. The Sourirajan model contains experimentally determined contributions to the ion partition coefficients (via intramembrane ion activity coefficients) and has been used to model the rejection of synthetic sea water (ionic strength of ~0.5 M, mainly NaCl) containing nine ionic species [73]. Although this model predicts the observed very high rejection (>90%) of all species (including monovalent ones) using RO membranes, it has never been applied to NF, and it is not clear whether it is capable of predicting the high selectivity between mono and multivalent ions that is one of the major characteristic features of NF. We can summarize the majority of the work on RO modeling by stating that these models, at least in their current form, are unsuitable for predicting the high multivalent and moderate to low monovalent ion rejection observed for NF membranes [26].

Before the introduction of the HET model, important experimental and theoretical work in the area of NF was performed [33, 41, 68, 70, 82–86]. These works were devoted to the study of neutral solutes, single salts, and ternary ion mixtures (two salts with at least one ion in common) at relatively low ionic strengths. Although, in accordance with conventional wisdom, a drop in counter-ion selectivity was observed in binary electrolyte mixtures, for example, $LiCl/MgCl_2$ with a common co-ion (here Cl^-) [85], there are examples of mixtures, such as $NaCl/Na_2SO_4$, for which mono-divalent selectivity actually increases with feed ionic strength [87]. Typical experimental results for NF were interpreted using the SC model [62–65] or its homogeneous limit (see, e.g., [33]), the ET model (which includes neither Hindered transport effects for ions nor the other interactions, aside from the electrostatic one, in the ion partitioning). Within the ET model, $K_{i,d}$, $K_{i,c}$, $\gamma_i^{f(p)}$, and $\bar{\gamma}_i$ are all set equal to unity in the ENP and ion partitioning equation (see Table 3).

Starting in 1995, NF theory has evolved, and one now commonly uses the hindered transport theory for cylindrical pores to both incorporate the steric term in ion partitioning and estimate the diffusive and convective hindrance factors $K_{i,d}$, $K_{i,c}$. Various attempts have also been made to include interactions other than electrostatic by incorporating them into the intramembrane activity coefficient $\bar{\gamma}_i$. The theory of concentrated electrolyte solutions has not yet been reliably extended to NF, because even if the bulk activity coefficients $\gamma_i^{f(p)}$ have been measured and can be predicted for simple salts at high concentrations, it is difficult to extend such results to complicated ionic mixtures and obtain reliable methods for evaluating intramembrane activity coefficients, $\bar{\gamma}_i$ (see, however, Refs. [72, 88]).

The ET model treats ions as point charges and replaces ion activities by concentrations. The ionic parameters entering into this simplified theory are the ion feed concentrations, valences, and bulk diffusion coefficients. The membrane is described by only two of the membrane parameters already introduced above: the effective membrane charge density X_m and the effective thickness l_{eff}. The HET model is the generalization of the ET model to include hindered transport effects, and this is the model that will be adopted here in our analysis of membrane filtration data (section 2.7). Given the uncertainty concerning the role and importance of interactions other than the electrostatic and steric/hydrodynamic hindrance ones, we will not attempt to account for any supplementary interactions (beyond those incorporated in the HET model).

2.4. Hindered Electro-Transport Theory

The HET model is a special limiting case of the general homogeneous transport model presented in section 2.3 [29] (this model is also sometimes called the Electrostatic and Steric [ES] Hindrance model [30] or the Donnan-steric-pore model [DSPM] [31]). The HET model treats ions as hard spherical charged particles and accounts for steric effects in the effective intra-membrane ion activities (Table 3). Within this model, $\gamma_i^{f(p)}$ is set equal to unity and $\bar{\gamma}_i = (\Phi_i^s)^{-1}$ in the ion partitioning equations; the diffusive and convective hindrance factors $K_{i,d}$ and $K_{i,c}$ are calculated using hindered transport theory for cylindrical pores. No other interactions other than the electrostatic and steric/hydrodynamic ones are incorporated into the model. The ion parameters entering into this model are

- Ion feed concentration c_i^f
- Valence z_i
- Ion radius r_i
- Bulk ion diffusion coefficient D_i (temperature dependent).

The membrane is characterized by four membrane parameters:

- The effective pore radius r_p
- The effective membrane charge density X_m
- The effective thickness l_{eff}
- The specific pure water membrane hydraulic permeability L_p^0.

Whereas for a given nanofilter, X_m and l_{eff} may—and do—depend on the electrolyte solution being filtered, r_p and L_p^0 are taken to be fixed parameters (the temperature dependence of $L_p^0 \propto \eta^{-1}$ is taken into account via the temperature dependence of the solution viscosity, assumed to be that of ultrapure bulk water).

There is compelling evidence coming from ion transport in membranes with known pore sizes, such as biological channels and zeolites, that a good starting point for estimating the ion size in a nanopore is the ion Pauling crystal radius (Table 2) . Studies of the selectivity of ions of the same valence appear to corroborate this choice [35, 36] (the current *ad hoc* choice of using the Stokes-Einstein radius for ions appears to based on the misconception that ion diffusivity in bulk solutions is determined by the same mechanisms controlling the diffusivity of neutral solutes). Although the HET model is appealing because of its relative simplicity and its capacity to account for electrostatic and hindered transport effects, one should keep in mind that it has not been derived from first principles but is, rather, a hybrid theory that reduces to the Hindered Transport theory for neutral solutes when the ion valences z_i are set to zero and reduces to the ET model when the effective ion radius r_i is set to zero (recall that the ET model, which is the homogeneous limit of the pore level space charge model, accounts only for electrostatic interactions; see Table 2). Modifications to intramembrane ion diffusivity resulting from interactions are taken into account implicitly via the tortuosity factor τ.

2.4.1. Nanofiltration Model Parameters

2.4.1.1. Pure Water Permeability, L_p^0 The specific pure water membrane hydraulic permeability L_p^0 can be obtained directly by measuring the volume flux density j_v of ultrapure water as a function of applied transmembrane pressure ΔP:

$$j_v = \frac{-L_p^0 \Delta P}{l_m} \tag{110}$$

Care should taken, however, if the larger pore-supporting layers are thick enough to contribute to the total pressure drop across the composite system. Within the framework of the effective cylindrical pore model, we can write

$$L_p^0 = \left(\frac{r_p^2 l_m}{8\eta l'_{eff}} \right) \tag{111}$$

where l'_{eff} is an effective membrane thickness associated with the specific pure water membrane hydraulic permeability L_p^0. If the actual membrane thickness is unknown, one can

directly measure only pure water membrane hydraulic permeability $\bar{L}_p^0$

$$\bar{L}_p^0 = \frac{L_p^0}{l_m} = \left(\frac{r_p^2}{8\eta l'_{eff}}\right)$$

2.4.1.2. Effective Pore Radius r_p The effective pore radius r_p can be estimated by fitting the hindered transport theory to the experimental rejection of model neutral solutes (with known size) as a function of volume flux density [30, 31, 75]: The limiting rejection at high volume flux density (equal to the filtration reflection coefficient), depends only on the ratio of solute to pore size. For certain membranes, such as ceramic ones, the effective pore radius r_p can also be estimated from N_2 adsorption/desorption measurements or bubble point measurements [38, 89].

Attempts have also been made to estimate the pore size or effective membrane thickness from the measured flux of pure water using the simple Hagan-Poiseuille equation for cylindrical pores modified by replacing the actual thickness of the NF layer by an effective one [see Eq. (111)], where the effective "permeability" thickness $l'_{eff} = l_m\tau'/\varphi_p$ incorporates porosity (φ_p) and tortuosity (τ') effects. Unfortunately, l'_{eff} must be determined first before this method can be used to estimate r_p, and there is some evidence that the effective thickness estimated using other methods might not be the same as the effective "permeability" thickness (for this reason, we have used a prime to differentiate l'_{eff} and τ' from the effective membrane thickness and tortuosity, l_{eff} and τ, that enter into the effective ion diffusivity, $\bar{D}_i$ [Eq. (56)]).

Attempts have been made to include (cylindrical) pore size distributions into NF transport models, with the conclusion apparently being that models with a single effective pore size seem to work best [90]. An explanation for this result may be found in percolation theory: despite the complicated three-dimensional pore structure and pore distribution of real nanofilters, there will always be a well-defined bottleneck in the system, and the radius of this bottleneck can be taken as the effective membrane pore size [38, 91].

2.4.1.3. Effective Membrane Thickness l_{eff} The effective membrane thickness l_{eff} can also be estimated by fitting the hindered transport theory to the experimental rejection of model neutral solutes, or salts, as a function of volume flux density, as this parameter determines the slope of the rejection curve at low volume flux density. It turns out, however, that the effective membrane thickness estimated in this way depends on the size of the solute or choice of salt (somewhat mysteriously, the general trend observed is l_{eff} decreasing with increasing neutral solute radius). It also appears as if the values of l_{eff} obtained by fitting the HET theory to the experimental rejection of single salts as a function of volume flux density are much larger than those obtained for neutral solutes and may even vary as a function of salt type, concentration, and pH [35, 36, 92].

If the effective pore radius r_p has been estimated using other means, then the Hagan-Poiseuille relation can also be used to estimate an effective membrane thickness l'_{eff}. In general, one finds that the various methods for determining "l_{eff}" do not give a consistent value, indicating that each transport quantity (neutral solute rejection, electrolyte rejection, and hydraulic permeability) may have its own effective "tortuosity." For each physical quantity, this tortuosity translates in part the difference between the simple cylindrical pore structure that is at the basis of almost all model calculations and the more complicated structure of real nanofilters.

2.4.1.4. Effective Membrane Charge Density X_m The membrane charge density can be estimated indirectly by fitting the HET model to the experimental rejection of salts as a function of volume flux density [31, 35, 36, 75, 77, 79]: the limiting rejection at high-volume flux density (equal to the salt filtration reflection coefficient), depends on the ratio of ion to pore size, ratio of co- and counter-ion intramembrane mobilities $|z_2|\bar{D}_2/(|z_1|\bar{D}_1)$, and membrane charge density. The fitted values of the effective membrane charge density X_m are a faithful representation of the actual physical membrane charge densities only if no other interactions, other than the electrostatic and steric ones, are important. If other, neglected, interactions are indeed important, then the adjusted charge densities will try to compensate for the missing interactions by taking on values that are different from the actual

physical ones. One of the advantages of estimating X_m from salt rejection is that rejection is determined nearly entirely by the active NF layer (the wider pore supporting layers usually have a negligible influence on ion rejection).

Other methods for estimating the membrane charge density include measuring: the streaming potential tangential to the membrane surface (advantage: probes NF active layer; caveat: probes only membrane front surface charge and not the effective charge density within the core of the NF membrane) [32, 34, 93]; the electrophoretic mobility of the powder used to make the membrane (same advantage and caveat as in previous item) [7, 22, 38, 89, 91]; or the electric filtration or streaming potential across the membrane and various supporting layers (advantage: probes charge density within the core of the NF membrane; caveat: probes not only active NF layer but also the supports) [94–99].

A more fundamental method involves constructing detailed physicochemical models of the pore wall surface to estimate the effective membrane charge density X_m from the surface density of ionizable groups and the equilibrium constants that control the dissociation of the sites and the specific adsorption of salt ions [100]. Despite the appeal of this more detailed method, a rather large number of parameters, such as the equilibrium constants, need to be fit because they cannot yet be determined at the molecular level [101].

The effective membrane charge density estimated using one or more of the above techniques tends to give values that vary considerably as a function of salt type, concentration, and pH. To handle this complexity, attempts have been made to find a more or less universal isotherm of the Freundlich type to account for the concentration dependence of X_m [30–32, 34, 48, 49]:

$$X_m \approx (X_m^0)^{1-a} c_{\text{salt}}^a \tag{112}$$

where X_m^0 is a reference charge density and the exponent a is usually close to 0.5 (the value predicted by electric double theory for planar charged surfaces, provided that the surface [$\sim\zeta$] potential is assumed to remain constant). It has been suggested that in using Eq. (112) the salt concentration should be measured in equivalents or ionic strength. The latter choice is sometimes justified by examining the surface charge density-zeta potential relation for sufficiently weak constant zeta potentials and planar surfaces ($\sigma_{\text{ek}} \propto \zeta I^{1/2}$) and noting that the exponent a is equal to 0.5 in this case. Despite some utility to using this method, it appears to be too limited to account for the observed variations of X_m as a function of salt type/salt mixtures, concentration, and pH (e.g., the "constant" X_m^0 will depend on salt type and may even change sign as a function of pH).

Although in general, X_m increases with increasing feed concentration, it usually increases slower than the concentration itself (exponent a less than one), leading to a normalized membrane charge density $\xi = X_m/c_i^f$, and therefore rejection, which usually decreases with increasing concentration. Anomalous behavior, however, has sometimes been found for salts, such as $CaCl_2$, possessing divalent cations; in this case, salt rejections that increase with increasing salt concentration have been observed (see, e.g., Fig. 4 of Ref. [32]).

2.5. Numerical Method for Solving the Nanofiltration Transport Model

In general, solving the complete system of nonlinear algebraic/ordinary differential equations describing ion partitioning and transport in NF is a relatively involved numerical problem (analytical mathematical solutions exist only for certain single salt solutions [99]). A major difficulty in any numerical treatment comes from the appearance of the unknown ion permeate concentrations in the ENP equations themselves via the filtration condition [Eq. (59)], which means that the model must be solved iteratively, as we now discuss (see Fig. 23) [30, 33, 41, 68, 70].

We denote the known ion feed concentrations by c_i^f *(real)* and the unknown ion permeate concentrations by c_i^p *(real)*, which are the solutions to the transport model equations. For a given value of volume flux density j_v, the iterative numerical method used for solving the transport model works as follows. Using an initial guess for c_i^p, the permeate Donnan potential is calculated using Eq. (73). This interfacial potential is then used to obtain the intramembrane ionic concentrations at the permeate–membrane interface. These concentrations can then be used as the starting boundary conditions for integrating the nonlinear ENP

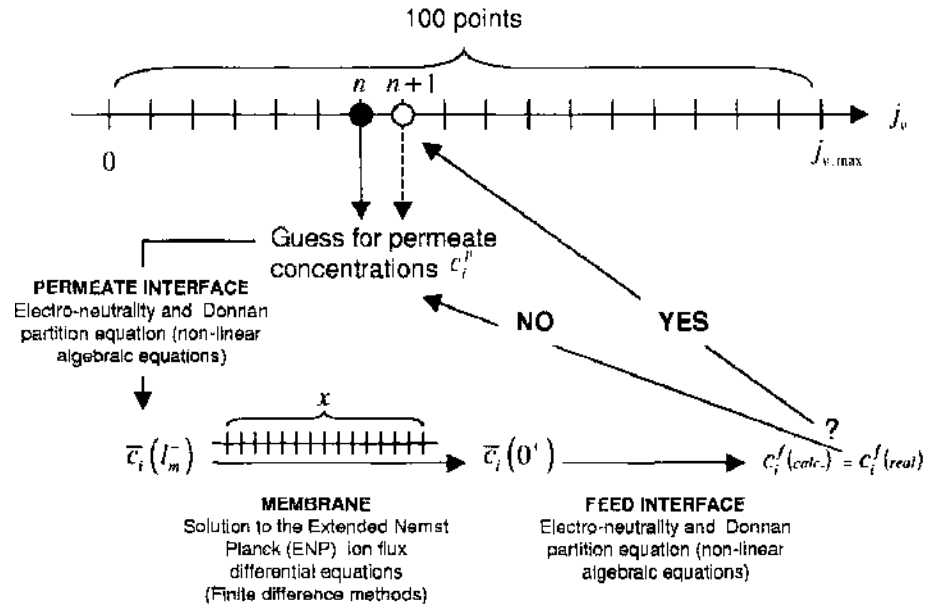

Figure 23. Iterative procedure used to solve the transport model and thereby calculate ionic rejection, electric filtration potential, and applied pressure as a function of volume flux density.

ion flux system of ODEs [Eq. (54)] backward across the membrane to the feed–membrane interface. The intramembrane ionic concentrations at the feed–membrane interface are then used in conjunction with the ion partitioning equations to calculate first the feed Donnan potential $\Delta\phi_D^f$, and then the ion feed concentrations $c_i^f(cal.)$. If the ion feed concentrations obtained by solving the model $c_i^f(cal.)$ agree (to within some preestablished tolerance) with the known values $c_i^f(real)$, then the iteration stops and the values used for c_i^p in the current calculation are the correct numerical solution to the problem. If, however, $c_i^f(cal.) \neq c_i^f(real)$, then new starting values are chosen for c_i^p and the iteration continues. Via this iteration, the guessed values c_i^p converge to the correct solution $c_i^p(real)$. The calculated ion rejection for the current value of j_v is then given by $R_i = 1 - c_i^p(real)/c_i^f(real)$ [cf. Eq. (3)]. To calculate ion rejection as a function of j_v, the current working value of j_v is incremented, and the iterative procedure is repeated (see Fig. 23).

The outputs of the above numerical algorithm are the correct ion permeate concentrations and concentration profiles within the membrane. Once these are known, the electric filtration potential $\underline{\Delta}\Phi^F$ and its various components (Donnan, diffusion, and streaming) can be calculated using Eq. (71) (Donnan) or by integrating Eq. (62) across the membrane (diffusion and streaming). Once the electric potentials are known, the applied pressure $\underline{\Delta}P$, at the given volume flux density, can be calculated using Eq. (98).

Until recently, this numerical solution has only been performed within the scope of the ET and HET models for mixtures of three ions (equivalent to mixtures of two salts with one ionic species, either a co-ion or counter-ion, in common) [30, 33, 41, 68, 70]. Such mixtures have also been studied by numerically solving the more complicated Maxwell-Stefan transport equations [72] (the results based on the Maxwell-Stefan model do not seem to be qualitatively different from those obtained using the ENP equations, and for the moment it is not clear whether the Maxwell-Stefan approach is more useful than the ENP one for NF modeling). Recently, however, a nanofiltration simulation code, NanoFlux, has been developed that allows solutions to the HET model to be obtained for up to 11 ionic species and composite membrane systems with up to three distinct layers [35, 36] (Fig. 22).

2.6. Principles of Membrane Characterization and Nanofiltration Performance Simulation

In this section, we explain how to characterize a nanofilter by setting up a limited single-salt database. We then show how this database can be used to simulate the performance of a nanofilter vis-à-vis arbitrary ion mixtures [33, 35, 36] (also see sections 1.2 and 1.4).

2.6.1. Neutral Solute and Single salt Characterization Protocol

A typical membrane characterization study involves all or some of the following steps:

1. Measure the pure water membrane volume flux density j_v^w as a function of applied pressure to obtain the pure water membrane hydraulic permeability $\bar{L}_p^0 = L_p^0/l_m$.
2. Measure the rejection of model neutral solutes (with known radii) as a function of volume flux density, and then fit the HT model to these data to establish the effective pore radius r_p and effective thickness l_{eff}^{ns} for neutral solutes (ns) (which may depend on solute size).
3. Measure the rejection of single-salt solutions (with known ionic radii) as a function of volume flux density j_v, and then fit the HET model to these data to establish the effective membrane charge density X_m and effective thickness l_{eff} for salts. One typically uses (1:1), (2:2), (1:2), and (2:1) salts such as NaCl, $MgSO_4$, Na_2SO_4, $CaCl_2$, or $MgCl_2$, usually at various values of pH and feed concentration.
4. Measure the transverse streaming potential (perpendicular to the membrane surface), and then fit the HET model to these data to establish the effective membrane charge density X_m and effective thickness l_{eff} for salts.
5. Measure the volume flux density j_v of the single salt solutions as a function of pressure, and then fit the HET model to these data to establish the effective membrane charge density X_m and effective thickness l_{eff}.
6. Estimate the membrane surface charge density σ_i by measuring the electrophoretic mobility of the powder used to prepare ceramic membranes or the tangential streaming potential (parallel to the membrane surface). The effective volumetric membrane charge density X_m can then be estimated using Eq. (50).

A typical single-salt characterization protocol (item 3 above) might involve carrying out measurements at, say, pH 3, 7, and 10 for three different salt feed concentrations (say 5×10^{-4}, 5×10^{-3}, 5×10^{-2} [mol/l]) [35, 36]. Other single-salt membrane characterization studies found in the literature do not necessarily follow this protocol and may be more limited [33].

The goal of most NF modeling studies to date has been to compare the salt rejection performance of different nanofilters and also to determine how well (over a range of pH, salt feed concentration, and relative salt mole fraction) the rejection and separation of multielectrolyte mixtures can be predicted by electro-transport theory from single-salt filtration results. To calculate the ion rejection and electric filtration potential within the HET model, the relevant parameters that must be supplied as input to the model are

- c_{tot}^f, total salt feed concentration [mol/m^3]
- x_s^f, salt feed mole fractions [mol/mol]
- X_m, effective membrane charge density [mol/m^3]
- r_i, the effective ion radius [m]
- r_p, the effective membrane pore size [m]
- l_{eff}, the effective membrane thickness [m]. To calculate j_v as a function of ΔP, in addition to the above parameters,
- $\bar{L}_p^0 = L_p^0/l_m$, the pure water hydraulic permeability

must be supplied also.

The NF modeling studies that appear in the literature (see Table 3) can be grouped on the basis of the transport model adopted and the methods used to estimate the effective ion radius (r_i) and membrane parameters (X_m, r_p, l_{eff}, L_p^0/l_m).

2.6.2. Membrane Database

Once the effective membrane pore radius has been estimated by filtering model solutes (or some other method), the two parameters characterizing a membrane/salt pair within the scope of the HET model (X_m, l_{eff}) can be determined, for single salts, in a variety of ways (section 2.4.1).

One of the methods discussed in detail here consists of estimating the value of the relevant membrane parameters, as a function of feed concentration and pH, via a numerical fitting

procedure. The best fit membrane parameter values for X_m and l_{eff} minimize the difference between the experimental and theoretical rejections. For a given membrane, the parameters X_m and l_{eff} may vary as a function of the salt concentration c_s^f and pH^f of the feed [35, 36].

At low or high pH and sufficiently low salt concentration, it is important to account for the nonnegligible influence on salt transport of the acid or base used to adjust the pH. In other cases, it is useful to examine the measured rejections of trace ions (including H^+ and OH^-) to justify the choice of sign for the membrane charge density and test the overall coherency of the model (contrary to what obtains for single salts, the ionic rejections in multielectrolyte mixtures are a sensitive gauge of the internal consistency of the transport model adopted) [47].

Other methods for determining X_m have already been discussed in section 2.4.1.4. In addition to the fitting method, we will also present here results based on estimating X_m from either the tangential streaming potential or the electrophoretic mobility (measured on the powder used to prepare ceramic membranes).

2.6.3. Simulations for Multielectrolyte Mixtures

Once the membrane characterization step is finished, one typically tries to simulate the membrane performance vis-à-vis more complicated salt mixtures by varying the relative salt proportions for different total feed concentrations and pH. In the field of NF, up until recently, only ternary ion mixtures were studied. Theoretical ion rejection predictions for single-salt and multielectrolyte mixtures are obtained by solving numerically the transport model, using suitable input parameters.

NF membranes come in a variety of materials, pores sizes, and thicknesses. The studies of the rejection performance of ceramic and organic nanofilters that can be found in the literature are all part of an attempt to better assess the filtration possibilities offered by NF membranes. It is hoped that these studies will lead to better ways to use existing membranes and point out paths to the development of new, higher-performance nanofilters. The only way to do this in an efficient and cost-effective way is to elucidate the structure–property relation for these membranes through detailed modeling studies. It is also important to go beyond the binary electrolyte solutions, with one common species usually studied in research labs to study the more complicated mixtures actually encountered in real-world industrial filtration problems.

One of the bottlenecks holding back the development of NF in industry is the lack of computer modeling tools in this area. To meet this very need in the area of NF, we have developed a user-friendly computer simulation program, NanoFlux, that can be used to characterize nanofilters and predict their rejection properties vis-à-vis complicated mixtures of neutral and charged solutes. NanoFlux can be used to simulate transport in the NF range by solving the hindered transport ENP ion flux equations and the averaged Stokes equations numerically [35, 36]. Using this tool, which provides a reliable and robust method for predicting the performance of NF membranes, we present here experimental results and theoretical predictions for binary and ternary salt mixtures, as well as results for real fluids possessing up to seven dominant ionic species.

It is of considerable interest to determine how well the rejection of multicomponent ionic mixtures can be predicted by electro transport theory from single-salt results. The membrane parameters obtained from data for single salts can be used to estimate the values of these same parameters for the multielectrolyte mixtures. We have developed an interpolation-weighting method [35, 36] that is a generalization of the mixing rule for X_m proposed in Ref. [33]. This mixing rule allowed the effective membrane charge density for a binary salt mixtures to be estimated by linear interpolation from fitted single-salt values obtained at nearly the same total salt concentration. This mixing rule requires that single-salt experimental results be obtained at approximately the same concentration and pH used for the salt mixtures to be studied. We get around this constraint by introducing solution pH as a further variable and implementing an interpolation/extrapolation scheme in the feed concentration-pH plane.

The effective charge densities and effective membrane thickness obtained by fitting electro-transport theory to the rejection data for single salts at a limited number feed

concentrations and pH values constitute the single salt database for a given salt/membrane pair. By using a suitable interpolation/extrapolation method, the values of these two parameters can be estimated for each salt/membrane pair at feed concentrations and pH values that were not studied experimentally. A suitable weighting method can then be used to estimate the values of these same parameters for any multielectrolyte mixture at any total feed concentration and pH.

Once we have a complete database for a given membrane, established using a limited number of carefully selected experiments, we can study the predicative power of the model with respect to salt mixtures. We assume that membrane parameters for a mixtures of N_s salts can be estimated using a simple weighting scheme:

$$X_m^{mix} = \sum_{s=1}^{N_s} w_s X_m^s \tag{113}$$

$$I_{eff}^{mix} = \sum_{s=1}^{N_s} w_s I_{eff}^s \tag{114}$$

where w_s represents the weight of salt s in the mixture as a molar/mass fraction of the salt in the solution. We have proposed three different methods for determining the weight w_s:

- WCC: weighting by concentration at constant total concentration
- WII: weighting by ionic strength at constant total ionic strength
- WIC: weighting by ionic strength at constant total concentration.

The last method (WIC) especially is used to increase the weight of salts containing multivalent ions.

For the first method (WCC), the weight of salt s in the mixture is taken to be equal to the salt mole fraction $w_s = x_s^f = c_s^f / c_{tot}^f$. For the other methods (WII and WIC), the weight of each salt in the mixture is determined by the ionic strength fraction $w_s = I_s / I_{tot}$, where

$$I_s = \frac{1}{2} \sum_{i=1}^{2} z_{i,s}^2 c_{i,s}^f \tag{115}$$

is the ionic strength of salt s and

$$I_{tot} = \sum_{s=1}^{N_s} I_s \tag{116}$$

is the total ionic strength. For the WCC and WIC methods, the parameters X_m and I_{eff} for each salt are taken in the single salt database at the same concentration as the total salt concentration of the mixture and at the same pH. For the WII method, in contrast, these parameters are evaluated in the single-salt database at a concentration that ensures that the ionic strength of a component salt will be equal to the total ionic strength of the mixture.

2.7. Applications of the NF Transport Model to Polymer and Ceramic Nanofilters

Following earlier RO and UF studies [42, 50, 70, 83, 94, 95, 102], many NF studies have been carried out for organic nanofilters [31–34, 55, 56, 75, 77, 85, 86, 103–107] and inorganic nanofilters [7, 22, 37–38, 92, 108–114]. Although it not possible to discuss all the results obtained in the NF studies up to this time, we will illustrate here typical NF behavior by using the methods described above for membrane characterization and simulation to present results for a selection of nanofilters (the characterization methods used are in parentheses):

1. Commercial organic NTR-7450 nanofilter (single-salt database)
2. Desal5DK and NTR-729 (HN PVD1) commercial nanofilters (tangential streaming potential)
3. comparative study of two commercial organic nanofilters (NF200, Desal5DL), and a commercial ceramic TiO_2 membrane at the borderline between UF and NF (single-salt database)

4. Homemade Hafnia nanofilter (electrophoretic mobility)
5. Homemade Titania nanofilter(single salt database and electrophoretic mobility).

Ion properties needed for input in the model calculations presented below are listed in Table 2. In reading certain of the figures presented below, it should be noted that the symbols farthest to the right and just below the NanoFlux simulation curves are not experimental data points but serve rather to identify the curves (using the legend provided). In the legends of the figures presenting ion rejection, the numbers placed next to the ion symbols are the values of $K_{i,d}D_i$ in units of 10^{-9} m^2 s^{-1}.

2.7.1. NTR-7450 Nanofilter

2.7.1.1. Experimental Protocol In Ref. [33], a detailed experimental and modeling study of two nanofilters (Nitto Denko NTR-7410 and NTR-7450) was carried out. These membranes have a negatively charged active layer of sulfonated polyether sulfone and a molecular weight cut-off (MWCO) below 1000 Da (estimated from more recent neutral solute rejection studies, which indicate a pore size ~0.8 nm). To characterize the membrane charge density, rejection measurements for single salts (NaCl, KCl, $MgSO_4$, Na_2SO_4, $CaCl_2$, $MgCl_2$) were performed. Here we discuss only the higher-performance membrane, the NTR-7450, for which the most extensive results were reported.

2.7.1.2. Single-Salt Database The experimental rejection results as a function of volume flux density for these 1 : 1, 2 : 2, 1 : 2, 2 : 1 ($|z_{cation}|$, $|z_{anion}|$) salts were analyzed using the ET model (incorporating only Donnan [charge] exclusion) via a numerical fitting procedure to determine the optimal values of the two parameters (X_m and l_{eff}) that characterize the membrane/salt pair. The single salts were studied at natural pH over a wide feed concentration range (10^{-3} [mol/l] -- 1 [mol/l]). Overall, behavior thought to be typical of a negatively charged NF membrane was found: a strong drop in rejection with increasing

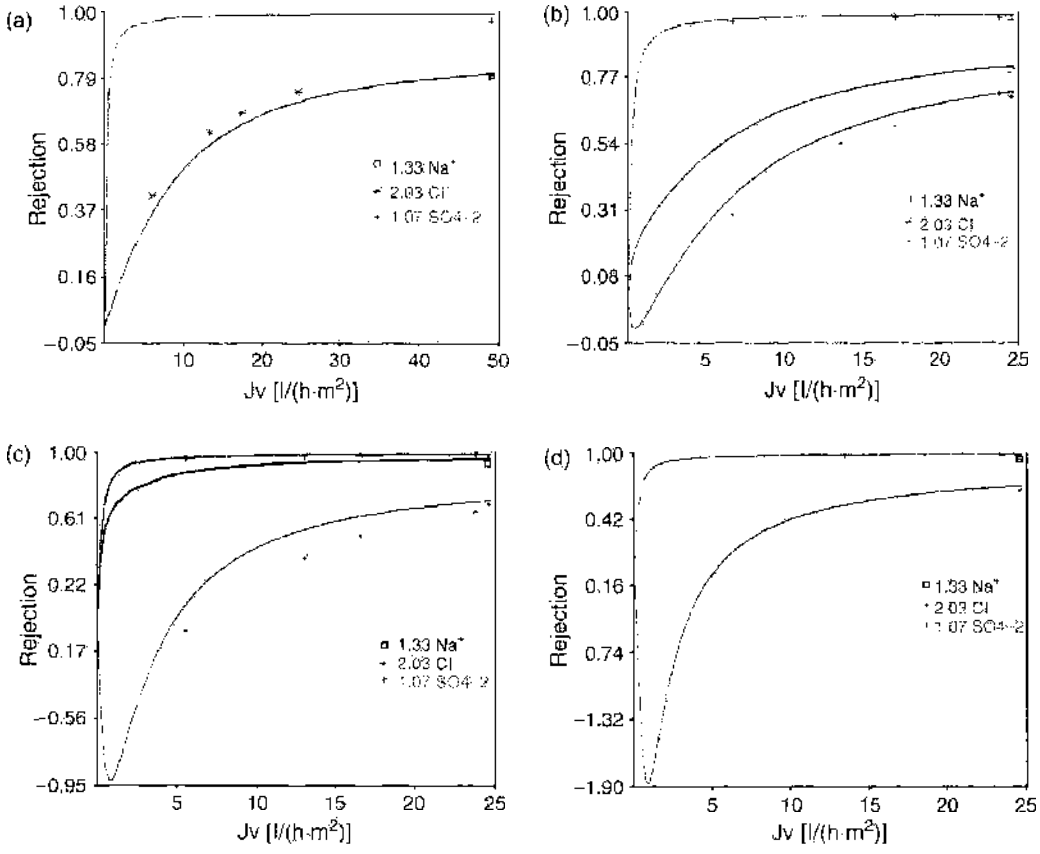

Figure 24. Ion rejection versus volume flux density; experimental data and ET model simulations for the NTR-7450 nanofilter at various salt mole fractions for $NaCl/Na_2SO_4$ mixtures at total feed concentration of 0.01 M and natural pH: (a) 100/trace, (b) 20/80, (c) 80/20, (d) trace/100.

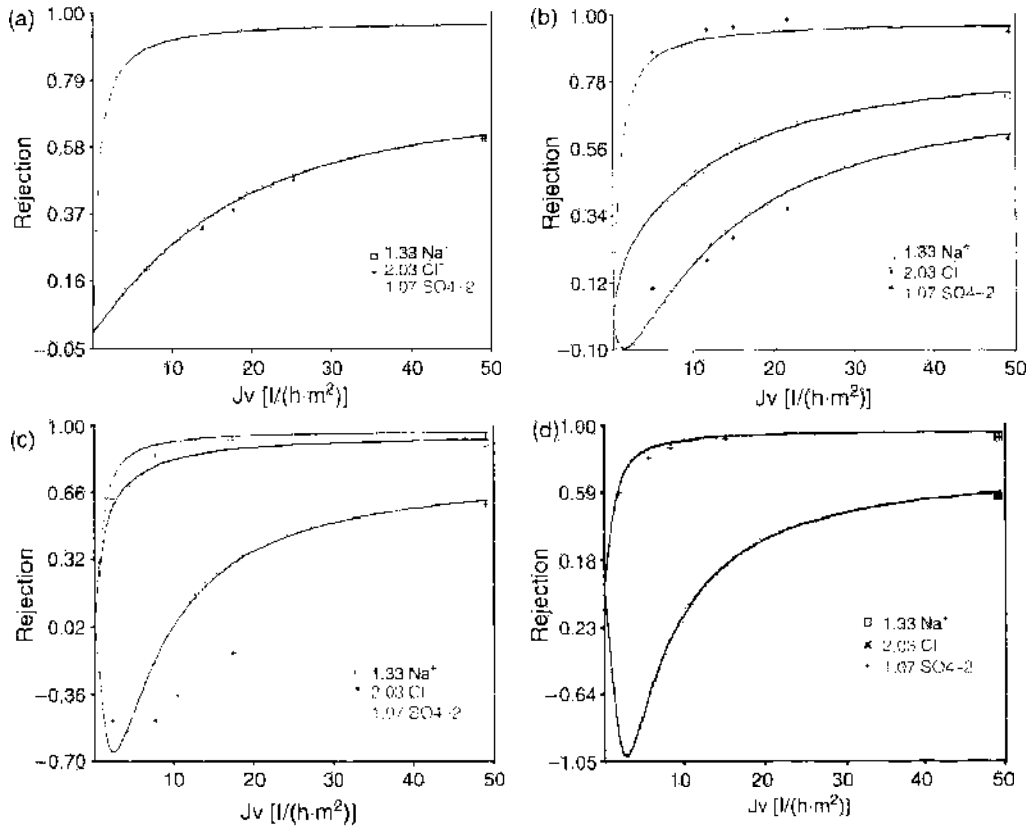

Figure 25. Ion rejection versus volume flux density: experimental data and ET model simulations for the NTR-7450 nanofilter at various salt mole fractions for $NaCl/Na_2SO_4$ mixtures at total feed concentration of 0.05 M and natural pH: (a) 100/trace, (b) 20/80, (c) 80/20, (d) trace/100.

feed concentration, with measured or extrapolated rejection approaching zero in the high-concentration range (Fig. 3 of Ref. [33]) for all salts studied. The charge parameter X_m depended strongly on salt type ($|z_{cation}|$, $|z_{anion}|$) and feed concentration (Fig. 4 of Ref. [33]), and the thickness parameter l_{eff} depended slightly on the membrane and salt mixture studied. Although the fitted effective membrane charge density exhibited a Freundlich-type behavior,

$$\log X_m = a \log c_s + \text{const.} \tag{117}$$

with an exponent close to 0.5, the constant term clearly depended on salt type (even if the salt concentration were measured in equivalents or be replaced by ionic strength). Despite the increase of the fitted values of the effective membrane charge density X_m as a function of salt concentration for all salts studied [33], the normalized membrane charge density ξ itself decreases, leading to typical NF behavior: salt rejection decreasing with increasing concentration.

The results for the single salts correspond closely, but not exactly, to the typical behavior expected theoretically for a negatively charged NF membrane that rejects ions mainly by charge (Donnan) exclusion: the experimental rejection order was (2 : 1) < (1 : 1) < (2 : 2) < (1 : 2) (Fig. 3 of Ref. [33]), whereas the expected theoretical rejection order for the ET model is (2 : 1) < (2 : 2) < (1 : 1) < (1 : 2). It should be kept in mind, however, that the expected result is based on the physically unrealistic assumption that the effective membrane charge density is the same for all salts. The relatively high observed rejection of the 2 : 2 salt could be explained by a specific sulfate adsorption that gives the membrane a higher negative charge density in this case than in the case of a 1 : 1 salt.

Although the estimated pore radius of 0.8 nm implies that hindered transport effects cannot be entirely neglected, the single-salt database established in Ref. [33] within the framework of ET model can still be used to perform simulations for salt mixtures, as the fitted values of the effective membrane parameters X_m and l_{eff} will naturally try to compensate for the interactions that were left out of the model.

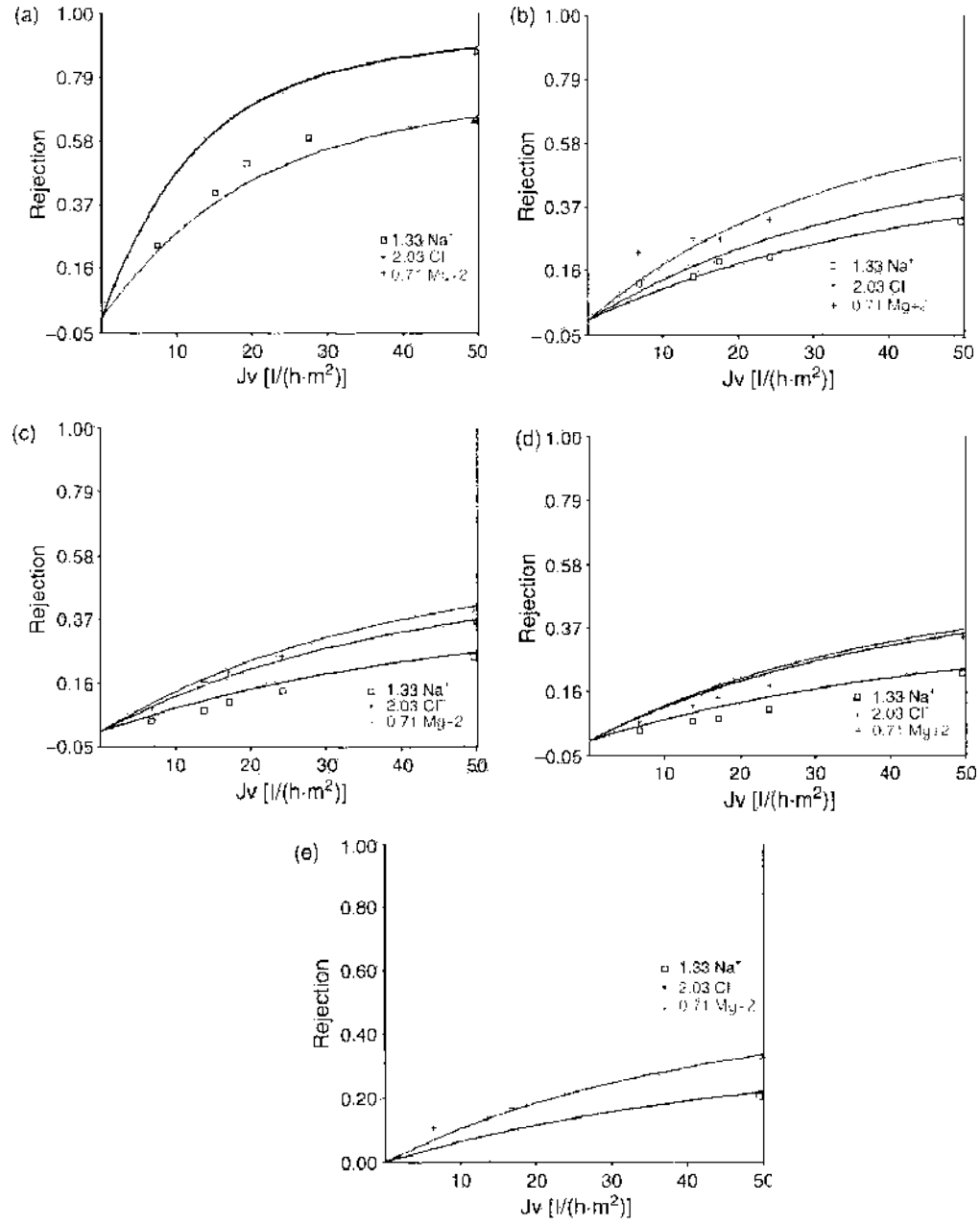

Figure 26. Ion rejection versus volume flux density; experimental data and ET model simulations for the NTR-7450 nanofilter at various salt mole fractions for $NaCl/MgCl_2$ mixtures at total feed concentration of 0.03 M and natural pH: (a) 100/trace, (b) 20/80, (c) 50/50, (d) 80/20, (e) trace/100.

Although some single salts were studied up to 1 [mol/l] in feed concentration in Ref. [33], binary salt mixtures, including $NaCl/Na_2SO_4$ and $NaCl/MgCl_2$, were only studied in the concentration range between 0.01 [mol/l] and 0.05 [mol/l]. Simulations of salt mixtures performed with NanoFlux in the ET model mode ($r_i = 0$), using the single-salt ET model database established in Ref. [33], corroborate the modeling results found in this reference; namely, that the rejection behavior of ternary ion mixtures can be reasonably well predicted by the ET model from the single-salt results, using an appropriate weighting scheme.

2.7.1.3. Binary $NaCl/Na_2SO_4$ Electrolyte Mixtures Using the method outlined in section 2.5, we present in Figs. 24 and 25 ET model simulations at various mole fractions for $NaCl/Na_2SO_4$ mixtures (100/trace, 20/80, 80/20, and trace/100) at total feed concentrations c_{tot}^f of 0.01 (Fig. 24) and 0.05 [mol/l] (Fig. 25).

The experimental and modeling results for the NTR-7450 membrane and $NaCl/Na_2SO_4$ mixtures (with varying salt proportions) reveal high sulfate rejection (>90%) with low to

negative chloride rejection for majority Na_2SO_4, and very high sulfate rejection (>95%) with moderate chloride rejection for majority NaCl. This is typical negatively charged membrane NF behavior for such [1:1]–[1:2] binary salt mixtures: an increase in the divalent co-ion (sulfate) rejection at low Na_2SO_4 mole fraction and negative monovalent co-ion (chloride) rejection observed and predicted at low flux (pressure) when this species is in the minority. The latter leads to very high mono-divalent co-ion (anion) selectivity, $S(Cl^-/SO_4^{2-}) = T_{Cl^-}/T_{SO_4^{2-}}$, at intermediate membrane volume flux density j_v, and the possibility of efficiently separating mono- from multivalent anions using negatively charged nanofilters. Although the simulations indicate that this intermediate flux selectivity should be enhanced at lower feed concentration (Fig. 24), there are unfortunately no data at low flux in [33] that would allow us to confirm this prediction. The increase of the limiting, high flux rejections with decreasing feed concentration is also another signature of typical NF behavior.

2.7.1.4. Binary NaCl/$MgCl_2$ Electrolyte Mixtures In Fig. 26, we present simulations at various mole fractions for NaCl/$MgCl_2$ mixtures (100/trace, 20/80, 50/50, 80/20, and trace/100) at a total feed concentrations c_{tot}^f of 0.03 [mol/l].

The experimental and modeling results for the NTR-7450 membrane and NaCl/$MgCl_2$ mixtures [33] reveal modest magnesium rejections (<40%) that tend to increase with decreasing $MgCl_2$ mole fraction, and intermediate-to-low sodium rejections that decrease with increasing $MgCl_2$ mole fraction. This intermediate-to-low rejection is typical of a negatively charged nanofilter for such [1 : 1]–[2 : 1] binary salt mixtures and leads to modest mono-divalent counter-ion (cation) selectivity over the whole relative mole fraction range. In contrast to what is obtained for minority co-ions in NaCl/Na_2SO_4 mixtures, there is, in particular, no negative rejection of the minority counter-ion. The NanoFlux simulation for the 80/20 NaCl/$MgCl_2$ mixture (minority $MgCl_2$) is a severe test for the transport model: compared with Na^+, the slightly higher observed Mg^{2+} rejection can only be correctly predicted by the transport model if the ratio of di- to monovalent cation mobility is slightly greater than one (NanoFlux uses $\hat{\mu}_{Mg^{2+}}/\hat{\mu}_{Na^+} = 2\hat{D}_{Mg^{2+}}/\hat{D}_{Na^+} = 2D_{Mg^{2+}}/D_{Na^+} = 1.07$). For this mixture, the Mg^{2+} rejection is a sensitive function of the Mg^{2+} diffusivity, $\bar{D}_{Mg^{2+}}$—a 30% decrease in this value would lead to a Mg^{2+} rejection curve that nearly coincides with the Na^+ one over the experimentally studied membrane volume flux density j_v range (and then crosses over to lower values at higher j_v); a 50% decrease in $\bar{D}_{Mg^{2+}}$ would lead to a nonmonotonic Mg^{2+} rejection curve that reaches a maximum at ~30 $lh^{-1}m^{-2}$ and is always much lower than the Na^+ rejection; a 30% increase in $\bar{D}_{Mg^{2+}}$ would lead to a Mg^{2+} rejection curve that overestimates the experimental rejection by a factor of 2 at higher j_v.

2.7.1.5. Nanofiltration of Artificial Seawater Using the NTR-7410 and NTR-7450 nanofilter, the NF of artificial seawater has also been studied experimentally [104]. This artificial seawater contains about 35 g/l (~0.5 [mol/l]) of NaCl with lower concentrations of divalent anions (sulfate, 0.028 [mol/l]) and cations (magnesium, 0.0425 [mol/l]) and is formally equivalent to a ternary 85/06/09 NaCl/Na_2SO_4/$MgCl_2$ salt mixture at a total feed concentration of 0.495 [mol/l]. In Figure 27, we present NanoFlux simulations for this quaternary ion mixture of Na^+, Cl^-, Mg^{2+}, and SO_4^{2-} (in Ref. [104], a modeling study was not carried out for this case).

Although the looser and more weakly charged NTR-7410 membrane showed poor artificial seawater rejection performance, the NTR-7450 showed moderately high sulfate rejection (~80%), in spite of the relatively high feed concentration, but at the same time, moderate Mg^{2+} (~35%) to low Na^+/Cl^- (<15%) rejection. The monodivalent anion selectivity was sufficiently high for the NTR-7450 nanofilter to be considered useful for separating SO_4^{2-} from the other ions in this artificial seawater. Simulations of artificial seawater rejection, performed with NanoFlux using the ET model single-salt NTR-7450 database [33, 104], show good agreement with experiment. Using the WC weighing method, the simulations account well for the monovalent ion rejection but underestimate somewhat the divalent rejection (Fig. 27a). In contrast, using the WCI weighing method (which gives more weight to salts possessing multivalent ions), the simulations account well for the divalent ion rejection but overestimate somewhat the monovalent rejection at higher volume flux density (Fig. 27b).

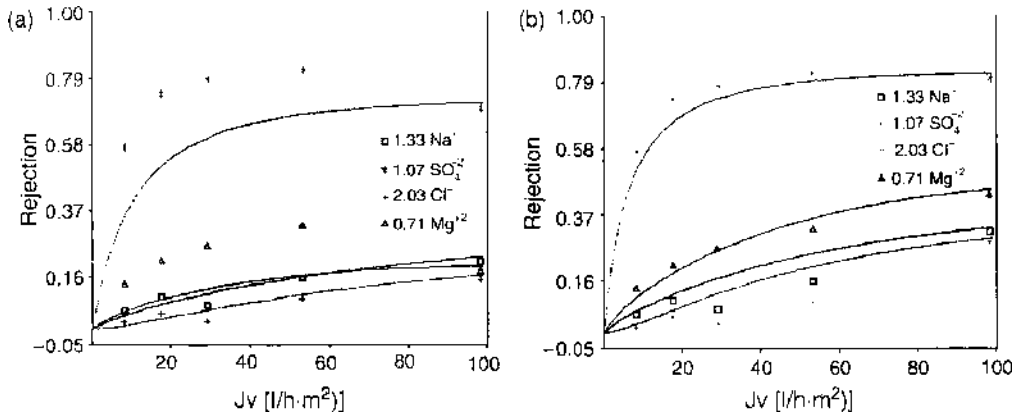

Figure 27. Ion rejection versus volume flux density; experimental data and ET model simulations for the NTR-7450 nanofilter and artificial sea water (Na^+, 0.480 M; Cl^-, 0.595 M; Mg^{2+}, 0.043M; SO_4^{2-}, 0.028 M) (a) WC weighting method (b) WCI weighting method.

The results presented here for the NTR-7450 nanofilter indicate that under certain circumstances, rejection performance can be reasonably well explained by the ET model, incorporating only Donnan exclusion. The reason has already been evoked: the simulations for multielectrolyte mixtures are based on a single-salt database, and the fitted single-salt values of X_m and l_{eff} for the ET model naturally try to compensate for the missing contributions of other physically important interactions that may have been left out of the model. As a consequence, compared with what one would obtain with a hypothetical HET model database, the fitted single salt values of X_m and l_{eff} for the ET model will generally be higher to make up for the neglected hindered transport effects (steric exclusion and hindered diffusion and convection).

However, as we will see later (sections 2.7.3.4, 2.7.3.5), the simplified ET model is not capable of accounting for the observed selectivity of ions of the same valence but different size. The observed selectivity of such ions requires generalizing the model to include other interactions, and we show that, unlike the ET model, the HET model (section 2.4) allows us to explain the observed selectivity both for Cl^- and NO_3^- and for Na^+ and K^+, provided that we adopt the crystal (Pauling) choice for ion radius.

2.7.2. Desal5DK and NTR-729 (HN PVD1) Nanofilters

In [32, 34], two tight organic nanofilters were studied: Desal5DK (MWCO 200-300 Da) and NTR-729 (HN PVD1) (MWCO <200 Da). The MWCO was determined by measuring the rejection of uncharged organic molecules (alcohols and sugars). Single salts (NaCl, Na_2SO_4, $CaCl_2$) and ternary ion mixtures ($NaCl/Na_2SO_4$ and $NaCl/CaCl_2$) were also studied in order to characterize the electrolyte rejection performance of these two membranes. Similar NF studies were carried out for organic nanofilters in Refs. [31, 33, 55, 56, 75, 77, 85, 86, 103–107, 115].

The effective membrane charge density X_m was estimated from the zeta potential ζ, determined experimentally from tangential streaming potential measurements (Fig. 28). These measurements seem to indicate that for both membranes and all the salts studied, the membrane charge density is positive below an IEP (isoelectric point) located at pH ~4 and negative above. The surface charge density of an exposed planar surface σ_{ek} can then be calculated from the measured zeta potential via

$$\sigma_{ek} = \left(2\varepsilon RT \sum_i c_i \left[\exp\left(\frac{-z_i F\zeta}{RT}\right) - 1\right]\right)^{1/2} \tag{118}$$

where c_i is the bulk ion concentration used in the measurements. In the limit of weak zeta potential, $(|z_i|F\zeta/RT) < 1$, this expression gets simplified to

$$\sigma_{ek} \approx \frac{\varepsilon\zeta}{\lambda_D} \tag{119}$$

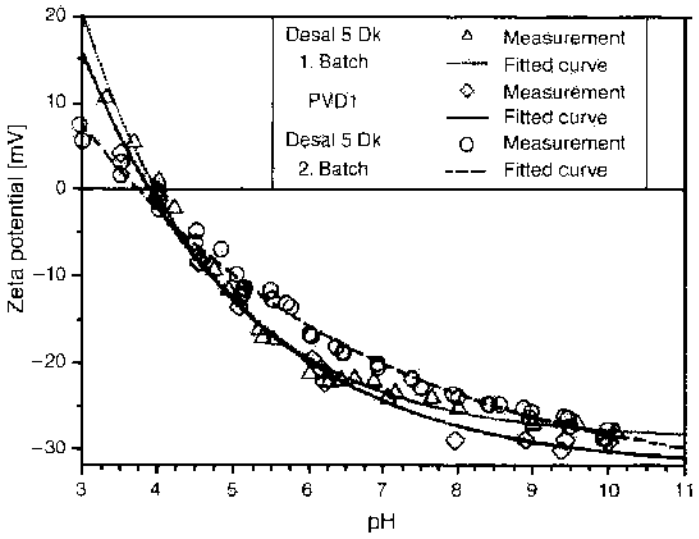

Figure 28. Zeta potential ζ determined experimentally (data) as a function of bulk pH from tangential streaming potential measurements, Desal5DK and NTR-729 (HN PVD1) nanofilters. Reprinted with permission from [34], Hagmeyer and Gimbel, *Sep. Purif. Technol.* 15, 19 (1999). © 1999, Elsevier.

where

$$\lambda_D = \left(\frac{\varepsilon RT}{2F^2 I}\right)^{1/2} \tag{120}$$

is the usual Debye length based on the ionic strength I.

By assuming that the pore wall surface charge density can be estimated from the exposed planar surface one (i.e., $\sigma_i \approx \sigma_{ek}$), the effective membrane charge density can be estimated from Eq. (50), provided that the effective pore radius r_p is known. In Refs. [32, 34], the effective pore radius for an effective cylindrical pore was not estimated directly from neutral solute measurements but, rather, determined by fitting the salt rejection model to experiment; for the Desal5DK, this procedure led to a value for pore radius (~1.05–1.82 nm, depending on membrane batch) that is a factor of two to four bigger than more recent estimates based on neutral solute rejection [115].

2.7.2.1. Single Salts By also using the effective membrane thickness l_{eff} as an adjustable parameter (independent of salt and operating conditions), it was found that [1 : 1] single-salt rejection as a function of salt concentration (Fig. 29) and pH (Fig. 30) at various volume flux densities could be reasonably well predicted by the hindered ENP model, albeit without the steric term in ion partitioning [32, 34]. As expected for NF, the [1 : 1] salt (NaCl) rejection decreases with increasing concentration.

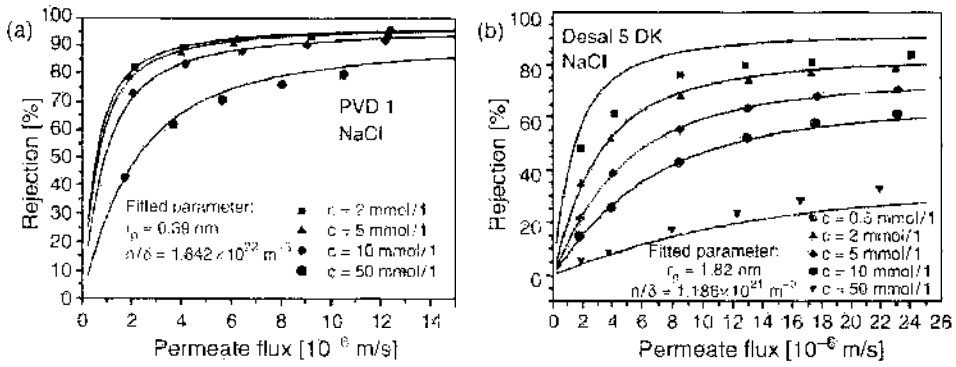

Figure 29. NaCl Rejection versus volume flux density for different salt concentrations at natural pH; experimental data and predictions of the hindered ENP model (without steric partitioning), using zeta-potential measurements to estimate membrane charge density (a) NTR-729 (HN PVD1); (b) Desal5DK. Reprinted with permission from [34], Hagmeyer and Gimbel, *Sep. Purif. Technol.* 15, 19 (1999). © 1999, Elsevier.

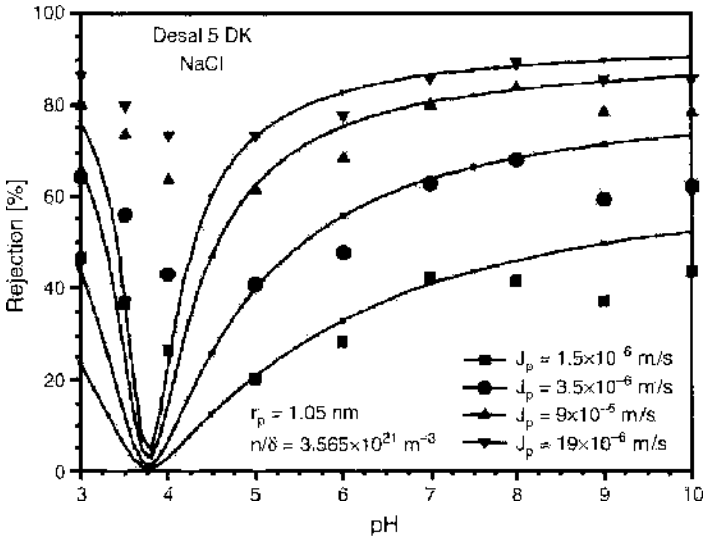

Figure 30. NaCl Rejection versus pH (Desal5DK) for various values of volume flux density at a salt concentration of 0.002 M; experimental data and predictions of the hindered ENP model (without steric partitioning), using zeta-potential measurements to estimate membrane charge density. Reprinted with permission from [34], Hagmeyer and Gimbel, *Sep. Purif. Technol.* 15, 19 (1999). © 1999, Elsevier.

For the salt possessing a divalent cation ($CaCl_2$), both membranes exhibited what may be considered at first sight to be atypical NF behavior: $CaCl_2$ rejection by the Desal5DK increased monotonically with increasing salt concentration over the range from 0.5 to 50 mM (Fig. 4b of Ref. [32]); for the NTR-729 nanofilter, over the same concentration range, $CaCl_2$ rejection first decreased and then increased with increasing salt concentration (Fig. 4d of Ref. [32]). Because this type of behavior cannot be explained using the negative effective membrane charge densities obtained from the zeta-potential measurements, it was suggested that an extended HET model (Table 3), including a Born exclusion term, could account in a reasonable way for such results [32, 115].

As noted in Refs. [32, 34] the IEP for the Desal5DK and NaCl salt, obtained using zeta-potential measurements, seemed to be one unit lower than the effective IEP indicated by the rejection measurements.

2.7.2.2. Binary NaCl/Na_2SO_4 Electrolyte Mixtures Thanks to the negative membrane charge density predicted by the streaming potential method, it was also found that the rejection of NaCl/Na_2SO_4 mixtures at a total salt concentration of 0.01 M for the NTR-729 and 0.002 M for the Desal5DK at natural pH could be well accounted for by the model (including negative rejection of Cl^- at low flux when NaCl is in the minority) (Fig. 31).

2.7.2.3. Binary NaCl/$CaCl_2$ Electrolyte Mixtures For the Desal5DK, negative rejection of Na^+ was observed at low flux for minority NaCl in NaCl/$CaCl_2$ mixtures. Such behavior could not be accounted for within the scope of the extended HET model using the negative membrane charge density predicted by zeta-potential measurements. This type of negative rejection for a minority monovalent cation is most probably an indication of positive membrane charge density (see section 2.7.3.3).

2.7.3. Comparative Study of NF200, Desal5DL, and Membralox Nanofilters

We present here part of a detailed experimental and theoretical study of the rejection of single salts and multielectrolyte mixtures by a ceramic TiO_2 (SCT Membralox) nanofilter at the borderline between ultra- and nanofiltration, as well as by two tighter organic nanofilters (NF200, Desal5DL) [35, 36]. Using NanoFlux in the HET model mode, the predictions for ion rejection for multielectrolyte solutions are obtained by solving numerically the hindered extended Nernst-Planck (ENP) ion flux equations. We find that, depending on the operating conditions, the looser ceramic nanofilter does not necessarily perform less well than the tighter organic ones. We also examine how well the rejection of multielectrolyte mixtures

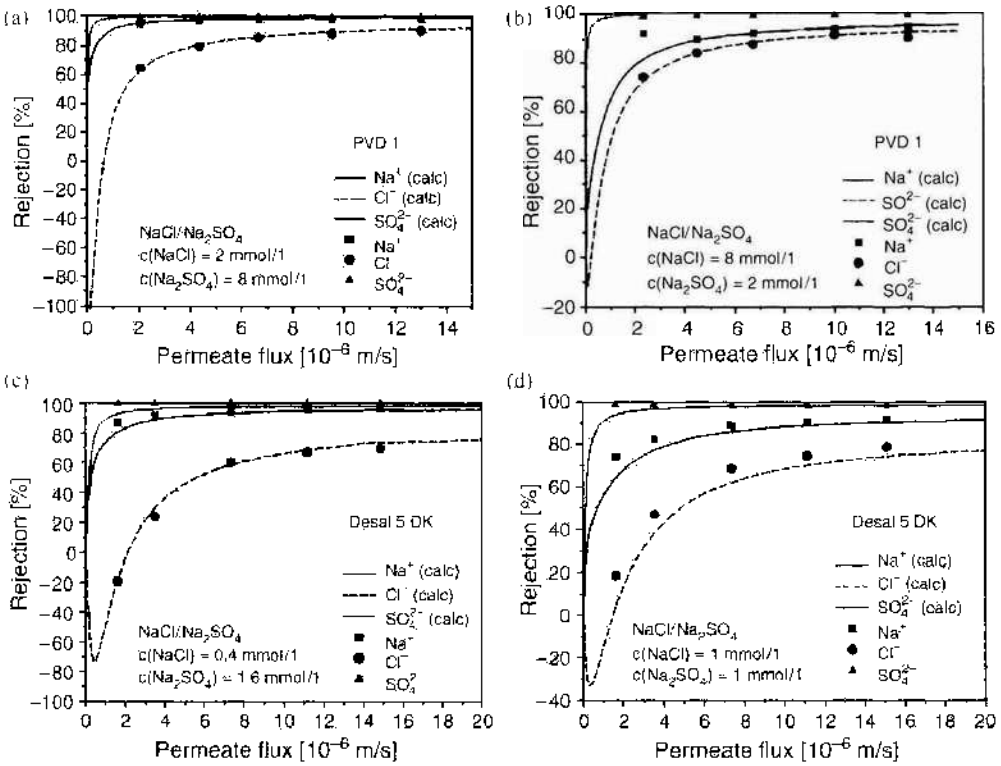

Figure 31. Ion rejection versus volume flux density for $NaCl/Na_2SO_4$ mixtures; experimental data and predictions of the hindered ENP model (without steric partitioning) at natural pH (using zeta-potential measurements to estimate membrane charge density): (a) 20/80 $NaCl/Na_2SO_4$, NTR-729 (HN PVD1), (b) 80/20 $NaCl/Na_2SO_4$, NTR-729 (HN PVD1), (c) 20/80 $NaCl/Na_2SO_4$, Desal5DK, and (d) equimolar (50/50) mixture, Desal5DK. Reprinted with permission from [34], Hagmeyer and Gimbel, *Sep. Purif. Technol.* 15, 19 (1999). © 1999, Elsevier.

can be predicted by hindered electro-transport theory, using a single-salt database, over a wide range of relative salt mole fractions.

The relatively high charge densities of ceramic nanofilters can induce strong electrostatic interactions, which can in turn lead to high limiting ionic rejection despite ionic sizes much smaller than the membrane pore size. The relatively large pore size of these ceramic NF membranes implies that ion rejection is controlled primarily, but not uniquely, by the long-range electrostatic interactions. The pore size is estimated experimentally from N_2 adsorption/desorption (ceramic membrane), and the rejection of model neutral solutes (organic nanofilters). An adjustable effective membrane thickness is introduced to account not only for morphological but also possible electrokinetic tortuosity effects.

2.7.3.1. Experimental Protocol The ceramic titania nanofilter studied (SCT US Filter, Membralox® NF Filter, MWCO 1000 Da) is a lightly sintered nanophase granular porous medium possessing an effective pore radius of $r_p \sim 1.5$ nm. The organic nanofilters studied (DOW FilmTEC NF200, MWCO 200 Da, $r_p \sim 0.38$ nm and GE-Osmonics Desal5DL, MWCO 300 Da, $r_p \sim 0.58$ nm) are tighter polymer membranes. To establish the single-salt NanoFlux database, rejection measurements were conducted on the ceramic membrane using single-salt solutions of NaCl, $NaNO_3$, $MgSO_4$, Na_2SO_4, and $CaCl_2$ at pH 3, 4, 6, and 9 for three different feed concentrations (10^{-3}, 10^{-2}, 10^{-1} [mol/l]). Similar measurements were also carried out on the two organic nanofilters, using single-salt solutions at pH 3, 7, and 10 for three different feed concentrations (5×10^{-4}, 5×10^{-3}, 5×10^{-2} [mol/l]). By varying the relative salt proportions, measurements were then carried out on a variety of mixed-salt solutions for different total salt feed concentrations and values of pH. Operating conditions were chosen to reduce concentration polarization (feed flow rates of ~360 l/h and ~600 l/h for the ceramic and organic membranes, respectively).

2.7.3.2. Single-Salt Database Using NanoFlux, the two parameters characterizing the membrane/salt pair within the scope of our model, namely, the effective charge density X_m

and effective membrane thickness l_{eff}, were determined, via a numerical fitting procedure, for the single salts as a function of feed concentration and pH. As stated earlier, we attempt to account for possible electrostatic hindrance contributions to the effective tortuosity (not included directly in the usual hindered diffusion coefficients) by allowing l_{eff} to be an adjustable parameter on the same footing as X_m. The best-fit parameter values minimize the difference between the experimental and theoretical rejections.

We find that X_m and l_{eff} vary as a function of the salt concentration c_s^f and pH^f of the feed. At low pH and salt concentration, we have accounted for the nonnegligible influence on salt transport of the acid (HCl) used to adjust the pH (see, e.g., Fig. 32). In other cases, we have, whenever possible, included the measured rejections of trace ions (including H^+ and OH^-) to justify our choice for the sign of the membrane charge.

The results of this analysis of single salts constitute the internal NanoFlux database. For NaCl there is an apparent IEP between pH 6 and 7 for the SCT membrane (amphoteric behavior, Fig. 33a), where X_m changes sign and l_{eff} appears to have a tendency to pass through a minimum (Fig. 33b). The effective membrane thickness for NaCl and ceramic membrane (Fig. 33b) appears to decrease with increasing salt concentration (as electrical effects get increasingly screened) and is generally much greater than the actual estimated thickness of the active layer (~1 μm). As noted earlier, this behavior is not yet well understood. For NaCl, the NF200 membrane appears to be negatively charged over almost the whole concentration and pH range studied experimentally (IEP near pH 5). Specific adsorption of the divalent Ca^{2+} cation, in contrast, appears to render both the TiO_2 membrane and the organic membranes positively charged over a large part of the concentration and pH range studied. The database for the SCT ceramic membrane and $CaCl_2$ is shown in Figs. 34a, 34b. We observe that at fixed feed concentration X_m, although mainly decreasing with pH, remains positive over the whole pH range studied. Furthermore, at fixed pH, X_m increases with increasing feed concentration. These results presented (Fig. 34b) again confirm that the effective membrane thickness l_{eff} is always much greater than the actual thickness of the NF active layer (~1 μm) and does indeed appear to vary with the operating conditions (feed concentration and pH). Despite its relatively large pore radius, the TiO_2 membrane possesses effective membrane charge densities high enough to lead to high limiting cation rejection at acid pH: The Na^+ limiting rejections are in the 24–65% range for NaCl when the feed concentration is near 10^{-2} [mol/l] and the pH is far enough from the IEP (<4 or >8); the Ca^{2+} limiting rejections are in the 30–95% range when the feed concentration is 10^{-2} [mol/l] and the pH is less than 10. Because NaCl and $CaCl_2$ rejection tends to decrease with

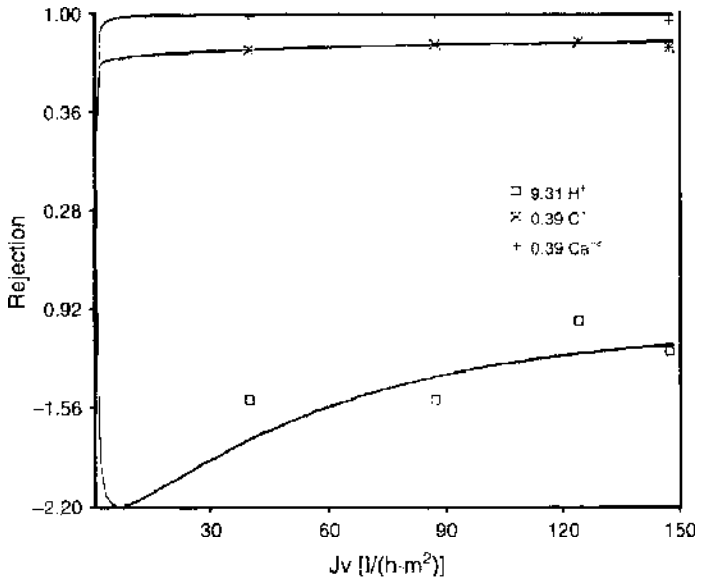

Figure 32. Ion rejection versus volume flux density: 15/85 $HCl/CaCl_2$ mixture and NF200 nanofilter; experimental data and HET model fit used to set up the single salt database ($CaCl_2$ concentration 0.0055 M, pH 3; fitted model parameters: $X_m = +0.057$ M and $l_{eff} = 15.7$ μm).

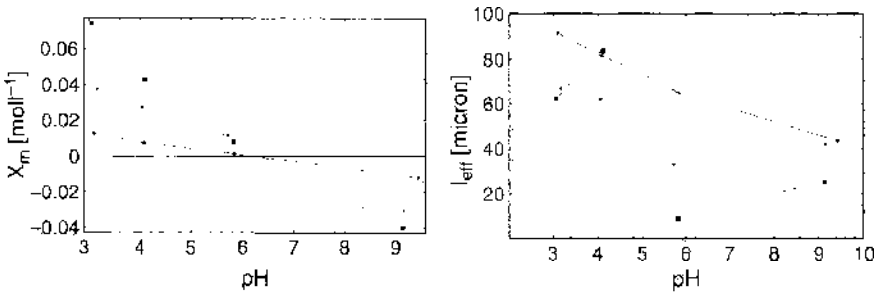

Figure 33. Salt database parameters for NaCl and SCT nanofilter (a) Effective membrane charge density X_m versus feed pH. (b) Effective membrane thickness l_{eff} versus feed pH (squares, 10^{-1} M; stars, 10^{-2} M; diamonds, 10^{-3} M). Reprinted with permission from [35], Palmeri et al. *Desalination* 147, 231 (2002). © 2002, Elsevier.

increasing salt concentration, for these salts the SCT ceramic membrane exhibits typical NF behavior. The organic nanofilters, however, can exhibit the type of $CaCl_2$ rejection behavior discussed in section 2.7.2.

2.7.3.3. Binary NaCl/CaCl$_2$ Electrolyte Mixtures We present here a part of our comparative study using binary and ternary electrolyte mixtures [35, 36]. The estimated values of X_m and l_{eff} for mixtures were obtained from the NanoFlux database using the interpolation and weighting scheme (WIC) presented earlier (section 2.6.3), in which the weight of each salt in the mixture is based on its ionic strength, rather than its concentration (cf. Ref. [33]).

In Figures 25–29, we present experimental results and NanoFlux simulations for binary $NaCl/CaCl_2$ mixtures at a total feed concentration of $c_{tot}^f = 10^{-2}$ [mol/l] and natural pH^f (5–6.5) for various relative salt mole fractions (nearly pure NaCl, majority NaCl, equimolar, majority $CaCl_2$, nearly pure $CaCl_2$). For nearly pure salts with traces, we present only NanoFlux simulations, as the single pure salt results are part of the NanoFlux database. For future experiments, it should be kept in mind that it is helpful to have trace ion rejection results in hand when fitting the transport model to the data.

In most of the cases studied here at natural pH, X_m is negative for pure NaCl and positive for pure $CaCl_2$. Natural pH is also close to the IEP for NaCl and some of the membranes studied, and this further complicated matters, because ion rejection is a rapidly varying function of pH in the range around the IEP (see, e.g., Fig. 30). These experimental results therefore present a severe test for the HET model and the NanoFlux database. The model predictions, discussed below, are in generally good agreement with the experiment, the only exception being for the *Desal5DL* nanofilter and the 90/10 $NaCl/CaCl_2$ mixture.

2.7.3.3.1. Nearly Pure NaCl In Figure 35 we show rejection results for nearly pure NaCl with trace amounts of $CaCl_2$. In this case the NaCl results are nearly identical to those used for establishing the single salt database.

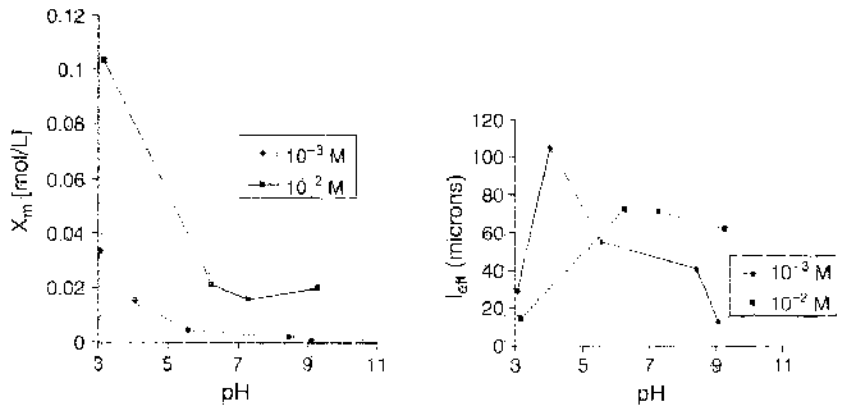

Figure 34. Salt database parameters for $CaCl_2$ and SCT nanofilter (a) Effective membrane charge density X_m versus feed pH. (b) Effective membrane thickness l_{eff} versus feed pH (squares, 10^{-2} M; diamonds, 10^{-3} M). Reprinted with permission from [36], Lefebvre et al., *Sep. Pur. Tech.* 32, 117 (2003). © 2003, Elsevier.

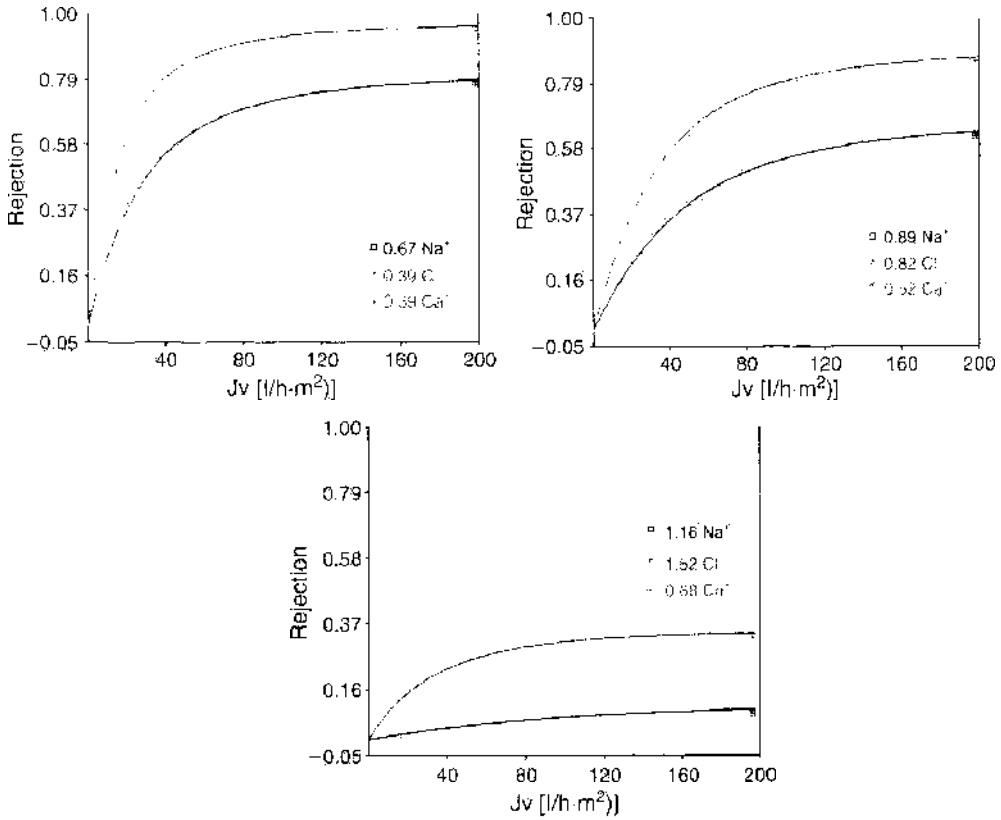

Figure 35. Ion rejection versus volume flux density: HET model calculations for a 100/trace binary $NaCl/CaCl_2$ mixture at a total feed concentration of $C_{tot}^f = 10^{-2}$ M and natural pH^f (5–6.5) (a) NF200 (b) Desal5DL (c) SCT, Membralox.

2.7.3.3.2. Majority NaCl For majority NaCl (Fig. 36) and the *NF200* nanofilter, we observe moderate rejection and separation of divalent cations Ca^{2+} from monovalent ones Na^+. Because of the moderate negative effective membrane charge density predicted by the NanoFlux database for this mixture, the simulations for the 90/10 mixture are in good agreement with experiment. For the *Desal5DL*, however, the observed selectivity is reasonably high for this mixture, in disagreement with the NanoFlux predictions. In this case, the experimental rejection results would indicate rather a positive membrane charge density, whereas the NanoFlux database predicts a moderate negative one. In this case, it turns out that none of the weighting methods presented in section 2.6.3 are capable of giving sufficient weight to the positive membrane charge density contributed by the minority $CaCl_2$. For a 95/05 mixture and the *SCT* nanofilter, the observed rejection and cation selectivity are both low, in good agreement with the NanoFlux predications (thanks to the weak positive membrane charge density predicted by the NanoFlux database). This comparative study shows that at this feed concentration, composition, and pH, the looser *SCT* membrane performs less well than the organic nanofilters.

2.7.3.3.3. Equimolar Mixture In Figure 37, we present experimental results and NanoFlux simulations for the three nanofilters for 50/50 binary mixtures. For the organic nanofilters, we observe good separation of divalent cations Ca^{2+} from monovalent ones Na^+, especially at low to intermediate volume flux, where Na^+ is concentrated in the permeate (negative rejection). Overall, the agreement between the simulations and experiment is reasonably good, although the NanoFlux database does tend to overestimate slightly the positive membrane charge density for the *Desal5DL*.

2.7.3.3.4. Majority $CaCl_2$ In Figure 38, we present experimental results and NanoFlux simulations for 10/90 mixtures for the *NF200* and *Desal5DL* nanofilters and for 20/80 mixtures for the ceramic membrane. For the organic nanofilters, we observe very good separation of divalent cations Ca^{2+} from monovalent ones Na^+, especially at low to intermediate volume flux, where Na^+ is strongly concentrated in the permeate (strong negative rejection).

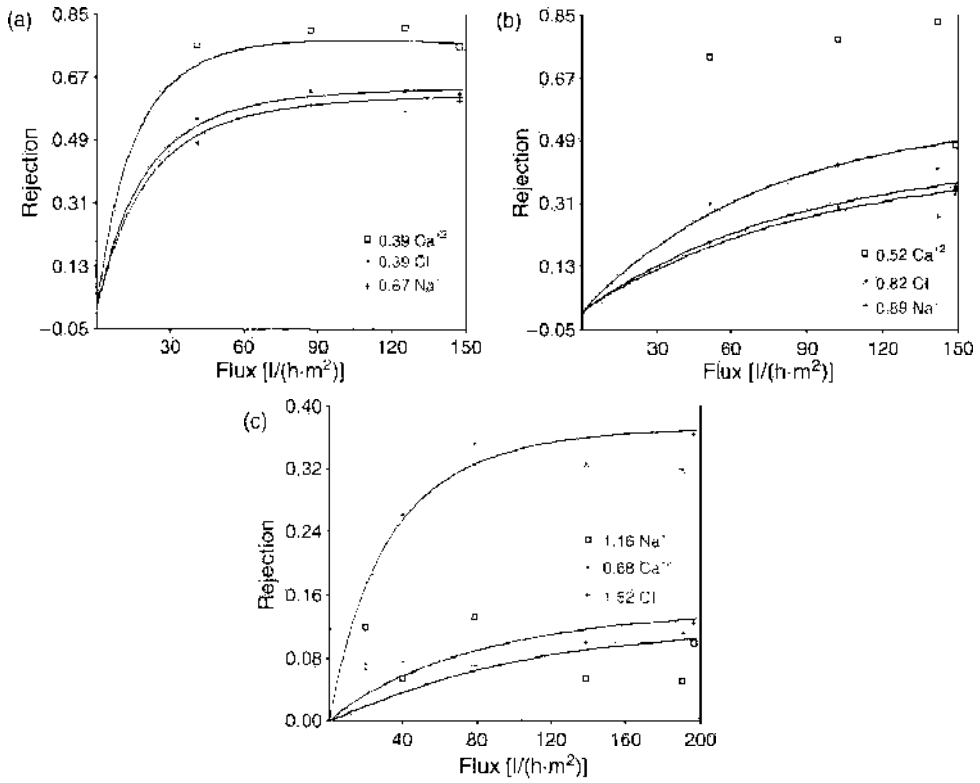

Figure 36. Ion rejection versus volume flux density: Experimental results and HET model simulations for a binary $NaCl/CaCl_2$ mixture with majority NaCl at a total feed concentration of $C_{tot}^f = 10^{-2}$ M and natural pH^f (5–6.5) (a) 90/10 mixture, NF200 (b) 90/10 mixture, Desal5DL (c) 95/05 mixture, SCT, Membralox. Reprinted with permission from [36], Lefebvre et al., *Sep. Pur. Tech.* 32, 117 (2003). © 2003, Elsevier.

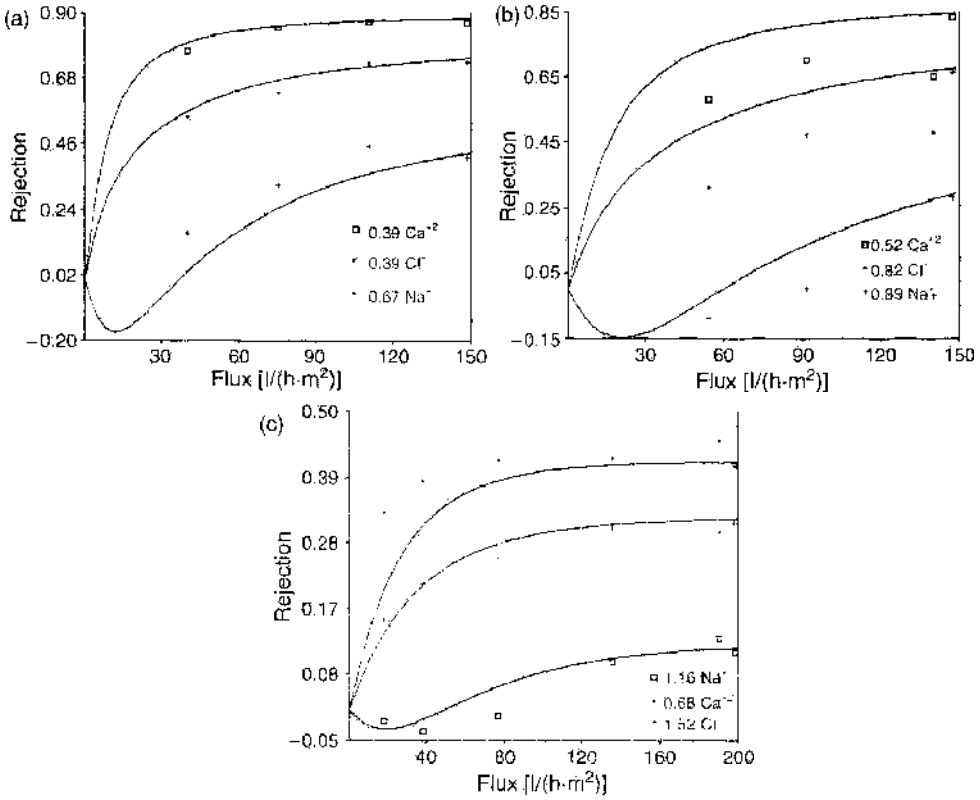

Figure 37. Ion rejection versus volume flux density: Experimental results and HET model simulations for a equimolar binary $NaCl/CaCl_2$ mixture at a total feed concentration of $C_{tot}^f = 10^{-2}$ M and natural pH^f (5–6.5) (a) NF200 (b) Desal5DL (c) SCT, Membralox. Reprinted with permission from [35], Palmeri et al. *Desalination* 147, 231 (2002). © 2002, Elsevier.

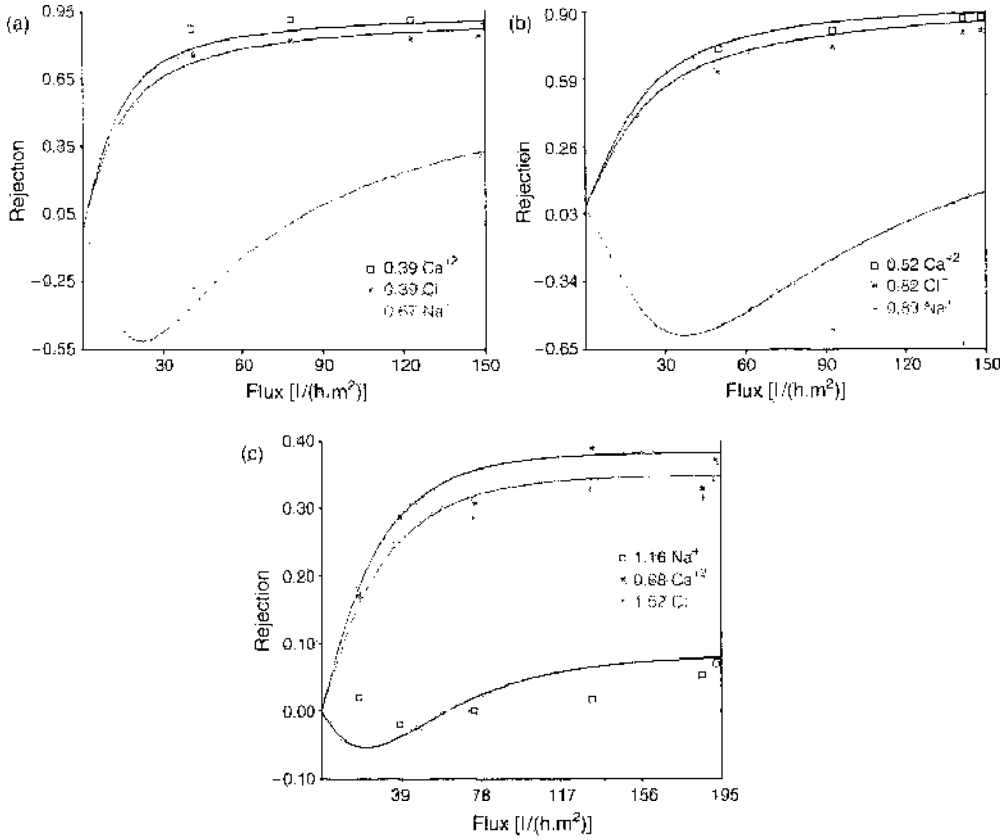

Figure 38. Ion rejection versus volume flux density: Experimental results and HET model simulations for a binary NaCl/$CaCl_2$ mixture with majority CaCl2 at a total feed concentration of $C_{tot}^f = 10^{-2}$ M and natural pH^f (5–6.5) (a) 10/90 mixture, NF200 (b) 10/90 mixture, Desal5DL (c) 20/80 mixture, SCT, Membralox. Reprinted with permission from [36]: Lefebvre et al., *Sep. Pur. Tech.* 32, 117 (2003). © 2003, Elsevier.

For the SCT nanofilter, we observe and predict low Na^+ and moderate Ca^{2+} rejection and therefore modest monodivalent cation selectivity. Thanks to the moderate to high positive charge density predicted by the NanoFlux database, the simulations are in good agreement with experiment; in particular, they can account for the strong negative rejection of the monovalent co-ion (Na^+) observed at low flux for the two organic nanofilters.

2.7.3.3.5. Nearly Pure $CaCl_2$ In Figure 39 we show rejection results for nearly pure $CaCl_2$ with trace amounts of NaCl. In this case, the $CaCl_2$ results are identical to those used for establishing the single-salt database.

2.7.3.3.6. Summary In Figures 35–39 we have presented simulations of multielectrolyte solutions of NaCl and $CaCl_2$ for several relative salt proportions, at a total salt concentration of 10^{-2} [mol/l] and natural pH for the ceramic and two organic nanofilters. On these plots, we note that the NanoFlux predictions for mixtures going from majority NaCl (Fig. 36) to equimolar (Fig. 37), and finally to majority $CaCl_2$ (Fig. 38) obtained using the internal database are in generally good agreement with experiment. Although the predicted effective membrane charge density can take on positive and negative values, the same order of ion rejection is observed [$R(Ca^{2+}) > R(Cl^-) > R(Na^+)$] and predicted in all cases. In the conditions studied here, it is also possible to class the membranes according to their overall performance: R(NF200 > R(Desal5DL) > R(SCT), which follows the estimated pore size.

In Figure 38, we observe that the rejection of a small amount of Na^+ added to $CaCl_2$ can be negative at low volume flux and is always much lower than that of Ca^{2+}; such behavior is a clear signature of a positive membrane charge. The simultaneous high rejection of Ca^{2+} and low Na^+ rejection at low volume flux in 50/50 mixtures (Fig. 37) is also a clear sign of a positive membrane charge. The high rejection of Ca^{2-} for positively charged membranes is mainly because of strong Donnan/steric exclusion at the feed/membrane interface (Figs. 37–39). The low rejection of Na^- for positively charged membranes is a result of its relatively

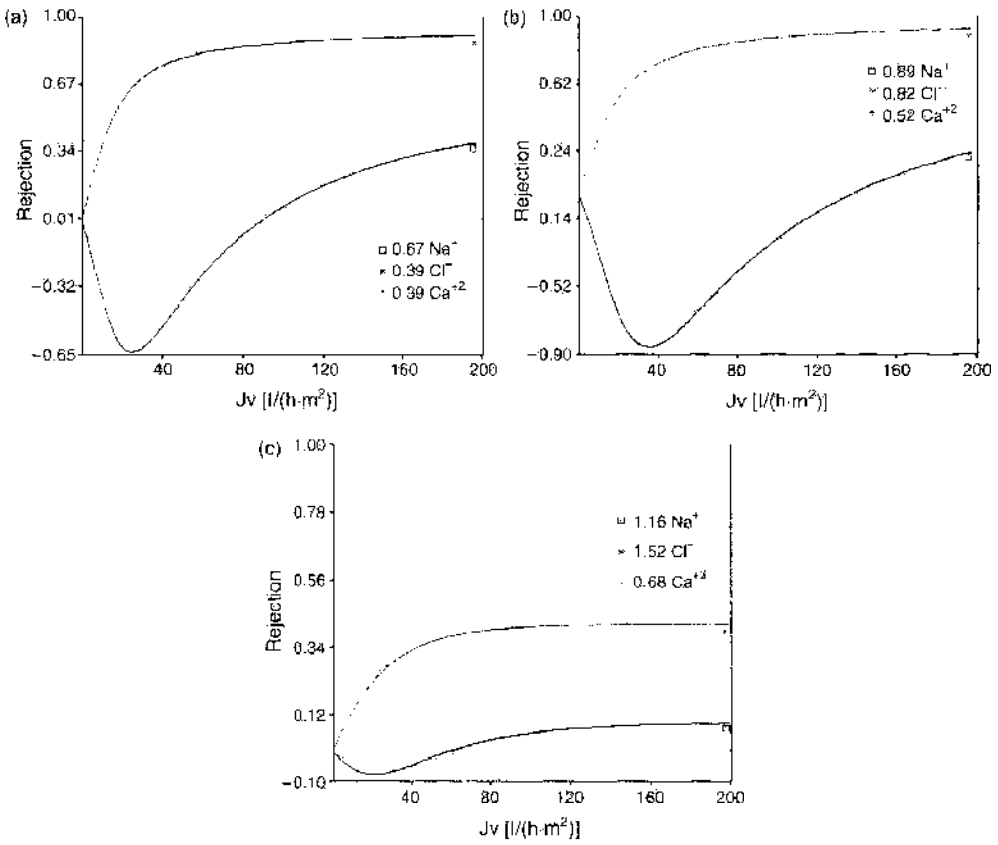

Figure 39. Ion rejection versus volume flux density: HET model calculations for a trace/100 binary $NaCl/CaCl_2$ mixture at a total feed concentration of $C_{tot}^{f} = 10^{-2}$ M and natural pH^{f} (5–6.5) (a) NF200 (b) Desal5DL (c) SCT, Membralox.

weak Donnan/steric exclusion, combined with its strong electrical migration in the streaming potential, which tends to favor the transmission of co-ions. In Figure 36, we observe that, in contrast to what occurs for Na^+ in majority $CaCl_2$ (Figs. 38, 39), the rejection of a small amount of divalent cation (Ca^{2+}) added to NaCl is always higher than that of Na^+. Somewhat surprisingly at first sight, this behavior is observed irrespective of the sign of the membrane charge. For majority $CaCl_2$ and positive membrane charge, the large observed gap between $R(Ca^{2+})$ and $R(Na^+)$ (Figs. 36c and 36b) is a result of the strong Donnan/steric exclusion of Ca^{2+} (already evoked earlier). For negative membrane charge, the gap between $R(Ca^{2+})$ and $R(Na^+)$, now smaller (Fig. 36a), still exists, as the strong Donnan attraction for Ca^{2+} is completely counterbalanced by its stronger retardation in the membrane streaming potential resulting from the higher relative mobility, $\bar{\mu}_i = z_i \bar{D}_i$, of Ca^{2+} in the membrane compared with that of Na^+. The change in membrane polarity observed for the organic nanofilters as the $CaCl_2$ mole fraction is increased (going from Fig. 35 to Fig. 39) probably occurs because in the case of majority $CaCl_2$, specific adsorption of the divalent cation renders the membrane positively charged; in contrast, in the case of majority NaCl, natural pH is above the IEP (at this total salt concentration), and therefore the membrane is negatively charged. The simulations presented here indicate that this evolution from negative to positive effective membrane charge density is well accounted for by the NanoFlux database, except for the Desal5DL nanofilter and 90/10 $NaCl/CaCl_2$ mixture.

This comparative study shows that at a total salt concentration of 10^{-2} [mol/l] and natural pH, the organic nanofilters, thanks in great part to their smaller pore size, outperform their ceramic counterpart.

2.7.3.4. Ternary Electrolyte Mixtures

2.7.3.4.1. NaCl/CaCl₂/HCl Mixtures In Figure 40 we present experimental results and NanoFlux simulations for the *SCT* nanofilter for 45/50/05 ternary mixtures of $NaCl/CaCl_2$/HCl, and NanoFlux simulations only for the *NF200* and Desal5DL nanofilters for 45/45/10

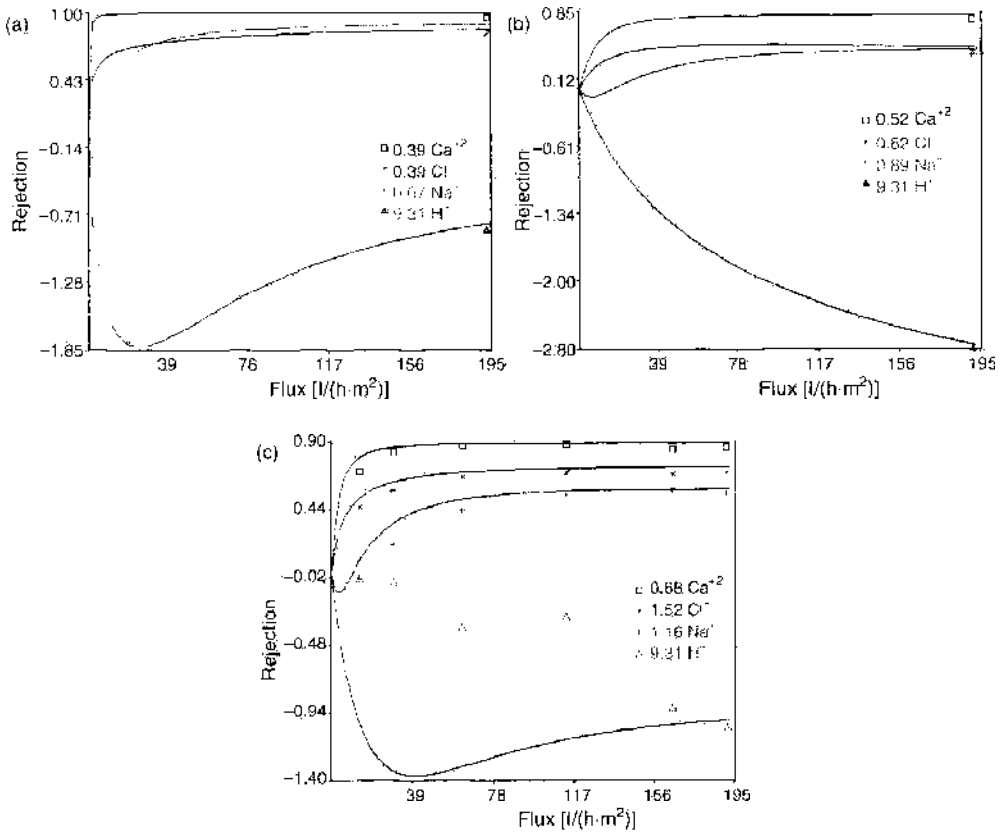

Figure 40. Ion rejection versus volume flux density: HET model simulations for the (a) NF200 and (b) Desal5DL nanofilters for 45/45/10 ternary mixtures of NaCl/$CaCl_2$/HCl; (c) experimental results and HET model simulations for the *SCT* nanofilter for a 45/50/05 ternary mixture of NaCl/$CaCl_2$/HCl (salt concentration of $C^f_{tot} = 10^{-2}$ M and pH 3). Reprinted with permission from [36], Lefebvre et al., *Sep. Pur. Tech.* 32, 117 (2003). © 2003, Elsevier.

ternary mixtures of NaCl/$CaCl_2$/HCl (at a total salt concentration of $c^f_{tot} = 10^{-2}$ [mol/l] and pH 3). For the SCT membrane, both negative H^+ rejection and very high salt cation rejections are observed experimentally and predicted theoretically, even at high volume fluxes. This type of rejection behavior could be useful in industry as an economic way of separating acids from salts by simultaneous acid concentration in the permeate and salt rejection in the retentate. Thanks to its relatively high positive membrane charge density at low pH, the *SCT* membrane performs as well as the organic nanofilters under these operating conditions. The higher hydraulic permeability of the ceramic membrane [about 21 l/(h m^2 bar) for pure water] leads to a higher productivity, which indicates that, all other factors considered equal, under these operating conditions the larger pore ceramic membrane might be the better choice.

In Figure 41a, we present experimental results and NanoFlux simulations for the SCT membrane for ion rejection as a function of feed pH for NaCl/$CaCl_2$/HCl mixtures at a total feed salt concentration (NaCl + $CaCl_2$) of 0.011 M and pH > 3. The NanoFlux simulations account well for the increase in NaCl and $CaCl_2$ rejection with decreasing pH and predict a strong drop in Cl^- rejection at pH less that 3 (unfortunately, at this total feed salt concentration, we do not have experimental data in this pH range). To examine more carefully ion rejection in the pH range (5–10) where the added acid (HCl) is so dilute that it has little direct influence on salt transport, we present in Fig. 41b, experimental results and NanoFlux simulations for the SCT membrane for ion rejection as a function of feed pH for NaCl/$CaCl_2$ mixtures at a total feed salt concentration (NaCl + $CaCl_2$) of 0.01 [mol/l]. Because the volume flux density reaches a maximum (Fig. 42a) and the electrical filtration potential vanishes (Fig. 42b) there, the pH (~8.7) at which the three ion rejection curves cross (Fig. 41b) is the IEP for this mixture.

2.7.3.4.2. $NaNO_3$/NaCl/$CaCl_2$ Mixtures In Figure 43, we present experimental results and NanoFlux simulations for the two organic nanofilters and simulations only for the ceramic

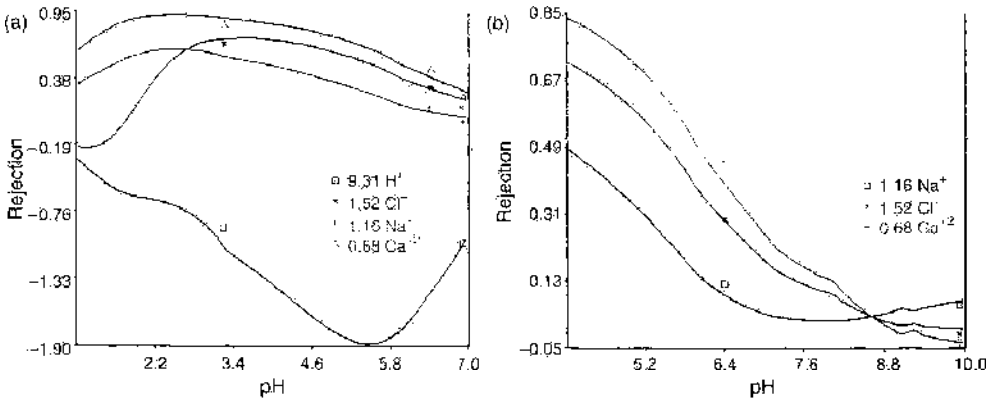

Figure 41. Ion rejection versus pH: Experimental results and HET model simulations for the SCT nanofilter for (a) equimolar NaCl/$CaCl_2$ mixtures + HCl and (b) equimolar NaCl/$CaCl_2$ mixtures [fixed feed salt concentration (NaCl + $CaCl_2$) of 0.01 M].

nanofilter for equimolar ternary mixtures of $NaNO_3$/NaCl/$CaCl_2$ at $c_{fi}^{f} = 1.5 \times 10^{-2}$ [mol/l], pH^f 5.3. Thanks to the predicted positive effective membrane charge density, we observe once again good separation of divalent cations from monovalent ones at intermediate volume flux. These important results, obtained without adjustable parameters using the internal NanoFlux database, for a relatively complex salt mixture with four distinct ionic species, show the coherence of our choice of ionic radii. Within the scope of our model, the gap that opens between the rejection curves of the two monovalent anions (Cl^- and NO_3^-) at high volume flux is entirely caused by the difference in ionic crystal radius. This difference in size influences their partitioning into the membrane. More important, it also strongly modifies the relative anion diffusivity in the membrane ($\bar{D}_{Cl^-}/\bar{D}_{NO_3^-} \approx 5$) with respect to that in the bulk ($D_{Cl^-}/D_{NO_3^-} \approx 1$) and leads to a higher rejection for the smaller, more mobile counter-ion (Cl^-) at high volume flux because of migration in the electric field engendered by the streaming potential (which, because of the positive membrane charge, tends to retard more mobile anions more strongly than less mobile ones). Neither the ET model (without hindrance effects) nor the HET model using the Stokes-Einstein ionic radii can explain the results presented in Figure 43 (because these two anions have nearly identical bulk diffusivities, both of these models predict nearly identical anion rejections). However, we observe in Figure 43 that the HET model with the crystal choice of ionic radius allows us to account for the difference in ion selectivity for anions (NO_3^- and Cl^-) of the same valence, but very different bare size. Moreover, the simulations also indicate that the looser ceramic nanofilter should perform less well than the organic nanofilters under these filtration conditions.

2.7.3.5. Nanofiltration of Real Drinking Water (NF200) Real drinking water can contain seven or more predominant ions (and a large number of traces) and cannot easily be resolved

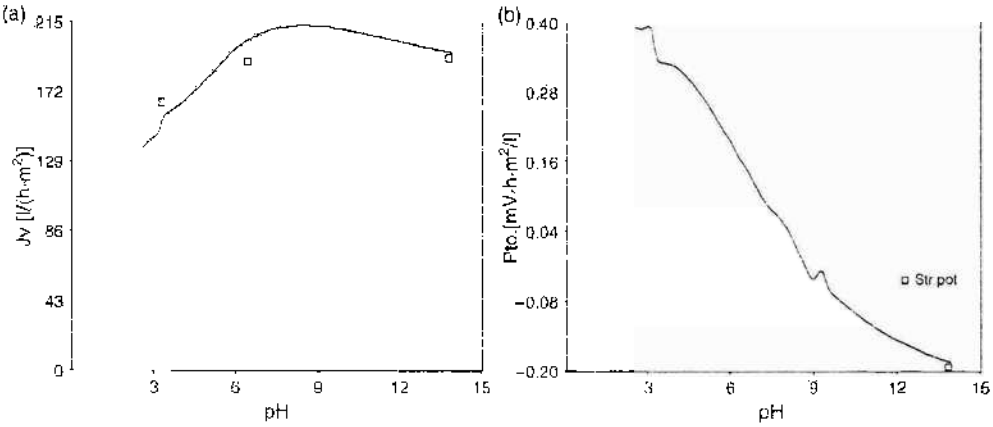

Figure 42. SCT nanofilter, equimolar NaCl/$CaCl_2$ mixtures + HCl (fixed applied pressure 10 bar) (a) Volume flux density versus pH, experimental results and HET model simulations; (b) reduced streaming potential, ν_r, versus pH, HET model simulations [fixed feed salt concentration (NaCl + $CaCl_2$) 0.01 M].

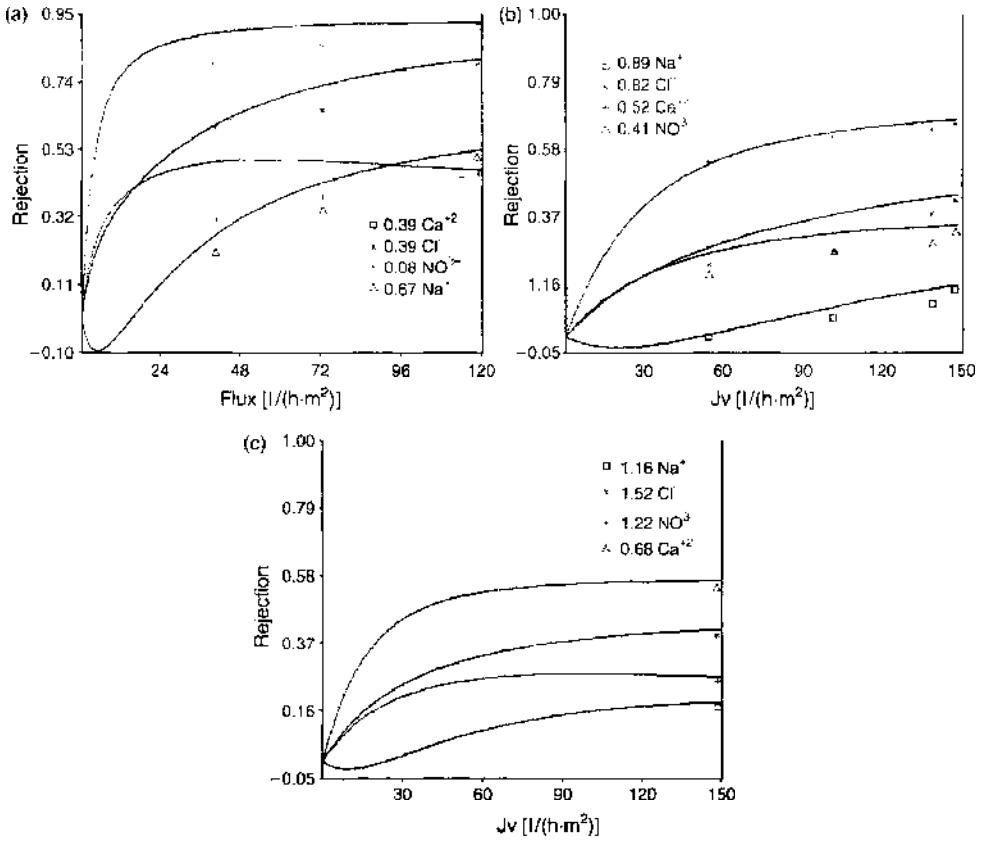

Figure 43. Ion rejection versus volume flux density for equimolar ternary mixtures of $NaNO_3/NaCl/CaCl_2$ at $C_{tot}^f = 1.5 \times 10^{-2}$ M, pH^f 5.3: experimental results and HET model simulations for the (a) NF200 and (b) Desal5DL nanofilters; (c) NanoFlux simulations for the *SCT* nanofilter. Reprinted with permission from [35], Palmeri et al., *Desalination* 147, 231 (2002). © 2002, Elsevier.

into a mixture of different salts. To be able to use NanoFlux to estimate the membrane parameters for arbitrary ion mixtures, we have developed a method to first transform a given ion mixture into an equivalent mixture of generic ions and then transform this mixture of generic ions into a mixture of at most three generic salts contained in the single salt

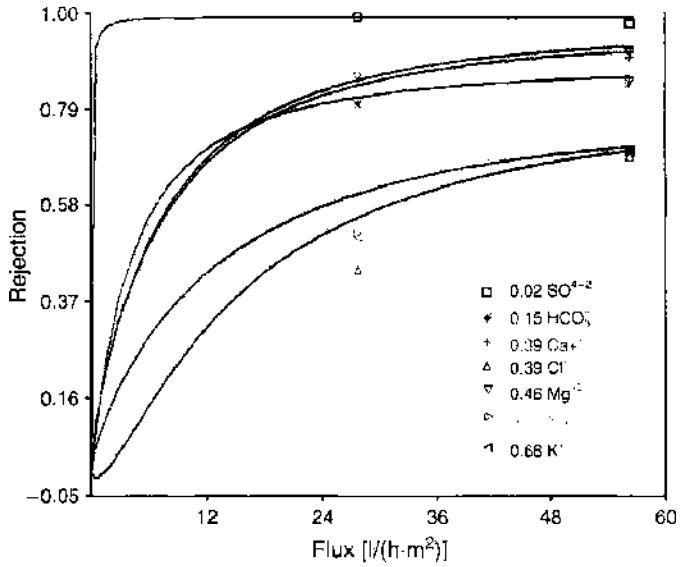

Figure 44. Ion rejection versus volume flux density: Experimental results and HET model simulations for the NF200 nanofilter and real drinking water (seven predominate ionic species at a total ionic strength of 0.016 M and pH 8.1) (estimated values of membrane parameters: $X_m = -3.59 \times 10^{-2}$ M, $l_{eff} = 12.76$ μm); (see Table 4 for ion concentrations).

database [35, 36]. In Figure 44 we see that simulation performed using NanoFlux permits us to account for the full complexity of real drinking water ionic rejection for the NF200 nanofilter (in Table 4, we list the ionic concentrations for the seven predominate ionic species in the drinking water at pH 8.1 and total ionic strength 0.016 [mol/l]).

The simulations account for the very high rejection (>98%) of the sulfate ion (present at relatively low concentrations), the high bicarbonate (HCO_3^-) and divalent cation (Ca^{2+} and Mg^{2+}) rejections (>80%), and the moderate monovalent cation (K^+ and Na^+) and chloride (Cl^-) rejections. This type of rejection performance shows that nanofiltration can be useful for reducing the amount of sulfate and decreasing the concentration of divalent cations (water softening). The simulations not only reproduce the correct order of rejection for all the seven species but also predict the absence of monovalent cation (K^+ and Na^+) selectivity for this membrane. Within the HET model, this last result is caused by the combination of higher bulk diffusivity and larger crystal ion radius of K^+ compared with Na^+. As a result of hindered transport effects, this results in the same intramembrane diffusivity for both of these species. The roughly equivalent predicted cation rejection shows that, in this particular case, cation electrical migration in the membrane (roughly the same for K^+ and Na^+) predominates over the steric exclusion effect in the partition coefficient (stronger for the larger K^+ than for smaller Na^+). These encouraging results indicate that modeling could indeed be useful in real water treatment NF.

2.7.4. Homemade Hafnia Ceramic Nanofilter

A hafnia ceramic nanofilter [37, 38] and a new generation of titania nanofilters [7, 22] have recently been introduced with pore sizes that are smaller than those usually attributed to the currently known commercial ceramic nanofilters, We discuss in this and the next subsection the nanofiltration of neutral solutes and electrolytes by these membranes. Similar NF studies were carried out for inorganic nanofilters in Refs. [89, 92, 108–114].

We treat the hafnia nanofilters prepared and studied in our laboratory as consolidated granular porous media and use the hindered transport model for neutral solutes and, neglecting ion size, the ET model for ions without any adjustable parameters to account for the observed limiting rejection of neutral and charged species.

2.7.4.1. Neutral Solutes In Figure 45, the hindered transport theory has been used for neutral solutes to predict, using the experimentally determined solute and membrane pore radii, the limiting rejection (obtained at high volume flux) of four organic molecules. The effective membrane pore radius was estimated from the hydraulic radius $r_H \approx 0.75$ nm, measured by N_2 adsorption/desorption, using structural models for ceramic membranes prepared from metal oxides (three-dimensional packings of hard spheres) that indicate that $r_p = 1.4 \times r_H \approx 1.0$ nm. There is good agreement between the theoretical rejection of neutral model solutes and experiment for this nanofilter, especially considering that no adjustable parameters have been introduced [37, 38].

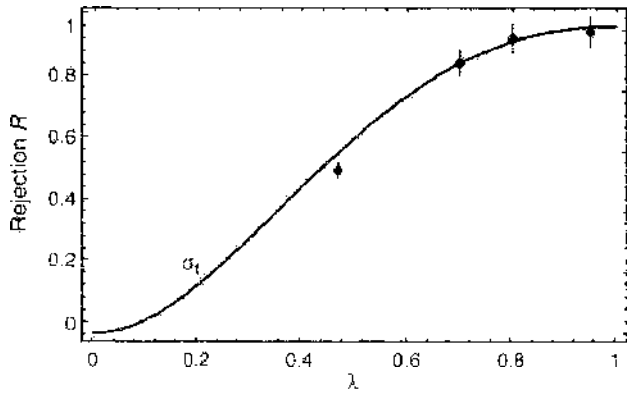

Figure 45. Limiting neutral solute rejection as a function of $\lambda = r_s/r_p$: Hafnia nanofilter experimental data for sucrose (MW 342), PEG 400 (MW 400), PEG 600 (MW 600), and PEG 1000 (MW 1000); spherical solute rejection coefficient, σ_t (solid curve), predicted by the capillary pore hindered transport theory. Reprinted with permission from [38], Palmeri et al., *J. Membr. Sci.* 179, 243 (2000). © 2000, Elsevier.

Table 4. Ionic concentrations in drinking water nanofiltered with the NF200 membrane.

Ion	Na^+	K^+	Mg^{2+}	Ca^{2+}	Cl^-	SO_4^{2-}	HCO_3^-
Concentraion [mmol/l]	8.38	0.20	1.1	1.3	6.74	0.30	6.03

2.7.4.2. Single Salts To use the ET model to calculate the limiting rejection of symmetric and asymmetric single salts without any adjustable parameters, we use the electrophoretic mobility μ_E, measured on the ceramic powder used to prepare the membrane, to estimate the effective membrane charge density. Under certain conditions, it is possible to use the simplified Smoluchowski equation to translate the measured μ_E into an estimate for membrane material electrokinetic surface charge density, σ_{ek} (Fig. 46). These conditions are weak zeta-potential ζ, and thin electrical double layer thickness ($\sim\lambda_D$), compared with r_{agg}, the radius of the powder particles (agglomerates),

$$\lambda_D \ll r_{agg} \tag{121}$$

In this case, $\mu_E \approx \varepsilon\zeta/\eta$ and $\sigma_{ek} \approx \varepsilon\zeta/\lambda_D$ [see Eqs. (118)–(120)]. Under the assumption that $\sigma_i \approx \sigma_{ek}$, it is possible to obtain an estimate for the membrane volume charge density, X_m (provided the membrane hydraulic radius is known, see above):

$$X_m \approx 0.10\frac{\sigma_{ek}}{r_H} = 0.30\frac{\mu_E I^{1/2}}{r_H} \tag{122}$$

with X_m and I in [mol/l], μ_E in $\mu C/cm^2$, μ_E in $(\mu m/s)/(V/cm)$, and r_H in nm [37, 38]. As discussed in section 2.4.1.4, this method for estimating X_m is similar to the tangential streaming potential method, in that the surface charge density of an exposed membrane material surface is probed and not the surface charge density in the pore interior.

When the theoretical (ET model) limiting rejections for three symmetric and two asymmetric salts are plotted as a function of the normalized membrane charge density, we establish curves that serve as a signature for membranes that reject ions mainly by electrostatic interactions. We then compare, using the experimentally determined effective membrane charge densities [obtained using the results in Fig. 46 and Eq. (122)], the theoretical predictions for the limiting rejection with the experimental results for the five salts and, aside from one experimental point, find reasonably good agreement without any adjustable parameters (Fig. 47).

If the limiting rejections of symmetric salts are only slightly asymmetric about the IEP (because of the different diffusivities of the cation and anion), the limiting rejections of asymmetric salts are, on the contrary, highly asymmetric, because of the marked change in co- and counter-ion valences when the membrane charge changes sign and the roles of

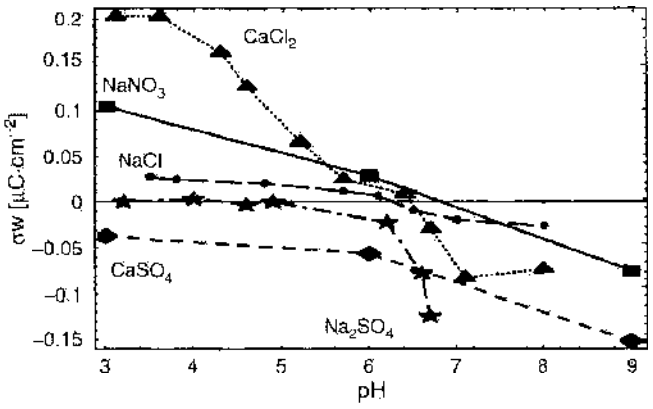

Figure 46. Hafnia nanofilter experimental data for the surface charge density σ_i as a function of the bulk (feed) solution pH (estimated from the electrokinetic surface charge density σ_{ek} deduced from the measured electrophoretic mobility). Reprinted with permission from [38], Palmeri et al., *J. Membr. Sci.* 179, 243 (2000). © 2000, Elsevier.

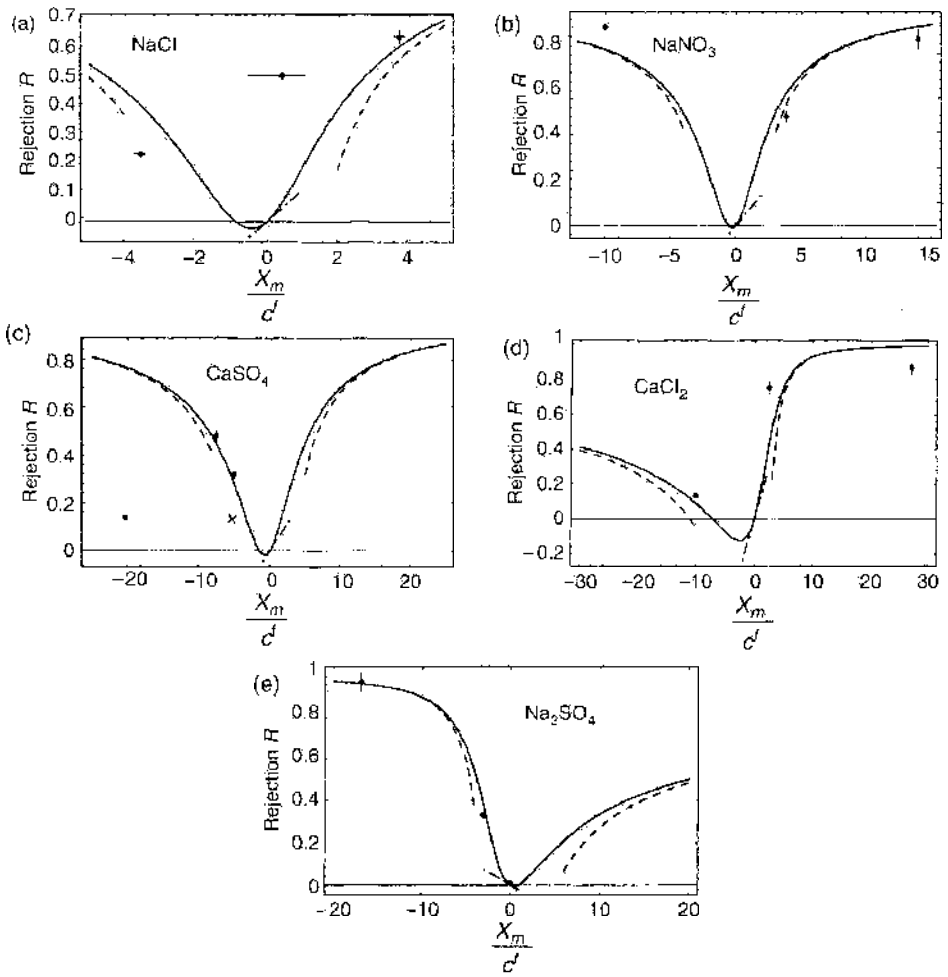

Figure 47. Hafnia nanofilter experimental data and theoretical predictions for the limiting salt rejection, R as a function of normalized membrane charge density (eletrophoretic mobility measurements used to estimate membrane charge density): exact homogeneous theory results (solid curves), weak charge homogeneous results (dot-dash curves), homogeneous good co-ion exclusion (GCE) results (dashed curves); salt concentration 10^{-3} M: (a) NaCl, (b) $NaNO_3$, (c) $CaSO_4$, (d) $CaCl_2$, and (e) Na_2SO_4. Reprinted with permission from [38], J. Palmeri et al., *J. Membr. Sci.* 179, 243 (2000). © 2000, Elsevier.

co- and counter-ion are reversed. Taking as an example the experimentally relevant case of a (1 : 2) and (2 : 1) salts, we see that for one membrane charge polarity, there will be a divalent co-ion that will be strongly rejected by Donnan exclusion at high membrane charge, whereas the monovalent counter-ion will only be weakly attracted by the membrane, leading to high rejection; for the opposite membrane charge polarity, conversely, the monovalent co-ion will only be weakly excluded and the divalent counter-ion will be strongly attracted by the membrane, leading to a low rejection, which can even become strongly negative for small values of normalized membrane charge density $\xi = X_m/c_s^f$. This asymmetry in the rejection is mainly a result of the strong influence of co- and counter-ion electrochemical valences on the co-ion Donnan partition coefficient. This valence asymmetry leads to the strongly skewed, S-shaped, theoretical rejection curves for the two asymmetric salts presented in Figure 47, which provides a clear signature of electrostatic interactions.

2.7.5. New Ceramic Titania Nanofilter

In Refs. [7, 22], a new titania nanofilter has been prepared and its filtration performance compared with a wide range of commercial ceramic nanofilters. These experimental studies led to the conclusion that this new generation of TiO_2 membranes has a tighter porous structure than that usually attributed to the currently known commercial ceramic nanofilters. To characterize the rejection properties of this nanofilter, we use the hindered transport model for neutral solutes and, now including ion size, the HET model for ions. In addition to

setting up a single-salt database for this membrane, we also use the electrophoretic mobility μ_p to estimate the effective membrane charge density (as we did for the hafnia nanofilter discussed above). This last method allows us to compare, as a function of pH, the predicted single salt rejection with experiment.

2.7.5.1. Neutral Solutes A wide range of neutral solutes with MW ranging from 32 to 2000 Da were filtered using the new TiO_2 nanofilter. If we fit the hindered transport model for neutral solutes to the limiting rejection data, we obtain the curves appearing in Figure 48. Although the effective solute radius for small roughly spherical neutral solutes, such as methanol, glucose, and sucrose, is meaningful and well known, the same cannot be said for the PEG series. These last molecules probably tend to untangle somewhat and probably cannot be reliably modeled as hard spheres (which, we recall, is a prerequisite for justifying the validity of the hindered transport model used here). As a consequence, there is no true consensus in the literature concerning the effective radius of the PEG series. For this reason, we have presented the data for the PEG series (400, 600, 1000, 1500) using two different estimates for the effective solute size found in the literature. The results presented in Figure 48 indicate that the effective pore size for this nanofilter TiO_2 lies in the range between 0.5 and 1.0 nm. By giving more weight to the smaller solutes, for which more reliable size estimates are known, we arrive at a rough estimate of $r_p \approx 0.92$ nm for the effective pore radius of this membrane (in rough agreement with N_2 adsorption/desorption measurements [22]). Although it would be desirable to refine this estimate using other model solutes, this is the value we use below when we apply the HET model to ions.

2.7.5.2. Single Salts The salt filtration performance of the new TiO_2 nanofilter was characterized by studying the rejection as a function of transmembrane pressure of NaCl, $NaNO_3$, KCl, Na_2SO_4, and $CaCl_2$ at a feed concentration of 10^{-2} [mol/l] and of NaCl and Na_2SO_4 at 10^{-1} [mol/l] for five to seven values of pH (between 2 and 11). The pH was adjusted using the acids and bases of the respective salts (HCl, NaOH, HNO_3, KOH, H_2SO_4, and $Ca(OH)_2$). Although ion rejection was usually measured at only two values of pressure (6 and 15 bar), more complete results were obtained for NaCl, KCl, and Na_2SO_4 at 10^{-2} [mol/l] and pH 11 ($\Delta P = 4, 6, 8, 10, 12$, and 15 bar). The electrophoretic mobility was measured for NaCl, KCl, and Na_2SO_4 at 10^{-3} [mol/l] and NaCl at 10^{-2} [mol/l].

The membrane properties (X_m and l_{eff}) for each salt at each feed concentration and pH studied experimentally were obtained by fitting the HET model to the experimental R_i versus ΔP data. As described in section 2.6.2, the fitting procedure we use takes into account the presence of the acids and bases of the respective salts used to adjust the pH (although near natural pH, H^+, and OH^- are usually trace species, at low and high pH, the presence of acids or bases can considerably modify the transfer of the salt cation and anion, leading to unequal rejections for these species; see, e.g., Fig. 32). The fitted values of X_m

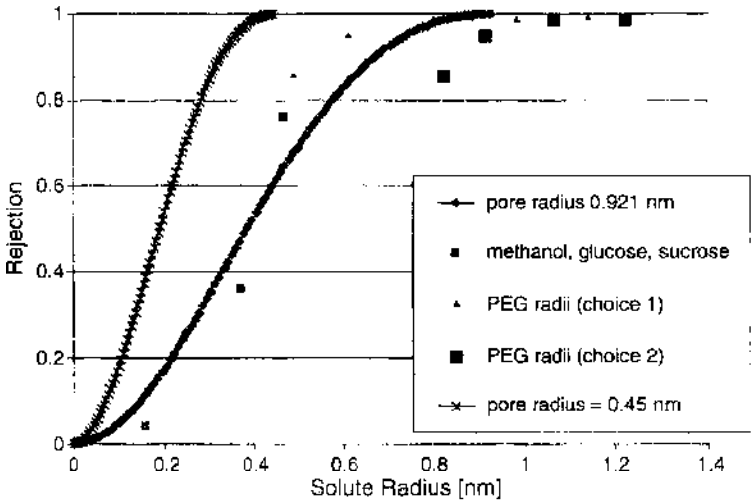

Figure 48. Limiting neutral solute rejection as a function of solute radius: Titania nanofilter experimental data and predicted rejection using the capillary pore hindered transport theory for two different pore radii.

and l_{eff} were used to create the NanoFlux single-salt database for this nanofilter. For $CaCl_2$, NaCl, and Na_2SO_4 these results are presented in Figures 49–53, where we observe typical behavior for an amphoteric nanofilter. Once again we observe that although X_m increases with increasing feed concentration, it increases more slowly than the concentration itself, leading to a normalized membrane charge density ξ, and therefore rejection, that decreases with increasing concentration. For [1 : 1] salts (NaCl, Figs. 50 and 52), we note that X_m is positive below a membrane IEP located at a feed pH close to 7 and negative above (the IEP of an exposed TiO_2 surface is thought to be close to 6). The effective membrane charge density X_m is generally positive and higher at low than at high pH for the salt with a divalent cation ($CaCl_2$), although there appears to be a slight increase in the charge density amplitude at higher values of pH (Figs. 49 and 51). For the salt with a divalent anion (Na_2SO_4) X_m (Fig. 53) is always negative and tends to increase in amplitude with increasing pH (although once again there may be some slight nonmonotonic behavior near natural pH, in the range pH 6–8). This type of behavior for salts possessing divalent ions is thought to be caused by specific divalent ion adsorption at the surface of the membrane pores.

Because salt rejection was usually measured at only two values of ΔP (and the corresponding volume flux densities j_v were not made available), the fitted values of l_{eff} (Figs. 51b–53b)

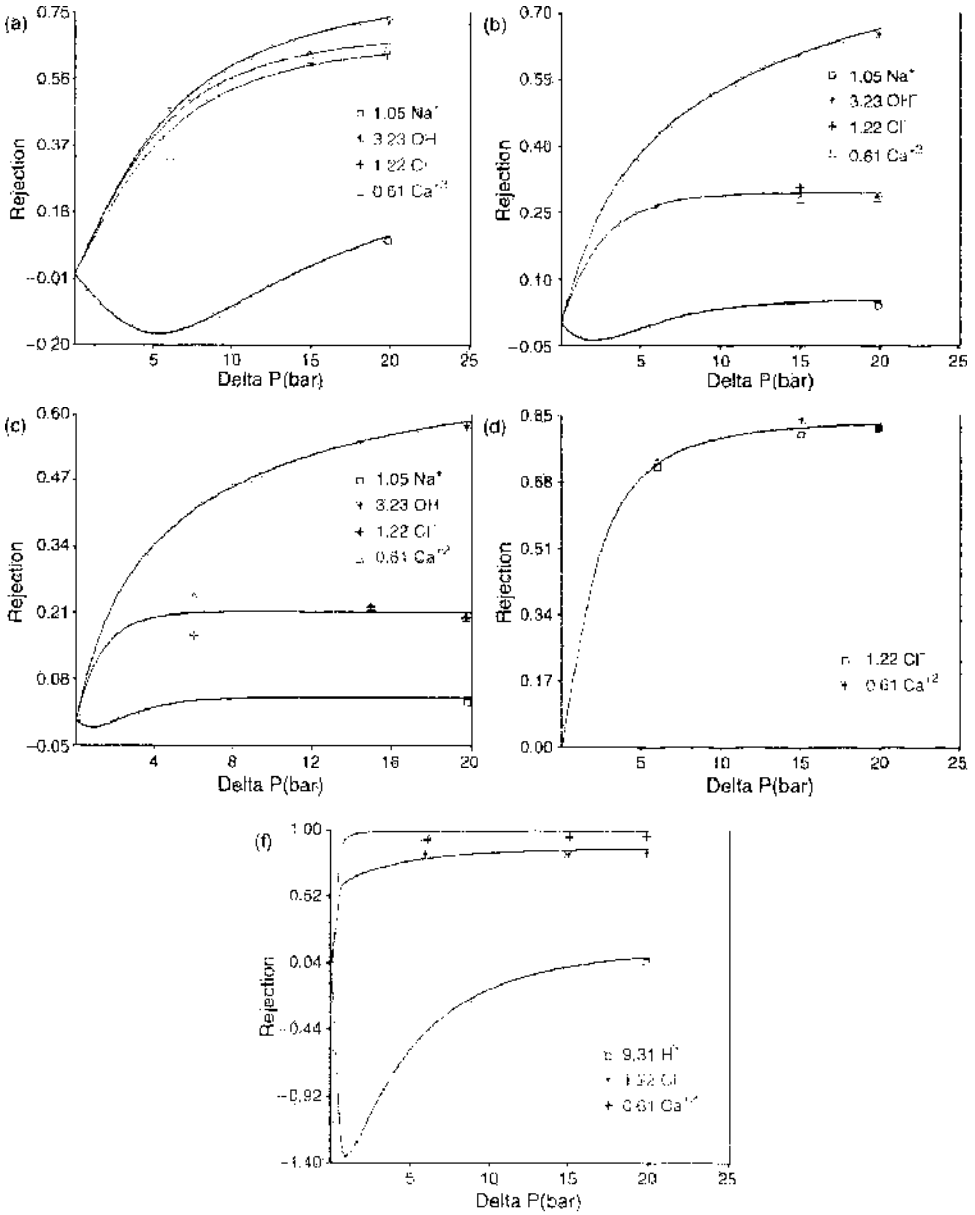

Figure 49. Ion rejection vs. transmembrane pressure: Experimental results and HET model fits: 0.01 M $CaCl_2$ and titania nanofilter: (a) pH 11 + NaOH, (b) pH 9 + NaOH, (c) pH 7 + NaOH, (d) pH 5, and (e) pH 2.5 + HCl.

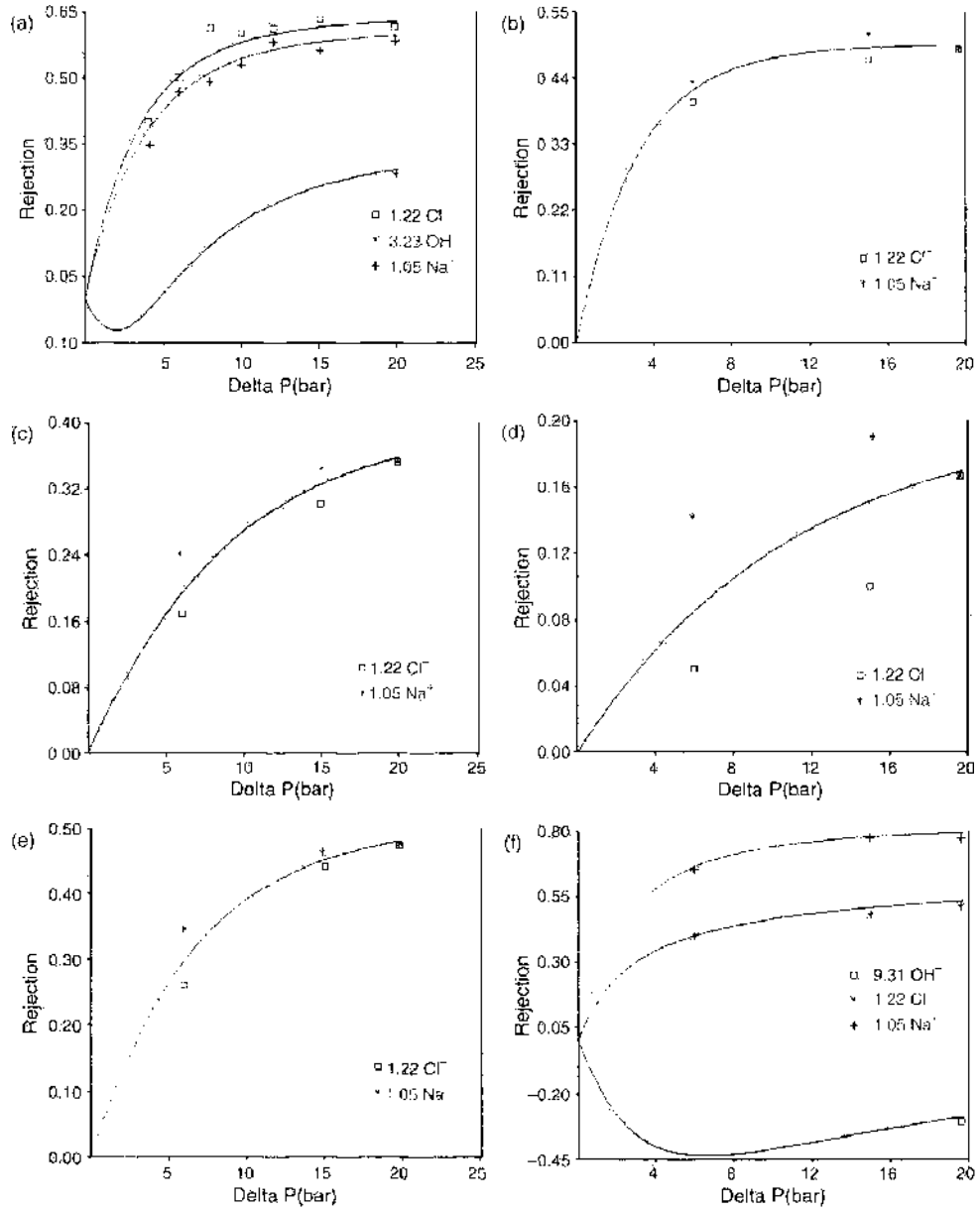

Figure 50. Ion rejection vs. transmembrane pressure: Experimental results and HET model fits: 0.01 M NaCl and Titania nanofilter: (a) pH 11 + NaOH; (b) pH 8; (c) pH 7; (d) pH 6.5; (e) pH 5; and (f) pH 2.5 + HCl.

are probably less reliable than those of X_m (Figs. 51a–53a); this could explain the scatter observed in Figures 51b–53b (l_{eff} measures the rate at which the rejection approaches its limiting value, and this dependence is easier to get a handle on when R_i versus j_v data are used to perform the fitting). Because electrophoretic mobility, but not rejection, measurements

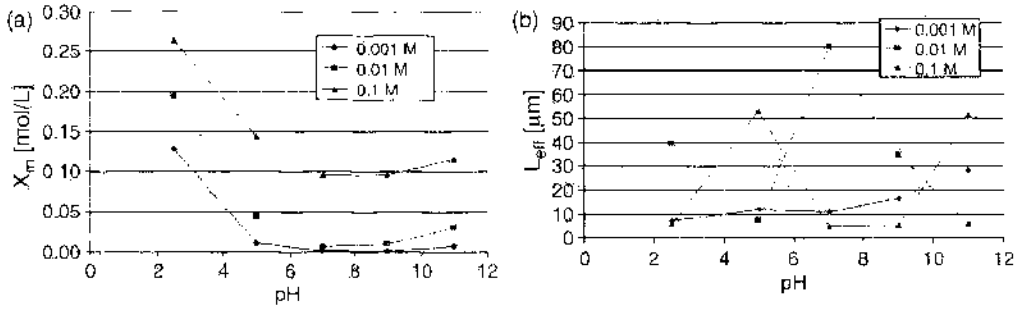

Figure 51. Titania nanofilter: $CaCl_2$ NanoFlux HET model database: (a) effective membrane charge density X_m vs. pH; (b) effective membrane thickness l_{eff} vs. pH (salt concentrations 0.1, 0.01, 0.001 M).

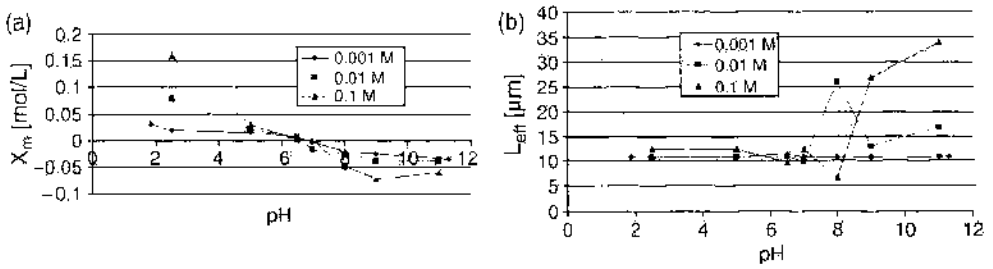

Figure 52. Titania nanofilter: NaCl NanoFlux HET model database: (a) effective membrane charge density X_m vs. pH; (b) effective membrane thickness l_{eff} vs. pH (salt concentrations 0.1, 0.01, 0.001 M).

were carried out at 10^{-3} [mol/l], to extend the database we have used an extrapolation method to estimate values for X_m and l_{eff} at this feed concentration (as well as to estimate these quantities for $CaCl_2$ at 10^{-1} [mol/l], a concentration for which rejection measurements were not carried out for this salt). As a consequence, the values of X_m and l_{eff} appearing in Figures 51–53 for a feed concentration of 10^{-3} [mol/l] are probably less reliable than at 10^{-2} [mol/l].

In Figure 54, we plot the experimental and simulated salt rejection as function of pH at a constant applied pressure of 15 bar for NaCl at 10^{-3} (Fig. 54a) and 10^{-2} [mol/l] (Fig. 54b) and Na_2SO_4 at 10^{-3} [mol/l] (Fig. 54). The predicted rejection is calculated using the value of X_m estimated from the measured electrophoretic mobility (see section 2.7.4.2). The "experimental" rejection for Na_2SO_4 at 10^{-3} [mol/l] has, as explained earlier, been estimated by extrapolating the experimental results obtained at 10^{-2} and 10^{-1} [mol/l] to the lower concentration for which there are no experimental rejection data. At low or high pH, we see that the added acid or base strongly modifies the single-salt rejection and leads to unequal anion and cation rejections (cf. Refs. [32, 34]). For NaCl, we clearly see the IEP at which the effective membrane charge density vanishes (Fig. 54a, 54b); for Na_2SO_4, however, X_m remains negative over the whole pH range studied, and there is no visible IEP (Fig. 54c).

The generally good agreement between experiment and the simulations using the measured electrophoretic mobility to estimate the effective membrane charge density X_m provides further evidence for the utility of this approximate method for predicting the rejection performance of a nanofilter. We can conclude once again that the experimental and simulation results obtained for the Titania nanofilter have the signature of a membrane that rejects ions mainly by electrostatic interactions.

2.7.5.3. Binary NaCl/Na_2SO_4 Electrolyte Mixtures Using the single-salt database for this nanofilter, we have also simulated the rejection of NaCl/Na_2SO_4 mixtures at various relative salt fractions (100/00, 80/20, 60/40, and 50/50), a constant total feed concentration of 0.05 [mol/l], and pH 8.5 (Fig. 55). Although NanoFlux correctly predicts the negative chloride rejection at low to intermediate pressure and positive chloride rejection at high pressure, the simulations seem to underestimate the amplitude of the predicted negative effective membrane charge density. The simulations are in qualitative, but not quantitative, agreement with experiment, for they systematically underestimate the sodium and sulfate rejections at higher Na_2SO_4 mole fraction. More extensive measurements of salt mixtures are needed before any definite conclusions can be reached concerning the usefulness of NanoFlux for simulating the performance of this new ceramic nanofilter vis-à-vis electrolyte mixtures.

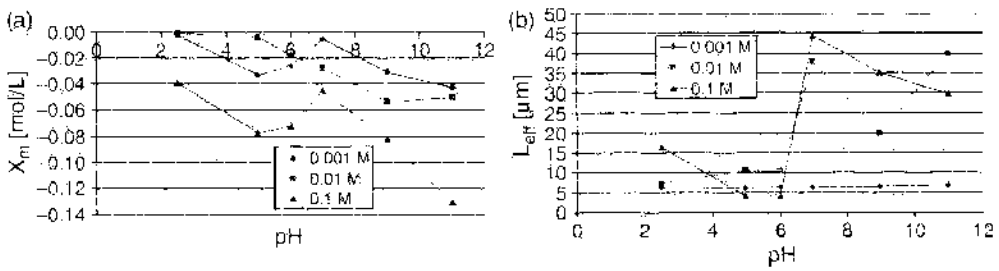

Figure 53. Titania nanofilter: Na_2SO_4 NanoFlux HET model database: (a) effective membrane charge density X_m vs. pH; (b) effective membrane thickness l_{eff} vs. pH (salt concentrations 0.1, 0.01, 0.001 M).

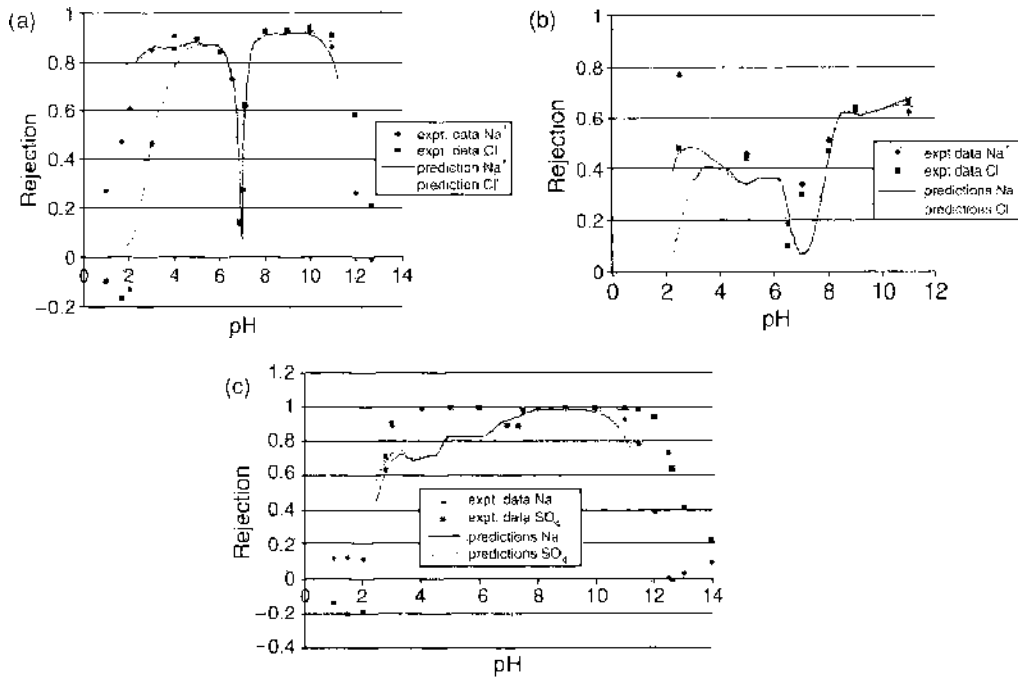

Figure 54. Ion rejection vs. pH, experimental results and HFT model simulations using electrophoretic mobility data: titania nanofilter: (a) NaCl 0.001 M; (b) NaCl 0.01 M; and (c) Na_2SO_4 0.001 M.

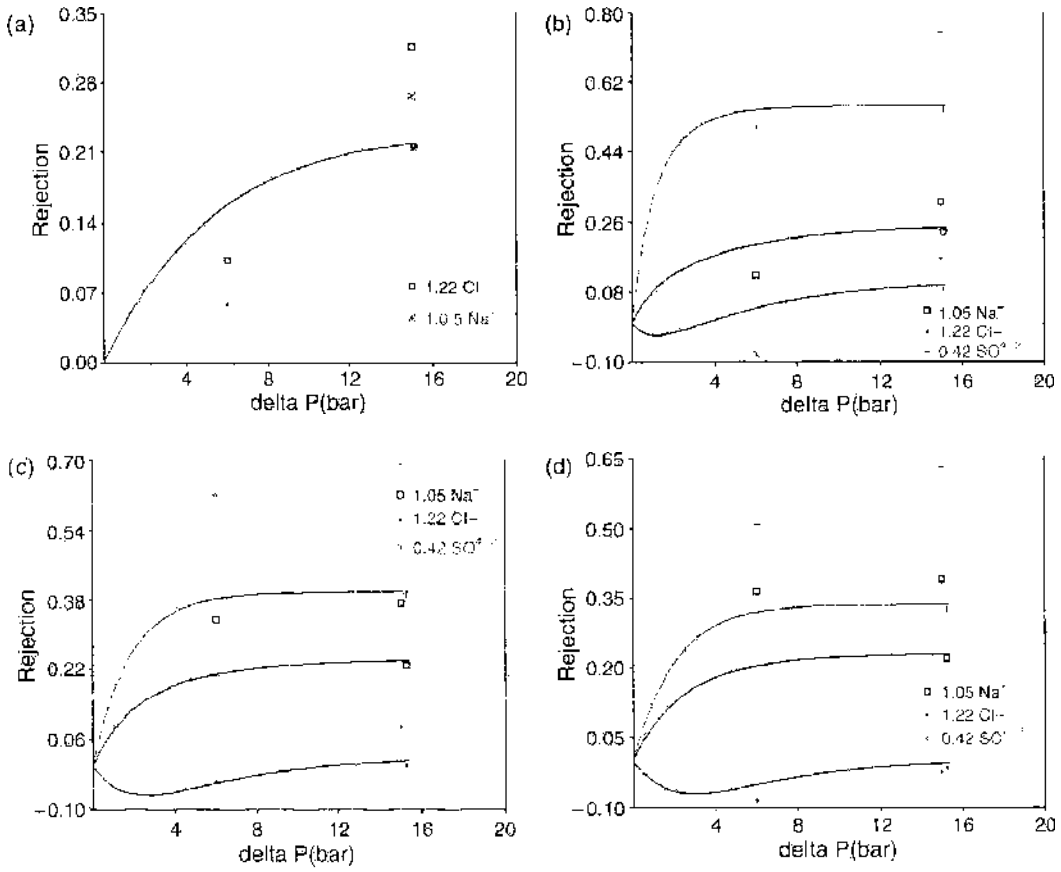

Figure 55. Ion rejection vs. transmembrane pressure: experimental results and NanoFlux HFT model predictions (electrophoretic mobility measurements used to estimate membrane charge density): Titania nanofilter. NaCl/Na_2SO_4 mixtures, pH 8.5: (a) 0.050 M NaCl/0.0 M Na_2SO_4; (b) 0.050 M/0.012 M; (c) 0.050 M/0.036 M; and (d) 0.050 M/0.055 M.

2.8. Conclusions

In this section of the chapter, we presented the state of the art in nanofiltration modeling and showed that the various experimental methods currently employed for characterizing nanofilters can be used to determine a limited number of single-salt model parameters, such as effective pore radius and effective membrane thickness and (volumetric) charge density. When these effective transport model parameters are used to perform NF simulations of multielectrolyte mixtures, we have shown that it is possible to obtain good agreement with experiment not only for ternary and quaternary ion mixtures but also for real drinking water containing seven predominant ionic species. These encouraging results indicate that the types of mesoscopic NF transport models presented here have matured sufficiently for them to be used to simulate reliably multimodule/multistage NF plants.

Despite this optimism, there remains much to do in the area of NF modeling: extending the models to deal with water treatment and industrial effluent applications; extending the NF models to the high concentrations range (>1 [mol/l]) by shedding light on the importance in nanopores of both ion activity and the cross-coupling terms appearing in the Maxwell-Stefan models; and clarifying the role and importance of nonelectrostatic interactions. Computer simulation methods will be useful at each step—not only at the mesoscopic and macroscopic levels presented in this chapter, but also at the molecular level necessary for elucidating the fundamental nature of the interactions between ions and charged nanoporous media.

3. COMPUTER-AIDED SIMULATION AND DESIGN OF NANOFILTRATION PROCESSES

3.1. Introduction

In the past, attention tended to concentrate on the development and optimization of membranes and membrane elements/modules [3, 4, 116], whereas recently, focus has been centered on actual process development (e.g., process planning, design, and operational optimization of membrane plants). Because of diminishing sources of raw materials and energy, as well as an increase in environmental awareness, process development, governed by a process-oriented rationale, is gaining in significance. Increasing demands are being placed on the operational reliability of technical processes in terms of ecological effect, safety, product quality, and economic efficiency.

However, one point of criticism is, essentially, the relatively lengthy periods of development, particularly when opening new areas of application. The reason for these delays is that results from numerous preliminary tests, involving the medium to be treated, are needed to design membrane units reliably, while scale-up from pilot feed volume (flow approx. 0.1 m^3/h) to industrial level involves considerable input, despite the modular structure of membrane processes. Depending on the structure of the process selected, other operational conditions, which have to be considered during the planning stage, prevail in industrial membrane plants. Because of the lack of supportive simulation programs that allow operating conditions to be estimated, the most vital design parameters have often to be determined using time-consuming and cost-intensive pilot plant experiments. During pilot plant operation, optimization is mostly based on predominantly empiric values resulting from the user's expertise. This also prolongs process development. Designing and constructing industrial membrane processes without practical testing at pilot level entails a great deal of uncertainty.

Until now, it has only been possible to develop marketable design programs for reverse osmosis (RO) processes, with which the steady-state operation of an industrial process can be estimated with any adequate degree of precision. However, the operational behavior of reverse osmosis plants is calculated by using simplifying approaches that involve neglecting concentration polarization and feed-side pressure loss or the assumption of constant membrane rejection.

Strong similarity exists between reverse osmosis and nanofiltration with regard to the structural type of the membrane elements and systems engineering, as well as mass transport processes.

The affinity between the two processes in terms of the membrane elements available, operating mode, and plant design has led, in the past, to the tools, developed for reverse osmosis, being used partially for the computer-aided processing of process analysis to design nanofiltration processes. However, because the simplifying assumptions that are permissible for reverse osmosis, are not applicable to nanofiltration, the plant, designed with these tools, shows, in reality, major deviations from the simulated operating conditions. As a result, it is not possible to make reliable predictions for the operating behavior of NF processes based on simulation.

Because of the considerably lower transmembrane pressure difference in nanofiltration processes, feed-side pressure loss has a key influence on separation behavior (the feed-side pressure loss of a membrane element can be up to 0.7 bar). Rejection reacts much more sensitively to changes in membrane flux density (permeate flux density) and salt concentration, with the result that the membrane elements arranged in series exhibit different rejection values because of feed-side pressure loss.

In the mid 1990s, composite membranes were developed and brought onto the market. These membranes allow higher membrane hydraulic permeabilities at equivalent rejection properties for nanofiltration (and also reverse osmosis), and thus a further reduction in the transmembrane pressure difference required.

The following section will deal with the simulation of industrial nanofiltration processes. The main focus is on the modeling and simulation of the separation characteristics of spiral wound elements/modules, while (Fig. 9) considering mainly the separation properties characteristic of nanofiltration processes. The previous shortcomings in the simulation and design of NF processes can thus be abolished and a reliable way of dealing with process analysis tasks is made available. Furthermore, process development can be speeded up considerably by using computer-aided parameter studies for optimization purposes. The study was verified by applying a process simulation prototype to a real case study.

3.2. Process Simulation for Developing Membrane Processes

With the exception of reverse osmosis, the problem concerning the modeling and appropriate simulation of pressure-driven membrane processes (microfiltration, ultrafiltration, nanofiltration) has not, so far, been solved satisfactorily, the main reason being the numerous interactions between the various components in the solution to be filtered as well as the membrane matrix. Pronounced nonidealities and coupling effects occur on the membrane surface and in the membrane. Other reasons are, for example,

- Many physically proven or semiempirical model concepts deal with the description of local mass transport on a small membrane area. It is possible to model the separation behavior of nanofiltration membranes relatively accurately for a local approach [117, 118]. However, because of the structural arrangement of the large area inside the membrane elements, upscaling these models to an industrial membrane module is not possible without further work (integration of the membrane area, consideration of aspects reducing driving force).
- The detailed modeling of mass transport on the membrane involves a considerable degree of work, and the models can only be applied to the membrane elements to a certain extent. In industrial processes, numerous membrane elements, which interact to achieve the separation objective, are interconnected partially in multiple stages (Fig. 56). In process simulation, the calculation of the individual membrane elements (in this part, membrane element means the smallest part of membrane arrangement in the membrane module: one to six, or maximum eight membranes/elements are incorporated in one spiral wound membrane module [see Fig. 59]) with accurate mass transport models involves much numerical input, which can increase considerably in process calculations.
- Despite numerous investigations, no satisfactory models have been developed for the formation of biological films (biofouling), adsorption of organic substances or formation of inorganic coatings (scaling) [119, 120].
- The membrane or the treated solution react to variations in many of the operating parameters (temperature, viscosity, pressure, concentration, pH value, hydrodynamics,

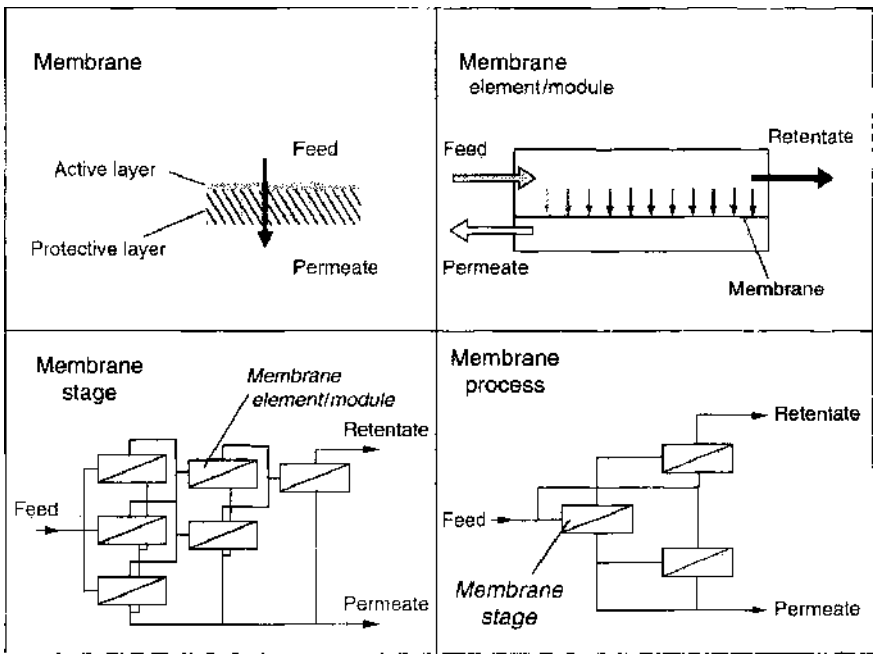

Figure 56. Illustration of membrane processes from the membrane, through the membrane element/module, up to the membrane stage and membrane processes. Adapted from [20].

etc.) by a change in separation behavior. Determining membrane separation behavior for the most important parameters and modeling the results via regression analysis with nonphysically proven models is time consuming and expensive. In addition, extrapolation in ranges outside the measurement points is not reliable [121].

As a result of these aspects, mathematical tools play a rather subsidiary role in the development of membrane processes. Reliable up-scaling to industrial level is seldom possible without pilot-scale tests (stage directly before industrial scale), and optimization is mostly conducted on an empirical basis, usually involving the designer's expertise. Depending on the level of experience involved, this increases the time and the costs for development.

In process simulation of reverse osmosis, some models can be supplemented by simplifying assumptions for mass transport on the membrane as well as for hydraulic flow conditions in membrane elements. These include constant membrane rejection, neglect of concentration polarization, constant pressure loss, or constant yield for the membrane elements. As for reverse osmosis, these "short-cut methods" could be used to simulate industrial processes, with good approximation, via a membrane element analysis [122–125].

For such idealized approaches to the filtration of pure electrolyte mixtures, useful simulation programs are available for optimizing and designing reverse osmosis processes (Table 5) [126], usually in the form of software developed by the membrane manufacturer and only applicable to his own membranes. Two exceptions are the programs RODESIGN and USRRO from the Institute for Process Engineering at the Technical University (RWTH) in Aachen, Germany.

Because of the similar operational mode and membrane elements (spiral wound elements) for nanofiltration and reverse osmosis, the design and configuration of nanofiltration

Table 5. Commercially available process simulations programs for reverse osmosis processes (as of July 2001).

Manufacturer	Membrane	RO software
Dow Chemicals	FilmTec	Rosa
Hydranautics	Hydranautics	RoDesign, Rodata
Koch	Fluid Systems	Ropro 6.1, Costpro
Osmonics	Osmonics, Desal	WinFlows
Toray, Ropur, Trisep	Toray, Ropur, Trisep	WinCarol 1, 2p flows
Technical University (RWTH) Aachen[a]		RODESIGN USRRO für AspenPlus™

[a] Institute for Process Engineering (IVT) at the Technical University (RWTH) Aachen, Prof. Melin/Prof. Rautenbach.

processes were partially modeled on the basis of existing RO processes for seawater desalination [127]. Because nanofiltration is mostly used for water softening or brackish water desalination, filtration is usually carried out at low transmembrane pressure differences, also because of the low salt concentration and low membrane rejection at low osmotic pressure difference. As a result of this, the feed-side pressure loss has a decisive influence on the operation of nanofiltration processes and, therefore, should not be neglected. Calculations by Van der Meer [128] have shown that this can affect the optimum configuration of NF processes. Furthermore, mass transport in nanofiltration is caused by several simultaneous and interactive transport mechanisms (cf. Fig. 7), resulting in the fact that the rejection of nanofiltration membranes is much more dependent on changes in concentration. Thus, membrane elements/modules, arranged in series, display very different separation characteristics, whose calculation using the simplified reverse osmosis models partially results in considerable deviations from actual operating behavior in reality.

3.3. Model Development and Simulation of Nanofiltration Processes

To avoid the disadvantages of the simulation programs for reverse osmosis, we developed [129–137] a simulation program, NF-PROJECT, for nanofiltration processes. However, this program is not to be considered as a replacement for practical pilot-scale tests for plant design performed by an expert but, rather, as an additional computer-aided tool for process designers to use in the planning, designing, and optimizing of NF processes, whereby:

- The extension of options incorporated into the development phase,
- The definition of process (operating) alternatives, which should be considered in detail and,
- The appropriate degree of reliability required for industrial upscaling can be achieved in a quicker, less expensive and more efficient manner.

First of all, the structure of membrane processes (section 3.3.1) will be presented in terms of the design possibilities for the entire membrane area to be installed. The results will then be used to develop a procedure for the simulation of membrane processes (section 3.3.2), which includes a methodology concept and model development, as well as model equations for characterizing and simulating the separation behavior of NF membrane elements. In addition, the estimation of model parameters, which are adapted to a system (membrane/model solution), will be illustrated.

3.3.1. Structure of Membrane Processes

3.3.1.1. Connection of Membrane Elements/Modules If, in a filtration process, the entire membrane area is composed of several membrane elements/modules, then an optimum arrangement is required. Basically, membrane elements/modules can be arranged in series or in parallel (Fig. 57). In a series arrangement, the retentate of the upstream membrane element provides the feed for the downstream element, whereas, in a parallel arrangement, the feed quality is the same for all membrane elements. For both arrangements, the entire permeate consists of partial permeates from the individual elements, resulting in a mixed concentration in the entire permeate volume flow.

Because of the high flow rate, the individual permeate volume flow in a spiral wound element is low compared to the feed volume flow. Therefore, in large-scale treatment plants, several spiral wound modules are usually arranged in series to obtain the permeate yield required. As can be seen in Figure 57, which shows modules arranged in series, there is a constant rise in feed concentration for the downstream elements and a decrease in feed volume flow because of permeate withdrawal. If pressure loss and concentration polarization are considered, the effective driving force for mass transport can decrease quickly, also affecting the separation result considerably. Therefore, it is of paramount importance to examine the filtration conditions of the individual elements and, particularly, the last critical membrane element in the series arrangement in which feed concentration is at its highest and flow rate at its lowest. A simulation process is particularly conducive to the examination of filtration conditions.

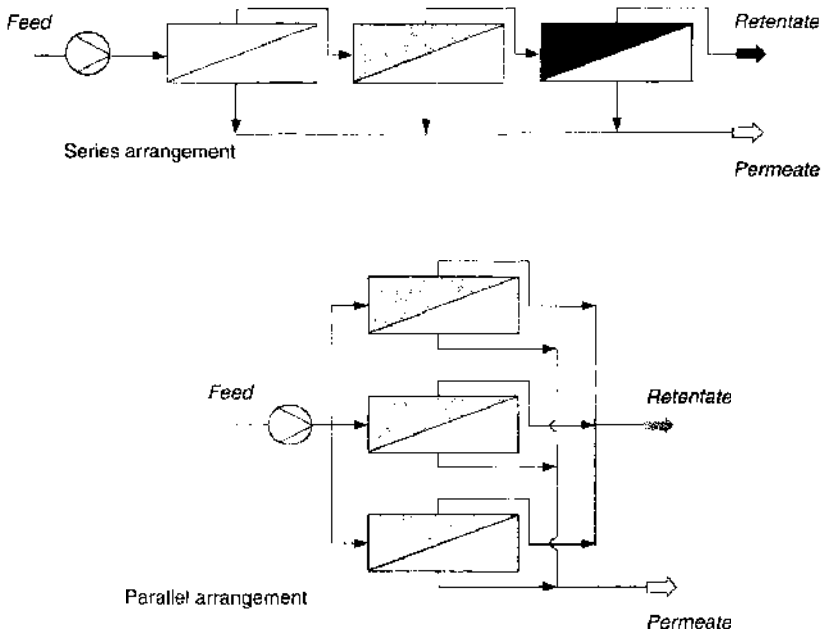

Figure 57. Series and parallel arrangement of membrane elements/modules.

In design processes, attention should be given to the maximum feed and minimum retentate volume flows, as specified by the manufacturer. Flow through an element causes pressure loss, which should not exceed a maximum value, as otherwise damage to the membrane elements can occur (exceedingly high shear force on the membrane surface, "telescoping"). Because of the increase in concentration polarization on the membrane surface, which occurs at low feed volume flows, a minimum feed volume flow, based on empirical values, is also specified. Hence, for parallel arrangements, a greater degree of energy is needed because the minimum volume feed flow has to pass through each element.

3.3.1.2. Configuration of Membrane Elements/Modules in a Filtration Stage For the installation of very large membrane areas with spiral wound elements in industrial treatment plants, pressure pipes (membrane elements arranged in pressure pipes form the membrane module) forming the membrane module, in which up to six membrane elements (in exceptional cases up to eight) arranged in series, are used. In the planning and design of an industrial filtration stage, two structures, which allow a parallel or series arrangement of the pressure pipes, have become established [121]:

- Tree structure
- Feed-and-bleed structure

The tree structure is used for very large treatment plants in particular (Fig. 58).

Depending on feed volume flow, several pressure pipes are grouped into parallel blocks, which are connected in series. The retentate volume flow of one block serves as the feed volume flow for the downstream block. Because of the decrease in volume flow, each downstream block contains fewer pressure pipes than the previous block, so that flow over the membrane elements is ensured. However, one disadvantage of the tree structure is its poor capacity to adapt to fluctuations in the feed volume flow or feed quality. Optimum flow conditions can only be achieved to an approximate degree because of the discrete element size and the gradual reduction in the flow cross section. If the feed volume flow is modified, it is possible to exceed the maximum permissible or fall below the minimum required volume flows in the individual membrane elements.

Furthermore, pressure losses in the membrane elements vary. When fluctuations in concentration occur, the permeate flows through the membrane elements change, as does the feed volume flows in the downstream blocks. As a consequence, permeate yield cannot be easily changed. One advantage, however, is the low energy consumption (no circulation pumps, cf. feed-and-bleed structure in Fig. 59), as well as the short residence time in the

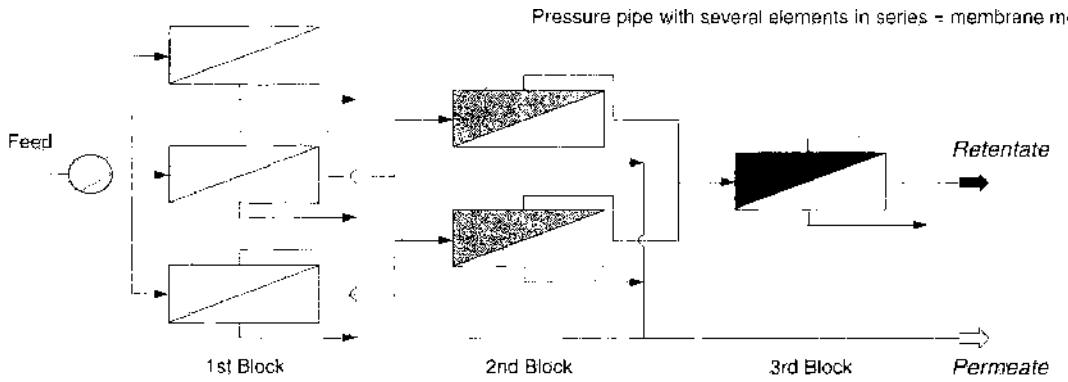

Figure 58. Tree-structure arrangement of pressure pipes with several membrane elements in series.

filtration stage. The tree structure is applied in large-scale treatment plants when few fluctuations in feed concentration are to be expected and when there is low estimated potential for organic or biological fouling on the membrane (e.g., seawater treatment after adequate pretreatment or as a second filtration stage in the treatment of leachate from landfills). The feed-and-bleed structure is used for small-scale treatment plants, and preferably for high fouling potential in the feed solution (Fig. 59).

The optimum or required flow conditions are ensured by internal recirculation cycles operated by circulation pumps. A small "bleed" flow is withdrawn from the recirculation cycle in a controlled manner. The size of the bleed flow allows permeate yield to be set over a large area. For this type of operation, it should be noted that the retentate is remixed in the recirculation mode, thus producing longer residence times for the substances retained in the system. However, the feed concentration for the membrane elements also increases, depending on the circulation rate. Compared to the tree structure, this arrangement results in a change of separation performance because the higher feed concentration leads to an increase in permeate concentration and to a decrease in permeate flux. Moreover, feed-and-bleed operation incurs higher energy costs, caused by the additional circulation pumps.

In addition to the quality required for the water to be treated, the reason for choosing a particular process structure depends essentially on the size of the feed volume flow and the flexibility required of the process (e.g., variable setting of yield).

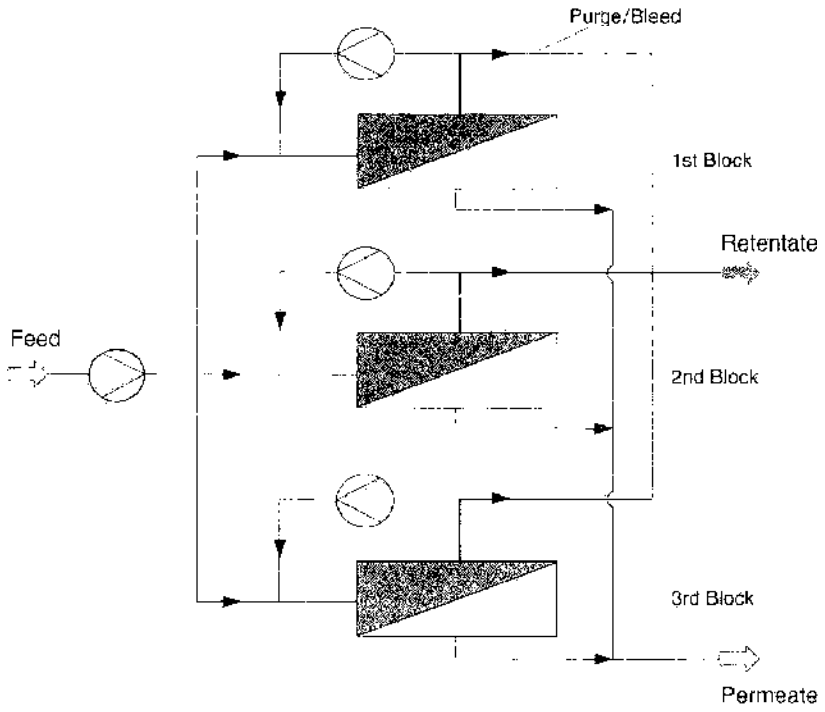

Figure 59. Feed-and-bleed arrangement of pressure pipes with several membrane elements in series.

3.3.1.3. Multistage Unit Arrangements Depending on the objectives defined for product quality, one filtration stage may not be capable of producing the separation effect required. In such cases, the membrane in operation does not have adequate selectivity properties (or poor rejection), or the degree of product purity cannot be achieved for the yield required. Multistage unit arrangement (membrane cascade) can solve this problem.

Only one-dimensional cascades are generally used in membrane technology, whereby the feed volume flow is divided into a retentate and a permeate volume flow. Multidimensional cascades that can separate a mixed substance into several components will not be dealt with in this chapter.

Membrane cascades can be defined as symmetrical or asymmetrical, indicating the way in which the filtration stages are linked. The following two diagrams show the types of two-stage membrane cascades most commonly used. Figure 60 illustrates a two-stage cascade in which the permeate from the first filtration stage is filtered in a second stage. This type of operation requires a second force pump because the permeate from the first stage is without pressure.

Conversely, Figure 61 shows a two-stage cascade in which the retentate from the first filtration stage is filtered in the second stage. If the feed-side pressure loss is low compared to the transmembrane pressure difference, a main feeder pump is not required after the first filtration stage. Without a recirculation mode, the cascade illustrated in Figure 61 cannot be differentiated from a single-stage arrangement.

3.3.2. Methodology for Simplified Simulation of Nanofiltration Processes

The entire membrane area in industrial membrane processes is modular in structure (cf. section 3.3.1). In nanofiltration and reverse osmosis involving pretreatment of the medium to be purified, standardized 8″ spiral wound elements are preferably used and arranged in a certain configuration to form one entire membrane area. Industrial spiral wound elements are approximately 200 mm in diameter and roughly 1000 mm in length and can basically be connected in series for any number at all (the membrane area A_m for each spiral wound module is usually roughly between 30 and 40 m^2).

Figure 62 [138] shows a stage-by-stage break-down of the process system. The entire process is considered to be a "black box," broken down gradually into process groups or subgroups and finally into process elements. Individual membrane elements can be understood as process elements.

This procedure is defined as "decomposition of a process system" [139]. On the final level, the membrane element is regarded as a black box, converting input variables into output variables (volume flow, pressure difference, and concentration), thus having one function (Fig. 63).

As a consequence, the entire process can be simulated via sequential calculation and modeling of the separation behavior of the membrane elements. This so-called element-by-element analysis has already been applied successfully to simulate reverse osmosis processes [140]. Compared to the numerical integration of differential balances of mass, material,

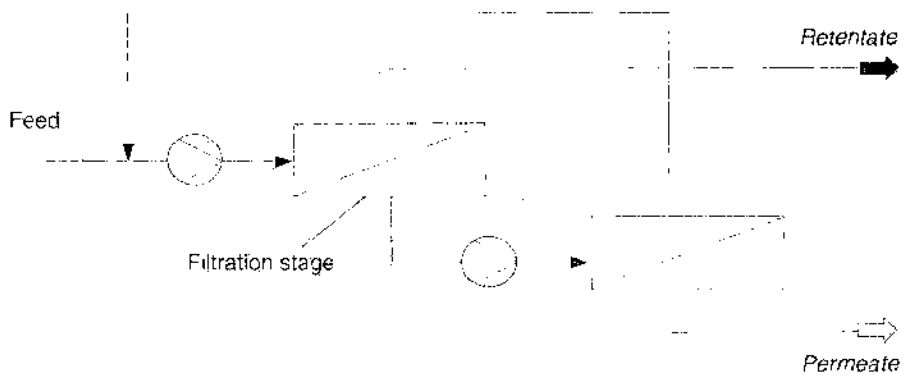

Figure 60. Two-stage symmetrical cascade with follow-up permeate filtration, reprinted with permission from [135], M. Noronha et al. *J. Membr. Sci.* 202, 217 (2002), © 2002, Elsevier.

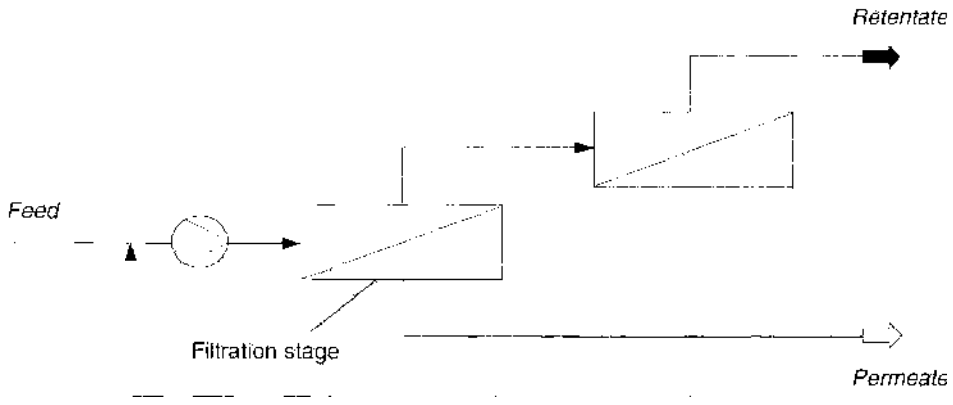

Figure 61. Two-stage symmetrical cascade with follow-up retentate filtration.

and impulses throughout the entire process, considerable time can be saved for complex processes with recirculation, as there is less numerical calculation.

The objective underlying the development of a simulation process for nanofiltration was to keep the complexity of the entire modeling process as low as possible (estimation of fewer and simpler model parameters) while using a simple model for mass transport through membrane elements. In many cases, very accurate and complex models, considering the high numerical calculation, do not produce a better result for the prediction of process behavior under real conditions, compared to rigorously simplified black box models for the simulation of reverse osmosis processes. Therefore, it is crucial for the simulation of nanofiltration processes to define a meaningful balance between the type of models used and the detailing of models to obtain significant results. Basically, a procedure based on the principle "as accurate as necessary" has proven favorable [141].

3.3.2.1. Modeling the Separation Behavior of Nanofiltration Membrane Elements A modeling process that involves differential equations for feed-side and permeate-side pressure loss as well as feed-side and permeate-side concentration changes is very elaborate as a result of the flows crossing in the spiral wound element [121]. When permeate volume flow in the membrane element is low compared to the feed volume flow (yield $Y < 0.1$), calculations for the feed can be performed using mean logarithmic values for transmembrane pressure difference ΔP and mean arithmetical values for the bulk concentration of component i c_i^b with good approximation. This is usually true for nanofiltration processes.

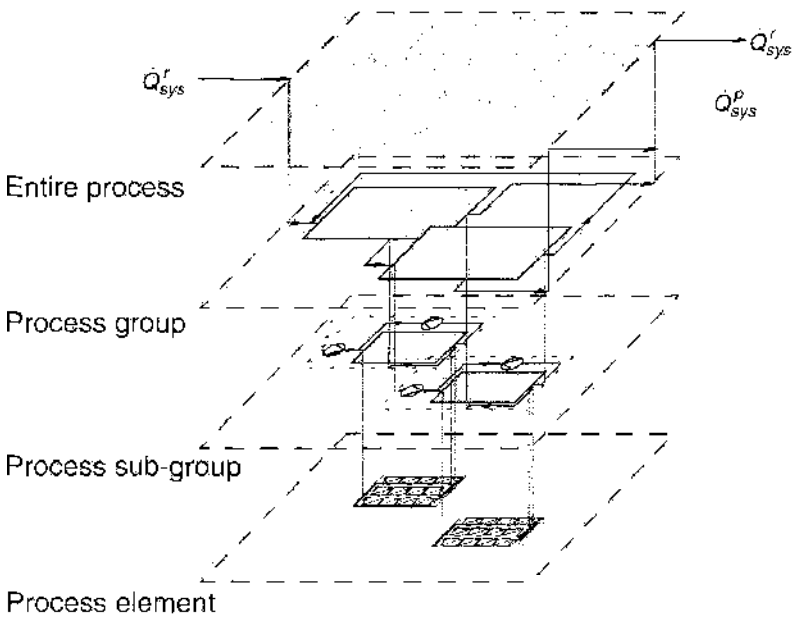

Figure 62. Stage-by-stage break-down of the process system.

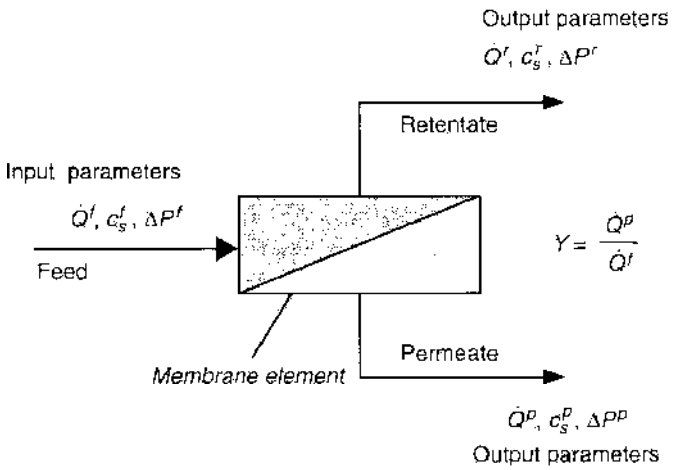

Figure 63. Input and output parameters of one membrane element.

The model structure for the mathematical description of isotherm mass transport in nanofiltration membrane elements (spiral wound modules) is based on equations for local mass transport. It was assumed that the permeate-side process parameters can be calculated from the averaged feed-side process parameters at the inlet and outlet of the membrane element (mean logarithmic value for transmembrane pressure difference ΔP and mean arithmetic value for the concentration of component i in the bulk stream c_i^b) by suitable model equations for the quasi-local mass transport. It was assumed that characterization was conducted using a binary electrolyte solution. The model used to characterize and simulate NF spiral wound membrane elements is characterized by the following properties and assumptions:

- Calculation of the permeate flux based on the simple solution–diffusion model
- Use of the van't Hoff equation for osmotic pressure in diluted electrolyte mixtures
- Incorporation of concentration polarization at the membrane surface
- Adaptation of the feed-side mass transport coefficient to flow conditions according to Schock and Miquel
- Calculation of real membrane rejection according to Spiegler and Kedem
- Use of the extended Spiegler-Kedem model according to Schirg and Widmer
- Use of an empirical equation by a membrane manufacturer to calculate the feed-side pressure loss in spiral wound elements

In the following, the features and assumptions of the model will be explained in detail:

3.3.2.1.1. Membrane Volume Flux Density (Permeate Flux Density) j_v The permeate flux can be equated to the transmembrane volume water flux density ($j_v = J_W$) with good approximation. It has a linear dependence on the net pressure difference [17, 117]. The pressure in the header for the permeate in the spiral wound element is neglected (permeate pressure is at ambient pressure) [127] [see Eq. (97)], where the global osmotic reflection coefficient $\Sigma = 1$]:

$$j_v = J_W = \bar{L}_p^0 \cdot (\Delta P - \Delta\Pi) \tag{123}$$

where J_W is the transmembrane volume water flux density [m³/m²h], $\bar{L}_p^0$ is the pure water membrane hydraulic permeability [m²/m²h.bar], ΔP is the the transmembrane pressure difference [bar], and $\Delta\Pi$ is the osmotic pressure difference [bar].

3.3.2.1.2. Osmotic Pressure Difference $\Delta\Pi$ The thermodynamic expression for osmotic pressure can be calculated for diluted solutions according to the van't Hoff equation

$$\Pi_W = \frac{R \cdot T}{\bar{V}_W} \cdot \ln(1 - x_s^f) = -\frac{R \cdot T}{\bar{V}_W} \cdot \ln x_W = -\frac{R \cdot T}{\bar{V}_W} \cdot \ln a_W = \frac{R \cdot T}{\bar{V}_W} \cdot x_s^f \approx R \cdot T \cdot c_s \tag{124}$$

where Π_W is the osmotic pressure difference according to van't Hoff [bar], R is the gas constant [J/molK], T is the temperature [K], x_s^f is the mole fraction for salt [mol/mol],

$\bar{V}_{H}$ is the partial molar volume [m³], a_W is the activity coefficient, x_W is the mole fraction for water [mol/mol], and c_s is the salt concentration [mol/m³].

Then the osmotic pressure difference can be expressed as

$$\Delta\Pi = R \cdot T \cdot (c_s^w - c_s^p) \tag{125}$$

where c_s^w is the salt concentration at the membrane surface (wall) [mg/m³], and c_s^p is the salt concentration in the permeate [mg/m³].

In an isothermal approach, the term $R \cdot T$ can be assumed to be constant and can be summed up as a parameter b_W [bar/(g/m³)], the so-called van't Hoff coefficient:

$$\Delta\Pi = b_W \cdot (c_s^w - c_s^p) \tag{126}$$

3.3.2.1.3. Concentration Polarization Concentration polarization (see, section 1.2.4) on the membrane surface is an important phenomenon in membrane filtration because it reduces driving force. It will therefore be included in the model development process [17]. In this case, Eq. (14) will be applied:

$$\exp\left(\frac{J_w}{k_F}\right) = \frac{c_s^w - c_s^p}{c_s^b - c_s^p} \tag{127}$$

3.3.2.1.4. Flow Conditions for Membrane Elements In pressure pipes (membrane modules) arranged in series, the membrane elements are operated at different volume flows. The reason for this is that the retentate volume flow of the upstream element is the feed volume flow of the downstream element. This means that the feed volume flow for each further membrane element is reduced by the permeate volume flow of the upstream element. The average flow velocity of the feed solution along the membrane u in the membrane elements influences pressure loss and the mass transport between the laminar boundary layer and the bulk stream. Thus, feed velocity u has a direct effect on the level of concentration polarization because of changes in the mass transport parameter k_F. This parameter can be adapted individually according to Schock and Miquel [13], as Eq. (17):

$$k_F = 0.065 \cdot D_i^{0.75} \cdot d_H^{-0.125} \cdot \nu^{-0.625} \cdot u^{0.875} \tag{128}$$

The parameter, diffusion coefficient D_i, and kinematic viscosity ν of the solvent (water) are assumed to be constant.

3.3.2.1.5. Real Rejection $R_{s,Real}$ The Spiegler and Kedem [142] equation was chosen to calculate real rejection. This equation was extended by incorporating the concentration dependence of salt permeability according to Schirg and Widmer [143] ([cf. Eq. (35)]). This produced good agreement for the filtration of electrolyte solutions containing binary salts with the model results of the extended Nernst-Planck equation [144]:

$$R_{s,Real} = 1 - \frac{1-\sigma}{1-\sigma \cdot \exp((\sigma-1) \cdot J_W/\bar{P}_s)} \tag{129}$$

where σ is the reflection coefficient [-], and $\bar{P}_s$ is the salt membrane permeability [m/h].

According to Schirg and Widmer, salt membrane permeability $\bar{P}_s$ can be expressed as

$$\bar{P}_s = \alpha \cdot (c_s^w)^\beta \tag{130}$$

where α and β are the empirical coefficients [-]. This procedure allows the dependence of rejection on permeate flux and concentration typical for nanofiltration membranes to be expressed mathematically.

3.3.2.1.6. Maximum Real Salt Rejection $R_{s,Real,max}$ The maximum salt rejection of nanofiltration membranes (e.g., for sodium chloride) is considerably below one. Maximum real rejection $R_{s,Real,max}$ can be expressed by the Stavermann's reflection coefficient σ [143] and, according to Eq. (38), is

$$R_{s,Real,max} = \sigma \tag{131}$$

In simulating separation behavior, the feed-side pressure loss during flow through the spiral wound element must also be taken into consideration. As a result of tests conducted by a

membrane manufacturer on the pressure loss in numerous industrial spiral wound elements, an empirical equation, whereby the dependence of pressure loss ΔP^{loss} in each element on the average feed volume flow could be described, was determined:

$$\Delta P^f - \Delta P^r = \Delta P^{loss} = 8.56785 \cdot 10^{-3} \cdot \left(\frac{\dot{Q}^f + \dot{Q}^r}{2}\right)^{1.7} \tag{132}$$

Equation (132) is not needed to characterize a membrane element because the process parameters at the inlet and outlet are determined during a filtration experiment. Conversely, the equation is required to simulate membrane elements arranged in series because the outlet parameters have to be calculated only from the process parameters at the inlet.

The flux of dissolved salts is defined implicitly by the expressions in Eqs. (123) and (129), as $c_s^p = J/J_W$ and rejection $R_{s,\,Real}$, according to Eq. (3), can be expressed as

$$R_{s,\,Real} = 1 - \frac{c_s^p}{c_s^w} = 1 - \frac{J}{J_W \cdot c_s^w} \tag{133}$$

where J is the solute molar flux density [m^3/m^2h].

As this equation shows, for separation effects, the charge interactions on the membrane with the components of the electrolyte solution were not considered. Furthermore, the influence of temperature on water viscosity was not considered in the model equations (isothermal approach). It is preferable to carry out the characterization process within the operating temperature range of the treatment plant. Equations (123–131) contain free model parameters that, when characterizing an nanofiltration membrane or membrane systems with a model solution (binary electrolyte mixture), have to be estimated on the basis of experimental results and, ideally, are considered to be nearly constant in the range under study. One exception is the mass transport coefficient, which is adapted to the flow conditions. Thus, it is specified together with the flow velocity of the feed solution along the membrane u during the experiments and the hydraulic diameter d_H of the feed channel (Table 6).

3.3.3. Estimating the Free Model Parameters

The free model parameters are estimated on the basis of experimental data from filtration experiments that are to be considered as erroneous because of measurement inaccuracy. It is basically possible to estimate the parameters more accurately by adapting regression methodology if the percentage range of the data is known. However, to simplify matters, a less complicated method for minimizing square errors will be used in this chapter.

Pure water hydraulic permeability $\bar{L}_p^0$ can be determined simply and accurately by a filtration experiment using fully desalinated water. In this case, the transmembrane pressure difference range under study should ideally contain the pressure difference of the operating point of the treatment plant in question.

To estimate the model parameters b_W and k_F, the Eqs. (123), (126), and (127) are applied. Hence, it follows that:

$$\begin{aligned} J_W &= \bar{L}_p^0 \cdot (\Delta P - \Delta\Pi) \\ &= \bar{L}_p^0 \cdot [\Delta P - b_W \cdot (c_s^w - c_s^p)] \\ &= \bar{L}_p^0 \cdot \left[\Delta P - b_W \cdot (c_s^b - c_s^p) \cdot \exp\left(\frac{J_W}{k_F}\right)\right] \end{aligned} \tag{134}$$

Table 6. Free parameters for characterizing the separation behavior of NF membrane elements.

Parameter	Unit	Specification
$\bar{L}_p^0$	l/(m²·h·bar)	Pure water hydraulic permeability
b_W	bar/(g/l) or bar/(mS/cm)*	van't Hoff coefficient (osmotic pressure)
$k_F(u,\, d_H)$	l/(m²·h)	Feed-side mass transfer coefficient
σ	—	Staverman reflection coefficient
α and β	—	Coefficients with empirical character

*In the characterization process using NaCl, concentration was recorded by the parameter, electrical conductivity.

and

$$\frac{1}{c_s^b - c_s^p} \cdot \left(\Delta P - \frac{J_W}{\bar{L}_p^0} \right) = b_W \cdot \exp\left(\frac{J_W}{k_F} \right) \tag{135}$$

Equation (135) (the part on the right) is equivalent to an equation having the general form

$$f(x) = A_1 \cdot \exp(A_2 \cdot x) \tag{136}$$

where

$$A_1 = b_W \text{ and } A_2 = \frac{1}{k_F}$$

Because the process parameters J_W, $\bar{L}_p^0$, ΔP, c_s^b, and c_s^p can be determined by measurements (the feed-side process parameters at the inlet and outlet are averaged by logarithms for transmembrane pressure difference ΔP and arithmetically for concentration c_s^b (Fig. 4), the parameters b_W and k_F can be determined via an exponential regression (by minimizing square errors) of the function terms f (x) or f (J_W) over x or J_W [in Eq. (135); according to Eq. (122), j_v can be used instead of J_W].

Although the van't Hoff coefficient b_W is ideally considered as constant, this is not true for the mass transport coefficient k_F, which is basically influenced by flow conditions in the membrane element. Therefore, regression should be calculated via measurement points for which flow conditions diverge only slightly. Using Eq. (128), this parameter k_F can be transferred to other flow velocities and hydraulic diameters (by diffusion constant D_i = const.) if the averaged flow velocities u in the membrane element and the hydraulic diameter d_H [specification of the "reference points" k_F (u, d_H)] are known. This allows concentration polarization on the membrane surface to be estimated according to Eq. (127), from which concentration on the membrane surface c_s^m can be determined. Thus, real salt rejection $R_{s,Real}$ can be estimated according to Eq. (4), whose maximum value is equivalent to the reflection coefficient σ [see Eq. (131)].

By modifying Eq. (139) and by calculating the salt membrane permeability $\bar{P}_s$ for different concentrations, $\bar{P}_s$ can be expressed as a function of c_s^m. The empirical parameters α and β can then be estimated by potential regression (by minimizing square errors).

3.3.4. Sensitivity Analysis of the Model Parameters

The essential output parameters for the simulation of separation characteristics of nanofiltration membrane elements are permeate volume flow $\dot{Q}^p$ and permeate salt concentration c_s^p. Indirectly, the parameters are calculated from the membrane volume flux density (permeate flux) j_v and rejection R_s or R_i. The calculation result is influenced by the values for the model parameters. The estimation of the model parameters is subject to a certain degree of uncertainty because the measurement data from the filtration experiments are sufficiently accurate. As a result of these systematic errors, deviations can occur when calculating or simulating separation characteristics. The extent of these deviations, which are caused by the individual parameters, can be examined via a sensitivity analysis of the model parameters, which provides information on the significance of the individual model parameters for the calculation of the permeate flux density and rejection. It is then possible to estimate some parameters as accurately as possible (because of the large amount of data), whereas other parameters can be estimated using fewer measurement results.

In the following text, a sensitivity analysis is carried out so that the relative deviation of the calculated target parameters, permeate flux density j_v, and salt rejection R_s (based on concentration in the bulk feed c_s^b) can be studied for low, relative deviations (up to 10%) of an individual model parameter. The other model parameters remain constant.

According to Figure 64, the model parameters, pure water membrane permeability $\bar{L}_p^0$ and the van't Hoof coefficient b_W, have an almost identical and approximately linear influence on the calculation results of the permeate flux density ($\bar{L}_p^0$ is proportional, b_W is antiproportional). The other model parameters are of little significance for the simulated permeate flux density. Figure 65 shows a very strong influence of the reflection coefficient σ on the

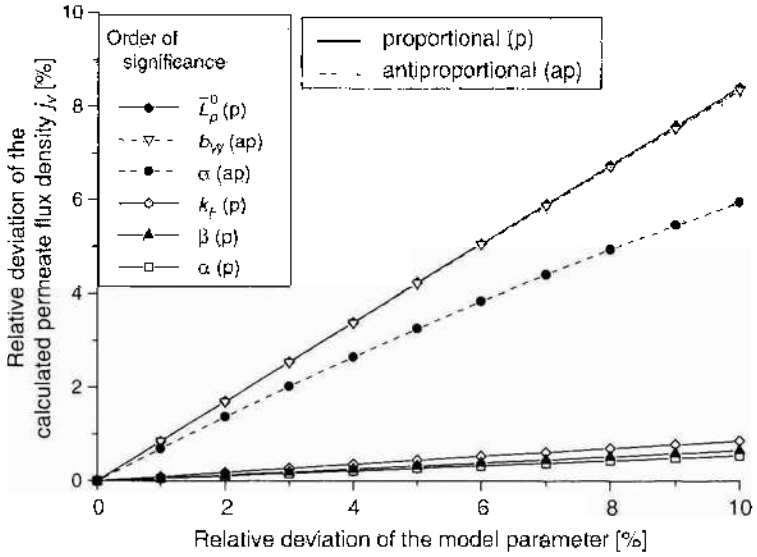

Figure 64. Relative deviation of the calculated permeate flux density j_v as a function of the relative deviation of the model parameters.

calculation of rejection, although the significance of the other parameters is negligible in comparison.

The sensitivity analysis was conducted on the basis of the following reference parameter: $\Delta P = 7$ bar, $c_s^b = 4.0$ mS/cm. For the model parameters, values that were in the range of the characterization results obtained experimentally were also assumed (see section 3.4). Depending on the reference parameter chosen and the values of the model parameters, slightly different sensitivities were produced, although the different degrees of significance for each parameter remained. To better estimate the significance of the individual model parameters on separation characteristics, it is advisable to record the entire deviation resulting from the sum of the subdeviations for equivalent relative changes in the individual parameters by determining the average values as a percentage, and therefore as a relative relation (Fig. 66).

Figure 66 illustrates that deviation during the calculation of permeate flux is dominated by the three parameters pure water permeability $\bar{L}_p^0$ (33.3%), the van't Hoff coefficient b_W (33.1%), and the reflection coefficient σ (25.4%). The accuracy of the estimation of the other parameters is of secondary importance for calculating the permeate flux.

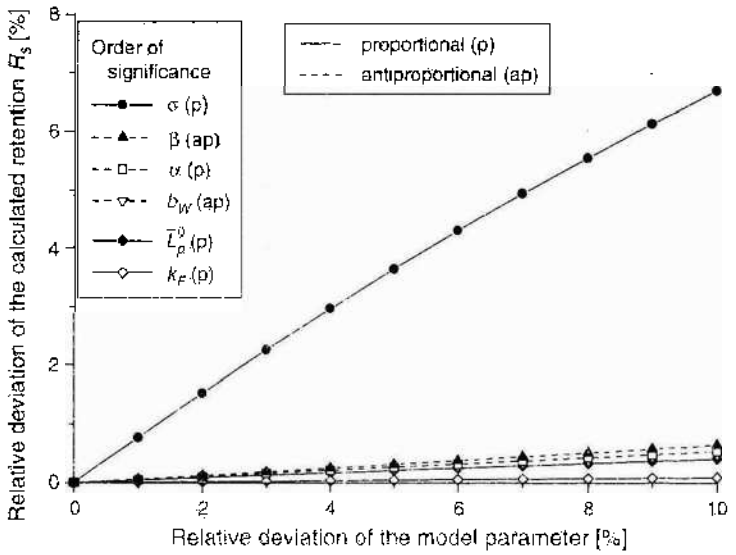

Figure 65. Relative deviation of the calculated rejection R as a function of the relative deviation of the model parameters.

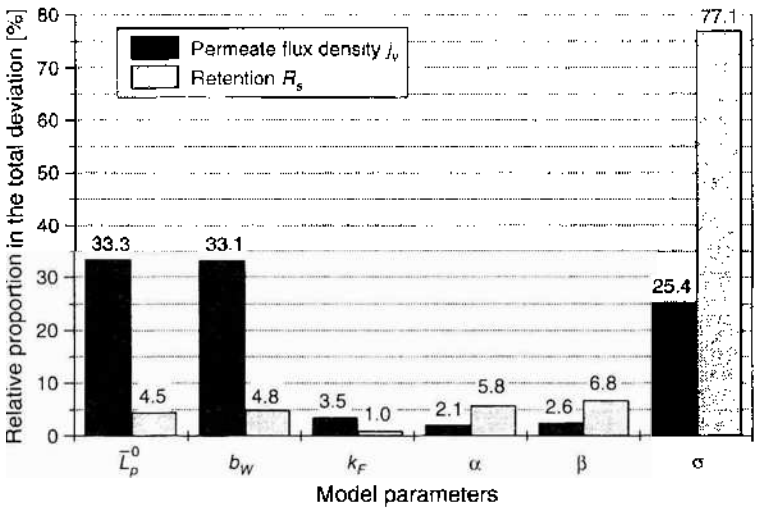

Figure 66. Relative part of deviation of model parameters in the total deviation of permeate flux density j_v and rejection R_s.

In contrast, the calculations for rejection depend primarily on the reflection coefficient (77.1%). With the exception of the mass transport coefficient k_F (1%), the remaining quantity (21.9%) is equally distributed over the other model parameters.

As expected, pure water hydraulic permeability $\bar{L}_p^0$ was to be estimated as accurately as possible for the calculation of the permeate flux density j_v. A relatively exact determination can be obtained by a simple filtration test. The van't Hoff coefficient can be approximated by plotting as many measurement points as possible. The feed-side mass transport coefficient k_F seems to play a subordinate role in the simulation of separation characteristics. In view of the fact that the reflection coefficient σ can only be estimated when a value for k_F exists, the significance of the mass transport coefficient for the accuracy of the reflection coefficient should not be neglected to any great extent. An exact value for the reflection coefficient σ is equally important for the calculation of permeate flux density and rejection. The significance of the empirical coefficients α and β should not be underestimated despite a low relative share in overall deviation in the simulation of rejection characteristics at various levels of concentration.

As a result, all model parameters should be estimated using as large a data record as possible.

3.4. Results of the Characterization of Membrane Elements and Computer-Aided Simulation and Design of Nanofiltration Processes

The presentation of the results on the characterization of the membrane elements can be divided into two sections, the first of which deals with the tests on various nanofiltration membrane elements and model solutions to determine their characterizability, as well as a comparative survey on the model parameters estimated. In the second section, the separation characteristics of the membrane elements are simulated by applying the model equations and parameters and are finally compared to the experimental results. Therefore, the first part of this section focuses on the verification of the methodology presented for the characterization of NF membrane elements, followed by the evaluation of the selected model equations based on the simulation results. For the characterization of the membrane elements, a test stand was used, as shown in Fig. 15.

3.4.1. Characterization of the Nanofiltration Membrane Elements

3.4.1.1. Determination of Pure Water Permeability There is no osmotic pressure difference when ultrapure water (fully desalinated water) is used in the determination of pure water hydraulic permeability. Hence, pure water hydraulic permeability $\bar{L}_p^0$ can be calculated simply from the permeate flux density j_v and the transmembrane pressure difference

[cf. Eq. (123) with $\Delta\Pi$]:

$$\bar{L}_p^0 = \frac{j_v}{\Delta P} \text{ for } \Delta\Pi = 0 \tag{137}$$

Determination of the pure water hydraulic permeability $\bar{L}_p^0$ for the membrane elements was carried out in a predefined pressure difference range. As far as energy is concerned, the overriding advantage, that nanofiltration membranes have over reverse osmosis membranes, is that operation can take place in the so-called hydraulic low-pressure difference range between $\Delta P = 5$–11 bar for many cases of application (e.g., low-contaminated process water from the food industry, water softening, etc.) because comparatively high membrane permeability with good rejection efficiency can be obtained at low energy consumption. For this reason, the membrane elements were investigated in a transmembrane pressure difference range of $\Delta P = 2$–13 bar (Fig. 67).

During the determination of pure water hydraulic permeability for the membrane elements according to Eq. (137), deviations from the linearity between permeate flux density and transmembrane pressure difference resulting at low transmembrane pressure differences were observed. This was caused by compaction effects from the membrane bags in the spiral wound module, which increased resistance for the permeate flow inside the membrane bags.

From a certain transmembrane pressure difference value, an approximately constant value for pure water hydraulic permeability, which was assumed as parameter L_p^0 for the operating range under study, was established. When the pressure difference was increased beyond this operating range, membrane permeability decreased as the result of an increase in the permeate-side pressure loss in the membrane bags [116]. Table 7 contains the experimental results of the pure water hydraulic permeability of four nanofiltration membrane elements under study.

The membrane elements under study were commercially available spiral wound modules made by DOW Chemicals (Liquid Separations) and FilmTec® membrane elements. Spiral wound elements are usually available with standardized diameters of 2.5″ (63.5 mm), 4″ (101.6 mm), and 8″ (203.2 mm), and in various lengths. We used elements with a diameter of 2.5″, a length of 40″ (1016 mm), and an active membrane area of $A_m \approx 2.1$ m^2 in our tests.

A comparison between Tables 7 and 8 (manufacturing data) brings to light an apparent correlation between the rejection and permeability properties of the membranes. The "open-pore" membrane NF1 has low rejection for NaCl, and thus a high pure water hydraulic permeability value. Membranes, which have better rejection properties, have lower pure water hydraulic permeability rates. However, a basic hypothesis for a direct connection is not acceptable. Although membrane selectivity is greatly influenced by cut-off and the rejection

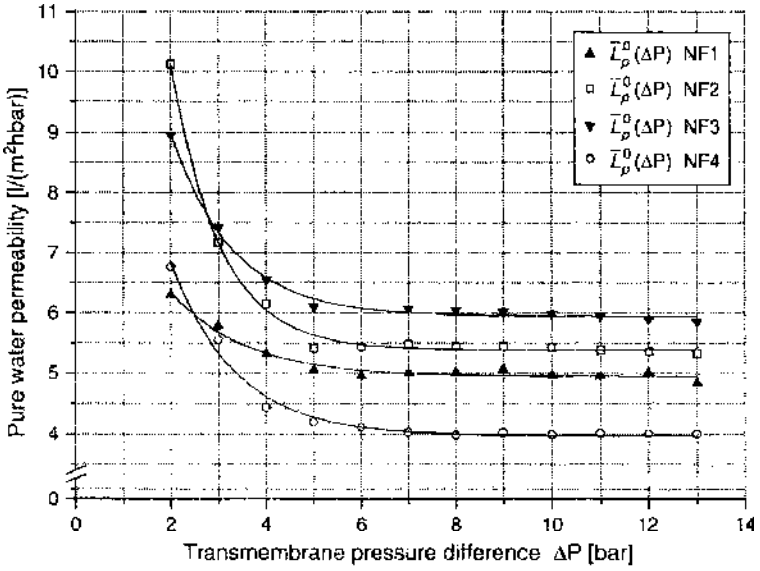

Figure 67. Determination of pure water permeability $\bar{L}_p^0$ for the membrane elements in a hydraulic differential pressure range of $\Delta P = 2$–12 bar at 293 K.

Table 7. Experimental results of pure water permeability for the membrane elements under study at 293 K.

Membrane element	Pure water hydraulic permeability $\bar{L}_p^0$
NF1	5.9 l/(m²h.bar)
NF2	5.4 l/(m²h.bar)
NF3	5.0 l/(m²h.bar)
NF4	4.0 l/(m²h.bar)

curve, the composition of the active layer in terms of pore homogeneity and pore density is important for permeability. Both these membrane properties can be modified and optimized separately.

3.4.1.2. Estimation of the Feed-Side Mass Transport Parameter k_F and the van't Hoff Coefficient b_W To estimate the parameters k_F and b_W, discontinuous concentration (batch) tests were conducted, using different membrane elements at various differential pressures. Model solutions (1 : 1 electrolyte NaCl for NF1–NF4 and, in addition, 2 : 2 electrolyte $MgSO_4$ for NF1) were used for the tests.

In presenting the experimental results, Eq. (135) is applied, except j_v is used instead of J_W.

$$\frac{1}{c_s^b - c_s^p} \cdot \left(\Delta P - \frac{j_v}{\bar{L}_p^0}\right) = b_W \cdot \exp\left(\frac{j_v}{k_F}\right) = f(j_v) \tag{138}$$

A general form of exponential regression according to Equation (136) with $x = j_v$ is used

$$f(j_v) = A_1 \cdot \exp(A_2 \cdot j_v) \tag{139}$$

with

$$A_1 = b_W \text{ and } A_2 = \frac{1}{k_F}$$

The value estimated for A_1 by regression analysis (square error minimization) corresponds to the y-axis intercept of $f(j_v = 0)$. Moreover, the slope of the curve, or the exponential degree A_2 of the function, reproduces the level of concentration polarization. Because of the reciprocal relation, a greater degree A_2 is equivalent to a small estimated value for the mass transport parameter k_F, whereby concentration polarization increases.

For illustration purposes, an introduction and discussion of the trend of the function $f(j_v)$ will be presented at this point, based on the results obtained for the system *NF1-$MgSO_4$* (Fig. 68).

The measurement results show that, at moderate and high $MgSO_4$ concentrations, corresponding to moderate to low permeate fluxes or permeate yields $Y < 10\%$, the model assumptions made are satisfied by the following characteristics:

- At different levels of transmembrane pressure difference, all curves for high concentrations of magnesium sulfate or low permeate fluxes aim at a similar value for the van't Hoff coefficient b_W [y-axis intercept for $f(j_v = 0)$].

Table 8. Manufacturing data on the rejection and cut-off characteristics of the membrane elements under study.

	Separation properties according to the manufacturers			
Membrane	Test conditions*	Permeate volume flow	Rejection (%)	Cut-off
NF 1	2 g/l NaCl, 5 bar, 25°C	No details	<45	ca. 300 g/mol
NF 45-2540	2 g/l $MgSO_4$, 5 bar, 25°C	158.3 l/h ± 20 %	95	
NF 2	2 g/l NaCl, 5 bar, 25°C	No details	70	ca. 200 g/mol
NF 70-2540	2 g/l $MgSO_4$, 5 bar, 25°C	133.3 l/h ± 20%	95	
NF 3	2 g/l NaCl, 5 bar, 25°C	No details	90	ca. 200 g/mol
NF 90-2540	2 g/l $MgSO_4$, 5 bar, 25°C	108.3 l/h ± 20%	95	
NF 4	2 g/l NaCl, 16 bar, 25°C	104 l/h ± 20%	99	ca. 100 g/mol
TW 30-2540				

*Standardised test conditions specified by membrane manufacturers.

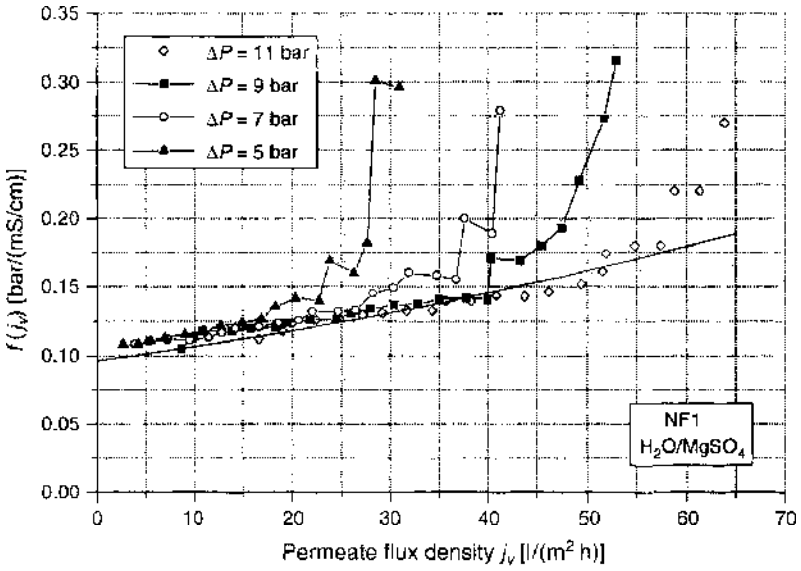

Figure 68. Trend of the function $f(j_v)$ for the system NF1–$MgSO_4$ at various transmembrane pressure differences ΔP (293 K) with fitting curve at $\Delta P = 11$ bar.

- For moderate to low permeate fluxes, the experimental results can be approximated using an exponential functional approach according Eq. (138).
- At low concentrations or high permeate fluxes, deviations from ideal operating behavior occur. The slope of the curves, showing the results, increases steeply. Therefore, the points in this range cannot be recorded by a trend based on the above-mentioned function [Eq. (138)]. This effect occurred for higher transmembrane pressure difference values in all the tests conducted and was probably caused by varying mass transport coefficients for the range under study. At the start of the test, comparatively high permeate fluxes were generated, but these decreased quite strongly when concentration in the storage tank was increased slightly. The average feed-side volume flow cannot be considered constant, particularly for this test period; the same is also true for the mass transport coefficient. The decrease in the permeate volume flow is lower for moderate and high feed concentrations. Therefore, in this part of the test, calculations can be carried out with a constant feed volume flow with good approximation ($k_F \approx$ const.).

During the characterization process for the membrane elements using NaCl, an effect typical for nanofiltration membranes at higher concentrations occurred. As concentration increased, the Debye length (characteristic measure for the thickness of the electric double layer [118]) decreased and the negative membrane charge was shielded to a greater extent. As a result, there was less exclusion of co-ions, and the anion concentration in the membrane increased. As a consequence, rejection decreased (this effect is also predicted in the formulation of the ideal Donnan equilibrium, see section 1).

Because the model concepts do not contain the extent to which rejection is influenced by charge interactions, deviation from the proposed model occurred in the experiments at low permeate fluxes. This effect was quite pronounced for the membrane element NF2 but was weaker for NF3. As for the membrane NF4 whose rejection properties border between nanofiltration and reverse osmosis, no strong decrease was recorded, even for higher concentrations of NaCl.

For these reasons, the regression analysis for the estimation of k_F and b_{II} was applied to the experimental results for moderate and high feed concentrations. The experimental points, which deviate from the model concepts for the above-mentioned reasons, were not included in the regression analysis but are recorded in the figures. For the experimental results, at a transmembrane pressure difference of $\Delta P = 11$ bar, the idealized functional trend (equalizing curve) was adapted to the measurement results via square error minimization and integrated into the figures to give an example.

Figures 69–71 show the functional trends $f(j_v)$ for the estimation of the parameters k_F and b_{II} for the membrane elements NF2–NF4, using the model solution NaCl. It can be

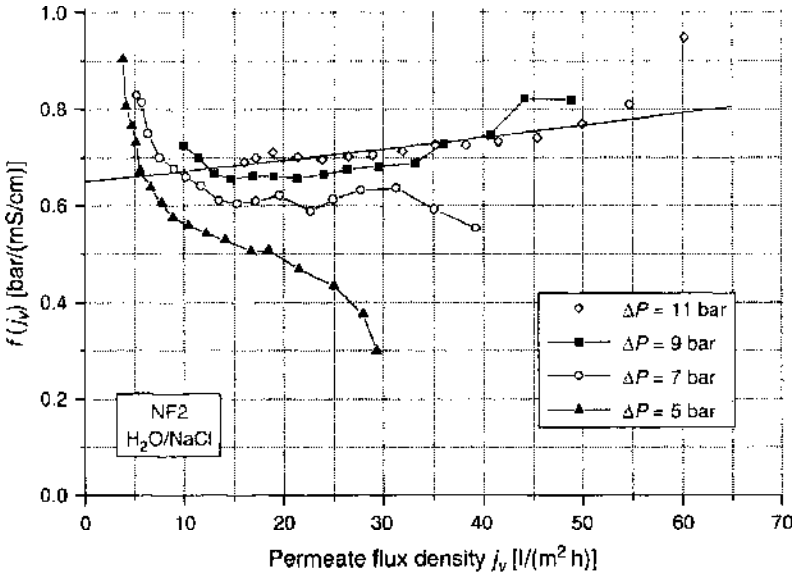

Figure 69. Trend of the function $f(j_v)$ for the system NF2–NaCl at various transmembrane pressure differences ΔP (293 K) with fitting curve at $\Delta P = 11$ bar. Reprinted with permission from [132], M. Noronha et al., *Ann. N. Y. Acad. Sci.* 984, 142 (2003). © 2003. New York Academy of Sciences, USA.

seen from the results that approximately the same values for the van't Hoff coefficient b_W can be estimated for all tests, even at different levels of transmembrane pressure difference, if the regression analysis is performed, as illustrated in the previous section (see also the following section). At higher transmembrane pressure differences, an increase in the developing concentration polarization was recorded that is expressed by the increase in the slope of the curves.

As for low transmembrane pressure difference levels, concentration polarization for NaCl is negligible (nonexistent or even negative gradient). For these cases, the concentration in the bulk stream (c_s^b) can be equated with the concentration on the membrane surface (c_s^w) and $k_f \to \infty$. Furthermore, strong charge interactions occur between the electrolyte solution and the membrane at high concentrations, greatly differentiating from ideal operating behavior (Fig. 69).

The system NF1–NaCl was a special case in the system under study. Rejection for the membrane NF1 was extremely low for monovalent ions compared to the other systems

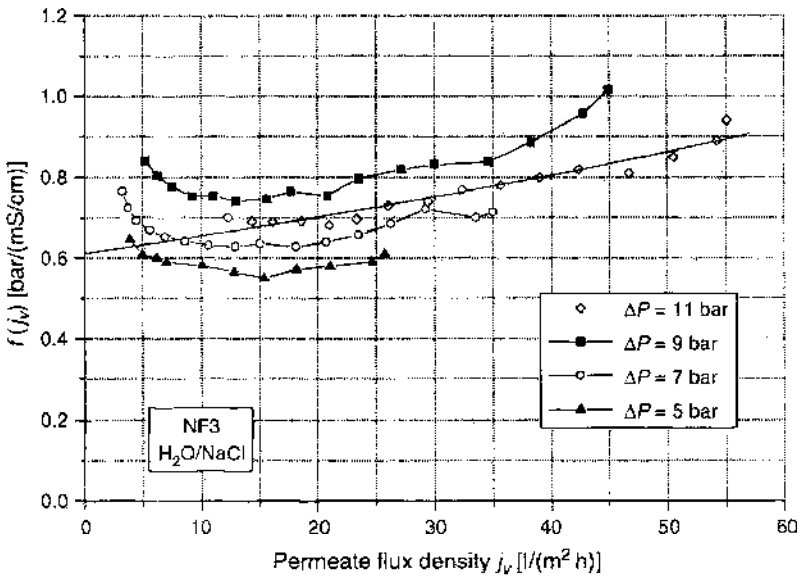

Figure 70. Trend of the function $f(j_v)$ for the system NF3–NaCl at various transmembrane pressure differences ΔP (293 K) with fitting curve at $\Delta P = 11$ bar.

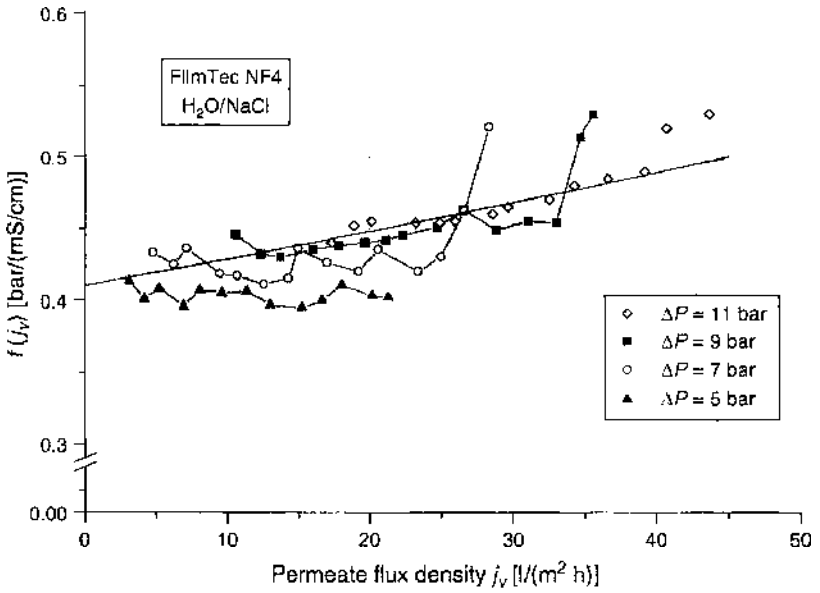

Figure 71. Trend of the function $f(j_v)$ for the system NF4–NaCl at various transmembrane pressure differences ΔP (293 K) with fitting curve at $\Delta P = 11$ bar.

studied. As feed concentration in the storage tank increased, a decrease in permeate flux could not be recorded because only low osmotic pressure difference could build up as a result of a small difference in transmembrane concentration (between feed and permeate). Thus, the presentation of the experimental results is different from the previous figures. The results of this test can be seen in Figure 72.

The parameters b_w and k_F cannot be estimated simply by regression analysis from Figure 72. However, judging from the experience gained in the tests, characterization by adding an additional assumption, is possible

- The low rejection allows the assumption to be made that concentration polarization, in the pressure difference and concentration range under study, can be neglected. On the basis of this assumption, it can be stated that the concentration in the bulk stream c_s^b

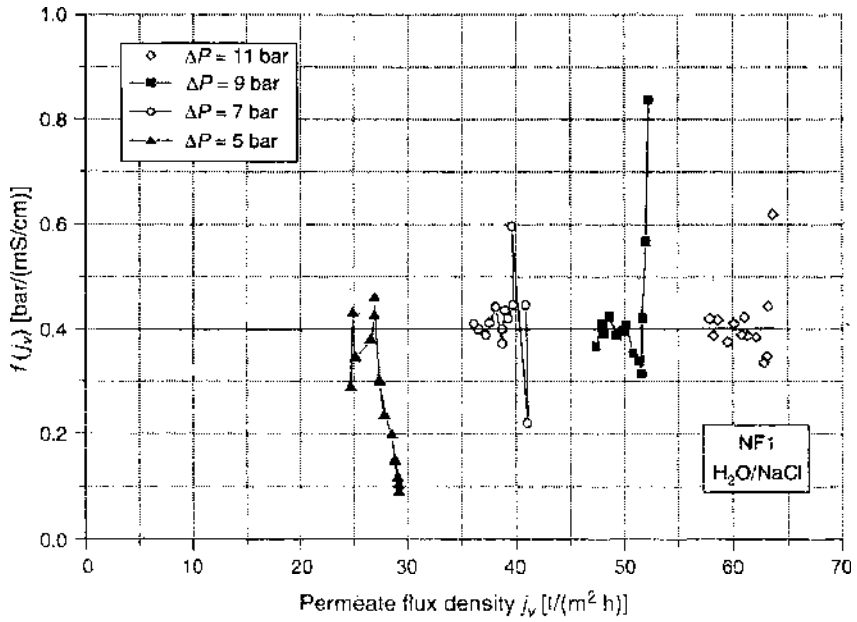

Figure 72. Trend of the function $f(j_v)$ for the system NF1–NaCl at various transmembrane pressure differences ΔP (293 K) with fitting curve at $\Delta P = 11$ bar.

is equivalent to the concentration on the membrane surface c_s''. As a result, Eq. (135) (instead of J_W, j_v is used) can be simplified with $k_F \to \infty$ to form

$$\frac{1}{c_s^b - c_s^p} \cdot \left(\Delta P - \frac{j_v}{\bar{L}_p^0}\right) = b_W \cdot \exp\left(\frac{j_v}{k_F}\right) \tag{140}$$

mit $k_F \to \infty$

$$\frac{1}{c_s^b - c_s^p} \cdot \left(\Delta P - \frac{j_v}{\bar{L}_p^0}\right) = b_W \tag{141}$$

The results for the pressure difference $\Delta P = 7, 9$, and 11 [bar] verify this assumption. The measurement points vary by one value for $b_W = 0.4$ [bar/(mS/cm)]. Measurement inaccuracies are partly the cause of the fluctuations.

To adapt the simulation procedure to different flow conditions and different industrial spiral wound elements, the mass transport coefficient k_F is to be specified in conjunction with flow velocity of the feed solution u, as well as the hydraulic diameter of the feed channel of the membrane d_H. For the mean flow velocity u in the membrane element, on which the mass transport coefficient is based, the relevant mean feed volume flow across the length of the membrane element must be determined. To this end, the arithmetic mean value is determined from the maximum and minimum feed volume flow recorded by those measurement points that are incorporated into the regression analysis. An average value is then calculated arithmetically from this value, and the constant retentate volume flow is 500 [l/h]. Figure 73 shows a graphic illustration of the procedure involved in determining the average feed volume flow.

The simplified calculation of the average feed volume flow can be conducted by using Eq. (142):

$$\bar{\dot{Q}} = 0.5 \cdot (\dot{Q}_{\max}^p + \dot{Q}_{\min}^p) + \dot{Q}^r \tag{142}$$

According to Schock and Miquiel [13], a constant hydraulic diameter of the channel of the membrane element of $d_H = 0.95$ [mm] and an effective cross-sectional area of $A_{eff} = 9.11 \cdot 10^{-4}$ [m^2] can be defined for the spiral wound elements with a diameter of 2.5" used in the experiments. Table 9 sums up the results from this section on characterization in which the estimated model parameters at two transmembrane pressure differences were compared

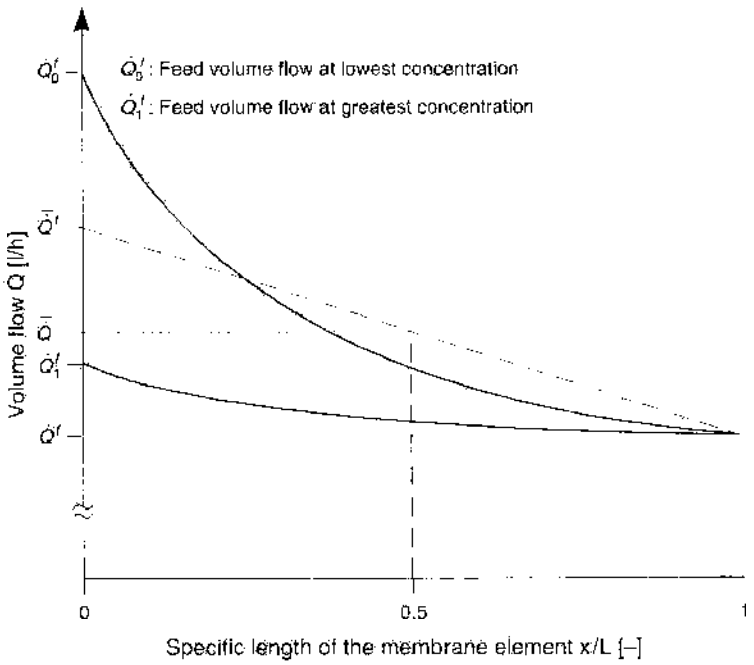

Figure 73. Graphic representation of the determination of the mean feed volume flow along the specific length of a membrane element.

Table 9. Summary of the results for the estimation of the van't Hoff coefficient b_M and the mass transport coefficient k_F.

System	ΔP [bar]	b_M [bar/(mS/cm)]	k_F [l/(m²h)]	$\dot{Q}$ [l/h]	u [m/s]	Re [-]
NF1–$MgSO_4$	5	0.0968*	50.914	514.5	0.157	149.11
	7	0.0967*	52.76	518.88	0.158	150.1
NF1–NaCl	9	0.4	$k_F \to \infty$	525	0.16	152
	11	0.4	$k_F \to \infty$	531	0.162	153.9
NF2–NaCl	9	0.5841	166.2	512	0.156	148.2
	11	0.6089	169.95	517.75	0.158	150.15
NF3–NaCl	9	0.682	146.29	513.75	0.157	149.4
	11	0.662	145.29	517.25	0.158	150.1
NF4–NaCl	9	0.423	242.37	511.25	0.156	148.2
	11	0.4406	236.10	514.25	0.157	149.15

*The unit for b_M for magnesium sulfate is [bar/(g/l)].

for one system. The terms $\Delta P = 5$ and 7 [bar] were selected for the tests with $MgSO_4$ and transmembrane pressure differences of $\Delta P = 9$ and 11 [bar] for the tests with NaCl. In addition, the table contains information on the average feed volume flows, flow velocity, and Reynolds number.

Table 9 shows there was good approximation and agreement for the parameters b_M and k_F in two separate experiments with different transmembrane pressure differences. The tests with the $MgSO_4$ model solution showed that the transmembrane pressure difference had no great influence on the parameters, whereas, for tests using the NaCl model solution for model parameter estimation, higher transmembrane pressure differences had to be chosen to suppress the nonideal filtration effects (to reduce the influence of the membrane fixed charge) that occurred. The average feed volume flow varies only very slightly. As a result, only a slight deviation in velocity u and the Reynolds number Re occurred in the experiments. The average Reynolds number of $Re = 150$ for the flow in the spiral wound elements is clearly in the laminar flow range.

3.4.1.3. Maximum Transmembrane Concentration Difference During the filtration experiments, the permeate flux density j_v decreased as electrolyte concentration increased in the storage tank. The osmotic pressure difference $\Delta\Pi$ increased and counteracted the transmembrane pressure difference ΔP. Osmotic pressure difference can be calculated from the difference between the permeate flux density of pure water and the permeate flux density of an electrolyte solution at constant transmembrane pressure difference by applying Eq. (123):

$$\Delta\Pi = \frac{\Delta P \cdot \bar{L}_p^0 - j_v}{\bar{L}_p^0} \tag{143}$$

or

$$\Delta\Pi = \Delta P - \frac{j_v}{\bar{L}_p^0} \tag{144}$$

If the permeate flux density decreases $j_v \to 0$, then the transmembrane pressure difference is equivalent to the osmotic pressure difference. According to the thermodynamic definition of osmotic pressure based on van't Hoff, it is true for diluted electrolyte solutions that there is a linear relation between the osmotic pressure of a solution and the electrolyte concentration. The following equation results for the osmotic pressure difference across the membrane [see Eq. (126)]:

$$\Delta\Pi = b_M \cdot (c_s'' - c_s^P) \tag{145}$$

Concentration at the membrane surface c_s'' can be calculated using the mass transport coefficient k_F, which was estimated individually for each experiment. Thus, the osmotic pressure difference according to Eq. (144) can be expressed as a function of the transmembrane concentration difference $c_s'' - c_s^P$. The trend of the function is shown in Figures 74–78 for all the systems studied, and linearity can be verified by applying Eq. (145).

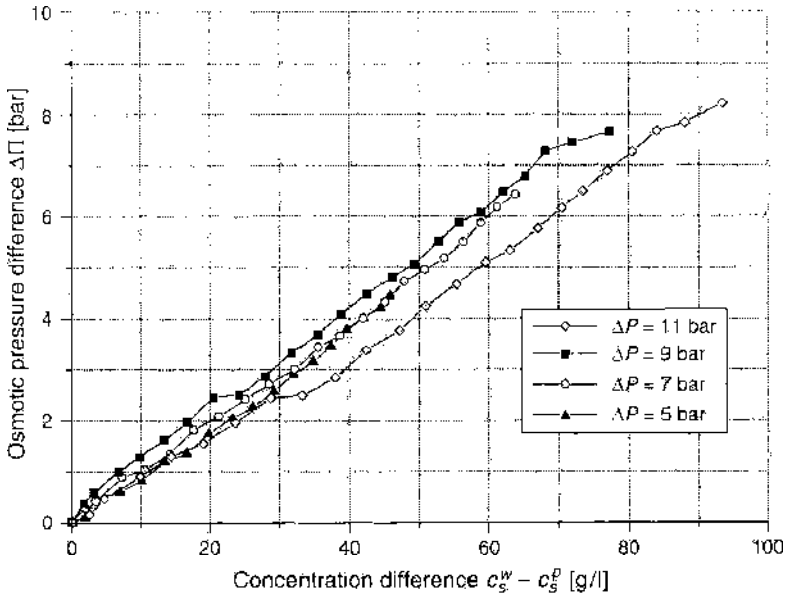

Figure 74. Osmotic pressure difference $\Delta\Pi$ as a function of the transmembrane concentration difference $c_s^w - c_s^p$ for the system NF1–$MgSO_4$ at various pressure differences ΔP (293 K).

The figures highlight the linear dependence of osmotic pressure difference on transmembrane concentration difference for low electrolyte concentrations. As feed concentration c_s^f in the storage tank and osmotic pressure difference rose, the transmembrane concentration difference $c_s^w - c_s^p$ also increased at first in a linear relation. The value for the van't Hoff coefficient b_w was almost the same (similar increase in the functions) at different transmembrane pressure differences ΔP. Thus, the linear dependence, expressed by Eq. (145), is given.

If the concentration of monovalent ions in the electrolyte in the storage tank continues to increase, an effect, typical for the separation behavior of nanofiltration membranes with high rejection, occurs (cf. Figs. 76 and 77). Although the permeate flux j_w continues to decrease because of the increase in feed concentration at a specified transmembrane pressure difference, and the osmotic pressure difference increases, the nanofiltration membrane reaches a maximum in transmembrane concentration difference $c_s^w - c_s^p$. If the feed concentration continues to increase, then a strong decrease in rejection occurs (as a result of reducing the

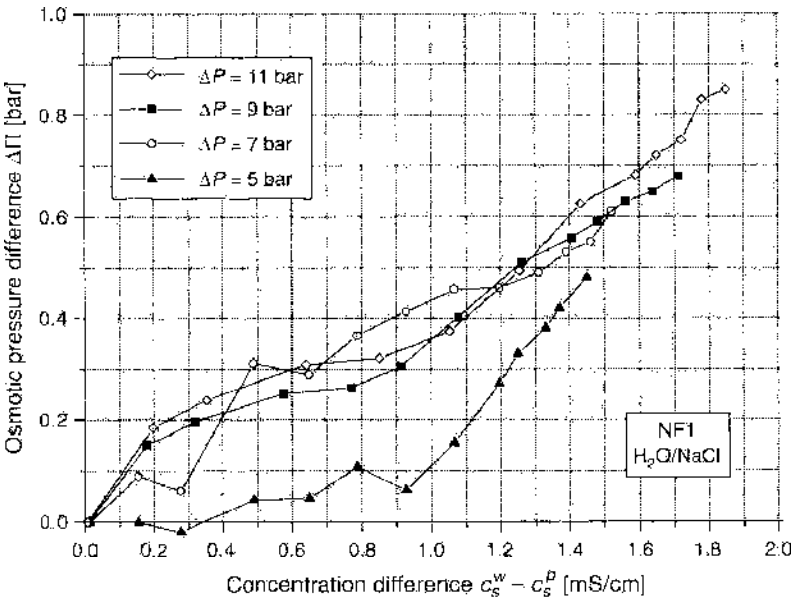

Figure 75. Osmotic pressure difference $\Delta\Pi$ as a function of the transmembrane concentration difference $c_s^w - c_s^p$ for the system NF1–NaCl at various pressure differences ΔP (293 K).

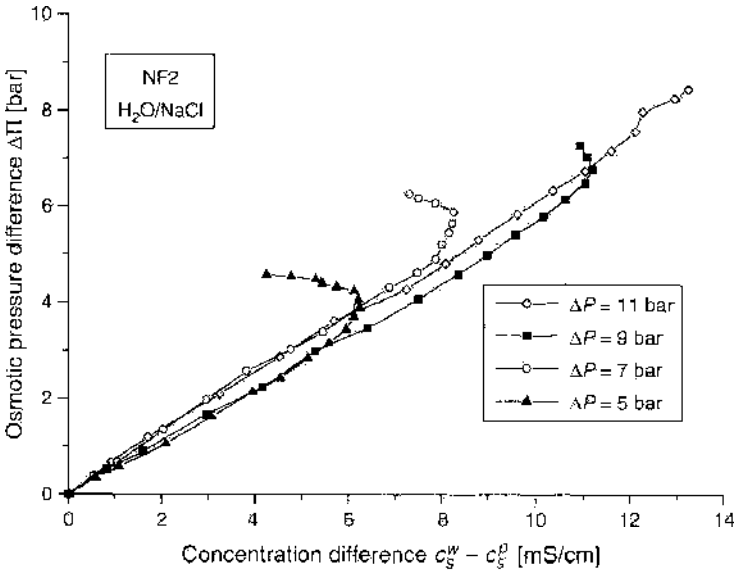

Figure 76. Osmotic pressure difference $\Delta\Pi$ as a function of the transmembrane concentration difference $c_s^w - c_s^p$ for the system NF2–NaCl at various pressure differences ΔP (293 K). Reprinted with permission from [132], M. Noronha et al. *Ann. N. Y. Acad. Sci.* 984, 142 (2003). © 2003. New York Academy of Sciences, USA.

influence of the membrane fixed charge). For this reason, the transmembrane concentration difference decreases further when osmotic pressure difference increases. Therefore, for one system studied at specified transmembrane pressure difference, the nanofiltration membrane was characterized by a maximum attainable transmembrane concentration difference across the membrane or by maximum "separation properties." This phenomenon becomes clearer when concentration difference is expressed as follows:

$$\begin{aligned} c_s^w - c_s^p &= c_s^w - (1 - R_{s,Real}) \cdot c_s^w \\ &= R_{s,Real} \cdot c_s^w \end{aligned} \tag{146}$$

It then follows for the range of functions considered:

$$|R_{s,Real} \cdot c_s^w|c_s^{f,0} > |R_{s,Real} \cdot c_s^w|c_s^{f,0} \text{ with } \Delta P = \text{ const.} \tag{147}$$

for $c_s^{f,0} > c_s^{f,1}$.

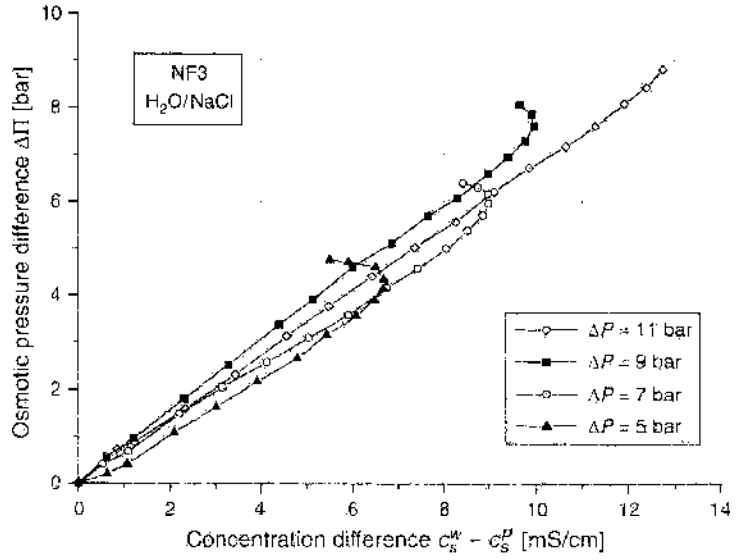

Figure 77. Osmotic pressure difference $\Delta\Pi$ as a function of the transmembrane concentration difference $c_s^w - c_s^p$ for the system NF3–NaCl at various pressure differences ΔP (293 K).

This means that the additional increase in concentration at the membrane surface $c_s^{II'}$ is overcompensated for by the reduction of rejection $R_{s,\,Real}$. Separation behavior at higher levels of transmembrane pressure difference is, according to the model equations, a response to ideal behavior. The influence of membrane fixed charge is suppressed to a greater extent, allowing higher maximum transmembrane concentration differences to be reached. Therefore, regression analysis was carried out for the systems NF2–NaCl and NF3–NaCl at higher transmembrane pressure differences ($\Delta P = 9$ and 11 bar). The dependence of osmotic pressure difference on transmembrane concentration difference can be considered as linear for the systems NF1–$MgSO_4$ (Fig. 74) and NF4–NaCl (Fig. 78).This was primarily a result of rejection, which is very high ($R_{s,\,Real} > 0.85$) in both systems, even at relatively high concentrations. In the system NF1–$MgSO_4$, a mixture of bivalent ions, which were retained very well at high concentrations, was filtered. A "densely structured" membrane, which can be defined as a reverse osmosis membrane because of its rejection for monovalent ions, was used in the system NF4–NaCl.

The results in Figure 75 illustrate that concentration polarization can be neglected for the system NF1–NaCl. The osmotic pressure difference is linearly dependent on the concentration difference in the bulk stream and in the permeate $c_s^b - c_s^p$. In comparison, the values for concentration difference were low.

3.4.1.4. Estimation of the Reflection Coefficient σ The reflection coefficient is considered a factor linking permeate flux density and electrolyte flux density. An ideal semipermeable membrane would only allow water to permeate ($\sigma = 1$), which would mean that rejection is $R_{s,\,Real} = 1$. In the limit $\sigma = 1$, the transport model adopted here reduces to the classic solution–diffusion model, for which the rejection increases monotonically from 0 at zero permeate volume flux to the limiting value of 1 as the permeate volume flux increases without bound (the functional form does, however, change from an exponential function of volume flux to an algebraic one when $\sigma = 1$). For more informations see section 2.2.1. A purely porous membrane cannot retain ions ($R_{s,\,Real} = 0$); as a consequence, an increase in permeate flux results in an increase in ions in the permeate (permeate concentration remains constant). Thus, the reflection coefficient is estimated by maximum rejection $R_{s,\,Real,\,max}$.

Basically, rejection rises when feed concentration is reduced and transmembrane pressure difference is increased (increase in permeate flux density). To determine the reflection coefficient, a filtration test at low feed concentration and a transmembrane pressure difference of, for example, $\Delta P = 11$ bar, should be performed. At this point, it should be stated that maximum rejection at $\Delta P = 5$, 7, and 9 bar only differs insignificantly from the values presented in Table 10.

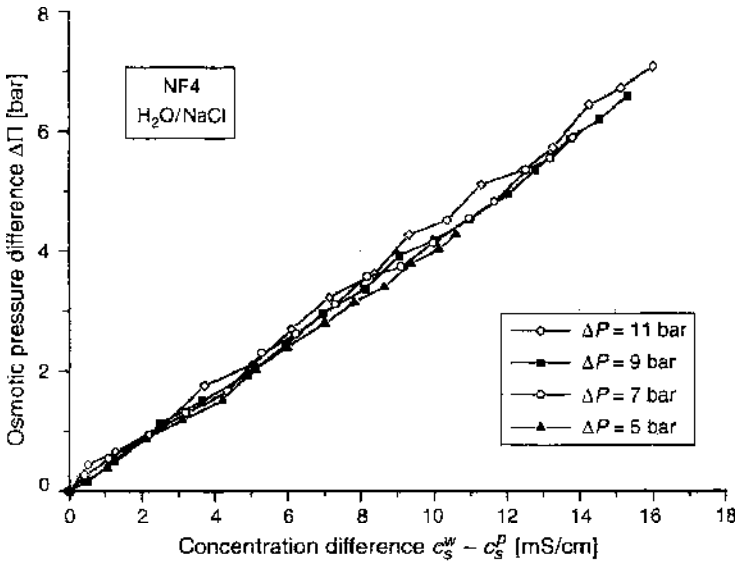

Figure 78. Osmotic pressure difference $\Delta\Pi$ as a function of the transmembrane concentration difference $c_s^w - c_s^p$ for the system NF4–NaCl at various pressure differences ΔP (293 K).

Table 10. Results of estimation of the reflection coefficient σ for the systems under study.

System	Reflection coefficient σ [-]
NF1–$MgSO_4$	0.996
NF1–NaCl	0.41
NF2–NaCl	0.97
NF3–NaCl	0.979
NF4–NaCl	0.993

From Table 10, it can be seen that, with the exception of the system NF1–NaCl, very high reflection coefficients $\sigma \geq 0.95$ were determined. The maximum rejection value $R_{s,Real,max} = \sigma$ expresses the rejection properties of a NF membrane, but only in a narrow operating range. The actual membrane characteristic is formed by rejection as feed concentration increases and at different transmembrane pressure differences. For the system NF1–NaCl, a low reflection coefficient of $\sigma = 0.41$ is specified, indicating a strong link between the partial flows of the water and the ions through the membrane, which has a comparatively low rejection for NaCl.

3.4.1.5. Estimation of the Empirical Parameters α and β The parameters α and β characterize the rejection of a NF membrane at different electrolyte concentrations. Schirg and Widmer [143] postulated that salt membrane permeability $\bar{P}_s$ is dependent on concentration at the membrane surface c_s^m and increases with the increase in concentration and can be characterized by the following equation:

$$\bar{P}_s = \alpha \cdot (c_s^m)^\beta \tag{148}$$

where α and β are the variable empirical parameters.

Because actual rejection $R_{s,Real}$, concentration at the membrane surface c_s^m, and permeate flux density j_v, as well as the refection coefficient σ, can be estimated or are known for various measurement points, Eq. (129) can be reformulated as follows:

$$\bar{P}_s = \frac{(\sigma - 1) \cdot j_v}{\ln((\sigma - R_{s,Real})/\sigma \cdot (1 - R_{s,Real}))} \tag{149}$$

Membrane permeability $\bar{P}_s$ can be plotted against membrane surface concentration c_s^m, and the parameters α and β can be estimated. The following figures show the results of this characterization step for all the systems under study (Figs. 79–83). As in section 3.4.1.2, at a transmembrane pressure difference of $\Delta P = 11$ bar, the idealized functional trend was adapted to the measurement results via square error minimization and integrated into the figures as an example.

With only a few exceptions, the figures show the dependence of salt membrane permeability on membrane surface concentration in the form of a potential function. There are clear differences in the functional trends at different hydraulic pressures for the system NF1–NaCl shown in Figure 80. These results could be predicted by the low reflection coefficient because this value ($\sigma = 0.41$) indicates a major coupling between the partial flows of the water and the ions. Accordingly, dissolved ions are also transported through the membrane to almost the same extent when transmembrane pressure difference increases. As a result, the relation of salt membrane permeability is almost proportional to transmembrane pressure difference.

There is no coupling of the partial flows for the systems NF2–NaCl and NF3–NaCl (Figs. 81 and 82). The fluctuations in the results lie within the scope of the measurement inaccuracies. Noteworthy is the higher ion permeability for the system NF2–NaCl at low transmembrane pressure differences, which is caused by the electrostatic interactions of the membrane with the electrolyte solution. These effects are suppressed at higher pressure differences and produce the same result at $\Delta P = 9$ and 11 bar (the experiments were performed separately). For higher electrolyte concentrations, the beginning of an exponential increase in salt permeability, which is also a result of the influence of electrostatic interactions, can be seen (Fig. 82; NF3–NaCl).

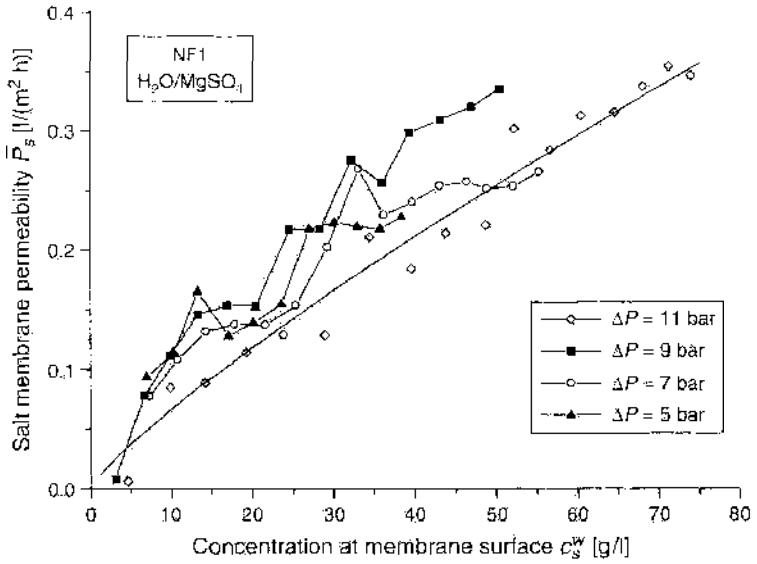

Figure 79. Salt membrane permeability $\bar{P}_s$ as a function of the concentration at the membrane surface c_s^w for the system NF1–$MgSO_4$ at various transmembrane pressure differences ΔP (293 K) with curve fitting at ΔP = 11 bar.

The results for the system NF4–NaCl best coincide with the assumption of the potential dependence of salt permeability on membrane surface concentration, compared to the other systems studied. For all transmembrane pressure differences, there was similar dependence, which verifies the functional trend even at higher concentrations.

Table 11 sums up the results of this section of the characterization procedure. To this end, the results for one system under study were compared at two transmembrane pressure differences (Table 11).

Table 11 illustrates that, with the exception of the system NF1–NaCl, the model parameters α and β, determined individually, show good approximation and agreement at different transmembrane pressure differences.

To summarize: The characterization method for NF membranes, presented in section 3.3.2, was successfully tested. The model parameters in the model equations could be estimated as examples, using five different systems and by regression via simple square error minimization. Each system studied was characterized by six individual model parameters that, in conjunction with the model equations, enable the simulation of separation characteristics of membrane elements to be carried out. This will now be verified in the next section.

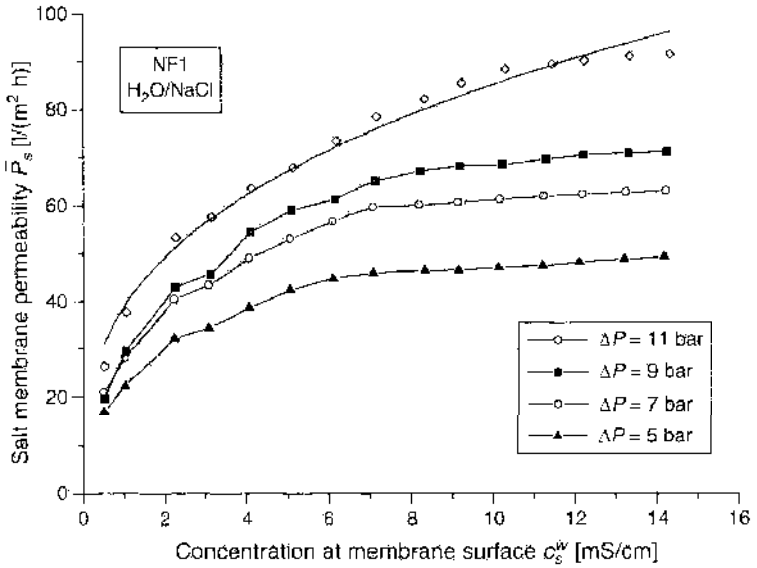

Figure 80. Salt membrane permeability $\bar{P}_s$ as a function of the concentration at the membrane surface c_s^w for the system NF1–NaCl at various transmembrane pressure differences ΔP (293 K) with curve fitting at ΔP = 11 bar.

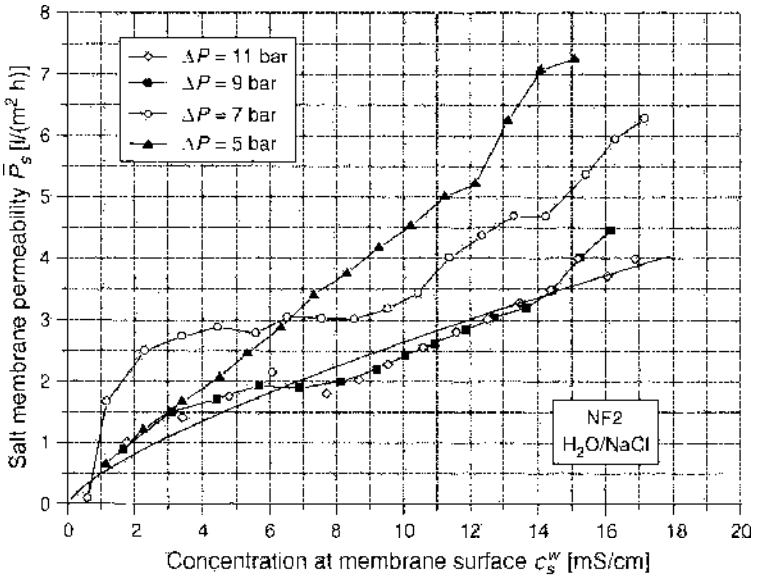

Figure 81. Salt membrane permeability $\bar{P}_s$ as a function of the concentration at the membrane surface c_s^w for the system NF2–NaCl at various transmembrane pressure differences ΔP (293 K) with curve fitting at ΔP = 11 bar. Reprinted with permission from [132], M. Noronha et al., *Ann. N. Y. Acad. Sci.* 984, 142 (2003). © 2003, New York Academy of Sciences, USA.

3.4.2. Simulation of the Separation Characteristics of NF Spiral Wound Modules

The characterization method for nanofiltration spiral wound modules, introduced in section 3.3, was applied to five different systems (membrane element/model solution). For each system, six individual model parameters, which allow the simulation of separation characteristics of membrane elements to be simulated at different hydraulic pressures and feed concentrations, were determined or estimated.

The following table (Table 12) contains the model parameters for the systems used for verification purposes and the simulation processes presented in this section. In addition, flow velocity u and hydraulic diameter $d_{H,2.5''}$ are specified for the mass transport coefficient k_F. (These details are needed for adapting the mass transport coefficient to flow conditions in industrial 8″ spiral wound elements.)

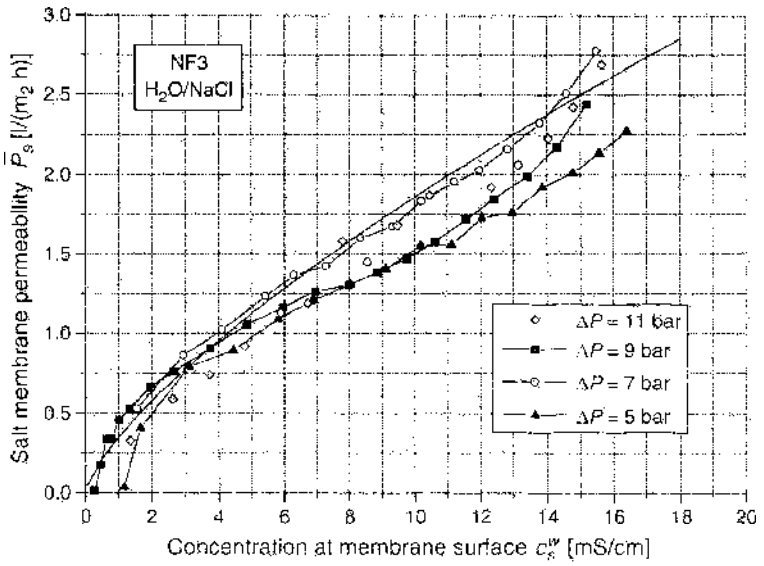

Figure 82. Salt membrane permeability $\bar{P}_s$ as a function of the concentration at the membrane surface c_s^w for the system NF3–NaCl at various transmembrane pressure differences ΔP (293 K) with curve fitting at ΔP = 11 bar.

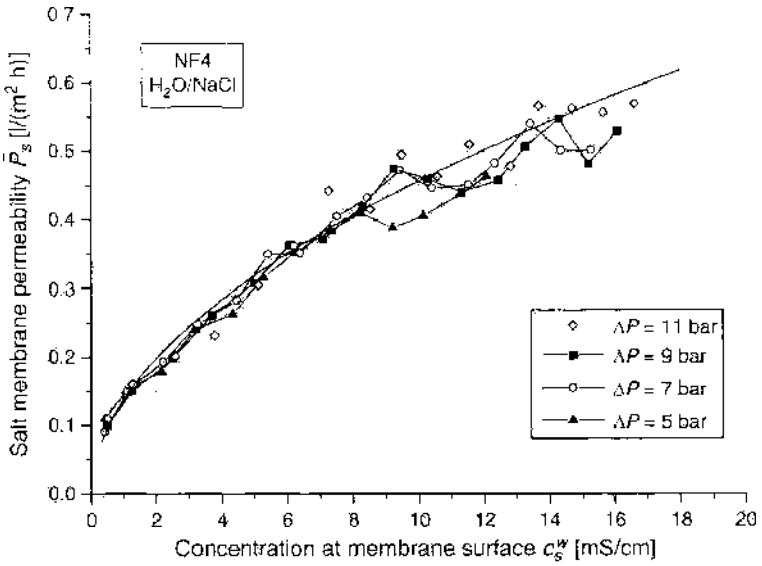

Figure 83. Salt membrane permeability $\bar{P}_s$ as a function of the concentration at the membrane surface c_s^w for the system NF4–NaCl at various transmembrane pressure differences ΔP (293 K) with curve fitting at $\Delta P = 11$ bar.

In this section, the model equations are verified so that the simulation of the separation characteristics of the membrane elements can be compared with the experimentally determined results and then evaluated. The model parameters were selected for systems with NaCl solution at a transmembrane pressure difference of $\Delta P = 11$ bar to rule out, as far as possible, nonideal separation behavior during the characterization process. The fluctuation in the model parameter did not depend on the transmembrane pressure difference for the system NF1–NaCl.

3.4.2.1. Simulation of the Permeate Flux Density in the Spiral Wound Elements The following simulation results show the extent to which the permeate flux density j_v in the spiral wound modules depends on concentration in the bulk stream c_s^b at different levels of transmembrane pressure difference ΔP (Figs. 84–88). The model parameters for the simulation of each system are taken from Table 12. The experimental data from the discontinuous concentration tests were also incorporated into the above figures, thus allowing simulation efficiency to be compared directly and evaluated.

The figures show good agreement between simulation and the experiments. Despite different separation characteristics, the permeate flux density can be described quite accurately as a function of concentration in the bulk stream, as well as a function of transmembrane pressure difference. For example, there is only a slight (linear) dependence of the permeate flux density on concentration for the system NF1–NaCl (Fig. 85), whereas for the systems NF1–$MgSO_4$, NF2–NaCl, and NF3–NaCl, a nonlinear dependence, typical for nanofiltration membranes, can be seen. For the system NF4–NaCl, a permeate flux density, characteristic of reverse osmosis membranes, as a function of feed concentration is obvious.

Table 11. Summary of the results for the estimation of the empirical coefficients α and β.

System	ΔP [bar]	α [-]	β [-]
NF1–$MgSO_4$	5	0.0168	0.6302
	7	0.0188	0.6177
NF1–NaCl	9	28.012	0.449
	11	35.94	0.37
NF2–NaCl	9	0.6499	0.6136
	11	0.6562	0.6063
NF3–NaCl	9	0.393	0.674
	11	0.373	0.686
NF4–NaCl	9	0.182	0.382
	11	0.169	0.403

Table 12. Overview of the estimated model parameters used for the simulation of the separation behavior of nanofiltration spiral wound modules.

Model parameters	NF1–$MgSO_4$	NF1–NaCl	NF2–NaCl	NF3–NaCl	NF4–NaCl
$\bar{L}_p^0$ [l/(m²h.bar)]	5.9	5.9	5.4	5.0	4.0
b_κ [bar/(mS/cm)]	0.0967*	0.4	0.6089	0.662	0.4406
k_f [l/(m²h)]	52.76	$k_f \to \infty$	169.95	145.29	236.10
$u_{25°}$ [m/s]	0.157	0.162	0.156	0.157	0.156
$d_{H,25°}$ [m]	$0.95 \cdot 10^{-3}$	$0.95 \cdot 10^{-3}$	$0.95 \cdot 10^{-3}$	$0.95 \cdot 10^{-3}$	$0.95 \cdot 10^{-3}$
σ [-]	0.996	0.41	0.97	0.979	0.993
α [-]	0.0188	35.94	0.6562	0.373	0.169
β [-]	0.6177	0.37	0.6063	0.686	0.403

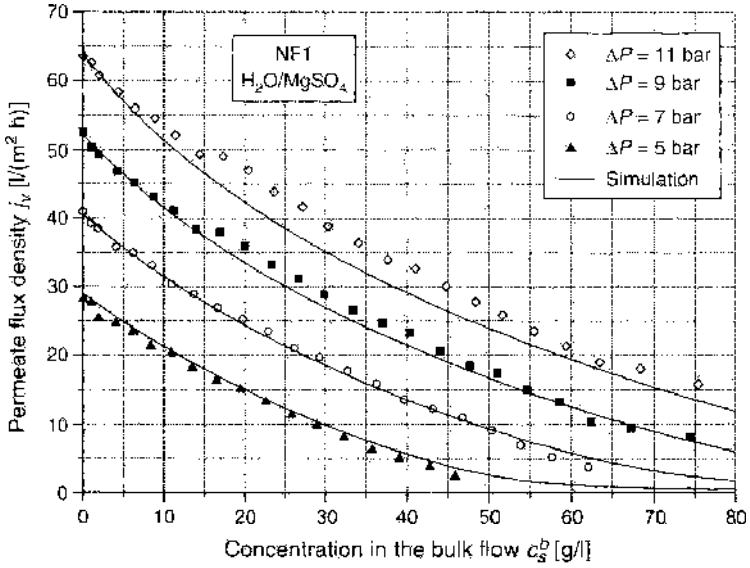

Figure 84. Comparison of simulation and experimental results—permeate flux density j_v as a function of concentration c_s^b at various transmembrane pressure differences ΔP for the system NF1–$MgSO_4$ (293 K), Reprinted with permission from [136], M. Noronha et al., *Desalination* 145, 207, (2002). © 2002, Elsevier.

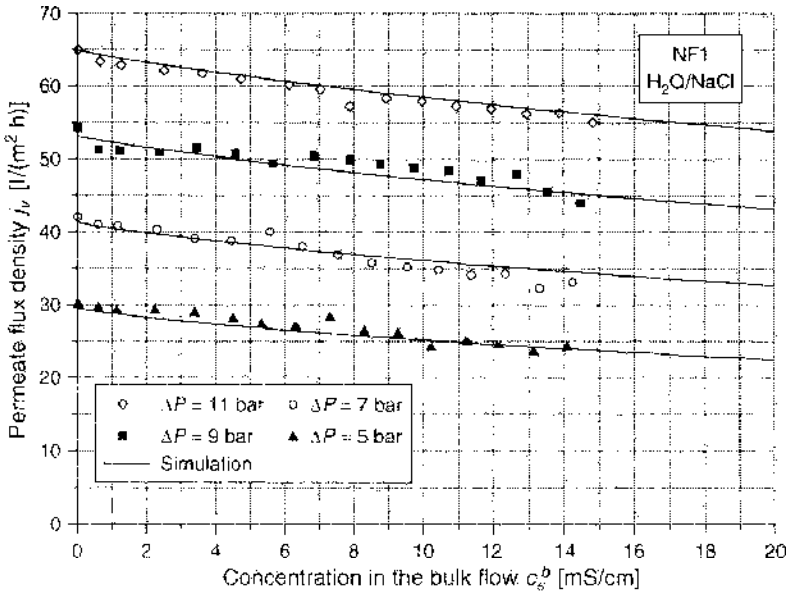

Figure 85. Comparison of simulation and experimental results—permeate flux density j_v as a function of concentration c_s^b at various transmembrane pressure differences ΔP for the system NF1–NaCl (293 K).

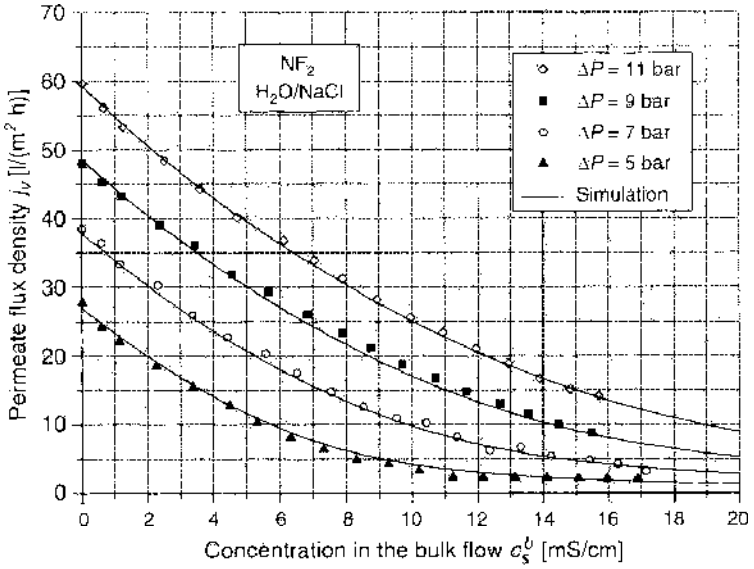

Figure 86. Comparison of simulation and experimental results—permeate flux density j_v as a function of concentration c_s^b at various transmembrane pressure differences ΔP for the system NF2–NaCl (293 K). Reprinted with permission from [132], M. Noronha et al. *Ann. N. Y. Acad. Sci.* 984, 142 (2003). © 2003, New York Academy of Sciences, USA.

3.4.2.2. Simulation of Rejection for the Spiral Wound Elements The following figures show the dependence of the apparent rejection R_i in the spiral wound elements on concentration in the bulk stream c_s^b at different levels of transmembrane pressure difference ΔP (Figs. 89–93). The model parameters for the simulation process are taken from Table 12.

The figures show that there is good agreement between the simulation of rejection in the membrane elements and real separation behavior. At electrolyte concentrations $c_i^B \rightarrow 0$, rejection is not dependent on transmembrane pressure difference, as can be seen from Eq. (129). As concentrations increase at lower transmembrane pressure differences, rejection is lower. For higher concentrations, membrane rejection decreases to a greater extent, particularly at lower transmembrane pressure differences. In simulation for this concentration range, real separation efficiency is overestimated, although there is qualitative agreement of the trend. For those systems, in which a decrease in rejection does not occur for these concentrations, there is agreement between experiment and simulation throughout the entire concentration and transmembrane pressure difference ranges under study (Figs. 89–93).

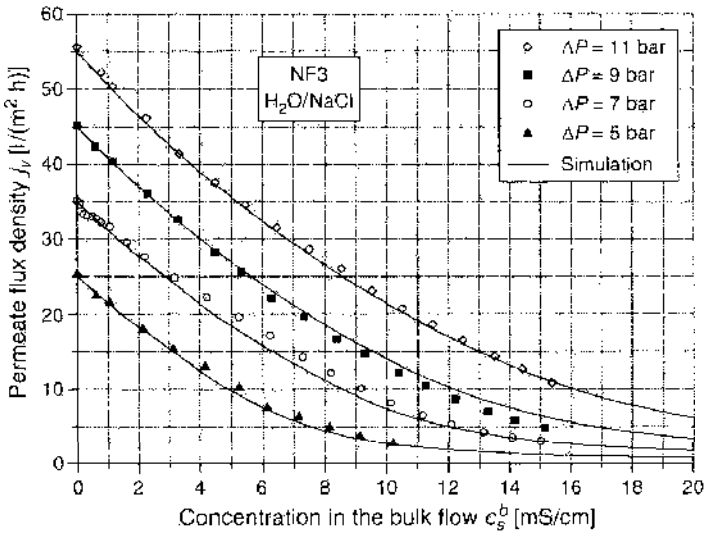

Figure 87. Comparison of simulation and experimental results—permeate flux density j_v as a function of concentration c_s^b at various transmembrane pressure differences ΔP for the system NF3–NaCl (293 K).

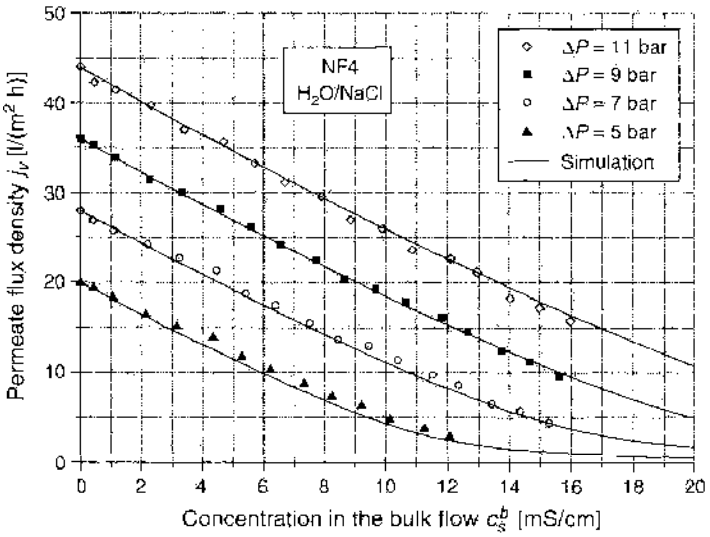

Figure 88. Comparison of simulation and experimental results—permeate flux density j_v as a function of concentration c_s^b at various transmembrane pressure differences ΔP for the system NF4–NaCl (293 K).

To summarize, the model equations, illustrated in section 3.3.2.1, are suitable for modeling the separation characteristics of nanofiltration membrane elements (spiral wound modules). The model parameters, estimated in section 3.4.1, allow possible simulation of membrane separation characteristics, which is adapted to the properties of the nanofiltration membranes as well as to the properties of the model solution. The simulation results agree qualitatively and quantitatively with the experimental results. Because of their degree of accuracy, the model equations can be instrumental for the design of nanofiltration plants for practical applications. One weak point is the simulation of membrane rejection at higher electrolyte concentrations, during which deviations from real behavior can occur.

3.5. Simulation of a Two-Stage Nanofiltration Process

The simulation of the separation characteristics of membrane elements lays the basis for the simulation of industrial membrane processes. In conjunction with the modeling of process structures (mass, material, and energy balances), the sequential calculation of membrane

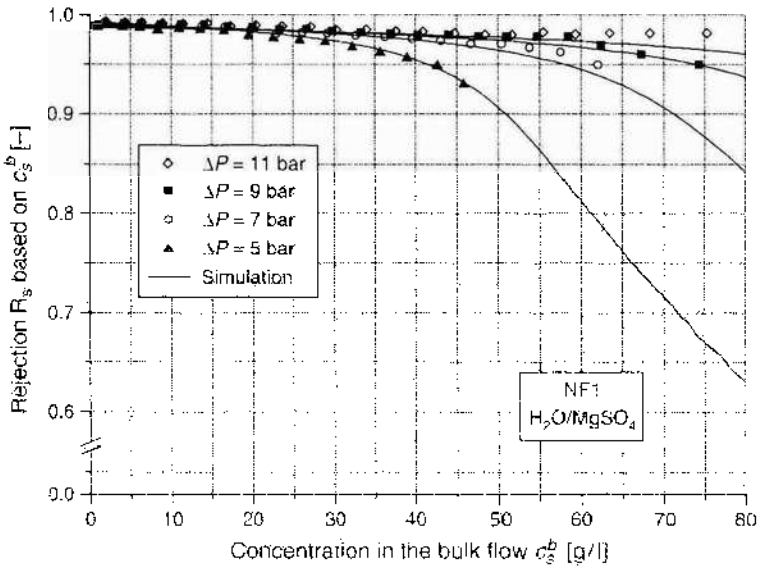

Figure 89. Comparison of simulation and experimental results—apparent rejection R_s as a function of concentration c_s^b at various transmembrane pressure differences ΔP for the system NF1–$MgSO_4$ (293 K). Reprinted with permission from [136], M. Noronha et al., *Desalination* 145, 207 (2002), © 2002, Elsevier.

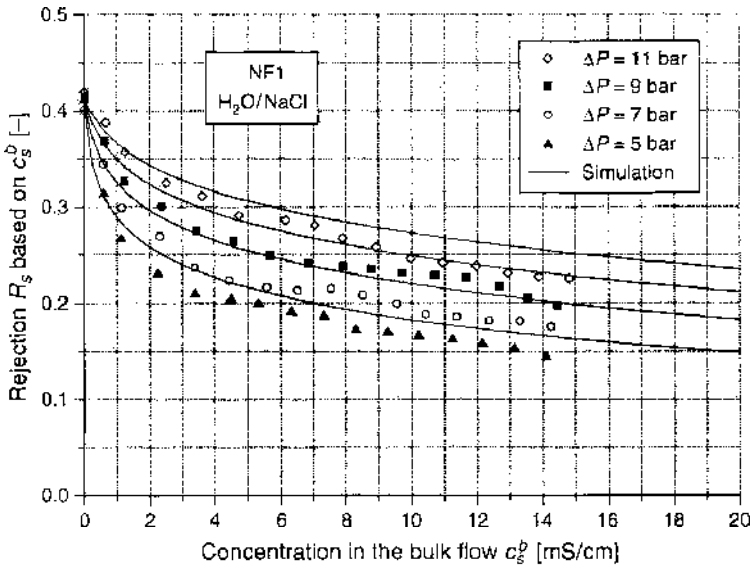

Figure 90. Comparison of simulation and experimental results—apparent rejection R_s as a function of concentration c_s^b at various transmembrane pressure differences ΔP for the system NF1–NaCl (293 K).

elements (membrane element analysis) provides an easy and efficient way of process analysis. Hence, conclusions can be drawn on the significance of certain process parameters or operating parameters, as well as on design specifications (cf. Figs. 60 and 61) for optimization purposes during the design and operating phases.

3.5.1. Simulation of Operating Conditions in Membrane Element Pressure Pipes

In industrial plants, several membrane elements are incorporated in one pressure pipe, together forming one membrane module. The permeate volume flow of a single spiral wound element is low compared to the feed volume flow. In most cases, permeate yield is less than 0.1 ($Y < 0.1$), making it necessary, in industrial membrane separation processes, to operate in membrane modules—several spiral wound elements—in series to obtain the permeate yield needed. Figure 94 shows a schematic representation of this type of operation (cf. Fig. 57).

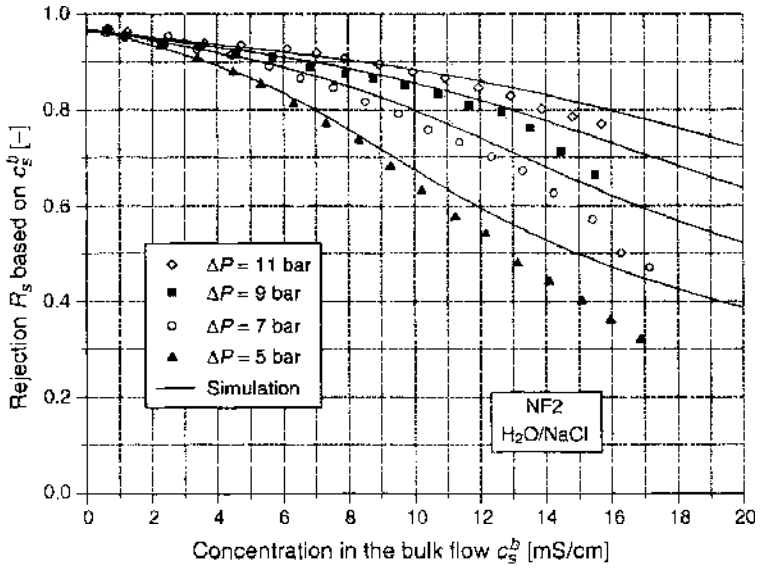

Figure 91. Comparison of simulation and experimental results—apparent rejection R_s as a function of concentration c_s^b at various transmembrane pressure differences ΔP for the system NF2–NaCl (293 K). Reprinted with permission from [132]. M. Noronha et al., *Ann. N. Y. Acad. Sci.* 984, 142 (2003). © 2003, New York Academy of Sciences, USA.

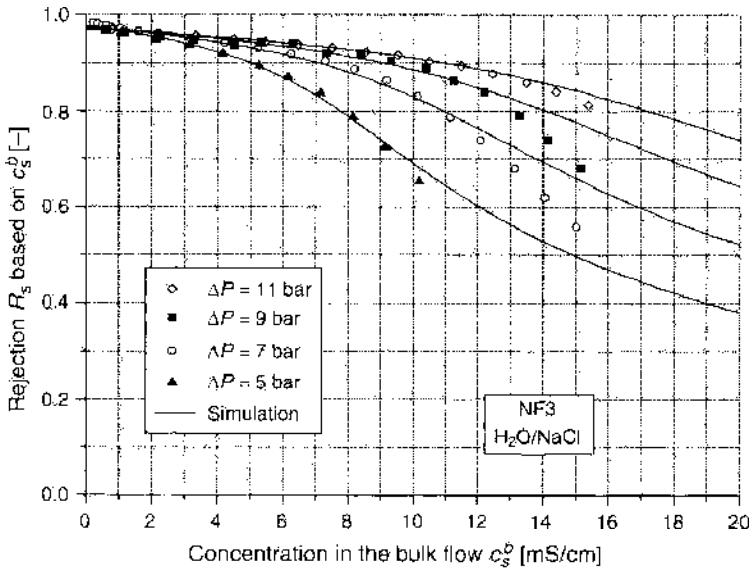

Figure 92. Comparison of simulation and experimental results—apparent rejection R_s as a function of concentration c_s^b at various transmembrane pressure differences ΔP for the system NF3–NaCl (293 K).

In industrial applications, the membrane elements are placed in a pressure pipe of appropriate length (Fig. 95). The headers for the permeate in the individual elements are interlinked and sealed against the outer feed-side volume flow. The accumulative permeate is withdrawn on both sides of the pressure pipe, with one outlet usually remaining closed.

The maximum number of elements in a series arrangement is limited by the feed-side concentration, the decrease in differential pressure, and flow reduction within the pressure pipe. Checking filtration conditions in the final membrane element is absolutely essential for plant dimensioning and proper operation of the membrane module. A membrane element analysis can be conducted for nanofiltration processes by applying the model equations to investigate the individual operating conditions of the membrane elements. In this way, the permeate productivity of the individual elements can be tested and the installation of an extra element can be considered and assessed in view of the additional investment costs.

Simulation is based on a sequential calculation of the individual industrial membrane elements (element-by-element analysis). The volume flow, the concentration, and the transmembrane pressure difference are determined at the inlet and outlet of each individual

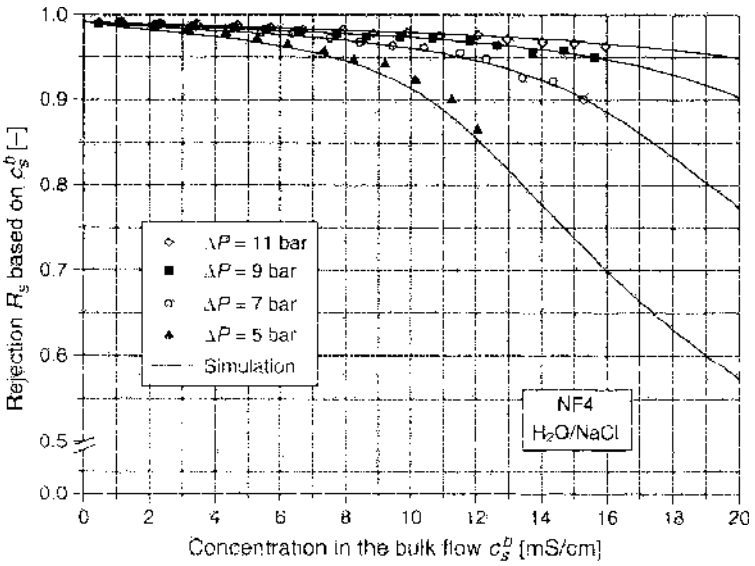

Figure 93. Comparison of simulation and experimental results—apparent rejection R_s as a function of concentration c_s^b at various transmembrane pressure differences ΔP for the system NF4–NaCl (293 K).

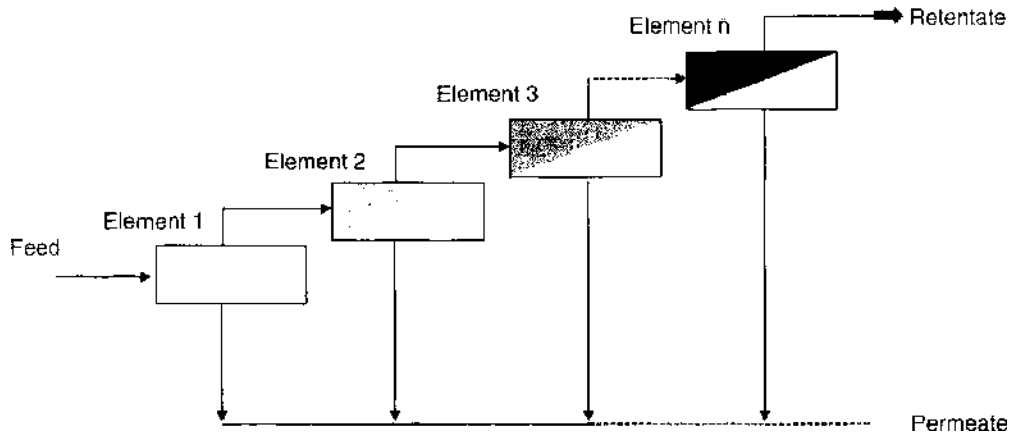

Figure 94. Flow diagram of a membrane module consisting of several membrane elements arranged in series.

membrane element. The outlet parameters of one element serve as inlet parameters for the downstream element. The following process parameters are calculated for each membrane element and applied to the averaged inlet and outlet parameters (logarithmic average for differential pressure and arithmetical average for concentration): hydraulic and osmotic pressure difference (ΔP and $\Delta\Pi$), feed-side concentration c_x^w and c_x^b, flow velocity of the feed solution u, mass transport coefficient k_F, permeate volume flow $\dot{Q}^p$, membrane volume flux density j_w, permeate concentration c_x^p, real and apparent membrane rejection $R_{x,Real}$, and R_x (based on salt concentration in the bulk flow c_x^b). In addition, further design aids (characteristic numbers) such as the volume flow ratio retentate/permeate and the permeate yield of the membrane element, for which reference values have been specified by the manufacturer, are defined. The entire equation system for the numerical solution to all process parameters for the membrane elements is contained in Appendix 2 [129].

Table 13 shows an example of the results of a membrane element analysis. Six membrane elements are arranged in series in a pressure pipe. Calculations are based on the model parameters for the system NF3–NaCl.

The results from Table 13 show how the continuous withdrawal of permeate along the length of the pressure pipe affects the operating conditions of the nanofiltration elements. Because of the decrease in transmembrane pressure difference and the increase in osmotic pressure difference, the permeate volume flow, obtained by the elements, constantly decreases. The permeate obtained from the final (sixth) membrane element is less than half as high as the permeate generated by the first membrane element. As a consequence of the increase in feed-side concentration and the reduction in permeate flux density, the rejection decrease causes an increase in permeate concentration from the first to the final spiral wound element. The following figure shows the variations in some selected operating parameters of the membrane elements arranged in series (Fig. 96).

3.5.2. Simulation of a Nanofiltration Process Using NF-PROJECT

We developed a steady-state simulation program, NF-PROJECT, with the objective of supporting the design, simulation, and optimization of a two-stage nanofiltration process

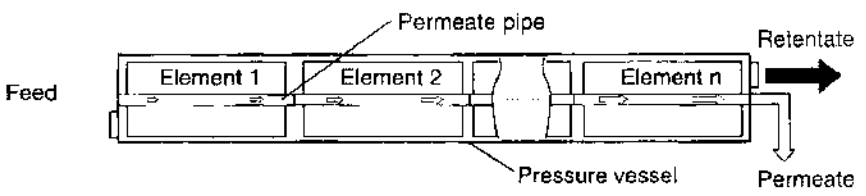

Figure 95. Technical realisation of a membrane module with a series arrangement of membrane elements in a pressure pipe. Reprinted with permission from [132], M. Noronha, *Ann. N. Y. Acad. Sci.* 984, 142 (2003). © 2003, New York Academy of Sciences, USA.

Table 13. Analysis of the membrane elements for an arrangement in series of six 8″ spiral wound elements (inlet conditions: c_s^f = 4.0 mS/cm, ΔP^f = 8.0 bar, $\dot{Q}^f$ = 12.0 m³/h).

	Membrane area per element A_m 37.16 m²					
System NF3–NaCl	Element 1	Element 2	Element 3	Element 4	Element 5	Element 6
Inlet volumeflow $\dot{Q}^f$ [m³/h]	12.00	11.09	10.29	9.61	9.03	8.54
Inlet concentration c_s^f [mS/cm]	4.00	4.31	4.62	4.93	5.22	5.49
Inlet press. difference (hydr.) ΔP^f [bar]	8.00	7.45	6.97	6.55	6.16	5.82
Mean press. difference ΔP [bar]	7.72	7.21	6.76	6.35	5.99	5.66
Pressure loss ΔP^{loss} [bar]	0.55	0.48	0.43	0.38	0.34	0.31
Osmotic press. difference $\Delta\Pi$ [bar]	2.94	3.07	3.19	3.29	3.38	3.45
Mean flow velocity $v_{K^{\prime\prime}}$ [m/s]	0.263	0.243	0.227	0.212	0.200	0.189
Mass transfer coeff. $k_{L,K^{\prime\prime}}$ [l/(m²h)]	223.06	208.56	195.94	185.05	175.69	167.71
Mean feed concentration c_s^b [mS/cm]	4.15	4.47	4.77	5.07	5.35	5.62
Membrane surface conc. c_s^m [mS/cm]	4.88	5.13	5.37	5.60	5.82	6.02
Retention R (based on c_s^b) [%]	94.58	93.96	93.20	92.30	91.22	89.95
Retention R_{Real} (based on c_s^m) [%]	95.39	94.74	93.96	93.03	91.93	90.63
Permeate volume flow $\dot{Q}^p$ [m³/h]	0.92	0.79	0.68	0.58	0.49	0.42
Permeate flux density j_v [l/(m²h)]	24.70	21.33	18.32	23.15	19.99	17.15
Permeability $\bar{L}_p$ [l/(m².bar)]	3.57	3.30	3.01	15.65	13.29	11.21
Permeate concentration c_s^p [mS/cm]	0.23	0.27	0.32	0.39	0.47	0.56
Outlet volume flow $\dot{Q}^r$ [m³/h]	11.08	10.29	9.61	9.03	8.54	8.12
Outlet concentration c_s^r [mS/cm]	4.31	4.62	4.93	5.22	5.49	5.74
Outlet press. difference (hydr.) ΔP^r [bar]	7.45	6.97	6.55	6.16	5.82	5.50
Volume flow ratio $\dot{Q}^r/\dot{Q}^p$ [-]	12.1	13.0	14.1	15.6	17.3	19.5
Element recovery $Y(\dot{Q}^p/\dot{Q}^f)$ [%]	7.6	7.1	6.6	6.0	5.5	4.9
Total permeate from the pressure pipe	Permeate volume flow $\dot{Q}^p$[m³/h]	3.87	Permeate recovery [%]			37.75
			Retention $\bar{R}$, (based on c_s^b) [%]			91.99
	Permeate concen. c_s^p [mS/cm]	0.39	Retention $\bar{R}$ (based on c_s^f) [%]			90.25
	Permeability $\bar{L}_p$ [l/m²h.bar]	2.58				

[129–133, 135–137]. The sequential-modular structure of processes involving membrane elements and pressure pipes (membrane module) enables simulation to be performed for processes of any size which essentially consist of a simulation sequence of individual membrane elements. Due to the interaction of the membrane elements in a certain pre-defined configuration, which reflects the process structure, the operating behavior of the entire process can be simulated.

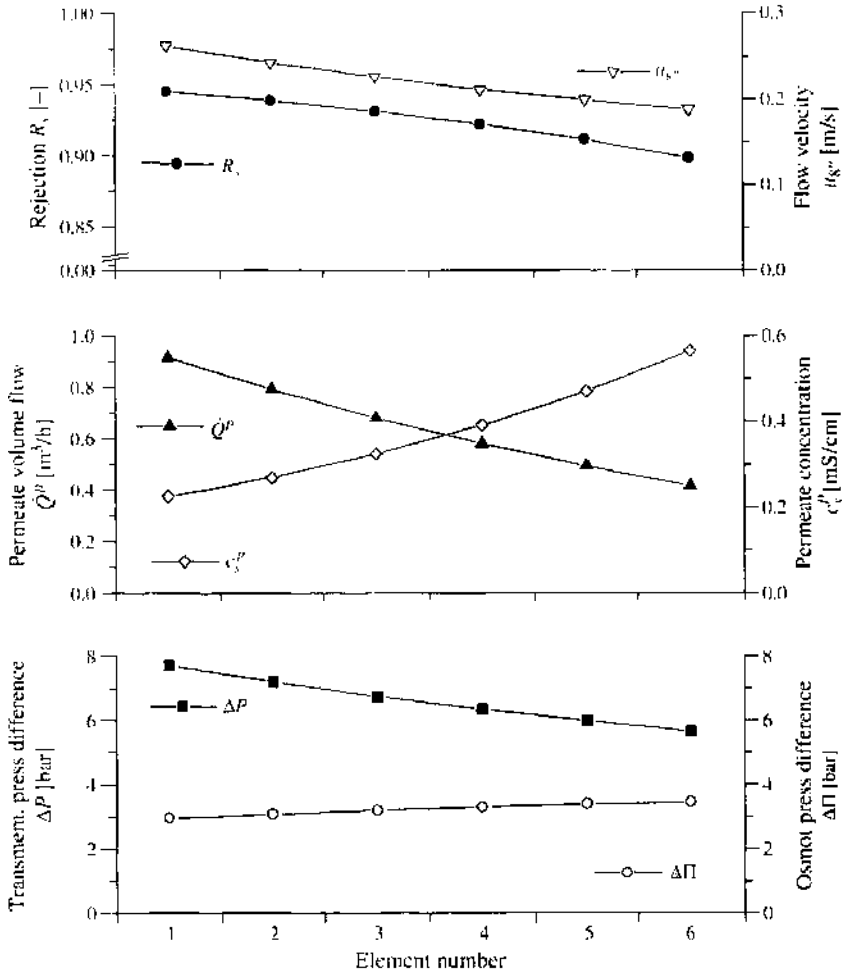

Figure 96. Operating conditions for membrane elements arranged in series in a membrane module.

3.5.2.1. Process Structure Basically, numerous arrangements are conceivable for nanofiltration processes. To evaluate the efficiency of process simulation using reliable operating data from a case study, we developed the process simulation tool NF-PROJECT based on the existing data of a demonstration plant in operation [129]. The plant is a two-stage treatment unit in the form of a two-stage symmetrical cascade with follow-up permeate filtration according to Figure 60 (Fig. 97).

Because the feed volume flow of the plant was lower than the minimum volume flow specified by the manufacturer for the membrane elements, both filtration stages were equipped with internal recirculation cycles and circulation pumps. A pressure pipe (membrane module), containing two 8″ spiral wound elements arranged in series (1″ × 2″) was fitted into

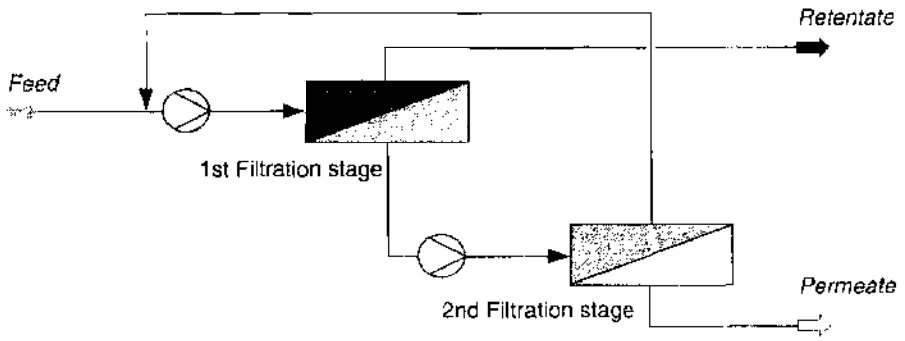

Figure 97. Simplified flow diagram of a two-stage membrane process in a symmetrical cascade with follow-up permeate filtration.

each filtration stage. By recording all volume flows by the integrated control system, partial permeate yields Y_1 and Y_2 can be specified separately. The permeate yields were set by control valves. The flow diagram in Figure 98 is an exact representation of the demonstration plant.

Because of internal recirculation, the simulation of a steady process state can only be solved by iteration, calculated in several recursive steps. The criterion for stopping the iteration process is the failure to reach a minimum relative deviation of the new approximation value from the previous value or exceeding a predefined maximum number of recursion steps. Initial estimation of the parameters for the recirculated streams into the recirculation cycles in each filtration stage was incorporated into the simulation process to optimize the run time of the program.

3.5.2.2. Input and Output Information Various types of input information are needed to simulate a nanofiltration process with the tool NF-PROJECT (Fig. 99).

3.5.2.2.1. Model Parameters The nanofiltration membrane elements, fitted into each filtration stage of the pilot plant, had to be characterized as a separate system by using a model solution (binary electrolyte solution). It was necessary for characterization to be conducted in a concentration and differential pressure range that was as near as possible to the operating point of the nanofiltration plant. The six model parameters, determined in the characterization process, were specified separately and individually to simulate the required separation characteristics of the membrane elements.

3.5.2.2.2. Configuration Parameters To ensure a certain amount of flexibility in designing the membrane area to be installed in each filtration stage, the possibility of predefining configuration parameters was considered. This essentially refers to the number of pressure pipes n_{PP} and the number of membrane elements arranged in series n_{ME} (this provides the necessary specification of the entire membrane area for one filtration stage at industrial scale: $n_{PP} \times n_{ME}$). The membrane area A_m, as well as the effective cross-sectional area A_{eff}, of an industrial 8" spiral wound element can fluctuate, depending on the manufacturer or even within one manufacturer's product series, although this is usually specified in the technical notes. The mass transport coefficient k_F can be adapted by defining the hydraulic diameter d_H of the industrial membrane element. The required flow over the membrane surface is obtained through the recirculation of the retentate. The volume stream entering the pressure pipe is defined and should be adapted to the number of membrane elements n_{ME} arranged in series and the selected permeate yield in the filtration stage Y. Accordingly, the recirculated permeate flow is kept constant.

3.5.2.2.3. Process Parameters Operating parameters have to be specified for the simulation of the two-stage process by defining a system feed concentration $c_s^{f,sys}$ in the model solution in the feed to the plant, the transmembrane pressure difference in the feed ΔP_1,

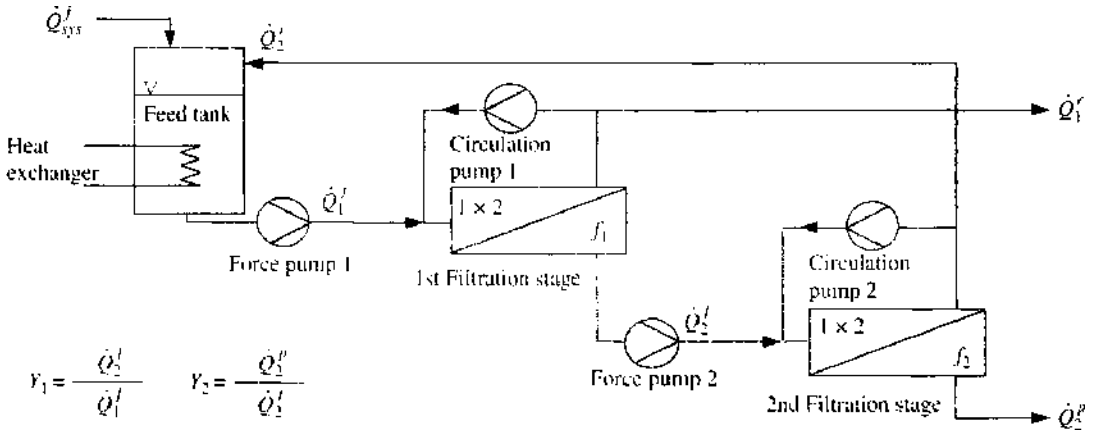

Figure 98. Flow diagram of the demonstration plant used. Reprinted with permission from [136], M. Noronha et al., *Desalination* 145, 207 (2002). © 2002, Elsevier.

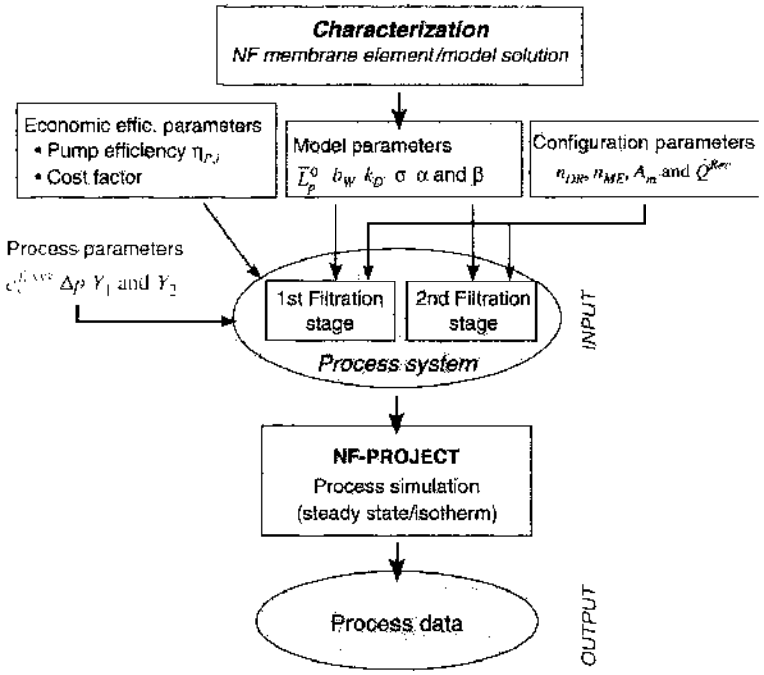

Figure 99. Input information needed for the application of NF project.

which has to be generated by the pressure pump in the first filtration stage as well as the partial permeate yields Y_1 and Y_2 in both filtration stages, whereby the entire system yield Y_{sys} is determined.

3.5.2.2.4. Economic Efficiency Parameters Economic efficiency parameters were defined to compare different operating modes and alternative treatment techniques during process analysis. The overall efficiency $\eta_{P,i}$ of the pumps (main feed and circulation pumps) or turbines $\eta_{T,i}$ is needed to calculate the electric power required. Centrifugal pumps, commonly installed in membrane plants, are responsible for major pressure losses, which also depend on volume flow [145]. Further cost factors such as electricity costs need to be known so as to determine specific energy costs.

The following table (Table 14) contains all the parameters that can be freely selected in the simulation program.

Once the process calculation has been completed, the program user is provided with the results in the form of a flow sheet (Fig. 100).

Process simulation for the demonstration plant was performed for the system NF3–NaCl in both filtration stages at $\Delta P_i = 10$ bar, $Y_1 = 0.75$, and $Y_2 = 0.85$ (equivalent to a total yield of $Y_{Sys} = 0.718$), and $c_s^{f,sys} = 3.5$ mS/cm and $\eta_P = 0.4$ for all pumps [145] (the following configuration parameters apply to both filtration stages: $n_{PP} = 1$, n_{ME}=2, $A_m = 36.17$ m^2, $A_{cff} = 0.0122$ m^2, $d_{H,sp} = 0.95 \cdot 10^{-3}$ m, $\dot{Q}_{in} = 10$ m^3/h).

The exact operating data and detailed information on the specific operating conditions of the individual membrane elements in both filtration stages are contained in Table 15. In evaluating the simulation results, it is important to ensure that the operating parameters are within the definition limits from the characterization process.

3.5.3. Process Analysis and Optimization

There is an increasing demand for small and medium-sized membrane plants to be flexible in operation, as their design cannot be based on a fixed operating point because of, for example, fluctuations in feed concentration. As far as complicated two-stage treatment plants are concerned, operational behavior is not straightforward. System adaptation or optimization without the appropriate aids can only be carried out in an empirical manner involving expert knowledge.

Process simulation by means of NF-PROJECT allows different operating states to be examined and analyzed, thus making it possible to define dimensions during planning and

Table 14. Summary of the selected parameters for process simulation.

Name	Unit	Specification
Model parameters from characterization (to be specified for both filtration stages)		
$\bar{L}_P^0$	[l/(m²h.bar)]	Pure water permeability
b_W	[bar²/(mS/cm)]	van't Hoff coefficient
k_F	[l/(m²h)]	Feed-side mass transfer coefficient
$u_{2.5''}$	[m/s]	Feed-side flow velocity in the membrane element
$d_{H,2.5''}$	[m]	Hydraulic diameter of the membrane element
σ	[-]	Reflection coefficient
α, β	[-]	Empirical parameter from characterization
Configuration parameters (to be specified for both filtration stages)		
n_{PIR}	[-]	No. of parallel pressure pipes
n_{ME}	[-]	No. of membrane elements arranged in series
A_m	[m²]	Active filtration area in industrial 8" spiral wound element
A_{cff}	[m²]	Effective cross-sectional area of the 8" spiral wound element
$d_{H,8''}$	[m]	Hydraulic diameter of the 8" spiral wound element
$\dot{Q}^{in}$	[m³/h]	Inlet volume flow of pressure pipes
Process parameters		
$c_S^{f,in}$	[mS/cm]	Concentration in feed of the demonstration plant
ΔP_1	[bar]	Hydraulic differential pressure in 1st filtration stage at inlet of pressure pipes
Y_1	[-]	Permeate recovery in the first filtration stage
Y_2	[-]	Permeate recovery in the second filtration stage
Economic efficiency parameters		
$\eta_{P,i}$	[-]	Overall degree of efficiency of pumps installed
$\eta_{T,i}$	[-]	Degree of efficiency for turbines (if installed)
$K_{electricity}$	[€/kWh]	Cost of electricity (cost factor)

design or to optimize an existing process in operation. A membrane plant can be optimally adapted to various separation problems by modifying different operating parameters such as partial yields in both filtration stages, feed concentration, or the transmembrane pressure difference in the first filtration stage and simulation of steady-state operating conditions.

Permeate concentration and permeate volume flow can be defined as target parameters. They are often governed by certain requirements that must be adhered to at all times. From

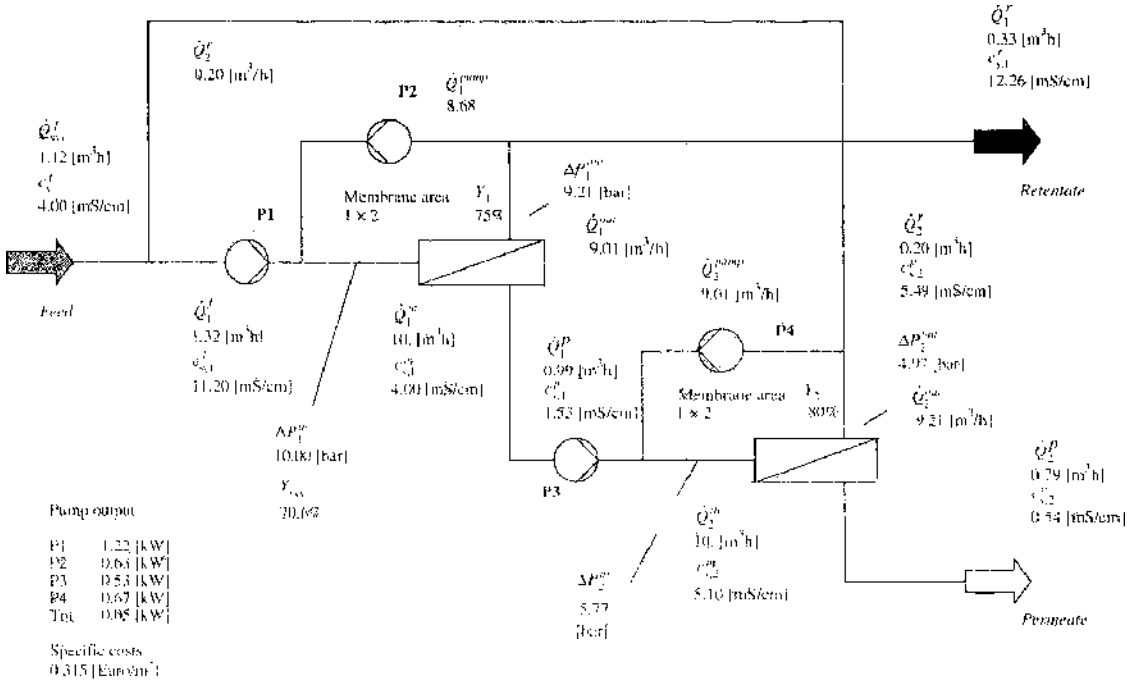

Figure 100. Flow diagram of the process and operating data for the two-stage NF process. Reprinted with permission from [136], M. Noronha et al., *Desalination* 145, 207 (2002). © 2002, Elsevier.

Table 15. Details of the operating data for the two-stage process.

	1st Filtration stage		2nd Filtration stage	
Feed volume flow $\dot{Q}^f$ [m³/h]	1.32		0.99	
Feed concentration c_χ^f [mS/cm]	4.22		1.53	
	Element 1	Element 2	Element 1	Element 2
Inlet volume flow $\dot{Q}^f$ [m³/h]	10.00	9.46	10.00	9.57
Inlet concentration c_χ^f [mS/cm]	11.20	11.76	5.10	5.30
Inlet press. difference (hydr.) ΔP^f [bar]	10.00	9.59	5.77	5.36
Mean press. difference ΔP [bar]	9.80	9.40	5.56	5.16
Pressure loss ΔP^{loss} [bar]	0.41	0.38	0.41	0.39
Osmotic press. difference $\Delta\Pi$ [bar]	7.04	7.09	3.22	3.24
Mean flow velocity u_{sw} [m/s]	0.221	0.21	0.222	0.214
Mass transfer coefficient $k_{f,sw}$ [l/(m²h)]	192.11	183.55	193.02	186.19
Mean feed concentration c_χ^b [mS/cm]	11.48	12.01	5.20	5.40
Membrane surface conc. c_χ^w [mS/cm]	12.54	12.91	5.59	5.72
Retention R_χ (based on c_χ^b) [%]	87.77	85.94	90.55	89.05
Retention $R_{\chi,Rmd}$ (based on c_χ^w) [%]	88.81	86.92	91.22	89.68
Permeate volume flow $\dot{Q}^p$ [m³/h]	0.54	0.45	0.43	0.36
Permeate flux density j_v [l/(m²h)]	14.54	12.09	11.69	9.60
Permeability $\bar{L}_p$ [l/(m²·h.bar)]	1.48	1.29	2.10	1.86
Permeate concentration c_χ^p [mS/cm]	1.4	1.69	0.49	0.59
Outlet volume flow $\dot{Q}^r$ [m³/h]	9.46	9.01	9.57	9.21
Outlet concentration c_χ^r [mS/cm]	11.76	12.26	5.30	5.49
Outlet press. difference (hydr.) ΔP^r [bar]	9.59	9.21	5.36	4.97
Volume flow ratio $\dot{Q}^r/\dot{Q}^p$ [-]	17.5	20.1	22.1	25.9
Element recovery Y ($\dot{Q}^p/\dot{Q}^f$) [%]	5.4	4.7	4.3	3.7
Permeate volume flow $\dot{Q}^p$ [m³/h]	0.988		0.79	
Permeate concentration c_χ^p [mS/cm]	1.53		0.54	
Retentate volume flow $\dot{Q}^r$ [m³/h]	0.33		0.20	
Retentate concentration c_χ^r [mS/cm]	12.26		5.49	

an economic viewpoint, the specific energy costs per cubic meter of treated permeate are specified as a target criterion at this point because electric power consumption for the pumps constitutes much of the running operating costs for membrane plants (in addition to costs for membrane replacement and plant repair).

The following section deals with process analysis and optimization, using the above-mentioned two-stage nanofiltration demonstration plant. The possibility of finely adjusting partial yields while maintaining the system (entire) yield from the two-stage demonstration plant is presented. We will also deal with the analysis of the effects of fluctuating feed concentrations on the operating behavior of the demonstration plant as well as the design supports for the planning phase of a membrane plant. A cost-effective operating point will be determined by adapting and optimizing the transmembrane pressure difference at constant feed concentration in the first filtration stage.

3.5.3.1. Adjusting Partial Yields at Constant System Yield The economic efficiency of membrane separation processes is mainly governed by permeate yield (also termed "system yield" in the following). During the planning of a membrane plant, system yield Y_{sys} is also defined as a target parameter. A high system yield for a membrane separation process results in a reduction in the quantity of retentate to be disposed of and an increase in the reusable permeate volume flow. In a simple series arrangement of two filtration stages in a cascade, the system yield is obtained by multiplying the partial yields Y_1 and Y_2 in both filtration stages. For a two-stage process with recirculation of the retentate volume flow from the second filtration stage, as shown in Figure 98, system yield can be expressed as a function of the partial yields in both filtration stages, as follows:

$$Y_{sys} = \frac{\dot{Q}_2^p}{\dot{Q}_{sys}^f}$$

$$\Leftrightarrow \dot{Q}_{sys}^f \cdot Y_{sys} = \dot{Q}_2^f \cdot Y_2$$

$$
\begin{aligned}
&= \dot{Q}_1^f \cdot Y_1 \cdot Y_2 \\
&= (\dot{Q}_{sys}^f + \dot{Q}_2^p) \cdot Y_1 \cdot Y_2 \\
&= \left(\dot{Q}_{sys}^f + \frac{\dot{Q}_2^p}{Y_2} \cdot (1 - Y_2)\right) \cdot Y_1 \cdot Y_2 \\
&= \dot{Q}_{sys}^f \cdot \left(1 + \frac{Y_{sys}}{Y_2} \cdot (1 - Y_2)\right) \cdot Y_1 \cdot Y_2 \\
\Leftrightarrow\ Y_{sys} &= \frac{Y_1 \cdot Y_2}{1 - Y_1 \cdot (1 - Y_2)}
\end{aligned} \tag{150}
$$

Therefore, according to equation (151), it is possible to vary the partial yields in both filtration stages while maintaining a predefined system yield. By modifying the partial yields, different operating points in the two-stage demonstration plant, which can be tested and compared to the target criteria, become established.

Figure 101 shows the different combinations possible for the partial yields, according to Eq. (151) for constant system yields of $Y_{sys} = 0.5, 0.6$, and 0.7. In addition, dotted curves are involved that represent the combinations of partial yields in a simple series arrangement of both filtration stages without recirculation of the retentate.

The different operating points resulting from the variation of the partial yields from the twostage demonstration plant were tested for a constant system yield $Y_{sys} = 0.7$ in terms of the target parameters, permeate volume flow, and permeate concentration, as well as the specific energy costs of the pumps. This provides valuable information not only for design purposes but also for optimizing the operation of the membrane plant.

In both filtration stages, the system NF3–NaCl was simulated for the membrane elements, using the values for the input parameters in section 3.5.2.2 except for total yields.

From Figure 102, it is evident that the optimum operating point from an economic viewpoint can be set when the partial yields in the first filtration stage Y_1 are reduced as far as possible, while the partial yield in the second filtration stage Y_2 is increased to reach the system yield required. Flow through the plant is maximized for a minimum partial yield Y_1. On the one hand, the decrease in Y_2 is limited by a maximum permissible partial yield Y_2 and by the system yield required because $Y_1 > Y_2$ must always be valid.

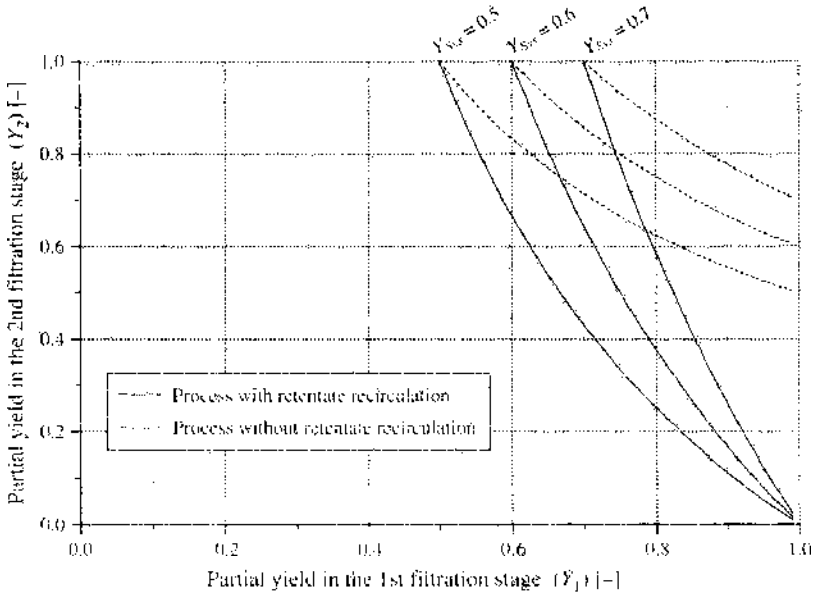

Figure 101. Different combinations of partial yields Y_2 and Y_1 at constant system recovery Y_{sys}. Reprinted with permission from [132]. M. Noronha et al. *Ann. N. Y. Acad. Sci.* 984, 142 (2003). © 2003 New York Academy of Sciences, USA.

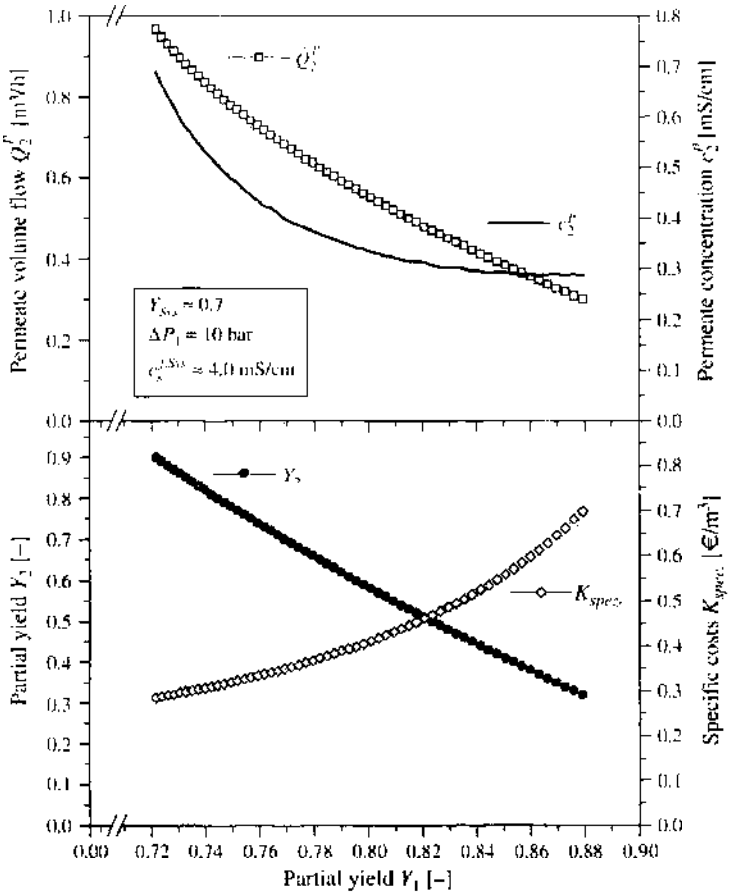

Figure 102. Permeate volume flow, permeate concentration as well as specific costs as a function of partial yields (at constant system yield). Reprinted with permission from [136], M. Noronha et al., *Desalination* 145, 207 (2002). © 2002, Elsevier.

On the other hand, a relatively poor permeate concentration (average permeate concentration from both filtration stages) becomes established for this economically optimum operating point. Average permeate quality (from ~0.7 mS/cm to ~0.3 mS/cm) can be greatly improved by increasing the partial yield in the first filtration stage, whereas system yield remains the same. In designing a two-stage membrane plant, attention should focus on reaching the required permeate concentration in the economically optimum operating point. Otherwise, a compromise between the required permeate concentration and permeate volume flow should be found, allowing for the priorities set by the target criteria.

3.5.3.2. Variation in Feed Concentration In general, membrane plants are designed for a fixed nominal state by using an economic efficiency parameter as an evaluation criterion, with the result that flexibility aspects during the actual design and dimensioning of the plant are neglected. However, if nominal design principles cannot be adhered to, process alternatives, which have greater "flexibility" toward external process parameters, can be more favorable. In this case, "flexibility" is defined as operating behavior that deviates from nominal operating conditions. Therefore, system behavior should be analyzed when changes in external process parameters occur.

For example, major fluctuations may occur in feed concentrations during the treatment of process water, particularly industrial process water from small and medium-sized enterprises. Concentration can change by ±30% within a few hours, but operating mode is not usually adapted as soon as the changes take place.

If a two-stage plant is designed for a specific feed concentration, failure to meet this concentration can considerably affect stringently regulated permeate values, if the operating mode remains unchanged. Figure 103 shows the dependence of permeate volume flow and permeate concentration on feed concentration for a fixed operating point of a demonstration plant ($\Delta P_1 = 10$ bar, $Y_1 = 0.75$, $Y_2 = 0.8$).

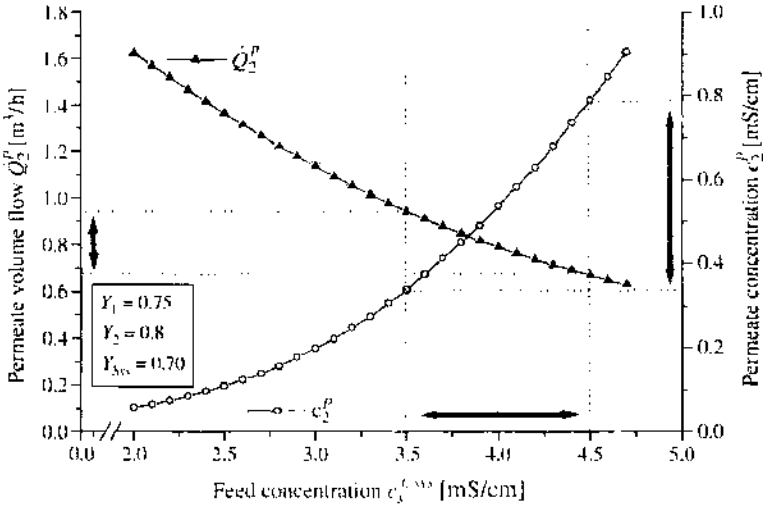

Figure 103. Permeate volume flow and permeate concentration of a two-stage nanofiltration plant as a function of feed concentration. Reprinted with permission from [136], M. Noronha et al., *Desalination* 145, 207 (2002). © 2002, Elsevier.

The figure illustrates that, for this operating point, the demonstration plant has a moderate degree of flexibility (major changes) as regards permeate volume flow and a slight degree of flexibility as regards permeate concentration when feed concentration changes. Table 16 shows percentage changes in the permeate concentration when the feed concentration fluctuates between 3.5 and 4.5 mS/cm with the nominated plant design feed concentration of 4.0 mS/cm.

From Table 16, it can be seen that fluctuations in feed concentration of ±12.5% around the operating point $c_3^{f,sys} = 4.0$ mS/cm cause greater percentage changes in permeate concentration, meaning that the operating behavior of the demonstration plant reacts very sensitively to the operating parameter, feed concentration. Although the permeate volume flow can change by +18.9%/−15.2%, even greater changes in permeate concentration are to be expected. For this case, the steady-state simulation process calculates changes to the extent of −37.0%/ + 46.3%.

In designing a two-stage nanofiltration plant for treating process water with major concentration fluctuations, it follows that the membrane plant must be overdimensioned (increase in flexibility). Hence operation in the nanofiltration plant can keep to the required permeate concentration even at maximum feed concentration.

3.5.3.3. Optimizing Transmembrane Pressure Difference After defining specific operating parameters (e.g., partial yields) for a nominal design of a two-stage nanofiltration membrane plant, variable operating parameters can be adapted or optimized to external parameters. In this case, the transmembrane pressure difference should be optimized in relation to feed concentration.

It is easy to understand that a rise in transmembrane pressure difference in the first filtration stage increases the permeate volume flow. However the increase in the energy required is out of proportion to the increase in the permeate volume flow. Similarly, an excessive reduction in transmembrane pressure difference, thus saving energy consumption,

Table 16. Change in permeate concentration when feed concentration fluctuates by ±12.5% from nominal design conditions.

$c_3^{f,sys}$ [mS/cm]	3.5	4.0	4.5
% change	−12.5%	—	+12.5%
$\dot{Q}_2^P$ [m³/h]	0.94	0.79	0.67
% change	+18.9%	—	−15.2%
$c_{3,2}^P$ [mS/cm]	0.34	0.54	0.79
% change	−37.0%	—	+46.3%

leads to a greater decrease in permeate volume flow. There is an increase in specific energy costs in both cases.

Optimum transmembrane pressure difference depends on feed concentration and on the selected partial yields in both filtration stages (or system yield). The following figure (Fig. 104) shows the extent to which the specific energy costs depend on transmembrane pressure difference. For this purpose, process analysis was carried out for two different levels of feed concentration ($c_s^{f,sys}$ = 1.5 mS/cm/4.0 mS/cm) at a defined system yield of $Y_{sys} \approx 0.7$ (Y_1 = 0.75; Y_2 = 0.8).

From Figure 104, it is evident that the dependence of the permeate volume flow is, as expected, almost linear to the transmembrane pressure difference in the first stage. Additional pressure difference of roughly 4 bar is needed at the higher feed concentration to achieve the same permeate volume flow as at the lower feed concentration. Permeate concentration can be improved with increasing pressure difference, but only up to certain values of pressure difference. This operating behavior was observed for both feed concentrations under study.

A decisive factor is that, as far as the target criterion, economic efficiency (defined by specific energy costs), is concerned, optimum transmembrane pressure difference can be determined in the first filtration stage that minimizes the specific energy costs. Optimum transmembrane pressure difference increases when feed concentrations rise. An excessive decrease in transmembrane pressure difference results in considerably higher specific energy costs, in comparison to an excessive increase of differential pressure.

To summarize, the steady-state process simulation tool NF-PROJECT allows efficient simulation of a two-stage nanofiltration process to be performed. The focus here is on

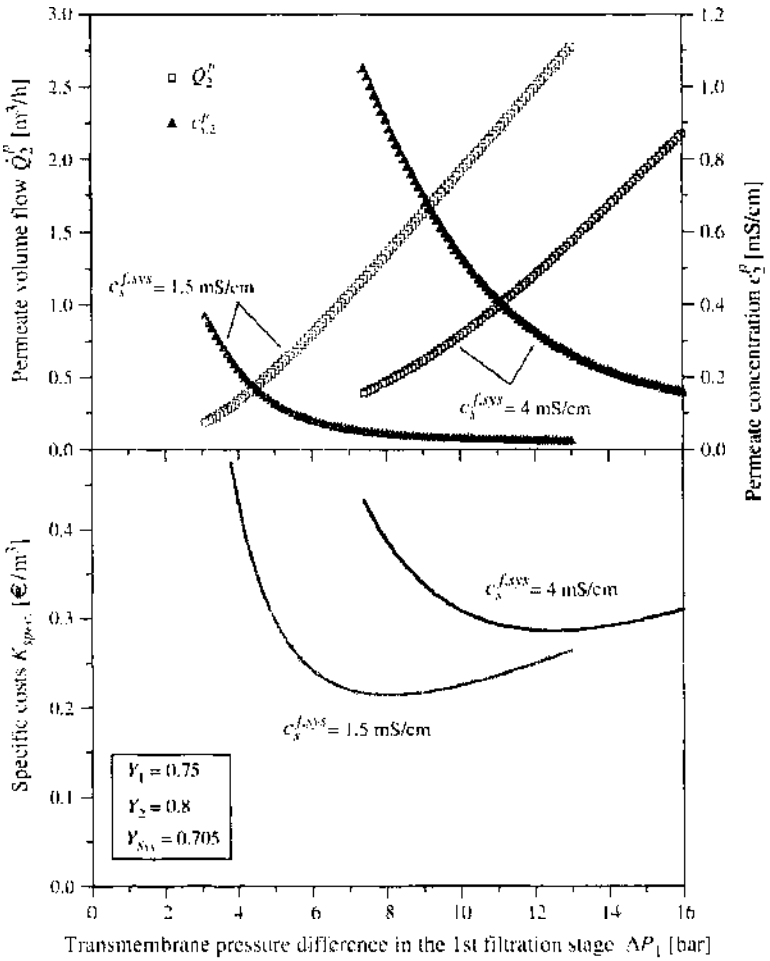

Figure 104. Optimization of transmembrane pressure difference in the first filtration stage at different feed concentrations.

a feed-and-bleed structure in which the size of the filtration stages can be varied by specifying the number of parallel pressure pipes (membrane modules) and membrane elements arranged in series. The model parameters from the characterization of the membrane elements and the model solution can be incorporated quite easily for each separate filtration stage, thus modeling and simulating the individual separation characteristics of the membrane system. Different problems can be analyzed and optimized in terms of process flexibility at various target criteria. Overall, simulation makes a valuable contribution to designing or optimizing the operation of a two-stage nanofiltration plant.

By using the simplified process simulation tool combined with MINLP methods (mixed-integer non-linear programming), issues concerning process synthesis or process design can also be dealt with [122, 141]. By predefining input/output conditions, configuration parameters as well as operating parameters of a nanofiltration process can be optimized.

APPENDIX 1

We present here approximate analytic expressions for the diffusive and the convective hindrance factors appearing in the HT and HET models [45]:

$$K_{i,d} = \frac{6\pi}{K_t(\lambda_i)} \text{ and } K_{i,c} = \frac{(2 - \Phi_i^S)K_s(\lambda_i)}{2K_t}$$

with

$$K_t(\lambda) = \frac{9}{4}\pi^2\sqrt{2}(1-\lambda)^{-5/2}\left[1 + \sum_{n=1}^{2} a_n(1-\lambda)^n\right] + \sum_{n=0}^{4} a_{n+3}\lambda^n$$

and

$$K_s(\lambda) = \frac{9}{4}\pi^2\sqrt{2}(1-\lambda)^{-5/2}\left[1 + \sum_{n=1}^{2} b_n(1-\lambda)^n\right] + \sum_{n=0}^{4} b_{n+3}\lambda^n$$

$a_1 = -73/60$, $a_2 = 77.293/50.4$, $a_3 = -22.5083$, $a_4 = -5.6117$, $a_5 = -0.3363$, $a_6 = -1.216$, $a_7 = 1.647$, $b_1 = 7/60$, $b_2 = -2.227/50.4$, $b_3 = 4.018$, $b_4 = -3.9788$, $b_5 = -1.9215$, $b_6 = 4.392$, $b_7 = 5.006$.

The variation of the diffusive and the convective hindrance factors as a function of $\lambda_i = r_i/r_p$ is presented in Figure A1.

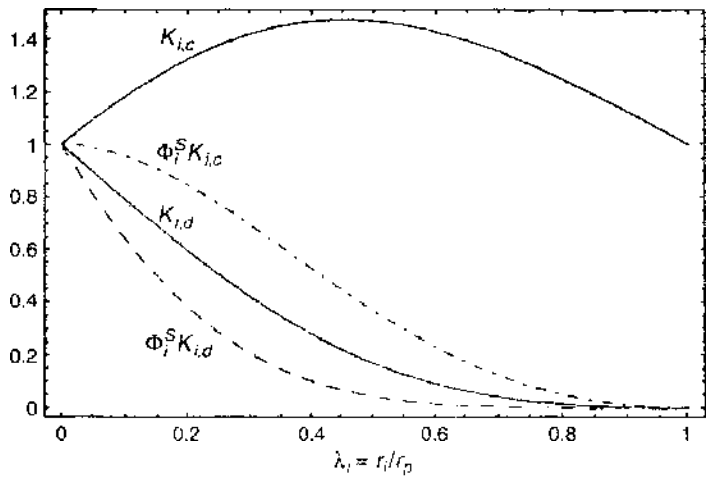

Figure A1. The diffusive hindrance factor $K_{i,d}$, product $\Phi_i^S K_{i,d}$, convective hindrance factor $K_{i,c}$, and product $\Phi_i^S K_{i,c}$ as a function of $\lambda_i = r_i/r_p$ [$\Phi_i^S = (1-\lambda_i)^2$ is the steric partitioning coefficient and $\sigma_i = 1 - \Phi_i^S K_{i,c}$ is the steric reflection coefficient].

APPENDIX 2

Reference model for simulating the separation behavior of membrane elements Figure A2 should help illustrate the following equations:

The parameters, volume flow, concentration and pressure are already known. The details in Table A1 and A2 are also available.

To simulate the separation behavior of an industrial 8" membrane element, the following equation system is solved numerically. The nine parameters from Tables A1 and A2, as well as the input parameters $\dot{Q}^f$, c_s^f, and ΔP^f, are known.

Mass balance

$$\dot{Q}^f = \dot{Q}^p + \dot{Q}^r \tag{A.1}$$

Material balance

$$\dot{Q}^f \cdot c_s^f = \dot{Q}^p \cdot c_s^p + \dot{Q}^r \cdot c_s^r \tag{A.2}$$

Concentration in the bulk flow

$$c_s^b = \frac{c_s^r + c_s^f}{2} \tag{A.3}$$

Mean transmembrane pressure difference

$$\Delta P = \frac{\Delta P^f - \Delta P^r}{\ln\left(\Delta P^f / \Delta P^r\right)} \tag{A.4}$$

Feed-side pressure loss in the membrane element [129]

$$\Delta P^{loss} = 8.56785 \cdot 10^{-3} \cdot \left(\frac{\dot{Q}^f + \dot{Q}^r}{2}\right)^{1.7} \tag{A.5}$$

$$\Delta P^f - \Delta P^{loss} = \Delta P^r \tag{A.6}$$

Permeate volume flow

$$\dot{Q}^p = j_v \cdot A_m \tag{A.7}$$

Permeate flux density = transmembrane water flux density

$$j_v = J_W \tag{A.8}$$

Transmembrane water flux density

$$J_W = \bar{L}_p^0 \cdot (\Delta P - \Delta\Pi) \tag{A.9}$$

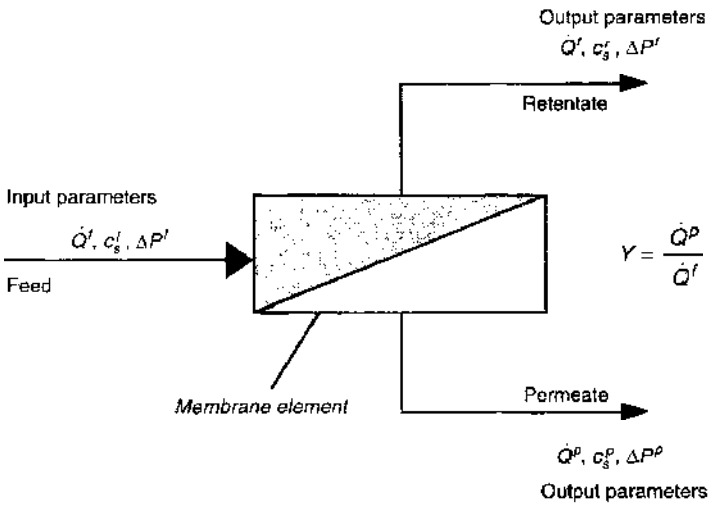

Figure A2. Input/output balance of a membrane element.

Table A1. Model parameters needed for simulating a membrane element.

Model parameter	Unit	Definition
L_p^0	l/(m²h.bar)	Pure water hydraulic permeability
b_W	bar/(g/l)	van't Hoff coefficient (osmotic pressure)
k_F ($u_{2.5''}$, $d_{H,2.5''}$)	l/(m²h)	Feed-side mass transport coefficient
σ	—	Staverman's reflection coefficient
α and β	—	Empirical coefficient

Osmotic pressure difference

$$\Delta\Pi = b_W \cdot (c_s^w - c_s^p) \tag{A.10}$$

Concentration polarization

$$\exp\left(\frac{J_W}{k_F}\right) = \frac{c_s^w - c_s^p}{c_s^b - c_s^p} \tag{A.11}$$

Real salt rejection

$$R_{s,real} = 1 - \frac{c_s^p}{c_s^w} \tag{A.12}$$

Real salt rejection

$$R_{s,real} = 1 \frac{1-\sigma}{1-\sigma \cdot \exp((\sigma-1)\cdot J_W/\overline{P}_s)} \tag{A.13}$$

Solute permeability (see Eq. 3.8)

$$\overline{P}_s = \alpha \cdot c_W^{\beta} \tag{A.14}$$

Feed-side mass transport coefficient (see Eq. 1.17)

$$k_F = 0.065 \cdot D_i^{0.75} \cdot d_{H,8''}^{-0.125} \cdot \nu^{-0.625} \cdot u_{8''}^{0.875} \tag{A.15}$$

Flow velocity of the feed solution along the membrane

$$u_{8''} = \frac{0.5 \cdot (\dot{Q}^f + \dot{Q}^r)}{A_{eff,8''}} \tag{A.16}$$

Diffusion coefficient (see Eq. 1.17)

$$D_i = \left(\frac{k_F(u_{2.5''}, d_{H,2.5''})}{0.065 \cdot d_{H,2.5''}^{-0.125} \cdot \nu^{-0.625} \cdot u_{2.5''}^{0.875}}\right) \tag{A.17}$$

For the set of equations solved numerically (Eqs. A.1–A.17), further information on the separation characteristics of the membrane element can be calculated:

Pure water permeability

$$\bar{L}_P^0 = \frac{\dot{Q}^p}{\Delta P \cdot A_m} \tag{A.18}$$

Rejection based on c_s^b

$$R_s = 1 - \frac{c_s^p}{c_s^b} \tag{A.19}$$

Table A2. Parameters needed for industrial 8'' membrane elements.

Parameter	Unit	Definition
$A_{m,8''}$	m²	Membrane area
$A_{eff,8''}$	m²	Effective cross-sectional area of the membrane
$d_{H,8''}$	m	Hydraulic diameter of the feed-channel of the membrane element

ACKNOWLEDGMENTS

Horst Chmiel, Valko Mavrov, and Mohan Noronha thank P. Klein for the technical and translation work, R. Weber for permission to use figures from his PhD thesis, J. Dorda for his work with the experiments, J. Massobrio and R. Klein-Kretzschmar for the computer simulation programs, and M. Golab for her technical cooperation, as well as all previous and current members of staff from the Institute for Environmentally Compatible Process Technology and the Department of Process Technology at the Saarland University, Saarbrücken, Germany, for their fruitful collaboration in the field of membrane processes.

John Palmeri and Xavier Lefebvre thank P. David, C. Guizard, J. Sandeaux, B. Maleyre, A. Andral, S. Genty, A. Deratani, M. Persin, and S. Condom, as well the members of *TECHNO-MEMBRANES* (P. Amblard, director), in Montpellier, France, for fruitful collaborations in the area of NF. We would also like to thank P. Fievet, M. Pontié, Z. Twardowski, and A. Yaroshchuk for helpful clarifying discussions.

LIST OF SYMBOLS

Latin Letters

A_m	m^2	Membrane area
A_{eff}	m^2	Effective cross-sectional area of membrane
a_W	—	Activity coefficient
b_W	bar/(g · l)	Van't Hoff coefficient
c_i	mg/m³; mol/m³	Concentration of component *i*/ion *i*, in general, and local concentration of ion *i*
$\bar{c}_i$	mol/m³	Intramembrane concentrations (ion *i*)
$c_i(x, r)$	mol/m³	Ion concentration in cylindrical pore (ion *i*)
c_i^b	mg/m³; mol/m³	Concentration of the component *i* in the bulk flow
c_i^f	mg/m³; mol/m³	Concentrations of the component *i* in the feed
c_i^p	mg/m³; mol/m³	Concentration of the component *i* in the permeate
c_i^w	mg/m³; mol/m³	Concentration of the component *i* at the membrane surface
c_j^f	mg/m³; mol/m³	Concentrations of the component *j* in the feed
c_j^p	mg/m³; mol/m³	Concentrations of the component *j* in the feed
c_s	mg/m³; mol/m³; mS/cm	Solute/salt concentration
c_s^b	mg/m³; mol/m³; mS/cm	Salt concentration in the bulk flow
c_s^f	mg/m³; mol/m³; mS/cm	Solute/salt concentration in the feed
$c_s^{f,sys}$	mg/m³; mol/m³; mS/cm	System solute/salt feed concentration
c_{tot}^f	mg/m³; mol/m³; mS/cm	Total salt concentration in the feed
c_s^p	mg/m³; mol/m³; mS/cm	Solute/salt concentration in the permeate
c_s^r	mg/m³; mol/m³; mS/cm	Solute/salt concentration in the retentate
c_s^w	mg/m³; mol/m³; mS/cm	salt concentration at the membrane surface (membrane wall)
C, C_s	mol/m³	Virtual salt and salt concentrations
d_H	m	Hydraulic diameter of the feed channel of the membrane element
D_i	m²/s	Diffusion coefficient for a component *i*/ion *i*
$\bar{D}_i$	m²/s	Intramembrane diffusion coefficients component *i*/ion *i*
$\bar{D}_{max}$	m²/s	Maximum intra-membrane ion diffusion coefficient
D_s	m²/s	Bulk diffusion coefficient
E_x		Electric field
F	C/mol	Faraday constant (F = 96 500 C/mol)

G	—	Function of Péclet number
I, I_s, I_{ion}	mol/m^3	Ionic strength (salt, total)
I_c	C/m^{2}s	Electric current density
j_i	mol/m^{2}h	Total molar flux density of component i/ion i
j_i	mol/m^{2}h	Local molar flux density
$j_{i,c}$	mol/m^{2}h	Convective molar flux density of component i/ion i
$j_{i,d}$	mol/m^{2}h	Diffusive molar flux density of component i/ion i
j_v	m^3/m^{2}h	Membrane volume flux density (permeate flux density)
j_v^w	m^3/m^{2}h	Pure water membrane volume flux density
J	mol/m^{2}h	Solute molar flux density
J_W	m^3/m^{2}h	Transmembrane water (solvent) volume flux density
k_B	J/K	Boltzmann constant ($k_B = 1.38 \times 10^{-23}$ J/K)
k_F	m/s	Feed-side mass transport coefficient
k_i	—	Ionic partition coefficient for ion i in the mixture
k_i^f; k_i^p	—	Feed (permeate) partition coefficient
K_D^0	m^2	Pure water Darcy hydraulic membrane permeability
$K_{i,c}$, $K_{i,d}$	—	Convective and diffusive hindrance factors of ion i
$K_{s,c}$; $K_{s,d}$	—	Convective and diffusive hindrance factors of solute
$K_{spec.}$	Euro/m^3	Specific costs
l_m	m	Active membrane layer thickness
l_{eff}	m	Effective active membrane layer thickness $l_{eff} = l_m\varphi_p/\tau$
l'_{eff}	m	Effective active membrane layer thickness associated with $\bar{L}_p^0$
l_{eff}^{ns}	m	Effective active membrane layer thickness for neutral salts
$L_{i,j}$	m^3/m.h.bar	Transport coefficients in mesoscopic irreversible thermodynamics
$\bar{L}_{i,j}$	m^3/m^{2}h.bar	Transport coefficients in macroscopic irreversible thermodynamics
L_p	m^3/m.h.bar	Specific solution membrane hydraulic permeability (in mesoscopic irreversible thermodynamics)
$\bar{L}_p$	m^3/m^{2}h.bar	Solution membrane hydraulic permeability (in general or macroscopic irreversible thermodynamics)
L_p^S	m^3/m.h.bar	Specific salt solution membrane hydraulic permeability
$\bar{L}_p^s$	m^3/m^{2}h.bar	Salt solution membrane hydraulic permeability
L_p^0	m^3/m.h.bar	Specific pure water membrane hydraulic permeability
$\bar{L}_p^0$	m^3/m^{2}h.bar	Pure water membrane hydraulic permeability
n_{ME}	—	Number of membrane elements
n_{pp}	—	Number of pressure pipes
N, N_s	—	Number of ions and salts in electrolyte mixture
p	bar	Local fluid pressure
P	bar	Average fluid pressure
ΔP, $\underline{\Delta P}$	bar	Transmembrane pressure difference
ΔP_m	bar	Intramembrane pressure difference
P^f	bar	Feed-side pressure

$\underline{\Delta}P^f$; $\underline{\Delta}P^p$	bar	Interfacial pressure jumps feed-side or permeate-side
ΔP^f; ΔP^p; ΔP^r	bar	Feed-side, permeate-side, retentate-side pressure difference
ΔP^{loss}	bar	Pressure loss in the membrane element (feed-side)
P^p	bar	permeate-side pressure
P^r	bar	Retentate-side pressure
$\bar{P}_s$	m/h	Solute permeability in general and macroscopic irreversible thermodynamic
P_s	m²/h	Solute permeability in mesoscopic irreversible thermodynamic
P_0	bar	Effective fluid pressure ($P_0 = P - \Pi$)
Pe	—	Péclet number
$\dot{Q}^f$	m³/h	Feed volume flow
$\dot{Q}^f_{sys}$	m³/h	System feed volume flow
$\dot{Q}^p$	m³/h	Permeate volume flow
$\dot{Q}^p_{sys}$	m³/h	System permeate volume flow
$\dot{Q}^r$	m³/h	Retentate volume flow
$\dot{Q}^r_{sys}$	m³/h	System retentate volume flow
r	m	Cylindrical pore radial coordinate
r_{agg}	m	Ceramic powder particle radius
r_H	m	Hydraulic radius of the membrane pores
r_i	m	Effective ion radius
r_p	m	Effective pore radius of the membrane
r_s	m	Solute radius
R	J/mol.K	Gas constant
R_s^∞	—	Limiting solute/salt membrane rejection
Re	—	Reynolds number
R_i	—	Rejection for a component i/ion i
$R_{i,Real}$	—	Real rejection for a component i
R_s	—	Solute/salt rejection
$R_{s,real}$	—	Real salt rejection
$R_{s,real,max}$	—	Maximum real salt rejection
$S_{i,j}$	—	Membrane selectivity
Sc	—	Schmidt number
Sh	—	Sherwood number
T	K	Temperature
T_i	—	Passage for a component i/ion i through the membrane
T_j	—	Passage for a component j/ion j through the membrane
u	m/s	Flow velocity of the feed solution along the membrane
V	m/h	Average solution velocity in the pore of the membrane
$\bar{V}_W$	m³	Partial molar volume
w_s	mol/mol; mg/mg	Molar/mass fraction of the salt in the solution
x	m	Transverse membrane coordinate
x_s^f	mol/mol; mg/mg	Molar/mass fraction of the salt in the solution
x_W	mol/mol	Mole fraction for water
X_m	mol/m³	effective membrane charge density (moles per unit pore volume) of the membrane
X_m^{max}	mol/m³	Maximum physical effective membrane charge density

X_m^0	mol/m^3	References charge density
Y	—; %	Membrane yield (recovery)
Y_{sys}	—; %	System yield, permeate yield
$z_{i,s}$; $z_{a,s}$; $z_{c,s}$	—	Valence of ion i, cation c, anion a in the solution

Greek Letters

α	—	Empirical coefficient
β	—	Empirical coefficient
γ_i, $\bar{\gamma}_i$, γ^f, γ^p	—	Bulk, feed, permeate intra-membrane activity coefficient (ion i)
Γ_D^f; Γ_D^p	—	Function of feed (permeate) Donnan potential
δ	m	Thickness of the laminar boundary layer
Δ; $\underline{\Delta}$		Finite Difference ... (final – initial) and (initial – final)
ε	C^2/J.m	Solution or water dielectric constant
ζ	mV	Zeta potential
η	Pa.s	Fluid dynamic viscosity
η^{eff}	Pa.s	Effective electrolyte dynamic viscosity
$\eta_{P,i}$	—	Overall efficiency of the pumps
$\eta_{T,i}$	—	Overall efficiency of the turbines
κ	—	Electroviscous coefficient
λ_s, λ_i	—	Relative solute and ion size
λ_c, λ_D	m	Debye lengths based on salt concentration and ionic strength
λ_m	m	Debye length based on effective membrane charge density
μ_E	(μm/s)/(V/cm)	Electrophoretic mobility
μ_s, μ_i, $\bar{\mu}_i$	J/mol	Electrochemical potential (bulk solute/salt, bulk ion, intra-membrane ion)
μ_i^f; μ_i^p	J/mol	Ionic electrochemical potential in the bulk feed (f) and permeate (p)
$\hat{\mu}_i$	m^2/s	Intramembrane effective mobility (ion i) $\hat{\mu}_i = z_i \bar{D}_i$
ν	m^2/s	Kinematic viscosity of the solution
v	m/h	Pore level fluid velocity
ν_i, $\nu_{a,s}$; $\nu_{c,s}$	—	Stoichiometric coefficient ion i/anion a and cation c
$\tilde{\nu}_j$	mV/(m^3/m^{2}h)	Reduced (flux) streaming potential
ν_p	mV/bar	Reduced (pressure) streaming potential
ξ	—	Normalized membrane charge density ($\xi = X_m/c^f$)
$\Delta\pi^f$; $\Delta\pi^p$	bar	Interfacial osmotic pressure jumps feed-side or permeate-side
Π	bar	Osmotic pressure
$\Delta\Pi$	bar	Osmotic pressure difference
$\underline{\Delta}\Pi_m$	bar	Intramembrane osmotic pressure difference
Π_{vH}	bar	Osmotic pressure difference according to van't Hoff
ρ	C/m^3	Ion charge density
σ	—	Local reflection coefficient in general and mesoscopic
σ_d, $\bar{\sigma}_d$	—	Osmotic reflection coefficient (meso- and macroscopic)
σ_f, $\bar{\sigma}_f$	—	Filtration reflection coefficient (meso- and macroscopic)
σ_{ek}	C/m^2	Electrokinetic surface charge density
σ_i	C/m^2	Pore wall surface charge density
σ_s	—	Local salt reflection coefficient
σ^*	—	Dimensionless pore wall surface charge density
Σ	—	Global osmotic reflection coefficient for an electrolyte mixture
τ; τ'	—	Tortuosity
ϕ	mV	Average intramembrane electric potential (mesoscopic)

$\tilde{\phi}$	—	Average dimensionless electric potential ($\tilde{\phi} = F\phi/RT$)
$\Delta\tilde{\phi}$	—	Dimensionless intramembrane potential difference
$\Delta\phi_D^f$; $\Delta\phi_D^p$	mV	(interfacial) feed-side (permeate) Donnan potential
ϕ_d	mV	Electric diffusion potential
$\Delta\phi'_{\text{lim}}$	mV	Limiting y-intercept of electric filtration potential
ϕ_s	mV	Electric streaming potential
φ_p	—	Membrane porosity
Φ^f; Φ^p	mV	Bulk feed and permeate electric potential
$\underline{\Delta}\Phi^F$	mV	Electric filtration potential difference $\underline{\Delta}\Phi^F = \Phi^f - \Phi^p$
$\underline{\Delta}\tilde{\Phi}^F$	mV	Dimensionless electric filtration potential
Φ^s, Φ_i^s	—	Solute, ion steric partition factor ($\Phi_i^s = (1 - \lambda_i)^2$)
ψ	mV	Local (pore level) electric potential
Ψ	mV	Local (pore level) electric potential due to electric double layer
$\tilde{\Psi}$	—	Dimensionless local electric potential

Acronyms

A	anion
c	convection
C	cation
d	diffusion
DSPM	Donnan Steric pore model
ENP	Extended Nernst-Planck
ES	Electric Steric
ET	Electro-Transport
f	feed; bulk feed
HT	Hindered Transport
HET	Hindered Electro-Transport
i	ion
IEP	Isoelectric Point
lim	limiting
MF	Microfiltration
MWCO	Molecular Weight Cut-Off
mix	mixture
N	total number of ions
N_s	number of salts in the mixture
NF	Nanofiltration
ns	natural salt
p	permeate
pH^f	pH of the feed
r	retentate
RO	Reverse Osmosis
s	solute/salt
tot	total
UF	Ultrafiltration
WCC	Weighting by Concentration at constant total Concentration
WII	Weighting by Ionic strength at constant total Ionic strength
WIC	Weighting by Ionic strength at constant total Concentration

REFERENCES

1. H. Chmiel, H. Strathmann, E. Streicher, and H. Schneider, *Chemie Ingenieur Technik* 55, 582 (1983).
2. M. Ernst, A. Bismarck, J. Springer, and M. Jekel, *J. Membr. Sci.* 165, 251 (2000).
3. F. Evangelista, *Ind. Eng. Chem. Process Des. Dev.* 24, 211 (1985).
4. F. Evangelista and G. Jonsson, *Chem. Eng. Commun.* 72, 69 (1988).
5. J. Cadotte, *Desalination* 70, 77 (1988).

6. B. M. Watson and C. D. Homburg, *Desalination* 72, 11 (1989).
7. R. Weber, H. Chmiel, and V. Mavrov, *Desalination* 157, 113 (2003).
8. P. Börgardts, Berichte aus Forschung, and Entwicklung, Nr. 1, Fraunhofer IRB Verlag (1996).
9. S. Mirza, amk-preprints OP 21, GVC Düsseldorf (2003).
10. S. Bhattacharya and S. Hwang, *J. Membr. Sci.* 132, 73 (1997).
11. B. Marinas and R. Urama, *J. Env. Eng.* 122, 292 (1996).
12. H. Niemi, J. Raimoaho, and S. Palosaari, "Chemical Technology and Metallurgy Series." Helsinki, 1986. pp. 1–32.
13. G. Schock and A. Miquel, *Desalination* 64, 339 (1987).
14. B. Tansel, W. Y. Bao, and I. N. Tansel, *Desalination* 129, 7 (2000).
15. G. Del Re. G. Di Giacomo. L. Aloisio, and M. Terreri, *Desalination* 119, 205 (1998).
16. F. G. Donnan, The theory of membrane equilibria. Chemical Reviews, Band 1 (1925).
17. G. Schneider. Ph.D. Thesis on Trennverhalten in Nanofiltrationsmembranen, Technical University (RWTH), Aachen, 1993.
18. S. P. Nunes and K.-V. Peinemann, "Membrane Technology in the Chemical Industry." Wiley-VCH, 2002.
19. J. Mohn, W. Heine, R. Rautenbach, R. Mellis, and K. Vossenkaul. Filtration and separation apparatus especially for biological-organic fluids with filter elements in the form of membrane pads. European Patent EP0707884 B1 (1995).
20. T. Melin and R. Rautenbach, "Membranverfahren." Springer. Berlin, 2003.
21. R. Weber. Ph.D. Thesis on Charakterisierung, Stofftransport und Einsatz keramischer Nanofiltrationsmembranen, Saarland University, Saarbrücken, 2001.
22. P. Puhlfürß, I. Voigt, R. Weber, and M. Morbé, *J. Membr. Sci.* 174, 123 (2000).
23. J. Israelachvili. "Intermolecular and Surface Forces," 2nd Edn. Academic Press, San Diego, 2000.
24. C. Van Oss. "Interfacial Forces in Aqueous Media." Marcel Dekker, New York, 1994.
25. L. Dresner, *Desalination* 15, 39 (1974).
26. V. M. Starov and N. V. Churaev, *Adv. Colloid Interface Sci.* 43, 145 (1993),
27. A. Yaroshchuk, *Adv. Colloid Interface Sci.* 85, 193 (2000).
28. B. Hille, "Ionic Channels of Excitable Membrane," 3rd Edn. Sinauer, Sunderland, MA, 2001.
29. W. M. Deen, B. Satvat, and J. M. Jamieson, *Am. J. Physiol.* 238, F126 (1980).
30. X.-L. Wang, T. Tsuru, M. Togoh, S. Nakao, and S. Kimura, *J. Chem. Eng. Japan* 28, 372 (1995).
31. W. R. Bowen and H. Mukthar, *J. Membr. Sci.* 112, 263 (1996).
32. G. Hagmeyer and R. Gimbel, *Desalination* 117 (1998).
33. T. Tsuru, M. Urairi, S. Nakao, and S. Kimura, *J. Chem. Eng. Jap.* 24, 518 (1991).
34. G. Hagmeyer and R. Gimbel, *Sep. Purif. Technol.* 15, 19 (1999).
35. J. Palmeri, J. Sandeaux, R. Sandeaux, X. Lefebvre, P. David, C. Guizard, P. Amblard, J.-F. Diaz, and B. Lamaze, *Desalination* 147, 231 (2002).
36. X. Lefebvre, J. Palmeri, J. Sandeaux, R. Sandeaux, P. David, B. Maleyre, C. Guizard, P. Amblard, J.-F. Diaz, and B. Lamaze. *Sep. Pur. Tech.* 32, 117 (2003).
37. P. Blanc, A. Larbot, J. Palmeri, M. Lopez. and L. Cot, *J. Membr. Sci.* 149, 151 (1998).
38. J. Palmeri, P. Blanc, A. Larbot, and P. David. *J. Membr. Sci.* 179, 243 (2000).
39. F. Helfrich, "Ion Exchange." McGraw-Hill, New York, 1962.
40. R. Schlögl. *Ber. Bunsenges. Physik. Chem.* 70, 400 (1966).
41. L. Dresner, *Desalination* 10, 27 (1972).
42. E. Hoffer and O. Kedem, *Desalination* 2, 25 (1967).
43. K. S. Spiegler and O. Kedem, *Desalination* 1, 311 (1966).
44. A. A. Sonin, "Charged Gels and Membranes" (E. Sélégny, Ed.), Vol. 1, p. 255, Reidel. Dordrecht, 1976.
45. W. M. Deen, *AIChE J.* 33, 1409 (1987).
46. E. H. Cwirko and R. Carbonell, *J. Colloid Interface Sci.* 129, 513 (1989).
47. A. E. Yaroshchuk, *Adv. Colloid Interface Sci.* 60, 1 (1995).
48. X.-L. Wang, T. Tsuru, S. Nakao, and S. Kimura, *J. Membr. Sci.* 103, 117 (1995).
49. X.-L. Wang, T. Tsuru, M. Togoh, S. Nakao, and S. Kimura, *J. Chem. Eng. Japan* 28, 186 (1995).
50. O. Kedem and A. Katchalsky, *J. Gen. Physiol.* 45, 143 (1961).
51. G. B. Westermann-Clark and J. Anderson, *J. Electrochim. Soc.* 130, 839 (1983).
52. H. J. M Hijnen. J. V. Van Daalen, and J. A. M. Smit, *J. Colloid Interface Sci.* 107, 525 (1985).
53. W. M. Deen, C. R. Bridges, B. M. Brenner, and B. D. Myers, *Am. J. Physiol.* 249, F374 (1985).
54. S. Nakao and S. Kimura, *J. Chem. Eng. Japan* 15, 200 (1982).
55. M. Perry and C. Linder, *Desalination* 71, 233 (1989).
56. P. Schirg and F. Widmer, *Desalination* 89, 89 (1992).
57. F. A. Morrison and J. F. Osterle, *J. Chem. Phys.* 43, 2111 (1965).
58. R. J. Gross and J. F. Osterle. *J. Chem. Phys.* 49, 228 (1968).
59. J. C. Fair and J. F. Osterle. *J. Chem. Phys.* 54, 3307 (1971).
60. L. Dresner and K. A. Kraus. *J. Phys. Chem.* 67, 990 (1963).
61. L. Dresner, *J. Phys. Chem.* 69, 2230 (1965).
62. P. Neogi and E. Ruckenstein. *J. Colloid Interface Sci.* 79, 159 (1981).
63. H. J. M. Hijnen and J. A. M. Smit, *Biophys. Chem.* 41, 101 (1991).
64. A. E. Yaroshchuk and S. S. Dukhin. *J. Membr. Sci.* 79, 133 (1993).
65. J. A. M. Smit, *J. Colloid Interface Sci.* 132, 413 (1989).

66. A. D. MacGillivray, *J. Chem. Phys.* 48, 2903 (1968).
67. H. U. Demisch and W. Pusch, *J. Colloid Interface Sci.* 69, 247 (1979).
68. L. Dresner, *J. Phys. Chem.* 76, 2256 (1972).
69. A. E. Yaroshchuk, *J. Membr. Sci.* 167, 163 (2000).
70. E. Hoffer and O. Kedem, *Ind. Eng. Chem. Process Des. Dev.* 11, 211 (1972).
71. F. Donnan, *Zeitschrift für Elektrochemie und angewandte physikalische Chemie* 17, 572 (1911).
72. T. R. Noordman, P. Vonk, V. H. J. T. Damen, R. Brul, S. H. Schaafsma, M. de Haas, and J. A. Wesselingh, *J. Membr. Sci.* 135, 203 (1997).
73. R. Rangarajan, M. A. Mazid, T. Matsuura, and S. Sourirajan, *Ind. Eng. Chem Process Des. Dev.* 24, 977 (1985).
74. G. Jacazio, R. F. Probstein, A. A. Sonin, and D. Yung, *J. Phys. Chem.* 76, 4015 (1972).
75. W. R. Bowen, A. W. Mohammed, and N. Hilal, *J. Membr. Sci.* 126, 91 (1997).
76. W. R. Bowen and A. W. Mohammed, *Trans. IchemE* 76, 885 (1998).
77. C. Labbez, P. Fievet, A. Szymczyk, A. Vidonne, A. Foissy, and J. Pagetti, *Sep. Purif. Technol.* 30, 47 (2003).
78. S. Sourirajan, "Reverse Osmosis." Academic Press, New York, 1970.
79. T. Matsuura and S. Sourirajan, *Ind. Eng. Chem Process Des. Dev* 20, 273 (1981).
80. H. Mehdizadeh and J. Dickson, *J. Membr. Sci.* 42, 119 (1989).
81. S. Chevalier, Ph.D. Thesis, "Modélisation Mathématique des Mécanismes de Transfert en Nanofiltration." University of Bordeaux II, France, 1999.
82. E. Hoffer and O. Kedem, *Ind. Eng. Chem Process Des. Dev.* 11, 226 (1972).
83. H. K. Lonsdale, W. Pusch, and A. Walch, *J. Chem. Soc., Faraday Trans. I* 71, 501 (1975).
84. D. Nielsen and G. Jonnson, *Sep. Sci. Tech.* 29, 1165 (1994).
85. A. Shenase, E. Staude, and A. E. Yaroshchuk, *Sep. Sci. Technol.* 30, 2865 (1995).
86. C. Bardot, E. Gaubert, and A. E. Yaroshchuk, *J. Membr. Sci.* 103, 11 (1995).
87. Z. Twardowski, Nanofiltration of concentrated aqueous salt solutions, US Patent 5 587 083 (1996).
88. A. J. Shor, K. A. Kraus, W. T. Smith, and J. S. Johnson, *J. Phys. Chem.* 72, 2200 (1967).
89. C. Labbez, P. Fievet, A. Szymczyk, A. Vidonne, A. Foissy, and J. Pagetti, *J. Membr. Sci.* 208, 315 (2002).
90. W. R. Bowen and J. S. Welfoot, *Chem. Eng. Sci.* 57, 1393 (2002).
91. J. Palmeri, P. Blanc, A. Larbot, and P. David, *J. Membr. Sci.* 160, 141 (1999).
92. R. Vacassy, J. Palmeri, C. Guizard, V. Thoraval, and L. Cot, *Sep. Purif. Technol.* 12, 243 (1997).
93. C. Labbez, P. Fievet, A. Szymczyk, E. Thomas, C. Simon, A. Vidonne, J. Pagetti, and A. Foissy, *Desalination* 147, 223 (2002).
94. G. Tanny, E. Hoffer, and O. Kedem, "Biological Aspects of Electrochemistry" (G. Milazzo, Ed.), p. 619. Birkhauser Verlag, Basel, Switzerland, 1971; *Experentia Suppl.* 18, 619 (1971).
95. G. Tanny and O. Kedem, *J. Colloid Interface Sci.* 51, 177 (1975).
96. Y. Elmarraki, M. Persin, J. Sarrazin, M. Cretin, and A. Larbot, *Sep. Pur. Tech.* 25, 493 (2001).
97. S. Condom, S. Chemlal, W. Chu, M. Persin, and A. Larbot, *Sep. Pur. Tech.* 25, 545 (2001).
98. A. E. Yaroshchuk and Y. P. Boiko, *Langmuir* 18, 5154 (2002).
99. X. Lefebvre, J. Palmeri, and P. David, *J. Phys. Chem. B* 108, 16811 (2004).
100. R. J. Hunter, "Foundations of Colloid Science." Clarendon Press, Oxford, 1987/1989, Vols. 1/2.
101. W. B. Samuel de Lint, P. Maarten Biesheuvel, and Henk Verweij, *J. Colloid Interface Sci.* 251, 131 (2002).
102. C. P. Minning and K. S. Spiegler, "Charged Gels and Membranes" (E. Sélégny, Ed.), Vol. 1, p. 277, Reidel, Dordrecht, 1976.
103. P. Eriksson, *Environ. Prog.* 7, 58 (1988).
104. T. Tsuru, M. Urairi, S. Nakao, and S. Kimura, *Desalination* 81, 219 (1991).
105. J. M. M. Peeters, J. P. Boom, M. H. V. Mulder, and H. Strathmann, *J. Membr. Sci.* 145, 199 (1998).
106. B. Van der Bruggen, J. Schaep, D. Wilms, and C. Vandecasteele, *J. Membr. Sci.* 156, 29 (1999).
107. Johan Schaep and Carlo Vandecasteele, *J. Membr. Sci.* 188, 129 (2001).
108. Stéphane Sarrade, Gilbert M. Rios, and Maurice Carlès, *J. Membr. Sci.* 97, 155 (1994).
109. G. M. Rios, R. Joulie, S. J. Sarrade, and M. Carlès, *AIChE J.* 42, 2521 (1996).
110. P. Baticle, C. Kiefer, N. Lakhchaf, A. Larbot, O. Leclerc, M. Persin, and J. Sarrazin, *J. Membr. Sci.* 135, 1 (1997).
111. C. Combe, C. Guizard, P. Aimar, and V. Sanchez, *J. Membr. Sci.* 129, 147 (1997).
112. R. Vacassy, C. Guizard, V. Thoraval, and L. Cot, *J. Membr. Sci.* 132, 109 (1997).
113. Toshinori Tsuru, Shin-ichi Wada, Shuhei Izumi, and Masashi Asaeda, *J. Membr. Sci.* 149, 127 (1998).
114. C. Labbez, P. Fievet, A. Szymczyk, A. Vidonne, A. Foissy, and J. Pagetti, *J. Membr. Sci.* 208, 315 (2002).
115. W. R. Bowen and J. S. Welfoot, *Chem. Eng. Sci.* 57, 1121 (2002).
116. F. Evangelista and G. Jonsson, *Chem. Eng. Commun.* 72, 83 (1988).
117. W. R. Bowen and H. Mukhtar, *J. Membr. Sci.* 112, 263 (1996).
118. T. Tsuru, M. Urairi, S. Nakao, and S. Kimura, *Desalination* 81, 219 (1991).
119. H.-C. Flemming, G. Schaule, T. Griebe, J. Schmitt, and A. Tamachkiarowa, *Desalination* 113, 215 (1997).
120. M. Otaki, S. Takizawa, and S. Ohgaki, *J. Water Sci. and Technol.* 38, 405 (1998).
121. R. Rautenbach, "Membranverfahren Grundlagen der Modul- und Anlagenauslegung." Berlin, Springer, 1997.
122. M. M. El-Hawagi, *AIChE Journal* 38, 1185 (1992).
123. K. K. Sirkar and G. Rao, *Ind. Eng. Chem. Process Des. Dev.* 20, 116 (1981).
124. K. K. Sirkar, P. T. Dang, and G. Rao, *Ind. Eng. Chem. Process Des. Dev.* 21, 517 (1982).
125. K. K. Sirkar and G. Rao, *Desalination* 48, 25 (1983).
126. E. Brauns, *Desalination & Water Reuse* 10/4, 18 (2001).

127. W. G. J. van der Meer, C. W. Aeijelts Averink, and J. C. van Dijk, *Desalination* 105, 25 (1996).
128. W. G. J. van der Meer, M. Riemersma, and J. C. van Dijk, *Desalination* 119, 57 (1998).
129. M. Noronha, Ph.D. Thesis on Effiziente Auslegung und Optimierung technischer Nanofiltrationsverfahren durch vereinfachte Prozesssimulation, University Saarbrücken, 2002.
130. M. Noronha, V. Mavrov, and H. Chmiel, in Preprints 9. Aachener Membrankolloquium, 241, 2001.
131. C. Blöcher, M. Noronha, L. Fünfrocken, J. Dorda, V. Mavrov, H. D. Janke, and H. Chmiel, *Desalination* 144, 143 (2002).
132. M. Noronha, V. Mavrov, and H. Chmiel, *Ann. N. Y. Acad. Sci.* 984, 142 (2003).
133. M. Noronha, V. Mavrov, and H. Chmiel, *Chemie Ingenieur Technik* 74, 70 (2002); *Computer-Aided Simulation for Optimising Nanofiltration Processes, Chem. Eng. Technol.* 11, 1065 (2002).
134. M. Noronha, T. Britz, V. Mavrov, H. D. Janke, and H. Chmiel, *Desalintion* 143, 183 (2002).
135. M. Noronha, V. Mavrov, and H. Chmiel, *J. Membr. Sci.* 202, 217 (2002).
136. M. Noronha, V. Mavrov, and H. Chmiel, *Desalination* 145, 207 (2002).
137. M. Noronha, V. Mavrov, and H. Chmiel, *Desalination* 152, 253 (2002).
138. E. Blass, in "Grundlagen der chemischen Technik," Otto Salle, 1989.
139. W. F. Daenzer, System Engineering, 2nd Edn. P. Hanstein-Verlag Köln, 1979.
140. M. C. Wilbert, F. Leitz, E. Abart, B. Boegli, and K. Linton, *Water Treatment Eng. Res.* Denver, CO, 1998.
141. S. Noronha, Ph.D. Thesis on Rechnergestützte Synthese verfahrenstechnischer Prozesse mit MINLP-Methoden, Technical University Hamburg-Harburg, 1998.
142. K. Spiegler and O. Kedem, *Desalination* 21, 203 (1966).
143. P. Schirg and F. Widmer, *Desalination* 89, 89 (1992).
144. T. Tsuru, S.-I. Nakao, and S. Kimura, *J. Chem. Eng. Japan* 24, 511 (1991).
145. Grundfos Pumps, Technische Informationen zu elektronisch geregelten Hochdruck-Kreiselpumpen (Typ CRNE) (2000).

CHAPTER 4

Constrained Grain Boundary Diffusion in Thin Copper Films

Markus J. Buehler,[1,2] T. John Balk,[1] Eduard Arzt,[1] Huajian Gao[1]

[1] *Max Planck Institute for Metals Research, Stuttgart, Germany*
[2] *California Institute of Technology, Pasadena, California, USA*

CONTENTS

ISBN: 1-58883-047-0

Handbook of Theoretical and Computational Nanotechnology
Edited by Michael Rieth and Wolfram Schommers
Volume 5: Pages (215–249)

1. INTRODUCTION

Materials in small dimensions have become an increasingly important topic of research in the last decade. Changes in material behavior resulting from the effects of surfaces, interfaces, and constraints are still not completely understood. The focus of this chapter is on the mechanical properties of ultrathin submicron copper films on substrates. In such materials, important effects of the film surface and grain boundaries occur, and the constraint of the film–substrate interface can govern the mechanical behavior.

Polycrystalline thin metal films, shown schematically in Fig. 1, are frequently deposited on substrate materials to build complex microelectronic devices and are a relevant example of materials in small dimensions. In many applications and during the manufacturing process, thin films are subjected to stresses arising from thermal mismatch between the film material and the substrate. This can have a significant effect on the production yield as well as on the performance and reliability of devices in service. In past years, an ever-increasing trend toward miniaturization in technology has been observed, stimulating a growing interest in investigating the deformation behavior of ultrathin metal films with film thicknesses well below 1 μm.

Different inelastic deformation mechanisms operate to relax the internal and external stresses on a thin film. Experiments have shown that for films of thicknesses between approximately 2 and 0.5 μm, the flow stress increases in inverse proportion to the film thickness (see, for example, Refs. [1–3]). This has been attributed to dislocation channeling through the film [4–6], where a moving threading dislocation leaves behind an interfacial segment. The relative energetic effort to generate these interfacial dislocations increases with decreasing film thickness, which explains the higher strength of thinner films. This model, however, could not completely explain the high strength of the thin films that was found in experiments [1]. More recent theoretical and experimental work [7–11] indicates that the strength of thin metal films often results from a lack of active dislocation sources rather than from the energetic effort associated with dislocation motion.

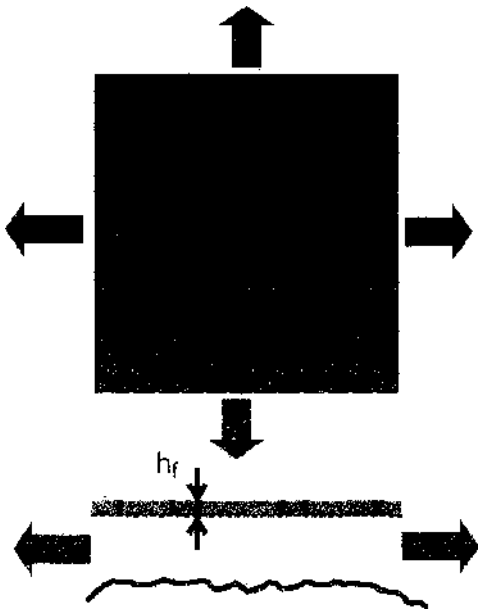

Figure 1. A polycrystalline thin film constrained by a substrate. The thin film is subject to biaxial loading as a result of thermal mismatch of film and substrate material.

The regime in which plastic relaxation is limited by dislocation nucleation and carried by the glide of threading dislocations reaches down to film thicknesses of about $h_f \approx 400$ nm. For yet-thinner films, experiments have revealed a film-thickness-independent flow stress [7]. *In-situ* transmission electron microscopy observations of the deformation of such ultrathin films reveal dislocation motion parallel to the film–substrate interface [7, 8]. This glide mechanism is unexpected, because in the global biaxial stress field, there is no resolved shear stress on parallel glide planes, indicating that there must be a mechanism involving long-range internal stresses that vary slowly on the length scale of the film thickness. For sufficiently thin films, these internal stresses have a pronounced effect on the mechanical behavior. Constrained diffusional creep [12] has provided what is so far the only feasible mechanism for such internal stresses to cause nucleation of dislocations on glide planes parallel to the surface.

This chapter contains three main parts. The first part reviews continuum mechanics modeling of constrained diffusional creep. The second part contains the results of molecular dynamics simulations of diffusional creep and plasticity in polycrystalline thin films. In the third part, we discuss relevant experimental results. Finally, we summarize all the results to develop a deformation mechanism map for ultrathin films on substrates.

2. CONTINUUM MODELING

The continuum model of constrained diffusional creep was developed by Gao and coworkers [12]. Diffusion can have a fundamentally different nature in thin films than in bulk materials. The constraint imposed by the strong bonding between film and substrate implies that no sliding can occur at the film–substrate interface. In contrast to previously proposed models of diffusion in thin films [13], the constraint of no sliding at the film–substrate interface renders diffusion in thin films an inherently transient phenomenon [12]. Therefore, steady-state solutions frequently used to describe grain boundary diffusion may not be applied. An additional constraint is that material transport cannot proceed into the substrate, and diffusion must therefore stop at the film–substrate interface. It was shown by Gao and coworkers [12] that constrained grain boundary diffusion leads to a new material defect, referred to as the grain boundary diffusion wedge.

Figure 2 illustrates the basic mechanism of constrained diffusional creep [12] in three stages. In stage 1, material is transported from the surface into the grain boundary. In stage 2, mass transport leads to the formation of a diffusion wedge, as more and more material flows into and accumulates in the grain boundary. The continuum model predicts that the traction along the grain boundary diffusion wedge becomes fully relaxed and cracklike on the scale of a characteristic time τ. This leads to extraordinarily large resolved shear stresses on glide planes that are parallel and close to the film–substrate interface, and that can cause emission of parallel glide dislocations in the last stage. Although the resolved shear stresses on the parallel glide planes induced by a diffusion wedge are similar to those generated by a crack, differences in the dislocation nucleation process may arise.

This section is briefly outlined as follows. We discuss the continuum mechanics model of constrained diffusional creep for different cases, including the homogeneous case, bimaterial interface, and coupled surface and grain boundary diffusion. We also present an extension of the continuum model to include a threshold stress for diffusion. Finally, we discuss a model of the critical condition for initiation of diffusion and a model for parallel glide dislocation nucleation from the diffusion wedge in the spirit of a model by Rice and Thomson for dislocation nucleation at crack tips [14].

2.1. Basics of the Continuum Modeling

In the continuum model, diffusion is treated as dislocation climb in the grain boundary. The basis is the solution for the normal traction σ_{xx} along the grain boundary resulting from the insertion of a single dislocation (material layer of thickness b) along $(0, \zeta)$ (corresponding to a climb edge dislocation). The coordinate system for the problem is depicted in Fig. 3. The solution for a single edge dislocation near a surface is used as the Green's function

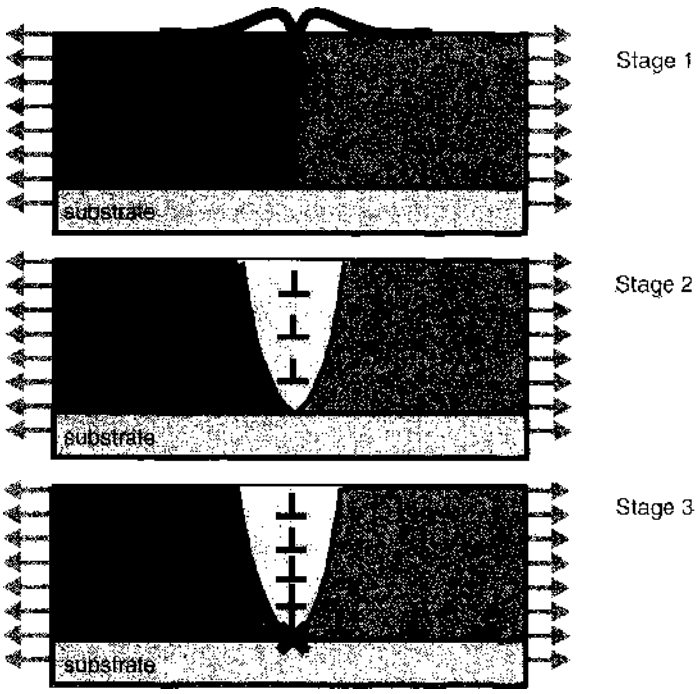

Figure 2. Mechanism of constrained diffusional creep. Material is transported from the surface into the grain boundary, leading to the formation of a diffusion wedge as material accumulates in the grain boundary. The diffusion wedge can be modeled as a pile-up of climb edge dislocations near the film–substrate interface, causing a cracklike singular stress concentration near the root of the grain boundary.

to construct a solution with infinitesimal Volterra edge dislocations [15–17]. The traction at position ζ resulting from a dislocation at ξ is

$$\sigma_{xx}(\zeta, \xi) = \frac{Eb}{4\pi(1-\nu^2)} K(\zeta, \xi) \tag{1}$$

where

$$K(\zeta, \xi) = \frac{1}{\zeta - \xi} - \frac{1}{\zeta + \xi} - \frac{2\zeta(\zeta - \xi)}{(\zeta + \xi)^3} \tag{2}$$

is the Cauchy kernel function for this particular problem, with E denoting Young's modulus and ν Poisson's ratio. For an arbitrary opening function $2u(\zeta)$ in a film with thickness h_f, the stress along the grain boundary is given by

$$\sigma_{xx}(\zeta, t) = \sigma_0 - \frac{E}{2\pi(1-\nu^2)} \int_0^{h_f} S(\zeta, \xi) \frac{\partial u(\xi, t)}{\partial \xi} \, d\xi \tag{3}$$

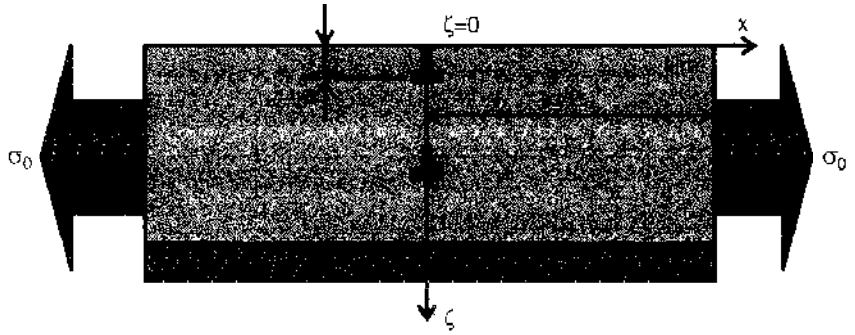

Figure 3. Coordinate system for the continuum mechanics analysis. The schematic shows climb edge dislocations in the grain boundary of a thin film on substrate.

where σ_0 is the stress in the absence of diffusion and $S(\zeta, \xi)$ is a Green's function kernel for the continuous dislocation problem (Cauchy kernel). For a dislocation near a free surface, $S(\zeta, \xi) = K(\zeta, \xi)$. The kernel function $S(\zeta, \xi)$ can also be established for a dislocation near a bimaterial interface [12, 18] or for periodic wedges [12]. The calculations in this chapter are mostly for an elastic film on a rigid substrate, although we do not give the Green's function kernel explicitly here.

The chemical potential relative to the free surface (with atomic volume $\Omega = a_0^3/4$ in face-centered cubic crystals where a_0 is the lattice parameter) is given by

$$\mu(\zeta, t) = \mu_0 - \sigma_{xx}(\zeta, t)\Omega \tag{4}$$

where μ_0 is an arbitrary reference constant. The corresponding atomic flux per unit thickness in the boundary is

$$j(\zeta, t) = -\frac{\delta_{gb} D_{gb}}{kT} \frac{\partial \mu(\zeta, t)}{\partial \zeta} = \frac{\delta_{gb} D_{gb}}{kT} \frac{\partial \sigma_{xx}(\zeta, t)}{\partial \zeta} \tag{5}$$

where k is the Boltzmann constant and T the absolute temperature. The parameter $\delta_{gb} D_{gb}$ denotes temperature-dependent grain boundary diffusivity. Equations (4) and (5) are coupled via mass conservation, as the flux divergence is related to the displacement rate through

$$2\frac{\partial u}{\partial t} = -\Omega \frac{\partial j(\zeta, t)}{\partial \zeta} \tag{6}$$

which can be combined with Eq. (5) as

$$\frac{\partial u}{\partial t} = -\frac{\delta_{gb} D_{gb} \Omega}{2kT} \frac{\partial^2 \sigma_{xx}(\zeta, t)}{\partial \zeta^2} \tag{7}$$

The derivative of $\sigma_{xx}(\zeta, t)$ with respect to time is given by

$$\frac{\partial \sigma_{xx}(\zeta, t)}{\partial t} = -\frac{E}{2\pi(1 - \nu^2)} \int_0^{h_f} S(\zeta, \xi) \frac{\partial^2 u(\xi)}{\partial \xi \partial t} \, d\xi \tag{8}$$

and inserting Eq. (7) into Eq. (8) yields the main governing equation

$$\frac{\partial \sigma_{xx}(\zeta, t)}{\partial t} = \frac{E \delta_{gb} D_{gb} \Omega}{4\pi(1 - \nu^2) kT} \int_0^{h_f} S(\zeta, \xi) \frac{\partial^3 \sigma_{xx}(\xi, t)}{\partial \xi^3} \, d\xi \tag{9}$$

for the grain boundary traction. Boundary and initial conditions are given as follows: for the continuity of chemical potential near the free surface,

$$\sigma_{xx}(\zeta = 0, t) = 0 \tag{10}$$

and for no sliding and no diffusion at the interface,

$$\frac{\partial \sigma_{xx}}{\partial \zeta}(\zeta = h_f, t) = \frac{\partial^2 \sigma_{xx}}{\partial \zeta^2}(\zeta = h_f, t) = 0 \tag{11}$$

Finally,

$$\sigma_{xx}(\zeta, t = 0) = \sigma_0 \tag{12}$$

sets the initial condition for the transient problem.

The problem given by Eq. (9) can be expressed by the method of separation of variables in the form of an expansion series

$$\sigma_{xx}(\zeta, t) = \sigma_0 \sum_{n=1}^{\infty} c_n \exp(-\lambda_n t/\tau) f_n(\zeta/h_f) \tag{13}$$

where

$$\tau = \frac{4\pi(1-\nu^2)\mathrm{k}Th_f^3}{ED_{gb}\delta_{gb}\Omega} \tag{14}$$

is a characteristic time and λ_n, f_n, and c_n denote the eigenvalues, eigenfunctions, and coefficients. The coefficients are determined from the initial condition at $t = 0$. It is important to note that $\tau \sim h_f^3$, similar to the classical Coble creep equation [19]. To solve the equations numerically, the problem is transformed into a standard Cauchy-type singular equation for f_n''' [12]. The Gauss–Chebyshev quadrature developed by Erdogan et al. [20, 21] can be used to solve such equations. The opening displacement $u(z, t)$ is given by

$$u(\zeta, t) = -\frac{2\pi(1-\nu^2)h_f\sigma_{tt}}{E}\sum_{n=1}^{\infty} c_n\lambda_n^{-1}\left(1-\exp\left(-\lambda_n t/\tau\right)\right) f_n''(\zeta/h_f) \tag{15}$$

The solution procedure can be summarized in the following steps: first, find eigenvalues and eigenfunctions; second, find the coefficients c_n, and third, calculate the traction and displacement from Eqs. (13) and (15).

The dislocations "stored" in the grain boundary represent additional material in the boundary. With respect to the lattice distortion around the diffusion wedge, the dislocations in the grain boundary exemplify a type of geometrically necessary dislocation [22] that causes nonuniform plastic deformation in the thin film. The eigenvalues measure the rate of decay of each eigenmode. The results showed that the higher eigenmodes decay much faster than the first eigenmode, so the diffusion process is dominated by the first eigenmode [12].

Figures 4, 5, and 6 show several numerical examples. Figure 4 shows the stress intensity factor normalized by the corresponding value for a crack versus the reduced time $t^* = t/\tau$ for identical elastic properties of substrate and film material (homogeneous case), rigid substrate (copper film and rigid substrate), and soft substrate (aluminum film and epoxy substrate). Table 1 summarizes the material parameters used for the calculation. In the table, μ_{film}/μ_{subs} is the ratio of the shear moduli.

Figure 5 shows the opening displacement along the grain boundary for several instants in time for the case of soft film on rigid substrate, and Fig. 6 shows the traction along the boundary for various instants in time. These examples illustrate that in the long time limit $t \to \infty$, the solution approaches the displacement profile of a crack.

For constrained diffusional creep to proceed, both grain boundary diffusion and surface diffusion need to be active. In the original paper on constrained diffusional creep [12],

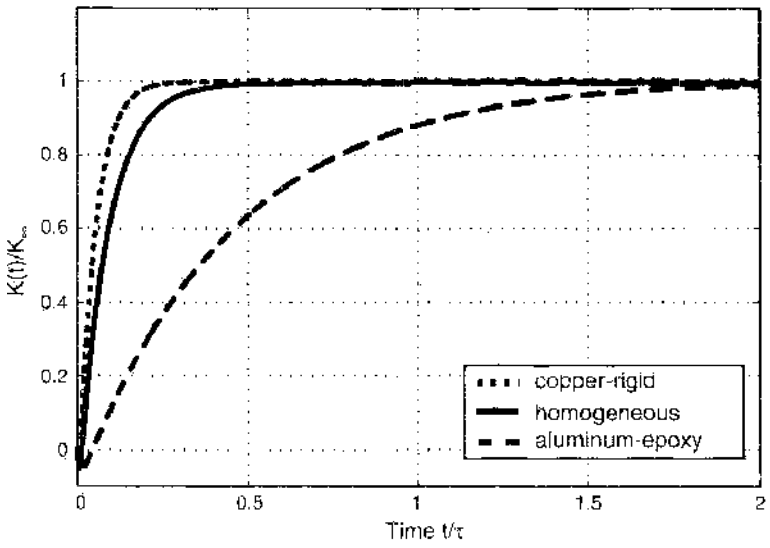

Figure 4. Development of stress intensity factor over time for the cases of an elastically homogeneous film on substrate, a rigid substrate, and a soft substrate. The convergence to the stress intensity factor of a crack is fastest for a rigid substrate and slowest for a soft substrate.

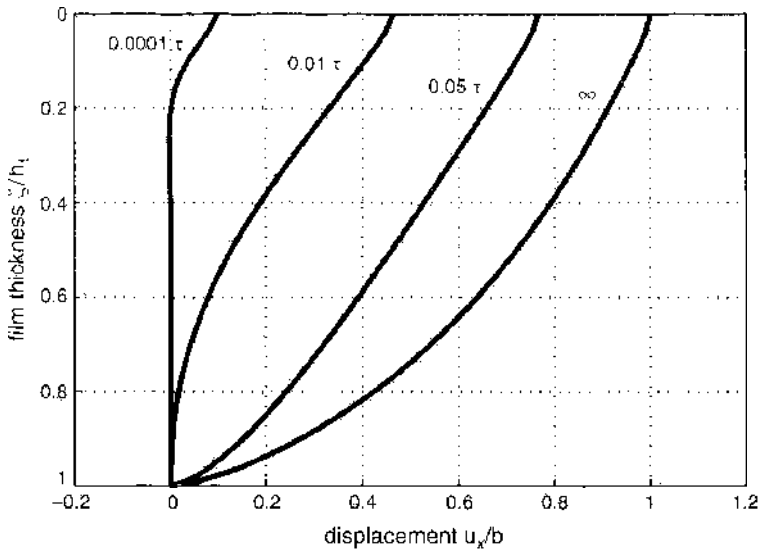

Figure 5. Development of grain boundary opening u_x normalized by a Burgers vector over time, in the case of a copper film on a rigid substrate. The loading σ_0 is chosen such that the opening displacement at the film surface ($\zeta = 0$) at $t \to \infty$ is one Burgers vector.

surface diffusion was assumed to be infinitely fast relative to grain boundary diffusion. This implies that grain boundary diffusion is the rate-limiting factor. To account for cases when surface diffusion is slower than grain boundary diffusion, or for cases when surface and grain boundary diffusion occur on comparable timescales, the model was extended in a later publication to also include the effect of surface diffusion [18]. We now briefly review this model.

The atomic flux on a free surface may be expressed as

$$j_s(s,t) = \frac{\delta_s D_s}{kT} \frac{\partial \mu_s}{\partial s} \tag{16}$$

Here $\partial \mu_s / \partial s$ refers to the gradient in chemical potential along the free surface, and $\delta_s D_s$ is the temperature-dependent coefficient of surface diffusion. The chemical potential of an

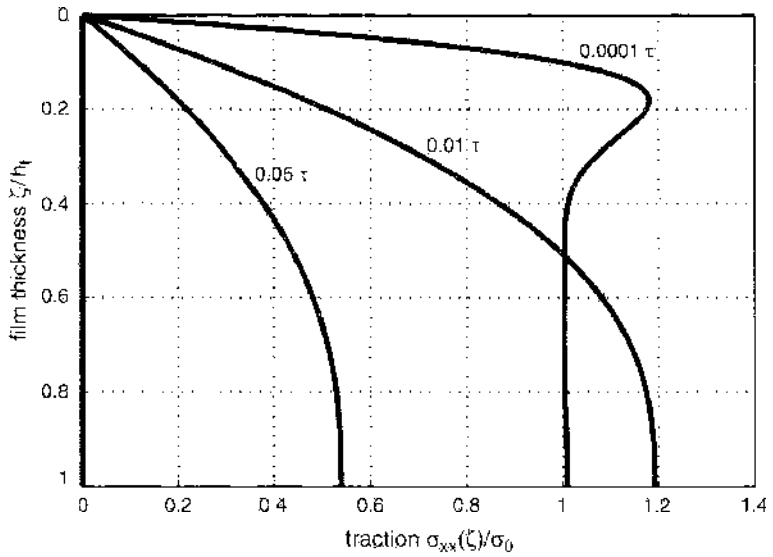

Figure 6. Development of grain boundary traction σ_{xx}/σ_0 over time for the case of a copper film on a rigid substrate. The grain boundary traction approaches σ_0 when $t \to 0$, and the grain boundary traction relaxes to zero when $t \to \infty$.

Table 1. Material parameters for calculation of stress intensity factor over the reduced time.

	ν_{film}	$\nu_{\text{substrate}}$	$\mu_{\text{film}}/\mu_{\text{substrate}}$
Cu/rigid	0.32	—	0
Al/epoxy	0.3	0.35	23.08
isotropic	—	—	1

atom at surface is

$$\mu_s = \mu_0 - \Omega\gamma_s\kappa(s, t) \tag{17}$$

where the contribution from elastic energy is neglected, following Rice and Chuang [23]. Here, γ_s is the surface energy and $\kappa(s, t)$ is the local surface curvature. Assuming that the surface slope is small, the governing equation for the surface evolution can be expressed by Mullins' equation [24]:

$$\dot{y}(x, t) = -\frac{\delta_s D_s \gamma_s \Omega}{kT} y''''(x, t) \tag{18}$$

where y measures the deviation of the surface relative to the flat surface and $\dot{y}$ is the time derivative of y. The boundary and initial conditions for the present problem are given as

$$y'(0, t) = \cos(\Psi) \qquad y'(d/2, t) = y'''(d/2, t) = 0 \qquad \text{and} \qquad y(x, 0) = 0 \tag{19}$$

where d is the grain size in the x-direction, with $d/2$ referring to the midpoint of the grain, as shown in Fig. 3. The parameter

$$\Psi = \cos^{-1}\left(\frac{\gamma_{gb}}{2\gamma_s}\right) \tag{20}$$

is the angle of grain boundary groove to be calculated from γ_s and the grain boundary energy γ_{gb}.

Solving the fully coupled grain boundary and surface diffusion problem is rather difficult. In [18] it was proposed that the two problems be solved separately by assuming that the surface retains a small slope such that the kernel function $S(z, \zeta)$ remains invariant during surface diffusion. The link between the two governing Eqs. (9) and (18) is the continuity of chemical potential at the intersection of the grain boundary and the free surface

$$\sigma_{gb}(0, t) = \gamma_s\kappa(0, t) = \gamma_s y''(0, t) \tag{21}$$

and that of atomic flux

$$\delta_{gb} D_{gb} \sigma'_{gb}(0, t) = -2\delta_s D_s \gamma_s y'''(0, t) \tag{22}$$

For the case of infinitely fast grain boundary diffusion, a characteristic time for stress decay can be defined as

$$\tau_s = \frac{kTh_f^3(1 - \nu^2)}{E\delta_s D_s \Omega} \tag{23}$$

Note that τ_s is defined 4π larger than that adopted in Ref. [18].

In Ref. [18], solutions are reported for different ratios of the rate of surface diffusion relative to grain boundary diffusion and vice versa. The ratio $\Delta = \tau_{gb}/\tau_s$ determines the relative importance of grain boundary to surface diffusion, where τ_{gb} is equal to τ defined in Eq. (14). For all values of Δ, constrained grain boundary diffusion leads to exponential relaxation of grain boundary traction, and the relaxation results in a singular stress field at the root of the grain boundary. Another important finding was that in all cases (even if grain boundary diffusion is comparable in rate to surface diffusion), the characteristic timescales

with the cube of the film thickness $\tau \sim h_f^3$. The main result reported in Ref. [18] is that an effective diffusivity could be defined according to an empirical mixing rule

$$\tau_{\text{eff}} = \frac{4\pi k T h_f^3 (1-\nu^2)}{\delta_{\text{eff}} D_{\text{eff}} \Omega E} \tag{24}$$

where

$$\delta_{\text{eff}} D_{\text{eff}} = \delta_{\text{gb}} D_{\text{gb}} \frac{\Delta}{\Delta + \alpha} \tag{25}$$

and α is a constant to be determined by matching the relaxation behavior for different values of Δ. In Ref. [18], α was determined to be around 1/3.

2.2. Average Stress and Thermal Cycling Experiments

Weiss and coworkers [25] extended the continuum model based on a convolution procedure to model their thermal cycling experiments. The average stress in the film is calculated and compared to direct measurement in the laboratory.

Because the averaged grain boundary traction follows an exponential time decay [12], the average stress in the grain boundary can be approximated as

$$\hat{\sigma}_{\text{gb}}(t) = \sigma_0 \exp(-\lambda_0 t/\tau) \tag{26}$$

with a geometry-dependent constant

$$\lambda_0 = 8.10 + 30.65 h_f/d \tag{27}$$

Here, d is the grain size, and σ_0 is the reference stress in the absence of diffusion, as discussed in Section 2.1. Equation (27) is an empirical formula and is valid for $0.2 \le h_f/d \le 10$. The loading rate of applied stress with respect to temperature is given by

$$\frac{d\sigma_0}{dT} = -\Delta\alpha M_f \tag{28}$$

Then, with $\dot{T}$ as the time derivative of the temperature (heating or cooling rate),

$$\hat{\sigma}_{\text{gb}}(t) = \sigma_0 \exp\left[-\lambda \int_{T_{\text{start}}}^{T} \frac{d\zeta}{\dot{T}\tau(\zeta)}\right] - M_f \Delta \dot{T} \int_{T_{\text{start}}}^{T} \exp\left[-\frac{\lambda}{\dot{T}}\left(\int_{\zeta}^{T} \frac{d\xi}{\tau(\xi)}\right)\right] \frac{1}{\dot{T}}\, d\zeta \tag{29}$$

where T is the temperature at time t, and T_{start} is the starting temperature. The average stress σ in the film is related to σ_0 and $\hat{\sigma}_{\text{gb}}$ as

$$\sigma = \sigma_0 - (\sigma_0 - \hat{\sigma}_{\text{gb}})\Theta \tag{30}$$

where

$$\Theta = \frac{4h_f}{d} \tanh\left(\frac{d}{4h_f}\right) \tag{31}$$

Equation (30) was obtained from an analysis of a periodic array of cracks in a thin elastic film analyzed by Xia and Hutchinson [26]. For a given experimentally measured stress σ, the average stress in the grain boundary $\hat{\sigma}_{\text{gb}}$ is given by

$$\hat{\sigma}_{\text{gb}} = \frac{1}{\Theta}(\sigma - \sigma_0) + \sigma_0 \tag{32}$$

The average film stress depends on the ratio of grain size to film thickness.

With full grain boundary relaxation and no further diffusion, the average stress follows a thermoelastic line with a reduced slope of

$$\frac{d\sigma}{dT} = -\Delta\alpha M_f (1-\Theta) \tag{33}$$

2.3. Single Edge Dislocations in Nanoscale Thin Films

Mass transport from the film surface into the grain boundary was modeled as a climb of infinitesimal edge dislocations [12, 18]. However, diffusion into the grain boundary must proceed with at least one atomic column. At the nanoscale, dislocation climb in the grain boundary becomes more of a discrete process. Grain boundary diffusion requires insertion of discrete climb dislocations into the grain boundary, a fact that has not been accounted for by the continuum model so far.

To investigate this effect, we consider a single edge dislocation climbing along a grain boundary in an elastic film of thickness h_f on a rigid substrate. The elastic solution of edge dislocations in such a film can be obtained using the methods described in Refs. [15, 27].

The geometry is shown in Fig. 3. A dislocation placed inside the film is subjected to image forces arising from the surface and the film–substrate interface. The image stress on a dislocation for different film thicknesses is shown in Fig. 7. Between the film surface and the film–substrate interface, the image force is found to attain a minimum value at $\zeta_{EQ} \approx 0.4h_f$.

From the energetic point of view, a minimum critical stress is required to allow a single climb edge dislocation to exist in the grain boundary. The thicker the film, the smaller this critical stress. This analysis suggests that consideration of single, discrete dislocations could become very important for nanoscale thin films. For films around 5 nm in thickness, the minimum critical stress for one stable dislocation in the grain boundary approaches 1 GPa. The requirement that an edge dislocation in the film be in a stable configuration could be regarded as a necessary condition for the initiation of constrained grain boundary diffusion.

2.4. Initiation Condition for Diffusion

Considerations similar to those in the previous section were employed to determine conditions under which diffusion could initiate. In Ref. [28], a criterion for the initiation of grain boundary diffusion is proposed, following the spirit of the Rice–Thomson model [14]. It is postulated that the condition for initiation of diffusion is a local criterion, independent of the film thickness.

The main assumption is that grain boundary diffusion is initiated when a test climb dislocation near the surface is spontaneously inserted into the grain boundary. Considering the force balance on the critical configuration of an edge dislocation located one Burgers vector away from the free surface, as shown in Fig. 3, a critical lateral stress

$$\sigma_0^{\text{crit}} > \frac{E}{8\pi(1-\nu^2)} \tag{34}$$

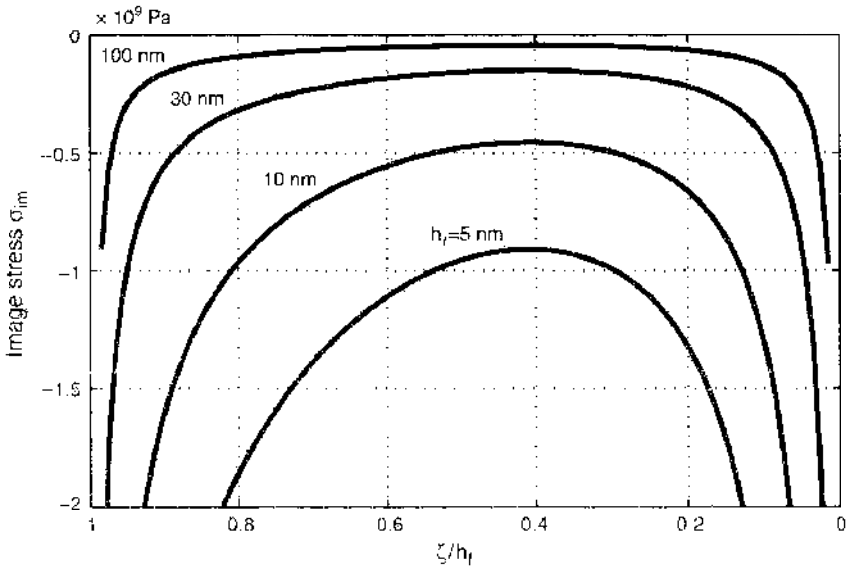

Figure 7. Image stress on a single edge dislocation in a thin film for different film thicknesses ranging from 5 to 100 nm.

can be defined for spontaneous insertion of the test dislocation into the grain boundary. Note that E should be interpreted here as the local modulus of the grain boundary near the surface, which could be much smaller than the bulk modulus. This result implies that a critical stress independent of the film thickness is required for the onset of grain boundary diffusion.

2.5. Nucleation Criterion for Parallel Glide Dislocations

A criterion based on a critical stress intensity factor K^{PG} was proposed for the nucleation of parallel glide dislocations at grain boundary diffusion wedges [28].

The stress intensity factor at the root of a crack or diffusion wedge is defined as

$$K = \lim_{\zeta \to h_\Gamma} \left\{ [2\pi(\zeta - h_\Gamma)]^s \sigma_{xx}(0, \zeta) \right\} \tag{35}$$

where s refers to the stress singularity exponent that can be determined from Ref. [29].

$$\cos(s\pi) - 2\frac{\alpha - \beta}{1 - \beta}(1 - s)^2 + \frac{\alpha - \beta^2}{1 - \beta^2} = 0 \tag{36}$$

The parameters α and β are Dundur's parameters, which measure the elastic mismatch of film and substrate material.

It is assumed that the diffusion wedge is located close to a rigid substrate, and the corresponding Dundur's parameters for this case are $\alpha = -1$ and $\beta = -0.2647$. The singularity exponent is found to be $s \approx 0.31$ for the material combination considered in our studies (compared to $s = 0.5$ in the case of a homogeneous material). Close to the bimaterial interface, we calculate the stress intensity factor

$$K = A \times \lim_{\zeta \to h_\Gamma} \left(\frac{\partial u_x(\zeta)}{\partial \zeta} (1 - (\zeta/h_\Gamma)^2)^s \right) (\pi h_\Gamma)^s \tag{37}$$

where

$$A = \frac{E}{1 - \nu^2} \frac{(1 - \alpha)}{4 \sin(\pi s)} \left(\frac{3 - 2s}{1 + \beta} - \frac{1 - 2s}{1 - \beta} \right) \tag{38}$$

The stress intensity factor provides a link between the atomistic results and continuum mechanics. To calculate the stress intensity factor from atomistic data, the atomic displacements of the lattice close to the diffusion wedge are calculated and the stress intensity factor is then determined using Eq. (37).

A common approach to study the nucleation of dislocations from defects is to balance the forces on a test emergent dislocation [14]. The force on a dislocation element is referred to as Peach–Koehler force, which can be written as $d\mathbf{F}_d = (\sigma \cdot \mathbf{b}) \times d\mathbf{l}$, where $d\mathbf{l}$ is the element length vector and σ is the local stress [16]. A dislocation is assumed to be in an equilibrium position when $F_d = 0$. Following the Rice-Thomson model [14], we consider the force balance on a probing dislocation in the vicinity of a dislocation source to define the nucleation criterion. The probing dislocation is usually subject to an image force attracting it toward the source, as well as a force resulting from applied stress driving it away from the source. The image force dominates at small distances, and the driving force caused by applied stress dominates at large distances. There is thus a critical distance between the dislocation and the source at which the dislocation attains unstable equilibrium. Spontaneous nucleation of a dislocation can be assumed to occur when the unstable equilibrium position is within one Burgers vector of the source.

Nucleation of parallel glide dislocations from a crack in comparison to that from a diffusion wedge is shown in Fig. 8. The crack case is treated similarly as in Ref. [14], and the forces involved are F_c because of the crack tip stress field, F_{image} from the crack surface (image dislocation), and F_{step} because of the creation of a surface step, which is assumed to be negligible in comparison of F_{image}.

Close to a diffusion wedge, $F_{\text{step}} = 0$ because no surface step is involved, and a dipole must be created to nucleate a parallel glide dislocation from the wedge. This leads to a

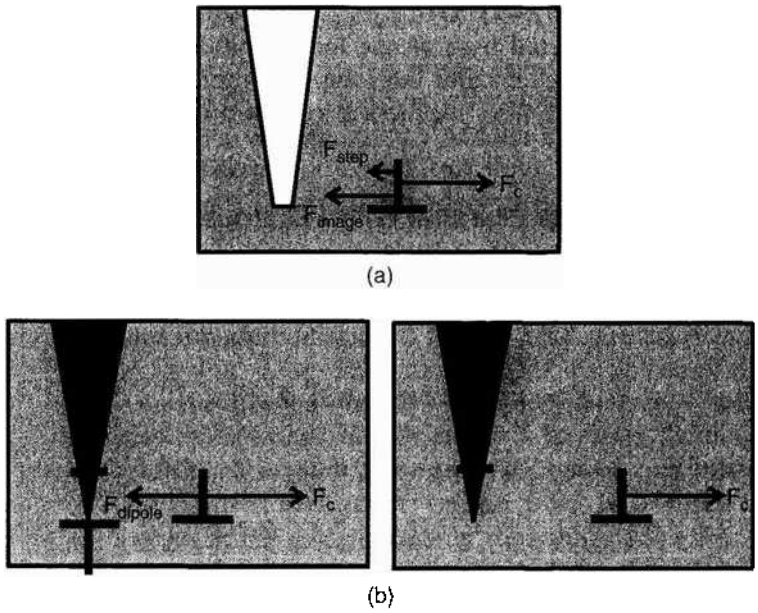

Figure 8. Force balance on a dislocation near (a) a crack (top) and (b) a diffusion wedge (bottom).

dipole interaction force F_{dipole}. The dipole consists of a pair of dislocations of opposite signs, one pinned at the source and the other trying to emerge and escape from the source. The pinned end of the dipole has the opposite sign of the climb dislocations in the diffusion wedge and can be annihilated via climb within the grain boundary. Such annihilation breaks the dipole free and eliminates the dipole interaction force so that the emergent end of the dipole moves away to complete the nucleation process. Therefore, it seems that there could be two possible scenarios for dislocation nucleation at a diffusion wedge. In the first scenario, the nucleation condition is controlled by a critical stress required to overcome the dipole interaction force. In the second scenario, the nucleation criterion is controlled by the kinetics of climb annihilation within the grain boundary, which breaks the dipole interaction by removing its pinned end and setting the other end free. The force balance on the dislocation is illustrated in Fig. 8 for two different, subsequent instants in time.

We assume that dislocation nucleation at a diffusion wedge is stress controlled (rather than kinetics controlled), and the first scenario of dislocation nucleation described above is adopted. This assumption has been verified by recent molecular dynamics simulations [28]. With this assumption, it is possible to define a nucleation criterion in terms of a critical stress intensity factor. We illustrate the critical condition for dislocation nucleation in Fig. 9. A force balance on a dislocation near a crack tip at a rigid bimaterial interface leads to the critical stress intensity factor for dislocation nucleation from a crack

$$K_{cr}^{PG} = \frac{E(2\pi b)^s}{8\pi(1-\nu^2)} \tag{39}$$

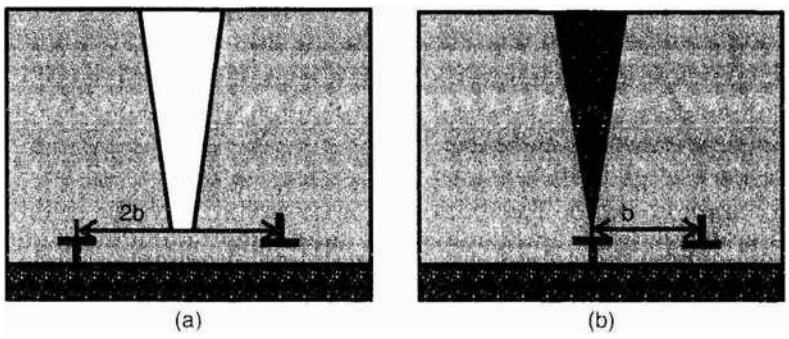

Figure 9. Nucleation of parallel glide dislocations from (a) a crack and (b) a diffusion wedge.

In comparison, a balance of critical stress required to break the dipole interaction in front of a diffusion wedge yields a similar nucleation criterion

$$K_{\mathrm{dw}}^{\mathrm{PG}} = \frac{E(2\pi b)^{\frac{1}{2}}}{4\pi(1-\nu^2)} \tag{40}$$

For copper with $b = 2.56$ Å, $E \approx 150$ GPa, and $\nu = 0.33$, typical values are $K_{\mathrm{cr}}^{\mathrm{PG}} \approx 12.5$ MPa $\times$ $\mathrm{m}^{\frac{1}{2}}$ and $K_{\mathrm{dw}}^{\mathrm{PG}} \approx 25$ MPa $\times$ $\mathrm{m}^{\frac{1}{2}}$. We note a factor of 2 difference in the critical K-values, $K_{\mathrm{dw}}^{\mathrm{PG}}/K_{\mathrm{cr}}^{\mathrm{PG}} = 2$, for dislocation nucleation at a diffusion wedge and at a crack tip.

2.6. Constrained Grain Boundary Diffusion with Threshold Stress

In recent molecular dynamics and discrete dislocation simulations [28, 30, 31] of constrained diffusional creep in thin films, it has been shown that the stress does not relax to zero in the film. Also, a critical stress σ_0^{crit} is found to be necessary to initiate diffusion. In addition to the theoretical considerations (see Section 2.4), experimental results of stress–temperature plots during thermal cycling also indicate a threshold stress for diffusion [8]. In the following, we extend the continuum model to include a threshold stress.

Equation (9) is the governing equation for the problem of constrained diffusional creep. Assuming a threshold stress σ_t for grain boundary diffusion, the boundary conditions are now modified as

$$\sigma_{xx}(\zeta = 0, t) = \sigma_t \tag{41}$$

and

$$\frac{\partial \sigma_{xx}}{\partial \zeta}(\zeta = h_t, t) = \frac{\partial^2 \sigma_{xx}}{\partial \zeta^2}(\zeta = h_t, t) = 0 \tag{42}$$

The initial condition remains the same

$$\sigma_{xx}(\zeta, t = 0) = \sigma_0 \tag{43}$$

We consider the possibility that σ_t may be different under tension and compression. That is, no grain boundary diffusion can occur when

$$\sigma_t^- < \sigma_{xx}(0, t) < \sigma_t^+ \tag{44}$$

where $\sigma_{xx}(0, t)$ is the stress at the site of initiating climb edge dislocations near the entrance to the grain boundary.

Using superposition,

$$\sigma_{xx}(\zeta, t) = \sigma_t + \tilde{\sigma}(\zeta, t) \tag{45}$$

we obtain the governing equation for $\tilde{\sigma}(\zeta, t)$ as

$$\frac{\partial \tilde{\sigma}_{xx}(\zeta, t)}{\partial t} = \frac{E D_{\mathrm{gb}} \delta_{\mathrm{gb}} \Omega}{4\pi(1-\nu^2)\mathrm{k}T} \int_0^{h_t} S(\zeta, \xi) \frac{\partial^3 \tilde{\sigma}_{xx}(\xi, t)}{\partial \xi^3} d\xi \tag{46}$$

The boundary conditions are

$$\tilde{\sigma}_{xx}(\zeta = 0, t) = 0 \tag{47}$$

$$\frac{\partial \tilde{\sigma}_{xx}}{\partial \zeta}(\zeta = h_t, t) = \frac{\partial^2 \tilde{\sigma}_{xx}}{\partial \zeta^2}(\zeta = h_t, t) = 0 \tag{48}$$

and the initial condition is

$$\tilde{\sigma}_{xx}(\zeta, t = 0) = \sigma_0 - \sigma_t \tag{49}$$

These equations are identical to those of Ref. [12], except that the initial condition is effectively reduced. Therefore, we can simply use the previous solution [see Eq. (26)] to obtain the average stress along the grain boundary as

$$\hat{\sigma}_{gh}(t) = (\sigma_0 - \sigma_i)\exp(-\lambda_0 t/\tau) + \sigma_i \tag{50}$$

Figure 10(a) shows a numerical example of the decay of the average stress in the film as given by Eq. (30) both with and without threshold stress. The parameter σ_i^+ is assumed to be 65 MPa. For comparison, experimental stress relaxation curves for 200- and 800-nm Cu films are presented in Fig. 10(b). The experimental results show that the film stress does not decay to zero but, instead, approaches a plateau value.

We can now generalize the convolution procedure described by Weiss et al. [25]

$$\frac{d\sigma_0}{dT} = -\Delta\alpha M_f \tag{51}$$

Then,

$$\hat{\sigma}_{gh}(t) = \sigma_i + (\sigma_0^{start} - \sigma_i)\exp\left[-\lambda\int_{T_{start}}^{T}\frac{d\zeta}{\dot{T}\tau(\zeta)}\right] - M_f\Delta\dot{T}\int_{T_{start}}^{T}\exp\left[-\frac{\lambda}{\dot{T}}\left(\int_{\zeta}^{T}\frac{d\xi}{\tau(\xi)}\right)\right]\frac{1}{\dot{T}}\,d\zeta \tag{52}$$

The average stress in the film as measured in experiment is calculated from $\hat{\sigma}_{gh}(t)$ by using Eq. (30).

2.7. Discussion and Summary of Continuum Modeling

We summarize the main results of the continuum modeling: first, the continuum model predicts an exponential decay of stress in the thin film with a characteristic time $\tau \sim h_f^3$, similar to the classical Coble creep [19]. A new defect referred to as a "diffusion wedge" is built up by the pileup of edge dislocations in the grain boundary [12] on the order of the characteristic time τ. Second, the continuum model predicts that the deformation field near a diffusion wedge becomes cracklike on the order of the characteristic time τ [12, 18]. Third, for nanoscale thin films, the effect of discrete dislocations becomes important as the image stress on a single dislocation reaches several hundred megapascal [32]. Fourth, treatment of atomic diffusion from a free surface into the grain boundary by the climb of discrete edge dislocations suggests a threshold stress for diffusion initiation independent of film thickness [28, 30, 32]. Finally, a condition for the nucleation of parallel glide dislocations

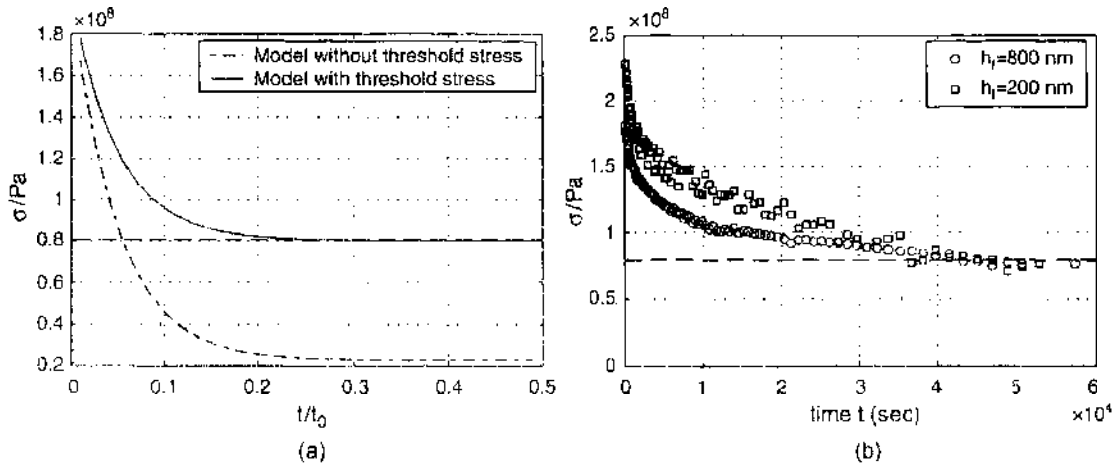

Figure 10. (a) Prediction of stress decay by the continuum model with and without threshold stress. (b) Experimental results of stress decay at 250°C for $h_f = 200$ nm and $h_f = 800$ nm.

from a grain boundary diffusion wedge has been derived based on the force balance on a probing dislocation, in the spirit of the Rice–Thomson model [32].

The continuum modeling provided key input toward the understanding of the plasticity of ultrathin films. However, some of the atomic aspects of diffusion could not be understood from the standpoint of continuum modeling alone. This lack of understanding motivated the development of atomistic models.

3. ATOMISTIC MODELING

Under the guidance of the continuum model [12, 18, 27], atomistic simulations have proven to be capable of providing a detailed description of how parallel glide dislocations are nucleated near a diffusion wedge. In the following sections we summarize the main results of recent molecular dynamics simulations of constrained grain boundary diffusion [28, 30, 32].

Large-scale atomistic modeling provides a helpful tool for investigating material phenomena from a fundamental perspective. The methodology of atomistic simulations together with their strengths and shortcomings are discussed in another chapter of this book [33].

3.1. Large-Scale Atomistic Simulations of Plasticity in Polycrystalline Thin Films

It was proposed that traction relaxation along grain boundaries in thin films significantly alters the mechanism of dislocation nucleation and motion [7, 12]. In a recent paper [30], the effect of grain boundary traction relaxation on the plasticity of polycrystalline thin films was investigated, with the focus being the dynamics of defect evolution in films both with and without traction relaxation.

The molecular dynamics simulations showed that the relaxation of grain boundary tractions changes the dislocation microstructure and triggers different stress relaxation mechanisms in thin films. Threading dislocations dominate when tractions along the grain boundaries are not relaxed, as shown in Fig. 11(a). If the grain boundary tractions are relaxed, parallel glide dislocations dominate, as in Fig. 11(b). Threading dislocations were found to be mostly complete dislocations, whereas a strong tendency to nucleate partial dislocations is seen in the case of parallel glide dislocations in the nanometer-sized grains. This is qualitatively consistent with the results of atomistic modeling the deformation of nanocrystalline materials [34, 35]. Twinning along parallel planes becomes an active deformation mechanism at high strain rates. Figure 12 shows that threading dislocations dominate

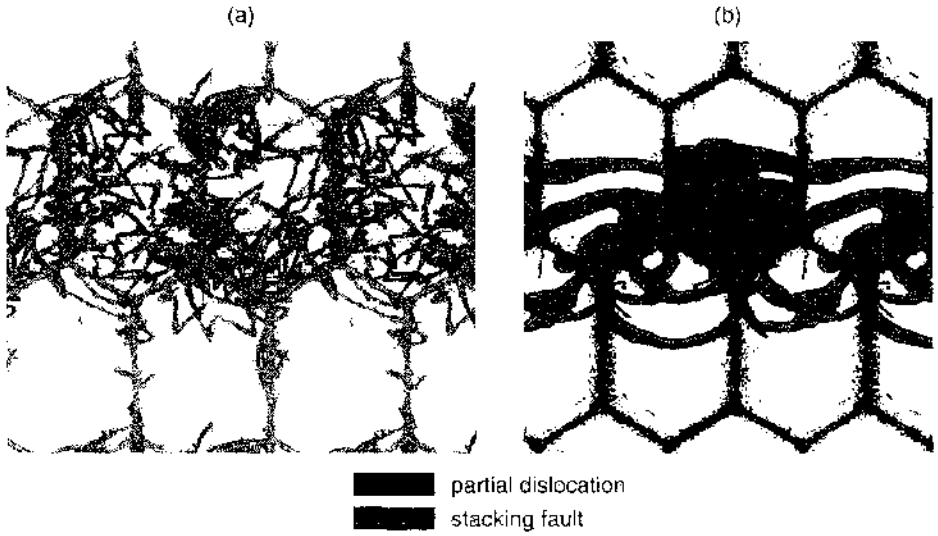

Figure 11. Plasticity in a polycrystalline thin film (a) without and (b) with grain boundary traction relaxation. When grain boundary tractions are not relaxed, threading dislocations dominate plasticity. In contrast, when the tractions are relaxed, parallel glide dislocations dominate. The plot shows dislocations as curved lines, and stacking faults as dark areas.

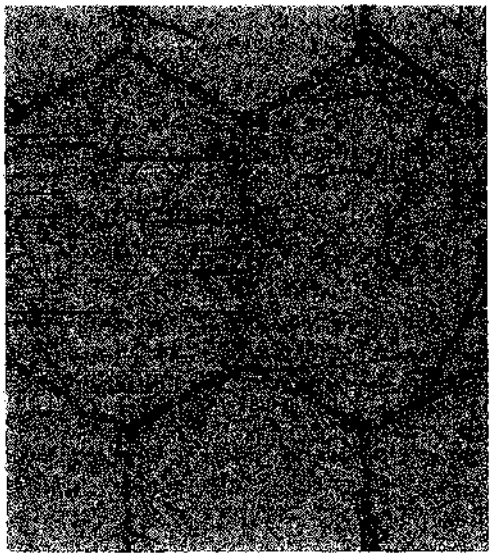

Figure 12. Plasticity in a polycrystalline thin film without grain boundary traction relaxation. The threading dislocations dominate. The plot shows a view on the surface, showing creation of surface steps as dark lines.

plasticity when grain boundary relaxation is shut down. Threading dislocations leave surface steps as they glide through the crystal.

Further studies in Ref. [30] focused on the influence of grain boundary structure on the nucleation of parallel glide dislocations.

A tricrystal model was considered with different types of grain boundaries, as shown in Fig. 13(a), to investigate the difference between low-energy (symbol A in the plot) and high-energy grain boundaries (symbol B in the plot). Low-energy grain boundaries are composed of an array of misfit grain boundary dislocations that serve as multiple nucleation sites for dislocations. It was observed that low-energy grain boundaries provide more fertile sources for threading dislocation nucleation. At such a boundary, dislocations are often observed to nucleate close to the misfit dislocations. This could be referred to as an intrinsic condition, as the structure of the grain boundary leads to local stress magnification at the misfit dislocations that serve as the source of parallel glide dislocations. Because it is possible that the incipient dislocations are nucleated on different glide planes, dislocation reactions may take place when several of them combine to form a single dislocation. The formation of jogs was observed in the dislocation line, generating trails of point defects that significantly hinder the motion of dislocations.

In the more homogeneous high-energy grain boundaries, there is inherently no preferred nucleation site, in which case triple junctions of grain boundaries serve as the nucleation

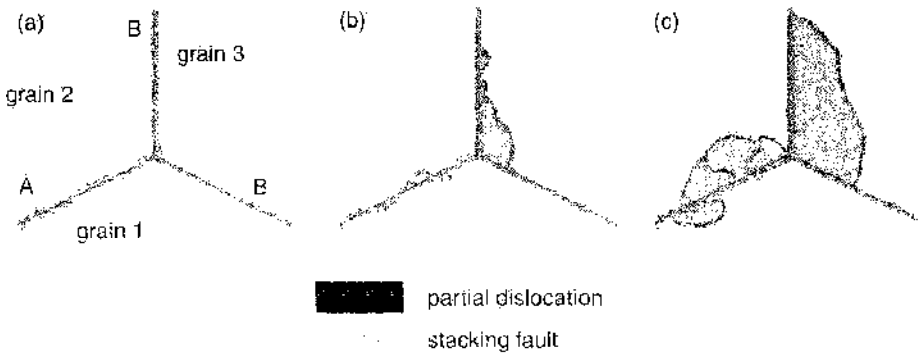

Figure 13. A temporal sequence of nucleation of parallel glide dislocations from grain boundaries in a triple junction model. Grain boundary type A refers to low-energy grain boundaries, and B corresponds to high-energy grain boundaries.

site. A temporal sequence of dislocation nucleation from a grain boundary triple junctions is shown in Fig. 13(a)–(c).

3.2. Atomistic Modeling of Diffusional Creep

Atomistic modeling of thin-film mechanics may become routine with the advent of massively parallel computers on time- and length-scales comparable with those usually attained in experimental investigations. Because of the time limitation of the classical molecular dynamics method (time intervals typically $<10^{-8}$ seconds), simulations of diffusional creep were performed at elevated temperatures to accelerate the dynamics of grain boundary diffusion [33].

The phenomenon of grain boundary diffusion wedge and the associated dislocation mechanisms persist at very high temperatures, making it possible to simulate this phenomenon using classical molecular dynamics [36, 37]. At elevated temperatures, grain boundary diffusion in a bulk material was recently successfully modeled [36], where grain sizes up to 15 nm were considered in a model system of palladium. Recent work [36, 38, 39] suggests that at elevated temperatures, the grain boundary structure of metals may transform into a liquid-like structure with a width up to several nanometers, which was referred to as a "glassy phase." Glassy phases in grain boundaries were found in copper at homologous temperatures as low as $T_h \approx 0.4$ [39, 40]. Experimental evidence for glassy intergranular phases was discussed in Ref. [41]. Such phase transformation at the grain boundary plays a significant role in the plastic properties at elevated temperatures because each different grain boundary structure has significant influence on the diffusion [38, 39].

To investigate creep behavior, the sample was loaded according to a prescribed strain field. An important result of the simulations was that diffusion cannot relax stresses in such thin films completely. These observations are qualitatively consistent with the predictions of Eq. (34) and are in agreement with experimental results.

The snapshots in Fig. 14 show how the displacement changes as material diffuses into the grain boundary. The horizontal coordinates have been stretched by a factor of 10 in x-direction to make the crystal lines clearly visible; that is,

$$[x, y, z]^{\text{new}} = [10\,x, y, z]^{\text{orig}} \tag{53}$$

This technique helps to highlight the additional half-planes of atoms close to the grain boundary.

To illustrate diffusional motion of atoms in the grain boundary, we color each atom with diffusive displacement δz larger than a few Burgers vectors. Figure 15 plots these atoms for several instants in time. Diffusion leads to significant surface grooving, with groove depths of up to several nanometers. One can clearly identify the wedge shape of the diffused atoms. The atomistic simulations show that atoms inserted into the grain boundary instantaneously crystallize, rendering the structure of the grain boundary invariant (this was observed for temperatures below 1150 K; at higher temperatures, the width of the grain boundary increases slightly). The atoms transported along the grain boundary may add to either one of the two grains, illustrating that the continuum mechanics assumptions [12, 18, 27] are also valid on the atomistic level. A frequently observed phenomenon is the emission of dislocations from the grain boundary on inclined ⟨111⟩ glide planes [6, 34], corresponding to the "classical" threading dislocations that become operative when stresses in the film are high enough to allow nucleation of dislocations [34, 36].

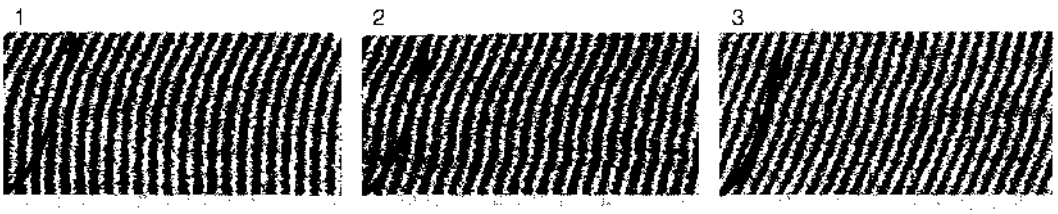

Figure 14. Lattice distortion near a diffusion wedge. The field becomes cracklike as the diffusion wedge builds up. The black lines correspond to the continuum solution of constrained grain boundary diffusion [12, 18] for $t \to \infty$.

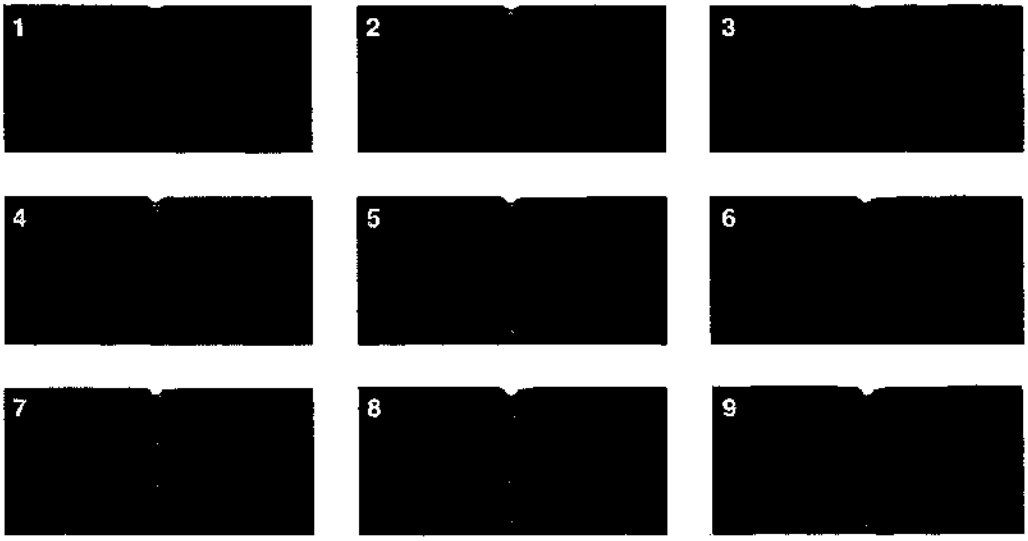

Figure 15. Formation of a grain boundary diffusion wedge. Atoms with significant diffusive displacement δz over time are highlighted. The plot shows that a diffusion wedge is formed by insertion of material into the grain boundary. The diffusion wedge develops at a relatively short timescale.

3.3. Atomistic Modeling of Nucleation of Parallel Glide Dislocations from Diffusion Wedges

Here we summarize the main results of the atomistic simulations that focused on the nucleation of parallel glide dislocations from diffusion wedges.

It was confirmed that thinner films require a higher critical stress for threading dislocation nucleation from the grain boundary, in qualitative agreement with the notion that the strength of thin films increases inversely to the film thickness [6]. In films thinner than 10 nm, extremely high stresses are required to nucleate inclined dislocations, which renders this mechanism almost impossible. This was also verified in a recent paper by Shen [42], in which the scaling of the strength of thin films with respect to the film thickness was investigated.

Continuum theory assumes that parallel glide dislocations are nucleated when the stress field around the diffusion wedge becomes cracklike. Critical stress intensity factors (SIFs) for dislocation nucleation measured from the atomistic simulations are shown in Table 2 for different simulations. Equation (37) was used to determine the SIF from the atomistic simulation results of the displacement field near the diffusion wedge. The critical SIF for the nucleation of parallel glide dislocations appears to be independent of film thickness and had similar values at $T_h = 0.8$ and $T_h = 0.9$.

For films thinner than 20 nm, parallel glide dislocations are not observed in our bicrystal model, as the cohesive strength of the film material is reached before the nucleation condition is met.

As reported in Refs. [28, 32], dislocation nucleation at a diffusion wedge can be divided into different stages, as shown in Fig. 16(a). After the critical SIF is achieved, a dislocation

Table 2. Critical stress intensity factors K^{PG} for nucleation of parallel glide dislocations near a diffusion wedge and a crack.

Temperature T (K)	Film thickness h_f (nm)	K^{PG} (MPa × m$^{\alpha}$)
	Crack	
300	27.2	4.95
	Diffusion wedge	
1150	27.2	11.91
1250	27.2	11.35
1250	34.2	11.23

Source: The data are taken from Ref. [28].

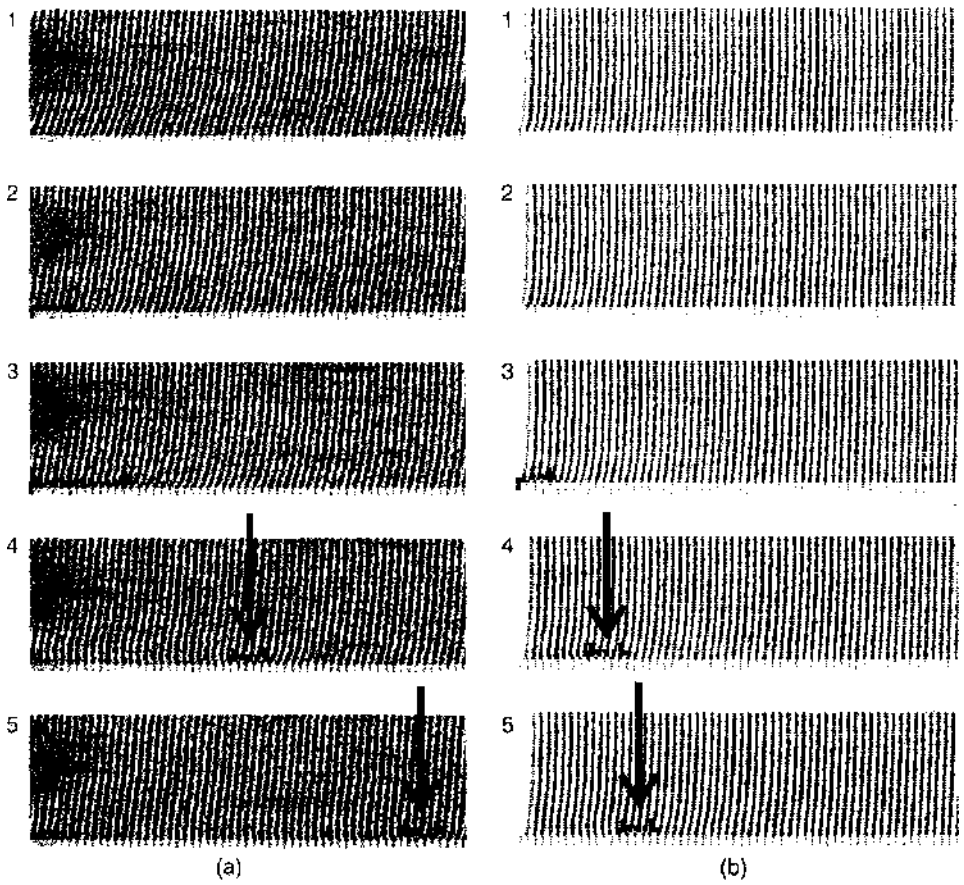

Figure 16. Atomistic details of the nucleation process of parallel glide dislocations from (a) a diffusion wedge and (b) a crack. The black line in the first snapshot of column (a) gives the solution of the continuum theory of constrained grain boundary diffusion [12, 18] for $t \to \infty$.

dipole is formed. One end of the dipole is pinned in the grain boundary, whereas the dislocation at the other end of the dipole slides away from the grain boundary. Subsequently, the pinned dislocation is annihilated or "dissolves into" the grain boundary, and the dislocation at the right end of the dipole begins to move away from the nucleation site. The parallel glide dislocation glides on a slip plane parallel to the plane of the film at a distance of a few Burgers vectors above the film–substrate interface (and is therefore completely inside the film material). The dislocation moves a small distance away from the grain boundary to its equilibrium position. When stresses in the film become larger, the film responds by moving farther away from the grain boundary. The nucleation process is highly repeatable. It was found that every time a parallel glide dislocation is nucleated, one climb edge dislocation is annihilated, leading to a decay in stress intensity. After a nucleation event, the time required to nucleate the next parallel glide dislocation is determined by the time required for diffusion to recover the critical stress intensity. This time increment is much less than the initial time required to form the diffusion wedge. After the first dislocation is nucleated, more and more parallel glide dislocations are observed. In our confined, finite simulation geometry, the emitted parallel glide dislocations form a "secondary pileup" close to the boundary of the simulation cell.

The nucleation of parallel glide dislocations from a crack in a similar geometry is shown in Fig. 16(b). The chosen loading rate was higher than in the previous case, and the temperature in the simulations was about 300 K. After an incipient dislocation is formed, a dislocation nucleates and moves away from the crack tip. The crack tip is blunted, and each time a parallel glide dislocation is nucleated, one surface step is formed. This process is also highly repeatable. The nucleation of parallel glide dislocations from a crack tip was observed at a loading rate a few orders of magnitude higher than in the case of a diffusion wedge, and there seemed to be no rate limitation in the case of a crack. As in the case of a diffusion

wedge, the dislocation glides on a parallel glide plane a few Burgers vectors above the film–substrate interface. The critical stress intensity factor for parallel glide dislocation nucleation from a diffusion wedge is about 2.3 times larger than that for a crack. This value was in good agreement with the estimated factor of two based on the Rice–Thomson model.

3.4. Discussion of Atomistic Simulation Results

When classical mechanisms of plastic deformation based on creation and motion of dislocations are severely hindered in thin films on substrates, constrained diffusional creep provides an important mechanism for stress relaxation, leading to the formation of a new type of defects called the grain boundary diffusion wedges. We have performed a set of large-scale atomistic simulations to investigate the properties of such diffusion wedges. Atomistic simulations show that material is indeed transported from the surface into grain boundaries and that such transport leads to a crack–like stress field causing the nucleation of parallel glide dislocations near the film–substrate interface. The atomistic simulations of parallel glide dislocations emitted near the root of the grain boundary have further clarified the mechanism of constrained grain boundary diffusion in thin films.

Computer simulations provide evidence that diffusion initiation occurs at a critical applied stress $\sigma_0^{\text{crit}} \approx 1.6$ GPa in copper, independent of the film thickness. Continuum analysis in Eq. (34) at $T = 0$ K for initiation of diffusion supports this finding and predicts a critical stress $\sigma_0 \approx 6$ GPa, also independent of the film thickness. The fact that the continuum analysis indicates a higher value could be explained by the higher temperature used in the simulations, in contrast to the continuum mechanics analysis at 0 K. It was found in Ref. [43] that the critical stresses for dislocation nucleation are about five times smaller at room temperature than at 0 K, thus matching the value measured in the atomistic simulations. It has recently been shown that stress distribution in thin films over different grains is highly inhomogeneous [44]. In some grains, extremely high stresses of several gigapascal are observed. This provides sufficiently large stresses to initiate diffusion and a possible explanation of why parallel glide dislocation nucleation only occurs at specific grain boundaries in the experiments.

In films thinner than 5 nm, image stresses on climb dislocations can be as large as 1 GPa (see Section 2.3). This can severely hinder climb-mediated diffusional creep and indicates that the behavior of discrete dislocations needs to be considered in nanoscale thin metal films. This is supported by the atomistic results showing that stress cannot be completely relaxed in extremely thin films. These results are in qualitative agreement with experimental results that often shown relatively large residual stresses in extremely thin films [2].

The diffusion wedge has properties similar to a crack, but it requires a larger SIF to nucleate a dislocation. The reason for this is that in the case of a diffusion wedge, a dislocation dipole needs to be formed, and the dipole interaction force is twice as strong as the image force on an emergent dislocation near a crack tip. We have studied common and distinct properties observed in atomistic simulations of the two kinds of defects (crack versus diffusion wedge) along the grain boundary at elevated temperatures. For a crack, the following was observed: as the applied stress σ_0 is increased, the normal stress σ_{xx} along the grain boundary remains zero throughout the film thickness, consistent with the traction-free condition along the crack faces; the loading rate can be much higher than in the case of diffusional creep (there is no rate-limiting factor on dislocation nucleation); dislocation nucleation occurs at a relatively small stress intensity factor; and dislocation nucleation starts with an incipient dislocation close to the crack tip.

In contrast, for a diffusion wedge the following can be summarized: the loading rate must be slow enough for diffusion to remain as the dominant relaxation mechanism—at high loading rates, dislocation activities on inclined planes are observed instead of grain boundary diffusion; to nucleate a parallel glide dislocation, dislocation climb in the grain boundary must occur to annihilate part of an incipient dipole (on atomistic timescales, this is an extremely slow process—(for a crack, dislocation nucleation is fast); dislocation nucleation starts when the stress intensity factor reaches a critical value required to create a dislocation dipole near the diffusion wedge; and there exists a minimal thickness for parallel glide dislocation nucleation: If the film is very thin, the applied stress reaches the cohesive strength of the material before the critical stress intensity factor K^{PG} for dislocation nucleation is reached.

The two types of defects have significantly different timescales associated with dislocation nucleation. A crack is a ready source for dislocations, whereas a diffusion wedge has an intrinsic characteristic time associated with the dislocation climb. No essential difference in the mechanism of parallel glide dislocation nucleation from a diffusion wedge has been observed in the temperature range $0.8 < T_h < 0.9$.

4. EXPERIMENTAL STUDIES

Since its proposal in 1999, the model for constrained diffusional creep [12] has been further developed in light of experimental results [7, 35]. Weiss et al. [25] invoked the constrained diffusional creep model to explain the occurrence of a stress drop observed during the first heating cycle of thin copper films. They also used constrained diffusional creep to model the stress–temperature curves measured during thermal cycling of several films and found good agreement for a 500 nm copper film, albeit by assuming a very large grain size. Later, the discovery of parallel glide dislocations [45] provided experimental support for the constrained diffusional creep model. In turn, constrained diffusional creep furnished the basis for the interpretation of certain experimental results, especially in regard to the mechanisms for the creation and emission of parallel glide dislocations. In the following sections, we present key experimental results and their connection to the model of constrained diffusional creep.

4.1. Thermomechanical Behavior of Thin Copper Films

A series of thin copper films, ranging in thickness from 2 μm down to 35 nm, was produced by magnetron sputtering under ultrahigh vacuum. All films were annealed immediately thereafter in the deposition chamber, without breaking vacuum, yielding oxide-free unpassivated copper films. The substrates used for the films were (001)-oriented single crystalline silicon that had been coated with 50 nm amorphous silicon oxide and 50 nm amorphous silicon nitride before copper deposition. Thus, the interface between film and substrate is crystalline/amorphous. The average grain size, as determined from focused ion beam (FIB) and transmission electron microscopy (TEM) measurements, ranged from 1.5 times the film thickness (for the 2-μm film) to 2.5 times the film thickness (for the 100-nm film). X-ray diffraction measurements revealed that all films had a strong [111] fiber texture, albeit with a small population of [100]-oriented grains for films thicker than 200 nm. Thus, the vast majority of grains within each film, including the grains imaged using TEM and presented below, are oriented with a (111) plane parallel to the substrate.

The thermomechanical behavior of each film was determined by subjecting it to a thermal cycle between room temperature and 500°C. Because copper possesses a higher coefficient of thermal expansion than silicon, an equibiaxial compressive stress evolves in the film during heating, and a tensile stress evolves during cooling. This coupling of stress and temperature in the film/substrate system enables the thermomechanical loading of thin films, and a variety of thermal paths can be employed to generate compressive and tensile stresses of varying magnitude. In the examples presented below, simple thermal cycles starting at room temperature, progressing up to 500°C and then returning to 50°C were performed. Heating and cooling rates were 6 K/min, except for final cooling below 100°C, which proceeded at 4 K/min because of the limited cooling capacity of the oven.

An example of the thermomechanical behavior of an ultrathin copper film is presented in Fig. 17. The stress within this 100-nm film was initially 360 MPa. During heating, the tensile stress decreased and a compressive stress was achieved by 210°C. The compressive stress rose in magnitude with further heating but then dropped after reaching a maximum at 260°C. The stress level decreased slightly during heating to 320°C and then became more compressive during heating to 500°C. From this point on, the stress evolution was monotonic with temperature: cooling produced a tensile stress and subsequent heating in the second cycle produced a compressive stress again. No stress drops were observed in the second cycle or later.

The stress drop that occurs above 250°C in the 100-nm film, as well as in all thicker films measured in this study, appears to be the result of constrained diffusional creep, as previously

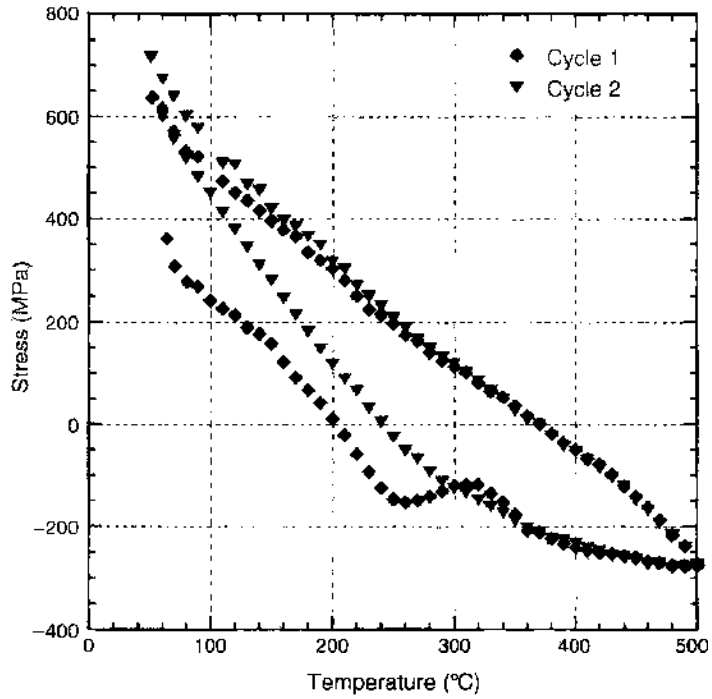

Figure 17. The first two thermal cycles of a 100-nm copper film. During the first heating segment, a stress drop is observed at 260°C, which is attributed to constrained diffusional creep. Subsequent thermal cycles are highly repeatable, with no stress drop.

explained by Weiss et al. [25]. The temperature of 250°C, which represents a homologous temperature of 0.4, is apparently sufficient to activate surface and grain boundary diffusion and lead to the formation of diffusion wedges during heating. Only when the relaxation of stress at the grain boundaries is saturated, in this case at a temperature well above 300°C, does stress increase again. The lack of the stress drop during the second and later thermal cycles is explained by the stress level: at 250°C in the second cycle, film stress is only −26 MPa, which may be insufficient to cause outward diffusion of copper atoms from the grain boundaries, and therefore no stress relaxation occurs.

The second cycle in Fig. 17 deviates from the first cycle during the final stages of cooling (below ~200°C), perhaps because of the thermal drift of the sample. This, however, is an inherent error in the experimental technique and gives a good measure of the error one should assign to the absolute stress values that are reported. The film strength is typically taken to be the flow stress measured at the end of a thermal cycle. Thus, in this case, the strength of the 100-nm film would simply be given by the average of the two stresses measured at 50°C at the end of cooling: 676 ± 39 MPa.

Although film strength generally increases with decreasing film thickness [2, 25, 46], unpassivated copper films deviate from this trend below 400 nm [7]. Instead of rising continuously, the film strength exhibits a plateau between 650 and 700 MPa for films 400 nm and thinner. This is apparent in Fig. 18, which shows the second thermal cycle for a 200-nm copper film, along with the second cycle for the 100-nm film from Fig. 17. The two films exhibit virtually identical thermomechanical behavior, with the film strengths at 50°C (695 ± 9 MPa for the 200-nm film) and the flow stresses at 500°C matching very closely. Although the 500°C flow stress does become slightly more compressive in thinner films, the plateau in 50°C film strength persists down to a thickness of 35 nm.

To explore whether the stress–temperature cycles, such as those shown in Figs. 17 and 18, represent steady-state behavior, a 50-nm copper film was thermally cycled at two different rates. In addition to the standard 6 K/min rate, a complete cycle was performed at 1 K/min; both are portrayed in Fig. 19. Because of the extremely small film thickness, this comparison allows us to investigate whether grain boundary diffusion and constrained diffusional creep are able to proceed to completion within the time frame of these experiments. The heating segments of each cycle are somewhat different, but they yield roughly the same 500°C

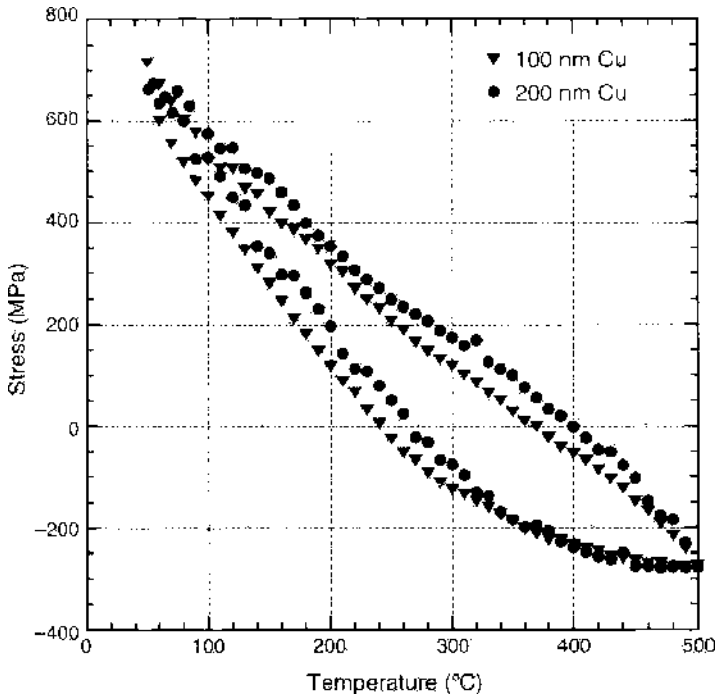

Figure 18. The second thermal cycle of a 200-nm copper film, along with the second cycle of the 100-nm film from Fig. 17. Both films exhibit the same thermomechanical behavior, with the same stress levels at 500° and 50°C.

flow stress; namely, 322 ± 14 MPa. However, there is a large discrepancy in stress evolution during cooling, especially between 350° and 200°C. Within this temperature range, the lower cooling rate permits significantly more stress relaxation. This indicates that the standard 6 K/min used throughout this study is too fast to allow constrained diffusional creep to reach steady state and that grain boundary diffusion may be the rate-limiting step in this

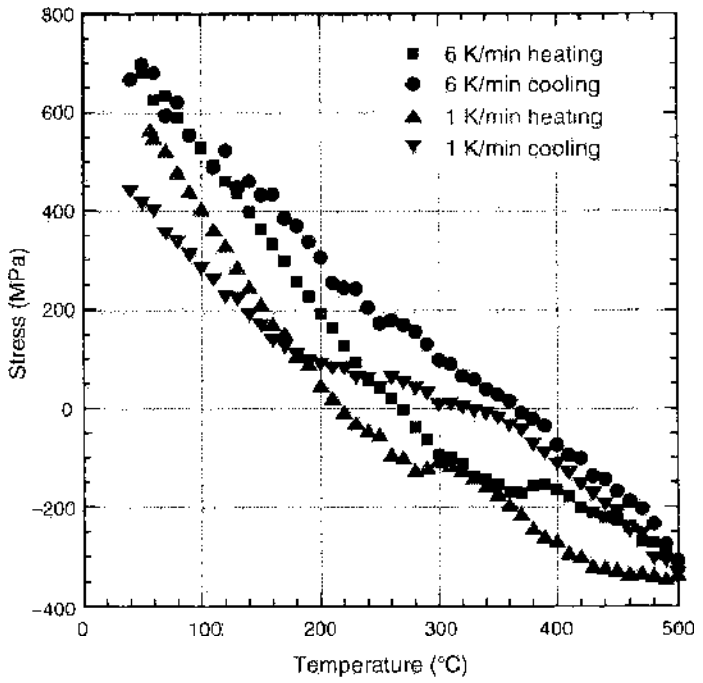

Figure 19. Two thermal cycles of a 50 nm copper film, conducted at different heating and cooling rates. Although the same 500°C flow stress is reached in both cases, the stress evolution during cooling is seen to depend strongly on cooling rate, indicating that the standard rate of 6 K/min is too fast to allow constrained diffusional creep to proceed to completion.

temperature regime. The final cooling curves below 200°C appear to be offset by approximately 200 MPa, but they exhibit the same slope, indicating that constrained diffusional creep is equally slow in both cases, or that constrained diffusional creep is no longer able to provide stress relaxation below 200°C.

4.2. Transmission Electron Microscopy Observations of Dislocation Behavior

Thermal cycling experiments were also conducted *in-situ* in the TEM to elucidate the deformation mechanisms underlying the thermomechanical behavior illustrated in Figs. 17–19. These figures clearly showed that films in this thickness range ($\leq$200 nm) exhibit a plateau in strength, which indicates that the Mathews–Freund–Nix mechanism involving threading dislocations is saturated or has been replaced. As discussed below, *in-situ* observations of dislocation motion revealed that a new, alternative deformation mechanism does indeed dominate in ultrathin, unpassivated copper films.

Figure 20 shows an example of parallel glide dislocations in a small grain within a 200-nm copper film. There are four dislocations oriented roughly perpendicular to the diffraction vector g in the TEM micrograph. During subsequent heating, these dislocations moved in the direction of g and underwent glide across the entire width of the grain. In this image of the [111]-oriented grain, the projected width of all inclined {111} planes is 70 nm. On the basis of their length and the extent of their motion (up to 300 nm), the dislocations must therefore have moved on the (111) plane parallel to the film/substrate interface. Because of this, the observed motion was termed "parallel glide" [7].

An important consequence of glide occurring parallel to the film/substrate interface is that the Burgers vector of the dislocations, which must lie within the (111) glide plane, is parallel to the plane of the film. However, the biaxial film stress that evolves in the film during thermal cycling does not produce a resolved shear stress on this plane, and it therefore cannot be directly responsible for the motion of parallel glide dislocations. Both of these points, however, are addressed by the constrained diffusional creep model [12], which aids the interpretation of these experimental results. As predicted by the theoretical simulations and discussed further below, parallel glide is a consequence of constrained diffusional creep.

Additional experimental observations have clarified several details of this deformation mechanism. Figure 21 shows another example of parallel glide dislocations, extending from

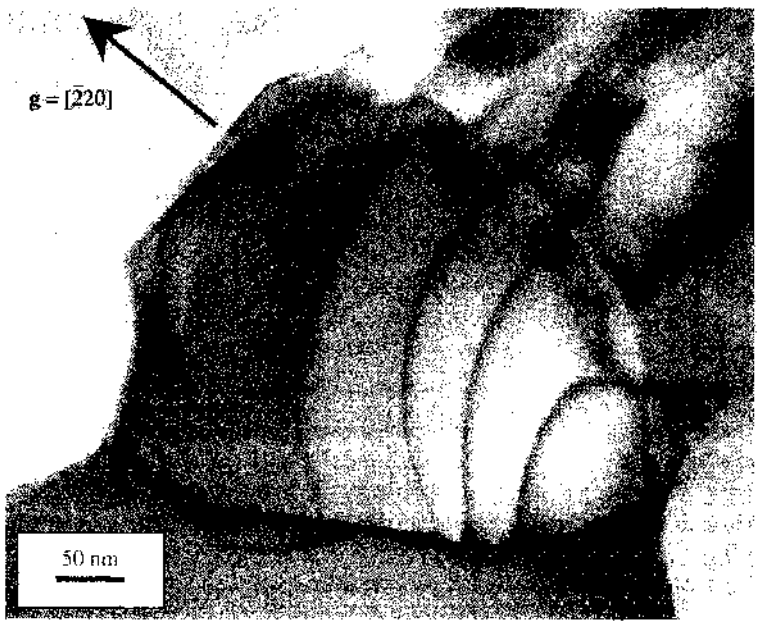

Figure 20. Transmission electron micrograph of parallel glide dislocations in a 200-nm copper film. These edge-oriented dislocations underwent glide in the direction of the diffraction vector g. On the basis of the extent of their motion, the only possible glide plane is the (111) plane parallel to the film–substrate interface.

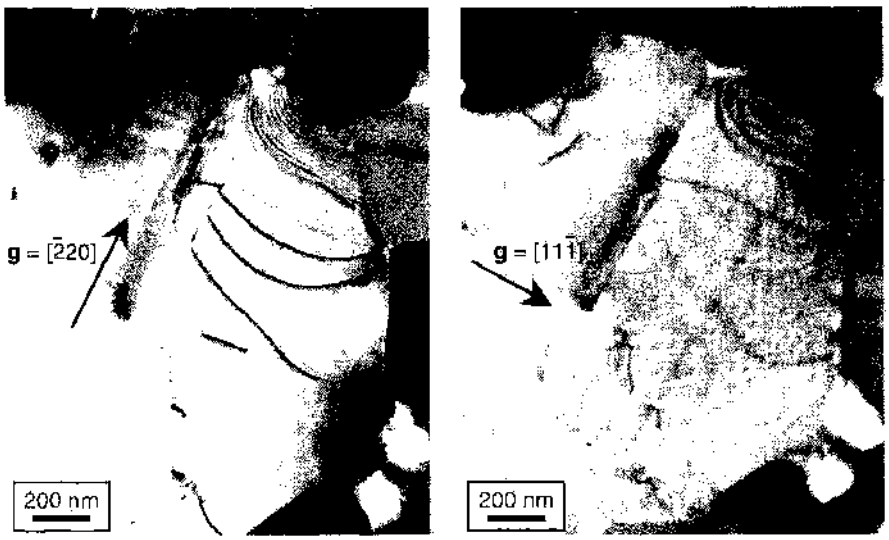

Figure 21. (a) Three parallel glide dislocations are visible in this transmission electron (TEM) micrograph of a 200-nm copper film. Their (111) glide plane, which is also the plane of this image, contains the Burgers vector **b**. (b) TEM of the same location, but with a different diffraction vector. The three parallel glide dislocations are invisible here, indicating that **b** is perpendicular to [11$\bar{1}$]. On the basis of these images, **b** must be parallel to [$\bar{2}$20], and the dislocations thus have predominantly edge character.

the twin in the middle of the micrographs to the grain boundary at the right. In Fig. 21(a), three dislocations are visible, but in Fig. 21(b), they are invisible, indicating that the Burgers vector is perpendicular to the [11$\bar{1}$] direction. Moreover, the Burgers vector lies within the (111) plane and must therefore be parallel to the [$\bar{2}$20] diffraction vector in Fig. 21(a). The dislocations thus have predominantly edge character, as they are oriented roughly perpendicular to **b** and **g** in Fig. 21(a). This is a general feature of parallel glide dislocations, which are always emitted with edge character. During subsequent glide, which can involve interaction with other dislocations and with obstacles such as twins and grain boundaries, the parallel glide dislocations may bow into a curved shape and attain mixed character.

In-situ TEM observations [7] have revealed that parallel glide dislocations are emitted from sources at triple junctions and grain boundaries. Typically, these grain boundaries (or one of the grain boundaries leading to the triple junction) are oriented roughly perpendicular to the Burgers vector. This indicates that the diffusion wedge added to the grain boundary is indeed essentially an array of edge dislocations, which are eventually emitted and undergo parallel glide.

In all cases in which it was measured [7, 45], the tilt angle between grains bounding a parallel glide source was found to lie between 6° and 6.5°. Tilting and diffraction experiments near a ⟨112⟩ zone axis revealed that the tilt angle is 6°, not 66° (i.e., the 60° ambiguity inherent to the comparison of [111] electron diffraction patterns was eliminated). This provided a key piece of information for input into the atomistic simulations [28, 30, 32] and allowed the introduction of grain boundaries that were suitable for constrained diffusional creep and the emission of parallel glide dislocations in the simulated cooling experiments.

By tilting the specimen, one can image the inclined grain boundaries and observe the position of parallel glide dislocations by determining exactly where they terminate. TEM micrographs [7] reveal that the dislocations meet the grain boundaries at the film–substrate interface. Thus, the parallel glide plane is located at the bottom of the grain, albeit some small distance above the silicon nitride. From high-resolution TEM micrographs [47], it was observed that the silicon nitride layer is not atomically flat but, instead, contains hills and valleys, with a peak-to-valley height of approximately 2 nm. Given the observation that parallel glide occurs over large distances, without cross-slip events, the glide plane cannot lie directly at the film–substrate interface, but instead must be situated several nanometers above it.

Multiple families of parallel glide dislocations are sometimes also observed, as shown in Fig. 22. Three families, each oriented roughly perpendicular to one of the three $\langle\bar{1}10\rangle$ directions within the (111) film plane, are located at the bottom, right, and top-left corners of the grain. In contrast to other examples of parallel glide (e.g., Fig. 19), the dislocations in Fig. 22 accommodate strain symmetrically within the film plane. This appears to be a result of the grain size, as smaller grains rarely exhibit multiple families of dislocations.

Finally, copper films passivated with an aluminum oxide layer were also investigated for comparison with the observations of the unpassivated films presented above. Although their thickness and grain size are identical to the unpassivated films, passivated films do not exhibit parallel glide. Instead, threading dislocations are generated. As they glide through the film on inclined $\{111\}$ planes, they deposit straight segments along $\langle\bar{1}10\rangle$ directions at the film–substrate interface, as shown in Fig. 23. Passivation of the film surface completely shuts down parallel glide, providing strong evidence that surface diffusion is an essential component of this deformation mechanism.

4.3. Interpretation of Experimental Observations

The observations of parallel glide can be explained with the help of the constrained diffusional creep model. The finding that an unpassivated film surface is required for parallel glide supports the claim that constrained diffusional creep is the mechanism responsible for stress relaxation and plastic deformation in ultrathin copper films. The stress drop observed during the first heating cycle of a copper film (e.g., in Fig. 17) is explained nicely by the constrained diffusional creep model. Finally, other models of thin film deformation are unable to explain parallel glide, as the biaxial film stress that evolves during thermal cycling does not generate a resolved shear stress on the (111) plane parallel to the substrate and therefore cannot directly drive the dislocation motion presented here.

Because parallel glide is the dominant mode of dislocation motion in copper films 200 nm and thinner, and as parallel glide appears to be a consequence of constrained diffusional creep, we can check whether constrained diffusional creep mediates the entire amount of plasticity during a thermal cycle. According to the constrained diffusional creep model, atoms diffuse from the surface into the grain boundaries of a film under tension, assuming that temperature and stress are sufficiently high. For an appropriately oriented grain, this is

Figure 22. Transmission electron micrograph of a grain exhibiting multiple families of parallel glide dislocations, one each at the bottom, right, and top left corners of the grain. The families are each oriented roughly perpendicular to one of the three $\langle\bar{1}10\rangle$ directions within the (111) film plane.

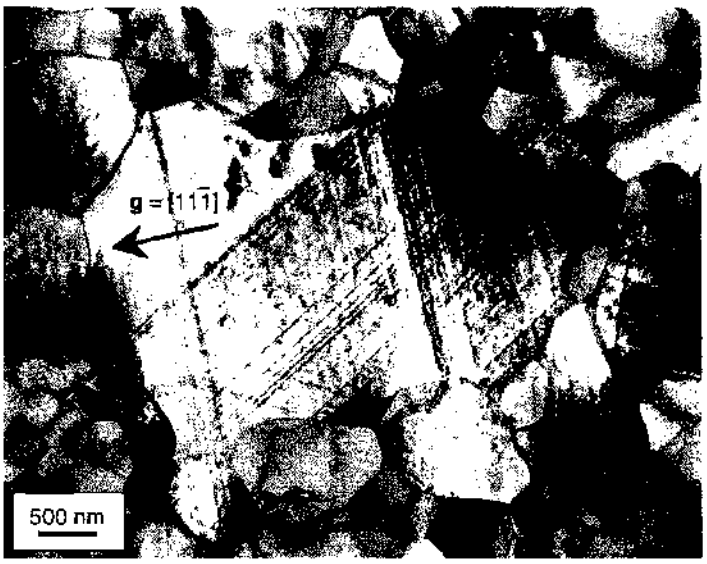

Figure 23. When passivated with an aluminum oxide layer, 200-nm copper films no longer exhibit parallel glide. Instead, threading dislocations are activated, which glide through the film and generate straight slip traces at the film–substrate interface.

equivalent to adding edge dislocations at the grain boundary. For each edge dislocation, the addition of the extra half-planes increases the grain length by b, the magnitude of the Burgers vector. We can therefore calculate how many parallel glide dislocations should exist within a given grain:

$$d_{\text{grain}}\varepsilon_{\text{plastic}} = N_d b \tag{54}$$

where d_{grain} is the grain length parallel to **b**, $\varepsilon_{\text{plastic}}$ is the plastic strain measured from the stress–temperature plot for a thermal cycle, and N_d is the number of parallel glide dislocations.

Application of Eq. (54) to TEM observations yields excellent agreement. In Fig. 24, a schematic of the grain and parallel glide dislocations from Fig. 20, tilted back to simulate a three-dimensional view, has been drawn. The parallel glide plane, shaded gray in the figure, is located at the bottom of the grain, near the film–substrate interface. The dislocations are roughly perpendicular to **b** and are distributed over the length of the grain. The relevant values for Eq. (54) are $d_{\text{grain}} = 400$ nm and $\varepsilon_{\text{plastic}} = 0.30\%$ for a 200-nm copper film. The required number of dislocations is thus $N_d = 4.7$. Four dislocations were observed in the grain. The remainder, 0.7, is insufficient to necessitate the emission of a fifth dislocation.

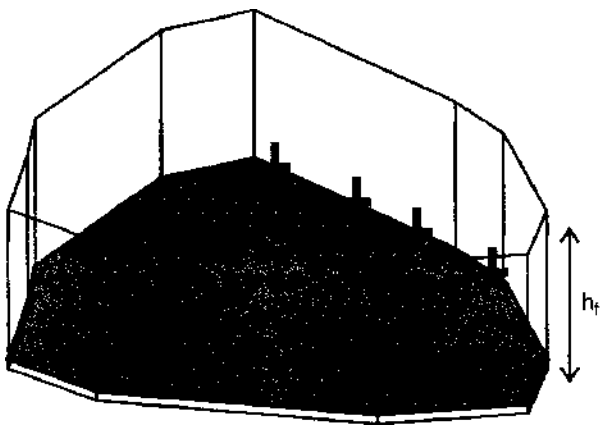

Figure 24. Schematic of the grain and parallel glide dislocations from Fig. 20. The glide plane is at the bottom of the grain, near the film–substrate interface, and the dislocations are distributed across the width of the grain. The number of parallel glide dislocations corresponds to the average amount of plastic strain exhibited by the film during thermal cycling.

More specifically, however, this "missing" partial dislocation should simply remain in the grain boundary, as there is no driving force for its emission.

In other words, a criterion for the occurrence of parallel glide is the presence of multiple dislocations in a grain boundary. Once an additional dislocation, or perhaps a partial dislocation, is formed in the grain boundary, the repulsive force between them causes the emission of the first dislocation into the grain. Based on comparisons between Eq. (54) and TEM observations, the presence of a partial dislocation appears to be the more likely case. This leads to a slightly modified equation that accounts for the emission criterion:

$$d_{\text{grain}}\varepsilon_{\text{plastic}} = \left(N_d + \frac{1}{2}\right)b \tag{55}$$

For larger grains, where many dislocations should undergo glide, the difference between Eqs. (54) and (55) may be insignificant. However, as grain size decreases toward the nanoregime, the exact form of Eq. (55) becomes important. The additional 1/2 may need to be replaced by a different quantity, but this possibility requires further investigation.

A consequence of Eqs. (54) and (55) is that there is a critical length scale for the formation of a parallel glide dislocation; namely, roughly $b/\varepsilon_{\text{plastic}}$. In grains smaller than this quantity, less than a single dislocation is required to mediate the entire amount of plasticity. In this case, the partial dislocation remains in the grain boundary. Indeed, almost no dislocation motion is observed in 50-nm copper films, which undergo a plastic strain of 0.25% during a thermal cycle and therefore have $b/\varepsilon_{\text{plastic}} = 102$ nm. The median grain size in a 50-nm copper film is only 99 nm (i.e., more than half of the grains require less than a single parallel glide dislocation, and only a small minority of the grains are sufficiently large [>150 nm] for parallel glide to occur at all). In 50-nm films, parallel glide was observed in relatively large grains (i.e., >200 nm), supporting the concept of a critical length scale.

The multiple families of parallel glide dislocations in Fig. 22 indicate that plastic strain is accommodated along all possible $\langle\bar{1}10\rangle$ directions within the (111) film plane, as should be the case for an equibiaxial stress state. In many cases, especially in smaller grains, parallel glide occurs in only one or two directions. This is likely a result of the character of the remaining grain boundaries, which may allow some degree of diffusion but still be unsuitable for the emission of parallel glide dislocations. In addition, in small grains, the emission of parallel glide dislocations from a grain boundary may alter the stress state sufficiently to hinder the insertion of diffusion wedges into the remaining grain boundaries.

Copper films with 200 nm thickness have been presented here to illustrate parallel glide. Although these films, which yielded the TEM observations presented above, are thicker than those that were simulated, it has been experimentally confirmed [7] that parallel glide is the dominant mode of dislocation motion in films between 50 and 200 nm thick. Note that 50-nm films exhibit little dislocation activity, but that which does occur always takes place via parallel glide.

Parallel glide is a consequence of constrained diffusional creep (i.e., the actual deformation mechanism is constrained diffusional creep). The motion of parallel glide dislocations does not mediate plasticity. Rather, it redistributes, across the width of the grain, the strain fields of the edge dislocations contained within the diffusion wedges. By the time parallel glide occurs, constrained diffusional creep has already provided plastic strain by increasing the grain dimension. Thus, in terms of strain accommodation, it does not matter where the parallel glide dislocations are situated within the grain. This is fundamentally different from conventional dislocation slip and threading dislocation motion, which progressively mediate plastic strain as glide occurs.

5. MODELING THE EXPERIMENTAL RESULTS WITH CONTINUUM THEORY

In addition to aiding the interpretation of the TEM observations of parallel glide, the constrained diffusional creep model can be used to generate the stress–temperature curve for a thermal cycle. This was done by Weiss et al. [25] for copper films, although certain discrepancies between simulated and experimental curves could not be overcome. The model has

since been modified to include a threshold stress for constrained diffusional creep, which has led to better agreement in the high-temperature regime, as presented below.

5.1. Experimental Estimate of the Threshold Stress

Experimental results provided an estimate of the threshold stress in thin copper films. Constant-temperature stress relaxation experiments were performed with films ranging in thickness from 100 nm to 2 μm. During cooling from 500°C, the sample was held at 250°C for 16 h, and the amount of stress reduction was monitored. The final stress measured in each film is listed in Table 3. For film thicknesses between 100 nm and 1 μm, the relaxed stress level is very consistent, with an average value of 81 MPa [see also Fig. 10(b)]. This is surprising, given the large variation in stress as a function of film thickness, as determined from standard thermal cycles. Only the 2-μm film exhibits a lower stress.

The data in Table 3 indicate that the concept of a threshold stress for constrained diffusional creep is valid for all copper films below micrometer size. It is also in agreement with the notion of an athermal stress component in thin films, as discussed by Kobrinsky et al. [2, 48, 49]. The athermal stress cannot be relaxed by thermally activated mechanisms such as constrained diffusional creep. Kobrinsky's results [2, 48] also indicate a thickness-independent threshold stress for silver films between 250 and 860 nm.

5.2. Fit of the Continuum Theory to Experimental Results

In this section we discuss some fits of the extended continuum mechanics model with threshold stress to the experimental results.

5.2.1. Modeling of Thermal Cycling Experiments

As reported in Refs. [25, 50], the grain boundary diffusivity for copper is given by

$$\delta_{gb} D_{gb}(T) = 5 \times 10^{-15} \exp\left(-\frac{Q_b}{RT}\right) \text{m}^3\,\text{s}^{-1} \tag{56}$$

with activation energy $Q_b = 104$ kJ/mole. We consider two film thicknesses of 100 and 600 nm. The threshold stresses for the grain boundary average stress are estimated from the experimentally measured average stress in the film by Eq. (32) and are approximated to be $\sigma_t^+ = 65$ MPa and $\sigma_t^- = -65$ MPa. In the following text we assume that $E = 124$ GPa, $\nu = 0.34$ and $\Delta\alpha = 1.3 \times 10^{-5}$ K^{-1}. In Figs. 25 and 26 we show a comparison between experiment and the continuum model with threshold stress for steady-state thermal cycling of thin films of thickness $h_f \approx 100$ nm (Fig. 25) and 600 nm (Fig. 26).

In both cases, some qualitative agreement is found, especially at elevated temperatures. For the 600-nm film, the agreement at low temperatures during the cooling cycle (upper curve) is not as good as for high temperatures. This could partly be explained by the fact that, because of the rather large film thickness, not only parallel glide dislocations are present, but threading dislocations are also nucleated and relieve stresses, as observed in the experiment in Ref. [7]. During cooling of the film, diffusional creep dominates at high temperatures, but threading dislocations may dominate at low temperatures. Because the continuum model does not account for threading dislocations, the stresses at low temperatures (upper left corner in the plot) are overestimated. At high temperatures during the heating cycle, the stress at the grain boundary relaxes to the value associated with the threshold stress σ_t^-, and

Table 3. Average film stresses measured after isothermal relaxation at 250°C for 16 h.

h_f (nm)	100	200	800	1000	2000
$\sigma_{250°C,\,\text{relaxed}}$	80	73	85	85	43

Note: All films between 100 nm and 1 μm exhibit nearly the same stress, with an average value of 81 MPa. On the basis of the experimental data, 65 MPa was taken to be the threshold stress at the grain boundary; that is, the high-temperature flow stress of thin copper films following maximum relaxation by constrained diffusional creep.

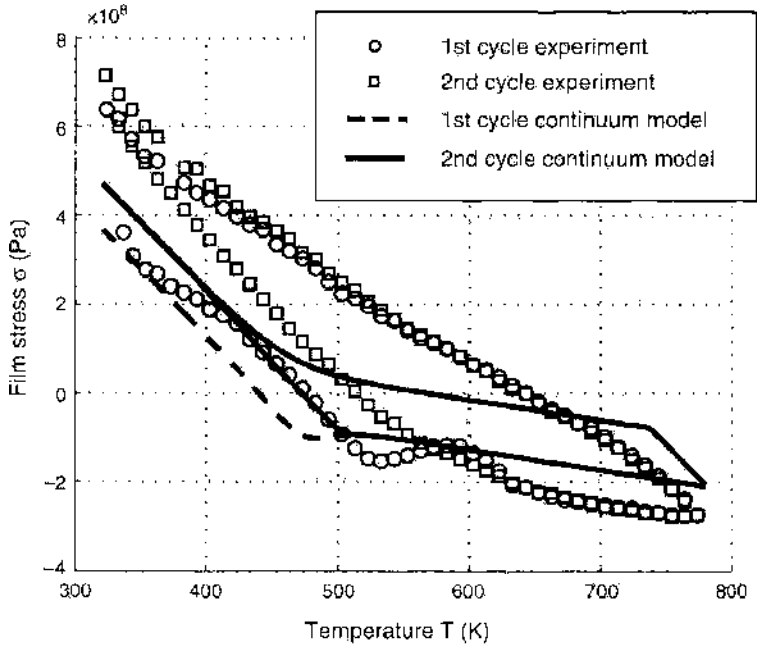

Figure 25. Fit of continuum model with threshold stress to the experimental data from Fig. 17. The film thickness is $h_f = 100$ nm and grain boundary diffusivities are as in Ref. [50].

the experimental measurements and continuum modeling of the average stress in the film agree quite reasonably.

The fits show that the introduction of a threshold stress based on experimental data represents an improvement of the previous model. Unlike in Ref. [25], where the grain size had to be adjusted to improve agreement, the parameters used here are identical to those used in the experiments (same grain size, same ratio of grain size to grain diameter, same cooling and heating rates, etc.). The most important difference is that without the threshold stress, the numerically estimated curves are very "thin" in contrast to the experimental results. The thermal slope, which is apparent at high temperatures during the cooling cycle, can only be reproduced with the generalized model, including a threshold stress.

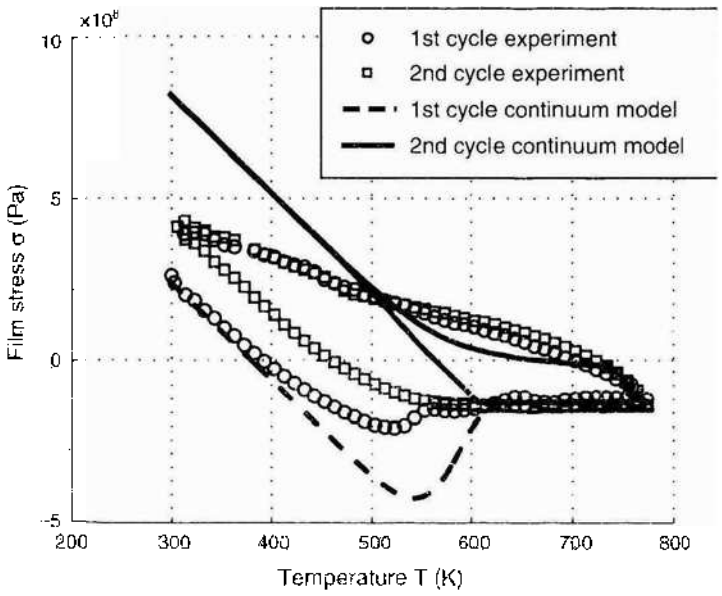

Figure 26. Fit of continuum model with threshold stress to experimental data. The film thickness is $h_f = 600$ nm and grain boundary diffusivities are as in Ref. [50].

5.2.2. Estimation of Diffusivities from Experimental Data

Another interesting aspect is the estimation of diffusivities from the experimental data. It can be observed in Fig. 26 that the stress decrease in the first heating cycle is larger in the experiment than in the simulation. When the diffusivities reported in the literature are used, the maximum compressive stress is overestimated by a factor of two (a similar observation was also made in the paper by Weiss et al. [25], Fig. 10). This could be because the diffusivities used in the continuum mechanics model are smaller than the actual experimental value. Figure 27 shows a fit of the continuum mechanics model to the experimental data, with a threshold stress $\sigma_i^* = -65$ MPa for a 600-nm film, as obtained from experiment (see discussion above). Fitting the maximum compressive stress to the experimental results by adjusting the diffusivity yields a diffusivity 80 times higher than in the literature. Possible reasons for this could be the fact that the grain boundary structure strongly influences the diffusivities. In the literature, a dependence of the diffusivities on grain boundary structure has been proposed (for further discussion, see, for instance, Refs. [28, 35]). Such considerations have not been taken into account in modeling diffusion in thin films so far, but they may explain the observations discussed above.

The fitted grain boundary diffusivity is given by

$$\delta_{gb} D_{gb}(T) = 4 \times 10^{-13} \exp\left(-\frac{Q_h}{RT}\right) \mathrm{m}^3 \mathrm{s}^{-1} \tag{57}$$

The characteristic time for a film with $h_f = 20$ nm at a temperature of about 90% of the melting point is then on the order of 10^{-8} s. This supports the idea that constrained grain boundary diffusion can be modeled with classical molecular dynamics, as such simulations are typically limited to a timescale of around 1×10^{-8} s [28, 33].

Finally, we compare calculations with the new estimate for diffusivities to the experimental results. In Fig. 28 we show a comparison of experiment and the continuum model with threshold stress for steady-state thermal cycling of thin films with film thickness $h_f \approx 100$ nm. In Fig. 29 we show a comparison of experiment and the continuum model with threshold stress for film thickness $h_f \approx 600$ nm.

6. MAP OF PLASTIC DEFORMATION MECHANISMS

The results from the numerical modeling together with the experimental findings [7] were used to qualitatively describe different deformation mechanisms that occur in submicron thin films. It was proposed in Ref. [30] that there exist four different deformation regimes: (A) deformation with threading dislocations, (B) constrained diffusional creep with

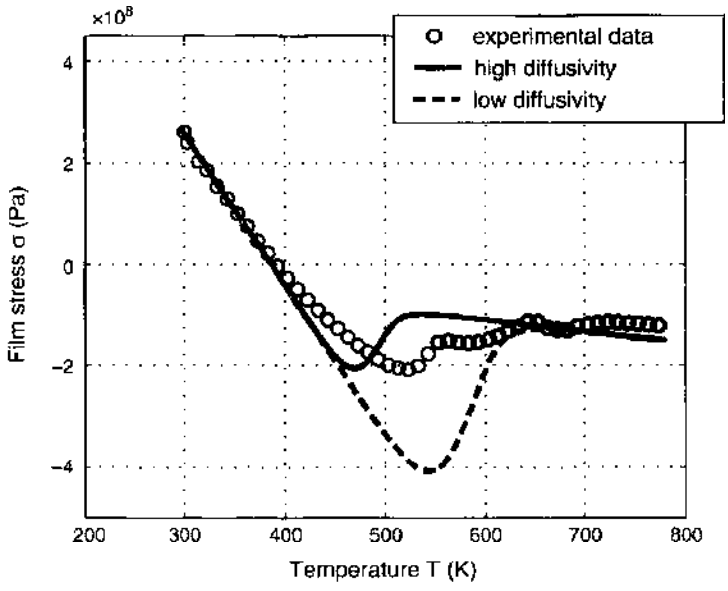

Figure 27. Fit of diffusivities to the experimental data based on the first heating curve of the 600-nm film.

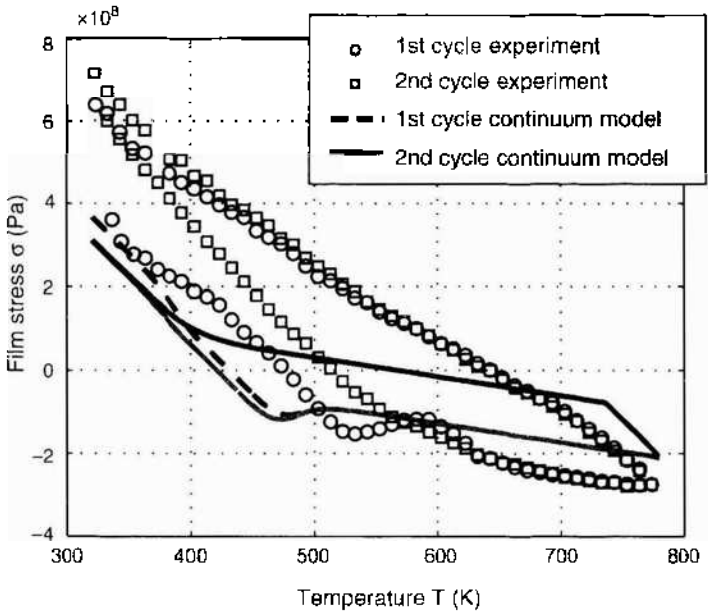

Figure 28. Fit of continuum model with threshold stress to experimental data. The film thickness is $h_f = 100$ nm, and grain boundary diffusivities are fitted to experimental data.

subsequent parallel glide, (C) constrained diffusional creep without parallel glide, and finally, for the thinnest films, and (D) no stress relaxation mechanism (no diffusion and no dislocation motion possible). A schematic "deformation map" is plotted in Fig. 30. This plot shows the critical applied stress to initiate different mechanisms of deformation as a function of the film thickness. Note that it is assumed that loading is applied very slowly and that temperature is sufficiently high for diffusive processes to occur.

The critical applied stress to nucleate threading dislocations scales with $1/h_f$ [4–6]. The $1/h_f$ scaling has also been found in two-dimensional molecular dynamics simulations [34]. For films thicker than a material-dependent value, regime (A) is the dominant deformation mechanism. For thinner films, the stress necessary to nucleate threading dislocations is larger than that required to initiate grain boundary diffusion. In this regime (B), diffusion dominates stress relaxation and causes a plateau in the flow stress, as shown by experimental

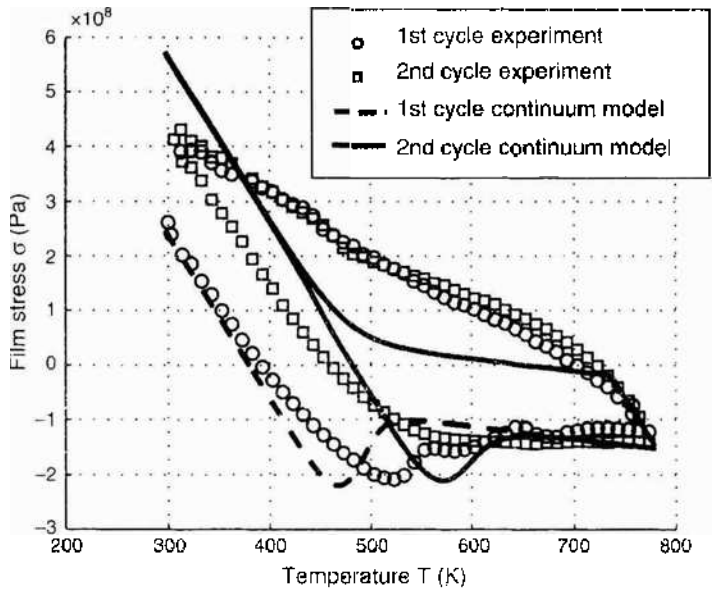

Figure 29. Fit of continuum model with threshold stress to experimental data. The film thickness is $h_f = 600$ nm, and grain boundary diffusivities are fitted to experimental data.

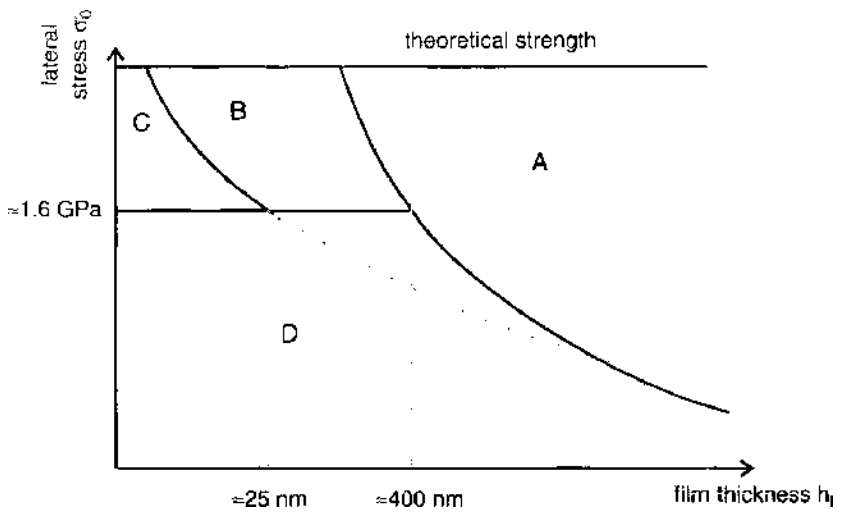

Figure 30. Deformation map of thin films as a function of film thickness, summarizing different stress relaxation mechanisms in ultrathin films on substrates [30].

results [7, 8] and later by discrete dislocation modeling [31]. Parallel glide helps to sustain grain boundary diffusion until the overall stress level is below the diffusion threshold, which is independent of the film thickness. For yet thinner films, our MD simulations revealed that grain boundary diffusion stops before a sufficient stress concentration for triggering parallel glide is obtained. The onset of regime (C) can be described by the scaling of the critical nucleation stress for parallel glide with $1/h_f^s$ ($s = 0.5$ for the homogeneous film/substrate case). In this regime, the flow stress again increases for smaller films due to the back stress of the climb dislocations in the grain boundary, effectively stopping further grain boundary diffusion. If the applied stress is lower than the critical stress for diffusion, no stress relaxation is possible. This is referred to as regime (D).

The yield stress of thin films resulting from these considerations is summarized in Fig. 31 for different film thicknesses. For thicker films, the strength increase is inversely proportional to the film thickness, as has been shown in several theoretical and experimental studies [1, 5, 7, 9]. If the film thickness is small enough such that grain boundary diffusion and parallel glide are the prevailing deformation mechanisms, the film strength is essentially independent of h_f, as seen in experiment [7] and as later shown by the discrete dislocation model [31]. However, for films thinner than $h_f \approx 30$ nm, discrete dislocation modeling [31] predicts a further increase in strength with decreasing film thickness.

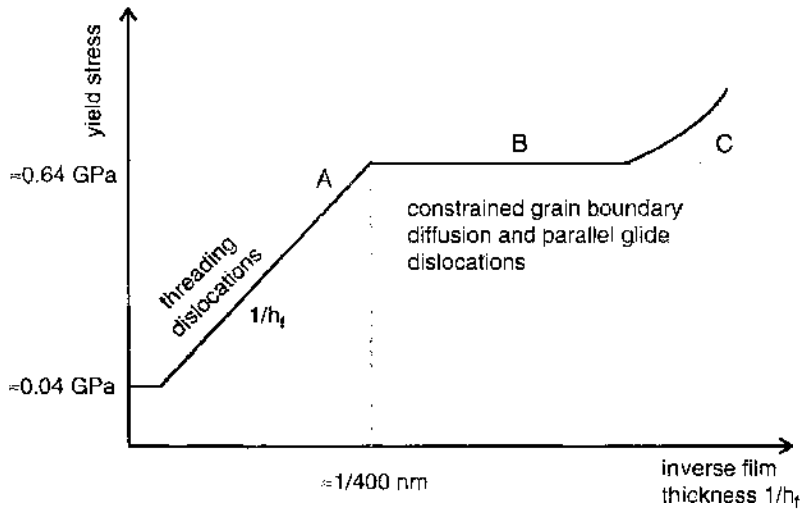

Figure 31. Strength of thin films as a function of film thickness. The film thickness of $h_f \approx 400$ nm, as well as the plateau yield stress of 0.64 GPa, are taken from experimental results [7, 8]. Further details are given in Ref. [30].

The existing understanding is mostly qualitative. A few data points from experiment, simulation, or theory were taken to draw the deformation map. Future studies could focus on a more quantitative study of the different deformation mechanisms and provide a systematic study of transition from one regime to the other. Mesoscopic simulations [31], as applied to constrained diffusional creep and nucleation of parallel glide dislocations, could play an important role in these studies.

7. SUMMARY AND CONCLUSIONS

In this chapter we have reviewed recent theoretical, numerical, and experimental activities investigating the mechanical properties of submicron thin films on substrates.

Theoretical modeling predicted the existence of so-called grain boundary diffusion wedges. This model was later successfully used to explain experimental observations of parallel glide dislocations, which verified the prediction that dislocations with Burgers vector parallel to the film plane could be emitted from the tip of a diffusion wedge. The experimental results, together with the theoretical predictions, guided molecular dynamics studies that confirmed this concept at the atomic scale.

A new and significant result reported in this chapter is the modeling of thermal cycling of ultrathin films using continuum theories. With the new concept of a threshold stress, we qualitatively reproduced experimental results. Additional discussion was devoted to estimates of the grain boundary diffusivity from experimental data. It was found that diffusivities are higher than reported in the classical literature [50], which may be attributed to the dependence of diffusivities on the grain boundary structure. A deformation map describing numerous novel deformation mechanisms in thin metal films was developed to summarize the main findings.

The examples reported in this chapter exemplify the richness of phenomena that can occur as the dimensions of materials shrink to nanometer scale.

ACKNOWLEDGMENTS

We thank Gerhard Dehm and Alexander Hartmaier for many helpful discussions on the experimental and modeling work described here. M.B. acknowledges fruitful discussions with Dieter Wolf on modeling diffusional creep with molecular dynamics. The simulations reported in this work were carried out at the Max Planck Society Supercomputer Center in Garching.

REFERENCES

1. R.-M. Keller, S. P. Baker, and E. Arzt, *Acta Mater.* 47, 415 (1999).
2. M. J. Kobrinsky and C. V. Thompson, *Appl. Phys. Lett.* 73, 2429 (1998).
3. R. P. Vinci, E. M. Zielinski, and J. C. Bravman, *Thin Solid Films* 262, 142 (1995).
4. L. B. Freund, *J. Appl. Mech.* 54, 553 (1987).
5. W. D. Nix, *Metall. Trans. A* 20, 2217 (1989).
6. W. D. Nix, *Scripta Mater.* 39, 545 (1998).
7. T. J. Balk, G. Dehm, and E. Arzt, *Acta Mater.* 51, 4471 (2003).
8. G. Dehm, T. J. Balk, B. von Blanckenhagen, P. Gumbsch, and E. Arzt, *Z. Metallk.* 93, 383 (2002).
9. B. von Blanckenhagen, P. Gumbsch, and E. Arzt, *Modelling Simulation Mat. Sci. Eng.* 9, 157 (2001).
10. M. Legros, K. J. Hemker, A. Gouldstone, S. Suresh, R.-M. Keller-Flaig, and E. Arzt, *Acta Mater.* 50, 3435 (2002).
11. B. von Blanckenhagen, P. Gumbsch, and E. Arzt, *Philos. Mag. Lett.* 83, 1 (2003).
12. H. Gao, L. Zhang, W. D. Nix, C. V. Thompson, and E. Arzt, *Acta Mater.* 47, 2865 (1999).
13. M. D. Thouless, J. Gupta, and J. M. E. Harper, *J. Mat. Res.* 8, 1845 (1993).
14. J. R. Rice and R. Thomson, *Philos. Mag.* 29, 73 (1974).
15. Z. Suo and J. W. Hutchinson, *Int. J. Solids Struct.* 25, 1337 (1989).
16. J. P. Hirth and J. Lothe, "Theory of Dislocations," Wiley-Interscience, New York, 1982.
17. J. D. Eshelby, in "Dislocations in Solids" (F. R. N. Nabarro, Ed.), Vol. 1, p. 167, North-Holland, Amsterdam, 1979.
18. L. Zhang and H. Gao, *Z. Metallk.* 93, 417 (2002).
19. R. L. Coble, *J. Appl. Phys.* 41, 1679 (1963).

20. F. Ergodan, G. D. Gupta, and T. S. Cook, "Methods of Analysis and Solutions of Crack Problems," pp. 168–425. Nordhoff International Publishing, Leyden, Netherlands, 1973.
21. F. Ergodan and G. D. Gupta, *Q. Appl. Math.* 30, 525 (1972).
22. H. Gao, Y. Huang, W. D. Nix, and J. W. Hutchinson, *J. Mech. Phys. Solids* 47, 1239 (1999).
23. J. R. Rice and T.-J. Chuang, *J. Am. Ceram. Soc.* 64, 46 (1981).
24. W. W. Mullins, *J. Appl. Phys.* 28, 333 (1957).
25. D. Weiss, H. Gao, and E. Arzt, *Acta Mater.* 49, 2395 (2001).
26. Z. C. Xia and J. W. Hutchinson, *J. Mech. Phys. Solids* 48, 1107 (2000).
27. L. Zhang, Ph.D. thesis, Stanford University, 2001.
28. M. J. Buehler, A. Hartmaier, and H. Gao, *J. Mech. Phys. Solids* 51, 2105 (2003).
29. A. R. Zak and M. L. Williams, *J. Appl. Mech.* 30, 142 (1963).
30. M. J. Buehler, A. Hartmaier, and H. Gao, *Model. Sim. Mat. Sci. Eng.* 12, 351 (2004).
31. A. Hartmaier, M. J. Buehler, and H. Gao, *Defect Diffusion Forum* 224–225, 107 (2004)
32. M. J. Buehler, A. Hartmaier, and H. Gao, *Mat. Res. Soc. Symp. Proc.* 779, W4.7.1 (2003).
33. M. J. Buehler and H. Gao, "Handbook of Theoretical and Computational Nanotechnology," Chap. 4. American Scientific Publishers, Stevenson Ranch, CA, 2004.
34. H. van Swygenhoven, P. M. Derlet, and A. Hasnaoui, *Phys. Rev. B* 66, 024101 (2002).
35. D. Wolf, V. Yamakov, S. R. Phillpot, and A. K. Mukherjee, *Z. Metallk.* 94, 1052 (2003).
36. V. Yamakov, D. Wolf, S. R. Phillpot, and H. Gleiter, *Acta Mater.* 50, 61 (2002).
37. R. Würschum, S. Herth, and U. Brossmann, *Adv. Eng. Mat.* 5, 365 (2003).
38. P. Keblinski, D. Wolf, S. R. Phillpot, and H. Gleiter, *Phil. Mag. Lett.* 76, 143 (1997).
39. P. Keblinski, D. Wolf, S. R. Phillpot, and H. Gleiter, *Phil. Mag. Lett.* 79, 2735 (1999).
40. P. Lagarde and M. Biscondi, *Mem. Etud. Sci. Rev. Met.* 71, 121 (1974).
41. E. Budke, C. Herzig, S. Prokofjev, and L. Shvindlerman, *Defect Diffusion Forum* 156, 21 (1998).
42. Y.-L. Shen, *J. Mater. Res.* 18, 2281 (2003).
43. J. R. Rice and G. B. Beltz, *J. Mech. Phys. Solids* 42, 333 (1994).
44. R. Spolenak, N. Tamura, B. Valek, R. S. Celestre, A. A. MacDowell, T. Marieb, H. Fujimoto, W. L. Brown, J. C. Bravman, H. A. Padmore, B. W. Batterman, and J. R. Patel, *Phys. Rev. Lett.* 90, 096102 (2003).
45. T. J. Balk, G. Dehm, and E. Arzt, *Mat. Res. Soc. Symp. Proc.* 673, 2.7.1 (2001).
46. R. Venkatraman and J. C. Bravman, *J. Mater. Res.* 8, 2040 (1992).
47. G. Dehm, B. J. Inkson, T. J. Balk, T. Wagner, and E. Arzt, *Mat. Res. Soc. Symp. Proc.* 673, 2.6.1 (2001).
48. M. J. Kobrinsky and C. V. Thompson, *Acta Mater.* 48, 625 (2000).
49. M. J. Kobrinsky, G. Dehm, C. V. Thompson, and E. Arzt, *Acta Mater.* 49, 3597 (2001).
50. H. J. Frost and M. F. Ashby, "Deformation-Mechanism Maps," 1st ed., p. 21. Pergamon Press, Oxford, 1982.

CHAPTER 5

Chemical Reaction and Flow Modeling in Fullerene and Nanotube Production

Carl D. Scott
NASA Johnson Space Center, Houston, Texas, USA

Samir Farhat
Laboratoire d'Ingéniérie des Matériaux et des Hautes Pressions, Villetaneuse, France

Robert B. Greendyke
Department of Mechanical Engineering, University of Texas at Tyler, Tyler, Texas, USA

CONTENTS

ISBN: 1-58883-047-0

Handbook of Theoretical and Computational Nanotechnology
Edited by Michael Rieth and Wolfram Schommers
Volume 5: Pages (251–327)

1. INTRODUCTION

The development of processes to produce fullerenes and carbon nanotubes has largely been empirical. Fullerenes were first discovered in the soot produced by laser ablation of graphite [1] and then in the soot of electric arc evaporated carbon [2]. Techniques and conditions for producing larger and larger quantities of fullerenes depended mainly on trial-and-error empirical variations of these processes, with attempts to scale them up by using larger electrodes and targets and higher power. Various concepts of how fullerenes and carbon nanotubes were formed were put forth, but very little was done based on chemical kinetics of the reactions. This was mainly due to the complex mixture of species and complex nature of conditions in the reactors. Temperatures in the reactors varied from several thousand degrees Kelvin down to near room temperature. There are hundreds of species possible, ranging from atomic carbon to large clusters of carbonaceous soot, metallic catalyst atoms to metal clusters, to complexes of metals and carbon. Most of the chemical kinetics of the reactions and the thermodynamic properties of clusters and complexes have only been approximated. In addition, flow conditions in the reactors are transient or unsteady and three-dimensional, with steep spatial gradients of temperature and species concentrations. All these factors make computational simulations of reactors very complex and challenging.

This article addresses the development of the chemical reactions involved in fullerene production and extends this to production of carbon nanotubes by the laser ablation/oven process and by the electric arc evaporation process. In addition, the high-pressure carbon monoxide (HiPco) process is discussed. The article is in several parts. The first one addresses the thermochemical aspects of modeling and considers the development of chemical rate equations, estimates of reaction rates, and thermodynamic properties where they are available. The second part addresses modeling of the arc process for fullerene and carbon nanotube production using 0D, 1D, and 2D, fluid flow models. The third part addresses simulations of the pulsed laser ablation process using time-dependent techniques in 2D, and a steady-state 2D simulation of a continuous laser ablation process. The fourth part addresses steady-state modeling in 0D and 2D of the HiPco process. In each of the simulations, there is a variety of simplifications that are made that enable one to concentrate on one aspect or another of the process. There are simplifications that can be made to the chemical reaction models (e.g., reduction in number of species by lumping some of them together in a representative species). Other simulations are carried out by eliminating the chemistry altogether in order to concentrate on the fluid dynamics. When solving problems with a large number of species in more than one spatial dimension, it is almost imperative that the problem be decoupled by solving for the fluid dynamics to find the fluid motion and temperature history of "particles" of fluid moving through a reactor. Then, one can solve the chemical rate equations with complex chemistry following the temperature and pressure history. One difficulty is that often, mixing with an ambient gas is involved. Therefore, one needs to take dilution and mixing into account. This changes the ratio of carbon species to background gas. Commercially available codes may have no provision for including dilution as part of the input. One must write special solvers for including dilution in decoupled problems.

The article addresses both fullerene production and single-wall carbon nanotube (SWCNT) production. There are at least two schemes or concepts of SWCNT growth. This article will only address growth in the gas phase by carbon and catalyst cluster growth and SWCNT formation by the addition of carbon. There are other models that conceive of SWCNT growth as a phase separation process from clusters made up of carbon and metal catalyst, with the carbon precipitating from the cluster as it cools. We will not deal with that concept in this article. Further research is needed to determine the rates at which these composite clusters form, evaporate, and segregate.

2. REACTION SCHEMES AND THERMODYNAMIC PROPERTIES

This section deals with the formation of fullerenes and SWCNTs via precursor species, clusters of carbon, and metal catalysts. Two basic processes are considered: one being processes that involve carbon vaporized at high temperatures such as the arc process and the laser ablation process; the other a gas phase process in which carbon is supplied by carbon monoxide at high pressure (the HiPco process).

2.1. Carbon and Fullerene Kinetics

Various workers have studied the kinetics of the formation of carbon clusters. Bernholc and Phillips [3] solved the Smoluchowski equations for carbon clusters C_n up to $n = 25$ using a reaction probability, or kernel, based on a scaled derivative of the Gibbs free energy. Their work included both negative and positive ions, in addition to neutral clusters. Using this technique, they predicted the distribution of clusters, including the presence of magic numbers. Creasy and Brenna [4, 5] used a simple model in which clusters grew by attachment of only the small clusters C, C_2, and C_3. The reaction rates were estimated from gas kinetic rates. Subsequently, Creasy [6] developed more complex reaction models that allowed for multiple steps, in an attempt to account for "magic number" clusters. His analysis produced cluster and fullerene distributions up to about $n = 450$ that depended on the initial concentration of small carbon molecules. The higher the initial density, the greater was the average size cluster, and the more the distribution shifted toward larger clusters at steady state. The reaction rates in their model did not depend on temperature.

2.1.1. Model of Krestinin and Moravsky

Krestinin et al. [7] developed a reaction scheme for fullerene formation. Krestinin and Moravsky [8] applied the model to an arc process, where they achieved reasonable agreement with measured fullerene production, considering the approximations made in the arc flow field. They were able to explain the relatively constant ratio of C_{60} to C_{70} seen in arc experiments. The objective of their model was to depict carbon vapor condensation in an arc reactor. Because of the lack of thermodynamic data for the various clusters, the model was formulated, to the extent necessary, not to rely on that data. Many reactions are written as separate forward and backward reactions, or only in terms of condensation and not decomposition of clusters. They rejected formulating a scheme that includes all carbon clusters, as well as their ions, due to the complexity of experimental verification. As experimental data becomes available and simulations are made, the model can be validated and rate coefficients and reactions can be refined. Their rates are based on measurements using ionic gas chromatography published in the literature [9–12]. Carbon clusters up to $n = 31$ are assumed to be highly reactive chains, cycles, and polycycles. Clusters with $n = 32$ to 79 are closed shells, where the main growth or decomposition is from C_2 attachment or detachment, respectively. That odd-n clusters are less stable than even clusters is attributed to a lack of resonance stabilization. Their model reflects a 251-kJ/mol lower enthalpy of formation of even-n numbered clusters as compared with odd-n numbered clusters. Upon decomposition, odd clusters tend to eject C, rather than C_2 [13]. Clusters with $n = 80$ or greater are assumed to be soot (denoted Z in the tables). In the calculations of Krestinin et al. [7], they assumed that soot takes on a size distribution and that soot reactions are heterogeneous. The reaction

rate then depends on the surface area of the soot particle. (In later applications [14] of this model to nanotube production discussed in this article, the model is modified so that soot is treated as a single gas phase species.)

Reaction equations and rate coefficients from [7] are given in Arrhenius form in Table 1 for the fullerene model.

$$k = A \exp\left(\frac{-E}{RT}\right) \tag{1}$$

The thermodynamic properties for these clusters were determined from existing data for C, [15], C_2, [16], C_3–C_{10}, [17], and C_{60F} and C_{70F}, [18]. The enthalpy of formation for clusters

Table 1. Gas phase chemistry for Fullerene model.[a]

Reaction	A ($cm^3\ s^{-1}\ mol^{-1}$)	β	E/R (K)
1. Chemistry of small clusters (C–C_{10})			
$C + C \leftrightarrow C_2$	2.00×10^{14}	0	0
$C + C_2 \leftrightarrow C_3$	2.00×10^{14}	0	0
$C_2 + C_2 \leftrightarrow C_3 + C$	2.00×10^{15}	0	9040
$C_2 + C_3 \leftrightarrow C_4$	2.00×10^{14}	0	0
$C_1 + C_3 \leftrightarrow C_4$	2.00×10^{14}	0	0
$C_1 + C_4 \leftrightarrow C_5$	2.00×10^{14}	0	0
$C_2 + C_3 \leftrightarrow C_5$	2.00×10^{14}	0	0
$C_{n-m} + C_m \leftrightarrow C_n$	2.00×10^{14}	0	0
$n = 6, 10$ and $m = 1, n/2$			
2. Chemistry of cycles and polycycles (C_{11}–C_{30})			
$C_{n-m} + C_m \leftrightarrow C_n$	2.00×10^{14}	0	0
$n = 11, 31$ and $m = 1, 15$			
3. Formation of fullerenes			
$C_{n-m} + C_m \leftrightarrow C_n$	2.00×10^{14}	0	0
$n = 32, 46$ and $n - 31 \leq m \leq 15$			
4. Growth of fullerene shells			
$C_n + C \leftrightarrow C_{n+1}$	2.00×10^{14}	0	0
$n = 32, 78$ excluding $n = 59, 69$			
$C_n + C_2 \rightarrow C_{n+2}$	4.00×10^{08}	0	0
$C_{n+2} \rightarrow C_n + C_2$	3.20×10^{13}	0	61900
$n = 32, 59$ excluding $n = 58$			
$C_n + C_2 \rightarrow C_{n+2}$	4.00×10^{08}	0	0
$C_{n+2} \rightarrow C_n + C_2$	3.20×10^{13}	0	61900
$n = 60, 77$ excluding $n = 68$			
$C_n + C_3 \leftrightarrow C_{n+2} + C$	1.00×10^{15}	0	0
$n = 32, 77$			
5. Formation and decay of fullerene molecules			
$C_{60} \rightarrow C_{60F}$	5.00×10^{13}	0	37745
$C_{60} + C \rightarrow C_{60F}$	2.00×10^{14}	0	0
$C_{58} + C_2 \rightarrow C_{60F}$	4.00×10^{08}	0	−30196
$C_{60F} \rightarrow C_{58} + C_2$	8.00×10^{12}	0	61900
$C_{58} + C_3 \rightarrow C_{60F} + C$	8.00×10^{14}	0	0
$C_{60F} + C \rightarrow C_{61}$	2.00×10^{14}	0	10065
$C_{60F} + C_2 \rightarrow C_{62}$	2.00×10^{14}	0	10065
$C_{60F} + C_3 \rightarrow C_{63}$	2.00×10^{14}	0	10065
$C_{70} \rightarrow C_{70F}$	1.20×10^{14}	0	37745
$C_{69} + C \rightarrow C_{70}$	2.00×10^{14}	0	0
$C_{68} + C_2 \rightarrow C_{70}$	4.00×10^{08}	0	−30600
$C_{70} \rightarrow C_{68} + C_2$	2.50×10^{14}	0	0
$C_{68} + C_3 \rightarrow C_{70} + C$	1.40×10^{15}	0	49925
$C_{70} + C \rightarrow C_{71}$	2.00×10^{14}	0	10065
$C_{70} + C_2 \rightarrow C_{72}$	2.00×10^{14}	0	10065
$C_{70} + C_3 \rightarrow C_{73} + C$	2.00×10^{14}	0	10065

[a] Forward rate constants k are calculated assuming Arrhenius temperature dependence $k = AT^{\beta} \exp(-\frac{E}{RT})$ where A is the pre-exponential factor, β is the temperature exponent, and E is the activation energy. Constants A, β, and E are from Krestinin et al. [7].

with $n = 11$ to 59, 61 to 69, and 71 to 79 were estimated by interpolating the values between $n = 10$ and 60. The entropy of formation was estimated by interpolation between $n = 5$ and 60. The specific heats were set at values corresponding to $T > 2000$ K where fully excited vibration and rotation is achieved. Then, $C_p/R = 3n - 2$ for $n \geq 6$. The complete set of thermodynamic coefficients for the fullerene model is listed in Table 2. These coefficients are in the old NASA format where the various thermodynamic functions are calculated by the formulas:

$$\frac{C_{pi}}{R} = A_{1i} + A_{2i}T + A_{3i}T^2 + A_{4i}T^3 + A_{5i}T^4 \tag{2}$$

$$\frac{h_i}{RT} = A_{1i} + A_{2i}T/2 + A_{3i}T^2/3 + A_{4i}T^3/4 + A_{5i}T^4/5 + A_{6i}/T \tag{3}$$

$$\frac{s_i}{R} = A_{1i}\ln(T) + A_{2i}T + A_{3i}T^2/2 + A_{4i}T^3/3 + A_{5i}T^4/4 + A_{7i} \tag{4}$$

where R is the universal gas constant, h_i is the specific enthalpy of the ith species, and s_i is the specific entropy. For the clusters for which thermodynamic properties were interpolated, it can be seen from the values in Table 2, that C_{pi} and s_i are constant with respect to temperature. Thus, they are rather approximate. In most simulations, this does not pose a problem because of dilution. The fully excited approximation for C_p is not very significant due to dilution and the high temperatures used in production of fullerenes and nanotubes. In such case, the energy equation for the flow does not depend significantly on the energetics of the carbon reactions.

2.1.2. Reduced Carbon Cluster Scheme

Because of the significant computer time required for models containing large numbers of species used in computational fluid dynamic (CFD) simulations, large models are impractical for simulating complex time-dependent flows, such as pulsed laser ablation. To overcome this limitation of CFD codes, it is almost imperative that the number of species in the chemical reaction models be reduced to a manageable number. An effort to do this was accomplished for simulating the HiPco process and likewise for the carbon fullerene and carbon/metal-vapor SWCNT processes. Gökçen et al. [19] showed that in simulations of the flow in the HiPco reactor, the number of catalyst particles Fe_n for $n > 2$ could be lumped into a single representative iron cluster Fe_c, and the 200 SWCNTs in their model could be reduced to a single representative nanotube, CNT. They compared the production of CO_2 using both models and showed that they produced similar results for a constant temperature case. This enabled Gökçen et al. to use the model in their simulations of the HiPco reactor, thus saving much computer time. Their full and reduced models will be discussed in more detail later.

In a similar way, we have reduced the fullerene model of Krestinin et al. [7]. In the reduced fullerene model, we have lumped all carbon cluster C_n with $n > 3$ into a single representative species CC. For carbon balance in the reaction equations, we specify the number of carbons in CC to be 40. The feedstock for growth of CC and the fullerene C_{60} are the small carbon molecules C, C_2, and C_3. These small molecules coalesce to form CC, which then forms C_{60}. A soot Z is also formed from CC. This soot is considered a single species of constant $n = 80$. The reduced fullerene model is given in Table 3, and the corresponding thermodynamic coefficients are given in Table 4. The thermodynamic coefficients for CC and Z correspond to C_{40} and C_{80} in the full fullerene model. These coefficients were derived from interpolations of properties as indicated above.

2.2. Metal Catalyst Schemes

When pure carbon is used as the feedstock for reactions in high-temperature processes, the product is usually amorphous carbon chains and rings, fullerenes, graphitic particles, and soot. At some conditions multiwall carbon nanotubes (MWNT) are formed. However, if some metal catalysts are added, there is a preference to form single-wall carbon nanotubes. SWCNTs have many interesting and unique properties. They may range from metallic to

Table 2. Thermodynamic coefficients for carbon clusters.[a]

i	A_{1i}	A_{2i}	A_{3i}	A_{4i}	A_{5i}	A_{6i}	A_{7i}
1H	2.5205176E + 00	1.8268312E − 04	−3.1504542E − 08	2.5371109E − 12	−6.2267852E − 17	8.4851595E + 04	5.8203836E + 00
1L	1.9031864E + 00	4.0200238E − 03	−9.0395391E − 06	8.1759092E − 09	−2.5854092E − 12	8.4826660E + 04	7.2917617E + 00
2H	4.0753780E + 00	3.3239978E − 04	−1.2344909E − 08	−7.0714041E − 13	2.8222317E − 17	9.9788114E + 04	9.6847543E − 01
2L	5.4993641E + 00	1.8891470E − 03	−1.3226503E − 05	1.6061423E − 08	−5.8286773E − 12	9.9140682E + 04	−7.7146073E + 00
3H	4.9032746E + 00	1.1113409E − 03	−7.5331984E − 08	−4.8099305E − 13	8.9121604E − 17	9.6812289E + 04	1.5052816E − 01
3L	3.6042014E + 00	7.5373711E − 03	−1.1558984E − 05	8.8850242E − 09	−2.5287216E − 12	9.7010617E + 04	6.1103710E − 00
4H	4.9032746E + 00	1.1113409E − 03	−7.5331984E − 08	−4.8099305E − 13	8.9121604E − 17	1.1492855E + 05	1.5052816E − 01
4L	3.6042014E + 00	7.5373711E − 03	−1.1558984E − 05	8.8850242E − 09	−2.5287216E − 12	1.1512688E + 05	6.1103710E + 00
5H	1.1592118E + 01	8.5502931E − 04	−1.2817463E − 07	7.7473555E − 12	1.6260603E − 16	1.1368121E + 05	−3.5115388E − 01
5L	1.1731935E + 01	−2.5681572E − 02	7.8642726E − 05	−7.8483519E − 08	2.6116987E − 11	1.1495211E + 05	2.9295593E − 01
6	16	0	0	0	0	149572	−61.28986
7	19	0	0	0	0	157121	−77.6175
8	22	0	0	0	0	178812	−93.94515
9	25	0	0	0	0	186965	−110.2728
10	28	0	0	0	0	178963	−126.6004
11	31	0	0	0	0	181413.9	142.9281
12	34	0	0	0	0	183864.9	159.2557
13	37	0	0	0	0	186315.8	−175.5834
14	40	0	0	0	0	188766.8	−191.911
15	43	0	0	0	0	191217.7	−208.2387
16	46	0	0	0	0	193668.6	−224.5663
17	49	0	0	0	0	196119.6	240.894
18	52	0	0	0	0	198570.5	−257.2216
19	55	0	0	0	0	201021.5	−273.5493
20	58	0	0	0	0	203472.4	−289.8769
21	61	0	0	0	0	205923.3	−306.2045
22	64	0	0	0	0	208374.3	−322.5322
23	67	0	0	0	0	210825.2	−338.8598
24	70	0	0	0	0	213276.2	−355.1874
25	73	0	0	0	0	215727.1	−371.5151
26	76	0	0	0	0	218178	−387.8427
27	79	0	0	0	0	220629	−404.1704

continued

Table 2. Continued.

28	82	0	0	0	0	223079.9	−420.498
29	85	0	0	0	0	225530.9	−436.8257
30	88	0	0	0	0	227981.8	−453.1533
31	91	0	0	0	0	230432.7	−469.481
32	94	0	0	0	0	232883.7	−485.8086
33	97	0	0	0	0	265530.6	−502.1362
34	100	0	0	0	0	237785.6	−518.4639
35	103	0	0	0	0	270432.5	−534.7916
36	106	0	0	0	0	242687.4	−551.1192
37	109	0	0	0	0	275334.4	−567.4468
38	112	0	0	0	0	247589.3	−583.7745
39	115	0	0	0	0	280236.3	−600.1021
40	118	0	0	0	0	252491.2	−616.4297
41	121	0	0	0	0	285138.1	−632.7574
42	124	0	0	0	0	257393.1	−649.085
43	127	0	0	0	0	290040	−665.4127
44	130	0	0	0	0	262295	−681.7403
45	133	0	0	0	0	294941.9	−698.068
46	136	0	0	0	0	267196.8	−714.3956
47	139	0	0	0	0	299843.8	−730.7233
48	142	0	0	0	0	272098.7	−747.051
49	145	0	0	0	0	304745.7	−763.3785
50	148	0	0	0	0	277000.6	−779.7062
51	151	0	0	0	0	309647.5	−796.0338
52	154	0	0	0	0	281902.5	−812.3615
53	157	0	0	0	0	314549.4	−828.6891
54	160	0	0	0	0	286804.4	−845.0168
55	163	0	0	0	0	319451.3	−861.3444

continued

Table 2. Continued.

i	A_{1i}	A_{2i}	A_{3i}	A_{4i}	A_{5i}	A_{6i}	A_{7i}
56	166	0	0	0	0	291706.3	−877.6721
57	169	0	0	0	0	324353.2	−893.9997
58	172	0	0	0	0	296608.1	−910.3274
59	175	0	0	0	0	329255.1	926.655
60H	9.9843418E + 01	7.8857558E − 02	−3.0608799E − 05	5.1957690E − 09	−3.2188408E − 13	2.6670488E + 05	−5.4587488E + 02
60L	3.3579084E + 01	4.2844440E − 01	−3.1712321E − 04	4.7546257E − 08	2.7677699E − 11	3.0465122E + 05	1.4832875E + 02
61	181	0	0	0	0	334156.9	−959.3103
62	184	0	0	0	0	306411.9	−975.638
63	187	0	0	0	0	339058.8	−991.9655
64	190	0	0	0	0	311313.8	−1008.293
65	193	0	0	0	0	343960.7	1024.621
66	196	0	0	0	0	316215.6	−1040.949
67	199	0	0	0	0	348862.6	−1057.276
68	202	0	0	0	0	321117.5	1073.604
69	205	0	0	0	0	353764.4	−1089.931
70H	1.0677602E + 02	1.0200334E − 01	−3.9562455E − 05	6.7122022E − 09	−4.1568097E − 13	2.9769320E + 05	−5.9941734E + 02
70L	−3.1366983E + 01	3.3484410E − 01	9.8587783E − 05	−4.4663983E − 07	2.2008836E − 10	3.4260294E + 05	1.4891614E + 02
71	211	0	0	0	0	358666.3	−1122.587
72	214	0	0	0	0	330921.3	−1138.914
73	217	0	0	0	0	363568.2	−1155.242
74	220	0	0	0	0	335823.2	−1171.57
75	223	0	0	0	0	368470.1	1187.897
76	226	0	0	0	0	340725	−1204.225
77	229	0	0	0	0	373372	−1220.553
78	232	0	0	0	0	345626.9	−1236.88
79	235	0	0	0	0	378273.9	−1253.208
80	238	0	0	0	0	350528.8	−1269.536

[a] H = 1000 to 20,000 K; L = 300 to 1000 K.

Table 3. Reduced fullerene model reaction scheme.

	A	η	E/R
Cluster growth			
$C + C = C_2$	2.0E + 14	0	0
$C + C_2 = C_3$	2.0E + 14	0	0
$C2 + C_2 = C_3 + C$	2.0E + 15	0	9040
$C3 + C = 0.100CC$	2.0E + 13	0	0
$C3 + C_2 = 0.125CC$	2.0E + 13	0	0.0
$C3 + C_3 = 0.150CC$	2.0E + 13	0	0.0
$CC + C = 1.025CC$	2.3E + 14	0	0.0
$CC + C_2 \Rightarrow 1.05CC$	2.3E + 14	0	0.0
$CC \Rightarrow 0.95CC + C_2$	3.2E + 13	0	61900
Fullerene formation			
$CC + C_3 \Rightarrow 0.70C_{60} + C$	2.0E + 13	0	0
$CC + C_2 \Rightarrow 0.70C_{60}$	4.0E + 9	0	−30196
$CC + C \Rightarrow 0.6833333C_{60}$	2.0E + 13	0	0
Fullerene disintegration			
$C_{60} \Rightarrow 1.45CC + C2$	8.0E + 13	0	61900
Soot formation			
$CC + CC \Rightarrow Z$	4.0E + 13	0	0
$CC + C_2 \Rightarrow 0.525Z$	4.0E + 8	0	−30600
$CC + C_3 \Rightarrow 0.5375Z$	6.92E + 10	0.5	0
$C_{60} + Z \Rightarrow 1.75Z$	1.26E + 12	0	10098
$CC + C_3 \Rightarrow 0.525Z + C$	2.0E + 11	0	0
$Z + C_3 \Rightarrow 1.0375Z$	4.0E + 12	0	0
$Z + C_2 \Rightarrow 1.025Z$	4.0E + 12	0	0
$Z + C \Rightarrow 1.0125Z$	4.0E + 12	0	0

Table 4. Thermodynamic property NASA coefficients for reduced fullerene model plus some other species used in plasma simulations.

AR	IVTAN AR 1	G	300.000 20000.000 1000.00		1
0.25199477E + 01	−0.22858382E − 04	0.74655237E − 08	−0.90208251E − 12	0.36063733E − 16	2
−0.75393340E + 03	0.42492779E + 01	0.25670200E + 01	−0.44283132E − 03	0.98495011E − 06	3
−0.88424193E − 09	0.27879189E − 12	−0.75176371E + 03	0.40801018E + 01		4
C	GMcB 20 K 0C 1	G	300.000 20000.000 1000.00		1
0.23205176E − 01	0.18268312E − 03	−0.31504542E − 07	0.25371109E − 11	−0.62267852E − 16	2
0.84851595E + 05	0.58203836E + 01	0.19031864E + 01	0.40200238E − 02	−0.90395391E − 05	3
0.81759092E − 08	−0.25854092E − 11	0.84826660E + 05	0.72917617E + 01		4
C_3	GMcB 20 K 0C 2	G	300.000 20000.000 1000.00		1
0.40753780E + 01	0.33239978E − 03	−0.12344909E − 07	−0.70714041E − 12	0.28222317E − 16	2
0.99788114E + 05	0.96847543E + 00	0.54993641E + 01	0.18891470E − 02	−0.13226503E − 04	3
0.16061423E − 07	−0.58286773E − 11	0.99140682E + 05	0.77146073E + 01		4
C_5	GMcB 20 K 0C 3	G	300.000 20000.000 1000.00		1
0.49032746E + 01	0.11113409E − 02	−0.75331984E − 07	−0.48099305E − 12	0.89121604E − 16	2
0.96812289E + 05	0.15052816E + 00	0.36042014E + 01	0.75373711E − 02	−0.11558984E − 04	3
0.88850242E − 08	−0.25287216E − 11	0.97010617E + 05	0.61103710E + 01		4
$C60_L$	C 60	0 0	G	0300.00 5000.00 1000.00	1
0.17800000E + 03	0.00000000E + 00	0.00000000E + 00	0.00000000E + 00	0.00000000E + 00	2
0.30151000E + 06	−0.9429827E + 03	0.17800000E + 03	0.00000000E + 00	00.00000000E + 00	3
0.00000000E + 00	0.00000000E + 00	0.30151000E + 06	−0.9429827E + 03		4
CC	C 40	G	300.00 5000.000 1000.00		1
0.11800000E + 03	0.00000000E + 00	0.00000000E + 00	0.00000000E + 00	0.00000000E + 00	2
0.2524912E + 06	−0.6164297E + 03	0.11800000E + 03	0.00000000E + 00	0.00000000E + 00	3
0.00000000E + 00	0.00000000E + 00	0.2524912E + 06	−0.6164297E + 03		4
Z	C 80	0 0	G	0300.00 5000.00 1000.00	1
0.2380000E + 03	0.00000000E + 00	0.00000000E + 00	0.00000000E + 00	0.00000000E + 00	2
0.3505288E + 06	−0.1269536E + 04	0.2380000E + 03	0.00000000E + 00	0.00000000E + 00	3
0.00000000E + 00	0.00000000E + 00	0.3505288E + 06	−0.1269536E + 04		4

continued

Table 4. Continued.

Species in the arc plasma					
Ni	GMcB 20 K 0Ni 1		G	300.000 20000.000 1000.00	1
0.36971152E + 01	−0.82867716E − 03	0.18628604E − 06	−0.11986930E − 10	0.23752778E − 15	2
0.50060051E + 05	0.72075154E + 00	0.42140643E + 01	−0.10224755E 01	0.25272825E − 04	3
−0.24064628E − 07	0.78454681E − 11	0.50323075E + 05	0.58841215E 01		4
Ni−	GMcB 20 K 0Ni 1E	−1	G	300.000 20000.000 1000.00	1
0.21013259E + 01	0.71871149E − 03	−0.11060734E − 06	0.67741068E − 11	−0.13425799E − 15	2
0.14040022E + 06	0.89762594E + 01	0.12260499E + 00	0.14956310E − 01	−0.30951078E − 04	3
0.26889803E − 07	−0.83015704E − 11	0.14047983E + 06	0.16941765E + 02		4
Y	IV 25 K 0Y 1		G	300.000 25000.000 1000.00	1
0.79437350E + 00	0.13579116E − 02	−0.12031792E − 06	0.31899976E − 11	−0.15582902E − 16	2
0.51410499E + 05	0.18158732E + 02	−0.66965149E + 01	0.65805915E − 01	−0.14851900E − 03	3
0.13342009E − 06	−0.41975353E − 10	0.51184455E − 05	0.45676826E + 02		4
Y+	0Y 1E	−1	G	300.000 25000.000 1000.00	1
0.30001765E + 01	0.19353870E 04	0.10693682E − 07	−0.93577306E 12	0.20474488E − 16	2
0.12272102E + 06	0.46280979E + 01	−0.10156546E + 02	0.94627761E 01	−0.20487420E − 03	3
0.17857051E − 06	−0.55138220E − 10	0.12325328E + 06	0.57606297E + 02		4
C+	GMcB 20 K 0C 1E	−1	G	300.000 20000.000 1000.00	1
0.25063181E + 01	0.16390834E − 05	−0.41024961E − 08	0.78583063E − 12	−0.23326192E − 16	2
0.21547022E + 06	0.43269073E + 01	0.26069164E + 01	−0.48079487E − 03	0.83960952E − 06	3
−0.64172956E 09	0.18061570E − 12	0.21545410E + 06	0.38615888E + 01		4
C_2	121286C 4E	−1	G	0300.00 5000.00 1000.00	1
0.06500180E + 02	0.04228632E 01	−0.01790717E − 04	0.03404812E − 08	−0.02403978E − 12	2
0.24662108E + 06	−0.11488894E + 02	0.02343028E + 02	0.16429811E − 01	−0.15279858E − 04	3
0.07343826E − 07	−0.15822743E − 11	0.24662184E + 06	0.09826204E + 02		4
C_3	121286C 5E	−1	G	0300.00 5000.00 1000.00	1
0.08078081E + 02	0.05743464E − 01	−0.02436405E − 04	0.04638916E − 08	−0.03278909E − 12	2
0.23886116E + 06	−0.01953023E + 03	0.02115273E + 02	0.02326331E + 00	−0.02109499E − 03	3
0.09072734E 07	−0.15400926E − 11	0.23886181E + 06	0.10976027E + 02		4
C_4	GMcB 20 K 0C 4		G	300.000 20000.000 1000.00	1
0.49032746E + 01	0.11113409E − 02	−0.75331984E − 07	−0.48099305E 12	0.89121604E − 16	2
0.11492855E + 06	0.15052816E + 00	0.36042014E + 01	0.75373711E − 02	−0.11558984E − 04	3
0.88850242E − 08	−0.25287216E − 11	0.11512688E + 06	0.61103710E + 01		4
C_5	GMcB 20 K 0C 5		G	300.000 20000.000 1000.00	1
0.11592118E + 02	0.85502931E − 03	−0.12817463E − 06	0.77473555E − 11	−0.16260603E − 15	2
0.11368121E + 06	−0.35115388E + 02	0.11731935E + 02	−0.25681572E − 01	0.78642726E − 04	3
−0.78483519E − 07	0.26116987E 10	0.11495211E + 06	−0.29295593E + 02		4
HE	120186HE 1		G	0300.00 5000.00 1000.00	1
0.02500000E + 02	0.00000000E + 00	0.00000000E + 00	0.00000000E + 00	0.00000000E + 00	2
−0.07453750E + 04	0.09153489E + 01	0.02500000E + 02	0.00000000E + 00	0.00000000E + 00	3
0.00000000E + 00	0.00000000E + 00	−0.07453750E + 04	0.09153488E + 01		4

semiconducting, depending on their chirality and diameter. The current understanding of their formation does not allow us to predict from chemical kinetics their relative abundance in a given production process. To the authors' knowledge, no one has developed a chemical kinetics model of particular types of nanotubes. Therefore, in the following models, carbon nanotubes will be treated as a single species, with no consideration of types. At present, there are several concepts of how SWCNTs form, but we will consider here only those that depend on gas phase reactions in which metal clusters are involved. It is assumed in this article that gas phase reactions govern the rate of the formation of SWCNTs and not diffusion or segregation of carbon from metal catalyst particles.

Metal catalyst clusters are formed from metals vaporized from electrodes in the arc process, from composite targets in laser ablation processes, or from decomposition of metal-containing precursor gases, such as iron pentacarbonyl in the HiPco process.

Iron Cluster Formation and Evaporation

Several authors have developed the kinetics of iron cluster formation and evaporation. Girshick and his coworkers published a series of articles on iron cluster nucleation and growth [20–26]. They used modified classical aerosol cluster theory to develop nucleation, growth, and evaporation rates. They compared plasma-generated iron atom nucleation and

cluster evolution with measurements. Their basic equations for the rates of cluster growth are given by the collision frequency. Evaporation is considered as a function of cluster size by accounting for its volume and surface tension. They expressed the net rate of change of iron monomers as

$$\frac{Dn_1}{Dt} = \frac{R}{\rho_g} - \rho_g n_1 \sum_{j=1}^{\infty} \beta_{1j} n_j + \sum_{j=2}^{\infty} (1 + \delta_{2j}) R_j^e n_j \tag{5}$$

while for dimers and all larger clusters they write

$$\frac{Dn_k}{Dt} = \frac{\rho_g}{2} \sum_{i+j=k} \beta_{ij} n_i n_j - \rho_g n_k \sum_{j=1}^{\infty} \beta_{jk} n_j + R_{k+1}^e n_{k+1} - R_k^e n_k \tag{6}$$

In these equations, R is the rate of monomer generation/depletion by chemical processes, n_j is the number of j-mers per unit mass of gas, β_{ij} is the collision frequency for i-mers with j-mers, and E_j is the evaporation coefficient. Adding the Kronecker delta δ_{2j} accounts for two monomers formed from each dimer. The collision frequency function is taken from ideal gas kinetic theory for the free molecule regime

$$\beta_{ij} = r_1^2 \left[\frac{8\pi kT}{m_i} \left(\frac{1}{i} + \frac{1}{j} \right) \right]^{1/2} \left(i^{1/3} + j^{1/3} \right)^2 \tag{7}$$

The evaporation coefficient is written

$$R_j^e = \beta_{i,j-1} n_s \exp\left(\Theta \left[j^{2/3} - (j-1)^{2/3} \right] \right) \tag{8}$$

where n_s is the equilibrium saturation number density, Θ is a dimensionless surface energy

$$\Theta = \frac{\sigma s_1}{kT} \tag{9}$$

where σ is the surface tension, and s_1 is the surface area of the monomer.

The saturation number density n_s can be calculated using the perfect gas law and the vapor pressure

$$p_s = p_s^o \exp\left(\frac{-E_s}{kT} \right) \tag{10}$$

where p_s^o is the coefficient of the vapor pressure expression.

Rate coefficients for gas phase kinetics can be derived in Arrhenius form from these expressions for β_{ij} and E_j. The evaporation rate coefficient can be expressed as

$$k_j = A_j T^{1/2} \exp\left(-\frac{E_j}{kT} \right) \tag{11}$$

where

$$E_j = \left(\sigma s_1 \left[j^{2/3} - (j-1)^{2/3} \right] - E_s \right) \tag{12}$$

and

$$A_j = r_1^2 \left[\frac{8\pi}{m_i} \left(\frac{1}{i} + \frac{1}{j} \right) \right]^{1/2} \left(i^{1/3} + j^{1/3} \right) \frac{p_s^o}{k} \tag{13}$$

The rate coefficients developed from this analysis were published for iron clusters in [27].

2.3. High-Pressure Carbon Monoxide Disproportionation Models

The high-pressure carbon monoxide (HiPco) process begins with iron pentacarbonyl diluted in carbon monoxide. This mixture is injected near room temperature into a high-temperature reactor, where it mixes rapidly with hot carbon monoxide. As the temperature increases above about 600°C, $Fe(CO)_5$ decomposes into FeCO and Fe, which then react to form dimers of iron. These iron dimers coalesce with iron atoms and other dimers to form Fe_3 and Fe_4. Coalescence continues and larger and larger clusters of iron are formed.

For modeling the HiPco reactor, Dateo et al. [28] adopted the rate coefficients of Krestinin et al. [29] for iron cluster condensation and evaporation. These coefficients are based on assumptions, such as, clusters up to $n = 4$ are considered to be in the gas phase; above that they are considered to be condensed phase with rate coefficients for reactions with smaller clusters having reached their asymptotic limit. Evaporation is assumed to be negligible for clusters larger than $n = 9$; and condensation and growth of iron clusters occurs mainly through reactions with Fe_4 and smaller clusters. The rate coefficients that they used were developed through considerations of the dependence of equilibrium constants on the formation energy and standard reduced thermodynamic potential. They accounted for the collision frequency and its dependence on size when computing the rate coefficients for cluster growth. These reactions and rates from [29] are given in Table 5.

After Krestinin et al. [29] published their results for iron cluster chemistry, Vlasov et al. [30] developed rate coefficients for iron cluster kinetics that takes into account nonequilibrium effects associated with the difference between the gas temperature and the internal temperature of the iron clusters. They made their calculations of decomposition of clusters within the framework of the statistical theory of unimolecular reactions, in which they treated only the attachment and detachment of monomers. The nonequilibrium effects are manifested by depletion of internal energy by detachment and gain of internal energy by attachment of monomers. Nonequilibrium effects are seen most vividly for clusters up to $n = 20$. After that, there seems to be a smooth variation in the equilibrium constant and rate coefficients. They plotted their equilibrium constants, decomposition rate coefficient, and recombination coefficients as functions of cluster size for temperatures from 1000 K to 3000 K in Figs. 3, 4, and 5, respectively, of their article [30]. One present author (CDS) curve fit these figures and obtained Arrhenius expressions for the rate coefficients. These coefficients for $n < 51$ are given in Table 6. For $n > 50$ the constants in these expressions can easily be extrapolated. A comparison of evaporation rate coefficients at $T = 1380$ K is given in Fig. 1; and recombination coefficients at $T = 1500$ K are given in Fig. 2. It is apparent there is a strong influence nonequilibrium effects associated with atom attachment and evaporation (Vlasov), particularly for small clusters. The recombination rates of Girshick, where classical gas kinetics governs attachment, are probably overestimated for small clusters.

2.3.1. Decomposition of $Fe(CO)_5$

There are several sources of reaction rates for $Fe(CO)_5$ decomposition. Krestinin, Smirnov, and Zaslonko [29] included a two-step decomposition scheme when simulating the decomposition of $Fe(CO)_5$ and the condensation of Fe. Their decomposition reactions are:

$$Fe(CO)_5 \rightarrow FeCO + 4CO \tag{14}$$

$$FeCO + M \rightarrow Fe + CO + M \tag{15}$$

The rate coefficient for (14) was taken from [158]. They inferred the rate coefficient for (15) from the shock tube data. Their complete reaction set is given in Table 7. Note that the formation of dimers in their scheme is allowed by the reactions

$$FeCO + FeCO \rightarrow Fe_2 + 2CO \tag{16}$$

$$FeCO + Fe \rightarrow Fe_2 + CO \tag{17}$$

Because FeCO can react to form Fe_2, the direct nucleation of Fe_2 from two Fe atoms is not required. Due to the nature of the closed shell electronic structure of Fe, it is unlikely that

Table 5. Iron carbonyl and iron cluster model of Krestinin, Smirnov, and Zaslonko [29].

	A	η	E_a/R
1. Iron carbonyl reactions			
$Fe(CO)_5 \Rightarrow FeCO + 4CO$	2.0E + 15	0.0	20130.9
$FeCO \Rightarrow Fe + CO$	6.0E + 14	0.0	10317.1
$Fe + CO + M \Rightarrow FeCO + M$	5.0E + 14	0.0	0.0
2. Fe nucleation			
$FeCO + FeCO \Rightarrow Fe_2 - CO + CO$	6.0E + 14	0.0	1006.5
$FeCO + Fe \Rightarrow Fe_2 + CO$	6.0E + 14	0.0	0.0
$Fe + Fe + M \Rightarrow Fe_2 + M$	6.0E + 14	0.0	0.0
3. Formation small clusters			
$Fe_2 + FeCO \Rightarrow Fe_3 + CO$	6.0E + 14	0.0	0.0
$Fe_3 + FeCO \Rightarrow Fe_4 + CO$	6.0E + 14	0.0	0.0
$Fe_4 + FeCO \Rightarrow Fe_5 + CO$	6.0E + 14	0.0	0.0
$Fe_2 + Fe + M \Rightarrow Fe_3 + M$	5.0E + 15	0.0	0.0
$Fe_3 + Fe \Rightarrow Fe_4$	5.0E + 11	0.0	0.0
$Fe_4 + Fe \Rightarrow Fe_5$	3.0E + 13	0.0	0.0
4. Evaporation of small clusters			
$Fe_2 + M \Rightarrow Fe + Fe + M$	1E15 (1E16)	0.0	16104.7
$Fe_3 + M \Rightarrow Fe_2 + Fe + M$	1E16 (1E17)	0.0	22143.9
$Fe_4 \Rightarrow Fe_3 + Fe$	1E13 (2E13)	0.0	27679.9
$Fe_5 \Rightarrow Fe_4 + Fe$	2E14 (7E14)	0.0	30699.5
$Fe_6 \Rightarrow Fe_5 + Fe$	2E15 (4E15)	0.0	32712.6
$Fe_7 \Rightarrow Fe_6 + Fe$	5E15 (1E16)	0.0	33719.2
$Fe_8 \Rightarrow Fe_7 + Fe$	1E16 (2E16)	0.0	34222.4
$Fe_9 \Rightarrow Fe_8 + Fe$	4E16 (4E16)	0.0	35229.0
5. Fe-atom exchange			
$Fe_2 + Fe_2 \Rightarrow Fe_3 + Fe$	3.0E + 14	0.0	0.0
$Fe_2 + Fe_3 \Rightarrow Fe_4 + Fe$	3.0E + 14	0.0	0.0
6. Coagulation of small clusters			
$Fe_3 + Fe_2 \Rightarrow Fe_4$	5.0E + 13	0.0	0.0
$Fe_2 + Fe_3 \Rightarrow Fe_5$	1.0E + 14	0.0	0.0
$Fe_2 + Fe_4 \Rightarrow Fe_6$	3.0E + 14	0.0	0.0
$Fe_3 + Fe_3 \Rightarrow Fe_6$	3.0E + 14	0.0	0.0
$Fe_3 + Fe_4 \Rightarrow Fe_7$	3.0E + 14	0.0	0.0
$Fe_4 + Fe_4 \Rightarrow Fe_8$	3.0E + 14	0.0	0.0
7. Heterogeneous reaction in the c-phase ($n >= 5$)			
$Fe + Fen \Rightarrow Fe(n + 1)$	2.3E + 13	0.0	0.0
$FeCO + Fen \Rightarrow Fe(n + 1) + CO$	2.3E + 13	0.0	0.0
$Fe_2 + Fen \Rightarrow Fe(n + 2)$	2.3E + 13	0.0	0.0
$Fe_3 + Fen \Rightarrow Fe(n + 3)$	2.3E + 13	0.0	0.0
$Fe_4 + Fen \Rightarrow Fe(n + 4)$	2.3E + 13	0.0	0.0
$Fen + Fem \Rightarrow Fe(n + m)$	k_{nm}	0.0	0.0
$k_{nm} = Z_{11}[(n^{1/3} + m^{1/3})/2]^2 [(n + m)/2nm]^{1/2}$			

two ground state atoms are likely to form Fe_2. It probably requires one or both atoms to be in excited states to achieve Fe recombination [27]. The rate coefficient for the reaction

$$Fe + Fe + M \rightarrow Fe_2 + M \tag{18}$$

given in Table 5 was inferred from shock tube data. Because formation of iron clusters is very rapid in the shock tube experiments, it is possible that reactions (16) and (17) dominate. This was discussed in [27].

Smirnov inferred iron pentacarbonyl decomposition rates from shock tube measurements [32] of absorption spectrophotometry of Fe atoms and parent molecules. Vlasov et al. [33] included them in a review of metal compound decomposition. However, there was a difference in the $Fe(CO)_5$ decomposition rate of one order of magnitude. It is not clear which rate is correct. Rumminger et al. [34] compiled a set of reactions for the inhibition of flames by iron pentacarbonyl. They included recombination reactions from Seder, Ouderkirk, and

Table 6. Rate coefficients for iron pentacarbonyl decomposition and recombination.

	High-pressure Ames[a]			High-pressure Smirnov[b]			Low-pressure (fall-off) Smirnov[b]		
Reaction	A ($cm^3\ s^{-1}\ mol^{-1}$)	η	E/R (K)	A ($cm^3\ s^{-1}\ mol^{-1}$)	η	E/R (K)	A ($cm^3\ s^{-1}\ mol^{-1}$)	η	E/R (K)
$Fe(CO)_5 \rightarrow Fe(CO)_4 + CO$	4.62×10^{20}	−1.96	21028.3	4.26×10^{20}	−1.85	20447	1.22×10^{74}	−16.78	20447
$Fe(CO)_4 + CO \rightarrow Fe(CO)_5$[c]	3.50×10^{10}	0	0						
$Fe(CO)_4 \rightarrow Fe(CO)_3 + CO$	6.96×10^{22}	−2.14	14346.3	2.85×10^{21}	−1.87	16598	2.89×10^{57}	−12.41	16598
$Fe(CO)_3 + CO \rightarrow Fe(CO)_4$[c]	1.30×10^{13}	0	0						
$Fe(CO)_3 \rightarrow Fe(CO)_2 + CO$	8.70×10^{19}	−1.58	14679.8	2.09×10^{21}	−1.85	17921	2.10×10^{67}	−9.11	17921
$Fe(CO)_2 + CO \rightarrow Fe(CO)_3$[c]	1.80×10^{13}	0	0						
$Fe(CO)_2 \rightarrow FeCO + CO$	3.96×10^{21}	−2.29	18799.4	4.07×10^{19}	−1.46	13110	7.92×10^{53}	−5.4	13110
$FeCO + CO \rightarrow Fe(CO)_2$[c]	1.50×10^{13}	0	0						
$FeCO + M \rightarrow Fe + CO + M$	4.87×10^{19}	−0.90	2874.5	1.073×10^{23}	−2.6	6495	1.073×10^{23}	−2.6	6495
$Fe + CO + M \rightarrow FeCO + M$[d]	1.00×10^{15}	0	0						

[a] Ref. [28].
[b] Ref. [32].
[c] Ref. [35].
[d] Ref. [34].

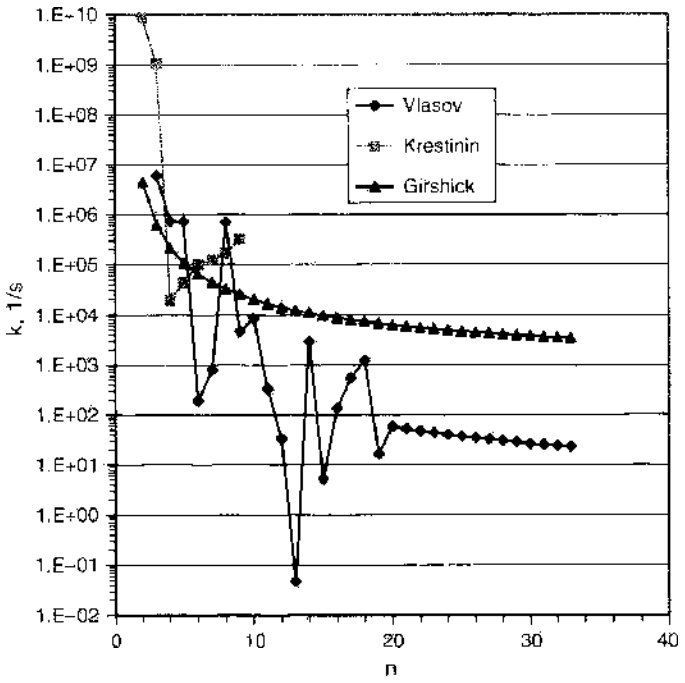

Figure 1. Comparison of iron cluster evaporation rate coefficients at 1380 K versus number of atoms in nickel clusters.

Weitz [35]. Using more recent bond energy measurements from Sunderlin et al. [36] and accurate *ab initio* calculations of Ricca [37], Dateo et al. [28] calculated the equilibrium constants for decomposition/recombination reactions of $Fe(CO)_n$. With the association rates of Seder et al. [37], they calculated the dissociation rates that are denoted "Ames" in Table 7. Because the HiPco reactor that they modeled is at many atmospheres pressure, they did not give rate coefficients for the low-pressure fall-off regime. Rate coefficients for the iron carbonyl dissociation reactions of Smirnov [32] are also given in Table 7.

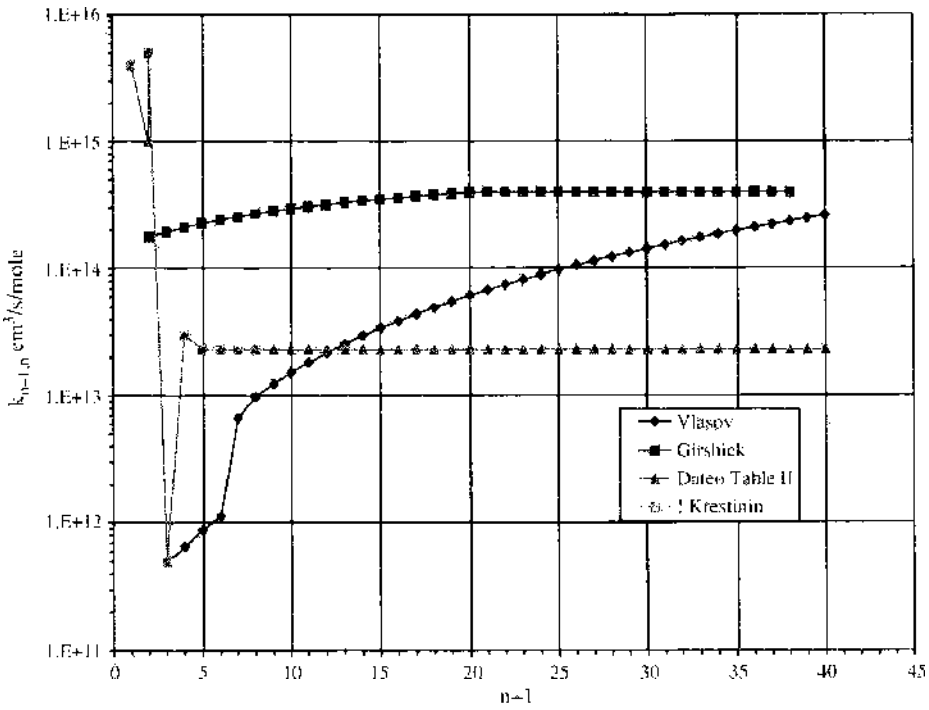

Figure 2. Iron cluster recombination rates at 1500 K. Iron atoms attaching to clusters of size $n - 1$ forming clusters of n-atoms.

Table 7. Fits to Vlasov Fig. 5 recombination rates.

	A	η	E_a/R
$Fe_3 + Fe \Rightarrow Fe_4$	1.28E + 10	0.5	0
$Fe_4 + Fe \Rightarrow Fe_5$	1.70E + 10	0.5	0
$Fe_5 + Fe \Rightarrow Fe_6$	2.24E + 10	0.5	0
$Fe_6 + Fe \Rightarrow Fe_7$	2.89E + 10	0.5	0
$Fe_7 + Fe \Rightarrow Fe_8$	1.73E + 11	0.5	0
$Fe_8 + Fe \Rightarrow Fe_9$	2.53E + 11	0.5	0
$Fe_9 + Fe \Rightarrow Fe_{10}$	3.18E + 11	0.5	0
$Fe_{10} + Fe \Rightarrow Fe_{11}$	3.90E + 11	0.5	0
$Fe_{11} + Fe \Rightarrow Fe_{12}$	4.71E + 11	0.5	0
$Fe_{12} + Fe \Rightarrow Fe_{13}$	5.60E + 11	0.5	0
$Fe_{13} + Fe \Rightarrow Fe_{14}$	6.57E + 11	0.5	0
$Fe_{14} + Fe \Rightarrow Fe_{15}$	7.63E + 11	0.5	0
$Fe_{15} + Fe \Rightarrow Fe_{16}$	8.77E + 11	0.5	0
$Fe_{16} + Fe \Rightarrow Fe_{17}$	1.00E + 12	0.5	0
$Fe_{17} + Fe \Rightarrow Fe_{18}$	1.13E + 12	0.5	0
$Fe_{18} + Fe \Rightarrow Fe_{19}$	1.27E + 12	0.5	0
$Fe_{19} + Fe \Rightarrow Fe_{20}$	1.42E + 12	0.5	0
$Fe_{20} + Fe \Rightarrow Fe_{21}$	1.58E + 12	0.5	0
$Fe_{21} + Fe \Rightarrow Fe_{22}$	1.74E + 12	0.5	0
$Fe_{22} + Fe \Rightarrow Fe_{23}$	1.92E + 12	0.5	0
$Fe_{23} + Fe \Rightarrow Fe_{24}$	2.11E + 12	0.5	0
$Fe_{24} + Fe \Rightarrow Fe_{25}$	2.30E + 12	0.5	0
$Fe_{25} + Fe \Rightarrow Fe_{26}$	2.50E + 12	0.5	0
$Fe_{26} + Fe \Rightarrow Fe_{27}$	2.72E + 12	0.5	0
$Fe_{27} + Fe \Rightarrow Fe_{28}$	2.94E + 12	0.5	0
$Fe_{28} + Fe \Rightarrow Fe_{29}$	3.17E + 12	0.5	0
$Fe_{29} + Fe \Rightarrow Fe_{30}$	3.41E + 12	0.5	0
$Fe_{30} + Fe \Rightarrow Fe_{31}$	3.66E + 12	0.5	0
$Fe_{31} + Fe \Rightarrow Fe_{32}$	3.92E + 12	0.5	0
$Fe_{32} + Fe \Rightarrow Fe_{33}$	4.19E + 12	0.5	0
$Fe_{33} + Fe \Rightarrow Fe_{34}$	4.47E + 12	0.5	0
$Fe_{34} + Fe \Rightarrow Fe_{35}$	4.76E + 12	0.5	0
$Fe_{35} + Fe \Rightarrow Fe_{36}$	5.06E + 12	0.5	0
$Fe_{36} + Fe \Rightarrow Fe_{37}$	5.37E + 12	0.5	0
$Fe_{37} + Fe \Rightarrow Fe_{38}$	5.69E + 12	0.5	0
$Fe_{38} + Fe \Rightarrow Fe_{39}$	6.01E + 12	0.5	0
$Fe_{39} + Fe \Rightarrow Fe_{40}$	6.35E + 12	0.5	0
$Fe_{40} + Fe \Rightarrow Fe_{41}$	6.70E + 12	0.5	0
$Fe_{41} + Fe \Rightarrow Fe_{42}$	7.06E + 12	0.5	0
$Fe_{42} + Fe \Rightarrow Fe_{43}$	7.43E + 12	0.5	0
$Fe_{43} + Fe \Rightarrow Fe_{44}$	7.81E + 12	0.5	0
$Fe_{44} + Fe \Rightarrow Fe_{45}$	8.19E + 12	0.5	0
$Fe_{45} + Fe \Rightarrow Fe_{46}$	8.59E + 12	0.5	0
$Fe_{46} + Fe \Rightarrow Fe_{47}$	9.00E + 12	0.5	0
$Fe_{47} + Fe \Rightarrow Fe_{48}$	9.42E + 12	0.5	0
$Fe_{48} + Fe \Rightarrow Fe_{49}$	9.85E + 12	0.5	0
$Fe_{49} + Fe \Rightarrow Fe_{50}$	1.03E + 13	0.5	0
$Fe_{50} + Fe \Rightarrow Fe_{51}$	1.07E + 13	0.5	0
Fits to Vlasov evaporation rates			
$Fe_4 \Rightarrow Fe_3 + Fe$	4.255E + 13	0	24660
$Fe_5 \Rightarrow Fe_4 + Fe$	4.323E + 13	0	24720
$Fe_6 \Rightarrow Fe_5 + Fe$	4.574E + 13	0	36140
$Fe_7 \Rightarrow Fe_6 + Fe$	5.287E + 13	0	34380
$Fe_8 \Rightarrow Fe_7 + Fe$	5.196E + 13	0	25020
$Fe_9 \Rightarrow Fe_8 + Fe$	5.562E + 13	0	31990
$Fe_{10} \Rightarrow Fe_9 + Fe$	5.859E + 13	0	31250
$Fe_{11} \Rightarrow Fe_{10} + Fe$	7.06E + 13	0	35970
$Fe_{12} \Rightarrow Fe_{11} + Fe$	5.095E + 13	0	38700
$Fe_{13} \Rightarrow Fe_{12} + Fe$	5.875E + 13	0	47040
$Fe_{14} \Rightarrow Fe_{13} + Fe$	6.321E + 13	0	32840
$Fe_{15} \Rightarrow Fe_{14} + Fe$	6.45E + 13	0	41610

continued

Table 7. Continued.

	A	η	E_a/R
$Fe_{16} \Rightarrow Fe_{15} + Fe$	6.178E + 13	0	37050
$Fe_{17} \Rightarrow Fe_{16} + Fe$	7.468E + 13	0	35380
$Fe_{18} \Rightarrow Fe_{17} + Fe$	6.98E + 13	0	34180
$Fe_{19} \Rightarrow Fe_{18} + Fe$	7.509E + 13	0	40220
$Fe_{20} \Rightarrow Fe_{19} + Fe$	7.076E + 13	0	38380
$Fe_{21} \Rightarrow Fe_{20} + Fe$	7.40298E + 13	0	38617.6229
$Fe_{22} \Rightarrow Fe_{21} + Fe$	7.59216E + 13	0	38769.36455
$Fe_{23} \Rightarrow Fe_{22} + Fe$	7.78134E + 13	0	38914.9169
$Fe_{24} \Rightarrow Fe_{23} + Fe$	7.97052E + 13	0	39054.78564
$Fe_{25} \Rightarrow Fe_{24} + Fe$	8.1109E + 13	0	39206
$Fe_{26} \Rightarrow Fe_{25} + Fe$	8.34888E + 13	0	39319.20281
$Fe_{27} \Rightarrow Fe_{26} + Fe$	8.53806E + 13	0	39444.49644
$Fe_{28} \Rightarrow Fe_{27} + Fe$	8.72724E + 13	0	39565.61064
$Fe_{29} \Rightarrow Fe_{28} + Fe$	8.91642E + 13	0	39682.82685
$Fe_{30} \Rightarrow Fe_{29} + Fe$	9.1372E + 13	0	39856
$Fe_{31} \Rightarrow Fe_{30} + Fe$	9.29478E + 13	0	39906.55531
$Fe_{32} \Rightarrow Fe_{31} + Fe$	9.48396E + 13	0	40013.50488
$Fe_{33} \Rightarrow Fe_{32} + Fe$	9.67314E + 13	0	40117.43669
$Fe_{34} \Rightarrow Fe_{33} + Fe$	9.86232E + 13	0	40218.52357
$Fe_{35} \Rightarrow Fe_{34} + Fe$	1.0377E + 14	0	40423
$Fe_{36} \Rightarrow Fe_{35} + Fe$	1.02407E + 14	0	40412.78232
$Fe_{37} \Rightarrow Fe_{36} + Fe$	1.04299E + 14	0	40506.23296
$Fe_{38} \Rightarrow Fe_{37} + Fe$	1.0619E + 14	0	40597.39881
$Fe_{39} \Rightarrow Fe_{38} + Fe$	1.08082E + 14	0	40686.39369
$Fe_{40} \Rightarrow Fe_{39} + Fe$	1.09974E + 14	0	40773.32304
$Fe_{41} \Rightarrow Fe_{40} + Fe$	1.11866E + 14	0	40858.28466
$Fe_{42} \Rightarrow Fe_{41} + Fe$	1.13758E + 14	0	40941.36951
$Fe_{43} \Rightarrow Fe_{42} + Fe$	1.15649E + 14	0	41022.66227
$Fe_{44} \Rightarrow Fe_{43} + Fe$	1.17541E + 14	0	41102.24195
$Fe_{45} \Rightarrow Fe_{44} + Fe$	1.19433E + 14	0	41180.18238
$Fe_{46} \Rightarrow Fe_{45} + Fe$	1.21325E + 14	0	41256.55265
$Fe_{47} \Rightarrow Fe_{46} + Fe$	1.23217E + 14	0	41331.41751
$Fe_{48} \Rightarrow Fe_{47} + Fe$	1.25108E + 14	0	41404.83774
$Fe_{49} \Rightarrow Fe_{48} + Fe$	1.2529E + 14	0	41377
$Fe_{50} \Rightarrow Fe_{49} + Fe$	1.28892E + 14	0	41547.56942

Iron clusters are formed from FeCO and Fe combining and agglomerating. Krestinin et al. [29] developed a set of iron cluster reactions and thermodynamic data. Their reactions and rate coefficients are given in Table 5. They contend that due to low pressure, FeCO decomposition is controlled by the bimolecular activation step. Thus, the rate of decomposition of FeCO is commensurate with the reactions

$$FeCO + FeCO \Rightarrow Fe_2 + CO + CO \tag{19}$$

$$FeCO + Fe \Rightarrow Fe_2 + CO \tag{20}$$

Because of this, Fe_2 and larger clusters are produced in large quantities during FeCO decomposition. Therefore, it is not necessary that direct formation of Fe_2 nucleation occur via Fe-atom recombination. Further growth of iron clusters is dominated by coagulation of these clusters. Evaporation of small clusters was estimated based on classical theory. However, These rates did not lead to good agreement with measurements. Therefore, they were adjusted as given in Table 5. The original rate coefficients are given in parentheses.

2.3.2. CO Attachment to Iron Clusters

In the development of the model for the high-pressure carbon monoxide reactor, Dateo et al. [28] assumed that CO attaches to iron clusters beginning at Fe_{10}. There is some data [38, 39] that suggests that CO will attach to smaller clusters and may attach to larger clusters in greater numbers. However, multiple bonding of CO probably does not alter significantly the rate of production of carbon nanotubes (Boudouard reaction). To keep their model simpler, only Fe_nCO are considered for $n > 9$ and no multiple attachments of CO to the

clusters. This reaction forms the first of a three-step model for the production of carbon nanotubes.

2.3.3. Formation of Carbon Nanotube Reactions

The second of the three steps for the formation of carbon nanotubes in the Dateo model is detachment of CO from Fe_nCO. The final step is the conversion of Fe_nCO to a carbon nanotube.

$$Fe_nCO + CO \rightarrow \beta Fe_nC_{NT} + \frac{1+\beta}{2}CO_2 + (1-\beta)Fe_nCO \tag{21}$$

where $\beta = 1/(2n_{NT} - 1)$ and n_{NT} is the average number of carbon atoms in a carbon nanotube formed in Fe_n-C_{NT}. In the calculations of Dateo et al. [28], they let $n_{NT} = 3000$. In the calculations of Scott et al. [27], they let $n_{NT} = 999$ due to a limitation in the input format of CHEMKIN [40].

2.3.4. Inerting or "Death" of Clusters

Daniel Colbert, while at Rice University, suggested that carbon nanotubes stop growing due to lack of iron clusters or due to carbonizing of the iron cluster to which the nanotube is attached during growth. Iron clusters may become overcoated with carbon that blocks the formation of nanotubes. This results in their "death" as a useful catalyst, and nanotube growth stops. To account for this possibility, the following two types of reactions are included in the Dateo model

$$Fe_n \rightarrow Fe_n^* \tag{22}$$

$$Fe_nC_{NT} \rightarrow Fe_n^*C_{NT} \tag{23}$$

Fe_n^* and $Fe_n^*C_{NT}$ are clusters and nanotubes that have been poisoned with carbon to the extent that they cannot catalyze the reactions and cease to grow. The HiPco reaction model of Dateo et al. [28] is summarized in Table 8.

Table 8. Full iron pentacarbonyl and iron cluster HiPco model of Dateo et al. [28].

	A ($cm^3\ s^{-1}\ mol^{-1}$)	η	E_a/k (K)
Thermal decomposition and formation of small iron clusters from FeCO fragment reaction			
1. Ames carbonyl rates			
$Fe(CO)_5 \Rightarrow Fe(CO)_4 + CO$	4.620E + 20	−1.96	21028.30
$Fe(CO)_4 + CO \Rightarrow Fe(CO)_5$	3.500E + 10	0.00	0.00
$Fe(CO)_4 \Rightarrow Fe(CO)_3 + CO$	6.960E + 22	−2.14	14346.30
$Fe(CO)_3 + CO \Rightarrow Fe(CO)_4$	1.300E + 13	0.00	0.00
$Fe(CO)_3 \Rightarrow Fe(CO)_2 + CO$	8.700E + 19	−1.58	14679.80
$Fe(CO)_2 + CO \Rightarrow Fe(CO)_3$	1.800E + 13	0.00	0.00
$Fe(CO)_2 \rightarrow FeCO + CO$	3.960E + 21	−2.29	18799.40
$FeCO + CO \rightarrow Fe(CO)_2$	1.500E + 13	0.00	0.00
$FeCO + M \Rightarrow Fe + CO + M$	4.870E + 19	−0.90	2874.50
$Fe + CO + M \Rightarrow FeCO + M$	1.000E + 15	0	0
2. Formation and growth of small iron clusters			
Krestinin			
$Fe + Fe + M \Rightarrow Fe_2 + M$	4.00E + 15	0	0
$Fe_2 + Fe(+M) \Rightarrow Fe_3(+M)$	5.00E + 15	0	0
Krestinin recombination rates			
$Fe_3 + Fe \Rightarrow Fe_4$	5.10E + 11	0	0.00E + 00
$Fe_4 + Fe \Rightarrow Fe_5$	3.00E + 13	0	0.00E + 00
$Fe_5 + Fe \Rightarrow Fe_6$	1.10E + 12	0	0.00E + 00
$Fe_6 + Fe \Rightarrow Fe_7$	1.50E + 12	0	0.00E + 00
$Fe_7 + Fe \Rightarrow Fe_8$	7.90E + 12	0	0.00E + 00
$Fe_8 + Fe \Rightarrow Fe_9$	1.00E + 13	0	0.00E + 00
$Fe_9 + Fe \Rightarrow Fe_{10}$	1.30E + 13	0	0.00E + 00

continued

Table 8. Continued.

3. Thermal decomposition of small iron clusters				
Krestinin				
$Fe_2 + M \rightarrow Fe + Fe + M$	1.00E + 15	0	16102.93	
$Fe_3 + M \rightarrow Fe_2 + Fe + M$	1.00E + 16	0	22141.54	
$Fe_4 \Rightarrow Fe_3 + Fe$	1.00E + 13	0	27676.92	
$Fe_5 \Rightarrow Fe_4 + Fe$	2.00E + 14	0	30696.22	
$Fe_6 \Rightarrow Fe_5 + Fe$	2.00E + 15	0	32709.09	
$Fe_7 \Rightarrow Fe_6 + Fe$	5.00E + 15	0	33715.52	
$Fe_8 \Rightarrow Fe_7 + Fe$	1.00E + 16	0	34218.74	
$Fe_9 \Rightarrow Fe_8 + Fe$	4.00E + 16	0	35225.17	
4. Coagulation of small iron clusters				
$Fe_2 + Fe_2 \Rightarrow Fe_4$	5.00E + 13	0	0	
$Fe_2 + Fe_3 \Rightarrow Fe_5$	1.00E + 14	0	0	
$Fe_2 + Fe_2 \Rightarrow Fe_3 + Fe$	3.00E + 14	0	0	
$Fe_2 + Fe_3 \Rightarrow Fe_4 + Fe$	3.00E + 14	0	0	
$Fe_2 + Fe_4 \Rightarrow Fe_6$	3.00E + 14	0	0	
$Fe_3 + Fe_3 \Rightarrow Fe_6$	3.00E + 14	0	0	
$Fe_3 + Fe_4 \Rightarrow Fe_7$	3.00E + 14	0	0	
$Fe_4 + Fe_4 \Rightarrow Fe_8$	3.00E + 14	0	0	
$Fe_2 + Fe_5 \Rightarrow Fe_7$	2.30E + 13	0	0	
$Fe_2 + Fe_6 \Rightarrow Fe_8$	2.30E + 13	0	0	
5. Coagulation of larger clusters				
$Fe_n + Fe \Rightarrow Fe_{n+1}$	2.30E + 13	0	0	$9 < n < 200$
$Fe_n + Fe_2 \Rightarrow Fe_{n+2}$	2.30E + 13	0	0	$9 < n < 199$
$Fe_n + Fe_3 \Rightarrow Fe_{n+3}$	2.30E + 13	0	0	$9 < n < 198$
$Fe_n + Fe_4 \Rightarrow Fe_{n+4}$	2.30E + 13	0	0	$9 < n < 197$
6. Attachment of CO to iron clusters				
$Fe_n + CO \Rightarrow Fe_nCO$	1.00E + 13	0	0	$9 < n < 201$
7. Desorption of CO from clusters				
$Fe_nCO \Rightarrow Fe_n + CO$	1.00E + 15	0	16000	$9 < n < 201$
8. Formation of SWCNTs				
$Fe_nCO + CO \Rightarrow \beta FenC_{NT} + (1 + \beta)/2CO_2 + (1 - \beta)Fe_nCO$	1.00E + 16	0	12500	$9 < n < 201$
9. End of growth of nanotubes (overcoating)				
$Fe_nCNT \Rightarrow DFe_nC_{NT}$	1.00E + 00	0	0	$9 < n < 201$
10. End of catalyst effectiveness				
$Fe_n \Rightarrow DFe_n$	1.00E + 03	0	0	$9 < n < 201$

$\beta = 1/(2n_{NT} - 1)$, $n_{NT} = 3000$ in Dateo et al. [28].

2.3.5. Reduced HiPco Model

The full model of Table 8 is very large, having 971 species and 1948 reactions. To simplify the model and make it useable in a 2D CFD code, Dateo et al. [28] collapsed or lumped all the iron clusters having $n > 2$ into a single representative cluster Fe_C. They also collapsed the other clusters as well, leaving the following 14 species: iron carbonyls [$Fe(CO)_5$, $Fe(CO)_4$, $Fe(CO)_3$, $Fe(CO)_2$, and FeCO], CO, CO_2, Fe, Fe_2, Fe_C, Fe_C·CO, Fe_CC_{NT}, Fe_C^*, and $Fe_C^*C_{NT}$. Their reduced model, listed in Table 9, has only 22 reactions.

2.4. Carbon Vapor Models of Carbon Nanotube Formation

Carbon vapor models are required for processes that start from vaporized carbon such as in laser ablation processes and the arc vaporization process. These processes, and how these models can be applied to them, are described in more detail in the subchapters of this chapter. Single-wall carbon nanotubes require a feedstock of carbon vapor plus vaporized metal catalysts. From this feedstock, clusters of carbon and nickel condense to form SWCNTs and impurities, such as soot and carbon-coated metal clusters. The general concepts of SWCNT formation fall into two or three categories. In order to form carbon nanotubes, it is necessary for the carbon to be catalyzed by nickel and other metals. Nucleation and growth of carbon nanotubes are not well understood; and there are many possible scenarios for

Table 9. Reduced iron pentacarbonyl and iron cluster HiPco model of Dateo et al. [28].

	A	η	E_a/k
1. Thermal decomposition and formation of small iron clusters from FeCO fragment			
Ames carbonyl rates			
$Fe(CO)_5 \Rightarrow Fe(CO)_4 + CO$	4.620E + 20	−1.96	21028.30
$Fe(CO)_4 + CO \Rightarrow Fe(CO)_5$	3.500E + 10	0.00	0.00
$Fe(CO)_4 \Rightarrow Fe(CO)_3 + CO$	6.960E + 22	−2.14	14346.30
$Fe(CO)_3 + CO \Rightarrow Fe(CO)_4$	1.300E + 13	0.00	0.00
$Fe(CO)_3 \Rightarrow Fe(CO)_2 + CO$	8.700E + 19	−1.58	14679.80
$Fe(CO)_2 + CO \Rightarrow Fe(CO)_3$	1.800E + 13	0.00	0.00
$Fe(CO)_2 \Rightarrow FeCO + CO$	3.960E + 21	2.29	18799.40
$FeCO + CO \Rightarrow Fe(CO)_2$	1.500E + 13	0.00	0.00
$FeCO + M \Rightarrow Fe + M + CO$	4.870E + 19	−0.90	2874.50
$Fe + CO + M \Rightarrow FeCO + M$	1.00E + 15	0	
2. Growth and evaporation of iron clusters			
$Fe + Fe + M \Rightarrow Fe_2 + M$	4.00E + 15	0	0
$Fe_2 + Fe + M \Rightarrow 3\alpha Fe_C + M$	5.00E + 15	0	0
$Fe_2 + M \Rightarrow Fe + Fe + M$	1.00E + 15	0	16102.93
$Fe_2 + Fe_2 \Rightarrow 4\alpha Fe_C$	5.00E + 13	0	0
$Fe_2 + Fe \Rightarrow Fe_3$	1.00E + 14	0	0
$Fe_2 + Fe_C \Rightarrow (1 + 2\alpha)Fe_C$	3.00E + 14	0	0
3. Attachment of CO on iron clusters			
$Fe_C + CO \Rightarrow Fe_C CO$	1.00E + 13	0	0
4. Desorption of CO from clusters			
$Fe_C CO \Rightarrow Fe_C + CO$	1.00E + 15	0	16000
5. Formation of SWCNTs			
$Fe_C CO + CO \Rightarrow \beta Fe_C C_{NT} + (1 + \beta)/2CO_2 + (1 - \beta)Fe_C CO$	1.00E + 16	0	12500
6. End of growth of nanotubes			
$Fe_C C_{NT} + Fe_C \Rightarrow \beta^* DFe_C C_{NT} + (1 - \beta)Fe_C C_{NT}$	3.5E14	0	0
7. End of catalyst effectiveness			
$Fe_C \Rightarrow \alpha^* DFe_C$	1000	0	0

$\beta = 1/(2n_{NT} - 1)$, $\alpha = 1/n_C$, $\alpha^* = n_C/n_C^*$,
$\beta^* = n_C/(n_C^* - n_C)$, $n_{NT} = 3000$, $n_C = 20$, $n_C^* = 40$.

carbon and nickel to condense in a reactor and then to grow nanotubes. An early scheme, called the "scooter mechanism" was envisioned by Smalley's group at Rice University. In it, carbon was envisioned to form fragments of graphene sheets that would tend to close into fullerenes. However, nickel or other metal catalyst atoms would attach to an open edge of the carbon cluster and "scoot" or move around, holding open the end of the tube, while small carbon clusters (e.g., C_2) would attach to the nascent nanotube that would continue to grow. In this scheme, carbon would condense first, then nickel would tend to agglomerate until a cluster of nickel at the end of the nanotube is so large as to become covered with carbon or graphite and cease to allow the nanotube to grow; or the metal cluster would detach from the nanotube, thus ending its growth. This scenario is supported by the observation that laser ablation nanotubes are almost never seen attached to metal clusters. It also conforms to the tendency for carbon to agglomerate first, followed by nickel, due to the stronger carbon–carbon bond and to the higher concentration of carbon than catalysts.

Another scheme that has much support involving vaporized carbon in SWCNT production is one in which metal catalysts are envisioned to form along with carbon clusters at high temperature in the arc vaporization process. As the mixture cools, carbon precipitates out of the cluster, and the energetics and geometry favor the formation of nanotubes. This is essentially a phase change phenomenon due to cooling of a mixture, especially eutectic mixtures of nickel, cobalt, and carbon. This scheme is supported by the observation that the ends of nanotubes, particularly bundles, are sometimes seen attached to metal clusters in arc produced material. Some clusters are seen to have a number of bundles attached in sort of a "sea urchin" pattern: see Fig. 3 and Fig. 4.

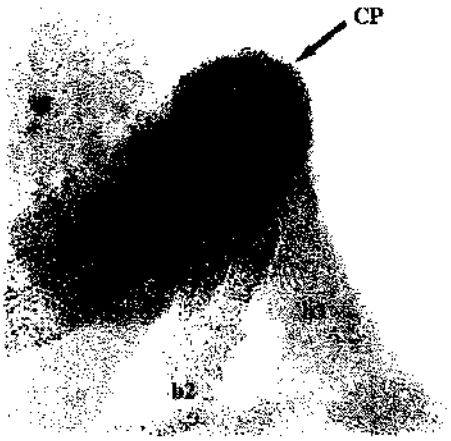

Figure 3. Nanotube bundles emanating from a nickel/cobalt catalyst particle. Courtesy A. P. Moravsky, MER Corp.

2.4.1. Nickel Cluster Nucleation and Growth

Nickel is used as a catalyst in both the laser ablation process and the arc vaporization process. Other metal catalysts that are commonly used are cobalt and yttrium. Because cobalt is a neighboring transition metal, it has similar properties to nickel. Yttrium properties are less well-known. For these reasons, only nickel will be discussed here. To assess why nickel did not produce nanotubes in the HiPco reactor, Scott and Smalley [42] tested the effect of the diatomic bond energy and the bond energy of nickel atoms with CO. The bond energy of Ni to Ni is larger than that of Fe to Fe, and also, the bond energy between CO and Ni is larger than between CO and Fe. To assess the effects of bond energies, simulations of the HiPco reactor were made using each metal as catalyst. To do the nickel catalyst simulation, it was necessary to create agglomeration and evaporation rates for nickel. The Girshick technique described in Eqs. (7)–(13) was used. The surface tension was adjusted until the activation energy for E_j equaled the Ni_2 bond energy. The activation energy for NiCO was set equal to its corresponding bond energy.

In principle, more accurate evaporation rate coefficients for small n can be calculated from the cross section data of Amentrout's group [43, 44]. They measured the dissociation of Ni atoms and small clusters from nickel clusters from $n = 2$ to 18 in a crossed beam apparatus in which they obtained collisions of the nickel clusters ions with xenon. They corrected their data for internal energy (pressure) effects; and they also suggested the following simple

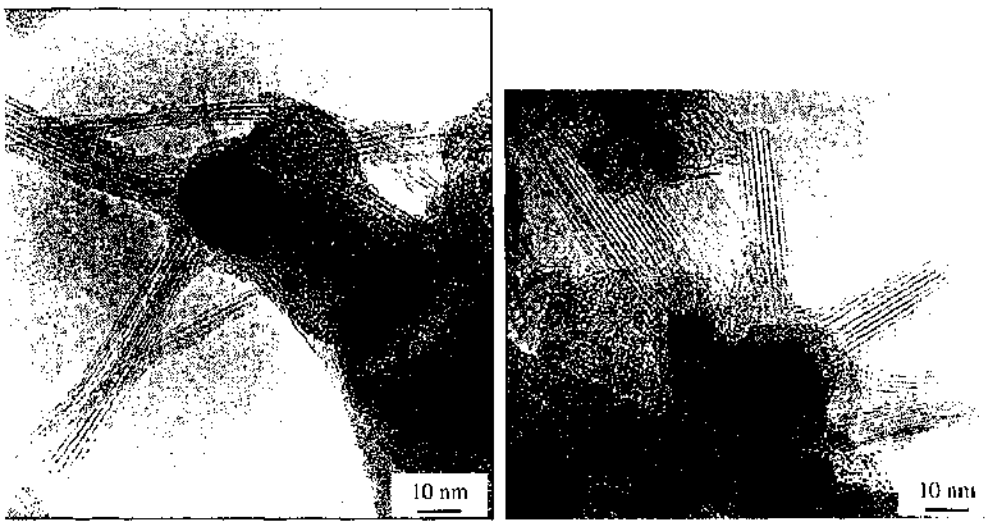

Figure 4. Nanotube bundles emanating from catalyst particles. Reprinted with permission from [41], J. Gavillet et al., *Carbon* 40, 1649 (2002). © 2002, Elsevier.

equation to fit their data.

$$\sigma(E) = \frac{\sigma_0(E - E_i - E_0)^N}{E} \tag{24}$$

where N and σ_0 are adjustable parameters, E is the relative kinetic energy, E_i is the internal energy of the cluster, and E_0 is the collision induced dissociation threshold energy. This provided an accurate and convenient formula for calculating rate coefficients from the expression

$$k_e = \frac{4}{\pi}\left(\frac{\mu}{2kT}\right)^{3/2} \int_0^\infty v^3 \exp\left[\frac{-\mu v^2}{2kT}\right]\sigma(v)\,dv \tag{25}$$

where k_e is the evaporation rate coefficient, μ is the reduced mass, $v = \sqrt{2E/\mu}$ is the relative velocity, and $\sigma(v)$ is the collision cross-section as a function of relative velocity. The main difficulty with this method is the need for the internal energy, which is not known for many clusters.

Because of the large number of possible nickel clusters, there seemed to be a need for reducing the model in some way. The option chosen [42] was to lump clusters greater than $n > 8$ into sizes 16, 32, ... 2048. We call this the "binary" model. Evaporation equations for these clusters are written

$$\mathrm{Ni}_n \rightarrow \mathrm{Ni}_{n/2} + \frac{n}{2}\mathrm{Ni} \tag{26}$$

which, in an approximate fashion, accounts for the nickel clusters not included in the model. Agglomeration rates for all nickel clusters and evaporation rate coefficients for $n \geq 16$ were determined from Girshick's method, Eqs. (7)–(13). These evaporation coefficients are given in Table 10a; and the agglomeration coefficients are given in Table 10b. The rate coefficients for $n \geq 16$ have been multiplied by n to account for the missing clusters between each n and $2n$.

2.4.2. Combined Carbon and Nickel Clusters to Form Carbon Nanotubes

One kinetics model that takes advantage of the fullerene model of Krestinin et al. was proposed by Scott [14]. The nickel model of Scott and Smalley [42] is added to the set of reactions for carbon to produce fullerenes and other large carbon clusters. Carbon and nickel clusters combine to form the nuclei for the growth of carbon nanotubes. The rates of nickel cluster formation and growth are as discussed previously, the growth of the combination carbon/nickel clusters can be obtained from the aerosol theory of Girshick as given in Eq. (7). Carbon clusters in the form of soot Z, and fullerenes C_{60} and C_{70} are assumed to be the precursors that combine to form nickel/carbon clusters, ZNi_C and $CFNi_C$. These clusters are the species that nucleate and grow nanotubes CNT. These reactions are given in Table 11. For specificity, soot is assumed to have 80 carbon atoms, while ZNi_C is assumed to have 80 carbon atoms and 1024 nickel atoms. CNT is assumed to have 999 carbon atoms. Whereas this is much fewer than in actual nanotubes, it can represent them; and the number of them will be correspondingly larger. The number 999 is purely arbitrary and can be selected to be something greater. However, in [42] it is chosen because the computer code used to solve the kinetic rate equations has a three-digit limit in the input format for number of atoms in the species definition.

2.4.3. Reduced Combined Carbon and Nickel Cluster Nanotube Scheme

As we saw in the reduced HiPco model, we can attempt to reduce the number of species and reactions by lumping most of the metal clusters as well as carbon clusters into representative clusters. Both active and inert (dead) clusters that combine the catalyst and carbon can also be lumped together into a single representative cluster. The species in this reduced model are Ar/He, C, C_2, C_3, C_r, Z (soot), C_{60}, Ni, Ni_2, Ni_3, Ni_C, ZNi_C, DZ, and $DZNi_C$. The subscript C on these symbols denote "cluster." The "D" on the symbol indicates a dead

Table 10. Nickel cluster evaporation coefficients and agglomeration coefficients.

Reaction	A ($cm^3\ s^{-1}\ mol^{-1}$)	β	E/R (K)
(a) Evaporation coefficients for $n = 32$ to 2048 based on Girshick's formulas, Eqs. (7)–(13)			
$Ni_{32} \rightarrow Ni_{16} + 16Ni$	9.38×10^{17}	−0.5	39127
$Ni_{64} \rightarrow Ni_{32} + 32Ni$	1.34×10^{18}	−0.5	40843
$Ni_{128} \rightarrow Ni_{64} + 64Ni$	1.96×10^{18}	−0.5	42194
$Ni_{256} \rightarrow Ni_{128} + 128Ni$	2.91×10^{18}	−0.5	43263
$Ni_{512} \rightarrow Ni_{256} + 256Ni$	4.36×10^{18}	−0.5	44109
$Ni_{1024} \rightarrow Ni_{512} + 512Ni$	6.61×10^{18}	−0.5	44780
$Ni_{2048} \rightarrow Ni_{1024} + 1024Ni$	1.01×10^{19}	−0.5	45312
(b) Nickel cluster agglomeration coefficients based on Girshick's formulas, Eqs. (7)–(13)			
$Ni + Ni \rightarrow Ni_2$	3.70×10^{12}	0.5	0
$Ni_2 + Ni \rightarrow Ni_3$	4.10×10^{12}	0.5	0
$Ni_3 + Ni \rightarrow Ni_4$	4.51×10^{12}	0.5	0
$Ni_4 + Ni \rightarrow Ni_5$	4.90×10^{12}	0.5	0
$Ni_5 + Ni \rightarrow Ni_6$	5.27×10^{12}	0.5	0
$Ni_6 + Ni \rightarrow Ni_7$	5.61×10^{12}	0.5	0
$Ni_7 + Ni \rightarrow Ni_8$	5.94×10^{12}	0.5	0
$Ni_2 + Ni_2 \rightarrow Ni_4$	4.16×10^{12}	0.5	0
$Ni_2 + Ni_3 \rightarrow Ni_5$	4.37×10^{12}	0.5	0
$Ni_2 + Ni_4 \rightarrow Ni_6$	4.60×10^{12}	0.5	0
$Ni_4 + Ni_3 \rightarrow Ni_6$	4.45×10^{12}	0.5	0
$Ni_3 + Ni_4 \rightarrow Ni_7$	4.59×10^{12}	0.5	0
$Ni_6 + Ni_2 \rightarrow Ni_8$	5.06×10^{12}	0.5	0
$Ni_5 + Ni_2 \rightarrow Ni_7$	4.83×10^{12}	0.5	0
$Ni_5 + Ni_3 \rightarrow Ni_8$	4.75×10^{12}	0.5	0
$Ni_4 + Ni_4 \rightarrow Ni_8$	4.67×10^{12}	0.5	0
$Ni_8 + Ni_8 \rightarrow Ni_{16}$	4.19×10^{13}	0.5	0
$Ni_{16} + Ni_{16} \rightarrow Ni_{32}$	9.41×10^{13}	0.5	0
$Ni_{32} + Ni_{32} \rightarrow Ni_{64}$	2.11×10^{14}	0.5	0
$Ni_{64} + Ni_{64} \rightarrow Ni_{128}$	4.74×10^{14}	0.5	0
$Ni_{128} + Ni_{128} \rightarrow Ni_{256}$	1.06×10^{15}	0.5	0
$Ni_{256} + Ni_{256} \rightarrow Ni_{512}$	2.39×10^{15}	0.5	0
$Ni_{512} + Ni_{512} \rightarrow Ni_{1024}$	5.36×10^{15}	0.5	0
$Ni_{1024} + Ni_{1024} \rightarrow Ni_{2048}$	1.20×10^{16}	0.5	0

particle that no longer reacts. As in the reduced HiPco model and the reduced fullerene model, the representative lumped clusters have specified numbers of atoms each just for the specificity required to satisfy element balance in the reaction.

Reaction rate coefficients may have to be adjusted slightly to make the results agree with those of the full model. This can be attempted by solving the problem parametrically, using a simple temperature and dilution profile that is representative of a given reactor or process. The reduced model for SWCNT production based on carbon vapor and metal catalysts is given in Table 12. Nickel is the metal chosen because it is most often used.

Table 11. Reactions to form nickel/carbon nuclei clusters and nanotubes.

	A	η	E/R
Nickel/carbon cluster formation			
$Z + Ni_{1024} \rightarrow ZNiC$	1.E16	0.5	0
$C_{60F} + Ni_{1024} \Rightarrow CFNiC$	1.E16	0.5	0
$C_{70F} + Ni_{1024} \rightarrow CFNiC + .1428571C_{70F}$	1.E16	0.5	0
Nanotube formation from Z and Ni			
$Z + ZNiC \Rightarrow 0.08008008008CNT + ZNiC$	1.E12	0.5	0
Nanotube formation from C_{60F}, C_{70F}, and Ni			
$C_{60F} + ZNiC \rightarrow 0.06006006006CNT + ZNiC$	1.E13	0.5	0
$C_{70F} + ZNiC \Rightarrow 0.07007007007CNT + ZNiC$	1.E13	0.5	0
Soot inerting			
$Z \Rightarrow DZ$	1.E2	0	0
$ZNiC \Rightarrow DZNiC$	1.E4	0	0

Table 12. Reduced carbon vapor/nickel catalyst model.

	A	η	E_a/k
$C + C = C_2$	2.00E + 14	0	0
$C + C_2 = C_3$	2.00E + 14	0	0
$C_2 + C_2 = C_3 + C$	2.00E + 15	0	9040
$C_3 + C = 0.100CC$	2.E + 14	0.00	0.00
$C_3 + C_2 = 0.125CC$	2.E + 14	0.00	0.00
$C_3 + C_3 = 0.150CC$	2.E + 14	0.00	0.00
Nin cluster agglomeration Rao method			
$Ni + Ni \Rightarrow Ni_2$	3.70479E + 12	0.5	0
$Ni_2 + Ni \Rightarrow Ni_3$	4.09656E + 12	0.5	0
$Ni_3 + Ni \Rightarrow 0.0039062NiC$	4.51E + 12	0.5	0
$Ni_3 + Ni_2 \Rightarrow 0.0048828NiC$	4.37E + 12	0.5	0
$Ni_3 + Ni_3 \Rightarrow 0.0058593NiC$	4.45E + 12	0.5	0
$Ni + NiC \Rightarrow 1.0009766NiC$	8.04E + 13	0.5	0
$Ni_2 + NiC \Rightarrow 1.0019531NiC$	5.96E + 13	0.5	0
$Ni_3 + NiC \Rightarrow 1.0029297NiC$	5.03E + 13	0.5	0
Rate estimated from WebElements Ni—Ni bond energy 203 kJ/mol			
$Ni_2 + M \Rightarrow Ni + Ni + M$	1.00E + 15	0	24476
Girshick evaporation rates with WebElements energy			
$Ni_3 \Rightarrow Ni_2 + Ni$	3.37E + 17	−0.5	28145
$NiC \Rightarrow 0.5NiC + 512Ni$	6.61E + 18	−0.5	44780
Carbon cluster agglomeration			
$CC + C = 1.025CC$	2.300E + 14	0	0
$CC + C_2 \Rightarrow 1.05CC$	2.300E + 14	0	0
$CC \Rightarrow 0.95CC + C_2$	3.2E13	0	61900
Fullerene formation			
$CC + C_3 \Rightarrow 0.70C_{60I} + C$	2.00E13	0	0
$CC + C_3 \Rightarrow 0.70C_{60F}$	4.00E + 09	0	−30196
$CC + C \Rightarrow 0.6833333C_{60I}$	2.00E13	0	0
Fullerene disintegration			
$C_{60I} \Rightarrow 1.45CC + C_2$	8.0E13	0	61900
$C_{60F} + C_3 \Rightarrow 0.7875Z$	2.00E + 13	0	10065
Soot formation			
$CC + CC \Rightarrow Z$	4.E13	0	0
$Z + C_3 = 1.0375Z$	4.E12	0	0
$Z + C_2 = 1.025Z$	4.E12	0	0
$Z + C = 1.0125Z$	4.E12	0	0
Nickel/carbon cluster evaporation			
$ZNiC \Rightarrow 0.9990234ZNiC + Ni + 0.0009766Z$	6.61E + 18	0	44780
Soot inerting			
$Z \Rightarrow DZ$	1.0E2	0	0
$ZNiC \Rightarrow DZNiC$	1.0E4	0	0
Nickel/carbon cluster formation			
$Z + NiC \Rightarrow ZNiC$	1.E16	0.5	0
Nanotube formation from Z and Ni			
$Z + ZNiC \Rightarrow 0.0800800800 8CNT + ZNiC$	1.E12	0.5	0
Nanotube formation from C60F and Ni			
$C_{60F} + ZNiC \Rightarrow 0.0600600600 6CNT + ZNiC$	1.E13	0.5	0

$CC = C_{10}$ Carbon cluster.
$Z = C_{30}$ Soot.
$NiC = Ni_{512}$ Nickel cluster.
$ZNiC = C_{30}Ni_{512}$ Nickel-Soot cluster.
$DZ = C_{30}$ Inert (dead) soot.
$DZNiC = C_{30}Ni_{512}$ Inert (dead) Nickel-soot cluster.
$C_{60I} = C_{60}$ Fullerene.

2.4.4. Results Comparing Full and Reduced Fullerene Models

To assure that a reduced model actually is capable of predicting the production of nanotubes, one can calculate both models for some representative simple cases such as a temperature profile linear in time. A comparison of the complete Krestinin et al. [7] model with the reduced fullerene model was presented in [14]. The time evolution of a carbon/nickel

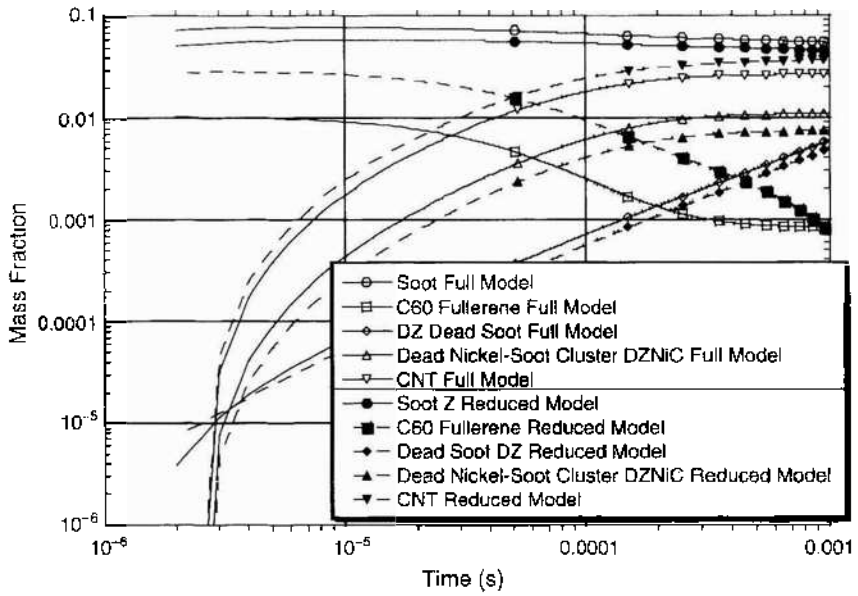

Figure 5. Carbon cluster and SWCNT production for full model (with modified rates) compared with reduced model with temperature ramp from 3500 to 1500 K in 1 μs.

vapor, with a temperature profile ramped from 3500 K to 1500 K, was calculated using a zero-dimensional code (AURORA code of CHEMKIN package [40]) for both models. The calculation of the production of carbon nanotubes and other clusters agree very well. Figures 5 and 6 show comparisons of the time evolution of various species and the production of SWCNTs. Whereas the comparison is very good (within 50%), the production of carbon nanotubes and other clusters must be compared with experiment to calibrate the rate coefficients used in the models.

The models discussed in Section 2 have been applied to various problems associated with the production of carbon nanotubes. The application of these models has taken various levels of fidelity and sophistication. Assessments of the models, particularly comparisons between full and reduced models, are given in this section. Section 3 contains results applied to the arc process, Section 4 addresses laser ablation process results, and Section 5 deals with the HiPco process. Two approaches are considered for solving the coupled fluid dynamics equations and the chemical kinetics of the models. Because complete fluid dynamics

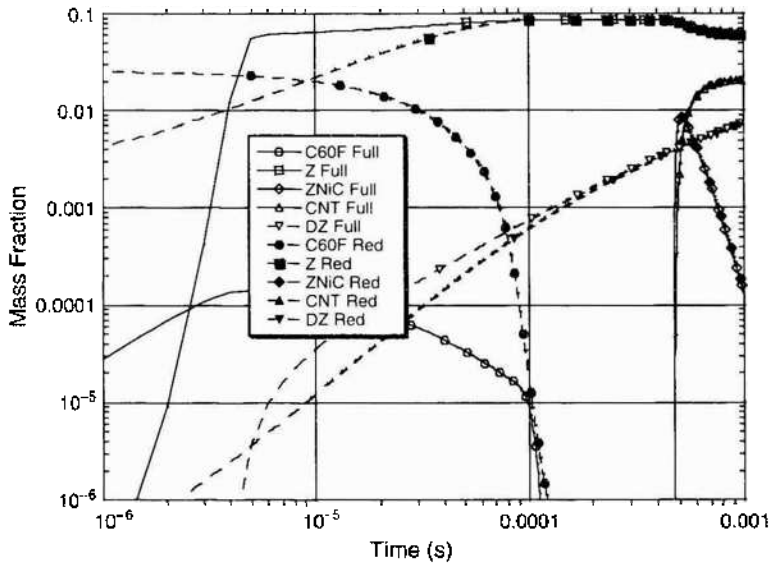

Figure 6. Comparison of cluster evolution and production of SWCNTs with full model (with modified rates) and the reduced model with temperature ramp from 3500 to 1500 K in 500 μs.

in three dimensions plus large models having hundreds of species presents a formidable computational task, we approach the solution by simplifications of two types. One is to reduce the size of the model by lumping many clusters into a single representative cluster, as in the "reduced" models. One can then use these reduced models in highly complex geometrical situations using multidimensional fluid dynamics equations. On the other hand, if high fidelity of chemical species and reactions is desired, then the chemistry and fluid dynamics solutions can be decoupled. The fluid dynamics equations are solved without chemical reactions; and then the complex chemical kinetics is developed along streak lines.

3. ANALYSIS AND MODELING OF CARBON ARC REACTORS

The arc discharge method, developed initially for fullerene synthesis [2], can also produce single-wall carbon nanotubes [45–48] by simply adding catalysts to the graphite and by changing process conditions. Compared with other synthesis techniques, the arc leads to temperatures higher than 5000 K, as measured by optical emission spectroscopy [49–51], thus insuring total and fast vaporization of graphite anode containing bimetallic catalysts in a background gas of helium [46], argon [46, 52], or mixtures of them [52, 53]. Catalysts that are commonly used are nickel and yttrium at about one to four molar percent [46]. Optimal conditions are obtained with this catalyst composition [46], for helium at a pressure of 660 mbar, and a current of 100 A. Nanotubes are collected in a soot, called "collaret," that is close to the cooled cathode. They seem to grow either in bundles or as individual tubes that coalesce readily into bundles. Laboratory scale reactors can produce up to 1 g of this collaret per 10-min batch run. The as-produced material contains nanotubes that are 1 to 1.4 nm in diameter and a few micrometers in length. Due to its relatively low cost, the arc discharge process is used to produce nanotubes commercially. Although prices are still high, they are in constant decrease. For example, the MER Corporation in the United States offers a soot synthesized by the electric arc method (Fig. 7) that contains 10% to 40% by mass of nanotubes at $50 per gram, compared with $2000 per gram a few years ago! Contrary to the competing process by chemical vapor deposition CVD in fixed [54–59] or fluidized beds [60, 61], nanotubes produced by arc are reputed to have excellent structural properties. They are quite straight and present fewer topological defects, probably because of the fast growth conditions. However, the major inconvenience of the arc process remains the presence of impurities such as catalysts and amorphous carbon mixed with the nanotubes. To take advantage of the good structural quality of nanotubes produced by arc, two solutions are possible. The first concerns the development of postsynthesis purification methods to remove these impurities. However, due to the large variety of carbon impurities (Fig. 8), such as amorphous carbon, graphitic nanoparticles, polyhedral carbon particles, onions, single-wall nanohorns (SWNHs), fullerenes, and some other forms of carbon with metal catalyst enclosed, purification is a very tedious task, and no purification technique is universally admitted today. In addition, this large variety of impurities renders the quantitative techniques developed to measure the amount of carbon nanotubes in the sample such as thermogravimetric analysis (TGA) or near-infrared (NIR) spectroscopy [62] not very reproducible. For these reasons,

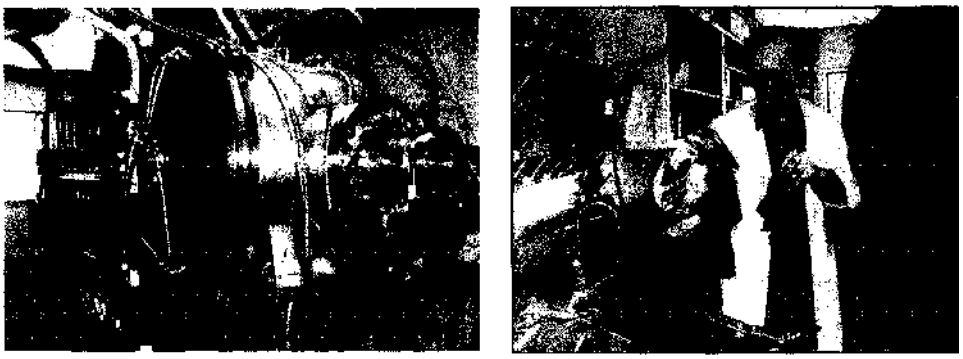

Figure 7. MER's industrial reactor of capacity ~100 g SWCNT soot per hour. On the left, it shows soot containing up to 20 wt% of nanotubes. Courtesy Alexander Moravsky.

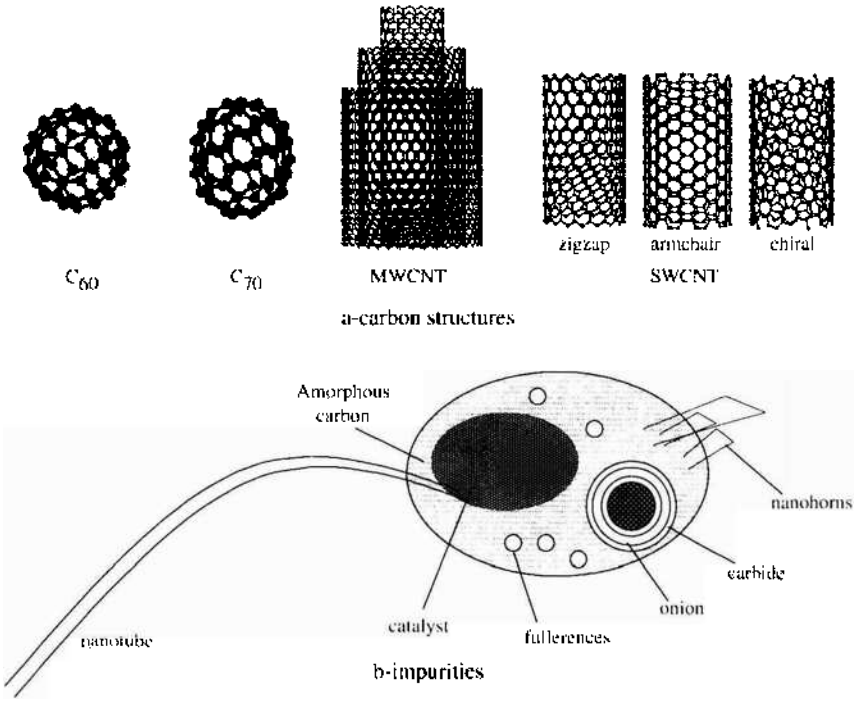

Figure 8. Schematic of (a) ideal structures and (b) impurities in the collected arc materials.

it is better to improve the process to increase nanotube yield during their formation. Hence, many experimental and theoretical studies have attempted to improve nanotube yield during arc synthesis and to provide a comprehensive understanding of the growth mechanism. For the future, there is an important challenge for scaling up, optimizing, and controlling the arc process to make it commercially viable. To perform these objectives, several experimental approaches were developed to study the effect of the different arc parameters on nanotube yield and structure. These studies were also complemented by several models, either phenomenological, to understand how and where nanotubes are formed, or macroscopic, to understand such processes as mass and heat transfer in the arc and their interconnection. When implemented into computational fluid dynamics (CFD) numerical codes, these models can predict temperature, species distribution, and fullerene yield or nanotube growth rate. In this section, we will summarize first the experimental approaches used to enhance fullerene or nanotube yield in the arc. Then, by a comparative survey of all synthesis processes, we will point out the specificity of the arc. Phenomenological models, as well as macroscopic multidimensional models at 0D, 1D, and 2D will be presented. These models were developed to predict the temperature and chemical species distributions, fullerene yield or nanotube growth rate.

3.1. Review of the Arc Process

Several laboratory-scale methods have been proposed to produce SWCNTs. Examples include condensation of laser [63, 64] vaporized carbon in the presence of catalysts, decomposition of hydrocarbons on supported [54–56], entrained [65–68] or fluidized bed catalysts, [59, 60], decomposition of carbon monoxide on supported catalysts [59], and a high-pressure technique called HiPco. This technique involving decomposition of carbon monoxide on gas phase metallo-organic carbon pentacarbonyl $Fe(CO)_5$ was developed more recently by Smalley's group at Rice University [69, 70]. Compared with these processes, the unique aspects of arc synthesis are the presence of the ions in the discharge and the formation of catalysts atoms and small carbon clusters C and C_2 at relatively high temperature. After giving a brief history of the arc, we will present in this section the uses of arc technique to produce carbon materials as fullerenes, multiwalled or single-wall carbon nanotubes. We will discuss in more detail the specific conditions of single-wall carbon nanotube formation.

3.1.1. History

Sir Humphry Davy of London, England, discovered the electric arc between two carbon electrodes in 1813. In 1844, the French physicist Léon Foucault studied physical phenomenon in the arc lamp. The first industrial use of the arc was achieved in 1862 to produce acetylene by a process developed by Marcellin Berthelot. In 1880, Louis Clerc replaced the oxygen flame for welding applications by the plasma of an electric arc. At the end of the nineteenth century, carbon arc welding (CAW) was intensively used for locomotive maintenance because the weld joints were hard and brittle due to the carbon flaking off into the weld puddle [71]. Since 1944, these discoveries opened the way to the thermal plasma synthesis of carbon materials.

The German physicist Otto Hahn obtained carbon chains when trying to create some heavy atoms by fixing neutrons during the evaporation of metals in a carbon arc. Harold Kroto and Dave Walton also observed these chains in 1970 during experiments simulating conditions of combustion in the formation of red giant stars. In 1990, fullerene synthesis was performed by Krätschmer et al. [2] (Fig. 9) of the Max Planck Institute in Heidelberg, Germany, under a helium atmosphere. One year later, in 1991, nanotubes were observed for the first time by S. Iijima [72–75] of the Japanese company NEC and by Bethune et al. [76]. Due to their unique combination of properties, nanotubes generated a lot of interest in the scientific community, and opened new fields of studies in science and technology. Since 1991, nanotube synthesis in the arc has been extensively developed and studied by several research teams around the world.

3.1.2. Experimental Approaches

Before presenting the different modeling approaches, we will briefly discuss the experimental approaches used to improve fullerene and nanotube arc processes.

3.1.3. Fullerenes versus Multiwalled Carbon Nanotubes

When the electric current is changed from direct (DC) to alternating (AC) current, nanotubes instead of fullerenes are formed in a deposit on the cathode. Hence, the arc discharge technique, first used to produce fullerenes [2], was then extended to producing multiwalled carbon nanotube [2, 77] synthesis by changing the conditions of the discharge in the same apparatus. Figure 8 illustrates ideal structures obtained in the soot. Multiwalled carbon nanotubes are formed inside a hard deposit that grows on the cathode at a speed of about 1 mm/min. They are organized in bundles with diameters between 2 and 30 nm [72, 77, 78]. Ebbesen et al. [45] and Ajayan and Iijima [77] proposed improvements in the classic process of Krätschmer and Huffmen. These studies showed that optimal growth conditions are different from of those of fullerenes. For example, the total pressure of helium is 660 mbars for nanotubes and only 200 mbars for fullerenes. The physical reason of this difference remains not very elucidated. Among the limited number of publications on this topic, we notice the work of Zhang et al. [79] on the effect of the helium pressure on the MWCNT

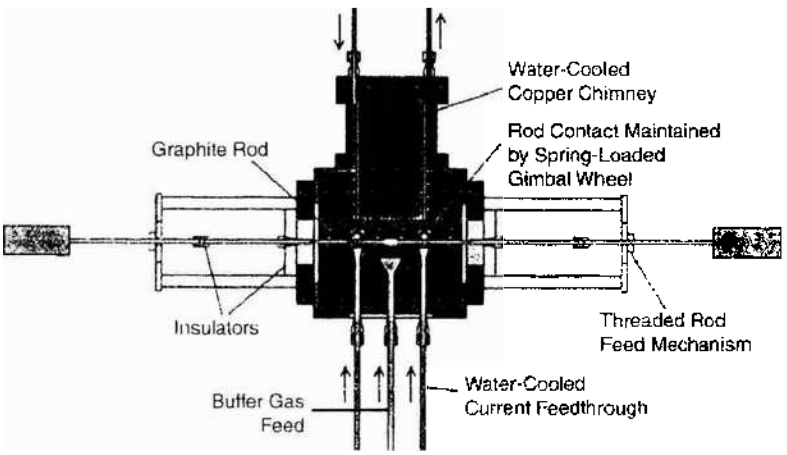

Figure 9. Krätschmer and Huffman arc reactor.

yield. They indicated that the increase in pressure enhances nanotube yield and decreases fullerene formation. Cadek et al. [80] reported a pressure of 660 mbar and a current density of 195 A/cm^2 as optimal conditions for MWCNT synthesis. Nanotube synthesis under an argon atmosphere was studied by Borisenko et al. [81] who showed that argon can improve MWCNT yield by a factor of 5–10 compared to helium in similar arc discharge conditions. A hydrogen discharge was also tested by Ando et al. [82] and Zhao et al. [83] to grow nanotubes with smaller diameters. Double-walled carbon nanotubes were produced using a mixture of argon and hydrogen by Hutchison et al. [84]. Finally, Jung et al. [85] studied the morphology and the structure of MWCNT produced in a mixed atmosphere of helium and acetylene in the arc. They noticed that the quantity of carbon nanoparticles, formed inside the cathodic deposit, increases when acetylene is added to the ambient gas. An important modification of the arc method was achieved using liquid nitrogen [85, 86] with the advantage of an easier recuperation of the products and a possible continuous synthesis. Another less efficient, but also less expensive method uses water instead liquid nitrogen [87].

3.1.4. Single-Wall Carbon Nanotubes

Single-wall carbon nanotubes were discovered by Iijima [72] in 1991 when adding iron to a graphite anode in the arc. Later, all the process parameters such as catalysts and inert gas composition, current density, pressure, gravity (orientation), and so forth, were varied to enhance nanotube yield. Several metallic particles were used as catalysts including cobalt [76], nickel [88], yttrium [89], manganese [90], scandium [91], lanthanum [92, 92], vanadium [93], cerium [94], gadolinium [95], and zirconium [92]. The presence of these catalysts leads to a large variety of metallic particles and carbides in the plasma and in the collected material. Currently, the most efficient catalyst is obtained by mixing two elements such as nickel–yttrium [46, 96], nickel–cobalt [97, 98], iron–nickel, [99, 100], or rhubidium–platinium [101]. According to Saito et al. [102], the efficiency of the Rh–Pt couple is comparable to Ni–Y. It is also noticed that these catalysts can change the diameter distributions in the interval 0.7–3 nm. On the other hand, Sugai et al. [102] used a pulsed discharge to synthesize fullerenes and SWCNTs using nickel and cobalt catalysts under an inert atmosphere of helium, argon, or krypton. Argon was found to be the best gas for fullerene production and krypton the most efficient for nanotubes. According to the authors, increasing the pulse duration increases nanotube and decreases fullerene yields, making a competition between these two kinetic pathways. The conventional electric arc is an unsteady process because of instabilities of cathodic spot. This leads to a nonhomogeneous distribution of the electric field in the plasma. The cathode spot instability results in random and erratic motion of a luminous spot along the cathode surface. Hence, Lee et al. [103] used a technique of rotation of the anode to create uniform plasma. This rotation generated a turbulence that accelerates carbon species perpendicularly to the anode. In this situation, carbon is not condensed on the surface of the cathode but collected on a graphite collector placed in the periphery of the plasma. According to the authors, increasing the speed of rotation increases nanotube yield and decreases nanotube diameter. This result was confirmed by Bae et al. [104]. Effects of gravity have been studied by Kanai et al. [105] who found that the absence of gravity forces can reduce convective fluxes of the inert gas increasing plasma volume. Consequently, the authors found an increase of the yield of nanotubes and an increase of their diameter. A key parameter for the arc is the erosion rate of the anode. This parameter depends on the input power, the chemical composition of the anode, the length of the arc, and the nature of the inert gas, the pressure, the cooling of electrodes as well as the geometry of the reactor. Not all these parameters are independent, increasing the complexity of the problem. Therefore, Zhang et al. [106] studied the dependence of the speed of erosion of the anode with the pressure and the nature of the inert gas (argon or helium). The authors found that, for low pressures between 100 and 300 mbar, the erosion rate of a pure graphite anode is lower in argon than in helium. This tendency is reversed for pressures between 300 and 900 mbar. Takizawa et al. [107] measured the quantity of soot formed in the reactor while varying the percentage of nickel and yttrium in the composition of the anode. They demonstrated that the addition of yttrium traces (0.1% at.) with the nickel increases soot yield by a factor of 2–3. This yield was not important when only nickel or yttrium was used as catalyst.

3.2. Analysis of the Arc Discharge

3.2.1. Description of the Experiment

The carbon arc apparatus consists of a static water-cooled reaction chamber with two cooled graphite rods. For the anode, a graphite rod filled with catalysts (Co, Fe, Ni, Y) is generally used. The cathode is made of pure graphite or copper. It was reported that copper does not improve the results and leads to a less-stable arc [108]. The distance between the anode and the cathode can be adjusted by moving the anode toward the cathode manually [46, 52] or automatically [49] using an optoelectronic system. A direct current (DC) for nanotube synthesis or alternating current (AC) for fullerene production passes through the electrodes, and plasma is created in the interelectrode region. Efficient operation is assumed to exist when the discharge is stable and the anode erosion rate is constant. This can be achieved by maintaining a constant voltage between the electrodes, which is closely related to the stability of the electrode spacing. The plasma is first ignited by contact between the anode and the cathode, which elevates the temperature of the contact point until evaporation of the anode material. Then, the anode is moved back to maintain a desired gap between the growing deposit on the cathode and the burning anode. An active plasma zone bounded by the deposit and the anode is created. This hot plasma zone produces carbon and catalyst vapors, which then diffuse to the cooled reactor regions. Carbon species and catalysts build up on the end of the cathode (called cathode deposit), and deposit forms a collaret around the cathode deposit. Soot is deposited on the reactor walls by free convection. The high temperature near the anode and the high energy density in the plasma insure vaporization of most of the anode material. The water-cooled cathode leads to high quench rates and high levels of super cooled or supersaturated vapor with nanotube formation. The quench process is uncontrolled, but arc products usually are soot on the reactor walls, web-like structures between the cathode and the chamber walls, a hard gray deposit at the cathode's end, and a rubber-like collaret rich in nanotubes around this deposit. Figure 10 shows scanning electron microscopy (SEM) and high-resolution transmission electron microscopy (HRTEM) micrographs of as-produced nanotubes.

3.2.2. Comparison with the High-Temperature Processes

The nanotubes produced by arc discharge are similar to those obtained in high-temperature processes such as laser or solar vaporization, and it is interesting to compare all these processes to point out the specificity of the arc. In high-temperature processes, the temperature is higher than 3500 K, permitting the total vaporization of the target or anode formed by graphite and catalyst. To achieve such high temperatures, high-energy densities are needed to atomize totally the solid and to form atoms of carbon C and catalyst M. When the temperature decreases in the cold region of the reactor, carbon reacts to form molecules of superior size and clusters composed only of carbon, such as C_2, $C_3 \ldots C_{60} \ldots$ CNT..., soot or composed of only metal as M_2, $M_3, \ldots, M_{cluster}$ or, finally, a mixture of them, C_nM_m. To understand these processes, it is necessary to quantify mass and energy fluxes at different conditions. In Table 13, a comparison of fluxes of mass and energy for the most important

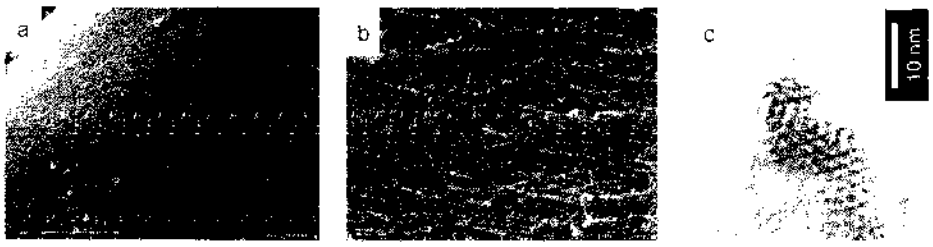

Figure 10. Micrograph of the as-produced collaret in the arc chamber: (a) and (b) are SEM micrographs at two magnifications [109] showing bundles of SWCNTs and impurities obtained with catalyst composition Ni : Y 4.2 : 1 atomic percent; (c) is a high-resolution HRTEM of the collaret produced in helium showing bundle of about 60 nanotubes. Reprinted with permission from [53], Hinkov et al, *J. Appl. Phys.* 95, 2029 (2004). © 2004, American Institute of Physics.

Table 13. Comparison of the arc process with other high-temperature processes used for SWCNT synthesis.

Process	Conditions	Energy density (W/m^2)	Vaporization flux (g/h)	Soot containing SWCNT rate (g/h)	Nanotubes (vol%)	Temperature and cooling rates
Arc discharge[a]	$I = 100$ A; $V = 38$ V $r_A = 3$ mm; $d_{AC} = 3$ mm He; $P = 660$ mbar	1.4×10^8	72	4.2	50 vol%	$T = 6500$ K Cooling rate = 7300 K/ms
	$I = 100$ A; $V = 22$ V $r_A = 3$ mm; $d_{AC} = 3$ mm Ar; $P = 100$ mbar	7.8×10^7	8	1.5	20 vol% 20 vol%	$T = 18000$ K Cooling rate = 4800 K/ms
Pulsed laser[b]	$\lambda_1 = 532$ nm $E_{pulse} = 250$–490 mJ $\nu_1 = 10$–30 Hz $\Phi_1$spot = 5–6 mm $t_{pulse} = 40$–50 ns $\lambda_2 = 1064$ nm $E_{pulse} = 300$–550 mJ $\Phi_2$spot = 6–7 mm Ar; $P = 500$ mbar	$1.3 \times 10^8 - 5.2 \times 10^8$	0.05	$3.3 \times 10^{-3} - 40 \times 10^{-3}$	60–90 vol%	Oven at 1200°C Target at 3500 K Cooling rate = 170–420 k/ms
Continious laser[c,d]	$\lambda = 10.6$ μm Φspot = 1 mm Ar; $P = 270$–530 mbar	4.3×10^8	0.1	0.13	80 vol%	Oven at 1200°C Target at 3500 K
Solar energy[e,f]	λ = sunlight Oven at 2 kW	7.4×10^6	1.77×10^{-4}	0.1	—	Target at 3550 K Cooling rate = 600 K/ms
	Power = 1300 W Φspot = 15 mm Ar; $P = 250$ mbar Oven at 50 kW He; $P = 450$ mbar Ni/Co = 2 : 2 at%	8.5×10^6	15	13	—	—

[a] Ref. [113].
[b] Ref. [63].
[c] Ref. [168].
[d] Ref. [169].
[e] Ref. [170].
[f] Ref. [171].

high-temperature processes is given. In this table, I and V are, respectively, the current and potential drop between electrodes, r_A is anode radius, d_{AC} is the distance between anode and cathode, P the pressure, λ is the laser wavelength, ν the frequency of the laser, E_{pulse} is the pulse energy, t_{pulse} is the duration between two pulses, and Φ is the laser or solar spot diameter. We notice that the arc process is by far the most efficient process in terms of erosion rate and produces 4.2 g/h of soot containing nanotubes. Nevertheless, for industrial applications, arc processes have at least two disadvantages: (1) This process is discontinuous and requires cycles of production/cleaning, (2) the nanotube concentration in the soot is relatively poor.

3.3. Specificity of the Arc

3.3.1. Specific Conditions for SWCNT Growth

Typical experimental conditions [109] for SWCNT synthesis in the arc are the following:

(i) The inert gas is helium.
(ii) The potential drop between the electrodes is $V = 40$ V.
(iii) The anode diameter $r_A = 3$ mm and the cathode diameter $r_C = 16$ mm.
(iv) The current density $j = 100$ to 350 A/cm^2.
(v) The interelectrode distance $d_{AC} = 1$ to 3 mm
(vi) The plasma = temperature ~6500 K.
(vii) The erosion rate = 70 g/h.
(viii) The pressure = 660 mbar.
(ix) The velocity of material leaving the anode as calculated by Farhat et al. [107] $u_{\text{anode}} = 78$ m/s and as estimated by Krestinin and Moravskii [7, 110], $u_{\text{anode}} = 2$ to 80 m/s for fullerene conditions.
(x) The dilution factor τ is the ratio of helium to carbon material leaving the interelectrode space: $\tau = 20$ to 30% [7, 110].
(xi) Mixing time τ_{mix} is a parameter introduced by Krestinin and Moravskii [7, 111] to measure the time that carbon material needs to be totally mixed with helium when leaving the interelectrode space: $\tau_{\text{mix}} = 2$ to 8 ms [7, 110].

Other parameters such as water flow-rate used to cool the cathode and loss by radiation from the plasma are reported in the literature [111, 112]. Gamaly and Ebbesen [113] proposed to estimate gas radiation simply from Stephan-Maxwell equation $Q_{\text{rad}} = \sigma T^4 = 5.67 \times 10^{-12}$ T^4 J/cm^2 s with T~4000 K. However, arcs are not usually optically thick. Therefore, this is not a good assumption.

3.3.2. Space Charge, Potential, and Electric Field Distributions

Space charge, potential, and electric field distributions have been described by Gamaly and Ebbesen [113] for multiwalled carbon nanotube conditions. According to them, the space distribution of the potential has a steep drop near the cathode in a region of positive space charge where practically the entire potential drop occurs, as shown in Fig. 11. They calculated this sheath length at $\Delta = 12$ μm for typical multiwalled carbon nanotube conditions with $V = 20$ V and $j = 150$ A/cm^2. This is also the distance of the main potential drop in the interelectrode region. Gamaly and Ebbesen [113] also estimated the average electric field in this region at $E = 2 \times 10^4$ V/cm and consider that the electric field in the outer region is several orders of magnitude lower.

3.3.3. Ionization State and Density of the Plasma

The interelectrode region is composed of a mixture of inert gas, carbon and catalyst atoms, and molecules. Figure 12 shows qualitatively 15 pictures of the development of the arc in the argon as the distance between the electrodes is changed. Light is emitted from atom and ion lines, as well as from C_2 and, possibly, CN molecules. The first ionization potential of some elements present in the plasma are summarized in Table 14. For a helium/carbon discharge without catalysts used for MWCNT synthesis, Gamaly and Ebbesen [113] estimated that the

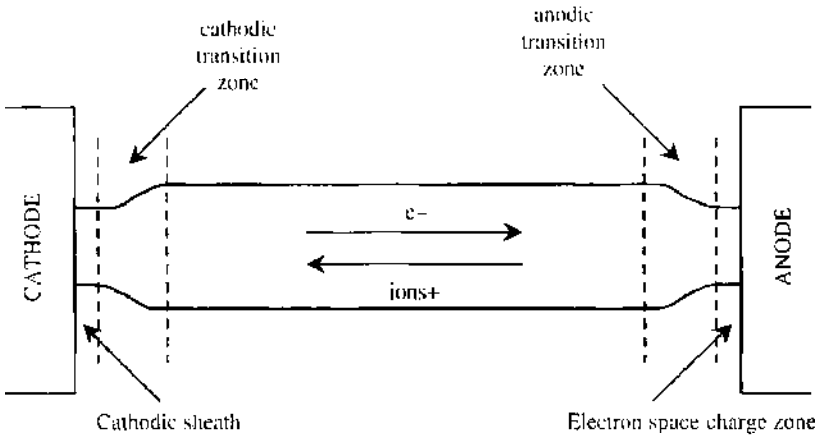

Figure 11. Space charge potential a dielectric field distribution in the arc.

carbon ion C^+ is the major ion, with the density in the plasma of $n_{C^+} = 5 \times 10^{15}$ cm^{-3} and near the cathode of $n_{C^+} = 6.9 \times 10^{13}$ cm^{-3}. The ion velocity was estimated at $v_{ion} = 1.8 \times 10^5$ cm/s. At these conditions, the flux of carbon to the cathode is 6.25×10^{19} carbon/s, and the number density of the plasma is dominated by helium with $n_{He} = 6.4 \times 10^{18}$ cm^{-3}. Nevertheless, Scott et al. found that yttrium and nickel ions are the major ions in the discharge when catalyst is added to the anode for SWCNT optimal conditions. Figures 13 and 14 show measured optical emission spectra and that calculated with the atomic emission spectroscopy Fortran program named AES and developed by J. Hornkohl of the Tennessee Space Institute.

3.4. Modeling Arc Process

After presenting the main results obtained by the analysis of the experimental arc process, we need to develop a systematic approach in order to establish a relation between nanotubes or fullerene yield and arc parameters. Before establishing such relations, it is legitimate to ask some questions.

- Where and how are nanotubes formed in the reactor and how can this perfect linear and symmetric structure be formed in such an anisotropic plasma?
- Why in the same reactor but with different conditions we obtain fullerenes C_{60} and C_{70}, MWCNT or SWCNT?

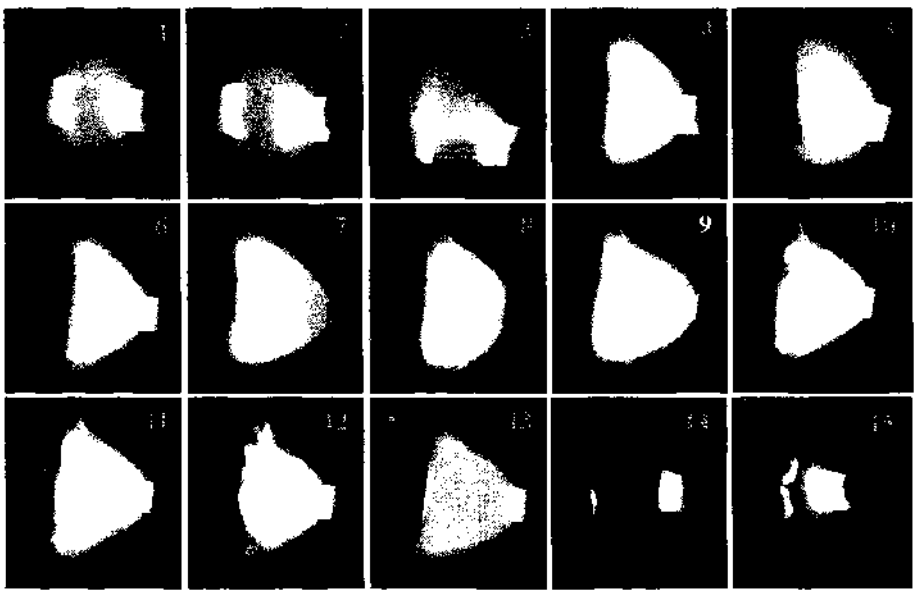

Figure 12. Development of the plasma in the interelectrode zone between the cathode on the left and the anode of 6-mm diameter on the right. Reprinted with permission from [115], I. Hinkov, Ph.D. Thesis, University Paris 13, France, 2004. © 2004.

Table 14. First ionization potential and energy of elements used in models.

	Y	Ni	C	Ar	He
First ionization potenital (ev)	6.38	7.63	11.26	15.76	24.87
Ionization energy (kJ/mol)	600	737	1086	1520	2372

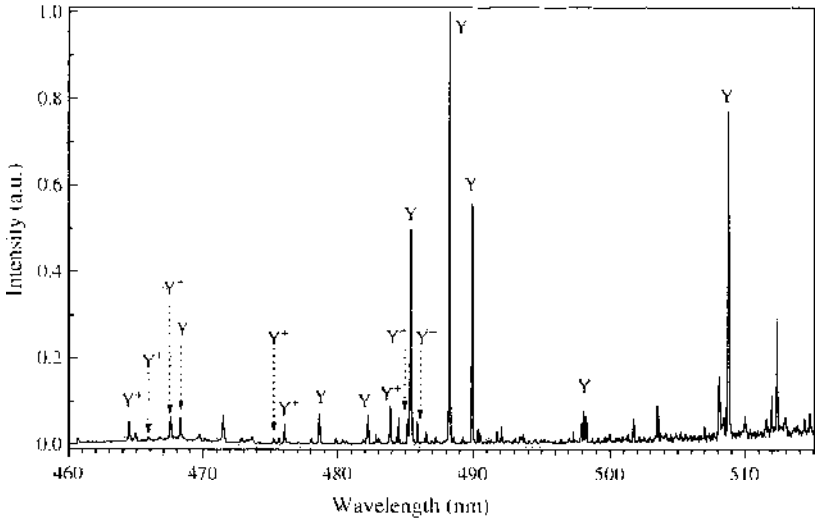

Figure 13. Measured optical emission spectra showing the predominance of yttrium ions.

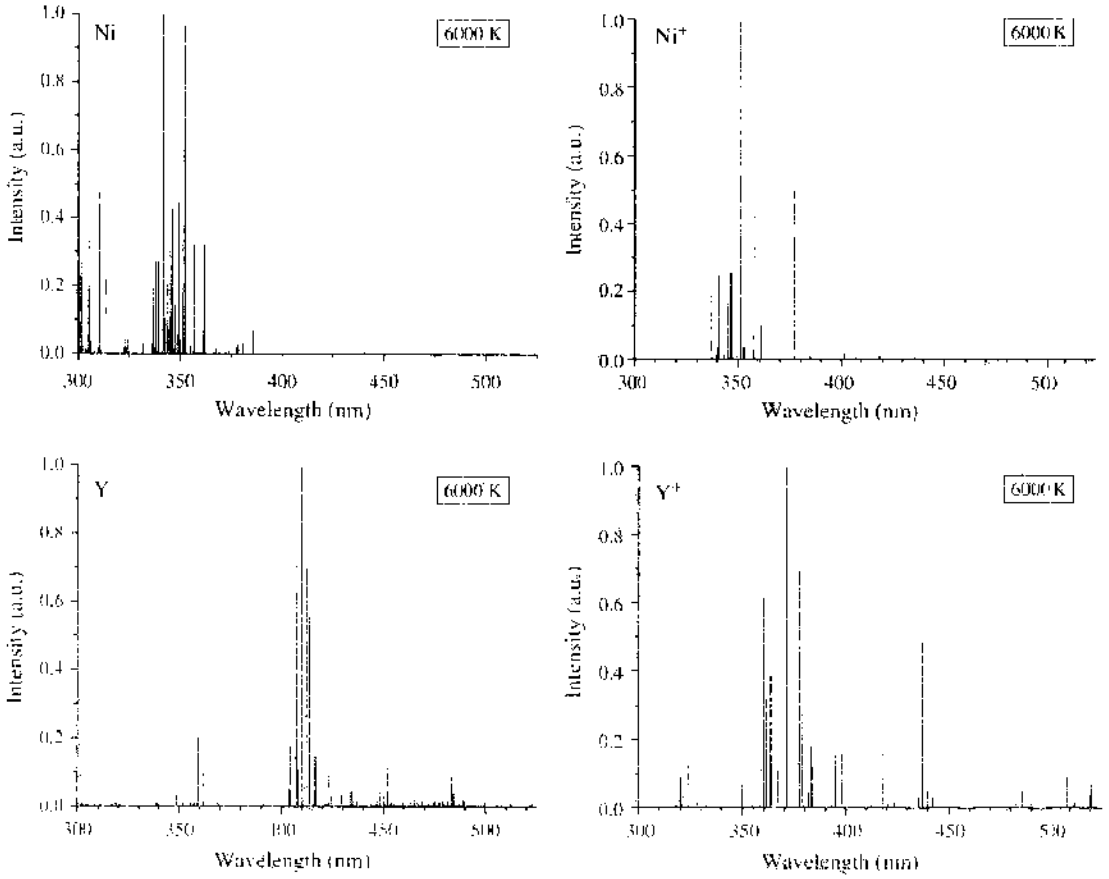

Figure 14. Calculated nickel and yttrium spectra [50].

- What are the growth precursors, and by which kinetic mechanisms are they formed and transported in the plasma? What is the role of the ions in the growth of nanotubes?
- What process parameters control this growth and how do they influence nanotube diameter and chirality?

Due to the complexity of time and space phenomena in the arc and the interconnection of several individual processes such as electric, mass, and energy transfer, answering all these questions is a difficult task without the help of modeling. Very few works are reported in the literature to determine arc characteristics in the specific conditions of fullerene or nanotube growth. We selected some approaches, developed mainly by Gamaly and Ebbesen [113] for multiwalled carbon nanotubes, Bilodeau et al. [114] and Kristinin and Moravskii [7, 110] for fullerenes, and by Hinkov [115], Scott [116], and Farhat et al. [109] for single-wall carbon nanotubes.

3.4.1. Phenomenological Growth Models

A quantitative description of nanotubes was first described by Gamaly and Ebbesen [113] based on the approximation of the distribution of density, velocity, and temperature of carbon vapors, electric charge, potential, and electric field in the arc. On this basis, the authors presented a scenario for the nanotube formation, growth, and termination in time and space scales. It is doubtful that some of the details of this model are correct. However, it points out some useful facts. Typical multiwalled nanotube conditions reported are obtained with the vaporization of pure graphite anode in a helium discharge chamber with P = 500 Torr, anode to cathode distance $d_{AC} \leq 1$ mm, a potential drop of $V = 20$ V, and a current density of $j = 150$ A/cm^2. At these conditions, average plasma temperature was assumed to be constant and ~4000 K. The deposit of area 0.5 cm^2 containing MWCNT grows at the cathode with a measured rate of 1 mm/min = 16 μm/s. Assuming the average material density of 1.5 g/cm^3, this corresponds to a flux of carbon of 1.3×10^{20} atoms cm^{-2} s^{-1} or a flow rate of 6.25×10^{19} atoms/s. At plasma temperature of 4000 K, calculated C^+ density in the plasma is $n_{C+} = 5 \times 10^{15}$ cm^{-3}, and near the cathode $n_{C+} = 6.9 \times 10^{13}$ cm^{-3}. The ion velocity was estimated at $v_{ion} = 1.8 \times 10^5$ cm/s, and the plasma is dominated by helium with $n_{He} = 6.4 \times 10^{18}$ cm^{-3}. Because the temperature of the plasma is close to the melting (4100 K) and boiling (4470 K) temperatures of graphite, carbon begins to evaporate, producing a thin layer of saturated carbon vapor near the cathode surface. By a kinetic theory calculation of the evaporation, the authors determine that the carbon vapor sheath density is $n_{vap} \sim 1.35 \times 10^{18}$ cm^{-3}, which is very close to the density of surrounding gas. The carbon vapor initially expands from the gas and forms a thin shield over the cathode surface. There the gas is cooled in a region very close to the cathode of only 2 to 3 μm in thickness having a temperature gradient of 26 K/cm. The saturated carbon is in fact diluted with helium in such way that the density after mixing is $n_{vap} \sim 4.8 \times 10^{17}$ cm^{-3}. According to the authors, the growth is due to the competitive input of two groups of carbon having different velocity distributions. The first group comes from the anode and has a Maxwellian velocity distribution. The second group is composed of ions accelerated in the gap between the positive space charge and the cathode. Due to the large difference in the first ionization potential between carbon (11.26 eV) and helium (24.87 eV), the major ion in the plasma is C^+. At a potential drop of $V = 20$ V, the ion velocity, calculated from the kinetic energy, equals 2×10^6 cm/s, which is 10 times higher than thermal velocity. The presented scenario of deposit growth consists of cycles of four events.

(1) Seed structure formation during the establishment of a steady ion current by collisions between $C^+ + C^+$ leading to C_2, which is the feedstock for the seed structure growth. The small characteristic time of C_2 formation (10^{-7}–10^{-8} s) permits forming about 10^7 seeds in a micrometer-thick layer.
(2) Mutishell tube growth during the stable stage of the discharge. Because the mean free path of carbon–carbon collisions (15 μm) is larger than the sheath thickness (2–3 μm), ions maintain perpendicular direction when moving to the cathode.
(3) Termination of tube growth is due to current instabilities caused by spot instability or spontaneous interruption and restriking of the discharge without significant changes in

external voltage or current. Another cause of the instability reported by the authors is due to the splitting of the current into thinner filaments threads that move randomly to the cathode.

(4) The tube ends are capped by a process involving the rearrangement of carbon having Maxwellian distribution in the absence of current.

Based on this model, and the assumption that the characteristic reaction time for carbon–carbon attachment is proportional to the carbon–carbon collision time, the authors estimated the time of creating a 1-μm-length tube with a diameter of 5 nm at ~0.02 s. Their conclusion is based on the qualitative agreement between the predicted time of these two groups with the experimental time ~0.07 s. Gamaly and Ebbesen pointed out the importance of cooling the cathode in reducing the velocity of carbons with Maxwellian distribution, thus reducing the perturbation amplitude and improving yield and quality of nanotubes. They finally concluded that the extremely high local field of $\sim 10^8$ V/cm as suggested by Smalley [117] to explain open-end nanotube growth is four orders of magnitude higher than their calculated average electric field of 20 V/10 mm $\sim 2 \times 10^4$ V/cm.

3.4.2. Plasma Models

The majority of the work of modeling electric arc discharge in the presence of carbon and inert gas assumed local thermodynamic equilibrium (LTE) [7, 109, 110, 113, 114, 118]. This assumption consists of considering a unique temperature to represent the plasma. Thus, the temperature of electrons T_e, ions T_i, and atoms and neutral molecules of the gas T_g are equal. This assumption has been justified by the work of Bilodeau et al. [114] concerning fullerene modeling in the arc. According to them, pure helium plasmas show departures from LTE at pressures of 10^4 Pa. However, their calculations demonstrate that carbon species dominate in the arc region, resulting in an increase of the electric conductivity in comparison to pure helium. As a result, the electric field is limited to values of 10 V/cm, thus limiting deviations from LTE. In order to verify this assumption, Hinkov [115] calculated features of a plasma used at specific conditions of SWCNT growth using the AURORA plasma software in the CHEMKIN collection [119]. This software predicts the steady state or time averaged properties of a well mixed or perfectly stirred plasma reactor. By modeling nonthermal plasmas, Aurora determines the ion, electron, and the neutral radical species concentrations and the electron temperature. Well-stirred reactors are characterized by a reactor volume, residence time or mass flow rate, heat loss or gas temperature, surface area, surface temperature, the incoming temperature and mixture composition, as well as the power deposited into the plasma for nonthermal systems. Figure 15 is a schematic representation of the well-mixed plasma reactor [119] and its adaptation to predict plasma compositions [115]. The reactor of volume $V = 0.6$ cm^3 and containing a reactive cathode surface area of $A_m = 2$ cm^2 is continuously fed by a mass flow of 1800 sccm coming from the anode erosion. The composition of the inlet flow is calculated at 4000 K using Ivtanthermo [120] equilibrium computer

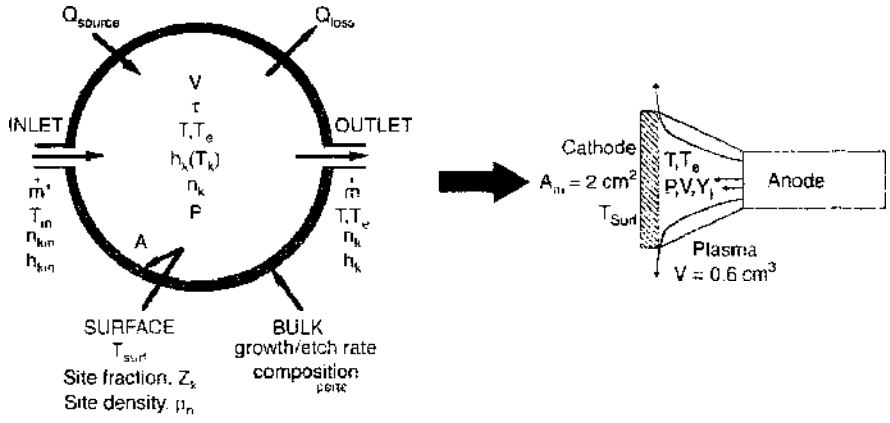

Figure 15. Schematic representation of a well-mixed plasma reactor [119] and its adaptation to predict plasma compositions Y_i for given T and T_e. Reprinted with permission from [115]. I. Hinkov, Ph.D. Thesis, University Paris 13, France, 2004. © 2004.

code with the initial composition of the anode C : Ni : Y 94.8 : 4.2 : 1 at.%, diluted by a factor of 20 in the helium, as suggested by Krestinin and Moravskii [110]. The model takes into account 92 species including carbon radicals C, C_2, C_3, ... C_{79}, fullerenes C_{60F} and C_{70F}, inert gas He, and ions Ni^+, Y^+, He^+, C^+, C_4^+, C_5^+, and C_{60}^+. All these species involve 562 electron and neutral reactions listed respectively in Tables 1 and 15. In addition to the homogeneous gas chemistry, the surface reactions listed in Table 16 were added to account for the growth and etching of carbon nanotubes assumed to grow at the cathode surface from small carbon atoms. The sticking coefficient of unity for the deposition and 0.1 for etching was arbitrarily chosen. Finally, ions recombine in the sheath by the application of the Bohm condition for ion fluxes to surfaces. Indeed, as suggested by Meeks et al. [119], it is reasonable to constrain the ion flux to a surface according to the Bohm criterion. This condition results in the maximum net flux of a particular ion to a surface equal to the product of the ion density and the Bohm velocity. No data are available for recombination of nickel and yttrium ions in the sheath, hence an arbitrary Bohm criterion of BOHM = 0.4 was chosen by Hinkov [116]. The calculations were performed with the following conditions, inert gas = helium, measured erosion rate $G_{\text{erosion}} = 17.2$ mg/s at 100 A, assumed dilution factor $\tau_{\text{dilution}} = 20$, and a total pressure $P = 660$ mbar, with and without the LTE assumption. In the first calculation, the LTE assumption with $T_g = T_{\text{ion}} = T_e = 6500$ K was assumed. The output results from AURORA are summarized in Table 17 and reveal a residence time of about 28 μs and a weak electronic density of 6.4×10^{14} cm^{-3}. The predicted total ion current density of 10.4 A/cm^2 corresponds to a total current of the order 20 A, based on a cathode surface area of 2.01 cm^2. This is much lower than 100 A, making the LTE assumption questionable. The second calculation was performed in the same conditions by maintaining gas temperature at $T = 6500$ K and varying electron temperature from 0.56 eV (6500 K) to 5.17 eV (60000 K) corresponding to varying the current from 20 to 200 A. The estimated ion mass fractions, plotted in Fig. 16, reveal that the major ion is Y^+ for the current intensity $I < 50$ A and Ni^+ for the current intensity $I > 50$. This result is explained by the low quantity of yttrium (1 at.%) added to the anode material, and to the weak energy of ionization of the yttrium. Increasing the current intensity, one forms more and more Ni^+ ions from nickel atoms. Figure 17 gives the evolution of calculated current density and electron temperature with electron density. In the optimal domain of current (80–120 A) for nanotube synthesis, the calculated electron density is between 1.25×10^{15} and 1.5×10^{15} cm^{-3}, and the electron temperature is 1.7–2.4 eV. Table 18 summarizes the plasma composition calculated for $I = 100$ A where the electron density of $n_e = 1.4 \times 10^{15}$ cm^{-3} is in good agreement with the measurements of Akita et al. [51] in the interval 10^{15}–10^{16} cm^{-3} for $T = 6000$ K as measured by optical emission spectroscopy in the following nanotube conditions: inert gas = helium, pressure $P = 300$ Torr, $G_{\text{erosion}} = 50$ mg/s, and the flow rate of carbon without catalysts is 5500 sccm. The calculations indicate that when the catalyst is present the major ion is Ni^+ with a molar fraction of 1.3×10^{-3} followed by Y^+ with a molar fraction of 4.7×10^{-4} and C^+ with a molar fraction of 1.3×10^{-4}. From these results, even if the LTE condition is not satisfied, the weak rate of ionization of the carbon (<0.3%) indicates clearly that C^+ ions cannot explain the fast nanotube growth rates, as was implied by the model of Gamaly and Ebbesen, described in Section 3.4.1.

Table 15. Electronic gas phase reactions considered in Hinkov [113].

Number	Reaction	A (cm^{-3} s^{-1} mol^{-1})	β	E (K)	Ref.
Ion 1	$C + e^- \leftrightarrow C^+ + e^- + e$	3.3×10^{20}	0	214420	[82]
Ion 2	$C^+ + C_3 \rightarrow C_4^+$	9.0×10^{9}	0	0	[82]
Ion 3	$C^+ + C_4 \rightarrow C_5^+$	6.0×10^{14}	0	0	[82]
Ion 4	$C^+ + e^- \leftrightarrow C$	3.6×10^{16}	−4.5	0	[83]
Ion 5	$C_{60F} \leftrightarrow C_{60}^+ + e$	1.33×10^{15}	0	65900	[84]
Ion 6	$Ni^+ + e^- \leftrightarrow Ni$	2.2×10^{20}	−4.5	0	[85]
Ion 7	$Y^+ + e \leftrightarrow Y$	2.2×10^{20}	−4.5	0	[85]
Ion 8	$He^+ + e \leftrightarrow He$	2.2×10^{20}	−4.5	0	[85]

Table 16. Surface reactions considered in Hinkov [113].

Number	Reaction	A ($cm^3\ s^{-1}\ mol^{-1}$)	β	E (K)
Deposition				
S_1	Ni + WL(S) → WLNi(S) (Stick)	1.0	0	0
S_2	Y + WL(S) → WLY(S) (Stick)	1.0	0	0
S_3	C + WL(S) → WLC(S) (Stick)	1.0	0	0
S_4	C_2 + WL(S) → WLC_2(S) (Stick)	1.0	0	0
S_5	C_3 + WL(S) → WLC_3(S) (Stick)	1.0	0	0
S_6	C_4 + WL(S) → WLC_4(S) (Stick)	1.0	0	0
S_7	C_5 + WL(S) → WLC_5(S) (Stick)	1.0	0	0
Etching				
S_8	C + WLC(S) → WL(S) + C_2 (Stick)	0.1	0	0
Recombination of ions				
S_9	$Ni^+ + e^-$ → Ni(BOHM)	0.4	0	0
S_{10}	$Y^+ + e^-$ → Y(BOHM)	0.4	0	0

Table 17. Plasma characteristics calculated by AURORA assuming LTE and $T_g = T_{ion} = T_e = 6500$ K.

Outlet Conditions
Specified inlet mass flow rate = 0.116 g/s
Outlet mass flow rate = 0.116 g/s
(which is based on a reactor density = 0.551×10^{-05} g/cm^3
and on a reactor volume = 0.6 cm^3
produces a residence time) = 0.284×10^{-04} s
Total ion current density = 10.4067 A/cm^2
Outlet and reactor temperature = 6500 K
Outlet and reactor pressure = 0.651 atm
Outlet and reactor density = 0.55074×10^{-05} g/cm^3
Outlet and reactor mean molecular weight = 4.5101 g/mol
Outlet molar flow rate = 0.25773×10^{-01} mol/s
Outlet volumetric flow rate = 21106 cm^3/s
(based on reactor pressure and temperature)
= 37833 SCCM
= 37.833 SLPM
Outlet and reactor electron temperature: Te = 6502.7 K
Te = 0.56036 eV

Outlet conditions for gas phase molecular species

Species	Mole fraction	Number density (cm^{-3})	mol/s	g/s	cm^3/s
e	8.7×10^{-04}	$6.4 \times 10^{+14}$	2.2×10^{-05}	1.2×10^{-08}	$1.8 \times 10^{+01}$
C	4.5×10^{-02}	3.3×10^{-16}	1.2×10^{-03}	1.4×10^{-02}	9.5×10^{-02}
C_2	2.0×10^{-05}	1.5×10^{-13}	5.2×10^{-07}	1.2×10^{-05}	4.2×10^{-01}
C_3	2.7×10^{-08}	2.0×10^{-16}	7.0×10^{-10}	2.5×10^{-08}	5.8×10^{-04}
C_4	6.5×10^{-16}	4.7×10^{-24}	1.7×10^{-17}	8.0×10^{-16}	1.4×10^{-11}
C_5	2.0×10^{-15}	1.5×10^{-23}	5.2×10^{-17}	3.2×10^{-15}	4.3×10^{-11}
He^+	5.4×10^{-13}	4.0×10^{-05}	1.4×10^{-14}	5.6×10^{-14}	1.1×10^{-08}
Ni^+	2.7×10^{-14}	2.0×10^{-14}	7.1×10^{-16}	4.2×10^{-14}	5.8×10^{-10}
Y^+	4.7×10^{-04}	3.5×10^{-14}	1.2×10^{-05}	1.1×10^{-03}	9.9×10^{-01}
C^+	1.3×10^{-02}	9.2×10^{-13}	3.2×10^{-04}	3.9×10^{-03}	$2.7 \times 10^{+00}$
C_2^+	1.1×10^{-12}	7.9×10^{-26}	2.8×10^{-14}	1.3×10^{-12}	2.3×10^{-08}
C_3^+	1.7×10^{-15}	1.2×10^{-03}	4.4×10^{-17}	2.6×10^{-15}	$3.6 \times 10^{+01}$
C_{60}^+	5.3×10^{-41}	3.9×10^{-25}	1.4×10^{-42}	9.9×10^{-39}	1.1×10^{-36}
Ni	1.7×10^{-03}	1.3×10^{-15}	4.4×10^{-05}	2.6×10^{-03}	$3.6 \times 10^{+01}$
Y	4.6×10^{-06}	3.4×10^{-12}	1.2×10^{-07}	1.1×10^{-05}	9.8×10^{-02}
He	9.5×10^{-01}	7.0×10^{-17}	2.5×10^{-02}	9.8×10^{-02}	$2.0 \times 10^{+04}$

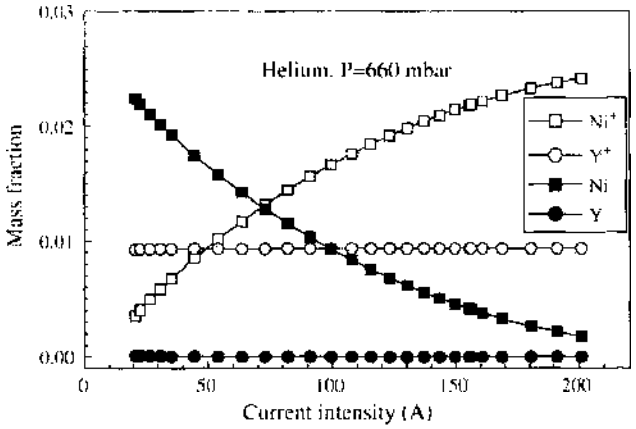

Figure 16. Predicted variations of ion mass fractions with the total current intensity. From [116], C. D. Scott, Report, 2003. Unpublished.

3.4.3. Zero-Dimensional Models

A zero-dimensional model for arc nanotubes synthesis was developed by Farhat et al. [109] and Hinkov [115] to calculate the equilibrium chemical composition in one point in the plasma, assuming LTE and given the gas temperature and pressure. The objective is to study the sensitivity of the kinetic model developed by Krestinin and Moravskii [118] in the specific conditions of nanotube growth.

3.4.3.1. Model Equations The multidimensional conservation model is reduced to zero spatial dimensions (0D) by assuming steady-state and a given temperature and zero velocity. The conservation equations can be written as a balance between an accumulation term on the left-hand side of Eq. (27) and chemical source term.

$$\frac{dY_i}{dt} = \omega_i \frac{M_i}{\rho} \qquad (i = 2, \ldots, n_s) \tag{27}$$

In this equation, n_s is the number of gas species, Y_i is the mass fraction, ω_i is the chemical molar production (mol cm^{-3} s^{-1}), and M_i is the molecular weight (g mol^{-1}), respectively, of species i, ρ is the total mass density (g cm^{-3}), and t is the time (s). The source term ω_i is calculated by considering R elementary reversible or irreversible reactions involving n_s reacting chemical species A_i.

$$\sum_{i=1}^{n_s} \nu'_{ir} A_i \underset{2}{\overset{1}{\leftrightarrow}} \sum_{i=1}^{n_s} \nu''_{ir} A_i \qquad (r = 1, \ldots, R) \tag{28}$$

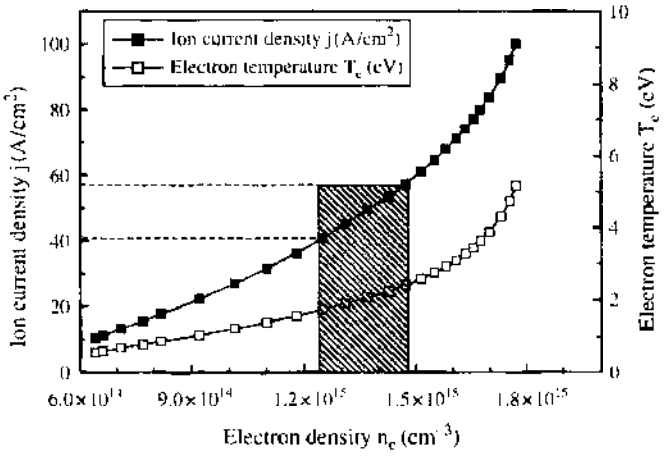

Figure 17. Plasma characteristics calculated by AURORA in the conditions $T_g = T_{ion} = 6500$ K and variable T_e. Hatched zone corresponds to the optimal domain of current intensity 80–120 A for nanotube synthesis. Reprinted with permission from [115], I. Hinkov, Ph.D. Thesis, University Paris 13, France, 2004. © 2004.

Table 18. Plasma composition calculated for $I = 100$ A in helium with $P = 660$ mbar.

Species	Mole fraction	Number density (cm^{-3})	mol/s	g/s	cm^3/s
e	1.9×10^{-03}	$1.4 \times 10^{+15}$	4.9×10^{-05}	2.7×10^{-08}	$4.0 \times 10^{+01}$
C	4.5×10^{-02}	$3.3 \times 10^{+16}$	1.2×10^{-03}	1.4×10^{-02}	$9.5 \times 10^{+02}$
C_2	2.0×10^{-05}	$1.5 \times 10^{+13}$	5.1×10^{-07}	1.2×10^{-05}	4.2×10^{-01}
C_3	2.7×10^{-08}	$2.0 \times 10^{+10}$	7.0×10^{-10}	2.5×10^{-08}	5.7×10^{-04}
C_4	6.3×10^{-16}	$4.6 \times 10^{+02}$	1.6×10^{-17}	7.9×10^{-16}	1.3×10^{-11}
C_5	2.0×10^{-15}	$1.5 \times 10^{+03}$	5.1×10^{-17}	3.1×10^{-15}	4.2×10^{-11}
He^+	7.0×10^{-12}	$5.1 \times 10^{+06}$	1.8×10^{-13}	7.2×10^{-13}	1.5×10^{-07}
Ni^+	1.3×10^{-03}	$9.4 \times 10^{+14}$	3.3×10^{-05}	1.9×10^{-03}	$2.7 \times 10^{+01}$
Y^+	4.7×10^{-04}	$3.5 \times 10^{+14}$	1.2×10^{-05}	1.1×10^{-03}	$1.0 \times 10^{+01}$
C^-	1.3×10^{-04}	$9.2 \times 10^{+13}$	3.2×10^{-06}	3.9×10^{-05}	$2.7 \times 10^{+00}$
C_4^+	1.0×10^{-12}	$7.7 \times 10^{+05}$	2.7×10^{-14}	1.3×10^{-12}	2.2×10^{-08}
C_5^+	1.6×10^{-15}	$1.2 \times 10^{+08}$	4.2×10^{-17}	2.5×10^{-15}	3.5×10^{-11}
C_{60}^+	6.5×10^{-41}	4.8×10^{-23}	1.7×10^{-42}	1.2×10^{-39}	1.4×10^{-36}
Ni	7.2×10^{-04}	$5.2 \times 10^{+14}$	1.8×10^{-05}	1.1×10^{-03}	$1.5 \times 10^{+01}$
Y	4.2×10^{-07}	$3.1 \times 10^{+11}$	1.1×10^{-08}	9.6×10^{-07}	8.9×10^{-03}
He	9.5×10^{-01}	$7.0 \times 10^{+17}$	2.5×10^{-02}	9.8×10^{-02}	$2.0 \times 10^{+04}$

where ν'_{ir} and ν''_{ir} are the stoichiometric mole numbers of the reactants and products, respectively, and A_i is the chemical symbol for the ith species. The chemical production rate ω_i of ith species can be written as a summation of the rate-of-progress variables for all the reactions involving the ith species:

$$\omega_i = \sum_{r=1}^{n_r} \Delta\nu_{ir} q_r \qquad (r = 1, \ldots, n_r) \tag{29}$$

where $\Delta\nu_{ir} = \nu''_{ir} - \nu'_{ir}$. The rate-of-progress variables q_r for the rth reaction is given by the difference of the forward rates 1 and the reverse rates 2 as:

$$q_r = k_{1r} \prod_{i=1}^{n_s} C_i^{\nu'_{ir}} - k_{2r} \prod_{i=1}^{ns} C_i^{\nu''_{ir}} \qquad (r = 1, \ldots, R) \tag{30}$$

where k_{1r} and k_{2r} are the forward and reverse rate coefficients of the rth reactions and C_i is the molar concentration of ith species. Reverse reactions are written explicitly in the forward sense. The forward rate constants are calculated for each reaction r by assuming Arrhenius temperature dependence:

$$k_{1r} = A_r T^{\beta_r} \exp\left(\frac{-E_r}{RT}\right) \qquad (r = 1, \ldots, R) \tag{31}$$

The rate-of-progress variables q_r are computed using CHEMKIN database and software package.

The condition of total mass fraction given by

$$\sum_{i=1}^{n_s} Y_i = 1 \tag{32}$$

3.4.3.2. Kinetic and Thermodynamic Data The gas phase chemistry used in this approach involves neutral carbon species and includes small clusters (C_1–C_{10}), cycles and polycycles (C_{11}–C_{31}), fullerene shells (C_{32}–C_{46}), fullerene clusters (C_{47}–C_{70}), and two fullerene molecules C_{60F} and C_{70F}. In addition, argon and/or helium, as well as nickel and yttrium, are considered as inert chemical species. There are at least 554 chemical reactions, listed in Table 1, that describe the chemical kinetics of carbon vapor condensation and clusters of different sizes in the arc. The source of these data and the formation enthalpies are discussed by Krestinin and Moravsky [118]. The symbols $\leftrightarrow$ and $\rightarrow$ in each reaction indicate that this reaction is reversible or irreversible, respectively. Finally, this model includes 81 carbon species (C_1, C_2 ..., C_{70}, C_{60F}, C_{70F}) involving all the reactions of Table 1. The thermodynamic properties of species are fitted in the temperature range of 300 to 20,000 K from

Ivtanthermo [120], JANAV [121], NASA [122], and CHEMKIN [40] databases and given in CHEMKIN (old NASA) format. This format presumes that the standard-state thermodynamic properties as standard-state molar heat capacity at constant pressure of the ith species c_{pi}^0, standard molar enthalpy H^0, and standard molar enthalpy S^0 are thermally "perfect" in that they are only functions of temperature and are given in terms of polynomial fits (Section 2–4). For small carbon species, argon, helium, nickel, and yttrium, the polynomial coefficients are listed in Table 4.

3.4.3.3. Solution Procedure The solution of differential algebraic equations (DAE) representing mass conservation Eqs. (27) and (32) employs a backward differential formula method implemented in LSODI package [123]. This software was designed to solve stiff DAE, and the solution procedure attempts time-integration from an initial guess of the variables. The initial composition of the gas was estimated at a given temperature and pressure using IVTANTHERMO [120] equilibrium computer code, with the initial composition of the anode C : Ni : Y 94.8 : 4.2 : 1 at.%, diluted by a factor of 20 in helium. Time-stepping improves the starting point by relaxing it closer to the steady-state solution. This solution method is much faster and much more stable in reaching steady-state convergence than the classical Newton iteration method. The model takes into account 84 equations corresponding to all the species including: radicals C, C_2, C_3, ..., C_{79}, fullerenes C_{60F} and C_{70F}, nickel Ni, yttrium Y, and inert gas He. These species involve the 554 reactions of Table 1. The typical time evolution of the solution for carbon atom mole fractions calculated at $T = 4000$ K and $P = 660$ mbar is given in Fig. 18. The characteristic reaction time to obtain steady-state C mole fraction is about 1 μs. At a cooler temperature, $T = 2000$ K, we start to form fullerenes from carbon clusters. Figures 19 and 20 show the time evolution of carbon clusters C_{58}, C_{59}, C_{60} and the fullerenes C_{60F} and C_{70F}, respectively. Fullerenes have a characteristic reaction time of about 10 μs. Finally, in Figs. 21a and 21b are plotted mole fractions of small carbon species and total fullerene yield versus temperature calculated in helium at 660 mbar. We can see from these figures that fullerenes start to be formed at 3000 K.

3.4.4. Turbulent Fan Jet Model

When the electrode spacing is very small, carbon is ejected from between the electrodes as a radially expanding jet. Krestinin and Moravsky [7, 110, 118] developed a model to describe the chemical processes taking place in a turbulent fan jet leaving the interelectrode space.

3.4.4.1. Model Formulation The turbulent jet model accounts for the main processes controlling fullerene formation in electric arc, namely (1) cooling and mixing of carbon vapor in a buffer gas, (2) reactions of cluster growth and decomposition under nonisothermal conditions, and (3) formation of soot particles and heterogeneous reactions on their surface. In this model, the flow from the arc zone is idealized as an axially symmetric fan jet represented in Fig. 22. The pressure gradient in the reactor, the temperature gradient in the gap,

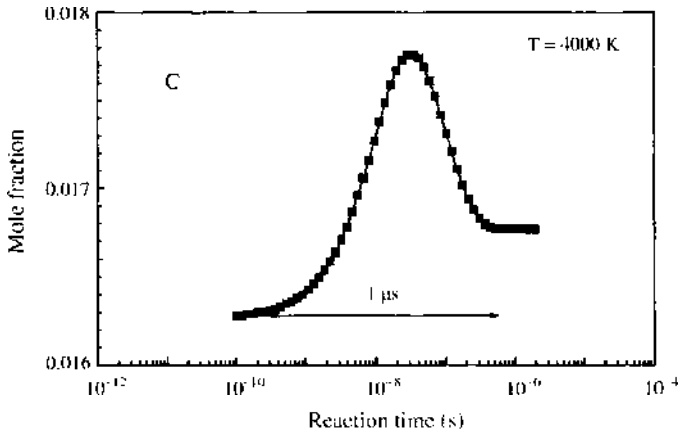

Figure 18. Time evolution of carbon atom mole fraction calculated in helium, at $P = 660$ mbar and $T = 4000$ K.

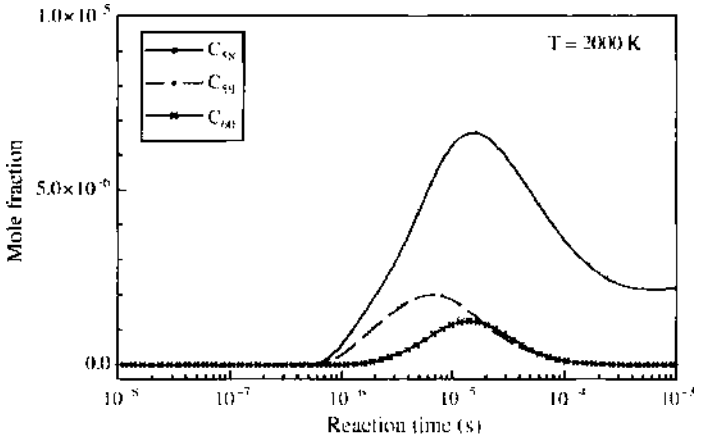

Figure 19. Time evolution of some carbon cluster mole fraction calculated in helium, at $P = 660$ mbar and $T = 2000$ K.

as well as the rate of inert gas diffusion inward the interelectrode zone were neglected. The model solves the gas dynamic equations governing the expansion of an initial volume ΔV_0 at the temperature T_0 with an initial high velocity U_0 of a jet surrounded by a pure and cold inert gas at T_{at}. The velocity profile U in the plane (z, r) representing a jet section is shown schematically in Fig. 22.

3.4.4.2. Model Equations The conservation equations are written within a boundary layer with turbulent mass and heat transfer across the jet in the following form:

$$\rho U \frac{\partial Y_i}{\partial r} = \frac{\partial}{\partial z} k_c \varepsilon_\tau \rho \frac{\partial Y_i}{\partial z} + M_i f_i \qquad (i = 1, \ldots, n_g) \tag{33}$$

$$\rho C_p U \frac{\partial T}{\partial r} = \frac{\partial}{\partial z} k_T \varepsilon_\tau \rho C_p \frac{\partial T}{\partial z} + f_T \tag{34}$$

where ε_τ is the coefficient of turbulent momentum transfer, k_c and k_T are empirical coefficients relating momentum transfer to mass and heat transfer, Y_i and T are, respectively, the mass fractions of the species i and the temperature at the longitudinal position, r, and transverse, z, coordinates of the jet. The terms f_i and f_T are the rates of mixture component formation and the rate of heat release due to chemical reactions, M_i are the molecular weights of the mixture components, ρ is the gas density, C_p is the mixture specific heat, and U is the mass-mean gas velocity. To solve these partial differential equations, the semiempirical theory of free turbulent jet developed by Abramovich [124] is applied. In this theory, the ratio between the half-width of a free turbulent jet b and the mixing length L is assumed

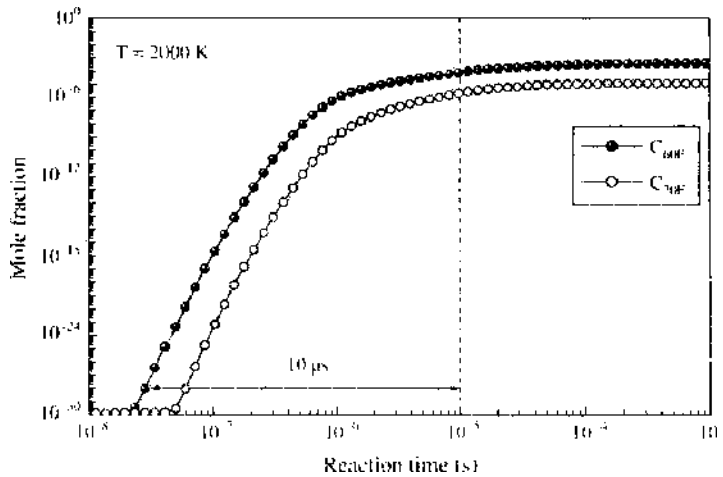

Figure 20. Time evolution of fullerene mole fraction calculated in helium, at $P = 660$ mbar and $T = 2000$ K.

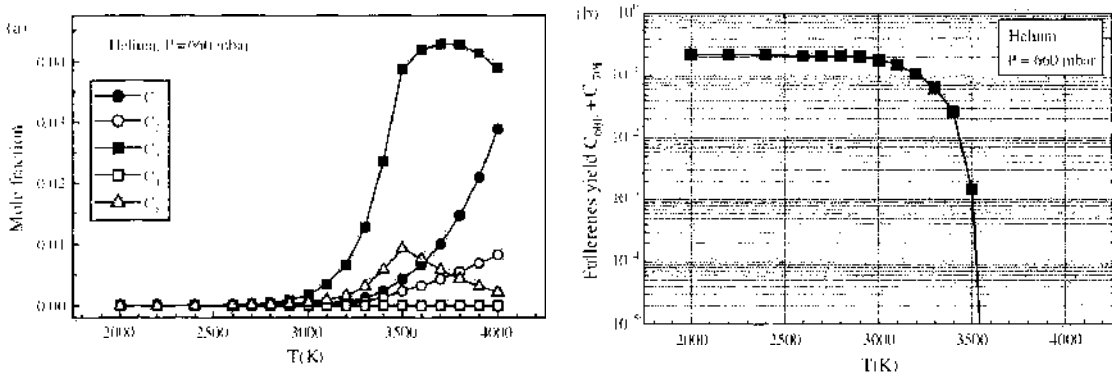

Figure 21. (a) Mole fractions of small carbon species calculated at equilibrium versus temperature calculated in helium at 660 mbar. (b) Total fullerene yield versus temperature calculated in helium at 660 mbar.

constant at each longitudinal position r of the jet. $L/b = \text{const.} \sim 0.2$. In addition, due to the jet symmetry, derivatives of all the variables with respect to z are equal zero at the jet center plane. Hence, temperature and concentration vary little within the turbulent mixing length $L(r)$ and can be assumed constant and equal to their values at $z = 0$. Thus, integrating the Eqs. (33) and (34) with respect to z over interval $[-L, L]$ yields to an approximate description of evolution of an elementary gas volume moving near the symmetry plane of a fan jet. By replacing the derivatives with respect to z by finite differences,

$$\frac{\partial Y_i}{\partial z} = \frac{Y_{0,i} - Y_i}{b}$$
$$\frac{\partial T}{\partial z} = \frac{T_{at} - T}{b} \tag{35}$$

partial differential Eqs. (33) and (34) are transformed via a procedure described in detail in [7] to a set of ordinary differential equations. These equations are written in CHEMKIN notation as following,

$$\frac{dY_i}{dt} = k_v(Y_{0,i} - Y_i) + \omega_i \frac{M_i}{\rho} \qquad (i = 1, \ldots, n_g) \tag{36}$$

$$\sum_{i=1}^{n_g} Y_i C_{p,i} \frac{dT}{dt} = \sum_{i=1}^{n_g} Y_i C_{p,i} k_T (T_{at} - T) + \omega_i h_i \frac{M_i}{\rho} \tag{37}$$

where Y_i and $Y_{0,i}$ are the mass fractions of mixture components including carbon black particles in the reaction volume and buffer gas, respectively, T is the temperature, ω_i is the chemical molar production of species i(mol cm^{-3} s^{-1}), M_i is the molecular weight (g mol^{-1}), ρ is the total mass density (g cm^{-3}), h_i is the specific enthalpy of the ith species (erg/g), $C_{p,i}$ is the specific heat at constant pressure of the ith species (ergs g^{-1} K^{-1}), and t is the

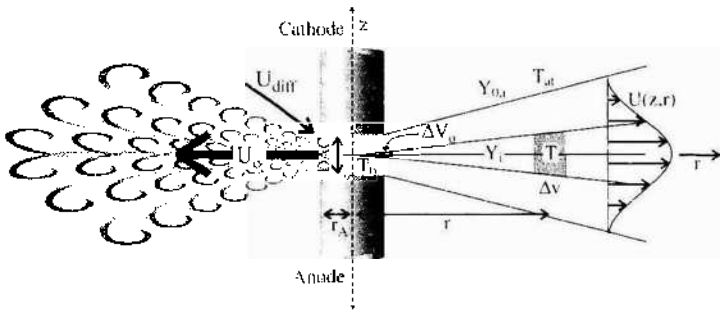

Figure 22. Schematic of the flow issuing from the electric arc zone as represented by Krestinin and Moravsky. Courtesy A. Moravsky.

time (s). The mass and heat transfer coefficients k_c and k_T are calculated by the empirical formulas:

$$k_c = \frac{0.32}{\tau_{mix} + 2t} \tag{38}$$

$$k_T = \frac{0.64}{\tau_{mix} + 2t} \tag{39}$$

where τ_{mix} is the time of turbulent mixing calculated from the flow velocity in the jet within the arc zone U_0 using Eq. (40).

$$\tau_{mix} = \frac{r_A}{U_0}\left(\frac{r_A}{d_{AC}}\right)^{0.5} \tag{40}$$

The flow velocity U_0 is calculated by Eq. (41) assuming that the carbon vapor in the arc zone is equilibrated with electrode graphite and taking the experimental value of the formation rate of fullerene carbon black, V_{soot}

$$U_0 = \frac{V_{soot} R T_0}{2\pi r_A d_{AC} P} \tag{41}$$

where d_{AC} is the anode to cathode distance, r_A is the anode radius, R is the universal gas constant, P is the helium pressure in the reactor, and T_0 the arc temperature calculated from the equilibrium pressure of the carbon cluster vapor over graphite. V_{soot} is determined from the measured rate of ablation of the anode

3.4.4.3. Numerical Results The representative experimental conditions of Krestinin and Moravskii are $P = 100$ to 760 Torr, $T_0 = 3600$ to 3900 K, and $U_0 = 2$ to 80 m/s. Under these experimental conditions, the model equations (36) and (37) were solved using the chemical gas model in Table 1 and Table 19. Figure 23 compare calculated and experimental fullerene yields as obtained by Krestinin and Moravsky [8] at different pressures.

3.4.5. One-Dimensional Models

In order to analyze the effect of arc process parameters on temperature and species profiles in (1D), Farhat et al. [109] used the highly structured computer packages SPIN and SURFACE CHEMKIN developed by Kee et al. [40] at Sandia for rotating disk CVD processes. The complex gas-phase chemical reaction mechanism representing carbon condensation from the arc was added into numerical simulations in a one-dimensional (1D) model.

Table 19. Soot nuclei and soot particle reaction rates, from Krestinin and Moravskii [116].

Reaction	A ($cm^3\ s^{-1}\ mol^{-1}$)	β	E
1. Formation of soot nuclei Z			
$C_{78} + C_2 \rightarrow Z$	4.0×10^{08}	0	60,8
$C_{78} + C_2 \rightarrow Z + C$	4.0×10^{08}	0	0
n, m = 1–10			
$C_{20+n} + C_{20+n} \rightarrow Z$	4.0×10^{14}	0	0
$C_{20+n} + C_{20+m} \rightarrow Z$	4.0×10^{14}	0	0
2. Heterogeneous reactions on soot particles[a]			
C_1 + soot ↔ soot	4.0×10^{03}	0	0
C_2 + soot ↔ soot	4.0×10^{03}	0	0
C_3 + soot → soot	4.0×10^{03}	0	0
n = 4–79			
C_n + soot → soot	4.0×10^{03} (1/m)$^{0.5}$	0	0
C_{80} + soot → soot	1.0×10^{03}	0	30
$C_{>80}$ + soot → soot	1.0×10^{03}	0	30

[a] The rate constants of heterogeneous reactions are given per unit aerosol surface area.

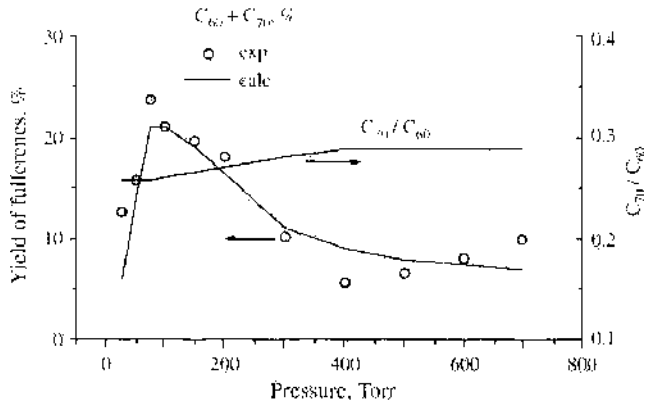

Figure 23. Comparison of experimental and calculated yield of fullerenes versus the pressure. The experimental molar ratio C_{70}/C_{60} is found to be invariably equal to 0.2. Reprinted with permission from [8], A. V. Krestinin and A. P. Moravsky, *Chem. Phys. Lett.* 286, 479 (1998). © 1998, Elsevier.

This model was formulated under specific conditions of nanotube growth in the interelectrode region. It solves for species, temperature, and velocity profiles in a steady-state, one-dimensional stagnation-point flow, with temperature-dependent fluid properties.

3.4.5.1. Model Formulation This model is a boundary value problem consisting of a set of ordinary differential equations, solved by a finite difference procedure. It assumes local thermal equilibrium (LTE) and solves the steady-state axial and radial momentum, species, and energy equations in one spatial dimension between the anode and the cathode. The model accounts for carbon deposition at the cathode by a set of surface reactions that simulates nanotube growth. The steady-state assumption is justified by the continuous adjustment of the interelectrode gap leading to a constant erosion rate of the anode, hence a constant condensation of carbon vapor close to the cathode. Local thermodynamic equilibrium was assumed based on the Bilodeau et al. [114] model for fullerene synthesis by arc discharge in the same range of pressure as nanotube synthesis.

3.4.5.2. Model Equations The governing equations that are solved in the SPIN code include continuity, radial momentum, species conservation, and thermal energy and are given below.

Continuity

$$\frac{1}{\rho}\frac{\partial \rho}{\partial t} = -\frac{\partial u}{\partial x} - 2V - \frac{u}{\rho}\frac{\partial \rho}{\partial x} = 0 \tag{42}$$

Radial momentum

$$\rho\frac{\partial V}{\partial t} = -\frac{\partial}{\partial x}\left(\mu\frac{\partial V}{\partial x}\right) - \rho u\frac{\partial V}{\partial x} - \rho V^2 - \frac{1}{r}\frac{\partial p}{\partial r} = 0 \tag{43}$$

Species continuity

$$\rho\frac{\partial Y_i}{\partial t} + \frac{\partial(\rho Y_i V_i)}{\partial x} + \rho u\frac{\partial Y_i}{\partial x} = M_i\omega_i \qquad (i = 1, \ldots, n_g) \tag{44}$$

Thermal energy

$$\rho c_p\frac{\partial T}{\partial t} = \frac{\partial}{\partial x}\left(\lambda\frac{\partial T}{\partial x}\right) - \rho c_p u\frac{\partial T}{\partial x} - \sum_{i=1}^{n_g}\left(c_{pi}\rho Y_i V_i\frac{\partial T}{\partial x} + \dot{\omega}_i h_i\right) + S_q(x) - Q_{\text{rad}} = 0 \tag{45}$$

Although these equations are stated in their transient form, the solution is obtained when all time derivatives are zero. In the governing equations, the independent variables are the distance normal to the cathode x (Fig. 24), and the time t. The dependent variables are axial u and radial V velocities, gas temperature T, gas-phase species mass fractions Y_i. The mass density is given by ρ and the specific heats at constant pressure by c_p. In the

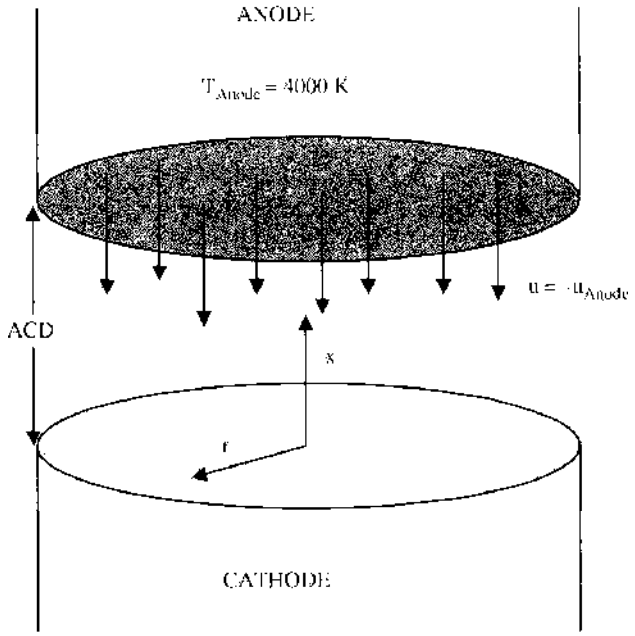

Figure 24. Simulation domain and boundary conditions.

radial momentum equation, p is the spatially varying component of the pressure [40]. The molecular weight and specific enthalpy of species i are given by M_i and h_i, respectively. The viscosity and thermal conductivity are μ and λ. The net chemical production rate of species i by gas-phase reaction is ω_i. The species diffusion velocity V_i is calculated from mixture diffusion coefficient and species gradient [40]. The source term $S_q(x)$ in the energy equation accounts for the electrical energy dissipated in the arc. It was assumed that it is distributed in the form of Gaussian centered at x_s with a (half) half-width of w_s by the equation:

$$S_q(x) = q\frac{1}{w_s}\sqrt{\frac{3}{\pi}}e^{\left[-\frac{3(x-x_s)^2}{w_s^2}\right]} \tag{46}$$

Here, q accounts for the total power integrated over its full spatial extent $q = \int_{-w_s}^{+w_s} S_q(x)\,dx$ and includes 100% of the net power added to the arc. The center of the interelectrode gap was chosen as the peak in the distribution x_s and w_s chosen to adjust the flatness of the distribution. In the current calculations, w_s was 0.15 cm, resulting in a very uniform distribution. The total energy q was calculated from measured electric power dissipated in the arc. It was corrected by the loss from arc plasma due to the gas convection. The radiative term Q_{rad} in the energy equation accounts for the net loss of energy by gas radiation. It was estimated from a curve fit of Owano [125] in atmospheric argon plasma by:

$$Q_{rad} = 1.065 \times 10^{14}\alpha \exp\left(\frac{-141170}{T}\right)\left(\frac{W}{m^3}\right) \tag{47}$$

with T the gas temperature in K and α a nonequilibrium factor accounting for the deviation from the equilibrium; $\alpha = 1$ for local thermal equilibrium (LTE). Gas radiation is negligible when helium is used. Gas kinetics, thermodynamic and transport properties of species are estimated in the same way as in Section 3.4.3.

3.4.5.3. Surface Chemistry Carbon nanotube growth is considered as a boundary condition at the cathode by a set of surface reactions simulating nanotube growth. As a first approach, the open-end tube growth (scooter) mechanism developed by Smalley [117] and illustrated in Fig. 25 by an African calabash structure decorated by hexagons and open on the top was implemented as a boundary condition. Open-ended nanotubes were first explained by the high local electric field in the region of nanotubes growth preventing their closure ends. More recently, catalysts such as Ni were thought to be attached to hold open the ends

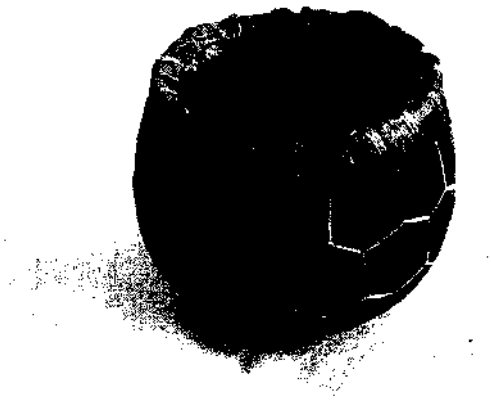

Figure 25. African calabash with structure decorated by hexagons and opened on the top.

of nanotubes and promoted growth. It was assumed that nanotube growth occurs at the cathode surface (Fig. 26) and that surface chemistry is controlled by the local terminated bond and not by the bulk nanotube bonds. Nanotube growth is based on the adsorption and desorption of three small carbon clusters (C_1 to C_3) to simulate nanotube growth. The surface reactions considered here are listed in Table 20, where CR represents the nanotube radical site at the open edge of the tube and CNT is assumed to be the unique "bulk" species. In the reaction (S1), for example, carbon atoms C react with a radical site CR to generate a new radical site CR and one incorporated carbon into the bulk nanotube CNT. The pre-exponential factor of these reactions was fixed arbitrarily at 2.50×10^{11} and was varied as a parameter from 3.0×10^{4} for carbon addition of C, C_2, and C_3 on soot [118] to 1.0×10^{13} for carbon addition on diamond [126, 127]. Because no other carbon phases are incorporated in this model, the total number of sites Γ is calculated by geometrical considerations from Hamada's indices n and m. We consider a triangular arrangement of carbon nanotubes within a bundle [128] (Fig. 25) and divide the number of atoms per hexagon by the area of the hexagon using the equation

$$\Gamma = \frac{3N_{at}}{3\sqrt{3}(d_{CNT} + d_{NT\text{-}NT})^2} \times \frac{1}{N_{Av}}$$

with N_{at} the number of atoms per unit cell (nanotube), d_{CNT} the nanotube diameter, $d_{NT\text{-}NT} = 0.340$ nm the distance between two adjacent nanotubes [128], and N_{Av} the Avogadro's number. For example, for a (10,10) nanotube, $d_{CNT} = 1.357$ nm and $N_{at} = 20$, hence the site density is $\Gamma = 6.66 \times 10^{-10}$ mol/cm^2. For comparison, this is lower than the diamond

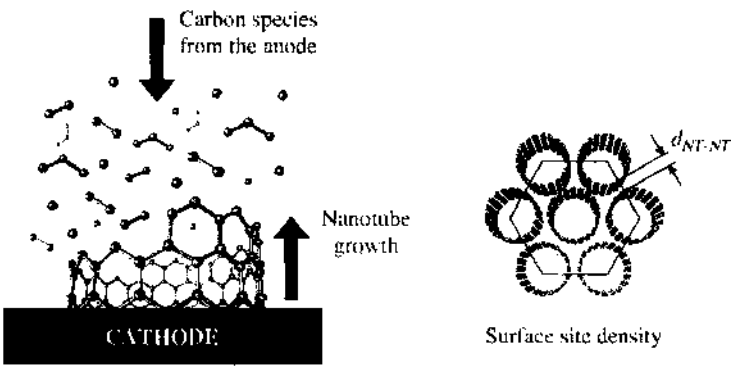

Figure 26. Gas-phase species reacting at the edge of an open nanotube and top view of growing bundles of nanotubes showing surface site density.

Table 20. Surface reactions considered in Farhat et al. [107].

Reaction	A ($cm^3\ s^{-1}\ mol^{-1}$)	β	E/R (K)
(S1) CR + C → CR + CNT	2.50×10^{11}	0.5	0.0
(S2) CR + C3 → CR + CNT + C2	2.50×10^{11}	0.5	0.0
(S3) CR + C2 → CR − CNT + C	2.50×10^{11}	0.5	0.0

site density [127] of 2.61×10^{-9} mol/cm^2. The surface site density is often assumed to be conserved; and the surface-species conservation equation is given by $(dZ_{CR}/dt) = (s_{CR}/\Gamma) = 0$, where Z_{CR} is surface species site fraction and Γ is the surface site density [40]. The chemical production s_{CR} of surface species by surface reactions is given by the sum over the rate-of-progress variables for all surface reactions. The rate of production s_{CR} expressed in mol cm^{-2} s^{-1} is converted to linear nanotube growth rate G in μm/s by using nanotube bulk mass density $\rho_{CNT} = 2.20$ g/cm^3 and molecular weight $M_{CNT} = 12.01$ g/mol using the equation

$$G = \frac{s_{CR} M_{CNT}}{\rho_{CNT}} \tag{48}$$

3.4.5.4. Boundary Conditions The axial gas velocity at the anode was estimated from the measured erosion rate Φ and the total gas density ρ by $u_{anode} = \Phi/(\rho A)$, where A is the anode surface area. For a stagnation-point flow problem, axial velocity at the cathode is zero. The anode temperature was always fixed at the average vaporisation temperature of graphite, $T_{anode} = 4000$ K. The temperature of the cathode T_C is predicted as a part of the solution by adding a radiative energy balance as a boundary condition. Close to cathode surface, the diffusive heat flux in the gas-phase is balanced by the thermal radiative heat loss to the anode given by: $\lambda \frac{\partial T}{\partial x}|_{cathode} = \sigma\varepsilon(T_C^4 - T_{anode}^4)F_{CA}$, where σ is the Stefan-Boltzmann constant, ε is the surface emissivity, and T_{anode} is the anode temperature to which the cathode radiates. The radiative exchange form factor is F_{CA}. At the anode, mass fractions are calculated at the equilibrium temperature of 4000 K, given a dilution factor τ. This factor accounts for the mixing of anode material with inert atmosphere and is defined by the ratio τ = (moles(C + Ni + Y))/(moles(C + Ni + Y + He)) × 100. In the case of evaporation of the mixture of 94 at.% C/5 at.% Ni/1 at.% Y, Krestinin and Moravsky [7, 110] reported that carbon vapor is diluted as much as $\tau = 20$ to 30 times by mixing with inert atmosphere. For the reduced model considered here, mass fractions at the anode were calculated using IVTANTHERMO [120] computer code. For the full model, mass fractions Y_i were calculated from a zero dimension (0D) model involving the following set of ordinary differential equations: $\rho(\partial Y_i/\partial t) = M_i\omega_i = 0 \quad (i = 1, \ldots, n_g)$, where the net chemical production rate ω_i is calculated, as discussed above, from all the reactions listed in Table 1.

3.4.5.5. Numerical Results Numerical simulation of nanotube growth in the arc reactor has been carried out by solving the set of model equations and the boundary conditions using the SPIN computer code for the full chemical model. The chemical model of Krestinin and Moravsky, developed originally for fullerene synthesis, was tested in typical single-wall nanotube growth conditions in the interelectrode region. For these calculations, helium used was as buffer gas, with a total pressure of $P = 660$ mbar and interelectrode gap of 3 mm. The measured electric power dissipated in the arc for 100 A electric current was $q = 1.24 \times 10^{07}$ W/m^2 and the dilution factor at the anode was fixed at $\tau = 20$. In these conditions, the measured erosion rate was $\Phi = 20.4 \times 10^{-03}$ g/s, and the calculated mass density of the gas at the equilibrium temperature of 4000 K is $\rho = 9.24 \times 10^{-06}$ g/cm^3. For a surface anode area of $A = 0.29$ cm^2, the axial velocity $u_{anode} = 7818$ cm/s was estimated at the anode from mass conservation. When small gaps are considered, the form factor F_{CA} should be accounted for. However, in these calculations it was set to unity. Calculated temperature profiles in the 3 mm interelectrode gap for pure helium are shown in Fig. 27. A maximum

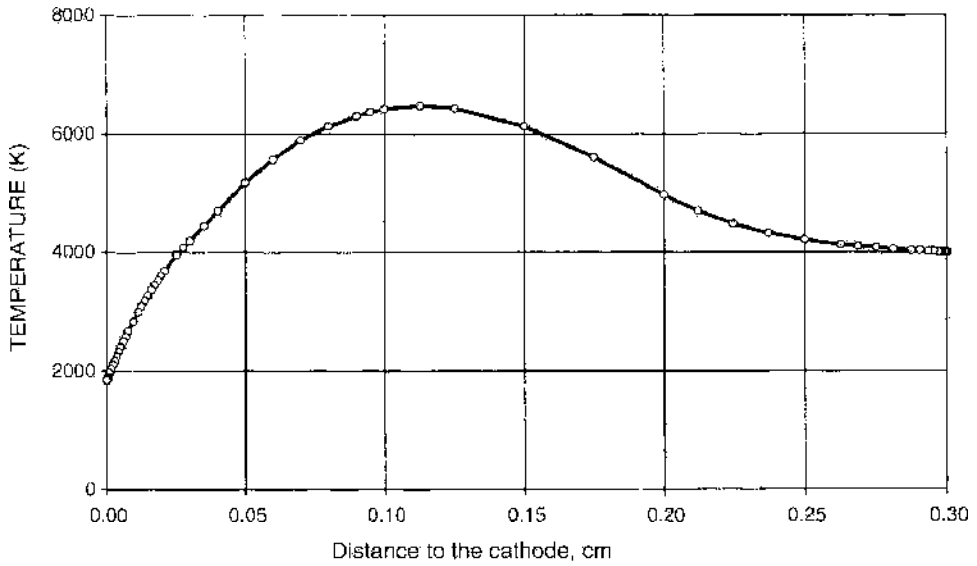

Figure 27. Calculated temperature profile in the interelectrode gap of the arc. Conditions are He, $P = 660$ mbar and $I = 100$ A.

temperature of ~6500 K is obtained at ~1 mm from the cathode and is in fairly good agreement with measured rotational temperature from optical emission spectroscopy performed by the Huczko group [49] (5300 K ± 500 K) in the center of the plasma with $I = 54$ A and $P = 880$ mbar). Nanotubes are created between 1200 K and 1800 K [129, 130]. Such temperatures are reached very close to the cathode, justifying the assumption of nanotube growth at the cathode surface. The calculated mole fractions of major carbon species are shown in Fig. 28. Due to the high temperature that exists throughout most of the gap, the discharge is dominated by atomic carbon. The regions close to the cathode and anode are cooler than the center of the plasma. This enhances carbon atom recombination and explains the two peaks of C_2 mole fraction shown in Fig. 28. The first peak is due to the recombination of C atoms close to the anode, and the second peak occurs at 0.3 mm from the cathode and is due to the competition between gas and surface chemistry. This second peak constitutes a feedstock for nanotube growth. Radiation intensity contours measured at 515 nm by the Huczko

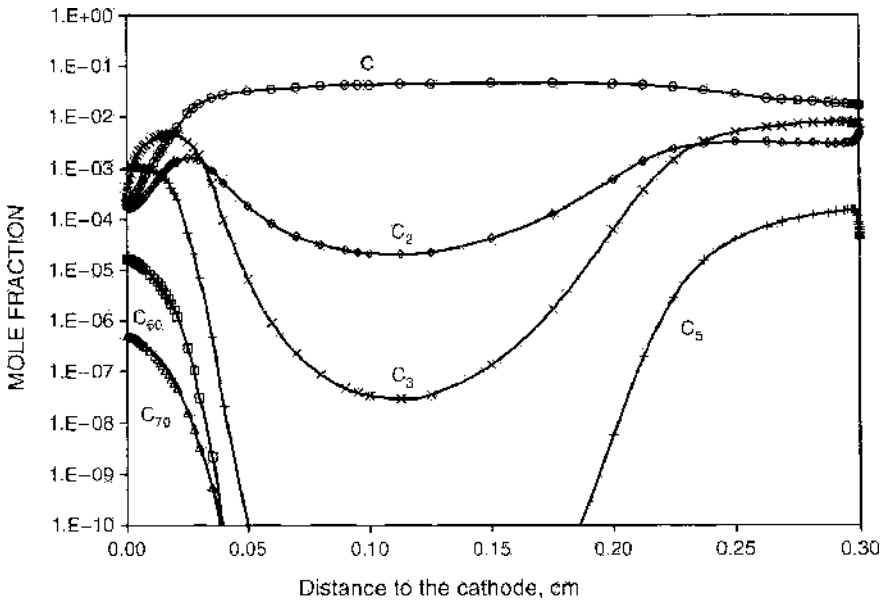

Figure 28. Calculated axial distribution of small carbon clusters and fullerenes in the interelectrode gap of the arc. Conditions are He, $P = 660$ mbar, $I = 100$ A, dilution factor $\tau = 20$.

group [49] indicate qualitatively the presence of two zones rich in C_2, in agreement with our calculations. It can be noted from Fig. 28 that decreases of C, C_2, and C_3 carbon species close to the cathode are due to the surface chemistry, and that fullerenes start to be formed at 0.3 mm close to the cathode. However, the (1D) model as developed here, is not able to calculate the distribution of fullerenes in all of the reactor. The region where fullerenes start to be formed is important from growth mechanism point of view and could be investigated by optical spectroscopy measurements. The calculated normalized species abundance at the cathode is plotted versus cluster size in Fig. 29. It shows a roughly Gaussian distribution of even-numbered clusters with 28–58 carbon atoms and two peaks for C_{60} and C_{70}. Inserted in Fig. 29 are the distributions of carbon clusters as measured under various experimental conditions for laser ablation of a graphite target by Kroto et al. [1] that show a similar behavior. The calculated number densities of major carbon species are listed in Table 21. Number densities of the buffer gas and the catalysts calculated from equation of state are fairly constant $n_{He} = 1.4 \times 10^{18}$ cm^{-3}, $n_{Ni} = 2.0 \times 10^{14}$ cm^{-3}, and $n_Y = 3.2 \times 10^{14}$ cm^{-3}.

Finally, the calculated nanotube growth rate using (10,10) is plotted in Fig. 30 for dilution factors 5, 10, and 20, as the pre-exponential factor of surface reactions varied from 3.0×10^4 carbon addition of C, C_2, and C_3 on soot [118] to 1.0×10^{13} corresponding to carbon addition on diamond [126, 127]. The results show that the predicted growth rate ranges from a few μm/min to 1000 μm/min.

3.4.6. Two-Dimensional Models

A two-dimensional (2D) approach was developed by Bilodeau et al. [114] for simulating carbon arc reactor for fullerene synthesis in helium or argon. The model solves velocities, temperature, and total concentration of carbon species in the two-dimensional axisymmetric space between the electrodes. The model accounts for carbon evaporation from the anode, deposition on the cathode, and condensation in the regions surrounding the arc.

3.4.6.1. Model Formulation Bilodeau et al. [114] assumed an axisymmetric laminar flow, steady-state, and local thermodynamic equilibrium (LTE). The anode erosion rate was assumed uniform and was obtained experimentally. The deposition on the surface of the cathode is governed by diffusion, with velocities of the order of 400 m/s. The drift of ionic species having a velocity 10 m/s due to the electric field was neglected. The input of energy

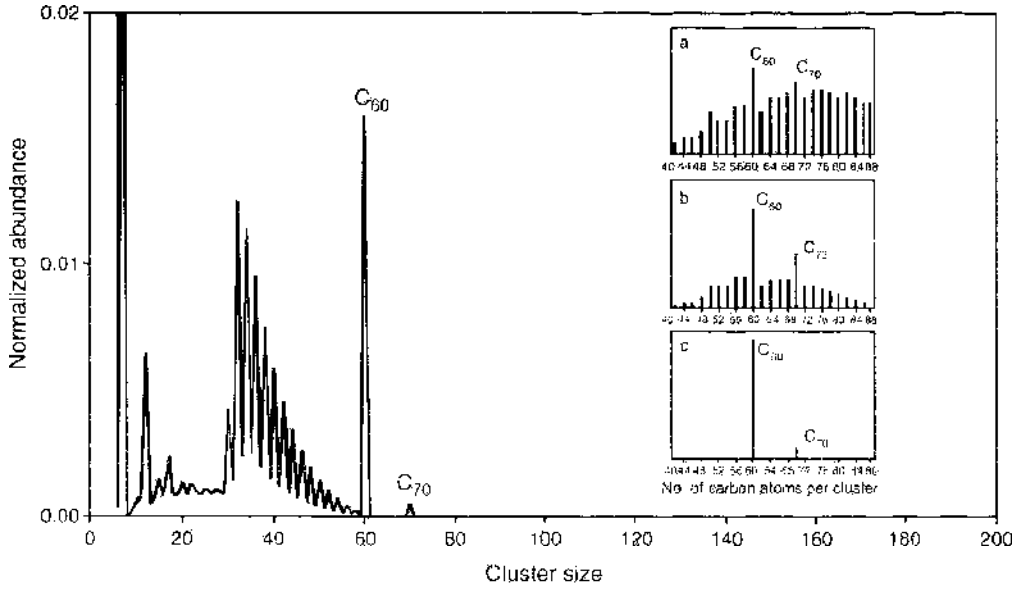

Figure 29. Calculated normalized species abundance at the cathode in nanotube growth in helium. $P = 660$ mbar, $I = 100$ A. In the right of this figure is superposed a comparison with Kroto et al. [1] measurements. (a) Low helium density over graphite target at time of laser vaporization. (b) High helium density over graphite target at time of laser vaporization. (c) Same as (b), but with addition of "integration cup" to increase time between vaporization and cluster analysis.

Table 21. Calculated number densities of small carbon clusters and fullerenes at three positions in the arc.

	T (K)	C density (cm^{-3})	C_2 density (cm^{-3})	C_3 density (cm^{-3})	C_{60} density (cm^{-3})	C_{70} density (cm^{-3})
Anode	4000	7.8×10^{15}	1.1×10^{-15}	1.1×10^{-15}	—	—
1 mm from the cathode	6472	1.2×10^{16}	2.9×10^{12}	2.8×10^{09}	—	—
Cathode	1837	1.7×10^{14}	8.5×10^{13}	6.0×10^{13}	2.6×10^{12}	7.0×10^{09}

A symbol —indicates negligible density. Conditions are helium with $p = 660$ mbar, $I = 100$ amps, $d_{AC} = 3$ mm, and the dilution factor = 20.

in the arc is due to ohmic heating and to the enthalpy flux of the electrons. Enthalpy diffusion due to species transport is considered, and radiation losses are considered using the net emission coefficient method with a plasma thickness of 0.5 mm. As shown in Fig. 31, two calculation domains were chosen to predict temperature and velocity distributions. The first domain, noted (1) in Fig. 31, represents the interelectrode gap of a thickness chosen equal to 1 or 4 mm. The second domain, noted (2) in Fig. 31, represents the entire reactor.

3.4.6.2. Model Equations

Continuity

$$\vec{\nabla} \cdot (\rho \vec{v}) = S_m \tag{49}$$

Axial and radial momentum conservation

$$\vec{\nabla} \cdot (\rho \vec{v} \vec{v}) = -\vec{\nabla} P + \vec{\nabla} \cdot (\mu \vec{\nabla} \vec{v}) + \rho \vec{g} + \vec{j} \times \vec{B} \tag{50}$$

Energy conservation:

$$\vec{\nabla} \cdot (\rho \vec{v} h) = \vec{\nabla} \cdot \left(\frac{\kappa}{c_p} \vec{\nabla} h \right) + \frac{j_x^2}{\sigma} + \frac{5}{2} \frac{k_B}{e c_p} \vec{j} \cdot \vec{\nabla} h - \vec{\nabla} \cdot \left(\frac{\kappa}{c_p} - \rho D_C \right) (h_C - h_g) \vec{\nabla} \omega_C - 4\pi \varepsilon_n + S_h \tag{51}$$

Carbon species conservation

$$\nabla \cdot (\rho v \omega_C) = \nabla \cdot (\rho D_C \nabla \omega_C) + S_m \tag{52}$$

In these equations, $\vec{v}$ is the gas velocity, P is the local pressure, μ the viscosity, ρ the mass density, g the gravitational acceleration, h the specific enthalpy, h_C and h_g the enthalpy of pure carbon and pure buffer gas, respectively, κ the thermal conductivity, c_p the heat capacity at constant pressure, ε_n the net emission coefficient, e the charge of the electron,

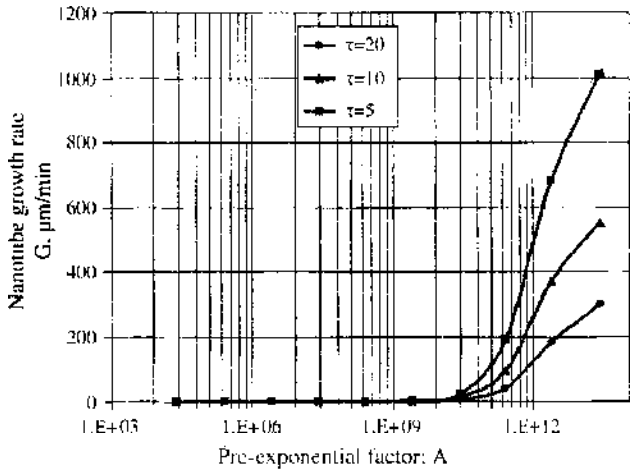

Figure 30. Calculated (10,10) nanotube growth rate versus pre-exponential factor A of the reactions (S1) to (S3) in Table 21 for different dilution factors. Conditions are He. $P = 660$ mbar, $I = 100$ A.

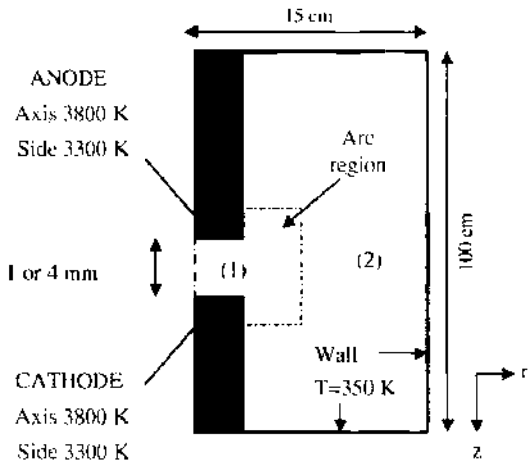

Figure 31. Two calculation domains in Bilodeau et al. [115] (2D) model: (1) arc region delimited by the two opposed movable graphite electrodes and (2) all the reactor.

k_B is the Boltzmann constant, σ the electrical conductivity, ω_C is the mass fraction of carbon species, and D_C is the diffusion coefficient of the carbon species. The axial current intensity $j_x = \sigma E$ is calculated from the linear electric field E, the conductance G, the total current intensity I, and the radius of the electrodes.

$$E = \frac{I}{G} = \frac{I}{2\pi \int_0^R \sigma r \, dr} \tag{53}$$

B is the magnetic field intensity:

$$B = \frac{\mu_0}{R} \int_0^R J_r \, dr \tag{54}$$

with μ_0 the magnetic permeability of vacuum. S_h and S_m are, respectively, heat and mass source terms. The mass source term S_m represents the carbon evaporation near the anode (positive term) or the condensation of the condensation of carbon species near the cathode (negative term).

3.4.6.3. Numerical Results The model equations presented above were solved using the SIMPLE method described by Patankar [131]. Boundary conditions are the following:

- On the reactor wall, the temperature $T = 350$ K, the axial and radial velocities $V_z = V_r = 0$, and the carbon composition $X_C = 0$.
- On the reactor axis, the radial velocity $v_r = 0$ and radial gradients $\partial\phi/\partial r = 0$; with $\phi = (T, X_C, V_z, J_z)$.
- At the anode and cathode tip, $T = 3300$ K on the side and $T = 2800$ K on the axis.

Typical temperature profile maps are shown on Fig. 32 for helium and argon in the two simulations domains (1) and (2) discussed above. For a 1-mm gap, the maximum temperature is ~12,000 K. When the gap distance is increased to 4 mm, this maximum temperature increases to over 17,000 K near the cathode. Bilodeau et al. attribute this difference to the lower carbon concentration and higher electrical resistivity. When argon is used instead of helium with a gap width of 4 mm, the temperature range (1500–5000 K) is wider in argon than in helium. In the temperature range 2000–3000 K assumed by the authors to be favorable for the formation of fullerene precursors, the carbon species concentration is higher in helium than in argon.

3.4.6.4. Flow and Heat Transfer Modeling More recently, Hinkov [115] compared the temperature profiles obtained in nanotube conditions for helium at 660 mbar and argon at 100 mbar. The model consists of Navier Stokes equations implemented in FLUENT computer code. For these calculations, only two species, namely carbon atoms and helium or argon without any chemical reactions were considered. A constant heat flux of

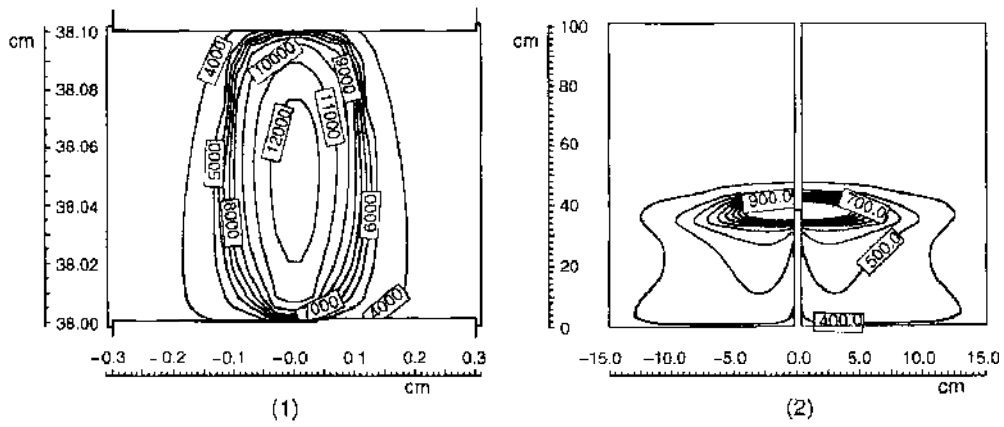

Figure 32. Temperature field in the interelectrode gap (1) and in all the reactor (2) calculated with helium, d_{ac} = 1 mm, I = 80 A, erosion rate = 9.98 mg/s, deposition rate = 4.71 mg/s, and P = 13.3 kPa. Reprinted with permission from [114], J.-F. Bilodeau et al., *Plasma Chem. Plasma Proc.* 18, 285 (1998). © 1998, Springer Science and Business Media.

6.5×10^9 ergs cm^{-2} s^{-1} for argon and 1.2×10^{10} for helium was considered from the measured power. The wall reactor temperature was 300 K. The anode and cathode temperatures are 4000 K and 2000 K, respectively. From Fig. 33, the calculated maximum temperature is 14,700 K for argon and 9080 K for helium. The lower thermal conductivity of argon leads to a much larger hot zone close to the cathode. This result could explain the higher observed nanotube yield when helium is used rather than argon.

3.5. Arc Modeling Concluding Remarks

Mathematical modeling of the carbon arc has been the subject of numerous studies where the objective was to better understand fullerene and nanotube growth, as well as to predict the chemical composition of species and the temperature distribution in the discharge. Several approaches were developed and permitted isolating the effects of thermal, kinetic, mixing, and electric processes on vaporization and condensation of carbon and metallic clusters. Compared with other high-temperature techniques, the uniqueness of the arc is the presence

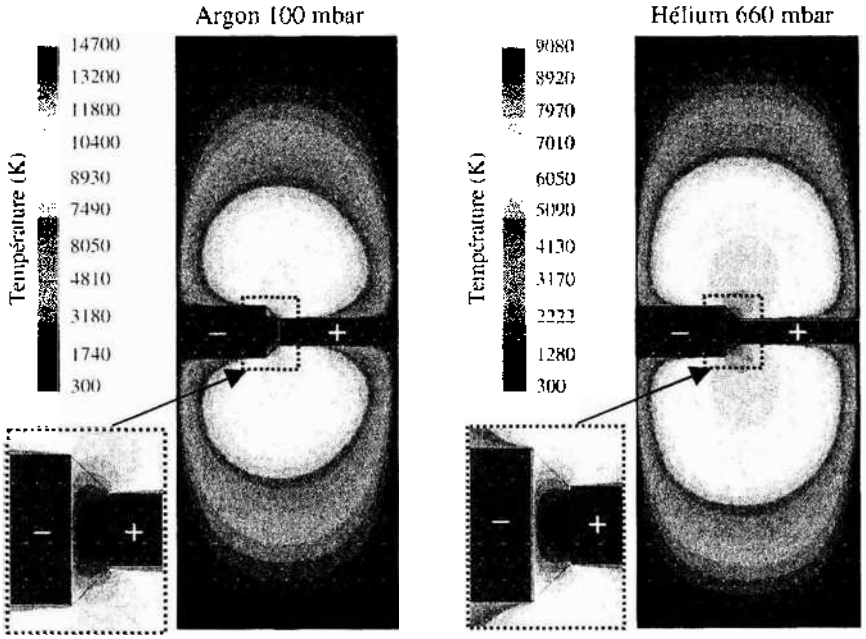

Figure 33. Comparison between argon and helium for optimal nanotube conditions. Reprinted with permission from [115], I. Hinkov, Ph.D. Thesis, University Paris 13, France, 2004. © 2004.

of ions. When a metallic catalyst is mixed to the graphite in the anode, the major ions as measured and calculated are found to be the catalyst ion Y^+ or Ni^+ and not C^+. Hence, in addition to its catalytic role, these metals play the role of current carriers in the discharge. In addition, the energy of ionization of the catalyst is weak; and the process of the anode vaporization is more efficient. Otherwise, the experimental results indicate that the limiting process in nanotube growth is the rate of anode erosion. It will be interesting to explore the effect of other types of catalysts with lower energies of ionization. In addition, we can conclude that the low density of carbon ions in the discharge does not explain the fast growth of nanotubes. Hence, carbon nanotube growth occurs from neutral precursors and could be modeled by a set of surface reactions simulating open nanotube growth exposed to a mass flux from the anode. Because in this approach nanotube surface chemistry is controlled by the local terminated bond and not by the bulk nanotube bond, a mechanistic approach based on the formal resemblance between the bonding and the structure between open nanotube and other carbon surfaces was proposed to explain nanotube growth. Predicted growth rates are in the range of 100 to 1000 μm/min. Nevertheless, a debate still exists on the reason why the nanotube is maintained open during the growth. Some authors attributed this fact to the high local electric field in the growth region close to the cathode; but the predicted values of this local field varies within four orders of magnitude from 10^4 to 10^8 V/cm. This suggest that further modeling efforts are needed to estimate with accuracy the electric field distribution in the connection with thermal, kinetic and turbulent mixing in multidimensional configuration. Further development of a modeling approach is in the direction of selecting more representative gas phase and surface reactions and using *ab initio* calculations of mechanisms and kinetic data. There is a real need for accurate kinetic data for the adsorption of small carbon clusters on open nanotubes of different diameters and chiralities or on pentagon–heptagon defects of closed nanotubes. Because we have evidence that SWCNTs may grow in the gas phase, further work in modeling the arc process will include gas phase production as proposed in [14]. There, gas-phase reactions for the production of SWCNTs are proposed to grow from carbon/nickel clusters using a formalism for the reactions like the one developed for the Boudouard reaction used in the high-pressure carbon monoxide process (HiPco) by Dateo et al. [28]. The calculations will be extended to two dimensions and possibly three dimensions in order to take into account both collaret and core deposit growth in the cathode region. Even though growth chemistry and surface site densities are very different for SWCNT growth in the collaret as compared with MWNT formation in the hard deposit, the formalism discussed in this paper remains valid, and could take into account simultaneous growth of these species in 2D or 3D configurations.

4. COMPUTATIONAL FLUID DYNAMICS ANALYSIS OF TRANSIENT CARBON PLUMES IN LASER-ABLATION SWCNT PRODUCTION

The use of computational fluid dynamics (CFD) simulation methods for the analysis of the flow fields resulting from the laser ablation of carbon targets in the production of single-wall carbon nanotube production is a relatively new practice, with most studies having been conducted only since the turn of the century. CFD techniques for the solution of the governing equations of fluid motion have been present since the advent of high-speed computers in the 1960s. The National Aeronautics and Space Administration (NASA) and various aircraft corporations originally developed CFD methods primarily for the solution of external flow fields surrounding aircraft and high-speed space vehicles leaving or returning to the earth's atmosphere. Additionally, CFD methods for the solution of internal flows such as those occurring through gas turbine engines were developed at the same time as external solution techniques or "codes." Recently, CFD methods have gained popularity in other fields of endeavor that are less "aeronautical" in nature such as the analysis of various forms of materials processing, or when the fluid dynamics equations are merged with equations of electrodynamic forces such as the Maxwell equations (in a group of techniques referred to as "magnetohydrodynamics" or MHD), to such diverse fields of study as the flow of charged

particles in the magnetosphere of the earth. Two excellent references for general conventional internal and external CFD techniques are the works of Hirsch [132, 133] and Hoffman and Chiang [134]. The former publication is more theoretical in nature than the latter; however, the latter provides a better introduction for the casual CFD code user.

Recent work in the application of CFD methods to laser ablation flow field studies have been accomplished by both the solution of the Euler equations [132], which ignore viscous effects in the solution technique, and by solution of the Navier-Stokes equations [132], which do incorporate viscous effects. Both methodologies will be examined as they have been applied to laser-ablation SWCNT production in the following paragraphs. All numerical techniques are approximations of the full partial differential equations of fluid motion, be they Euler or Navier-Stokes equations, and the solution of the governing PDEs calculated by computer codes will be highly dependent upon the boundary conditions applied. All transient solution methods are highly dependant on two factors: boundary conditions and the time step size taken at each time step. Transient methods rely on having accurate assessment of the current flow field and then extrapolate the current solution into the future by known mathematical methods. Therefore, no discussion of the CFD techniques as applied to laser ablation flow fields would be complete without a discussion of the boundary condition determination for the flow fields—such discussion will follow the examination of the basic numerical solution methodology for the Euler and Navier-Stokes equations.

4.1. Inviscid Solution of Carbon Plumes in Laser Ablation

Lobao and Povitsky [135] have successfully used a unique combined Eulerian and Lagrangian approach to the solution of the flow fields resulting from the rapid vaporization of carbon targets in the SWCNT oven. Note should be made that the phrase "Eulerian" in this sense refers to analysis by a fixed control volume, not to the governing inviscid fluid dynamics conservation equations—although Lobao and Povitsky do indeed use the Euler equations in their methodology. Lagrangian methods differ from Eulerian in that individual particles are tracked as they flow through space; and overall thermophysical parameters are then calculated by statistical techniques applied to the many particles in the flow field.

Lobao and Povitsky make the assumption that the inviscid Euler equations suffice for an analysis of the laser ablation of carbon due to the rapid time frames in which the ablation process occurs. The laser irradiation times for the laser ablation process as practiced at NASA Johnson Space Center are approximately 10 ns in duration, although the material may continue to ablate for several nanoseconds after the irradiation terminates. It should be noted however that viscous shear stresses, τ, are a function of velocity gradients wherein:

$$\tau_{ij} = \mu \frac{\partial v_i}{\partial x_j} \tag{55}$$

for a Newtonian fluid, where v_i is the velocity component in the "i" direction, x_j represents the "j" spatial direction, and μ is the viscosity. A direct physical dependency upon time in the viscous components of the flow physics does not exist then. Given the extreme velocity gradients that occur in the laser ablation process, with inlet velocities of the ablative carbon being of the order kilometers per second flowing into essentially quiescent argon gas, it is possible that even given the short time duration of the flow, viscous effects may be of significant enough magnitude that they cannot be ignored.

4.1.1. Solution Methodology

Lobao and Povitsky used the two-dimensional compressible Euler equations with a generalized curvilinear coordinate system in ξ, η coordinates. The equations can be represented in vector form by:

$$\frac{\partial Q}{\partial t} + \frac{\partial F}{\partial \xi} + \frac{\partial G}{\partial \eta} = S \tag{56}$$

where the vectors of conserved variables (Q, F, G, and S) are given by:

$$Q = \frac{\delta}{J}\begin{bmatrix} \rho \\ \rho u \\ \rho v \\ E \\ \rho C_1 \\ \rho C_2 \end{bmatrix} \qquad F = \frac{\delta}{J}\begin{bmatrix} \rho U \\ \rho u U + \xi_x P \\ \rho v U + \xi_y P \\ (E+P)U \\ \rho C_1 U \\ \rho C_2 U \end{bmatrix}$$

$$G = \frac{\delta}{J}\begin{bmatrix} \rho V \\ \rho u V + \eta_x P \\ \rho v V + \eta_y P \\ (E+P)V \\ \rho C_1 V \\ \rho C_2 V \end{bmatrix} \qquad S = \frac{1}{J}\begin{bmatrix} 0 \\ 0 \\ P \\ 0 \\ 0 \\ 0 \end{bmatrix} \tag{57}$$

In this formulation, ρ represents the local gas density, u and v are the local velocity components, U and V are the contravariant velocities, E is the total energy, and P is the pressure. C_1 and C_2 are the mass fractions of the two species. ξ_x, ξ_y, η_x, and η_y are the metrics of the coordinate transformation. J represents the Jacobian of the coordinate transformation, and δ is the radial axisymmetric coordinate in the η direction. The first equation represents the conservation of mass while the second and third equations are the conservation of momentum in two dimensions. The fourth equation is the conservation of energy while the final two equations are the "conservation of species" equations for the two chemical species, C_3 and Ar, used in the Lobao and Povitsky analysis. The gas is assumed to be a calorically perfect gas in their analysis. Excellent references for further elaboration on the Euler equations and their generalized coordinate versions can be found in [134, 136]. Lobao and Povitsky use a second-order upwind scheme for the conservation equations called "MUSCL" [133] and they use a central relaxing total variation diminishing (TVD) scheme best described in their paper [135]. The Lagrangian scheme used by Lobao and Povitsky to solve for particle motion in the flow field is not well described in their paper other than the fact that it is based on a second-order Runge-Kutta scheme and yields particle streak lines in the resulting carbon plume.

Lobao and Povitsky considered an axisymmetrical flow domain that was 25 cm in the longitudinal direction by 5 cm in the lateral dimension with a structured grid giving a grid size of 250 x 50 computational nodes. Initial conditions inside the flow chamber were a pressure of 1 atm and a temperature of 1500 K for the argon in simulation of a high-pressure ablation process and also for a pressure of 10^{-6} atm for a low-pressure ablation case in their paper. The boundary conditions at the site of the laser irradiation are given as 100 atm of pressure at a temperature of 5000 K. The irradiation boundary condition was allowed to propagate for 20 ns with an initial time step of 10^{-11} s. The ablation boundary condition is then replaced by the flow chamber conditions, and the entering plume of C_3 is allowed to propagate downstream. Time steps in the Lobao and Povitsky method were controlled by adjustment of the Courant-Friedricks-Lewy, or CFL, number given the fixed even grid spacing.

4.1.2. Results

Lobao and Povitsky simulated a number of variations upon the standard conditions used in the laser ablation at NASA Johnson Space Center, and qualitative comparisons were made between the parametric variations, although no comparisons were made to existing experimental data [137] for shock front expansion. As previously mentioned, two variations

on the chamber pressure were simulated and showed consistent physical results in that the C_3 plume expanded more rapidly in the lower chamber pressure than in the 1 atm pressure case.

Other variations on the standard operating conditions that Lobao and Povitsky examined included the influence of carbon injection velocity on the flow field dynamics. Initially, the entrance velocity of the carbon plume was set to zero and the plume allowed to propagate by virtue of the pressure differential. Additional injection velocities were simulated in their paper, although few results were shown. A final variation examined by Lobao and Povitsky was the effect of the interaction of multiple laser irradiations upon overall plume dynamics. The standard processing of SWCNT calls for irradiation of 10 ns duration for the first pulse followed 50 ns later by a second pulse of 10 ns duration. This process then repeats on a 60 Hz cycle. Lobao and Povitsky allow for a similar double-plume injection however using a gap of 16 μs between irradiation intervals. The main effect of the multiple plume interaction noted by Lobao and Povitsky was the increase in plume temperatures observed from the reflected shock waves re-compressing the plume from wall and plume interactions.

4.2. Navier-Stokes Solutions of Carbon Plumes in Laser Ablation

Greendyke et al. [138–143] have conducted a number of studies of the carbon plume resulting from laser ablation of a carbon surface in SWCNT production using a full Navier-Stokes solution of the flow equations. In preliminary work [138], it was determined that the viscous stress terms could not be ignored given that the background flow was approximately 3 cm/s yet the carbon plume entrance velocity was of the order 5 km/s. Such large differences in velocity would necessarily lead to large viscous stress terms (as explained in the previous section) given the magnitude of the inevitable velocity gradients.

In his first study [138], Greendyke used the VULCAN code [144], which was originally designed for the study and analysis of internal supersonic combustion processes in hypersonic propulsion applications. The code was selected for its ability to handle mixed elliptical, parabolic, and hyperbolic flow field equations. The code solves the generalized curvilinear Navier-Stokes equations described by:

$$Q_t + (E - E_v)_\xi + (F - F_v)_\eta + (G - G_v)_\zeta = S$$

where Q_t, E, F, G, and S are vectors describing the conserved variables included in the conservation of mass, momentum, energy, and species conservation equations as best described by White and Morrison [144]. E_v, F_v, and G_v represent the viscous flux vectors and are also described in [144]. In addition to the full Navier-Stokes equations, the VULCAN code also contains several turbulence model formulations, and Greendyke selected the k-ω model of Pope (described, along with other turbulence models in [145]) for his studies. The VULCAN code uses several solution methodologies for the Navier-Stokes equations, and Greendyke selected the time-accurate fourth-order Runge-Kutta methodology option of the VULCAN code that is based on a method first developed by Jameson et al. [146] for the solution of the Euler equations. In general, however, any CFD code capable of mixed flow regimes would work well in laser ablation plume development studies—a very good synopsis of modern CFD codes can be found in Laney [147] and at the accompanying Web site [148].

4.2.1. Boundary Condition Determination at Ablative Surfaces

Before any CFD code can be accurately run for the solution of carbon plumes, it is necessary to correctly determine the boundary conditions at the ablative surface—without the boundary conditions correctly determined, no CFD code can predict reliable results. However, very little experimental information was available for the boundary conditions at the surface of the laser ablation carbon target. The only known thermophysical quantities had been the carbon mass ablation rate of 1.6×10^{-6} g/laser pulse in argon, and the approximate energy of 300 mJ over the 5-mm laser spot size. The original studies of Greendyke et al. [138, 139] assumed that the carbon mass was injected into the flow field through the 10 ns duration of the laser pulse. A simultaneous solution of both the ideal gas equation

$$PV = NRT \tag{58}$$

and the Clausius-Claperon equation:

$$P = P_{ref} \cdot e^{\frac{\Delta H_{vap}}{RT}} \tag{59}$$

resulted in a density of 10.59 kg/m^3, a gas temperature of 5211 K, a vapor pressure of 377 atm, and a carbon injection velocity of 1900 m/s at the target surface. In those studies, however, the resulting propagating carbon plumes exceeded the shock front locations data gathered by Puretzky et al. [140] past the 200 μs postablation time.

In later studies [140, 143], the ablation time was assumed to be 15 ns—the additional 5 ns worth of ejected ablation material coming after the termination of the laser pulse. The resulting solution of ideal gas and Clausius-Claperon equations showed that while the temperature of the injected carbon was relatively insensitive to the additional ablation time (T = 4950 K), the vapor pressure of the carbon plume dropped considerably to approximately 100 atm. The corresponding density was an order of magnitude less, 1.039 kg/m^3, and the plume injection velocity rose to 5228 m/s due to the lower molecular weight. Chemical equilibrium was assumed at the ablation surface, and the CHEMKIN [40] code was used to determine inlet carbon species mass fractions for C through C_5 (no data being available in CHEMKIN for C_6). C_3 and C_5 were found to be the dominant species at the ablation surface inlet with the mass fraction of C_3 being 0.463 and C_5 being 0.426. The next contributors to the inlet flow were C_2 and C_4 with species mass fractions of 0.044 and 0.059, respectively. The atomic carbon mass fraction was nearly negligible at 0.008.

4.2.2. Flow Domain Gridding

After the correct determination of flow field boundary conditions, the domain of interest needs to be resolved into a computational grid for the calculation of flow field characteristics. Greendyke [140] originally used a 2D axisymmetric solution methodology for the flow field volume with a 2D grid. At the time of his first investigation into laser ablation carbon flow fields, little was known of the resulting flow field and the degree to which the carbon plume would propagate into the flow field downstream of the carbon targets or the region in the outer quartz tube of the laser ablation oven. Figure 34 shows the original axisymmetric grid that was used by Greendyke in the original investigations. Figure 34, however, displays a symmetrical grid about the $y = 0$ axis. Only the portions for $y \geq 0$ are used in the actual axisymmetric flow field calculations. One problem encountered was that the grid only extends

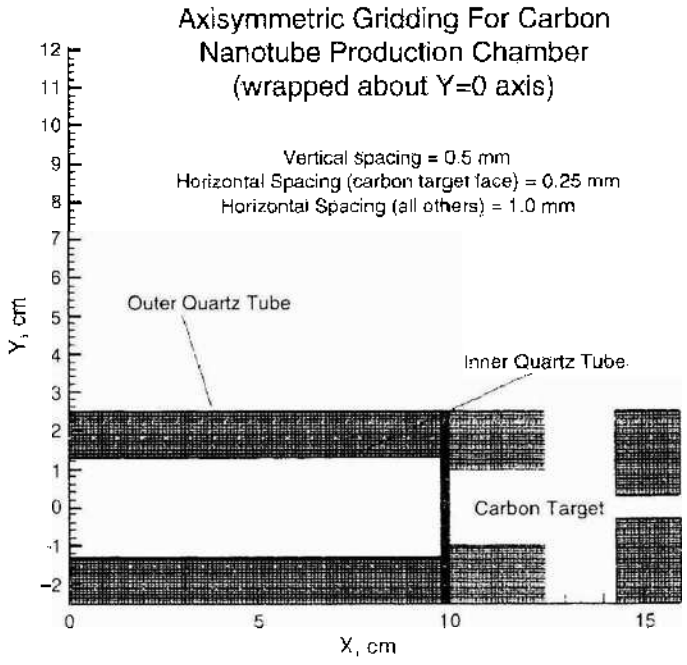

Figure 34. Laser-ablation oven gridding.

to 10 cm in front of the carbon target and boundary conditions at the upstream portion of the background argon flow reflected the pressure wave resulting from ablation boundary conditions back into the propagating carbon flow. In later studies, Greendyke et al. [142–145] used a "primary grid" (Fig. 35) with 0.5-mm grid node locations for the first 10 cm in front of the ablation surface for the inner quartz tube alone as in the first work [140–141], with a "secondary grid" of 0.5-mm vertical spacing and 5-cm horizontal spacing out to a point 55-cm upstream of the carbon target. The elongated flow field region under consideration alleviated the problem of reflecting pressure waves returning to influence the carbon plume's propagation into the argon background flow.

Multiple gridding software options are available to the researcher, with varying degrees of complexity to use. The most convenient of the available gridding software codes is the *Mesh Generator* software [149] available as an "add-on" package to Amtec Engineering Inc.'s *Tecplot* software [150]. The *Mesh Generator* is capable of outputting grid information in both the ASCII format and the PLOT3D form (PLOT3D is a graphics package for CFD use that is available from the Open Channel Foundation—see their Web site referenced in [151]) used by many commercially available CFD codes such as the VULCAN code [146].

4.2.3. Flow Field Solution Procedures Used by Greendyke et al.

In all of the studies by Greendyke et al. [140–145], the same procedure was used throughout. After determination of the boundary conditions, the first priority of the simulations was the solution of the "base" argon flow. The global elliptical viscous method of the VULCAN code was used with diagonal approximate-factorization in axisymmetric fashion for this part of the simulation. Full k-ω turbulence modeling and a mixture of thermally perfect gases options were chosen. The solution was allowed to converge until a sixth-order reduction in the L2 norm was observed.

Actual simulation of the carbon plume resulting from the laser-ablation of the target could proceed with the base flow established. To simulate the carbon plume, a jet of carbon was allowed to enter at a density, with the boundary conditions described above, from the first five grid point locations in the grid block immediately in front of the carbon target corresponding to 2.5 mm in actual length. Flow enters axisymmetrically having a radius of the laser beam's spot size. The time-accurate Runge-Kutta solution procedure was applied to the restart files from the base flow simulation for 100 (or 150 in later studies) time steps of 0.1 ns each—corresponding to the actual duration of a laser pulse. The restart files from this "carbon-injection" simulation were themselves used in subsequent simulations with the carbon mass flow injection deleted in the input data file for VULCAN. An isothermal wall boundary condition was used in place of the carbon injection condition with a temperature

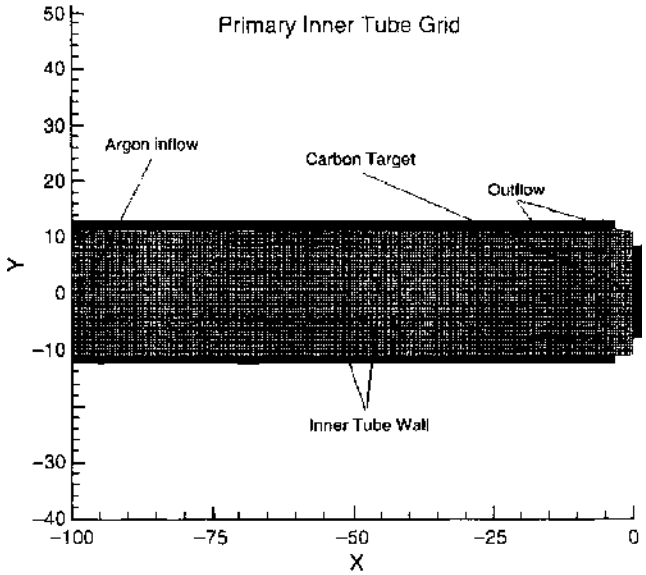

Figure 35. "Primary" grid spacing in revised studies of laser ablation plumes.

set to slightly higher (1773 K) than the initial ambient conditions in the nanotube production chamber. This boundary condition was held constant until 60 ns of simulated time had passed, and then the ablation boundary condition was reinitiated for another 15 ns of simulated time to correspond to the second laser ablation of the processing on a 60 Hz cycle as practiced at NASA Johnson Space Center. The flow with the developing carbon plume was simply allowed to develop naturally to whatever point in time required by manipulation of the time step size and maximum number of iterations allowed in the VULCAN input data file.

4.2.4. Results of Navier-Stokes Simulations

For the original work with full Navier-Stokes solution methods, Greendyke et al. used only C_3 as the injected species at the carbon ablation boundary points to determine flow field characteristics and plume propagation into the background argon gas. No chemical reactions were allowed in these studies. Figure 36 shows the result of the C_3 injection simulations at 200 μs postinjection time and indicates the classic "smoke ring" profile of the carbon plume observed by several experimental investigations. Further confirmation of the accuracy of the Navier-Stokes modeling was presented by Greendyke et al. [143] using only C_3 as the injected carbon species without chemical reactions. Good comparisons were obtained with experimental observations of carbon plume propagation conducted by Puretzky et al. [137] for the earlier postinjection times. As the flow field solutions were allowed to progress, however, computational results for the leading edge of the carbon plume began to overtake experimental results at the 1-ms point of postinjection time. Temperature contours compared favorably to experimental results as well in this study, as can be seen in Fig. 37.

In later studies [142–145], Greendyke et al. added chemical reaction mechanisms to the flow field solution methodologies. The first reaction model [140] was a 12-species, 14-reaction model for the formation of carbon molecules up to C_6 including the ion species of C^+, C_4^+, and C_5^+ as well as electron concentrations. The chemical reaction model was a reduced form of the reaction mechanism for the formation of C_{60} and C_{70} fullerenes developed by Krestinin and Moravsky [8]. The primary purpose of the inclusion of higher species and chemical reactions was twofold. The first purpose was to see what effect condensation of the carbon species would have on flow field dynamics and temperature profiles. The second purpose was to determine if formation of the C_6 molecule, as it is not injected in the boundary conditions, would provide some indication to the thermophysical conditions for higher carbon molecule formation. The formation of C_6 would then serve as an "indicator species" for more complex carbon molecule formation. One discrepancy in this initial study with chemical reaction mechanisms was immediately observed—temperature profiles with chemical reaction mechanisms quickly exceeded the temperature profiles from earlier work—and this result was first thought to be the result of energy being released into the flow field from the condensation of lighter carbon species. However, in later work, Greendyke et al. [144] discovered that the high temperatures were the result of excessive time steps being used in combination with chemical reactions. If the time steps for the initial laser

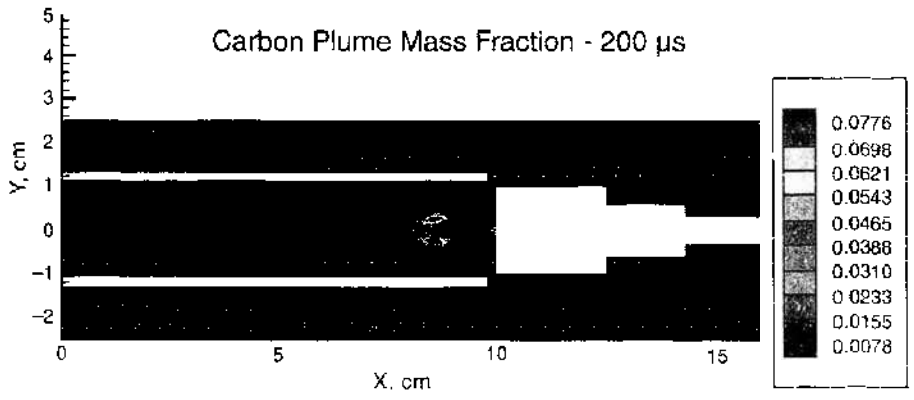

Figure 36. C_3 mass fraction contours at 200 μs.

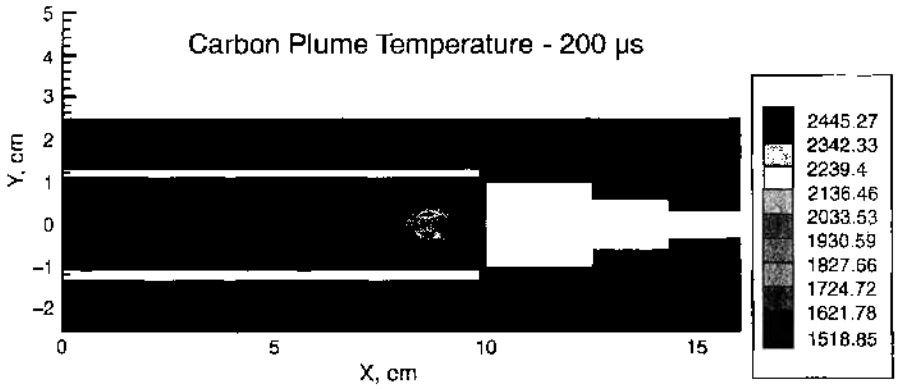

Figure 37. Temperature contours at 200 μs for C_3 studies of Greendyke et al. Reprinted with permission from [142], R. B. Greendyke et al., *J. Nanosci. Nanotechnol.* 4, 441 (2004). © 2004, American Scientific Publishers.

ablation boundary conditions were decreased to 0.01 ns, temperature profiles in argon background gases returned to similar, although not identical, profiles for the original work with C_3. A curious result of this work was that even with the higher temperature profiles, leading edge propagation of the carbon plume was comparable to the earlier work [138], but deviated from the experimental work of Puretzky et al. [137] at postablation onset times at, or beyond, 1 ms. A possible cause for the higher plume propagation speed of the calculated results than experimental could be the curve-fit data incorporated into the input files used in the VULCAN code for diffusion of the higher species of carbon. No data was available for the higher carbon species, and data for C and C_2 was simply extrapolated for higher species. As is generally known, lighter species will diffuse faster than heavier species.

It is impractical to use the full C_{60} and C_{70} model for fullerene formation of Krestinin and Moravsky. All flow field solution methods such as the VULCAN code have to solve the species continuity equations at each grid point in the considered flow field domain. Computational intensity therefore increases with the number of grid points and species by the relationship $CPU \propto (NS)^2$ where CPU indicates *CPU* processor time, N is the number of grid point locations in the domain, and S is the number of chemical species. As a result, for the flow field grid described in [138], computational times of up to 30 min were required for a single iteration at a time step of 10^{-13} s, thereby rendering such CFD studies impractical.

In the same studies [141–143], work began by Greendyke et al. on duplicating a series of parametric experimental studies conducted at NASA Johnson Space Center [152]. The latest work [143] represented the culmination of the computational simulations to duplicate the set of experiments. For this study, the 12-species model originally used was replaced by an 11-species model with 14 reactions—which is given in Table 22. The goals of this study were to gain insight into the thermophysical characteristics of the flows under differing pressures, background gas temperatures, different background gas chemical species, and differing diameters of the quartz inner tube of the laser ablation oven. A secondary goal was again to attempt to define "indicators" in the flow field solutions of the carbon plume that would provide insight in the refinement of the laser ablation SWCNT processing and allow improvement of the method for increased production. Unfortunately, in the set of experiments that this study was based on, it was not possible to determine the actual quantities of SWCNT produced in the experiments. Only the total carbon ablated was available, thereby negating the ability to do a direct comparison between computational studies and SWCNT production.

However, certain insights were still available from the computational study. One of the main results of Greendyke's study was a direct correlation between plume expansion into the background gas and the amount of recovered carbon from the experiments. A plume expansion factor, ϕ, was defined by Greendyke as

$$\phi = \iiint \left[\frac{\rho_{carbon}}{\rho} \sqrt{x^2 + y^2} \right] dV \tag{60}$$

Table 22. Simplified carbon chemistry model used in laser ablation simulation.

REACTION	A ($cm^3\ s^{-1}\ mol^{-1}$)	β	T_a (K)
Reaction Rate Coefficients [where $k_f = A^* T B^* \exp(-T_a/T)$]			
1. $C + e- \Leftrightarrow C+ + e- + e-$	5.46E − 04	0	214420
2. $C + C \Leftrightarrow C_2$	2.00E + 14	0	0
3. $C + C_2 \Leftrightarrow C_3$	2.00E + 14	0	0
4. $C_2 + C_2 \Leftrightarrow C_3 + C$	2.00E + 15	0	9040
5. $C_2 + C_2 \Leftrightarrow C_4$	2.00E + 14	0	0
6. $C + C_3 \Leftrightarrow C_4$	2.00E + 14	0	0
7. $C + C_4 \Leftrightarrow C_5$	2.00E + 14	0	0
8. $C_2 + C_3 \Leftrightarrow C_5$	2.00E + 14	0	0
9. $C + +C_3 \Leftrightarrow C_4^+$	9.00E + 09	0	0
10. $C + +C_4 \Leftrightarrow C_5^-$	6.00E + 14	0	0
11. $C + +e- \Leftrightarrow C$	3.60E + 16	−4.5	0
12. $C_3 + C \Leftrightarrow C_6$	2.00E + 14	0	0
13. $C_4 + C_2 \Leftrightarrow C_6$	2.00E + 14	0	0
14 $C_3 + C_3 \Leftrightarrow C_6$	2.00E + 14	0	0

where

$$\frac{\rho_{carbon}}{\rho} = \sum_{\substack{carbon \\ species}} \frac{\rho_i}{\rho} \tag{61}$$

or, the local summation of the individual carbon species' mass fractions. The plume expansion factor provided a relative measure from one case to the next of the propagation of carbon throughout the flow field assuming the carbon plume originates at the origin, as it does in all cases in [143]. The plume expansion factor provided a direct relative measure of the expansion of carbon throughout the flow field.

Varying the thermophysical characteristics of the background gas resulted in widely different plume development at similar points in time. Figures 38–40 indicate the difference in both leading edge propagation of the carbon plume for argon, helium, and N_2 background gases at 100 μs postablation time. The resulting plume expansion factors for the variation of background gases is seen in Fig. 41, which shows that the higher the plume expansion factor, the lower the mass of recovered material from the laser ablation when compared to the experimental results of Arepalli et al. [152]. Similar results were obtained for the other variations of background gas temperature, pressure, and the inner tube diameter of the

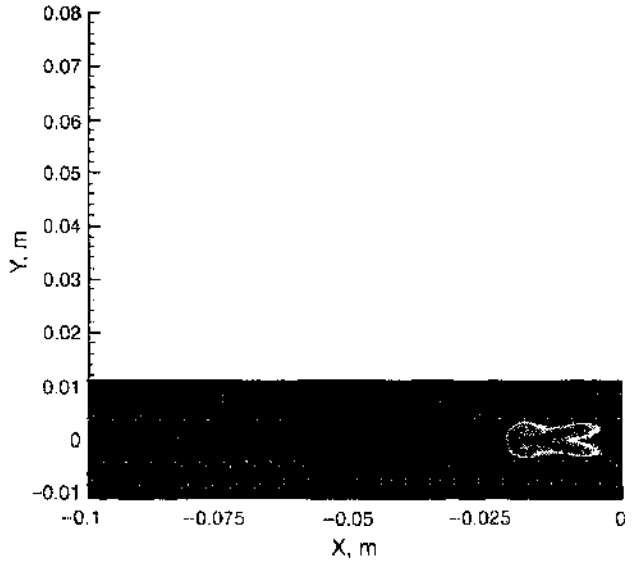

Figure 38. Carbon plume propagation in Ar at 100 μs postablation onset.

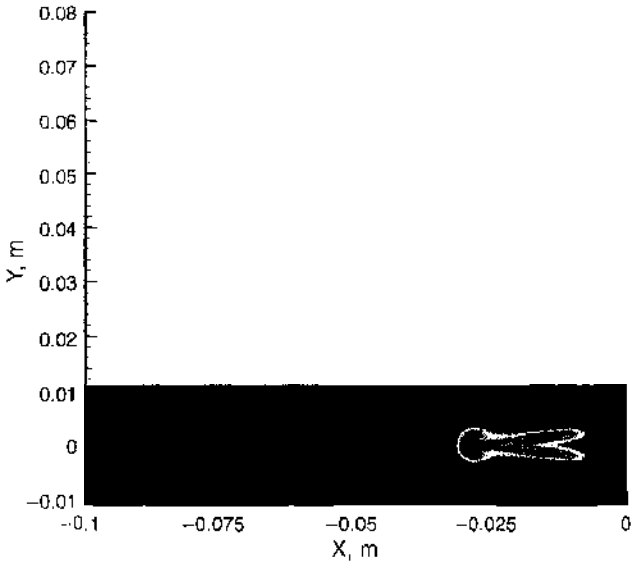

Figure 39. Carbon plume propagation in N_2 at 100 μs postablation onset.

laser ablation oven with one noticeable discrepancy—the case where the inner quartz tube was reduced from its nominal 1-inch diameter used in standard processing to a diameter of 1/2 inch. Experimental results showed that the narrower diameter case should result in a reduced quantity of mass being recovered from laser ablation, whereas the inverse relationship seen with the plume expansion factor plotted in Fig. 42 indicates that the mass recovered should have been higher than the nominal one inch diameter case. With the exception of this one case, the plume expansion factor did provide the best "indicator" yet of the amount of ablative carbon material that could be recovered from laser ablation studies. However, the plume expansion factor did not provide a direct quantitative relationship for the carbon recovered, but it did provide a qualitative relative measure from one case to the next. A possible cause of this discrepancy may be the result of the high concentration of carbon in the small diameter case resulted in more absorption of laser energy by the ablation products. This reduced the energy flux to the target, resulting in less ablation.

Other results from the latest study [143] did provide thermal and species concentration profiles for the parametric variations that can be used in separate decoupled solutions with more complex chemical models (such as the Krestinin and Moravsky model in [8]) using the

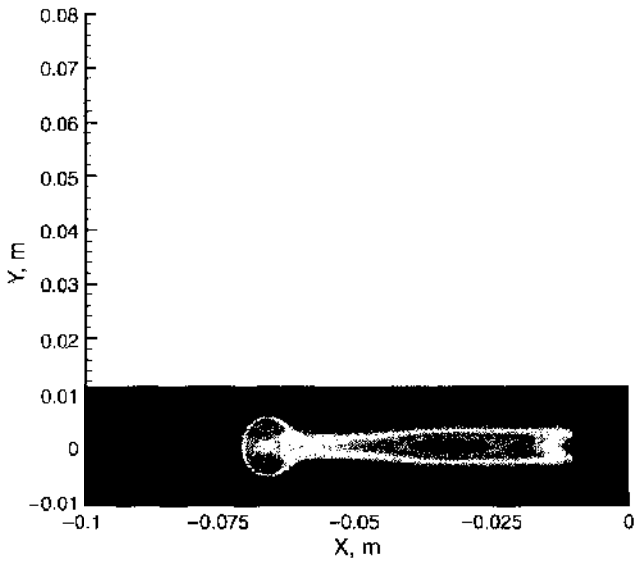

Figure 40. Carbon plume propagation in He at 100 μs postablation onset.

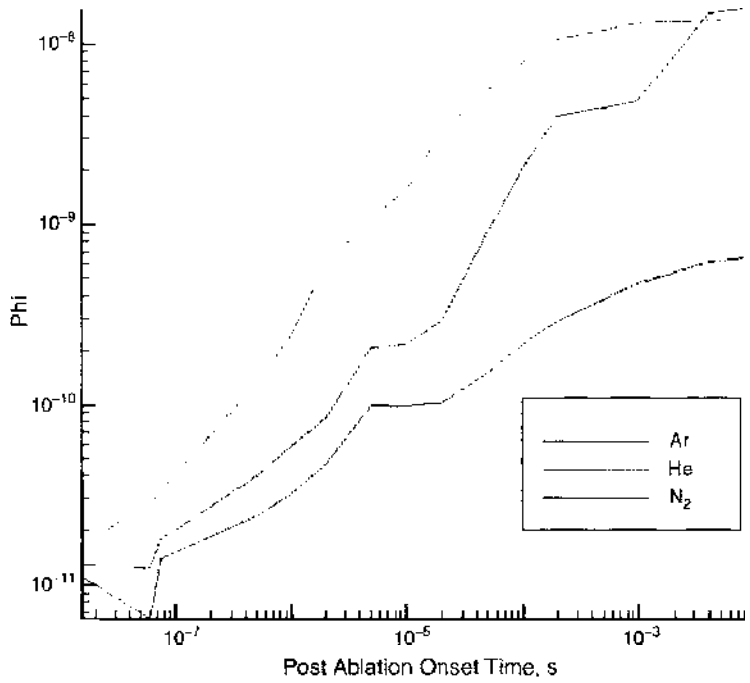

Figure 41. Plume expansion factor for varying background gases.

CHEMKIN software [40]. At the present time, Greendyke and Scott are continuing these decoupled studies with a refined grid mesh in the immediate ablation area of the carbon target for times ranging from ablation onset up to the first few microseconds after ablation onset. The flow field solutions at different points in postablation onset times that result from this study can be combined into a single solution file via use of the *Tecplot* [150] software. The resulting solution data file can then be input into the *CFD Analyzer* [153] add-on feature to the *Tecplot* package. Once the user has specified the location of basic flow field properties in the file, such as pressure and temperature, the *CFD Analyzer* package can automatically integrate streak lines or particle trajectories over the time domain of the composite flow field solution file. All flow field properties and chemical compositions along the streak lines are then returned by the software for analysis with the decoupled methodology previously

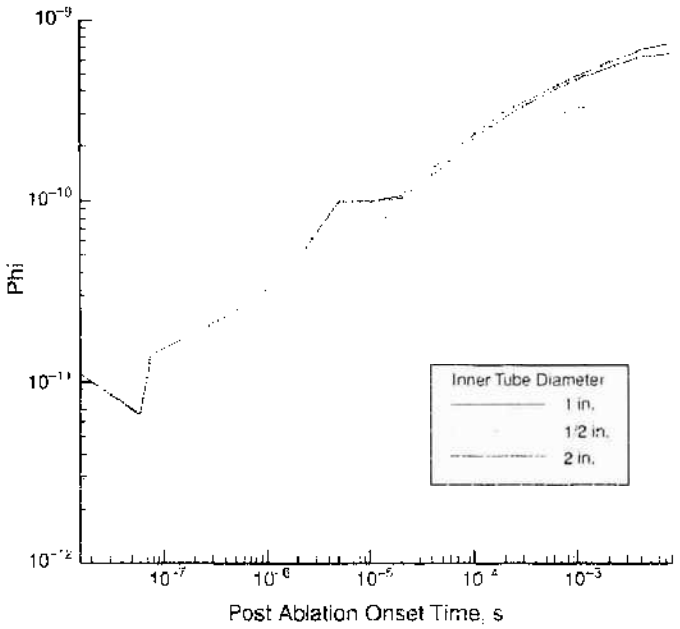

Figure 42. Plume expansion factor for differing inner quartz tube diameters of the laser ablation oven.

described. Results from decoupled calculations along streak lines will be discussed in the next section.

4.3. Chemical Kinetics Along Streak Lines in Pulsed Laser Ablation

For CFD problems having more than one dimension, adding a large chemical kinetics model would overwhelm even supercomputers. Solutions would take days or weeks of computer time to solve. In many cases, it is useful to decouple the problem and solve the fluid dynamics and energy equations without chemical reactions. The history of temperature, pressure, and mixing (dilution) with an external gas can be determined along streak lines. For steady-state problems such as the arc or HiPco process, as was described in Section 2.3.1, one can easily integrate the position divided by velocity to obtain the time at corresponding points in the flow. The CFD solution provides all other properties, except the detailed chemical species. One can then use a chemical kinetics code, such as the AURORA code of CHEMKIN, to solve the chemical rate equations along the streak line, as a function of time. For time-dependent solutions of the flow equations, as is needed for dynamic situations such as the laser ablation process, a similar technique can be used to follow a sample "particle" of the flow as time evolves. However, the process requires having the solution at various times during the development of the flow. With these solutions described in Section 4.2, one can do a similar integration of the distance/velocity. For example, in some preliminary calculations we have the evolution of the solution along a number of streak lines that start next to the laser ablation target. These streak lines are shown in Fig. 43. Integrating the distance divided by velocity, we obtain the time interval between points and therefore, the time at each location. Then we have the flow field properties as a function of time. The temperature (Fig. 44) and pressure profiles were then input into the AURORA code to solve the chemical rate equations for the evolution of the species along the streak line. One such preliminary solution is shown in Fig. 45 for the complete model along one of the streak lines. The rate coefficients for this calculation were not accurate; therefore, it only represents the methodology, not accurate results.

4.4. Conclusions from CFD Modeling

The current limitations of reduced carbon chemical reaction mechanisms and the resulting computational overhead that would result from higher order chemistry models severely hinder the analysis of laser ablation SWCNT production by CFD methods when CFD is used

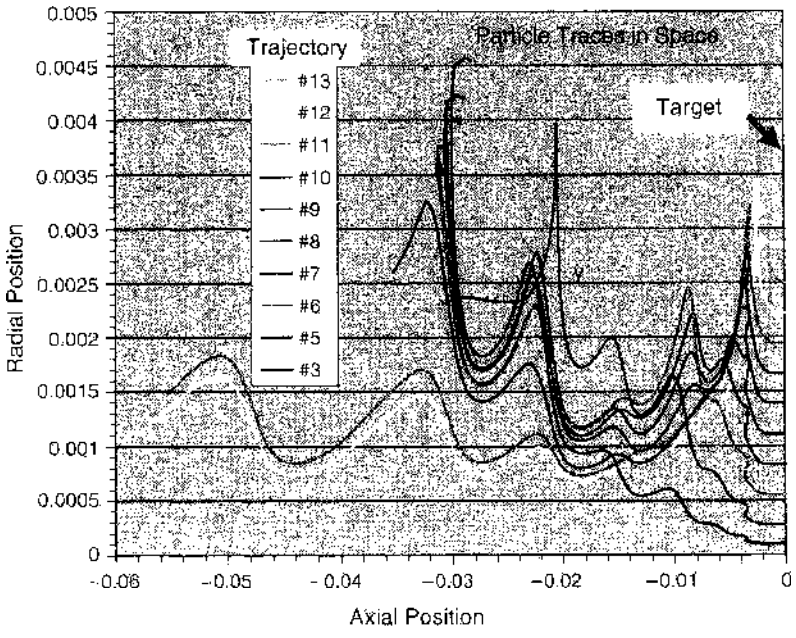

Figure 43. Streak lines in space for laser ablation axisymmetric calculation.

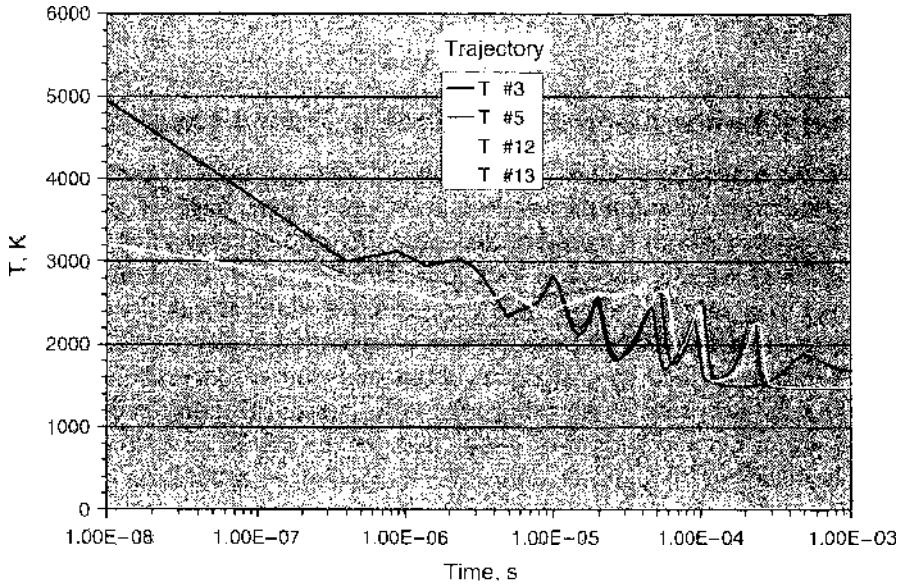

Figure 44. Temperature histories along selected streak lines for laser ablation calculations.

by itself. However, this does not mean that useful information for the study of SWCNT production is unobtainable—the use of the plume expansion factor formulated by Greendyke et al. [143] and outlined in the previous section does yield insight into the possible enhancement of SWCNT production by aerodynamic means alone. The information provided—chemical profiles of "building block" species, temperature profiles, relative localized densities of the chemical species, and so forth—can provide input data for decoupled studies with chemical reaction codes that do not have the dependency of CPU time on grid resolution and number of grid points considered. Indeed, it is possible that in the future, unconventional CFD methods such as direct simulation Monte Carlo methods [154] or molecular dynamics methods [155] could more completely simulate at least the initial onset of ablation in the flow field, as they do not have the same relationship between the number of chemical species and computational overhead—although such methods have difficulties of their own that make their use questionable at the present time.

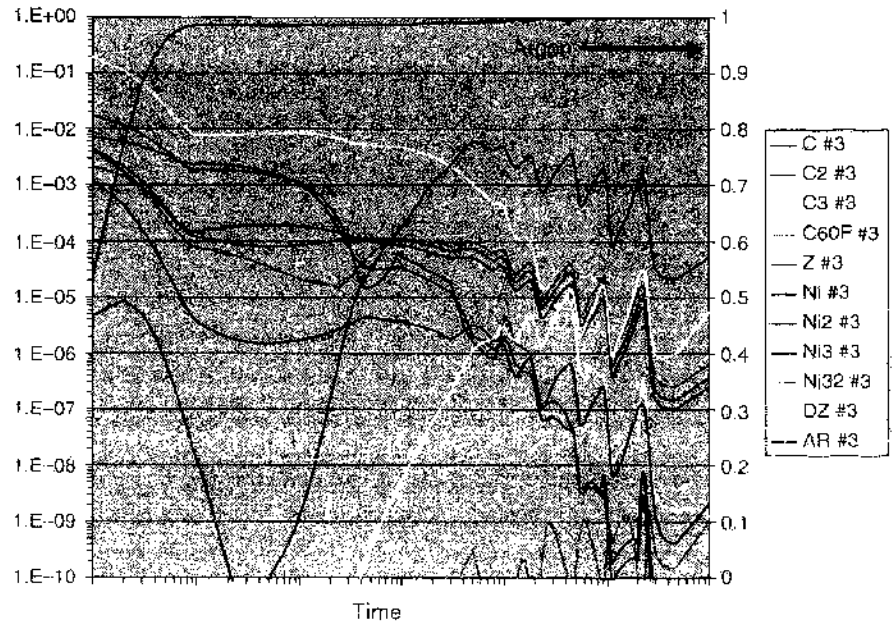

Figure 45. Example of evolution of species mass fractions along streak line in laser ablation. Arbitrary evaporation rate coefficients were used in calculation, therefore data is not accurate but only shown as an example of methodology.

5. COMPUTATIONAL SIMULATION OF THE HIPCO SWCNT PRODUCTION PROCESS

A new method for the production of SWCNT that is receiving much attention at the current time is the high pressure carbon monoxide, or HiPco, process, first developed by Nikolaev et al. [156]. Two of the main problems in the production of SWCNT are the ability to produce them in economically viable quantities and to produce them with predetermined structures that have unique properties such as their chirality. Although the HiPco process does not necessarily address the latter problem, it is a possible answer to the former. The HiPco process is a continuous gas production reactor that uses a relatively cold input stream of CO and iron pentacarbonyl, $Fe(CO)_5$, that is injected into the reactor with impinging streams of heated CO in a "showerhead" configuration (Fig. 46). As the iron pentacarbonyl is heated by the impinging streams, it decomposes releasing the Fe atoms, which then condense into metallic iron clusters. The clusters serve as catalysts for SWCNT development. The SWCNT begin to develop from the iron clusters when CO molecules interact with the iron catalyst and form an iron cluster with the developing SWCNT forming on it and CO_2 molecules.

Computational simulations of the HiPco using reacting-gas computational fluid dynamics (CFD) have not been common. One of the primary investigations into the process has been the work of Dateo et al. [27] and Gökçen et al. [19], who conducted extensive work first on a reduced chemical reaction model for the HiPco process and then combined this model with a simplified CFD code to produce a parametric analysis of the HiPco process. Work by other researchers such as Povitsky and Salas [157] have focused on the actual aerodynamics of the HiPco process to insure the best mixing of the iron pentacarbonyl and carbon monoxide streams for SWCNT production. Scott et al. [31] also conducted research on the HiPco process with limited CFD methods that used a chemical reaction model that is decoupled from the flow field solution method.

5.1. Reacting Gas Modeling of the HiPco Process

Dateo, Gökçen, and Meyyappan published a two-part paper [19, 27] that modeled their chemical reaction mechanism [27] in the first part, and the application of that chemical reaction mechanism [19] couples with a CFD solution methodology for the analysis of the HiPco reactor chamber. The first paper established their chemical reaction mechanism that can be broken down into three fundamental parts: the decomposition of the iron pentacarbonyl steps, iron catalyst growth and evaporation, and, finally, carbon nanotube formation.

Dateo et al. noted that the iron pentacarbonyl will begin to decompose at temperatures above 500 K, which is the situation as the inlet $Fe(CO)_5$ stream initially encounters the hotter stream of CO. The decomposition mechanism is modeled in five steps:

$$Fe(CO)_5 \leftrightarrow Fe(CO)_4 + CO$$

$$Fe(CO)_4 \leftrightarrow Fe(CO)_3 + CO$$

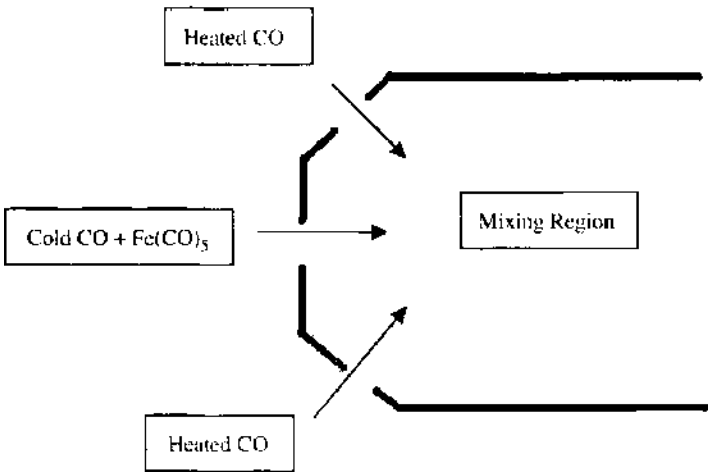

Figure 46. Schematic of a generalized "showerhead" HiPco reactor chamber.

$$Fe(CO)_3 \leftrightarrow Fe(CO)_2 + CO$$
$$Fe(CO)_2 \leftrightarrow FeCO + CO$$
$$FeCO + M \leftrightarrow Fe + CO + M$$

Chemical reaction rates for the dissociation were estimated by Dateo et al. by use of experimental data from Lewis et al. [158] and Engelking and Lineberger [159]. The reverse reaction rates were taken from Seder et al. [160].

Iron cluster formation in the second part of their model was based on the rates of Krestinin et al. [29], wherein their model is based on the reaction mechanisms:

$$Fe_m + Fe_n \rightarrow Fe_{m+n} \qquad (n = 1 \text{ to } 4)$$
$$Fe_m \rightarrow Fe_{m-1} + Fe$$
$$FeCO + Fe_m \rightarrow Fe_{m+1} + CO$$
$$FeCO + FeCO \rightarrow Fe_2 + 2CO$$

It is noted that iron evaporation will occur at higher temperatures, and the condensation of carbon into SWCNT requires higher temperatures for proper formation.

Condensation of the carbon atoms is accomplished by a modification of the Boudouard reaction [161]:

$$2CO(g) \rightarrow C(s) + CO_2(g)$$

into the three-step process suggested by Boudart [162]:

$$Fe_m + CO \rightarrow Fe_m \bullet CO$$
$$Fe_m \bullet CO \rightarrow Fe_m + CO$$
$$Fe_m \bullet CO + CO \rightarrow Fe_m \bullet C_{NT} + CO_2$$

The final composition of the reaction model in [27] consists of 971 species in 1948 chemical reactions. Because computational effort in chemically reacting flow fields is proportional to the square of the number of species multiplied by the number of grid points, the initial model in [27] was reduced for CFD analysis. The reduction was accomplished by grouping the iron cluster species that contain three or more atoms of iron into a single species. This regrouping of the iron related species results in a much more computationally feasible model that has 14 species and 22 reactions—well within the capabilities of most modern CFD codes.

Both the full and the reduced models were used in a simple 0D parametric study that examined variations of temperature, pressure, and $Fe(CO)_5$ partial pressure at the gas injection interface. The main findings of Dateo et al. in part 1 of their paper [27] determined that increasing the temperature in the HiPco chamber speeds up the decomposition of the iron pentacarbonyl but at the same time increases iron cluster evaporation. Increasing the pressure was found to speed up the Boudouard reaction and slow down iron pentacarbonyl decomposition. Increasing $Fe(CO)_5$ partial pressures speeds up both decomposition of the iron pentacarbonyl and the formation of iron clusters. When the reduced and full chemistry models were compared in the 0D model, it was found that the two models gave acceptable comparison to each other over the range of parameters studied.

5.2. CFD Modeling of the HiPco Process

In part 2 of the work [19], Gökçen et al. incorporated their reduced three-part chemical model for SWCNT formation into a Navier-Stokes flow field solver for axisymmetric nonequilibrium flows. The fundamental equations they used were expressed in vector form as:

$$\frac{\partial U}{\partial t} + \frac{\partial F}{\partial x} + \frac{1}{y}\frac{\partial (yG)}{\partial y} = W + \frac{H}{y} \tag{62}$$

where

$$U = \begin{bmatrix} \rho \\ \rho_1 \\ \cdot \\ \cdot \\ \rho_{14} \\ \rho u \\ \rho v \\ E \end{bmatrix}, \qquad F = \begin{bmatrix} \rho u \\ \rho_1 u + j_{1x} \\ \cdot \\ \cdot \\ \rho_{14} u + j_{14x} \\ \rho u^2 + P + \tau_{xx} \\ \rho uv + \tau_{xy} \\ u(E + P + \tau_{xx}) + v\tau_{xy} + q_x \end{bmatrix}$$

$$G = \begin{bmatrix} \rho v \\ \rho_1 v + j_{1y} \\ \cdot \\ \cdot \\ \rho_{14} v + j_{14y} \\ \rho uv + \tau_{xy} \\ \rho v^2 + P + \tau_{yy} \\ v(E + P + \tau_{yy}) + u\tau_{yx} + q_y \end{bmatrix}, \qquad W = \begin{bmatrix} w \\ w_1 \\ \cdot \\ \cdot \\ w_{14} \\ 0 \\ 0 \\ 0 \end{bmatrix}, \quad \text{and} \quad H = \begin{bmatrix} 0 \\ 0 \\ \cdot \\ \cdot \\ 0 \\ 0 \\ P + \tau_{\theta\theta} \\ 0 \end{bmatrix} \tag{63}$$

The first 15 equations in the set represent the mass conservation equations for overall mass and the 14 species. The latter equations are the conservation of momentum in two directions and the conservation of energy equation. The H-vector reflects changes in the fundamental equations that are required by the axisymmetric geometry, and the W-vector term in the overall equation represents the source vector for chemistry effects. The equations were discretized into a finite-volume approach using a Steger-Warming flux-vector splitting [63]. The coupled gas dynamics and flowfield dynamics solution method used an implicit Gauss-Seidel relaxation method [163]. The domain of the HiPco reactor was split into two blocks, one modeling the inlet conical "showerhead" region, and the second for the cylindrical downstream portion of the flow. Laminar flow was assumed throughout the study.

Results from the CFD simulation showed that there was an optimum pressure and temperature for the growth and development of SWCNT that agreed with their previous part 1 of their paper as stated in the previous section. In addition, the variations of temperature and pressure showed good agreement with experimental results. An interesting conclusion of their study, (not elaborated upon in the paper) is the belief that improved mixing in the flow field domain of the HiPco reactor would not lead to greater iron cluster (and therefore SWCNT) production. Gökçen et al., however, allowed that work was needed to improve the chemical modeling before they could conclusively respond about mixing improvement.

5.3. Other HiPco Modeling Efforts

Povitsky and Salas [157] also attempted a CFD analysis of the HiPco flow field regime with the goal of improving the mixing of the iron precursors. Their technique was to use a combination of an Eulerian-based flow field solution code named FLUENT [164] for the Navier-Stokes solution of the flow field without chemical reactions, and a Lagrangian solution method to track the particles of the flow and the resulting parameters of the flow field through which they pass. The FLUENT code used a k-ε turbulence model in the solution procedure as implemented by Povitsky et al. In addition, FLUENT also provided the Lagrangian methodology for the particle trace simulations.

The primary purpose of the Povitsky work was to examine multiple geometric configurations of the HiPco reactor including the angle of the impinging CO jets and the number of jets used to determine the optimum configuration of the "showerhead" reactor chamber. An interesting result of their work showed that rapid mixing of the flow geometrically does not imply rapid temporal mixing of the flow. The best geometry for good heating of the iron precursor flow through the center of the reactor chamber was found to be a single central jet containing the precursor gas with three inlet jets for the heated CO with an angle of 30 degrees between the centerline and the impinging hot CO jets.

5.3.1. Production of SWCNTs/CO_2

The solution to the chemical kinetics of nanotube production for the HiPco process was developed using two methods. In the first method, Dateo et al. [27] and Gökçen et al. [19] implemented their kinetics model first by applying it parametrically to constant temperature and pressure conditions. They then reduced the model and followed a similar procedure to show that their reduced model produced about the same amount of CO_2 as their full model. They then included these models in an axisymmetric full Navier-Stokes CFD solver and concluded that their reduced model adequately represented the results of the full model (see details in Section 2.3.). The second approach was a decoupled method in which Povitsky [165] solved Euler equations with a turbulence model to find streak lines. Scott et al. [31] then used the solutions along streak lines and solved the kinetics equations with the chemical kinetics code of CHEMKIN to find the evolution of CO_2 and other species in the HiPco reactor. They used the chemical reaction models developed by Dateo et al. as well as investigated variations of those models. The time history of the temperature and dilution due to mixing were found along the streak lines calculated by Povitsky [165] and Povitsky and Salas [166]. Sample stream paths are shown in Fig. 47. The variations were developed to investigate the effect of various assumptions about the nucleation rate and the number of clusters in the model on carbon creation and cluster size distributions. Figure 48 shows the evolution of carbon nanotubes attached to clusters of iron as a function of iron cluster size. One can see that at long times, the largest cluster starts to increase relative to the other clusters. This indicates that larger clusters should be included in the model. However, the amount

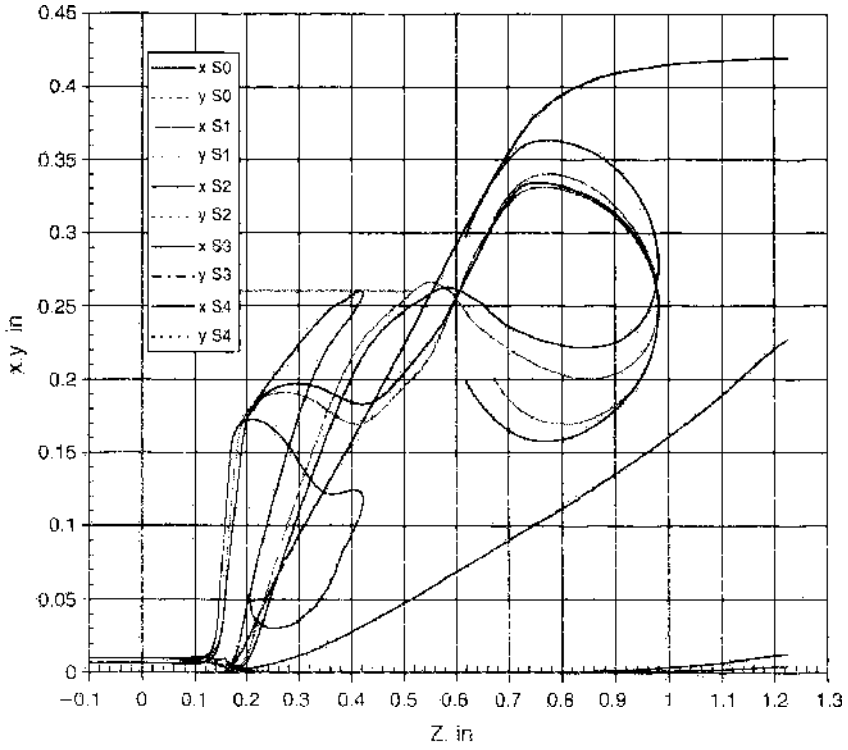

Figure 47. x- and y-coordinates along four typical streak lines versus the axial coordinate z, in mixing zone of HiPco reactor, calculated by the FLUENT code.

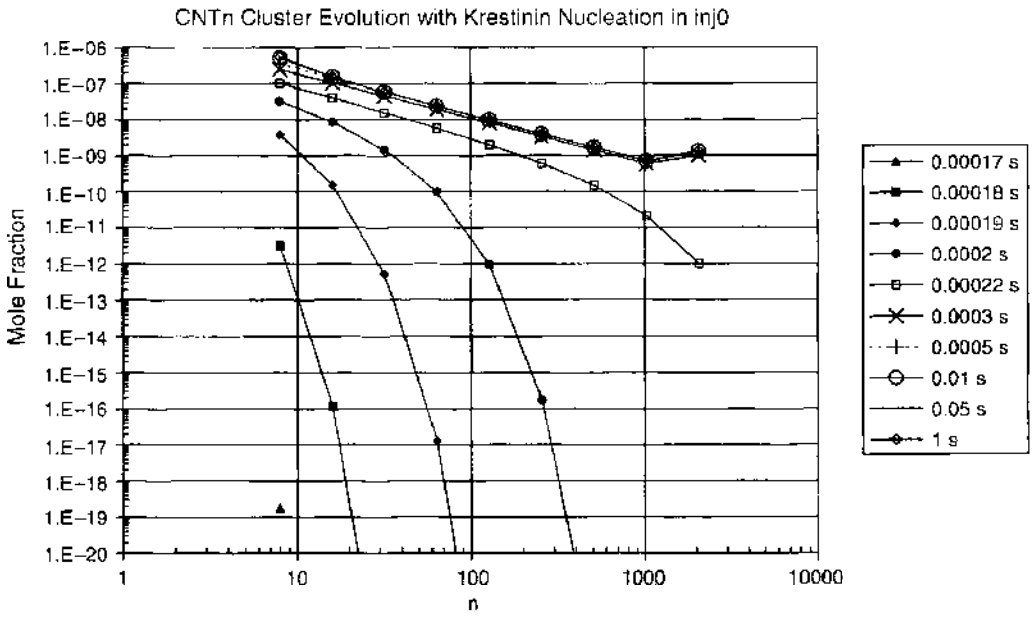

Figure 48. Carbon nanotube cluster distributions at various times in trajectory no. inj0 of HiPco reactor. Reprinted with permission from [27], C. D. Scott et al., *J. Nanosci. Nanotechnol.* 3, 63 (2003). © 2003, American Scientific Publishers.

of carbon nanotubes is dominated by the small cluster population. Therefore, from the standpoint of predicting carbon production, the model is quite adequate and does not need augmenting with larger metal clusters. However, the models tend to over predict the amount of carbon produced as compared with experiments, as seen in Fig. 49.

5.3.2. Assessment of Nickel as Catalyst for HiPco

Due to the fact that iron tends to evaporate at fairly low temperatures compared with nickel, it was anticipated that nickel might be a better catalyst for the HiPco reactor. However, when nickel tetracarbonyl was injected as the catalyst into the reactor, no carbon nanotubes were produced. The reason was not clear, as nickel is very effective in the arc and laser ablation processes. Modeling the nucleation and evaporation of metals allowed Scott and Smalley [42] to conclude that the higher binding energy and stability of nickel as compared with iron was the principle factor that contributed to no growth of nanotubes when nickel-only was included as catalyst. A comparison of calculations of the production of SWCNTs

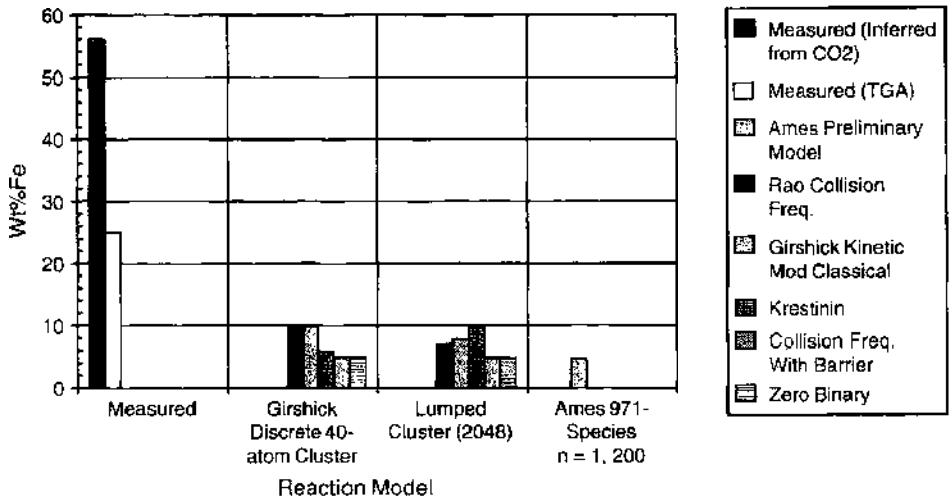

Figure 49. Calculated and measured iron fraction in product of HiPco reactor. Reprinted with permission from [27], C. D. Scott et al., *J. Nanosci. Nanotechnol.* 3, 63 (2003). © 2003, American Scientific Publishers.

took into account iron-species rate coefficients and rate coefficients adjusted for the binding energies of nickel. It was found that almost no nanotubes were produced when the values corresponding to the nickel bond energies were used in the rate coefficients for evaporation and for the NiCO bond. It was found that the metal-CO bond energy has a major influence on the production of CO_2. The higher NiCO bond energy almost eliminates production of CO_2, whereas the smaller bond energy of FeCO leads to significant production. Also, the rate of dimer dissociation and small cluster evaporation affects the production of CO_2 by limiting the rate of cluster growth, and thus the number of clusters available to catalyze SWCNT growth. This suggests that CO reacts with metal clusters and removes atoms from them by forming MeCO, which has the effect of enhancing the evaporation rate and reducing SWCNT production. It appears that the stronger bond between nickel and CO tends to extract nickel from clusters. It is like an enhanced evaporation that prevents nickel cluster growth in high-pressure CO. Therefore, very few clusters are formed that can catalyze SWCNT formation and growth.

5.3.3. Production of Catalyst Particles Prior to Injection Into HiPco Reactor

An investigation of a potential procedure for injecting pre-made catalyst particles was studied using models of the HiPco process. It was envisioned that a laser could dissociate $Fe(CO)_5$ in the injector of the HiPco apparatus. Laser dissociation instead of thermal dissociation would free iron atoms for nucleation and growth prior to mixing with hot CO. One might be able to control the size of the iron clusters and thus affect the production of SWCNTs in a favorable way. Instead of fabricating the device, it would be reasonable just to be able to compute the results and assure that the experiment is worth building. A calculation was made assuming that all iron carbonyl is completely dissociated prior to injection into the main reactor. This is a truncated model (clusters up to $n = 40$). The inlet flow is then allowed to relax to form iron clusters and iron clusters with CO attached. From Fig. 50, one can see that it takes about 0.1 to 1 ms for a fairly uniform distribution of iron clusters to form at this condition. The model only allows CO to bind to Fe_n clusters for $n > 10$, therefore, the small clusters have no CO attached, whereas the larger ones all have attached CO. The possibility of the clusters catalyzing SWCNT formation depends on the residence time in the cool (400 K) zone. The design of the inlet can be tailored to meet a wide range of residence times by adjusting the inlet tube diameter and length. It is apparent that a CW laser might

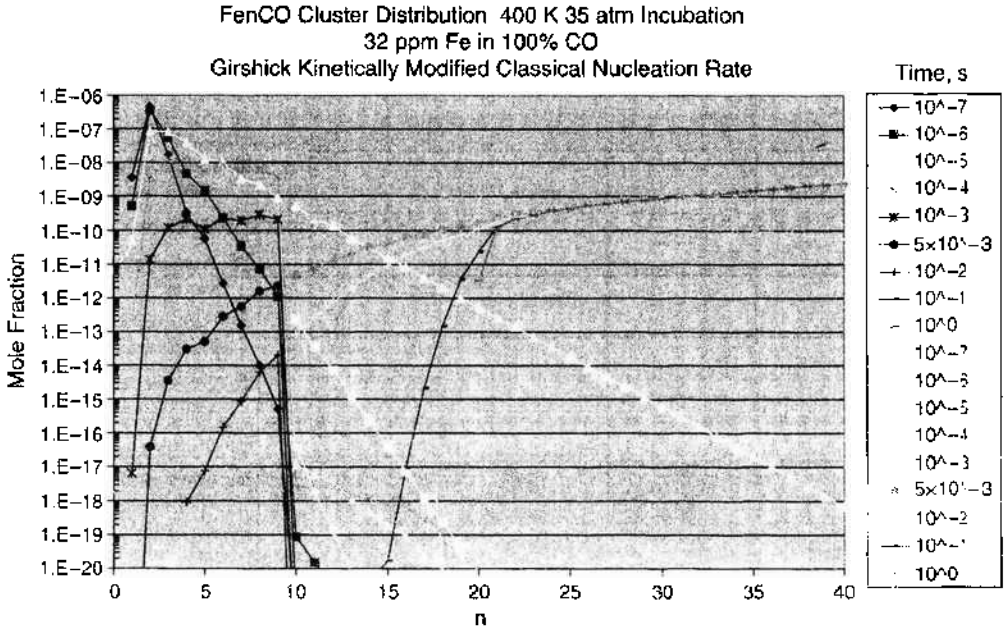

Figure 50. Iron cluster distribution at various times in inlet to HiPco reactor, starting from fully dissociated iron pentacarbonyl at 35 atmospheres and 400 K.

result in overheating, therefore, a pulsed laser might be better. It could be timed such that a slug of gas that is dissociated then flows into the main reactor in the time between pulses. Another adjustable parameter could be the partial pressure of $Fe(CO)_5$, controlled by controlling the temperature of its container. If small clusters are needed, then short residence times are indicated; but if larger clusters are needed, then longer residence times would be preferred.

6. CONCLUSIONS

Modeling of fullerene and carbon nanotube formation involves understanding how the species react chemically and evolve in time. Time evolution of conditions modeled used various degrees of fidelity in solving the fluid dynamics equations of motion. Calculations were done for one degree or another using computational fluid dynamics. The kinetics involves knowing how nanotubes are formed from simpler species; that is, a concept of how they grow. This is not an easy question to answer, particularly in the case of single-wall carbon nanotubes. In this chapter, we have assumed the fullerene chemical kinetics model of Krestinin et al. that was, to some extent, validated by comparisons with measured production. We have applied modeling to the arc process and the laser ablation process; and we have used their carbon model as the basis for carbon cluster growth in models of SWCNT production. Growth of SWCNTs requires the introduction of metal catalysts; and we included the nucleation and growth of nickel clusters to represent catalysts in the arc and laser ablation processes.

Unfortunately, the kinetics of nickel cluster growth is not well documented in the literature; therefore, we have taken extensive liberties to approximate the kinetics of nickel. We have posed the mechanisms of cluster formation and growth using the aerosol theory developed by Girshick, which essentially treats cluster growth as a kinetically controlled process. Evaporation of these clusters was treated in their theory as determined from knowledge of the bulk vapor pressure and surface tension. Several variations of the kinetics model of the HiPco process for SWCNT production were reviewed. The essential results at the current stage of development indicate that these models can predict measured trends in production, but the absolute quantity of carbon (nanotubes) is overpredicted.

We have reviewed various degrees of approximation in the kinetics models and have shown attempts to reduce the size of HiPco and the carbon vapor models. Reasonable comparisons between the full and reduced models were shown.

It should be emphasized that the kinetics models are approximate and preliminary. They await validation and refinement based on comparisons with measurements. As pointed out, the nickel evaporation model can be refined by using measured cross-sections and accounting for internal energy. It is possible that the intermediate clusters should be combinations of carbon and a few nickel atoms, rather than forming carbon, then nickel, followed by combining the two types of clusters. The current models show how we were guided by the observation that metal clusters are seen in the product. However, there are molecular dynamics models [167] that carbon and nickel co-condense. That model indicates further coalescence of nickel and carbon into larger clusters that may be followed by segregation of carbon from the metal catalysts. There are also some electron diffraction measurements that show crystalline metal carbides in the clusters seen in the product.

We have shown computational fluid dynamics models of the arc, laser ablation, and HiPco processes. The highest dimension of any of the calculations, thus far, is two-dimensional. It is apparent from experiment that the flow fields are three-dimensional. Thus, future work should be extended to three dimensions for problems when the chemistry is decoupled from the flow field. However, it appears that even 1D calculations can yield important insight and understanding of the flow and its chemical kinetics.

ACKNOWLEDGMENT

The authors would like to thank Ivaylo Hinkov for his help in the preparation of this manuscript.

REFERENCES

1. H. W. Kroto, J. R. Heath, S. C. O'Brien, R. F. Curl, and R. E. Smalley, *Nature* 318, 162 (1985).
2. W. Krätschmer, L. D. Lamb, K. Fostiropoulos, and D. R. Huffman, *Nature* 347, 354 (1990).
3. J. Bernholc and J. C. Phillips, *Phys. Rev. B* 33, 7395 (1986).
4. W. R. Creasy and J. T. Brenna, *Chem. Phys.* 126, 453 (1988).
5. W. R. Creasy and J. T. Brenna, *J. Chem. Phys.* 92, 2269 (1990).
6. W. R. Creasy, *J. Chem. Phys.* 92, 7223 (1990).
7. A. V. Krestinin, A. P. Moravskii, and P. A. Tesner, *Chem. Phys. Rep.* 17, 1687 (1998).
8. A. V. Krestinin and A. P. Moravsky, *Chem. Phys. Lett.* 286, 479 (1998).
9. G. Von Helden, M.-T. Hsu, N. Gotts, and M. T. Bowers, *J. Phys. Chem.* 86, 8182 (1993).
10. G. Von Helden, N. Gotts, and M. T. Bowers, *Nature* 363, 60 (1993).
11. J. M. Hunter, J. L. Fye, and N. F. Jarrold, *J. Chem. Phys.* 99, 1785 (1993).
12. J. M. Hunter, J. L. Fye, E. J. Roskamp, and N. F. Jarrold, *J. Phys. Chem.* 98, 1810 (1994).
13. P. P. Radi, T. L. Bunn, P. R. Kemper, M. E. Molchan, and M. T. Bowers, *J. Chem. Phys.* 88, 2809 (1988).
14. C. D. Scott, *J. Nanosci. Nanotech.* 4, 368 (2004).
15. V. P. Glushko, ed., "Termodinamicheskie Svolstva Individual'nykh Veshchest. Spravochnik," Vol. 2, Book 1, Nauka, Moscow, 1978.
16. R. S. Udahl, Y. Bao, and W. M. Jackson, *Chem. Phys. Lett.* 178, 425 (1991).
17. J. M. L. Martin, J. P. Francois, and R. Gijbels, *J. Chem. Phys.* 95, 9420 (1991).
18. C. J. Pope and J. B. Howard, *J. Phys. Chem.* 99, 4306 (1995).
19. T. Gökçen, C. E. Dateo, and M. Meyyappan, *J. Nanosci. Nanotech.* 2, 535 (2002).
20. S. L. Girshick, C.-P. Chiu, and P. H. McMurry, *Plasma Chem. Plasma Proc.* 8, 145 (1988).
21. S. L. Girshick and C.-P. Chiu, *Plasma Chem. Plasma Proc.* 9, 355 (1989).
22. S. L. Girshick, C.-P. Chiu, and P. H. McMurry, *Aerosol Sci. Technol.* 13, 465 (1990).
23. S. L. Girshick and C.-P. Chiu, *J. Chem. Phys.* 93, 1273 (1990).
24. S. L. Girshick, *J. Chem. Phys.* 94, 826 (1991).
25. S. L. Girshick, C.-P. Chiu, R. Muno, C. Y. Wu, L. Yang, S. K. Singh, and P. H. McMurry, *J. Aerosol Sci.* 24, 367 (1993).
26. N. Rao, S. Girshick, J. Heberlein, P. McMurry, S. Jones, D. Hansen, and B. Micheel, *Plasma Chem. Plasma Proc.* 15, 581 (1995).
27. C. D. Scott, A. Povitsky, C. E. Dateo, T. Gökçen, P. A. Willis, and R. E. Smalley, *J. Nanosci. Nanotech.* 3, 63 (2003).
28. C. E. Dateo, T. Gökçen, and M. Meyyappan, *J. Nanosci. Nanotech.* 2, 523 (2002).
29. A. V. Krestinin, V. N. Smirnov, and I. S. Zaslonko, *Sov. J. Chem. Phys.* 8, 689 (1991).
30. P. A. Vlasov, I. S. Zaslonko, and Yu. K. Karasevich, *High Temperature* 36, 189 (1998).
31. K. E. Lewis, D. M. Golden, and G. P. Smith, *J. Am. Chem. Soc.* 106, 3905 (1984).
32. V. N. Smirnov, *Kinetics and Catalysis*, 34, 391 (1992).
33. P. A. Vlasov, I. S. Zaslonko, Yu. K. Karasevich, and V. N. Smirnov, *Kinetics and Catalysis* 40, 611 (1999).
34. M. D. Rumminger, D. Reinelt, V. Babushok, and G. T. Linteris, *Combust. Flame* 116, 207 (1999).
35. T. A. Seder, A. J. Ouderkirk, and E. Weitz, *J. Chem. Phys.* 85, 1977 (1986).
36. L. S. Sunderlin, D. Wang, and R. R. Squires, *J. Am. Chem. Soc.* 114, 2788 (1992).
37. A. Ricca, *Chem. Phys. Lett.* 350, 313 (2001).
38. E. K. Parks, K. P. Kerns, and S. J. Riley, *J. Chem. Phys.* 112, 3384 (2000).
39. K. P. Kerns, E. K. Parks, and S. J. Riley, *J. Chem. Phys.* 112, 3394 (2000).
40. R. J. Kee, F. M. Rupley, J. A. Miller, M. E. Coltrin, J. F. Grear, E. Meeks, H. K. Moffat, A. E. Lutz, G. Dixon-Lewis, M. D. Smooke, J. Warnatz, G. H. Evans, R. S. Larson, R. E. Mitchell, L. R. Petzold, W. C. Reynolds, M. Caracotsios, W. E. Stewart, P. Glarborg, C. Wang, and O. Adigun, CHEMKIN Collection, Release 3.6, Reaction Design, Inc., San Diego, CA, 2001.
41. J. Gavillet, A. Loisear, F. Ducastelle, S. Thair, P. Bernier, O. Stephan, J. Thibault, and J.-C. Charlier, *Carbon* 40, 1649 (2002).
42. C. D. Scott and R. E. Smalley, *J. Nanosci. Nanotech.* 3, 75 (2003).
43. L. Lian, C.-X. Su, and P. B. Armentrout, *J. Chem. Phys.* 96, 7542 (1992).
44. P. B. Armentrout, *Annu. Rev. Phys. Chem.* 52, 423 (2001).
45. T. W. Ebbesen and P. M. Ajayan, *Nature* 358, 220 (1992).
46. C. Journet, W. K. Maser, P. Bernier, A. Loiseau, M. Lamy de La Chapelle, S. Lefrant, P. Deniard, R. Lee, and J. E. Fischer, *Nature* 388, 756 (1997).
47. A. Huczko, H. Lange, A. Resztak, and P. Byszewski, *High Temp. Chem. Process.* 4, 125 (1995).
48. A. Huczko, H. Lange, P. Byszewski, M. Poplawsks, and A. Starski, *J. Phys. Chem. A* 101, 1267 (1997).
49. P. Byszewski, H. Lange, A. Huczko, and J. F. Behnke, *J. Phys. Chem. Solids* 58, 11 (1997).
50. C. D. Scott, S. Farhat, and I. Hinkov, "Analysis of Emission Spectra From Arc in Production of Single-Wall Carbon Nanotubes," Internal LIMHP Report, 2002.
51. S. Akita, H. Ashihara, and Y. Nakayama, *Jpn. J. Appl. Phys.* 39, 4939 (2000).
52. S. Farhat, M. Lamy de La Chapelle, A. Loiseau, C. D. Scott, S. Lefrant, C. Journet, and P. Bernier, *J. Chem. Phys.* 115, 10 (2001).
53. I. Hinkov, J. Grand, M. Lamy de la Chapelle, S. Farhat, C. D. Scott, P. Nikolaev, V. Pichot, P. Launois, J. Y. Mevellec, and S. Lefrant, *J. Appl. Phys.* 95, 2029 (2004).

54. J. H. Hafner, M. J. Bronikowski, B. R. Azamian, P. Nikolaev, A. G. Rinzler, D. T. Colbert, K. A. Smith, and R. E. Smalley, *Chem. Phys. Lett.* 296, 195 (1998).
55. B. C. Satishkumar, A. Govindaraj, R. Sen, and C. N. R. Rao, *Chem. Phys. Lett.* 293, 47 (1998).
56. J.-F. Colomer, J.-M. Benoit, C. Stephan, S. Lefrant, G. Van Tendeloo, and J. B. Nagy, *Chem. Phys. Lett.* 345, 11 (2001).
57. H. M. Cheng, F. Li, X. Sun, S. D. M. Brown, M. A. Pimenta, A. Marucci, G. Dresselhaus, and M. S. Dresselhaus, *Chem. Phys. Lett.* 289, 602 (1998).
58. A. Peigney, C. Laurent, F. Dobigeon, and A. Rousset, *J. Mater. Res.* 12, 613 (1997).
59. H. Dai, A. G. Rinzler, P. Nikolaev, A. Thess, D. T. Colbert, and R. E. Smalley, *Chem. Phys. Lett.* 260, 471 (1996).
60. Y. Wang, F. Wei, G. Luo, H. Yu, and G. Gu, *Chem. Phys. Lett.* 364, 568 (2002).
61. Y. Wang, Z. Zhang, H. Liu, X. Xu, G. Pa, Z. Guo, Y. Liu, X. Han, and G. Lan, *Spectrochim. Acta A* 58, 2089 (2002).
62. M. E. Itkis, D. E. Perea, S. Niyogi, S. M. Rickard, M. A. Hamon, H. Hu, B. Zhao, and R. C. Haddon, *Nano Lett.* 3, 309 (2003).
63. T. Guo and R. E. Smalley, in "Recent Advances in the Chemistry and Physics of Fullerenes and Related Materials" (R. S. Ruoff and K. M. Kadish, Eds.). Electrochemical Society Pennington, NJ, and Reno, Nevada, 1995.
64. A. Thess, R. Lee, P. Nikolaev, H. J. Dai, P. Petit, J. Robert, C. H. Xu, T. H. Lee, S. G. Kim, A. G. Rinzler, D. T. Colbert, G. E. Scuseria, D. Tomanek, J. E. Fischer, and R. E. Smalley, *Science* 273, 483 (1996).
65. R. Sen, A. Govindaraj, and C. N. R. Rao, *Chem. Phys. Lett.* 267, 276 (1997).
66. H. M. Cheng, F. Li, G. Su, H. Y. Pan, L. L. He, X. Sun, and M. S. Dresselhaus, *Appl. Phys. Lett.* 72, 3282 (1998).
67. H. M. Cheng, F. Li, X. Sun, S. D. M. Brown, M. A. Pimenta, A. Marucci, G. Dresselhaus, and M. S. Dresselhaus, *Chem. Phys. Lett.* 289, 602 (1998).
68. G. G. Tibbetts, D. W. Gorkiewicz, and R. L. Alig, *Carbon* 31, 809 (1993).
69. P. Nikolaev, M. J. Bronikowski, R. K. Bradley, F. Rohmund, D. T. Colbert, K. A. Smith, and R. E. Smalley, *Chem. Phys. Lett.* 313, 91 (1999).
70. K. Bradley, "Large Scale Production of Single-wall Carbon Nanotubes." Ph.D. Thesis, Rice University, 2000.
71. A history of welding: Available at http://www.weldinghistory.org/htmlhistory/wh_index.html.
72. S. Iijima, *Nature* 354, 56 (1991).
73. S. Iijima, *Mater. Sci. Eng. B* 19, 172 (1993).
74. S. Iijima, T. Ichihashi, and Y. Ando, *Nature* 356, 776 (1992).
75. S. Iijima and T. Ichihashi, *Nature* 363, 503 (1993).
76. D. S. Bethune, C. H. Chang, M. S. DeVries, G. Gorman, R. Savoy, J. Vazquez, and R. Beyers, *Nature* 363, 605 (1993).
77. P. M. Ajayan and S. Iijima, *Nature* 358, 23 (1992).
78. W. S. Bacsa, D. Ugarte, A. Chatelain, and W. De Heer, *Phys. Rev. B* 50, 15473 (1994).
79. H. Zhang, D. Wang, X. Xue, B. Chen, and S. Peng, *J. Phys. D* 30, L1 (1997).
80. M. Cadek, R. Murphy, B. McCarthy, A. Drury, B. Lahr, R. C. Barklie, M. Panhuis, J. N. Coleman, and W. J. Blau, *Carbon* 40, 923 (2002).
81. D. N. Borisenko, N. N. Kolesnikov, M. P. Kulakov, and V. V. Kveder, *Int. J. Nanosci.* 1, 235 (2002).
82. Y. Ando, X. Zhao, S. Inoue, and S. Iijima, *J. Crystal Growth* 237, 1926 (2002).
83. X. Zhao, M. Ohkohchi, M. Wang, S. Iijima, T. Ichihashi, and Y. Ando, *Carbon* 35, 775 (1997).
84. J. L. Hutchison, N. A. Kiselev, A. Krinichnaya, A. Krestinin, R. Loutfy, A. Moravsky, V. M'uradan, E. O'braztsova, V. Sloan, S. Terekhov, and D. Zharkov, *Carbon* 39, 761 (2001).
85. S. H. Jung, M. R. Kim, and S. H. Jeong, S. U. Kim, O.-J. Lee, K.-H. Lee, J.-H. Suh, and C.-C. Park, *Appl. Phys. A* 76, 285 (2003).
86. M. Ishigami, J. Cumings, A. Zettl, and S. Chen, *Chem. Phys. Lett.* 319, 457 (2000).
87. H. W. Zhu, X. S. Li, B. Jiang, C. L. Xu, Y. F. Zhu, D. H. Wu, and X. H. Chen, *Chem. Phys. Lett.* 366, 664 (2002).
88. Y. Saito, T. Yoshikawa, M. Inagaki, M. Tomita, and T. Hayashi, *Chem. Phys. Lett.* 204, 277 (1993).
89. M. Yudasaka, T. Komatsu, T. Ichihashi, Y. Achiba, and S. Iijima, *J. Phys. Chem. B* 102, 4892 (1998).
90. P. M. Ajayan, C. Colliex, J. M. Lambert, P. Bernier, L. Barbedette, M. Tence, and O. Stephan, *Phys. Rev. Lett.* 72, 1722 (1994).
91. Y. Saito, M. Okuda, T. Yoshikawa, S. Bandow, S. Yamamuro, K. Wakoh, and K. Sumiyama, *Jpn. J. Appl. Phys.* 33, L186 (1994).
92. R. S. Ruoff, D. C. Lorents, B. Chan, R. Malhotra, and S. Subramoney, *Science* 259, 346 (1993).
93. S. Bandow and Y. Saito, *Jpn. J. Appl. Phys. Pt. 2*, 32, L1677 (1993).
94. Y. Yosida, *Appl. Phys. Lett.* 62, 3447 (1993).
95. S. A. Majetich, M. E. McHenry, J. O. Artman, N. T. Nuhfer, and S. W. Staley, *Phys. Rev. B* 48, 16845 (1993).
96. Y. Ando and X. Whao, *Mol. Cryst. Liq. Cryst.* 340, 707 (2000).
97. M. Takizawa, S. Bandow, T. Torii, and S. Iijima, *Chem. Phys. Lett.* 302, 146 (1999).
98. G. T. Kim, J. G. Park, Y. W. Park, K. Liu, G. Düsberg, and S. Roth, *Synth. Met.* 103, 2551 (1999).
99. S. Seraphin and D. Zhou, *Appl. Phys. Lett.* 64, 2087 (1994).
100. Y. Saito, T. Koyama, and K. Kawabata, *Z. Phys. D* 40, 421 (1997).
101. Y. Saito, Y. Tani, N. Miyagawa, K. Mitsushima, A. Kasuya, and Y. Nishina, *Chem. Phys. Lett.* 294, 593 (1998).

102. T. Sugai, H. Omote, S. Bandow, N. Tanaka, and H. Shinohara, *J. Chem. Phys.* 112, 6000 (2000).
103. S. J. Lee, H. K. Baik, J. Yoo, and J. H. Han, *Diam. Relat. Mater.* 11, 914 (2002).
104. J. C. Bae, Y. J. Yoon, S.-J. Lee, K. M. Song, and H. K. Baik, *Carbon* 40, 2905 (2002).
105. M. Kanai, A. Koshio, and H. Shinohara, T. Miemo, A. Kasuya, Y. Ando, and X. Zhao, *Appl. Phys. Lett.* 79, 2967 (2001).
106. H. Zhang, X. Xue, D. Wang, Y. He, and Sh. Peng, *Mater. Chem. Phys.* 58, 1 (1999).
107. M. Takizawa, S. Bandow, M. Yudasaka, Y. Ando, H. Shimoyama, and S. Iijima, *Chem. Phys. Lett.* 326, 351 (2000).
108. T. W. Ebbesen, ed., "Carbon Nanotubes. Preparation and Properties." CRC Press, Boca Raton, FL, 1997.
109. S. Farhat, I. Hinkov, and C. D. Scott, *J. Nanosci. Nanotechnol.* 4, 377 (2004).
110. A. V. Krestinin and A. P. Moravskii, *Chem. Phys. Rep.* 18, 515 (1999).
111. T. W. Ebbesen, *Ann. Rev. Mater. Sci.* 24, 235 (1994).
112. T. W. Ebbesen, H. Hiura, J. Fujita, Y. Ochiai, S. Matsui, and K. Tanigaki, *Chem. Phys. Lett.* 209, 83 (1993).
113. F. G. Gamaly and T. W. Ebbesen, *Phys. Rev. B* 52, 2083 (1995).
114. J.-F. Bilodeau, J. Pousse, and A. Gleizes, *Plasma Chem. Plasma Proc.* 18, 285 (1998).
115. I. Hinkov, Ph.D. Thesis, University Paris 13, France, 2004.
116. C. D. Scott, Report on Trip to LIMHP Université Paris 13 (2003).
117. R. E. Smalley, *Mater. Sci. Eng. B* 19, 1 (1993).
118. A. V. Krestinin and A. P. Moravsky, "Dynamics of Fullerene Formation in a Carbon Arc Process," personal communication. The data cited in this communication combines the data from two papers in Russian published in *Khimicheskaya Fizika* issued as a version in English named *Chemical Physics Reports*. Those two papers in English are Refs. 7 and 108.
119. E. Meeks, H. K. Moffat, J. F. Grcar, and R. J. Kee, *Aurora: A Fortran Program for Modeling Well Stirred Plasma and Thermal Reactors with Gas and Surface Reactions*, Release 3.6, Reaction Design, Inc., San Diego, 2001.
120. L. V. Gurvich, V. S. Iorish, D. V. Chekhovskoi, and V. S. Yungman, *IVTANTHERMO-A Thermodynamic Database and Software System for the Personal Computer. User's Guide.* CRC Press, Boca Raton, FL, 1993.
121. JANAF, "Thermochemical tables, National Standards Reference Data Series," Report NSRDS-NBS: Dow Chemical Company, distributed by Clearinghouse for Federal Scientific and Technical Information, PB168370, 1965.
122. B. J. McBride and S. Gordon, "FORTRAN IV Program for Calculation of Thermodynamic Data," NASA Report NASA TN-4097, 1967.
123. A. C. Hindmarsh, ODEPACK, A Systematized Collection of ODE Solvers, Scientific Computing (R. S. Stepleman, Ed.), Amsterdam, 55–64, 1983.
124. G. N. Abramovich, "Applied Gas Dynamics," Nauka, Moscow, 1969.
125. T. G. Owano, HTGL Report No. T-279, "Non-Equilibrium behavior in a flowing, atmospheric pressure plasma," Stanford University, 1991.
126. B. W. Yu and S. L. Girshick, *J. Appl. Phys.* 75, 8 (1994).
127. D. G. Goodwin, *J. Appl. Phys.* 74, 6888 (1993).
128. A. Peigney, Ch. Laurent, E. Flahaut, R. Bacsa, and A. Rousset, *Carbon* 39, 507 (2001).
129. H. Kataura, Y. Kumazawa, Y. Maniwa, Y. Ohtsuka, R. Sen, S. Suzuki, and Y. Achiba, *Carbon* 38, 1691 (2000).
130. A. A. Puretzky, D. B. Geohegan, H. Schittenhelm, X. Fan, and M. A. Guillorn, *App. Surf. Sci.* 552, 197 (2002).
131. S. V. Patankar, "Numerical Heat Transfer and Fluid Flow." McGraw-Hill, New York, 1980.
132. C. Hirsch, "Numerical Computation of Internal and External Flows, Vol. 1: Fundamentals of Numerical Discretization." John Wiley & Sons, New York, 1990.
133. C. Hirsch, "Numerical Computation of Internal and External Flows. Vol. 2: Computational Methods for Inviscid and Viscous Flows." John Wiley & Sons, New York, 1990.
134. K. A. Hoffman and S. T. Chiang, "Computational Fluid Dynamics for Engineers," Vols. 1 and 2, Engineering Education System, Wichita, US, 1993.
135. D. C. Lobao and A. Povitsky, AIAA Paper 2003-3923, 33rd AIAA Fluid Dynamics Conference, Orlando FL, 2003.
136. K. A. Hoffman, S. T. Chiang, S. Siddiqui, and M. Papadakis, "Fundamental Equations of Fluid Mechanics." Engineering Education System, Wichita, US, 1996.
137. A. A. Puretzky, D. B. Geohegan, X. Fan, and S. J. Pennycook, *Appl. Phys. A* 70 (2000).
138. R. B. Greendyke, "NASA Contractor Report on Grants NAG 9-39 and 9-54" (W. Hyman, D. Sickorez, M. Miller, and W. Tarkington, Eds.), Vol. 1, pp. III–14, Summer, 2001.
139. R. B. Greendyke and C. D. Scott, Report at Annual APS March Meeting 2002, Indianapolis, IN, 2002.
140. R. B. Greendyke, C. D. Scott, and J. Swain, AIAA paper 2002-3026, AIAA/ASME 8th Joint Thermophysics and Heat Transfer Conference, St. Louis, MO, 2002.
141. R. B. Greendyke, J. Swain, and C. D. Scott, NASA/Rice University Workshop on SWCNT Growth Mechanisms (Invited speaker/author), Boerne, TX, 2003.
142. R. B. Greendyke, J. Swain, and C. D. Scott, *J. Nanosci. Nanotechnol.* 4, 441 (2004).
143. R. B. Greendyke, J. E. Swain, T. Stein, L. Ray, and C. D. Scott, AIAA Paper 2004-0807, AIAA 42nd Aerospace Sciences Meeting, Reno, NV, 2004.
144. J. A. White and J. H. Morrison, AIAA paper 99-3360, 1999. (Also see: http://vulcan-cfd.larc.nasa.gov).
145. D. C. Wilcox, "Turbulence Modeling for CFD," 2nd Edn, DCW Industries, Inc., La Canada, CA, 1998.
146. A. Jameson, W. Schmidt, and E. Turkel, AIAA Paper 81–1259, 1981.
147. C. B. Laney, "Computational Gas Dynamics," Cambridge University Press, Cambridge, UK, 1998.

148. Available at: http://capella.colorado.edu/~laney/home.htm.
149. "Mesh Generator Users Manual." Amtec Engineering Inc., Bellevue, WA, 1999 (see also: http://www.amtec.com).
150. "Tecplot User's Manual– Version 9.2, Release 1." Amtec Engineering Inc., Bellevue, WA, 2002 (http://www.amtec.com).
151. Available at: http://www.openchannelfoundation.org/projects/PLOT3D.
152. S. Arepalli, W. A. Holmes, P. Nikolaev, V. G. Hadjiev, and C. D. Scott, *J. Nanosci. Nanotechnol.* 4, 762 (2004).
153. "CFD Analyzer™ User's Manual, Version 3.0." Amtec Engineering Inc., Bellevue, WA, 2002.
154. G. A. Bird, "Molecular Gas Dynamics and the Direct Simulation of Gas Flows," Oxford University Press, Oxford, 1994.
155. D. Frenkel and B. Smit, "Understanding Molecular Simulation," 2nd Edn. Academic Press, New York, 2002.
156. P. Nikolaev, M. J. Bronikowski, R. K. Bradley, F. Rohmund, D. T. Colbert, K. A. Smith, and R. E. Smalley, *Chem. Phy. Lett.* 313, 91 (1999).
157. A. Povitsky and M. D. Salas, *AIAA J.* 41, 2143 (2003).
158. K. E. Lewis, D. M. Golden, and G. P. Smith, *J. Am. Chem. Soc.* 106, 3905 (1984).
159. P. C. Engelking and W. C. Lineberger, *J. Am. Chem. Soc.* 101, 5569 (1979).
160. T. A. Seder, A. J. Ouderkirk, and E. Weitz, *J. Chem. Phys.* 85, 1977 (1986).
161. G. Boudouard, *Ann. Chem. Phys.* 24, 5 (1901).
162. M. Boudart, *AIChE J.* 18, 465 (1972).
163. C. B. Laney, "Computational Gas Dynamics," Cambridge University Press, Cambridge, UK, 1998.
164. "FLUENT 5.0 Users Manual, 2000," Fluent Inc., Lebanon, NH (see also: http://www.fluent.com).
165. A. Povitsky, ICASE Report 2000-18, *Computers and Fluids (International Journal)*, accepted for publication, 2001.
166. A. Povitsky and M. Salas, ICASE Report No. 2001-04, NASA CR 2001-210662, 2001.
167. S. Maruyama and Y. Shibuta, *Mol. Cryst. Liq. Cryst.* 387, 87 (2002).
168. E. Muñoz, W. K. Maser, A. M. Benito, M. T. Martinez, G. F. De la Fuente, and Y. Maniette, *Carbon* 38, 1445 (2000).
169. A. Foutel-Richard, Ph.D. Thesis, CNAM, France, 2003.
170. T. Guillard, S. Cetout, G. Flamant, and D. Laplaze, *J. Mater. Sci.* 35, 419 (2000).
171. D. Laplaze, P. Bernier, W. K. Maser, G. Flamant, T. Guillard, and A. Loiseau, *Carbon* 36, 685 (1998).

CHAPTER 6

Modeling Gas Adsorption in Amorphous Nanoporous Materials

M. B. Sweatman
Department of Chemical and Process Engineering, University of Strathclyde, Glasgow, United Kingdom

N. Quirke
Department of Chemistry, Imperial College, South Kensington, London, United Kingdom

CONTENTS

ISBN: 1-58883-047-0

Handbook of Theoretical and Computational Nanotechnology
Edited by Michael Rieth and Wolfram Schommers
Volume 5: Pages (329–378)

1. INTRODUCTION

1.1. Scope

Materials with amorphous nanoporous surfaces are widely used in industry as adsorbents, particularly for applications where selective adsorption of one fluid component from a mixture is important. Some materials, such as PX21 [1], an ultrahigh surface area carbon activated by treatment with potassium hydroxide, are quoted to have a (BET) surface area higher than 3000 m^2/g! A back of the envelope calculation reveals that, if taken at face value, the pore-walls of this material generally consist of only one graphitic layer. Analysis of adsorption isotherms for PX21 by the methods described later in this chapter reveals that most of the nanoporosity in this material is on the scale of 3 nm or less. At this scale, adsorption is dramatically influenced by nanoscale (surface) geometry, molecular size, and the influence of both on cohesive energies. Naturally, to model adsorption in PX21, and in many other similar materials, a successful approach will require an atomic-scale model of the surface and a molecular theory of adsorption equilibrium.

Traditionally, adsorption onto surfaces is described by "isotherm" equations [1–9] that attempt to encode all of the relevant physics with a few fitted parameters, largely ignoring the complex interaction of surface geometry and fluid physics. These approaches have provided limited insight and, as a consequence, limited confidence. The advent of modern methods based on statistical mechanics and fast computers has radically changed this state of affairs. To a significant degree, the physics of adsorption is now well understood, and today methods for modeling adsorption in nanoporous amorphous materials are generally limited only by the complexity of the surface model, the patience of the modeler, and the quality of experimental reference data.

This chapter reviews progress that has been made in the past two decades concerning the modeling of equilibrium gas adsorption in amorphous nanoporous materials. Much of the discussion will focus on modern statistical mechanical methods, such as classical density functional theory (DFT) [10, 11] and Monte-Carlo simulation [12–14], as well as the surface models employed (i.e., the surface characterization). We will be concerned only with amorphous materials that predominantly contain nanopores. Pore sizes have been classified [1] in terms of micropores (<2 nm), mesopores (2–50 nm), and macropores (>50 nm). But in our case, we are interested in pores that are less than ~10 times the size of an adsorbed particle because fluid behavior in these pores is changed most dramatically compared to bulk gas behavior. This means that for some simple but industrially important molecular fluids such as nitrogen, carbon dioxide, hydrogen, short alkanes, and water, we are interested in pores with widths less than about 5 nm, (i.e., micropores and the smallest mesopores).

As with any modeling exercise, the aim is to make predictions that can be validated experimentally. When designing new materials, the accuracy of gas adsorption prediction is required to be quantitative, not merely qualitative. So we concentrate here on methods that have been applied to make quantitative predictions for real materials. We will see that even the most modern methods are not completely satisfactory. For example, adsorption isotherms for some simple gases in activated carbons can be predicted with accuracy close to that of experiments at super- or near-critical temperatures. But the same confidence does not yet extend to significantly subcritical gases. Nevertheless, for some systems the bottleneck for materials design optimization is now shifted significantly toward their manufacture (i.e., our ability to produce large amounts of material that have nanoscopic properties within a specified tolerance). So the benefits of successful models are clear—they enable accurate prediction of selective adsorption thereby greatly enhancing our ability to design new and better adsorbents.

Finally, we will not consider systems that exhibit significant chemisorption. Physisorption [1] describes a relatively weak bond between adsorbent and adsorbate such that the adsorbate can be recovered without harming the adsorbing material, for example by a reduction in pressure and moderate increase in temperature. Typically, this means adsorbate–surface interactions are due to van der Waals interactions, that is, to induced dipole–induced dipole (also called dispersion, or London) interactions or relatively weak polar interactions

(permanent dipole–permanent dipole, for example). In contrast, chemisorption describes adsorbate–adsorbent bonds that are roughly as strong as bonds that form the material.

Most of our experience and most of the relevant published research concerns activated carbons, but we will attempt to broaden the discussion to other materials that fit the above classification. So we will also mention modeling of adsorption in nanoporous silica xerogels [1]. Amorphous materials such as controlled pore glasses [15] are mostly mesoporous and, although industrially important with novel phase behavior, are outside the scope of this review. Zeolites [1] are industrially important nanoporous adsorbents but are crystalline and also outside the scope of this review. Many polymers do fit within our classification in that they can be nanoporous, amorphous, and industrially important adsorbents. But we will not consider them because polymer science is a vast field in its own right [16].

1.2. Materials

Amorphous nanoporous carbons include materials such as active carbons, carbon fibers, carbon molecular sieves, and carbon xerogels. Many books and review articles [1, 4, 6–9, 17–19] have been written about their manufacture, composition, characterization, and utilization. Briefly, they are generally formed by carbonization of a precursor such as peat, coconut shell, or polymer. Carbonization consists of heat treatment in an inert atmosphere that drives off much of the noncarbon elements leaving a disordered array of graphitic sheets (a graphitic sheet is composed of a single layer of carbon atoms). In carbon xerogels, these sheets coagulate into densely packed nanoscopic beads. In graphitizable carbons, these sheets are thought to be hexagonally bonded internally and to form many layered stacks, whereas in nongraphitizable carbons (see Fig. 1 for example) the sheets are thought to occur singly or in stacks of only a few sheets. The precise nature of the bonding internal to the sheets in nongraphitizing carbons is still a matter of debate [18–21]. Earlier models that proposed hexagonally bonded flat sheets seem to be giving way to models of curved sheets formed from fullerene-like fragments or from graphene sheets with five- and seven-membered ring defects. The "active" prefix implies chemical and/or physical treatment that encourages the formation of nanoporosity and can be applied before or after carbonization. Despite this intense treatment, appreciable noncarbon elements can remain particularly around the edges of graphene sheets, generally in the range of 1–10% by weight. These noncarbon elements, such as hydrogen, oxygen, and sulfur, are often present in the form of functional groups (e.g., OH) that might influence pore geometry and the affinity for polar adsorbates.

The manufacture of active carbons is a global industry, with around half a million tons [7] manufactured each year primarily to store, sieve, purify, separate and decolor a wide range of liquid and gas mixtures. They are also used in catalytic processes. They comprise the most

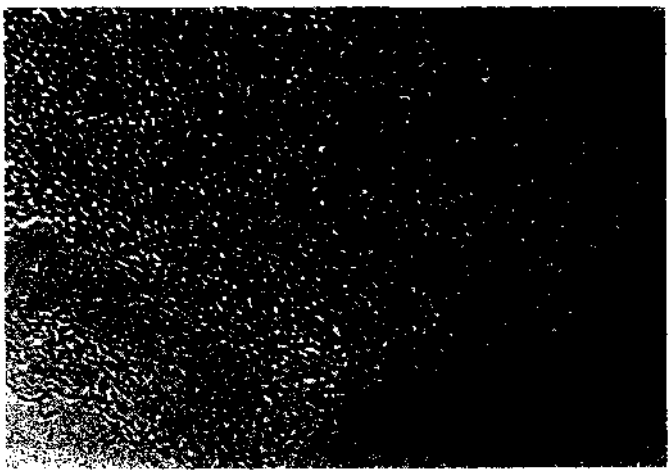

Figure 1. High-resolution electron micrograph of carbon prepared from Saran polymer (scale bar is 50 Å). Reprinted in part with permission from P. J. F. Herris and S. C. Tang, *Philos. Mag. A* 76, 667 (1997). © 1997. Taylor & Francis.

Figure 2. High-magnification SEM micrograph for acid-catalyzed TMOS xerogel. Reprinted in part with permission from T. R. Bryans, V. L. Brawner, and E. L. Quitevis. *J. Sol-Gel Sci. Technol.* 17, 211 (2000). © 2000, Kluwer.

industrially important class of amorphous adsorbent because of their very high surface area and low cost. There is great interest in tuning their properties for particular applications.

Amorphous silica oxide xerogels [1, 9] (see Fig. 2 for example) are prepared by gelation from solution. Dehydration of the hydrogel can lead to a relatively compact xerogel formed from tightly packed nanoscopic beads, each about 2 nm or more in diameter. The solution chemistry and preparation conditions can be varied to arrive at a wide range of gel structures; for example, under certain conditions the beads can coagulate into secondary colloidal structures [1]. Naturally, adsorption isotherms are also varied depending on the degree of microporosity versus mesoporosity, the surface chemistry of each bead, and their interaction with an adsorbing gas.

Silica gels are inexpensive and have found widespread use [9] as adsorbents, dessicants, and catalyst supports because of their affinity for polar molecules. Although their adsorptive behavior has attracted interest [22–25] from a qualitative viewpoint, to our knowledge there has been no work on quantitative predictions using modern methods that make comparison with experiment. Perhaps this is for the future. Because of this, we will have relatively little to say about them except to remark on their interesting adsorptive behavior.

1.3. Objectives

One of the most useful properties of amorphous nanoporous materials is their high adsorptive capacity. Not surprisingly, the main objective of efforts to model these materials is usually to predict adsorption. In particular, the aim is to make predictions for a range of adsorbates over a range of conditions with as much accuracy and as little input data as possible. Clearly, there will be a compromise between the amount of input data and the range and accuracy of output data. Often, the desired aim is to make predictions for a range of adsorbates over a range of temperatures and pressures given a single adsorption isotherm of a single "probe" adsorbate. So, for example, it might be desired to predict the adsorption of methane at ambient temperatures on an activated carbon given only the adsorption of nitrogen at 77 K up to its saturation pressure (1 bar).

Given that most applications involving these materials involve selective adsorption, the ultimate aim is often much more demanding and important [4, 9] than stated above. Very often the aim is to predict the adsorption of a specified fluid mixture of any bulk phase mole fraction given a single probe adsorption isotherm. Clearly, the addition of $n - 1$ dimensions to the pure adsorption problem, where n is the number of components in the mixture, can make predictions much more difficult and time consuming.

This last point introduces another factor, namely the compromise between accuracy and speed. Sometimes the particular industrial application might require predictions to be made quickly so that the experience of making predictions is "interactive." We will see later that if this is the case, then calculation of mixture adsorption isotherms using molecular simulation directly is out of the question, particularly if there are several components in the mixture. Clearly, any model should be simplified as far as possible provided its predictions are consistent with experimental error.

Other properties such as transport coefficients and adsorption energies can be important for materials and industrial processes. But in this chapter we will concentrate on equilibrium adsorption.

1.4. Issues

Surface characterization is an important part of the modeling process. Little insight into the behavior of adsorbates can be gained without it. Clearly, it is not possible to generate a model that describes every atom in a macroscopic sample of *amorphous* nanoporous adsorbent. The aim then is to create a model that captures the most significant features of the surface so that sufficiently accurate predictions can be made.

The surface model must be calibrated by adjusting any free parameters to fit experimental data. The most common [1, 2, 26–28] experimental method for characterization of amorphous adsorbents involves measurement of adsorption isotherms of one or more probe adsorbates. Of course, the probe should be sensitive to the significant features of the surface so that the pore model can be accurately calibrated. In the case of active carbons, the most significant feature is the pore width if simple gases like methane are to be studied. So the ideal probe will be strongly attracted to the surface to reduce experimental error, it will remain fluid at all locations in the adsorbent to avoid pore-blocking, and it will be subcritical so that capillary condensation can be used to discriminate pore width. Generally, the probe will become more sensitive to pore width as its temperature is lowered toward its triple-point. But venturing too close to the triple-point runs the risk of pore-blocking. Traditionally [1, 4, 7], nitrogen at 77 K is used as a probe following the conventional Brunauer-Emmett-Teller (BET) method.

Many modern studies employ a "pore-size distribution" (PSD) to characterize the pore network in a material. However, statements about the pore network geometry should usually be considered with caution for several reasons. Most importantly, it is not a well-defined property because the geometry of a curved surface is dependent on the adsorbate. Second, it is not yet possible to measure directly the pore network geometry of a real amorphous nanoporous material with respect to any adsorbate. Instead, we can only make rather crude inferences on the basis of indirect measurements, such as adsorption isotherms and adsorption energies, and crude pore models. And these measurements are often easily confused by competing influences such as pore width and the strength of adsorbate–surface interactions [29–31]. Yet despite these pitfalls, a great many studies [27, 32–43] have tended to concentrate on prediction of pore-size distributions rather than prediction of adsorption.

For polar molecules, the polarity of the surface plays an important role in their adsorption. The complex interaction between pore width and surface charge distribution might require several probes to be used to distinguish competing effects. For example, nonpolar argon might be used to generate a PSD, while water adsorption could be used to assess surface polarity for the given PSD. Recent studies involving titration [44, 45] are thought to provide greater detail with respect to particular surface functional groups (e.g., nitrogen, phosphorus or oxygen functional groups). Other measurements [21] that provide characteristics of the surface include x-ray diffraction and high-resolution transmission electron microscopy

(HRTEM) from which average pair-distribution functions can be obtained, and spectroscopy, which also measures the type and number of functional groups present (much more detail about experimental methods can be found in [21]).

Often the material's surface is considered to be inert in the sense that it does not react in any way to the presence of the adsorbate. Clearly, this is inappropriate for modeling materials that are known to swell appreciably such as unexpanded clays [1] or some polymers [16]. But for materials like nongraphitizing active carbon where the *chemical* bonding between graphitic sheets is thought to be relatively [18] strong, this is thought to be a reasonable approximation [46].

It is important to be clear about exactly what an experiment measures. In the case of the most common surface characterization measurement, the adsorption isotherm, it is the number of moles of adsorbate in an accessible volume in excess of the number of moles of adsorbate that would fill this volume if it had a uniform density equal to the bulk adsorbate density ρ_f^b, that is,

$$N^{ex} = N_{V_f}^{tot} - \rho_f^b V_f \tag{1}$$

where N^{ex} is the excess number of moles of adsorbate, and $N_{V_f}^{tot}$ is the experimentally measured total number of moles of adsorbate in a volume V_f that includes all the accessible pore space and none of the inaccessible pore space. $N_{V_f}^{tot}$ is measured directly in an experiment, either gravimetrically or volumetrically, but V_f is not well defined because it is impossible in an experiment to distinguish gas adsorbed in accessible pore space, V_f^p, from gas in the experimental bulk volume, V_f^b. So we can write

$$V_f = V_f^p + V_f^b \tag{2}$$

As explained carefully by Neimark and Ravikovitch [47], it is standard practice to define V_f by measuring the total adsorption of helium at a particular pressure and temperature. If it is assumed that the excess adsorption of helium is zero, then we have $V_f = N_{V_{He}}^{tot}/\rho_{He}^b$ and using (1) again

$$N^{ex} = N_{V_f}^{tot} - \frac{\rho_f^b}{\rho_{He}^b} N_{V_{He}}^{tot} \tag{3}$$

All the quantities on the right-hand side of (3) can be measured directly in an experiment. A problem with this definition is that it is well-known that helium can experience significant adsorption, especially in the narrowest pores and at low temperature. So this definition of V_f and N^{ex} should be viewed as a calibration. This should be contrasted with the usual definition of excess adsorption in theoretical models

$$N_{the}^{ex} = N_{V_{the}}^{tot} - \rho_{f,the}^b V_{the} \tag{4}$$

where V_{the} is the pore volume accessible to fluid in the theoretical model, and $\rho_{f,the}^b$ is used to distinguish the modeled bulk density from the experimental bulk density at a particular pressure. So theoretical model predictions are exact when

$$N_{V_f^p}^{tot} - N_{V_{the}}^{tot} = \rho_f^b \frac{N_{V_{He}^p}^{tot}}{\rho_{He}^b} - \rho_{f,the}^b V_{the} \tag{5}$$

For a perfect model, $N_{V_f^p}^{tot} = N_{V_{the}}^{tot}$ and $\rho_f^b = \rho_{f,the}^b$ in which case we must set $V_{the} = N_{V_{He}^p}^{tot}/\rho_{He}^b$ to ensure that perfect agreement with experiment is obtained. For a perfect model, $N_{V_{He}^p}^{tot}$ can be obtained from the model itself. Neimark and Ravikovitch [47] argue that this definition should be used for any model. They show that the adsorption of helium in the low-pressure (Henry's law) limit depends strongly on temperature, so the temperature at which $N_{V_{He}^p}^{tot}$ is obtained experimentally can have a dramatic impact on calculated values of N^{ex} for supercritical or near-supercritical adsorbates. Essentially the same conclusions are reached by Myers and Monson [48]. They also suggest that helium calibration should be standardized.

Ozdemir et al. [49] argue that the above arguments are correct only for a rigid adsorbent. For an adsorbent that swells, V_{the} should be reduced by a volume equal to the amount of swelling. Murata et al. [50] describe a different approach to calculating total adsorption. Unfortunately, their argument is circular and their results are entirely dependent on fitting an isotherm equation to an experimental isotherm.

Another popular measurement concerns the "heat of adsorption," although precisely which heat quantity is measured will depend on experimental setup and procedure. Several books [1, 3, 6, 14] relate this heat to the "isosteric heat," which is calculated from at least two adsorption isotherms of the same system at different temperatures. We will describe the relation between these quantities later after first presenting some thermodynamics. We mention them here because they provide another example of the difficulty in comparing experimental measurements and model predictions.

Fluids in pores exhibit richer phase behavior compared to the bulk phase. This topic alone has motivated numerous books [14, 51–53], articles [54], journal sections, and careers and is still a growing field of study. The counterparts of equilibrium bulk phase transitions like the gas–liquid transition are generally shifted to other bulk pressures and temperatures when fluid is confined to a pore. The magnitude of this shift depends on the pore size, geometry, and the nature of the fluid–surface interaction. A modified [55] form of Kelvin's equation [56] predicts this shift for the liquid–gas transition for a cylindrical pore

$$k_B T \ln\left(\frac{\mathrm{P}_{\mathrm{sat}}}{\mathrm{P}}\right) = \frac{2\gamma_{\mathrm{lg}} \cos\theta}{R(\rho_l - \rho_g)} \tag{6}$$

provided R, the pore radius, is very large compared to the adsorbate particle size. Here, θ is the "contact angle" [51] required to stabilize a droplet of liquid on an isolated surface, γ_{lg} is the gas–liquid surface tension at bulk coexistence, ρ_l and ρ_g are the bulk liquid and gas densities at coexistence, and P_{sat}/P is the ratio of the bulk saturation pressure to the confined saturation pressure.

For fluids confined in pores with relatively strong fluid–surface interactions, like subcritical nitrogen in the graphitic pores of active carbons, the pressure at which capillary condensation occurs steadily reduces with pore size. For pore sizes that we are concerned with, the Kelvin equation is no longer accurate [38, 57] and alternative theories are needed. An accurate theory should be able to reproduce the correct condensation pressure for a pore of any size and be able to predict the modulation of this transition caused by packing effects in the smallest pores. In addition, surface phase transitions that have no bulk counterpart such as prewetting are possible for sufficiently smooth surfaces. These transitions are sensitive to the nature of both fluid–fluid and fluid–surface interactions and they can be influenced by the shifted bulk transitions [58]. So, for example, it is possible for prewetting to be preempted by capillary condensation as pressure increases toward saturation in sufficiently small pores. For the systems considered in this review, capillary condensation is the most useful transition because it is very sensitive to pore size.

Phase behavior in amorphous nanoscopic materials is complicated further by pore connectivity and proximity [22, 23, 59–61]. For example, the equilibrium capillary condensation pressure of a pore can be reduced if neighboring pores are smaller. This proximity effect can be important for systems in which fluid–fluid interactions are relatively strong compared to fluid–surface interactions (xenon adsorbed in a high porosity xerogel [23], for example). But for most of the systems considered here, fluid–surface interactions are relatively strong, so this proximity effect is likely to be less significant and many studies choose to ignore it.

1.5. Difficulties

Poor equilibration is a factor that complicates both experimental and theoretical studies of adsorption. It covers several phenomena, including metastability, pore-blocking, and poor diffusion. It is further complicated by the connectivity of the network of pores. Each of these mechanisms can lead to hysteresis where the adsorption and desorption curves are not identical. For example, Fig. 3 shows adsorption and desorption curves for argon on SBA-16 [62] (an ordered mesoporous silica consisting of 9.5-nm spherical cavities connected

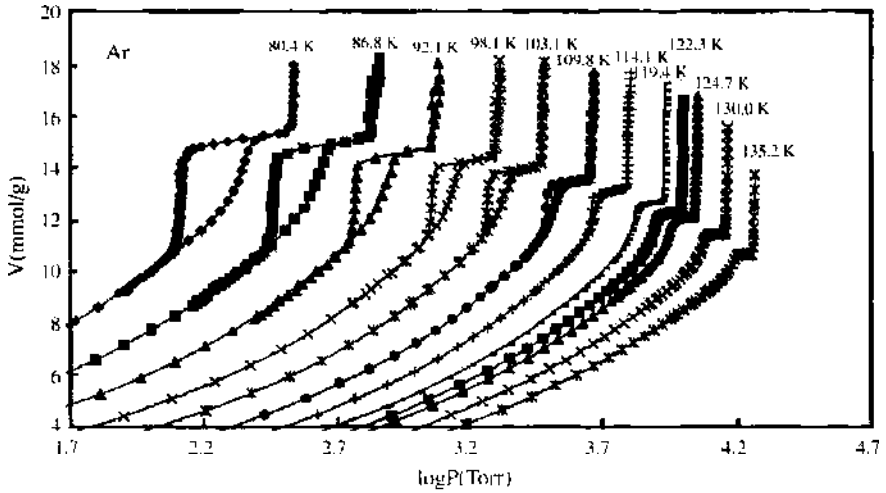

Figure 3. Temperature dependence of hysteresis of argon on SBA-16. Reprinted with permission from [62], Morishige and Tateishi, *J. Chem. Phys.* 119, 2301 (2003). © 2003, American Institute of Physics.

through 2.3-nm openings) for a range of temperatures. In this case, the hysteresis loop vanishes at a temperature well below the bulk critical temperature. The relative importance of metastability versus pore-blocking has been debated for decades. Early pore network analysis methods [63] often relied on pore-blocking as the prime hysteresis mechanism. But recent work by Kierlik and colleagues [23, 59, 60] and Monson and colleagues [22, 61] demonstrates that metastability is sufficient to account for various types of hysteresis seen in experiment.

Metastability indicates that a system is at a state of local rather than global stability. In terms of gas adsorption in inert solids, metastable states are located at the local minima of the grand-potential surface. They have a lifetime that depends on the height of the free-energy barrier between neighboring state. Or, in other words, their stability depends on the probability of a random (thermal) fluctuation with sufficient magnitude to escape the basin of attraction of the metastable state. Essentially, the higher the free-energy barrier, the longer the expected lifetime of the metastable state. In experiments, this can be observed as hysteresis if the lifetime of a metastable state exceeds the patience of the experimenter. For fluids adsorbed in idealized model pores, hysteresis can be induced both by surface phase transitions, such as prewetting, and by the shifted counterparts of bulk transitions, notably capillary condensation. For adsorption in amorphous materials, the picture is much more complicated [22, 23, 59–61]. If a single pore can be either gas-like or liquid-like at a particular pressure due to metastability with an experimentally long lifetime, then an estimate for the number of potential metastable states corresponds to the number of possible permutations for all pores in the sample that have this property, an astronomical number for a macroscopic sample. This can only be an estimate because this way of counting states ignores the effect of fluid in one pore on fluid in neighboring pores. This proximity effect will shift the equilibrium and metastable transitions to other pressures depending on whether neighboring pores are filled with gas or liquid. Consequently, condensation can proceed via avalanches or cascades as condensation in one pore triggers condensation in neighboring pores.

This picture emerged from the work of Kierlik and coworkers [23, 59, 60] and Monson and co-workers [22, 61] who studied this phenomenon with lattice DFT and Monte Carlo models of high-porosity mesoporous glasses and xerogels. They find that they can qualitatively reproduce experimental isotherms and hysteretic behavior for these materials if their models allow for metastability and the proximity effect (but not pore-blocking). Their approach also allows them to predict how phase behavior depends upon temperature, porosity, and the relative strength of gas–gas to gas–surface interactions. Metastability in regular mesoporous materials has been studied by Neimark and coworkers using both DFT [64–66] and a "gauge-cell" Monte Carlo method [67]. They find that the hysteresis loops in these materials can be

reproduced quite well with simple geometric surface models appropriate to the particular material, and that for these materials pore-blocking is probably not responsible for hysteresis.

Pore-blocking [1, 68] is thought to occur when condensate in a filled pore cannot escape to the reservoir, even though the pressure is below its equilibrium cavitation pressure, because the route to the reservoir is blocked by a smaller connecting pore that is also filled with condensate. If this blocked state is not metastable, then it must be caused by poor diffusion of condensate in the larger pore through the blocking smaller pore. If this is the case, then one can also imagine that pore-blocking occurs during adsorption as well as desorption. In experiments, poor diffusion can test the patience of experimenters, and for very poorly diffusing systems the experimenter can be deceived, thinking that all the pores have achieved equilibrium (if only metastable) when in fact a significant portion have not. For many years, this was widely thought to be the dominant factor in producing hysteresis [68]. Models based on this mechanism were developed to analyze pore network connectivity [63]. However, recent analysis [69] based on molecular dynamics (MD) simulations questions the existence of pore-blocking for simple fluids in "ink-bottle" geometries. Sarkisov and Monson [69] found that for a Lennard-Jones (LJ) fluid and one particular pore configuration, the larger pore could empty before the smaller connecting pore emptied, that is, that diffusion through the smaller pore was not hampered (Fig. 4). Vishnyakov and colleagues [70] found similar results using Monte Carlo (MC) simulation. Nonetheless, they [70] continue to use the "pore-blocking" terminology for pore configurations where the smaller pore is not too small compared to the larger pore and both pores empty simultaneously on desorption. But their terminology could be misleading as their MC study does not account for dynamics (i.e., diffusion) but instead considers only metastability. Nevertheless, pore-blocking due to poor diffusion is still considered an important hysteresis mechanism for simple fluids by some workers [71]. It seems that more work focusing on molecular dynamics is needed to establish the existence and significance of pore-blocking for a range of fluids, surfaces and networks.

Fortunately, hysteresis caused by metastability is less important or absent for nanoporous materials and simple gas mixtures (i.e., for most of the systems considered in this review). Using a mean-field density functional theory Ravikovitch and colleagues [72] find that metastability related hysteresis of nitrogen at 77 K in spherical silica pores is essentially a mesoscopic phenomenon that generally occurs in pores larger than about 6 nm. Similar conclusions are likely for other pore geometries and subcritical gases, although the precise onset of hysteresis with pore width will be sensitive to the particular system.

For more complex systems, poor diffusion is significant. For example, studies [73] involving water adsorption in model active carbons that have polar surface sites have shown that water can adsorb at the entraces to pores, thereby potentially blocking the access of other adsorbed gases (although this study did not investigate dynamics). And Nakashima et al. [74] report activated diffusion in a particular activated carbon using carbon dioxide as a probe at 273 K. In the case of materials that swell, for example, many clays and polymers, the swelling process might be completed only very slowly.

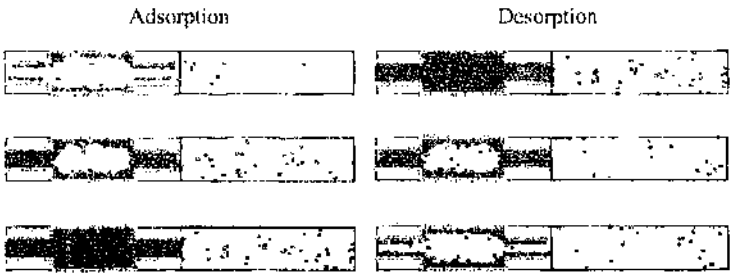

Figure 4. Computer graphics visualization of the filling (with increasing pressure) and emptying (with decreasing pressure) of a Lennard-Jones fluid in an "ink-bottle" pore whose walls are formed from hexagonally arranged Lennard-Jones particles. Note there are periodic boundaries in the direction of the pore (left–right) and normal to the plane of (into) the diagram. The right-hand volume in each case is a grand-canonical "control" volume while diffusion into and out of the left hand volume occurs via molecular dynamics. Reprinted with permission from [69], Sarkisov and Monson, *Langmuir* 17, 7600 (2001). © 2001, American Chemical Society.

Moreover, if fluid becomes very dense within a pore, it can freeze [75] at a temperature that is shifted with respect to the bulk freezing temperature. Pore (and surface) freezing is exacerbated by relatively strong fluid–surface interactions [76–78] and by pore-junctions [79] and pits [80] (i.e., the kind of heterogeneous surfaces expected in amorphous materials). Freezing of simple fluids in ideal pores has been investigated in detail using grand-canonical Monte Carlo simulation by Radhakrishnan and coworkers [76, 77, 81–83]. They find that for relatively strong fluid–surface interactions, freezing on the surfaces of pore-walls occurs at higher temperatures than freezing in the remainder of the pore, which itself can occur at higher temperatures than in the bulk at the same pressure. Figure 5 shows the global phase diagram for freezing of a Lennard-Jones fluid in a model slit-pore at 1 atmosphere as calculated by Radhakrishnan et al. For the systems with the strongest relative fluid–surface interactions, they find that freezing can occur in narrow pores at temperatures about 20% above the bulk freezing temperature at this pressure. Although there might be some problems associated with simulating freezing in the grand-canonical ensemble,[1] their simulation results for freezing in ideal pores compare well with experiments on real porous materials [76].

Based on these results, if we consider the nitrogen–graphitic pore system at 77 K, which has a high relative fluid–surface interaction strength [76, 77], α, close to 2.5 if typical gas–surface interaction parameters are used [72], we see that according to the phase diagram of Radhakrishnan et al., (Fig. 5) nitrogen might freeze in narrow pores at a temperature about 20% above its bulk freezing temperature [84] (63.3 K) at 1 atmosphere (i.e., close to 76 K). We can expect that it will freeze in even narrower pores at lower pressures and slightly higher temperatures. This could have a major impact on traditional pore characterization experiments [1, 2, 6] that routinely use nitrogen at 77 K, including the BET analysis of surface area. It indicates that studies that have analyzed nanoporous carbonaceous materials with nitrogen at 77 K could be flawed because it is conceivable that frozen, hexatic [76], glassy, or poorly diffusing nitrogen has blocked access to the normally accessible porous network. Indeed, this possibly has occurred for at least one system frequently analyzed in the literature [35, 38, 85–88], namely the adsorption of nitrogen at 76 K on AX21 (a carbon related to PX21). Figure 6a compares a typical isotherm for this system with the corresponding isotherm on another high surface area carbon [88] (PRC16), while Figure 6b shows the corresponding isotherms at 77 K for several low surface area carbons that are thought [89] not to contain significant microporosity. Because in all these materials adsorption is dominated by the strength of the gas–surface interaction, one should expect that significant adsorption in microporous carbons will occur for $P \ll 0.01$ mbar, as is the case for PRC16 in Fig. 6a. That adsorption is insignificant for nitrogen in AX21 below this pressure indicates that it is not significantly nanoporous (or at the very least that the fraction of pores less than 1 nm or so in width is tiny [90]), like the low surface area carbons in Fig. 6b. But analysis of carbon dioxide adsorption on AX21 with a simple "polydisperse slit-pore" model [91] (described later) indicates the opposite (i.e., AX21 probably is significantly nanoporous). So it seems that the experimental result for nitrogen at 77 K in AX21 could be erroneous, possibly because of poor diffusion.

The work of Radhakrishnan et al. indicates that to avoid pore-blocking of this kind, probes should be employed at a temperature well above their bulk triple-point temperature, say at least 30% higher. Clearly, a compromise temperature is required so that the adsorbate is sufficiently mobile while remaining sufficiently sensitive to the surface and to pore width.

Other factors that can complicate the interpretation of gas adsorption in nanoporous amorphous materials include molecular sieving and swelling. No two adsorbates experience the same amorphous surface. Molecular sieving can result if one adsorbate can reach regions of the pore network that are inaccessible to another adsorbate because it is too large to fit through any of the connecting pores. This effect is clearly very dependent on the connectivity of the pore network. As pores fill with fluid, the pressure exerted on the pore walls changes.

[1] A crystalline solid simulated at fixed volume with periodic boundaries also has a fixed lattice site density in a conventional simulation. So, the system cannot attain the true equilibrium lattice site density at the specified chemical potential unless, somehow, the correct density is known in advance. In our view, this argument holds regardless of system size and particle creation/annihilation statistics.

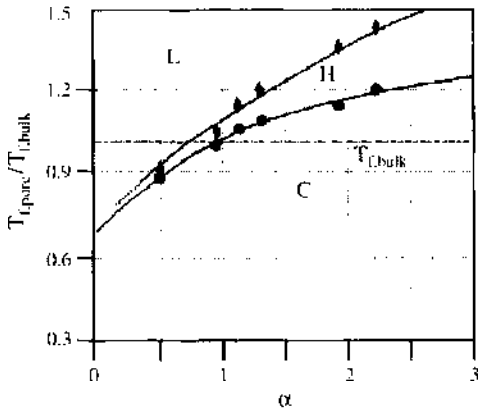

Figure 5. Global freezing phase diagram of a fluid in a slit-pore with physical width three times that of a fluid particle. Three different phases are observed; liquid (L), hexatic (H), and crystalline (C). Symbols are simulation results while lines are a guide to the eye. The dashed line represents an extrapolation of the phase boundaries on the basis of MC simulations without free-energy calculations. The phase transition temperature is plotted relative to the bulk freezing temperature for a range of relative gas–surface to gas–gas interaction strengths, α. Reprinted with permission from [76], Radhakrishnan, et al., *J. Chem. Phys.* 116, 1147 (2002). © 2002, American Institute of Physics.

If this pressure is different from the pressure in the bulk, then a net force will be exerted on the pore walls. For materials like activated carbons, the pore walls are fairly rigid and usually modeled to be inert. But for some clays and polymers, this solvation force results in considerable swelling.

Clearly, poorly diffusing and sieving systems present additional modeling challenges because a description of the pore network connectivity is required in addition to an understanding of molecular-scale behavior in individual pores. Methods for describing nanoporous amorphous solids will be described later in Section 3. Materials that swell can be described in the osmotic ensemble [92], which is specified by fixed pressure, temperature, fluid phase chemical potential, and number of "solid" particles. However, relatively little fundamental work [48, 93, 94] seems to have been published on this subject concerning systems of relevance to us. Analysis of swelling seems to be much more developed in the field of polymer science [16].

The length of the above discussion serves to illustrate the difficulties associated with interpreting adsorption (and desorption) isotherms. Considerable progress has now been made concerning our fundamental understanding of fluid behavior in amorphous materials, but a great deal more remains for the future.

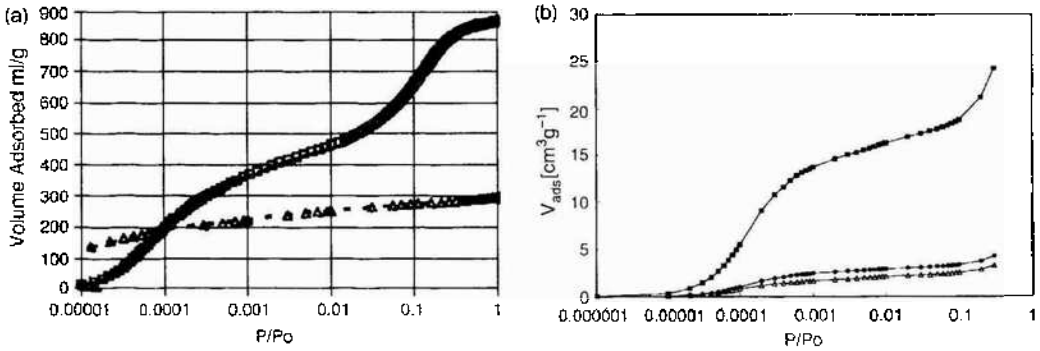

Figure 6. (a) Experimental adsorption of nitrogen (cm^3 at STP per gram of carbon) at 76.1 K in AX21 (squares) and PRC16 (triangles) activated carbons (the lines are fitted to this data). Pressure is plotted relative to the condensation pressure of nitrogen at this temperature (i.e., about 1 bar). Reprinted with permission from [88], Quirke and Tennison, *Carbon* 34, 1281 (1996). © 1996, Elsevier. (b) Experimental adsorption (cm^3 at STP per gram of carbon) of nitrogen at 77 K on three low surface area carbons: Vulcan (squares), Sterling (circles), and graphite (triangles) (the lines are a guide to the eye). Pressure is relative to the condensation pressure of nitrogen at this temperature (i.e., 1 bar). Reprinted with permission from [89], Kluson and Scaife, *J. Porous Mater.* 9, 115 (2002). © 2002, Kluwer.

1.6. A Little Thermodynamics

An adsorbed fluid is in equilibrium with its bulk gas phase when its temperature and chemical potentials are constant throughout the system. So a natural ensemble with which to study adsorption is the grand-canonical ensemble. The relevant free-energy is the grand potential, Ω, which is a function of the chemical potential of each fluid component, μ_i, at fixed temperature, T, and volume, V. The starting point for many treatments of the thermodynamics of adsorption is the fundamental relation

$$\Omega = E - TS - \sum_i \mu_i N_i \tag{7}$$

where E is the energy, S is the entropy, and N_i is the number of particles of type i. While the fixed V constraint is certainly appropriate for inert adsorbents, it is not appropriate for flexible adsorbents. Porous carbons have successfully been modeled as rigid adsorbents, but materials such as polymers, gels, xerogels, and clays are known to swell or contract appreciably during the process of adsorption and desorption. For these materials, it can be more appropriate to let the material achieve mechanical (pressure) equilibrium with the bulk gas while constraining the number of particles that form the adsorbent, N_0. Myers and Monson [48] have developed the thermodynamics of this system in terms of "solution thermodynamics" (i.e., the adsorbent is treated as another fluid phase with fixed N_0). Their treatment corresponds to an osmotic ensemble [92] for which the fundamental relation is

$$\mu_0 N_0 = E - TS - \sum_i \mu_i N_i + PV \tag{8}$$

They show that the thermodynamics of a rigid system can be deduced from that of the osmotic ensemble by ultimately fixing V (i.e., that the grand-canonical ensemble view of adsorption is a special case of the osmotic view).

For amorphous carbons, this picture might be valuable in the future if it is shown that swelling is important for these materials. For now, we will follow the usual grand-canonical approach and begin by considering the adsorbent as completely inert so that it is described solely by an external potential. If we treat amorphous systems as extensive (i.e., doubling the size of the system doubles the grand potential), then we can develop a thermodynamic framework as follows. The work done on the system is written

$$dE = \omega dV + TdS + \sum_i \mu_i dN_i \tag{9}$$

where ω is the energy per unit volume required to increase the volume of the system at constant S and N_i. How can this possibly be achieved for an amorphous system? Well, at least in principle, we can imagine an insulating impenetrable barrier, or magic piston, that confines adsorbate and heat to a particular region of the material. Because we take the surface to be inert, it has zero thermal conductivity and heat capacity. Increasing the volume of this magic piston so that all the gas remains within the material requires work to be done by the contained adsorbate.

Substituting (9) into (7) gives

$$d\Omega = \omega dV - SdT - \sum_i N_i d\mu_i \tag{10}$$

which means that we can identify $\Omega = \omega V$ and so

$$Vd\omega = -SdT - \sum_i N_i d\mu_i \tag{11}$$

from which we obtain expressions for the adsorption and grand potential at fixed temperature and volume

$$N_i = -\frac{\partial \Omega}{\partial \mu_i}; \quad d\Omega = -\sum_i N_i d\mu_i \tag{12}$$

These expressions are crucial to the development of thermodynamic theories such as ideal adsorbed solution theory [95], which will be discussed later, for the analysis of experimental data such as the heat of adsorption, which will be discussed next, and for checking the accuracy and consistency of statistical mechanical calculations based on molecular simulation and theory [11].

The "isosteric heat," q_{st}, is defined via the isosteric method [1], which consists of analyzing the variation of pressure with temperature at fixed adsorption, that is,

$$q_{st} = \frac{T}{\rho_b}\left(\frac{\partial P}{\partial T}\right)_{V,N^{ex}} \tag{13}$$

Note that when analyzing experimental data, it is usually the excess adsorption that is held fixed. When analyzing model data, however, either the absolute or excess adsorption can be held fixed. This should not cause confusion provided the constraint is made explicit, and much of the following discussion is unchanged by this choice. In the following, we will employ fixed excess adsorption, which requires definition of adsorbed and bulk volumes, V_a and $V_b = V_a + V_c$, so that $N^{ex} = N_a - N_b = \rho_a V_a - \rho_b V_b$. To see how (13) is related to a heat measured in an experiment, we will specialize to a pure gas and use (11) to obtain

$$\frac{V_b}{N_b}\left(\frac{\partial P}{\partial T}\right)_{V,N^{ex}} = \frac{S_b}{N_b} + \left(\frac{\partial \mu}{\partial T}\right)_{V,N^{ex}} \tag{14}$$

as $-P$ is the grand-potential density of the bulk gas. To evaluate the differential of the chemical potential at fixed excess adsorption, we need to develop an "excess" thermodynamic framework. This can be achieved by defining

$$F^{ex} = F_a - F_b = E_a - TS_a - E_b + TS_b \tag{15}$$

Then, using (9) gives

$$\begin{aligned} dF^{ex} &= \omega dV_a + \mu dN_a - S_a dT + PdV_b - \mu dN_b + S_b dT \\ &= \omega^{ex} dV_a + PdV_c + \mu dN^{ex} - S^{ex} dT \end{aligned} \tag{16}$$

We now use a mathematical identity (a Maxwell relation)

$$\left(\frac{\partial \mu}{\partial T}\right)_{V,N^{ex}} = \frac{\partial}{\partial T}\left[\left(\frac{\partial F^{ex}}{\partial N^{ex}}\right)_{T,V}\right]_{V,N^{ex}} = \frac{\partial}{\partial N^{ex}}\left[\left(\frac{\partial F^{ex}}{\partial T}\right)_{N^{ex},V}\right]_{T,V} = -\left(\frac{\partial S^{ex}}{\partial N^{ex}}\right)_{T,V} \tag{17}$$

and the fact that entropy is extensive if the grand-potential density and temperature are fixed to obtain

$$q_{st} = \frac{T}{\rho_b}\left(\frac{\partial P}{\partial T}\right)_{V,N^{ex}} = T\left(\frac{\partial S_b}{\partial N_b}\right)_{P,T} - T\left(\frac{\partial S^{ex}}{\partial N^{ex}}\right)_{T,V} \tag{18}$$

The right-hand expressions here are both measurements of the heat evolved when particles are reversibly added to a system under different conditions. This is why the isosteric expression (13) is called a "heat." It is also sometimes [1, 48, 96] called the "differential enthalpy" of adsorption because the enthalpy $H = E + PV$. From this definition we find

$$dH^{ex} = TdS^{ex} + \mu dN^{ex} - V_c dP + \omega^{ex} dV_a \tag{19}$$

so that if $V_c = 0$,

$$\frac{H_b}{N_b} - \left(\frac{\partial H^{ex}}{\partial N^{ex}}\right)_{T,V} = T\left(\frac{\partial S_b}{\partial N_b}\right)_{P,T} - T\left(\frac{\partial S^{ex}}{\partial N^{ex}}\right)_{T,V} \tag{20}$$

which is equal to the isosteric heat. Note that if absolute adsorption is employed, then we have

$$q_{st} = \frac{T}{\rho_b}\left(\frac{\partial P}{\partial T}\right)_{V_a,N_a} = T\left(\frac{\partial S_b}{\partial N_b}\right)_{P,T} - T\left(\frac{\partial S_a}{\partial N_a}\right)_{T,V_a}$$
$$= \frac{H_b}{N_b} - \left(\frac{\partial H_a}{\partial N_a}\right)_{T,V_a} + V_a\left(\frac{\partial P}{\partial N_a}\right)_{T,V_a} \tag{21}$$

which no longer consists purely of enthalpy related terms. So we prefer description in terms of a reversible "heat."

The heat measured in an experiment depends entirely on the apparatus and procedure. But whatever the experiment, the isosteric heat itself cannot ever be measured *directly* because it is simply not possible for N_a or N^{ex} to vary in an equilibrium system at constant P, V_a, and T. Indeed, terms of the type [14, 97] $(\partial S_a/\partial N_a)_{V_a,T,P}$ or $(\partial S^{ex}/\partial N^{ex})_{V_a,T,P}$ are meaningless as they are overconstrained. To relate the isosteric heat to an experimental measurement might require consideration of other constraints. For example, the constant volume or "differential" heat of adsorption [98, 99] is

$$q_d = T\left(\frac{\partial S_b}{\partial N_b}\right)_{T,V} - T\left(\frac{\partial S_a}{\partial N_a}\right)_{T,V} = q_{st} + \left(\frac{\partial E_b}{\partial N_b}\right)_{T,V} - \frac{H_b}{N_b} \tag{22}$$

where the last two terms on the right-most-side sum to $-k_BT$ for an ideal molecular gas. An experiment [99] that can measure this heat comprises two chambers, one is an evacuated chamber that contains the adsorbent and is connected via a valve to the other, bulk chamber. If the gas is ideal, then the reversible heat measured leaving both chambers on opening the valve is the differential heat of adsorption. Another alternative mentioned in the literature [98, 100] is the "equilibrium" heat of adsorption

$$q_{eq} = T\left(\frac{\partial S_b}{\partial N_b}\right)_{P,T} - T\left(\frac{\partial S^{ex}}{\partial N^{ex}}\right)_{P,T} = q_{st} + \frac{T}{\rho^{ex}}\left(\frac{\partial \omega^{ex}}{\partial T}\right)_{V,N^{ex}} = \frac{H_b}{N_b} - \frac{H^{ex}}{N^{ex}} + \frac{\omega^{ex}}{\rho^{ex}} \tag{23}$$

which is perhaps the most intuitive heat of adsorption, although it is difficult to imagine an adsorption experiment that could measure it in practice. Note the ω^{ex}/ρ^{ex} term in (23) vanishes if we use Vuong and Monson's [98] definition of enthalpy, $H = E - \omega V$, and if absolute rather than excess measurements are made, then the "*ex*" superscripts also vanish.

1.7. General Classification of Models

All models of gas adsorption in nanoporous amorphous materials require a model of the adsorbing surface and a model of gas adsorption on this surface. These surface and "isotherm" models can be classified separately, and they will be described in the next two sections accordingly.

We classify isotherm models in terms of whether they are based on a lattice or are continuum theories. We classify continuum approaches separately as classical density functional theory and Monte Carlo simulation. We classify surface models in terms of whether they are based on a few free parameters (scalar models), many similar parameters (vector models), or arbitrarily complex 3D representations. The classification of models in this way can be debated, but we have chosen a scheme that groups models roughly according to their complexity and accuracy. We make no apology for not mentioning absolutely every such model in the literature.

2. ADSORPTION ISOTHERMS

We focus in this review on methods that can generate adsorption isotherms for any given external potential, that is, inert surface. Many popular engineering or empirical approaches to generating adsorption isotherms are actually combinations of particular theories and particular surface models. For example, the Langmuir isotherm can be derived [1] by considering the statistical mechanics of monolayer adsorption on an isolated plane surface using a lattice model and several crude approximations. So we will not discuss these engineering or empirical isotherms until later in the context of surface models.

2.1. Lattice Models

A lattice model restricts the Hamiltonian so that the system consists of a discrete lattice of sites. Many different lattice topologies can be imagined, but one of the simplest and most well-known 3D models is the Ising Model [54, 101] that consists of a cubic lattice where each site, s_i, can be either occupied ($s_i = 1$) or unoccupied ($s_i = 0$). The Hamiltonian for a pure fluid is then

$$H = -\varepsilon \sum_{ij} s_i s_j + \sum_i V_i^{ext} s_i \tag{24}$$

where the "ij" sum is restricted to nearest-neighbor pairs and $\varepsilon > 0$ is the interaction energy if a pair of sites are both occupied. The external field, V_i^{ext}, can be different for each site if desired. The lattice spacing is often taken to be about the same size as a particle.

There is no restriction on how the statistical mechanics of a lattice model is solved. Usually, a Monte Carlo method [22, 54] or a mean-field theoretical treatment is invoked [22, 54, 101]. The advantage of this fluid model is efficiency. Solutions, either approximate analytic or by stochastic methods, can be obtained quickly compared to "off-lattice" or continuum molecular models. This is useful for mapping phase diagrams and important for investigating critical phenomena and finite-size effects for which very large systems are required. The critical behavior of the lattice model can then be related to a continuum model if they are of the same universality class, that is, the discretization of the fluid on the scale of σ, the particle size, is unimportant when considering long-range fluctuations near a critical point. They are also useful for quickly modeling the more complex confining geometries where the lack of symmetry in V_i^{ext} can make application of continuum approaches more difficult. On the other hand, the lattice discretization is significant when considering short-range phenomena such as packing in narrow pores because much of the short-range correlation information is absent. So it seems that lattice models are not well suited to accurate studies of adsorption in nanoscopic pores, particularly if a fluid mixture is present where the components have quite different sizes.

Because of this limitation, lattice models are generally not used to predict accurately gas adsorption and selectivity in nanoscopic amorphous materials (so we will keep our discussion of lattice models brief). Rather, most lattice model studies are focused on understanding the physics of adsorption phenomena. For example, lattice models have been employed to investigate wetting [102, 103], capillary condensation [104, 105], and adsorption in pores with energetic [31, 106, 107] and geometric nonuniformities [31] (e.g., striped pores [108], pore-end effects [109]) or with reduced symmetry [110].

2.2. Density Functional Theory

Classical density functional theory (DFT) is the most successful theory of nonuniform equilibrium fluids. Since its initial development for quantum systems [111–113] and extension to classical systems [114–116], it has been one of the most useful tools for understanding confined fluid behavior alongside molecular simulation. The central ideas and main developments are described in several books [10, 51, 117] and are repeated only briefly here.

The classical density functional formalism [114] is developed in the grand-canonical ensemble, although extensions to the canonical ensemble have been made recently [118, 119]. Our description here applies to a continuum model, but we note that DFT is equally valid

when applied to lattice models [108]. The grand potential, Ω, is expressed as a functional of the set of one-body densities, $\{\rho(\mathbf{r})\}$, where $\mathbf{r}$ represents all static degrees of freedom (positions, orientations, etc.) of a molecule. The global minimum of Ω with respect to variation of $\{\rho(\mathbf{r})\}$ at fixed chemical potential and temperature corresponds to the equilibrium Ω^0 and equilibrium set $\{\rho^0(\mathbf{r})\}$. So specification of $\Omega[\{\rho(\mathbf{r})\}]$ and a method for finding its global minima are central to any DFT study. The grand-potential functional is related to the intrinsic Helmholtz free-energy functional, F, via

$$\Omega[\{\rho(\mathbf{r})\}] = F[\{\rho(\mathbf{r})\}] + \sum_i \int d\mathbf{r}\rho_i(\mathbf{r})[V_i^{ext}(\mathbf{r}) - \mu_i] \tag{25}$$

where V_i^{ext} is an external one-body potential, μ_i is the chemical potential, and i labels the component of the mixture. In many adsorption studies, the adsorbent is regarded as completely inert, exerting its influence through V_i^{ext}. So DFT is well suited to materials that do not swell appreciably.

The problem now is to specify $F[\{\rho(\mathbf{r})\}]$. The ideal gas contribution, F^{id}, is known for rigid particles leaving only the excess contribution to be specified. For flexible molecules, however, F^{id} is generally unknown and quite complicated, although suitable approximations can be found for some systems [120–122]. So we will consider only rigid particles here. The great advantage that theories have over molecular simulations is the ease with which solutions for the adsorption can be found. In some very simple cases, analytic solutions to DFTs are possible [10]. But for accurate work, solutions must be obtained by numerical integration and iteration. The speed with which numerical solutions are found depends crucially on the degree of symmetry in the underlying Hamiltonian. Wherever there is symmetry, an associated integration can be performed analytically, or at least outside the iterative solution loop. Therefore, DFTs for spherical particles in idealized geometries, like slits, cylinders, and spherical pores, are much easier to solve than DFTs for nonspherical particles adsorbed on amorphous surfaces. Indeed, in the latter case molecular simulation may well be more efficient!

For spherical models of the gas molecules of interest to us, the short-range repulsive "core" is usually treated by a hard-sphere term, F_{HS}^{ex}, with the remainder treated by a perturbation, F_p. With the ideal gas contribution we have

$$F = F^{id} + F^{ex} = k_B T \sum_i \int d\mathbf{r}\rho_i(\mathbf{r})\{\ln[\Lambda_i^3\rho_i(\mathbf{r})] - 1\} + F_{HS}^{ex} + F_p \tag{26}$$

where Λ_i is the thermal de Broglie wavelength, usually an irrelevant constant in DFT. Unfortunately, F^{ex} is not known exactly for any nontrivial 3D system so approximations are needed.

The development of approximate hard-sphere functionals could fill a chapter of its own. Less attention has been paid to treatment of the perturbation contribution [123, 124]. Indeed, in every application of DFT to materials characterization known to us, the same perturbation term is used

$$F_p = \frac{1}{2}\sum_{ij} \iint d\mathbf{r}_1 d\mathbf{r}_2 \rho_i(\mathbf{r}_1)\rho_j(\mathbf{r}_2)\phi_{ij}^p(r_{12}) \tag{27}$$

where $\phi_{ij}^p(r)$ is the perturbation potential and $r_{12} = |\mathbf{r}_1 - \mathbf{r}_2|$. If a Lennard-Jones potential is used, then according to the WCA [125] convention

$$\phi_{ij}^p(r) = \begin{cases} 4\varepsilon_{ij}(x^{-12} - x^{-6}); & x > 2^{1/6} \\ -\varepsilon_{ij}; & x \le 2^{1/6} \end{cases} \tag{28}$$

where $x = r/\sigma_{ij}$, and σ and ε are the Lennard-Jones length and energy parameters, respectively. Usually, a cutoff in the range of $\phi_{ij}^p(r)$ is used to avoid lengthy numerical integrations. This type of mean-field perturbation is very common throughout the DFT literature because of its simplicity, but it is not that accurate [123], particularly at low temperatures [124].

The development of DFT methods in materials characterization has closely followed the development of hard-sphere functionals. The first such study [39] employed a pure fluid local density approximation for this contribution

$$F_{HS}^{ex} = \int d\mathbf{r} f_{HS}^{ex}[\rho(\mathbf{r}); d] \tag{29}$$

where f_{HS}^{ex} is the excess (relative to the ideal gas) free-energy density of a uniform hard-sphere fluid with hard-sphere diameter d, for example the Carnahan-Starling [126] equation of state. But this functional cannot describe the packing of particles in very narrow pores and so is not a good choice for accurate studies of nanoporous materials. Consequently, despite its simplicity, it is rarely used [127].

Much greater accuracy can be achieved, at greater numerical expense, with a weighted density approximation (WDA) or "non-local" DFT. The "smoothed density approximation" (SDA2) of Tarazona [128] is one such approach and is known [66, 129, 130] to be quite accurate for adsorption studies. Most DFT characterization studies have used this functional [26, 36, 38, 86–89, 131] and, we believe, it is incorporated in the "DFT+" materials characterization software [37, 40, 41, 132–134]. It ascribes the excess free-energy per particle, ψ^{ex}, at a point in the fluid nonlocal character

$$F_{HS}^{ex} = \int d\mathbf{r}\rho(\mathbf{r})\psi_{HS}^{ex}[\bar{\rho}(\mathbf{r}); d] \tag{30}$$

where

$$\bar{\rho}(\mathbf{r}_1) = \int d\mathbf{r}_2 \rho(\mathbf{r}_2) w[r_{12}; \bar{\rho}(\mathbf{r}_1)] \tag{31}$$

and

$$w(r; \rho) = w_0(r) + \rho w_1(r) + \rho^2 w_2(r) \tag{32}$$

The density-independent weight functions, w_0, w_2, and w_2, are chosen to reproduce accurately thermodynamic and structural properties of the uniform fluid, including the Carnahan-Starling equation of state, and have a range equal to d.

Recently, the fundamental measure functional (FMF), developed originally by Rosenfeld [135, 136] and by Kierlik and Rosinberg [137], has been employed [129] in characterization studies. It also employs three linearly independent and density-independent weight functions

$$\begin{aligned} w_i^{(3)}(r) &= \Theta(R_i - r) \\ w_i^{(2)}(r) &= \delta(R_i - r) \\ \mathbf{w}_i^{(2v)}(\mathbf{r}) &= \delta(R_i - r)\frac{\mathbf{r}}{r} \end{aligned} \tag{33}$$

where $\Theta(r)$ and $\delta(r)$ are the Heaviside step- and Dirac delta-functions, respectively. But now the weight functions have a range $R_i = d_i/2$, making this theory twice as fast to solve as the SDA2 (the same number of integrations are required). Note that it is also formulated naturally for mixtures, whereas the SDA2 requires modification [138, 139] for this purpose. The functional is written

$$F_{HS}^{ex} = k_B T \int d\mathbf{r}\Phi(\{n_\alpha(\mathbf{r}), \mathbf{n}_\alpha(\mathbf{r})\}) \tag{34}$$

where

$$\Phi = -n_0 \ln(1 - n_3) + \frac{n_1 n_2 - \mathbf{n}_{v1} \cdot \mathbf{n}_{v2}}{1 - n_3} + \frac{n_2^3 - 3n_2 \mathbf{n}_{2v} \cdot \mathbf{n}_{2v}}{24\pi(1 - n_3)^2} \tag{35}$$

and the weighted densities are

$$n_\alpha(\mathbf{r}_1) = \sum_i \int d\mathbf{r}_2 \rho_i(\mathbf{r}_2) w_i^{(\alpha)}(r_{12}); \quad \mathbf{n}_{\alpha v}(\mathbf{r}_1) = \sum_i \int d\mathbf{r}_2 \rho_i(\mathbf{r}_2) \mathbf{w}_i^{(\alpha v)}(r_{12}) \tag{36}$$

The three other linearly dependent weight functions are

$$w_i^{(1)}(r) = \frac{w_i^{(2)}(r)}{4\pi R_i}$$
$$\mathbf{w}_i^{(1v)}(\mathbf{r}) = \frac{\mathbf{w}_i^{(2v)}(\mathbf{r})}{4\pi R_i} \tag{37}$$
$$w_i^{(0)}(r) = \frac{w_i^{(1)}(r)}{R_i}$$

Also note the intriguing vectorial weight functions $\mathbf{w}^{(1v)}$ and $\mathbf{w}^{(2v)}$ that generate vectorial weighted densities $\mathbf{n}_{1v}$ and $\mathbf{n}_{2v}$, respectively. These vectorial functions are required to allow deconvolution of hard-sphere Mayer bond [135, 140]. Equation (35) corresponds to the original FMF; other prescriptions for Φ have been proposed recently [141, 142] that are more accurate, particularly for DFT studies of solids. However, none of these advanced prescriptions has yet to be employed in materials characterization studies.

Putting (25) and (26) together with the minimal Ω principle gives the Euler-Lagrange equation for the densities

$$\rho_i^0(\mathbf{r}) = \rho_{bi} \exp\left(-\beta\left(V_i^{ext}(\mathbf{r}) - \mu_i^{ex} + \left(\frac{\delta F^{ex}}{\delta \rho_i(\mathbf{r})}\right)_{\{\rho^0(\mathbf{r})\}}\right)\right) \tag{38}$$

where the excess chemical potential $\mu_i^{ex} = \mu_i - k_B T \ln(\Lambda_i^3 \rho_{bi})$, $\beta = 1/k_B T$, and ρ_{bi} is the bulk density corresponding to μ_i. Because the last term on the right-hand side depends on $\{\rho^0(\mathbf{r})\}$, which is also the solution on the left-hand side, the EL equations can be solved by simple (Picard) iteration. Alternatively, if a gradient (Newton) method [143] is used, then many fewer iterations might be required to reach a desired level of accuracy, but at greater numerical expense for each iteration.

The accuracy of a DFT approximation can be assessed in a variety of ways. One choice is to analyze the hierarchy of uniform fluid direct correlation functions,

$$c_{ij\ldots}^{(n)}(\rho_u) = -\beta\left(\frac{\delta^n F^{ex}}{\delta\rho(\mathbf{r}_1)\ldots\delta\rho(\mathbf{r}_n)}\right)_{\rho_u} \tag{39}$$

where ρ_u is a uniform density. The complete hierarchy of these functions expresses all the information content of the DFT because they are the coefficients of a functional Taylor series expansion in density of F^{ex}. They can be compared with the corresponding functions generated from computer simulations of the same system. Usually for spherical particles it is sufficient to compare the second-order coefficient, the pair-direct correlation function $c_{ij}^{(2)}(r)$, for a range of uniform densities. This function contains significant information regarding fluid structure because it is related to the uniform total pair-correlation function, $h_{ij}(r)$, [and hence the pair-distribution function $g_{ij}(r) = h_{ij}(r) + 1$] via the uniform fluid Ornstein-Zernike relation.

$$h_{ij}(r_{12}) = c_{ij}^{(2)}(r_{12}) + \sum_k \int d\mathbf{r}_3\, \rho_k c_{ik}^{(2)}(r_{13}) h_{kj}(r_{32}) \tag{40}$$

which is a direct consequence of the Legendre transform (25). Also, spatial integration of $c_{ij}^{(2)}(r)$ using the hierarchy of sum-rules [10] generates the equation of state of the uniform fluid, that is,

$$\mu_i^{ex}(\{\rho\}) = -k_B T \sum_j \int_0^1 d\alpha \rho_j \int d\mathbf{r}\, c_{ij}^{(2)}(r; \{\alpha\rho\}) \tag{41}$$

Alternatively, one can analyze the performance of the functional in extreme limits, such as the 2D limit that corresponds to confinement to a flat surface. Whatever density functional is employed, it is especially important for adsorption studies that the theory is consistent with

respect to the Gibbs adsorption equation [11], that is, it should satisfy (12) at constant temperature and volume. Any theory that does not satisfy this relation will become less accurate as adsorption increases [11]. All of the above DFTs will satisfy the Gibbs adsorption equation provided the choice of hard-sphere diameter is independent of chemical potential [11].

It is well-known that the LDA functional cannot reproduce packing effects because there is no particle size-dependent information in $c_{ij}^{(2)}(r)$. The SDA2 and FMF functionals, on the other hand, generate quite accurate $c_{ij}^{(2)}(r)$ up to high bulk densities. In fact, the FMF reproduces the Percus-Yevick [117] $c_{ij}^{(2)}(r)$ exactly for a hard-sphere mixture [144]. The FMF for hard spheres also possesses desirable dimensional crossover properties in that it is quite accurate for hard disks in 2D and exact for hard rods in 1D.

Due to the accuracy of both the SDA2 and FMF functional for hard spheres, the limiting factor in accuracy of this DFT approach is generally the mean-field perturbation term for attractive interactions (27) and the spherical model of gas molecules. Methods have been devised that avoid these limitations [120, 123, 124, 145], but none of them have been used in characterization studies.

In the above theories, the Lennard-Jones parameters, σ and ε, and the hard-sphere diameter, d, can be chosen independently. Several theoretical methods have been suggested for fixing d, given σ and ε, such as the Barker-Henderson [117, 146] (BH), Weeks-Chandler-Anderson [117, 125] (WCA), Lado [147], and Rosenfeld [148] prescriptions. However, given the inherent inaccuracies in the above approximations, particularly the mean-field perturbation term (27), it is more appropriate to fit the free parameters to reference data (i.e., experiment or molecular simulation data). Lu et al. [149] choose to fit d so that theory agrees with Monte Carlo simulation for the coexisting bulk densities of a Lennard-Jones fluid, whereas Walton and Quirke [150] fit d along an isotherm. But this still leaves σ and ε to be decided if comparison is to be made with experiment. Early studies [39] of nitrogen adsorption at 77 K with the LDA functional chose $\sigma = d$ and ε to reproduce the bulk liquid density and pressure at 1 bar. Later, Ravikovitch et al. [129] compared several methods and concluded that fitting $\sigma = d$ and ε to experimental data for bulk liquid–gas coexisting pressures and densities for a range of temperatures was the most convenient and accurate approach.

For mixtures of Lennard-Jones fluids, the cross-interaction parameters are required. By far, the most popular method employs the Lorentz-Berthelot (LB) combining rules

$$\sigma_{ij} = \frac{(\sigma_{ii} + \sigma_{jj})}{2}; \quad \varepsilon_{ij} = \sqrt{\varepsilon_{ii}\varepsilon_{jj}} \tag{42}$$

This can be useful for gas–gas interactions dominated by dispersion forces, for example those between methane and nitrogen. But for less symmetric molecular interactions, such as between methane and water, it is likely that cross-interactions will need to be fitted to mixture data, such as the solubility.

2.3. Monte Carlo Simulation

The equilibrium statistical mechanics of a Hamiltonian can be solved, to within statistical error, with Monte Carlo and molecular dynamics simulations. Not surprisingly, these methods, and Monte Carlo simulation in particular, are popular for characterization and adsorption studies. Due to the popularity of books [12–14] in this field and detailed articles [90, 151] we will not dwell on the theory here.

Whereas with DFT the grand-canonical ensemble is the most convenient choice, with Monte Carlo simulation in particular the choice of ensemble is completely open. As described earlier, the grand-canonical ensemble is best suited to rigid, inert adsorbents, whereas the osmotic ensemble [92] is suited to swelling materials like polymers and clays.

A molecular Monte Carlo simulation is an attempt to sample the relevant microstates of an ensemble in accordance with the laws of equilibrium statistical mechanics [152], that is, the Boltzmann equation

$$p_i = Q^{-1} \exp(E_i); \quad Q = \sum_i \exp(E_i) \tag{43}$$

where p_i is the probability of occurrence of microstate i, E_i is its energy, and the sum is over all relevant microstates. Properties of interest, or ensemble averages, are then

$$\langle A \rangle = \sum_i p_i A_i \tag{44}$$

where angle brackets denote an ensemble average and A_i is the value for microstate i. Usually, many millions of states are sampled by starting the system from a particular configuration (described by the system volume and specification of each static degree of freedom for each initial molecule) and performing a sequence of small moves (a Markov chain). In a grand-canonical ensemble Monte Carlo (GCMC) simulation, three types of move are attempted at random. Attempts are made to randomly displace, create, or destroy particles resulting in equilibration of temperature and chemical potential. Usually, moves are designed to satisfy microscopic reversibility, so creation and destruction attempts are attempted with equal probability. The decision to accept or refuse the attempted move is formulated to ensure that the system explores all relevant states in line with the Boltzmann equation (43); this is Boltzmann sampling. An osmotic ensemble Monte Carlo simulation consists of a mixture in which the number of particles of at least one of the components is held fixed. Random creation and destruction attempts are made for the other components to equilibrate their chemical potentials, and random system volume changes and particle displacements are also made to equilibrate pressure and temperature.

With today's computing power, simulations of several hundred to several thousand particles are typical. Molecules are often modeled with multisite combinations of Lennard-Jones potentials and partial charges. To enable such a relatively small system to mimic a macroscopic system requires the use of periodic boundary conditions. Provided the system is sufficiently large, these periodic boundaries will not significantly affect results. A system is considered sufficiently large when distant particles become uncorrelated. For example, the pair-distribution function, which is a measure of density correlations, should effectively decay to unity at a range that is less than the simulation box length. This means that the size of the simulated system will depend on the range of interactions and the thermodynamic proximity of the system to critical points. For "long-range" interactions, such as those between Coulombic charges, a compromise on system size is usually needed.

The use of periodic boundaries requires a strategy for treating interactions whose range is longer than the simulation box length to avoid particles interacting with their periodic images. For "short-range" interactions, such as the Lennard-Jones interaction and quadrupole–quadrupole interactions, suitable approximations that ignore correlations beyond a range longer than the box length can be implemented. Alternatively, these interactions can be truncated at a cutoff distance, r_c, less than the box length. A general method for smoothing the resulting potential to facilitate calculation of quantities derived from the gradient of the pair-potential, such as pressure, involves applying a ramp for molecule–molecule separations slightly less than r_c. For example, the intermolecular potential between two rigid molecules whose centers are separated by a distance r_{ij} and with relative molecular orientation φ can be written

$$\phi_{ij}(r_{ij}, \varphi) = \begin{cases} \sum_{ab} \phi_{ab}(r_{ab}); & r_{ij} < r_r \\ \dfrac{r_c - r_{ij}}{r_c - r_r} \sum_{ab} \phi_{ab}(r_{ab}); & r_r \le r_{ij} \le r_c \\ 0; & r_{ij} > r_c \end{cases} \tag{45}$$

where ϕ is a pair potential, i and j are molecular indices, the "ab" sum is over all pairs of sites (a sites are on molecule i and b sites are on molecule j), ϕ_{ab} is the "uncut" spherical pair-potential between sites a and b, r_{ab} is the distance between sites a and b, and $r_r < r_c$ is the ramp separation. The bulk pressure calculated via the virial route [13] is now

$$P = k_B T \left\langle \frac{N}{V} \right\rangle - \left\langle \frac{1}{3V} \sum_{i<j} r_{ij} \frac{\partial \phi_{ij}}{\partial r_{ij}} \right\rangle \tag{46}$$

where N is the total number of molecules present, V is the simulation box volume, and

$$r_{ij}\frac{\partial \phi_{ij}}{\partial r_{ij}} = \begin{cases} \sum_{ab} \dfrac{\partial \phi_{ab}}{\partial r_{ab}} \dfrac{\mathbf{r}_{ab}\cdot\mathbf{r}_{ij}}{r_{ab}}; & r_{ij} \le r_t \\ \sum_{ab} \dfrac{\partial \phi_{ab}}{\partial r_{ab}} \dfrac{\mathbf{r}_{ab}\cdot\mathbf{r}_{ij}}{r_{ab}} \left(\dfrac{r_c - r_{ij}}{r_c - r_t}\right) - \dfrac{r_{ij}\phi_{ab}}{r_c - r_t}; & r_t < r_{ij} < r_c \\ 0; & r_{ij} > r_c \end{cases} \tag{47}$$

For "long-range" interactions that do correlate at ranges beyond the box length, special techniques are needed to make progress. Many such techniques have been suggested for Coulombic interactions [153], including the Ewald method [13]. These methods are needed only to treat long-range Coulombic interactions, such as the dipole–dipole interaction or partial charge distributions that mimic these interactions. Several of these techniques have been tested recently by Seaton and coworkers [153] in the context of water adsorption in slit-pores using grand-canonical Monte Carlo simulation. They find that a method due to Heyes and van Swol [154] is the most efficient in their application and see no reason why this should not be a general result.

As the density of the system increases, it becomes increasingly unlikely that attempted creation or destruction moves will be accepted because the probability of formation of a cavity at equilibrium reduces with increasing density. Nitrogen adsorbed in narrow graphitic pores at 77 K and 1 bar, for example, is so dense that it might actually freeze. Not only does this manifest as an experimental difficulty associated with poor diffusion, but it also hinders simulations because the low probability of creation and destruction results in poor statistics even for very long simulations. Many approaches have been suggested in the literature to combat this difficulty, including cavity bias [155], excluded volume mapping [156], and staged insertion [157]. Staged insertion is an "extended ensemble" method whereby microstates that do not contribute to the ensemble are sampled to provide an alternative, "easier," path between microstates that do contribute to the ensemble. Of course, these extended states are not counted when calculating ensemble averages. The other methods look for suitable "holes" within which to attempt particle insertion. Any potential sampling bias is then corrected.

To reproduce experiment accurately, any molecular model must be calibrated. In gas adsorption experiments, we need adsorbate molecular models to be accurate both for gas-like and liquid-like densities. Often, molecular models are calibrated by requiring that bulk gas–liquid coexistence properties like density and pressure are accurately reproduced. Essentially, this means finding bulk gas and liquid states for a particular molecular model that have identical chemical potential and pressure. Before the invention of the Gibbs ensemble [158], this would typically have involved calculating the chemical potential and pressure along each phase branch separately [12, 159], a lengthy process particularly if the molecular model is to be optimized to reproduce experiment. However, the Gibbs ensemble [12, 158, 160–166] has revolutionized this process as it generates coexisting phases with a single simulation.

In its simplest guise, a Gibbs ensemble Monte Carlo (GEMC) simulation can be pictured as a canonical ensemble where phase separation of a system occurs without an interface. It answers the question, "What is the most likely, or equilibrium, partitioning of particles between two (separated) simulation boxes if their total number, the total volume and temperature are held constant?" Essentially, it locates the minimum of the total Helmholtz free-energy, or equivalently the minimum of the sum of the Helmhotz free-energies of each simulation box. We know that in a phase separated "one-box" canonical ensemble, the interface will move to equilibrate the chemical potential and pressure in each phase. In a GEMC simulation, equilibration is facilitated by "interbox" moves that allow particles and volume to transfer from one box to the other. As with any simulation, periodic boundaries are applied to each simulation box, and each box must be sufficiently large to render finite-size effects insignificant. The Gibbs ensemble can also be used to study confined fluids, either in equilibrium with a bulk phase [167, 168] or with another confined phase [169, 170]. The reader

is directed toward the many detailed accounts of the Gibbs ensemble for specifics regarding Monte Carlo moves and acceptance ratios.

Neimark and Vishnyakov have employed a restricted version of the Gibbs ensemble, called a "gauge-cell" [67, 171], to study hysteresis in first-order phase transitions of confined fluids. With this simulation method, the confined system, fluid in a slit pore, for example, is allowed to exchange particles, but not volume, with a fixed volume simulation of the bulk fluid, the gauge-cell. In this way, chemical potential and temperature, but not grand-potential density or pressure, are equilibrated. So, the aim of this method is simply to generate an ensemble with specified chemical potential and constrained density. The equilibrated chemical potential and density can be adjusted by adding or deleting particles in the gauge-cell. In this way, an entire isotherm including stable, metastable, and unstable sections can be simulated, thereby revealing the potential extent of hysteresis. Actually, this method is similar to another Gibbs method for simulating confined fluids [167] where the bulk phase pressure rather than the bulk phase volume is fixed except that this method is less stable with respect to density fluctuations along metastable portions of phase branches.

The liquid–gas phase diagram of a molecular model can be sketched quite efficiently by performing GEMC simulations for a sufficient number of temperatures, or by implementing a thermodynamic scaling method [172]. Alternatively, the thermodynamic integration route of Mehta and Kofke [173] can be employed to generate the coexistence curve given an initial point on the curve generated by GEMC. Whatever method is used, great care is required as T approaches the critical temperature, T_c, because the range of density correlations diverges at T_c. For this reason, usually no attempt is made to calibrate a molecular model near the critical region, although finite-size scaling methods [174, 175] do exist that would allow this.

Ensemble averages are calculated by analyzing the statistics generated by the simulation. First, one has to decide when the system has reached equilibrium. All configurations sampled before this point are discarded. If the remaining configurations are analyzed without knowledge of the underlying distribution of states, then a straightforward block-averaging scheme can be adopted [13]. Alternatively, a histogram that plots the order-parameter of interest (density, for example) against probability of occurrence can be analyzed [12]. Generally, this will reveal a single Gaussian-like peak from which the statistics can be measured. If there is more than one statistically significant peak, it means that the simulation has sampled more than one phase and configurations corresponding to the unwanted phase should be discarded. The equilibrium phase is that with the highest peak (i.e., is most likely), while the other peak corresponds to a metastable state. For a first-order phase transition, the difference in the height of these peaks and the depth of the trough between them (or the free-energy barrier) will increase nearly linearly with system-size.

3. ADSORBENT MODELS

Scalar surface models are those that describe the surface in terms of only a few separate measures, the surface area and gas–surface interaction energy, for example. Vector models provide more detail in that one or more of these measures are described by a distribution. The obvious example here is a surface described by a distribution of pore widths. 3D surface models are arbitrarily complex.

3.1. Scalar Models

Much of the early work in adsorption employed empirical adsorption equations. Standard texts [1–8] on adsorption provide good accounts of their development. Over the years, some of these isotherm equations have been given a proper statistical mechanical grounding, for example the Langmuir isotherm [1, 176], and many have been extended and adapted to a wide range of systems. They are simply too numerous to list completely, but notable equations that can be found in the above-mentioned books include those of Henry, Langmuir, Hill-de Boer, Brunauer-Emmett-Teller (BET), Brunauer-DDT, Anderson-Brunauer, Hill, Frenkel-Halsey-Hill, Dubinin-Radushkevitch, Dubinin-Astakhov, Dubinin-Stoeckli, Dubinin-Izotova,

Freundlich, Toth, Horvath-Kawazoe, and so on. More recently we have had equations from Keller [177, 178], a patchwise supersite isotherm [179], the approach of Ustinov and Do [34], a modified BET-Kelvin isotherm [35], various 2D equations of state [180, 181], an improved Horvath-Kawazoe isotherm [182], extended or multisite or multilayer or improved Langmuir isotherms [183–185], the multispace adsorption model (MSAM) [186], vacancy solution theory [187] (VST), a neural network approach [188], a modified Toth equation [189], a "generalized adsorption isotherm" [190], other virial approaches [191–193], and so on and so forth.

Some of these isotherms are used to model adsorption in amorphous materials, and some of them are used to describe adsorption in idealized pores or on sites with a particular energy and are then convoluted with a predefined distribution of sites or energies described by a few parameters. Some of them are described as generalized, while others are limited to describing only supercritical adsorption, or only subcritical adsorption, or have some other limitation. Some of them have been compared with each other for a few adsorbents, but given their number it is impractical to expect a thorough comparative analysis. Faced with this plethora of options and limitations, the novice, or even the experienced, engineer might be daunted and confused as to which approach to choose. What is more, the sheer number of these isotherms surely hints at an underlying flaw, for if any of them were generally accurate there would be no need to invent so many options. One might also wonder why it is that given the existence of theories for adsorption that are, in principle, exact, such as density functional theory, that any research continues with these approaches. Clearly, their popularity is related to their simplicity rather than their accuracy or applicability. Generally, more accurate approaches involve description of a material in terms of a vector or 3D model and adsorption theories based on fundamental statistical mechanical approaches such as density functional theory or Monte Carlo simulation.

3.2. Vector Models

3.2.1. Quenched-Annealed Model

Some materials have been modeled using the quenched-annealed (QA) model [194–196]. The quenched-annealed system consists of a mixture of quenched (immobile, solid adsorbent) particles and annealed (mobile, fluid adsorbate) particles. Local properties of the fluid system are determined for a given configuration of quenched particles, but global properties are obtained by averaging over all possible quenched configurations with the appropriate weight. The power of liquid-state physics techniques can be brought to bare on this QA system if the "replica" trick [197] is employed. This consists of considering another, different "replica" system that can have the same statistics as the QA system. In the replica system, the solid adsorbent particles are now mobile and there are s noninteracting copies of the fluid system (of course, each replicated fluid system still interacts with the solid adsorbate particles).

At the heart of the replica trick is the mathematical identity

$$\ln \Xi = \lim_{s \to 0} \frac{(\Xi^s - 1)}{s} \tag{48}$$

This allows the globally averaged properties of the QA system to be described in terms of corresponding properties of the replica system in the limit $s \to 0$. This trick was formulated originally for the spin-glass system [198] but has been adapted to amorphous (or disordered) adsorbents and other systems [197] where some disorder is quenched such as with random sequential adsorption.

The replica trick is commonly employed [25] in the context of integral equation theory for bulk fluids. More recently [196], it has been implemented in a fundamental measure density functional theory. An integral equation theory consists of two parts, a set of Ornstein-Zernike (OZ) relations for a fluid mixture and a set of closure relations that provide sufficient constraint. For a uniform fluid of spherical particles, the appropriate OZ relations are given in (40). The original replica OZ equations of Madden and Glandt [195, 199] were

corrected by Given and Stell [194] to give

$$\begin{aligned} h_{qq} &= c_{qq} + \rho_q c_{qq} \otimes h_{qq} \\ h_{aq} &= c_{aq} + \rho_q c_{aq} \otimes h_{qq} + \rho_a c_c \otimes h_{aq} = h_{qa} \\ h_{aa} &= c_{aa} + \rho_q c_{aq} \otimes h_{qa} + \rho_a c_c \otimes h_{aa} + \rho_a c_b \otimes h_c \\ h_c &= c_c + \rho_a c_c \otimes h_c = h_{aa} - h_b \\ c_c &= c_{aa} - c_b \end{aligned} \tag{49}$$

where h and c are the total and pair-direct correlation function, respectively, which are functions of the radial distance, subscripts q and a indicate quenched and annealed particles, respectively, and $\otimes$ denotes a real-space convolution. Closure relations can be obtained from density functional arguments but are generally approximations based on the Euler-Lagrange equation (38). For example, the popular Percus-Yevick [117] closure can be used

$$c_{ij}(r) = \{1 - \exp[\beta\phi_{ij}(r)]\}[h_{ij}(r) + 1] \tag{50}$$

where ϕ_{ij} is the pair potential between components i and j. This coupled set of equations can be solved using fast Fourier transform methods [200] provided the set h_{qq} (or c_{qq}) and the volume-averaged densities, ρ_i, are provided as input and an approximation for c_b (such as $c_b(r) = 0$, the Madden-Glandt approximation [194, 195]) is specified. Finally, the volume-averaged densities must be related to bulk fluid properties if adsorption isotherms [201] are to be generated (to be clear, the density ρ_a, corresponding to the average density of annealed (adsorbed) particles will generally be different to the bulk (reservoir) density).

Studies with these replica OZ equations are generally limited to fundamental studies of phase behavior for a range of adsorbates in gels and, as far as we are aware, they have not been used to accurately predict adsorption in real materials. One can speculate that they might be employed in this context by fitting ϕ_{qq} (or h_{qq}) to experimental data (e.g., an isotherm of a probe adsorbate). In one study [201], Vega et al. provided realistic pair-potentials for methane in a silica xerogel as input and derived two routes to calculate bulk fluid properties. They found good agreement with computer simulation at a supercritical temperature for methane adsorption. It seems plausible that the inverse problem, that is, generating ϕ_{qq} (h_{qq}) as output, can be attempted. This could then be used to generate adsorption isotherms for other adsorbates. However, as noted in the above study [201] and elsewhere [25], it is likely that the replica OZ method will be less suitable for systems significantly perturbed from bulk behavior (i.e., for subcritical fluids and denser, nanoporous xerogels). More recent work has shown that under these circumstances, metastable states significantly influence adsorption and hysteresis. So an integral equation approach based on a crude closure approximation will struggle to be accurate. Although the replica OZ approach has been useful for studying gels, it seems unlikely that it will be as useful for active carbons. For example, the graphene sheets thought to form active carbons are clearly not spherical particles. On the other hand, graphene sheets can be modeled as assemblies of spherical carbon atoms.

3.2.2. Polydisperse Independent Ideal Pore Models

By far the most popular modern model for characterizing porous adsorbents is the polydisperse independent ideal pore model. Quite simply, the adsorption in a number of independent ideal pores with a range of sizes is added together (or integrated over for a continuous distribution) to give the total amount adsorbed per gram of material at a particular pressure

$$N(P) = \int_0^\infty dH f(H) v(H, P) \tag{51}$$

Here, $f(H)$ is called a pore-size distribution (PSD), $v(H, P)$ is the "kernel" of "local" *excess* isotherms (for comparison with experiment), and the mass of material is measured in a vacuum. The kernel is pregenerated and the PSD is optimized to minimize the difference, usually measured in terms of the root-mean-square (rms) deviation, between an experimental isotherm and the isotherm calculated from (51).

The simplest geometries that generate a confined pore space are slits, cylinders, and spheres. We can take advantage of the planar symmetry of fluid adsorbed in an ideal slit pore to re-express the thermodynamics of adsorption. Quite simply, we can replace the work term ωdV in (9) with $\sigma dA + fdH$ to obtain

$$d\Omega = \sigma dA + fdH - SdT - \sum_i N_i d\mu_i \tag{52}$$

where now we can identify $\Omega = \sigma A$. Here, σ is the energy per unit area required to increase adiabatically the area of the slit pore system, A, at constant pore width, H, and f is the energy required to increase adiabatically the width of the slit pore system at constant A. In terms of the diagonal components of the pressure tensor, we can identify

$$\sigma = -\int_{\infty} dz P_{xx}(z) = -\int_{-\infty}^{\infty} dz P_{yy}(z) \tag{53}$$

and

$$f = -P_{zz}A = -A\sum_{ia}\int_{-\infty}^{\infty} dz \rho_{ia}(z)\frac{\partial V_{ia}^{w}(z)}{\partial z} \tag{54}$$

where V_{ia}^{w} is the interaction between a single wall and site a on adsorbate molecule i (either wall can be chosen because of reflection symmetry about $H/2$). Here, z is chosen to be the distance normal to the plane of the slit pore and x and y indicate directions orthogonal to z. The solvation pressure, P_s, is the pressure normal to the slit required to stabilize the pore with width H and is equal to the difference between the internal and external pressures, $P_s = P_{zz} - P_b$.

In a slit pore, the external potential, $V_{ia}^{ext}(z)$, is the sum of contributions from each wall,

$$V_{ia}^{ext}(z) = V_{ia}^{w}(z) + V_{ia}^{w}(H - z) \tag{55}$$

To preserve transverse symmetry the gas–solid potential is usually constructed by "smearing" out individual gas–solid atom contributions. The well-known Steele potential [202] performs this integration for each layer of a graphitic surface to arrive at the rather accurate gas–solid interaction

$$V_{ia}^{w}(z) = 2\pi\rho_w\sigma_{iaw}^2\varepsilon_{iaw}\Delta_w\left[\frac{2}{5}\left(\frac{\sigma_{iaw}}{z}\right)^{10} - \left(\frac{\sigma_{iaw}}{z}\right)^{4} - \frac{\sigma_{iaw}^4}{3\Delta_w(0.61\Delta_w + z)^3}\right] \tag{56}$$

where ρ_w is the density of atoms in the wall, Δ_w is the interlayer spacing between graphitic sheets (usually taken to be 114 nm $^{-3}$ and 0.335 nm, respectively [5, 202]), and σ_{iaw} and ε_{iaw} are the gas–solid interaction length and strength parameters, respectively. These parameters can be determined by fitting to experiment, just as with the gas–gas parameters. But we leave discussion of this until later.

If we measure a continuous slit-PSD in terms of the internal surface area of slit pore per unit pore width per gram, then the total internal surface area and volume per gram of material are

$$A = \int_0^{\infty} dH f(H); \quad V = \frac{1}{2}\int_0^{\infty} dH H f(H) \tag{57}$$

But these quantities are absolute values, and we know that the surface area and volume of any porous material can only be measured with respect to a particular adsorbate (i.e., to the modeled form of V_{ia}^{w}). A simple method for obtaining adsorbate specific quantities is to define a "chemical" surface, or boundary, that describes the region of pore space to which the adsorbate has access. For example, Fig. 7 is a schematic diagram showing the difference between physical and chemical pore width

$$H_c = H_p - \delta H \tag{58}$$

The pore width, H, is then substituted by H_c in (51) and (57).

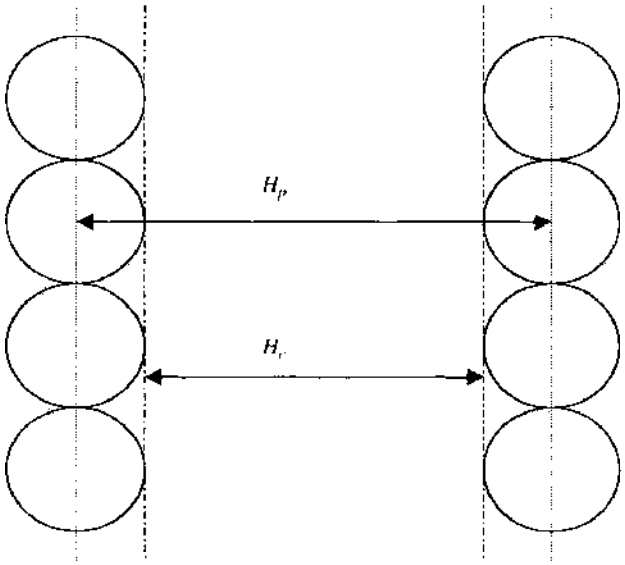

Figure 7. Schematic diagram showing the difference between physical and chemical widths in a slit pore.

Usually, this boundary is arbitrarily defined to reside at one-half the width (ie., σ) of a wall atom inside the pore. So for graphitic walls, δH is often taken to be 0.34 nm. Others [203] have defined this surface to coincide with the surface $V_i^{ext}(z) = 0$ for spherical particles. Another choice could be to define an effective "hard-wall" pore in a similar fashion to the BH and WCA prescriptions for the effective hard-sphere diameter of a spherical atom. In this case, the chemical width equivalent to the BH prescription for a single-site particle is

$$H_c = 2\int_0^{H/2} dz \exp\left[-\beta V_i^{rep}(z)\right] \tag{59}$$

where $V_i^{rep}(z)$ is the repulsive contribution to the external potential. Just as with WCA theory, this repulsive contribution could be defined as

$$V_i^{rep}(z) = \begin{cases} V_i^{ext}(z) - V_i^{\min}; & z < z_i^{\min} \\ 0; & z > z_i^{\min} \end{cases} \tag{60}$$

where $V_i^{\min}$ is the minimum value of V_i^{ext} that occurs at $z_i^{\min}$. With parameters corresponding to a model of methane in a graphitic slit ($\varepsilon_{ia}/k_B = 70.7$ K and $\sigma_{ia} = 0.357$ nm), this gives $\delta H = 0.328$ nm for methane in a very wide slit pore at 293 K. With this method, the chemical width is dependent on temperature, the adsorbate, and the pore width.

If the experimental pore volume is calibrated with helium, an effective chemical pore width for helium will be required, as discussed in Section 1.4. The excess adsorption is then calculated as

$$N(P) = \int_0^H dH f(H)\left[v^{ab}(H, P) - \frac{\rho_b(P)}{\rho_{He}} v_{He}^{ab}(H)\right] \tag{61}$$

where $v^{ab}(H, P)$ is the *absolute* local adsorption and ρ_{He} is the corresponding bulk density and $v_{He}^{ab}(H)$ is the absolute local adsorption for helium at the calibration temperature and pressure. However, most studies of this type avoid using a helium calibrated pore width and instead use an arbitrary chemical pore width, for example $H_p - 0.34$ nm, which leads to inconsistencies with experiment.

If the dependence of the local isotherms on pore width is not an analytic function, we must instead represent the adsorption integral as a sum. In turn, if our local isotherms are not analytic, then (51) becomes a matrix equation [204].

$$\mathbf{N}(P) = \mathbf{v}(H_c, P)\mathbf{dH}(H_c)\mathbf{f}(H_c) \tag{62}$$

where **dH** is diagonal. The next step is to define the range and number of pore widths. Davies et al. [204] carefully describe the issues that influence these choices, and we will base the following discussion on their work. They argue that the number of pore widths, which is equal to the length of the column vector f, should be set equal to the number of pressure data points, which is equal to the length of the column vector N, to ensure that the unique "feasible" solution, if it exists, is found (they define a feasible solution to be one for which each element of **f** is non-negative). This assumes that all the column vectors of v are linearly independent. But if a feasible solution does not exist, then the choice of the number of pore widths is less clear. They also recommend using a cutoff in the upper range of H_c to ensure the linear independence of the columns of v, as local isotherms tend to become increasingly similar for large H_c. Actually, this constraint is dependent on the upper range and resolution of pressure data because, for subcritical gases, the maximum pore width that can be resolved depends on experimental pressure resolution close to the bulk gas–liquid phase transition. They suggest these constraints because they suppose that the characterization process is of little use if more than one solution is obtained from (62). Of course, the usefulness of a characterization technique can only be defined with respect to a particular aim. If the aim is to make accurate adsorption predictions on the basis of a characterization, then it is not clear that uniqueness of PSDs is important. But if the PSD itself (i.e., f), is the focus of investigation (e.g., the aim might be to determine the effect an activation processes on a material), then uniqueness is important. They also recommend the use of regularization techniques to smooth **f** so that it is more physically appealing and less sensitive to small perturbations in experimental data. Regularization techniques are somewhat arbitrary. The smoother the resulting PSD as a result of regularization then, by definition, the less sensitive it will be to small perturbations in the data to be fitted, which means that the PSD will be less sensitive to experimental error. Choosing a regularization technique on the grounds of what is physically appealing could be quite misleading. Finally, on grounds of simplicity, they recommend using uniform intervals in H_c, which reduces **dH** to a scalar constant. This final constraint is questionable. In line with the requirement that local isotherms comprising the kernel should be linearly independent, it seems more sensible instead if the intervals in H_c are chosen to maximize this requirement, (i.e., to maximize the difference in the local isotherms). Typically, this means choosing an interval that increases with H_c, perhaps exponentially.

Active carbons are usually modeled with the polydisperse ideal slit-pore model. Although the precise nature of the pore surface must depend on the precursor and treatment, there is recent evidence from high-resolution electron microscopy [18, 20] (HREM) that the pore surface of nongraphitizing carbons is formed from curved fullerene-like fragments with 5, 6, and 7-membered rings. A random arrangement of these elements produces a rather tortuous pore-space. Whatever the nature of the surface, the polydisperse slit-pore model can be quite successful [28] for activated carbons and some simple near-supercritical gases.

Ideal cylindrical and spherical pores have also been used in polydisperse pore models. Ravikovitch et al. [129] model the interaction of a LJ particle with an ideal cylindrical surface with radius R_p with

$$V_{iw}^{cyl}(r) = \pi^2 \rho_w \varepsilon_{iw} \sigma_{iw}^2 \left\{ \begin{array}{l} \frac{63}{32}\left[\frac{R_p - r}{\sigma_{iw}}\left(1 + \frac{r}{R_p}\right)\right]^{-10} \times F\left[-\frac{9}{2}, -\frac{9}{2}; 1; \left(\frac{r}{R_p}\right)^2\right] \\ -3\left[\frac{R_p - r}{\sigma_{iw}}\left(1 + \frac{r}{R_p}\right)\right]^{-4} \times F\left[-\frac{3}{2}, -\frac{3}{2}; 1; \left(\frac{r}{R_p}\right)^2\right] \end{array} \right\} \tag{63}$$

where r is the radial coordinate measured from the cylinder's axis and $F(\alpha, \beta, \chi, \delta)$ is the hypergeometric function [200]. The "chemical" internal surface area and volume are now

$$A = \int_0^\infty dR_c f(R_c); \quad V = \frac{1}{2}\int_0^\infty dR_c R_c f(R_c) \tag{64}$$

where $R_c = R_p - \delta R$ is the chemical pore radius. This model was used to study adsorption in a regular mesoporous material (MCM-41 [129]) that consists of long parallel channels but could also be used to study amorphous materials in place of the usual slit-pore model.

Ravikovitch and Neimark [72] modeled the interaction of LJ particles with an ideal spherical surface of radius R_p using

$$V_{iw}^{ext}(r) = 2\pi\rho_w\varepsilon_{iw}\sigma_{iw}^2\left[\begin{array}{l}\frac{2}{5}\sum_{n=0}^{4}\left(\frac{\sigma_{iw}^{10}}{R_p^n r^{10-n}} + (-1)^n\frac{\sigma_{iw}^{10}}{R_p^n(r-2R_p)^{10-n}}\right)\\ \frac{2}{5}\sum_{n=0}^{3}\left(\frac{\sigma_{iw}^{4}}{R_p^n r^{4-n}} + (-1)^n\frac{\sigma_{iw}^{4}}{R_p^n(r-2R_p)^{4-n}}\right)\end{array}\right] \tag{65}$$

Now, the chemical surface area and volume are

$$A = \int_0^\infty dR_c f(R_c); \quad V = \frac{1}{3}\int_0^\infty dR_c R_c f(R_c) \tag{66}$$

This model was also used to study regular porous materials, this time containing cage-like pores.

The first DFT characterization method [39] employed a "local" DFT (29) to generate the local isotherms. But more recent DFT work [38] has used one of the "nonlocal" theories described in Section 2.2, that is, either the SDA2 or FMF for hard spheres [augmented by a simple mean-field term for attractive forces (27)]. These theories require each component of the adsorbate to be modeled as a spherical particle. To solve the Euler-Lagrange equation (38) for the density, these theories also require, at least, calculation of $\delta F^{ex}/\delta\rho_i(\mathbf{r})$ for each iteration of the solution method. Ultimately this requires many integrations of the form

$$I(\mathbf{r}_1) = \int d\mathbf{r}_2 f(\mathbf{r}_2) w(r_{12}) \tag{67}$$

where f has the symmetry of the confining geometry and w is a spherically symmetric weight function. For ideal slit-pores, we can make use of cylindrical symmetry to obtain

$$I(z_1) = 2\pi\int dz_2 f(z_2) W(z_2 - z_1) \tag{68}$$

where

$$W(z) = \begin{cases}\int_{z}^{\infty} dr_{12} r_{12} w(r_{12})\\ \mathbf{i}_z z\int_{|z|}^{\infty} dr_{12} w(r_{12})\end{cases} \tag{69}$$

for scalar and (FMT) vectorial weight functions where $\mathbf{i}_z$ is the unit vector normal to the plane of the pore walls. Because $W(z)$ can be calculated outside of any iteration loop, solution of a nonlocal spherical DFT in planar symmetry is essentially a 1D integration problem. With FMT, each $W(z)$ can be calculated analytically to give [135]

$$\begin{aligned} W_i^{(3)}(z) &= \frac{(R_i^2 - z^2)}{2}\\ W_i^{(2)}(z) &= R_i\\ W_i^{(2v)}(z) &= z\mathbf{i}_z \end{aligned} \tag{70}$$

for $|z| < R_i$, and 0 otherwise. A great deal of work has used either the SDA2 or FMT nonlocal DFTs to analyze adsorption in slit-pores ranging from fundamental studies of fluid behavior [10, 54, 205] to materials characterization studies [27, 38].

Solution of nonlocal DFTs in cylindrical geometries is more complicated, particularly for FMT. Generally, the characteristic integral can now be expressed in the cylindrical coordinates of the confining geometry (Fig. 8a)

$$I(r_1) = 4\int_0^\infty dr_2 r_2 f(r_2) W(r_1, r_2) \tag{71}$$

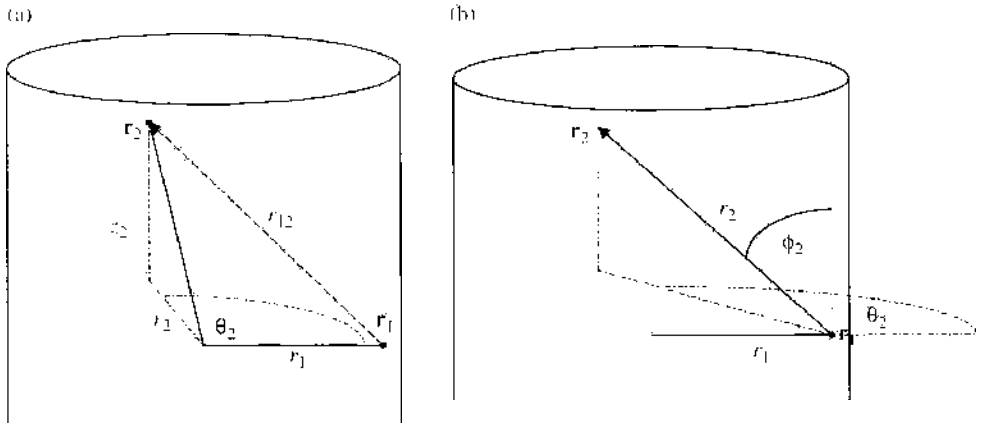

Figure 8. Schematic diagrams describing (a) cylindrical coordinates and (b) spherical coordinates in a cylindrical geometry.

where

$$W(r_1, r_2) = \int_0^{\pi} d\theta_2 \int_c^{\infty} dr_{12} \frac{r_{12} w(r_{12})}{\sqrt{r_{12}^2 - c^2}} \tag{72}$$

and

$$a = r_1^2 + r_2^2; \quad b = 2r_1 r_2; \quad c = \sqrt{a - b\cos\theta_2}; \quad r_{12}^2 = c^2 + z_2^2 \tag{73}$$

Once again, solution of a nonlocal DFT becomes a one-dimensional integration problem because, generally, $W(r_1, r_2)$ can be calculated outside of the solution integration loop. But to calculate $W(r_1, r_2)$, we first need to deal with the integrable singularity at $r_{12} = c$. This can be achieved with the substitution $t^2 = r_{12} - c$ to obtain

$$W(r_1, r_2) = 2\int_0^{\pi} d\theta_2 \int_0^{\infty} dt \frac{(t^2 + c) w(t^2 + c)}{\sqrt{t^2 + 2c}} \tag{74}$$

which is integrable for reasonably smooth weight functions, w. For example, for the FMT weight function $\alpha = 3$, we obtain

$$W_i^{(3)}(r_1, r_2) = \int_0^{\theta_i^{\max}} d\theta_2 \sqrt{R_i^2 - c^2}; \quad \theta_i^{\max} = \cos^{-1}\left(\max\left(-1, \frac{(a - R_i^2)}{b}\right)\right) \tag{75}$$

But the FMT weight functions with $\alpha = 2$ and $\alpha = 2v$ are not sufficiently smooth to allow calculation of $W(r_1, r_2)$ by numerical integration using (74) (these FMT weight functions involve spherical delta-functions). For these weight functions, we obtain from (74)

$$W_i^{(2)}(r_1, r_2) = R_i \int_0^{\theta_i^{\max}} d\theta_2 \frac{1}{\sqrt{R_i^2 - c^2}} \tag{76}$$

and

$$W_i^{(2v)}(r_1, r_2) = \left(r_2 \int_0^{\theta_i^{\max}} d\theta_2 \frac{\cos(\theta_2)}{\sqrt{R_i^2 - c^2}} - \frac{r_1 W_i^{(2)}(r_1, r_2)}{R_i} \right) \mathbf{i}_{r_1} \tag{77}$$

where $\mathbf{i}_{r_1}$ is the unit vector pointing in the direction of $\mathbf{r}_1$ from the center of the cylinder. But, once again, these integrals have singularities at $\theta_2 = \theta_i^{\max}$ for $r_1 > R_i$. This time they can be avoided by using the substitution $t^2 = \theta_i^{\max} - \theta_2$ to obtain

$$W_i^{(\alpha)}(r_1, r_2) = \begin{cases} 2R_i \displaystyle\int_0^{\sqrt{\theta_i^{\max}}} dt \frac{t}{\sqrt{R_i^2 - a + b\cos(\theta_i^{\max} - t^2)}}; & \alpha = 2 \\ \left(2r_2 \displaystyle\int_0^{\sqrt{\theta_i^{\max}}} dt \frac{t\cos(\theta_i^{\max} - t^2)}{\sqrt{R_i^2 - a + b\cos(\theta_i^{\max} - t^2)}} - \frac{r_1 W_i^{(2)}(r_1, r_2)}{R_i} \right) \mathbf{i}_{r_1}; & \alpha = 2v \end{cases} \tag{78}$$

For $r_1 > R_i$, these integrals become

$$W_i^{(\alpha)}(r_1, r_2) = \begin{cases} \dfrac{\pi R_i}{\sqrt{2b}}; & \alpha = 2 \\ \dfrac{\pi(r_2 - r_1)\mathbf{i}_{r_1}}{\sqrt{2b}}; & \alpha = 2v \end{cases} \tag{79}$$

in the limit $\theta_i^{\max} \to 0$. The singularities in (78) for $r_1 \le R_i$ can be avoided by reordering the characteristic integral, that is, by writing

$$I(r_1) = 4\int_0^{\pi} d\theta_2 \int_0^{\infty} dr_2 r_2 f(r_2) W'(r_1, r_2, \theta_2) \tag{80}$$

where

$$W'(r_1, r_2, \theta_2) = \int_{r_{12}}^{\infty} dr_{12} \frac{r_{12} w(r_{12})}{\sqrt{r_{12}^2 - c^2}} \tag{81}$$

But now the problem is two-dimensional and its solution is somewhat complicated with this route. So for $r_1 \le R_i$, we advise that the more efficient two-dimensional route devised by Figueroa-Gerstenmaier et al. [206] is followed. They use spherically symmetric coordinates (see Fig. 8b) to obtain the characteristic integral

$$I(r_1) = \int_0^{2\pi} d\theta_2 \int_0^{\pi} d\phi_2 \int_0^{\infty} dr_2 r_2^2 \sin\phi_2 f(x) w(r_2) \tag{82}$$

where

$$x^2 = r_1^2 + r_2^2 \sin^2\phi_2 + 2r_1 r_2 \sin\phi_2 \cos\theta_2 \tag{83}$$

For the FMT weight functions with $\alpha = 2$ and $\alpha = 2v$, this characteristic integral becomes

$$I_i^{(\alpha)}(r_1) = 4R_i^2 \int_0^{\pi} d\theta_2 \int_0^{\pi/2} d\phi_2 \sin\phi_2 \begin{cases} f(x'); & \alpha = 2 \\ \sin\phi_2 \cos\theta_2 f(x')\mathbf{i}_{r_1}; & \alpha = 2v \end{cases} \tag{84}$$

where

$$x'^2 = r_1^2 + R_i^2 \sin^2\phi_2 + 2r_1 R_i \sin\phi_2 \cos\theta_2 \tag{85}$$

These 2D integrals are devoid of singularities.

So, to recap, for cylindrical geometries the most efficient method for calculating the characteristic integral is to use (71) with (74) for smooth weight functions, which gives (75) for the $\alpha = 3$ weight function in the FMF. The numerical integration remaining inside the iterative solution loop is then one-dimensional. Similarly, the most efficient method for the $\alpha = 2$ and $\alpha = 2v$ weight functions in the FMF is to use (78) for $r_1 > R_i$, which becomes (79) in the limit $\theta_i^{\max} \to 0$. But for $r_1 \le R_i$ we recommend using the 2D integrals (84) with (85) for these weight functions.

The most straightforward method for solving the characteristic integral for spherical geometries is by 3D fast Fourier transforms (FFTs) [200]. The convolution theorem yields

$$I(r_1) = IFT[f(k)w(k)] \tag{86}$$

where IFT denotes the inverse 3D Fourier transform operation and k indicates the 3D Fourier transformed quantity. For the linearly independent FMT weight functions, we have

$$\begin{aligned} w_i^{(3)}(k) &= \frac{4\pi}{3k^3}[\sin(kR_i) - kR_i\cos(kR_i)] \\ w_i^{(2)}(k) &= \frac{4\pi R_i}{k}\sin(kR_i) \\ w_i^{(2v)}(\mathbf{k}) &= -i\mathbf{k}w_i^{(3)}(k) \end{aligned} \tag{87}$$

Lastoskie et al. [38] used the SDA2 functional to model the adsorption of nitrogen at 77 K in graphitic slit-pores and calculated PSDs for three microporous carbons, including AX21. They found that the nonlocal theory could generate a much better fit to experimental isotherms than the local DFT. By calibrating their molecular models to adsorption on a low surface area carbon (Vulcan), they obtained PSDs for each of the high surface area carbons. However, they did not remark on the similarity of the nitrogen isotherms on Vulcan and AX21, which indicates the possibility of poor diffusion in AX21. The SDA2 version of DFT has been used in various studies of porous carbons [40, 41, 133]. Kowalczyk et al. [40] and Puziy et al. [41] have both compared predictions of the DFT+ software with the characterization method of Do and coworkers [35, 85]. Kowalczyk et al. find that the DFT+ software fits experimental isotherms better than the method of Do and colleagues. Both groups claim that there is good agreement between the two methods for prediction of PSDs, but we are inclined to disagree for adsorption in nanopores. Dombrowski et al. [36] and Scaife et al. [86] have both performed studies concerning characterization of activated carbons with the SDA2 DFT used to model the adsorption of both nitrogen and argon at 77 K in graphitic slit-pores. The aim of this work is to assess the agreement between PSDs predicted by different adsorbates. But each of these studies could well be flawed because of the low temperature used. Indeed, at 77 K argon is 7 K *below* its triple point, so one should not expect it to be a useful probe of pore structure at this temperature. Unsurprisingly, these studies make rather different conclusions regarding the consistency of PSDs generated by different adsorbate probes. Dombrowski et al. conclude that there is good agreement (although this is not obvious from their results), whereas Scaife et al. conclude the opposite.

Ravikovitch et al. [27] used the SDA2 DFT and model graphitic slit-pores (56) to analyze the adsorption of nitrogen and argon at 77 K (each up to their respective saturation pressures) and carbon dioxide at 273 K (up to 1 bar) on several activated carbons. They calibrate all gas–surface interactions to adsorption on low surface area carbons and find quite good agreement for PSDs generated by the different adsorbate probes on each high surface area material (see Fig. 9, for one example). Indeed, the apparent level of agreement is remarkable considering their calibration method, the range of temperatures and adsorbates employed, and that argon is 7 K below its triple point. Unfortunately, they do not make predictions for gas adsorption using these PSDs, so it is not clear how accurate their method actually is. Ravikovitch and colleagues have also performed several other studies with the SDA2 DFT in cylindrical [207] and spherical [72] pores to investigate adsorption and hysteresis in regular mesoporous materials. Olivier and coworkers [208, 209] have used a similar method to analyze the pore structure in clays and related materials.

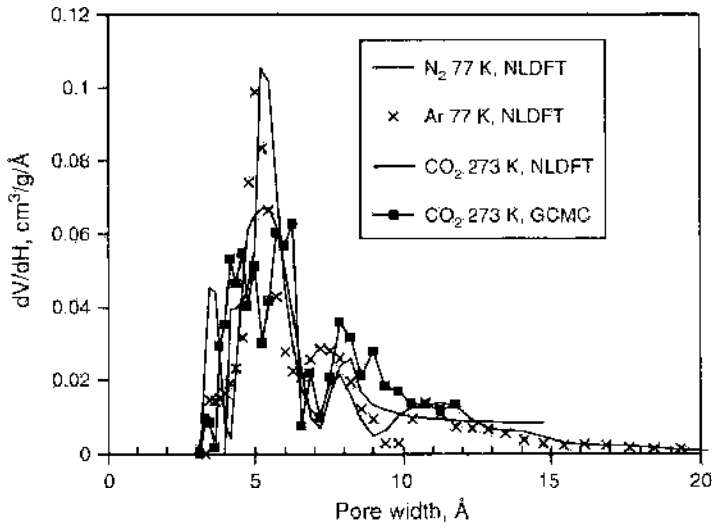

Figure 9. Pore-size distribution of CFCMS carbon fiber calculated from nitrogen, argon, and subatmospheric carbon dioxide adsorption isotherms using nonlocal DFT and grand-canonical MC simulations to generate the kernel. Reprinted with permission from [27], Ravikovitch, et al., *Langmuir* 16, 2311 (2000). © 2000, American Chemical Society.

Although FMT has become the method of choice for fundamental DFT studies in confining geometries [205, 210], it has yet to be employed to characterize real nanoporous materials. For those unfamiliar with this theory, it might appear more complex than the SDA2 theory, but in fact it is often more efficient for calculation of the kernel. Indeed, the FMF should be preferred to the SDA2 DFT in very narrow cylinders because it is exact in the 1D limit. However, given the crude nature of the approximation for weak attractive forces (27), there might not actually be much to gain by adopting the FMT functional. Goulding et al. [211] were the first (as far as we are aware) to employ FMT in cylindrical geometries, but they did not publish details of their solution method. They found substantial size selectivity for hard-sphere mixtures in nanoscopic cylinders. The 2D integration method corresponding to (82) with (83) was first described by Figueroa-Gerstenmaier et al. [206] who examined the adsorption of a Lennard-Jones fluid in nanoscopic cylinders and found that the behavior differed significantly from that in similarly sized slit-pores (although this difference reduced as pore-size increased), and that the FMF [augmented by (27)] was quite accurate even in the smallest pores studied (i.e., close to the 1D limit), when compared with grand-canonical MC simulation results. Gu et al. [212] use the same 2D integration method to examine the adsorption of hydrogen in carbon nanotubes at low temperatures where quantum effects become significant. They employ a path-integral approach that involves modeling quantum particles by unusual classical ring-polymers. Although the general approach involving path-integrals is interesting, their particular model ring-polymer is very crude. In their model, every site on a ring-polymer interacts with every other via hard-sphere repulsion when, in fact, only adjacent sites on the same ring-polymer should interact with a *harmonic* interaction and only sites with the same label (from 1 to N) on *different* ring-polymers should interact via hard-sphere repulsion.

Ravikovitch and colleagues [129] have compared the performance of the SDA2 and FMF DFTs [plus the mean-field term (27)] against grand-canonical MC simulations for adsorption of a LJ fluid in nanoscopic slit-pores and cylinders. They find that the SDA2 functional generally produces a slightly more structured fluid than the FMF functional, and that when molecular model parameters are fitted to reproduce bulk data (such as coexisting liquid and gas densities and pressures), both theories perform quite well compared to MC simulation even in very narrow pores. The largest deviations from simulation results are observed at the highest bulk densities (pressures) and, for SDA2, in the narrowest cylinders. Unfortunately, they do not solve the FMF in cylindrical geometries, so its behavior in the approach to the 1D limit (where the FMF is exact) is not assessed.

Despite the undoubted gains made using DFT to generate the kernel, some concerns remain. First, there is no *explicit* evidence that the DFTs and models described earlier in this review are able to predict accurately adsorption in real materials, either of the same gas used to generate the PSD at other temperatures or of other gases at any temperature. Although DFT has proved popular for fundamental studies of the behavior of simple fluids in ideal pores and for material characterization studies, there are no studies, to our knowledge, that make predictions for adsorption in real materials using DFT. We can expect, given the accuracy of nonlocal DFTs in ideal pores for simple fluids, that it might be quite accurate for predicting adsorption of simple fluids in active carbons. But we have no right to expect similar accuracy for more complex fluids with significantly nonspherical molecular shapes or with electrostatic moments, such as butane and water. Further work is needed to establish whether current DFT methods are sufficient to model a range of gases adsorbed in a range of real materials, or whether more sophisticated functionals and models are required. Second, most nonlocal DFTs are very numerically demanding; possibly too demanding to be of much use for predicting gas mixture adsorption. Each additional component of a mixture adds an additional dimension to the kernel. This means that, although nonlocal DFTs can be much quicker than MC simulation for generation of the kernel, they are still very expensive numerically for mixtures. Much faster methods are desired for this purpose and they will be described in the next chapter.

Several studies use the polydisperse ideal-pore model and GCMC simulation to generate the kernel. Quirke and Tennison [88] analyzed the adsorption of nitrogen at 77 K and methane at 313 K on an activated carbon PRC16. They find poor agreement between

graphitic slit-pore PSDs generated from each adsorbate probe and for the resulting adsorption predictions. They attribute the lack of agreement to the enhanced interaction of nitrogen at 77 K relative to methane at 313 K on electrostatic or polar surface sites (nitrogen has an electric quadrupole moment, whereas methane does not). Although this is certainly conceivable, a more simple explanation of the poor agreement is their calibration method for each gas–surface interaction, which employs a low surface area carbon as the calibration material. Gusev et al. [213] have used GCMC and the polydisperse independent slit-pore model to generate PSDs for methane at 308 K on BPL-6 activated carbon and are then able to predict methane adsorption at higher temperatures (333 K and 373 K) with good accuracy. This is encouraging, but is not a particularly stringent test of the model. Lopez-Ramon and colleagues [43] have used similar methods to obtain PSDs for three different adsorbates (CH4, CF6, and SF6) that probe different pore width ranges (due to their different molecular size). They then "stitch" these PSDs together to obtain the "global" PSD for Carbosieve G [43] and to analyze pore network connectivity. Unfortunately, there is poor agreement between PSDs generated by the different probes in the region of overlap of their pore-width ranges. The authors attribute this lack of agreement to two factors: (1) in any region of overlap, one probe will be more sensitive than another and better agreement could be obtained with a different method for solving the adsorption integral (51), and (2) that their calibration method is inaccurate. They use second-virial coefficients to calibrate gas–gas interactions and adsorption on a low surface area carbon to calibrate gas–surface interactions.

The early work of Samios et al. [214] should be regarded with caution as they employ carbon dioxide at 195 K, which is considerably below its triple-point temperature, as a probe of pore structure in activated carbon. However, later work by Samios and colleagues [215] using similar methods makes good predictions for adsorption of carbon dioxide at 298 K based on a PSD obtained from nitrogen adsorption at 77 K on the same material (Norit RB4). The reverse process, that is, prediction of nitrogen adsorption at 77 K using the PSD based on carbon dioxide adsorption at 298 K is less accurate but encouraging nevertheless. They also make generally good predictions for adsorption of these gases at the same temperatures based on PSDs obtained from carbon dioxide adsorption at 195 K and 308 K, but they do not show the resulting fits to experiment at 195 K and 308 K so it is not clear whether these results are significant. The consistency between the adsorption of nitrogen at 77 K and carbon dioxide at 298 K is remarkable considering the range of temperatures employed, their calibration method for gas–surface interactions (they calibrate to a low surface area carbon), and the very different PSDs obtained for each gas and temperature. Their success can probably be attributed in part to their imposition of an additional constraint (compared to other work in this area), that is, they require each PSD to have the same total volume (although it is not clear how they choose this volume).

Ravikovitch et al. [27] obtain quite good agreement between PSDs generated with the polydisperse slit-pore model and kernels generated by grand-canonical MC simulation and classical DFT for adsorption of carbon dioxide at 273 K on a number of activated carbons (see Fig. 9 for example). They calibrate gas–gas interactions to reproduce bulk coexistence data and gas–surface interactions to reproduce adsorption on a low surface area carbon. Unfortunately, as stated earlier, they make no adsorption predictions so it is not clear whether the apparent agreement in their PSDs translates to good predictive capability.

Sweatman and Quirke [28] use this model and grand-canonical MC simulation to generate kernels to analyze the adsorption of carbon dioxide, methane, and nitrogen on three activated carbons at 293 K. They find quite good agreement between experimental isotherms and isotherms predicted on the basis of carbon dioxide PSDs (see Fig. 10). They calibrate gas–gas interactions by developing new molecular models using Gibbs ensemble simulations and reference experimental data for liquid–gas coexistence densities and pressures over a range of temperatures, and they calibrate gas–surface interactions by fitting to adsorption on a low surface area carbon (modeled as a porous material rather than a flat surface). These results are encouraging, but once again they are not a severe test of the model because nitrogen and methane are substantially supercritical at 293 K. Finally, using the same methods these workers analyze adsorption of nitrogen at 77 K and carbon dioxide at 293 K on

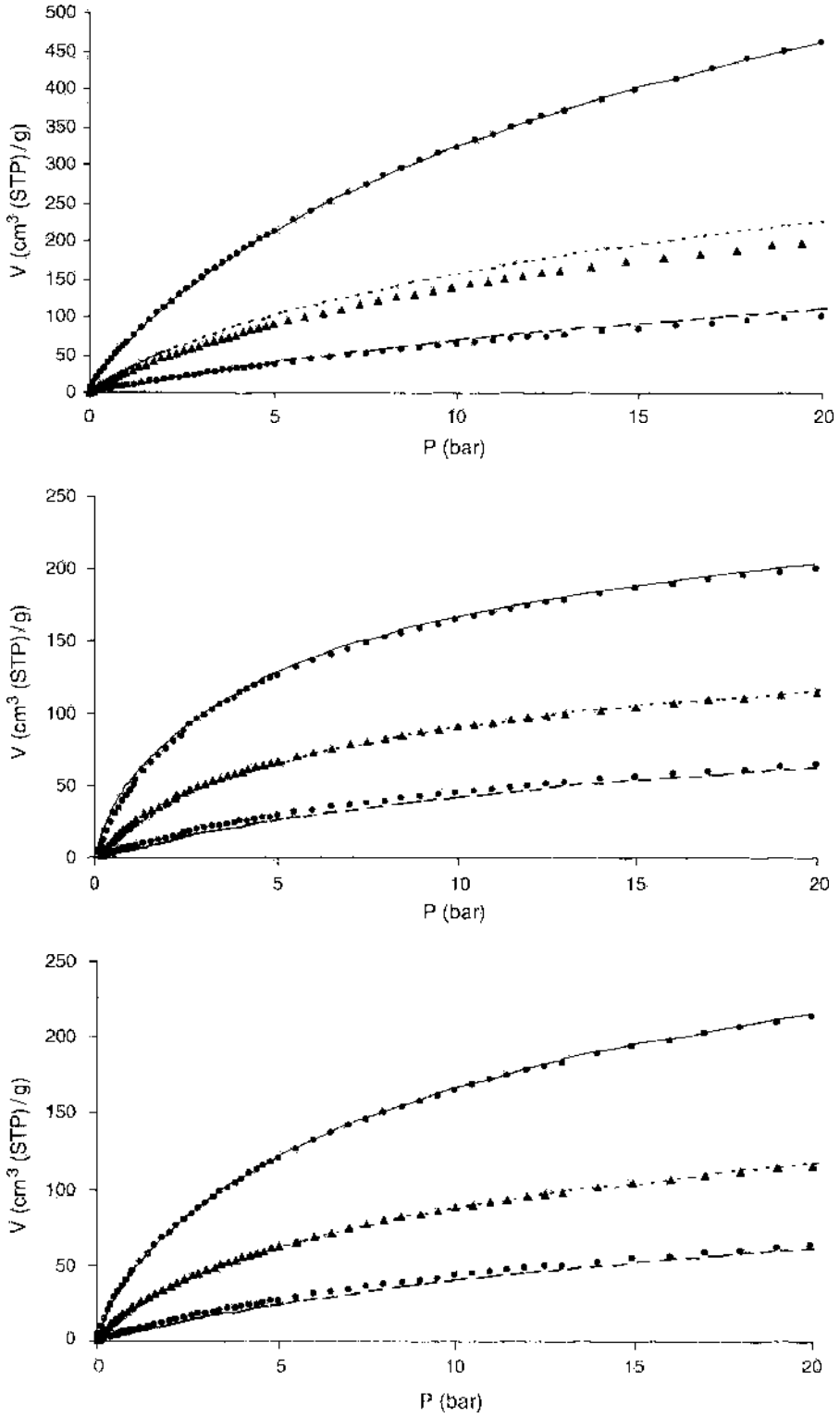

Figure 10. Experimental adsorption isotherms for carbon dioxide (top circles), methane (triangles), and nitrogen (bottom circles) in three activated carbons at 298 K. The full lines are fits to the carbon-dioxide data using a slit-PSD and a kernel generated by grand-canonical MC simulation. The other lines are adsorption predictions based on these PSDs. Reprinted with permission from [28], Sweatman and Quirke, *Langmuir* 17, 5011 (2000). © 2001, American Chemical Society.

AX21 [91]. They find poor agreement between PSDs for each probe gas and consequently poor predictive capability. They conclude that, most likely, the poor agreement is caused by poor diffusion of nitrogen at 77 K in AX21 (possibly caused by freezing; see Section 1.5). However, it could also be caused by calibration of gas–surface interactions to a low surface area carbon. Note that in this case, the serious discrepancies are unlikely to be caused by enhanced adsorption of nitrogen at 77 K on electrostatic surface sites because carbon dioxide adsorption is underpredicted using the nitrogen PSD. So this result questions the interpretation of Quirke and Tennison [88].

So what can we draw from this body of work? It seems that all this work suffers the same limitation, that is, that gas–surface interactions are calibrated to reproduce adsorption on low surface area carbons and applied to analyze adsorption on high surface area carbons that might have quite different effective gas–surface interaction strengths [215]. Some success has been gained, but usually these are not stringent tests of the surface model. The exception to this conclusion is the work of Samios and colleagues [216], who obtain quite good agreement between adsorption isotherms for nitrogen at 77 K and carbon dioxide at 298 K on a single carbon. Unfortunately, they do not obtain consistent PSDs. It seems that further work is required using these methods, including adsorption prediction for a range of super- and subcritical gases for a range of materials.

3.3. 3D Models

Despite the undoubted success of the polydisperse independent pore model for mimicking the behavior of some systems, for example the adsorption of weakly polar near- or supercritical gases on activated carbon [28, 213, 215], it is known to be inadequate for a range of other important systems. Its failure is the result of two factors: (a) the modeled uniformity of individual pores, and (b) the independence of these pores.

In real materials, there will be both geometric and energetic nonuniformities that result in phenomena that the ideal pore model cannot capture. Indeed, it cannot even clearly distinguish energetic from geometric nonuniformity or one kind of geometry from another. For example, Davies and Seaton [30] and Bojan and Steele [29] have modeled the adsorption of simple fluids in ideal pores with a variety of cross-sectional shapes using Monte Carlo simulation. They find that the geometry of the pore cannot reliably be determined from an adsorption isotherm alone. And Gac and coworkers [31] find using Monte Carlo simulation that the adsorption isotherms of a simple fluid are quite similar when adsorbed in pores with different energetic and geometrical nonuniformities. Maddox and coworkers [79] have investigated the influence of pore-junctions on adsorption of a model of nitrogen at 77 K using molecular simulation. They found that this geometric nonuniformity resulted in pore-blocking and that similarly sized independent pores did not exhibit this phenomenon. Papadopoulous et al. [109], Kozak et al. [217], and Gelb [218] have studied the influence of boundary conditions on adsorption in smooth-walled pores of finite length using Monte Carlo simulation and mean-field DFT. Essentially, they find that adsorption metastability is reduced if one end of the pore is closed with an attracting (Lennard-Jones) wall and that desorption metastability is reduced for an open-ended pore. The more recent work of Gelb [218] suggests that this simple picture is complicated by other considerations such as temperature, pore width, and pore length. Ultimately, ideal pores of infinite length exhibit enhanced hysteresis because the formation of menisci is suppressed. For strongly dipolar molecules, like water, Brennan and colleagues [73, 219] find that energetic nonuniformities can lead to water adsorbing at pore entrance, potentially blocking them, a phenomenon that is also absent from the polydisperse independent pore model. Kierlik and colleagues [23, 59, 60] have demonstrated that pores, or regions, in an amorphous material can have an important influence on neighboring regions for subcritical fluids. Their work concerning concerning lattice models of high porosity disordered materials (silica gels) has shown that the independent pore model would not be able to provide a full account of their adsorption phase behavior.

Clearly, characterization of nanoporous materials in terms of a polydisperse independent pore model is a gross approximation. For activated carbons, high-resolution electron

micrographs [18, 20] indicate that the slit-pore model might be a reasonable starting point, whereas for other materials, like silica gels, it might not be as accurate. So there can be great value in developing surface models that address specific issues such as energetic or geometric nonuniformity or pore–pore interactions. However, a surface model that can capture all of these effects is likely to be very complex. If energetic and geometric nonuniformity are predominantly short-range in nature and if pore–pore interactions are long-range, then an accurate model will probably be described over a wide range of length scales. Essentially, an accurate model will need to capture nanostructure and network topology. Recent articles [21, 219] have addressed the development of detailed 3D surface models in some depth. Here, we present a summary of some of these models, concentrating on those that have been subjected to comparison with adsorption experiments for nanoporous materials, that is, the models of Segarra and Glandt [220] and the reverse Monte Carlo (RMC) models of Gubbins and colleagues [73, 221–223].

Segarra and Glandt [220] modeled an activated carbon as a collection of randomly oriented graphitic disks. Each disk represents two circular graphene layers held parallel to each other at a distance of 0.335 nm. Each layer is uniform, and adsorbate-layer interactions are modeled by a "smeared-out" Lennard-Jones interaction, which varies only with distance perpendicular to the layer and from its circular axis. Each realization of a carbon surface is generated by performing a canonical Monte Carlo simulation of hard disks at equilibrium (see Fig. 11). Adsorption isotherms are generated with GCMC simulation and a single parameter, the disk radius, was varied (from 0.5 to 1.0 nm) to make comparison with experimental results for the adsorption of methane and ethane at about 300 K. To model the adsorption of water an additional adsorbate–dipolar disk edge interaction was introduced. The complexity of surfaces generated by this method allows a degree of geometric and energetic nonuniformity and pore–pore interaction. But it is essentially a scalar model, so it is no surprise that quantitative agreement with experiment for adsorption isotherms was not obtained.

Thomson and Gubbins [222] modeled an activated carbon with "reverse Monte Carlo" (RMC). This is essentially a method whereby a structural measure of the simulated nanoporous carbon, its carbon atom–carbon atom radial distribution function, for example,

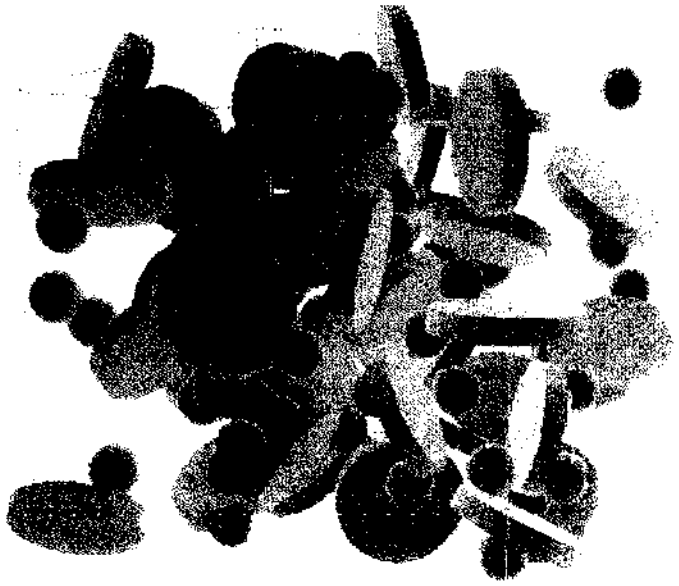

Figure 11. Representation of a 3D model of an activated carbon (platelets) and adsorbed gas (spheres). The platelet configuration is generated by a MC procedure. Reprinted with permission from [220], Segarra and Glandt, *Chem. Eng. Sci.* 49, 2953 (1994). © 1994, Elsevier.

is stochastically optimized to fit experimental data by allowing a large number of small fluctuations in the modeled surface.

In one method [221, 222], the model consists of a number of flat graphene sheets contained within a given volume, and three types of move are performed: (a) random translational and orientational moves of a graphene sheet, (b) random creation or deletion of aromatic rings on the edge of a graphene sheet, and (c) occasional creation or deletion of a complete, randomly generated graphene sheet. The RMC simulation is initialized from a randomly generated realization consisting of a number of randomly generated graphene sheets and the moves are accepted if the deviation of the instantaneous simulated carbon–carbon distribution function from experimental data, which is obtained from scattering experiments on a macroscopic sample, is reduced (and rejected otherwise). Entire graphene sheets are created or deleted to prevent the average density from deviating too far from a desired value. This is a "downhill" optimization procedure, and so the name "reverse Monte Carlo" is not entirely appropriate. Once the surface is generated by RMC (see Fig. 12 for example), GCMC is employed to model the adsorption of nitrogen where each carbon surface atom and each nitrogen atom is represented by a Lennard-Jones site. Thomson and Gubbins [222] found that nitrogen adsorption at 77 K on carbon a-MCMB was accurately predicted for pressures less than about 10^{-3} bar, but significant deviation from experiment was observed above this pressure. They argue that this is because their simulation cell, which was cubic with each side 10 nm, is not sufficiently large to properly capture the contribution from pores larger than about 1.5 nm or so. It remains to be seen how large the simulation box-size should be to capture the correct behavior. Another consideration is that they follow earlier work and calibrate gas–surface interactions to a low surface area carbon. Gavalda and colleagues [221] used the same method to model nitrogen adsorption in carbon aerogels. In their study, nitrogen adsorption in the nanoporous carbon beads that form the aerogel was poorly predicted at all pressures. They suggest that this could be due to poor calibration of gas–surface interactions, to imprecise calculation of the material's density, or due to insufficient sophistication of the surface model. This last factor seems unlikely given the

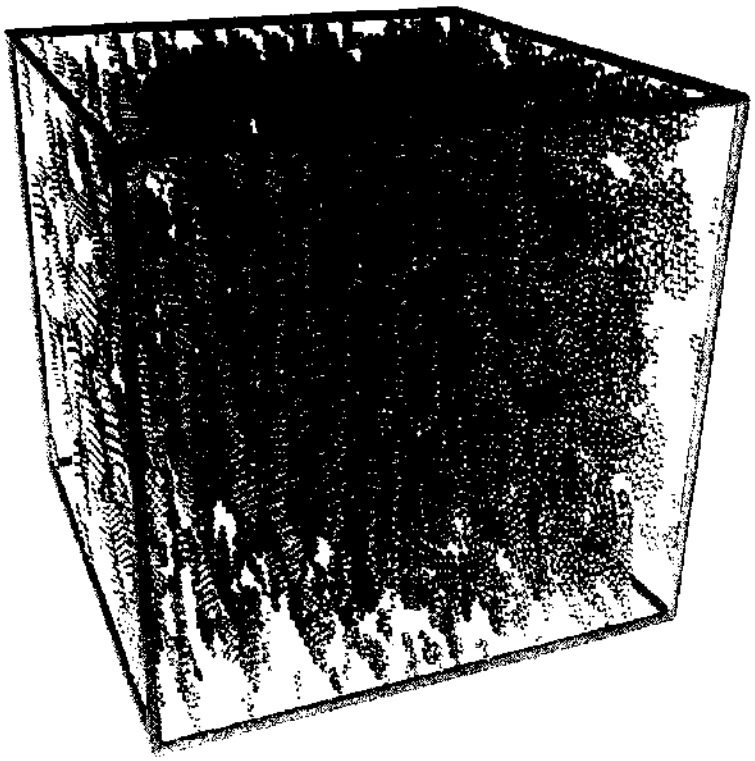

Figure 12. Representation of a 3D model of an activated carbon formed from graphene-like sheets via a reverse MC method. Reprinted with permission from [222]. Thomson and Gubbins, *Langmuir* 16, 5761 (1999). © 1999, American Chemical Society.

ability of much simpler models, such as the polydisperse slit-pore model, to describe nitrogen adsorption on active carbons.

Brennan and coworkers [73] have also used this method to study the adsorption of water in a graphitizable carbon. In addition to adopting this method to generate a carbon surface, they also randomly decorated the edges of graphene sheets with oxygen sites (represented by LJ sites with embedded partial charges), with a range of average oxygen densities. They find that this model is potentially able to reproduce pore-blocking due to water adsorption, but make no comparison with experiment. Pikunic et al. [223] considered a somewhat different RMC approach where individual carbon atom moves are attempted. Moves are accepted or rejected to optimize the fit to three target structural measures, the experimental structure factor, the average bond angle ($2\pi/3$), and the average number of carbon atoms bonded with three neighboring carbon atoms (carbon atoms are considered to be neighbors if the separation of their centers is between specified limits). These measures are weighted and a simulated annealing optimization algorithm is employed. For a model mimicking a glassy carbon formed by heat treatment at 2773 K, they generated a nitrogen adsorption isotherm at 77 K with GCMC but, again, make no comparison with experiment.

The most generally applicable of these different 3D modeling approaches is the RMC method of Pikunic et al. [224] as there are minimal arbitrarily imposed constraints. For example, the RMC method of Thomson and Gubbins [222] imposes the existence of graphene sheets comprised entirely of aromatic rings. In principle, one could imagine applying the RMC method of Pikunic and colleagues to any amorphous material provided the target data is known, that is, the structure factor, average bond angle and density of the most important component (i.e., carbon atoms in activated carbons). Adsorption isotherms can then be generated for a given adsorbate molecular model by GCMC. This is an attractive method, but it is numerically intensive compared to the polydisperse independent pore model, for example.

Two competing methods are immediately obvious for the prediction of mixture adsorption on a RMC-generated surface. The most accurate method is to simply perform GCMC simulations of the desired mixture. But this is laborious, particularly if one wishes to obtain data for a range of mixtures (for the purpose of design optimization, for example). A much quicker alternative would be to employ a theory that can predict mixture adsorption based on pure component isotherms only. This is the aim of ideal adsorbed solution theory [95] (IAST). Although IAST is extremely easy and quick to use, it is useful only for ideal (or nearly ideal) mixtures (i.e., mixtures where the interactions of each component are quite similar). This theory and its limitations are detailed in the next section along with other approaches to predicting mixture adsorption on the basis of pure component isotherms.

3.4. Calibrating Interactions

Just as with adsorbate–adsorbate interactions, adsorbent–adsorbate interactions should be calibrated when using molecular models of adsorbate and adsorbent. For example, if we consider the Steele potential, a popular model for the interaction of a Lennard-Jones adsorbate site with a graphitic surface, we see that it is defined by four parameters, interlayer spacing Δ, solid density ρ_s and the LJ length and energy parameters, σ_{ss} and ε_{ss}. How should we set the values of these parameters for a high surface area carbon such as AX21?

First, it should be realized that there are actually only two independent parameters to be calibrated, as we can set $\varepsilon = \Delta\rho\varepsilon_{ss}$. In every case [27, 28, 38, 39, 88, 131, 170, 203, 213–215, 220, 222, 225–230] in the literature, the remaining parameters are calibrated to reproduce adsorption on graphite or a low surface area carbon such as Sterling or Vulcan. Sometimes, the "standard" values $\varepsilon_{ss}/k_B = 28$ K and $\sigma_{ss} = 0.34$ nm, and the Lorentz-Berthelot rules (42) are used to derive adsorbate–adsorbent interactions. These parameters were obtained from studies of graphite [5, 202], so use of these parameters still corresponds to calibration to a low surface area carbon.

This approach (i.e., fitting to a low surface area carbon) is a reasonable first approximation but it should not necessarily be expected to yield consistent results for high surface area carbons. Quite simply, the surface of a high surface area carbon is very different from that of a

low surface area carbon. So, for example, when using the polydisperse slit-pore model to characterize an activated carbon, one should not expect PSDs generated by different adsorbates to be consistent if the adsorbate–adsorbent interactions have been calibrated to a low surface area carbon. Yet it is often expected that PSDs generated in this way will be consistent. If one wishes to use PSDs in a predictive capacity (i.e., to predict adsorption of a pure or mixed gas on the basis of a PSD generated by another gas), then it would be more appropriate to calibrate the individual pure fluid adsorbate–adsorbent interaction parameters to a reference high surface area carbon. The premise here is that surfaces of all high surface area carbons are more similar to each other than they are to any low surface area carbon. The same kind of approach should probably be employed when analyzing any amorphous adsorbent.

4. PREDICTING GAS MIXTURE ADSORPTION

In nature, most fluids are mixtures. In industry, nanoporous amorphous adsorbents like activated carbons are used for a variety of purposes, but most of them involve the separation of one fluid component from another. Here we discuss advances in modeling the equilibrium adsorption of gas mixtures in these materials.

The problem that fluid mixtures present is concerned with the additional degrees of freedom generated by each component after the first. For pure fluids, we need specify only the bulk pressure and temperature, so an adsorbed phase diagram is relatively easy to map. But for mixtures it becomes increasingly difficult to map the adsorbed phase diagram as the number of fluid components increases.

If we consider one method for predicting pure fluid adsorption, the adsorption integral (62), and attempt to adapt it to mixtures, we find that we need to specify an $n+1$-dimensional kernel (at a fixed temperature) for an n-component mixture. If we represent the kernel at a fixed temperature by a matrix of, say, 10 elements for pressure, pore width and each bulk mole fraction, we find that the number of data entries is 10^{n+1}, a rather large number, even for small n. So it is quite impractical to try to generate the kernel by calculating each data entry using a numerically intensive method such as MC simulation or even nonlocal DFT. Alternatively, a 2-D kernel can be generated as needed for a mixture with specified composition, although this is still a lengthy computation that needs to be repeated for each different mixture.

On the other hand, it is unlikely that any method for predicting mixture adsorption in nanoporous amorphous materials will be successful generally unless it models the behavior of fluid mixtures at the nanoscale. So our goal is to create a method that is both accurate at the nanoscale and very quick. This is precisely why this problem is difficult, interesting, and important. An accurate and fast method would be of use both in probing the physical chemistry of mixed adsorption and in practical applications to, for example, adsorbent design.

Every approach to this problem in the literature is based on modeling the adsorption of the pure components and using a fast theory to make predictions for the mixture. The modeling of pure component adsorption was discussed in the previous sections. Various methods have been used, ranging from simple "scalar" characterizations of the surface and empirical adsorption equations, to complex 3D models of the surface and Monte Carlo simulation of adsorption. Most of these methods have been adapted to predict mixture adsorption.

The additional element needed to make predictions for the mixture is a theory that predicts mixture adsorption given pure component data as input. A number of methods have been attempted based on extending "empirical" pure adsorption equations to mixtures. For example, the Langmuir [9, 177, 185, 231, 232], Dubinin-Radushkevich [233], Dubinin-Astakhov [234], and Toth [189] isotherms and neural-network [188] and virial [9, 191–193] methods have been adapted in this way to analyze a variety of gas mixture systems. In these approaches, parameters describing the adsorbed gas mixture are determined by fitting to the pure component data. As with their pure component progenitors, we do not detail these methods.

One of the most significant theories for predicting gas mixture adsorption is based on a thermodynamic treatment of adsorption at a surface. In 1965, Myers and Prausnitz [95] invented ideal adsorbed solution theory (IAST), which is essentially an extension of ideal

solution theory [235] to adsorption. This theory for the adsorbed mixture takes as its only input the pure component isotherms, all at the same temperature. It is able to make predictions for gas mixture adsorption at this temperature up to a pressure that is limited by the input data. There is no constraint on how the input isotherms are described. For example, one could fit straight-line segments between a set of data points. But usually the input data is described in terms of a smooth adsorption equation such as the Langmuir [186, 231, 236], Dubinin-Radushkevich [237], or Toth [186] isotherms. In 1995, Cracknell and Nicholson [238] suggested that the original theory should be recast in terms of the total, or absolute, grand potential rather than the "spreading pressure," which, according to them, is the negative of the excess (over bulk) grand-potential density. Vuong and Monson [239] arrived at the same conclusion, which was later proved by us [240]. However, we note that in the original 1965 paper the theory is initially developed in absolute, rather than excess, terms.

IAST makes no assumptions about the nature of the adsorbent other than it is inert. We are not aware of any development of IAST to other ensembles, such as the osmotic ensemble that can be used to model swelling materials. IAST itself is not based on any nanoscopic model, but the pure component isotherms can be. This means that IAST can be combined with a model of the surface, such as a polydisperse pore model. This attractive feature has been used by several groups [131, 187, 241, 242] to improve gas mixture adsorption prediction beyond the standard application of IAST. Note that a surface model defined in terms of a PSD [242] seems to be preferred [241] to one defined in terms of a distribution of gas–surface interaction energies [243, 244] (or an ED).

Accurate prediction of mixture adsorption in nanoporous adsorbents requires a theory that models both the adsorbent and adsobate at a nanoscopic level. Or, in the language of AST, a theory is required that can calculate the effect of the surface on activity coefficients [245]. Given the success of DFT and molecular simulation in modeling pure gas adsorption, one should expect them to be successful in predicting mixed gas adsorption as well. Gusev and O'Brien [230] and Seaton and colleagues [228, 229] have used a slit-PSD to model activated carbons and Monte Carlo simulation to model the adsorption of gas mixtures. Using a PSD generated from the pure methane adsorption isotherm and a methane GCMC kernel, Gusev and O'Brien [230] find that they are unable to predict satisfactorily the adsorption of methane/ethane gas mixtures at 308 K in BPL-6 activated carbon at moderate to high pressures using the same PSD and a GCMC mixture kernel, although they find better agreement with experiment at low pressure. Davies and Seaton [228] used the same methods to study these gases on a range of activated carbons. They find that pure component adsorption is predicted quite well for both gases for a range of temperatures above 293 K up to high pressure (about 30 bar or so) on several carbons using a PSD generated from the pure ethane isotherm at 293 K (see Fig. 13 for example). This is despite using gas-surface interactions that have been optimized for adsorption on low surface area carbons. They also find that selectivity is predicted quite well at relatively low pressure (1 bar or less) but is less satisfactory at higher pressures. They compare the use of MC simulation with IAST for predicting mixture adsorption and find close agreement, presumably because the mixture is relatively ideal under the conditions analyzed. Heuchel and coworkers [229] analyze carbon dioxide/methane mixtures at ambient temperature up to 17 bar. They find that, generally, better predictions for gas mixture adsorption can be obtained as more and more input data is used (i.e., using several pure gas isotherms as input is better than using just one). They attribute this to obtaining a more accurate PSD as more input data is used. For example, Fig. 14 compares predicted isotherms of several carbon dioxide–methane mixtures, based on a PSD generated by fitting to both pure carbon dioxide and methane isotherms simultaneously, against experimental data. The mixture isotherms, generated using the same PSD and GCMC kernels, are not particularly accurate. Also, they find that they cannot accurately fit a PSD to all of their data, including the mixture data.

Despite some encouraging results, these are not particularly stringent tests of the model because the probe gas (ethane or carbon dioxide at ambient temperature) is only marginally subcritical and is used to predict adsorption of the probe gas at higher temperatures and methane adsorption at supercritical temperatures to moderate pressure only (less than 20 bar). Mixture adsorption prediction is also limited to low or moderate pressures. Overall,

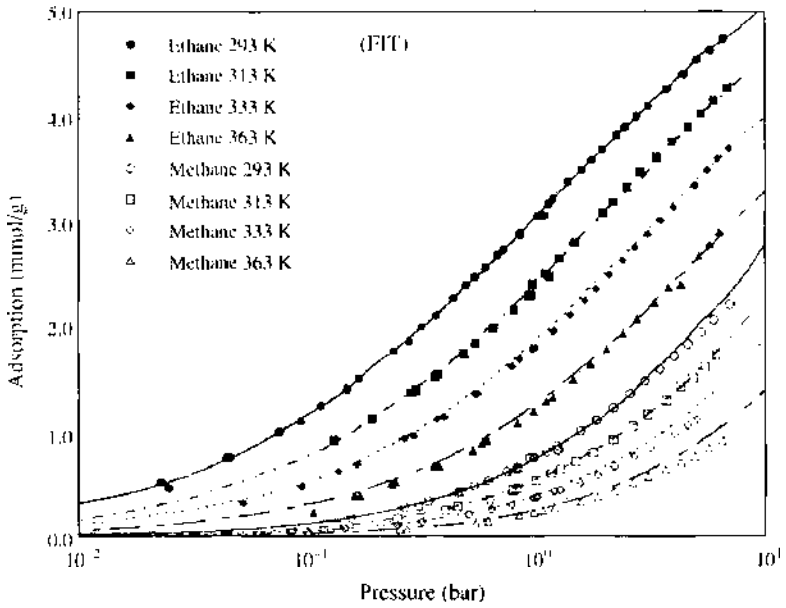

Figure 13. Adsorption of pure ethane and methane on Nuxit activated carbon at various temperatures. Lines are predictions based on a PSD generated by fitting to the pure ethane isotherm at 293 K and kernels generated by grand-canonical MC simulation. Symbols are experiment. Reprinted with permission from [228], Davies and Seaton, *AIChE J.* 46, 1753 (2000). © 2000, AIChE.

the predictions for mixed gas adsorption in this work are somewhat disappointing considering the level of sophistication. In all of this Monte Carlo simulation work, a likely cause of error is due to calibration of the molecular models. In each case, gas–surface interaction parameters are fitted to reproduce adsorption on a low surface area carbon. The assumption is that this parameterization is valid for high surface area carbons. We feel that this assumption is highly optimistic. The simplicity of the slit-pore model might also be important.

There have been no attempts to predict gas mixture adsorption in nanoporous materials with a nonlocal DFT of the type detailed in Section 2.2. But, recently, we have found some success with a particularly simple, "trimmed-down," nonlocal DFT [240] that is able to predict the adsorption of gas mixtures in graphitic slit-pores both accurately and quickly using as input a single pure gas adsorption isotherm only. Preliminary application of this method to a range of activated carbons is encouraging [216]. We will describe this method and its

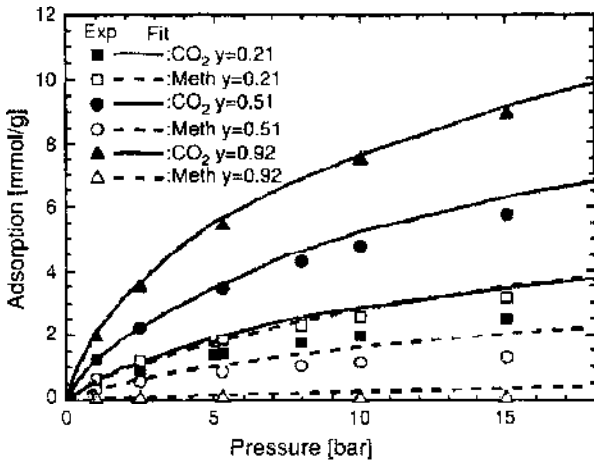

Figure 14. Adsorption of carbon dioxide–methane mixtures on A35/4 activated carbon at 293 K. Lines are predictions based on a slit-PSD generated by fitting simultaneously to both pure carbon dioxide and methane isotherms and kernels generated by grand-canonical MC simulation. Symbols are experiment. Results are shown for three values of the bulk molar fraction of carbon dioxide, y. Reprinted with permission from [229], Heuchel et al., *Langmuir* 15, 8695 (1999). © 1999, American Chemical Society.

relation to IAST in detail, drawing substantially on our published work [240]. In summary, this success stems from two key advances. The first concerns calibration of the molecular models, that is, we calibrate gas–surface interactions to reproduce pure gas adsorption on a reference high surface area carbon. The second concerns our novel and simple DFT.

We start by equating chemical potentials in the bulk and adsorbed phases.

$$\mu_{ai} = \mu_{bi} \tag{88}$$

where subscripts a and b are used to distinguish adsorbed and bulk quantities. Writing the chemical potential in terms of a reference chemical potential for the pure fluid

$$\mu_i(T, \Omega, \{V_i^{ext}\}, \{x\}) = \mu_i^0(T, \Omega_i^0, V_i^{ext}) + k_B T \ln(x_i \gamma_i(T, \Omega, \Omega_i^0, \{V_i^{ext}\}, \{x\})) \tag{89}$$

we obtain

$$z_{ai}^0(T, \Omega_{ai}^0, V_i^{ext}) x_{ai} \gamma_{ai}(T, \Omega_a, \Omega_{ai}^0, \{V_i^{ext}\}, \{x_a\}) = z_{bi}^0(T, \Omega_{bi}^0) x_{bi} \gamma_{bi}(T, \Omega_b, \Omega_{bi}^0, \{x_b\}) \tag{90}$$

where the 0 superscript denotes the pure component quantity, x_i and γ_i are the mole fraction and activity coefficient for component i, respectively, and

$$z_i = \exp(\beta \mu_i) \tag{91}$$

is the activity. So far, we have yet to specify how Ω_i^0, the grand potential of the pure reference state, relates to Ω, the grand potential of the mixed state, at the same temperature. Following the convention with ideal solution theory, we decide to choose Ω_i^0 such that $\gamma_i = 1$ in the low-density limit. To discuss the consequences of this choice in the most accessible manner, we use basic results from DFT rather than the arguments put forward by Rudisill and LeVan [246] and ourselves [240]. From the fundamental equations of DFT [(25) and (26)], we have

$$\begin{aligned} \beta\Omega = &\sum_i \int d\mathbf{r} \rho_i(\mathbf{r}) \{\ln[\Lambda_i^3 \rho(\mathbf{r})] - 1\} + \beta F^{ex} \\ &- \sum_i \int d\mathbf{r} \rho_i(\mathbf{r}) [\ln(\Lambda_i^3 \rho_{bi}) + \beta \mu_i^{ex} - \beta V_i^{ext}(\mathbf{r})] \end{aligned} \tag{92}$$

which with the Euler-Lagrange equation (38) in the low-density limit becomes

$$-\beta\Omega = \sum_i \int d\mathbf{r} \rho_i(\mathbf{r}) = \sum_i \rho_{bi} c_i \tag{93}$$

where c_i is a constant. From (88), (89), and the low-density result $\beta\mu_i = \ln(\Lambda_i^3 \rho_{bi})$, we have in this limit

$$\rho_{bi}(T, \Omega_b, \{x_b\}) = x_{ai} \rho_{bi}^0(T, \Omega_{ai}^0, V_i^{ext}) \tag{94}$$

Putting these two results together gives

$$-\beta\Omega_i^0 = \rho_{bi}^0 c_i = \frac{\rho_{bi}}{x_{ai}} c_i = \int d\mathbf{r} \frac{\rho_{ai}(\mathbf{r})}{x_{ai}} = -\beta\Omega \tag{95}$$

Finally, substituting this result in (90) gives the nonideal adsorbed solution theory (NIAST) relations

$$z_{ai}^0(\Omega_a) x_{ai} \gamma_{ai}(\Omega_a, \{x_a\}) = z_{bi}^0(P) x_{bi} \gamma_{bi}(P) \tag{96}$$

where each quantity on the left also depends on temperature and the surface, and each quantity on the right also depends on just the temperature. Ω_a is the grand potential of the adsorbed mixture and P is the pressure of the bulk mixture (for a bulk fluid $\Omega = -PV$). Because we have yet to make any approximations, the NIAST relations are exact and equivalent to the Euler-Lagrange equations. The NIAST equations relate adsorbed concentrations to bulk concentrations in terms of pure fluid equations of state and activity

coefficients. If for the moment we assume that all the activity coefficients are known, then for fixed Ω_a and $\{x_b\}$, if we can determine all the pure fluid adsorbed equations of state $z_i^0(\Omega_a)$ and bulk equations of state $z_i^0(P)$, then the only remaining unknown quantities are $\{x_a\}$ and P. Because we also know that $\Sigma_i x_{ai} = 1$, we actually have $n + 1$ equations with $n + 1$ unknown quantities. So this set of equations can be solved by matrix inversion. Of course, the activity coefficients are generally not known exactly and approximations for them must be sought, except in the low-density limit where we have defined $\gamma_i = 1$.

The total adsorption can be obtained by substituting (11) into (89) (with $\Omega_i^0 = \Omega = \omega V$) to obtain

$$\frac{1}{N_a} = \frac{-1}{V_a}\sum_i x_{ai}\left(\frac{\partial \mu_i}{\partial \omega_a}\right)_T = \frac{-1}{V_a}\sum_i x_{ai}\left[\left(\frac{\partial \mu_i^0}{\partial \omega_a}\right)_T + \frac{k_B T}{x_{ai}}\left(\frac{\partial x_{ai}}{\partial \omega_a}\right)_T + \frac{k_B T}{\gamma_{ai}}\left(\frac{\partial \gamma_{ai}}{\partial \omega_a}\right)_T\right] \tag{97}$$

Use of (11) again and the fact that $\sum_i x_i = 1$ gives the desired adsorption relation

$$N_a^{-1} = \sum_i x_{ai}(N_{ai}^0)^{-1} - \frac{k_B T}{V_a}\sum_i \frac{x_{ai}}{\gamma_{ai}}\left(\frac{\partial \gamma_{ai}}{\partial \omega_a}\right)_T \tag{98}$$

which reduces to Henry's law in the low-density limit where $\gamma_i = 1$.

Equations (96) and (98) are exact relations for the concentration and amount of each component in the adsorbed phase. Their solution requires knowledge of bulk and adsorbed equations of state for each pure component and all activity coefficients. We assume that the pure fluid equations of state are known. So expressions for the activity coefficients are required. The most obvious approximation is to set $\gamma_{ai} = \gamma_{bi}$, which yields "equal mixing adsorbed solution theory" (EMAST) [240]

$$z_{ai}^0(T, \Omega, V_i^{ext})x_{ai} = z_{bi}^0(T, P)x_{bi} \tag{99}$$

This approximation will be less useful if gas–surface interactions significantly affect mixing in the adsorbed phase. So we can expect this approximation to be less accurate with increasingly different gas–surface interactions for each component. We note that it is not necessary to set $\gamma_{ai} = \gamma_{bi} = 1$ (i.e., the fluid mixture is *not* approximated to be ideal). EMAST simply approximates mixing to be the same, ideal or not, in the bulk and adsorbed phases. IMAST (ideal mixing) is EMAST with $\gamma_{ai} = \gamma_{bi} = 1$. IAST can be obtained from IMAST by using the ideal gas approximation for z_i^0 to give

$$P_{ai}^0(T, \Omega, V_i^{ext})x_{ai} = P_b x_{bi} \tag{100}$$

Clearly, this approximation will be less accurate as pressure increases.

We compared IAST against a particularly simple DFT and found that our novel DFT [240] was significantly more accurate for predicting the adsorption of a model of a nonideal gas mixture, carbon dioxide and hydrogen, in ideal graphitic slit-pores. For relatively ideal gas mixtures, such as a model of methane and carbon dioxide, there was little difference in accuracy. In principle, our DFT approach is not limited in application by the input data as is the case with IAST (i.e., once a DFT model is defined it can be applied at any pressure and temperature). Although the IAST approach was still quicker by far, our DFT method was sufficiently quick to be considered interactive (i.e., an isotherm in an ideal slit pore could be generated in under a second on a desktop PC).

Our DFT method, as with all DFT approaches applied to materials characterization, treats gas molecules as hard spheres with a mean-field perturbation. Although accurate nonlocal theories for hard-sphere fluids exist, they are numerically intensive and inappropriate for quick calculations. So we used a local theory, using the FMF (i.e., the PY) equation of state for bulk hard-sphere mixtures. We approximate the intrinsic excess Helmholtz free-energy with (27), (28), and (29)

$$F^{ex} = \int d\mathbf{r}\varphi_{HS}^{PY}(\{\rho(\mathbf{r})\}) + \frac{1}{2}\sum_{ij}\iint d\mathbf{r}_1 d\mathbf{r}_2 \rho_i(\mathbf{r}_1)\rho_j(\mathbf{r}_2)\phi_{ij}^p(r_{12}) \tag{101}$$

To simplify matters further, we adopted the slit-pore geometry and symmetrically parameterized the density into three slabs. In this respect, our DFT has parallels with the MSAM model of Gusev and coworkers [186], which divides pore space into two regions, a strongly adsorbed region and the remainder.

Our model is presented schematically in Fig. 15 with the density profile represented by the vertically shaded region. It symmetrically parameterizes density profiles in terms of the set $\{H_p, \delta H, \rho_{1i}, \rho_{2i}, \rho_{3i}, \sigma_{bi}, \delta\sigma_{bi}, z^*\}$, where each element is non-negative. Parameters with a subscript "i" can be different for each fluid component, otherwise they are the same for all components. The slit width, H_p, describes the physical width of the slit (i.e., H_p is the distance normal to the walls between wall atom centers. The region where the density is zero, described by $\delta H = H_p - H_c$, prohibits fluid particles from overlapping wall particles. The three regions or "slabs" of density represent (1) a monolayer of fluid strongly adsorbed at the wall with density ρ_{1i} and width $z_{1i} = \min(\sigma_{bi} + \delta\sigma_{bi}, H_c/2)$, (2) a thick layer of adsorbed fluid with density ρ_{2i}, and (3) the remaining fluid in the center of the slit with density ρ_{3i} and width z^*.

For both the external potential and ideal gas contributions of slab 1 to the grand potential [see (25) and (26)], we transform slab 1 so that it has width $\delta\sigma_{bi}$ while conserving the total number of particles (i.e., it has density $\rho_{1i}^* = \rho_{1i} z_{1i}/\delta\sigma_{bi}$). This is represented by the horizontally shaded region in Fig. 15. In summary, the grand potential is written [240]

$$\Omega = F^{ex} + 2A\sum_i \left\{ \begin{array}{l} \delta\sigma_{bi}\rho_{1i}^*[V_i^{ext} + \ln(\Lambda_i^3\rho_{1i}^*) - \mu_{bi} - 1] \\ \quad + z_{2i}\rho_{2i}[\ln(\Lambda_i^3\rho_{2i}) - \mu_{bi} - 1] + z^*\rho_{3i}[\ln(\Lambda_i^3\rho_{3i}) - \mu_{bi} - 1] \end{array} \right\} \quad (102)$$

where $z_{2i} = H_c/2 - z_{1i} - z^*$ and V_i^{ext} is the strength of gas–surface interactions. Because of this transformation of slab 1 for the external potential and ideal gas contributions only, in effect our prescription for F^{ex} is a crude nonlocal approximation.

Minimization of (102) with respect to the density with all other parameters held fixed, that is, variation of $\{\rho_{1i}, \rho_{2i}, \rho_{3i}, z^*\}$ at fixed $\{T, H_p, \delta H, \sigma_{bi}, \delta\sigma_{bi}, \sigma_{ai}, \varepsilon_{ai}, V_i^{ext}, \mu_{bi}\}$, gives the equilibrium state according to this simple model.

The bulk LJ parameter set, $\{\sigma_{bi}, \varepsilon_{bi}\}$, is determined by fitting to pure bulk fluid reference pressure–density isotherms for a given temperature, T, with $H_p \to \infty$. The adsorbed parameter set is determined by estimating δH and $\delta\sigma_{bi}$, fixing V_i^s by fitting to the low-density limit of each pure fluid adsorption isotherm, and then fitting $\{\sigma_{ai}, \varepsilon_{ai}\}$ to the entire range of each pure fluid adsorption isotherm. A downhill simplex algorithm initialized near to $\{\sigma_{bi}, \varepsilon_{bi}\}$ was used to find the local minimum of the rmsd (root-mean-square-deviation) of this fit.

For prediction of mixture adsorption, the same DFT model is solved to determine $\{\rho_{1i}, \rho_{2i}, \rho_{3i}, z^*\}$ with all the other parameters fixed, the bulk fluid composition, x_{bi}, known,

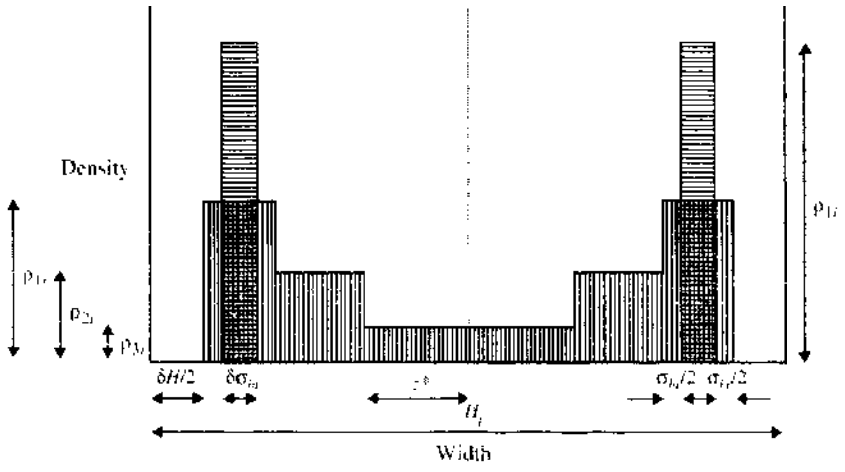

Figure 15. Schematic diagram of the simple density functional model used to predict mixture adsorption given the adsorption of the pure components in an ideal slit-pore. Reprinted with permission from [240]. Sweatman and Quirke, *Langmuir* 18, 10443 (2002). © 2002, American Chemical Society.

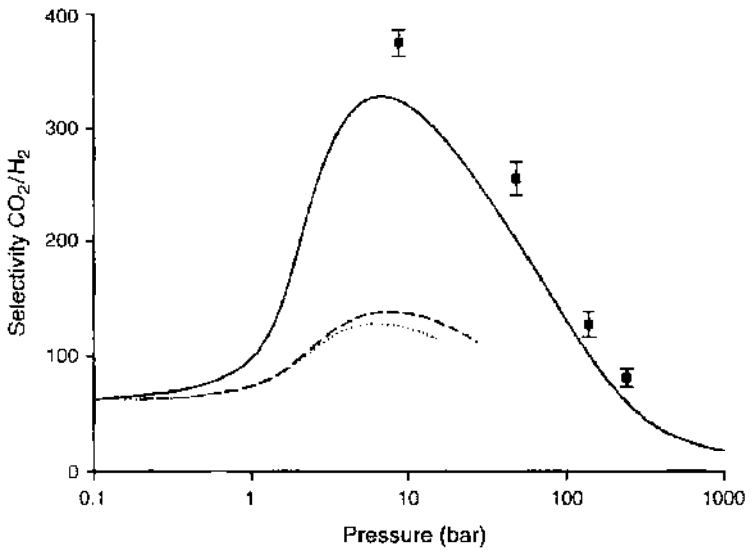

Figure 16. Selectivity for a model carbon dioxide–hydrogen mixture in an ideal graphitic slit with physical width of 1 nm from an equimolar bulk mixture at 295 K. Symbols are grand-canonical MC simulation data and lines are the predictions of theory (see text for details); slab-model DFT (solid line), IMAST (dashed line), and IAST (dotted line). Reprinted with permission from [240], Sweatman and Quirke, *Langmuir* 18, 10443 (2002). © 2002, American Chemical Society.

and imposition of the LB rules (42) to define cross-interactions. It was demonstrated [240] that this DFT model is not unduly sensitive to small variations in the estimated parameters δH and $\delta\sigma_{ht}$ for a highly nonideal mixture.

Figure 16 shows the selectivity

$$S_{12} = \frac{\rho_{a1}\rho_{b2}}{\rho_{a2}\rho_{b1}} \tag{103}$$

for a model of an equimolar bulk mixture of carbon dioxide and hydrogen in an ideal graphitic slit-pore [modeled with a Steele potential (56)] with a physical width of 1 nm at 295 K. It shows, in this case, that the simple DFT generates significantly better predictions than IAST. It is not yet known whether more complex DFT models will be required to maintain this performance advantage for more complex mixtures, such as water and alkanes.

This result is encouraging, but the acid test is application to a real adsorbent. We have applied [216] our simple DFT approach to predict the adsorption of mixtures of carbon dioxide, carbon monoxide, nitrogen, and methane in several activated carbons at ambient temperature up to about 40 bar, and we will report these results in due course.

5. CONCLUSIONS

The adsorption of gas in nanoporous amorphous materials is a complex process. But after a century of effort, it seems that we are at last making significant progress based largely on an improved understanding of adsorption in terms of equilibrium statistical mechanics. A great deal of research in the past into this problem has tended to be based on extremely simplified modeling both in terms of the surface and adsorption isotherms. This is still the case today, although the more sophisticated approaches covered in this chapter seem to be gaining wider acceptance. This is fortunate, as it seems that many of the "traditional" approaches employed in connection with gas mixture adsorption are very limited or easy to misinterpret. For example, in the introduction we highlighted the need to be careful about interpreting experiments. The helium pore volume calibration and isosteric method are important cases here. But perhaps the most important conclusion in this respect concerns the use of nitrogen at 77 K to characterize active carbons. The use of nitrogen at 77 K and any other probe gas at temperatures close to its triple point should be considered carefully. If they are used to analyze strongly adsorbing materials, problems with diffusivity may well occur. We also observe in the literature that relatively little research is published concerning the prediction

of gas mixture adsorption compared to the amount that is published concerning materials characterization. It seems to us that given the industrial importance of predicting the selectivity, this imbalance needs correction.

Activated carbons are the most important industrial adsorbents and so it is no surprise that there is a great deal of research in this area. It seems somewhat fortunate that for these materials, a relatively simple model of the surface (i.e., the polydisperse independent slit-pore model) is reasonably successful for modeling the adsorption of simple gases, at least at super- or near-critical temperatures. But this does not mean that this strategy will necessarily be successful for other materials or more complex adsorbates or lower temperatures. For example, materials that swell significantly might well require an altogether different approach. And even for inert surfaces, the polydisperse independent pore model is inadequate for systems where it is important to distinguish energetic and geometric heterogeneity, or where pore–pore interactions are important (in amorphous hysteretic systems, for example).

It seems that new methods are needed to predict adsorption in a wide range of materials under a wide range of conditions. The ideal method will be nearly as straightforward as the polydisperse independent pore model and yet be sufficiently sophisticated that it can represent both energetic and geometric nonuniformities and include pore–pore interactions. It should also be quantitatively accurate and flexible so that it can be fitted to reference data. The RMC method of Pikunic and colleagues [223] is certainly sophisticated but is numerically expensive and has yet to demonstrate its accuracy. The lattice DFT method of Kierlik and colleagues and Sarkisov and coworkers [60] is more efficient but lacks sufficient accuracy at molecular length-scales. Finally, even if such a model can be developed, it is not clear what experimental data will be required to characterize materials. Quite possibly, characterization on the basis of a single probe gas will be inadequate.

REFERENCES

1. F. Rouquerol, J. Rouquerol, and K. Sing, "Adsorption by Powders and Porous Solids." Academic Press, New York, 1999.
2. S. J. Gregg and K. S. W. Sing, "Adsorption, Surface Area and Porosity." Academic Press, London, 1991.
3. D. M. Young and A. D. Crowell, "Physical Adsorption of Gases." Butterworths, London, 1962.
4. A. Dabrowski, *Adv. Colloid Interface Sci.* 93, 135 (2001).
5. W. A. Steele, "The Interaction of Gases with Solid Surfaces." Pergamon, Oxford, 1974.
6. D. M. Ruthven, "Principles of Adsorption and Adsorption Processes." Wiley, Chichester, 1984.
7. H. Jankowska, A. Swiatkowski, and J. Choma, "Active Carbon." Ellis Horwood, New York, 1991.
8. R. C. Bansal, J. Donnet, and F. Stoeckli, "Active Carbon." Marcel Dekker, New York, 1988.
9. R. T. Yang, "Gas Separation by Adsorption Processes." Imperial College Press, Singapore, 1997.
10. R. Evans, in "Fundamentals of Inhomogeneous Fluids" (D. Henderson, Ed.), p. 85. Marcel Dekker, New York, 1992.
11. M. B. Sweatman, *Mol. Phys.* 98, 573 (2000).
12. B. Smit and D. Frenkel, "Understanding Molecular Simulation: From Algorithms to Applications." Academic, New York, 1996.
13. M. P. Allen and D. J. Tildesley, "Computer Simulation of Liquids." Clarendon Press, Oxford, 1987.
14. D. Nicholson and N. G. Parsonage, "Computer Simulation and the Statistical Mechanics of Adsorption." Academic Press, London, 1982.
15. D. Enke, F. Janowski, and W. Schwieger, *Microporous Mesoporous Mater.* 60, 19 (2003).
16. F. A. Escobedo and J. J. de Pablo, *Phys. Rep.* 318, 86 (1999).
17. S. Sircar, T. C. Golden, and M. B. Rao, *Carbon* 34, 1 (1996).
18. P. J. F. Harris, *Int. Mater. Rev.* 42, 206 (1997).
19. F. Rodriguez-Reinoso and A. Linares-Solano, in "Chemistry and Physics of Carbon" (P. A. Thrower, Ed.), Vol. 21, Marcel Dekker, New York, 1988.
20. P. J. F. Harris, A. Burian, and S. Duber, *Philos. Mag. Lett.* 80, 381 (2000).
21. T. J. Bandosz, M. J. Biggs, K. E. Gubbins, Y. Hattori, T. Iiyama, K. Kaneko, J. Pikunic, and K. Thomson, in "Chemistry and Physics of Carbon" (L. R. Radovic, Ed.), Vol. 28. Marcel Dekker, New York, 2003.
22. L. Sarkisov and P. A. Monson, *Phys. Rev. E* 65, 011202 (2002).
23. E. Kierlik, P. A. Monson, M. L. Rosinberg, and G. Tarjus, *J. Phys.: Condens. Matter* 14, 9295 (2002).
24. M. Schmidt, E. Scholl-Paschinger, J. Kofinger, and G. Kahl, *J. Phys.: Condens. Matter* 14, 12099 (2002).
25. V. Krakoviack, E. Kierlik, M. L. Rosinberg, and G. Tarjus, *J. Chem. Phys.* 115, 11289 (2001).
26. M. L. Lastoskie and K. E. Gubbins, *Adv. Chem. Eng.* 28, 203 (2001).
27. P. I. Ravikovitch, A. Vishnyakov, R. Russo, and A. V. Neimark, *Langmuir* 16, 2311 (2000).

28. M. B. Sweatman and N. Quirke, *J. Phys. Chem. B* 105, 1403 (2000).
29. M. J. Bojan and W. A. Steele, *Carbon* 36, 1417 (1998).
30. G. M. Davies and N. A. Seaton, *Carbon* 36, 1473 (1998).
31. W. Gac, A. Patrykiejew, and S. Sokolowski, *Thin Solid Films* 298, 22 (1997).
32. D. Lozano-Castello, D. Cazorla-Amoros, A. Linares-Solano, and D. F. Quinn, *J. Phys. Chem. B* 106, 9372 (2002).
33. P. Kowalczyk, A. P. Terzyk, and P. A. Gauden, *Langmuir* 18, 5406 (2002).
34. E. A. Ustinov and D. D. Do, *Langmuir* 18, 4637 (2002).
35. C. Nguyen and D. D. Do, *Langmuir* 15, 3608 (1999).
36. R. J. Dombrowski, D. R. Hyduke, and M. L. Lastoskie, *Langmuir* 16, 5041 (2000).
37. Z. Y. Ryu, J. T. Zheng, M. Z. Wang, and B. J. Zhang, *Carbon* 37, 1257 (1999).
38. M. L. Lastoskie, K. E. Gubbins, and N. Quirke, *J. Phys. Chem. US* 97, 4786 (1993).
39. N. A. Seaton, J. P. R. B. Walton, and N. Quirke, *Carbon* 27, 853 (1989).
40. P. Kowalczyk, A. P. Terzyk, P. A. Gauden, R. Leboda, E. Szmechtig-Gauden, G. Rychlicki, Z. Y. Ryu, and H. Q. Rong, *Carbon* 41, 1113 (2003).
41. A. M. Puziy, O. I. Poddubnaya, A. Martinez-Alonso, F. Suarez-Garcia, and J. M. D. Tascon, *Appl. Surf. Sci.* 200, 196 (2002).
42. D. P. Cao, W. C. Wang, Z. G. Shen et al., *Carbon* 40, 2359 (2002).
43. M. V. Lopez-Ramon, J. Jagiello, T. J. Bandosz, and N. A. Seaton, *Langmuir* 13, 4435 (1997).
44. C. Conteseu, J. Jagiello, and J. A. Schwartz, *Langmuir* 9, 1754 (1997).
45. J. Jagiello, T. J. Bandosz, and J. A. Schwartz, *Carbon* 32, 1026 (1994).
46. N. Kobayashi, T. Enoki, C. Ishii, K. Kaneko, and M. Endo, *J. Chem. Phys.* 109, 1983 (1998).
47. A. V. Neimark and P. I. Ravikovitch, *Langmuir* 13, 5148 (1997).
48. A. L. Myers and P. A. Monson, *Langmuir* 18, 10261 (2002).
49. E. Ozdemir, B. I. Morsi, and K. Schroeder, *Langmuir* 19, 9764 (2003).
50. K. Murata, M. El-Merraoui, and K. Kaneko, *J. Chem. Phys.* 114, 4196 (2001).
51. J. S. Rowlinson and B. Widom, "Molecular Theory of Capillarity." Oxford University Press, Oxford, 1982.
52. D. E. Sullivan and M. M. Telo da Gama, in "Fluid Interfacial Phenomena" (C. A. Croxton, Ed.), p. 45. Wiley, Chichester, 1986.
53. D. Henderson, "Fundamentals of Inhomogeneous Fluids." Marcel Dekker, New York, 1992.
54. R. Evans, *J. Phys.: Condens. Matter* 2, 8989 (1990).
55. R. Evans and U. M. B. Marconi, *Chem. Phys. Lett.* 114, 415 (1985).
56. W. M. Thomson, *Philos. Mag.* 42, 448 (1871).
57. J. P. R. B. Walton and N. Quirke, *Mol. Sim.* 2, 361 (1989).
58. R. Evans and U. M. B. Marconi, *Phys. Rev. A* 32, 3817 (1985).
59. E. Kierlik, M. L. Rosinberg, G. Tarjus, and P. Viot, *Phys. Chem. Chem. Phys.* 3, 1201 (2001).
60. E. Kierlik, P. A. Monson, M. L. Rosinberg, L. Sarkisov, and G. Tarjus, *Phys. Rev. Lett.* 87, 055701 (2001).
61. H. J. Woo, L. Sarkisov, and P. A. Monson, *Langmuir* 17, 7472 (2001).
62. K. Morishige and N. Tateishi, *J. Chem. Phys.* 119, 2301 (2003).
63. N. A. Seaton, *Chem. Eng. Sci.* 46, 1895 (1991).
64. A. V. Neimark, P. I. Ravikovitch, and A. Vishnyakov, *Phys. Rev. E* 65, 031505 (2002).
65. P. I. Ravikovitch and A. V. Neimark, *Colloid Surface A* 187, 11 (2001).
66. A. V. Neimark, P. I. Ravikovitch, and A. Vishnyakov, *Phys. Rev. E* 62, R1493 (2000).
67. A. V. Neimark and P. I. Ravikovitch, *Phys. Rev. E* 62, 4611 (2000).
68. D. H. Everett, in "The Solid-Gas Interface" (E. A. Flood, Ed.), Vol. 2. Marcel Dekker, London, 1967.
69. L. Sarkisov and P. A. Monson, *Langmuir* 17, 7600 (2001).
70. A. Vishnyakov and A. V. Neimark, *Langmuir* 19, 3240 (2003).
71. J. C. Groen, L. A. A. Peffer, and J. Perez-Ramirez, *Microporous Mesoporous Mater.* 60, 1 (2003).
72. P. I. Ravikovitch and A. V. Neimark, *Langmuir* 18, 1550 (2002).
73. J. K. Brennan, K. T. Thomson, and K. E. Gubbins, *Langmuir* 18, 5438 (2002).
74. M. Nakashima, S. Shimada, M. Inagaki, and T. A. Centeno, *Carbon* 33, 1301 (1995).
75. H. Dominguez, M. P. Allen, and R. Evans, *Mol. Phys.* 96, 209 (1999).
76. R. Radhakrishnan, K. E. Gubbins, and M. Sliwinska-Bartkowiak, *J. Chem. Phys.* 116, 1147 (2002).
77. R. Radhakrishnan, K. E. Gubbins, and M. Sliwinska-Bartkowiak, *J. Chem. Phys.* 112, 11048 (2000).
78. M. Schneemilch, N. Quirke, and J. R. Henderson, *J. Chem. Phys.* 120, 2901 (2004).
79. M. W. Maddox, N. Quirke, and K. E. Gubbins, *Mol. Sim.* 19, 267 (1997).
80. A. R. Turner and N. Quirke, *Carbon* 36, 1439 (1998).
81. R. Radhakrishnan and K. E. Gubbins, *Mol. Phys.* 96, 1249 (1999).
82. R. Radhakrishnan, K. E. Gubbins, and M. Sliwinska-Bartkowiak, *Phys. Rev. Lett.* 89, 076101 (2002).
83. R. Radhakrishnan, K. E. Gubbins, A. Watanabi, and K. Kaneko, *J. Chem. Phys.* 111, 9058 (1999).
84. P. W. Atkins, "Physical Chemistry." Oxford University Press, Oxford, 1998.
85. D. D. Do, C. Nguyen, and H. D. Do, *Colloids Surf. A* 187, 51 (2001).
86. S. Scaife, P. Kluson, and N. Quirke, *J. Phys. Chem. B* 104, 313 (2000).
87. M. L. Lastoskie, N. Quirke, and K. E. Gubbins, *Stud. Surf. Sci. Catal.* 104, 745 (1997).
88. N. Quirke and S. R. R. Tennison, *Carbon* 34, 1281 (1996).
89. P. Kluson and S. Scaife, *J. Porous Mater.* 9, 115 (2002).
90. M. B. Sweatman and N. Quirke, *Mol. Sim.* 27, 295 (2001).
91. M. B. Sweatman and N. Quirke, *Langmuir* 17, 5011 (2001).

92. F. A. Escobedo, *J. Chem. Phys.* 113, 8444 (2000).
93. J. Shen and P. A. Monson, *Mol. Phys.* 100, 2031 (2002).
94. J. Milewska-Duda, J. Duda, A. Nodzenski, and J. Lakatos, *Langmuir* 16, 5458 (2000).
95. A. L. Myers and J. M. Prausnitz, *AIChE J.* 11, 121 (1965).
96. D. M. Shen, M. Bulow, F. Siperstein, M. Engelhard, and A. L. Myers, *Adsorption* 6, 275 (2000).
97. H. H. Pan, J. A. Ritter, and P. B. Balbuena, *Langmuir* 14, 6323 (1998).
98. T. Vuong and P. A. Monson, *Langmuir* 12, 5425 (1996).
99. S. Brunauer, "The Adsorption of Gases and Vapours." Oxford University Press, London, 1945.
100. S. Sircar, R. Mohr, C. Ristic, M. B. Rao, *J. Phys. Chem. B* 103, 6539 (1999).
101. D. Chandler, "Introduction to Modern Statistical Mechanics." Oxford University Press, New York, 1987.
102. C. Ebner and W. F. Saam, *Phys. Rev. B* 35, 1822 (1987).
103. D. P. Landau and K. Binder, *Phys. Rev. B* 41, 4633 (1990).
104. K. Binder and D. P. Landau, *J. Chem. Phys.* 96, 1444 (1992).
105. E. V. Votyakov, Y. K. Tovbin, J. M. D. MacElroy, and A. Roche, *Langmuir* 15, 5713 (1999).
106. A. J. Ramirez-Pastor, D. Stacchiola, M. S. Nazzarro, J. L. Riccardo, and G. Zgrablich, *Surf. Sci.* 449, 43 (2000).
107. F. Bulnes, A. J. Ramirez-Pastor, and V. D. Pereyra, *J. Mol. Cat. A* 167, 129 (2001).
108. P. Rocken and P. Tarazona, *J. Chem. Phys.* 105, 2034 (1996).
109. A. Papadopoulou, F. van Swol, and U. M. B. Marconi, *J. Chem. Phys.* 97, 6942 (1992).
110. A. P. Malanoski and F. van Swol, *Phys. Rev. E* 66, 041602 (2002).
111. P. Hohenberg and W. Kohn, *Phys. Rev.* 136, B864 (1964).
112. W. Kohn and L. J. Sham, *Phys. Rev.* 140, A1133 (1965).
113. N. D. Mermin, *Phys. Rev.* 137, A1441 (1965).
114. R. Evans, *Adv. Phys.* 28, 143 (1979).
115. C. Ebner, W. F. Saam, and D. Stroud, *Phys. Rev. A* 14, 2264 (1976).
116. W. F. Saam and C. Ebner, *Phys. Rev. A* 15, 2566 (1977).
117. J. P. Hansen and I. R. McDonald, "Theories of Simple Liquids." Academic, London, 1986.
118. A. Gonzalez, J. A. White, F. L. Roman, S. Velasco, and R. Evans, *Phys. Rev. Lett.* 79, 2466 (1997).
119. J. A. White and A. Gonzalez, *J. Phys.: Condens. Matter* 14, 11907 (2002).
120. M. B. Sweatman, *J. Phys.: Condens. Matter* 15, 3875 (2003).
121. C. W. Woodward, *J. Chem. Phys.* 94, 3183 (1991).
122. E. Kierlik and M. L. Rosinberg, *J. Chem. Phys.* 99, 3950 (1993).
123. M. B. Sweatman, *Phys. Rev. E* 63, 031102 (2001).
124. M. B. Sweatman, *Phys. Rev. E* 65, 011102 (2002).
125. J. D. Weeks, D. Chandler, and H. C. Andersen, *J. Chem. Phys.* 54, 5237 and 5422 (1971).
126. N. F. Carnahan and K. E. Starling, *J. Chem. Phys.* 51, 635 (1969).
127. D. L. Valladares, F. R. Reinoso, and G. Zgrablich, *Carbon* 36, 1491 (1998).
128. P. Tarazona, *Phys. Rev. A* 31, 2672 (1985).
129. P. I. Ravikovitch, A. Vishnyakov, and A. V. Neimark, *Phys. Rev. E* 64, 011602 (2001).
130. A. V. Neimark, P. I. Ravikovitch, and A. Vishnyakov, *J. Phys.: Condens. Matter* 15, 347 (2003).
131. P. Kluson, S. Scaife, and N. Quirke, *Sep. Purif. Technol.* 20, 15 (2000).
132. K. M. Steele and W. J. Koros, *Carbon* 41, 253 (2003).
133. Z. Y. Ryu, J. T. Zheng, M. H. Wang, and B. J. Zhang, *J. Colloid Interface Sci.* 230, 312 (2000).
134. M. Kruk, M. Jaroniec, and J. Choma, *Carbon* 36, 1447 (1998).
135. Y. Rosenfeld, *Phys. Rev. Lett.* 63, 980 (1989).
136. S. Phan, E. Kierlik, M. L. Rosinberg, B. Bildstein, and G. Kahl, *Phys. Rev. E* 48, 618 (1993).
137. E. Kierlik and M. L. Rosinberg, *Phys. Rev. A* 42, 3382 (1990).
138. G. S. Heffelfinger, K. E. Gubbins, U. Marini Bettolo Marconi, and F. van Swol, *Mol. Sim.* 2 (1989).
139. Z. Tan, K. E. Gubbins, U. Marini Bettolo Marconi, and F. van Swol, *J. Chem. Phys.* 90, 3704 (1989).
140. M. Schmidt, *Phys. Rev. E* 62, 4976 (2000).
141. P. Tarazona, *Phys. Rev. Lett.* 84, 694 (2000).
142. Y. Rosenfeld, M. Schmidt, H. Lowen, and P. Tarazona, *J. Phys.: Condens. Matter* 8, L577 (1996).
143. L. J. D. Frink and A. G. Salinger, *J. Comput. Phys.* 159, 407 (2000).
144. J. L. Lebowitz, *Phys. Rev.* 133, A895 (1964).
145. N. N. Neugebauer and M. V. Szombathely, *Stud. Surf. Sci. Catal.* 128, 99 (2000).
146. J. A. Barker and D. Henderson, *J. Chem. Phys.* 47, 4714 (1967).
147. F. Lado, *Phys. Lett. A* 89, 196 (1982).
148. Y. Rosenfeld, *J. Chem. Phys.* 98, 8126 (1993).
149. B. Q. Lu, R. Evans, and M. M. Telo da Gamma, *Mol. Phys.* 55, 1319 (1985).
150. J. P. R. B. Walton and N. Quirke, *Chem. Phys. Lett.* 129, 382 (1986).
151. D. Nicholson, *J. Chem. Soc. Farad. Trans.* 92, 1 (1996).
152. R. P. Feynman, "Statistical Mechanics." Perseus Books, Reading, MA, 1998.
153. M. Jorge and N. A. Seaton, *Mol. Phys.* 100, 2017 (2002).
154. D. M. Heyes and F. van Swol, *J. Chem. Phys.* 75, 5051 (1981).
155. D. H. L. Yau, S. Y. Liem, and K. Y. Chan, *J. Chem. Phys.* 101, 7918 (1994).
156. G. L. Deitrick, L. E. Scriven, and H. T. Davis, *J. Chem. Phys.* 90, 2370 (1989).
157. D. A. Kofke and P. T. Cummings, *Mol. Phys.* 92, 973 (1997).
158. A. Z. Panagiotopoulos, *Mol. Phys.* 61, 813 (1987).

159. D. Fincham, D. J. Tildesley, and N. Quirke, *J. Chem. Phys.* 84, 4535 (1986).
160. A. Z. Panagiotopoulos, *Mol. Sim.* 9, 1 (1992).
161. E. A. Escobedo, *J. Chem. Phys.* 115, 5642 (2001).
162. T. Kristof and J. Liszi, *Mol. Phys.* 94, 519 (1998).
163. J. N. C. Lopes and D. J. Tildesley, *Mol. Phys.* 92, 187 (1997).
164. W. R. Smith and B. Triska, *J. Chem. Phys.* 100, 3019 (1994).
165. M. B. Sweatman and N. Quirke, *Mol. Sim.* 30, 23 (2004).
166. A. Z. Panagiotopoulos, N. Quirke, M. Stapleton, and D. J. Tildesley, *Mol. Phys.* 63, 527 (1988).
167. S. C. McGrother and K. E. Gubbins, *Mol. Phys.* 97, 955 (1999).
168. W. R. Smith and H. L. Vortler, *Chem. Phys. Lett.* 249, 470 (1996).
169. A. Z. Panagiotopoulos, *Mol. Phys.* 62, 701 (1987).
170. M. L. Lastoskie, K. E. Gubbins, and N. Quirke, *Langmuir* 9, 2693 (1993).
171. A. Vishnyakov and A. V. Neimark, *J. Phys. Chem. B* 105, 7009 (2001).
172. K. Kiyohara, T. Spyriouni, K. E. Gubbins, and A. Z. Panagiotopoulos, *Mol. Phys.* 89, 965 (1996).
173. M. Mehta and D. A. Kofke, *Chem. Eng. Sci.* 49, 2633 (1994).
174. N. B. Wilding, *Phys. Rev. E* 52, 602 (1995).
175. N. B. Wilding, *J. Phys.: Condens. Matter* 9, 585 (1997).
176. I. Langmuir, *J. Am. Chem. Soc.* 38, 2221 (1916).
177. F. Dreisback, R. Staudt, and J. U. Keller, *Adsorption J. Int. Ads. Soc.* 5, 215 (1999).
178. J. U. Keller, *Physica A* 166, 173 (1990).
179. E. Bottani and W. A. Steele, *Adsorption* 5, 81 (1999).
180. A. D. Soule, C. A. Smith, X. N. Yang, and L. T. Limi, *Langmuir* 17, 2950 (2001).
181. M. Sudibandriyo, Z. J. Pan, J. E. Fitzgerald, R. L. Robinson, and E. A. M. Gasem, *Langmuir* 19, 5323 (2003).
182. L. S. Cheng and R. T. Yang, *Adsorption* 1, 187 (1995).
183. K. Wang and D. D. Do, *Adsorption* 5, 25 (1999).
184. C. E. Webster and R. S. Drago, *Microporous Mesoporous Mater.* 33, 291 (1999).
185. N. V. Choudhury, R. V. Jasra, and S. G. T. Bhat, *Sep. Sci. Tech.* 30, 2337 (1995).
186. V. Gusev, J. A. O'Brien, C. R. C. Jensen et al., *AIChE J.* 42, 2773 (1996).
187. L. P. Ding and S. K. Bhatia, *Carbon* 39, 2215 (2001).
188. M. Carsky and D. D. Do, *Adsorption* 5, 183 (1999).
189. W. S. Appel, M. D. LeVan, and J. E. Finn, *Ind. Eng. Chem. Res.* 37, 4774 (1998).
190. R. Staudt, F. Dreisback, and J. U. Keller, *Adsorption* 4, 57 (1998).
191. S. M. Taqvi and M. D. LeVan, *Ind. Eng. Chem. Res.* 36, 2197 (1997).
192. J. Ghassemzadeh, L. F. Xu, and T. T. F. A. Tsotsis, *J. Phys. Chem. B* 104, 3892 (2000).
193. L. F. Xu, T. T. Tsotsis, and M. Sahimi, *J. Chem. Phys.* 114, 7196 (2001).
194. J. A. Given and G. Stell, *J. Chem. Phys.* 97, 4573 (1992).
195. W. G. Madden and E. D. Glandt, *J. Stat. Phys.* 51, 537 (1988).
196. M. Schmidt, *Phys. Rev. E* 66, 041108 (2002).
197. J. A. Given, *Phys. Rev. A* 45, 816 (1992).
198. M. Mezard, G. Parisi, and M. A. Virasoro, "Spin Glass Theory and Beyond." World Scientific, Singapore, 1987.
199. W. G. Madden, *J. Chem. Phys.* 96, 4522 (1992).
200. W. H. Press, S. A. Teukolsky, W. T. Vetterling, and B. P. Flanney, "Numerical Recipes in Fortran 77: The Art of Scientific Computing." Cambridge University Press, Cambridge, 1992.
201. C. Vega, R. D. Kaminsky, and P. A. Monson, *J. Chem. Phys.* 99, 3003 (1993).
202. W. A. Steele, *Surf. Sci.* 36, 317 (1973).
203. K. Kaneko, R. F. Cracknell, and D. Nicholson, *Langmuir* 10, 4606 (1994).
204. G. M. Davies, N. A. Seaton, and V. S. Vassiliadis, *Langmuir* 15, 8235 (1999).
205. M. Schmidt, *J. Phys.: Condens. Matter* 15, S101 (2003).
206. S. Figueroa-Gerstenmaier, F. J. Blas, J. B. Avalos, and L. F. Vega, *J. Chem. Phys.* 118, 830 (2003).
207. P. I. Ravikovitch, S. C. O. Domhnaill, A. V. Neimark, F. Schuth, and K. K. Unger, *Langmuir* 11, 4765 (1995).
208. J. P. Olivier and M. L. Occelli, *Microporous Mesoporous Mater.* 57, 291 (2003).
209. J. P. Olivier and M. L. Occelli, *J. Phys. Chem. B* 105, 623 (2001).
210. H. Lowen, *J. Phys.: Condens. Matter* 14, 11897 (2002).
211. D. Goulding, J. P. Hansen, and S. Melchionna, *Phys. Rev. Lett.* 85, 1132 (2000).
212. C. Gu, G. H. Gao, and Y. X. Yu, *J. Chem. Phys.* 119, 488 (2003).
213. V. Gusev, J. A. O'Brien, and N. A. Seaton, *Langmuir* 13, 2815 (1997).
214. S. Samios, A. K. Stubos, N. K. Kanellopoulos, R. F. Cracknell, G. K. Papadopoulos, and D. Nicholson, *Langmuir* 13, 2795 (1997).
215. M. B. Sweatman and N. Quirke, submitted to *J. Phys. Chem. B.*
216. S. Samios, G. K. Papadopoulos, T. Steriotis, and A. K. Stubos, *Mol. Sim.* 27, 441 (2001).
217. E. Kozak, G. Chmiel, A. Patrykiejew, and S. Sulzolowski, *Phys. Lett. A* 189, 94 (1994).
218. L. D. Gelb, *Mol. Phys.* 100, 2049 (2002).
219. J. K. Brennan, T. J. Bandosz, K. T. Thomson, and K. E. Gubbins, *Colloid Surf. A* 187, 539 (2001).
220. E. I. Segarra and E. D. Glandt, *Chem. Eng. Sci.* 49, 2953 (1994).
221. S. Gavalda, K. E. Gubbins, Y. Hanzawa, K. Kaneko, and K. T. Thomson, *Langmuir* 18, 2141 (2002).
222. K. T. Thomson and K. E. Gubbins, *Langmuir* 16, 5761 (2000).

223. J. Pikunic, C. Clinard, N. Cohaut, K. E. Gubbins, J. M. Guet, R. J. M. Pellenq, I. Rannov, and J. N. Rouzaud, *Langmuir* 19, 8565 (2003).
224. J. Pikunic, R. J. Pellenq, K. T. Thomson et al., *Stud. Surf. Sci. Catal.* 132, 647 (2001).
225. A. Vishnyakov, P. I. Ravikovitch, and A. V. Neimark, *Langmuir* 15, 8736 (1999).
226. R. F. Cracknell, D. Nicholson, S. R. Tennison, and J. Bromhead, *Adsorption* 2, 193 (1996).
227. P. N. Aukett, N. Quirke, S. Riddiford, and S. R. Tennison, *Carbon* 30, 913 (1992).
228. G. M. Davies and N. A. Seaton, *AIChE J.* 46, 1753 (2000).
229. M. Heuchel, G. M. Davies, E. Buss, and N. A. Seaton, *Langmuir* 15, 8695 (1999).
230. V. Gusev and J. A. O'Brien, *Langmuir* 14, 6328 (1998).
231. S. Qiao, K. Wang, and X. Hu, *Langmuir* 16, 5130 (2002).
232. R. Bai, *Chem. Eng. Sci.* 55, 5165 (2000).
233. G. O. Wood, *Carbon* 40, 231 (2002).
234. K. Nieszporek, *Adsorption J. Int. Ads. Soc.* 8, 45 (2002).
235. J. S. Rowlinson and F. L. Swinton, "Liquids and Liquid Mixtures," Butterworths, London, 1982.
236. A. Malek and S. Farooq, *AIChE J.* 42, 3191 (1996).
237. N. Sundaram, *Langmuir* 11, 3223 (1995).
238. R. F. Cracknell and D. Nicholson, *Adsorption* 1, 16 (1995).
239. T. Vuong and P. A. Monson, *Adsorption* 5, 183 (1999).
240. M. B. Sweatman and N. Quirke, *Langmuir* 18, 10443 (2002).
241. K. Wang, S. Z. Qiao, and X. Hu, *Ind. Eng. Chem. Res.* 39, 527 (2000).
242. S. Qiao, K. Wang, and X. Hu, *Langmuir* 16, 1292 (2000).
243. D. P. Valenzuela, A. L. Myers, O. Talu, and I. Zwiebel, *AIChE J.* 34, 397 (1988).
244. K. Wang, S. Z. Qiao, and X. J. Hu, *Sep. Purif. Technol.* 20, 243 (2000).
245. R. Van der Vaart, C. Huiskes, H. Bosch, and T. Reith, *Adsorption* 6, 311 (2000).
246. E. N. Rudisill and D. Levan, *Chem. Eng. Sci.* 47, 1239 (1992).

CHAPTER 7

Sliding Friction at the Atomic Scale

Annalisa Fasolino

Theoretical Physics, IMM, Radboud University Nijmegen, Nijmegen, The Netherlands; van 't Hoff Institute for Molecular Sciences (HIMS), and Van der Waals-Zeeman Institute, Universiteit van Amsterdam, Amsterdam, The Netherlands

CONTENTS

ISBN: 1-58883-047-0

Handbook of Theoretical and Computational Nanotechnology
Edited by Michael Rieth and Wolfram Schommers
Volume 5: Pages (379–436)

1. SLIDING FRICTION: FROM MACROSCOPIC RULES TO MICROSCOPIC UNDERSTANDING

Sliding of two bodies against each other usually leads to friction, which acts against the mutual movement and transforms (part of) the mechanical energy into heat. This phenomenon is one of the oldest problems in physics and certainly one of the most important for practical applications. Nevertheless, so far remarkably little is understood about the fundamental microscopic processes responsible for friction and wear. Recent years have witnessed a surge of interest in understanding the microscopic origin of friction as a result of the increased control in surface preparation, the development of local probes like the atomic force microscope and friction force microscope and of the quartz crystal microbalance (QCM), and the interest for possible applications in nanotechnology. The final goal of research on friction at the atomic scale is to become able to control and inhibit/enhance friction by understanding the relevant mechanisms of energy dissipation in a given situation. From the experimental point of view, atomic force microscopy (AFM) studies on clean surfaces are expected to clarify the intrinsic aspects of friction by eliminating most of the unknown effects related to surface asperities, contaminants, and roughness. These conditions define a problem that becomes tractable from a theoretical point of view. The findings of these experimental techniques have attracted the interest of theoreticians during the past years also thanks to the currently available supercomputers that make it possible to carry out numerical simulations of systems approaching the size of those of interest for the understanding of the above AFM measurements albeit not yet on the appropriate timescales.

The microscopic origin of sliding friction is still largely unknown. This is in a sense not surprising because sliding friction (or just friction in the following) is essentially a macroscopic concept. Friction is defined as the force that opposes the beginning and continuation of motion of a body sliding onto another. This macroscopic force arises from microscopic interactions between the atoms of the two materials, but a detailed description of all the processes that can occur at a real interface is not only prohibitive but also not needed. In fact, this effective force can be described phenomenologically by means of very simple rules that have been known for more than 200 years.

Leonardo da Vinci had observed that the friction force is independent of the area of contact, as beautifully illustrated in a drawing of the *Codex Atlanticus* reported in the book on sliding friction by Bo Persson [1] and in the review article by Jacqueline Krim [2] showing identical blocks of wood being pulled with sides of different size touching the table. The phenomenological laws governing sliding friction in a very wide range of conditions have then been discovered and rediscovered many times and now go under the name of Amonton or Coulomb. In most experimental conditions, for a given pair of contacting surfaces, the friction force is just proportional to the load and is independent of the contact area, surface roughness, and sliding velocity. The force needed to put a body in motion is higher than that needed to keep it in motion, namely static friction is higher than dynamic friction.

Despite the fact that the contacting surfaces are in general poorly characterized, with asperities and polluted in several ways, these simple rules have been good enough to identify, by trial and error, pairs of materials that have high or low friction as needed. It is just this simplicity that makes a phenomenological approach so powerful, all complex processes occurring at the interface, being cast into few rules that can be used in engineering applications as well as in everyday life. Everybody knows which shoes to wear when the ground is slippery. However, these simple rules cannot be derived by fundamental laws, and indeed deviations from them are often observed [3]. The static friction force is often found to increase with time, a phenomenon called aging, and the kinetic friction is not constant but increases linearly at high velocity.

At the microscopic level, the simple macroscopic laws of friction become completely inadequate. Studies at the molecular level often reveal a behavior that is markedly different from that of macroscopic bearings. In this regime, dissipation of mechanical energy is dominated by atom–atom interactions, surface registry, vibrational and excitation spectra, and by nonlinear dynamics leading to new phenomena like velocity-dependent forces and even possible frictionless sliding.

Friction processes take place on a large spectrum of length scales, but a real understanding of this phenomenon begins at the nanometer scale. The interest in understanding the atomic-scale processes giving rise to friction is not only motivated by the hope to understand and control macroscopic friction in the future, but it is interesting in itself for fundamental physics as well as for application in nanotechnology. Atomic-scale processes that can lead to energy dissipation are phononic and electronic excitations, rupture or modifications of chemical bonds, and creation and diffusion of defects at the interface. One of the challenges for computational physics is the need to examine processes that occur on very different timescales, femtoseconds for electronic excitations, picoseconds for phonons up to much longer timescales of up to seconds for soft phonon modes and conformational changes in organic layers [4].

The questions are formidable, and the possible applications and, in general, the relevance for society is enormous.

In this quest, as theorists we are still very poorly armed. A few simplified, nonlinear models have been studied extensively and have indeed contributed to form some important concepts of friction at the atomic scale, particularly about the role of commensurability of the contacting surfaces and of stability and instability of a sliding state. In most of these models, the substrate is rigid, one-dimensional (1D), and at zero temperature. However, simple as they are, nonlinear dynamical systems are still a challenge, particularly for driven and damped systems with many degrees of freedom [5], and their study forms a field of research in itself where both physicists and mathematicians are very active. Another possible approach is via extensive molecular dynamics simulations with more realistic atomic interactions and geometries. This route is usually taken to understand processes of wear and plastic deformations and the role of thin layers of lubricant between solid surfaces. The time and length scales for a truly realistic approach are still beyond reach as will be discussed in more detail later and the computer simulations so heavy that only few cases can be studied.

The current status of research has been the subject of several review articles, each with its focus and merits. A general introduction can be found at the Web site devoted to friction of the University of Basel [6]. The book of Persson [1, 7] has quickly become a classic in the field. Its focus is on models that can give a rationale for the behavior of lubricated contacts and macroscopic friction, which are the ones currently most relevant for industrial applications. The review by Singer [8] and that by Robbins and Müser [9] are instead dedicated to a review of the models put forward to describe friction at the atomic scale, the latter being particularly focussed on realistic molecular dynamics approaches. The reviews by Morita, Fujisawa, and Sugawara [10], by Carpick and Salmeron [11], by Gnecco, Bennewitz, Gyalog, and Meyer [12] and by Krim [2] are mostly focused on experimental techniques and report results for many different sliding systems as well as a discussion of some interpretative theoretical models. In particular, [10–12] are focused on AFM studies, whereas [2] illustrates the use of the QCM and reports also a beautiful historical introduction to the topic of friction.

When confronted with the task of writing this review article, I have felt overwhelmed by the difficulty of summarizing a field of research that is so young and so complex. My motivation in writing this article is to attract the attention of people working in different fields of theoretical and computational physics on this topic and to provide a basis for further studies. Due to its phenomenological approach, the study of macroscopic friction, also called *tribology* (literally meaning science of rubbing), has been in the hands of a large but rather closed and applied engineering community. Friction at the atomic scale, or *nanotribology*, instead can be interesting and can profit from the knowledge coming from many fields, from mathematics to material science, so that an article in this broad handbook can have a role in enlarging the community of scientists contributing to this important topic.

1.1. Focus and Outline of This Review

This review gives a detailed account of the most used nonlinear models for sliding friction that have led to concept forming. For their generality, similar models have been studied already in different contexts, and they have accounted for the first burst of theoretical and computational activity in the field. Besides providing, at present, the most solid results, they also constitute a bulk of knowledge that cannot be ignored before proceeding to more realistic approaches. Details of computational techniques are given in the last section, which can be skipped if the reader is already familiar with them.

This review is organized as follows. In Section 2, the phenomenology of macroscopic friction is briefly reviewed and will serve as a basis to go over to the new phenomena occurring at the nanoscale.

In Section 3, the conceptual difference between static and dynamic friction will be qualitatively introduced. An intuitive view of how nonlinear interactions between the sliding surfaces can lead to dissipative processes as a consequence of the relative motion is presented in Section 4.

In Section 5, I will describe the new AFM and QCM experimental techniques that give access to measuring friction at the atomic scale together with key experimental results.

In Section 6, we introduce the first and most insightful nonlinear model of friction at the atomic scale, the Tomlinson model. This model is not only historically important because it has been the first to be proposed to understand the microscopic origin of friction between solid surfaces but is also the most used to analyze AFM experiments. The Tomlinson model consists of just one body, coupled elastically to a moving support and interacting with the substrate via a periodic potential. This model will be discussed in great detail and will be used to make contact with several experimental AFM results, as those described in Section 5. In particular, the Tomlinson model gives account for the observed atomic-scale stick-slip motion in terms of elastic instabilities.

Next, in Section 7 we introduce the Frenkel-Kontorova (FK) model, where the surface layer is modeled by a harmonic chain and the substrate is described, as in the Tomlinson model, by a rigid periodic modulation potential. The FK model is particularly suitable to describe the effects of commensurability between the contacting surfaces that have been shown to play an important role, as discussed within the section on key experimental results. We will first discuss the Hamiltonian version of this model, where no dissipative terms are introduced. It turns out that this model provides a way to describe exactly the onset of friction as due to phononic excitations.

In Section 8, extensions of the FK models to include driving and frictional terms are presented. For driven and damped systems, our knowledge is still fragmented. Only some regimes have been investigated in some detail. These results show that the collective behavior of sliding systems can be extremely complex and that the resulting friction may depend critically on the applied force and damping mechanisms.

In Section 9, we briefly review the results of molecular dynamics (MD) studies of systems with realistic interactions. In Section 10, theoretical challenges, and perspectives are discussed. Finally, relevant numerical methods, and particularly the Langevin approach, are described in Section 11.

2. THE RULES OF MACROSCOPIC SLIDING FRICTION

The phenomenological laws that describe macroscopic friction go under the name of Amonton or Coulomb laws. They can be summarized as follows:

- The static friction force F, which has to be overcome to put a body in motion, is proportional to the load L (often simply the weight of a body) via a coefficient μ that is independent of the contact area and surface roughness, namely

$$F = \mu L \tag{1}$$

  The coefficient of proportionality μ is specific for the pair of surfaces in contact and, if present, of the lubricant layer in between.
- The force needed to put a body in motion is higher than the one needed to keep it in motion, namely the static friction coefficient μ_s is higher than the dynamic friction coefficient μ_k (where the subscript s is for static and k is for kinetic). The friction force is, in not too extreme situations, independent of the sliding velocity. This type of velocity-independent friction is often called dry friction as opposed to viscous friction, which has a linear dependence on velocity.

A careful account of these findings is given in [1, 7], which I briefly summarize here. The fact that static friction depends only on the load and not on the contact area is due to the fact that every macroscopic surface presents some roughness. It is the effective area of contact ΔA, which is much smaller than the whole surface, which will sustain the applied load $L = Mg$, M being the mass of the upper body. By assuming that each junction forming the contact is in a state of incipient plastic flow, namely that it is subjected to the largest compressive stress σ_c that can be sustained by the material without exhibiting plastic deformations, one can write

$$L = Mg = \sigma_c \Delta A \tag{2}$$

a relation that allows estimation of ΔA. For steel on steel, with $\sigma_c = 10^9$ N/m^2, an effective contact area 10^{-5} times smaller than the apparent area of contact is derived [7]. A further step to go over to an estimate of the friction force between nonlubricated surfaces was done around 1940 by Bowden and Tabor [13]. They assumed that the friction force is the force required to shear the junctions of area ΔA between the solids, which is given by $F = \tau_c \Delta A$, where τ_c is the yield stress during shear. By combining this expression with the expression of ΔA derived above, one finds the linear proportionality of the friction force to the applied load, which describes correctly the experimental results as

$$F = \tau_c \Delta A = \frac{\tau_c}{\sigma_c} L \equiv \mu L \tag{3}$$

The values μ_s and μ_k for a variety of systems are reported in Table 7.5 of [1]. For many surfaces that are not intentionally lubricated, the ratio μ_k/μ_s is close to 0.5. This value is also found for most lubricants that interact weakly with the surfaces, like hydrocarbons. For fatty acids and inorganic layered systems, which have stronger interactions with the surfaces, this ratio is close to unity. Qualitatively, a value close to 0.5 is attributed to the presence of a fluidized lubricant layer, whereas a larger value is related to a more organized structure of the lubricant [14].

When a lubricant is present between the sliding surfaces, two regimes can be identified: hydrodynamic lubrication and boundary lubrication [15]. The first is the most used in macroscopic bearings. In this case, the viscous lubricant may develop a pressure that is high enough to keep the surfaces apart. The friction force, which can be calculated using the Navier-Stokes equations of hydrodynamics, increases with increasing sliding velocity. If the velocity becomes small, the pressure developed by the lubricant decreases and the two surfaces can come in solid contact, being separated by only one or few monolayers of lubrication molecules. This is the regime of boundary lubrication where the friction force becomes usually much higher and roughly independent of the sliding velocity. If the load is high enough,

the molecules can even be completely removed from the contact region, leading to very high sliding friction and wear. This phenomenon is usually avoided by adding to the lubricant oil additives like fatty acids, hydrocarbon chains with polar end groups. These molecules will form monolayers tightly bound to the surface. In this regime, the properties of the monolayers in the region of closest contact between the surfaces play a crucial role in determining the macroscopic friction. An understanding at the atomic scale of the response of an adsorbed monolayer to an external driving force is therefore as relevant for the boundary lubrication regime as for the sliding of clean solid surfaces without lubricants. We will come back to this issue in Sections 8 and 9.

3. STATIC *VERSUS* DYNAMIC FRICTION

Here we present an intuitive picture of the different origin of static and dynamic friction, illustrated by the cartoon picture of Fig. 1. Most models of sliding friction at the atomic scale are constructed by considering a mobile set of atoms, representing a tip or an adsorbed atomic layer interacting with a rigid substrate. For the purpose of illustration, it is convenient to represent the mobile atoms by a one-dimensional array of particles connected by springs of natural length b in interaction with a sinusoidal potential V_{per} with period representing the lattice spacing a of the substrate. We will see later that this description is the one given by the Frenkel-Kontorova model [16] described in Section 7.

At rest, the atoms will adjust to minimize their total potential energy. As a result of the competition between the elastic intrachain interactions favoring spacing b and the nonlinear forces due to V_{per} favoring spacing a, the minimum energy configuration will, in general, be a complex function of the ratio a/b and of the ratio between the elastic constants and the amplitude of the periodic potential. For the simple case of a perfectly commensurate match of the lattice parameters of the surfaces in contact (i.e., $a = b$), every atom will find itself in a minimum of the potential. The static friction force, defined as the force needed to bring each atom of the chain up to the top of the potential hills, would be maximal

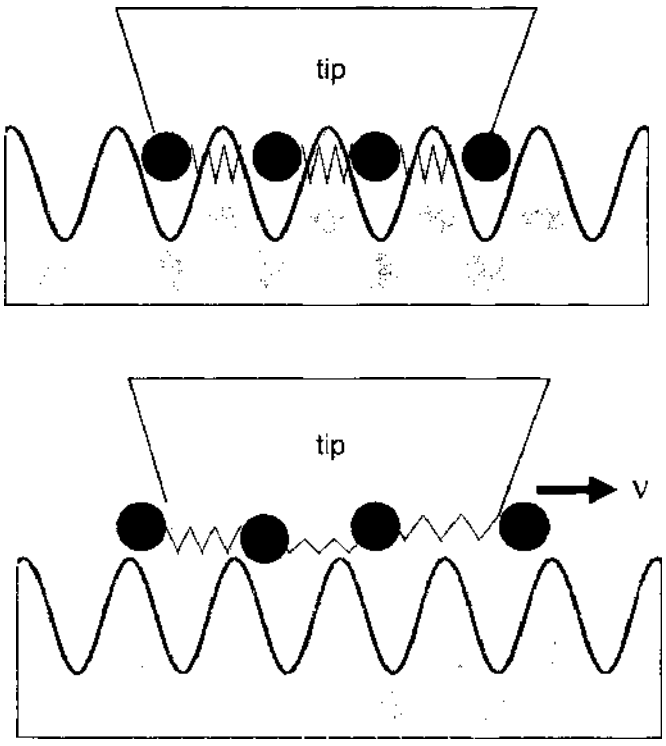

Figure 1. Cartoon description of static and dynamic friction. Top: static friction is the force needed to untrap the system from the energy minimum corresponding to static equilibrium. Bottom: Once the body is in motion, dynamic friction results from all processes that cause the sliding to not occur rigidly, namely from any excitations, such as vibrations of the particles, occurring in the sliding layer or in the substrate (see text).

in this case and proportional to the potential amplitude. The other extreme case occurs when a and b are not a simple fraction of each other (i.e., when their ratio cannot be expressed as a rational number). In this case, the contact is said to be incommensurate. If the interaction with the substrate is not too strong, the positions of the atoms of the chain will be continuously distributed over the periodic potential (see also Fig. 14). In this situation, a small displacement of all atoms would not change the total energy, as on average there will be as many atoms moving downhill and gaining potential energy as atoms moving upwards and loosing potential energy. Therefore, even an infinitesimally small force would be enough to displace the chain, so that the static friction would vanish. Such a situation can be very relevant at the atomic scale for the sliding of two perfectly ordered flat surfaces onto each other. For a generic pair of surfaces and for a generic sliding direction, incommensurability of the lattice parameters is more the rule than the exception, and indeed evidence of this behavior has been experimentally found (see Section 5.3.4).

Once the upper surface starts sliding, be it with finite or vanishing friction force, in absence of dissipative processes, conservation of energy would imply that it could slide indefinitely if it would move as a whole onto the rigid substrate. Dynamic friction results from all processes which cause the sliding to not occur rigidly; namely, that processes of excitations as well as plastic deformations occur during the motion either in the sliding body or in the underlying surface. In Section 7 we will see how, within simplified models, the process of transformation of kinetic energy into heat, leading to dynamic friction, can be followed in detail. In Section 8, dynamic friction is shown to be a strongly nonlinear function of velocity.

4. HOW MOTION CAN LEAD TO DISSIPATION

In the previous section, we have introduced the concept of static and dynamic friction for a simple model of the sliding system.

The key feature that makes it extremely interesting to study the motion onto a *spatially periodic* substrate with period a described by a potential energy of the form

$$V(x) = V_0\left[1 - \cos\left(\frac{2\pi}{a}x\right)\right] \tag{4}$$

is that, in the frame of the center of mass x, which moves with a given sliding velocity v (i.e., $x = vt$), the external potential leads to a *time periodic* force

$$F(t) = -\frac{dV}{dx} = -\frac{2\pi}{a}V_0 \sin\left(\frac{2\pi}{a}vt\right) \tag{5}$$

acting on the moving particles. The frequency

$$\Omega = \frac{2\pi v}{a} \tag{6}$$

is often called the *washboard frequency*. Therefore, the presence of the periodic substrate has two important consequences: first, it brings in the nonlinear forces given by Eq. (5); second, it leads to a time-dependent force that can generate resonances with inherent excitations of the sliding system. These facts are the origin of the complex dynamics exhibited by the model systems that will be described in the following sections.

The washboard frequency can become resonant with particular phonon modes of the sliding system and involve in sequence other modes due to anharmonicities. Therefore, close to these resonances, in a system driven by an external force, a large increase of the driving force leads to only a marginal increase of the average velocity, and the work done is turned into oscillatory motion. The resulting friction as a function of the applied force is highly nonlinear and dependent on the damping rate due to the interactions with the substrate [17]. Conversely, in an undriven, undamped system moving with initial velocity close to some resonances, the excited phonon can couple in cascade to other phonon modes via nonlinear terms leading to a decay of the center of mass velocity [18]. In other words, the motion on the periodic substrate becomes a probe of the spectrum of excitations and anharmonicities of the sliding system.

5. EXPERIMENTAL PROBES OF FRICTION AT THE ATOMIC SCALE

During the past decade, remarkable developments in surface physics and nanotechnology, notably the use of the atomic force microscopes and of the quartz crystal microbalance, have provided the possibility to perform well-defined measurements of friction on well-characterized materials at the micro- and nanoscales. These state-of-the-art local probes with nanometer sensitivity, which are often operated in ultrahigh vacuum (UHV), are proving essential to make a step forward in our understanding of the origin of friction. Here we briefly review the most important techniques and some important experimental results that suggest that the laws of macroscopic friction do not hold at the micro- and nanoscales.

5.1. The Atomic Force and Friction Force Microscopes

The atomic force microscope [19] has become in the past decade one of the most powerful instruments for measuring and imaging surfaces at the nanoscale level. In an AFM instrument, a small sharp tip, typically of 10–100 nm, is attached to a cantilever and brought close to a surface as done also in scanning tunneling microscopy (STM) experiments. The forces due to the interaction of the tip with the surface lead to a deflection of the cantilever, which is usually measured by means of a laser beam deflection method. AFM is suitable to measure metallic as well as nonconducting samples. AFM images of surfaces that show atomic details can be found in many papers and Web sites. A topographic image of the surface is the one obtained by recording the variation of height of the tip, which yields a constant repulsive force while the tip scans the surface.

For measurements of friction, the tip is moved at a constant velocity along given scanning lines on the surface. The lateral forces give rise also to a twisting of the cantilever. When the atomic force microscope is supplemented by a four-quadrant photodetector, this instrument can measure lateral and vertical forces independently [20]. Extremely low forces in the range nN to pN can be detected. The effective forces can be derived from the measured deflection of the cantilever, which is characterized by the three force constants describing elastic deformations for in-plane and vertical distortions. Typically, the force constants characterizing the cantilever are such that the spring constant for torsional in-plane distortions (k_x, k_y) are much stiffer than for vertical deflection (k_z). Moreover, if x is taken along the scanning direction, usually $k_y > k_x$. For a silicon cantilever, these values are estimated on the basis of continuum mechanics in [21] to be $k_x = 4.03$ N/m, $k_y = 101.1$ N/m, $k_z = 0.2$ N/m. The high ratio of torsional and normal spring constant results in a relatively small frictional force signal. The group of Joost Frenken in Leiden has recently developed a new type of cantilever with four arms, the so called tribolever [22, 21], which allows enhancement of the frictional signal by making k_z larger than k_x and k_y. The estimated values for this instrument are $k_x = k_y = 5.75 \pm 0.15$ N/m, $k_z = 26 \pm 1$ N/m [23].

Because the lateral forces in the direction of the motion are by definition the friction forces, this variant of AFM, also called lateral force microscopy (LFM) or friction force microscopy (FFM), has triggered the beginning of the new field of *nanotribology*, the study of friction at the atomic level. We note that studies of friction and adhesion are always done in the so-called contact mode, namely with the tip probing the repulsive short range part of the tip–surface interactions [11]. FFM measurements can be done in several types of environments: UHV, ambient air, controlled atmosphere, and liquids [11]. Here, we will focus on UHV and ambient air measurements.

The first measurements of friction with this technique were performed in 1987 by Mate et al. [24] using a tungsten tip on graphite. At the nanometer scale, the lateral forces measured while scanning the surface show a sawtooth behavior corresponding to what is called *stick-slip* motion. The measured lateral force grows almost linearly until it drops suddenly and then starts growing again. The lateral forces measured on the (100) surface of copper show that the sawtooth periodicity is the one of the underlying surface [25]. This makes that atomically resolved images of surfaces can be obtained also by imaging the lateral forces. The stick-slip behavior observed at the atomic scale can be understood on the basis of simple models such as the Tomlinson model, which we will discuss in detail in Section 6, as due

to the fact that the tip stays predominantly close to potential minima, with sudden jumps among them. A recent detailed theoretical/experimental study [26] of AFM images obtained in this regime on graphite substrates shows, however, that, strictly speaking, the AFM images are not *atomically resolved* but rather *hollow site resolved*, as they reveal the periodicity of the potential minima of the hollow sites of the hexagonal graphite lattice rather than the actual atomic positions. This is shown in Fig. 2. This means that it is not always possible to image the full atomic structure of the surface, as only the minima of the tip–surface interaction potential are in contact with the tip for a significant time. Another important characteristic of the measured friction force is also the hysteresis or friction loops found between forward and backward scans [24].

For completeness, we note that recently the new technique called dynamic force spectroscopy or noncontact force microscopy has been introduced. The method is based on the measurement of the resonance frequency as a function of the resonance amplitude of the oscillated cantilever [27, 28]. This technique has been shown to be able to measure the tip–surface potential with true atomic resolution, allowing also the detection of defects. However, this technique does not allow linking the atomic corrugation to the friction force, and it is therefore not very relevant in the context of this review.

5.2. Quartz Crystal Microbalance

A role as important as that played by AFM studies for the development of nanotribology is that of studies performed by means of the QCM [2]. The technique aims at probing energy dissipation by measuring the conversion of mechanical energy into heat at the molecular level. The mechanisms of energy dissipation are traced back to the generation of phononic and electronic excitation in the sliding layer or in the substrate. The QCM consists of a single crystal of quartz that has very little internal dissipation, so that it oscillates at a very sharp frequency, typically 5–10 MHz, with a quality factor Q near 10^5, depending on its mass and elastic constants. The oscillations are driven by applying a voltage to thin metal electrodes applied on the quartz surface. The QCM has been first used to monitor thin crystal growth

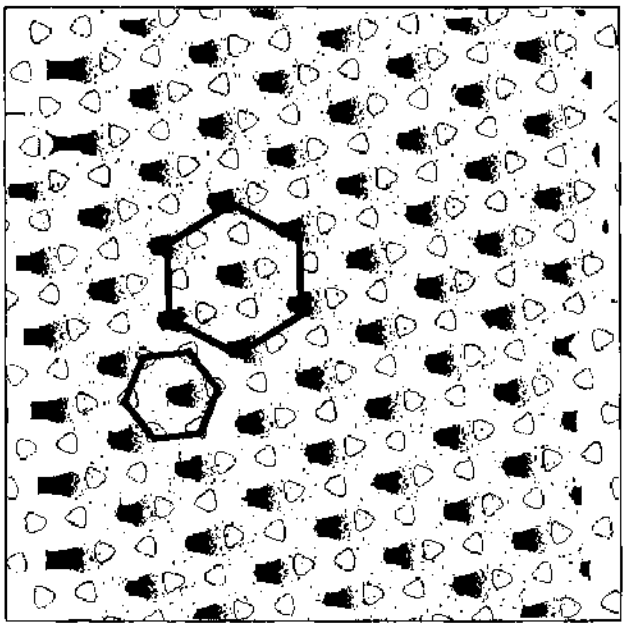

Figure 2. Contour plots of the two-dimensional potential used in [26] to describe the interaction with the graphite substrates. The maxima of the potential, indicated by open triangles, correspond to the positions of the carbon atoms in the surface layer, which form hexagonal rings with lattice spacing of 1.42 Å. The black dots, which represent the tip positions at all times in the simulations, show that the tip stays predominantly at the hollow sites of the surface, so that only these minima of the potential are profiled by the tip. Therefore, the measured lateral forces in AFM experiments show a periodic structure with the periodicity of 2.46 Å of the hollow sites rather than the carbon atomic positions. Reprinted with permission from [26], H. Hölscher et al., *Phys. Rev. B* 57, 2477 (1998). © 1998, American Physical Society.

with submonolayer sensitivity [29]. Thin films can be deposited on the electrodes, lowering the resonance frequency with a shift proportional to the mass of the adsorbates.

Jacqueline Krim and coworkers [30–33] have widened the scope of this instrument by noting that the resonance is broadened by any frictional energy dissipation due to the relative motion of the adsorbate layer and the microbalance. Data obtained with this technique are analyzed under the assumption that the friction force has a viscous behavior proportional to the velocity, which can be written as

$$F = \eta v A_c \qquad \eta = \frac{\rho}{\tau} \tag{7}$$

where A_c is the true area of contact, v is the sliding velocity, and the damping coefficient η is written in terms of ρ, the mass per unit area of the sliding layer, and of a characteristic slip time τ. The solution of the equation of motion of a particle in presence of a constant damping gives an exponentially decaying velocity. The slip time τ represents the time it takes for the film speed to drop to $1/e$ times the original value assuming it is stopped by frictional forces of the type of Eq. (7) alone. A short slip time corresponds to high friction and *vice versa*. The slip time can be derived by the shifts of the inverse quality factor $\delta(Q^{-1})$ and of the frequency δf via the relation [30]

$$\delta(Q^{-1}) = 4\pi\tau\delta f \tag{8}$$

With the QCM, it is possible to measure friction only if it is relatively low so that significant sliding occurs and an appreciable broadening is observed. Therefore, this technique has been mostly used to study the frictional behavior of rare gases on metal surfaces. In this case, the interactions of the adsorbate layer with the metal substrate can be described by weak van der Waals interactions modeled by Lennard-Jones potentials [34–36].

The assumption of a viscous force linear with velocities has been tested experimentally by Mak and Krim [33] and found to hold for complete monolayers both solid and fluid, whereas at lower coverages a sublinear dependence has been observed. The sliding velocities reached in these experiments are estimated to be in the range of μm/s to cm/s [30, 33]. Recently, a promising new technique called quartz crystal resonator has been proposed [37] to reach velocities of a few m/s.

The results obtained by the QCM are of extreme importance in addressing the role of commensurability between the lattices of the sliding layer and of the substrate and to study the contribution of electronic excitations to frictions. We will describe the most significant experimental results on these two aspects in Sections 5.3.4 and 5.3.5, respectively.

5.3. Key Experimental Results

5.3.1. Dependence of Friction on Contact Area

According to the macroscopic definition given by Eq. (1), the ratio of lateral to vertical forces yields the friction coefficient. Therefore, FFM can in principle be used to measure the friction coefficient directly [38]. However, the usefulness of this macroscopic definition of the friction coefficient is due to the independence of the macroscopic friction force from the apparent contact area as discussed in Section 1. Intuitively, one does not expect this relation to hold when two perfectly ordered, flat surfaces are brought into contact. In FFM experiments, however, only the surface can be perfectly characterized, whereas such a control of the tip is still beyond reach. The dependence of the contact area on the load has been interpreted in terms of models of continuum mechanics that describe the contact area between a sphere (tip) and a plane (sample) first studied by Hertz [39], who showed that the contact area A grows with the load L as a power law with exponent 2/3, namely $A \sim L^{2/3}$. This relation implies the same dependence $\sim L^{2/3}$ for the friction force as a consequence of Eq. (1). The dependence on the relative effect of elasticity to adhesion, which is not included in the Hertzian model, has been incorporated by two refined models, the Johnson-Kendall-Roberts (JKR) [40] and the Derjaguin, Müller, Toporov (DMT) [41] models, which apply to soft contacts with short-range adhesion and to stiff materials with long-range adhesion, respectively.

The results of Carpick et al. [42] on mica have been interpreted in terms of the JKR [40] model, whereas Enachescu et al. [43] identify the DMT model appropriate to describe the contact of a W tip with the (111) hydrogen terminated diamond surface. More details on these models and their applicability can be found in [11, 43]. Moreover, in [43] the dependence of the friction force on the contact area has been addressed by a clever combination of AFM and scanning tunneling microscopy (STM) techniques. The dependence of the measured friction as a function of the load is found to follow the same behavior of the measured conductance, showing convincingly that indeed, at the nanoscale, friction is proportional to the contact area, at variance with the macroscopic behavior.

5.3.2. Velocity and Temperature Dependence

Typical velocities in FFM experiments are extremely slow, ranging from a few nm/s up to μm/s. The dependence of friction for velocities in this range has been experimentally studied by means of AFM by different groups [24, 25, 33, 44–50]. Depending on the investigated systems and on the experimental conditions, different and somewhat contradictory results for the velocity dependence have been found.

In the original experiments of Mate et al. [24], the authors state that the frictional forces of a tungsten tip on graphite shows little dependence on velocity for scanning velocities up to 400 nm/s. A similar behavior up to velocities of several μm/s has been reported also in the work of Zwörner et al. [49], where friction on different carbon structures has been studied. However, an increase of the friction force has been observed even for small velocities in [25, 46, 48] where it has been attributed to thermally activated processes leading to a logarithmic dependence of friction on the sliding velocity. A nonlogarithmic dependence of friction on velocities has been observed in [50] where it is attributed to an effective two-dimensional motion of the tip, and no temperature effects are invoked. All these results are interpreted in the framework of the Tomlinson model described in Section 6. We will describe there the theoretical arguments that lead to a logarithmic dependence of friction on velocity as proposed by Gnecco et al. [48] and by Sang et al. [51].

5.3.3. Load Dependence

The friction force depends on the applied load L for macroscopic friction between multicontact surfaces. As discussed in Section 5.3.1, a power law dependence $L^{2/3}$ is instead predicted for a single Hertzian contact. Such a dependence has been observed experimentally for relatively large tips on different substrates, hydrogenated diamond [43], mica [42], and carbon compounds [52, 53]. The results reported by Mate et al. [24] for graphite suggest rather a linear dependence, although deviations toward a lower exponent appear at low loads.

Atomistic computational studies have been performed for two very different cases. In a molecular dynamics study [54] of an extended 5×5-atom Cu(111) tip on Cu(111), a linear relation between friction and load is derived. The authors note that because the contact area in the simulation cannot change with the load, as in macroscopic contacts, the increase of friction must be due to a linear increase of the average shear stress τ_c. By studying tips of different area (from 3×3 up to 9×9 atoms), the friction force is also found to scale linearly with contact area. For a point-like contact formed by one carbon atom on graphite, the friction force is found to scale with load as a power law with exponent $\sim$1.5 [55]. A slightly smaller exponent $\sim$1.3 is found for larger undeformable graphite tips on graphite [56]. An *ab initio* total energy calculation for Pd monolayers on graphite [38] finds a sublinear relation not further specified.

Other nanoscale aspects that depend on the load, like the type of motion and the effective potential corrugation, have been studied in a few experimental [57–60] and theoretical papers [55, 61].

In [57], a NaF(001) surface is studied. Clear sublattice atomic periodicity with high and low peaks allowing to distinguish Na and F sites are measured for loads up to tens of pN. By further increase of the load, only the large peaks remain, and above 6 nN an abrupt increase of the friction force occurs. The latter effect is attributed to large deformations of the surface at this load. A similar behavior is found in [59]. Maps with periodic spacing

shorter than a unit cell have been reported also for a β-$MoTe_2$ surface [62]. A model for this surface has been proposed in [63].

In [58], Fujisawa et al. present a very interesting study of graphite with loads ranging from 22 nN to 327 nN. They show, at 44 nN, a change of motion from smooth sliding to sa more and more pronounced stick-slip as a function of the load. Furthermore, in the stick-slip regime, they find the tip motion to have a two-dimensional zig-zag character at intermediate loads going over to a one-dimensional motion at the highest loads. They give a qualitative interpretation of their results as due to increasing interaction with the core of the substrate atoms. Interpretation of the images at different load by means of a static two-dimensional Tomlinson model with Lennard-Jones interaction with the substrate [64] are presented in [61]. The observed change of motion with load is also reproduced in [55] by MD simulations based on a realistic interaction potential for graphite [65].

A very recent AFM study by Sokoliuc et al. [66] has also reported the transition from stick-slip motion to continuous sliding on cleaved NaCl by reducing the load. Hysteresis disappears in the sliding regime, and the friction therefore drops below the accuracy of the instrument. The observed behavior is the one expected on the basis of the Tomlinson model, and the drop of the kinetic friction corresponds to the disappearance of the elastic instabilities, which are the main cause of dissipation, as will be discussed in Section 6. Actually, the change of behavior of the friction force reported in [66] closely resembles the one reported in Fig. 10 in going from $\lambda > 1$ to $\lambda < 1$. Therefore, no assumptions concerning the presence of large contacts and incommensurability effects are invoked, contrary to the experiment of Hirano et al. [67] and Dienwiebel et al. [23], which will be discussed in Section 5.3.4.

Another interesting aspect of studying the load dependence is that it gives the possibility of probing the effective tip–surface interaction potential. This argument has been suggested in [58] and has been pursued by Riedo et al. [60] and in [55]. In [60], the motion of the silicon tip on a mica substrate is related to the thermally activated motion on an effective sinusoidal interaction potential. From the dependence of the measured friction force on scanning velocity, the authors extract the values of the potential barrier as a function of the applied load, finding a power-law dependence with exponent ~1.2 [68]. The computational study for graphite point-like and extended contacts mentioned above [55, 56] find that the potential corrugation varies with the same exponent (~1.5 for point-like, ~1.3 for extended contacts) found for the dependence of friction on load. This finding suggests a direct link between atomistic friction and energy barriers for diffusion.

5.3.4. Effect of Commensurability

For a tip constituted by several atoms or for a whole adsorbed layer as studied by means of the QCM, commensurability effects become crucial in determining the effective friction force. As we will discuss in Section 7, within the 1D Frenkel-Kontorova model, for an infinitely extended incommensurate contact, the static friction is found to vanish [69]. Frictionless sliding of incommensurate contacts also at finite and large velocities has been predicted in [70], and this effect has been named superlubricity. In [67], experimental evidence for this superlubric behavior is found in an STM study in ultrahigh vacuum of a W(011) surface sliding on a clean Si(100) surface. The use of STM instead of AFM for measurements of sliding friction is not common, and I refer to the paper for experimental details. The area of contact is estimated to be a few nanometers squared. The authors report a drop of the friction force from 90 nN to less than 3 nN (sensitivity of the experimental setup) in going from a commensurate to an incommensurate contact. Similar behavior had been observed by the same group also for the sliding on mica surfaces [71]. The authors claim that these experimental results support the prediction of superlubricity of [70].

The friction on graphite substrates is currently studied in the group of Joost Frenken in Leiden by means of a new generation AFM setup, the so called tribolever [22, 21] mentioned in Section 5.1. For this surface, it is conjectured [21, 23] that the tip cleaves a flake of graphite when brought into contact so that the effective system under study is the contact of a graphite flake with a graphite surface. These studies show that also for finite but large contacts of about hundred atoms, the friction force becomes vanishingly small [21] when the sliding occurs in a generic direction where the registry between tip and substrate is incommensurate.

The friction force is studied there over a range of substrate rotation angles. Two peaks of high friction with a value of 360 and 203 ±2 pN are found at angles of 0 and 61 degrees. In between, a wide angular range of ultralow friction close to the detection limit of the instrument is found. A fit of the data by means of an extended 2D Tomlinson model indicates that the contact is formed by a symmetric hexagonal flake of 96 atoms. Also, these authors call superlubricity the extremely low friction found for sliding along directions in which the tip and the substrate are incommensurate. It should be noted however that in [70], the prediction of superlubricity applies to velocities up to many order of magnitude higher than what can be attained in this type of experiment. Instead, these results certainly support the fact that the kinetic friction tends to zero in the quasistatic limit for incommensurate contacts. We will come back to this point in Section 7.

Interestingly, in other measurements presented in [21, 23], there is also evidence that the tip can suddenly get locked in a commensurate registry with a sudden increase of the friction force. This result is attributed to the contact formed by a graphite flake loosely attached to the tip, which rotates under the effect of the torque exerted by the surface on the nearly aligned flake.

The second group of results that addresses more directly the dependence on commensurability are the ones obtained by the QCM for rare gas adsorbed on atomically smooth and atomically rough metal surfaces [31, 32, 72–74]. The adsorbed film can be either fluid or solid depending on temperature and pressure [31]. The results of these studies clearly indicate the role of commensurability. Krim and coworkers showed for Kr monolayers on gold substrates [31] that incommensurate solid monolayers did not exhibit any static friction force. Both solid and liquid monolayers were showing a viscous force law (e.g., a linear dependence of friction on velocity). Even more impressive is the fact that incommensurate solid monolayers display a viscous friction much weaker than fluid monolayers [31]. Another evidence that indeed the incommensurate registry was at the origin of the very low friction force for solid monolayers is that only in this case, contrary to fluid layers, the measured friction was found to depend on the roughness of the substrate. Recently, the results for Kr on gold have been confirmed in [73, 74], which report also the detection of the depinning transition from a locked to a sliding state by slowly increasing the amplitude of the substrate oscillations. Again, qualitatively, these findings can be understood in terms of the Frenkel-Kontorova model. More specifically, these data have been interpreted by detailed numerical simulations based on Lennard-Jones potentials, which can reproduce quite well the weak van der Waals interactions between the rare gas atoms and between adsorbate and substrate [34–36]. Persson and Nitzan [75] use instead a Morse-like potential for the interaction with the substrate and Lennard-Jones between rare gas atoms. The results of [34–36] lead the authors to conclude that dissipation is dominated by phonon excitations. Conversely, friction is attributed to electronic excitations in [75]. We come back to this still unresolved controversy in the following Section 5.3.5.

5.3.5. Electronic Friction

Any excitation that can couple to the motion can be responsible for the occurrence of friction. In the case of metals, the possibility of friction due to electronic excitations could, in principle, contribute to friction as much or more than phononic processes. An experimental proof of the importance of electronic friction on metal surfaces, which had been discussed in several theoretical papers [75–80], is given in the QCM study of Dayo et al. [81] where the sliding of nitrogen onto lead is studied across the superconductor phase transition in the lead substrate. A sudden drop of friction to about half its value is observed at the onset of superconductivity in the substrate. The slip time is substantially longer when the lead substrate is in the superconducting state than when it is in the normal state. By analyzing their results, the authors find that, if the reduction of friction is interpreted as an abrupt drop of the conduction electron contribution when the lead enters the superconducting state, then the phononic and electronic friction should be approximately equal in magnitude. However, they note that the number of conducting electrons is not expected to drop suddenly at the transition. Indeed, the sudden collapse of friction at the superconducting transition is a puzzling result, as argumented by Persson and Tosatti [82].

In a comment to Dayo et al. [81], another group [83] reports an experiment, nominally for the same system of Dayo et al. and with improved cryogenics conditions, without finding any jump of the friction force at the superconducting lead transition. They assume that a small amount of surface disorder is enough to pin the adsorbed film at low temperature as expected on the basis of the theoretical work of Volokitin and Persson [80]. Krim [84] answers by stressing the importance of surface preparation, which is apparently not the same in the two experiments. Renner et al. report more extensive results in [85], finding that the nitrogen film is always rigidly pinned to the substrate at low temperature so that there is no friction, and therefore no effects at the superconducting transition can be expected. Again, differences in surface preparation must be invoked to reconcile these results with those of [81]. While waiting for further experimental evidence on better characterized metal films, many theoretical papers are contributing to an ongoing discussion on the mechanisms of electronic friction and on the relation to the superconducting transition [86–92].

6. THE TOMLINSON MODEL

In this section, we present a simple one-dimensional model, introduced by Tomlinson in 1929 in the paper "A molecular theory of friction" [93], which captures the main atomistic features giving rise to static and dynamic friction as well as the transition from uniform sliding to stick-slip motion. This model turns out to be very useful in analyzing experimental FFM results [49, 94], as shown in Section 5.1. Because, in its simplicity, this model is ideal to understand many aspects characterizing friction and energy dissipation at the atomic scale, we will present its properties with more details than what can be found in research papers. This section is mostly based on [9, 95] and is supplemented by original material.

6.1. Potential Energy and Dynamics

The Tomlinson model describes a particle of mass m attached via a spring to a support sliding with constant velocity v in an external periodic potential representing the substrate, as illustrated in Fig. 3. Pictorially, one can see the atom as bound by the spring to its own bulk sliding onto a crystalline surface. Vibrations of the spring can then be dissipated via the damping term into the bulk and lead to energy dissipation.

The total potential energy V^{tot} can be written as:

$$V^{tot} = V_{el} + V_{per} = \frac{1}{2}K(x - x_s)^2 + V_0\left[1 - \cos\left(\frac{2\pi}{a}x\right)\right] \tag{9}$$

The first term V_{el} represents the elastic energy due to the spring of strength K with x the position of the particle and $x_s = vt$ the position of the moving support with respect to the periodic substrate. The substrate potential V_{per} has periodicity a and varies between zero and $2V_0$. The minimum of V_{tot} is found for $x = x_s = na$ with $n = 0, 1, 2, \ldots$. The static

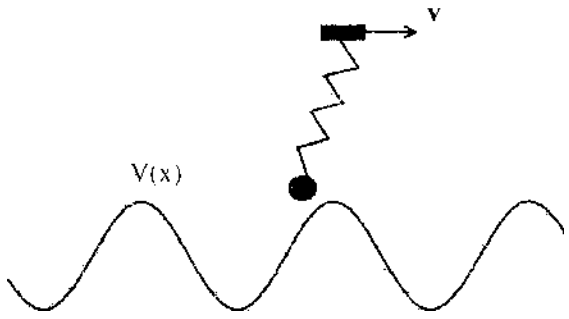

Figure 3. Schematic illustration of the Tomlinson model. A particle of mass m attached via a spring to a support sliding with constant velocity v in an external periodic potential representing the substrate.

friction force is given by the maximum of the force $-dV_{per}/dx$

$$F_{static} = \frac{2\pi}{a} V_0 \tag{10}$$

The dynamics resulting from V^{tot} is studied with the addition of a viscous damping term proportional to the velocity of the particle. This term represents a possible coupling to external degrees of freedom in the substrate such as bulk lattice vibrations (phonons) and is added to counterbalance the drive constituted by the moving support.

The equation of motion is:

$$m\frac{d^2x}{dt^2} = F_{el} + F_{per} + F_v = -K(x - x_s) - V_0\frac{2\pi}{a}\sin\left(\frac{2\pi x}{a}\right) - m\eta\frac{dx}{dt} \tag{11}$$

where the subscript *el*, *per*, and *v* represent elastic, periodic, and viscous, respectively. The solution of Eq. (11) is periodic, with period na/v [95]:

$$x\left(t + \frac{na}{v}\right) = x(t) + na \qquad \text{for integer } n \tag{12}$$

Usually, $n = 1$. Only in the underdamped regime ($\eta < \sqrt{K/m}$) jumps of the tip with periodicity larger than one lattice parameter (i.e., $n > 1$) occur. It is convenient to rewrite Eq. (11) in adimensional units. We multiply each term of Eq. (11) by $2\pi/(Ka)$ so that by defining

$$\tilde{x} = \frac{2\pi x}{a}, \qquad \tilde{t} = \frac{t}{\tau}, \qquad \tilde{\eta} = \eta\tau \quad \text{with} \quad \tau = \sqrt{\frac{m}{K}}, \qquad \lambda = \frac{V_0(2\pi)^2}{(Ka^2)} \tag{13}$$

Eq. (11) becomes

$$\frac{d^2\tilde{x}}{d\tilde{t}^2} = -(\tilde{x} - \tilde{x}_s) - \lambda\sin(\tilde{x}) - \tilde{\eta}\frac{d\tilde{x}}{d\tilde{t}} \tag{14}$$

From now on, when using adimensional units, we drop the tilde sign on all of them. The timescale τ is the inverse of the natural frequency ω_0 of the spring.

Now we go back to discuss the total potential energy in rescaled variables

$$V_{tot} = \frac{1}{2}(x - x_s)^2 + \lambda[1 - \cos(x)] \tag{15}$$

The conservative force deriving from V_{tot} is

$$F = -\frac{dV_{tot}}{dx} = F_{el} + F_{per} = -(x - x_s) - \lambda\sin(x) \tag{16}$$

Two different regimes, with a single or more minima of V_{tot} for all values of x_s, can be identified for values of λ smaller or larger than one. The occurrence and the implications of these two regimes become clear by looking at the forces as well as at the total energy.

The condition of equilibrium $F = F_{el} + F_{per} = 0$ implies

$$(x - x_s) = -\lambda\sin(x) \tag{17}$$

A graphical solution of the above equation, as reported in [9], shows that for $\lambda < 1$ there is only one stable solution for any value of x_s, whereas multiple solutions are possible for $\lambda > 1$. In fact, the left-hand side represents a straight line with slope 1 and the right-hand side starts off with slope λ. The solutions for which the second derivative of V_{tot} with respect to x is positive (i.e., $1 + \lambda\cos(x) > 0$) define the possible metastable states of the system. For $\lambda < 1$, $1 + \lambda\cos(x) > 0$ always and no instabilities can occur. For $\lambda > 1$, instead, $1 + \lambda\cos(x)$ can pass through zero for certain values of x. More and more metastable states appear as λ increases. In this case, even if the support moves very slowly, the second derivative of the potential is bound to vanish at some point so that the particle is not in equilibrium anymore, and sudden jumps between different metastable minima cannot be avoided. In Fig. 4 from [64],

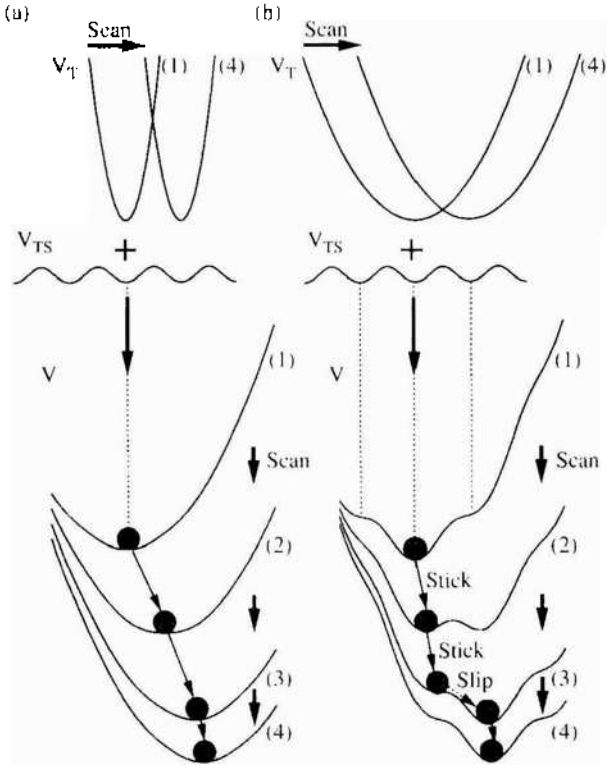

Figure 4. The total potential energy in the Tomlinson model is the sum of the elastic energy due to the spring (V_T in the figure, V_{el} in the text) and of the particle surface interaction (V_{TS} in the figure and V_{pot} in the text) from [64]. Two cases for (a) a stiff cantilever and (b) a soft cantilever are presented. (1)–(4) present the time evolution while the particle is drawn onto the substrate by the moving support. For the stiff cantilever, the total potential V_T is nearly parabolic and the particle is always located at the minimum. Conversely, for the soft cantilever, several metastable points, corresponding to local minima, appear and the particle sticks in one local minimum and jumps abruptly to the next minimum when the barrier between two minima disappears. Reprinted with permission from [64], N. Sasaki et al., *Phys. Rev. B* 54, 2138 (1996). © 1996, American Physical Society.

the elastic and periodic potential and the resulting V_{tot} are shown schematically for two cases with λ smaller or larger than one. The metastable states for $\lambda > 1$ here show up very clearly as a series of relative minima in V_{tot}.

On the basis of this model, uniform sliding at the velocity $\langle \dot{x} \rangle \sim v$ occurs for $\lambda < 1$. The only source of energy dissipation comes from the viscous term, which vanishes in the limit $v \to 0$. Note that the vanishing of kinetic friction does not imply vanishing static friction, as the periodic surface potential always pins the particle. For $\lambda > 1$, a discontinuous stick-slip motion occurs and opens a new channel for energy dissipation. Part of the energy gain due to the sudden jump to the next minimum can be converted into vibrations of the particle. In presence of some damping mechanism, this energy abandons the interface and is dissipated into phonons (heat) or other excitations. Thus, when the stiffness of the interaction of the atom with its own bulk is weaker than the one with the other surface, finite friction results also in the limit of low sliding velocity contrary to viscous friction, which vanishes in the quasistatic limit.

The two regimes of motion (uniform sliding and stick slip), are shown in Fig. 5a where we plot the position of the particle as a function of time for the two values $\lambda = 0.5$ and $\lambda = 3$ obtained by solving numerically Eq. (14) with damping $\eta = 2$. Incidentally this value of η corresponds to the critical damping of a damped oscillator of natural frequency ω_0 [5]. In Eq. (14), $\omega_0 = 1$. One can see that the uniform sliding for low λ goes over to stick-slip motion at higher λ. The increase of x occurs gradually for $\lambda = 0.5$, whereas for $\lambda = 3$, it occurs in steps, the particle remaining in a given minimum until it jumps to the next one very suddenly. The corresponding velocities $\dot{x}$ for $v = 0.08$ are shown in Fig. 6. For $\lambda = 0.5$, the velocity is always different from zero and close to v, whereas for $\lambda = 3$ it is close to zero in the sticking region and reaches values much higher than v during the short slip time.

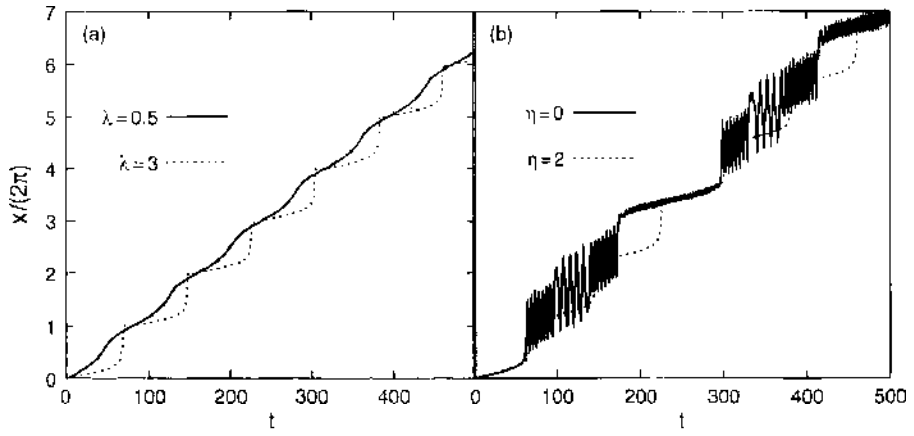

Figure 5. Time dependence of the particle position for support velocity $v = 0.08$. (a) solid line: $\lambda = 0.5$, $\eta = 2$ (critical damping); dotted line: $\lambda = 3$, $\eta = 2$. Note the transition from smooth sliding for $\lambda < 1$ to stick-slip behavior with rapid jumps of one substrate lattice parameter for $\lambda > 1$. (b) Comparison of damped and undamped motion in the stick-slip regime with $\lambda = 3$; solid line: $\eta = 0$; dotted line: $\eta = 2$ [same as in (a)]. Note the complex undamped motion, with several frequencies of oscillation and less well defined periodicity.

In Fig. 5b, we compare the stick-slip trajectory calculated for $\lambda = 3$ at critical damping to the one obtained by solving the equation of motion with $\eta = 0$. After each slip, strong oscillations take place, and also the stick-slip motion becomes more erratic, with a less defined time periodicity. One can see that, despite its simplicity, in the undamped or underdamped limit, this model shows complex dynamics, typical of nonlinear systems. For the Tomlinson model, the natural frequency of the spring $\omega_0 = 1$ becomes $\omega = \sqrt{d^2V_{tot}/dx^2}|_{x=2n\pi} = \sqrt{1 + \lambda \cos x}|_{x=2n\pi} = \sqrt{1 + \lambda}$ close to the minima of the periodic potential. However, from Fig. 5b one can see that the oscillations of the particle calculated with $\eta = 0$ are not simply given by this frequency. Certainly one of the most challenging aspects faced by theoretical studies of atomistic friction is that one has to describe a situation that is always away from equilibrium. All regions of the potential are probed during the motion contrary to most solid-state problems where usually the situations of interest concern atoms that are close to equilibrium positions so that a harmonic approximation can be applied. We refer to [95] for a discussion of the nonlinear aspects of the model that are particularly marked, with chaos

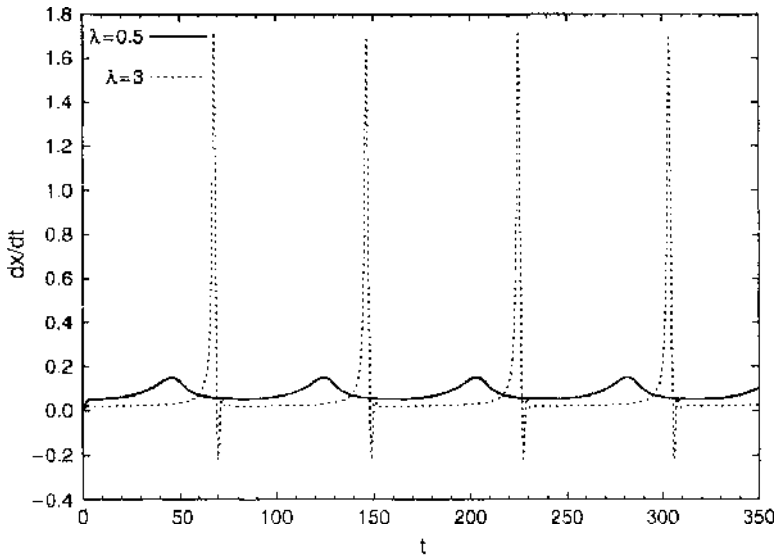

Figure 6. Time dependence of the particle velocity $\dot{x}$ for support velocity $v = 0.08$ and critical damping $\eta = 2$. Solid line $\lambda = 0.5$, dotted line $\lambda = 3$. In the smooth sliding regime for $\lambda = 0.5$, the particle velocity is always different from zero and close to v, whereas for $\lambda = 3$, the velocity is nearly vanishing in the sticking region and reaches values much higher than v during the short slip time.

and bifurcation behavior, for the case $\lambda > 1$, low damping, and high velocities, which are less relevant for the typical regime of AFM experiments.

In Fig. 7 we show the corresponding total energy given by

$$E_{tot} = \frac{1}{2}\left(\frac{dx}{dt}\right)^2 + V_{tot} \tag{18}$$

calculated for $\eta = 2$. The total energy starts from zero with the particle in a minimum of V_{per}, the spring at the equilibrium distance, and zero velocity. For $\lambda = 0.5$, the behavior of the total energy parallels that of the potential energy term V_{per} with maxima of height 2λ. The particle moves adiabatically along the potential energy surface due to the periodic potential V_{per}, and the spring remains almost at the rest length. For $\lambda = 3$ instead, when the support starts moving, the total energy increases due to the stretching of the spring reaching a value higher than the potential barrier 2λ. Then, the particle jumps and the energy gets totally dissipated during the rapid slip motion. The rise time is clearly much longer than the time during which the slip occurs. In the following Section 6.2, we show how the Tomlinson model can be used to describe AFM experiments. In Section 6.3, we give an exact definition of the friction forces that are derived from the measured lateral forces in an AFM experiment, and in Sections 6.4 and 6.5, we describe in detail the forces in the different regimes and we give typical values for them.

6.2. The Tomlinson Model for the Interpretation of AFM Experiments

The Tomlinson model gives a simple but appropriate description of AFM experiments. The moving support can be seen as the moving cantilever during a scan of the surface. The spring through which the particle is attached to the moving support represents the cantilever stiffness. The case $\lambda < 1$ corresponds to a stiff spring, $\lambda > 1$ to a soft one. The fact that a single particle can represent small but finite tips, with tens to thousands of atoms, relies on the approximation, that goes under the name of Tomlinson-Prandtl or independent oscillator (IO) model. The atoms of the tip are considered as a set of particles, spaced with the lattice parameter of the substrate, each attached to the moving support by a spring with same force constant and not interacting with each other. Therefore, the motion of each atom is the same. Within this approach, the motion of a single atom given by the Tomlinson model represents the average of the real tip–surface contact [9, 49].

The sinusoidal potential V_{per} may be thought as given by an ordered array of atoms in a crystalline surface. This approximation, which amounts to taking only the first Fourier component with wavevector $2\pi/a$ of the periodic potential, is rather well justified because higher

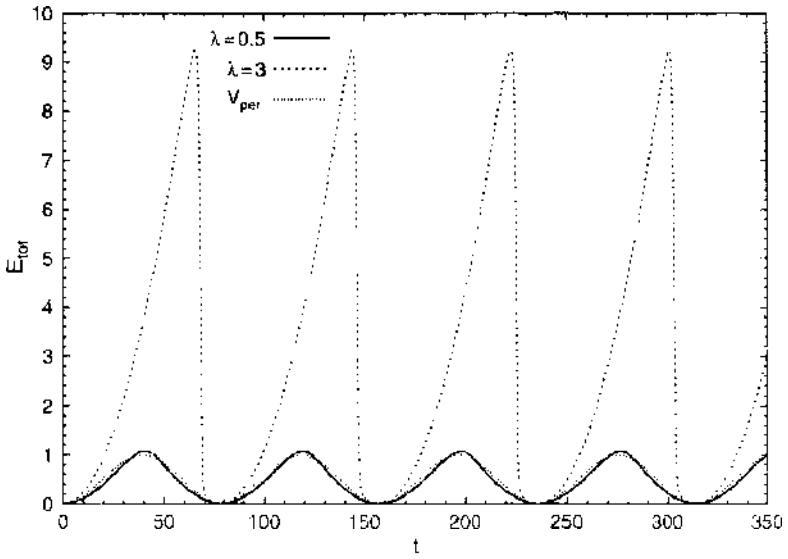

Figure 7. Time dependence of the total energy E_{tot} [Eq. (18)] for $v = 0.08$, $\eta = 2$, and two values of λ: solid line $\lambda = 0.5$, dotted line $\lambda = 3$. The thin dotted line gives V_{per} for $\lambda = 0.5$ (see text).

components are known to decay exponentially. Moreover, it is supported by *ab initio* calculations such as the one of [96]. In Fig. 8, we show the potential, calculated by *ab initio* pseudopotential total energy calculations, felt by a pyramidal Si_4H_9 tip sliding on a GaAs (110) surface represented by a 6-bilayer slab [96]. The tip is placed at fixed distance from the surface and moved at different positions on it along the paths indicated in Fig. 9. The structure is then fully relaxed, and the resulting total energy and forces are reported in Fig. 8. The approximate sinusoidal behavior of these quantities is apparent.

The values of the amplitude V_0 of the periodic potential are not always known. In principle, as shown in [55, 66], they can be extracted from the measured forces. Further knowledge can result from the noncontact spectroscopy described at the end of Section 5.1. Typical values range between 0.1 eV and 1 eV. The fact that experimentally a stick-slip behavior is observed indicates that the regime that applies is the one for $\lambda > 1$. Actually, as described in Section 5.3.3, also the transition between the two regimes has been observed [58, 66].

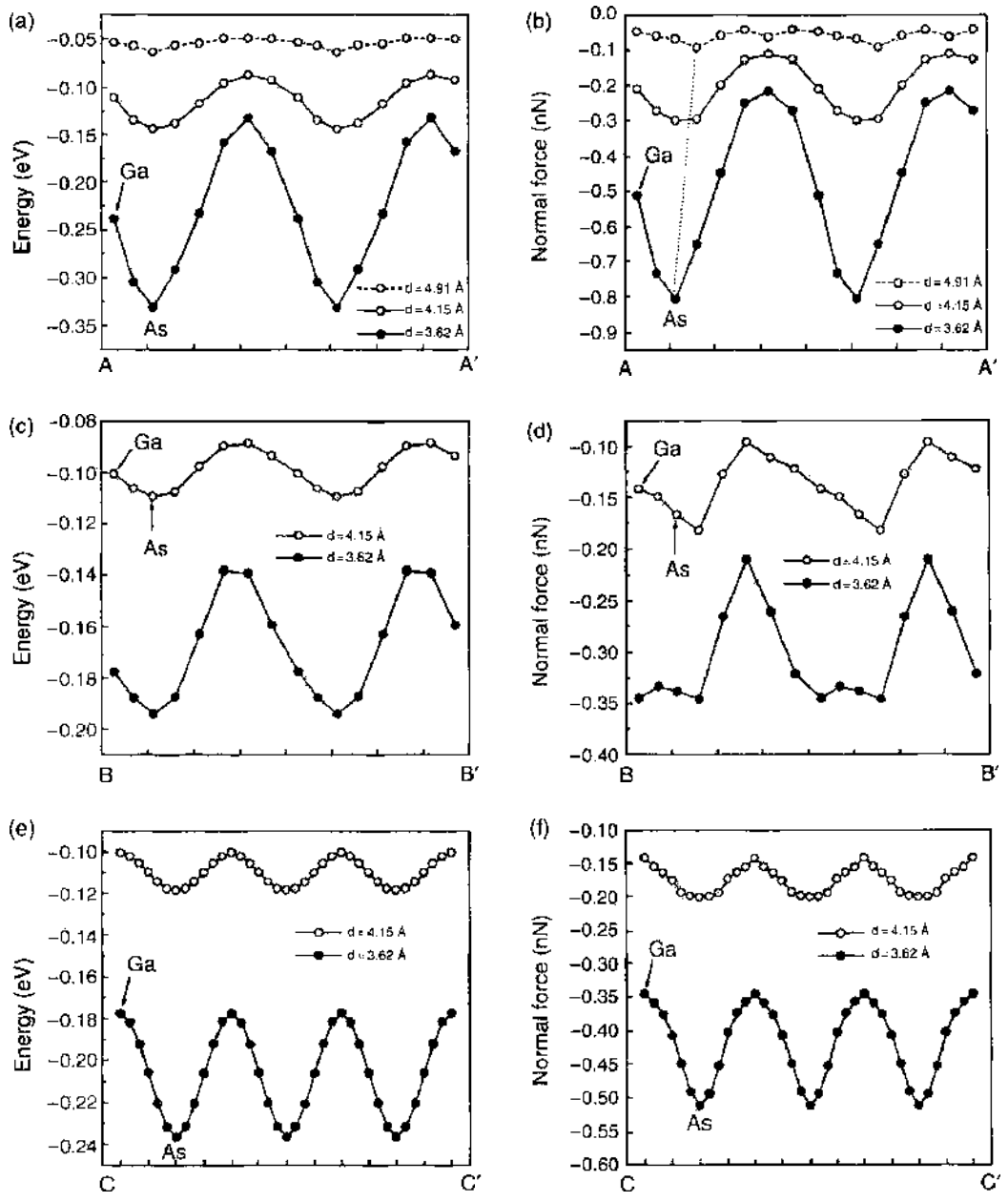

Figure 8. (a) Total energy and (b) forces calculated *ab initio* for a Si tip on GaAs(110) along the paths given in Fig. 9 for several values of the tip-surface distance d. The sinusoidal behavior found in these calculations supports the representation of the substrate as a rigid periodic potential used in the Tomlinson model. Reprinted with permission from [96]. S. H. Ke et al., *Phys. Rev. B* 60, 11631 (1999). © 1999, American Physical Society.

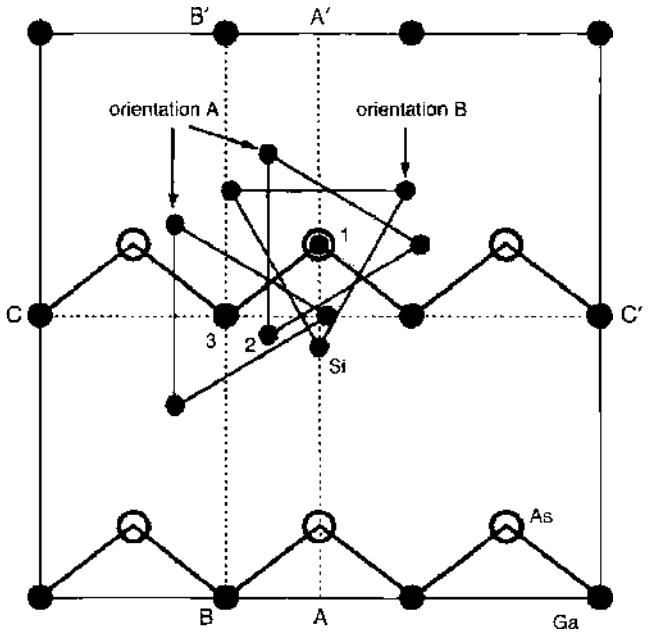

Figure 9. Top view of the (unrelaxed) GaAs(110) surface showing as dotted lines the paths along which the calculations of Fig. 8 are performed. White circles correspond to As atoms, black circles to Ga atoms. Reprinted with permission from [96], S. H. Ke et al., *Phys. Rev. B* 60, 11631 (1999). © 1999, American Physical Society.

Because the AFM scans are performed by moving the cantilever along a line on the surface, even a simple one-dimensional model turns out to be appropriate in first approximation. Several extensions have been used to make the model more realistic. In particular, extensions to 2D and 3D periodic modulation as well as other specific tip–surface interactions have been considered in [21, 26 50, 55, 63, 64, 97], leading to an impressive agreement with experimental results [26]. In [63], a two-dimensional model for a lattice with the symmetry of the NaCl lattice has been proposed, revealing the two-dimensional character of the lateral forces as well as sublattice periodicity, as also observed in experiments [59].

As discussed in Section 5.1, FFM can measure the force F_x felt by the cantilever along the motion, the so-called *lateral force*. In the following Section 6.3, we examine how the representation of friction in terms of lateral forces can be reconciled with the dissipation of energy due to the viscous forces describing the coupling η to bulk excitations.

6.3. Expression of the Friction Force in Terms of Lateral Forces

Consider again the equation of motion of the Tomlinson model given by Eq. (14) with $x_s = vt$ corresponding to the case of a support moving with constant velocity

$$\ddot{x} + \eta\dot{x} + \lambda \sin(x) + x - vt = 0 \tag{19}$$

For the periodic motion Eq. (12) with $n = 1$, the energy dissipated in one period $2\pi/v$ ($a = 2\pi$ in adimensional units) is

$$\Delta W = \int_0^{2\pi} F_\eta \, dx = \eta \int_0^{2\pi} \dot{x} dx = \eta \int_0^{2\pi/v} \dot{x}^2 \, dt \tag{20}$$

and the friction force is given by

$$F_{fric} = \frac{\Delta W}{2\pi} \tag{21}$$

Now we can multiply both sides of Eq. (19) by $\dot{x}$ and integrate over one period:

$$\int_0^{2\pi/v} \dot{x}\ddot{x} \, dt + \eta \int_0^{2\pi/v} \dot{x}^2 \, dt + U_0 \int_0^{2\pi/v} \dot{x} \sin x \, dt + \int_0^{2\pi/v} \dot{x}x \, dt - v \int_0^{2\pi/v} t\dot{x} \, dt = 0 \tag{22}$$

By use of the definition Eq. (21) and by integrating the last term by parts, Eq. (22) becomes

$$\frac{1}{2}\dot{x}^2\Big|_0^{2\pi/v} + 2\pi F_{fric} + U_0(1-\cos x)\Big|_0^{2\pi/v} + \frac{1}{2}x^2\Big|_0^{2\pi/v} + v\int_0^{2\pi/v} x\,dt - 2\pi x\left(\frac{2\pi}{v}\right) = 0 \quad (23)$$

Due to the periodicity of the solution Eq. (12), the first and third term of Eq. (23) vanish and Eq. (23) can be written as

$$2\pi F_{fric} - \frac{1}{2}(2\pi)^2 + v\int_0^{2\pi/v} x\,dt = 0 \quad (24)$$

We introduce $\xi = x - vt$. We can rewrite the last expression, obtaining

$$\begin{aligned} 2\pi F_{fric} &= \frac{1}{2}(2\pi)^2 - v\int_0^{2\pi/v} \xi\,dt - v^2\int_0^{2\pi/v} t\,dt \\ &= \frac{1}{2}(2\pi)^2 - v\int_0^{2\pi/v} \xi\,dt - \frac{v^2}{2}\left(\frac{2\pi}{v}\right)^2 = -v\int_0^{2\pi/v} \xi\,dt \end{aligned} \quad (25)$$

Because $vt - x = -\xi$ is the lateral force F_x, we obtain an alternative expression of the friction force

$$F_{fric} = \frac{v}{2\pi}\int_0^{2\pi/v} F_x\,dt \equiv \langle F_x \rangle \quad (26)$$

where $\langle\cdot\rangle$ indicates a time average. Thus, finally we have proven that

$$\eta\int_0^{2\pi/v} \dot{x}^2\,dt = \frac{v}{2\pi}\int_0^{2\pi/v} F_x\,dt \quad (27)$$

This relation allows one to reconcile the lateral friction force as defined within the context of AFM experiments, which is not dissipative in nature as it represents the work done to slide two interacting surfaces over a finite distance, with the dissipated energy due to the damping term $\eta\dot{x}$.

6.4. Friction Force in the Tomlinson Model

In the Tomlinson model, the lateral force F_x is given by

$$F_x = K(x_s - x) \quad (28)$$

or, in adimensional units

$$F_x = (x_s - x) \quad (29)$$

As demonstrated in the previous Section 6.3, the time average of this force $\langle F_x \rangle$ is defined as the frictional force F_{fric}. In Fig. 10, we show the lateral forces F_x calculated during the trajectory shown in Fig. 5. For $\lambda < 1$, $\langle F_x \rangle$ oscillates around zero, yielding an average value F_{fric}, which vanishes in the limit $v \to 0$. Notice that the maxima of this force represent the static friction force that would be needed to pull the particle over the potential barrier and set it in motion. The small deviations of the maxima of F_x from λ are due to the damping term $\eta dx/dt$, which is not negligible for $\lambda < 1$. This regime has also been recently observed [66], as discussed in Section 5.3.3.

For $\lambda > 1$, the stick-slip motion gives a sawtooth behavior of the lateral force similar to the one observed in most AFM experiments [25]. Although the particle sticks in the potential minima, the lateral force increases roughly linearly. The slope of this growth can be used to determine the stiffness of the cantilever as suggested in [11, 98, 99]. The effective spring

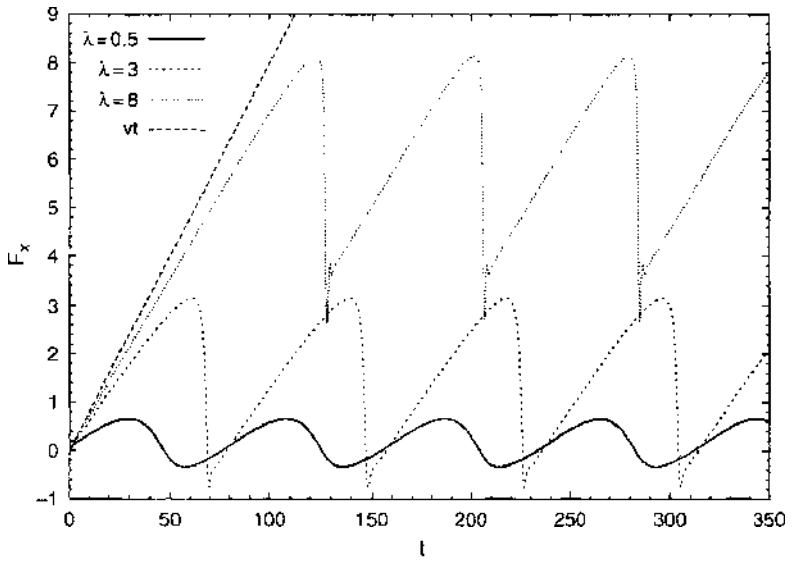

Figure 10. Time dependence of the forces for $v = 0.08$, $\eta = 2$, and three values of λ, $\lambda = 0.5, 3, 8$ as indicated. For $\lambda < 1$, $\langle F_x \rangle$ oscillates around zero, yielding an average value F_{fric} which vanishes in the limit $v \to 0$. For $\lambda > 1$, the stick-slip motion gives a sawtooth behavior of the lateral force similar to the one observed in most AFM experiments. The straight line vt gives the limiting slope expected for large values of the potential amplitude. The lateral forces for $\lambda = 8$ show a feature that is commonly observed in experiments, namely the first linear increase starting from rest lasts longer than the ones in following sticking regions (see text).

constant of the total system formed by the cantilever of stiffness K and by the tip–surface contact can be described as a series of two springs as

$$K_{eff} = \left(\frac{1}{K} + \frac{1}{K_{contact}} \right)^{-1} \tag{30}$$

where $K_{contact}$ is the stiffness of the tip–surface contact, namely the second derivative of V_{per} at equilibrium, $K_{contact} = \partial^2 V_{per}/\partial x^2|_{x=x_{min}}$. With our form of V_{per} [Eq. (9)], we have for $K_{contact}$

$$K_{contact} = \frac{4\pi^2 V_0}{a^2} \tag{31}$$

For large V_0 (or equivalently large λ in adimensional units), K_{eff} tends to the bare cantilever stiffness K. In Fig. 10, we have reported also a calculation with a large $\lambda = 8$. One can see that, in this case, the slope of the lateral forces tends to the slope v, which is the one obtained for $K_{eff} = K$ with $K = 1$ in our units. The lateral forces for large $\lambda = 8$ show also another feature that is commonly observed in experiments; namely, the first linear increase starting from rest lasts longer than the ones in following sticking regions [26]. Again, the maximum value of the lateral force represents the static friction force. For $\lambda > 1$, the frictional force F_{fric} is finite and grows with increasing λ.

6.5. Parameters of the Model in Physical Units

When written in adimensonal units, the Tomlinson model can describe two very different situations. In fact, in AFM, problems two kinds of dynamics are present: the slow motion of the massive cantilever, with typical resonant frequency of 10^4–10^6 Hz and the fast vibrations of atoms in the contact area, with typical frequency of 10^{12} Hz. Due to the extremely large difference of timescales, these two dynamical modes can be decoupled [100]. Typical values of the mass and of the stiffness of the cantilever used in AFM experiments are respectively $m \sim 10^{-11}$ kg and $K = 10$ N/m, with scanning velocities ranging from nm/s to μm/s. The corrugation V_0 depends on the nature of the substrate and on the applied load: as mentioned in Section 6.2, it can typically vary from 0.1 eV to 1 eV. Assuming critical damping,

the damping parameter in this case results to be $\eta = 2\sqrt{K/m} = 6.4 \cdot 10^5\ s^{-1}$. Converting these values of the parameters in adimensional units (indicated explicitly by the tilde), taking for example $V_0 = 0.5$ eV, $v = 10$ nm/s, and $a = 0.246$ nm (lattice constant of graphite), one gets $\lambda \simeq 5.2$, $\tilde{v} \simeq 0.8 \times 10^{-3}$, and $\tilde{\eta} = 2$.

However, it is also possible to adopt an atomistic approach, in which the dynamics of the atom, instead of the motion of the whole cantilever, is considered. In this extreme situation, m represents the mass of the atomic contact between the tip and the cantilever (e.g., for a carbon atom of mass $m \simeq 10^{-26}$ kg), and the velocity v is typical of atomic motion ($v \simeq 1$ m/s) [55]. Using these new values of m and v and taking the same values of V_0, K, and a as in the previous case, we obtain the same values of the adimensional parameters, $\lambda \simeq 5.2$, $\tilde{v} \simeq 0.8 \times 10^{-3}$, and $\tilde{\eta} = 2$. Note that in this case, $\eta \simeq 10^{-13}\ s^{-1}$. Thus, the same adimensional parameters may correspond to very different physical values of the masses and of the scanning velocities. In order to integrate Eq. (14) numerically, a value of the time step $\tilde{h}$ has to be chosen. Then, $h = \tilde{h}\sqrt{m/K}$. Choosing for example $\tilde{h} = 10^{-3}$, we find $h \sim 10^{-8}$ s for $m = 10^{-10}$ kg and $h \sim 10^{-16}$ s for $m = 10^{-26}$ kg. Note that this latter value of h is the one typically used in atomistic MD simulations. This means that we can in principle solve Eq. (14) with a fixed value of the time step and of the adimensional parameters, still describing diverse situations where the dynamical processes take place on timescales that differ by several orders of magnitude.

6.6. Thermal Effects in the Tomlinson Model

Up to now we have considered the statics and the dynamics of the Tomlinson model at $T = 0$ (i.e., in the absence of thermal fluctuations). However, it has been pointed out that thermal effects can be relevant for the frictional dynamics and can be responsible for the logarithmic dependence of the friction force on the scannning velocity [48, 51] mentioned in Section 5.3.2. This issue has been theoretically analyzed by using a simple thermal activation probabilistic approach [48] as well as by means of numerical simulations of the Tomlinson model at finite temperature [51]. These studies have shown that temperature can be effective in overcoming the potential barriers ΔE, activating jumps of the tip between minima of the total potential energy V_{tot}. The situation is schematically illustrated in Fig. 11, which shows V_{tot} as a function of x for three different values of x_s. At $T = 0$, the tip can jump when the maximum between two metastable minima disappears, namely when $\Delta E = 0$. On the other hand, if $T \neq 0$, jumps of the tip can occur, particularly for values of the barrier ΔE that are

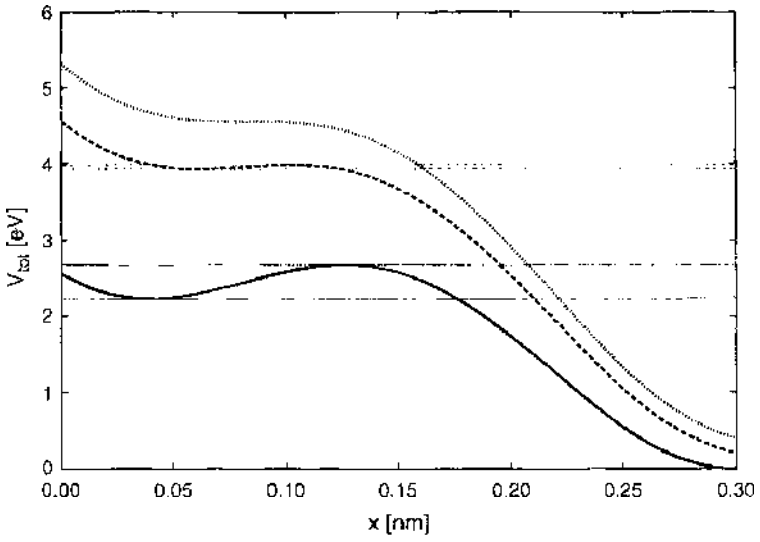

Figure 11. V_{tot} as a function of x for three different values of x_s. The distance between horizontal lines of the same type indicates the energy barrier ΔE between subsequent minima. At $T = 0$, the tip can jump when the maximum between two metastable minima disappears, namely when $\Delta E = 0$, as shown in the topmost case. If $T \neq 0$, jumps of the tip can occur as a consequence of thermal excitation, particularly for values of the barrier ΔE that are comparable to the thermal energy $k_B T$ (see text).

comparable to the thermal energy $k_B T$. In this case, the displacement of the cantilever is smaller than the one needed to observe a jump at $T = 0$, resulting in a lower friction force for finite temperatures.

The role of thermal activation on the dynamics of the tip can be understood within the simplified model proposed in [48], which has been used to explain the velocity dependence of the friction force observed in the experiments [25, 46, 48]. Let us consider a point-like particle in a well of the potential V_{tot} of Eq. (15). If p indicates the probability to find the particle in this minimum, $1 - p$ is the probability of the tip to jump to the next, lower minimum. The master equation that describes this process (assuming that the particle can only jump from the higher to the lower minimum, and not *vice versa*) has the form

$$\frac{dp(t)}{dt} = -f_0 \exp\left(\frac{-\Delta E(t)}{k_B T}\right) p(t) \tag{32}$$

where f_0 is an attempt frequency and $\Delta E(t)$ is the energy barrier between these minima. Equation (32) can be rewritten as

$$\frac{dp(F_x)}{dF_x} = \frac{dp}{dt}\left(\frac{dF_x}{dt}\right)^{-1} = -f_0 \exp\left(\frac{-\Delta E(F_x)}{k_B T}\right)\left(\frac{dF_x}{dt}\right)^{-1} p(F_x) \tag{33}$$

Assuming that F_x depends linearly on x_s with slope k_{eff}, we have

$$\frac{dF_x}{dt} = \frac{dF_x}{dx_s}\frac{dx_s}{dt} = k_{eff} v \tag{34}$$

In [48], it is also assumed that the energy barrier ΔE depends linearly on the lateral force, that is,

$$\Delta E(F_x) = \nu(F^* - F_x) \tag{35}$$

where F^* is the force needed to induce a jump at $T = 0$ and ν is of the order of V_0/F_{static}. Given these facts and imposing the maximum probability transition condition

$$\frac{d^2 p(F_x)}{dF_x^2} = 0 \tag{36}$$

we obtain the result of Gnecco et al. [48]

$$F_x(v) = F^* + \frac{k_B T}{\nu} \ln\left(\frac{k_{eff}\nu}{f_0 k_B T} v\right) \tag{37}$$

Thus, the friction force $F_{fric} = \langle F_x \rangle$ depends logarithmically on the scanning velocity v at a given temperature T. This is called linear creep regime, because the energy barrier ΔE vanishes linearly with the lateral force. The essential ingredient in this approach is the activated hopping between potential wells, which can be determined solely by thermal fluctuations.

In a more recent work, combining numerical simulations with analytical considerations, Sang et al. [51] have corrected the logarithmic dependence Eq. (37) in order to account for ramped creep that should be important at not too small velocities. The main improvement of the above reasoning lies in the modification of Eq. (35). The authors prove that the dependence of the barrier on the lateral force is given by

$$\Delta E = \mu(F^* - F_x)^{3/2} \tag{38}$$

where $\mu = 4\sqrt{2}V_0/(3F^*)$. Inserting Eq. (38) in Eq. (33) and following the same steps leading to Eq. (37), it can easily be seen that in this case, the dependence of the lateral force on scanning velocity becomes

$$F_x = F^* - \left(\frac{k_B T}{\mu}\right)^{2/3} \left| \ln\left(\frac{3\mu K \sqrt{F^*} v}{2 f_0 k_B T}\right) \right|^{2/3} \tag{39}$$

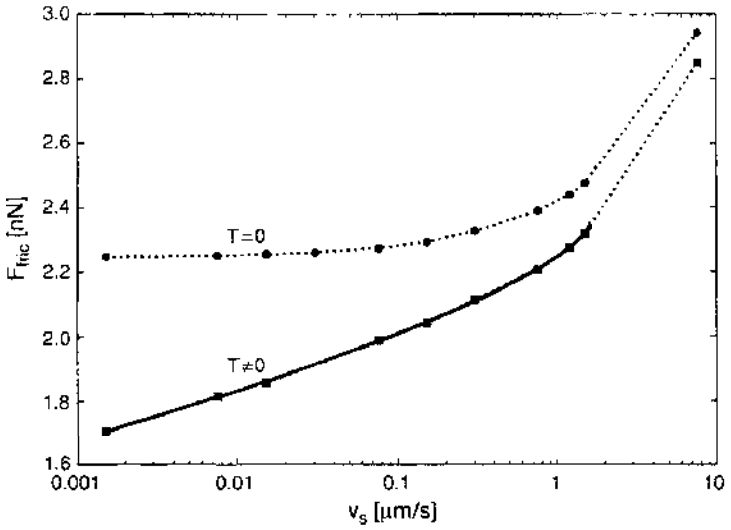

Figure 12. Friction force at $T =$ and $T = 300$ K as a function of the support velocity v. Notice the logarithmic scale used for v. Although a small dependence on the velocity is found also at $T = 0$, thermal fluctuations are the main contribution to the velocity dependence of atomistic friction at low velocities (see text).

The relation Eq. (39) is applicable for large λ in a wide range of velocities, while the linear creep holds in the small velocity regime, that is, for velocities satisfying the condition

$$v < \frac{4\pi V_0}{m\eta a}\frac{k_B T}{K}\exp\left(-\frac{F^* V_0}{k_B T}\right) \tag{40}$$

Figure 12 shows a comparison of the friction force as a function of sliding velocity for $T = 0$ and $T = 300$ K, from which it is evident that, at very low velocities, the main source of velocity dependence comes from thermal fluctuations and that the functional form Eq. (39) can successfully be used to describe the data for $T \neq 0$.

7. UNDAMPED, UNDRIVEN, FRENKEL-KONTOROVA MODEL

The Frenkkel Kontorova (FK) model, introduced in 1938 to describe dislocations in crystals [16], has been applied not only to this problem [101] but also to a variety of quasi one-dimensional physical phenomena such as charge-density waves [102–104], adsorbate layers on surfaces [105], and Josephson junction [106]. This model has taken a prominent role also in the field of sliding friction because it is ideally suited to study effects related to the commensurability of the sliding lattices. In particular, it is the prototype model to describe systems where competition between two incommensurate lengths determines the ground state energy. The FK model describes the surface by a harmonic chain in interaction with a substrate represented by a rigid periodic potential. Its ground state properties depend on the ratio of the lengths involved, the chain lattice spacing b and the period of the potential a. For incommensurate values of these two lengths, Aubry [107] has shown that, at a critical value of the coupling to the periodic potential, the ground state of the system displays a structural transition (Aubry transition) from a floating to a pinned configuration. Below this threshold, the ground state can be shifted by an infinitesimally small force, namely the system displays a vanishing static friction force. Therefore, if the macroscopic rules of friction would hold, one might expect a frictionless regime also in a dynamic situation. Indeed, for this case, Shinjo and Hirano [70] have predicted that for incommensurate values of the chain lattice parameter to the period of the modulation, a *superlubric* regime should exist where the chain would slide indefinitely without kinetic friction but with a recurrent exchange of kinetic energy between center of mass and internal vibrations. This work was followed by the STM study [67] quoted in Section 5.1 showing, at the low velocities attained in this type of experiments, a drop of the friction force to values below experimental resolution in going from commensurate to incommensurate contacts for a W tip

sliding on the Si(001) surface. A similar finding has recently been reported also for the sliding on graphite [23]. As described in Section 7, the prediction of frictionless sliding also at high velocities of [70] is oversimplified [18]. Moreover, the term *superlubricity* has been criticized in several papers [66, 108] because it suggests a transition to zero friction that can be compared to superfluidity or superconductivity, whereas there is no threshold value of the velocity below which the kinetic friction vanishes. Nevertheless, the term *superlubricity* has become very popular and used to describe low friction in the quasistatic limit accessible by AFM [23].

We present in this section the Hamiltonian version of the static and dynamic incommensurate FK model, which has led to the prediction of superlubricity, whereas in the following Section 8 we will consider the FK and FK-like models with driving and damping.

The dynamics deriving from the FK potential energy without the addition of external forces and dissipative terms conserves the energy and, strictly speaking, cannot be used to describe frictional properties. In [18, 70], the dynamics of the undriven FK chain without dissipative terms is studied as a function of the initial center of mass velocity and of the coupling to the substrate potential. The interest of this approach is that the center of mass motion can couple only to a finite number of excitations provided by the phonon spectrum of the chain, which can be described exactly. In this way, this model represents the simplest exact atomistic model of friction where one can follow in detail how mechanical energy is transformed into heat, or in other words how translational energy of the body as a whole can be transformed into vibrational energy.

The FK model has also been studied for the commensurate case $a = b$ in [109] to study the effect of impurities and the appearance of localized modes.

7.1. Static FK Model

The FK model [16] has been introduced as the potential energy describing a harmonic chain in interaction with a periodic substrate. Here we write it with the definition of parameters for which an exact value of the critical coupling at which the Aubry transition [69] occurs has been derived [110]. For N particles in one dimension, connected by springs and placed in a periodic potential, the total energy can be written as the sum of a harmonic and a periodic term

$$V_{tot}(x) = V_{harm} + V_{per} = \sum_{n=1}^{N} \left[\frac{1}{2}(x_{n+1} - x_n - b)^2 + \frac{\lambda}{(2\pi)^2}\left(1 - \cos\left(\frac{2\pi}{a}x_n\right)\right)\right] \tag{41}$$

As in the Tomlinson model, here also λ represents the ratio of the coupling to the periodic potential to the harmonic spring constant. If in the Tomlinson model, the limit of strong coupling ($\lambda > 1$) is the one suitable to describe the AFM data described in Section 5.1, for the FK model we will consider more in detail the limit of weak coupling, which applies to the experimental QCM results of Section 5.3.4.

The two lengths a and b are the period of V_{per} and the unstretched spring length, respectively. In absence of V_{per}, the position of the particles is simply given by $x_n = nb + \alpha$, where α is an arbitrary phase.

If the ratio of the two lengths a and b is a rational, namely $b/a = M/N$, with M and N integers, the registry is commensurate. This implies a finite periodicity $Nb = Ma$ of the system. For two arbitrary surfaces in contact, this case is rather unlikely. The most interesting case is the incommensurate case where the ratio $r = b/a$ is an irrational number, namely it cannot be expressed as the ratio of two integers. This means that one cannot define a finite period of the total system. This is why the model for incommensurate contacts is usually considered in the thermodynamic limit, in which the number of particles N tends to infinity.

One can define the *winding number* as the mean distance between the particles over an infinite range. The boundary conditions can be fixed in such a way that the winding number is kept at the unstretched length of the springs, namely

$$b = \lim_{n-n' \to \infty} \frac{x_n - x_{n'}}{n - n'} \tag{42}$$

The presence of two incommensurate lengths is the reason of a complex behavior of the model. The interparticle potential V_{harm} favors a uniform separation b between the particles, whereas the potential V_{per} tends to pin the particles at the minima of the periodic potential, therefore favoring a spacing a. Aubry [69] has shown that the ground state positions x_n can be described by the *hull* function $f(x)$ as

$$x_n = f(nb + \alpha) = nb + \alpha + g(nb + \alpha) \tag{43}$$

The function $f(x)$ is a strictly increasing function that depends on the ratio $r = b/a$, and $g(x)$ is periodic with the same period of V_{per}. The function $g(x)$ is also called the *modulation function* because it describes the variation of the ground state positions from the equidistant spacing resulting from V_{harm} alone. Aubry has shown that, for irrational values of r, $f(x)$ is an analytic function for values of $\lambda < \lambda_c$, where $\lambda_c(r)$ is a critical value that depends on r, whereas for $\lambda > \lambda_c$ the increase of $f(x)$ occurs only by discontinuities. Therefore, the transition occurring at λ_c is called the *breaking of analyticity* or Aubry transition [69]. This transition is signaled also by other quantities, in particular by the existence of a zero frequency phason mode below λ_c, which moves to finite frequency (the so-called phonon gap) at the Aubry transition [111, 112].

In [111], the equivalence of the equilibrium states of the FK model to the standard map [5, 113] is also demonstrated. It is following this route that the precise determination of λ_c and of several critical exponents has been obtained by MacKay [110]. Greene [114] has numerically shown that for $r = \tau_g$ and its inverse τ_g^{-1}, the critical value λ_c is the largest, where $\tau_g = \frac{\sqrt{5}-1}{2}$ is the golden mean. Mackay [110] has developed a successful renormalization approach that gives $\lambda_c(\tau_g) = 0.971635406$.

In principle, the hull and modulation functions contain all the information about the ground state. However, there is no analytic solution for these functions, so that in practice one proceeds the other way around. Usually, the period a of the potential is taken $a = 1$ so that r becomes equal to the rest chain spacing b. The potential energy Eq. (41) is minimized for a large but finite number of atoms N, and the ground state configuration $\{x_n\}$ gives approximations for a discrete set of points in the period of f and g:

$$f(nb \text{ modulo } a) = x_n \text{ modulo } a \tag{44}$$

$$g(nb \text{ modulo } a) = x_n - nb \tag{45}$$

The minimum energy configuration must be found by numerical calculations which require to introduce some approximations.

First periodic boundary conditions are introduced, that is,

$$x_{n+N} = x_n + Nb \tag{46}$$

In this way, it is possible to fulfill the requirement (42). Second, we need to deal with the irrational number r that, as already said, does not allow definition of a finite period of the total system. It is well-known that the golden mean, τ_g, can be approximated by the ratio of successive Fibonacci numbers ($F_1 = 1$, $F_2 = 1$, $F_n = F_{n-1} + F_{n-2}$ for $n > 2$), namely

$$\tau_g = \lim_{n \to \infty} \frac{F_n}{F_{n+1}} \tag{47}$$

If the period of the potential is $a = 1$, so that $r = b$, the number of particles N and the winding number b of the nth approximant in numerical implementation of the FK model are therefore defined as:

$$N = F_{n+1} \qquad b = \frac{F_n}{F_{n+1}} = \frac{M}{N} \tag{48}$$

The true FK model with infinite number of particles and a true irrational b can now be seen as the limit of these approximants for $n \to \infty$.

Within these approximations, Aubry and André [115] and Aubry and Le Daeron [116] proved that a relaxation method starting on an equidistant input configuration, $x_n = nb + \alpha$, always converges to the true ground state.

In Fig. 13, the hull and modulation functions are shown for two values of λ above and below λ_c, showing the occurrence of a structural transition. Continuity of the modulation functions means that the particles are uniformly distributed over all possible values of V_{per}, or, equivalently, that x_n modulo a form a dense set in the unit cell of the periodic potential. Discontinuities, instead, signal the occurrence of forbidden region of the potential. This feature is illustrated in Fig. 14 where the ground state positions are shown for λ below and above λ_c.

Another way to express the modulation function and its change across the Aubry transitions, which can be more intuitive for solid-state physicists, is the one given by our group in [117–119]. Once the model has been defined on a lattice with N sites with periodic boundary conditions as defined in Eqs. (46) and (48), one can write the modulation function explicitly in terms of the deviations from the equidistant spacing b, which describes the ground state for $\lambda = 0$ as

$$y_n = x_n - nb - Q = g(nb \text{ modulo } 1) \qquad Q = \frac{1}{N}\sum_n x_n \tag{49}$$

where $a = 1$, and Q represents the center of mass position. One can then rewrite Eq. (41) as

$$V_{tot} = \sum_{n=1}^{N}\left[\frac{1}{2}(y_{n+1} - y_n)^2 + \frac{\lambda}{(2\pi)^2}(1 - \cos(nq + 2\pi y_n + 2\pi Q))\right] \tag{50}$$

where we have defined the substrate modulation wavevector

$$q = 2\pi b = 2\pi\frac{M}{N} \tag{51}$$

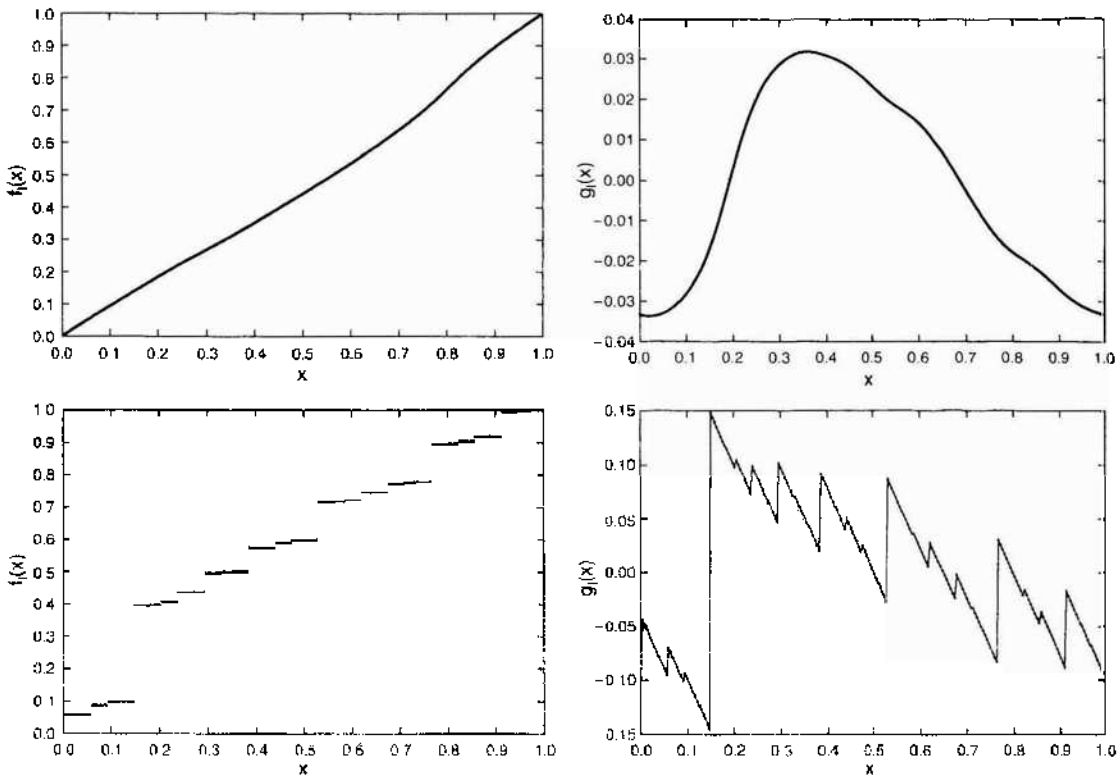

Figure 13. Top: the hull function $f(x)$ (left) and the modulation function $g(x)$ (right) for $\lambda = 0.7 < \lambda_c$. Bottom: same for $\lambda = 1.4 > \lambda_c$ calculated for a system of $N = 233$ particles on a periodic potential of period $a = 1$. The winding number b is chosen to be an approximation of the golden mean τ_g as $b = 144/233$. Although these figures consist of a discrete set of points, obtained according to the prescription Eq. (45), continuity for $\lambda < \lambda_c$ is apparent. For $\lambda > \lambda_c$, the modulation and hull functions become discontinuous

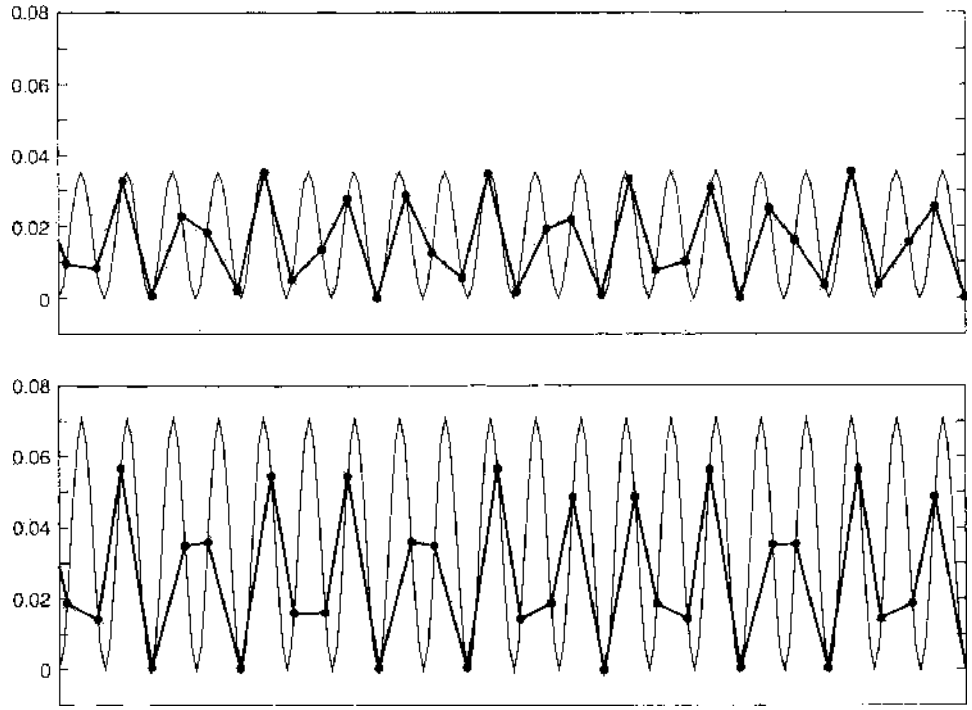

Figure 14. The positions of the particles in the ground state configuration for $\lambda = 0.7 < \lambda_c$ (top) and $\lambda = 1.4 > \lambda_c$ (bottom). Notice that for $\lambda < \lambda_c$, the particles are distributed at all positions in the periodic potential, whereas for $\lambda > \lambda_c$, forbidden regions around the potential maxima appear. Only part of the system formed by $N = 233$ particles as in Fig. (13) is shown.

In the limit of weak coupling, it is convenient to go over to their Fourier transformed coordinates defined as

$$y_k = \frac{1}{N}\sum_n e^{-ikn} y_n \qquad \text{with} \qquad k = \frac{2\pi K}{N} \qquad \text{and} \qquad K \in \left(-\frac{N}{2}, \frac{N}{2}\right] \tag{52}$$

which represent the phonon modes of the system for $\lambda = 0$. The dispersion for the linear chain with $\lambda = 0$ is

$$\omega_k = 2\left|\sin\left(\frac{k}{2}\right)\right| \tag{53}$$

It is then to be expected that, in the limit of weak coupling, the deviations from the equidistant spacing y_n will be modulated with the wavevector q as due to the frozen-in phonon ω_q. For weak coupling $\lambda \ll \lambda_c$, the Fourier transform related to q has the strongest amplitude, and the amplitudes of higher harmonics mq scale as $\lambda^{|m|}$. Indeed, as shown in the top panel of Fig. 15, the amplitude of the low Fourier components $|y_k|^2$ is very pronounced for $\lambda < \lambda_c$ and washed out at $\lambda > \lambda_c$. In the bottom panel of Fig. 15, the amplitudes are ordered as a function of mq so that the exponential decay shows up clearly. Notice, however, that the finite numerical precision makes that the high order components cannot be calculated numerically. Therefore, the ground state in the low λ regime can be seen as the unperturbed state modulated by a number of harmonics with the periodicity of the substrate potential.

The Aubry transition has important consequences for the static friction force, which in the context of the FK model is also called the depinning force [69] and is defined as follows. If we apply a force F to each atom of the chain, the equilibrium condition of the system obeys, if a stable state exists, $F = -\partial V_{tot}/\partial x_n$ or

$$2x_n - x_{n+1} - x_{n-1} + \frac{\partial V_{per}}{\partial x_n} - F = 0 \tag{54}$$

The static friction force F_s is defined as the critical value for which the chain will not be anymore at equilibrium and will start sliding or, in other words, F_s is the value for which (54) has one or more solutions for $F < F_s$ and no solution for $F > F_s$.

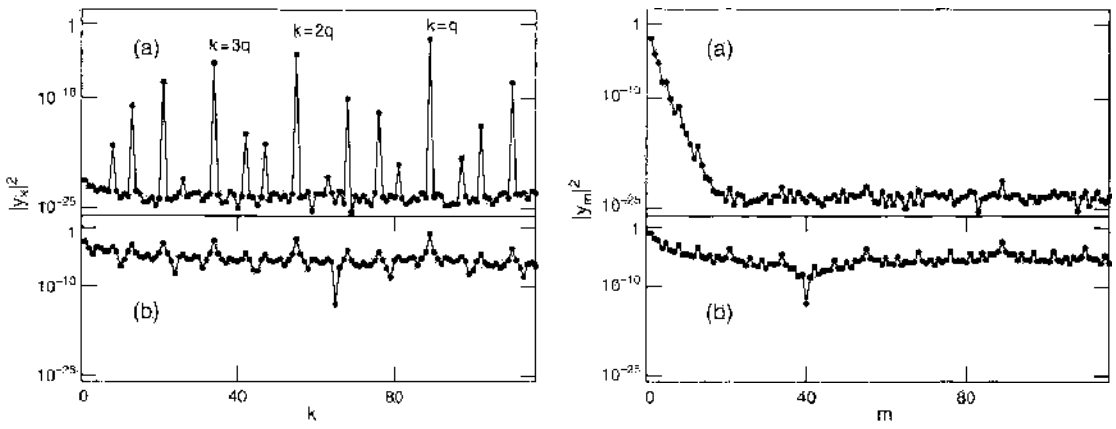

Figure 15. Left: Amplitude of the Fourier transform of the displacements from equidistant spacing in the FK chain $|y_k|^2$ given by Eq. (52) for (a) $\lambda < \lambda_c$ and (b) $\lambda > \lambda_c$. Notice that the component related to the modulation wavevector q [Eq. (51)] has the strongest amplitude and that the amplitudes of higher harmonics mq scale as $\lambda^{|m}$ (notice logarithmic scale). Right: The amplitude of the Fourier transform of the displacements from equidistant spacing in the FK chain are plotted as a function of multiples of the modulation wavevector q for (a) $\lambda < \lambda_c$ and (b) $\lambda > \lambda_c$ (see text).

Below the Aubry transition, the chain is not locked by the periodic potential and an arbitrary small value of F is enough to cause the sliding and to let all stationary stable states disappear, namely $F_s = 0$.

For $\lambda > \lambda_c$, some energy is needed to bring the particles over the forbidden regions, the tops of the potential hills. In order to produce an infinitesimal translation to the right, energy is needed to bring the particle, situated at the left side of a forbidden region, over the top at the right hand side of it. The energy that is needed to overcome the largest discontinuities in the hull function is called the *depinning energy* or the *Peierls-Nabarro* barrier. The Peierls-Nabarro barrier E_{PN} and the friction force F_s start to grow at λ_c with a critical exponent Ψ [110].

$$E_{PN}(\lambda), F_s(\lambda) \propto (\lambda - \lambda_c)^{\Psi} \qquad \Psi \approx 3.0117222 \tag{55}$$

Before closing this section, we quote a number of interesting papers for further studies. In [120], the Aubry transition is described in relation to the devil's staircase. Chou and Griffiths [121] give analytical and numerical strategies to find the ground state of the FK and similar models. Also, the effect of perturbation due to additional harmonics to V_{per} is examined. In [122], the existence of an Aubry transition for a realistic model of an incommensurate gold/gold interface is found. An incommensurate gold grain boundary has been found to be stable by high resolution electron spectroscopy [123]. This study therefore shows the occurrence of vanishing static friction for this real system when the grain boundaries are unstrained. In [124], the effect of finite chains with open boundary conditions is examined. In [125, 126], quasiperiodic potentials are investigated. In [127], the conditions for the existence of a transition analogous to the Aubry transition are derived for a generalized FK model where the harmonic intrachain interactions are replaced by a modified Morse potential, which can represent better interatomic interactions. Xu et al. [128] generalize the FK model to a diatomic chain. The effect of quantum fluctuations on the Aubry transition is studied in a numbers of papers of this group, which are reviewed in [129].

Weiss et al. have also studied the FK-Tomlinson model [108], which adds to each atom in the chain a harmonic interaction with a rigid upper body as in the Tomlinson model. This model exhibits a structural transition, similar to the Aubry transition of the FK model.

7.2. Dynamic FK Model

As already mentioned, the prediction of superlubricity [70] follows from a study of the dynamics of the incommensurate FK model. For its importance, it is worthwhile to treat this topic in detail.

We follow the notation of Shinjo and Hirano [70] and define the FK Hamiltonian obtained by supplementing the potential energy Eq. (41) with a kinetic energy term,

$$\mathcal{H} = T + V_{harm} + V_{per} = \sum_{n=1}^{N} \left[\frac{p_n^2}{2} + \frac{1}{2}(q_{n+1} - q_n - b)^2 + \frac{\lambda}{2\pi} \sin\left(\frac{2\pi q_n}{a}\right) \right] \tag{56}$$

where q_n and p_n are the particle positions and momenta, b is the equilibrium spacing of the chain for $\lambda = 0$, and λ is as in Eq. (41) the strength of the coupling scaled to the elastic spring constant. Notice the difference of notation with respect to Eq. (41) where the positions were denoted as x_n. Moreover, there is a difference of a factor 2π. This is due to the fact that for the dynamics, the first derivative of the potential energy, namely the forces, are the relevant quantities so that the present definitions leads to a simpler form of the equations of motion. With this definition, the Aubry transition takes place at $\lambda_c = 0.1546\ldots$ [130].

The incommensurable ratio of b to the period a of the periodic potential is chosen as the golden mean as described in the previous section by choosing $a = 1$, $b = \tau_g = (1 + \sqrt{5})/2$ expressed through commensurate approximants according to Eq. (47). Periodic boundary conditions $q_{N+1} = q_1 + Nb$ are implemented according to Eqs. (46) and (48). In [70], the number N of particles considered in approximating the golden mean is not mentioned. As argued in [18, 117, 119], a too small approximant could be the reason for the absence of dissipation, named superlubricity reported in this paper in a wide range of velocities. The center of mass (CM) position and velocity are defined for convenience as

$$Q = \frac{1}{N} \sum_n q_n, \qquad P = \frac{1}{N} \sum_n p_n \tag{57}$$

The undamped and driven dynamics is studied by giving the CM an initial kinetic energy and monitoring whether this energy is transferred to the internal motion. In this way, this Hamiltonian model can be used to study the frictional properties by monitoring how the translational CM kinetic energy is transferred to the internal motion of the atoms of the chain. To this purpose, the relative position and velocities of atom n with respect to the CM are defined as

$$\bar{p}_n = p_n - P \qquad \bar{q}_n = q_n - Q \tag{58}$$

With this notation,

$$\mathcal{H}(\bar{p}_i, \bar{q}_i; P, Q) = N\frac{P^2}{2} + \sum_i V_{per}(\bar{q}_i + Q) + \mathcal{H}_0(\bar{p}_i, \bar{q}_i) \tag{59}$$

where $\mathcal{H}_0(\bar{p}_i, \bar{q}_i)$ involves only the degrees of freedom of the internal motion, so that the coupling of the internal motion to the translational degrees of freedom P and Q comes only through the periodic potential.

The authors solve the equation of motion resulting from Eq. (7) with initial conditions for the CM velocity $P = P_0$, $\bar{q}_n$ corresponding to the ground state of the system and all $\bar{p}_i = 0$. The normalization used to define P is such that all $p_n(t = 0) = P_0$. Notice that for a given initial velocity P_0, particles pass over the minima of the potential with the washboard frequency $\Omega = 2\pi P_0$. Shinjo and Hirano find two regimes of motion, a frictional and a superlubric regime and draw the phase diagram sketched in Fig. 16, where the two regimes are given as a function of the CM initial velocity and of the coupling strength λ. The *superlubric* regime is characterized by a recurrent increase and decrease of translational energy. This regime is characterized as the one where the kinetic friction force, defined as the average value of the force resulting from the periodic potential given by

$$F = \frac{1}{N}\dot{P} = -\frac{\partial V_{per}(\bar{q}_i + Q)}{\partial Q} \tag{60}$$

vanishes. Therefore, for all values of the sliding velocity and coupling λ of Fig. 16, the chain would slide with no dissipation. In the following Section 7.3, it will be shown that this

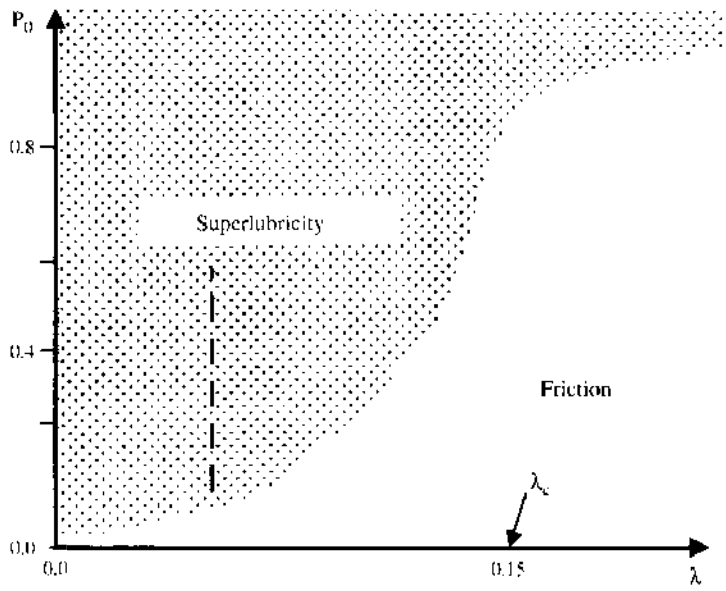

Figure 16. Sketch of the phase diagram presented in Ref. [70], with superlubric and frictional behavior for ranges of values of the initial CM velocity P_0 and coupling to the substrate λ. The vertical dashed line drawn for $\lambda = 0.5 \sim \lambda_c/3$ indicates the range of initial velocities for which simulations are presented in Fig. 18. The superlubric behavior described in Ref. [70] corresponds to the initial behavior of the CM as shown in Fig. 17 but does not account for the decay of CM velocities found in longer simulations (see Fig. 18).

recurrent behavior with no kinetic friction breaks down as a result of parametric resonances, which have not been found by Shinjo and Hirano.

Notice that the superlubric regime in Fig. 16 extends up to velocities as high as more than twice the frequency of the zone boundary phonon of the chain, namely hundreds of m/s. In fact, a value of $P_0 = 1$ gives a washboard frequency $\Omega = 6.28$. As given in Eq. (53), the maximum frequency of the chain is $\omega = 2$. To estimate the velocity in physical units, P_0 should be rescaled by the factor $a\sqrt{K/m}$. By taking for the lattice constant a, the harmonic force constant K, and the mass m of silicon, one finds that the value of P in m/s is given by $P(m/s) = 1.3 \times 10^3 P_0$.

These findings have been thoroughly reexamined in [18, 117, 119] described in Section 7.3, showing that the conclusions drawn in [70] are oversimplified as a result of either too short simulation times or of too small system sizes.

7.3. Conversion of Translational Energy into Heat: An Exact Model

In this section, we present the results obtained in our group, by Consoli et al. [18, 117–119] who have reexamined the finding presented in the previous section, coming to different conclusions. The model studied is exactly the same of [70], described in the previous Section.

The time evolution of the CM momentum is studied mostly for $\lambda \sim \lambda_c/3$ and several values of P_0. According to the phase diagram of [70], a superlubric behavior with recurrent and persistent exchange of energy between CM and internal energy should be observed for this value of λ and $P_0 \geq 0.1$. Consoli et al. find this type of situation only in the very initial phase of motion as shown in Fig. 17. Here there is indeed an oscillatory behavior of P around the value of the velocity corresponding to the washboard frequency $P = \Omega/(2\pi)$, going back to the initial value P_0 after each period of oscillation. However, this behavior does not continue indefinitely as it should in the superlubric regime.

In Fig. 18, the temporal behavior of the CM velocity is shown on a larger timescale for several initial values P_0. A nontrivial time evolution with oscillations of varying period and amplitude is found. This is related to the resonant coupling to particular modes of the chain with wavevector related to the modulation periodicity q. A very fast decay of the CM velocity occurs for $P_0 \sim \omega_q/(2\pi)$. Note again that the dynamics is studied in the absence of a damping term in the equations of motion and that therefore the decay of the CM velocity is only due to the excitations of phonons, which for this simple model are treated exactly. A similar, but

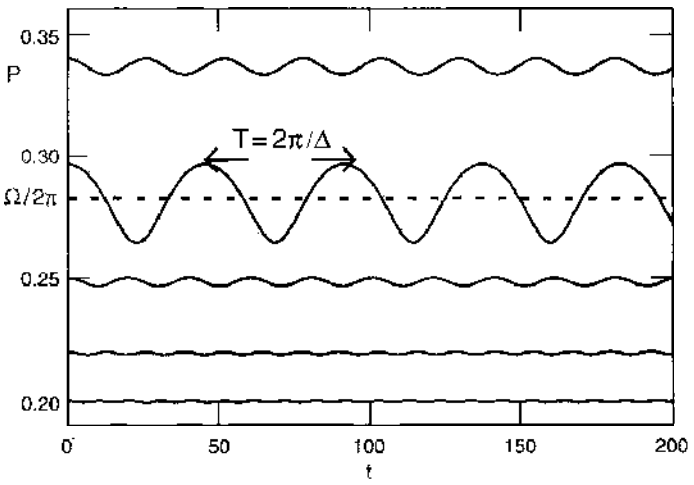

Figure 17. Initial behavior of the CM velocity P for $N = 144$, $b = 233/144$, and weak coupling $\lambda = 0.015 \sim \lambda_c/10$ for a few values of the initial CM velocity P_0 around the main resonance at $P = \omega_q/(2\pi)$. The solid lines are calculated by integrating the full system of equations (61) and are extremely well reproduced by the dashed lines, which are obtained by solving the minimal set of Eqs. (62) (see text). Reprinted with permission from [18], L. Consoli et al., *Phys. Rev. Lett.* 85, 302 (2000). © 2000, American Physical Society.

much slower, decay is found for $nP_0 \sim \omega_{nq}/(2\pi)$. In the study of the driven underdamped FK [17] discussed later in Section 8, it is shown that at these superharmonic resonances, the differential mobility is extremely low. Reference [18] presents an analytical description in terms of the phonon spectrum, which explains the complex time evolution of the CM velocity and identifies the dissipative mechanism that is triggered by these resonances. The oscillatory motion of the CM in the initial phase of the motion shown in Fig. 17 leads to excitation of phonon modes via a sequence of parametric excitations involving more modes in cascade. This mechanism is particularly effective close to the harmonic resonances at ω_{mq}, which act as a *driving* term for the onset of dissipation via subsequent complex parametric excitations.

It is useful to show how this mechanism, which represents a common feature of nonlinear lattices, can be followed in detail by means of the following theoretical approach. The N equations of motions resulting from the Hamiltonian Eq. (56) are solved numerically, for example, by a Runge Kutta algorithm, with initial momenta $p_n = P_0$ and $q_n(t = 0)$

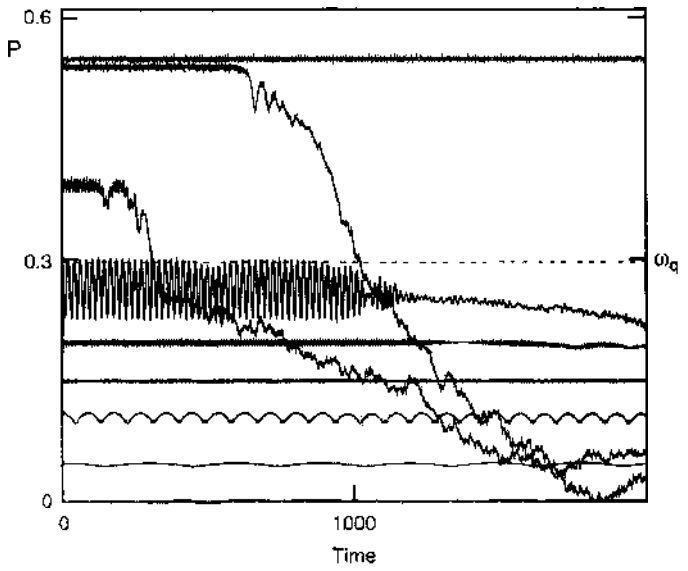

Figure 18. Temporal behavior of the CM velocity P for $N = 233$, $\lambda = 0.05$. Each solid line corresponds to a different initial value P_0. The dashed line corresponds to the main resonance, at $P_0 = \omega_q/(2\pi) = 0.2966$. The solid dots correspond to higher resonances.

corresponding to the ground state obtained by minimizing numerically the potential energy Eq.(41). With the definitions of Eq. (57) and by writing $q_n = nb + x_n + Q$, the equations of motion for the deviations x_n from a rigid displacement read

$$\ddot{x}_n = x_{n+1} + x_{n-1} - 2x_n + \lambda \cos(qn + 2\pi x_n + 2\pi Q) \tag{61}$$

In the limit of weak coupling λ, it is convenient to go from real to reciprocal space by defining Fourier transformed coordinates $x_k = \frac{1}{N}\sum_n e^{-ikn}x_n$ and $x_n = \sum_k e^{ikn}x_k$, where $k = 2\pi K/N$ with $K \in (-N/2, N/2]$, and the normalization is chosen to remove the explicit N-dependence in the equations of motion, which become:

$$\ddot{x}_k = -\omega_k^2 x_k + \frac{\lambda}{2N}\sum_n e^{-ikn}\left[e^{iqn}e^{i2\pi Q}e^{i2\pi x_n} + c.c.\right] \tag{62}$$

$$\ddot{Q} = \frac{\lambda}{2N}\sum_n \left[e^{i2\pi Q}e^{iqn}e^{i2\pi x_n} + c.c.\right] \tag{63}$$

with ω_k given by Eq. (53). Equation (63) is expanded in x_n as:

$$\ddot{x}_k = -\omega_k^2 x_k + \frac{\lambda}{2}\sum_{m=0}^{\infty}\frac{(i2\pi)^m}{m!}\sum_{k_1\ldots k_m}\left[e^{i2\pi Q}x_{k_1}\cdots x_{k_m}\delta_{k_1+\cdots+k_m,-q+k}\right.$$
$$\left.+(-1)^m e^{-i2\pi Q}x_{k_1}\cdots x_{k_m}\delta_{k_1+\cdots+k_m,q+k}\right] \tag{64}$$

Because in the ground state the only modes present in order λ are $x_q = x_{-q} = \lambda/2\omega_q^2$, the CM is coupled only to these modes up to second order in λ:

$$\ddot{Q} = i\lambda\pi\left(e^{i2\pi Q}x_{-q} - e^{-i2\pi Q}x_q\right) \tag{65}$$

$$\ddot{x}_q = -\omega_q^2 x_q + \frac{\lambda}{2}e^{i2\pi Q} \tag{66}$$

$$\ddot{x}_{-q} = -\omega_q^2 x_{-q} + \frac{\lambda}{2}e^{-i2\pi Q} \tag{67}$$

In Fig. 17, the behavior of $P(t) = \dot{Q}(t)$, obtained by solving the minimal set of Eq. (65) with the appropriate initial conditions $Q(t=0) = 0$, $P(t=0) = P_0$, $x_q(t=0) = \lambda/(2\omega_q^2)$, $\dot{x}_q(t=0) = 0$, with the one obtained from the full system of Eq. (61). Equation (65) reproduces very well the initial behavior of the CM velocity, which displays oscillations of frequency Δ around the value $\Omega/(2\pi)$, but does not predict the decay occurring at later times because, as we show next, this is due to coupling to other modes. To this aim, we analyze the relation between the initial CM velocity P_0 and $\Omega/2\pi$.

The initial behavior of the CM motion (Fig. 17) can be described by the *ansatz*:

$$Q(t) = \frac{\Omega}{2\pi}t + \alpha_+ \sin(\Delta_+ t) + \alpha_- \sin(\Delta_- t) \tag{68}$$

Inserting the *ansatz* (68) in the coupled set of Eq. (65), keeping only terms linear in $\alpha_\pm$, both $\Delta_\pm$ are found as roots of:

$$\Delta^2 = \lambda^2\pi^2\left[2Z(0) - Z(\Delta) - Z(-\Delta)\right] \tag{69}$$

$Z(\Delta)$ being the impedance

$$Z(\Delta) = \frac{1}{\omega_q^2 - (\Omega + \Delta)^2} \tag{70}$$

In general, Eq. (69) has (besides the trivial solution $\Delta = 0$) indeed two solutions, related to the sum and difference of the two basic frequencies in the system, ω_q and Ω:

$$\Delta_\pm \cong \left|\omega_q \pm \Omega + \frac{\lambda^2\pi^2}{2\omega_q(\Omega \pm \omega_q)^2} + \cdots\right| \tag{71}$$

Close to resonance, $\Omega \sim \omega_q$, the amplitude α_- dominates (see below), and the CM oscillates with a single frequency $\Delta = \Delta_-$ as shown in Fig. 17. Very close to resonance [more precisely, $\omega_q < \Omega < \omega_q + (2\lambda^2\pi^2/\omega_q)^{\frac{1}{3}}$], the root Δ_- becomes imaginary, signaling an instability. In fact, the system turns out to be bistable as P_0 passes through $\omega_q/(2\pi)$ [18].

Analytically, the relation between Ω and P_0 and the amplitudes $\alpha_\pm$ is determined by matching the *ansatz* (68) with the initial condition:

$$\alpha_\pm = \frac{\lambda^2\pi\Omega}{2\omega_q^2}\frac{1}{(\omega_q \pm \Omega)^3} \tag{72}$$

$$P_0 = \frac{\Omega}{2\pi} + \frac{\lambda^2\pi\Omega}{2\omega_q^2}\left[\frac{1}{(\Omega+\omega_q)^2} + \frac{1}{(\Omega-\omega_q)^2}\right] + \cdots \tag{73}$$

Notice that this equation, which is derived by keeping only linear terms in α_-, is not accurate enough to describe in detail the instability around ω_q where α_- diverges.

An initial behavior similar to that for $P_0 \simeq \omega_q/(2\pi)$ is observed in Fig. 18 for $nP_0 \simeq \omega_{nq}/(2\pi)$. Each of these resonances can be studied as done for the main resonance at ω_q by taking into account terms in higher order in λ in Eq. (64). For $n = 2$, Eq. (64) shows that x_{2q} is driven in next order in λ by x_q:

$$\ddot{x}_{2q} = -\omega_{2q}^2 x_{2q} + i2\lambda\pi e^{i2\pi Q} x_q \tag{74}$$

When $2\pi Q \simeq \Omega t$, x_q will be $\simeq \lambda e^{i\Omega t}$, so that x_{2q} is forced with amplitude λ^2 and frequency 2Ω, yielding resonance for $2\Omega = \omega_{2q}$. Because x_{2q} couples back to x_q, we have a set of equations similar to Eq. (65), but at order λ^2.

This approach shows that the coupling of the CM to the main harmonics nq cannot explain the onset of friction causing the decay of the CM velocity seen in Fig. 18 at later times. The decay of P is due to the fact that the oscillatory behavior of P in the initial phase of the motion leads to parametric resonances involving other modes as shown next. Because x_q is by far the largest mode in the early stage, one can consider second-order terms involving x_q in Eq. (64):

$$\ddot{x}_k = -\left[\omega_k^2 + 2\lambda\pi^2\left(e^{i2\pi Q}x_{-q} + e^{-i2\pi Q}x_q\right)\right]x_k \tag{75}$$

Insertion of the solution obtained above for x_q [Eq. (66)] and Q [Eq. (68)] yields

$$\ddot{x}_k = -\left[\omega_k^2 + A + B\cos(\Delta t)\right]x_k \tag{76}$$

with $A = 2(\lambda\pi)^2/Z(0)$ and $B \sim \alpha_-$. Clearly, Eq. (76) is a Mathieu parametric resonance [131, 132] for mode x_k. The relevance of parametric resonances has been recently stressed [133]. However, in this case, due to the coupling of the CM to the modulation mode q, resonances are not with the washboard frequency Ω but with $\Delta \sim \Omega - \omega_q$. Therefore, instability windows are found around $\omega_k^2 + A = (n\Delta/2)^2$. Because Δ is small close to resonance, one expects to find instabilities for acoustic modes with k small. Indeed, as shown in Fig. 19a, the decay of the CM is accompanied by the exponential increase of the modes $k = 2, 3, 4$ and, with a longer rise time, $k = 1$. However, the instability windows resulting from Eq. (76), shown in Fig. 19b, cannot explain the numerical results of Fig. 19. In Eq. (65), the only linear terms left out in Eq. (75) are couplings with $x_{k\perp q}$, which are much higher order in λ. Nevertheless, these terms are crucial, as they may cause new instabilities due to the fact that, for small k, they are also close to resonance. In [18], it is shown that a wider range of instabilities, which accounts for the behavior found by solving the full system of equations (61), is found by solving the coupled set of equations for mode $x_{\pm k}$ and $x_{k\pm q}$. This mechanism where a parametric resonance is enhanced by coupling to near resonant modes is quite general in systems with a quasicontinuous spectrum of excitations and is related to the one proposed [134] in explaining instabilities in the Fermi Ulam Pasta chain in a different physical context.

In [117, 118], this mechanism is shown to lead to a dynamical transition in the system, which is analogous to the Aubry transition for the static model. Without giving the details

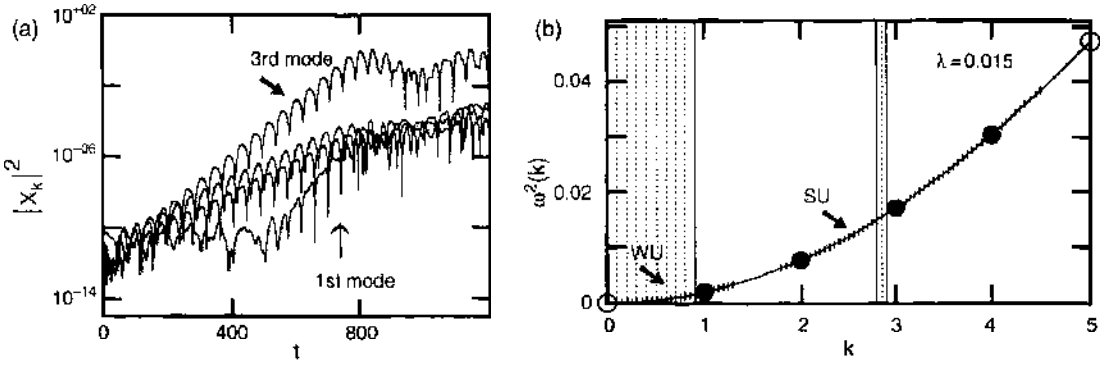

Figure 19. (a) Exponential growth of the amplitude of the Fourier tranform $|x_k|^2$ of the first four acoustic modes from Eq. (61) for $N = 144$, $\lambda = 0.015$, and $P_0 = 0.29$. The parametric excitation of these modes is the cause of the decay of the CM velocity. Notice that the third mode has the fastest growth. (b) Dispersion relation for a chain of $N = 144$ atoms (k are in units of $2\pi/144$). The unstable modes shown in panel (a) are indicated by solid dots. The shaded k ranges are the instability windows resulting from the Mathieu-type Eq. (76), which cannot give account of the instability leading to exponential growth found in the simulations. Conversely, the wiggled regions of the phonon dispersion are the instability ranges obtained by considering also modes $x_{k\pm q}$ (see text). These instability ranges give account of the found instabilities and of the shortest rise time of the third mode, which falls in the middle of the instability range. Reprinted with permission from [18], L. Consoli et al., *Phys. Rev. Lett.* 85, 302 (2000). © 2000, American Physical Society.

of the analytical results derived in those papers, we point out that indeed the average of the friction force given by Eq. (60), which is proportional to $\Sigma_n \cos(2\pi q_n/a)$, can vanish or be finite depending on whether the positions are uniformly distributed over the potential or not, namely

$$\langle \dot{P} \rangle = 0 \quad \text{if} \quad q_n \text{ modulo } a \quad \text{is continuous} \tag{77}$$

$$\langle \dot{P} \rangle \neq 0 \quad \text{if} \quad q_n \text{ modulo } a \quad \text{is discontinuous} \tag{78}$$

Therefore, the initial phase of the motion, in which indeed a recursive exchange of kinetic energy between the CM and internal modes occurs without dissipation, goes over to a dissipative regime with decay of the CM velocity P when the continuous modulation of the atomic position disappears as a consequence of phonon excitations.

For computer simulations, it is important to realize that parametric resonances give rise to instability energy windows leading to exponential growth of the amplitude of phonons in that energy range. Therefore, if the chain is too small, the discreteness of the spectrum can lead to a situation where no modes fall inside the instability range. As shown in Fig. 20 for $N = 144$, the CM velocity P quickly decays, whereas for $N = 21$ no decay exists as predicted in [18] on the basis of the previous treatment, which allows one to estimate the conditions for the existence of resonant growth of modes as a function of N. The effect of decreasing chain lengths has been studied also by Sokoloff [135], who analogously predicts vanishing friction for nanoscale solids due to the discreteness of the phonon spectrum.

In Fig. 21, all energy terms are examined. Initially, the system possesses only the CM kinetic energy E'_{kin}, which decays to zero with time, being transferred into potential energy and kinetic energy of the phonons in equal parts. At the end of the simulation, where complete energy transfer has occurred from the CM to the internal modes, the modes roughly behave as expected from equipartition as $|x_k|^2 \sim 1/\omega_k^2$ [119]. More detailed studies should be performed to establish this fact with certainty. For the driven damped FK model, small deviations from equipartition are found in [17].

Lastly, there is also another type of parametric resonances that also lead to decay of the initial momentum [136]. Based on our expansion (65), we find that modes $x_{q/2}$ are parametrically excited by the oscillatory motion of the CM:

$$\ddot{x}_{q/2} = -\omega^2_{q/2} x_{q/2} + i\lambda\pi\left(e^{i2\pi Q} x_{q/2} - e^{-i2\pi Q} x_{3q/2}\right)$$

$$\ddot{Q} = i\lambda\pi\left(e^{i2\pi Q} x_{-q} - e^{-i2\pi Q} x_q\right) - \lambda\pi^2\left(e^{i2\pi Q} x^2_{q/2} + e^{-i2\pi Q} x^2_{q/2}\right) \tag{79}$$

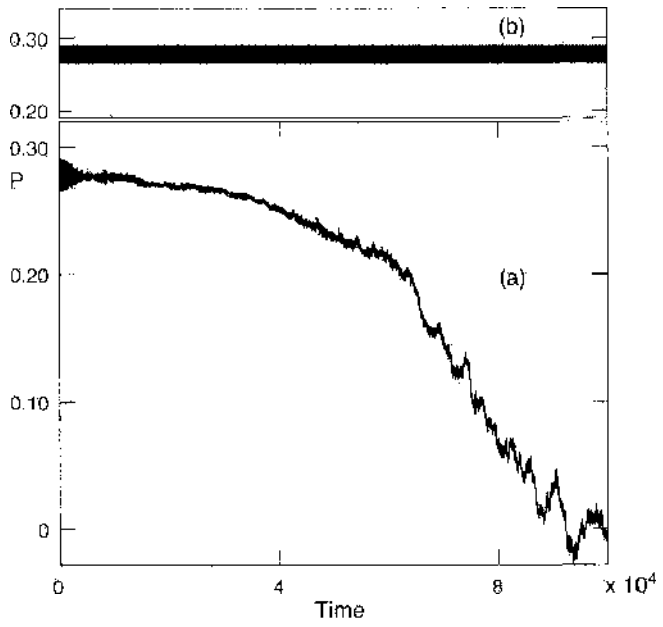

Figure 20. Temporal behavior of P for $\lambda = 0.015$ and $P_0 = 0.29$ for two values of N. (a) $N = 144$, (b) $N = 21$. In the last case, no decay occurs due to the discreteness of the spectrum, which prevents modes from becoming unstable (see text).

These resonances give instability regions (leading to excitation of internal motion and thus to frictional behavior) centered around the values $\omega_{M1} = 2\omega_{\frac{q}{2}}$ and $\omega_{M2} = 2\omega_{\pi-\frac{q}{2}}$. When compared to the standard Mathieu equation, the parametric resonances described by Eq. (79) can be considered peculiar for two reasons: first, the equation for mode $x_{\frac{q}{2}}$ is in fact a set of two coupled equations (x_k being a complex number). Second, the back coupling to the resonant mode $x_{\frac{q}{2}}$ in the equation for the CM motion drives Q inside and outside the instability window, which is not a standard feature of this type of phenomena.

In conclusion, for the 1D FK model, a dynamic frictionless superlubric regime cannot exist because the resonant coupling of the CM to the modes nq or $(\frac{q}{2}, \pi - \frac{q}{2})$ gives rise to an effective damping for the system via a cascade of couplings to more and more modes via the nonlinear terms in Eq. (65). An *apparent superlubricity* can arise in numerical calculations (thus with finite N) and can be attributed to the discreteness of the spectrum on the scale of the size of the instability windows.

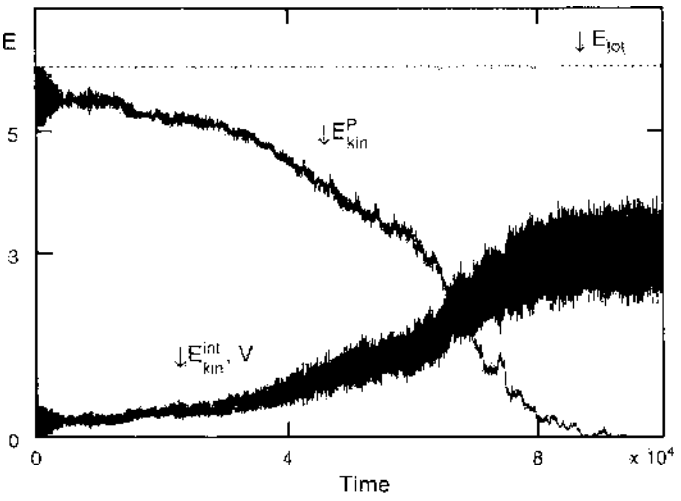

Figure 21. Temporal behavior of kinetic and potential energy terms for the case of Fig. 20a. The potential energy V and internal kinetic energy E^{int}_{kin} are not distinguishable in the figure.

7.4. Relation to Sine-Gordon Equation

Notice that the dynamics of FK model given by Eq. (56) represents the discrete version of the well-known sine-Gordon equation, which can be derived from Eq. (41) by letting N go to infinity while keeping the system size constant so that the interparticle distance goes to zero [132]. The term resulting from the harmonic intrachain coupling $x_{n+1} + x_{n-1} - 2x_n$ becomes the second derivative of the continuous variable $\phi(x, t)$ yielding:

$$\frac{\partial^2 \phi}{\partial t^2} = \frac{\partial^2 \phi}{\partial x^2} + \lambda \sin(\phi) \tag{80}$$

This is why the FK model is also called the discrete sine-Gordon equation. The sine-Gordon equation is exactly solvable [137] and has solutions in the form of solitons or solitary waves. In discrete models, *kinks* are analogous to solitons. The relation to the continuous sine-Gordon equation and its solutions is used in [138] to study the kink dynamics in finite FK chains. Resonance mechanisms due to the interplay between kink velocity and the phonons of the chain are also outlined in this paper and shown to lead to energy localization at the surfaces.

8. DRIVEN, DAMPED DYNAMICS

An important step toward the understanding of friction at the atomic scale is to be able to describe the response of a system of strongly interacting atoms to an external driving force in presence of a periodic potential and of some damping mechanism at finite temperature. This knowledge is relevant to understand nanoscale friction as well as macroscopic friction in the boundary lubrication regime described in Section 2. This step implies studying the nonequilibrium dynamics of driven systems of interacting particles onto periodic substrates, a complex phenomenon with many facets depending on temperature, boundary conditions, range, strength and nature of interactions, commensurability, and external fields. The steady-state in these experimental situations are usually studied by means of the Langevin dynamics with viscous dissipative terms and stochastic forces as described in Section 11.3. The resulting complex dynamics, particularly in an underdamped regime, is all but fully explored and understood.

For noninteracting atoms, this problem reduces to the diffusion of a Brownian particle in presence of a periodic potential, a situation that has been studied intensively, particularly in the context of surface diffusion and crystal growth, and which, about a half-century after the seminal work of Kramers [139], is by now almost completely understood [132, 140]. In Section 8.1, we review the main results due to Kramers for the driven motion of a single atom on periodic potentials at $T = 0$ and $T \neq 0$. In the same section, we compare these results with those resulting from the simplest system of interacting particles: a harmonic dimer. This simple example [141] illustrates how the interplay between interatomic interactions and thermal fluctuations can lead to new effects. Then in Sections 8.2 and 8.3, we go over to a description of the main results obtained for more complex driven systems at $T = 0$ and $T \neq 0$.

8.1. Driven Motion of Single Particles and Dimers

Let us reexamine the main results due to Kramers [132, 139, 140] to appreciate the effect brought in when considering not a single but many interacting particles. Consider the motion in presence of a 1D periodic potential.

$$m\ddot{x} + m\eta\dot{x} = -\frac{2\pi}{a} V_0 \sin\left(\frac{2\pi}{a} x\right) + F + f(t) \tag{81}$$

As described in detail in Section 11.3, the friction η and the noise $f(t)$ describe the coupling to nondescribed degrees of freedom, which serve as a heat bath. The fluctuation dissipation theorem requires

$$\langle f(t) f(t') \rangle = 2m\eta k_B T \delta(t - t') \tag{82}$$

where k_B is the Boltzman constant and T the temperature.

This equation can be made adimensional by introducing a characteristic time

$$\tau = \frac{a}{2\pi}\left(\frac{m}{k_B T}\right)^{1/2}$$

and by defining

$$\tilde{x} = \frac{2\pi}{a}x, \quad \tilde{t} = \frac{t}{\tau}, \quad \tilde{\eta} = \eta\tau, \quad \tilde{V}_0 = \frac{V_0}{(k_B T)}$$

$$\tilde{f} = \frac{f}{k_B T}\frac{a}{2\pi}, \quad \tilde{F} = \frac{F}{k_B T}\frac{a}{2\pi}$$

For typical values $m \sim 2 \times 10^{-26}$ kg, $T = 300$ K, $a \sim 2$ Å, we have $\tau \simeq 70$ fs. In adimensional units, and dropping the tildes on all rescaled variables, the equation of motion becomes

$$\ddot{x} + \eta\dot{x} = -V_0 \sin x + f + F \tag{83}$$

with

$$\langle f(t)f(t')\rangle = 2\eta\delta(t - t') \tag{84}$$

Consider first the situation at $T = 0$ by setting $f = 0$. When a constant force F is applied to a particle, the total potential is a corrugated plane with slope F. Local minima, where the particle can be locked exist for small forces and disappear at forces $F_f = V_0$ (or $2V_0\pi/a$ in physical units). Thus, by slowly increasing F, the atom goes from a locked to a running state when the force exceeds the static friction force $F = F_f$. Then, the particle slides with constant drift velocity v on the substrate, resulting in a linear relation between v and F for high values of the driving force:

$$F = \eta v \tag{85}$$

The relation between the applied force and the average drift velocity is called velocity–force characteristic and its slope defines the *mobility* B as

$$B = \frac{v}{F}$$

Conversely, if the force is decreased when the particle is in the running state, the critical force for the transition to the locked state may be shifted to a lower value F_b due to the inertia of the motion. In the underdamped regime identified in [132], $\eta/\sqrt{V_0} < 1.19$, the value of the backward force is

$$F_b = 4\eta\frac{\sqrt{V_0}}{\pi}$$

In the underdamped regime, the forward critical force F_f is larger than the backward value F_b so that hysteresis can occur. In other words, at $T = 0$ the particle is bistable for values of the force between F_b and F_f, as it can either be locked at the bottom of a local minimum or in a running state where the energy gain between potential minima compensates the energy loss due to friction. Notice that the forward force F_f does not depend on the damping, whereas the backward value F_b depends linearly on it. Therefore, the bistable region shrinks with increasing η and vanishes at $\eta \leq \eta_c = \frac{\pi}{4}\sqrt{V_0}$. For forces $F < F_b$, only the locked state exists.

Kramers considered the effect of thermal fluctuations and obtained a formula for the rate at which the particle switches between the stationary locked and running state, showing that the $T = 0$ bistability disappears at finite temperatures. Moreover, the particle has always the chance to get untrapped because of thermal fluctuations so that also the locked state at forces below F_b is, strictly speaking, not locked anymore. However, when the thermal energy is much less than the energy barrier, the drift velocity, and hence the mobility, will vanish, although the particle can occasionally jump from well to well. In this situation, one talks about *creep* motion. The threshold between creep and running motion is not sharp but can

be identified by an increase of the mobility. Computationally, the creep regime is obviously the most difficult to study, and it is often disregarded in the studies of many interacting particles that will be discussed in Section 8.3.

The situation for interacting particles is more complex, and very intriguing results have been reported that suggest that bistability can survive at finite temperatures for chains of interacting particles [142, 143].

We compare now the driven motion of a single particle with that of a dimer, formed by two particles interacting via a harmonic potential with force constant K and equilibrium length b. The stretching frequency of the dimer is thus $\omega_0 = \sqrt{2K}$. By comparing these results to those obtained for a single atom, it is easy to understand how interatomic interactions together with thermal fluctuations can lead to new effects.

In Fig. 22, we show the velocity–force characteristic for the monomer and for a dimer with $b = \tau_g a$ on a periodic substrate of depth $V_0 = 2.5$ at $T = 0$, where hysteresis appears for forces between F_b and F_f. In Fig. 23, thermal fluctuations are considered, and the threshold value of the force for motion disappears. As a consequence, the mobility is always different from zero when $F \neq 0$. Note that the energy barrier is only 2.5 times the thermal energy. We have reported also the analytical behavior derived by Kramers in the limit of large η for the velocity as a function of the driving force:

$$v = \left\{ \left[\frac{\eta^2}{4} + V_0 \cos\left(\arcsin\left(\frac{F}{V_0} \right) \right) \right]^{1/2} - \frac{\eta}{2} \right\} \left(e^{-(2V_0 - F\pi)} - e^{-(2V_0 + F\pi)} \right) \tag{86}$$

where $2V_0 - F\pi$ and $2V_0 + F\pi$ are the energy barriers for forward and backward motion, respectively (note that in adimensional units $\pi = a/2$). As we can see from Fig. 23b, Eq. (86) reproduces the simulation results for $F < 1$, but this range increases for larger values of V_0, where the activated processes are more pronounced. The behavior of the mobility for large F, where the particle performs a drift motion with a small contribution of the noise term, can be shown to be [1]

$$F = \eta v \left(1 + \frac{V_0^2}{2v^4} \right) \tag{87}$$

In particular, if F is very large compared to V_0, the term in parentheses tends to one and the characteristic curve becomes linear:

$$F \simeq \eta v \tag{88}$$

We note in passing that Fig. 8.8b in [1], which reports the same results as in Fig. 23, is only a sketch and that the numerical values given there are not exact.

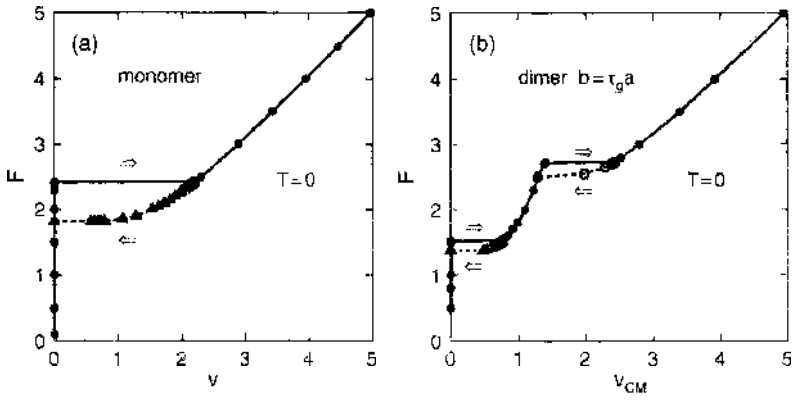

Figure 22. Velocity–force characteristic of a monomer (a) and a dimer with $b = \tau_g a$ (b) on a periodic substrate of depth $V_0 = 2.5$ at $T = 0$. For the monomer, hysteresis appears for forces between F_b and F_f (see text). For the dimer, a second hysteresis loop appears for CM velocity $v_{1,0}$ where the washboard frequency is in resonance with the stretching frequency of the dimer $\omega_0 = (2K)^{1/2}$, exciting the internal degrees of freedom.

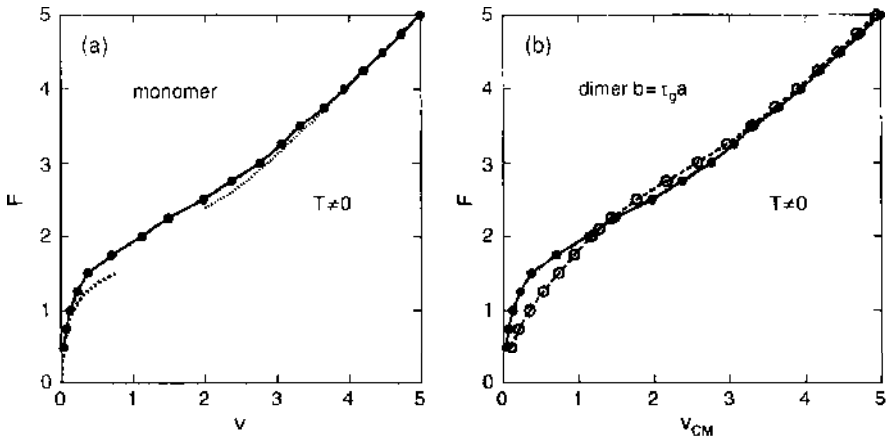

Figure 23. Velocity–force characteristic of (a) a monomer (filled circles) and (b) of a dimer with $b = \tau_0 a$ (open circles) compared to the monomer (filled circles) at $T \neq 0$ on a periodic substrate of depth $V_0 = 2.5$ (in units of $K_B T$). At $T \neq 0$, the threshold value of the force for motion disappears in both cases. In (a), the limiting behavior for low velocity given by Eq. (86) and for high velocity by Eq. (87) are plotted with dotted lines. Notice that the dimer drift velocity is much higher than that of a single atom when the drift velocity is less than the natural stretching frequency.

Next we consider the dimer. Equation (81) can easily be generalized for this case [141], and the motion of the center of mass (CM) can be monitored. The presence of the frequency ω_0 brought in by the interparticle interaction gives rise to a richer dynamic behavior. As for the monomer, a critical force F_f^{dim}, which depends on the value of b, is needed to achieve motion for $T = 0$ as shown in Fig. 22b. For larger values of F, the velocity increases as a function of the external force, but at a certain value of the force $F = F_r$, another plateau appears in the $v_{CM} - F$ characteristic (v_{CM} being the CM mean velocity), signaling a dynamic crossover in the system. Finally, keeping increase of the force, the linear regime is recovered as shown in Fig. 22. As described in Section 4, in the CM frame, the external potential leads, for a drift motion $x_{CM} \sim v_{CM} t$, to a time-periodic force acting on the particles, with "washboard" frequency given by v_{CM}. The force F_r, where the second plateau appears, physically corresponds to the point where the washboard frequency is in resonance with the stretching frequency of the dimer $\omega_0 = \sqrt{2K}$, exciting the internal degrees of freedom. In correspondence with the two plateaus in the characteristic curve, two regions of hysteresis and bistability are found. Thus, when F is decreased, a first hysteresis occurs in proximity of $v_{CM} = \omega_0$, at a value $F < F_r$, where the characteristic curve has a discontinuous derivative, while a second hysteresis is found when F is decreased further from F_f and another critical value F_b^{dim}, where $v_{CM} = 0$, is obtained as for the monomer. The qualitative behavior is the same for different b [141], but the values of F_f^{dim} and F_b^{dim} can differ significantly as a function of b.

The behavior outlined for $T = 0$ smears out at finite temperatures. The static friction force vanishes and no bistabilities and hysteresis are present, as shown in Fig. 23. The most noticeable result coming out of the comparison between the behavior of a single atom and a dimer is that for weak forces, the dimer drift velocity becomes much higher than that of a single atom when the drift velocity is less than the natural stretching frequency. However, this behavior reverts when the forces get larger and the drift velocity comes close to the frequency ω_0 corresponding to the stretching vibration of the dimer. The mechanism of excitation has been studied in detail in [141] and shown to consist of a parametric excitation of the stretching mode due to the drift CM velocity.

For completeness, we mention that the motion of atoms on periodic potentials is very important for thermal diffusion, which is described by Eq. (81) with $F = 0$. Information about the diffusive behavior of the particles is obtained by computing the mean square displacement (MSD) $\langle x^2(t) \rangle$, where $\langle \cdot \rangle$ denotes the average over the realizations. The diffusion coefficient D is defined by

$$D = \lim_{t \to \infty} \frac{\langle x^2(t) \rangle}{2t} \tag{89}$$

Usually, it is assumed that the dependence of D on temperature should follow the Arrhenius law:

$$D = D_0 \exp(-E_a) \tag{90}$$

where D_0 is a prefactor and E_a is the activation energy for diffusion, scaled to $k_B T$. In Eq. (90), both D_0 and E_a are assumed to be T independent. However, some recent studies have already shown that there may be deviations from the Arrhenius behavior [144–146]. Deviations from Arrhenius behavior is also found for the dimer [141] except for the commensurate case $b = a$.

8.2. Driven Systems at $T = 0$

The dynamics of the driven damped incommensurate FK model at zero temperature has been thoroughly studied in two subsequent papers by Strunz and Elmer [17]. The overdamped limit taking $\ddot{x} = 0$ has been treated in [103]. In the underdamped limit, this situation has been studied for a small number of particles ($N < 10$) in [147, 148]. More results for incommensurate and commensurate cases at finite temperature are discussed also in relation to the results at $T \neq 0$ in the following Section 8.3.

In [17], Strunz and Elmer start from the equation of motion of the FK model for a chain of lattice spacing b with a periodic potential of periodicity a in presence of a driving force $\tilde{F}$ and a damping term η:

$$\ddot{x}_n + \gamma \dot{x}_n = x_{n+1} + x_{n-1} - 2x_n - \lambda \sin(x_n) + F \tag{91}$$

with $\gamma = \eta/\sqrt{km}$, $\lambda = (2\pi/a)^2 V_0/K$, and $F = (2\pi/a)\tilde{F}/K$. Lengths and time are in units of $a/(2\pi)$ and $\sqrt{m/K}$, respectively, where m is the mass of the particles and K the force constant of the harmonic interactions. We note that these units correspond to those of the potential energy Eq. (41) so that the critical value at which the Aubry transition occurs is $\lambda = \lambda_c = 0.971635406$. Chains of N particles (with N = ranging from 144 to 2584) with periodic boundary conditions $x_{n+N} = x_n + Nb$, with b expressed as $b = 2\pi M/N$ are considered mostly for incommensurate ratios of the equilibrium chain spacing $b = (3 - \sqrt{5})/2$. Smaller values of N as well as nearly commensurate ratios are also considered for comparison. In the first paper, they consider the underdamped regime with $\gamma = 0.5$ and in the second one the case with extremely weak damping $\gamma = 0.05$.

By writing the sliding velocity v as the time average of the particle velocities

$$v = \langle \dot{x} \rangle = \lim_{T \to \infty} \frac{1}{T} \int_0^T \frac{1}{N} \sum_{n=1}^{N} \dot{x}_n \, dt \tag{92}$$

and by defining an effective temperature T^*, related to the fluctuations of the particle velocities as

$$T^* = \lim_{T \to \infty} \frac{1}{T} \int_0^T \frac{1}{N} \sum_{n=1}^{N} (\dot{x}_n - v)^2 \, dt \tag{93}$$

the kinetic friction force as a function of the sliding velocity v can be obtained by equating the work of the force to the energy dissipated by the damping as

$$F = \gamma v \left[1 + \frac{T^*}{v^2} \right] \tag{94}$$

Equation (94) shows that, once in motion, the chain can slide indefinitely if $\gamma = 0$ and that the mobility $B = v/F$ is always less or equal to the value $1/\gamma$, which applies in the limit of zero coupling to the substrate (i.e., $\lambda = 0$).

The authors point out that a state that is compatible with the symmetry of the problem is the *uniform sliding* state where every particle performs the same motion shifted in time

by t_1, namely $x_{n+1}(t) = x_n(t + t_1)$, which can be described by generalizing the modulation function Eq. (43) to a *dynamic modulation function* as

$$x_n(t) = an + vt + \alpha + g(an + vt + \alpha) \tag{95}$$

where α is an arbitrary phase.

The velocity force characteristics for the uniform sliding state is studied analytically by solving Eq. (94) by use of the *ansatz* Eq. (95) for the uniform sliding state. The behavior of $F(v)$ is shown in Fig. 24. The velocity force characteristic is found to be non-monotonic as a result of resonances. The difference from the kinetic friction γv without interactions with the substrate is given in the inset. One can see a series of peaks, which imply that a large increase of the force is needed to achieve a small increase of velocity. The work done by the force is only partially turned into kinetic energy of the CM of the chain and leaks away via the damping of the internal oscillatory motion. These results are another manifestation of the resonant behavior generated by the washboard frequency that we have discussed qualitatively in Section 4 and in more detail in Section 7.2.

Note that the velocity force characteristic shown in Fig. 24 only addresses the role of kinetic friction of the uniform sliding state with sliding velocity v. The transition from locked to running states and the occurrence of fluid sliding states is studied by Strunz and Elmer in the second paper for very weak damping.

The other important finding concerns the stability of the uniform sliding state. Two types of resonances, due to the washboard frequency, are shown to lead to instabilities of the uniform sliding state indicated by dotted lines in Fig. 24. The first type are the resonances due to coupling of the CM to the phonon modes with the wavevector of the modulation potential $q = 2\pi b/a$ and to its harmonics nq. Resonances occur at values of the velocity $v_n = \omega_{nq}/(2\pi n)$. As described in Section 7, the excitation of these phonons gives rise to dissipation via the subsequent parametric excitation of more and more modes. The second type

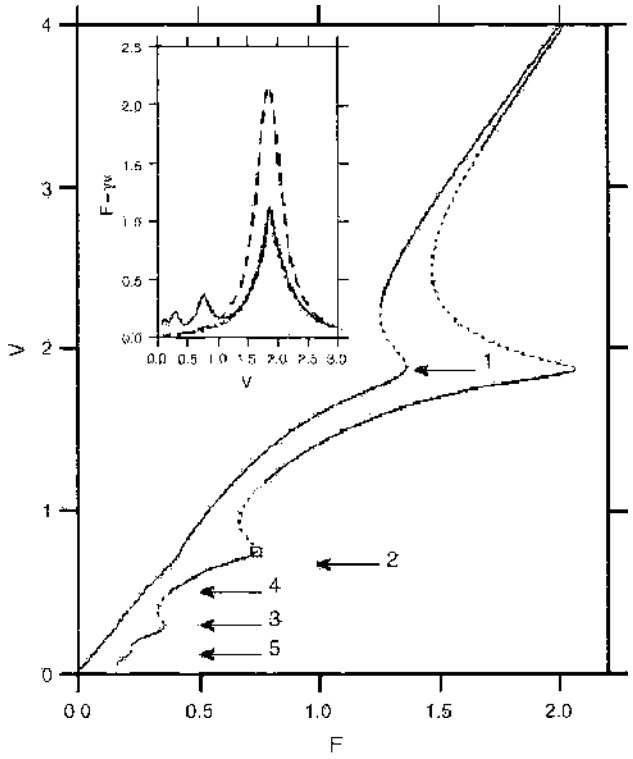

Figure 24. Velocity force characteristic of the uniform sliding state described by the *ansatz* of Eq. (95) from Ref. [17]. Solid and dotted lines indicate stable and unstable solutions, respectively. The parameters are $b = (3 - \sqrt{5})/2$, $\gamma = 0.5$, and $\lambda = 1$ (left curve) and $\lambda = 2$ (right curve). The arrows denote the resonant values of v given by $v_n = \omega_{nq}/(2\pi n)$ where the number indicates the value of n. Reprinted with permission from [17], T. Strunz and Elmer, *Phys. Rev. E* 58, 1601 (1998). © 1998, American Physical Society.

of instability is given by parametric resonances that describe the decay of n washboard waves into two phonons of wavevector $na/2 \pm q$, also described in Section 7. In presence of damping, parametric resonances occur only beyond a certain threshold of the coupling $\sim\gamma^{1/n}$.

Close to each resonance of the first type, where the velocity–force characteristic of the uniform sliding state have a negative slope, the system becomes bistable, but now the two stationary states are both running. The system can organize in domains of different uniform sliding states, as shown in Fig. 25. Two types of domains appear, each being characterized by uniform sliding with particle densities either larger or smaller than $1/a$. Neighboring domains are separated by domain walls of finite size. All domain walls move with the same velocity, which can be different from the center of mass velocity. These two-domain solutions are not found in numerical simulations for values of the registry close to an integer. It is remarkable that domain formation occurs also in the case of commensurate registry where, intuitively, a uniform sliding state should be the most favored [149]. There are no rules to predict which will be the structure of the domains. The two-domain state can become unstable toward multidomain formation, particularly near higher order resonances that are relatively close to each other. The authors conjecture that the appearance of domain formation should lead to hysteretic behavior at each resonance, which could be observed experimentally.

In the second paper [17], the authors examine the underdamped regime for extremely weak damping $\gamma = 0.05$. A decreasing damping increases the complexity of the motion, and spatiotemporal chaos appears. The focus is now on the transition between the locked stationary state and the sliding states and on the chaotic sliding states. Hysteresis loops are observed between three types of solutions: the stationary *locked* state, the chaotic sliding state, which the authors call *fluid sliding state*, and the *solid sliding* state, which corresponds to a motion with practically no internal vibrations. The latter, which corresponds to the highest mobility $B = 1/\gamma$, becomes the only solution for very high values of the driving force. The authors note that in principle all sliding states that do not attain the maximum mobility could be called fluid sliding states, but they restrict it to states with spatiotemporal chaos that appear for extremely weak damping and were not found in the regime $\gamma = 0.5$ studied in the first paper. They ascertain the chaotic nature of these states by studying their Lyapunov exponents. The velocity force characteristics of the fluid sliding state is almost featureless contrary to the case of Fig. 24, where domain formation occurred. Interestingly, the chaotic nature of the fluid sliding state does not depend on the commensurability of the chain but represents a general feature at low damping.

The authors investigate also the situation with values of the interparticle distance close to commensurate. In this case, by increasing the drive, they observe a rather sharp transition

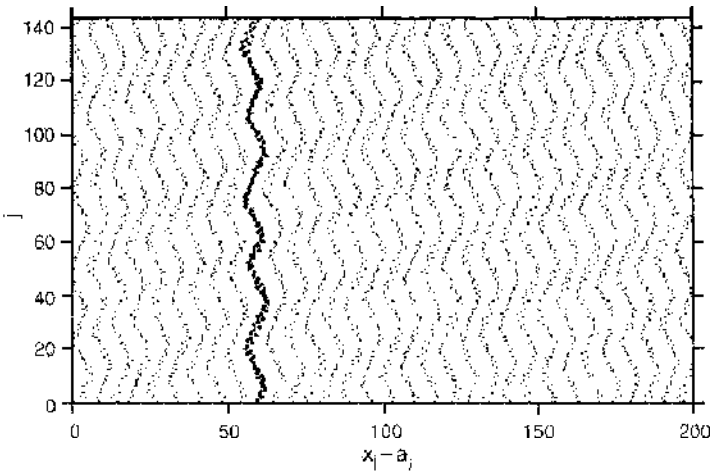

Figure 25. Dynamical domains of different particle density. A series of snapshots taken at equidistant time steps ($\delta t = 2\pi/\omega$) are shown. A particular zig-zag shaped snapshot is highlighted. The zigs and zags correspond to two different kinds of domains that are characterized by uniform sliding. Parameters: $N = 144$, $M = 55$, $\lambda = 2$, $\gamma = 0.5$, $F = 0.8$. Reprinted with permission from [17]. T. Strunz and Elmer, *Phys. Rev. E* 58, 1601 (1998). © 1998, American Physical Society.

from the fluid sliding state to a state with domain formation. One type of domain is so small that they can be seen as traveling kinks. Examples of a kink dominated sliding state and of the fluid sliding solution are given in Fig. 26. This transition displays no hysteresis for long-enough chain, whereas short chains display bistability between the different sliding states. The authors suggest that the hysteresis found in studies at finite temperature by Braun and coworkers [105, 150, 151] could be due to limited chain lengths. However, in [151], hysteresis is said not to be affected by finite size effects. We discuss further the results of Braun and coworkers in the following Section 8.3.

The fluid sliding state can also be characterized by the effective temperature T^*, defined as the average kinetic energy in frame comoving with the center of mass [Eq. (93)], due to excitation of phonon modes. The authors pose the question whether the spatiotemporal chaos can be considered equivalent to a system in thermal equilibrium. This question has been posed also in the context of thermal diffusion [152, 153]. They find that although the velocity distribution is Gaussian, small deviations from equipartition are present, so that they conclude that the chaotic state is not in thermal equilibrium, which is to be expected for a driven system.

8.3. Driven Systems at $T \neq 0$

The results for driven and damped motion at finite temperatures are not yet so clear cut and are certainly the most difficult to review in a coherent fashion. The models used are more complex, aiming at describing particular adsorbate layer-surface systems and are therefore more difficult to compare. However, from the studies we discuss next, the role of interactions in the sliding layer are consistently shown to lead to complex, hysteretic dynamics also at finite temperatures, irrespective of the dimensionality of the system. We remind that, as discussed in Section 8.1, at finite temperature, creep motion due to thermal excitations is always possible. However, because it corresponds to a vanishing mobility, as in the original references, we will loosely use the term *pinned* or *locked* for states in the creep regime.

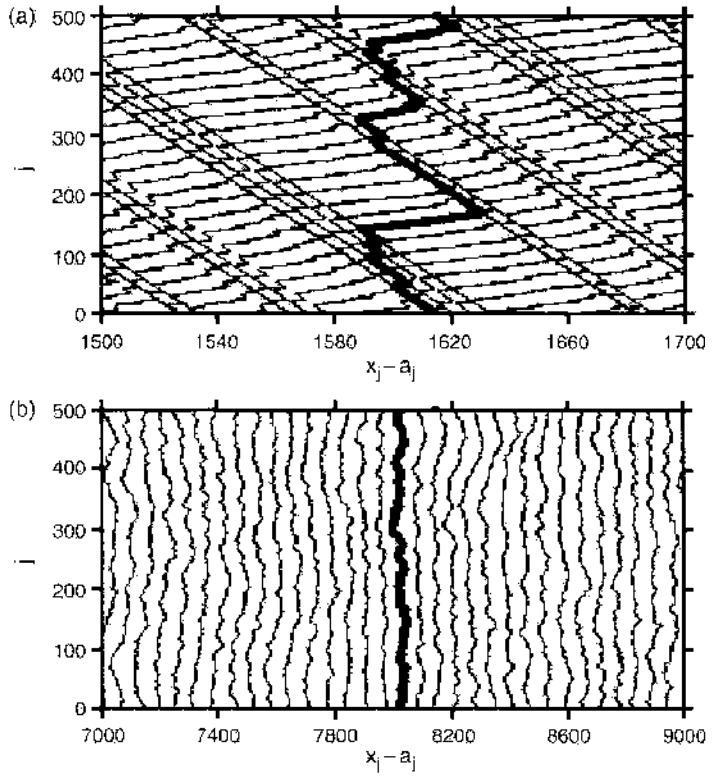

Figure 26. The dynamics of the kink-dominated sliding state (a) and of the fluid sliding state (b). Several snapshots are taken at equidistant time steps (a) $\delta t = 2\pi/v$, (b) $\delta t = 20\pi/v$. In each case, a particular snapshot is highlighted. Parameters are (a) $F = 0.2$, (b) $F = 0.3$ and $N = 500$, $M = 25$ (i.e., $b = \pi/10$), $\lambda = 2$, $\gamma = 0.05$. Reprinted with permission from [17], T. Strunz and Elmer, *Phys. Rev. E* 58, 1601 (1998). © 1998, American Physical Society.

Pioneering work on the problem of the driven motion of adsorbed monolayers has been done by Persson [15]. Single adsorbates and clusters are studied in [154]. In [15], Persson studies the Langevin dynamics of a system of particles interacting via Lennard-Jones potentials (with energy ϵ at the equilibrium distance r_0) on a corrugated square lattice surface described by a potential of the form:

$$V_{per}(x, y) = V_0 \left[2 - \cos\left(\frac{2\pi}{a}x\right) - \cos\left(\frac{2\pi}{a}y\right) \right] \tag{96}$$

Parameters are chosen to describe Xe on the Ag(100) with a ratio of r_0 to the lattice spacing a of the substrate $r_0/a = 1.56$. At half coverage, depending on the ratio of the relevant energies ϵ and V_0, the minimum energy structure of the adsorbate is either a commensurate $c(2 \times 2)$ lattice at large V_0/ϵ or an incommensurate triangular structure at low V_0/ϵ. Such an incommensurate structure is also obtained at coverages slightly higher than a half.

The commensurate $c(2 \times 2)$ structure melts at a temperature $T_c = 1.2\epsilon$ for $V_0/\epsilon = 2$. Below T_c, this structure is strongly pinned by the substrate. In this case, the adsorbate begins to slide for applied forces higher than a threshold value F_f. For forces above this threshold, the layer goes over from a $c(2 \times 2)$ lattice to a fluid state that resembles the triangular incommensurate unpinned structure found for low coupling to the substrate. When the force is then decreased, the system gets pinned again at a lower value of the force $F_b < F_f$ as found for a single particle. Persson draws the general conclusion that hysteresis will always be present in velocity–force characteristics for a solid commensurate adsorbate structure. We note that hysteresis is a process that, in general, depends on the rate with which the force is changed and that should vanish in the adiabatic limit. This issue is not addressed in the papers quoted in this section. The presence of hysteresis is justified by the analogy of the process leading to the pinned structure when the force is decreased to a nucleation process. The fluid state becomes unstable against formation of solid $c(2 \times 2)$ islands. These islands move into a fluid that acts as a drag force giving rise to energy dissipation and leading to a heating of the fluid. When the layer is in the fluid sliding state, it is possible to characterize it by the effective temperature T^*, which can be calculated from the particle velocities during the simulations as [155]

$$k_B T^* = m\frac{(\langle \dot{x}^2 \rangle - \langle v \rangle^2)}{2} \tag{97}$$

$v = \langle \dot{x} \rangle$ being the drift velocity. Alternatively, T^* can be calculated by equating the energy transferred to the layer by the external force to the energy transferred to the substrate, yielding

$$k_B T^* = k_B T + m\frac{F^2}{2m\eta\bar{\eta}}\left(1 - \frac{\eta}{\bar{\eta}}\right) \tag{98}$$

where $\bar{\eta} = F/(mv)$. Indeed, at a force lower than F_f, an increase of the layer temperature occurs. By analyzing several simulations, the force F_b at which the fluid system goes back to the $c(2 \times 2)$ pinned structure is found to occur at $F_b = F_f/2$ or when the temperature in the layer reaches (from above) the melting temperature T_c. Hysteresis is then expected whenever solid adsorbate structures can be formed. Moreover, the result $F_b = F_f/2$ implies a ratio of kinetic to static friction of 0.5 as found experimentally in many sliding systems (see also Section 2). Another important finding is that while reducing the force, the velocity jumps discontinuously to zero at F_b. The layer cannot sustain a constant sliding. If the layer were driven by a spring moving at constant velocity as done in macroscopic experiments, stick-slip motion would be observed.

Conversely, no hysteresis and bistability is found for the liquid layer above T_c, nor in the case of weak coupling to the substrate or away from exact half coverage where the adsorbate layer is incommensurate.

In successive works, the situation of commensurate adsorbates has been examined by Granato and Ying [143], whereas an incommensurate situation close to commensurability, which is similar to the one studied by Persson in [15] close but not exactly at half coverage,

has been studied by Braun and coworkers in an anisotropic 2D model in [105, 150] and in 1D in [151]. Incommensurate contacts are studied in [150].

The study of Granato and Ying [143] aims at verifying how general is the finding of hysteresis [15] in the transition from a locked state to a fluid sliding state for a commensurate contact in Lennard-Jones systems. They consider a pinned commensurate overlayer within a uniaxial 2D FK-model

$$\mathcal{H} = \sum_{i,j} \left[\frac{p_{ij}^2}{2m} + \frac{K_x}{2}(x_{i+1,j} - x_{ij} - b)^2 + \frac{K_y}{2}(x_{i,j+1} - x_{ij})^2 - V_0 \cos\left(\frac{2\pi x_{ij}}{a}\right) \right] \tag{99}$$

where the second and the third term represent intrachain and interchain harmonic interactions.

Simulations at finite temperature are performed, as usual, by Langevin dynamics. Due to the harmonic interactions, the particles have a fixed number of neighbors contrary to the case of interactions with a finite range like the Lennard-Jones potential. Therefore, even at high temperature, when no long-range order exists anymore, the fluid keeps some order [156] and strictly speaking cannot be called a fluid. For the same reason, the process of melting of this structure cannot go via topological defects such as dislocations. With this caveat in mind, the equilibrium structure is a chain-like commensurate structure that displays a melting transition at a critical temperature T_c to a fluid that is depinned from the substrate. A hysteretic transition is found also for this system, confirming one of the main findings of [15] for Lennard-Jones systems. Also in this study, the layer temperature is monitored as described above. At $T < T_c$, when the layer begins to slide at F_f, its temperature remains very close to the substrate temperature T. The system is a *solid sliding state*, with no internal motion; the sliding structure is indistinguishable from the solid pinned phase, if periodic boundary conditions are used. However, the structure becomes incommensurate, as for Lennard-Jones systems, if a small misfit is considered. Therefore, the force causes a transition from a commensurate pinned phase to a sliding incommensurate solid. By reducing the force, a behavior similar to the one described by Persson is found, including overheating of the sliding layer leading to a "dynamical" melting and the velocity gap with resulting stick-slip behavior. The authors also show that hysteresis disappears if the substrate temperature is higher than T_c. The only difference with respect to Persson's results [15] is that the ratio of static to kinetic friction is not found to be 0.5. Moreover, as shown in [157], the general features of the dynamics survives also in presence of weak disorder.

Lastly, we note that, due to the strong anisotropy of the potential, the system is quasi–one-dimensional, but the authors say they find a similar hysteretic behavior in more isotropic situations. As argued by Granato and Ying, one would expect the dimension to be relevant. The drift velocity of a commensurate layer is limited by the nucleation and mobility of defects like kinks and antikinks. In one dimension, the kinks are excited at any finite temperature, whereas in two dimensions, kinks become domain walls that require a finite activation energy to be formed for $T < T_c$. It is a pity that the effect of thermal fluctuations and of dimensionality have not been addressed systematically also within the conventional 1D and 2D FK model, as to make a direct contact with results obtained without thermal fluctuations like the ones of [17].

The issue of dimensionality comes back also in the work of Braun and coworkers [105, 142, 150, 151]. In [105, 150], they study a generalized 2D FK model for nearly commensurate contacts, in the underdamped regime at finite temperature by means of Langevin dynamics. The FK model is extended by replacing the harmonic interatomic interactions by an exponential interaction with a repulsive core. Moreover, the periodic potential is not a simple cosine function but a rectangular, strongly anisotropic potential meant to describe a surface with corrugated channels like W(112) on which Na atoms are adsorbed. However, as pointed out by the authors, this model has the same features of the FK model, in that the substrate is rigid and the commensurability of the lattice parameters of the mobile lattice of atoms and substrate can be chosen at will. The ground state in this case is pinned and consists of commensurate regions separated by kinks. The sliding state, starting at $F = F_f$, is a kink running state in which only the kinks and not the individual atoms move. The forward force F_f

can be estimated, in analogy to the one-particle case, as the effective Peierls-Nabarro energy barrier E_k for the motion of a kink in the tilted periodic potential [158] as $F_f = \pi E_k/a$, where a is the substrate lattice parameter along the channels. Contrary to the previously described case of commensurate contacts, while increasing the force, the sliding state passes through a hierarchy of (hysteretic) depinning transitions and a highly nontrivial velocity force characteristic. The system goes through different stages with a different organization of the domains up to a state where all atoms are running and the mobility is maximal. If the force is decreased from the state with highest mobility where kinks do not exist anymore, the system goes back directly to the pinned state at a force F_b.

As discussed above, a remarkable and surprising fact is that the authors find a similar behavior also in one dimension [151]; hysteresis occurs also in this case both at $T = 0$ and $T \neq 0$. The reason for this behavior is found in collective effects that forbid a single particle to go over to the running state due to the interactions with the neighbors, so that the system has to go as a whole from one state to the other. The transition from the locked to running state proceed via avalanches of particle motion that cannot go backwards when the force is slowly decreased, whence the hysteresis [151]. Strunz and Elmer [17] point out the similarity of the velocity force characteristics found at $T \neq 0$ in [105, 142, 150, 151] with their results at $T = 0$ for the cases close to commensurate registry and low damping. One of the intermediate transitions between the locked state and the highest mobility state is similar to the transition from the kink-dominated regime to the fluid sliding that we have discussed in the previous Section 8.2, although a fully chaotic sliding state is not reached. Strunz and Elmer conjecture that the presence of hysteresis at finite temperature might be due to the finite size of the system, but in [151] the authors exclude this possibility. Finally, in [142] also, incommensurate contacts are studied, leading to the conclusion that hysteresis occurs, both in 1D and 2D, irrespective of the commensurability, for not too high temperatures. The results are compatible with those of [15] but as in [143], the prediction $F_b = F_f/2$ is not confirmed. Therefore, the relation to friction in macroscopic lubricated contacts is not yet established firmly.

The stick-slip dynamics of strongly pinned 1D chains with both periodic and free boundary conditions is studied in [159, 160]. In [159], strong enhancement of the friction with respect to uncoupled oscillators is found, confirming that the interatomic interactions in the sliding layer act as an additional source of friction. Moreover, in [133], this group of authors show that the center of mass velocity of finite, small chains ($N = 10$ to 100) displays a discontinuous behavior as a result of resonances in the system. This finding can be explained by studying the resonant behavior of phonon modes due to the center of mass motion onto a periodic potential along the same lines discussed in Section 7.

The dynamics of the driven FK model in presence of quasiperiodic potentials at finite temperature has been addressed in [161], following a study of Vanossi et al. [126] at $T = 0$. Other interesting results are obtained by considering the effect of an additional force, transverse with respect to the sliding direction [157]. In [162], instability toward transverse motion is shown to lead to a non-monotonic behavior of the velocity for increasing applied force, leading to a sudden locking for increasing force as in a security fuse device.

9. MOLECULAR DYNAMICS STUDIES WITH REALISTIC INTERACTION POTENTIALS

The equations of motion for all models presented in the previous sections are not soluble analytically due to the nonlinear interactions between the sliding system and the underlying surface and are usually integrated numerically by one of the techniques described in Section 11. The second-order systems of differential equations can be either transformed into a dynamical system of first-order differential equations, which are then solved by Runge-Kutta–like methods, or discretized directly as in the Verlet approach. The latter route is the one usually followed in molecular dynamics (MD) simulations. MD studies of sliding systems are much more complex than for systems at equilibrium. As discussed in this review, the motion onto a periodic substrate can couple to the internal motion of the sliding system and lead to transformation of translational kinetic energy into random thermal motion.

The flow of the produced heat into the bulk, which occurs in experimental situations, has to be obtained in numerical simulations by coupling the system to a heat bath. Temperature regulation does not pose problems in ordinary MD simulations, and several types of thermostats have been developed [163, 164]. However, these algorithms remove heat equally in the whole sample, whereas the production of heat in sliding systems is strongly localized at the sliding interface. Therefore, a Langevin approach as described in Section 11.3, where more heat is removed from the fastest atoms, is usually preferred. Moreover, it would be desirable to have both sliding layer and substrate described by mobile atoms on such a length scale as to allow a quasi-continuum of phonon modes, including longwavelength acoustic modes. This is practically impossible to achieve, so that usually the substrate is kept rigid, removing a possible source of dissipation. Lastly, as discussed in Section 6.5, the microscopic dynamics implies integration steps of the order of fs, and therefore motion on the length scale of hundreds of lattice parameters with the typical velocity of AFM experiments which ranges from nm/s to μm/s would require simulation times of hundreds of seconds for large arrays of particles, which is several orders of magnitudes longer than what is currently possible to achieve. However, it is interesting to study also higher ranges of velocities, which can be relevant for the operation of nanomechanical devices. Conversely, MD simulations based on microscopic realistic interaction potentials can be very useful to describe irreversible quasistatic processes, like plastic deformations, indentation, and wear [9, 165]. Although the majority of computational studies of atomistic friction are based on classical potentials, a few *ab initio* studies of the energetics of a tip in contact with a surface have been carried out [96, 166].

It is beyond the scope of this review to give a comprehensive description of the physical systems and models that have been studied by detailed MD simulations. The review of Robbins and Müser [9] is more specifically focused on this approach. I will rather quote a few representative and complementary studies that give a glimpse of the type of systems and approaches that can be addressed in this way.

Studies of the dynamics of lubricants and rare gases can safely be carried out by representing the substrate as a rigid modulation potential in view of the fact that the bonded interactions in the substrate are much stronger than the ones within the sliding atomic or molecular layer. Moreover, for these cases, the weak van der Waals dipolar interactions are well represented by Lennard-Jones (LJ) radial potentials for which the forces can be very efficiently evaluated. Calculations for Kr and Xe on metal surfaces [34, 36] have been performed to evaluate the slip time measured in the QCM experiments [31, 72], reproducing the viscous frictions found experimentally. As mentioned in Section 5.3.5, the relative contribution of electronic and phononic friction is still a matter of debate. References [34, 36, 167, 168] support a phononic mechanism. Tomassone and Sokoloff [169] have studied the effect of steps and of random impurities, which should always be present on real surfaces. The viscous behavior is present also in presence of steps, but random impurities are found to increase the force necessary to unpin the layer so that the experimental results can only be justified if the impurities have strength much weaker than the substrate potential or have extremely small concentrations.

Pioneering extensive MD simulations of atomistic friction have been performed by Landman et al. for a Si-tip on the Si(111) surface [170] and for a CaF_2 tip on the layered CaF_2 surface [171]. In these simulations, stick-slip behavior is found as well as possible wear. The same qualitative features, stick-slip behavior as well as possible wear when the sliding does not occur between close-packed (111) planes, is found in the very careful study of Sorensen et al. [54] of different contacts between a Cu tip on Cu(111) and Cu(100) surfaces. In the study of Sorensen et al., the tip is realistically represented by a pyramidal structure with 5×5 Cu atoms in the bottom layer, which is in contact with the Cu surface. Interatomic interactions are derived by the effective medium theory [172]. Such a geometry can represent an AFM tip but it also provides a first approach to understand the processes occurring at asperity contacts on macroscopic surfaces, although they are usually of much larger micrometer size. One particularly interesting result of this work is the mechanism of stick-slip motion on extended contacts. The tip moved discontinuously between fcc and hcp positions on the surface with a dislocation mechanism rather than with a rigid jump of the

whole tip. Several other interesting results, particularly the persistence of stick-slip behavior in presence of wear, are presented in this paper. It should also be noted that only full three-dimensional approaches allow study of the load dependence of atomistic friction discussed in Section 5.3.3.

Stick-slip behavior without wear has been found by Harrison et al. [173] in MD simulations of hydrogen terminated diamond (111) surfaces described by the bond order potential due to Brenner [174]. The absence of wear appears to be a general characteristic of passivated surfaces [175, 176].

It is interesting to notice that in all these detailed calculations, reference to the results of simpler Tomlinson and FK model is made to guide the interpretation of complex results as well as with the purpose of validating their accuracy and generality.

In particular, in [177], Müser addresses the question of whether FK-like models are suitable to describe realistic incommensurate contacts. In this case, within the FK model, a finite static friction force is expected for a value of $\lambda > \lambda_c$ (see Section 7.1), namely for interactions with the substrate much larger than intrasurface interactions. For such large intersurface interactions, however, one would expect not only elastic instabilities but also plastic instabilities, including material transfer. This conjecture is confirmed in [178] by detailed molecular dynamics simulations of two crystalline incommensurate surfaces, each constituted by four to six atomic layers, with intra- and intersurface interactions modeled by LJ potentials of depth ϵ_0 and ϵ_1, respectively. It is shown that when intersurface interactions dominate on intrasurface interactions, the onset of friction only takes place when intermixing of the atoms originally belonging to either surface occurs. Moreover, mixing is suppressed due to large activation energy barriers up to $\epsilon_1/\epsilon_0 \sim 8$, where already elastic instabilities leading to a finite static friction force would have been expected within the FK model. These results lead the authors to conjecture that (wearless) static friction between incommensurate surfaces can only be due to finite contacts or to adsorbate atoms. Because for general sliding directions contacting surfaces are practically always incommensurate, the ubiquitous presence of static friction cannot simply be explained within the FK models as caused by elastic instabilities. The presence of adsorbates, so-called third bodies, between sliding layers is currently considered one of the possible mechanisms for the occurrence of static friction for large (infinite) incommensurate contacts.

10. THEORETICAL CHALLENGES

New experimental probes of friction for the sliding onto clean, well-defined surfaces have revealed that the simple macroscopic phenomenological rules that describe macroscopic friction are completely inadequate at the atomic scale. In this regime, friction is dominated by interatomic interactions, surface registry, and vibrational and electronic excitation spectra. In principle, at this scale, the very concept of friction could not be needed, and the occurrence of energy dissipation could be related to a particular microscopic quantum mechanical mechanism. But even if we were able to carry out such calculations for realistic materials and geometries on the appropriate timescale, this knowledge would not directly help in establishing general trends and concepts and in guiding the search for new functional situations. The challenge of theoretical nanotribology is just to take an approach like the one that has guided the description of macroscopic tribology and identify general mechanisms to be cast into some simple rules that can be used to describe the behavior of large classes of materials, types of contacts, and different regimes of sliding velocity and applied forces.

A theoretical description of friction at the nanoscale is still in its infancy. In this review, I have focused my attention on the most studied nonlinear models of atomistic friction, the Tomlinson and Frenkel Kontorova models, which indeed provide a few general concepts that can guide in addressing more detailed issues. Despite their simplicity, these models account qualitatively for the main features observed experimentally; in particular, the occurrence of stick-slip motion, almost vanishing (quasi)static friction for weakly interacting and incommensurate contacts, and nonlinear dependence on external load. However, even if the physical systems are strongly simplified within these approaches, the behavior for driven and damped systems of many interacting particles has not been fully explored, and many

questions remain open. As discussed, in particular in Section 8, within similar models, details of the interatomic interactions can affect substantially the response to external forces. Thermal effects that can be safely neglected for macroscopic objects become relevant. The very rich dynamic behavior displayed by these systems opens the way to new effects and functionality of nanocontacts. A tendency that is certainly present in the theoretical community and that will surely bear fruit in the future is the use of the results of realistic MD approaches and *ab initio* calculations to establish suitable parameters for simplified models. Therefore, becoming familiar with the results of the nonlinear models discussed in this review is a necessary step to proceed and approach more complex and realistic situations.

11. NUMERICAL METHODS

In this section, we briefly illustrate some numerical techniques commonly used for the molecular dynamics simulations of atomistic models of molecular systems. MD consists of solving the classical equations of motion for a system of N particles interacting via a potential U, using approximate methods. There are many reviews available on the fundamentals of classical MD simulations [163, 164, 179, 180]. In the following, we will outline the most popular integrators of the equations of motion, namely the Runge-Kutta method, the Verlet algorithm (with explicit treatment of frictional forces), and the Langevin dynamics, which is used to describe the motion of systems at finite temperature.

First of all, we note that for a system of N particles, the $3N$ equations of motion

$$m\ddot{\mathbf{r}}_i = -\frac{\partial U}{\partial \mathbf{r}_i} = \mathbf{F}_i \tag{100}$$

can be written as a system of first-order differential equations (i.e., as a dynamical system) by making the substitution

$$\begin{cases} \mathbf{x}_i = \mathbf{r}_i \\ \mathbf{y}_i = \dot{\mathbf{r}}_i \end{cases} \tag{101}$$

Thus, Eq. (100) becomes

$$\begin{cases} \dot{\mathbf{x}}_i = \mathbf{y}_i \\ \dot{\mathbf{y}}_i = \dfrac{\mathbf{F}_i}{m} \equiv \mathbf{a}_i \end{cases} \tag{102}$$

Introducing the variables

$$\mathbf{z} = \begin{pmatrix} \mathbf{x}_1 \\ \vdots \\ \mathbf{x}_N \\ \mathbf{y}_1 \\ \vdots \\ \mathbf{y}_N \end{pmatrix} \tag{103}$$

and

$$\mathbf{f} = \begin{pmatrix} \mathbf{y}_1 \\ \vdots \\ \mathbf{y}_N \\ \mathbf{a}_1 \\ \vdots \\ \mathbf{a}_N \end{pmatrix} \tag{104}$$

Eq. (102) can be rewritten as

$$\dot{\mathbf{z}} = \mathbf{f} \tag{105}$$

Equation (105) represents a dynamic system that, given a certain set of initial values of $\mathbf{z}$, has a unique evolution in time (i.e., a unique t-flow mapping).

11.1. Runge-Kutta Methods

This method can be applied to a system of first-order ordinary differential equations of the type of Eq. (105)

$$\dot{\mathbf{z}}_i(t) = \mathbf{f}_i(\mathbf{z}_1(t), \ldots, \mathbf{z}_{2N}(t); t), \qquad i = 1, \ldots, 2N \tag{106}$$

In the Runge-Kutta 4 scheme the solution at time $t + h$, where h is the time step, is given by

$$\mathbf{z}_i(t+h) = \mathbf{z}_i(t) + h\left(\frac{\mathbf{k}_i^{(1)}}{6} + \frac{\mathbf{k}_i^{(2)}}{3} + \frac{\mathbf{k}_i^{(3)}}{3} + \frac{\mathbf{k}_i^{(4)}}{6}\right) + O(h^5) \tag{107}$$

where $\mathbf{k}_i^{(1)}$, $\mathbf{k}_i^{(2)}$, $\mathbf{k}_i^{(3)}$, and $\mathbf{k}_i^{(4)}$ are defined as

$$\begin{aligned}
\mathbf{k}_i^{(1)} &= \mathbf{f}_i(\mathbf{z}_1(t), \ldots, \mathbf{z}_{2N}(t); t) \\
\mathbf{k}_i^{(2)} &= \mathbf{f}_i\left[\mathbf{z}_1(t) + \frac{h}{2}\mathbf{k}_1^{(1)}, \ldots, \mathbf{z}_{2N}(t) + \frac{h}{2}\mathbf{k}_{2N}^{(1)}; t + \frac{h}{2}\right] \\
\mathbf{k}_i^{(3)} &= \mathbf{f}_i\left[\mathbf{z}_1(t) + \frac{h}{2}\mathbf{k}_1^{(2)}, \ldots, \mathbf{z}_{2N}(t) + \frac{h}{2}\mathbf{k}_{2N}^{(2)}; t + \frac{h}{2}\right] \\
\mathbf{k}_i^{(4)} &= \mathbf{f}_i\left[\mathbf{z}_1(t) + h\mathbf{k}_1^{(3)}, \ldots, \mathbf{z}_{2N}(t) + h\mathbf{k}_{2N}^{(3)}; t + h\right]
\end{aligned}$$

Higher order Runge-Kutta methods have better truncation error but also require more computation time (i.e., more evaluations of $\mathbf{f}_i$). A more accurate evolution of the Runge-Kutta algorithm is represented by the possibility to adjust the mesh width h during the calculation [181]. In this manner, the solution is continuously monitored and the time step is modified to ensure that the user-specified accuracy is maintained.

11.2. Verlet Algorithm

In a Hamiltonian problem, the symplectic condition and microscopic reversibility are inherent properties of the true time trajectories that are the exact solution of the Hamilton equation. Specifically, the symplectic condition ensures that a generic transformation of the dynamic variable is canonical. Symplectic transformations preserve many dynamic properties of the phase space that the exact trajectories are known to exhibit, such as the conservation of the phase space volume. A stepwise integration defines a t-flow mapping, which may or may not retain these properties. Non-symplectic integrators, such as the Runge-Kutta, are generally believed to be less stable in the long-time integration of the equations of motion [182]. This is why popular MD symplectic algorithms like Verlet are considered more robust and stable. However, when non-Hamiltonian features, like a damping term, are explicitly considered in the dynamics, the symplectic property of the algorithm is not relevant.

The velocity Verlet is derived by discretizing directly the Newtonian equations of motion without first transforming them to a system of first-order differential equations. The algorithm advances positions and velocities as follows:

$$\begin{cases}
\mathbf{v}_i\left(t + \dfrac{h}{2}\right) = \mathbf{v}_i(t) + \dfrac{h}{2}\mathbf{a}_i(t) + O(h^2) \\
\mathbf{r}_i(t+h) = \mathbf{r}_i(t) + h\mathbf{v}_i(t) + \dfrac{h^2}{2}\mathbf{a}_i(t) + O(h^3) \\
\mathbf{v}_i(t+h) = \mathbf{v}_i\left(t + \dfrac{h}{2}\right) + \dfrac{h}{2}\mathbf{a}_i(t+h) + O(h^2)
\end{cases} \tag{108}$$

The algorithm is self-starting. Given the values at t, positions at $t + h$ and velocities at $t + h/2$ are calculated from the acceleration at time t. Then, $\mathbf{a}_i(t + h)$ is computed from the advanced positions. Calculation of the forces $\mathbf{F}_i = m\mathbf{a}_i$ is the most time-consuming part. Finally, the velocity is advanced from $t + h/2$ to $t + h$. In this way, at each time step only $3dN$ variables have to be kept in memory at each time step, where d is the dimensionality of the system and N the number of particles. In Eq. (108), the forces $\mathbf{F}_i$ are assumed to be dependent only on the coordinates $\mathbf{r}_i$. In the presence of a frictional force proportional to $\mathbf{v}_i$, this is not the case any more, and the new force will be

$$\mathbf{G}_i = \mathbf{F}_i - m\eta\mathbf{v}_i \tag{109}$$

While in the Runge-Kutta method Eq. (107), velocity-dependent forces can be treated straightforwardly, without formal changes in the algorithm, in velocity Verlet it is necessary to make some changes in Eq. (108), which now becomes

$$\begin{cases} \mathbf{v}_i\left(t + \dfrac{h}{2}\right) = \mathbf{v}_i(t)\left(1 - \eta\dfrac{h}{2}\right) + \dfrac{h}{2}\mathbf{a}_i(t) + O(h^2) \\ \mathbf{r}_i(t + h) = \mathbf{r}_i(t) + h\mathbf{v}_i(t) + \dfrac{h^2}{2}[\mathbf{a}_i(t) - \eta\mathbf{v}_i(t)] + O(h^4) \\ \mathbf{v}_i(t + h) = \mathbf{v}_i\left(t + \dfrac{h}{2}\right) + \dfrac{h}{2}[\mathbf{a}_i(t + h) - \eta\mathbf{v}_i(t + h)] + O(h^2) \end{cases} \tag{110}$$

It is easy to show that Eq. (108) is replaced by

$$\begin{cases} \mathbf{v}_i\left(t + \dfrac{h}{2}\right) = \mathbf{v}_i(t)\left(1 - \eta\dfrac{h}{2}\right) + \dfrac{h}{2}\mathbf{a}_i(t) + O(h^2) \\ \mathbf{r}_i(t + h) = \mathbf{r}_i(t) + h\mathbf{v}_i(t) + \dfrac{h^2}{2}[\mathbf{a}_i(t) - \eta\mathbf{v}_i(t)] + O(h^4) \\ \mathbf{v}_i(t + h) = \left(1 + \eta\dfrac{h}{2}\right)^{-1}\left[\mathbf{v}_i\left(t + \dfrac{h}{2}\right) + \dfrac{h}{2}\mathbf{a}_i(t + h)\right] + O(h^2) \end{cases} \tag{111}$$

11.3. Langevin Dynamics

It has been recognized that the issue of temperature regulation is a very delicate one in MD study of surface friction. Compared to other types of thermostats, the Langevin approach (a velocity-dependent damping plus stochastic forces as required by the fluctuation dissipation theorem) has the advantage of removing heat where it is generated.

Consider an adsorbate system, consisting of N particles, on a rigid substrate and suppose that an external force $\mathbf{F}_{ext}$ acts on each of the adsorbates. The adsorbate–substrate potential is $V = \sum_{i=1}^{N} v(\mathbf{r}_i)$ and the adsorbate–adsorbate interaction is given by $U = \frac{1}{2}\sum_{i,j(i\neq j)} u(\mathbf{r}_i - \mathbf{r}_j)$. Different forms for v and u can be chosen (e.g., v can be taken as a periodic potential and u as a Lennard-Jones). The equation of motion for the particle coordinate $\mathbf{r}_i(t)$ is

$$m\ddot{\mathbf{r}}_i + m\eta\dot{\mathbf{r}}_i = -\frac{\partial V}{\partial \mathbf{r}_i} - \frac{\partial U}{\partial \mathbf{r}_i} + \xi_i + \mathbf{F}_{ext} \tag{112}$$

where an explicit damping term $-m\eta\dot{\mathbf{r}}_i$ has been introduced (η is the friction coefficient), and the effect of finite temperature is taken into account by the stochastically fluctuating forces ξ_i. The components ξ_i^{α} of ξ_i are related to the friction coefficient η via the dissipation–fluctuation theorem:

$$\langle \xi_i^{\alpha}(t)\xi_j^{\beta}(0)\rangle = 2mk_B T\eta\delta_{\alpha\beta}\delta_{ij}\delta(t) \tag{113}$$

Moreover, the mean value of $\xi_i(t)$ should vanish:

$$\langle \xi_i(t)\rangle = 0 \tag{114}$$

We describe here how to solve numerically this problem, by restricting it to the simple case given by the low-density limit. In such a situation, the interparticle potential U can be neglected, and one can consider the problem of the motion of a single adsorbate. It can be shown that in this case, the motions in the x and y directions are decoupled; thus, it is enough to consider a one-dimensional model. The equation of motion for the particle coordinate $x(t)$ is

$$m\ddot{x} + m\eta\dot{x} = -\frac{\partial V}{\partial x} + \xi + F_{ext} \tag{115}$$

The fluctuation–dissipation theorem Eq. (113) then becomes

$$\langle \xi(t)\xi(0)\rangle = 2m\eta k_B T\delta(t) \tag{116}$$

The Newtonian dynamics of the system can be studied numerically by using, for example, one of the methods described above (Runge-Kutta or velocity Verlet with frictional forces). The stochastic force f is drawn at each time step from a Gaussian distribution with zero mean and variance given by

$$\langle \xi^2(t)\rangle = 2m\eta k_B \frac{T}{h} \tag{117}$$

The method of Box and Muller [163] can be used to generate numbers with a Gaussian distribution. It consists in generating a couple of uniform random numbers s_1 and s_2 in (0, 1) and calculating

$$\zeta_- = (-2\ln s_1)^{1/2}\cos(2\pi s_2) \tag{118}$$

and

$$\zeta_+ = (-2\ln s_1)^{1/2}\sin(2\pi s_2) \tag{119}$$

In this way, ζ_- and ζ_+ are Gaussian random numbers with zero mean and unit variance. A Gaussian number with mean a and variance σ can simply be obtained by the transformation

$$\xi_\pm = a + \sigma\zeta_\pm \tag{120}$$

In our case [Eqs. (114)–(117)], $a = 0$ and $\sigma = 2m\eta k_B T/h$. The stochastic force $\xi(t)$ at time t is calculated as the average of ξ_+ and ξ_-:

$$\xi(t) = \frac{1}{2}(\xi_+ + \xi_-) \tag{121}$$

In particular, it is convenient to extract ξ_- and ξ_+ according to Eqs. (118)–(120) at the beginning of the simulation, and then to use for ξ_- at each time step the value of ξ_- calculated at the previous time step and so on. In this way, only one Gaussian number has to be calculated every time step (except the first), thus avoiding the need to perform an extra calculation of ζ_-, which saves computational time, as the logarithm and the square root are quite expensive operations.

ACKNOWLEDGMENTS

I should like to thank my collegues and coworkers, Titus van Erp, Luca Consoli, Claudio Fusco, Bastiaan Huisman, Ted Janssen, Jan Los, Hubert Knops, and Misha Katsnelson for many useful discussions and for their support. A special thanks goes to Claudio Fusco for his many useful contributions to this work. Also, discussions with Elisa Riedo, Sylvia Speller, and Joost Frenken are gratefully acknowledged. This work has partially been supported by the FOM (Fundamenteel Onderzoek der Materie) and by NWO (Nederlandse organisatie Wetenschappelijke Onderzoek) project no. 015.000.031.

REFERENCES

1. B. N. J. Persson. "Sliding Friction: Physical Principles and Applications." Springer-Verlag, Berlin, Heidelberg, 1998.
2. J. Krim, *Surf. Sci.* 500, 741 (2002).
3. F. J. Elmer, *J. Phys. A* 30, 6057 (1997).
4. M. Salmeron, S. Kopta, E. Barrena, and C. Ocal, in "Fundamentals of Tribology and Bridging the Gap Between the Macro- and Micro/Nanoscales" (B. Bhushan, Ed.), pp. 41–52. NATO ASI Series E: Applied Sciences. Kluwer Academic Publishers, Dordrecht, The Netherlands, 2001.
5. J. V. José and E. J. Saletan, "Classical Dynamics, A Contemporary Approach." Cambridge University Press, Cambridge, 1998.
6. The tutorial devoted to friction can be found either at http://www.nanoworld.unibas.ch/nano/frictionmodule/ or at http://www.frictionmodule.nano-world.org/
7. B. N. J. Persson, *Surf. Sci. Rep.* 33, 83 (1999).
8. I. L. Singer, *J. Vac. Sci. Technol. A* 12, 2605 (1994).
9. M. O. Robbins and M. H. Müser, in "Handbook of Micro/Nano Tribology" (B. Bhushan, Ed.), p. 717. CRC Press, Boca Raton, FL, 2001.
10. S. Morita, S. Fujisawa, and Y. Sugawara, *Surf. Sci. Rep.* 23, 1 (1996).
11. R. W. Carpick and M. Salmeron, *Chem. Rev.* 97, 1163 (1997).
12. E. Gnecco, R. Bennewitz, T. Gyalog, and E. Meyer, *J. Phys.: Condens. Matter* 13, R619 (2001).
13. F. P. Bowden and D. Tabor, "Friction and Lubrication." Methuen, London, 1967.
14. See Tables I and II of Ref. [15].
15. B. N. J. Persson, *Phys. Rev. B* 48, 18140 (1993).
16. Ya. I. Frenkel and T. A. Kontorova, *Zh. Eksp. Teor. Fiz.* 8, 89 (1938).
17. T. Strunz and F.-J. Elmer, *Phys. Rev. E* 58, 1601 (1998); *Phys. Rev. E* 58, 1612 (1998).
18. L. Consoli, H. J. F. Knops, and A. Fasolino, *Phys. Rev. Lett.* 85, 302 (2000).
19. G. Binnig, C. F. Quate, and Ch. Gerber, *Phys. Rev. Lett.* 56, 930 (1986).
20. G. Meyer and N. M. Amer, *Appl. Phys. Lett.* 53, 1045 (1988).
21. M. Dienwiebel, Ph.D. Thesis, University of Leiden, The Netherlands.
22. Available at http://www.physics.leidenuniv.nl/sections/em/ip/welcome.htm.
23. M. Dienwiebel, G. J. Verhoeven, N. Pradeep, J. W. M. Frenken, J. A. Heimberg, and H. W. Zandbergen, *Phys. Rev. Lett.* 92, 126101 (2004).
24. C. M. Mate, G. M. McClelland, R. Erlandsson, and S. Chiang, *Phys. Rev. Lett.* 59, 1942 (1987).
25. R. Bennewitz, T. Gyalog, M. Guggisberg, M. Bammerlin, E. Meyer, and H.-J. Güntherodt, *Phys. Rev. B* 60, R11301 (1999).
26. H. Hölscher, U. D. Schwarz, O. Zwöner, and R. Wiesendanger, *Phys. Rev. B* 57, 2477 (1998).
27. H. Hölscher, W. Allers, U. D. Schwarz, A. Schwarz, and R. Wiesendanger, *Phys. Rev. Lett.* 83, 4780 (1999); U. D. Schwarz, H. Hölscher, and R. Wiesendanger, *Phys. Rev.* 62, 13089 (2000).
28. R. Garcia and R. Perez, *Surf. Sci. Rep.* 47, 197 (2002).
29. C. Lu and A. W. Czanderna, "Applications of Piezoelectric Quartz Crystal Microbalance." Elsevier, Amsterdam, 1984.
30. J. B. Sokoloff, J. Krim, and A. Widom, *Phys. Rev. B* 48, 9134 (1993).
31. J. Krim, D. H. Solina, and R. Chiarello, *Phys. Rev. Lett.* 66, 181 (1991).
32. J. Krim, *Sci. Am.* 275, 74 (1996); J. Krim and A. Widom, *Phys. Rev.* 38, 12184 (1988); A. Widom and J. Krim, *Phys. Rev.* 34, 1403 (1986).
33. C. Mak and J. Krim, *Phys. Rev. B* 58, 5157 (1998).
34. M. Cieplak, E. D. Smith, and M. O. Robbins, *Science* 265, 1209 (1994).
35. E. D. Smith, M. O. Robbins, and M. Cieplak, *Phys. Rev. B* 54, 8252 (1996).
36. M. S. Tomassone, J. B. Sokoloff, A. Widom, and J. Krim, *Phys. Rev. Lett.* 79, 4798 (1997).
37. S. Berg and D. Johannsmann, *Phys. Rev. Lett.* 91, 145505 (2003).
38. W. Zhong and D. Tománek, *Phys. Rev. Lett.* 64, 3054 (1990).
39. H. J. Hertz, *Reine Angew. Math.* 92, 156 (1881).
40. K. L. Johnson, K. Kendall, and A. D. Roberts, *Proc. R. Soc. London A* 324, 301 (1971).
41. B. V. Derjaguin, V. M. Müller, and Y. P. Toporov, *J. Colloid Interface Sci.* 53, 314 (1975); V. M. Müller, B. V. Derjaguin, and Y. P. Toporov, *Colloids Surf.* 7, 251 (1983).
42. R. W. Carpick, N. Agraït, D. F. Ogletree, and M. Salmeron, *J. Vac. Sci. Technol. B* 14, 1289 (1996).
43. M. Enachescu, R. J. A. van den Oetelaar, R. W. Carpick, D. F. Ogletree, C. F. J. Flipse, and M. Salmeron, *Phys. Rev. Lett.* 81, 1877 (1998).
44. V. N. Koinkar and B. Bhushan, *J. Vac. Sci. Technol. A* 14, 2378 (1996).
45. F. Heslot, T. Baumberger, and B. Perrin, *Phys. Rev. E* 49, 4973 (1994).
46. T. Bouhacina, J. P. Aimé, S. Gauthier, and D. Michel, *Phys. Rev. B* 56, 7694 (1997).
47. Y. Hoshi, T. Kawagishi, and H. Kawakatsu, *Jpn. J. Appl. Phys.* 39, 38 (2000).
48. E. Gnecco, R. Bennewitz, T. Gyalog, Ch. Loppacher, M. Bammerlin, E. Meyer, and H.-J. Güntherodt, *Phys. Rev. Lett.* 84, 1172 (2000).
49. O. Zwörner, H. Hölscher, U. D. Schwarz, and R. Wiesendanger, *Appl. Phys.* A66, S263 (1998).
50. R. Prioli, A. F. M. Rivas, F. L. Freire, Jr., and A. O. Caride, *Appl. Phys. A* 76, 565 (2003).
51. Y. Sang, M. Dubé, and M. Grant, *Phys. Rev. Lett.* 87, 174301 (2001).

52. U. D. Schwarz, O. Zwörner, P. Koster, and R. Wiesendanger, *Phys. Rev. B* 56, 6987 (1997).
53. E. Riedo and H. Brune, *Appl. Phys. Lett.* 83, 1986 (2003).
54. M. R. Sørensen, K. W. Jacobsen, and P. Stoltze, *Phys. Rev. B* 53, 2101 (1996).
55. C. Fusco and A. Fasolino, *Appl. Phys. Lett.* 84, 699 (2004).
56. C. Fusco and A. Fasolino, in "Advances in Science and Technology" (P. Vincenzini and F. Zerbetto, Eds.), Vol. 44, p. 293. Techna Group, Faenza, 2004.
57. S. Fujisawa, E. Kishi, Y. Sugawara, and S. Morita, *Phys. Rev. B* 52, 5302 (1995).
58. S. Fujisawa, K. Yokoyama, Y. Sugawara, and S. Morita, *Phys. Rev. B* 58, 4909 (1998).
59. M. Ishikawa, S. Okita, N. Minami, and K. Miura, *Surf. Sci.* 445, 488 (2000).
60. E. Riedo, E. Gnecco, R. Bennewitz, E. Meyer, and H. Brune, *Phys. Rev. Lett.* 91, 084502 (2003).
61. N. Sasaki, M. Tsukada, S. Fujisawa, Y. Sugawara, S. Morita, and K. Kobayashi, *Phys. Rev. B* 57, 3785 (1998).
62. H. Hölscher, W. Radberg, U. D. Schwarz, A. Hasbach, K. Wandelt, and R. Wiesendanger, *Phys. Rev. B* 59, 1661 (1999).
63. H. Hölscher, U. D. Schwarz, and R. Wiesendanger, *Europhys. Lett.* 36, 19 (1996).
64. N. Sasaki, K. Kobayashi, and M. Tsukada, *Phys. Rev. B* 54, 2138 (1996).
65. J. H. Los and A. Fasolino, *Phys. Rev. B* 68, 024107 (2003).
66. A. Socoliuc, R. Bennewitz, E. Gnecco, and E. Meyer, *Phys. Rev. Lett.* 92, 134301 (2004).
67. M. Hirano, K. Shinjo, R. Kaneko, and Y. Murata, *Phys. Rev. Lett.* 78, 1448 (1997).
68. The data presented in Fig. 2 of Ref. [60] are proportional to $L^{1/2}$ although the caption reads that the fit of the data is linear. C. Fusco, E. Riedo, private communication.
69. M. Peyrard and S. Aubry, *J. Phys. C* 16, 1593 (1983).
70. K. Shinjo and M. Hirano, *Surf. Sci.* 283, 473 (1993).
71. M. Hirano, K. Shinjo, R. Kaneko, and Y. Murata, *Phys. Rev. Lett.* 67, 2642 (1991).
72. C. Daly and J. Krim, *Phys. Rev. Lett.* 76, 803 (1996).
73. L. Bruschi, A. Carlin, and G. Mistura, *Phys. Rev. Lett.* 88, 046105 (2002).
74. A. Carlin, L. Bruschi, M. Ferrari, and G. Mistura, *Phys. Rev.* 68, 045420 (2003).
75. B. N. J. Persson and A. Nitzan, *Surf. Sci.* 367, 261 (1996).
76. B. N. J. Persson, *Phys. Rev. B* 44, 3277 (1991).
77. J. B. Sokoloff, *Phys. Rev. B* 52, 5318 (1995).
78. S. Tomassone and A. Widom, *Phys. Rev. B* 56, 4938 (1997).
79. L. S. Levitov, *Europhys. Lett.* 8, 499 (1989).
80. B. N. J. Persson and A. I. Volokitin, *J. Chem. Phys.* 103, 8679 (1995).
81. A. Dayo, W. Alnasrallah, and J. Krim, *Phys. Rev. Lett.* 80, 1690 (1998).
82. B. N. J. Persson and E. Tosatti, *Surf. Sci. Lett.* 411, L855 (1998).
83. R. L. Renner, J. E. Rutledge, and P. Taborek, *Phys. Rev. Lett.* 83, 1261 (1999).
84. J. Krim, *Phys. Rev. Lett.* 83, 1262 (1999).
85. R. L. Renner, P. Taborek, and J. E. Rutledge, *Phys. Rev. B* 63, 233405 (2001).
86. A. Liebsch and S. Gonçalves, and M. Kiwi, *Phys. Rev. B* 60, 5034 (1999).
87. V. L. Popov, *Phys. Rev. Lett.* 83, 1632 (1999).
88. T. Novotný and B. Velický, *Phys. Rev. Lett.* 83, 4112 (1999).
89. J. B. Sokoloff, M. S. Tomassone, and A. Widom, *Phys. Rev. Lett.* 84, 515 (2000).
90. L. W. Bruch, *Phys. Rev. B* 61, 16201 (2000).
91. B. N. J. Persson, *Solid State Commun.* 115, 145 (2000).
92. J. B. Sokoloff, *J. Phys. Condens. Matter* 14, 5277 (2002).
93. G. A. Tomlinson, *Philos. Mag. Ser.* 7, 905 (1929).
94. D. Tománek, W. Zhong, and H. Thomas, *Europhys. Lett.* 15, 887 (1991).
95. J. S. Helman, W. Baltensperger, and J. A. Holyst, *Phys. Rev. B* 49, 3831 (1994).
96. S. H. Ke, T. Uda, R. Perez, I. Stich, and K. Terakura, *Phys. Rev. B* 60, 11631 (1999).
97. H. Hölscher, U. D. Schwarz, and R. Wiesendanger, *Surf. Sci.* 375, 395 (1997).
98. M. A. Lantz, S. J. O'Shea, A. C. F. Hoole, and M. E. Welland, *Appl. Phys. Lett.* 70, 970 (1997).
99. R. W. Carpick, D. F. Ogletree, and M. Salmeron, *Appl. Phys. Lett.* 70, 1548 (1997).
100. Y. S. Leng and S. Jiang, *Phys. Rev. B* 63, 193406 (2001).
101. See, e.g., J. C. Hamilton, R. Stumpf, K. Bromann, M. Giovannini, K. Kern, and H. Brune, *Phys. Rev. Lett.* 82, 4488 (1999); Y. N. Gornostyrev, M. I. Katsnelson, and A. V. Trefilov, *Phys. Rev.* 60, 1013 (1999) and references therein.
102. J. B. Sokoloff, J. E. Sacco, and J. F. Weisz, *Phys. Rev. Lett.* 22, 1561 (1978).
103. L. Floría and J. J. Mazo, *Adv. Phys.* 45, 505 (1996).
104. S. N. Coppersmith, *Phys. Rev. B* 30, 410 (1984).
105. O. M. Braun, T. Dauxois, M. V. Paliy, and M. Peyrard, *Phys. Rev. Lett.* 78, 1295 (1997).
106. B. D. Josephson, *Phys. Lett.* 1, 251 (1962).
107. S. Aubry and L. de Seze, *Festkörperprobleme* XXV, 59 (1985).
108. M. Weiss and F. J. Elmer, *Phys. Rev.* 53, 7539 (1996).
109. O. M. Braun and Y. S. Kivshar, *Phys. Rev. B* 43, 1060 (1991).
110. R. S. MacKay, Ph.D. Thesis, Princeton University, 1982; reprinted in R. S. MacKay, "Renormalization in Area Preserving Maps," World Scientific, Singapore, 1993; R. S. MacKay, *Physica D* 50, 71 (1991).
111. S. Aubry, R. S. MacKay, and C. Baesens, *Physica D* 56, 123 (1992).
112. See, e.g., Refs. [103, 125].

113. B. V. Chirikov, *Phys. Rep.* 52, 263 (1979).
114. J. Green, *J. Math. Phys.* 20, 1183 (1979).
115. S. Aubry and P. Y. Le Daeron, *Physica D* 8, 381 (1983).
116. S. Aubry and G. André, *Ann. Israel. Phys. Soc.* 3, 133 (1980).
117. L. Consoli, H. J. F. Knops, and A. Fasolino, *Phys. Rev. E* 64, 016601 (2001).
118. L. Consoli, H. J. F. Knops, and A. Fasolino, *Europhys. Lett.* 60, 342 (2002).
119. A. Fasolino, L. Consoli, and H. J. F. Knops, Technical Proceedings of the ICCN 2001 Intl. Conf. on Computational Nanoscience. (Available at http://www.cr.org/publications/ICCN2001/).
120. S. Aubry, *Physica D* 7, 240 (1983).
121. W. Chou and R. B. Griffiths, *Phys. Rev. Lett.* 56, 1929 (1986); R. B. Griffiths and W. Chou, *Phys. Rev. B* 34, 6219 (1986).
122. F. Lançon, *Europhys. Lett.* 57, 74, (2002).
123. F. Lançon, J. M. Pénisson, and U. Dahmen, *Europhys. Lett.* 49, 603, (2000).
124. A. Vanossi, A. Franchini, and V. Bortolani, *Surf. Sci.* 502, 437 (2002).
125. T. S. van Erp, A. Fasolino, O. Radulescu, and T. Janssen, *Phys. Rev. B* 60, 6522 (1999).
126. A. Vanossi, J. Röder, A. R. Bishop, and V. Bortolani, *Phys. Rev. E* 63, 017203 (2000); *Phys. Rev. E* 67, 016605 (2003).
127. C.-I. Chou, C.-L. Ho, B. Hu, and H. Lee, *Phys. Rev. B* 57, 2747 (1998).
128. A. Xu, G. Wang, S. Chen, and B. Hu, *Phys. Rev. B* 58, 721 (1998).
129. B. Hu and B. Li, *Physica A* 288, 81 (2000).
130. In Ref. [70], this value is approximated to $\lambda_c \sim 0.14$.
131. M. Abramowitz and I. A. Stegun, Eds., "Handbook of Mathematical Functions." Dover, New York, 1970.
132. H. Risken, "The Fokker-Planck Equation." Springer-Verlag, Berlin, Heidelberg, 1996.
133. H. G. E. Hentschel, F. Family, and Y. Braiman, *Phys. Rev. Lett.* 83, 104 (1999).
134. G. Christie and B. I. Henry, *Phys. Rev. E* 58, 3045 (1998).
135. J. B. Sokoloff, *Phys. Rev. Lett.* 71, 3450 (1993); *J. Phys. Condens. Matter* 10, 9991 (1998).
136. L. Consoli, A. Fasolino, H. J. F. Knops, and T. Janssen *Ferroelectrics* 250, 111 (2001).
137. See, e.g., G. Lamb, "Elements of Soliton Theory." Wiley, New York, 1980.
138. A. Kwaśniewski, P. Machnikowsky, and P. Magnuszewski, *Phys. Rev. E* 59, 2347 (1999).
139. H. A. Kramers, *Physica* 7, 284 (1940).
140. P. Hänggi, P. Talkner, and B. Borkovec, *Rev. Mod. Phys.* 62, 251 (1990).
141. C. Fusco and A. Fasolino, *Thin Solid Films* 482, 34 (2003).
142. O. M. Braun, T. Dauxois, M. V. Paliy, and M. Peyrard, *Phys. Rev. E* 55, 3598 (1997).
143. E. Granato and S. C. Ying, *Phys. Rev. B* 59, 5154 (1999).
144. S. Yu. Krylov and L. J. F. Hermans, *Phys. Rev. B* 65, 092205 (2002).
145. J. C. Hamilton, *Phys. Rev. Lett.* 77, 885 (1996).
146. F. Montalenti and R. Ferrando, *Phys. Rev. B* 59, 5881 (1999).
147. S. Watanabe, S. H. Strogatz, H. S. J. van der Zant, and T. P. Orlando, *Phys. Rev. Lett.* 74, 379 (1995); S. Watanabe, H. S. J. van der Zant, S. H. Strogatz, and T. P. Orlando, *Physica D* 97, 429 (1996).
148. A. V. Ustinov, M. Cirillo, and B. A. Malomed, *Phys. Rev. B* 47, 8357 (1993).
149. W. Ellenbroek and H. J. F. Knops, private communication.
150. M. Paliy, O. Braun, T. Dauxois, and B. Hu, *Phys. Rev. E* 56, 4025 (1997).
151. O. Braun, A. R. Bishop, and J. Röder, *Phys. Rev. Lett.* 79, 3692 (1997).
152. D. I. Kopelevich and H. C. Chang, *Phys. Rev. Lett.* 83, 1590 (1999).
153. C. Fusco and A. Fasolino, in "Advances in Science and Technology" (P. Vincenzini and F. Zerbetto, Eds.), Vol. 44, p. 249. Techna Group, Faenza, 2004.
154. B. N. J. Persson, E. Tosatti, D. Fuhrmann, G. Witte, and Ch. Wöll, *Phys. Rev. B* 59, 11777 (1999).
155. The Gaussian distribution of velocities is here taken as a proof of thermal equilibrium. This assumption is criticized in Ref. [17].
156. V. L. Pokrovsky and A. L. Talapov, "Theory of Incommensurate Crystals." Soviet Scientific Reviews Vol. 1. Harwood Academic, Glasgow, 1984.
157. E. Granato and S. C. Ying, *Phys. Rev. Lett.* 85, 5368 (2000).
158. O. M. Braun, T. Dauxois, M. V. Paliy, and M. Peyrard, *Phys. Rev. B* 54, 321 (1996).
159. Y. Braiman, F. Family, and H. G. E. Hentschel, *Phys. Rev. E* 53, R3005 (1996); *Phys. Rev. B* 55, 5491 (1997).
160. Z. Zheng, B. Hu, and G. Hu, *Phys. Rev. B* 58, 5453 (1998).
161. L. Gao, J. Gu, and B. Hu, *Phys. Rev. B* 66, 064309 (2002).
162. O. M. Braun, M. V. Paliy, and B. Hu, *Phys. Rev. Lett.* 83, 5206 (1999).
163. M. P. Allen and D. J. Tildesley, "Computer Simulation of Liquids." Clarendon Press, Oxford, 1987.
164. D. Frenkel and B. Smit, "Understanding Molecular Simulation." Academic Press, London, 2002.
165. A. E. Filippov, J. Klafter, and M. Urbakh, *Phys. Rev. Lett.* 92, 135503 (2004) and references therein.
166. M. R. Jarvis, R. Perez, and M. C. Payne, *Phys. Rev. Lett.* 86, 1287 (2001).
167. M. O. Robbins and J. Krim, *MRS Bull.* 23, 23 (1998).
168. A. Buldum and S. Ciraci, *Phys. Rev. B* 60, 1982 (1999); A. Buldum, D. M. Leitner, and S. Ciraci, *Phys. Rev. B* 59, 16042 (1999).
169. M. S. Tommasone and J. B. Sokoloff, *Phys. Rev. B* 60, 4005 (1999).
170. U. Landman, W. D. Luedtke, and M. W. Ribarsky, *J. Vac. Sci Technol. A* 7, 2829 (1989).
171. U. Landman, W. D. Luedtke, and E. M. Ringer, *Wear* 153, 3 (1992).

172. K. W. Jacobsen, J. K. Norskov, and M. J. Puska, *Phys. Rev. B* 35, 7423 (1987); K. W. Jacobsen, *Comments Condens. Matter Phys.* 14, 129 (1988).
173. J. A. Harrison, C. T. White, R. J. Colton, and D. W. Brenner, *Phys. Rev. B* 46, 9700 (1992).
174. D. W. Brenner, *Phys. Rev. B* 42, 9458 (1990).
175. Y. S. Leng and S. Y. Jiang, *J. Am. Chem. Soc.* 124, 11764 (2002).
176. J. N. Glosli and G. M. McClelland, *Phys. Rev. Lett.* 70, 1960 (1993).
177. M. H. Müser and M. O. Robbins, *Phys. Rev. B* 61, 2335 (2000).
178. M. H. Müser, *Tribol. Lett.* 10, 15 (2001); *Computer Phys. Commun.* 146, 54 (2002).
179. H. C. J. Berendsen and W. F. van Gunsteren, in "Dynamics Simulation of Statistical-Mechanical Systems" (G. P. F. Ciccotti and W. G. Hoover, Eds.), p. 43. North Holland, Amsterdam, 1986.
180. P. Procacci and M. Marchi, in "Advances in the Computer Simulations of Liquid Crystals" (P. Pasini and C. Zannoni, Eds.), p. 333. Kluwer Academic Publishers, Dordrecht.
181. R. L. Burden and J. D. Faires, "Numerical Analysis," PWS Publishing Company, Boston, 1989.
182. S. K. Gray, D. W. Noid and B. G. Sumpter, *J. Chem. Phys.* 101, 4062 (1994).

CHAPTER 8

Diffusion in Elastically Strained Solids

Vladimir A. Borodin
RRC Kurchatov Institute, Moscow, Russia

Maria G. Ganchenkova
Helsinki University of Technology, Espoo, Finland

CONTENTS

ISBN: 1-58883-047-0

Handbook of Theoretical and Computational Nanotechnology
Edited by Michael Rieth and Wolfram Schommers
Volume 5: Pages (437–555)

1. INTRODUCTION

Diffusion in solids is important in many physical applications as the main and, in many cases, the only means of mass transfer in a solid. In our everyday life, we seldom deal with the manifestations of diffusion in solids, which is usually extremely slow at room temperature. However, an appropriate increase of temperature (from tens to thousands degrees Celsius, depending on solid) accelerates mass transfer by diffusion, allowing the transformation of material microstructure within reasonable times. The temperature can be increased on purpose, in order to modify the properties of material itself, but often temperature rise is a consequence of other processes occurring in the material or its surroundings. Thanks to the diffusion acceleration, a controlled annealing at high temperatures is often included as part of a technological chain aimed at the production of microstructures with desirable properties. On the other hand, when materials are working at increased temperatures, diffusion-controlled modification of the initial microstructure can lead to noticeable degradation of material properties. Due to its practical importance, diffusion in solids is extensively studied, both experimentally and theoretically, and there exist many monographs covering various aspects of this problem (see, e.g., [1–5]).

One of the interesting problems concerning diffusion in solids is how diffusion proceeds in an elastically stressed material. Indeed, any solid on the earth is strained to a certain degree, due to gravity forces, atmospheric pressure, and so forth. The temperature rise itself can lead to stresses in the solid, if the accompanying thermal expansion is restricted in that or other way. Normally, the stresses are so low (in comparison to parameters characterizing the ideal strength of solid, such as the elastic moduli) that their effects on the processes occurring in solids at the level of nanometer length scales are negligible. However, in modern technologies it is not a rare case when the elastic stresses are sufficiently high to affect the diffusion and the evolution of diffusion-controlled microstructures.

A technological example, where the stress effect on diffusion is extremely important, is related to microelectronics, which is at present one of the main applications one thinks about when dealing with nanotechnologies. The 30-year run of the semiconductor industry has been driven by the tremendous scientific and manufacturing work that has centered on complementary metal-oxide-semiconductor (CMOS) technology. The technological improvements of CMOS chips are best exemplified by Moore's law, which predicts that transistor size scales down every 18 months, allowing for greater performance per transistor and increased transistor packing density. One of the promising directions of CMOS development is the use of strained Si technology.

Strained Si technology enables improvements in CMOS performance and functionality via replacement of the bulk, cubic-crystal Si substrate with a Si substrate that contains a tetragonally distorted, biaxially strained Si thin film at the surface. Due to changes in crystal symmetry by the elastic deformation, the strained Si film has electronic properties that are superior to those of bulk Si. Specifically, the strained Si film has greater electron and hole mobilities, which translate into greater drive current capabilities for n- and p-type MOS transistors, respectively. The ability to tailor the performance of strained Si technology for each specific application will have a far-reaching impact, from high-speed products like microprocessors and field-programmable gate arrays, to the low-power products used in wireless communications and other mobile devices.

However, the proper control of strained material performance requires adequate account of stress gradients acting as driving forces for diffusion. Indeed, the channel's electronic properties are controlled by impurities (dopants) specifically designed to add extra electrons or "holes" into the channel material. A particular percentage of a particular dopant produces a particular set of electronic properties. Stress effects on dopant diffusion have been blamed for significant deviations in the device characteristics for both *n*-type and *p*-type metal-oxide semiconductor transistors.

The effect of stress on diffusion must be accounted for in different situations. Sometimes, the stress dependence of diffusion coefficients is used for the better understanding of diffusion mechanisms in complicated systems, for example, when the diffusion can occur through several mechanisms, which are acting simultaneously. This situation is met in silicon, where self-diffusion can be mediated by both vacancies and interstitials. Even more complicated is diffusion in ordered intermetallic alloys, where up to three different mechanisms with very similar predicted activation energies can operate in parallel [6]. The measured temperature dependence of the diffusivity does not allow separation of the relative contributions from different mechanisms. In contrast to the temperature-dependence, the measurements of diffusion in pressurized samples provide information about the dominant diffusion mechanisms, which normally demonstrate qualitatively different response to the action of external loads [7]. For instance, the application of hydrostatic pressure decreases the equilibrium concentration of interstitials and increases that of vacancies [8]. Correspondingly, the external pressure suppresses self-diffusion mediated by interstitials but increases that mediated by vacancies [9].

In addition to stresses caused by external loading of a solid material, internal stresses perhaps cause an even bigger effect in nanostructures. Internal stresses can be distributed uniformly over some part of material, as was the case in the strained Si example. The deformation of material is achieved by the nanostructure preparation technique, such as epitaxial growth of thin layers at substrates with somewhat different lattice spacing, or results from thermal and geometric effects. Alternatively, nanostructures can be composed of nanosize objects that serve as localized stress sources. Such nanostructures are especially typical in applications related to material irradiation with fast particles on accelerators and in nuclear facilities. For example, ion implantation is often used for creation of buried layers of new phase nanoclusters, which, depending on the nanocluster properties, can be used in various micro- and optoelectronic devices: field transistors, flash memories, optical waveguides, switches, and so forth. In neutron-irradiated materials working in active cores of nuclear reactors, nanosize clusters appear in the form of dislocation loops, voids, gas bubbles, and second-phase precipitates.

When nanostructures include ensembles of nanoscale objects, the growth and mobility of these objects is often closely related to diffusion. For instance, the growth of new phase clusters in ion-implanted samples is performed by annealing at high temperatures, so that the implanted impurity atoms could diffuse to clusters. The evolution of nanoscale objects is provided by diffusion currents of appropriate particles (impurity atoms and/or self-point defects—vacancies and interstitials). If the stresses created by the nanosize objects are high, they can noticeably affect the efficiency of particle diffusion in the vicinity of these objects. And indeed, the stresses around the nanosize objects can be quite high. In order to get a feeling of the stress magnitude, let us estimate the stresses acting at the surface of a spherical void with the radius R of, say, 10 nm. A void of this size is sufficiently big in order to be described with such macroscopic parameter as the surface energy, γ, so that the normal stress at its surface, σ_r, can be written down simply as

$$\sigma_r = \frac{-2\gamma}{R}$$

With a typical value of $\gamma \sim 1$ J/m^2 [10], this gives $\sigma_r \sim 200$ MPa; that is, not much below the yield stress of many metals. Even higher stresses are reached close to the cores of dislocations, which are intrinsic defects for any crystalline solid. In metals, dislocations constitute a substantial part of the microstructure, and it is not easy to decrease the dislocation

density below 10^7 cm/cm^3. In microelectronic materials (first of all, in silicon), the intrinsic dislocation densities are orders of magnitude lower, but dislocations (in the form of dislocation loops) often appear in a big number as a by-product of material processing by irradiation. Note that in contrast to phase transformations, which allow stress relaxation around second-phase particles, dislocations create in their vicinity elastic stresses that cannot be relaxed in principle.

Due to the importance of applications, where diffusion takes place in elastically strained structures, researchers require adequate means for the treatment of such situations, in order to make reasonable predictions of nanostructure behavior during processing and operation. Here we collect the published approaches and methods devoted to this particular aspect of diffusion in solids. This inevitably forces us to discuss the basic concepts of diffusion, because, in order to investigate the effects of stress on diffusion in crystalline solids, it is necessary to understand the mechanisms of the diffusion itself. However, we deliberately avoid here the multiple aspects of diffusion, which are not related in that or other way to our main topic.

Quite generally, diffusion is the way in which individual atoms in a solid move, making quick irregular jumps in different possible directions, allowed by their interaction with surrounding atoms. Sometimes, jumping atoms are able to make many sequential jumps, as is the case for impurities (i.e., atoms of elements that are not the main crystal constituents), which are located in interstitial positions of the host lattice. On the contrary, the diffusion of atoms of the crystalline lattice (self-diffusion) or impurities occupying lattice site position (such impurity atoms are called "substitutional") cannot proceed without mediating objects—vacancies and interstitials—because the direct exchange of position of neighboring atoms in the lattice is impossible. A vacancy is simply an empty lattice site and any of its neighbor atoms can jump into it. However, the vacancy will reappear at the position of the atom that made the jump, and the jumps become permitted for all atoms surrounding the vacancy in the new position. In other words, even though the vacancy is not a real material object and its movement is a chain of host lattice atom jumps by only one interatomic distance each, it is convenient to treat vacancies as quasiparticles, in exactly the same way as impurity atoms jumping over the interstitial positions in the lattice. Nearly the same situation is met in the case of self-interstitials, which in many solid lattices consist of two host lattice atoms, forming a dumbbell with the "center of mass" located on the lattice site. Such pair of atoms sharing a lattice site behaves as a unique object, which is sometimes called "interstitialcy" [11], in order to differentiate it from an atom (no matter, impurity or the host lattice atom), jumping from one interstitial position to another. An interstitialcy moves, when one of the dumbbell atoms returns to the site position, while the other one shifts closer to a nearest neighbor atom, pushing it away from the lattice site and creating a new atomic pair, located on the site of the pushed away atom. Such interstitialcy can be treated, like vacancy, as a quasiparticle that moves on the lattice as an entity, even though the atoms that constitute this quasiparticle change each time it changes position. In what follows, we will be mainly interested in the diffusion objects that are able to move as an entity (such as interstitial impurities, vacancies, and interstitialcies, which we will generally refer to as "particles" or "point defects"), while the movement of the host lattice atoms, which is a secondary process mediated by self-point defects, will not be addressed in detail. Neither will we treat here the diffusion of complex defects, consisting of several particles (such as divacancies, which are mobile in many solids).

Diffusion in solids can be considered as a multiscale problem and, depending on the length scales at which a particular aspect of diffusion is considered, the approaches to treat the diffusion can be quite different. Individual atomic jumps occur at the length scale of one interatomic distance (several angstroms) and their description must account for the atomic structure of the lattice in a straightforward way. The approaches used at this level are largely numerical and aim at the definition of the probabilities of individual atomic jumps. Most often, these probabilities are defined in terms of the jump energetics, which is estimated either by molecular statics methods or by molecular dynamics. On the other hand, the long-range diffusion of particles occurs at the length scales, comparable to the distances between particle sinks and traps, which in nanostructures means from tens to hundreds of nanometers. In this length-scale range, the diffusion can be described, at a choice, by atomistic methods

(e.g., molecular dynamics or lattice kinetic Monte Carlo) or the continuum ones, based on the use of differential equations of diffusion. When the evolution of the nanostructure constituents (such as nanoclusters) is important, diffusion over length scales exceeding intersink distances can be treated by methods that are able to describe diffusional mass transport in a complete ensemble of diffusing particles, sinks and traps.

The advantage of such multilevel approach to the description of diffusion is that the results of the more detailed treatment can be used as input and boundary conditions for the less detailed one. As a result, consideration of diffusion at different levels provides the overall consistency of diffusion description. Following the multiscale approach, we start the discussion of different aspects of the effects of elastic stresses on diffusion with the description of particle diffusion on the atomistic level. This is very important for the basic understanding of the diffusion features and especially for obtaining the basic parameters, which characterize individual atomic jumps. However, such a treatment is quite a formidable task, which is far beyond analytical approaches and whose progress is made available by the fast development of efficient numerical computation means. The advantages and shortcomings of the atomistic treatments of diffusion will be considered in more detail in Section 2, both for the diffusion in general and as applied to the possibilities to incorporate the effects of stress on diffusion, in particular.

The atomistic approaches give very detailed information about the behavior of individual jumping particles, but due to hardware limitations they are essentially limited to microscopic lattices, consisting of maximum several millions of atoms. However, in practical applications, especially related to technology, one often deals with diffusion in systems of the real-life length scales (above micrometers), which are beyond the possibilities of atomic level simulations. On the other hand, such systems consist of many diffusing particles of the same kind, and it is sufficient to know overall characteristics of the whole particle ensemble. For example, in order to find the rate of nanocluster growth as a result of impurity absorption from the surrounding matrix, one should know only the average impurity currents to cluster, which do not require detailed description of the movement of individual atoms in the cluster vicinity. Hence, it is possible to treat the diffusional mass transfer in the framework of a continuum approach that describes diffusion using partial differential equations (of parabolic or elliptic types) for the concentration of particles in the material.

One of the main features of the continuum approach is the description of the spatial distribution of particles in terms of particle concentration, defined usually as the number of particles per unit volume of material. From the practical point of view, this unit volume should be "physically small," so that it would contain sufficiently large number of particles, but still the particle distribution within the volume could reasonably be considered as uniform. However, in crystalline solids it is often more convenient to define concentration in probabilistic terms, that is as a probability density to find a particle on a lattice site. Concentration c introduced in this way is dimensionless, and the concentration "per unit volume" can be formally defined as c/Ω, where Ω is the average volume occupied by one atom in the lattice ("atomic volume"). Naturally, this does not allow us to treat c as the number of particles in the atomic volume. Nonetheless, the probabilistic treatment allows introduction of the concept of particle concentration at the length scales, comparable to the interatomic distance a, and thus permits microscopic derivation of parameters characterizing particle movement, such as diffusion coefficients.

The time and space evolution of diffusing particle concentration can be described by a set of differential equations. One of these is quite general and is simply the particle number density conservation law. In the simplest case, when only one type of diffusing particles is present in the solid and there are no sources or sinks of diffusing particles, it can be written down as

$$\frac{\partial c}{\partial t} + \operatorname{div} \mathbf{j} = 0 \tag{1}$$

where j is the particle current density. The second equation relates the current density j to the concentration c and can be obtained from the general nonequilibrium thermodynamics (see, e.g., [12]), which predicts that the spatial currents of particles in a slightly nonequilibrium systems can be expressed in terms of spatially nonuniform chemical potential, μ,

of diffusing particles. Namely, where the chemical potential is a slowly varying function of spatial coordinates, in the sense that $a|\nabla\mu| \ll \mu$, one can assume direct proportionality between the particle current density and the gradient of chemical potential,

$$j_n = -D_{nm}c\frac{\partial\mu}{\partial x_m} \tag{2}$$

where the set of proportionality factors D_{nm} (with $m, n = 1, 2, 3$ enumerating the Cartesian coordinates) is called the diffusion coefficient tensor and Einstein summation rule is implied. Having in mind that for dilute particle solution the relation between the chemical potential and the particle concentration is given by [13]

$$\mu = \ln c \tag{3}$$

we come to the desired relation

$$j_n = -D_{nm}\frac{\partial c}{\partial x_m} \tag{4}$$

In a particular case of completely isotropic diffusion, the diffusion tensor should have diagonal form with equal nonzero elements, $D_{nm} = D\delta_{nm}$, where δ_{nm} is the Kronecker's tensor. Correspondingly, Eq. (4) is reduced to the isotropic form,

$$\mathbf{j} = -D\nabla c \tag{5}$$

which is known in the literature as Fick's law, where D is the scalar diffusion coefficient. Note that in the derivation of Eq. (5), we have directly used the assumption of low concentration of diffusing particles in the matrix, so that it might be inapplicable to the case of diffusion of the main constituents of a crystal, for which concentrations are in any case not small. However, as it has already been mentioned, the movement of atoms in the lattice occurs as a result of diffusion of defects of crystalline structure (vacancies and interstitial atoms). The concentration of these point defects is normally quite low, and their diffusion is nicely described by the Fick's law.

Involving a very limited number of phenomenological parameters (first of all, diffusion coefficients), the continuum approach allows prediction of the diffusion-related effects with the help of much less complicated numerical techniques than those involved in the atomistic approaches. Often, even analytical treatments are possible. However, like any phenomenological theory, the continuum approach parameters cannot be obtained within the approach itself but should be defined either from experiment or from the knowledge accumulated at the atomistic level or from both. Indeed, the most important experimental finding about the diffusion coefficients is that their temperature dependence can be described by Arrhenius law,

$$D = D_0 \exp\left(\frac{-E_m}{k_B T}\right) \tag{6}$$

where E_m is referred to as the migration energy, D_0 is a certain numerical factor (diffusion coefficient preexponent), k_B is the Boltzman factor, and T is the absolute temperature. For any particular pair of "diffusing particles–host material," this expression is usually valid in broad temperature ranges, where the atomistic nature of particle diffusion does not change. The Arrhenius law, expressing diffusion coefficient in terms of the energy parameter E_m, largely simplifies numerical estimates of diffusion coefficients, because the energy can be calculated at one temperature (normally, absolute zero) and then used for diffusion coefficient scaling with temperature. The evaluation of the preexponential factor D_0 is generally much less important, especially having in mind that very often (though not without formidable exceptions), it varies in a quite narrow range of 0.01–1 cm^2/s. The only problem that remains is to understand, what the migration energy E_m is from the atomistic point of view and how we can get it. As shown in Section 2, it is not so easy to define this value correctly, regardless of formidable increase in the understanding of the atomistic picture of diffusion jumps during the past half century.

The fact that the detailed information about the microscopy of elementary diffusion jumps is hidden in the phenomenological parameters creates the link between the atomistic and continuum treatments of diffusion. It is possible to calculate diffusion coefficients by atomistic computations and then use them for purely continuum description. In complicated situations, where the experimental determination of diffusion coefficients is essentially impossible (e.g., when several diffusion mechanisms act at the same time, allowing measure of only the average rate of mass transfer), numerical atomistic treatments remain the only way to estimate diffusion coefficients, as well as other phenomenological parameters that can affect the diffusion (e.g., the efficiencies of diffusing particle interaction with various traps).

The proper understanding of the stress effects on diffusion is also impossible without efficient numerical means for the estimation of migration energies of diffusing particles, which are the key parameters modified by the elastic strains. Unfortunately, diffusion coefficients in stress fields cannot be described by a simple formula of the type of Eq. (6). Therefore, in Section 3 we demonstrate how the information about the kinetics of individual diffusion jumps can be converted into the macroscopic description in terms of diffusion equations. The presentation closely follows the general approach to anisotropic diffusion in stress fields developed by Dederichs and Schroeder [14] but takes into account additional restrictions imposed by defect behavior in equilibrium positions [15]. In the framework of this approach, the diffusion coefficients will be expressed in terms of both the individual jump probabilities and the geometry of possible diffusional jumps. The correlation of diffusion coefficients to the parameters of individual point defects for particular lattices will be discussed in Section 4.

Up to now, we discussed only the ways to describe the diffusion of particles in a perfect infinite crystal, assuming that there are no other processes that can affect particle behavior during the diffusion. In real life, such situations are rare and are met mostly in experiments specially tailored for the measurement of diffusion coefficients. On the contrary, practical applications in modern nanotechnologies normally involve much more complex situations, when diffusing particles are created, captured by internal sinks and interact with other particles, nucleating various particle clusters. A typical example is the ion-beam synthesis in microelectronics, where host materials are implanted with impurity atoms and subsequently annealed at high temperatures in order to force impurity clustering. In such applications, diffusion plays an important but intermediate part, determining the quality of the obtained microstructures but not being the main aim of the process. A very similar situation but with the opposite consequences is met in nuclear technologies, where the diffusion of point defects and impurities in irradiated structural materials leads to highly undesirable modifications of the initial material microstructure as a result of defect clustering into voids, dislocation loops, and second-phase particles. Evidently, in physical tasks, where the interactions of diffusing particles with other components of material microstructure are of interest, additional modifications of diffusion equations are necessary. A common approach for diffusion description in solids with multiple sinks is given by the chemical rate theory, which will be described in Section 5.

Finally, in Section 6 we give several examples of physical phenomena that crucially depend on the inter-relation of diffusion and stress. The selection of examples is related mainly to scientific interests of the authors and is far from being exhaustive.

2. DIFFUSION AT THE ATOMIC LENGTH SCALE

In order to understand how elastic deformation affects diffusion in solids, one has, first of all, to realize clearly the atomic mechanisms of diffusion jumps. Indeed, the methods used to determine the parameters of jumping particles are basically the same for stress-free and stressed material. Therefore, we start from the discussion of different concepts of the elementary diffusion events and the corresponding numerical methods for evaluation of appropriate jump parameters; first of all, particle energies in critical positions on the jump trajectory. After that, we discuss how these particle energies are modified by elastic deformation of the solid, which physical parameters for the description of particle interaction with elastic field should be introduced and which methods are applied for analytical and numerical estimation of these parameters.

2.1. Diffusion in Solids: History and Modern Understanding

2.1.1. The Absolute Rate Theory

Usually, the diffusion coefficient is defined as a proportionality constant between the mean squared shift of position of a diffusing particle after some time t and the time itself. The simplest model of this kind involves random one-dimensional jumps of a particle with a certain frequency Γ. In order to reflect the limitations imposed by the solid state, the length of individual jump ΔX can be considered constant. Then, a probability to find a particle at a certain distance from the initial point after time t can easily be calculated (first it was done by Einstein in the beginning of the twentieth century for a more general case, allowing different directions and lengths of individual jumps), and the diffusion coefficient may be expressed in terms of Γ and ΔX as

$$D = \frac{1}{2}\Gamma(\Delta X)^2 \tag{7}$$

the factor 1/2 arising from the possibility of jumps in two directions.

The length of an individual jump entering Eq. (7) is defined by an implicit assumption inherent to theory of diffusion in solids, namely that the initial and the final positions of the individual jump are nearest neighbors. Correspondingly, the distance traveled by a diffusing particle in one diffusion jump is of the order of the interatomic distance, a. This assumption is usually well justified, although in real-life one can meet examples when this is not the case, especially when particles are jumping near lattice imperfections. In the simplest case, such imperfection can be another particle. For example, in ordered intermetallics, individual vacancies in a divacancy can jump between the second nearest neighbor positions [6].

In contrast to the jump length, the frequency of jumps in (7) is not easy to find from the first principles. The most important indication of the possible microscopic mechanisms of diffusion is provided by experimentally observed fact that the dependence of the diffusion rate on temperature follows Arrhenius law, which often arises in physical phenomena that require thermal activation. This prompts the idea that diffusion also requires thermal activation, and a jumping particle must surmount a free-energy barrier, ΔG_m. Following this idea, until the late 1950s, the theory of diffusion in a crystalline phase was formulated in terms of the absolute rate theory borrowed from chemical reaction kinetics. In this approach, the transition of an atomic system from the initial to the final state occurs as a result of continuous variation of atomic coordinates, so that the atomic system passes through a continuously changing set of intermediate atomic configurations. Evidently, among this set of configurations there exists the one (called "activated complex") from which the system evolution toward the initial and the final configuration is equally probable. The potential energy of the system in this configuration is assumed to be the highest along the transition trajectory. The formalism of absolute rate theory, being applied to an individual atomic jump in a crystal, leads to the following relation for the diffusion coefficient [16]

$$D = \gamma a^2 \nu_0 \exp\left(-\frac{\Delta G_m}{k_B T}\right) \tag{8}$$

where γ is a numerical constant accounting for the geometry of the lattice (similar to factor 1/2 in Equation (7)) and ν_0 is a certain vibration frequency. Correspondingly, the jump rate is expressed as $\Gamma = \nu_0 \exp(-\Delta G_m/kT)$. An adequate estimation of ν_0 remains an extremely complicated problem, but for practical purposes the rough estimate of $\nu_0 \approx 10^{13}$ Hz works well.

The free energy change as a result of the transition can be written down as [13]

$$\Delta G_m = \Delta U_m - T\Delta S_m \tag{9}$$

where ΔU_m is the change of the crystal potential energy associated with the diffusing particle transition from the equilibrium position to the position corresponding to the top of thermodynamic barrier, and ΔS_m is the respective change of the crystal entropy. Correspondingly, the temperature dependence of the jump frequency is determined by the potential energy

change, whereas the entropy change contributes only to the temperature-independent pre-exponential factor.

The main problem of the absolute rate theory is related to the approximations used for calculation of ΔG_m. The cornerstone of the absolute rate theory is the assumption that a diffusion jump occurs sufficiently slowly (at least in the neighborhood of the transition state), so that the crystal around the jumping particle equilibrates to a degree justifying the thermodynamic description of the transition state in terms of the free energy. As far as the entropy change is concerned, in the case of individual particle jump it is related to the modification of the atomic vibrational modes. It is well-known that defects in equilibrium positions change the vibration frequency spectrum of the lattice, leading to the appearance of localized vibration modes. The assumption of the sufficiently long-lived transition state allows estimation of the vibration frequency spectrum for a particle in the transition position in a steady-state approximation. The same is true for the potential energy, which can be calculated assuming that the atoms around the jumping particle are in mechanical equilibrium, and thus the potential energy along the jump trajectory is a unique function of particle coordinates.

However, it is generally believed nowadays that the thermodynamical approach can be justified only while particles are vibrating close to well-defined positions in the lattice, where the energy of their interaction with the surrounding lattice is at minimum. The locations of these "equilibrium" positions at the bottoms of local "potential wells" depend on the particular combination of diffusing particle and the host lattice, coinciding usually either with lattice sites or with high-symmetry interstitial positions. While remaining close to equilibrium positions, the particles perform thermal vibrations with the frequency $\nu_0 \sim 10$ THz and only under very favorable conditions acquire an energy that allows a particle to shift so far from the equilibrium position that the jump to another nearby equilibrium position becomes possible. The transition is very rapid, taking the time of the order of an atomic vibration. Under these circumstances, the use of a thermodynamically equilibrium transition state can be a remarkable oversimplification. It seems more reasonable to assume from the very beginning that in application to diffusion, the probability of the elementary event is defined not by the free energy change, but by the potential energy difference due to transition from the equilibrium state to the transition one.

For systems consisting of many atoms, like a crystal with diffusing particle, the potential energy is a complicated multidimensional function of coordinates of all atoms. The way in which the energy varies with the atomic coordinates is usually referred to as potential energy surface. In the diffusion theory, one is usually interested in the so-called stationary points of this surface, that is, the points where the derivatives of the energy surface with respect to all atomic coordinates vanish. In all stationary points, atomic systems are in mechanical equilibrium, because the negative gradient of potential energy with respect to coordinates of an atom is, by definition, the force acting on this atom. As known from the mathematical functional analysis, among the stationary points it is possible to select the minimum points, which correspond to the stable equilibrium state of the system in the sense that any shift of atoms from the stable atomic configuration leads to the increase of the potential energy of the system. Evidently, there can be many minima on the energy surface. This is particularly true for crystalline solids, where any local minimum is replicated infinite times due to translational symmetry. If a system is in the local minimum, it can pass into another minimum located nearby only provided its energy first increases, the value of the increase being dependent on the system trajectory in the phase space. Restricting ourselves to trajectories that connect the initial equilibrium state with the selected final one, we can always select the trajectory (or a set of trajectories), where the biggest energy increase along the trajectory, E_m, is the lowest among all possible trajectories. The point in the phase space where this "minimax" energy value is reached is usually called "saddle point." As can easily be understood, the saddle point corresponds to mechanically equilibrium state of the systems; however, this equilibrium is unstable with respect to the small shifts in directions along the minimax trajectory.

Strictly speaking, a real transition from one equilibrium position to another one must not follow only the minimax trajectory. It can be shown, however, [17] that the minimax

trajectories have the biggest statistical weight among all possible transitions, so that one can assume in (9)

$$\Delta U_m = E_m$$

As a result, the task of the definition of the diffusion jump rates is reduced in the absolute rate theory to the definition of the stationary points on the potential energy surface. For any realistic model of the interatomic interaction, there is little chance to do it analytically. Therefore, a whole group of computational techniques based on the principles of absolute rate theory has been developed, which is referred to as "molecular statics" in physics or "molecular mechanics" in chemistry.

2.1.2. Molecular Statics

From the computational point of view, the basic assumption of the absolute rate theory, namely that the environment of a jumping particle accommodates to the current particle position along the jump trajectory, is very helpful, even if not strictly justified. The basic physical idea behind the numerical techniques is that the jumping particle can be used as a probe, which can be shifted from its equilibrium position and scan the energy surface, assuming full relaxation of the atomic system in each probe position (by assumption, the system has enough time to reach an equilibrium state). The aim of molecular statics is to find space positions of the probe atom, where its potential energy is either minimal or makes a saddle point. Thus, from the technical point of view, molecular statics is a set of efficient schemes for finding extrema of multidimensional functions. Some of these techniques are described in this section.

As a zero-order approximation, one can assume that for any spatial position of the probe atom, the full relaxation of all remaining atoms results in the same atomic configuration pattern, independent of the way the probe atom reached this position. Under this assumption, the potential energy of the probe particle is a unique function of the probe atom position, and one can introduce the "reduced" potential energy surface as a three-dimensional function of particle spatial coordinates, which is obtained from the full multidimensional energy surface by minimization with respect to positions of all lattice atoms. The stationary points of the reduced energy surface directly determine the equilibrium and saddle point positions of the particle, as shown in Fig. 1. When the reduced energy surface is known, it is possible to find the lowest minima, which can be considered as the equilibrium positions of the jumping particle, and to identify the valleys leading to the lowest energy barriers between the neighboring equilibrium positions. It should be kept in mind, however, that the reduced

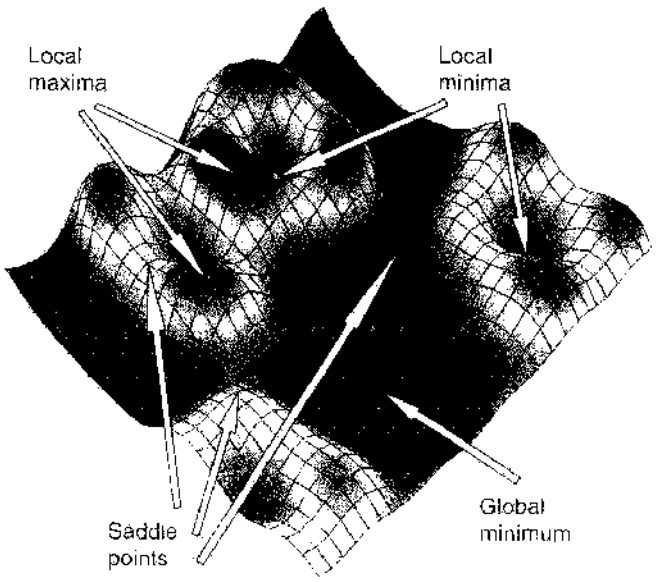

Figure 1. A schematic reduced energy surface (in two-dimensional case) and various stationary points on it.

potential energy surface is only a rough approximation, and the potential energy of the particle turns out to be sensitive to the way the jumping atom reaches a certain spatial point. In computational practice, it is not the rare case where, selecting the same initial atomic configuration (i.e., the relaxed configuration around a probe particle in an equilibrium position) and shifting the probe atom to the desired final position by a sequence of steps along some path (with full relaxation of the jumping particle environment at each step), somewhat different final values of the potential energy can be obtained, depending on the selected trajectory and the number of intermediate steps.

Before the description of the energy calculation techniques, several remarks are necessary. First of all, though formally there are no restrictions on the way how the particle potential energy surface is scanned, in practice a certain sequence of steps is followed. First of all, the full-scale scan of the potential energy surface is quite demanding in terms of computational resources, especially when the interaction potential is determined from quantum mechanics considerations, while the biggest part of the resulting information is simply a waste, as only stationary points are of any interest. For this reason, geometry optimization should be done before starting to study a defect incorporated into a crystal. Geometry optimizations typically attempt to locate minimums on the potential energy surface in order to predict equilibrium structures of crystalline systems. *A priori* guesses can often be made based on the crystal symmetry consideration, or a quick search assuming a rigid surrounding lattice can be made. All successful optimizations locate a stationary point, although not always the one that was intended. In fact, relaxation of sufficiently big atomic systems with essentially unknown minimum location and hence, with a wide freedom for the choice of the initial configurations (quite common situation in the modeling of, e.g., metallic glass structure), can result in extremely exotic final atomic arrangements corresponding to local energy minima. Because most minimization algorithms can only go downhill on the energy surface, they are able to locate the minimum that is uniquely defined by the starting point, as illustrated in Fig. 2. When more than one energy minimum for a diffusing particle is suspected, it makes sense to perform a conformational search in order to distinguish the deepest minimum. In order to locate more than one minimum or to locate the global energy minimum, one should be able to generate different starting points, each of which is then minimized. Some specialized minimization methods can make uphill moves to seek for minima lower in energy than the nearest one, but no algorithm has yet proved capable of locating the global energy minimum from the arbitrary starting position.

Geometry optimizations may be used to locate not only the minimum energy structures but transition atomic structures as well, though except for the self-evident situations, this is not the best approach. Usually, there is a definite difference in the methods used for the determination of the equilibrium and saddle point positions and energies of the jumping particles. Indeed, in case of equilibrium positions, the local energy minimum is achieved,

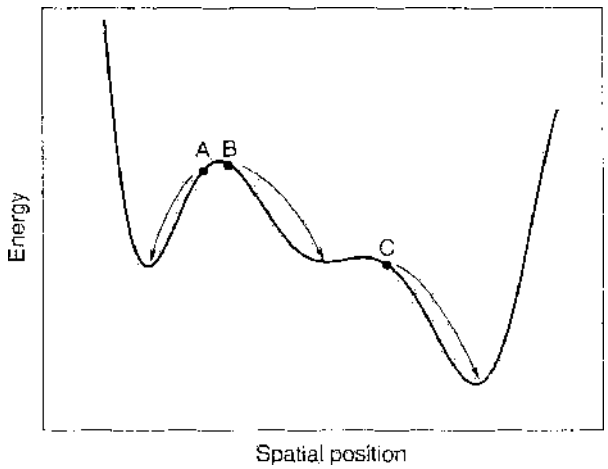

Figure 2. A schematic energy profile and minima that would be obtained starting from three initial points A, B, and C.

and so the conceptually simple energy minimization schemes are applied: no matter where exactly the atoms start (as long as they do not start too far from the supposed local energy minimum positions) and what are the atom trajectories, they eventually come to the desired final state. On the contrary, the saddle point positions and energies can depend on the particle trajectory, which requires additional efforts in selection of appropriate jump trajectories. Hence, reliable location of saddle points is done using special methods that explicitly consider information about the equilibrium particle positions and make search over the possible transition trajectories, as described below.

Second, the requirement of the full elastic relaxation during energy minimization, though much complicating the finding of extremum positions of the probe particle, is a must. Historically, starting with Huntington's work [18], the equilibrium, and even the saddle point configurations of jumping particles, were often calculated with the help of the rigid lattice approximation. However, even in the case of equilibrium positions, which can often be nicely located assuming the rigid lattice, such a model gives poor estimates for the defect formation energy. Indeed, the formation of defects inside the crystal changes the total forces acting on the atoms in the vicinity of the defect. These nonzero forces shift the atoms surrounding the defects to new positions, where the forces vanish and the system gets a thermodynamically preferable configuration with a minimum potential energy. As a result, the formation energy of a defect obtained in the rigid lattice approach turns out to be much higher than that obtained including the relaxation of the lattice atoms after the defect formation [19]. The difference becomes even more catastrophic in the case of saddle point configurations, where the energy can be overestimated by an order of magnitude.

Finally, one should remember that the accuracy of the molecular statics is inherently limited by the basic assumption of thermodynamic equilibrium. There are no objections for use of this technique for getting information about the equilibrium configuration geometry and energy, because the average time spent by atom in an equilibrium position is sufficient to reach both elastic and thermal equilibration of the atomic system. However, for transition states along the diffusion jump trajectory, there is no chance to know *a priori* the time that the atom spends at each point of the path. Thus, one cannot predict how much the system will relax at each atomic step, and, consequently, the assignment of a set of static configurations accompanying the particle movement is no more than approximation.

2.1.2.1. Energy Minimization Schemes As already stated, finding the equilibrium state characteristics is equivalent to the minimization of the total system energy, which is a unique function of all atomic coordinates. When this function is specified, the minimization can be treated as a purely formal mathematical problem: given a function U, which depends on a number of independent variables $x_1, x_2, \ldots, x_{3N}$, where N is the number of atoms in the system, find those values of these variables that provide the minimum value of U. In the minimum point all the first derivatives of the function vanish,

$$g_i \equiv \frac{\partial U}{\partial x_i} = 0 \tag{10}$$

while all the eigenvalues of the second derivatives matrix (or Hessian matrix),

$$H_{ij} = \frac{\partial^2 U}{\partial x_i \partial x_j} \tag{11}$$

are positive.

For multidimensional functions, the efficient location of the minimum is achieved by numerical methods, which iteratively change the atomic coordinates in such a way that the consecutive atomic configurations have progressively lower energies, until the minimum is reached. One can classify minimization algorithms into two groups: those that use derivatives of the energy with respect to the coordinates and those that do not. In turn, derivative methods can use either only the first derivatives or both the first and the second ones. Thus, three major approaches to finding a minimum of a function of many variables can be

summarized as follows:

- The first group of methods includes the so-called **search methods**. These methods use only values of the function itself. They are usually slow and inefficient but are very simple to program, as deriving cumbersome formulas for derivatives is not necessary. In spite of their inefficiency, the search algorithms are infallible and always find a minimum. For this reason, they are often used as an initial step, when the starting point in optimization is far from the minimum. Another disadvantage of search techniques is that they are very inefficient for a large number of optimized variables and converge very slowly when the number of variables exceeds 10.
- The family of **gradient methods** uses the values of the function and its gradients. These are currently the most popular methods in molecular static calculations. Among the most familiar members of this family are the steepest descent method and the conjugate gradient method [20]. This group of methods shows much better convergence rate than search methods and requires computer memory for storage, which scales as the number of particles N, since only $3N$ first derivatives are needed.
- The third group of methods has the name **Newton methods.** These are the most rapidly converging algorithms, which require values of the function, its first and second derivatives. The memory required for storing the Hessian matrix is proportional to N^2 (which may be prohibitive for simulation of large crystals). Therefore, a group of algorithms following from the Newton method has been developed and is called quasi-Newton methods. The main idea behind these algorithms is to use not the actual Hessian matrix but its current approximation. The typical members of this group are Davidon-Fletcher-Powell (DFP) or, for instance, Broyden-Fletcher-Goldfarb-Shanno (BFGS) algorithms. The detailed description of these algorithms can be found in [20].

Generally, the use of derivatives is beneficial, because they provide information about the shape of the energy surface and, if used properly, can significantly enhance the efficiency with which the minimum is located. Moreover, the higher is the order of derivatives employed by the algorithm, the more accurate its predictions are. Let us demonstrate it for a simple case of a system with two degrees of freedom (e.g., a two-dimensionally diffusing particle) described by potential energy function $U(\mathbf{x})$, where $\mathbf{x}$ is an observation point with Cartesian coordinates (x_1, x_2). Let us assume that the position of the particle is in some point $\mathbf{x}^0 = (x_1^0, x_2^0)$. Our goal is to find an optimal direction and length for a particle step from position $\mathbf{x}^0$ to some new position $\mathbf{x}$. What is meant by "optimal" depends on the particular type of the search. When the minimum of $U(\mathbf{x})$ is looked for, the optimum step should result in the largest energy decrease among all the possible step. The search for the saddle point is generally more sophisticated, because one usually finds saddle points following uphill valleys in the energy surface, and the optimum direction must keep the particle on the bottom of the valley, rather than simply increase the particle energy.

In any case, starting from the point under consideration, there is a 2π region of possible directions for the step. In order to choose between the possible directions, let us fix the step length h and consider a trial circle centered on the particle position and having the radius equal to the step length. Then, the displacement of the particle in the direction of some angle θ can be written down as

$$\Delta x_1 = x_1 - x_1^0 = h\cos\theta \quad \text{and} \quad \Delta x_2 = x_2 - x_2^0 = h\sin\theta \tag{12}$$

Let us select the step length h sufficiently small so that the potential energy in a close vicinity of point $\mathbf{x}^0$ could be reasonably approximated with a Taylor expansion to the second order in h,

$$U(\mathbf{x}) = U(\mathbf{x}^0) + g_1(\mathbf{x}^0)\Delta x_1 + g_2(\mathbf{x}^0)\Delta x_2 + \frac{H_{11}(\mathbf{x}^0)}{2}\Delta x_1^2 + \frac{H_{22}(\mathbf{x}^0)}{2}\Delta x_2^2 + H_{12}(\mathbf{x}^0)\Delta x_1 \Delta x_2 \tag{13}$$

where $\mathbf{g}$ and $\mathbf{H}$ are the gradient and the Hessian matrix, respectively.

If one retains only the first derivatives of the energy, expression (13) after simple transformation becomes:

$$U(\theta) = U(\mathbf{x}^0) + h[g_1(\mathbf{x}^0)\cos\theta + g_2(\mathbf{x}^0)\sin\theta] \tag{14}$$

which has two extremum values (one maximum and one minimum) on the trial circle, at angles θ_{ex} defined by the relation

$$\tan\theta_{ex} = \frac{g_2(\mathbf{x}^0)}{g_1(\mathbf{x}^0)} \tag{15}$$

The knowledge about the position of energy minimum on the trial contour can directly be used for the search of the potential energy minimum. Indeed, the direction from $\mathbf{x}^0$ toward the position of the minimum is evidently the optimum one, because it provides the biggest energy decrease for a step of any length h, which is sufficiently small to justify the use of linear approximation (14). On the other hand, the predictive force of the linear approximation is restricted. For instance, it gives little help for the selection of minimization step length, which usually requires more information than simply the knowledge of gradients in the starting point of the step. In the case of the saddle point search, the linear approximation gives an indication of the step direction only under very special conditions. For example, when $\mathbf{x}^0$ lays exactly on the bottom of the energy surface valley, which leads to the saddle point, the step can be directed toward the contour point, where the energy is the maximum one. However, when $\mathbf{x}^0$ deviates from the valley bottom, this "uphill" strategy can easily increase the deviation, driving the system toward an energy maximum, instead of a saddle point.

On the contrary, the account of the second derivatives in the Taylor expansion gives information about the local curvature of the energy surface. This information is crucial when the particle is in the vicinity of those special features of the potential surface, where the gradient or one of it component vanish. These features include stationary points (minimums, maximums, saddle points) and special lines (the tops of crests and the bottoms of valleys). In the most efficient energy minimization methods and nearly in all saddle point search methods, the investigation of the valley bottoms is of particular importance, because the atomic system trajectories in the phase space usually follow valley bottoms. On the other hand, when that or other stationary point is reached, the signs of the Hessian matrix eigenvalues allow one to determine the type of the point: a maximum (when all eigenvectors are negative), a minimum (all eigenvectors are positive), or a saddle (some eigenvalues are negative and some positive; when the potential energy depends on more than two variables, the number of negative eigenvalues determines the saddle point order).

The algorithms that use information about the local topology of the energy surface, as given by the second derivatives, gain qualitatively new possibilities compared to methods using only the first derivatives. For example, as discussed above, a first-order method is unable to follow an energy valley unless one applies some procedures returning the system to valley bottom after a step in the direction parallel or antiparallel to the gradient (an example of such correction procedure will be discussed below in relation to the drag method). On the contrary, the knowledge of the Hessian matrix makes it possible to follow approximately the valley bottom until the system comes close to a stationary point. The exact position of this point can be located, if necessary, by refined search techniques.

An instructive example, originally considered by Cerjan and Miller [21], illustrates how a second-order algorithm permits to trace a valley in the potential energy surface. Let us consider again a two-dimensionally moving particle located in point $\mathbf{x}_0$ near a valley bottom, but not exactly on it, Fig. 3a. When the Hessian in point $\mathbf{x}_0$ is known, one can approximate the particle energy with expansion (13), which can be rewritten for points on the trial circle as

$$U(\theta) = U(\mathbf{x}^0) + \frac{h^2}{4}[H_{11}(\mathbf{x}^0) + H_{22}(\mathbf{x}^0)] + h[g_1(\mathbf{x}^0)\cos\theta + g_2(\mathbf{x}^0\sin\theta)]$$
$$+ \frac{h^2}{4}\{[H_{11}(\mathbf{x}^0) + H_{22}(\mathbf{x}^0)]\cos 2\theta + 2H_{12}(\mathbf{x}^0)\sin 2\theta\} \tag{16}$$

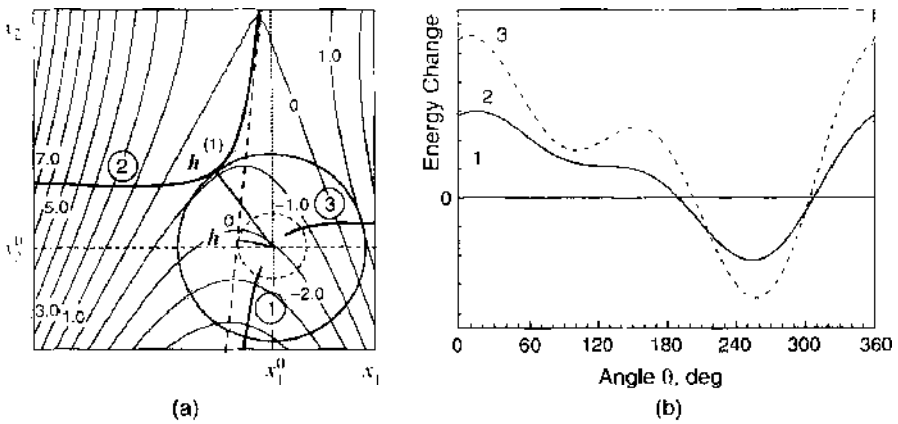

Figure 3. (a) A contour map of a valley in the potential energy surface U(**x**) and various circular contours around an observation point $\mathbf{x}^0$. The valley bottom line is shown by the dashed line; the distance from observation point to the valley bottom line is denoted as h^0. The branches of the optimal direction curve, as predicted by eigenvector following algorithm, are numbered according to Fig. 4a. $\mathbf{h}^{(1)}$ is the smallest step vector corresponding to parameter $\lambda^{(1)}$. (b) The angular dependence of U for trial contours with different radii: (1) $h = h^0$; (2) $h = h^{(1)} = 2.6h^0$; (3) $h = 4h^0$.

In contrast to the linear approximation, the presence of the second harmonics in θ can result in up to four extrema (local minima and local maxima) that can be used for selection of step direction. Naturally, the step length h must not be too small, because when h is smaller than the distance h^0 between the observation point and the valley bottom (see Fig. 3a), the angular dependence of U has only two extremum points (one minimum and one maximum), Fig. 3b. When h exceeds h^0, the trial circle scans both sides of the valley. Gradually increasing the step length, it is possible to reach the circle, where flex point appears on the angular dependence of U (see curve 2 in Fig. 3b). With the further increase of the trial circle radius, there appear two minima in the angular dependence of the potential energy on the trial circle, which approximately locate the points where the valley bottom enters and leaves the region surrounded by the trial circle. In other words, increasing the trial circle radius, one can approximately trace the bottom valley for all step lengths up to some, h_{max}, which is determined by physical restrictions [such as, for instance, the validity of the potential energy approximation with quadratic form (13)]. Correspondingly, one can approximately trace the valley bottom, selecting the step length close to h_{max}, and follow this bottom in the direction of the lower or the higher energy minimum, depending on the search direction. Evidently, in the new position the system will not be exactly on the bottom of the potential energy valley. Indeed, not the real energy surface, but only its local quadratic approximation is used for the selection of step direction. Also, an energy minimum on the trial circle fixes exactly the valley bottom only if the latter crosses the circle normally to the circle tangent, which is seldom the case. Nonetheless, a reasonable selection of the length step keeps the system *in the vicinity* of the bottom valley, and thus the trial circle search can be repeated in the new position until the system comes close to a stationary point.

There are two possibilities for calculating the derivatives that are used in modern codes. When the interaction energy is defined analytically, the derivatives can be calculated straightforwardly, and the appropriate mathematical formulae can be incorporated into the program. Another approach is to compute derivatives numerically by approximating the slope of an energy function (or its gradient in the case of second derivatives) by finite differences. Unfortunately, the use of energy derivatives is not always possible, so that one is left with the minimization algorithms that rely only on the energy values. However, these methods are much less popular than those using energy derivatives, and here we will restrict ourselves only to the latter.

There are many factors that must be taken into account when choosing the most appropriate algorithm (or combination of algorithms) for a given problem; the best minimization algorithm being the one that provides the answer as quickly as possible and uses the least amount of computer memory. No single minimization method has yet proved to be the best for all atomistic simulation problems, and so most commercial software packages

offer a choice of methods. For example, quite different methods are applied when the interatomic interactions are calculated from quantum mechanical principles and when they are defined in terms of phenomenological interaction energies. These approaches require so different computational efforts to calculate the energies and their derivatives in individual configurations that many-step algorithms, quite appropriate for classical atomic systems, become absolutely forbidden for quantum mechanical approaches. On the other hand, quantum mechanics is usually applied to systems with small amount of atoms (at best a half-thousand), whereas classical systems include many thousands and even millions of atoms. Some operations that are inherent to minimization procedures (such as matrix inversions), being trivial for small systems, become formidable for systems containing thousands of atoms.

Among the first-order minimization algorithms, two methods are most frequently used in atomistic simulations: the steepest descent and the conjugate gradients. The main idea behind the first-derivatives methods is the gradual change of the atomic coordinates along a sequence of directions, which moves the system closer and closer to the minimum point. The starting point for each iteration step is the atomic configuration obtained at the previous step, and the difference between the techniques is usually the algorithm, specifying how the set of directions is selected. The initial configuration of the system, serving as a staring point for the first iteration, remains usually the responsibility of the researcher.

2.1.2.1.a. The Steepest Descent Minimization The steepest descent method moves atoms in the direction along the instantaneous forces acting on atoms (this direction is that of the steepest-descent). In the $3N$ dimensional space of all atomic coordinates, $\mathbf{x} = (x_1, \ldots, x_{3N})$, the generalized force can be expressed as

$$F_i(\mathbf{x}) = -\frac{\partial U(\mathbf{x})}{\partial x_i} \quad (i = 1, \ldots, 3N) \tag{17}$$

An iteration step that starts from some system configuration $\mathbf{x}^n$ (where superscript n enumerates steps) begins from calculation of the force acting at the initial configuration, which is related to the gradient of potential energy in this point, $\mathbf{g}^n$, as

$$\mathbf{g}^n = -\mathbf{F}(\mathbf{x}^n)$$

and then the atoms are shifted along the line $\mathbf{x} = \mathbf{x}^n - b^n\mathbf{g}^n$ in $3N$-dimensional space (where b^n is a parameter characterizing the shift along the line), until the point is reached where the generalized force vanishes. In other words, the gradient at the starting geometry is followed downhill the energy surface by increasing the free parameter b^n until the energy starts to rise. Then, the value $b^n_{\min}$ corresponding to the local minimum of energy along the line is found by any standard technique [20] of one-dimensional minimum location, using the last three iteration points as a starting guess. The new system configuration obtained, $\mathbf{x}^{n+1} = \mathbf{x}^n - b^n_{\min}\mathbf{g}^n$, is used as the initial position for the next iteration step. In particular, the gradient at this approximate minimum, $\mathbf{g}^{n+1}$, is reevaluated and then the atoms are shifted in the direction opposite to $\mathbf{g}^{n+1}$ until the energy begins to rise again. The advantage of this minimization scheme is that it will always approach a minimum. It is simple and only requires storage of the gradient. However, in certain situations this straightforward minimization scheme is far from the optimum one.

Indeed, after the energy minimization along some vector $\mathbf{h}^n$, the energy gradient in the minimum point, $\mathbf{g}^{n+1}$, should have vanishing projection on the minimization direction, which means that $\mathbf{h}^n$ and $\mathbf{g}^{n+1}$ are perpendicular in this point,

$$\mathbf{h}^n \cdot \mathbf{g}^{n+1} = 0 \tag{18}$$

Because in the steepest descent method the direction of a step is antiparallel to the energy gradient at the starting point of the step ($\mathbf{h}^{n+1} = -\mathbf{g}^{n+1}$), condition (18) means that the direction of the next step is strictly orthogonal to the previous one, $\mathbf{h}^n \cdot \mathbf{h}^{n-1} = 0$. The shortcoming of this requirement can be understood if we consider the behavior of the trajectory leading from the initial system state to the final minimum. At the first step, the system moves toward the nearest valley in the potential energy surface and then descends along this valley

in a zigzag line oscillating around the valley bottom as it moves downhill. When the valley is narrow and an initial step is at an angle to the valley direction, the necessity to make each next step in the perpendicular direction to the previous one forces the system to move in small steps from one valley side to another. As a result, convergence toward the minimum point implies many iterations and is quite slow. For this reason, the steepest descent algorithm of energy minimization is usually used for quick relaxation of sufficiently simple starting geometries or as a backup algorithm, if the more sophisticated methods are unable to lower the energy function value.

2.12.1.b. Conjugate Gradients Minimization In the conjugate gradients method, the first step of minimization procedure is aimed at locating a valley in the potential energy surface and is done, similar to the steepest descent approach, against the direction of the gradient, $\mathbf{h}^0 = -\mathbf{g}^0$. However, the conjugate gradients method performs the descent along the valley cleverly using information about the potential energy shape and makes consecutive steps in a more flexible way than in the case of steepest descent, that is, more or less along the valley bottom instead of perpendicular to one another. The idea behind the selection of step direction can be demonstrated by the following reasoning.

Let us assume that after $n-1$ steps of minimization of the potential function U, the system has reached point $\mathbf{x}^n$ in $3N$-dimensional space of atomic coordinates, and we are looking for a better direction $\mathbf{h}^n$ for step n, as compared to the steepest descent (where one assumes $\mathbf{h}^n \| \mathbf{g}^n$). In order to improve the selection, we must first specify what is wrong with the steepest descent selection. One of the problems is that the energy gradient is orthogonal to the previous minimization direction $\mathbf{h}^{n-1}$ in the starting point of step n, but not in its final point $\mathbf{x}^{n+1}$ (corresponding to the energy minimum along direction $\mathbf{h}^n$), because the energy gradient rotates along the step in order to ensure that the final gradient $\mathbf{g}^{n+1}$ is orthogonal to $\mathbf{h}^n$. This means that while at the beginning of step n the energy is minimized along direction $\mathbf{h}^{n-1}$, at the end of the step this must not be so. In order to improve the minimization algorithm, we may ask ourselves whether it is possible to select step direction $\mathbf{h}^n$, so that in the final position of step n the potential energy would be minimized along both directions, $\mathbf{h}^{n+1}$ and $\mathbf{h}^n$? In mathematical terms, this is equivalent to requirement $\mathbf{g}^{n+1} \cdot \mathbf{h}^{n-1} = 0$. Moreover, if such selection strategy were possible for any step, it would mean, by induction, that after any step the energy would remain minimized along all the direction tested before, that is

$$\mathbf{g}^n \cdot \mathbf{h}^j = 0 \quad \text{for all } j < n \tag{19}$$

Correspondingly, after $3N$ steps we would reach the minimum along $3N$ noncollinear directions, which means that the minimum of the potential energy would be reached.

Unfortunately, it is not possible to satisfy Eq. (19) for an arbitrary potential, but it can be achieved in an important special case, where the potential energy function can be sufficiently well approximated by a harmonic function, which can be written in a general form as

$$U(\mathbf{x}) = U(\mathbf{x}_0) + \frac{1}{2}\sum_{i,j} H_{ij}(x_i - x_{0j})(x_j - x_{0j}) + \cdots \approx U(\mathbf{x}_0) + \frac{1}{2}(\mathbf{x} - \mathbf{x}_0) \cdot \mathbf{H} \cdot (\mathbf{x} - \mathbf{x}_0) \tag{20}$$

where $\mathbf{x}_0$ is the position of energy minimum, H is a constant Hessian matrix, and the last term is written down as a formal matrix product. Let us assume now that at step $n-1$, one has performed the minimization of the energy function along some direction h^{n-1}, and the system is in the state $\mathbf{x}^n$. According to Eq. (20), the value of the gradient $\mathbf{g}$ in point $\mathbf{x}^n$ equals to

$$\mathbf{g}^n = \mathbf{g}(\mathbf{x}^n) = -\mathbf{H} \cdot (\mathbf{x}^n - \mathbf{x}_0)$$

For the next possible direction, let us consider some $\mathbf{h}^n$, so that the minimization will be performed along the line $\mathbf{x} = \mathbf{x}^n + b^n\mathbf{h}^n$. Evidently, when the minimum will be found in some point $\mathbf{x}^{n+1}$, the value of the gradient in this point will be

$$\mathbf{g}^{n+1} = \mathbf{g}(\mathbf{x}^{n+1}) = -\mathbf{H} \cdot (\mathbf{x}^{n+1} - \mathbf{x}_0) = \mathbf{g}^n - b^n_{\min}\mathbf{H} \cdot \mathbf{h}^n \tag{21}$$

The condition $\mathbf{g}^{n+1} \cdot \mathbf{h}^{n-1} = 0$ is the equivalent to the requirement

$$\mathbf{h}^{n-1} \cdot \mathbf{H} \cdot \mathbf{h}^{n} = 0 \tag{22}$$

Vectors $\mathbf{h}^n$ and $\mathbf{h}^{n-1}$ satisfying Eq. (22) are called "conjugate" [20]. We thus see that the movement along direction $\mathbf{h}^n$ does not spoil the minimization along the previous step direction $\mathbf{h}^{n-1}$ when one selects conjugate step directions and not the orthogonal ones.

Restriction (22) still permits more than one choice of $\mathbf{h}^n$, which means that each next minimization step can be made independent of the previous one [22]. The selection of the step direction can be uniquely specified if one expresses $\mathbf{h}^n$, according to the original Fletcher-Reeves algorithm [23], in the form of a simple recursive relation,

$$\mathbf{h}^{n} = \mathbf{g}^{n} + \gamma^{n-1}\mathbf{h}^{n-1} \tag{23}$$

where γ^{n-1} is a scalar factor and assumes additionally that the gradient vectors in the beginning and the end of each step are orthogonal,

$$\mathbf{g}^{n} \cdot \mathbf{g}^{n-1} = 0 \tag{24}$$

Note, by the way, that even though the considered minimization method is called "conjugate gradient," it is the successive minimization directions that are conjugate, and not the gradients.

The conditions of orthogonality and conjugacy allow us to express the scalar constants $b^n_{\min}$ and γ^n as [24]

$$b^{n}_{\min} = \frac{\mathbf{g}^{n} \cdot \mathbf{g}^{n}}{\mathbf{h}^{n} \cdot \mathbf{H} \cdot \mathbf{h}^{n}} = \frac{\mathbf{g}^{n} \cdot \mathbf{h}^{n}}{\mathbf{h}^{n} \cdot \mathbf{H} \cdot \mathbf{h}^{n}} \quad \text{and} \quad \gamma^{n} = \frac{\mathbf{g}^{n+1} \cdot \mathbf{g}^{n+1}}{\mathbf{g}^{n} \cdot \mathbf{g}^{n}} \tag{25}$$

The most remarkable feature of conjugate direction selection according to (23) is that there is no necessity in the knowledge of the Hessian matrix to get a set of directions $\mathbf{h}^n$, regardless of the fact that the introduction of conjugate directions explicitly required it, and thus the ideology of the conjugate gradient approach is that of a second-order derivative method, rather than that of a purely first-derivative one. However, instead of calculating the new gradients after each step of linear minimization with the help of Eq. (21), one can find them by direct differentiation of the potential energy in the final point of the step and then use relation (25) to calculate scalar factor γ^n entering (23). Correspondingly, the method can be applied to a potential function of any shape, not necessarily to that which is fairly quadratic. Naturally, the number of iterations in this case will exceed that of $3N$, which is required to reach the minimum of a purely quadratic function of $3N$ variables.

As an improvement of the conjugate gradient scheme, Polak and Ribiere [24] proposed to select scalar constants γ^n in the form:

$$\gamma^{n} = \frac{(\mathbf{g}^{n+1} - \mathbf{g}^{n}) \cdot \mathbf{g}^{n+1}}{\mathbf{g}^{n} \cdot \mathbf{g}^{n}}$$

When the energy surface in the vicinity of the minimum point is described by a purely quadratic function, these constants coincide with those given by (25), as all gradients will be orthogonal. However, in reality, the energy functions are only approximately quadratic, and the Polak-Ribiere method performs better than the original Fletcher-Reeves algorithm, at least for the functions that were examined [24, 25].

The conjugate gradient method is one of the most popular minimization techniques in quantum mechanical calculations for locating the minimum of the Kohn-Sham energy functional [26], because of comparatively fast convergence and the use of only the first derivatives of the system energy. Some of the conjugate gradients method based algorithms adopted for these CPU-time expensive calculations have been reviewed, for example, in [22].

2.1.2.1.c. Newton-Raphson Method Second-order methods use explicitly not only the first derivatives but also the second derivatives of the energy surface to locate a minimum. The simplest second-order method is the Newton-Raphson method.

Strictly speaking, the Newton-Raphson algorithm is usually applied in order to locate the points where a function becomes equal to zero and is in this case a first derivative algorithm. Its application for the search of minima on the potential energy surface is possible, as it is equivalent to the search of zeros of the potential energy gradients, which must vanish in any stationary point.

The idea of the method can be illustrated if we consider a one-dimensional potential energy function $U(\mathbf{x})$, which is known at some point x^n together with its first and second derivatives. At a small distance δx from x^n the potential energy and its gradient can be represented in terms of Taylor series:

$$\begin{aligned} U(x^n + \delta x) &= U(x^n) + g(x^n)\delta x + \tfrac{1}{2}H(x^n)\delta x^2 + O(\delta x^3), \\ g(x^n + \delta x) &= g(x^n) + H(x^n)\delta x + O(\delta x^2) \end{aligned} \tag{26}$$

where $H(x) = d^2U/dx^2$. When x^n is close to point x^0, where g vanishes, the nonlinear terms can be neglected, and the distance $\delta x = x^0 - x^n$ can immediately be defined from the requirement $g(x^n + \delta x) = 0$, which gives

$$\delta x = -\frac{g(x^n)}{H(x^n)} \tag{27}$$

If, however, the accuracy of the zero point found using linear approximation for the energy gradient is insufficient, we can recalculate the first and second derivatives of the energy in the point $x^{n+1} = x^n + \delta x$ and make another step, moving again purely along the tangent to function g. Assuming that n is the number of a step in this iterative procedure, one obtains the following recursive formula for the location of energy minimum:

$$x^{n+1} = x^n - \frac{g(x^n)}{H(x^n)} \tag{28}$$

The same reasoning can easily be extended for a multidimensional case, in which case expression (28) can be rewritten as:

$$\mathbf{x}^n = \mathbf{x}^n - \mathbf{g}^n \cdot (\mathbf{H}^n)^{-1} \tag{29}$$

where $\mathbf{g}$ and $\mathbf{H}^{-1}$ are now the multidimensional gradient and the inverse Hessian matrix, respectively.

As shown in [20], the Newton-Raphson step length decreases with each iteration as

$$\delta x^{n+1} = -(\delta x^n)^2 \frac{H(x^n)}{2g(x^n)} \tag{29A}$$

Expression (29A) shows that Newton-Raphson method converges quadratically, increasing the number of significant digits in x_n by approximately a factor of two after each step. This feature makes this method a good choice for the finding of minima of potential energy function, provided its first and second derivatives can easily be evaluated.

However, the method has some shortcomings that can be divided in two groups. The first one is related to the method itself. Indeed, it works well only provided the Hessian matrix is positively defined in all iteration points, otherwise the minimization can become unstable. This implies that a good initial guess of the minimum is an important prerequisite for the convergence of iteration procedure. In practice, they usually first apply a more rough method to get close to the energy minimum before initializing the Newton-Raphson minimization procedure. The second disadvantage of the method is in the necessity of calculation, inversion, and storage of Hessian matrix at each step, which is potentially time and memory consuming.

There exist variations of the Newton-Raphson method (see [20]), many of which aim at avoiding the calculation of the full matrix of second derivatives. A family of methods, called quasi-Newton methods, requires only first derivatives and gradually construct the inverse Hessian matrix as the calculation proceeds. The "quasi" prefix is added, because one uses in

calculations not the real Hessian matrix, but its approximation at the current step. Indeed, the decrease of the potential function at the next step is guaranteed only provided the Hessian matrix is positively defined. However, when following a pure Newton step, as described above, one generally has no *a priori* confidence how far is the current system state from the minimum position and cannot be sure about the positively defined Hessian. To avoid this problem, it has been suggested to start with a positively defined, symmetric Hessian matrix to build up the approximation $\widetilde{H}$ that remains positively defined and symmetric during the whole iteration procedure, while tending to the correct inverse Hessian matrix by the end of iteration procedure. In other words, the sequence of matrices $\widetilde{H}^n$ (where i indicates the iteration number) must obey the following rule

$$\lim_{n\to\infty} \widetilde{H}^n = H^{-1}$$

Having moved from position $\mathbf{x}^n$ to the next one $\mathbf{x}^{n+1}$, in the quasi-Newton minimization we do not have to recalculate the inverse Hessian matrix $\widetilde{H}^{n+1}$ at the next step, but can simply obtain it from the inverse Hessian matrix of the previous step. Several variants of this procedure have been developed, such as DFP, BFGS, or, for instance, Murtaugh-Sargent (MS) schemes [27]. In particular, DFP formula for the inverse Hessian matrix update looks like

$$\widetilde{H}^*_{i-1} = \widetilde{H}_1 + \frac{(\mathbf{x}^{n+1} - \mathbf{x}^n) \otimes (\mathbf{x}^{n-1} - \mathbf{x}^n)}{(\mathbf{x}^{n+1} - \mathbf{x}^n) \cdot (\mathbf{g}^{n+1} - \mathbf{g}^n)} - \frac{[\widetilde{H}^n \cdot (\mathbf{g}^{n+1} - \mathbf{g}^n)] \otimes [\widetilde{H}^n \cdot (\mathbf{g}^{n-1} - \mathbf{g}^n)]}{(\mathbf{g}^{n+1} - \mathbf{g}^n) \cdot \widetilde{H}^n \cdot (\mathbf{g}^{n+1} - \mathbf{g}^n)} \tag{30}$$

where sign $\otimes$ denotes the direct matrix product. The detailed derivation of expression (30) can be found in [24, 25].

One simple way in which it may be possible to speed up the Newton-Raphson method is to use the same Hessian matrix for several successive steps of the Newton-Raphson algorithm with only the gradients being recalculated at each iteration. A widely used algorithm is the block-diagonal Newton-Raphson method, in which just one atom is moved at each iteration. This only leaves those terms that involve the coordinates of the atom being moved and reduces the problem to the trivial one of inverting a 3×3 matrix. However, the block-diagonal approach can be less efficient when the motions of some atoms are closely coupled, such as the concerted movements of connected atoms.

The choice of minimization algorithm is dictated by a number of factors, including the storage and computational requirements, the relative speeds with which the various parts of the calculation can be performed, the availability of analytical derivatives, and the roughness of the method. The Newton-Raphson method can be computationally demanding for systems with many atoms and can also require a significant amount of storage. Thus, any methods that require the Hessian matrix to be stored may present memory problems when applied to systems containing thousands of atoms. For calculations performed using molecular statics technique for systems of considerable size, therefore, the steepest descent and conjugate gradients methods are the most widely used.

On the other hand, quantum mechanical calculations are restricted to systems with relatively small numbers of atoms, and so storing the Hessian matrix is not a problem. As the energy calculation is often the most time-consuming part of the calculation, it is desirable that the minimization method chosen take as few steps as possible to reach the minimum. For many levels of quantum mechanics theory, analytical first derivatives are available. However, analytical second derivatives are rarely available and can be expensive to compute. The quasi-Newton methods are thus particularly popular for quantum mechanical calculations.

2.1.2.2. Saddle-Point Search Techniques Transition structures are generally more difficult to describe than equilibrium geometries. Let us consider, in particular, a jump of a single atom from one equilibrium position to another. If one assumes that the cooperative motion of atoms in crystal adjusts their configuration to the instantaneous position of the jumping atom, molecular statics method can be used as an approximate method for getting the migration path for this atom and for calculating the atom energy along this path. Where the reduced potential energy surface for the jumping atom remains a reasonable approximation, one can scan the space among the initial and final positions of a diffusion jump

and select the valleys in the energy surface that lead to the lowest saddle points. In fact, this method gives quite reasonable indication of the possible positions of saddle points and the topology of the potential surface in their vicinity, even though requires quite formidable computation resources. In contrast, where the energy of the jumping particle depends on the prehistory of particle movement, the search for true saddle points by simply scanning over the phase space of all possible positions of crystal atoms is hardly possible. This is especially true when crystal relaxations involve computationally demanding techniques, such as those involving quantum mechanics calculation of interatomic interactions. Therefore, the search for the saddle point positions usually heavily relys on physical assumptions concerning the most appropriate trajectory of a particle jump. Correspondingly, there always remains a risk of the saddle point algorithm failure if the implied assumptions turn out to be incorrect.

For the past 40 years of computational condensed matter development, different methods have been proposed for finding diffusion jump paths and saddle points. Typically, the search for the saddle point starts from the local minimum on the potential energy surface (stable equilibrium position of the jumping particle) and then traces the trajectory stepwise, in a sequential manner [28]. The selection of the atom shift length and direction at each step can be done in different ways. In some of the algorithms, the direction of the atom shift is selected exclusively from the properties of the energy surface in the close vicinity of the current point in the phase space. The main disadvantage of these algorithms is that there is no guarantee that in the end of the trajectory, the jumping particle reaches the desired final position (in another stable equilibrium position) and, even if it does, the selected trajectory will lead to the real saddle point. Therefore, a number of methods of saddle point search use information about both the initial and final positions of the jump (for a good review, the reader is referred to [29]).

2.1.2.2.a. Eigenvector Following Method The common problem that all developed methods meet is an uncertainty in obtaining the minimum energy path and, therefore, the saddle point location. This uncertainty results from the fact that more than one path can connect the initial and the final points of the diffusion jumps, whereas the methods used for tracing the transition path converge to that closest to the initial guess. To our knowledge, there exists only one method related to the direct scan of the space that makes it possible, at least in principle, to avoid this uncertainty and find the real minimum energy path and saddle point. This method is known under the name of "eigenvector following" (detailed qualitative description of the method can be found in [21]). The basic idea of the method is related to the scanning of the potential energy surface in the vicinity of a current point of a trajectory, as discussed in relation to Eq. (16). That is, the true energy surface is approximated by a quadratic form similar to Eq. (16), though in an appropriate multidimensional space, and the steps are made along the potential energy valley approximately located using the trial circle contours. In terms of classification introduced in Section 2.1.2.1, the eigenvector following method belongs to the group of second-derivative methods where the first and second derivatives are used for finding the most appropriate direction of motion. However, in contrast to the cases described in that section, where we looked for the direction leading downhill on the energy surface, now we follow the direction leading uphill from the minimum energy configuration. The use of second harmonics allows us to reach a good accuracy of the extrema values and to clarify the types of the stationary points found along the path. For instance, when the Hessian matrix at a stationary point does not have any positive eigenvectors, then energy function has reached its maximum value. If the Hessian matrix at a stationary point has one negative eigenvector, that is, one downhill direction (i.e., the direction along which the potential energy passes through the maximum), the stationary point is called a simple saddle point; if there are two negative eigenvectors, double saddle point; and so on.

The basics of the algorithm for finding a saddle point following local normal modes were first discussed in the works of Crippen and Scheraga [30] and Hilderbrandt [31]. In the first proposed algorithms, a step direction along the jump trajectory is selected in such a way that along one of the modes the step must be done in uphill direction, whereas along the others toward the lower potential energy. A more advanced approach to the selection of the

step directions was proposed by Cerjan and Miller [21], who used the Lagrange multiplayer technique for tracing the valleys in the potential surface. Let us assume that after some steps along the minimum energy trajectory, the investigated atomic system is in a point $\mathbf{x}_0$ of a p-dimensional space of the system degrees of freedom (e.g., a $3N$-dimensional space of atomic coordinates), and the potential energy function $U(\mathbf{x})$ in a point $\mathbf{x}$ in the vicinity of $\mathbf{x}_0$ is approximated by a quadratic form:

$$U(\mathbf{x}) = U(\mathbf{x}_0) + \mathbf{g} \cdot \Delta\mathbf{x} + \frac{1}{2}\Delta\mathbf{x} \cdot \mathbf{H} \cdot \Delta\mathbf{x} \tag{31}$$

where $\Delta\mathbf{x} = \mathbf{x} - \mathbf{x}_0$. Following the ideology described in relation to equation (16), let us look for the minima of the potential energy on the p-dimensional hypersphere of radius h with the center in the current point x_0. This can be done by minimizing the function

$$L(\Delta\mathbf{x}, \lambda) = U(\mathbf{x}) + \frac{\lambda}{2}(h^2 - \Delta\mathbf{x} \cdot \Delta\mathbf{x}) \tag{32}$$

where λ is a Lagrange multiplier, with respect to both $\Delta\mathbf{x}$ and λ. The requirement of the vanishing derivative of L with respect to λ guarantees that $\Delta\mathbf{x}$ remains at the hypersphere surface (i.e., $\Delta\mathbf{x} \cdot \Delta\mathbf{x} = h^2$), while the vanishing derivative over $\Delta\mathbf{x}$ specifies an equation for possible values of λ. The simplest form of this equation can be obtained if one rotates the local coordinate system in such a way that the Hessian matrix becomes diagonal,

$$\tilde{H}_{ij} = \left(\mathbf{T} \cdot \mathbf{H} \cdot \mathbf{T}^{-1}\right)_{ij} = H^{(i)}\delta_{ij}$$

where T is the unitary matrix of the appropriate coordinate transformation and $H^{(i)}$ are the Hessian matrix eigenvalues (without the loss of generality, we can assume that they are ordered in the increase). Then the requirement of the minimum of L over $\Delta\mathbf{x}$ leads to the equation

$$h^2 = \sum_{i=1}^{p} \frac{\tilde{g}_i^2}{(\lambda - H^{(i)})^2} \tag{33}$$

where $\tilde{g}_i$ are the components of the gradient vector in the coordinate system of the diagonalized Hessian, $\tilde{\mathbf{g}} = \mathbf{T} \cdot \mathbf{g}$. As can easily be seen, for a fixed hypersphere radius h, this equation is equivalent to a polynomial of power p, which can have up to $2p$ extrema, λ_j, each specifying a unique direction $\Delta\mathbf{x}_j = \mathbf{T}^{-1} \cdot \Delta\tilde{\mathbf{x}}_j$, where $\Delta\tilde{\mathbf{x}}_j$ defines energy extremum position in the rotated coordinate system,

$$(\Delta\tilde{x}_j)_i = \frac{\tilde{g}_i}{\lambda_j - H^{(i)}} \tag{34}$$

When λ is specified, the corresponding energy increases can be found from the relation

$$U(\lambda) - U(\mathbf{x}_0) = \frac{1}{2}\sum_{i=1}^{p} \frac{\tilde{g}_i^2(2\lambda - H^{(i)})}{(\lambda - H^{(i)})^2} \tag{35}$$

In the discussion above, the free parameter was the length step h, so that for any eigenvalue λ_j, Eqs. (34) and (35) are implicit functions of h. The locus of the eigenvectors predicted by (34) for an example two-dimensional system is shown in Fig. 3a. As can be seen, there are three branches of the locus curve, two of them (curves 1 and 3) start from the observation point and tend with the increase of h either to the valley bottom (when going downhill) or up the valley wall. Only when the trial circle radius exceeds some critical value $h^{(1)}$, intersection of the trial circle with the locus curve branch on the opposite side of the valley becomes possible. For $h > h^{(1)}$ there are two possible eigenvectors, both of which are directed uphill. However, only one of them tends to the valley bottom as the circle radius increases.

For a more quantitative analysis of the energy behavior in the vicinity of the observation point, it was proposed in [21] to treat λ as a free parameter. Then, Eq. (33) also becomes a parametric dependence and the number of possible eigenvalues for a certain length step h

(i.e., the number of energy extrema on the hypersphere in a p-dimensional space of the system degrees of freedom) is determined by the number of intersections of the function $\Delta^2(\lambda)$, which is equal to the right-hand side of Eq. (33), with the line $\Delta^2 = h^2$. The behavior of $\Delta^2(\lambda)$ is shown in Fig. 4a for the simplest case of a system with two degrees of freedom and in Fig. 4b for a more general case, which demonstrates that in a system with p degrees of freedom there are $p - 1$ parabola-like sections, each section being confined between two neighboring eigenvalues of the Hessian. The λ values, corresponding to the minima of individual parabolic sections, are denoted as $\lambda^{(k)}$, where $k = 1, \ldots, p - 1$.

It is seen in Figs. 4a and 4b that, as far as x_0 is a point where no components of the gradient vector $\tilde{g}$ vanish (i.e., it is not a stationary point and does not lie on a special line, such as a valley bottom), sufficiently small step lengths h provide only two energy extremum points on the hypersphere, which are determined by the intersection of the line $\Delta^2 = h^2$ with the branches at $\lambda < H^{(1)}$ and $\lambda > H^{(p)}$. These branches correspond to the pair of locus curve branches starting from the observation point, as shown in Fig. 3. Only when some minimum value of h is achieved, there appear additional minima and maxima on the trial hypersphere, which can be used for tracing energy valleys.

The selection of the eigenvalue λ_j and the corresponding eigenmode $\Delta\mathbf{x}_j$ determining the direction of the next algorithm step depends on the shape of the energy surface. In what follows, we are interested in two situations, when the observation point is close either to the minimum of the energy surface (i.e., all Hessian matrix eigenvalues are positive) or to the valley bottom (i.e., $H^{(1)} < 0$, while all other Hessian eigenvalues are positive). The qualitative behavior of the system energy as a function of λ is shown in Figs. 4c and 4d.

If the observation point is located in the region of a minimum (Fig. 4c) and one is interested in locating this minimum, the choice of $\lambda = 0$ gives, evidently, the lowest energy that can be achieved in one step. The expression for the optimal step is then $\Delta\mathbf{x} = -\boldsymbol{H}^{-1} \cdot \mathbf{g}$, which is recognized as the Newton-Raphson step. However, when going uphill, the selection of appropriate λ is not so evident.

In the original algorithm of Cerjan and Miller, the jump length and orientation are determined by selecting $\lambda = \lambda^{(1)}$. This is, however, not the optimum choice, as the corresponding eigenvector can lead quite far from the valley bottom (see Fig. 3a). As follows from the

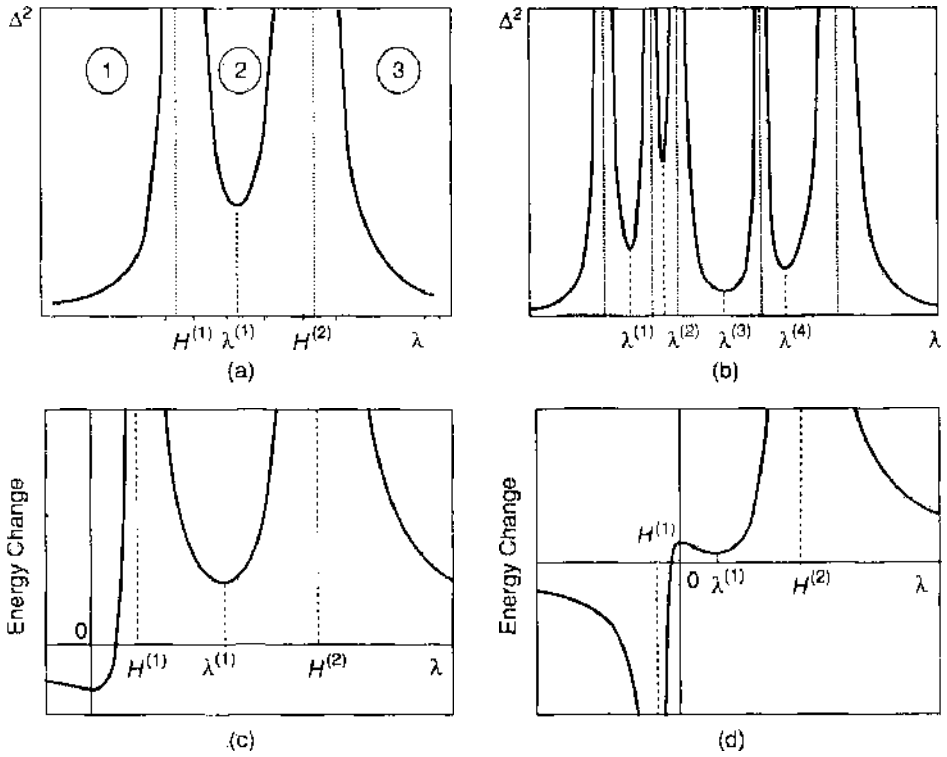

Figure 4. Function $\Delta^2(\lambda)$ for (a) 2 and (b) 5 degrees of freedom and for two kinds of potential energy behavior: (c) near a minimum of potential energy surface and (d) near a first-order saddle point.

same figure, a better result can be achieved if λ tends from above to the Hessian eigenvalue $H^{(1)}$, which not only increases the step length but also improves the accuracy of the valley bottom following as well. The smallest among the Hessian eigenmodes is selected, because it is assumed that following the direction of the smallest energy surface curvature, one comes to the lowest-energy saddle point. However, the latter assumption is not necessarily correct, and one can never exclude a possibility that a saddle point that will be reached if one selects λ close to (more exactly, slightly exceeding) another Hessian eigenvalue will be lower in energy than that reached by following the smallest Hessian eigenvalue.

When looking for a saddle point on the energy surface, one usually starts from some minimum of the potential energy. However, closer to the saddle point, one inevitably reaches the region where one of the Hessian eigenvalues is negative, while the eigenvalue $\lambda^{(1)}$ can be either positive (as in Fig. 4d) or negative. In both cases, however, there are two extrema of the energy in the range of λ between $H^{(1)}$ and $H^{(2)}$, because the first energy derivative must vanish also at $\lambda = 0$ [21]. When $\lambda^{(1)} > 0$ (i.e., the observation point is near an energy valley bottom), in moving from $\lambda^{(1)}$ to $H^{(1)}$ one passes through the energy maximum at $\lambda = 0$, which is, evidently, the best selection for the step. Indeed, in the case of purely quadratic energy surface, this step will lead exactly to the saddle point. In the opposite case of $\lambda^{(1)} < 0$, discussed in detail by Cerjan and Miller [21], the same selection of $\lambda = 0$ provides the best step direction. Indeed, in this case the observation point is close to a crest on the energy surface, rather than to the valley bottom; that is, it lies above the saddle point. Hence, one must minimize the energy during the step in order to reach saddle point, and the minimum is reached at zero λ.

A drawback of the original Cerjan and Miller scheme of λ selection [21] is that it does not care about finding and following any particular energy valleys. As a result, the algorithm leads uphill from the initial energy minimum along quite arbitrary trajectory, and only when the observation point reaches a region where the energy exceeds that of the nearest saddle point, the system is driven to this saddle point by an artificial Newton-Raphson minimization. Hence, regardless of the fact that this selection scheme does finally lead to a saddle point, it is completely useless for the case of diffusion path search, because one can never say to which minimum energy path the saddle point thus obtained corresponds and whether a different choice of the initial step will not lead to a different saddle point. Later on, a number of alternative possibilities for eigenvalue selection has been discussed (see, e.g., [32, 33] and references therein), but these are not very useful for diffusion description either, dealing mainly with small atomic ensembles typical for chemical applications. In fact, the standard ideology of diffusion path search implies tracing the bottom of one and the same energy valley until a saddle point is reached, and thus at the first step of the procedure it makes sense to scan the real energy surface around the starting position corresponding to an energy minimum, in order to find the valleys leading from it and only then apply eigenvector following algorithm, tracing each valley separately.

Despite the reliable ideological basis of the eigenvector following method, the necessity of calculation and inversion of the Hessian matrix at each point along the search trajectory restricts this algorithm to atomic systems with rather small number of degrees of freedom, like those discussed, for example, in [21]. An attempt to overcome this restriction involved the introduction of hybrid eigenvector-following/conjugate-gradients approach [34], which used iterative methods to find the smallest eigenvalue and the corresponding eigenvector, which is then followed uphill. Thus, the direct diagonalization of the Hessian matrix was avoided. The search for a minimum at each point of the path was performed using conjugate gradients method. The method worked well in the framework of tight-binding approach to the investigation of interstitial jumps in a 216 atomic Si crystal confined within a periodic boundary cell. However, it is not clear if this method can be applied for tracing the transition path using quantum mechanical energy calculations.

2.1.2.2.b. Drag (Reaction Coordinate) Method Due to the fact that second-order derivative techniques are extremely time and computer-memory consuming, much attention in the literature is paid to methods that implement the principles of the first-order derivative algorithms. The simplest of these methods is the "drag" or "reaction coordinate" method [28].

In quite general terms, the reaction coordinate method is applied to many-atomic systems that have many degrees of freedom and can transform from one state to another by continuous variation of atomic parameters (e.g., atom positions) associated with these degrees of freedom. The reaction coordinate is one specific path in the multidimensional space of atomic parameters, connecting the initial and the final configurations. This path can be selected as a linear interpolation or based on a series of potential energy calculations on a grid of points located along the expected trajectory and approximately tracing the energy surface valley. In order to follow the transition, the drag coordinate is introduced as the coordinate along the preselected path. The transition is then performed along the path stepwise from the initial to the final value. At each step, the drag coordinate is fixed and the total energy is minimized by relaxation of the remaining degrees of freedom. After the system is dragged along the whole path, the saddle point can be found by inspection or, if more accuracy is needed, by using mathematical techniques to interpolate between the grid points.

In molecular statics modeling of diffusion jumps of individual atoms, this scheme is largely simplified by the fact that the atoms around the jumping atom are allowed to adjust their positions to instantaneous position of the jumping atom, and thus the drag path is simply a line in a 3D space of positions of the jumping atom. As a general rule, the path starts from an equilibrium position of the jumping atom. Typically, it ends in the expected final position of the atom, but this is not mandatory. The diffusing particle is dragged along the path stepwise from the initial position to the position corresponding to the final value of reaction coordinate, which must not, strictly speaking, be the expected final position. At each step, the drag coordinate is fixed and the total energy is minimized, assuming that each atom in a model crystal has three degrees of freedom, except for the jumping atom. In simplest cases, when there is a high confidence that the drag path comes through the saddle point (e.g., when saddle point is located from symmetry considerations), the jumping atom can be fixed on the path during the relaxation. However, usually this atom is also allowed to move, but only in the directions that are normal to the drag coordinate. As a result of the energy minimization, all atoms shift from their earlier positions into the new ones, so that after each step the ensemble of atoms changes its configuration. The tracer atom also can deviate from the drag path if its relaxation normal to the drag path is allowed. After the relaxation is over, the jumping atom is shifted in the direction of the drag coordinate and a new relaxation is performed. This cycle is repeated until the final position is reached. The saddle point position and energy can then be extracted from the dependence of the energy of the atomic ensemble on the drag coordinate. In order to obtain good estimates of saddle point position, the shifts along the drag coordinate should not be too big, because with the increase of the shift length there increases a chance that relaxation of the crystal atoms will lead to a spurious energy minimum, as discussed in the beginning of this section. On the other hand, too small shifts increase the number of calculations without improving the quality of intermediate configurations. The reasonable trade-off is typically reached at the number of steps along the drag coordinate of the order 100.

The advantage of the drag method is that in moving along a transition path, the jumping atom is not forced to follow a prescribed trajectory. The trajectory selection by this algorithm fully takes into account the dynamic accommodation of the jumping atom environment during the transition. This method works well in many cases, but in some instances it may give ambiguous results. For example, one can meet situations when there exist more than one equivalent, or nearly equivalent transition paths, as it happens, for example, for vacancy jump in bcc iron, see Fig. 5. In these situations, several trajectories are possible, and in order to get a clear understanding of the transition pattern, the scan of the energy potential surface in the vicinity of the saddle point might be necessary. The main shortcoming of the drag method is the necessity to use minimization schemes at each tracer atom step. As a result, calculation of even one diffusion event is very time consuming, which practically precludes its use when the atomic relaxation is done using quantum mechanical methods for the description of interatomic interactions.

2.1.2.2.c. Chain-of-States Methods In order to reduce considerably the amount and especially the time of calculations, another class of methods has been proposed, which directly

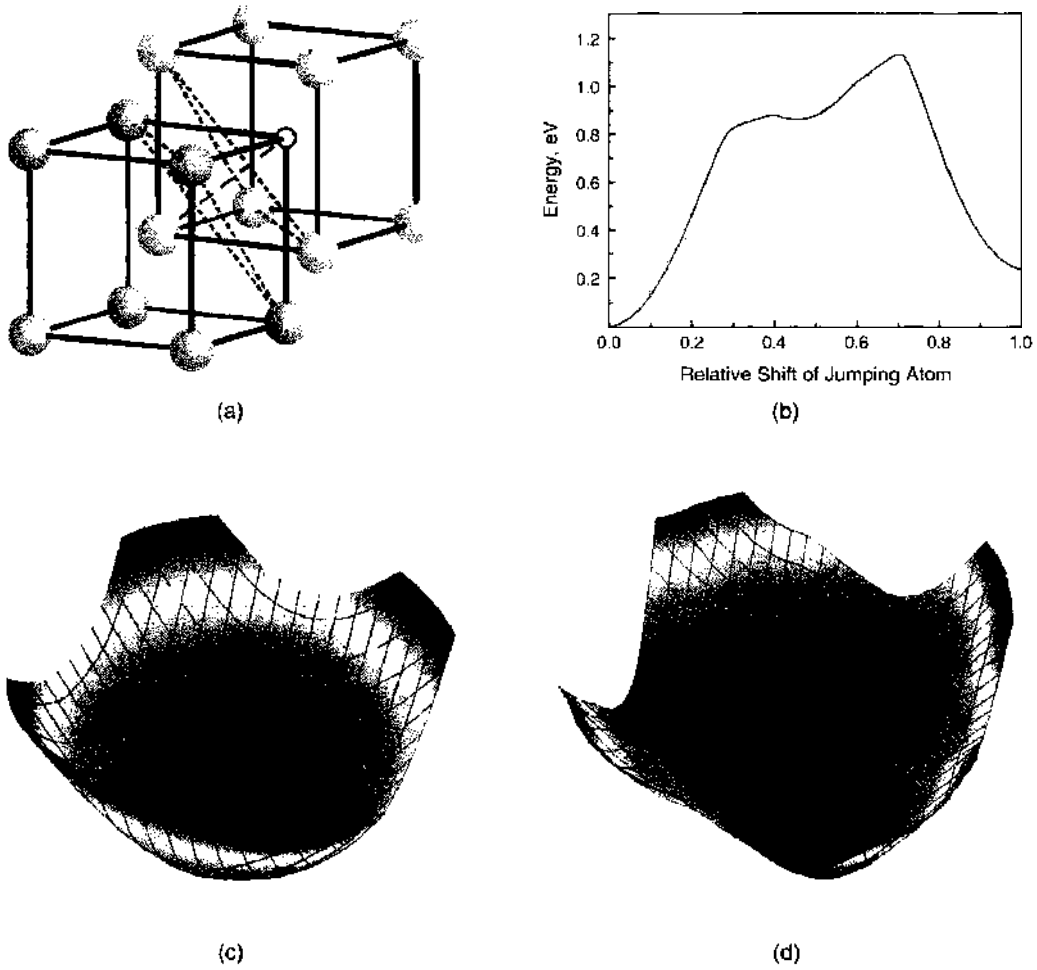

Figure 5. Vacancy jump in bcc crystal. (a) The jump geometry. (b) A typical energy variation for an atom dragged along the jump trajectory. The heights of two maxima are the same for monatomic crystal, but in a more general case (e.g., in ordered binary alloy of B2 type) may be different, as shown in the figure. (c) Potential energy surface in the (111) plane that is normal to the vacancy jump direction and crosses the jump trajectory at the distance 0.1 h from the initial position of the jumping atom (h is the jump length). (d) The same for the (111) plane crossing the jump trajectory at the distance 0.25 h, that is, near the saddle point of the jump. It is clearly seen that there are three equivalent positions of the lowest energy, which means that there are three possible jump paths and three possible saddle point positions. Calculations for figures (c) and (d) were done using Johnson's potential for iron [71].

employs information not only about the initial and final jump positions, but about the initial and final atomic configurations of simulation crystal as well. In this approach, a "guess" trajectory of the jumping atom between the initial and the final position is selected and split by several grid points, usually positioned at the same distance L between neighboring points. Then, a set of images (or replicas, or "states") of the simulation crystal is generated. In the first replica, the jumping atom is positioned in the initial jump position, in the second one in the first grid point, and so on, until the final jump position is occupied in the last crystal replica. The first and the last replica remain fixed, while the intermediate images in the ordered chain are optimized simultaneously in a concerted way. At each iteration step, the complete relaxation of each intermediate image is done under a constraint that the jumping particles interact not only with the crystal atoms, but also with two fictitious atoms, located in the positions of jumping atom in the next and the previous image in the chain. The interaction potential is usually the simple harmonic one, as if the jumping and the fictitious atoms were connected by elastic springs. So, in the chain-of-states methods, one minimizes the "object function"

$$S(\mathbf{R}_1, \ldots, \mathbf{R}_{p-1}) = \sum_{i=1}^{p} U(\mathbf{R}_i) + \sum_{i=1}^{p} \frac{Pk}{2} (|\mathbf{R}i - \mathbf{R}_{i-1}| - L)^2 \tag{36}$$

where P is the number of images, U is the image energy, k is the spring constant, and $\mathbf{R}_i$, $\mathbf{R}_{i-1}$ define the neighboring image positions along the path. One of the first implementations of this approach to finding the minimum energy path was called "plane elastic band" method. Initially, the springs of a zero natural length L were used, but this kind of object function failed in many situations and, later on, the expression for the object function was modified to take into account nonzero natural length between images, which was introduced as an average separation of images along the optimal path. However, this modification can result in an aggregation of images and, sometimes, in the path self-crossing near the minimum positions. This can be remedied by including an additional repulsive term to keep images apart. However, as shown by simulations, this algorithm does not lead to the convergence to the minimum energy path and to real saddle-point configuration.

In attempt to find more appropriate algorithm, the local update plane (LUP) algorithm has been proposed, where the energy minimization of each image i takes place only within the plane with the normal n_i aligned along the local tangent to the path, which is defined as the line segment connecting the next and previous images in the chain:

$$\mathbf{n}_i = \frac{\mathbf{R}_{i+1} - \mathbf{R}_{i-1}}{|\mathbf{R}_{i+1} - \mathbf{R}_{i-1}|}$$

The local tangents are updated after several iterations. However, images in this method are not connected, which can make the image distribution along the path quite chaotic. Moreover, in order to get an appropriate result by this technique, one needs a good initial guess for the path. Otherwise, if there are several possible paths connecting the initial and final positions, the algorithm can lead to a complete mess, mixing points from the different paths.

The most advanced version of the chain methods with the fixed initial and final states of a transition has been proposed by Jonsson et al. [29, 35] and is widely known as nudged elastic band (NEB). This method incorporates the features of both the "elastic band" method and LUP method. The first one ensures continuity of the transition path by adding spring interaction between adjacent images, thus mimicking an elastic band. The second method contributes a better convergence of the minimum energy path and saddle point. The elastic band is brought to the transition path by sequential optimization, involving the minimization of the force acting on the images in the chain and defined as:

$$\mathbf{F}_i = -\nabla U(\mathbf{R}_i) + \mathbf{F}_i^s$$

where the spring force $\mathbf{F}_i^s$ is

$$\mathbf{F}_i^s = k_{i+1}(\mathbf{R}_{i+1} - \mathbf{R}_i) - k_i(\mathbf{R}_i - \mathbf{R}_{i-1})$$

The main feature that distinguishes NEB from the other techniques of the same group is the use of force projections, referred to as "nudging." This means that at the iteration step of the energy minimization, the true force and the spring force are decomposed into components parallel and perpendicular to the path, and the relaxation uses only the true force component perpendicular to the path and only the spring force component along the path. In this way, the spring forces do not interfere with the convergence of the elastic band to the minimum energy path, while the true force does not affect the distribution of images along the path. In the NEB method, there is no competition between the true forces and the spring forces. The strength of the spring forces can be varied by several orders of magnitude without affecting the equilibrium position of the band.

In contrast to methods based on a sequential "drag" along the potential energy surface, the simultaneous optimization of several crystal images can be done by parallel computation or simply on a cluster of networked computers (see [29] and references therein), which makes NEB especially appropriate for time- and memory-consuming approaches, such as *ab initio*. Sometimes, it is possible to combine NEB with other methods. For example, a combination of dimer/NEB methods was applied for the investigation of adatom dimer formation on a crystal surface [35].

However, as shown by calculations, NEB methods should be treated with certain care in order to provide the good elastic band convergence to the minimum energy path. In particular, the number of the intermediate images requires optimization, because when too many images are used, kinks can form on the elastic band. As the minimization algorithm is applied, the kinks can continue to oscillate back and forth, preventing the band from converging to the path. It should also be taken in mind that the elastic band tends to be pulled off the energy minimum path when the path is curved. If the path is curved in the saddle point, this can lead to an overestimate of the saddle point energy. This problem was, in particular, observed in calculations of the exchange diffusion process in a Si crystal [35].

Finally, one should pay attention to the optimization of the initial trajectory of the jumping atom in the crystal images. A bad initial guess for the trajectory can result in completely unphysical final configuration of the system. An example of such situation is shown in Fig 6, which demonstrates the results of simulation of a divacancy formation in Si using NEB method implemented in Vienna *ab initio* Simulation Package (VASP) [36]. An initial guess trajectory in the form of a straight line connecting the initial and final positions of a vacancy jump resulted in too small distance between the initial position of the jumping atom in the central images and one of the lattice site atoms, which caused very strong repulsion between these atoms. Already after the first relaxation step, this strong repulsion shifted the central part of the image chain unreasonably far from the true jump trajectory. Positions of the intervening atom in the central image are also far from its original lattice site. Evidently, regardless of the fact that the resulting image chain was stable against further relaxation, predictions of this simulation attempt have no practical value. This kind of a problem is specific to NEB; it does not appear, for instance, in step-by-step methods.

To avoid the problem of the incorrect initial guess, hybrid techniques can be applied. An initial trajectory curve can be adjusted by such methods as activation–relaxation technique (ART) [37], or repulsive bias potential method (RPB) [38]. These methods are based on the

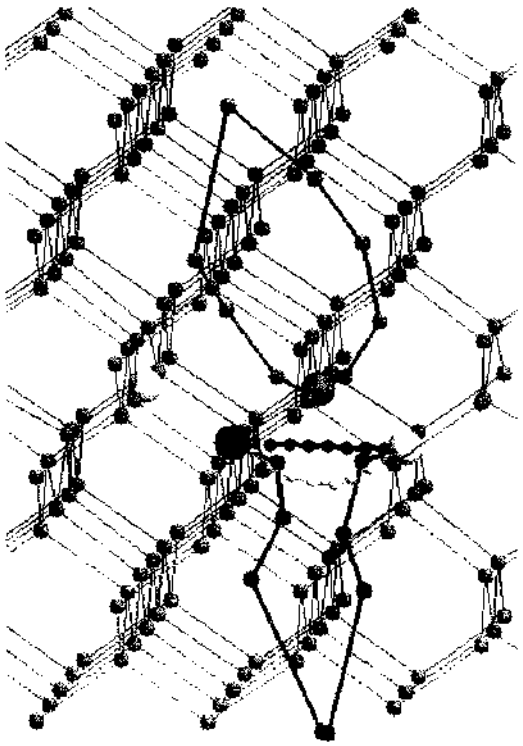

Figure 6. "Jump trajectories" obtained using NEB method for a diffusion jump in direction ⟨110⟩ leading to divacancy formation in Si. Initial locations of two vacancies and the jumping atom are shown by bigger white and cyan spheres, respectively. The initial guess for the jumping atom locations in the images is along straight line (as indicated by small spheres along yellow trajectory). The strong repulsive interaction of central images of the jumping atom with a close neighbor atom (marked by bigger red sphere) results in completely unreasonable displacements of both the jumping atom (cyan trajectory) and the close neighbor atom (red trajectory). The correct image chain is shown in white.

principle of activation of the current state, followed by relaxation to a new minimum. For example, in RPB method, the activation of the state is performed by application of a short-range repulsive potential at the initial position of a jumping atom, which makes the initial atom state unstable, while the subsequent relaxation pushes this atom to a nearby minimum configuration. The use of a local bias potential has also been suggested for dynamic simulation of the rare events that has got the name of accelerated molecular dynamics [39, 40]. However in the RPB method, the potential is fixed and exceeds the saddle point energy, which does not allow one to use this method for dynamical calculations nor to yield the exact transition path in the original potential energy surface.

2.1.3. Dynamical Approaches

The main feature of the absolute rate theory approach is the assumption that the rates of diffusion jumps can be expressed completely in terms of the free energy of only one particle that performs diffusional transition, while all the surrounding atoms are treated as a thermostat. It seems more reasonable to assume, however, that diffusion jumps involve collective behavior of the jumping atom and the remaining atoms in the crystal, especially the atoms in the close vicinity of the jumping one. In order to describe the collective behavior of atoms in the lattice, a more rigorous, many-body approach was proposed by Vineyard [41] in the late 1950s. This approach starts essentially from the same idea as that used earlier by Zener, that a big crystal can be considered as a statistical ensemble of vibrating atoms and the relative probability of that or other particular configuration can be described using some equilibrium distribution function over different configurations. Correspondingly, the jump rate is proportional to the ratio of this distribution function values for the transition and the equilibrium states. However, in contrast to Zener, who considered the distribution over the states of the jumping particle only, Vineyard applies equilibrium statistics to all atoms in the crystal. Because all calculations are performed in the complete phase space, the many-body character of the problem is introduced from the very beginning. In Vineyard's model, atoms are considered as quantum oscillators with completely independent degrees of freedom, each degree of freedom having, generally, its own basic vibration frequency. In the equilibrium state, each atom has 3 degrees of freedom, so that $3N$ different basic frequencies ν_i can be considered (where N is the number of atoms in the crystal). On the contrary, transition state is considered as the state where the vibrational degree of freedom of the jumping atom in the direction of the jump is frozen, so that only $3N - 1$ vibrational degrees of freedom with basic frequencies ν_i^* are present. The resulting jump rate for sufficiently high temperatures ($k_B T \gg h\nu_i$, where h is the Planck's constant) can be written down as

$$\Gamma = \frac{\prod_{i=1}^{3N} \nu_i}{\prod_{i=1}^{3N-1} \nu_i^*} \exp\left(\frac{-E_m}{k_B T}\right) \tag{37}$$

where E_m is the jump activation energy.

The advantage of Vineyard's approach is that it does not demand that the jump proceeds slowly. In contrast to the absolute rate theory, the transition state is not the top of the free-energy barrier, but a special configuration of the crystal atoms, for which the jump frequency is accompanied with the least increase in the crystal potential energy above the static potential; the activation energy being just this potential energy increase. In other words, it was predicted that migration parameters are associated with the crystal constrained in the transition configuration, although the configuration must be very short-lived, and it is *a priori* unclear how this configuration looks like.

Later on, Rice [42, 43] introduced a "dynamical theory" of diffusion, which emphasized the microscopic character of the jump process. Here, Γ is developed by going over to normal vibrations of all atoms and presenting the atomic dislocations from the lattice equilibrium positions as the sums of contributions from individual vibration modes. As a result, it becomes possible to make thermodynamic averaging not over atoms but over the vibration mode spectrum. Possibly, the most important qualitative achievement of the dynamical theory, as introduced by Rice, is the criterion of diffusion jump: a migrating atom makes a diffusion jump, provided it shifts in the jump direction sufficiently far from the rest position,

while the surrounding atoms move aside from the jump trajectory, making a "hole" through which the migrating atom jumps.

The dynamical approach allows one to estimate the rate of diffusion jumps completely based on the selected normal vibration statistics and places no time restrictions during the jump. In fact, the transition is instantaneous, as, after the critical shifts of the migrating atom and its surrounding atoms are achieved, their subsequent fate is assumed predetermined. However, the mathematical treatment by Rice involves serious simplifications, and the resulting expressions contain too many fitting parameters. A detailed discussion of the merits and difficulties of the dynamical approaches by Rice and Vineyard can be found in the paper of Glyde [44].

One of the most serious simplifications of the Rice's theory is that two basic events constituting the diffusion jump (achievement of sufficiently big amplitude of the migrating atom and the formation of sufficiently big "hole") are treated as being completely statistically independent. A tentative justification of this treatment was that the displacements of surrounding atoms in the critical configuration are much less than that of the migrating atom, and thus the "hole" appears much more often than the migrating atom uses it. This justification is not convincing, however, because in the critical configuration, the jumping atom interacts with atoms in its immediate vicinity at the very strong repulsive part of interatomic potential, which enables quite high (sometimes up to ten percent of interatomic distance) shifts of atoms surrounding the moving one. Such shifts cannot be achieved simply by thermal vibrations of these atoms, and it becomes necessary to consider the collective behavior of the whole "activated complex," consisting of the jumping atom and its nearest neighbors in the critical configuration. A step in this direction was done by Flynn [45], who demanded that the diffusion jump occurs, when some critical value is reached not by the displacement of an individual atom, but by the so-called "reaction coordinate," which is expressed in terms of coordinates of all atoms in the activated complex:

$$x = \left(\mathbf{R}_m - \frac{1}{n} \sum_{k=1}^{n} \mathbf{R}_k \right) \mathbf{e}$$

where $\mathbf{R}_m$ is the radius-vector of the jumping atoms, summation is over the radius-vectors of n its neighbors belonging to the activated complex, and $\mathbf{e}$ is the unit vector in the direction of the jump. Expressing fluctuations of reaction coordinate in terms of the phonon structure, it is possible to obtain the jump frequency in terms of the vibration frequencies, amplitudes of individual phonon modes, and the critical value of the reaction coordinate, the latter being the fitting parameter of the theory. Particular calculations for vacancy diffusion in fcc metal lattices [45], made using the Debye phonon spectrum of defect-free lattice, give the jump rate in the form.

$$\Gamma = \gamma_1 \nu_D \exp\left(-\gamma_2 \frac{\mu \Omega}{k_B T} \delta^2 \right) \tag{38}$$

where γ_1, γ_2 are constants of the order of unity, but depending on the crystal lattice symmetry, μ is the shear modulus of material and δ is the fraction of interatomic distance corresponding to the critical shift of the migrating atom.

As can be seen, the "energy barrier" $\mu\Omega\delta^2$ arises due to the work of the activated complex against the elastic forces. Quite nice correlation of this energy barrier with experimental values of migration energy in fcc metals indicates that dynamical approach reflects the picture of individual jumps much better, at least qualitatively, than the rate-theory method.

Later on, a number of improvements of dynamical approaches have been proposed. For example, while the above mentioned approaches treated atomic vibrations in the purely harmonic approximation, Toller et al. [46] derived more general expression for the jump rate, which is valid under appropriate conditions for crystals containing arbitrary but smooth anharmonicities. Their results reduce to those of earlier formulations, when the potential energy surface in the saddle point is planar, and to Vineyard's form, in particular, when the potentials are treated using harmonic approximations. In addition, however, the approach

incorporates the short-term memory of the dynamical system and can deal with anharmonicities, which cause the saddle surface to become curved.

However, in order to estimate accurately the rates of diffusion jumps in the framework of dynamical approach, one has to know exact dynamics of atomic ensembles, which are not analytically tractable for complex systems. In these cases, the dynamic behavior of crystals having any given masses and interatomic forces should be treated by numerical methods, such as molecular dynamics.

2.1.4. Molecular Dynamics

The molecular dynamics (MD) method is a computer simulation technique where the time evolution of a set of interacting atoms is followed by integrating their equations of motion, which are constructed in accordance with the laws of classical mechanics. Writing the second Newton's law for an arbitrary atom i in a simulated atomic array constituted by N atoms as

$$\frac{d^2\mathbf{R}_i}{dt^2} = \frac{\mathbf{F}_i}{m_i} \tag{39}$$

one sees that the spatial positions $\mathbf{R}_i$ of all the atoms can be determined at any moment of time, provided one knows the atom masses m_i, the forces $\mathbf{F}_i$ acting on each atom due to its interactions with other atoms, and the set of initial atomic positions and velocities.

Formally, molecular dynamics is a deterministic technique: when initial atomic positions and velocities are specified, the subsequent time evolution is *in principle* completely determined. The computer calculates a trajectory in a $6N$-dimensional phase space ($3N$ positions and $3N$ momenta). However, such trajectory is usually not considered to be particularly interesting by itself. Rather, molecular dynamics is employed as a statistical mechanics method, which is justified for ergodic systems, where the time average of a certain physical value coincides with the average over a set of configurations distributed according to some statistical distribution function, or a statistical ensemble. A trajectory obtained by molecular dynamics provides such a set of configurations. Therefore, a physical quantity is simply calculated as an arithmetic average of the instantaneous values acquired by it during the MD run.

MD simulations can be used to measure thermodynamic properties of a simulated material, using statistical physics as the link between the microscopic behavior and thermodynamics. In the limit of very long simulation times, one can expect the phase space to be fully sampled, and in that limit, statistical averaging process would yield the thermodynamic properties. In practice, the runs are always of finite length, and one should exert caution to estimate when the sampling has reached equilibrium.

Molecular dynamics is a very powerful technique but has limitations that one should be aware of when interpreting the obtained results. First of all, like no other technique, MD is sensitive to the choice of atomic interaction potentials. In molecular dynamics, atoms move under the action of instantaneous forces resulting from atom interactions with one another. As described earlier, these forces are usually obtained as the gradients of a "potential energy function" that depends on the positions of the atoms. As the atoms move, their relative positions change and forces change as well. A simulation reproduces the behavior of the system realistically, if interatomic forces are similar to those with which real atoms would interact when arranged in the same configuration. For this reason, great efforts are devoted to the development of appropriate interaction potentials for different atomic systems. Practically always, these potentials are "classical," as calculation of interatomic forces from the "first principles" in the framework of MD (as proposed, e.g., in [47]) requires prohibitively huge computation resources.

Second, typical MD simulations can be performed on systems containing thousands or, perhaps, millions of atoms, and for simulation times ranging from a few picoseconds to hundreds of nanoseconds. While these numbers are certainly respectable, time and/or size limitations are important for applications related to the study of diffusion in solids.

When speaking about time limitations, as applied to diffusion studies, both the "internal" time of the problem and the CPU time are important. A simulation is reliable from the

point of view of its duration when the "internal" time of simulation run (that is, the value of parameter t by the end of the run) is much longer than the relaxation time of the quantities we are interested in. Individual diffusion jumps are rare events, and the simulation times t in nanosecond range allow typically only several jumps of each migrating atom. On the other hand, in order to follow smoothly the atomic trajectories and keep the crystal temperature close to the average value, the duration of one "internal" time step is normally of the order few femtoseconds (10^{-15} s), so that a typical MD run requires 10^6–10^7 iterations, which means a lot of CPU time for sufficiently large simulation crystals. As a result, the determination of diffusion coefficients (as well as migration energies, defined from the temperature dependence of diffusion coefficients) by molecular dynamics requires additional tricks allowing to construct sufficiently long jump trajectories [48].

A limited system size can also constitute a problem, when correlation length for an investigated physical property is comparable with the computation cell size. A method to overcome this problem is known as "finite size scaling" and consists of computing a physical property A using several boxes with different sizes L, and then fitting the results on a relation

$$A(L) = A_0 + \frac{A_1}{L^n}$$

using A_0, A_1, and n as fitting parameters. Then A_0, corresponding to the limit of $A(L)$ at system size tending to infinity, can be taken as an estimate for the "true" physical quantity.

In diffusion modeling, the limited size of atomic ensemble is an important factor. Even 10^6 atoms in the simulation cell constitute quite small part of a real crystal, and so appropriate boundary conditions are necessary in order to mimic the interaction of atoms close to the cell surface with the rest of material. Periodic boundary conditions are often used in MD simulations of the diffusion in the bulk of material. The use of periodic boundary conditions precludes the use of small simulation crystals, where the elastic interaction of diffusing particle with the atoms outside the computation cell is important. Additionally, the use of periodic boundary conditions can lead to fictitious localization of diffusing particles near the periodic boundaries due to the accumulation of computer inaccuracy. As demonstrated in [48], the frequency of diffusion jumps can depend on the distance of the jumping particle from the simulation crystal boundary, which is a purely computational artifact related to the necessity of atomic translation in order to include interaction with atoms outside the periodic boundaries.

The typical sequence of steps for the MD simulation of thermally activated diffusion includes:

- Creation of the model crystal and creation of a diffusing particle in it;
- Relaxation of the obtained system by a static or quasidynamic technique, using the assumed interatomic potentials;
- Heating of the simulation crystal by assigning to the atoms randomly distributed velocities with the only limitation that the total kinetic energy would correspond to the desired temperature;
- Integration of the equations of motion.

Time integration algorithms are usually based on "finite difference methods," where time is discretized on a finite grid, the "time step" Δt being the distance between consecutive points on the grid. Knowing the atomic positions and velocities at time t, the integration scheme gives these quantities at a later time $t + \Delta t$. By iterating the procedure, the time evolution of the system can be followed for long times.

When selecting the integration algorithm, it is important to remember that each iteration step involves computation error, and thus the algorithm should guarantee that tens of millions of iteration steps do not lead to the significant loss of accuracy. Usually, there are two basic sources of computation errors. The first of them is related to the accuracy with which the finite difference method approximates the true solution. Finite difference methods are usually based on a Taylor expansion truncated at some term. These errors are intrinsic to the algorithm and do not depend on the implementation. The accuracy of approximation is usually achieved by the selection of appropriately small integration step Δt. For instance,

the Verlet algorithm has this type of errors proportional to Δt^4 for each integration time step. Another error source can be related to a particular implementation of the algorithm (i.e., to the finite number of digits used in computer arithmetics). Round-off errors decrease with the decrease of Δt slower than the approximation errors and dominate in the small Δt limit. Using the highest possible precision helps to keep round-off errors at a minimum.

The two most popular integration methods for MD calculations are the Verlet algorithm and predictor-corrector algorithm. Here they are described only briefly; for detailed information about these algorithms, the reader is referred to [49–51].

The basic idea of Verlet algorithm is to write two third-order Taylor expansions for the atomic positions $\mathbf{R}_i(t)$, one forward and one backward in time:

$$\mathbf{R}_i(t+\Delta t) = \mathbf{R}_i(t) + \dot{\mathbf{R}}_i(t)\Delta t + \frac{1}{2}\ddot{\mathbf{R}}_i(t)\Delta t^2 + \frac{1}{6}\dddot{\mathbf{R}}_i(t)\Delta t^3 + O(\Delta t^4)$$

$$\mathbf{R}_i(t+\Delta t) = \mathbf{R}_i(t) - \dot{\mathbf{R}}_i(t)\Delta t + \frac{1}{2}\ddot{\mathbf{R}}_i(t)\Delta t^2 - \frac{1}{6}\dddot{\mathbf{R}}_i(t)\Delta t^3 + O(\Delta t^4)$$

where points over the value denote corresponding time derivatives. Adding the two expressions gives the basic form of Verlet algorithm,

$$\mathbf{R}_i(t+\Delta t) = 2\mathbf{R}_i(t) - \mathbf{R}_i(t-\Delta t) + \ddot{\mathbf{R}}_i(t)\Delta t^2 + O(\Delta t^4)$$

Because we are integrating Newton's equations, $\ddot{\mathbf{R}}_i(t)$ is just the force divided by the mass, and the force is in turn a function of positions $\mathbf{R}_i(t)$. The truncation error of the algorithm is of the order of Δt^4, even if the third derivatives do not appear explicitly. This algorithm is at the same time simple to implement, accurate and stable.

The velocities in this version of the Verlet algorithm are not directly generated, because they are not needed for the time evolution. However, they are required to compute the kinetic energy, whose evaluation is necessary to test the conservation of the total energy and to check the temperature stability during the computation run. One could compute the velocities from the positions by using

$$\dot{\mathbf{R}}_i(t) = \frac{\mathbf{R}_i(t+\Delta t) - \mathbf{R}_i(t-\Delta t)}{2\Delta t}$$

However, the error associated to this expression is of the order Δt^2 rather than Δt^4. Another problem of Verlet algorithm is that atomic positions are defined by two preceding time steps and thus cannot be used for the first integration step. Therefore, the first step should be done using some other method, for example, predictor–corrector algorithm.

Predictor–corrector algorithms are another commonly used class of methods to integrate the equations of motion. Those most frequently used in molecular dynamics include three parts for each time integration step: predictor, force evaluation, and corrector. At the predictor stage, one "predicts" the atomic positions and their time derivatives (up to a certain order q) at time $t + \Delta t$, from the same quantities known at time t, by means of a Taylor expansion. Among these quantities are, of course, the second derivatives (accelerations). The force evaluation part involves computing of the forces acting on atoms in the predicted positions, for instance, by taking the gradient of the interaction potential. The resulting accelerations, as defined by Newton's law, will be in general different from the "predicted accelerations." The difference between the two constitutes an "error signal." At the corrector stage, the obtained error signal is used to "correct" atomic positions and their derivatives.

In a molecular dynamics simulation, a system state is characterized by a set of global parameters, such as density, temperature, or pressure. In a standard calculation, the density is controlled by the choice of the simulation cell volume V, while pressure remains free to change. The time integration of Newton's equations guaranties the conservation of the total energy, but the temperature is free to fluctuate. In the statistical mechanics parlance, these simulations correspond to the "microcanonical" or NVE ensemble, because the fixed

quantities are the number of particles, the volume, and the energy. On the other hand, the pressure and the temperature are measured during the run.

There are several important alternatives to the NVE ensemble, where one integrates Newton's equations modified in such a way that sampling is performed in another statistical ensemble. One such ensemble is the isobaric–isoenthalpic (NPH) one considered in [52]. The particle coordinates are specified there relative to the simulation box and the volume V of the box is treated as a dynamical variable, while the conserved quantities are the external pressure P and the enthalpy $H = E + PV$. In another scheme, developed by Parrinello and Rahman [53], the shape of the box can vary as well as the volume. This scheme is especially promising for simulation of defect kinetics in crystals subject to external loads. One more ensemble is the canonical (NVT) one, as considered by Nosè [54] and Hoover [55]. They achieve the maintenance of the temperature with the help of a time-dependent friction driven by the difference between the instantaneous kinetic energy and its expected average of $3Nk_BT/2$.

Every time the state of the system changes, i.e., when the global parameters, such as pressure or temperature in NVE ensemble, are not stationary, but relax toward a new value it is necessary to wait for the system to reach thermal equilibrium before collecting data. The state change may be induced deliberately or occur spontaneously, for instance, when the system undergoes a phase transition. One of the most important transients is associated with the onset of MD simulation: the selection of initial velocities is normally completely random, and a certain time (of the order of several to few hundreds picoseconds, depending on the temperature) is necessary in order to achieve an equilibrium phonon distribution.

2.2. The Effects of Elastic Deformation on Microscopic Diffusion Parameters

2.2.1. Particle Energies in an Elastically Strained Material

The reasons why elastic stresses affect the diffusion can easily be understood looking at Fig. 7. First of all, the energies of a defect in equilibrium and saddle point position change as compared to the unloaded material, because the creation of a defect and relaxation of lattice atoms around it requires additional work against the strains. Second, nonhydrostatic loads usually decrease the symmetry of the lattice, and the saddle point energies become sensitive to the direction of the jump even for those jumps that had exactly the same saddle point energies in a more symmetric unloaded lattice.

In order to describe quantitatively the effect of stress on the particle migration energy, it is convenient to recall that the migration energy is the difference of the energies of particle formation in the saddle point, E_s, and in the equilibrium position, E_f, and to consider these energies separately, starting from the energy of the particle in the equilibrium position. Because the elastic strains, ε_{ij}, are normally much smaller than unity, one can formally present E_f as a Taylor series expansion in the powers of the elastic strain. Retaining terms up to the second order, we obtain [56]

$$E_f = E_f^0 - P_{ij}^e \varepsilon_{ij} - \frac{1}{2}\alpha_{ijkl}^e \varepsilon_{ij}\varepsilon_{kl} \tag{40}$$

where E^0f is the defect formation energy in the stress-free material, and P_{ij}^e and α_{ijkl}^e are tensors of, respectively, second and fourth order, which depend on the type of the defect and the surrounding matrix, but not on the elastic stress. In writing down equation Eq. (40) and further on we use Einstein summation rule (i.e., summation over repeated subscripts in the products of tensors is implied). The second-order tensor P_{ij}^e is usually referred to as the elastic dipole tensor, because its eigenvalues define the "strength" of three mutually orthogonal force pairs (dipoles) that, being applied in the defect position, produce the same elastic field as the point defect (a more detailed explanation is given below, in relation to Kanzaki forces). The fourth-order tensor α_{ijkl}^e describes the effects related to the defect polarization and is called, correspondingly, polarization tensor. Superscript e indicates that both tensors are related to a defect located in equilibrium position.

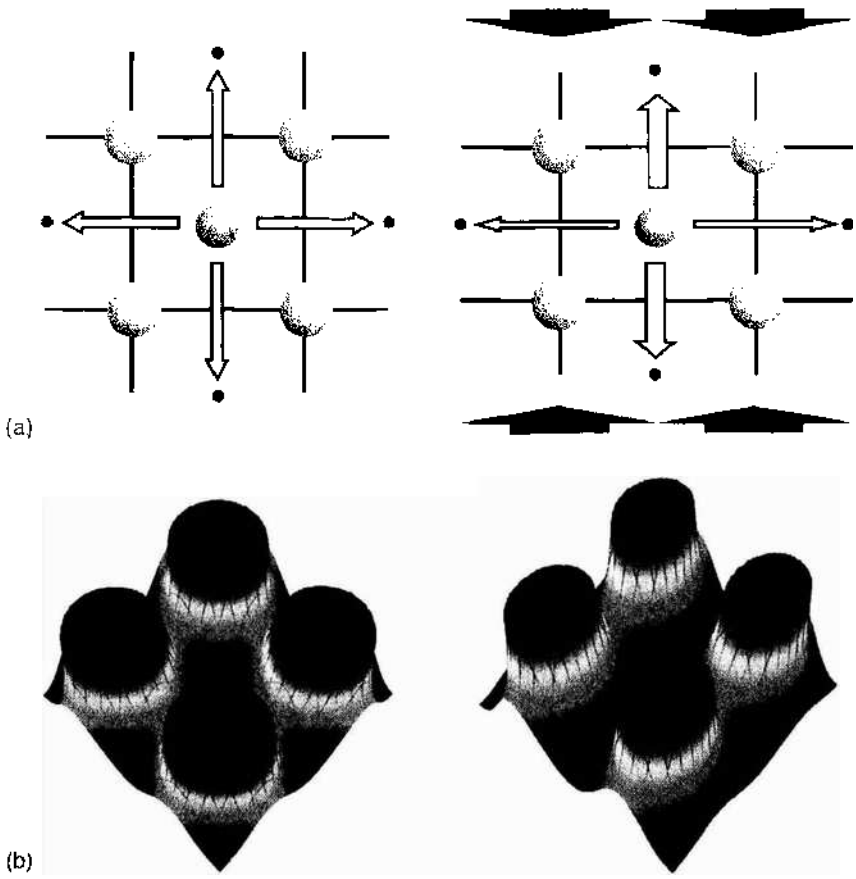

Figure 7. (a) Anisotropic distortion of crystalline lattice by external stresses and (b) corresponding modification of the potential energy surface for the jumping atom.

For point defects located in a saddle-point position, the elastic stress effect is exactly the same, but for one additional feature. As can be seen in Fig. 7, nonhydrostatic load changes the distances between atoms anisotropically, and thus the jumps that were completely equivalent in the stress-free lattice become dependent on the direction of the jump. Correspondingly, the energy of the defect in the saddle point, E_s, can be written down as

$$E_s(\mathbf{h}) = E_s^0 - P_{ij}^s(\mathbf{h})\varepsilon_{ij} - \frac{1}{2}\alpha_{ijkl}^s(\mathbf{h})\varepsilon_{ij}\varepsilon_{kl} \tag{41}$$

where E_s^0 is the energy of the defect formation in saddle-point in the stress-free lattice, and the dipole and polarization tensors in saddle point position depend on the jump direction, specified here by the vector $\mathbf{h}$, connecting the initial and final jump positions.

In writing down Eqs. (40) and (41), we made two implicit assumptions. The first one is related to the selection of the reference state, from which the energy is measured. In the stress-free material, this reference state is the energy of the ideal lattice, either without the defect (for interstitial defects) or with the defect replaced by the host lattice atom (for substitutional defects). In the case of the strained lattice, it is convenient to define the defect formation energy with respect to the loaded ideal lattice. Such choice of the reference state is prompted by the simple reasoning that the energy required for the elastic deformation of the defect-free lattice should not be considered as a contribution to the defect formation energy, were it E_f or E_s. As a result, the formation energies in loaded and unloaded material are measured from different reference states. It must be emphasized, however, that this assumption does not affect the migration energy value, because the latter equals to the difference of the saddle point and the equilibrium defect energies, which correspond to the same loading state and thus are measured from the same reference. Correspondingly, the activation energy for a jump in direction $\mathbf{h}$ is given by

$$E_m(\mathbf{h}) = E_s(\mathbf{h}) - E_f = E_m^0 - [P_{ij}^s(\mathbf{h}) - P_{ij}^s]\varepsilon_{ij} \tag{42}$$

where $E_m^0 = E_s^0 - E_f^0$ is the migration energy in the stress-free lattice. In writing down Eq. (42), we have restricted ourselves to linear corrections in strain, because in practical applications one seldom has to account for the second-order corrections to the defect energies.

Second, in the case when the diffusing particle is a self-point defect (a vacancy or an interstitialcy), the reference state is normally defined assuming that the total number of atoms in the crystal before and after formation of the point defect does not change. In the case of vacancy formation, it is assumed that the atom removed from the vacant site is added somewhere at the surface of the crystal, while in the case of an interstitial an atom is removed from the crystal surface. In the externally stressed crystal, the addition or removal of the atom to the surface requires additional energy, $-\sigma_{nn}\Omega$ or $\sigma_{nn}\Omega$, respectively, where σ_{nn} is the normal stress acting on the crystal surface in the position, where the atom is added or removed. This contribution is important where the formation of vacancies or interstitials is considered, leading to the dependence of the equilibrium point defect concentration at the crystal surface on the surface orientation with respect to the external loads. However, it does not affect the migration energy.

2.2.2. Microscopic Derivation of Dipole Tensors

In the previous section, the force tensors were introduced on purely formal grounds, as proportionality factors between the particle energy change in strained material and the strains themselves. Here we discuss the microscopic nature of the force tensors and demonstrate how they can be expressed in terms of parameters, characterizing atomic interaction in a stress-free lattice. All calculations will assume that a diffusing particle is located in a defined position, either the equilibrium position or the saddle point one. Because the consideration is completely equivalent for both, we will omit in this section indexes indicating the particle position.

Let us assume that external loads cause in the material elastic deformations $\mathbf{u}^0$, strains ε_{ij}^0, and stresses σ_{ij}^0, while the corresponding parameters for the particle in the stress-free material are $\mathbf{u}'$, ε_{ij}', and σ_{ij}'. Assuming that in both cases the strains are sufficiently small, so that the linear elastic theory is valid, the stresses σ_{ij} and strains ε_{ij} in the strained lattice with the particle can be taken as superpositions of two contributions:

$$\sigma_{ij} = \sigma_{ij}^0 + \sigma_{ij}' \quad \text{and} \quad \varepsilon_{ij} = \varepsilon_{ij}^0 + \varepsilon_{ij}' \tag{43}$$

On the other hand, the energy of the crystal is a second-order functional of strains, and thus, in addition to the energies of the external elastic field (in a defect-free crystal) and the particle energy (in a stress-free crystal), it includes the energy of particle elastic interaction with the external strain field, ΔE^{el}, which can be written down as

$$\Delta E^{el} = \frac{1}{2}\int_V (\sigma_{ij}\varepsilon_{ij} - \sigma_{ij}^0\varepsilon_{ij}^0 - \sigma_{ij}'\varepsilon_{ij}')\, dV \tag{44}$$

Substituting here relations (43) and taking into account Hook's law, we can present ΔE^{el} as

$$\Delta E^{el} = \int_V \sigma_{ij}'\varepsilon_{ij}^0\, dV \tag{45}$$

or, integrating by parts,

$$\Delta E^{el} = \int_V \frac{d\sigma_{ij}'}{dx_j} u_i^0\, dV \tag{46}$$

Having in mind the stress equilibrium equation,

$$\frac{d\sigma_{ij}'}{dx_j} + f_i' = 0$$

where $\mathbf{f}'$ is the density of forces created by the defect in the bulk of the material, we get

$$\Delta E^{el} = -\int_{V'} (\mathbf{f}'\mathbf{u}^0)\, dV \tag{47}$$

As can be seen, the energy change depends on the distribution of forces that describe the action of the particle on the host material. In order to express ΔE^{el} in terms of the particle properties, one has to use an appropriate model allowing to present $\mathbf{f}'$ in analytical form. One of the most often used is the model where point defect is treated as a set of three mutually orthogonal force pairs (dipoles), localized in the point $\mathbf{r}'$, where the particle is located. Then, the components of the force density (written down in the coordinate system with the axes directed along the individual force pairs) are (see, e.g., [57])

$$f_i = -P^{(i)} \frac{d\delta(\mathbf{r} - \mathbf{r}')}{dx_i}$$

where $P^{(i)}$ $(i = 1, 2, 3)$ are factors characterizing the dipole strengths, and δ is the Dirac's delta function. Generally, the spatial orientation of the force pairs is determined by the local symmetry of the particle environment and must not coincide with the global coordinate axes, which can be selected arbitrarily, for example, along the global symmetry axes of the crystal. In a general coordinate system, the force density will have a more general form

$$f_i' = -P_{ij} \frac{d\delta(\mathbf{r} - \mathbf{r}')}{dx_j} \tag{48}$$

where the proportionality factors P_{ij} make a second-order tensor. Evidently, the eigenvalues of this tensor equal to $P^{(i)}$. Substituting (48) into (47), we get

$$\Delta E^{el} = -P_{ij}\varepsilon_{ij}^0 \tag{49}$$

which coincides with the first term in the energy change expansion in strains [e.g., equation (40)]. This explains why tensor P_{ij} is referred to as the dipole tensor.

Naturally, Eq. (48) is only an approximation. First of all, it follows from nowhere that the strains around the particle can be described by force density localized in a point. We can expect, however, that this force density, even if distributed in space, falls down sufficiently quickly as the distance from the defect increases. Second, our basic assumption that strains created by the particle obey linear elasticity theory (i.e., they are related to the stresses by Hooke's law) may fail very close to the particle. In this case, Eq. (47), whose derivation involved the direct use of Hooke's law, remains valid only if $\mathbf{f}'$ is treated as the density of fictitious forces (called Kanzaki forces [58]), that would produce in a linearly elastic material the same displacements as those created by the particle in the real lattice.

Due to the short-range nature of Kanzaki forces, only the region in the vicinity of the particle contributes to the integral in (47). In this region, one can neglect possible spatial variation of the external strains, presenting displacements $\mathbf{u}^0$ as

$$u_i^0(r) \approx u_i^0(\mathbf{r}') + \varepsilon_{ij}^0(\mathbf{r}')(r_j - r_j')$$

Having in mind that for a static particle the total force acting on the lattice must vanish

$$\int_{V'} \mathbf{f}'\, dV = 0$$

the energy change will still be given by Eq. (49) with

$$P_{ij} = \int_{V'} f_i(\mathbf{r}) r_j\, dV \tag{50}$$

The lattice analogue of this equation is, evidently,

$$P_{ij} = \sum_n f_i^n r_j^n \tag{51}$$

where $\mathbf{r}^n$ is the radius vector of atom n in the defect-free lattice, and summation in (51) is over all atoms surrounding the particle.

Summing up, the linear relation between the energy change associated with the creation of a particle in the strained material and the external strains is a direct consequence of the elastic interaction of the particle with the external strain field. The tensor of proportionality factors P_{ij} can be expressed completely in terms of parameters, characterizing the particle in the stress-free material. However, there remains the task of finding the values of the dipole tensor component in particular materials. Some ways to do it are discussed below.

2.2.3. Activation Volumes

An important particular loading scheme is hydrostatic loading of material with pressure p (here we assume p to be positive when the material is compressed), because it is often used in diffusion experiments specially tailored to estimate the effect of stress on diffusion (see, e.g., [7, 59]). The estimated parameter is pressure derivative of the measured diffusion coefficient D (or, more exactly, the limiting value of the pressure derivative at $p \to 0$)

$$V^* = -kT\frac{\partial \ln D(T, p)}{\partial p} = \frac{\partial \Delta G}{\partial p} \tag{52}$$

where ΔG is the free energy entering Arrhenius formula for D [of the type of Eq. (8)]. Usually, V^* is called the activation volume for diffusion. For different types of diffusing particles, $\ln D$ can decrease or increase with p, so that V^* can be either positive or negative [60]. In order to establish relation between V^* and the microscopic properties (such as the dipole tensors) of diffusing particles, it is necessary to consider which type of diffusion coefficient is measured.

In experiments aimed at the measurement of diffusion coefficient, it is a usual practice to measure diffusion coefficient D of the lattice atoms (self-diffusion) or that of substitutional impurities. In both these cases, the diffusion is mediated by self-point defects: most often by vacancies, though in some materials, such as Si, interstitialcy contribution can be important. As a result, diffusion coefficient D is proportional to the product of the mediating defect diffusion coefficient D_α by its concentration C_α [where subscript α denotes the type of mediating defect, vacancy ($\alpha = V$) or interstitialcy ($\alpha = I$)]. Self-diffusion experiments are typically performed in the conditions when the point defects are in the thermal equilibrium and thus their concentration is the thermally equilibrium one,

$$C_\alpha = \exp\left(\frac{-\Delta G_{f\alpha}}{k_B T}\right)$$

where $\Delta G_{f\alpha}$ is the free energy of formation of mediating defect. Correspondingly, the free energy of diffusion is given by the sum of contributions due to the formation of a mediating defect and its migration in the lattice, $\Delta G = \Delta G_{f\alpha} + \Delta G_{m\alpha}$. Correspondingly, the activation volume for self-diffusion is

$$V^* = V_{f\alpha} + V_{m\alpha} \tag{53}$$

where the defect formation volume $V_{f\alpha}$ and migration volume $V_{m\alpha}$ are defined as

$$V_{f\alpha} = \frac{d\Delta G_{f\alpha}}{dp} \quad \text{and} \quad V_{m\alpha} = \frac{d\Delta G_{m\alpha}}{dp} \tag{54}$$

It should be kept in mind, however, that relation (53) does not always hold true. Indeed, in engineering applications, one often meets situations where the concentration C_α of defects mediating self-diffusion is not the thermodynamically equilibrium one; in particular, it may be temperature independent. In this case, the diffusion activation volume will be equal to the migration volume $V_{m\alpha}$. A similar situation is met when one measures the diffusion coefficients for particles that are able to migrate by themselves, which is the case for interstitially diffusing impurities, or self-point defects on the lattice.

2.2.3.1. Phenomenological Relations for Diffusion Activation Volumes An accurate estimation of activation volumes is a difficult and time-consuming procedure that requires a detailed knowledge about the micromechanism of the diffusion process for the interpretation of the results. In order to have the means for a quick estimate of the relaxation volumes or for their comparison between different materials (or, say, the compositional variation in the same material), a number of phenomenological relations expressing relaxation volumes in terms of some bulk properties and other diffusion parameters were proposed. Possibly, the simplest relation of this kind was obtained by Keys [63] from purely empirical considerations:

$$V^* = 4\beta\Delta H \tag{61}$$

where β is the material compressibility and ΔH is the diffusion activation enthalpy.

One of the most interesting relations expresses V^* in terms of the entropy variation, ΔS, associated with the diffusion jump,

$$\Delta V^* = \frac{\beta}{\alpha_T}\Delta S \tag{62}$$

where α_T is the thermal expansion coefficient. This equation has been obtained by Lawson et al. [64] following the dynamical theory of diffusion of Rice [42]. As shown in [65], the ratio α_T/β is very similar for most of the bcc and fcc metallic lattices.

A relation, similar to (62), can also be obtained based on the observation [66] that the logarithm of the self-diffusion coefficients D for a number of metals varies linearly with V/V_1, where V and V_1 are, respectively, the specific volumes of the solid at the experimental temperature and that of the liquid at the melting point. Recalling relation (8), this means that the variation of the free energy of atom migration with temperature can be described as

$$\Delta G_m(T) \approx \Delta G_0 + \frac{\partial \Delta G_m}{\partial V} V_0 \alpha_T T \tag{63}$$

where ΔG_0 and V_0 are, respectively, the free energy and the specific volume of the matrix at absolute zero temperature. Expressing the volume derivative of the free energy change as

$$\frac{\partial \Delta G_m}{\partial V} = -\frac{1}{\beta V}\frac{\partial \Delta G_m}{\partial p} = \frac{V^*}{\beta V}$$

and comparing to the standard thermodynamic relation, $\Delta G = \Delta G_0 - T\Delta S$, one can express V^* in terms of the entropy variation ΔS,

$$\Delta V^* = \frac{\beta}{\alpha_T}\Delta S(1 + \alpha_T T) \tag{64}$$

which reduces to Eq. (62) if one neglects the thermal expansion contribution.

Having in mind that the value of ΔS can be estimated from the pre-exponential factor of the diffusion coefficient, relation (62) is sometimes used as an indication of the "size" of the defect responsible for the elementary events of diffusional mass transport. In particular, very big pre-exponential factor is considered as an indirect indication that the elementary diffusion jump involves correlated movement of many atoms. According to Zener [16], the diffusion entropy is directly proportional to the ratio $\Delta G_0/T_m$, where ΔG_0 is the change of the free energy of diffusion jump [cf. Eq. (8)] extrapolated to $T = 0$, and T_m is the melting temperature of the material. Hence, it is possible to relate the activation volume for diffusion and the migration energy in a stress-free crystal as

$$V^* \propto \Delta G_0$$

which correlates with Eq. (61).

The importance of the phenomenological approach is mainly in the indication of relationships between the diffusion and bulk parameters, but its usefulness for the calculation of

activation volume is low, as it is based on crude approximations. To get more quantitative information about the relaxation volumes, one must take into account the definite mechanism that governs the diffusion of particular particles in a particular material. Such detailed information can be obtained only by numerical simulations.

2.2.3.2. Numerical Methods for Determination of Activation Volumes As demonstrated in the beginning of this section, activation volume is defined in terms of relaxation volumes and crystal expansion volumes due to the presence of a migrating defect. The crystal expansion ΔV^{out} can be calculated in the crystal that is not externally stress and, moreover, it can be directly related to the trace of the defect dipole tensor (in corresponding position) [57]

$$\Delta V^{\text{out}} = \frac{\text{Tr}P_{ij}}{3B} \tag{65}$$

where B is the bulk modulus of material. The accurate definition of the relaxation volume is more complicated, as it involves calculation of the elastic energy stored in the defect crystal under stress. Therefore, it is a common practice to express relaxation volume in terms of the crystal expansion as

$$\Delta V^{\text{rel}} = -\Delta V^{\text{out}} + \underline{O}(p) \tag{66}$$

Indeed, this relation holds true, when one describes the crystal relaxation around the mediated defect completely in terms of the linear elasticity theory. In order to demonstrate this, let us determine relaxation volume ΔV^{rel} for a vacancy in equilibrium position, which we will simulate as a spherical hole of radius a in a purely elastic continuum. In order to take into account the elastic relaxation around the vacancy, which occurs even in the stress-free crystal, we assume that surface tension P_s is acting at the vacancy surface (forgetting for the time being that such macroscopic description is a very crude approximation for a hole of atomic size).

The main contribution to the pressure dependence of the vacancy formation energy comes from the variation of the elastic energy in the volume surrounding the vacancy, which can be written down as

$$E_f = E_{f0} + \frac{1}{2}\int_V (\sigma_{ij}\varepsilon_{ij} - \sigma_{ij}^0\varepsilon_{ij}^0 - \sigma_{ij}^d\varepsilon_{ij}^d)\, dV \tag{67}$$

where E_{f0} is the vacancy formation energy in the unloaded crystal, and σ_{ij} and ε_{ij} are stresses and strains in the loaded crystal with the vacancy; the same parameters with superscript 0 correspond to the stressed crystal without the defect, and those with superscript d to the unstressed matrix with the defect. The integration is over the volume outside the vacancy.

Let us decompose the strains and stresses in the stressed crystal with the defect as

$$\sigma_{ij} = \sigma_{ij}^0 + \sigma_{ij}' \quad \text{and} \quad \varepsilon_{ij} = \varepsilon_{ij}^0 + \varepsilon_{ij}' \tag{68}$$

where the primed values denote the modification of the original elastic fields by the presence of the defect. Then

$$\Delta E_f = E_f - E_{f0} = \int_V \sigma_{ij}^0\varepsilon_{ij}'\, dV + \frac{1}{2}\int_V (\sigma_{ij}'\varepsilon_{ij}' - \sigma_{ij}^d\varepsilon_{ij}^d)\, dV \tag{69}$$

where we have taken into account that, in the framework of the linear elasticity theory, $\sigma_{ij}^0\varepsilon_{ij}' = \sigma_{ij}'\varepsilon_{ij}^0$. Now, integrating the first term in (69) by parts, using Gaussian theorem and the equilibrium equations for σ_{ij}^0, we obtain

$$\int_{V-V^{\text{at}}} \sigma_{ij}^0\varepsilon_{ij}'\, dV = \int_{V-V^{\text{at}}} \frac{d(\sigma_{ij}^0 u_i')}{dx_j}\, dV - \int_{V-V^{\text{at}}} u_i' \frac{d\sigma_{ij}^0}{dx_j}\, dV = \int_{S_{\text{out}}} \sigma_{ij}^0 u_i' n_j\, dS - \int_{S_a} \sigma_{ij}^0 u_i' n_j''\, dS$$

where $\mathbf{n}$ is the vector of external unit normal to the crystal surface S_{out}, and $\mathbf{n}^v$ is the external normal to the surface S^v of the hole simulating the vacancy. Taking into account that $\sigma_{ij}^0 n_j = -pn_i$ and $\sigma_{ij}^0 n_j^v = -pn_i^v$, we can reduce (69) to

$$\Delta E_f = -p(\Delta V^{out} - \Delta V^v) + \frac{1}{2}\int_V (\sigma_{ij}'\varepsilon_{ij}' - \sigma_{ij}^d\varepsilon_{ij}^d)\,dV \tag{70}$$

where ΔV^{out} is the change of the crystal volume,

$$\Delta V^{out} = \int_{S_{out}} u_i' n_i\,dS \tag{71}$$

while ΔV^v is the increase of the vacancy volume:

$$\Delta V^v = \int_{S_v} u_i' n_i^v\,dS \tag{72}$$

Because the normal stress at the hole surface is equal to the surface tension, the boundary condition for σ_{ij}' is

$$\sigma_{ij}' n_j^v = (p - P_s)n_i^v \tag{73}$$

while far from the defect, the stresses and strains vanish. This boundary value problem for σ_{ij}' differs from that for σ_{ij}^d only by the renormalized boundary condition at the vacancy surface (in the latter case one should set p equal to zero). Correspondingly, we can write

$$\sigma_{ij}' = (p - P_s)\tilde{\sigma}_{ij} \quad \text{and} \quad \sigma_{ij}^d = -P_s\tilde{\sigma}_{ij}$$

where $\tilde{\sigma}_{ij}$ is a dimensionless tensor, the same in both cases. Analogous relations will hold for strains and displacements. Therefore, Eq. (69) can be rewritten as

$$\Delta E_f = -p\Delta V^{out} + p\Delta V^v - pP_s\int_V \tilde{\sigma}_{ij}\tilde{\varepsilon}_{ij}\,dV + \frac{p^2}{2}\int_V \tilde{\sigma}_{ij}\tilde{\varepsilon}_{ij}\,dV \tag{74}$$

The second term in the right-hand side of this equation can be written down as

$$p\Delta V^v = (p^2 - P_s p)\int_{S_v} \tilde{u}_i n_j^v\,dS$$

while the integral in the third term can be taken by parts, like it is done in Eg. (69), giving

$$pP_s\int_{V-V^v} \tilde{\sigma}_{ij}\tilde{\varepsilon}_{ij}\,dV = -pP_s\int_{S_v} \tilde{u}_i n_j^v\,dS$$

Summing up these relations, and taking into account that the last term in (74) is quadratic in external pressure, we finally obtain

$$\Delta E_f = -p\Delta V^{out} + \underline{O}(p^2) \tag{75}$$

which immediately gives Eq. (66).

However, relation (66) must not be valid when atomic displacements around the defect do not obey elasticity theory requirements. Therefore, ΔV^{rel} must not vanish completely. An indication that relaxation volume ΔV^{rel}, obtained as the derivative of formation energy, can differ from the total volume increase ΔV^{out} follows from the results of [67], where both volumes were estimated for the same defects using independent approaches.

Note that the possibility of vanishing relaxation volume ΔV^{rel} in the equilibrium vacancy position does not contradict to the fact that V^* quite noticeably differs from the atomic volume. Indeed, the energy of a vacancy in the saddle point E_s must not include the contribution from the work against the external forces, as the jump occurs much faster that the elastic wave associated with the transition through the saddle point reaches the surface of material. Hence, no compensation of ΔV^{rel} in the saddle point occurs, and the main part in

the difference $V^* - \Omega$ should be ascribed to the contribution from the migration activation volume V_m.

In computational practice, the two contributions to the relaxation volume have received considerably different attention. The main attention has been paid to the contribution related to the work of external forces, ΔV^{out}. The most widespread method of estimation of ΔV^{out} was proposed in different versions by several authors [68–71]. The approach is based on the fact that, according to the elasticity theory, the displacements created in an infinite elastic continuum by any localized defect, fall down sufficiently far from the defect as r^{-2}, where r is the distance to the defect. In a special case, where the defect is spherically symmetric and the material is isotropic, the displacement field $\mathbf{u}$ around the defect has the form

$$\mathbf{u} = C\frac{\mathbf{r}}{r^3} \tag{76}$$

where $\mathbf{r}$ is the radius-vector connecting the defect and the observation point, and C is a constant ("defect strength"). Correspondingly, the volume expansion in an infinite continuum, $\Delta V_\infty^{\text{out}}$, associated with the defect can be presented as a linear function of C:

$$\Delta V_\infty^{\text{out}} = \int u\, dS = 4\pi C \tag{77}$$

where integration is performed over an arbitrary closed surface containing the defect inside. In particular, all points of the surface can be shifted far away from the defect (in the limit, to infinity), so that the calculation of the relaxation volume of a defect is reduced to the calculation of the unknown parameter C, describing the long-range properties of a defect in an elastic continuum. In a more general case, when the defect is not spherically symmetric, displacement field around the defect and the volume expansion should be expressed in terms of the dipole tensor components [see, e.g., Eq. (65)].

In a finite size crystal, the defect relaxation volume, ΔV_f^{out}, differs from $\Delta V_\infty^{\text{out}}$. Indeed, in a finite lattice, the vanishing normal stress at the outer lattice surface gives rise to an additional term in the volume expansion, which is called "image force" correction. However, as shown in [72], these two quantities are linearly related to each other

$$\Delta V_f^{\text{out}} = \Delta V_\infty^{\text{out}}(1 + \gamma_E) \tag{78}$$

where $\gamma_E > 0$ is the Eshelby factor. In an isotropic lattice, the Eshelby factor can be expressed in terms of the Poisson ratio, ν_E, [72]

$$\gamma_E = 3\frac{1 - \nu_E}{1 + \nu_E}$$

while in a cubic lattice [71],

$$\gamma_E = \frac{4(C_{11} - C_{12}) + 12C_{44}}{5(C_{11} + 2C_{12})}$$

where C_{11}, C_{12}, and C_{44} are elastic constants (in Voigt's notation). Therefore, the defect strength C is useful to define the relaxation volume in the finite crystal as well.

If the elastic theory would be valid for all atoms around the defect, the defect strength could be found simply from the solution of the static elastic equation. However, in the immediate vicinity of the defect, the atomic displacements can be quite large (up to ten percent of interatomic distance) and the applicability of the elasticity theory is questionable. Moreover, the lattice symmetry is usually different from isotropic, and the defect must not be spherically symmetric (especially when this method is applied to a defect in saddle-point position). Therefore, a computational cell of few hundreds to few thousands of atoms is used to describe the inelastic strain pattern in the immediate vicinity of a crystal lattice defect. This cell, in which atoms may arbitrarily move in accordance with a given set of atomic interaction functions, is embedded in an elastic mantle, which represents the effect of the rest of the crystal, where the atomic shifts caused by the defect are sufficiently accurately described by the elasticity theory.

In the model, the simulated crystal is divided into three regions (usually of spherical shape). In region I, the atoms interact through pair potential $\Phi(r_{ij})$, and are free to move. Outside of region I, the atoms are treated as though they are imbedded in an elastic continuum. These atoms are further divided into regions II and III, where region II is composed of atoms that have neighbors in region I. Correspondingly, the outer radius r_2 of zone II is chosen so that the thickness of the zone would exceed the cutoff radius of the effective atomic interaction for the chosen interatomic potential. The second zone thus plays a role of a buffer between zones I and III, where zone III is an elastic continuum.

In the classical model of Johnson [71], the energy of the crystal is given by

$$E = \frac{1}{2}\sum_{i=1}^{N1}\sum_{\substack{j=1\\ j\neq i}}^{N1}\Phi(r_{ij}) + \sum_{i=1}^{N1}\sum_{k=1}^{N2}\Phi(r_{ik}) + aC + bC^2 \tag{79}$$

where the summation over i includes all atoms within region I (their number being denoted as N_1), the summation over j includes those atoms in region I, which interact with the ith atom, and the summation over k includes atoms in region II, which interact with the ith atom. The term aC accounts for the work done against the forces required to hold the perfect lattice in equilibrium, and the term bC^2 accounts for the energy stored within the elastic field. The energy for a particular configuration is given by $E - E_0$, where E_0 is the perfect lattice energy.

The coefficient a in Eq. (79) can be found by an explicit bond calculation in the perfect lattice with the requirement that the lattice is in equilibrium [73]. In a cubic lattice, this gives

$$a = 1 + \frac{4(C_{11} - C_{12}) + 12C_{44}}{15B} \tag{80}$$

The coefficient b is calculated from elastic theory by setting the energy stored in the elastic field outside region I equal to bC^2. This leads to

$$b = \frac{32\pi^2}{5N_1\Omega}\left[C_{44} + \frac{1}{3}(C_{11} - C_{12})\right]$$

As demonstrated by the simulations, the pressure term aC plays a somewhat more important role than the elastic term bC^2.

The force acting on atom i from atom j can be written down as

$$\mathbf{F}^{ij} = \frac{d\Phi}{dr^{ij}}\frac{\mathbf{r}^{ij}}{r^{ij}}$$

where $\mathbf{r}^{ij}$ is the vector connecting atom i to atom j, while the total force on atom i is

$$\mathbf{F}^{i} = \sum_{j}\mathbf{F}^{ij} + \sum_{k}\mathbf{F}^{ik}$$

where summations have the same meaning as in (79). The generalized force on the crystal arising from the elastic variable C is given by

$$F^{c} = -\frac{\partial E}{\partial C} = -\sum_{i}\sum_{k}\mathbf{F}^{ik}\frac{\partial \mathbf{r}^{k}}{\partial C} - a - 2bC$$

where $\mathbf{r}^k$ denotes position of atom k in region II.

The process for finding energy minima and saddle points is as follows: Initial vector positions of each atom within the crystal are chosen to approximate the configuration of interest. Each coordinate of each atom within the crystallite is varied in turn until the corresponding force component becomes zero, and then the value of C is adjusted so that F^c vanishes. The force on a given atom and the generalized elastic force are very nearly linear with displacement for small displacements. Thus, it is possible to find the force for a given variable and use linear extrapolation to the value where the force is zero. According to [71], 10 to 20 such iterations are required for the energy and the configuration to converge.

The estimates of the second contribution to the relaxation volume, resulting from the elastic energy variation, ΔV^{el}, are not so frequent. For example, simultaneous calculations of both contributions were done for vacancy, divacancy, and several small vacancy-germanium complexes in silicon [67]. The volume increase ΔV^{out} was found using slightly modified version of Johnson's method, where the atoms in the buffer zone II were allowed to move freely, in order to minimize the error related to the interaction of atoms across the border between the freely relaxing crystal internals and the "embedding continuum." In contrast, the contribution of the formation volume ΔV^{rel} was found from the slope of the elastic energy of pressurized crystal plotted as a function of applied pressure p. The influence of the pressure on the system was taken into account through the corresponding displacement field in the "embedding continuum" (zone III), where the displacement field has two components: one is related to the applied pressure, and the other is due to the presence of the defect, being correlated with displacements of atoms in zones II and I. The component associated with the applied pressure was calculated using Murnaghan's equation of state (EOS) [74], which describes the dependence of the volume on the applied pressure. Determination of the formation energies using Tersoff's semiempirical potential have shown that the formation energies have a tendency to decrease with increasing pressure for all the considered vacancy-type defects, Fig. 8, as could be expected *a priori*. Consequently, the value of ΔV^{c_rel} has the negative sign (Table 1). This conclusion is in agreement with the first-principles calculations performed independently by Antonelli and Bernholc [8] and Ganchenkova et al. [67], which predict the values of ΔV^{c_rel} very similar to those obtained in the model with Tersoff's potential. The obtained values of ΔV^{c_rel} have opposite sign to ΔV^{c_out} and are sufficiently large to compensate the contribution of the latter. Although the accuracy of the first-principles calculations can be limited by the small size of the simulation cell, it is difficult to imagine that in bigger simulation cells, the contribution of ΔV^{c_rel} to the activation volume can vanish completely.

2.2.4. Numerical Techniques for Estimation of Dipole Tensors

Several methods have been proposed for the estimation of dipole tensors. All of them inevitably rely on numerical methods, as the relaxation of atoms in the vicinity of diffusing particles are normally beyond the lattice description in the harmonic approximation

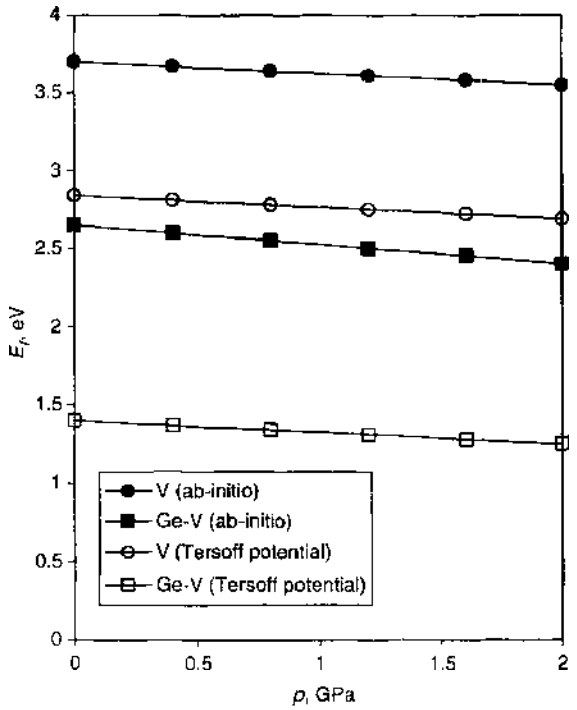

Figure 8. Dependence of defect formation energy on pressure for vacancy and vacancy-germanium complex in silicon. Calculations using density functional theory approach (VASP code) and Tersoff potential.

Table 1. Relaxation volumes for a vacancy and Ge-vacancy complex in silicon, according to [67]. Values in parenthesis indicate the corresponding volumes measured in units of the atomic volume Ω.

Defect	Simulation method	$\Delta V^{f,\mathrm{rel}}$, Å^3($\Omega$)	$\Delta V^{f,\mathrm{unr}}$, Å^3($\Omega$)	V_f, Å^3(Ω)
Vacancy	Tersoff	−13.30 (−0.63)	2.21 (0.11)	9.91 (0.47)
	DFT	−13.30 (−0.63)	—	—
Ge-V	Tersoff	−8.00 (−0.38)	1.64 (0.08)	14.64 (0.70)
	DFT	−16.70 (−0.80)	—	—

(i.e., assuming linear elastic response of the material), but vary in the degree to which analytical considerations are involved and what particularly is calculated numerically. Some of these methods are discussed below.

2.2.4.1. The Green's Function Approach The first group of approaches for finding the dipole tensors P_{ij} is based on the use of Kanzaki forces (e.g., [57]). In the literature, various schemes have been used to calculate P_{ij} and the associated relaxation volume ΔV. Among these is an approximate method introduced by Hardy [75] to study substitutional K^+ defects in NaCl and later extended [76] to vacancies in Na. This method has subsequently been applied for calculations of relaxation volumes for a wide range of defects, including interstitials (see, e.g., [77]). However, Hardy's results are obtained in the approximation that the anharmonicity of interaction between the host lattice atoms is neglected and breaks down for defects such as self-interstitials, which cause large lattice distortions. Therefore, more rigorous approaches for P_{ij} estimation using the results of computer simulation can be considered. For example, Schober [78] derived expressions for P_{ij} and ΔV using the Green's function method.

Here we discuss the Green's function method as applied to a foreign atom (defect) occupying an interstitial position in a host lattice. For simplicity, we assume that this interstitial position can be specified *a priori* (e.g., from symmetry consideration) and select it as the coordinate system origin. Following [78], we will assume that all ions interact via central pairwise forces. It can readily be shown that the results obtained are not influenced by this simple choice of model, but can be generalized to include many-body interactions. Denoting the lattice position of ion n as $\mathbf{r}^n$ ($1 \le n \le N$, where N is the total number of atoms in the crystal) and the distance between two atoms as $r^{nm} = |\mathbf{r}^n - \mathbf{r}^m|$, the energy E_c of the lattice in the absence of the defect can be presented as

$$E_c = \frac{1}{2} \sum_{n=1}^{N} \sum_{\substack{m=1 \\ m \neq n}}^{N} \Phi(r^{nm}, \{\xi\}^{nm}) \tag{81}$$

where $\Phi(r^{nm}, \{\xi\}^{nm})$ is the host–host pair potential function, which may depend, in addition to the distance between two atoms, on a set of other parameters, $\{\xi\}^{nm}$, which may be sensitive to the physical nature of interacting atoms. In practical calculations, these parameters are used as fitting parameters, and their number depends on the chemical composition of a particular solid.

The requirement that all atoms are in their equilibrium positions implies that the force $\mathbf{F}^n$ acting at any atom n vanishes, that is

$$\mathbf{F}^n = -\sum_{\substack{m=1 \\ m \neq n}}^{N} \mathbf{e}^{(nm)} \left. \frac{d\Phi(r)}{dr} \right|_{r=r^{nm}} = 0 \tag{82}$$

where $\mathbf{e}^{(nm)}$ is a unit vector directed from atom n to atom m. In a crystalline lattice with inversion symmetry, for any atom m one can find another atom k at exactly opposite position (i.e., $r^{nk} = r^{nm}$, $\mathbf{e}^{(nk)} = -\mathbf{e}^{(nm)}$), and Eq. (82) is satisfied independent of the particular form of the pair potential function. As a result, the most energetically favorable atomic configuration in the lattice is determined by energy minimization with respect to all or some of the fitting parameters (in particular, with respect to the interatomic separation).

When a defect is added in the coordinate origin, the surrounding atoms will shift from their ideal lattice positions by displacement vectors $\mathbf{u}^n$ due to the interaction with the introduced defect. The total energy of the defect lattice is given by:

$$E_{\text{tot}} = \frac{1}{2}\sum_{n=1}^{N}\sum_{\substack{m=1\\ m\neq n}}^{N}\Phi\left(\left|\tilde{\mathbf{r}}^{nm}\right|\right) + \sum_{n=1}^{N}\Psi\left(\left|\tilde{\mathbf{r}}^{n}\right|\right) \tag{83}$$

where Ψ is the defect–host interaction potential, $\tilde{\mathbf{r}}^n = \mathbf{r}^n + \mathbf{u}^n$ is the radius-vector of atom n in the defect lattice, and $\tilde{\mathbf{r}}^{nm} = \mathbf{r}^n + \mathbf{u}^n - \mathbf{r}^m - \mathbf{u}^m$. The values of the displacement vectors should be found from the requirement that after the relaxation all lattice atoms are again in mechanical equilibrium, so that

$$\sum_{\substack{m=1\\ m\neq n}}^{N}\tilde{\mathbf{e}}^{(nm)}\frac{d\Phi(r)}{dr}\bigg|_{r=\tilde{r}^{nm}} = -\tilde{\mathbf{e}}^{(n)}\frac{d\Psi(r)}{dr}\bigg|_{r=\tilde{r}^{n}} \equiv \widetilde{\mathbf{F}}(\tilde{r}^n) \tag{84}$$

where $\tilde{r}^{nm} = \left|\tilde{\mathbf{r}}^{nm}\right|$, $\tilde{\mathbf{e}}^{(nm)} = \tilde{\mathbf{r}}^{nm}/\tilde{r}^{nm}$, and $\tilde{r}^n = |\tilde{\mathbf{r}}^n|$, $\tilde{\mathbf{e}}^{(n)} = \tilde{\mathbf{r}}^n/\tilde{r}^n$. We can interpret this as the equilibrium equation of an ideal anharmonic crystal under the influence of an external force $\widetilde{\mathbf{F}}$. There are no analytical ways to solve these equations, unless the degree of anharmonicity is small. Then one can link this equation with harmonic lattice theory, expanding the left-hand side around the equilibrium positions:

$$\tilde{e}_\alpha^{(nm)}\frac{d\Phi(r)}{dr}\bigg|_{r=\tilde{r}^{nm}} = e_\alpha^{(nm)}\frac{d\Phi(r)}{dr}\bigg|_{r=r^{nm}} + \Phi_{\alpha\beta}^{nm}(u_\beta^m - u_\beta^n) + \Delta\Phi_\alpha^{nm} \tag{85}$$

where the subscripts indicate Cartesian coordinates, the nondiagonal components of the harmonic coupling matrix Φ (for $n \neq m$) are defined as

$$\Phi_{\alpha\beta}^{nm} = -\left[\frac{1}{r}\frac{d\Phi(r)}{dr}\right]_{r=r^{nm}}\delta_{\alpha\beta} - \left[r\frac{d}{dr}\left[\frac{1}{r}\frac{d\Phi(r)}{dr}\right]\right]_{r=r^{nm}} e_\alpha^{(nm)}e_\beta^{(nm)} \tag{86}$$

and $\Delta\Phi_\alpha^{nm}$ denotes the remaining part of the expansion, which is of the order of $(|\mathbf{u}^n - \mathbf{u}^m|/r^{nm})^2$. Substituting (85) into (84) and taking into account Eq. (82), we obtain:

$$\sum_{m=1}^{N}\sum_{\beta=1}^{3}\Phi_{\alpha\beta}^{nm}u_\beta^m = K_\alpha^n \tag{87}$$

where

$$\Phi_{\alpha\beta}^{nn} = -\sum_{\substack{m=1\\ m\neq n}}^{N}\Phi_{\alpha\beta}^{nm} \tag{88}$$

and the components of Kanzaki forces are defined as

$$K_\alpha^n = \widetilde{F}_\alpha(\tilde{r}^n) - \sum_{\substack{m=1\\ m\neq n}}^{N}\Delta\Phi_\alpha^{nm} \tag{89}$$

The range of $\mathbf{K}$ is determined by the range of the defect forces F and the anharmonicity.

The formal solution of (87) can be obtained with the help of the ideal lattice Green function matrix $\mathbf{G}$, which is simply the inverse of the harmonic coupling matrix, $\mathbf{G} = \Phi^{-1}$,

$$u_\beta^m = \sum_{n=1}^{N}\sum_{\alpha=1}^{3}G_{\beta\alpha}^{nm}K_\alpha^n \tag{90}$$

However, because both the anharmonic contributions and the forces $\widetilde{\mathbf{F}}$ depend on the displacements, relations (87) or (90) remain implicit equations for $\mathbf{u}^n$ and must be solved self-consistently. For a real system, this would involve the inversion of large $3N \times 3N$ matrices,

where N is the number of atoms affected by the coupling changes. In order to reduce the complexity of the problem, it is a usual practice (as suggested by Hardy [76]) to neglect the anharmonic terms in Kanzaki forces,

$$K_n'' = \tilde{F}_n(\tilde{r}'')$$

and simplify the expression for $\mathbf{u}$ to

$$\mathbf{u} = \mathbf{GF}(\mathbf{r} + \mathbf{u}) \tag{91}$$

Recalling the definition of the dipole tensor in terms of Kanzaki forces, Eq. (51), we obtain

$$P_{\alpha\beta}^{ff} = \sum_{n=1}^{N} r_\alpha'' \tilde{F}_\beta(\mathbf{r}'' + \mathbf{u}'') \tag{92}$$

This approximate formula has been applied to a wide range of defect types (see, e.g., the reviews [77, 79, 80] and references therein). However, Eqs. (91) and (92) are of practical use only for defects that lead to small shifts of the host lattice atoms (e.g., small impurity interstitials with a weak potential Ψ). A slight modification of Eq. (92), which yields essentially the same results, was proposed in [81]:

$$P_{\alpha\beta}^{D} = \sum_{n=1}^{N} (r_\alpha'' + u_\alpha'') \tilde{F}_\beta(\mathbf{r}'' + \mathbf{u}'') \tag{93}$$

2.2.4.2. Computer Relaxation Techniques As can be seen from the previous section, the main difficulty in the calculation of the polarization tensors is the determination of atomic displacements due to relaxation of the particle environment. It is possible, however, to perform the relaxation in the defect crystal straightforwardly, using some molecular statics approach with appropriate interaction potentials. In this way, the obtained atomic displacements are "exact" in the sense that there is no need to introduce harmonic approximation. The dipole tensor can thus be calculated directly from the displacements without the need for any of the approximations of the previous section.

In computer simulation performed by Schober [78] to test the Green's function approach, a model crystal was constructed in which atoms interacted and were free to move under the influence of an interatomic potential. The equilibrium atomic configurations and energies of defects were then found by minimizing the energy of the model with respect to the displacements of its constituent atoms. For point defect simulations, the crystal (region I) was surrounded by an outer mantle of atoms (region II), which were held fixed in their perfect lattice positions during the relaxation process. Provided region I is sufficiently large to include all the host lattice anharmonicity and the full range of the defect–host interaction, the defect displacement field obtained from the simulation can be used to determine Kanzaki forces from (89).

In addition, the dipole tensor can be obtained from the knowledge of the forces which act between regions I and II of the model. Holding the atoms of region II fixed during the simulation corresponds physically to applying to these atoms external forces $\mathbf{F}_{\text{ext}}$, which counteract the forces exerted by region I due to the presence of the defect. Assuming again that region I contains all the host lattice anharmonicity and the true defect–host forces, one gets [78]

$$P_{\alpha\beta}^{V} = \sum_{n} r_\alpha'' F_\beta^{\text{ext}}(\mathbf{r}'') \tag{94}$$

Essentially, this scheme has been applied by Schober [82] to a detailed investigation of vacancies and interstitials in copper and α-iron. The resulting values obtained, as well as the expected structure of these point defects, will be discussed in more detail in Section 4, below.

In an attempt to simulate the response of an infinite crystal, region II is sometimes allowed to relax, assuming that the atoms shift according to continuum expression [57]:

$$u_\alpha^n = -P_{\beta\gamma}\frac{dG_{\alpha\beta}(\mathbf{r}^n)}{dx_\gamma}$$

where $\mathbf{G}$ is the continuum limit of the Green's function of the infinite ideal host crystal. The elements of the dipole tensor $P_{\alpha\beta}$ thus become additional parameters in the energy minimization routine, very similar to the Johnson's scheme [71] described in Section 2.2.3.

Evidently, when the atoms in region II are allowed to relax, even assuming that atomic displacements correspond to the continuum elasticity, the direct summation of forces acting on atoms in region II by relation (94) is senseless. However, because all the forces acting in the atomic system can directly be calculated after the relaxation, the dipole tensors can be obtained by summation over the atoms in region I according to Eq. (93). Such an approach was followed in, for example, [83, 84], where it was applied for calculation of coefficients analogous to dipole tensor components for vacancies in iron.

2.2.4.3. Direct Expansion of Energy in Atomic Displacements In fact, after an atomic system with the defect is numerically relaxed, it is possible to use directly the information about the atomic shifts in order to calculate the dipole tensors, using the expansion of the interaction energy in powers of the displacements. In order to demonstrate it, we consider a particle in the equilibrium position; the saddle-point dipole tensor can be obtained along essentially the same lines. We restrict ourselves to a particular case of substitutional defect, which is obtained by removing one atom from ideal lattice and either replacing it with an atom of another kind (impurity), or leaving the site empty (which corresponds to creation of a vacancy). An interstitial defect can be treated similarly, as outlined in the previous section.

As discussed in Section 2.2.1, the defect formation energy in a stress-free lattice is measured from the ideal lattice energy, as given by Eq. (81). On the other hand, in the stressed lattice it is reasonable to measure the defect formation energy from the energy of the stressed lattice. Let us assume that an external elastic deformation is applied to the lattice in such a way that it creates in the material spatially uniform macroscopic strains ε_{kl} but no macroscopic rotations. Note that the last condition is not automatically fulfilled in computational practice, where it is quite common to introduce deformations by shifting the atoms at the crystal surface and keep their positions fixed, while the internal atoms are allowed to relax. As a result of atomic relaxation, the atoms acquire some new positions, $\mathbf{r}^n + \mathbf{v}^n$, where the shifts $\mathbf{v}^n$ are not necessarily small as compared to the interatomic separation. However, for any two atoms j and n, one can safely assume that $|\mathbf{v}^n - \mathbf{v}^j| \ll |\mathbf{r}^n - \mathbf{r}^j|$.

In a general case, it is not evident how to relate the shifts of each individual atom to macroscopic strains, one can only be sure that, as long as the deformations are elastic, these shifts scale linearly with the atom position, that is,

$$v_k^n = V_{kl}^n(\hat{\varepsilon})x_l^n, \quad (k, l = 1, 2, 3) \tag{95}$$

where x_l^n is the projection of the radius vector of atomic position $\mathbf{n}$ onto the Cartesian axis l and tensor $\mathbf{V}^n$ depends on both the combination of external strains and a particular lattice position. However, for simple lattices (e.g., a monatomic lattice with one atom in the primitive cell), all atoms must shift exactly according to the elasticity theory, that is,

$$v_k^n = \varepsilon_{kl}x_l^n \tag{96}$$

(note that in this case, the proportionality factors are independent of particular site location).

Because the elastic strains are, by definition, small, the energy of atomic system interacting via pair potentials is given by expansion

$$E_c^{\mathrm{el}} = E_c + \frac{1}{4}\sum_{n=1}^{N}\sum_{\substack{j=1\\ j\neq n}}^{N}(\mathbf{e}^{(nj)}, \mathbf{v}^j - \mathbf{v}^n)^2\frac{d^2\Phi(r)}{dr^2}\bigg|_{r=r^{nj}} + \ldots \tag{97}$$

where we have taken into account that the first-order term in the expansion vanishes due to (82),

$$\sum_{n=1}^{N}\sum_{\substack{j=1\\ j\neq n}}^{N}(e^{(nj)}, \mathbf{v}^j - \mathbf{v}^n)\frac{d\Phi(r)}{dr}\bigg|_{r=r^{nj}} = \mathbf{F}^n\mathbf{v}^n + \mathbf{F}^j\mathbf{v}^j = 0 \tag{98}$$

When relation (96) is valid, we can write down

$$(\mathbf{e}^{(nj)}, \mathbf{v}^j - \mathbf{v}^n) = -\varepsilon_{kl}e_l^{(nj)}e_k^{(nj)}r^{nj}$$

and get

$$E_c^{el} = E_c + \frac{1}{2}C_{klmp}\varepsilon_{kl}\varepsilon_{mp} \tag{99}$$

where the elastic moduli C_{klmp} are expressed in terms of pair potential derivatives as

$$C_{klmp} = \frac{1}{2}\sum_{n=1}^{N}\sum_{\substack{j=1\\ j\neq n}}^{N}e_k^{(nj)}e_l^{(nj)}e_m^{(nj)}e_p^{(nj)}(r^{nj})^2\frac{d^2\Phi(r)}{dr^2}\bigg|_{r=r^{nj}} \tag{100}$$

Now let us consider the situation where a defect is introduced in the central region of the crystal. Below we will assume that the number of atoms N in the simulation crystal is sufficiently big in order to neglect the influence of boundary conditions at the crystal surface on the response of atoms around the defect.[1] Let us assume that the position of the replaced atom is indexed by 1, and that the energy of pairwise interaction of the defect with regular atoms in the lattice is $\Psi(r^{1j})$. The replacement of atom in position 1, while all other atoms are kept in their position, modifies the energy of the crystal,

$$E_c^{def} = E_c + \sum_{n=2}^{N}W(r^{1n}) \tag{101}$$

where $W = \Psi - \Phi$. The force acting on the defect remains equal to zero,

$$\mathbf{F}^1 = -\sum_{n=2}^{N}\mathbf{e}^{(1n)}\frac{d\Psi(r)}{dr}\bigg|_{r=r^{1n}} = 0 \tag{102}$$

because this force vanishes exclusively due to the lattice symmetry, which is not affected for position 1. However, due to the difference between interatomic potentials Ψ and Φ, condition (82) for all other atoms in the lattice can be fulfilled only provided they are displaced from their positions by appropriate shifts $\mathbf{u}^n$. In contrast to the Green's function method, the current approach does not use any analytical approximations for the determination of atomic shifts, but applies numerical energy minimization methods, as described in the section devoted to molecular statics relaxation. When the atomic shifts are found, the energy can be expanded with respect to them,

$$E_c^d = E_c + \sum_{j=2}^{N}(\mathbf{e}^{(1j)}, \mathbf{u}^j - \mathbf{u}^1)\frac{dW}{dr}\bigg|_{r=r^{1j}} + \frac{1}{4}\sum_{n=1}^{N}\sum_{\substack{j=1\\ j\neq n}}^{N}(\mathbf{e}^{(nj)}, \mathbf{u}^j - \mathbf{u}^n)^2\frac{d^2\tilde{\Phi}(r)}{dr^2}\bigg|_{r=r^{nj}} + \cdots \tag{103}$$

where $\tilde{\Phi} = \Psi$, if one of the interacting atoms is the substitutional defect and $\tilde{\Phi} = \Phi$ otherwise. In writing down this expansion, we have used relation (82). The most remarkable feature of this result is that here we have the contribution to the energy already in the first order

[1] If, however, the crystal size is insufficient, additional measures should be taken to possibly minimize the influence of the boundaries. One possibility for that is the already mentioned embedding of the simulation crystal in an elastic continuum.

of the atomic shifts. The remaining double sum is the normal second-order contributions to the crystal energy.

When the same substitutional defect is formed in the strained lattice, the crystal energy E_c^{d-el} can be written in the same form (103), with the only difference that the shifts $\mathbf{u}^n$ must be replaced with the shifts $\mathbf{w}^n$ in the combined elastic field of the defect and external loads. Writing these shifts as

$$\mathbf{w}^n = \mathbf{u}^n + \mathbf{v}^n$$

we obtain the crystal energy in the form

$$E_c^{d-el} = (E_f^d + E_c^{el}) + \sum_{j=2}^{N} \left.\frac{dW}{dr}\right|_{r=r^{1j}} (\mathbf{e}^{(1j)}, \mathbf{v}^j - \mathbf{v}^1) + \frac{1}{2}\sum_{j=2}^{N} \left.\frac{d^2W}{dr^2}\right|_{r=r^{1j}} (\mathbf{e}^{(1j)}, \mathbf{v}^j - \mathbf{v}^n)^2$$
$$+ \frac{1}{2}\sum_{n=1}^{N}\sum_{\substack{j=1\\ j\neq n}}^{N} (\mathbf{e}^{(nj)}, \mathbf{u}^j - \mathbf{u}^n)(\mathbf{e}^{(nj)}, \mathbf{v}^j - \mathbf{v}^n) \left.\frac{d^2\tilde{\Phi}(r)}{dr^2}\right|_{r=r^{nj}} + \cdots \tag{104}$$

where $E_f^d = E_c^d - E_c$ is the so called configurational energy of the defect.

Now, as a first approximation we can assume that due to the linear nature of elasticity theory, $\mathbf{v}^n$ coincide with the elastic shifts of atoms in the absence of the defect. Making use of relation (96), the point defect formation energy modification due to the external load can be written down as

$$\Delta E_f^d = E_c^{d-el} - E_c^{el} - E_f^d = -P_{kl}\varepsilon_{kl} + \frac{1}{2}(C'_{klmp} - C_{klmp})\varepsilon_{kl}\varepsilon_{mp} \tag{105}$$

In this equation, the elastic moduli of the crystal, C'_{klmp}, are modified as compared to equation (100) by the presence of the defect,

$$C'_{klmp} = \frac{1}{2}\sum_{n=1}^{N}\sum_{\substack{j=1\\ j\neq n}}^{N} e_k^{(nj)} e_l^{(nj)} e_m^{(nj)} e_p^{(nj)} (r^{nj})^2 \left.\frac{d^2\tilde{\Phi}(r)}{dr^2}\right|_{r=r^{nj}} \tag{106}$$

Evidently, in a system with a very large number of particles, the correction of elastic moduli by an individual defect is negligible.

The linear in external strains term defines the dipole tensor, P_{kl}, which has the form

$$P_{kl} = -\sum_{j=2}^{N} e_k^{(1j)} e_l^{(1j)} \left[r\frac{dW}{dr}\right]_{r=r^{1j}} + \sum_{n=2}^{N}\left(\mathbf{u}^n, \sum_{\substack{j=1\\ j\neq n}}^{N} \mathbf{e}^{(nj)} e_k^{(nj)} e_l^{(nj)} \left[r\frac{d^2\tilde{\Phi}}{dr^2}\right]_{r=r^{nj}}\right) \tag{107}$$

The first sum in this equation is a direct analog of Hardy's approximation (92), with the only difference that the derivatives of the real forces are calculated on the ideal lattice positions and thus do not require the knowledge of the lattice atom shifts. The second sum arises due to the relaxation of the atoms around the defect and includes contributions due to the forces acting from the defect on the surrounding atoms and the effects related to the anharmonicity of atomic interaction. Though here we restrict ourselves to the linear approximation in $\mathbf{u}^n$, higher order terms can readily be obtained from the next terms of expansion (104).

In a special case where the defect is a vacancy, we have $\Psi \equiv 0$ and

$$P_{kl} = \sum_{n=2}^{N} e_k^{1n} e_l^{1n} \left[r\frac{d\Phi}{dr}\right]_{r=r^{1n}} - \frac{1}{2}\sum_{n=2}^{N}\sum_{\substack{j=2\\ j\neq n}}^{N} e_k^{(nj)} e_l^{(nj)} (\mathbf{e}^{nj}, \mathbf{u}^j - \mathbf{u}^n) \left[r\frac{d^2\Phi}{dr^2}\right]_{r=r^{nj}} \tag{108}$$

We thus see that the force tensors are completely determined by the interatomic potentials and the atomic shifts in a stress-free lattice.

2.2.4.4. Strain Derivatives Approach The most complicated, but at the same time the most straightforward approach, is called strain derivative method [85–87]. It is based on the consistent calculations of the total energy of a defect E^d in a lattice subject to the action of different modes of strain finding the energy derivatives with respect to the external strains. For example, the dipole tensor is found from the slopes of the crystal energy as functions of the strains as the strain tends to zero,

$$\left.\frac{\partial E^d}{d\varepsilon_{ij}}\right|_{\varepsilon_{ij}\to 0} = -P_{ij}^0 \tag{109}$$

In the worst case, the procedure uses six independent loading schemes (three uniaxial tensions along the principal coordinate axes and three shear strains) to obtain all the components of the dipole tensor. In symmetric lattices, the number of loading schemes can be reduced (e.g., two schemes are sufficient for bcc lattice and three for fcc lattice). A similar equation can be written for higher order polarization tensors as well. This kind of procedure for the calculations of dipole tensors has been suggested and performed first by Gillan [85, 86] for point defects in ionic crystals and later on was applied to a metallic c crystal by Puls and Woo [87]. Following [78], the simulation crystals in both cases contained the free central core of atoms (region I) surrounded by a mantle of immobile atoms (region II). The treatment of atoms in zone II was somewhat different, due to the nature of the considered systems. Although Gillan considered charged defects and supposed that displacements of the atoms in region II can be derived from the polarization density related to the induced charge, the calculation of the dipole and polarization tensors in metallic crystal in [87] used the condition that the atoms in elastic zone are strictly fixed in positions of appropriately strained, but defect-free lattice.

As demonstrated in [86], the strain derivative method is formally equivalent to the dipole tensor calculation with the help of equation (109), but only as long as the energy is calculated exactly. Otherwise, the strain derivative method should give better results. Indeed, equation (109) expresses the dipole tensor components in terms of the forces acting at the boundary between regions I and II. Small deviations of atomic positions in region I from the true equilibrium positions the atoms would have in an infinite crystal result in the inaccuracy of the crystal energy of the second order in these deviations, while the forces are affected already in the first order. In order to minimize the effect of the constraints imposed by fixing atoms in region II, the size of region I should be increased as much as possible, but then the forces in the region II become quite small, while the amount of surface atoms increases, which can also lead to the accumulation of inaccuracy.

The very direct way, in which the dipole tensor is calculated by strain derivative method, allows its application to defects in more complicated atomic environment than an ideal crystal. For example, dipole tensors for the saddle-point and equilibrium vacancy positions in the core of an edge dislocation in bcc iron were calculated in [88].

Using sufficiently large strains, one can determine also the nonlinear behavior of the energy as a function of strains. This allows the estimation of the higher-order polarization tensors. For example, diaelastic polarizabilties α_{ijkl} of vacancies and interstitials in copper were estimated by strain derivative method in [87].

3. PHENOMENOLOGY OF STRESS EFFECT ON DIFFUSION

3.1. From Elementary Jumps to Lattice Diffusion Equations

At the microscopic level, the description of particle diffusion is normally done in a statistical way. That is, one does not look at the trajectories of individual particles. Instead, one can consider the sites of a "lattice" consisting of all equilibrium positions of jumping particles. In some cases, this "jump lattice" can coincide with the real crystalline lattice, as is the case for diffusion of vacancies or substitutional atoms. However, the "jump lattice" can equally well be composed of a set of interstitial positions, which is quite a common case for impurity diffusion in host lattices (e.g., transition metals in silicon). Strictly speaking, in the latter case it is not even necessary that the type of the jump lattice coincides with the host one.

Therefore, in what follows, when referring to crystal lattice we always mean the "jump lattice."

In this section, we consider the simplest case of diffusion of particles of the unique type in a lattice with indistinguishable sites. Let us assume that at a certain time t and for an arbitrary lattice site indexed by some parameter $\mathbf{m}$ (we can consider $\mathbf{m}$ as, e.g., the radius-vector defining site position in some coordinate system), we know probability $\rho^{\mathbf{m}}(t)$ to find a particle in this site. Let us try to predict how big will be this probability after sufficiently small time interval Δt, assuming that the only reason for the site occupation variation is particle diffusion (in this context, "small" time means that more than one diffusion jump of a particle during this time is highly improbable). Evidently, if site $\mathbf{m}$ at time t is occupied by a particle, this particle can jump to one of the empty neighboring sites, say site $\mathbf{n}$, with probability $\lambda^{\mathbf{nm}}\Delta t$, where $\lambda^{\mathbf{nm}}$ is usually given by Arrhenius equation. On the contrary, if site $\mathbf{m}$ is not occupied, but the neighboring site is occupied, the reverse process is possible, with probability $\lambda^{\mathbf{mn}}\Delta t$. If we assume additionally that a probability to find a particle in an arbitrary site is low, so that a probability to find two particles at nearest-neighbor positions is negligible, then

$$\rho^{\mathbf{m}}(t + \lambda t) = \rho^{\mathbf{m}}(t) + \Delta t \sum_{\mathbf{n}} [\lambda^{\mathbf{mn}}\rho^{\mathbf{m}}(t) - \lambda^{\mathbf{nm}}\rho^{\mathbf{m}}(t)] \tag{110}$$

where summation is over all neighboring lattice sites accessible for a diffusion jump from site $\mathbf{m}$. Tending Δt to zero, one obtains master equation for diffusion in the form

$$\frac{\partial \rho^{\mathbf{m}}}{\partial t} = \sum_{\mathbf{n}} [\lambda^{\mathbf{mn}}\rho^{\mathbf{n}}(t) - \lambda^{\mathbf{nm}}\rho^{\mathbf{m}}(t)] \tag{111}$$

This master equation has already something in common with the diffusion equations defined in the Section 1 on purely phenomenological grounds. Indeed, here the particle distribution in space is treated probabilistically, and $\rho^{\mathbf{m}}(t)$ can be considered as particle concentration per lattice site. However, there are two important differences. First of all, transitions between neighboring positions are treated in Eq. (111) explicitly, and it contains no such phenomenological parameters as diffusion coefficient. Second, particle concentrations are specified on lattice sites and thus can attain completely uncorrelated values, while particle concentration c, entering differential Eq. (1), must be a smooth function of spatial positions. A direct consequence of these differences is the impossibility to transform equation (111) into a differential equation for general-form transition probabilities. Correspondingly, it makes little sense in the latter case to speak about diffusion coefficient (or even a diffusion coefficient tensor). However, where jump probabilities are given by standard Arrhenius relation,

$$\lambda^{\mathbf{nm}} = \nu_a \exp\left(\frac{-E_m^{\mathbf{nm}}}{k_B T}\right) \tag{112}$$

Eq. (111) can be reduced to a differential equation. Indeed, let us notice that the energy barrier for a diffusion jump, $E_m^{\mathbf{nm}}$, can be expressed as the difference between the system energies for two states, corresponding to particle in the jump saddle point and in the initial equilibrium position, that is,

$$E_m^{\mathbf{nm}} = E_s^{\mathbf{nm}} - E_f^{\mathbf{m}} \tag{113}$$

where, in contrast to the jump activation barriers, the values of system energies in saddle-point position, $E_s^{\mathbf{nm}}$, and in the equilibrium one, $E_f^{\mathbf{m}}$, can be uniquely defined only provided one specifies a common reference basis from which these energies are measured. Quite common selection of this reference energy, which will be accepted also here, is the energy of the perfect lattice in an unstrained state, in which case $E_s^{\mathbf{nm}}$ and $E_f^{\mathbf{m}}$ can be considered as the energies of particle formation in a saddle point or an equilibrium position, respectively.

Substituting (112) and (113) into (111) and introducing a renormalized concentration $w^{\mathbf{n}}$ [14],

$$w^{\mathbf{n}} = \rho^{\mathbf{n}} \exp(\beta E_f^{\mathbf{n}}) \tag{114}$$

where $\beta = 1/k_B T$, one can express the particle current between sites $\mathbf{n}$ and $\mathbf{m}$ as

$$j^{\mathbf{nm}} = \lambda^{\mathbf{nm}} \rho^{\mathbf{m}} - \lambda^{\mathbf{mn}} \rho^{\mathbf{n}} = \nu_0 e^{-\beta E_s^{\mathbf{mn}}} [w^{\mathbf{m}} - w^{\mathbf{n}}] \tag{115}$$

where we have used a common assumption that the saddle-point energy is independent of the jump direction. We can see that in terms of w, the transition is described as a difference of values of a function, which depends exclusively on site positions. At thermal equilibrium, where all particle currents vanish, the detailed balance requires

$$w^{\mathbf{m}} = \text{const} \tag{116}$$

Note that a similar condition for concentration ρ is valid only if $E_f^{\mathbf{m}}$ in all equilibrium positions is the same. It can be assumed that in the out of equilibrium conditions, where the detailed balance is no more valid, the renormalized concentration still remains a smooth function of site positions and, as such, can be approximated by a continuous function $w(\mathbf{r})$ of continuously varying space coordinates $\mathbf{r}$, which coincides in site positions with the discrete one, $w(\mathbf{r} = \mathbf{m}) = w^{\mathbf{m}}$.

The introduction of a continuous particle concentration has a direct advantage that now the difference $w^{\mathbf{m}} - w^{\mathbf{n}}$, where concentration values are defined in different spatial points, can be expressed in terms of the spatial derivatives of the concentration defined in one and the same spatial point,

$$w^{\mathbf{n}} - w^{\mathbf{m}} = w(\mathbf{r} + \mathbf{h}) - w(\mathbf{r}) \approx \mathbf{h}\nabla w(\mathbf{r}) + \frac{1}{2} h_i h_j \frac{\partial^2 w}{\partial x_i \partial x_j} + \cdots \tag{117}$$

where we have introduced the notation $\mathbf{h} = \mathbf{n} - \mathbf{m}$, while the master equation is reduced to

$$\frac{\partial \rho}{\partial t} = \mathbf{F}\nabla w + D_{kl} \frac{\partial^2 w}{\partial x_k \partial x_l} \tag{118}$$

where $\mathbf{F}$ is the drift force,

$$\mathbf{F} = \nu_0 \sum_h \mathbf{h} e^{-\beta E_s^h} \tag{119}$$

D_{kl} is the diffusion coefficient tensor,

$$D_{kl} = \frac{\nu_0}{2} \sum_h h_k h_l e^{-\beta E_s^h} \tag{120}$$

and the particle concentration $\rho(\mathbf{r})$ is a continuous representation of the on-site concentration $\rho^{\mathbf{m}}$. As discussed above, for the full time-dependent diffusion equation, this is possible only provided $E_f^{\mathbf{m}}$ can be approximated by a smooth function of spatial coordinates. However, in the case of steady-state diffusion, this additional restriction is not necessary.

As can easily be seen, the main contributions to the diffusion coefficient and the drift force are given by those jumps where the energy of the jump is the lowest one. In unstrained monatomic lattices, these jumps are normally to the first nearest neighbor positions, all having the same saddle-point energy, E_s^0. Due to the symmetry of the lattice, the drift force vanishes, while the diffusion coefficient tensor is reduced to

$$D_{kl} = D_0 \left\{ \frac{3}{N} \sum_i e_k e_l \right\} \tag{121}$$

where

$$D_0 = \frac{N}{6} \nu_0 h^2 e^{-\beta E_s^0} \tag{122}$$

N is the total number of the nearest neighbors (coordination number) of an atom in equilibrium position, h is the jump length, and summation in (121) is over all unit vectors $\mathbf{e} = \mathbf{h}/h$, connecting the equilibrium lattice position to its nearest neighbors. In the cubically symmetric lattices, which are widespread in the nature, the tensor in parentheses is reduced to the Kronecker's symbol δ_{kl}.

Under the action of external loads, the material deforms and the saddle-point energies become dependent on the particular direction of the jump. As discussed in Section 2, $E_s^{\mathbf{h}}$ can be expanded to the first order in strains as

$$E_s^{\mathbf{h}} = E_s^0 - P_{ij}^{\mathbf{h}} \varepsilon_{ij}(\mathbf{r}_s^{\mathbf{h}}) \tag{123}$$

where ε_{ij} are external strains acting in the saddle-point position of the jump. Assuming that the strains do not vary much on the length scale of one interatomic jump, it is usually possible to approximate

$$\exp(-\beta E_s^{\mathbf{h}}) \approx \exp[-\beta E_s^0 - \beta P_{ij}^{\mathbf{h}} \varepsilon_{ij}(\mathbf{r})] \left[1 + \frac{h}{2} \beta P_{ij}^{\mathbf{h}} (\mathbf{e} \nabla \varepsilon_{ij})\right]$$

where we have assumed that the saddle point is located in the middle of the diffusion jump. Substituting this relation into Eq. (118) and retaining only the terms up to the second order in h, one obtains

$$\frac{\partial \rho}{\partial t} = \tilde{\mathbf{F}} \nabla w + \frac{\partial}{\partial x_k} \tilde{D}_{kl} \frac{\partial w}{\partial x_l} \tag{124}$$

where

$$\tilde{\mathbf{F}} = \nu_0 h e^{-\beta E_s^0} \sum_{\mathbf{e}} \mathbf{e} \exp[-\beta P_{ij}^{\mathbf{h}} \varepsilon_{ij}(\mathbf{r})] \tag{125}$$

and

$$\tilde{D}_{kl} = D_0 \left\{ \frac{3}{N} \sum_{\mathbf{e}} e_k e_l \exp[-\beta P_{ij}^{\mathbf{h}} \varepsilon_{ij}(\mathbf{r})] \right\} \tag{126}$$

Normally, the force term appears only in a spatially nonuniform strain field, while in uniformly loaded material it vanishes, like in the case of unloaded crystal, for symmetry reasons. Indeed, for a jump in any direction $\mathbf{e}$, one can find another jump in the opposite direction, which should have exactly the same components of the dipole tensor. Omitting the drift term in (124), we obtain the continual diffusion equation in stress fields, first derived in [14]. For practical purposes, it is convenient to present it in a somewhat different form,

$$\tilde{D}_{ij} = D_0(\delta_{ij} + \theta_{ij}) \tag{127}$$

where the first term in the parentheses describes the isotropic part of the diffusion tensor and the second one is the correction due to the action of stresses,

$$\theta_{ij} = \frac{3}{N} \sum_{e} \left[e_i e_j \exp(-\beta P_{kl}^{\mathbf{h}} \varepsilon_{kl}(\mathbf{r})) - \frac{1}{3} \delta_{ij} \right] \tag{128}$$

The most interesting feature of the diffusion equation formulated in terms of the renormalized particle concentration is that the steady-state diffusion in strained lattice is insensitive to the effect of stress on the particle energy in equilibrium positions. The importance of this result comes from the fact that in diffusion tasks where boundary conditions can be expressed entirely in terms of the renormalized concentration (some examples are discussed in Chapters 5 and 6), only the dipole tensors in saddle-point positions of diffusion jumps play part in the kinetics of particle diffusion and capture by various sinks.

3.2. Diffusion Coefficients for Oriented Defects

Consideration in the previous section addressed the basic principles of derivation of continuous diffusion equation from atomistic considerations and, as such, treated the simplest type of particles, which are isotropic or, at least, cubically symmetric in the equilibrium positions. Particles in real lattices can be more complicated. The most important example of such particle is a dumbbell interstitial (as agreed upon in Section 1, we refer to it as an interstitialcy), which is characterized not only by the position of relevant lattice, but also by the dumbbell axis orientations. As an interstitialcy jumps from one site to another, its orientation changes [89]. In order to describe the diffusion of oriented point defects, the effect of their rotation should be included in a model, which requires generalization of the approach considered in the previous section.

Let us denote the probability to find a point defect with orientation μ in a site $\mathbf{m}$ of the lattice as $\rho_\mu^{\mathbf{m}}$. Evidently, it is sufficient to restrict our consideration to the most energetically favorable orientations. The total number of such orientations will be denoted as Z. In particular, in bcc lattice, the interstitialcies are supposed to be oriented along $\langle 110 \rangle$ directions ($Z = 6$) and in fcc along $\langle 100 \rangle (Z = 3)$ [89], as shown in Fig. 9.

The master diffusion equation that takes into account particle orientations may be written as [14]

$$\frac{\partial \rho_\mu^{\mathbf{m}}}{\partial t} = \sum_{\mathbf{n},\nu}{}' [\lambda_{\mu\nu}^{\mathbf{nm}} \rho_\nu^{\mathbf{n}} - \lambda_{\nu\mu}^{\mathbf{mn}} \rho_\mu^{\mathbf{m}}] \tag{129}$$

where $\lambda_{\mu\nu}^{\mathbf{mn}}$ is the probability of point defect transition from site $\mathbf{n}$ and orientation ν to site $\mathbf{m}$ with orientation μ. The prime over the summation sign indicates the absence of transition $\mathbf{n}\nu \to \mathbf{n}\nu$. The transition probability can be described as

$$\lambda_{\mu\nu}^{\mathbf{mn}} = \nu_0 \exp\left[-\beta E_m \begin{pmatrix} \mathbf{mn} \\ \mu\nu \end{pmatrix} \right] \tag{130}$$

where $E_{\mathbf{m}}\binom{\mathbf{mn}}{\mu\nu} = E_s\binom{\mathbf{mn}}{\mu\nu} - E_f\binom{\mathbf{n}}{\nu}$ is the migration barrier for the jump $\mathbf{n}\nu \to \mathbf{m}\mu$, $E_s\binom{\mathbf{mn}}{\mu\nu}$ is the energy of the point defect in a saddle point of the same jump, and $E_f\binom{\mathbf{n}}{\nu}$ is the energy of the point defect formation in site $\mathbf{n}$ with orientation ν (Fig. 10).

Let us reduce Eq. (129) to a differential equation. In general case, such reduction is difficult, as the sum in (129) includes transitions between different orientations of point defect in the same site (on-site rotations). However, this difficulty can be overcome in two limiting cases met in bcc and fcc lattices and corresponding, respectively, to equilibrium distribution of particles between on-site orientations and to long-range orientational memory of jumping particles.

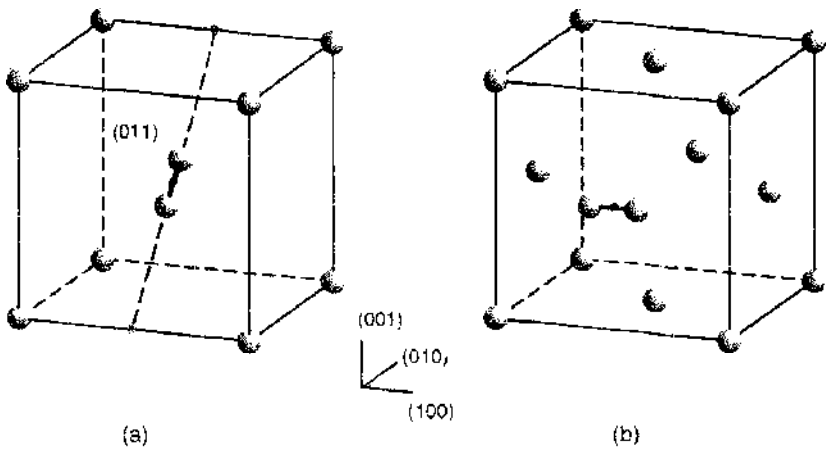

Figure 9. Orientations of interstitial dumbbells in equilibrium positions (a) in bcc lattice and (b) in fcc lattice.

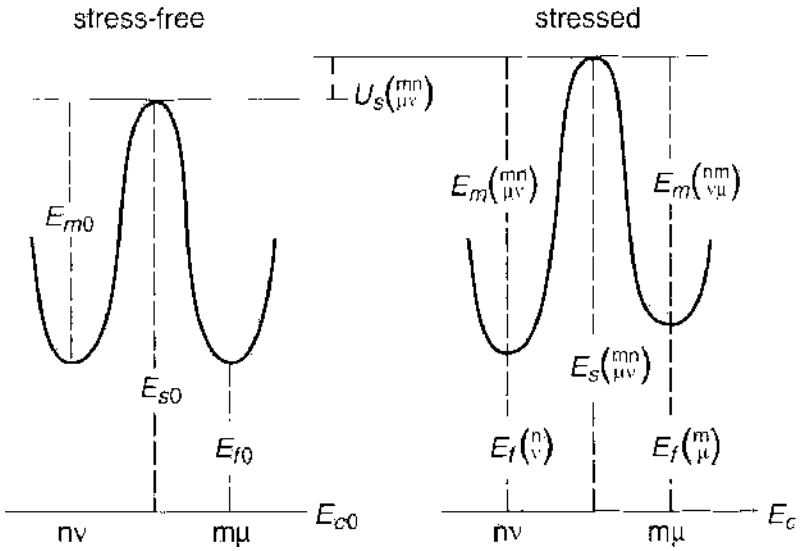

Figure 10. Energy profiles for diffusion jumps in stress-free and elastically stressed crystal. Notation for various energies is explained in text. Note that in both cases, the energies are measured from the energies of a defect-free crystal in a corresponding stress state.

3.2.1. Equilibrium Distribution of Point Defect Orientations on a Site

When the probability to find a defect on a site **m** with orientation μ is given by the thermal equilibrium distribution between orientations, we can write down

$$\rho_\mu^{\mathbf{m}} = \rho_{\mathbf{m}} \frac{\exp\left[-\beta E_f\left(\begin{smallmatrix}\mathbf{m}\\ \mu\end{smallmatrix}\right)\right]}{\sum_\mu \exp\left[-\beta E_f\left(\begin{smallmatrix}\mathbf{m}\\ \mu'\end{smallmatrix}\right)\right]} \tag{131}$$

where $\rho_{\mathbf{m}} = \sum_\mu \rho_\mu^{\mathbf{m}}$ is the overall probability to find a defect in site **m**.

Physically, this assumption means that a particle in a particular site forgets the way by which this site was reached. This situation seems to be encountered for dumbbell interstitials in bcc lattice for the following reasons. (i) The energy barrier for on-site interstitial rotation is nearly the same as that for the defect jump into the nearest neighbor site [89], and so the on-site rotation is possible. (ii) Even in the case of no on-site rotations, an interstitial can return into the same position with different orientation after several jumps. This means that after several jumps, any information about starting interstitial orientation is lost.

Master equation (129) in this case can be rewritten as

$$\frac{\partial \rho_\mu^{\mathbf{m}}}{\partial t} = \sum_{\mathbf{n}\neq\mathbf{m}} \bar{\lambda}_{\mathbf{mn}}[W_{\mathbf{n}} - W_{\mathbf{m}}] \tag{132}$$

where the averaged transition rate $\bar{\lambda}_{\mu\nu}^{mn}$ and the renormalized concentration $W_{\mathbf{m}}$ are given by

$$\bar{\lambda}_{\mathbf{mn}} = \frac{\nu_0}{Z} \sum_{\mu,\nu} \exp\left[-\beta\left(E_s\left(\begin{smallmatrix}\mathbf{mn}\\ \mu\nu\end{smallmatrix}\right) - E_f^0\right)\right] \tag{133}$$

and

$$W_{\mathbf{m}} = \frac{\rho_{\mathbf{m}}}{\sum_\mu \exp\left[-\beta E_b\left(\begin{smallmatrix}\mathbf{m}\\ \mu\end{smallmatrix}\right)\right]} \tag{134}$$

Here, $E_b\left(\begin{smallmatrix}\mathbf{m}\\ \mu\end{smallmatrix}\right) = E_f^0 - E_f\left(\begin{smallmatrix}\mathbf{m}\\ \mu\end{smallmatrix}\right)$ is the point defect binding energy at the site **m**, and E_f^0 is the energy of point defect formation in an unstressed crystal [this energy is independent both of particular site position **m** and of orientation μ (see Fig. 10)]. Note that $\bar{\lambda}_{\nu\mu}^{\mathbf{mn}} = \bar{\lambda}_{\nu\mu}^{\mathbf{mn}}$, and this equality has been taken into account when writing down Eq. (132).

Let us suppose that only the nearest-neighbor jumps are allowed, that is $\mathbf{n} - \mathbf{m} = \mathbf{h}$, where $\mathbf{h}$ is one of the vectors connecting site $\mathbf{m}$ with its nearest neighbors. Then the energy of the point defect in the saddle point of diffusional jump in direction $\mathbf{h}$ can be presented as

$$E_s\begin{pmatrix}\mathbf{mn}\\ \mu\nu\end{pmatrix} = E_s^0\begin{pmatrix}\mathbf{h}\\ \mu\nu\end{pmatrix} + U_s\begin{pmatrix}\mathbf{h}\\ \mu\nu\end{pmatrix} \tag{135}$$

where $E_s^0\left(\begin{smallmatrix}\mathbf{h}\\ \mu\nu\end{smallmatrix}\right)$ is the saddle-point energy of the point defect in the absence of external strains and $U_s\left(\begin{smallmatrix}\mathbf{h}\\ \mu\nu\end{smallmatrix}\right)$ is the energy of point defect interaction with external strains (see Fig. 10). If these strains are small, U_s can be presented as an expansion to the first order in applied strains ε_{kl} in saddle points [14]:

$$U_s\begin{pmatrix}\mathbf{h}\\ \mu\nu\end{pmatrix} = -P_{kl}^s\begin{pmatrix}\mathbf{h}\\ \mu\nu\end{pmatrix}\varepsilon_{kl}(\mathbf{r}_s) \tag{136}$$

where $P_{kl}^s\left(\begin{smallmatrix}\mathbf{h}\\ \mu\nu\end{smallmatrix}\right)$ is the dipole (force) tensor of the point defect in the saddle point of a jump, $\mathbf{r}_s$ is the radius-vector of the saddle point of the jump along $\mathbf{h}$, and the Einstein summation rule is implied (if not explicitly stated otherwise). The transition rate (133) is expressed in terms of continuously varying spatial functions ε_{kl} by using (135) and (136). If we also assume that the total probability to find a particle on-site, $\rho_{\mathbf{m}}$, and the renormalized probability, $W_{\mathbf{m}}$, can be approximated by continuous functions $c(\mathbf{r})$ and $w(\mathbf{r})$ (which can be interpreted as continuous particle concentration and renormalized concentrations, respectively), master equation (132) can be transformed into a differential equation:

$$\frac{\partial c}{\partial t} = \frac{\partial}{\partial x_i}\tilde{D}_{ij}\frac{\partial w}{\partial x_j} \tag{137}$$

where

$$\tilde{D}_{ij} = \frac{1}{2}\sum_{h} h_i h_j \Lambda(\mathbf{h}) \tag{138}$$

and

$$\Lambda(\mathbf{h}) \approx \frac{\nu_0}{Z}\sum_{\mu,\nu}\exp\left\{-\beta\left[E_m^0\begin{pmatrix}\mathbf{h}\\ \mu\nu\end{pmatrix} + U_s\begin{pmatrix}\mathbf{h}\\ \mu\nu\end{pmatrix}\right]\right\} \tag{139}$$

where $E_m^0\left(\begin{smallmatrix}\mathbf{h}\\ \mu\nu\end{smallmatrix}\right) = E_s^0\left(\begin{smallmatrix}\mathbf{h}\\ \mu\nu\end{smallmatrix}\right) - E_f^0$ is the migration barrier for the corresponding particle diffusion jump in unstrained crystal (see Fig. 10). In order to proceed a little further, we may apply the computer simulation results, showing [89] that $E_s^0\left(\begin{smallmatrix}\mathbf{h}\\ \mu\nu\end{smallmatrix}\right)$ for each particular jump direction $\mathbf{h}$ is very sensitive to the starting and final orientations ν and μ, and there always exist some pairs $\kappa = (\nu, \mu)$ with the lowest migration barrier, E_m^0, which give the main contributions to λ. Let the total number of such pairs be equal to z. Under these assumptions, Eq. (138) is reduced to

$$\tilde{D}_{ij} = D_0(\delta_{ij} + \theta_{ij}) \tag{140}$$

where $D_0 = (z\nu_0 N h^2/6Z)\exp(-\beta E_m^0)$ is the diffusion coefficient in an unstressed material, N is the coordination number, h is the distance between the neighboring sites, δ_{ij} is the Kronecker's symbol, and the anisotropy tensor θ_{ij} is given by

$$\theta_{ij} = \frac{3}{Nz}\sum_{\mathbf{e}}\sum_{\kappa=1}^{z} e_i e_j\left\{\exp\left[-\beta P_{kl}^s\begin{pmatrix}\mathbf{h}\\ \kappa\end{pmatrix}\varepsilon_{kl}\right] - 1\right\} \tag{141}$$

where $\mathbf{e} = \mathbf{h}/h$ are unit vectors directed toward nearest neighbor sites. The summation is performed over all jump directions and, for each $\mathbf{e}$, over all orientation pairs $\kappa = (\nu, \mu)$ that correspond to the lowest migration barrier E_m^0. As can easily be checked, in the absence of elastic strains, the diffusion tensor becomes isotropic, $\theta_{ij} = 0$. In the case of nonzero strains, the summation over the orientations in Eq. (141) requires additional information about the details of point defect jumps in particular crystalline lattices.

3.2.2. Long-Range Orientational Memory During Point Defect Migration

A different situation is met when no on-site rotations are allowed. This is characteristic for interstitialcies in fcc lattice, where the energy barrier for on-site rotations is higher than that for the migration jump [89]. If the orientation of an interstitialcy in a particular site is known, the orientation of this interstitialcy in any other site can be predicted unequivocally. Therefore, in the case of fcc lattice, four independent "channels" of interstitialcy diffusion exist (cf. Fig. 7 in [14]). They differ in orientations of interstitialcy in any chosen site, and these channels practically do not "mix up." As a result, for each channel, one must write its own master equation. To simplify the situation, we use the fact that the diffusion in each of these channels is physically equivalent. If we fix one (arbitrary) orientation of interstitial as a starting one for the diffusion and suppose that the diffusion channels differ in positions of starting orientation in a "primitive cell" (Fig. 11a), then the total concentration of interstitials can be presented simply as a sum of interstitial concentrations over sites of these "primitive cells." This approach is valid when point defect diffusion is treated at the length scales noticeably exceeding the size of this primitive cell.

The transformation of a one-channel master equation into a differential equation for diffusion of particles with orientational memory is less straightforward than it was in Section. 3.2.1. When a particle jumps from one site to another, its orientation changes and therefore its formation and saddle point energies change discontinuously from site to site and from jump to jump even in continuous strain fields. Consequently, neither $\rho_n^{\mathbf{m}}$, nor $\lambda_{\mu\nu}^{\mathbf{mn}}$ can be considered as continuous functions of spatial variables.

Let us assume that only the most energetically favorable configurations of dumbbell interstitials are present, namely those of the type ⟨100⟩. These orientations will be numbered 1, 2, or 3 according to the number of the coordinate axis, x_1, x_2, or x_3, along which the dumbbell axis is directed. Such interstitialcies can jump only into 8 nearest neighbor sites out of 12, and during the jump they rotate by 90° [89]. Because on-site rotations are suppressed, the fcc lattice can be considered as an overlay of four shifted simple cubic sublattices, such that in sites of each sublattice the defect orientations are the same, either along one of coordinate axes or no interstitials at all (Fig. 11b). In other words, the change of orientation during each diffusion jump can be described as a transition between different sublattices. It is convenient to number each sublattice according to the number of interstitial orientation (or zero, if the sublattice does not contain interstitials).

Let us suppose that initially an interstitial belongs to sublattice 1. If we define a renormalized probability to find point defect in site $\mathbf{m}$ of sublattice α, $W_{\mathbf{m}\alpha}$, as

$$W_{\mathbf{m}\alpha} = \rho_{\mathbf{m}\alpha} \exp\left[-\beta E_b \begin{pmatrix} \mathbf{m} \\ \alpha \end{pmatrix} \right] \tag{142}$$

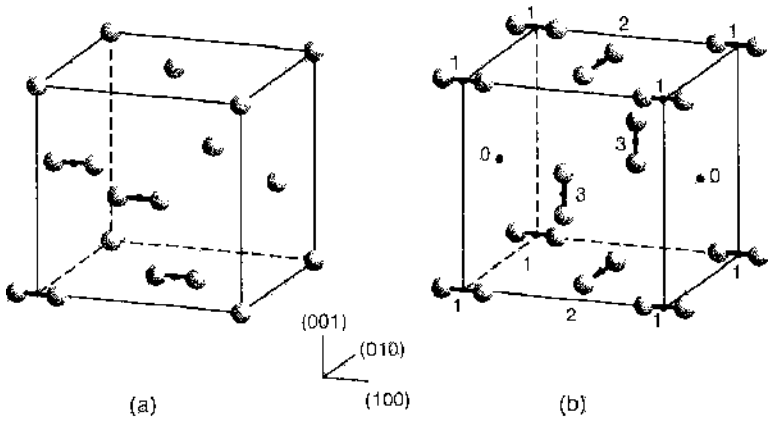

Figure 11. (a) Four nonequivalent positions for an interstitialcy with orientation [100], corresponding to four different diffusion channels in fcc lattice. (b) Orientations of interstitialcy on different sites of fcc lattice for one diffusion channel. Numbers indicate the sublattices of the fixed dumbbell orientation within the channel.

for $\alpha = 1, 2, 3$ and $W_{\mathbf{m}0} = \rho_{\mathbf{m}0} = 0$, then Eq. (129) can be rewritten as

$$\frac{\partial \rho_{\mathbf{m}1}}{\partial t} = \sum_{\mathbf{h}} {}^{13}\lambda^{\mathbf{h}}_{13}[W_{(\mathbf{m}+\mathbf{h})^3} - W_{\mathbf{m}1}] + \sum_{\mathbf{h}}{}^{12}\lambda^{\mathbf{h}}_{12}[W_{(\mathbf{m}+\mathbf{h})^2} - W_{\mathbf{m}1}] \tag{143}$$

where $\lambda^{\mathbf{h}}_{\alpha\beta} = \lambda^{\mathbf{h}}_{\beta\alpha} = \nu_0 \exp[-\beta E_{\mathbf{m}}(\overset{\mathbf{h}}{}_{\alpha\beta})]$ and the superscript $\alpha\beta$ at the summation sign implies summation over all vectors $\mathbf{h}$, relating site $\mathbf{m}$ in sublattice α to the "star" of nearest neighbor sites belonging to sublattice β.

Because all sites in each sublattice are equivalent, we may approximate $\rho_{\mathbf{m}\alpha}$ and $W_{\mathbf{m}\alpha}$ for each sublattice by continuous functions of coordinates $c_\alpha(\mathbf{r})$ and $w_\alpha(\mathbf{r})$. This allows us to transform Eq. (143) to the Fokker-Planck equation:

$$\frac{\partial c_1}{\partial t} = \frac{\partial}{\partial x_i} D^{12}_{ij} \frac{\partial w_2}{\partial x_j} + \frac{\partial}{\partial x_i} D^{13}_{ij} \frac{\partial w_3}{\partial x_j} + \Lambda^{13}(w_3 - w_1) + \Lambda^{12}(w_2 - w_1) \tag{144}$$

where $D^{\alpha\beta}_{ij}$ are partial diffusion coefficients,

$$D^{\alpha\beta}_{ij} = \frac{1}{4} D_0 \sum_{\mathbf{e}}^{\alpha\beta} e_i e_j \exp\left[-\beta U_s \left(\begin{matrix} \mathbf{e} \\ \alpha\beta \end{matrix} \right) \right] \tag{145}$$

and

$$\Lambda^{\alpha\beta} = \alpha^{-2} D_0 \sum_{\mathbf{e}}^{\alpha\beta} \exp\left[-\beta U_s \left(\begin{matrix} \mathbf{e} \\ \alpha\beta \end{matrix} \right) \right] \tag{146}$$

with $D_0 = a^2 \nu_0 \exp(-\beta E^0_m)$. Note that both $D^{\alpha\beta}_{ij} = D^{\beta\alpha}_{ij}$ and $\Lambda^{\alpha\beta} = \Lambda^{\beta\alpha}$, because the jump from orientation β to orientation α in a direction $\mathbf{e}$ should give the same contribution to sums (145) and (146) as the jump from orientation α to orientation β in the backward direction $-\mathbf{e}$, while the summation includes all vectors $\mathbf{e}$ in the same "star."

Important difference between Eqs. (143) and (144) is that in the first equation, concentrations are defined on different sublattices, whereas in the latter one they are continuously "smeared" over the whole volume of material. Repeating the same reasoning as applied to the sites in other sublattices, we obtain another pair of equations:

$$\frac{\partial c_2}{\partial t} = \frac{\partial}{\partial x_i} D^{21}_{ij} \frac{\partial w_1}{\partial x_j} + \frac{\partial}{\partial x_j} D^{23}_{ij} \frac{\partial w_3}{\partial x_j} + \Lambda^{21}(w_1 - w_2) + \Lambda^{23}(w_3 - w_2) \tag{147}$$

$$\frac{\partial c_3}{\partial t} = \frac{\partial}{\partial x_i} D^{31}_{ij} \frac{\partial w_1}{\partial x_j} + \frac{\partial}{\partial x_j} D^{32}_{ij} \frac{\partial w_2}{\partial x_j} + \Lambda^{13}(w_1 - w_3) + \Lambda^{32}(w_2 - w_3) \tag{148}$$

Thus, the diffusion in fcc lattice is described not by one diffusion equation, but by the set of three equations (144), (147), and (148). The right-hand sides of these equations include the terms corresponding to local transitions between different sublattices, as well as the contribution from long range diffusion within individual sublattices. However, these processes are important on different timescales. Indeed, the characteristic time for diffusion is of the order of L^2/D_0, where L is a characteristic distance of diffusion profile variation, whereas the characteristic time for local transitions between sublattices is $\sim a^2/D_0$. Because usually $L \gg a$, in the lowest order approximation we can omit the derivatives in these equations, thus obtaining $w_1 = w_2 = w_3$. Therefore, on the longer timescale, we can represent renormalized concentrations w_α as a sum of the average concentration,

$$w^{av} = \frac{1}{3}(w_1 + w_2 + w_3) \tag{149}$$

and small additional terms $w'_\alpha = w_\alpha - w^{av} \approx (a/L)^2 w^{av}$ that can be safely neglected for all practical purposes.

The equation for w^{av} can easily be obtained by summation of three equations for partial concentrations. The resulting equation does not contain "large" terms proportional to $\Lambda^{\alpha\beta}$,

while the second derivatives of w'_a can be neglected. Thus, on the long-term timescale, we obtain an equation

$$\frac{\partial c}{\partial t} = \frac{\partial}{\partial x_i}\widetilde{D}_{ij}\frac{\partial w^{av}}{\partial x_j} \tag{150}$$

where $c = (c_1 + c_2 + c_3)/3$ and $\widetilde{D}_{ij} = D_{ij}^{12} + D_{ij}^{23} + D_{ij}^{31}$. Equation (150) looks out very similar to (137), but there is a important difference. In the case of on-site equilibration, the particle concentration is directly proportional to renormalized concentration W, whereas in the case of long-range jump memory, this proportionality keeps only if the binding energy of an interstitial to a site does not depend on the sublattice, where it is located. If the latter condition is violated (e.g., due to the effect of nonhydrostatic stresses), the kinetics of sublattice filling should be followed using the complete set of equations. However, if only steady-state concentration distribution is of interest, there is no difference between the two limiting cases. The master equation for steady-state interstitial diffusion is reduced to the form proposed in [14], although the physical meaning of renormalized concentrations is completely different.

3.3. Diffusion Coefficients for More Complicated Lattices

Up to now, we considered diffusion on the lattice with one atom per primitive cell, which meant that all the sites were equivalent in terms of the site environments. One often meets situations when a primitive cell has more than one possible position for a diffusing defect in the primitive cell, which are not equivalent. The simplest example is diffusion of vacancies or tetrahedral interstitials on the diamond lattice, which is essentially an fcc lattice with two atoms in the basis. Neither of two basis atoms, however, is a center of inversion, and their environments are different, even though very similar from the symmetry point of view. Much more complicated situations can be met, which is the case for diffusion in complicated compounds, such as oxygen vacancy diffusion in high-temperature superconducting ceramics. When a particle can occupy several sites in an elementary cell and when these sites have essentially different geometrical and chemical environment, the analytical description of diffusion becomes quite a nontrivial task.

At present, only very limited analytical studies of diffusion on lattices with complicated primitive cells have been undertaken. For instance, diffusion in silicon (i.e., on the diamond lattice) has been considered by Daw and coauthors [90], who came to the conclusion that the diffusion coefficient introduced by Dederichs and Schroeder should be corrected in order to account for the nonequivalence of bond orientations of two basis atoms. Therefore, in this section, we briefly discuss diffusion on a nonprimitive lattice. To simplify the presentation, we restrict our consideration to a special situation of a monatomic solid with two sites in a primitive cell and the diffusing particles that have no preferred orientation in equilibrium position.

Let us define the probability to find a particle on a site with the radius vector $\mathbf{m}$ as $\rho^{|\mathbf{m}a|}$, where the location of the particle in one or another site in the primitive cell is indicated by index a (that is, $a = 1$ or 2). It is convenient to divide the whole lattice into two sublattices containing only that or other site types, so that $\rho^{|\mathbf{m}a|}$ can be alternatively referred to as the particle concentration on sublattice a. The master equations for particle concentrations on a sublattice must be of the form

$$\frac{\partial \rho^{|\mathbf{m}a|}}{\partial t} = \sum_{\mathbf{n}}[\lambda^{|\mathbf{m}a,\,\mathbf{n}b|}\rho^{|\mathbf{n}b|} - \lambda^{|\mathbf{n}b,\,\mathbf{m}a|}\rho^{|\mathbf{m}a|}] \tag{151}$$

where summation in the right-hand side is over the nearest neighbors of position $\mathbf{m}$, and $\lambda^{|\mathbf{m}a,\,\mathbf{n}b|}$ is the rate of the jumps from position $\mathbf{n}$ on sublattice b to position $\mathbf{m}$ on sublattice a. Recalling relation (112) and introducing reduced concentrations on the sublattices as

$$u^{|\mathbf{m}a|} = \frac{\rho^{|\mathbf{m}a|}}{\exp(-\beta E_f^{|\mathbf{m}a|})} \tag{152}$$

we get

$$\frac{\partial \rho^{[\mathbf{m}a]}}{\partial t} = \sum_{n} \lambda_s^{\mathbf{mn}} [w^{[\mathbf{n}b]} - w^{[\mathbf{m}a]}] \tag{153}$$

where

$$\lambda_s^{\mathbf{m}n} = \nu_0 e^{-\beta E_s^{\mathbf{mn}}} \tag{154}$$

Note that in the special case that we consider, Eqs. (153) for different sublattices are coupled, because the nearest neighbors of a site of type 1 must be sites of type 2 and *vice versa*, so that individual jumps are always between different sublattices. This fact allows us to omit the sublattice notation for $\lambda_s^{\mathbf{mn}}$. Also, we have taken into account that $\lambda_s^{\mathbf{mn}} = \lambda_s^{\mathbf{nm}}$, because the saddle-point energy is independent of the jump direction.

Difference equations (153) can be reduced to differential equations if we approximate the concentrations with continuous functions of space position $\mathbf{r}$. Very similar to the case of fcc lattice, discussed in Section 3.2, there is no *a priori* confidence that the probabilities on two sublattices can be approximated with one and the same function, but it is safe to assume that concentrations on each separate sublattice change monotonically from cell and can be approximated by continuous functions of special position ρ^a, so that $\rho^{[\mathbf{m}a]} \approx \rho^a(\mathbf{r} = \mathbf{m})$. Similarly, the reduced concentrations are also approximated with continuous functions w^a and w^b, which are defined everywhere in space. Thus it is possible to use in Eq. (153) the following Taylor expansion for concentration w^b in the point $\mathbf{n}$ on sublattice B, which is a nearest neighbor of site $\mathbf{m}$ on sublattice a:

$$w^b(\mathbf{n} \equiv \mathbf{m} + \mathbf{h}) = w^b(\mathbf{m}) + \mathbf{h}\nabla w^b(\mathbf{m}) + \frac{1}{2} \sum_{i,j=1}^{3} \frac{d^2 w^b(\mathbf{m})}{dx_i dx_j} h_i h_j + \underline{O}(h^3) \tag{155}$$

which upon substitution into (153) gives

$$\frac{\partial \rho^a}{\partial t} = \Lambda^a [w^b - w^a] + \mathbf{F}^a \nabla w^b + D_{ij}^a \frac{d^2 w^b(\mathbf{m})}{dx_i dx_j} \tag{156}$$

where

$$\Lambda^a = \sum_{\mathbf{h}^a} \lambda_s^{\mathbf{h}^a} \tag{157}$$

$$\mathbf{F}^a = \sum_{\mathbf{h}^a} \lambda_s^{\mathbf{h}^a} \mathbf{h}^a \tag{158}$$

$$D_{ij}^a = \frac{1}{2} \sum_{\mathbf{h}^a} \lambda_s^{\mathbf{h}^a} h_i^a h_j^a \tag{159}$$

and summation is over all vectors $\mathbf{h}^a$ that connect a site on sublattice a to nearest neighbor positions.

The two latter relations are very similar to those obtained for a monatomic cell lattice, Eqs. (125)–(126), with the only exception that summation in the drift force and diffusion tensor is over the star of vectors $\mathbf{h}^a$ that depends on the sublattice number. However, because all the jumps are between the opposite sublattices, for any jump in direction $\mathbf{h}^1$ from sublattice 1 to sublattice 2 one finds the jump in the reverse direction $\mathbf{h}^2 = -\mathbf{h}^1$ from sublattice 2 to sublattice 1. Because λ_s is not sensitive, whether the jump is forward or backward, this means that $\Lambda^1 = \Lambda^2 \equiv \Lambda$ and $D_{ij}^1 = D_{ij}^2 \equiv D_{ij}$, but $\mathbf{F}^1 = -\mathbf{F}^2 \equiv \mathbf{F}$.

Now, Eq. (156) represents a set of two equations, and the situation is very similar to that discussed in relation to Eqs. (144)–(148). Namely, having in mind the characteristic timescale reasoning, we can expect that the first term in the right-hand side of Eq. (156) dominates, tending to the establishing of the on-site equilibrium between two concentrations,

$$w^1 \approx w^2$$

Hence, it is convenient to introduce two new functions, that is, the total particle concentration in a primitive cell,

$$\rho = \rho^1 + \rho^2 = w^1 S^1 + w^2 S^2$$

where we have introduced brief notation $S^\alpha = \exp[-\beta E_f^\alpha(\mathbf{r})]$ and the difference $\delta w = w^2 - w^1$. The equations for these new functions will be

$$\frac{\partial \rho}{\partial t} = D_{ij}\frac{d^2 w}{dx_i dx_j} + \mathbf{F}^1 \nabla(\delta w) + D_{ij}\frac{d^2}{dx_i dx_j}\left(\frac{S^1 - S^2}{S^1 + S^2}\delta w\right) \tag{160}$$

and

$$\frac{\partial(\delta w)}{\partial t} = -\Lambda\frac{S^1 + S^2}{S^1 S^2}\delta w - 2D_{ij}\frac{d^2}{dx_i dx_j}\left(\frac{\delta w}{S^1 + S^2}\right) - \mathbf{F}^1 \nabla\left(\frac{S^1 S^2}{2S^1 S^2} w\right) + \frac{1}{2}D_{ij}\frac{d^2}{dx_i dx_j}\left(\frac{S^1 - S^2}{S^1 S^2} w\right) \tag{161}$$

where

$$w = \frac{2\rho}{S^1 + S^2}$$

Note that the temporal evolution of δw, as described by Eq. (161), is governed by the big first term in the right-hand side and occurs much faster than the change of the average cell concentration. Therefore, when we are interested in the timescales comparable to those typical for mass transfer by diffusion, the steady-state solution of Eq. (161) can be substituted into Eq. (160). Nonetheless, the spatial distribution of diffusing particles is described by two coupled equations. A certain simplification can be achieved, when the sites in the sublattices differ only in the spatial environment, but are completely equivalent with respect to defect formation energy, as is the case, for example, for vacancy diffusion on a diamond lattice. In this case, $S^1 = S^2 = S$ and the steady-state solution of Eq. (161) can be written down as

$$\delta w = -\frac{S}{2\Lambda}\mathbf{F}^1 \nabla\left(\frac{w}{S}\right) \tag{162}$$

When S is independent of the particle position, this results in the usual diffusion equation for the average cell concentration, but with the renormalized diffusion coefficient

$$D_{ij}^c = D_{ij} - \frac{F_i F_j}{2\Lambda} \tag{163}$$

which is essentially the result obtained in [90] by a method completely different from ours. In an unstrained lattice, as well as in a uniformly deformed one, $\mathbf{F} = 0$ due to the symmetry of the lattice, and hence the diffusion coefficient is given by formula (159), which is exactly the same as proposed by Dederichs and Schroeder. When the diffusion occurs in the nonuniform strain field ε, the correction is generally nonvanishing, but, being proportional to $(\nabla\varepsilon)^2$, must not be very big.

Relation (163) can be straightforwardly generalized for defects with noncubic symmetry in the equilibrium position. Such calculations can also be found in [90] for two defects in Si lattice, namely, a Si-B split interstitial and a vacancy, which is slightly noncubic in Si due to the Jahn-Teller distortion [91, 92].

3.4. Anisotropic *versus* Isotropic Description of Particle Diffusion

One of the main results of the previous section is that the most appropriate description of steady-state diffusion involves the use of renormalized concentration. In this case, steady-state diffusion depends only on the particle dipole tensors in saddle points of diffusion jumps

and not on those in equilibrium positions. However, it is quite a common practice in the literature to calculate defect currents to sinks (either spherical, such as voids [93–96], or linear, such as dislocations [97, 98]) using the energy parameters of defects located in equilibrium positions. Therefore, it makes sense to discuss the correlation between two approaches.

In order to proceed to standard equations employed for the description of diffusion in strain fields, it is sufficient to make two assumptions: (i) particles are isotropic dilatation centers both in equilibrium and in saddle point positions, and (ii) The relaxation volumes of particles in saddle point positions are the same as in equilibrium positions.

If we accept assumption (i), the equation relating the normal particle concentration c to the renormalized concentration w [either Eq. (134) or (142)] can be rewritten as

$$w = c\exp(\beta U_c) \tag{164}$$

where U_c is the elastic energy of a particle in equilibrium position. Similar to (136), this elastic energy can be written out as

$$U_c = -P_{kl}^c \varepsilon_{kl} \tag{165}$$

Having in mind that for an isotropic dilatation center

$$P_{kl}^c = P_0^c \delta_{kl} = K\Delta V^c \delta_{kl} \tag{166}$$

where P_0^c is the unique value characterizing the magnitude of the force tensor, K is the bulk modulus of material, and $\Delta V^c \equiv P_0^c/K$ is the point defect relaxation volume in equilibrium position, we obtain

$$U_c = -K\Delta V^c \varepsilon \tag{167}$$

where ε is the trace (hydrostatic part) of the strain tensor. If point defect anisotropy in the saddle point is neglected, Eq. (136) for U_s is reduced to the same form, with the saddle point relaxation volume $\Delta V^s \equiv \mathrm{Tr}(P_{kl}^s)/3K$ instead of ΔV^e.

The steady-state diffusion equation for concentration c is then

$$\frac{\delta}{dx_i} D_{ij}\left(\frac{\partial c}{dx_j} + \beta c \frac{\delta U_c}{dx_j}\right) = 0 \tag{168}$$

with

$$D_{ij} = D_{0i}\delta_{ij}\exp[\beta K(\Delta V_s - \Delta V_c)] \tag{169}$$

If assumption (ii) is now used in addition to assumption (i), the exponential in the right-hand side of Eq. (169) becomes equal to unity and (168) is reduced to the equation:

$$\mathrm{div}(\nabla c + \beta c \nabla U_c) = 0 \tag{170}$$

which is the diffusion equation employed in the cases, when no account of saddle point energy variations on the particle diffusion is taken.

As far as the validity of the simplifying assumptions is concerned, the weakest point is the assumption (i) for diffusing particle configuration in saddle points. As we had chance to see in Section 2, in saddle points the dipole tensors are anisotropic even for such defects as vacancies, whose equilibrium configurations can safely be considered as dilatation centers. For more complicated configurations, such as dumbbell interstitials, assumption (i) is invalid even in equilibrium positions, though to a certain extent its use can be justified, if equilibrium between different on-site orientations of interstitials is established. For example, in bcc lattices the thermal equilibrium is a reasonable assumption, whereas in fcc lattices local equilibrium between different sublattices in each diffusion channel can be adopted.

Assumption (ii), even though not at all evident, in many cases is a good approximation, as relaxation volumes of point defects in the saddle point and in the equilibrium position are indeed nearly equal [95]. However, in some cases this assumption can be completely

Table 2. The ratio $\Delta V_s/\Delta V_e$ for vacancies and interstitials, as calculated from the simulation results of [82].

	Cu	α-Fe
Vacancy	−24.0	1.03
Interstitial	1.02	1.11

misleading. As one can judge from Table 2, with the only exception of vacancies in copper, the ratio $\Delta V_s/\Delta V_e$ is close to unity, but for vacancies in copper it is not only much larger than unity, but has the negative sign (i.e., vacancy in the saddle point expands the lattice). It is interesting that the latter conclusion is obtained in two completely independent simulations [82, 87].

4. DIFFUSION COEFFICIENT IN STRAINED LATTICES

4.1. Diffusion Coefficient for Small Strains

Diffusion coefficient tensor defined by Eq. (138) depends on the strains in quite a complicated way. However, when the strains are sufficiently small, one can expand the anisotropy tensor to the first order in strains,

$$\theta_{ij} = \tilde{d}_{ijkl}\varepsilon_{kl} \tag{171}$$

where coefficients $\tilde{d}_{ijkl}$ constitute a fourth-order tensor that couples diffusion tensor with the strain tensor. The product $D_0\tilde{d}_{ijkl}$ is usually referred to as "elastodiffusion" tensor. An analytical expression for the coupling tensor can readily be derived from (141), but first let us briefly discuss what do we understand under small strains.

The strains acting at the length scales comparable to interatomic distances are always small as compared to unity, being limited by the values of $\varepsilon \sim 0.1$, corresponding to the theoretical strength limit of $\sim 0.1G$, where G is the material's shear modulus. In fact, when a metal sample is subjected to the action of external loads, the resulting elastic strains do not reach such high values, because of the plastic yield which limits the typical stresses by the level of the yield stress, which corresponds to elastic strains below 10^{-3}. (Naturally, plastic strains can be quite high, but plastic deformation occurs on length scales much bigger than the interatomic distances and do not directly affect the diffusion coefficients in the bulk of the material.) Because the typical values of the dipole tensor components are of the order of 10 eV [89], the migration energy corrections for such strain fields do not exceed 0.01 eV (or, in units of temperature, ~100 K). Experiments, where diffusion in solids occurs efficiently, require usually the temperatures much above this, so that the exponentials in (141) can be reasonably well represented by the first-order expansions in strains.

However, strain fields around internal stress concentrators act at nanometer length scales (i.e., not much larger then the interatomic distance). These local strain fields can noticeably exceed the limits posed by plastic relaxation requirements, especially very close to sinks, because they can not be eliminated by plastic flow due to the lack of plastic flow "carriers" at such length scales. Thus, the limits of elastic deformation at nanometer length scales are given only by the theoretical material strength. It can easily be checked that with the above mentioned values of the dipole tensor components, the stress-induced corrections can be comparable with the migration energies themselves. Correspondingly, it makes little sense to expand exponentials in (141) and the diffusion anisotropy tensor should be calculated exactly, possibly even including higher order terms in the migration energy expansion in strains, as discussed in Section 2.

Summing up, by small strains we will mean such strains that allow the expansion of the exponentials in (141) to the first order in strains. A particular value of the upper limit for small strains depends, naturally, on the particular material and the experimental temperature, but as a rule of thumb, the above-mentioned value of 0.1% will do quite well.

After the expansion the forth-order diffusion-stress coupling tensor is obtained in the form:

$$\tilde{d}_{ijkl} = \frac{3\beta}{N} \sum_{\mathbf{e}} e_i e_j \overline{P}^s_{kl}(\mathbf{e}) \tag{172}$$

where $\overline{P}^s_{kl}$ is the average of a dipole tensor for a jump along direction e over possible pairs of initial and final defect orientations,

$$\overline{P}^s_{kl}(\mathbf{e}) = \frac{1}{z} \sum_{\kappa=1}^{z} P^s_{kl}\begin{pmatrix}\mathbf{h}\\ \kappa\end{pmatrix} \tag{173}$$

Particular values of $\tilde{d}_{ijkl}$ can be determined only provided the geometry of the jump "star" in a particular material is known. The only positive statement that can be deduced from the explicit relation for $\tilde{d}_{ijkl}$ is that this tensor is symmetric with respect to exchange of indexes inside the first and the second index pairs, and thus in a general case it has only 36 independent components. A general representation of such tensor can be written down as a linear combination of the pair-wise products of six basic symmetric second-order tensors $\hat{\mathbf{b}}^{(k)}$, which are orthonormalized in the sense that

$$\sum_{i,j=1}^{3} \hat{b}^{(\alpha)}_{ij} \hat{b}^{(\beta)}_{ij} = \delta_{\alpha\beta} \tag{174}$$

A possible matrix representation for these tensors is

$$\begin{gathered}
\hat{\mathbf{b}}^{(1)} = \begin{pmatrix} 1 & 0 & 0 \\ 0 & 0 & 0 \\ 0 & 0 & 0 \end{pmatrix}; \quad \hat{\mathbf{b}}^{(2)} = \begin{pmatrix} 0 & 0 & 0 \\ 0 & 1 & 0 \\ 0 & 0 & 0 \end{pmatrix}; \quad \hat{\mathbf{b}}^{(3)} = \begin{pmatrix} 0 & 0 & 0 \\ 0 & 0 & 0 \\ 0 & 0 & 1 \end{pmatrix}; \\
\hat{\mathbf{b}}^{(4)} = \frac{1}{\sqrt{2}} \begin{pmatrix} 0 & 1 & 0 \\ 1 & 0 & 0 \\ 0 & 0 & 0 \end{pmatrix}; \quad \hat{\mathbf{b}}^{(5)} = \frac{1}{\sqrt{2}} \begin{pmatrix} 0 & 0 & 1 \\ 0 & 0 & 0 \\ 1 & 0 & 0 \end{pmatrix}; \quad \hat{\mathbf{b}}^{(6)} = \frac{1}{\sqrt{2}} \begin{pmatrix} 0 & 0 & 0 \\ 0 & 0 & 1 \\ 0 & 1 & 0 \end{pmatrix}
\end{gathered} \tag{175}$$

but other choices of basic tensors are possible as well (see, e.g., [14]). Using these basic tensors, the elastodiffusion tensor can be presented as

$$\tilde{d}_{ijkl} = \sum_{\alpha=1}^{6} \sum_{\beta=1}^{6} d^{(\alpha\beta)} \hat{b}^{(\alpha)}_{ij} \hat{b}^{(\beta)}_{kl} \tag{176}$$

with the elastodiffusion tensor eigenvalues $d^{(\alpha\beta)}$ being given by

$$d^{(\alpha\beta)} = \frac{3\beta}{Nz} \sum_{\mathbf{e}} \sum_{\kappa=1}^{z} \left\{ \sum_{i,j=1}^{3} \hat{b}^{(\alpha)}_{ij} e_i e_j \right\} \left\{ \sum_{k,l=1}^{3} \hat{b}^{(\beta)}_{kl} P^s_{kl}\begin{pmatrix} h \\ \kappa \end{pmatrix} \right\} \tag{177}$$

The number of independent constants can be noticeably reduced when lattice symmetry is explicitly taken into account. Below we will restrict our discussion with highly symmetric cubic lattices, first of all because it will suffice for demonstration how the coupling tensor is evaluated, and, second, because the very limited at present numerical data allowing to perform calculations "up to numbers" is available only for lattices with this symmetry.

In lattices with cubic symmetry, $\tilde{d}_{ijkl}$ must remain invariant with respect to a cyclic exchange of coordinate axis indices ($1 \to 2 \to 3 \to 1$). The set of basic matrices can than be subdivided into two subsets (matrices 1 to 3 and matrices 4 to 6), which transform through each other. In terms of tensor eigenvalues, this leaves only three essentially different values: $d^{(11)}$, $d^{(12)}$ and $d^{(44)}$, which can be expressed in terms of saddle-point dipole tensors as

$$d^{(11)} = \frac{\beta}{N} \sum_{\mathbf{e}} \left[e_1^2 \overline{P}^s_{11}(\mathbf{e}) + e_2^2 \overline{P}^s_{22}(\mathbf{e}) + e_3^2 \overline{P}^s_{33}(\mathbf{e}) \right] \tag{178}$$

$$d^{(12)} = \frac{1}{2}(\beta \overline{P}^s - d^{(11)}) \tag{179}$$

and

$$d^{(44)} = \frac{2\beta}{N}\sum_{\mathbf{e}}\left[e_1e_2\overline{P}^s_{12}(\mathbf{e}) + e_2e_3\overline{P}^s_{23}(\mathbf{e}) + e_3e_1\overline{P}^s_{31}(\mathbf{e})\right] \tag{180}$$

where $\overline{P}^s$ is the trace of the average saddle-point dipole tensor (173) for an arbitrary jump direction.

In the "crystallographic" coordinate system, where the Cartesian axes coincide with the cubic symmetry axes, the elastodiffusion tensor can be presented in a simple form, using Kronecker's symbols:

$$\tilde{d}_{ijkl} = \tilde{d}^{(1)}\delta_{ij}\delta_{kl} + \frac{1}{2}\tilde{d}^{(2)}(\delta_{ik}\delta_{jl} + \delta_{jk}\delta_{il}) + \tilde{d}^{(3)}\delta_{ij}\delta_{ik}\delta_{jl} \tag{181}$$

where $\tilde{d}^1 = d^{(12)}$, $\tilde{d}^{(2)} = 2d^{(44)}$, $\tilde{d}^{(3)} = d^{(11)} - d^{(12)} - 2d^{(44)}$ and no summation over repeated indices in this equation is implied. Equation (171) is also simplified to

$$\theta_{ij} = \tilde{d}^{(1)}\varepsilon\delta_{ij} + \tilde{d}^{(2)}\varepsilon_{ij} + \tilde{d}^{(3)}\varepsilon_{ij}\delta_{ij} \tag{182}$$

The first term contributes to the isotropic part of the diffusion tensor, while the second and the third terms depend on the local strain. Note that due to the presence of the third term in the r.h.s. of Eq. (182), its functional form is not retained in a coordinate system rotated with respect to the crystallographic one. Hence, due to this term there arises an interrelation between the lattice symmetry and the strain tensor symmetry.

Let us derive the explicit relations between the coefficients $\tilde{d}^{(k)}$ $(k = 1, 2, 3)$ and dipole tensors for different symmetries of jumping particles in the saddle points. Evidently, the simplest case is met when the particle has no preferred orientation in equilibrium position and retains complete cubic symmetry in saddle point position, so that $\overline{P}^s_{ij} = (\overline{P}^s/3)\delta_{ij}$. In this case, the only nonvanishing coefficient is $\tilde{d}^{(1)} = \beta\overline{P}^s/3$. However, in real life it is hard to imagine a situation where a particle in a saddle point would retain cubic symmetry. So let us consider more realistic cases. We restrict ourselves to monatomic lattices and first discuss a case of a nonoriented defect. A typical situation of this kind is vacancy diffusion in pure metals. After that, we will see how big a difference is for an oriented defect, such as a dumbbell self-interstitial.

4.2. Elastodiffusion Tensors in Cubic Lattices

4.2.1. Vacancies (Nonoriented Defects)

Vacancies are not oriented defects, and hence the stress-free diffusion coefficient in all cases considered below is given by $D_{0V} = \nu_0 a^2 \exp(-E^0_{mV})$. So, in order to completely specify the elastodiffusion tensors, it remains to express the factors $\tilde{d}^{(k)}$ in Eq. (181) in terms of dipole tensors in particular lattices.

4.2.1.1. Simple Cubic Lattice In a simple cubic lattice, a vacancy can jump into $N = 6$ equivalent positions in directions of type $\langle 100\rangle$. The jump distance is exactly equal to the lattice period a. From symmetry considerations, the vacancy in saddle point should have tetragonal symmetry, that is its dipole tensor has only two different nonzero components and can be written down as (to be specific, for the jump along x-axis)

$$\mathbf{P}^s([100]) = \begin{pmatrix} P_{11} & 0 & 0 \\ 0 & P_{22} & 0 \\ 0 & 0 & P_{22} \end{pmatrix} \tag{183}$$

So, the factors in equation (181) are reduced to $\tilde{d}^{(1)} = \beta P_{22}$, $\tilde{d}^{(2)} = \beta(P_{11} - P_{22})$, and $\tilde{d}^{(3)} = 0$.

No numerical estimates are available for this simple case of cubic lattice, because monatomic crystals practically never have such symmetry. So, the simple cubic lattice is discussed mainly for illustrative purposes.

4.2.1.2. BCC Lattice In a bcc lattice, point defects jump to the nearest neighbor sites located in ⟨111⟩-type directions. The number of nearest neighbors is $N = 8$, and the distance to them is $h = a\sqrt{3}/2$. According to the symmetry considerations, confirmed by calculations in [82], vacancies in the saddle point (assumed to be in the middle of the jump) have trigonal symmetry. In other words the dipole tensor has two independent components,

$$\mathbf{P}^s = \begin{pmatrix} P_{11} & P_{12} & P_{12} \\ P_{12} & P_{11} & P_{12} \\ P_{12} & P_{12} & P_{11} \end{pmatrix} \tag{184}$$

Numerical values of these components for α-iron are given in Table 3.

The factors in Eq. (181) are given by

$$\tilde{d}^{(1)} = \beta P_{11}, \quad \tilde{d}^{(2)} = 2\beta P_{12}, \quad \tilde{d}^{(3)} = -2\beta P_{12} \tag{185}$$

4.2.1.3. FCC Lattice In fcc lattice, point defects jump into the nearest neighbor sites located in the ⟨110⟩-type directions. The number of nearest neighbors $N = 12$, the distance to them is $h = a/\sqrt{2}$.

Vacancies in fcc lattice have the orthorhombic symmetry of saddle point, which results (for the jump direction [110]) in the dipole tensor of the form

$$\mathbf{P}^s = \begin{pmatrix} P_{11} & P_{12} & 0 \\ P_{12} & P_{11} & 0 \\ 0 & 0 & P_{33} \end{pmatrix} \tag{186}$$

The values of $\tilde{d}^{(k)}$ are

$$\tilde{d}^{(1)} = \frac{1}{2}\beta(P_{11} + P_{33}), \quad \tilde{d}^{(2)} = \beta P_{12}, \quad \tilde{d}^{(3)} = \frac{1}{2}\beta(P_{11} - P_{33} - 2P_{11}) \tag{187}$$

Numerical values of P_{kl} for copper are given in Table 4. The most remarkable result of computer simulations, obtained consistently in two independent calculations [82, 87], is the prediction that vacancy in a saddle point has a positive relaxation volume.

4.2.2. Dumbbell Interstitials (Oriented Defects)

As already mentioned, there are no monatomic simple cubic lattices, and hence it is hard to imagine what might be preferable interstitial orientations in such a lattice. Therefore, we come directly to more realistic lattices.

4.2.2.1. BCC Lattice According to [82], the most energetically favorable configuration of an interstitialcy in bcc lattice is ⟨110⟩ dumbbell. For this configuration, the total number of starting orientations for a diffusion jump is $Z = 6$, but the jumps to any one neighboring site are possible only from three of them. In turn, each possible starting configuration can result in two final configurations, so that $z = 6$. Let us calculate first the averaged dipole tensor $\overline{P}^s_{kl}$ for a jump in the direction $\mathbf{e} = (1/\sqrt{3})[111]$, which is the average value of dipole tensors at the saddle points over all lowest barrier jumps in this direction. For all other jump directions, $\overline{P}^s_{kl}$ can be obtained by rotation of the coordinate system.

The trajectories of all six possible jumps in the selected direction can be transformed one into another by cubic symmetry coordinate transformations. Therefore, the components of the dipole tensor for each particular jump can be expressed in terms of components of

Table 3. The components of the averaged dipole tensors in α-Fe, estimated using numerical values of individual point defect jumps from [82].

	P_{11}	P_{12}
Vacancy	−3.2 eV	−1.4 eV
Interstitial	18.7 eV	5.6 eV

Table 4. The components of the averaged dipole tensors in Cu, estimated based on numerical values of individual point defect jumps from [82].

	P_{11}	P_{33}	P_{12}
Vacancy	−0.5 eV	5.8 eV	−1.0 eV
Interstitial	14.7 eV	15.8 eV	3.0 eV

a dipole tensor p^{κ}_{kl} for an arbitrary reference jump κ. Summation of these dipole tensors gives the averaged dipole tensor, which has trigonal symmetry, as given by Eq. (184), with $P_{11} = \mathrm{Tr}(p^{\kappa}_{kl})/3$ and $P_{12} = (p^{\kappa}_{12} + p^{\kappa}_{23} + p^{\kappa}_{31})$ [15]. Corresponding values for α-iron are given in Table 3. It is interesting to note that dipole tensors p^{κ}_{kl} for each individual jump have the symmetry lower than trigonal (cf. [82]), so that the averaging over possible pairs of starting and final orientations increases the symmetry of the saddle point dipole tensor. In fact, interstitials behave in the average just like vacancies. Consequently, the expressions for factors entering Eq. (181) are of the same form as those for vacancies.

4.2.2.2. FCC Lattice In fcc lattice, the most energetically favorable orientation of a self-interstitial dumbbell is ⟨100⟩, while the jumps occur in ⟨110⟩ directions and are accompanied by interstitialcy rotation by 90°. Correspondingly, the number of initial jump orientations is $Z = 3$, but for any particular jump direction only two of them can contribute to the jump, and the final dumbbell orientation is uniquely determined by the initial orientation (i.e., $z = 2$).

Let us select the jump in direction [110] with the starting orientation $\nu = [100]$ and the final orientation $\mu = [010]$ as a reference and let us denote corresponding saddle-point dipole tensor as p^{κ}_{kl}. The symmetry of the jump requires $p^{\kappa}_{11} = p^{\kappa}_{22}$ and $p^{\kappa}_{13} = p^{\kappa}_{23} = 0$. Summation of the dipole tensors for all possible jump directions gives the averaged dipole tensor in the form of Eq. (186) with $P_{11} = p^{\kappa}_{11}$, $P_{33} = p^{\kappa}_{33}$ and $P_{12} = p^{\kappa}_{12}$ [15], that is the orthorhombic symmetry of the averaged dipole tensor is the same as that of an individual interstitialcy. Numerical values of the components of the averaged dipole tensor are given in Table 4.

Expressions for $\bar{d}^{(k)}$ are the same as for vacancies [see Eq. (187)], but the stress-free diffusion coefficient has a different pre-exponential factor $D_{0l} = (2\nu_0 a^2/3)\exp(-\beta E^0_{ml})$.

4.3. Medium Strains

The expansion of exponents in the r.h.s. of Eq. (143) to the first order in strains is justified when the interaction of point defects with the strain field is "weak," in the sense that $\beta U^{\kappa}_s \ll 1$ everywhere in the matrix. This simplification allows straightforward analytical treatment of the diffusion problem. For example, the "weak strain" approximation was used for the calculation of diffusion profile of particles near sinks that create in their vicinity elastic fields [14, 15, 99, 100].

Unfortunately, one can meet situations, where some particle sinks are very efficient stress concentrations. Two examples of such sinks are edge dislocations and crack tips in loaded materials. It can be easily checked that, for example, in the vicinity of the dislocation core the elastic interaction is "strong" ($\beta U^{\kappa}_s \gg 1$). Indeed, let us present the elastic correction to the saddle point energy for a jump in direction e with initial and final orientation pair κ in the form

$$U^{\kappa}_s = -\overline{P}^s[\varepsilon + p^{\kappa}_{kl}\varepsilon_{kl}] \tag{188}$$

where $p^{\kappa}_{kl} = \left[P^s_{kl}(\overset{e}{k}) - \overline{P}^s\delta_{kl}\right]/\overline{P}^s$ is the normalized deviatoric part of the dipole tensor. The hydrostatic part of the elastic interaction energy, $U^0_s = \overline{P}^s\varepsilon$, in the vicinity of an edge dislocation can be written down in the form

$$\beta U^0_s = \frac{R_s}{r}\sin\phi \tag{189}$$

where r is the distance from the particle to the dislocation, ϕ is the polar angle measured from the dislocation glide plane, and the well-known expression for the trace of strain tensor

near a dislocation [10] is substituted. The effective radius of the particle interaction with dislocation, R_s, is given by

$$R_s = \frac{(1-2\nu_E)\overline{P}^s}{2\pi(1-\nu_E)k_BT}b \tag{190}$$

where b is the value of dislocation Burgers vector, and ν_E is the Poisson ratio. Numerical estimates of these effective radii for interstitials (R_{si}) and vacancies (R_{sv}) in copper and α-iron at 750 K are given in Table 5. Because dislocation core radius is normally of the order of 2–3b, close to dislocation core one gets $R_s/b > 1$, so that the elastic interaction is rather "strong" than "weak."

We thus see that in order to determine the distribution of point defects in the vicinity of a dislocation, a straightforward expansion of the diffusion coefficient into a series in powers of strains cannot be justified. On the other hand, for the anisotropic diffusion coefficient keeping the strains in the exponentials, it is practically impossible to find in an analytical form either the concentration distribution around dislocation or the particle currents to it. In order to circumvent this difficulty, one can notice that although the ratio R_s/r near the dislocation core exceeds unity, it still remains comparable to it even in the case of interstitialcies. Hence, one can apply an approach [101] prompted by the particular form of dipole tensors that are dominated by relatively little varying diagonal components, while the components of the deviatoric dipole tensor are noticeably lower than $\overline{P}^s$. Hence, having in mind that the hydrostatic energy $U_s^{(1)}$ is independent of either the jump direction $\mathbf{e}$ or jump configuration κ, one can approximate the diffusion coefficient as [102]

$$D_{ij} = D_0 \exp(-\beta U_s^{(1)})(\delta_{ij} + \beta\overline{P}^s d'_{ijkl}\varepsilon_{kl}) \tag{191}$$

where

$$d'_{ijkl} = \frac{3}{zN}\sum_{\mathbf{e}}\sum_{\kappa=1}^{z} e_i e_j p_{kl}^{\kappa}(\mathbf{e}) \tag{192}$$

Tensor d'_{ijkl} is an analogue of $\tilde{d}_{ijkl}$ introduced by Eq. (172) in the case of small strains. In a cubic lattice, d'_{ijkl} has only three independent components. In a Cartesian coordinate system oriented along the principal crystallographic axes, it can be presented by an expansion in the form of (181). Numerical estimates of three independent coefficients $d'^{(k)}$ in this expansion are given in Tables 6 and 7. It can be seen that in copper the values of $d'^{(k)}$ are noticeably less than unity and nicely compensate for the relatively large strains near the dislocation core. In the case of iron, the compensation is tolerable only for the vacancy, while for interstitialcies approximation (191) remains rather poor. Nonetheless, even in the latter case, the expansion (191) remains valid at distances noticeably closer to the dislocation core, than in case of expansion (171), and it retains exponential dependence on the hydrostatic part of the elastic interaction energy. The retention of this dependence is essential, when one is interested in calculation of point defect currents to dislocations [102].

4.4. Large Strains

In case when particles move in regions of high stresses, it is essential for the correct determination of point defect currents to use diffusion coefficients in their original form (141). In this case, only numerical solution of diffusion equation is possible. Such an approach has been applied [103] for calculation of point defect and impurity distribution close to the tip

Table 5. Numerical estimates of effective interaction radii for vacancies and interstitialcies in α-iron and copper, using the dipole tensor values calculated in [82].

	α-Fe	Cu
R_{sv}	$5b$	$2b$
R_{si}	$27b$	$20b$

Table 6. Numerical estimates of $d^r(k)$ for α-iron, using computer-evaluated values of dipole tensors from [82].

	$d^{(1)}$	$d^{(2)}$	$d^{(3)}$
Vacancies	0	0.88	−0.88
Interstitials	0	0.6	−0.6

of a crack in an externally loaded material. Some examples of the predicted distributions are shown in Fig. 12.

The only simplification in particular lattices can be achieved by summation over different jump directions and by direct employment of the lattice symmetry. In examples below, we discuss vacancy diffusion coefficients, but the same reasoning holds true for any nonoriented defect.

4.4.1. Simple Cubic Lattice In a simple cubic lattice, a vacancy can jump into $N = 6$ equivalent positions along directions of type $\langle 100 \rangle$ and the dipole tensor has tetragonal symmetry, given by Eq. (183). In "crystallographic" coordinate system, the diffusion tensor is described by a simple relation

$$D_{ij} = D_0 \delta_{ij} \exp(\beta P^s_{22} \varepsilon + \beta (P^s_{11} - P^s_{22}) \varepsilon_{ij}) \tag{193}$$

4.4.2. BCC Lattice In BCC lattice, a vacancy can jump into $N = 8$ equivalent positions along directions of type $\langle 111 \rangle$ and the dipole tensor has trigonal symmetry, Eq. (184). The anisotropic diffusion tensor is given by

$$\begin{aligned} D_{ij} = D_0 \exp(\beta P^s_{11} \varepsilon) [\Phi^c_{ij} \cosh(2P^s_{12} \varepsilon_{12}) \cosh(2P^s_{12} \varepsilon_{13}) \cosh(2P^s_{12} \varepsilon_{23}) \\ + \Phi^s_{ij} \sinh(2P^s_{12} \varepsilon_{12}) \sinh(2P^s_{12} \varepsilon_{13}) \sinh(2P^s_{12} \varepsilon_{23})] \end{aligned} \tag{194}$$

where for the diagonal components

$$\Phi^c_{ij} = \Phi^s_{ij} = 1$$

while for the nondiagonal ones

$$\Phi^c_{ij} = \tanh(2P^s_{12} \varepsilon_{ij}) \quad \text{and} \quad \Phi^s_{ij} = \frac{1}{\tanh(2P^s_{12} \varepsilon_{ij})}$$

4.4.3. FCC Lattice In FCC lattice, vacancies jump into $N = 12$ nearest neighbor positions located along $\langle 110 \rangle$ directions and the dipole tensor has orthorhombic symmetry, Eq. (186). The diagonal components of the anisotropic diffusion tensor look out like

$$D_{ii} = \frac{1}{2} D_0 e^{\beta P^s_{11} \varepsilon} \{ e^{\beta (P^s_{33} - P^s_{11}) \varepsilon_{kk}} \cosh(P^s_{12} \varepsilon_{ik}) + e^{\beta (P^s_{33} - P^s_{11}) \varepsilon_{il}} \cosh(P^s_{12} \varepsilon_{il}) \} \tag{195}$$

where $i \neq k \neq l$ and no summation over repeated indices is implied. For nondiagonal components, one obtains

$$D_{ik} = \frac{1}{2} D_0 e^{\beta P^s_{11} \varepsilon + \beta (P^s_{33} - P^s_{11}) \varepsilon_{il}} \sinh(2P^s_{12} \varepsilon_{ik}) \tag{196}$$

where again $i \neq k \neq l$.

Table 7. Numerical estimates of $d^r(k)$ for copper, using computer-evaluated values of dipole tensors from [87].

	$d^{(1)}$	$d^{(2)}$	$d^{(3)}$
Vacancies	0.4	- 0.35	−0.85
Interstitials	0.01	0.13	−0.16

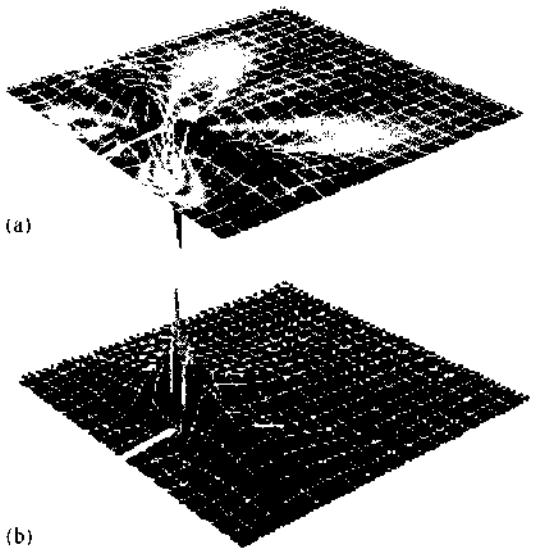

Figure 12. Impurity concentration profiles near the crack tip in bcc iron: (a) carbon at 300°C, (b) hydrogen at 20–50°C. In both cases, impurity equilibrium positions are in octahedral interstitial sites.

5. FROM CONTINUOUS DIFFUSION EQUATION TO CHEMICAL RATE EQUATIONS

5.1. Diffusion in a Medium with Particle Sinks

Diffusion equations considered up to now were derived from particle conservation equation (1), which takes into account only the diffusion of particles. As such, they do not treat either generation or loss of these particles inside the volume of the solid. Any steady-state distributions of particle concentration arise only due to concentration differences at external and/or internal surfaces of the solid. In real life, such situations are met mostly in experiments specially tailored for the measurement of diffusion transport rates of impurities in solids.

In applications, one often meets situations when diffusing particles are created, captured by internal sinks, and interact with other particles, nucleating various particle complexes. This is a common situation, when one deals with analytical description of the microstructure evolution in irradiated or implanted materials, where the sinks for implanted particles and/or generated self-point defects arise as a result of defect clustering into voids, dislocation loops, and secondary-phase particles. In order to describe such situations, one should consider modification of diffusion equations.

The simplest modification is required in order to account for particle creation. The necessity to include particle creation arises, for example, when one studies redistribution of impurity in samples during ion implantation, or the kinetics of point defects generated by neutron and fast particle irradiation. It can be done very straightforwardly, replacing (1) with

$$\frac{\partial c}{\partial t} + \operatorname{div} \mathbf{j} = K \tag{197}$$

where K is the rate of particle creation per unit time (and per unit lattice atom, when such concentration normalization is used). Here, K can depend on both the time and the spatial position, and normally the creation or implantation of particles is in no way related to their subsequent diffusional redistribution. For example, for the case of ion implantation, the rate of point defect creation can be calculated using specially adopted programs, such as SRIM [104].

Much more problems are met when one has to describe diffusion in a solid containing a system of sinks. By sinks of particles, we mean those regions in the material that can capture diffusing defects at their surfaces. All sinks can be classified as (see Fig. 13):

- Local sinks, whose largest size is much less than some characteristic length scale in the matrix. Examples of such sinks are voids and bubbles in irradiated materials or second-phase precipitates appearing during phase transformations.

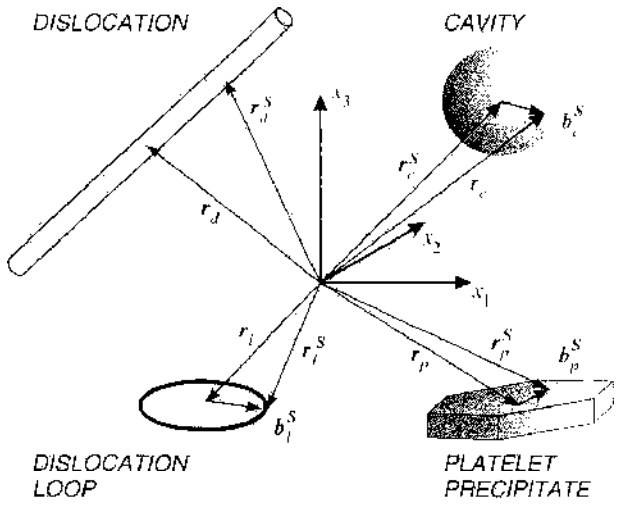

Figure 13. Different kinds of sinks, either local (cavities, precipitates, dislocation loops) or nonlocal (dislocations). Location of a sink is characterized by a vector $\mathbf{r}_k$ (where k indicates particular sink), while position of a point at the sink surface can be defined either in the global coordinate system (by vector $\mathbf{r}_k^s$) or with respect to the sink position (by vector $\mathbf{b}_k^s$).

- Linear sinks (e.g., network dislocations), whose length in one dimension is comparable to or noticeably exceeds the characteristic length scale in the matrix.
- Planar sinks (e.g., grain boundaries), whose sizes in two dimensions exceed the characteristic length scale in the matrix.

Evidently, this classification depends strongly on the choice of the characteristic length scale in the matrix. As long as we are interested in particle absorption by sinks, the relevant length scale is the average distance L_S traveled by particles before they are captured by sinks. In other words, L_S is of the order of intersink distance, provided no defect recombination is taken into account. Note that the requirement that the average intersink distance exceeds considerably the typical sink sizes means automatically that the total volume of such sinks constitutes only a small fraction of the whole volume of material, $S \ll 1$ (where S is the volume fraction occupied by sinks).

Typically, the sinks are distributed in the space of material at random. Moreover, sinks of the same physical nature can have different sizes, or spatial orientation, or some other differences in parameters characterizing each particular sink. The presence of multiple randomly distributed sinks with varying parameters makes the description of diffusion extremely complicated. Indeed, normally the sinks absorb particles at their surfaces, so that Eq. (197) is defined only in the domain between the sinks. At the surfaces of the sinks the concentration of particles is maintained at a certain level, which is determined by particle solubility in the surrounding material, or, in the case when diffusing particles are self-point defects—by thermal equilibrium concentration of defects in contact with a particular sink. Defining this concentration at the surface of sink n ($1 \le n \le N$, where N is the total number of sinks in the material) as $C_{\text{th}}^{(n)}$, we can write down a set of the boundary conditions as

$$c(\mathbf{r}_n^s, t) = C_{\text{th}}^{(n)}(\gamma_n) \tag{198}$$

where $\mathbf{r}_n^s$ is radius-vector of a point laying at the surface S_n of the sink and γ_n denotes the set of parameters characterizing the sink. The choice and the number of these parameters depend on the nature of corresponding sinks. For example, for a spherical void, γ_n includes only void radius R_n, while for second-phase particles this set of parameters can include information about the particle shape, composition, degree of grain boundary coherence to the matrix, and so forth.

When the total number of sinks, N, and the volume of material, V, are very big, it makes little sense to exactly solve diffusion equation of the type (197) in the multiply connected space between the sinks, even if it were possible. However, the exact solution of the diffusion

equation exists only for very simple systems (e.g., for two spherical sinks with fully absorbing surfaces [105]). The description of diffusion in a medium with particle sinks requires some special means of treatment.

The most straightforward numerical approach involves lattice kinetic Monte Carlo (MC) simulations. The specific nature of diffusion in crystals, which includes the presence of well defined equilibrium positions, the well defined jump directions, and practically instantaneous changes of equilibrium positions with well defined jump rates determined by local environment, makes it an excellent application for Monte Carlo simulations. In the most advanced versions, such as continuous time lattice kinetic Monte Carlo (CT-LKMC) [106], one can trace the system behavior at time scales up to microseconds, taking full account of lattice geometry and tracking computation progress in units of time, rather than in the number of MC steps.

Unfortunately, when the evolution of sinks is considered, purely numerical approaches are of rather limited applicability. Indeed, typically the sink concentrations rarely exceed 10^{15} cm^{-3}, and there is little chance to describe sink competition for diffusing particles with typical modern sizes of atomic arrays ($\sim 100 \times 100 \times 100$ lattice parameters). The situation becomes even worse, when one is interested in diffusion in stress fields, regardless of the fact that in an approach like MC, which involves only the local parameters, the incorporation of stresses in the description of particle diffusion is technically very straightforward. In fact, the only thing that is required is the account of stress effect on the jump energy barriers. But in practice, we are not aware of MC simulations of particle diffusion in stress fields. The reasons for that are quite evident. First of all, the jump barrier modification under the effect of stress can be described only provided one knows elastic force tensors of diffusing particles, which require a lot of computational efforts to be obtained and are rarely reported in the literature. Second, the applied stresses (if not hydrostatic) modify the symmetry of defects both in the equilibrium position and in the saddle points of diffusion jumps. As discussed in Section 2, the decisive part in the correct description of the stress effect on diffusion is played by the saddle point energy, which means that MC calculations should be done with the exact form of jump probabilities, instead of the most widespread schemes (Metropolis or Kawasaki [106]), which operate only with particle energies in equilibrium positions. Finally, when stresses are spatially nonuniform, the jump probabilities become space dependent, which requires calculation of jump probabilities at each MC step and drastically decreases the calculation efficiency.

On the other hand, in applications, the microstructural evolution of a material is addressed in order to interpret or predict the variation of macroscopic parameters. This situation is met in various physical tasks [107] where one wants to describe macroscopic properties (such as material volume, shape, electrical conductivity, elastic constants, viscosity, etc.) in a system of objects incorporated in a matrix with different physical properties. Such global properties are weakly sensitive to exact microstructural details and can be described by some average behavior of the ensemble of multiple incorporated objects (in our case, particle sinks).

The majority of modern analytical treatments of particle accumulation and absorption in materials with multiple randomly distributed sinks employ the so-called chemical rate theory, introduced originally for the description of chemical reactions in solutions. This concept was applied to the investigation of sink kinetics in irradiated materials in [108, 109]. The general philosophy of such an approach is very similar to the approaches used in analogous situations for the theoretical description of many-body problems (see, e.g., [110]). They assume that on the length scales noticeably exceeding the intersink separation, the material behaves as a homogeneous "effective lossy medium," while the efficiency of point defect capture by individual sinks is determined in an intuitively "self-consistent" manner. As a result, instead of exact concentration c, they introduce some average concentration, which coincides with c only in those regions of the matrix, where the sinks are absent.

The attempts to justify the rate theory from the "first principles" are rare [111–116] and very often are either limited to very specific systems [111–113, 115] or use too strong assumption [109, 114]. Nonetheless, the basic equations of the rate theory allow reasonable description of dilute sink systems in many practically important situations, while a self-consistent justification of the rate theory concept [116] allows one to apply it in nonevident cases,

for example where the sinks are nonuniformly distributed in space (which is quite typical for ion implantation tasks, Fig. 14) or when the sinks are ordered in space either partially (layering decomposition in a finite array of precipitates [117]) or fully (void lattice formation [118]).

Let us discuss the ideas and approaches used for the reduction of the exact diffusion problem in a matrix with multiple sinks to the description of diffusion in an "effective lossy medium."

5.2. Early Approaches to the Description of Diffusion in a Medium with Multisink Ensembles

5.2.1. "Cell" Model

The most straightforward approach, usually referred to as the "cell model," assumes that the total space of material can be separated between the sinks so that any sink is surrounded by a sink-free domain (or "cell") and all diffusing particles that are produced inside this domain are absorbed by the central sink. Various formulations of this model are available [97, 108, 109, 114, 119, 120–122]. Strictly speaking, this model is not statistical, as it is based on the direct solution of the original diffusion equations without any averaging over the sink array. Though for practical purposes this model is useful (e.g., sink strengths calculated on the basis of "cell" models roughly represent those obtained self-consistently in the effective medium approach [116]), it is not easy to justify its applicability except for the case of ordered systems of exactly the same sinks [114].

Because here we are interested in the illustration of the main ideas of the cell model, we consider the simplest case, when only one type of particles can diffuse in the matrix and their diffusion is described by Eq. (197) with spatially uniform particle generation rate K.

Let us consider first the case where all the sinks are of exactly the same type and form a spatially ordered array. Then we can split the space into the areas (cells) around sinks in such a way that they are centered at sinks, and the normal components of diffusion currents at the cell surfaces vanish [114, 120, 121]. In the considered particular case, the symmetry of the problems allows unique definition of a cell as Voronoi (or Wigner-Seitz) cell, while the spatial distribution of particle concentration in each cell is identical. Therefore, it is sufficient to solve diffusion Eq. (197) only in one cell, while the steady-state current of point defects, J,

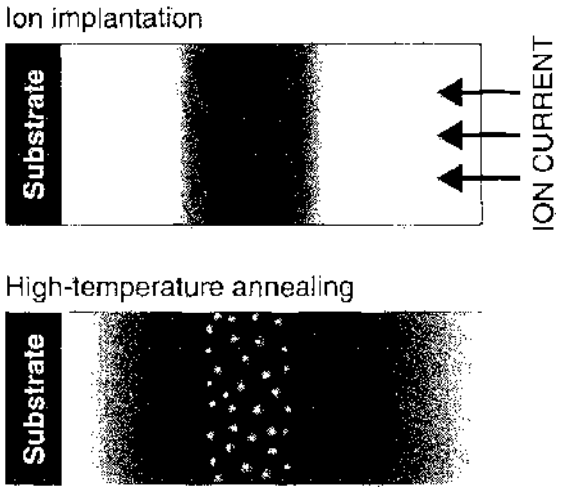

Figure 14. Radiation-induced synthesis of nanoclusters is a typical technological process, leading to nonuniform distribution of sinks in space. At the first stage, a thin layer on a substrate is implanted with ions on accelerator. The ions are stopped at some depth inside the layer, creating implant concentration profile distributed around the particle projection range (as shown by varying color density in the top figure). At the second stage, the sample is heated up to the temperature where implant diffusion is activated. If the implanted particle concentration exceeds the solubility in the matrix, a layer of precipitates is formed in the region of the maximum initial concentration (bottom figure).

to the central sink is determined by the matter conservation law,

$$J = \frac{KV_c}{\Omega} \tag{199}$$

where V_c is the volume of the cell. However, when the sinks are different, the symmetry arguments do not work and the shape of cells can be determined only after the complete solution of (197) is found.

In order to move somewhat further, we can modify an approach. Let us integrate Eq. (197) over the material volume between the sinks and apply the Gauss-Ostrogradsky theorem to the term with the current density. As a result, we get

$$\frac{\partial \langle c \rangle}{\partial t} + \frac{1}{V} \sum_{n=1}^{N} J_n = K \tag{200}$$

where $\langle c \rangle$ is the particle concentration averaged over the material volume V,

$$\langle c \rangle = \frac{1}{V} \int_V c \, dV \tag{201}$$

and J_n is the particle current to sink n,

$$J_n = D \int_{S_n} \nabla c \, dS \tag{202}$$

where integration is over the surface of the sink, S_n. In is intuitively clear that the particle current must be proportional to the difference between the average concentration and the equilibrium concentration at the surface of the sink. Assuming for simplicity that the equilibrium concentrations at all sink surfaces vanish (this condition is referred to as Smoluchowski boundary condition), we can write

$$J_n = Z_n D \langle c \rangle \tag{203}$$

where Z_n is some factor determined by the size and shape of the cell around sink n. In the radiation materials science literature, it is usual to refer to factors Z_n as "bias factors." This rather unusual name originated from the fact that under neutron irradiation, the main diffusing particles (vacancies and self-interstitials) are produced in exactly the same numbers, and in order for a sink to grow or shrink, it must be "biased," that is, capture different amounts of point defects per unit time. As can be demonstrated (see, e.g., [108]), this "bias" is largely determined by the factors Z_n.

Having in mind (203), we can represent Eq. (200) in the form of a classical balance equation,

$$\frac{\partial \langle c \rangle}{\partial t} = K - k_0^2 D \langle c \rangle \tag{204}$$

where $k_0^2 = \sum_{n=1}^{N} Z_n$ is called "sink strength for particle absorption" (or simply, sink strength).

It is interesting to mention that the derivation of (204) uses two implicit assumptions. First of all, it is assumed that bias factors are independent of the average concentration, but depend only on the shapes and sizes of both the sink and the cell. This basic assumption is automatically fulfilled in some formulations of the cell model (see, e.g., [123]), where it is postulated that the concentration at the surface of any cell is exactly $\langle c \rangle$. Second, there is no *a priori* confidence that cells defined by the condition of vanishing normal current at their surfaces can be chosen around each sink. In fact, the only case when one can be sure about the existence of such cells is that where the boundary concentrations at all sink surfaces are the same (without any loss of generality we can set them vanishing, $C_{\text{th}}^{(n)} = 0$) [121].

5.2.2. Effective Medium Approach

In the derivation of Eq. (204), we did not use the requirement that the sink system is periodic. However, in calculation of bias factors and sink strengths the periodicity is important, allowing one to consider only a limited number of essentially different cell shapes. When the sinks are distributed in space in an uncorrelated way, the size and shape of the cell for each individual sink is different, and the solution of diffusion equation in each separate cell does not simplify the task, even forgetting that the shape of the cell is not *a priori* known. Therefore, additional approximations are necessary to move forward.

It is at this junction where one applies the idea that for the description of macroscopic material behavior, the detailed information about the kinetics of each individual sink is largely excessive. In principle, it is sufficient to describe particle absorption by sinks in an "average" way, in terms of diffusion in some "lossy medium," where all sinks are "smeared" over the material volume. Historically, this was achieved in [111, 114] by introducing the probability density $f_N(\mathbf{r}_1, \ldots \mathbf{r}_N)$ to find N sinks in a particular realization where an arbitrary sink n $(1 \leq n \leq N)$ is located in the spatial position defined by radius-vector $\mathbf{r}_n$. Then, in addition to the spatial averaging of concentration according to Eq. (201), it is possible to average concentration over different possible spatial realization of sink ensembles, introducing concentration

$$C_0 = \int \langle c \rangle f_N(\mathbf{r}_1, \ldots, \mathbf{r}_N) \prod_{n=1}^{N} d\mathbf{r}_n \tag{205}$$

In a similar way, one can introduce ensemble-averaged sink strength as

$$k_0^2 = \sum_{n=1}^{N} \int Z_n f_N(\mathbf{r}_1, \ldots, \mathbf{r}_N) \prod_{n=1}^{N} d\mathbf{r}_n \tag{206}$$

The advantage of this definition is that all sinks of the same type should give exactly the same contribution to the sum, so that k_0^2 is determined, in fact, only by the sum over different sink types.

Although the ensemble averaging allows, in principle, to simplify the description of system behavior at the expense of transition from individual sinks to different sink types, this particular mode of its introduction does not provide any recipes for calculation of either sink strength, or the average concentration C_0. Therefore, the subsequent reasoning is largely intuitive. In particular, it can be expected [108] that in a spatially uniform sink ensemble $C_0 \approx \langle c \rangle$ and is given by an equation similar to (206),

$$\frac{\partial C_0}{\partial t} = K - k_0^2 D C_0 \tag{207}$$

with the only difference that the sink strength is given by (206). As for the sink strength, it is defined using an approach proposed by Maxwell [124] for determination of electrical resistance of suspension of spherical particles in a medium with different conduction properties. According to (202) and (203), the sink strength is determined by particle currents to individual sinks. In diluted sink system one can expect that a sink is surrounded by a region where there are no other sinks. On the other hand, far from the sink the system must still behave as a "lossy medium." Therefore, in the zero-order approximation, one can introduce some closed surface S_{out}, which encloses the sink and separates the space around the sink into two regions, namely, the sink-free region inside and the uniform "lossy continuum" outside. Then, the steady-state particle concentration in this combined medium, c_1 (which does not coincide with either c, or $\langle c \rangle$), is defined by equation

$$D\nabla^2 c_1 - k^2 c_1 = -K \tag{208}$$

where $k^2 = 0$ inside S_{out} and $k^2 = k_0^2$ outside it. At the separation surface, both the concentration and its first derivative must remain continuous. Solving this boundary-value problem and substituting c_1 instead of c into (202), it is possible to find bias factors for different sink types and thus the sink strengths. Particular calculations for the most important

sink geometries (spherical voids, circular dislocation loops, linear dislocations, planar grain boundaries) in the case of isotropic matrix can be found, for example, in [114], while the account of more complicated effects (in particular, related to the induced anisotropy of particle diffusion in stress field of sinks) remains an important direction of investigations in radiation materials science.

The described formulation of the rate theory allows one to calculate the sink strength to the end, and as such is widely used, but it has evident shortcomings from both conceptual and practical points of view. Indeed, this formulation leaves it completely unclear what is the exact relation between the real concentration c, the averaged concentration C_0, and the local concentration c_1, used for sink strength calculations. It follows from nowhere that the sink strength in (207) is exactly the same as in Eq. (208), as well as that the limiting value of c_1 far from the sink is C_0. Although the ensemble averaging of concentrations sounds reasonable, it is not quite evident why the sink strength should be averaged in the same manner, and why C_0 should satisfy Eq. (207) with just this sink strength. But the most essential methodological drawback of the standard "effective medium" approach is the definition of the average concentration as primarily the average over space. This spatial averaging is not only excessive, but, as will be shown below, substantially restricts the applicability of the rate theory, excluding from the very beginning the effects related to spatial non-uniformity of sink distribution.

As for the technical problems of this simplest formulation of the rate theory, one can mention at least the following. First of all, the introduction of the sink-free region near a sink required the assignment of the separation surface S_{out}, which is even less certain than the introduction of cell boundaries in the cell model, described in Section 2. In practical calculations, S_{out} is often shifted to the sink surface and the sink-free region is not at all specified [109]. Second, the currents to individual sinks are defined from Eq. (208), which contains the unknown sink strength as a fitting parameter. As a result, the total sink strength is expressed through itself, which requires additional efforts for obtaining the explicit expressions for the sink strength.

5.2.3. Alternative Justification of the Effective Medium Concept for Spherical Sink Ensemble

In order to calculate the sink strengths in a spatially uniform ensemble of spherical inclusions, one can use an alternative approach [111, 112, 115, 125], which is based on the explicit averaging of the approximate solution of diffusion equation over sink positions. Below, we will not discuss all the details of these papers, restricting ourselves to the most essential features of these approaches and leaving aside many details, especially the discussion of higher order corrections to the equations obtained below, which can be found in the original papers.

Let us assume that in some volume V of an infinite matrix, there are $N \gg 1$ spherical sinks. The position of the center of sink i will be denoted as $\mathbf{r}_i$ and sink radius as R_i. Because normally the sizes of sinks change "slow" when compared to the typical times of particle diffusion, we can assume that the concentration of point defects adiabatically follows the instantaneous sink ensemble configuration, so that one can restrict to the quasi steady-state diffusion equation, which here will be considered in the form,

$$\nabla^2 c = 0 \tag{209}$$

At the sink surfaces, the thermal equilibrium concentration of particles is maintained, Eq. (198), and this equilibrium can depend on the inclusion sizes, for example according to the Gibbs-Thomson relation

$$C_{\mathrm{th}}^{(i)} = C_{\mathrm{th}}^{(0)}\left(1 + \frac{2\gamma\Omega}{k_B T}\frac{1}{R_i}\right) \tag{210}$$

where $C_{\mathrm{th}}^{(0)}$ is the equilibrium concentration at a flat surface and γ is the sink surface energy. Far from the region V, the concentration tends to some constant value c_∞, which can be considered as a free parameter defined by a particular task. For the purposes of this paper,

it will suffice to restrict ourselves to the case where $c_\infty = C_{\text{th}}^0$, though in particular applications this restriction is not necessary (see, e.g., [126, 127]).

In a diluted sink array (i.e., when the intersink distance is much bigger than any sink size), it is possible to assume that in the zeroth-order approximation the sinks are point-like [112], so that the strength q_n of a sink is defined by relation

$$q_n = \int_{S_n} (\mathbf{e}^{(n)} \nabla c)\, dS \tag{211}$$

where $\mathbf{e}^{(n)}$ is the unit vector of external normal to the sink surface and the integration is over the sink surface S_n. Then, Eq. (209), which is valid only in the domain between the sinks, can be rewritten in the form defined in the whole material,

$$\nabla^2 c - \sum_{i=1}^{n} q_n \delta(\mathbf{r} - \mathbf{r}_n) = 0 \tag{212}$$

where δ denotes the Dirac's delta-function.

The solution of Eq. (212) tending to C_{th}^0 far from the sink array can be written down as

$$c = C_{\text{th}}^0 - \frac{1}{4\pi} \sum_{n=1}^{N} \frac{q_n}{|\mathbf{r} - \mathbf{r}_n|} \tag{213}$$

where sink strengths q_i must be found self-consistently. For this purpose, one can assume that in dilute sink ensembles the formal solution (213) can be valid also for finite-size sink (in other words, one can retain only the lowest order terms in the full multipole expansion of the solution [111]). Then, one obtains N equations for the determination of unknown q_i by demanding the fulfillment of boundary conditions at the sink surfaces,

$$\frac{q_i}{R_i} + \sum_{\substack{j=1 \\ j \neq i}}^{N} \frac{q_j}{|\mathbf{r}_j - \mathbf{r}_i|} = 4\pi [C_{\text{th}}^0 - C_{\text{th}}^{(i)}(R_i)] \approx -\frac{R_{\text{th}}}{R_i} \tag{214}$$

where $R_{\text{th}} = 8\pi C_{\text{th}}^0 \gamma \Omega / k_B T$.

In general, the sink strengths q_i in equation set (214) depend on all cluster positions and sizes, which makes the description of the ensemble evolution quite a complicated problem. In order to treat it, two complimentary approaches are possible. On the one hand, it is possible to specify some particular sink realization and then find the sink strengths numerically, regardless of the fact that for sufficiently big cluster systems, this can require large computer time and storage memory. Having in mind that the value of q_i determines the rate of cluster size variation,

$$4\pi R_i^2 \frac{dR_i}{dt} = D q_i \tag{215}$$

one can follow in this way the time evolution of the sink ensemble. Such an approach was applied in [117] to the investigation of the competition between Ostwald ripening and self-organization (layering) in a finite system of spherical clusters.

On the other hand, for macroscopic description of the cluster ensemble, one can use the ensemble averaging described above. For example, the average concentration is obtained by averaging over positions and sizes of all sinks,

$$C_0 = C_{\text{th}}^0 + [C_{\text{th}}^0(R_0) - C_{\text{th}}^0] s(\mathbf{r}, t) \tag{216}$$

where R_0 is some characteristic value of cluster radius (e.g., the initial or the average cluster radius), s is the nondimensional supersaturation of particles,

$$s = -\frac{C_\infty R_0}{R_{\text{th}}} \int dR_i \int_V d\mathbf{r}_i \frac{Q_i'}{|\mathbf{r} - \mathbf{r}_i|} f_1^{(i)} \tag{217}$$

$C_s = N/V$ is the average volume density of clusters, $Q_i^i(\mathbf{r}_i, R_i)$ is the average of q_i over positions and sizes of all sinks except the ith one, $f_1^{(i)}(\mathbf{r}_i, R_i)$ is the probability density to find this sink in position r_i with size R_i, and integration over cluster radii includes all the range of cluster size variation. In writing down (217), we have taken into account that all sinks are statistically independent, and summation in (213) gives simply the cluster number density.

In order to determine the average impurity supersaturation, Q_i^i is to be determined self-consistently. This can be done by averaging Eq. (214) with respect to parameters of all precipitates except the ith one. The result is

$$Q_i^i + C_s R_i \int_V \frac{Q_j^{ij}}{|\mathbf{r}_j - \mathbf{r}_i|} f_1^{(j)} d\mathbf{r}_j \, dR_j = -R_{\text{th}} \tag{218}$$

where Q_i^{ij} defines the average of q_i over positions and sizes of all sinks except sink i and sink j. In turn, the functions Q_i^{ij} are obtained by appropriate averaging of (214), which gives for sink i:

$$Q_i^{ij} + \frac{Q_j^{ij} R_i}{|\mathbf{r}_i - \mathbf{r}_i|} + C_s R_i \int_V \frac{Q_k^{kij}}{|\mathbf{r}_j - \mathbf{r}_i|} f_1^{(k)} d\mathbf{r}_k \, dR_k = -R_{\text{th}} \tag{219}$$

and a similar equation for sink j, where Q_i^{ijk} denotes the average of q_i over parameters of all sinks except sinks i, j, and k. Continuation of this procedure results, generally, in a hierarchy of equations for the moments of q_i [111, 112]. Strictly speaking, this equation set contains still many equations, but, in contract to (214), this hierarchy of equations can be truncated using some physical reasoning [116]. Evidently, the simplest way to proceed is to assume that q_i depends only on the parameters of the ith precipitate, $q_i = q_i(\mathbf{r}_i, R_i)$. This assumption means, in particular, that one neglects any correlations in the mutual disposition of precipitates (imposed, e.g., by the finite precipitate sizes). Then, the equation for Q_i^i can be written down in a closed form

$$Q_i^i(\mathbf{r}_i, R_i) + C_s R_i \int_V \frac{Q_i^i(\mathbf{r}_j, R_j)}{|\mathbf{r}_j - \mathbf{r}_i|} f_1^{(j)}(\mathbf{r}_j, R_j) \, d\mathbf{r}_j \, dR_j = -R_{\text{th}} \tag{220}$$

where we have taken into account that, due to the statistical equivalence of all sinks, Q_i^i and Q_j^j describe essentially the same functional dependence on sink position and size. For the same reason, the one-cluster distribution function does no depend explicitly on the sink index, so that the subscript in f_1 can be omitted. Multiplying (220) by $f_1(\mathbf{r}_i, R_i)$, integrating over the whole range of cluster radius variation, and using the normalization condition

$$\int f_1(\mathbf{r}, R) \, dR = n_s(\mathbf{r}) \tag{221}$$

where $n_s(\mathbf{r})$ is the specific number density of precipitates at point $\mathbf{r}$, one obtains

$$\overline{Q}(\mathbf{r}) + C_s \overline{R}(\mathbf{r}) \int_V \frac{n_s(\mathbf{r}')\overline{Q}(\mathbf{r}')}{|\mathbf{r} - \mathbf{r}'|} d\mathbf{r}' = -R_{\text{th}} \tag{222}$$

where

$$\overline{Q}(\mathbf{r}) = \frac{1}{n_s(\mathbf{r})} \int Q_i^i(\mathbf{r}, R) f_1(\mathbf{r}, R) \, dR \tag{223}$$

and

$$\overline{R}(\mathbf{r}) = \frac{1}{n_s(\mathbf{r})} \int R f_1(\mathbf{r}, R) \, dR \tag{224}$$

Taking into account Eqs. (216) and (217), we can reformulate (222) in the form of a conventional rate equation in a lossy medium,

$$\nabla^2 C - k^2 [C - C_{\text{th}}(\overline{R})] = 0 \tag{225}$$

where the sink strength k^2 is:

$$k^2(\mathbf{r}) = 4\pi C_v n_v(\mathbf{r})\overline{R}(\mathbf{r}) \tag{226}$$

Note that k^2 is defined here as a function of spatial position $\mathbf{r}$. We thus see that the statistical approach described in this section is indeed equivalent to the description of the precipitate system in terms of rate theory, while Eq. (222) is an integral equation formulation of the rate theory approach for a special case of spherical sinks.

5.3. Self-Consistent Justification of the Rate Theory

The treatment of a spatially homogeneous system of identical spherical sinks includes already the important features of an adequate approach. The most important achievement of this treatment is a clear demonstration of a hierarchical nature of the rate theory equations describing diffusion in a many-sink system. However, the hierarchy obtained in Section 5.2.3 is, in fact, that of approximate solutions of exact Eq. (209), which arises when boundary conditions at the sink surfaces are to be satisfied. It is possible to proceed in a somewhat different way [116], so that a statistical description of point defect diffusion in a many-sink system would lead to a hierarchy of diffusion equations themselves, irrespective of either the particular shapes of sinks or to the choice of boundary conditions. The only assumption that will be directly used at a certain point of the treatment is that the sink system is sufficiently dilute, in a sense described in the beginning of Section 3.3. This requirement is, by definition, satisfied for local sinks, so here we restrict our presentation to the discussion of local sinks. An expansion on nonlocal sinks can be found in [116].

5.3.1. Statistical Averaging of the Boundary Value Diffusion Problem

As already discussed, an arbitrary local sink n can be characterized by a set of parameters $\xi_n = (\mathbf{r}_n, \gamma_n)$, which includes sink position in the matrix, $\mathbf{r}_n$, and a set of other parameters, which we have denoted as γ_n. The complete set of parameters for all sinks will be briefly denoted as $\Xi = (\xi_1, \ldots, \xi_N)$ and the space of all possible parameter sets Ξ as $\{\Xi\}$.

For any particular realization Ξ of the sink system, the concentration c of point defects in the space between the sinks satisfies Eq. (197) with boundary conditions (198). In addition, an appropriate boundary condition on the outer surface of material should be defined. However, here we are interested in the case of $V \to \infty$ (and $N \to \infty$, so that the ratio N/V remains finite) and only demand the boundedness of c everywhere in the matrix as its volume tends to infinity. Evidently, the concentration satisfying this boundary-value problem depends not only on the spatial position $\mathbf{r}$ and time, but on the distribution of sinks as well, $c = c(\mathbf{r}, t|\Xi)$.

Normally, the timescale of particle concentration redistribution around the sinks, τ_s, is much shorter than that for evolution of the sink system itself. Therefore, in what follows we neglect the temporal evolution of the sink system when dealing with the problem of particle diffusion to sinks. This simplification imposes a certain limitation on the form of the particle diffusion Eq. (197). Indeed, the retention of the derivative term in (197) is reasonable only for those time-dependent tasks where the characteristic timescale is much shorter than τ_s. On the contrary, when timescales bigger or of the order τ_s are of interest, the point defect concentration profiles can be regarded as quickly accommodating to the instantaneous state of the sink system, and thus the diffusion problem should be treated as a steady-state one.

Equation (197) is defined only in the domain between the sinks, and for different realizations of the sink system the domains of definition of Eq. (197) are different. Because our aim is to average this equation over different realizations of the sink system, it is more convenient to rewrite (197) in such a form that it were defined in the whole volume of material and would automatically give correct values of concentration in the domain between the sinks. This can be achieved, much in the same way like it was done in Section 3.3.3.3, by incorporating the boundary conditions at sink surfaces into the diffusion equation itself,

$$\frac{\partial c}{\partial t} = K + D\nabla^2 c - \sum_{n=1}^{N} (\mathbf{j}\mathbf{e}^{(n)})\delta(S_n) \tag{227}$$

where $\delta(S_n)$ is the surface delta-function, defined as (see, e.g., [128])

$$\delta(S_n) = \int_{S_n} \delta(\mathbf{r} - \mathbf{r}_n^s)\, ds \tag{228}$$

where $\delta(\mathbf{r} - \mathbf{r}_n^s)$ is the three-dimensional Dirac's delta function and integration is over the points $\mathbf{r}_n^s$ belonging to the surface S_n of the nth sink (Fig. 13). This function has the property that for any function of spatial coordinates $f(\mathbf{r})$, the following relation holds [128]:

$$\int_V f(\mathbf{r})\delta(S_n)\, d\mathbf{r} = \int_{S_n} f(\mathbf{r}_n^s)\, dS$$

Equation (227) coincides with (197) in the domain of definition of the latter, whereas integration of (227) over the volume of material provides the correct particle currents to sinks, if the integral over the internal volume of sinks can be neglected. This latter assumption seems reasonable for dilute sink systems and corresponds to the neglect of particle generation and diffusional redistribution inside the sinks.

The next step is also very close in spirit to what is done in the preceding section. Namely, let us assume that the probability dP to find a system of sinks in a small volume $d\Xi = d\xi_1 d\xi_2 \ldots d\xi_N$ of the parameter space $\{\Xi\}$ around a point Ξ is given by some N-sink probability distribution function $f_N(\Xi)$ such that

$$dP = V^{-N} f_N(\Xi) d\Xi \tag{229}$$

The normalization condition is then, evidently,

$$V^{-N} \int_V f_N(\Xi) d\Xi = 1$$

Let us fix now m sinks ($0 \le m < N$), numbered as $i_1, i_2, \ldots, i_m$, and define the corresponding mth order moment of concentration in the matrix point $\mathbf{r}$ between fixed sinks, $C_m^{(i_1 \ldots i_m)}(r, t|\xi_{i_1}, \ldots, \xi_{i_m})$, as

$$C_m^{(i_1 \ldots i_m)} = \frac{V^{m-N}}{f_m^{(i_1 \ldots i_m)}} \int c(r, t|\Xi) f_N(\Xi) d\Xi_{(i_1 \ldots i_m)} \tag{230}$$

where we have introduced the m-sink distribution function $f_m^{(i_1 \ldots i_m)}$,

$$f_m^{(i_1 \ldots i_m)}(\xi_{i_1}, \ldots, \xi_{i_m}) = V^{m-N} \int f_N(\Xi) d\Xi_{(i_1 \ldots i_m)} \tag{231}$$

and integration in the phase space excludes the fixed sinks,

$$d\Xi_{(i_1 \ldots i_m)} = \prod_{\substack{n=1 \\ n \neq i_1, \ldots, i_m}}^{N} d\xi_n$$

The zero-order concentration moment C_0 is defined in the whole matrix volume and has the physical meaning of an average particle concentration in the material. The higher order concentration moments $C_m (m \ge 1)$ are defined only in the domain external to the fixed sinks, and integration in (230) is performed over positions of nonfixed sinks in this "external" domain (as f_N must prohibit sink overlap).

An equation for the mth moment of concentration can be obtained from (227) by averaging over parameters of all sinks, except the fixed ones.

$$\frac{dC_m}{dt} = K + D\nabla^2 C_m - D \sum_{\substack{n=1 \\ n \neq i_1, \ldots, i_m}}^{N} I_{m+1}^{(n|i_1 \ldots i_m)} \tag{232}$$

where the particle loss intensities I_{m+1} are given by

$$I_{m+1}^{(ni_1\ldots i_m)} = V^{-1}\int (\mathbf{e}^{(n)}\nabla C_{m+1}^{(i_1\ldots i_m n)})\varphi_{m+1}^{(n|i_1\ldots i_m)}\delta(S_n)\,d\xi_n \tag{233}$$

and $\varphi_{m+1}^{(n|i_1\ldots i_m)}$ is a conditional probability to find sink n with the parameter set ξ_n, when m other sinks have fixed parameter sets $\xi_k (k = i_1, \ldots, i_m)$:

$$\varphi_{m+1}^{(n|i_1\ldots i_m)}(\xi_n|\xi_{i_1}, \ldots, \xi_{i_m}) = \frac{f_{m+1}^{(i_1\ldots i_m n)}}{f_m^{(i_1\ldots i_m)}}$$

In order not to make subsequent expressions too cumbersome, we use a simpler notation, such as $\varphi_{m+1}^{(n|\ldots)}$, or even omit the superscripts, when the numbering of fixed sinks is unequivocal or unessential. Note that, due to normalization condition, $\varphi_1^{(n)} \equiv f_1^{(n)}$.

Substituting the definition of the surface delta-function into (233) and performing integration over the nth sink position, we obtain

$$I_{m+1}^{(n|\ldots)} = V^{-1}\int d\gamma_n \int_{S_n} dS[(\mathbf{e}^{(n)}\nabla C_{m+1}^{(i_1\ldots i_m n)})\varphi_{m+1}^{(n|\ldots)}]_{\mathbf{r}_n^s = \mathbf{r}} \tag{234}$$

The conditional probability $\varphi_{m+1}^{(n|\ldots)}(\mathbf{r}_n, \gamma_n|\ldots)$ should not change noticeably over the distances of the order of a sink size, that is

$$\varphi_{m+1}^{(n|\ldots)}(\mathbf{r}_n^s, \gamma_n|\ldots)\Big|_{\mathbf{r}_n^s = \mathbf{r}} \cong \varphi_{m+1}^{(n|\ldots)}(\mathbf{r}, \gamma_n|\ldots)$$

and thus $\varphi_{m+1}^{(n|\ldots)}$ would not contribute to the surface integral. Then, Eq. (234) is reduced to

$$I_{m+1}^{(n\ldots)} = V^{-1}\int d\gamma_n \varphi_{m+1}^{(n|\ldots)}(\mathbf{r}, \gamma_n)\int_{S_n} dS(\mathbf{e}^{(n)}\nabla C_{m+1}^{(i_1\ldots i_m n)})_{\mathbf{r}_n^s = \mathbf{r} - \mathbf{b}_n^s} \tag{235}$$

where $\mathbf{b}_n^s$ is the radius vector of surface point, defined in the local coordinate system originating at the sink position (see Fig. 13).

Substituting (235) into (232), we see that in order to determine the concentration moment C_m in a point $\mathbf{r}$ in the matrix surrounding m fixed sinks, one needs to know the concentration moments C_{m+1} for all systems, consisting of these sinks plus one more "probe" sink, placed near this point $\mathbf{r}$ in such a way that it "touches" $\mathbf{r}$ with some point of its surface. In other words, Eq. (232) represents in fact a hierarchy of equations that requires knowledge of the higher order solution in order to determine the lower order one.

The boundary conditions for C_m are determined by averaging Eq. (198) over the positions of all sinks except the m chosen,

$$C_m^{(i_1\ldots i_m)}(\mathbf{r}_k^s) = C_{1k}^{(k)}(\gamma_k) \quad \text{for } k = i_1, \ldots, i_m \tag{236}$$

A finite number of sinks always lies within a finite volume of material, and therefore additional assumptions are necessary to specify the concentration moment behavior far from the system of m fixed sinks. In particular, the boundedness of concentrations C_m far from the system of sinks is a reasonable boundary condition at infinity. This boundary condition at infinity can be made more specific, if we introduce the "concentration locality principle," postulating that any sink n contributes to the concentration field c only at distances not exceeding some "extinction length" λ_n from the sink, while its contribution to c quickly vanishes as $|\mathbf{r} - \mathbf{r}_n|/\lambda_n \to \infty$. This heuristic principle is physically reasonable and usually can be justified *a posteriori* [111, 112, 116]. An immediate consequence of the locality principle is that the nth sink contributes to the concentration in a matrix point $\mathbf{r}$ only provided it is located at distances within λ_n from this point. Then it is easy to show [116] that far from the fixed sink system the boundary conditions for concentration moments of the order $m > 0$ are reduced to

$$C_m(\mathbf{r} \to \infty) \to C_0 \tag{237}$$

while the only restriction on C_0 is that it should remain finite at infinity.

5.3.2. The Mean-Field Approximation

The discussion in the previous section demonstrates that instead of the exact solution of a particle diffusion equation in extremely complicated domain between the sinks, it is possible to reformulate the problem in terms of a hierarchy of diffusion equations for concentration moments, which describe the particle distribution in an "average" sense, that is, fixing a finite number of sinks that are of immediate interest and "smearing" all the remaining sinks over the matrix. Because the application of statistical treatment is reasonable only in the case when $N \gg 1$, the total number of equations in the hierarchy, though finite, is extremely big. However, very similar to the consideration of Section 5.2.3, we can now invoke physical arguments and truncate the hierarchy at some fixed value of m, which is a standard method of hierarchy uncoupling in statistical physics [110].

In this section, we restrict ourselves to the simplest case of the first-order hierarchy of rate equations, corresponding to truncation of the full hierarchy at $m = 1$. According to (232), the average particle concentration C_0 satisfies the equation

$$\frac{dC_0}{dt} = K + D\nabla^2 C_0 - D\sum_{n=1}^{N} I_1^{(n)} \tag{238}$$

where

$$I_1^{(n)}(\mathbf{r}) = V^{-1}\int d\gamma_n f_1^{(n)}(\mathbf{r}, \gamma_n) J_1^{(n)}(\mathbf{r}, \gamma_n) \tag{239}$$

and

$$J_1^{(n)}(\mathbf{r}, \gamma_n) = \int_{S_n} (\mathbf{e}^{(n)}\nabla C_1^{(n)})\Big|_{\mathbf{r}_n = \mathbf{r} - \mathbf{b}_n^*} dS \tag{240}$$

Calculation of $J_1^{(n)}(\mathbf{r}, \gamma_n)$ is quite nontrivial, because spatial derivatives of $C_1^{(n)}$ in the integrand for different surface points $\mathbf{r}_n^*$ are determined for the sink locations selected so that the sink "touches" spatial position $\mathbf{r}$ by corresponding surface point. However, when the length scale of spatial variation of the one-sink distribution function, L_f, considerably exceeds the sink size (which we can expect at least for dilute systems of local sinks), $J_1^{(n)}$ is approximately proportional to the particle current to nth sink located in point $\mathbf{r}$ [116],

$$J_1^{(n)}(\mathbf{r}, \gamma_n) = \int_{S_n} (\mathbf{e}^{(n)}\nabla C_1^{(n)})\Big|_{\mathbf{r}_n = \mathbf{r}} dS \tag{241}$$

At $m = 1$, Eq (232) for the ith sink ($i = 1, \ldots, N$) contains the loss terms $I_2^{(n|i)}$, which are defined by the gradients of point defect concentration $C_2^{(in)}(\mathbf{r}'|\xi_i, \xi_n)$ in the matrix point $\mathbf{r}'$ near sink n. In order to truncate hierarchy (232) at the level $m = 1$, one must approximate C_2 with the help of C_1 and C_0. The approximation formula should, evidently, be symmetric with respect to sink transposition and satisfy the concentration locality principle (i.e., for widely separated sinks, C_2 near each sink must be mainly determined by the parameters of this sink). However, even subject to these restrictions, the choice of the approximation formula is to a large extent voluntary [116]. The simplest and very evident choice is prompted by the following reasoning.

Far from the sink system, the concentration moments tend to the average concentration C_0. Therefore, the concentration deviations near the sinks, $\delta_m = C_0 - C_m$, are nonzero only in the immediate vicinity of sinks. Let us assume that for an arbitrary pair (i, j) of sinks $\delta_2^{(ij)}(\mathbf{r}'|\xi_i, \xi_j)$ is simply a sum of local concentration deviations $\delta_1^{(i)}(\mathbf{r}'|\xi_i)$ and $\delta_1^{(j)}(\mathbf{r}'|\xi_j)$, or, equivalently,

$$C_2^{(ij)}(\mathbf{r}'|\xi_i, \xi_j) = C_1^{(i)}(\mathbf{r}'|\xi_i) + C_1^{(j)}(\mathbf{r}'|\xi_j) - C_0(\mathbf{r}') \tag{242}$$

This relation constitutes the "mean-field" or "first-order additive" approximation for the concentration moments. Its substitution into $I_2^{(n|i)}$ gives

$$I_2^{(n|i)} \approx V^{-1}\int d\gamma_n \varphi_2^{(n|i)}(\mathbf{r}, \gamma_n|\xi_i) J_1^{(n)}(\mathbf{r}, \gamma_n). \tag{243}$$

where $I_1^{(n)}$ is given by (241) and depends on the first-order concentration moment. Hence, substitution of $I_2^{(n|i)}$ into (232) results in a closed-form equation set for $C_1^{(i)}(i = 1, \ldots, N)$. These equations look out very similar to the equation for C_0. Indeed, the particle loss efficiencies (239) and (243), entering equations for C_0 and C_1, respectively, differ only due to the difference between distribution functions $f_1^{(n)}(\xi_n)$ and $\varphi_2^{(n|i)}(\mathbf{r}, \gamma_n|\xi_i)$. However, when all sinks are statistically independent (i.e., their positions are completely uncorrelated), one can assume simply that

$$\varphi_2^{(n|i)}(\mathbf{r}, \gamma_n|\xi_i) = f_1^{(n)}(\xi_n) \tag{244}$$

for all sink pairs (i, j). It should be kept in mind that this assumption can never be strictly correct, because the overlapping of sinks is in any case not allowed, which already implies the correlation between sink positions. Nevertheless, for a dilute system of randomly distributed sinks, this approximation seems reasonable, even if not exact, because overlapping sink configurations in such system should give negligible contribution to point defect loss efficiencies.

If assumption (244) is accepted, then $I_2^{(n|i)} = I_1^{(n)}$. Subtracting Eq. (239) from (243) and neglecting the loss term $I_1^{(i)}$ (which is of the order of $V^{-1} \ll 1$), the following equations for the local concentration perturbations $\delta_1^{(i)}$ are obtained:

$$\frac{d\delta_1^{(i)}}{dt} = D\nabla^2\delta_1^{(i)} \tag{245}$$

while the boundary conditions are

$$\delta_1^{(i)}(\mathbf{r}_i^s) = C_{\text{th}}^{(i)} - C_0(\mathbf{r}_i^s) \tag{246}$$

and

$$\delta_1^{(i)} \to 0 \quad \text{far from the sink.}$$

The average point defect concentration does not vary much at the length scale of the order of sink size, and in the boundary conditions we may replace the average concentration $C_0(\mathbf{r}_i^s)$, defined in the sink surface point $\mathbf{r}_i^s$, with its value $C_0(\mathbf{r}_i)$ in the sink position point $\mathbf{r}_i$. After this substitution, it is possible to introduce a nondimensional function $v_1^{(i)}$,

$$\delta_1^{(i)} = [C_{\text{th}}^{(i)} - C_0(\mathbf{r}_i)]v_1^{(i)} \tag{247}$$

and the equation for the average concentration C_0 is finally reduced to

$$\frac{dC_0}{dt} = K + K_{\text{th}} + D\nabla^2 C_0 - k_0^2 D C_0 \tag{248}$$

where K_{th} describes particle emission from sinks,

$$K_{\text{th}} = \frac{D}{V}\sum_{n=1}^{N}\int C_{\text{th}}^{(n)}(\gamma_n) f_1^{(n)}(\mathbf{r}, \gamma_n) j_1^{(n)}(\mathbf{r}, \gamma_n) d\gamma_n \tag{249}$$

and k_0^2 is the sink strength, defined as

$$k_0^2 = \frac{1}{V}\sum_{n=1}^{N}\int f_1^{(n)}(\mathbf{r}, \gamma_n) j_1^{(n)}(\mathbf{r}, \gamma_n)\, d\gamma_n \tag{250}$$

where

$$j_1^{(n)}(\mathbf{r}, \gamma_n) = -\int_{S_n} (\mathbf{e}^{(n)}\nabla v_1^{(n)})|_{\mathbf{r}_n = \mathbf{r}}\, dS \tag{251}$$

and $v_1^{(i)}$ satisfies the boundary value problem

$$\frac{dv_1^{(i)}}{dt} = D\nabla^2 v_1^{(i)} \tag{252}$$

$$v_1^{(i)}(\mathbf{r}_i^s) = 1 \quad \text{and} \quad v_1^{(i)} \to 0 \quad \text{far from the sink.}$$

Equation (248) is our final aim, because it is the usual balance equation for the average point defect concentration in the matrix, while the set of equations (250)–(252) justifies the conventional procedure of sink strength calculation, as proposed in [108, 109], when each sink is inserted into a "lossy" continuum with some average point defect concentration C_0 and the local deviations of concentration are found in the sink vicinity, to be used afterwards to find k_0^2. However, the present treatment gives k_0^2 in a more general form as compared to the usual introduction of the sink strength.

First of all, here the sink strength is defined as a function of sink distribution and geometry only, but it does not depend on any parameters of material and irradiation. In other words, the sink strength is the intrinsic property of the sink system itself. The usual formulations of the rate theory simply postulate this statement without any justification. Second, the sink strength given by (250) explicitly depends on spatial positions of sinks (through the distribution function $f_1^{(n)}$) and thus the Laplace operator in (248) cannot, generally, be omitted. Only when the distribution of sinks is uniform in space [i.e., $f_1^{(n)} = f_1^{(n)}(\xi_n)$], the sink strength k_0^2 and concentration C_0 are constant throughout the matrix.

If all the sinks were different in their physical nature, the calculation of sink strength from (250) would remain quite a problem, as the total number of equations defining the functions $v_1^{(i)}$ would remain extremely large. However, real physical systems deal usually with sinks of the same physical nature, or with sinks belonging to a limited number of different types, so that all sinks of the same type are equivalent. Note that sinks equivalence is defined only with respect to particle absorption, but, as long as one is not interested in the sink system kinetics, physically different sinks that absorb particles in exactly the same way can be considered as belonging to the same type. In fact, it is sufficient that sinks of the same type have the same geometry and can be described by a unique expression for equilibrium point defect concentration at the sink surface. For example, spherical sinks with Smoluchowski boundary condition $C_{ih} = 0$ can include voids, gas bubbles, second phase precipitates, and so forth.

Introduction of sink types allows considerable simplification of sink strength calculation. Indeed, let us suppose that the material contains K different sink types, each comprising $N_p \gg 1$ sinks ($p = 1, \ldots, K$), so that $\sum_p N_p = N$. Because all sinks within a type are equivalent, the probability distribution function $f_N(\Xi)$ is symmetric with respect to permutation of parameter sets ξ_n corresponding to sinks of the same type. Therefore, $f_1^{(n)}$ is the same for them, and Eq. (251) gives a unique expression for particle current to all probe sinks of the same type. Hence, Eq. (250) for the sink strength can be rewritten as a sum over different sink types

$$k_0^2 = \sum_{p=1}^{k} (k_0^{(p)})^2 \tag{253}$$

where

$$(k_0^{(p)})^2 = n_p \int f_1^{(p)}(\mathbf{r}, \gamma_p) j_1^{(p)}(\mathbf{r}, \gamma_p)\, d\gamma_p \tag{254}$$

and $n_p = N_p/V$ is the average concentration of p-type sinks per unit volume of material. In agreement with the standard rate theory treatments, the total sink strength can be written as a sum of sink strengths for all sink classes in a material, and thus only K boundary-value problems of the type (250)–(252) should be solved in order to find the sink strength.

5.3.3 Higher-Order Corrections to the Sink Strength

In the preceding section, we discussed the case of very dilute sink system, when the hierarchy (232) can be truncated already at $m = 1$. In terms of its physical meaning, this approximation corresponds to the neglect of any diffusional interaction between individual sinks. This approximation is certainly valid for extremely diluted sink ensembles, where the volume fraction occupied by sinks is negligible, but can become insufficient, if the system contains close sink pairs, trios, and so forth. Such situation may arise when one tries to consider the effect of finite (though yet small, $S \ll 1$) total volume of sinks. In this case, it is necessary to take into account higher order corrections to the sink strength, and the first attempts to investgate the higher order corrections to sink strength were made already in [111, 112]. In this section, we briefly discuss how this can be done in terms of the statistical approach. In order not to involve unnecessary complications, we assume from the very beginning that all sinks are statistically independent and restrict ourselves to the steady-state form of diffusion equation (197).

In order to consider close-laying sink configurations, one has to account for diffusional interaction of sinks, which can be achieved by truncation of (232) at levels $m > 1$. As we will see, the bigger is the selected truncation levels, the bigger amount of sinks in close-laying configurations are taken into account. From the technical point of view, hierarchy truncation is acheved by introduction of an approximate relation, allowing to express the $(m + 1)$-th concentration moment in terms of lower-order moments. However, starting already from $m = 2$, the formulation of reasonable approximation expressions demands more sophisticated reasoning than simple intuitive considerations that led us to relation (242).

Let us assume that the concentration locality principle, as formulated in Section 5.3.1, is fulfilled for any sink in the sink system. Then it is tempting to assume that for any particular sink realization Ξ, the real concentration c can be presented as a sum of correlation functions

$$c(\mathbf{r}|\Xi) = \zeta_0(\mathbf{r}) + \sum_{n=1}^{N} \zeta_1^{(n)}(\mathbf{r}|\xi_n) + \sum_{n=1}^{N} \sum_{\substack{m=1 \\ m\neq n}}^{N} \zeta_2^{(mn)}(\mathbf{r}|\xi_n, \xi_m) + \cdots \tag{255}$$

so that ζ_0 is independent of sink positions, whereas $\zeta_1^{(n)}$, $\zeta_2^{(nm)}$, and so forth, depend only on positions of sinks denoted by corresponding superscripts. The definition implies that for any correlation order p, the corresponding correlation functions $\zeta_p^{(i_1 \ldots i_p)}$ essentially depend on the parameters of all p sinks and cannot be expressed as some linear combination of lower order correlation functions. In conjunction with the concentration locality principle, this means that $\zeta_p^{(i_1 \ldots i_p)} \to 0$ when the distance between any two sinks in the set $(i_1, \ldots, i_p)$ noticeably exceeds the maximum extinction length for these sinks, $\lambda_{\max}$. In other words, correlation function $\zeta_p^{(i_1 \ldots i_p)}$ does not vanish only in the vicinity of close configurations of p sinks. This property of correlation functions is especially convenient for dilute sink systems, where close configurations of several sinks are the rarer the bigger number of sinks they contain, and thus it is possible to introduce sequential approximations by omitting all correlations higher than the desired one.

When assumption (255) is valid, the average concentration C_0 defined by (230) has the form

$$C_0 = \zeta_0 + \sum_{n=1}^{N} \langle \zeta_1^{(n)} \rangle_n + \sum_{n=1}^{N} \sum_{\substack{m=1 \\ m\neq n}}^{N} \langle \zeta_2^{(nm)} \rangle_{nm} + \cdots \tag{256}$$

where the angular brackets mean averaging of corresponding value over parameters of sinks indicated by subscripts, that is

$$\langle \zeta_p^{(i_1 \ldots i_p)} \rangle_{(i_1 \ldots i_p)} = V^{-p} \int \zeta_p^{(i_1 \ldots i_p)} f_p^{(i_1 \ldots i_p)} d\xi_{i_1} \ldots d\xi_{i_p} \tag{257}$$

and $f_p^{(i_1 \ldots i_p)}$ is a p-sink distribution function, which is obtained from f_N by integration over parameters of all sinks except those fixed. When all sinks are statistically independent, the higher-order concentrations $C_p (p > 1)$ can be expressed in terms of lower-order

concentration moments and "concentration deviations" δ_p, which are expressed in terms of correlation functions of order p and higher [116]. In particular,

$$C_1^{(i)} = C_0 + \delta_1^{(i)} \tag{258}$$

$$C_2^{(ij)} = C_1^{(i)} + C_1^{(j)} - C_0 + \delta_2^{(ij)} \tag{259}$$

$$C_3^{(ijk)} = C_2^{(ij)} + C_2^{(jk)} + C_2^{(ik)} - C_1^{(i)} - C_1^{(j)} - C_1^{(k)} + C_0 + \delta_3^{(ijk)} \tag{260}$$

and so forth.

It can be seen that the retention in (255) of correlation functions whose order is lower or equal to some fixed value p has a consequence that concentration moments of the order higher than p become linear combinations of lower order concentration moments. In particular, the first-order additive approximation, as specified by Eq. (242), corresponds to omission in (255) of all correlations between individual sinks. It is therefore natural that in this approximation, the concentration field near a sink, described by (242), is not influenced by other sinks. A more detailed description includes, evidently, the account of close sink pairs in hierarchy (232), which can be achieved by the hierarchy truncation at the level $m = 2$, which corresponds to the second-order additive approximation. Let us briefly discuss this approximation, restricting ourselves to the steady-state diffusion equation.

In this case, the approximation formula for C_3 is obtained from (260) by setting $\delta_3 = 0$. The calculation of the third-order current $I_3^{(n|ij)}$ is noticeably simplified by the fact that the terms independent of the nth sink parameters do not contribute to it [116], so that

$$I_3^{(n|ij)} = I_2^{(n|i)} + I_2^{(n|j)} - I_1^{(n)} \tag{261}$$

and thus hierarchy (232) includes equations for correlation moments up to C_2. It is more convenient, however, to study equations not for C_2, but for the second-order deviations δ_2, introduced in (259). Taking a linear combination of equations (232) for $m = 0, 1, 2$ and neglecting the combination of terms $(I_2^{(ji)} + I_2^{(i|j)} - I_1^{(i)} - I_1^{(j)})/V$, which is of the order of $V^{-1} \ll 1$, one obtains

$$\nabla^2 \delta_2^{(ij)} = 0 \tag{262}$$

with the boundary conditions

$$\delta_2^{(ij)}(\mathbf{r}_i^s) = -\delta_1^{(j)}(\mathbf{r}_i^s) \approx -\delta_1^{(j)}(\mathbf{r}_i) \tag{263}$$

$$\delta_2^{(ij)}(\mathbf{r}_j^s) = -\delta_1^{(i)}(\mathbf{r}_j^s) \approx -\delta_1^{(i)}(\mathbf{r}_j) \tag{264}$$

and $\delta_2^{(ij)} \to 0$ far from the sink pair. Here it is assumed that the first-order concentration deviations from one sink do not vary much over the distances of the order of the other sink size. Then, $\delta_2^{(ij)}$ can be written down as

$$\delta_2^{(ij)}(\mathbf{r}) = -\delta_1^{(i)}(\mathbf{r}_j) v_2^{(i|j)}(\mathbf{r}) - \delta_1^{(j)}(\mathbf{r}_i) v_2^{(j|i)}(\mathbf{r}) \tag{265}$$

where functions $v_2^{(i|j)}$ [for any pair (i, j) of sinks] are independent of the first-order concentration deviations and, like $\delta_2^{(ij)}$, satisfy the Laplace equation, while boundary conditions at the sink surfaces are

$$v_2^{(i|j)}(\mathbf{r}_i^s) = 1 \quad \text{and} \quad v_2^{(i|j)}(\mathbf{r}_j^s) = 0 \tag{266}$$

An equation for the concentration moment C_1 is also conveniently replaced with that for the first-order deviation δ_1. Substituting (265) into the second-order current $I_2^{(n|ij)}$ and performing evident transformations, one easily obtains

$$\nabla^2 \delta_1^{(i)} - (k_1^{(i)})^2 \delta_1^{(i)} + G_1^{(i)} = 0 \tag{267}$$

where

$$(k_1^{(i)})^2 = -\frac{1}{V}\sum_{\substack{n=1\\ n\neq i}}^{N}\int d\gamma_n f_n^{(1)}(\mathbf{r},\gamma_n)\int_{S_n}(\mathbf{e}^{(n)}\nabla v_2^{(n|i)})\big|_{\mathbf{r}_n^s=\mathbf{r}}dS \tag{268}$$

and

$$G_1^{(i)} = \frac{1}{V}\sum_{n=1}^{N}\int d\gamma_n f_n^{(1)}(\mathbf{r},\gamma_n)\delta_n^{(1)}(\mathbf{r}_i|\mathbf{r},\gamma_n)\int_{S_n}(\mathbf{e}^{(n)}\nabla v_2^{(i|n)})\big|_{\mathbf{r}_n^s=\mathbf{r}}dS \tag{269}$$

Boundary conditions for $\delta_1^{(i)}$ are given by (246). Replacing in (246) the value of C_0 in a sink surface point with its value in the sink position point, we can express $\delta_1^{(i)}$ as

$$\delta_1^{(i)} = \delta_{\text{th}}^{(i)} - C_0(\mathbf{r}_j)v_1^{(i)} \tag{270}$$

where both $\delta_{\text{th}}^{(i)}$ and $v_1^{(i)}$ satisfy Eq. (267) with boundary conditions at the sink surface

$$v_1^{(i)}(\mathbf{r}_j^s) = 1, \quad \delta_{\text{th}}^{(i)}(\mathbf{r}_i^s) = C_{\text{th}}^i$$

and with vanishing boundary conditions at infinity. Then the balance equation for C_0 is identical to that obtained in the first-order approximation, Eq. (248), with the only modification that

$$K_{\text{th}} = -\frac{D}{V}\sum_{n=1}^{N}\int d\gamma_n f_1^{(n)}(\mathbf{r},\gamma_n)\int_{S_n}(\mathbf{e}^{(n)}\nabla\delta_{\text{th}}^{(n)})\big|_{\mathbf{r}_n=\mathbf{r}}dS \tag{271}$$

instead of (249). Note that, in contrast to the first-order approximation, one can express $\delta_1^{(i)}$ in terms of a unique function $v_1^{(i)}$ only when C_{th} is the same for all sinks and $\delta_{\text{th}}^{(i)} = C_{\text{th}}v_1^{(i)}$.

Comparison of Eqs. (267) and (245) reveals considerable difference between the governing equations for $\delta_1^{(i)}$ in the first- and the second-order approximation. Equation (245) describes diffusion to the ith sink in a matrix free of other sinks, whereas Eq. (267) contains the loss term with the sink strength $(k_1^{(i)})^2$, providing "screening" of deviations $\delta_1^{(i)}$ at large distances from corresponding sinks.

5.4. Nonlinear Effects of Stress Due to Statistical Averaging of Sink Ensembles

Up to now, the discussion in Section 5 was devoted to presentation of the basics of the rate theory, without considering the effects of stress on diffusion. Here we discuss how the general approach presented above can be generalized in order to include the effects of elastic fields on the particle diffusion. This consideration depends on the nature of the elastic strains.

5.4.1. Sink-Independent Elastic Strains

When the strains are created by some external loads and do not depend on the sink distribution in space, the generalization is straightforward, because the only difference as compared to Section 5.3 is that we should start from an anisotropic diffusion equation (137) instead of the isotropic one, Eq. (197). Let us restrict ourselves to the case of steady-state diffusion equation, which can be written down as

$$\frac{\partial}{\partial x_i}D_{ij}\frac{\partial w}{\partial x_j} + K = 0 \tag{272}$$

At sink surfaces, the concentration of particles is maintained equal to that in thermodynamic equilibrium. It means that the probability to find a particle (for generality, an oriented one) in a position $\mathbf{m}$ just one jump away from the surface of sink n is equal to

$$\rho_\mu^m = C_{\text{th}}(\gamma_n)\exp\left[\beta E_b\left(\frac{\mathbf{m}}{\mu}\right)\right] \tag{273}$$

where the thermally equilibrium concentration at sink surface depends, strictly speaking, on the normal stresses acting on the sink surface, because the attachment of a particle to sinks implies the shift of the sink boundary and thus requires the work against the stresses acting on the boundary. Averaging the probability ρ_μ^m either over particle orientation on site (for the case of easy particle on-site rotation), or over different jump sublattices (for long-range orientation memory), as done in Section 3, we obtain

$$w(\mathbf{r}_n^s) = C_{\text{th}}(\gamma_n) \tag{274}$$

Thus, it can be seen that in the case of elastically loaded materials, the steady-state diffusion is completely described in terms of renormalized concentration of particles, w, and is insensitive to the energies of particles in equilibrium positions.

Because the diffusion tensor is insensitive to sink parameters, the averaging over sink ensemble is performed in exactly the same way, as it is done in Section 5.3. In particular, the concentration moments are defined as

$$C_m^{(i_1 \ldots i_m)} = \frac{V^{m-N}}{f_m^{(i_1 \ldots i_m)}} \int w(r, t|\Xi) f_N(\Xi) d\Xi_{(i_1 \ldots i_m)} \tag{275}$$

and the hierarchy of equations for concentration moments is given by

$$\frac{\partial}{\partial x_i} D_{ij} \frac{\partial C_m}{\partial x_j} + K - D_0 \sum_{\substack{n=1 \\ n \neq i_1, \ldots, i_m}}^{N} I_{m+1}^{(n|i_1 \ldots i_m)} = 0 \tag{276}$$

where the particle loss intensities I_{m+1} are given by

$$I_{m+1}^{(n|i_1 \ldots i_m)} = \frac{1}{D_0 V} \int d\gamma_n \varphi_{m+1}^{(n|i_1 \ldots i_m)}(\mathbf{r}, \gamma_n) \int_{S_n} dS \left[D_{kl} e_k^{(n)} \frac{\partial C_{m+1}^{(i_1 \ldots i_m n)}}{\partial x_l} \right]_{\mathbf{r}_n = \mathbf{r} - \mathbf{b}_n^s} \tag{277}$$

Restricting ourselves to the first-order approximation (242) and expressing C_1 in terms of the average concentration and the normalized concentration deviation v_1 according to (258) and (247), we obtain for the average concentration C_0 an equation

$$\frac{\partial}{\partial x_i} D_{ij} \frac{\partial C_0}{\partial x_j} + K + K_{\text{th}} - k_0^2 D_0 C_0 = 0 \tag{278}$$

where K_{th} and k_0^2 are given by Eqs. (221) and (222), respectively, with

$$j_1^{(n)}(\mathbf{r}, \gamma_n) = -\frac{1}{D_0} \int_{S_n} \left[D_{kl} e_k^{(n)} \frac{\partial v_1^{(n)}}{\partial x_l} \right]_{\mathbf{r}_n^s = \mathbf{r}} dS \tag{279}$$

while Eq. (252) for $v_1^{(i)}$ should be replaced with the anisotropic form,

$$\frac{\partial}{\partial x_i} D_{ij} \frac{\partial v_1^{(i)}}{\partial x_j} = 0 \tag{280}$$

5.4.2. Internal Elastic Fields

In addition to external elastic fields, the particle sinks themselves can create in their vicinity elastic stresses. These stress fields can arise as a reaction of the local material inhomogeneity on the action of external stresses but can be equally well the inherent property of sinks.

Examples of the first kind are stress fields in an externally loaded material, which arise around crack tips and largely exceed the external loads, or stresses arising around second-phase inclusions with elastic constants different from those of surrounding material. On the other hand, dislocations create around themselves long range elastic fields [10] in the absence of any external loads. Evidently, in the case where the elastic fields are created by sinks themselves, it is no longer possible to neglect the elastic field dependence on sink positions during the ensemble averaging, as done in Section 5.4.1.

Let us start with the diffusion Eq. (272) with boundary conditions (274) and insert the boundary conditions into the diffusion equation

$$D_0 \frac{\partial}{\partial x_i}(\delta_{ij} + \theta_{ij}) \frac{\partial w}{\partial x_j} + K + \sum_{n=1}^{N} (\mathbf{j}\mathbf{e}^{(n)}) \delta(S_n) = 0 \tag{281}$$

where the diffusion coefficient tensor is written in the form of equation (127) and the particle current density is given by

$$j_k = -D_{kl} \frac{dw}{dx_l} \tag{282}$$

Using the averaging procedure of Section 5.4.1, we obtain the hierarchy for concentration moments C_m in the form

$$D_0 \nabla^2 C_m + D_0 \operatorname{div} \mathbf{E}_m + K - D_0 \sum_{\substack{n=1 \\ n \neq i_1 \ldots i_m}}^{N} \tilde{I}_{m+1}^{(n|i_1 \ldots i_m)} = 0 \tag{283}$$

where

$$E_{mk}^{(i_1 \ldots i_m)} = \frac{1}{f_m^{(i_1 \ldots i_m)}} \int \theta_{kl} \frac{dw}{dx_l} f_N(\Xi) d\Xi_{(i_1 \ldots i_m)} \tag{284}$$

and

$$\tilde{I}_{m+1}^{(n|i_1 \ldots i_m)} = -V^{-1} \int d\gamma_n \varphi_{m+1}^{(n|\ldots)}(\mathbf{r}, \gamma_n) \int_{S_n} dS(\mathbf{e}^{(n)}(\nabla C_{m+1}^{(i_1 \ldots i_m n)} + \mathbf{E}^{(i_1 \ldots i_m n)}))_{\mathbf{r}_n = \mathbf{r} - \mathbf{h}_n^i} \tag{285}$$

The evident new feature of the hierarchy is the appearance of terms depending on the stress-affected diffusion current, as determined by vector $\mathbf{E}_m$. Because the subsequent uncoupling procedure affects all other terms in (283) in a fashion already discussed in Section 5.3, only the contribution of $\mathbf{E}_m$ to the rate equations and the sink strengths is addressed below. To simplify presentation, we assume vanishing concentrations at the sink surfaces, $C_{th} = 0$.

Generally, when both w and θ_{kl} depend on positions of sinks, $\mathbf{E}_m$ cannot be directly expressed in terms of concentration moments. However, in dilute sink systems, further progress is possible due to the fact that any sink contributes to the overall stress field only in its immediate vicinity. Indeed, the elastic strains noticeably affect diffusion if the energy of their interaction with diffusing particles is not negligible with respect to $k_B T$. In the case of local sinks, the characteristic length L^{el} of strain decrease below the sensitivity level is of the order of the sink size. In the case of dislocations (linear sinks), L^{el} can noticeably exceed the transverse size of the dislocation core, however, the typical values of L^{el} in metals ($L_n^{el} \geq 1$ nm for vacancies and $L_n^{el} \leq 2$ nm for interstitials) are still considerably less than the average intersink separation. The consequence of this short-range nature of particle interaction with sinks is that in dilute sink systems, a diffusing particle elastically interacts mainly with the nearest sink. This consideration allows to immediately write down (285) in the standard form

$$\tilde{I}_{m+1}^{(n|i_1 \ldots i_m)} = -\frac{1}{V} \int d\gamma_n \varphi_{m+1}^{(n \ldots)}(\mathbf{r}, \gamma_n) \int_{S_n} dS \left(e_k^{(n)} (\delta_{kl} + \theta_{kl}^{(n)}) \frac{dC_{m+1}^{(i_1 \ldots i_m n)}}{dx_l} \right)_{\mathbf{r} = \mathbf{r} - \mathbf{h}_n^i} \tag{286}$$

where $\theta_{kl}^{(n)}$ is the anisotropic part of the diffusion coefficient due to the effect of elastic strains $\varepsilon_{ij}^{(n)}$ produced by sink n and the external strain ε_{ij}^{0} (not dependent on sink positions), if present.

The transformation of the term with the divergence of $\mathbf{E}_m$ is not so simple, as $\mathbf{E}_m$ is defined in an arbitrary space point, not necessary close to any sink. However, having in mind the locality of elastic stresses created by individual sinks, we may approximate the elastic strains in an arbitrary point of material as

$$\varepsilon_{ij} = \varepsilon_{ij}^{0} + \sum_{n=1}^{N} \varepsilon_{ij}^{(n)} \tag{287}$$

and restrict ourselves to the case when the internal stresses are small, so that θ_{kl} can be expanded to the first order in strains, giving

$$\theta_{kl} = \theta_{kl}^{0} + \sum_{n=1}^{N} \theta_{kl}^{(n)} \tag{288}$$

Then

$$E_{mk}^{(i_1 \ldots i_m)} = \theta_{mkl}^{(i_1 \ldots i_m)} \frac{dC_m^{(n|i_1 \ldots i_m)}}{dx_l} + \frac{1}{V} \sum_{\substack{n=1 \\ n \neq i_1 \ldots i_m}}^{N} \int \theta_{kl}^{(n)} \frac{dC_{m+1}^{(i_1 \ldots i_m n)}}{dx_l} \varphi_{m+1}^{(n|i_1 \ldots i_m)} d\xi_n \tag{289}$$

where $\theta_{mkl}^{(i_1 \ldots i_m)}$ is the anisotropic correction due to the external stress and the fixed sinks,

$$\theta_{mkl}^{(i_1 \ldots i_m)} = \theta_{kl}^{0} + \sum_{p=1}^{m} \theta_{kl}^{(i_p)}$$

In other words, approximation (288) allows one to express $\mathbf{E}_m$ in terms of $\mathbf{C}_m$ and $\mathbf{C}_{m+1}$, thus making it possible to apply the uncoupling procedure and self-consistently truncate the hierarchy set (283).

Here we restrict ourselves to the simplest mean-field approximation (242). In this case, we are left only with $\mathbf{E}_0$ and $\mathbf{E}_1$:

$$E_{0k} = \bar{\theta}_{0kl} \frac{dC_0}{dx_l} + \sigma_{0k} \tag{290}$$

and

$$E_{1k}^{(i)} = \bar{\theta}_{1kl}^{(i)} \frac{dC_1^{(i)}}{dx_l} + \sigma_{1k}^{(i)} \tag{291}$$

where

$$\bar{\theta}_{mkl}^{(i_1 \ldots i_m)} = \frac{1}{V} \sum_{\substack{n=1 \\ n \neq i_1 \ldots i_m}}^{N} \int \theta_{kl} \varphi_{m+1}^{(n|i_1 \ldots i_m)} d\xi_n \tag{292}$$

and

$$\sigma_{mk}^{(i_1 \ldots i_m)} = \frac{1}{V} \sum_{\substack{n=1 \\ n \neq i_1 \ldots i_m}}^{N} \int \theta_{kl}^{(n)} \frac{d\delta_1^{(n)}}{dx_l} \varphi_m^{(n|i_1 \ldots i_m)} d\xi_n \tag{293}$$

As discussed in Section 5.3.2, it is convenient to replace equations for the first-order concentration moments by those for concentration deviations $\delta_1^{(i)}$. Correspondingly, we are interested not so much in $\mathbf{E}_1$, but rather in $\delta\mathbf{E}_1 = \mathbf{E}_1 - \mathbf{E}_0$. When sinks are statistically independent, we have $\boldsymbol{\sigma}_1 \approx \boldsymbol{\sigma}_0$, so that

$$\delta E_{1k}^{(i)} = \bar{\theta}_{1kl}^{(i)} \frac{d\delta_1^{(i)}}{dx_l} + \left(\theta_{kl}^{(i)} - \frac{1}{V} \int \theta_{kl}^{(i)} f_1^{(i)} d\xi_i \right) \frac{dC_0}{dx_l} \approx \bar{\theta}_{1kl}^{(i)} \frac{d\delta_1^{(i)}}{dx_l} \tag{294}$$

Indeed, the spatial variation of C_0 occurs at the length scales comparable to those of the sink distribution function variation, that is, at least comparable to the intersink distances.

Thus in the vicinity of the ith sink the term proportional to ∇C_0 can be neglected. Making use of approximation (247), the equation for the nondimensional concentration deviation $v_1^{(i)}$ can be reduced to the form

$$\frac{\partial}{\partial x_k}(\delta_{kl} + \bar{\theta}_{1kl}^{(i)})\frac{\partial v_1^{(i)}}{\partial x_l} = 0 \tag{295}$$

with the same boundary conditions as before.

$$v_1^{(i)}(\mathbf{r}_i^s) = 1 \quad \text{and} \quad v_1^{(i)} \to 0 \quad \text{far from the sink.}$$

As for the equation for the average concentration, after simple transformations it can be reduced to

$$D_0\frac{\delta}{\delta x_k}(\delta_{kl} + \bar{\theta}_{0kl})\frac{\partial C_0}{\partial x_l} + K - k_0^2 D_0 C_0 = 0 \tag{296}$$

where the sink strength is defined as

$$\begin{aligned} k_0^2 = &\sum_{p=1}^{K} n_p \int \frac{\partial}{\partial x_k}\theta_{kl}^{(p)}\frac{\partial v_1^{(p)}}{\partial x_l} f_1^{(p)} d\xi_p \\ &- \sum_{p=1}^{K} n_p \int d\gamma_p f_1^{(p)}(\mathbf{r}, \gamma_p) \int_{S_p} dS \left[e_k^{(p)}(\delta_{kl} + \theta_{1kl}^{(p)})\frac{\partial v_1^{(p)}}{\partial x_l}\right]_{\mathbf{r}_p' = \mathbf{r} - \mathbf{h}_p'} \end{aligned} \tag{297}$$

where summation is over different sink types [cf. Eq. (253)] and, without much error, the derivatives in the surface integral in the last equation can be taken, assuming simply $\mathbf{r}_p = \mathbf{r}$. It is seen that the sink strength contains contribution from the volume integration, which is the direct consequence of the term σ_{ij} presence in equation (290). However, it is easy to reduce this term to integration over sink surfaces. Recollecting that in an elastically homogeneous matrix, both $v_1^{(p)}$ and $\theta_{kl}^{(p)}$ depend only on the relative distance $\mathbf{R}_p = \mathbf{r} - \mathbf{r}_p$, but not separately on the current position in space, $\mathbf{r}$, or sink position $\mathbf{r}_p$, i.e. $v_1^{(p)} = v_1^{(p)}(\mathbf{R}_p, \gamma_p)$, one can replace integration over $\mathbf{r}_p$ with integration over $\mathbf{R}_p$,

$$\int \frac{\partial}{\partial x_k}\theta_{kl}^{(p)}\frac{\partial v_1^{(p)}}{\partial x_l} f_1^{(p)} d\xi_p = -\int d\gamma_p \int_{V_{\text{out}}} d\mathbf{R}_p \frac{d}{dR_{pk}}\left(\theta_{kl}^{(p)}(\mathbf{R}_p, \gamma_p)\frac{\partial v_1^{(p)}(\mathbf{R}_p, \gamma_p)}{\partial R_{pl}}\right) f_1^{(p)}(\mathbf{r} - \mathbf{R}_p, \gamma_p)$$

where spatial integration is over the volume V_{out} outside the sink. Having in mind that a typical length scale of spatial variation of the sink distribution function f_1 exceeds considerably the size of the region around a sink, where the first-order concentration deviation $v_1^{(p)}$ is noticeably different from zero, we can approximate in the last integral $f_1^{(p)}(\mathbf{r} - \mathbf{R}_p) \approx f_1^{(p)}(\mathbf{r})$ and use the Gauss theorem, getting finally

$$k_0^2 = -\sum_{p=1}^{K} n_p \int d\gamma_p f_1^{(p)}(\mathbf{r}, \gamma_p) \int_{S_p} e_k^{(p)}(\delta_{kl} + \theta_{kl}^{0})\frac{dv_1^{(p)}}{dx_l} dS \tag{298}$$

Equations (296) and (295) represent a generalization of rate equations for the description of point defect kinetics in strained materials.

6. SOME PRACTICAL EXAMPLES OF STRESS-DIFFUSION COUPLING

In this chapter, we give several examples of physical phenomena, where the account of stress effects on diffusion plays an essential role in the adequate explanation of experimental phenomena. The examples are related mainly to radiation materials science, but this selection is only due to the fact that radiation materials science is one of the main scientific interests of the authors.

6.1. Void Swelling

6.1.1. Basics of the Swelling Theory

An unusual phenomenon observed in solids irradiated with energetic particles (neutrons, protons, α-particles or electrons in MeV energy range) is the gradual increase of material volume with the increase of irradiation dose. This phenomenon is known as radiation swelling and was discovered in metals [129], and later on was observed also in other types of solids. This discovery prompted intensive research, very much promoted by the necessity to understand the risks of swelling-induced degradation of structural materials in the active zones of fast neutron nuclear reactors. It is not our aim here to review the details of radiation swelling, which would be better read in special reviews and textbooks (an excellent compilation of facts related to void swelling can be found, for example, in [130, 131]). It is sufficient to mention that very soon after the discovery of radiation swelling in metals it became clear that at the microscopic level the reason for swelling is the formation of a large amount of cavities, either empty (then they are called "voids"), or gas-filled ("gas bubbles") with the sizes reaching 10–100 nm. As a result of matter conservation, formation of emptiness inside the material should be accompanied with the global increase of material volume, so very often this type of swelling is called "void swelling."

At a conceptual level, the void swelling phenomenon remained for some time a mystery. Indeed, it is well known that when particles penetrating a solid are sufficiently energetic, they can displace atoms from their positions, creating so-called Frenkel pairs, consisting of an interstitial and a vacancy. More energetic particles can originate even the cascades of atomic collisions, which create multiple interstitials and vacancies in the limited volume of material, and the determination of the number and spatial distribution of point defects after cascade cooling down is a vast field of activity in modern computational materials science. Nonetheless, vacancies and interstitials are produced in exactly the same amount. Let us assume additionally that all of them are produced as isolated defects (as known at present, this is not the case for cascade-producing irradiation because of the in-cascade defect clustering, but at the early times of the swelling theory that was unknown).

Swelling is normally observed at temperatures where vacancies are mobile (which is essential, because otherwise they would be unable to cluster) and interstitials are mobile as well (interstitials in metals are generally much more mobile than vacancies). During diffusional migration, a newly created point defect meets eventually either another point defect or a sink. In the case when two point defects meet each other, they either annihilate (in case when two opposite defects are met), or create a bound pair, which is a possible nucleus of a new cluster. On the other hand, when a point defect is captured by a sink, it simply disappears, while the shape of a sink changes in a way appropriate to a particular sink. The most important sinks for point defects in metals are edge dislocations, with line densities varying from 10^8 cm^{-2} to 10^{11} cm^{-2}, depending on the type of preliminary thermo-mechanical treatment. The capture of a point defect results in a shift of the dislocation extra-plane by one atomic volume. Now let us assume that in addition to dislocations, a system of voids is formed in the material. A capture of a diffusing vacancy increases the size of a void by one atomic volume, while a capture of an interstitial decreases it by the same amount. So, when a void grows with time, it must capture more vacancies than interstitials per unit time. Because the defects are produced at the same rate, the extra interstitials should be captured by something else, which in our simple model means by dislocations. We thus see that the explanation of swelling requires the presence of some mechanisms that could explain the partitioning of vacancies and interstitials between different types of sinks. This partitioning is the keystone of the theory of swelling and, as such, remained for a long time a hot subject for analytical models and computer simulations.

The main thing unclear at the time of swelling discovery was the reason for point defect partitioning between voids and dislocations. It cannot be related to point defect recombination, which is symmetric with respect to point defect types and, moreover, tends to suppress swelling by decreasing the number of vacancies available for void growth. To a certain extent, point defect partitioning can be related to differences in point defect clustering rate, because formation of tightly bound interstitial clusters (usually, in the form of dislocation loops)

from very mobile interstitials occurs much faster than formation of voids, which often happens after quite noticeable delay after the beginning of irradiation [132]. As a result, extra vacancies remain in the material volume and could, at least in principle, cluster to voids. It is interesting, that the fast clustering of interstitial can indeed result [133] in quite noticeable swelling, but this swelling is only transient and not related to voids, as it can be pronounced only at temperatures where vacancies are relatively immobile, and as such is observed only in some refractory metals, ceramics and compound semiconductors (such as SiC) [134]. Hence, the explanation of swelling required the mechanisms of point defect partitioning that were related to the properties of sinks themselves.

The first mechanism proposed for the explanation of different sink efficiencies for absorption of vacancies and interstitials was based on the account of elastic interaction of point defects with sinks [108, 135]. In the framework of different versions of the elastic interaction model, the calculation of point defect capture efficiencies (sink strengths) was done for both local sinks (voids and gas bubbles [93–96, 136, 137] and small dislocation loops [101, 138–140]) and for nonlocal ones (dislocations [77, 97, 98, 100, 141–144], grain boundaries [145], and surfaces of thin layer samples [147, 146]). Since the time of the first proposal, there appeared other models of point defect partitioning, related, for example, to the point defect absorption limitation at the sink surfaces [148–151], variation of point defect diffusion mode near a sink [152, 153], on to inverse Kirkendall effect in alloys [154]. Very popular is now the mechanism that takes into account that in the case of cascade producing irradiation, a part of defects can be formed as small planar interstitial clusters [155] that can move only one-dimensionally, in the direction normal to their extra plane [156]. It can easily be shown [157–159] that the efficiency of absorption of 1D moving clusters by sinks is pronouncedly different as compared to point defects diffusing in a normal 3D mode. However, all the other mechanisms, however important their contribution to swelling may be in separate cases, do not cancel the contribution from the elastic interaction of point defects with sinks.

In order to demonstrate the crucial role of point defect partitioning between sinks in a quantitative way, let us express the swelling rate in terms of parameters, characterizing point defect absorption by different sink types. By definition, swelling is the relative volume change of material as compared to its initial state (before irradiation). When voids are the only reason for swelling, the total volume increase exactly matches the volume of free space collected in the voids, so that the quantitative measure of swelling is the value

$$S = \frac{4\pi}{3V} \sum_n R_n^3 \tag{299}$$

where summation is over radii R_n of all voids in the volume of material. Correspondingly, the rate of swelling, dS/dt, is determined by the rates of growth of individual voids in the ensemble. If a spherical void (sink n in the total ensemble of sinks) has radius R_n and is located in some position $\mathbf{r}_n$, the rate of its volume change can be written down like

$$\frac{4\pi}{3} \frac{dR_n^3}{dt} = \int_{S_n} (\mathbf{e}^{(n)}, \mathbf{j}_V^{(n)} - \mathbf{j}_I^{(n)})\, dS \tag{300}$$

where $\mathbf{j}_\alpha^{(n)}$ is the current density of point defects of type α ($\alpha = V$ for vacancies and $\alpha = I$ for interstitials), expressed in terms of physical concentrations of point defects, $c_\alpha(\mathbf{r}|\Xi)$. Evidently, the definition of the exact growth rate of individual void in a particular sink environment is practically impossible. But the swelling value defined by Eq. (299) is defined by collective behavior of all voids, and it is a common practice to describe the void growth in the statistically averaged way in the framework of the rate theory (which was, in fact, first applied to radiation materials science in [108] just for this aim).

The averaging over all sinks except the selected void allows one to express the void growth rate in terms of the concentration moments $C_{\alpha 1}^{(n)}$. Assuming that the relation between the point defect current densities and point defect concentrations is in the form of the simple Fick's law (5), and using the mean field approximation and relations (258), (247), one easily obtains

$$\frac{dR}{dt} = \frac{1}{R}[Y_V D_V (C_{0V} - C_{V,\text{th}}(R)) - Y_I D_I C_{0I}] \tag{301}$$

where we have omitted the index of a void (because after statistical averaging, this equation is valid for any void in the ensemble), omitted the equilibrium concentration of interstitials (which is negligible in metals), and introduced factors Y_α, defined as

$$Y_\alpha = \frac{R}{4\pi}\int_{4\pi}\left.\frac{dv_{\alpha 1}}{dr}\right|_{r=R} d\omega \tag{302}$$

where $v_{\alpha 1}$ is defined by a corresponding boundary value problem [e.g., (252)] in its steady-state version, and the averaging is over the 4π solid angle. In the radiation materials science, such proportionality factors are referred to as "bias" factors, because the sign of their differences characterizes the sink "bias" to capturing that or other type of point defects. For example, when $v_{\alpha 1}$ is defined by Eq. (252), the direct solution gives $Y_i = Y_v = 1$, so that voids can be considered as "unbiased" sinks. However, as shown below, this statement becomes incorrect, when the effect of void stress field on point defect diffusion in its vicinity is taken into account.

Application of the statistical averaging procedure to Eq. (299) allows us to express the swelling rate as

$$\frac{dS}{dt} = \frac{4\pi}{3} n_v \int_0^\infty R^2 \frac{dR}{dt} f_1^{(v)}(R)\, dR \tag{303}$$

where n_v is the number density of voids and $f_1^{(v)}$ is the void size distribution function. Now, using the equation for the rate of void size change, it is possible to express the swelling rate in terms of the average concentrations of point defects.

In turn, the averaged concentrations of vacancies and interstitials are defined by the balance equations

$$D_\alpha \nabla^2 C_{0\alpha} + K + K_{\alpha,\mathrm{th}} - k_\alpha^2 D_\alpha C_{0\alpha} = 0 \tag{304}$$

where subscript α indicates point defect type. In writing this equation, we have taken into account that point defect concentrations quickly accommodate to sink ensemble parameters (so that quasi steady-state equations can be used) and neglected the point defect recombination, which is not important for qualitative reasoning given here. The spatial derivatives in this equation should be generally retained, and in some situations (e.g., swelling in thin metal layers) can play the crucial role, but when the damage occurs uniformly over large regions (a typical situation for neutron irradiation of reactor structural materials), they can be also omitted, so that (304) is reduced to a set of two algebraic balance equations with the evident solution

$$C_{0\alpha} = \frac{K + K_{\alpha,\mathrm{th}}}{k_\alpha^2 D_\alpha} \tag{305}$$

The sink strengths here are the sums of sink strengths of different sink types. For our purpose it is sufficient to restrict to the simplest situation, when in addition to voids, only one other sink type is present in the material, namely, network dislocations. Recalling the expression for the sink strength, equation (254), we can write down the void sink strengths for type α point defects as

$$(k_\alpha^{(v)})^2 = 4\pi n_v \int_0^\infty R Y_\alpha(R) f_1^{(v)} dR = 4\pi n_v \langle R Y_\alpha \rangle \tag{306}$$

where angular brackets are used in order to concisely indicate the averaging over void sizes. Similar to voids (see below), it can be shown that the sink strength of dislocations can be written down as

$$(k_\alpha^{(d)})^2 = Z_\alpha \rho_d \tag{307}$$

where ρ_d is the dislocation density (that is the total length of dislocation lines per unit volume) and Z_α is the dislocation bias factor. Like in the case of voids, when no effect of dislocation stress field on point defect diffusion is considered, $Z_v = Z_i$.

Now, collecting all things together, we obtain for the swelling rate,

$$\frac{dS}{dt} = (Z_I\langle RY_V\rangle - Z_V\langle RY_I\rangle)\frac{4\pi n_v \rho_d}{k_I^2 k_V^2}K + \frac{4\pi n_v}{k_V^2}[\langle RY_V C_{V,th}\rangle - \langle RY_V\rangle\langle C_{V,th}\rangle] \quad (308)$$

The second term in the right-hand side, which is related to vacancy redistribution between voids of different size according to Ostwald ripening mechanism, is normally completely unimportant in the theory of swelling for many reasons, among which is that swelling is usually pronounced at temperatures where the equilibrium concentration of vacancies is negligible. As for the first term, it also vanishes, if there is no difference in bias factors for voids and dislocations. In order to introduce the dependence of the bias factors on the type of point defects, one had to explain via which physical mechanisms the sinks differentiate between point defects of different types. The explanation was given in terms of the effect of stress on point defect diffusion in the vicinity of sinks.

6.1.2. Bias Factors of Spherical Cavities and Straight Dislocation Lines

Let us demonstrate how the inclusion of stress effect on diffusion is manifested in sink bias factors. In order to simplify notation, in Section 6.1.2 we will not specially indicate the point defect types, specifying them by appropriate subscripts (V for vacancies and I for interstitials) only where it is necessary to differentiate between point defect kinds.

In order to define the bias factors in the vicinity of different sink types in the framework of the rate theory, one has to find solution of corresponding diffusion equations for dimensionless concentration deviations of the first order, $v_{\alpha 1}$, which in the case of diffusion in the strain fields created by sinks themselves can be written down as (omitting, for brevity, the subscript indicating the point defect type)

$$\frac{d}{dx_k}D_{kl}\frac{dv_1}{dx_k} = 0 \quad (309)$$

where the diffusion coefficient depends only on external strains and strains created by the sinks themselves [cf. Eq. (295)]. The average strain contribution from other sinks will not be considered here, which is a good approximation in the case when sinks are distributed completely randomly in space. One should keep in mind, however, that this is not a general rule (see, e.g., [15]). The boundary conditions will be taken in a standard form:

$$v_1(\mathbf{r}_i^s) = 1 \quad \text{and} \quad v_1 \to 0 \quad \text{far from the sink}$$

In writing down the last boundary condition, special attention should be paid to the meaning of "far from the sink." For a spherical sink this condition can be safely set at an infinite distance from the sink. However, for linear sinks, such as dislocations, more careful definition of the outer boundary is necessary, as discussed below.

6.1.2.1. Spherical Sinks In order to study the point defect diffusion in the vicinity of a cavity, such as a void or a gas bubble, one needs to know first of all the distribution of strains in its vicinity. These strains are created by the normal stress σ_0 acting on the cavity surface, which is due to the surface tension γ and, in the case of gas bubbles, to the internal gas pressure P, so that $\sigma_0 = P - 2\gamma/R$. To be specific, in what follows we assume cavities to be spherical voids, though generalization for gas bubbles is straightforward.

In an infinite elastically isotropic medium the strains around a spherical sink are

$$\varepsilon_{ij} = \frac{\sigma_0}{4\mu}\left(\frac{R}{r}\right)^3(\delta_{ij} - 3n_i n_j) \quad (310)$$

where μ is the shear modulus of material, n_i is the directional cosine with respect to the i-th coordinate axis, and r is the distance from the void center, which coincides with the coordinate system origin. Note that $\mathrm{Tr}\varepsilon_{ij} = 0$, so that a spherical sink does not create hydrostatic pressure in its vicinity and, as such, does not interact with isotropic dilatation centers, at least in the first order in strains. Since for a long time after the discovery of swelling

the investigators did not differentiate between the effect of stress on point defects in saddle point and equilibrium positions (which, as shown in Section 3.4, is not always a bad approximation from the practical point of view), the point defect type dependence of bias factors could be predicted only taking into account the second-order effects caused by differences of elastic moduli of point defects and the bulk of material [93, 160], or taking into account the small elastic anisotropy, which is present to a small degree in any cubic metal [96, 137].

As we have already noted, the strains in the cavity neighborhood can be quite noticeable, however normally they never exceed 10^{-3}, so that in terms of the diffusion coefficient they can be considered as "weak" (see Section 4.1) and we can use the linear expansion of diffusion coefficient in strains. Assuming that the coordinate system axes are directed along the principal crystallographic axes of material, the diffusion coefficient has the form given by equations (127) and (182).

Since the corrections to the isotropic diffusion coefficient in equation (309) are small ($\theta_{ij} \ll 1$), it makes sense to look for a solution in the form of an expansion $v_1 = v_1^{(0)} + v_1^{(1)} + \ldots$, where $v_1^{(k)}$ is of the order of $(\sigma_0/\mu)^k$. The zero-order approximation for v_1 is obtained by setting $\theta_{ij} = 0$ and the solution of the corresponding equation is trivial, giving

$$v_1^{(0)} = \frac{R}{r} \tag{311}$$

Note that this solution is independent of either point defect type or lattice symmetry, which is quite natural, because this type of information is contained only in θ_{ij} and appears only in the first order corrections in strain.

The equation for the first order correction $v_1^{(1)}$ is obtained from (309) by retention of the terms linear in σ_0/μ. After some simple algebra, involving the explicit forms of both the elastic strains and the zero-order solution, one obtains

$$\nabla^2 v_1^{(1)} = \frac{6\sigma_0 R^4}{\mu r^6}\left\{\frac{5\tilde{d}^{(2)} + 2\tilde{d}^{(3)}}{20} + \frac{8\tilde{d}^{(3)}}{35}\sum_{k=1}^{3} P_4(n_k)\right\} \tag{312}$$

where P_4 are Legendre polynomials of the fourth order. Because Legendre polynomials as functions of directional cosines are eigenfunctions for the angular part of the Laplace operator, the solution for $v_1^{(1)}$ is straightforward, giving

$$v_1^{(1)} = \frac{6\sigma_0 R}{\mu r}\left\{\frac{5\tilde{d}^{(2)} + 2\tilde{d}^{(3)}}{240}\left(\frac{R^3}{r^3} - 1\right) + \frac{\tilde{d}^{(3)}}{35}\left(\frac{R^4}{r^4} - \frac{R^3}{r^3}\right)\sum_{k=1}^{3} P_4(n_k)\right\} \tag{313}$$

An interesting feature here is the angular dependence of point defect concentrations around spherical voids, which is absent in the zero-order counterpart and is a consequence of superposition of spherical symmetry of the void over the cubic symmetry of the point defect diffusion.

Restricting ourselves to the terms linear in strains and using Eq. (302), one immediately obtains

$$Y_\alpha = 1 + q_\alpha \frac{\sigma_0 \Omega}{k_B T} \tag{314}$$

where

$$q_\alpha = -\frac{5\tilde{d}_\alpha^{(2)} + 2\tilde{d}_\alpha^{(3)}}{40}\frac{k_B T}{\mu\Omega} \tag{315}$$

Having in mind that factors $\tilde{d}^{(k)}$ are inversely proportional to temperature, the values of q_α thus defined are temperature independent. The most important result is that factors q_α can be directly expressed in terms of dipole tensors of point defects in saddle points. In particular cases of bcc and fcc lattices, one has

$$q_\alpha(\text{bcc}) = -\frac{3}{20}\frac{P_{\alpha 12}}{\mu\Omega} \tag{316}$$

and

$$q_\alpha(\text{fcc}) = -\frac{3P_{\alpha 12} + P_{\alpha 11} - P_{\alpha 33}}{40\mu\Omega} \tag{317}$$

where the jump orientation averaged values of dipole tensors are meant for interstitials. Typically, the absolute values of q_α are of the same order of magnitude for both defect types ($\sim 10^{-2}$), but the sign is different, negative for interstitials and positive for vacancies [15].

6.1.2.2. Dislocations In the case of dislocations, the consideration is more complicated than in the case of spherical sinks, because dislocations are linear sinks and as such are oriented in space. This means, first of all, that in solving the boundary value problem (309) in the cell, surrounding a dislocation, it is reasonable to use a Cartesian coordinate system with special directions of its basis vectors $\mathbf{e}_1$, $\mathbf{e}_2$ and $\mathbf{e}_3$. In what follows, we assume that $\mathbf{e}_1$ is directed along the dislocation Burgers vector, $\mathbf{b}$, and $\mathbf{e}_3$ is directed along the dislocation line. Second, as the dislocation must not lie along a crystallographic axis even in cubic lattices, we should use the diffusion tensor in the form that is invariant with respect to the rotation of coordinate system. Having in mind that close to the dislocation line the elastic energy of point defects can be rather big, we use diffusion tensor in the form of Eq. (191).

Finally, the diffusion geometry in the case of linear sinks is two-dimensional, rather than three-dimensional, which requires certain modification of both the boundary condition at the outer boundary (far from the sink) and the definition of the sink strength [116]. In the case of two-dimensional diffusion the concentration locality principle is invalid and thus one can not, as in the case of local sinks, specify the boundary condition at the outer boundary by simply shifting it to infinity. Instead, the outer boundary should be selected in some self-consistent way. However, in diluted sink systems the dependence of the dislocation sink strength on the exact position of the outer boundary is very weak (logarithmic [97]) and so it is sufficient to select the outer boundary in the form of a cylinder with the radius R_d comparable to either half the average intersink distance, or k_0^{-1}. On the other hand, the sink strength of straight dislocation lines can be written down as

$$k_d^2 = -\frac{\rho_d}{D_0}\int d\gamma_d f_1^{(d)}(r, \gamma_p)\int_{\Gamma_d} e_k^{(d)} D_{kl}\frac{dv_l}{dx_l}d\Gamma \tag{318}$$

where $f_1^{(d)}$ is "one-dislocation" probability density, $\tilde{e}^{(d)}$ is the vector of outer normal to dislocation core and integration in the internal integral is along the contour Γ_d of the dislocation core cross-section (which is usually approximated by a circle of radius $r_0 \sim 2$–3 a).

As discussed in Section 4.3, in the case of dislocations, a direct expansion of the diffusion coefficient tensor into a series in stresses is not justified. In the case of isotropic diffusion, when no difference is made between the saddle-point and equilibrium configurations, it is well-known that the "weak" strain approximation [141] leads to qualitatively different predictions from the case, when the diffusion coefficient retains the exponential dependence on the elastic interaction energy of point defects with the dislocation stress field [97]. In particular, due to the specific angular dependence of dislocation stress field, the "weak strain" approximation predicts the elastic corrections to the sink strength, which are only of the second order of magnitude in dislocation strains ε_{ij}^d, which remains valid also in the case when diffusion anisotropy is taken into consideration [100].

However, diffusion in the vicinity of dislocation can be described in a mixed scheme, where the corrections to the isotropic contributions to the diffusion coefficient are treated in the explicit exponential form, while the anisotropic corrections are accounted only to the first order in stresses. In this case, the diffusion tensor has the form of Eq. (191), where the contribution from individual strains around a dislocation can be written down in a standard form (in polar coordinates (r, φ), see, e.g., [10]),

$$\beta P\varepsilon_{11} = -\frac{R_s}{2r}[(1+\gamma_E)\sin\varphi + \gamma_E \sin 3\varphi]$$

$$\beta P\varepsilon_{22} = -\frac{R_s}{2r}[(1-\gamma_E)\sin\varphi - \gamma_E \sin 3\varphi]$$

$$\beta P \varepsilon_{12} = -\frac{R_s}{2_r}\gamma_E[\cos\varphi + \cos 3\varphi]$$

and

$$\varepsilon_{13} = \varepsilon_{23} = \varepsilon_{33} = 0$$

where $\gamma_E = [2(1-2\nu_E)]^{-1}$, and R_s is defined by Eq. (190). As a result, the "hydrostatic" contribution to the interaction energy is given by Eq. (189).

Having in mind the mixed nature of the diffusion coefficient, it is possible to look for v_1 by sequential approximations. Indeed, following [97], we can approximate

$$v_1 = \exp\left(-\frac{1}{2}\beta U_s^0\right)(u^{(0)} + u^{(1)} + \cdots) \tag{319}$$

where $u^{(m)}$ is proportional to the m-th power of anisotropic corrections to the diffusion coefficient.

The zeroth-order approximation for v_1 is unaffected by diffusion anisotropy, and so $u^{(0)}$ is given by well-known relation [97, 98, 161]

$$u^{(0)} = \frac{Z^{(0)}}{2\pi}\left[K_0\left(\frac{2R_s}{r}\right) - \frac{K_0(\zeta_0)}{I_0(\zeta_0)}I_0\left(\frac{2R_s}{r}\right)\right] \tag{320}$$

where $Z^{(0)}$ is, as can easily be checked, the zero-order approximation to the dislocation bias factor,

$$Z^{(0)} = 2\pi\left[K_0(\zeta_d) - \frac{K_0(\zeta_0)}{I_{(0)}(\zeta_0)}I_0(\zeta_d)\right]^{-1} \tag{321}$$

where $\zeta_0 = |R_s|/2r_0$, $\zeta_d = |R_s|/2R_d$ and I_0, K_0 are the modified Bessel functions of the zeroth order. In our case, $\zeta_0 \geq 1$ and $\zeta_d \ll 1$ (see Table 5 for typical values of R_s), so that $Z^{(0)} \approx 2\pi/\ln(|R_s|/2R_d)$.

Note that the values of R_s entering the bias factor depend on the type of diffusing point defects, being directly proportional to the absolute value of the point defect relaxation volume in the saddle point of diffusion jump. Typically, in metals an interstitial causes much stronger local deformation than a vacancy, so that $\Delta V_I \gg |\Delta V_V|$ and, correspondingly, already in the zero-order approximation $Z_I^{(0)} > Z_V^{(0)}$. The difference is not so big,

$$\frac{(Z_I^{(0)} - Z_V^{(0)})}{Z_I^{(0)}} \approx \frac{\ln(\overline{P}_I^s/|\overline{P}_V^s|)}{\ln(2R_d/|R_{sV}|)} \approx 0.1 - 0.3 \tag{322}$$

but, as applied to radiation swelling, it is more than sufficient. However, in more subtle effects, where the competition between differently oriented dislocations plays the crucial part (examples are given in Sections 6.2 and 6.3, below), zero-order values of dislocation bias do not help much, as they are insensitive to dislocation orientations. For these purposes one needs to know the first-order corrections due to elastodiffusion. These were first obtained, under some simplifying assumptions, by Woo [101, 143] and later on, in general form, in [102].

The first-order corrections to the point defect distribution in the vicinity of a dislocation are calculated in essentially the same way, as for the case of spherical sinks, but look out noticeably more complicated. Therefore here we restrict ourselves to presentation of the first-order correction to the bias factor:

$$Z^{(1)} = \frac{(Z^{(0)})^2}{2\pi}\delta_0 \tag{323}$$

where δ_0 can be expressed in terms of the components of non-dimensional tensor d'_{ijkl}, entering Eq. (191),

$$\delta_0 = d'_{11} + d'_{22} + d'_{33} + 2\gamma_E(d'_{12} - d'_{11} - 2d'_{44}) \tag{324}$$

where the Voigt's notation of tensor components is used. It should be kept in mind that this equation relates δ_0 to the components of the diffusion tensor written down in the coordinate system related to dislocation [with the basis vectors $(\mathbf{e}_1, \mathbf{e}_2, \mathbf{e}_3)$]. Correspondingly, they can explicitly depend on the dislocation orientation with respect to the lattice symmetry axes. In order to identify a particular orientation of dislocation among many (say, K) possible in the lattice, we will mark below the dislocation-dependent values with a superscript, indicating dislocation orientation. For example, the basis vectors of the coordinate system related to the dislocation will be marked as $(\mathbf{e}_1^k, \mathbf{e}_2^k, \mathbf{e}_3^k)$ for dislocation orientation $k(1 \le k \le K)$, whereas the basis vectors in the crystallographic coordinate system will be referred to simply as $(\mathbf{e}_1, \mathbf{e}_2, \mathbf{e}_3)$, without superscripts.

In a particular case of the cubic lattice, the components of nondimensional tensor d'_{ijkl} in crystallographic coordinate system can be expressed in terms of three independent coefficient [similar to Eq. (171)], which can be transformed to the dislocation coordinate system by an appropriate spatial rotation, namely

$$d'^k_{ijlm} = d^{(1)}\delta_{ij}\delta_{lm} + \frac{1}{2}d^{(2)}(\delta_{il}\delta_{jm} + \delta_{jl}\delta_{im}) + d^{(3)}S^k_{ijlm} \tag{325}$$

where

$$S^k_{ijlm} = \sum_{p=1}^{3} T_{ip}T_{jp}T_{lp}T_{mp} \tag{326}$$

and $T_{im} = \mathbf{e}_i^k\mathbf{e}_m$ is an element of the coordinate system rotation matrix. Correspondingly, Eq. (324) is reduced to

$$\delta_0^k = \frac{1+\upsilon_E}{1-2\upsilon_E}d^{(1)} + \frac{1}{4}d^{(3)}\Phi^k \tag{327}$$

where Φ^k is determined by dislocation orientation with respect to the crystal symmetry axes,

$$\Phi^k = \frac{1}{1-2\upsilon_E}\left[\sum_{p=1}^{3}(\mathbf{e}_1^k\mathbf{e}_p)^2(\mathbf{e}_3^k\mathbf{e}_p)^2 + 1\right] + \sum_{p=1}^{3}(\mathbf{e}_3^k\mathbf{e}_p)^4 - 1 \tag{328}$$

The numerical estimates of the first-order corrections [102], based on dipole tensor values for interstitials and vacancies in iron [82] and copper [82, 87], indicate that their relative importance depends on both the lattice type and the kind of the defect. In bcc iron, the first-order corrections constitute 7–8% of the bias factors for both defect kinds. On the contrary, in fcc copper, the first–order corrections modify the bias factor of interstitials only by 2–3%, while the bias factor of vacancies is changed by nearly 20%.

It is interesting to mention that the orientational dependence of dislocation bias factors (and hence, the sink strength of dislocations with different orientations) requires adequate account of the cubic lattice symmetry in the diffusion tensor. When the cubically symmetric "star" of defect jump directions in the diffusion coefficient is approximated by isotropic distribution of jump directions, any information about the cubic symmetry of the lattice is lost [101].

6.1.3. The Effect of Void Bias on Swelling

Now that we have the dislocation and void bias estimates, let us return to Eq. (308), which determines the swelling rate, and consider the temperatures, where thermal concentration of vacancies is negligible. As can easily be seen, when the voids are sufficiently big (so that one could neglect the difference in void bias factors for interstitials and vacancies), the swelling rate is always positive, because the dislocations are biased towards the absorption of interstitials, $Z_I > Z_V$. Moreover, as the dislocation biases are not very much different for different materials, one should expect only weak dependence of the steady-state swelling rate on the particular material (steady-state means, in particular, that the void number density does not change much). This is indeed found for fcc materials, where the established swelling rate is normally of the order of 1%/dpa (here dpa, abbreviated form of "displacements per

atom," is a physical measure of irradiation dose) [132]. Approximately the same is true for the established swelling rate of bcc materials, in those rare cases, where this established rate is achieved (e.g., in vanadium doped with several percent of subsize impurities [162–165]). However, when one looks at the absolute values of swelling reached at a certain dose, it turns out that the swelling of bcc materials is much smaller than that of fcc materials. For example, pure vanadium (bcc) swells very little (less than 3% at 100 dpa), irrespective to the fact that cavities in neutron-irradiated vanadium are sometimes observed by transmission electron microscopy (TEM) [166, 167]. Possibly the most illustrative demonstration of the effect of crystalline structure on swelling was obtained in an experiment [168], where dual-phase steel with both fcc and bcc grains of essentially the same chemical composition was irradiated by 1 MeV electrons and exhibited swelling only in fcc grains. There exist various tentative explanations of this substantial difference in swelling resistance of bcc and fcc materials, among which one of the most attractive is related to the difference in the elastic interaction of point defects with dislocations [95].

Indeed, consider an irradiated material soon after the onset of irradiation, so that the main sinks for point defects are network dislocations, $\rho_d \gg 4\pi n_v \langle R \rangle$. Let us estimate the growth rate of an individual cavity, as given by Eq. (301). Writing down Eq. (314) as

$$Y_a = 1 + \frac{\Delta R_a}{R}$$

using the Gibbs-Thomson relation for the equilibrium vacancy concentration,

$$C_{V,\mathrm{th}}(R) = C^0_{V,\mathrm{th}}\left(1 + \frac{R_{GT}}{R}\right) \tag{329}$$

and neglecting nonlinear terms in bias corrections, we obtain

$$\frac{dR}{dt} = \frac{(Z_I - Z_V)K}{Z_I Z_V \rho_d R}\left[1 - \frac{R_c}{R}\right] - Y_V D_V C^0_{V,\mathrm{th}} \frac{R_{GT}}{R^2} \tag{330}$$

where

$$R_c = \frac{Z_V \Delta R_I - Z_I \Delta R_V}{(Z_I - Z_V)} \tag{331}$$

Note that in the case when cavities do not contain gas atoms, the value of R_c is positive and of the order of several nanometers [15]. When voids are big, the negative terms in the right-hand side of Eq. (330) can be neglected, whereas at small void sizes, these negative terms dominate. Correspondingly, only sufficiently big voids are able to grow, while smaller vacancy clusters tend to dissolve, even when they are created due to fluctuative events. The limiting size at which the rate of void growth vanishes is called the "critical" size.

As can be seen, there are two physical reasons for the existence of a critical void size. The most well known one is the vacancy evaporation from voids due to the Gibbs-Thomson effect (the thermal vacancy concentration at void surfaces exceeds that in the bulk of material). However, at the temperatures relevant for operation regimes of fusion and fission reactors, the thermal solubility of vacancies in most structural materials is too low to provide any barrier for void nucleation. Nonetheless, at these temperatures the growth of small voids remains hindered due to the intrinsic void bias [169].

Due to the necessity for nucleating voids to overcome a critical size, the formation of voids can occur only as a fluctuative process, which is usually treated in terms of the Fokker-Planck equation formalism (see, e.g., [170–174]). In full agreement with the general nucleation theory [174, 175], the evolution of void ensemble follows three consecutive stages: (i) the incubation period, when all new clusters have sizes below the critical one and can increase their sizes only due to fluctuations; (ii) the nucleation stage, which starts when some of fluctuatively created clusters reach the critical size and is characterized by intensive production of supercritical clusters at nearly constant rate, and (iii) the growth stage, when the already existing voids grow, but practically no new voids is nucleated. Evidently, the bigger is the critical void size, the longer is the duration of the incubation period. As concluded in [95]

on the basis of analysis of rather scarce experimental data, in the case of fcc metals, the relaxation volume of interstitials in saddle points of diffusion jumps is nearly twice as high as that for bcc metals, whereas the reverse is true for vacancies. As a result, the difference in the dislocation bias factors, entering the denominator of (330), can be much lower in fcc metals. Correspondingly, the critical radius for voids in bcc metals can be at least twice as high, requiring nearly an order of magnitude larger amount of vacancies in a critical void in bcc materials, which requires much more time. In other words, the critical void may turn out to be too big to form fluctuatively within a reasonable time [176]. Strictly speaking, the numerical estimates of relaxation volumes in [82] indicate their noticeable difference only for vacancies, but not for interstitials. So, in the absence of reliable data, the explanation of [95] can be neither rejected, nor accepted as the dominant one.

As alternative possibility remains, naturally, the hypothesis that void nucleation in metals is impossible, unless promoted by insoluble gases, which accumulate in void nuclei and prevent their collapse. In this case, the different response of fcc *versus* bcc materials can be attributed to different rates of accumulation of insoluble gases in them [177] or to the differences in the point defect production ratios and intracascade clustering (in the case of cascade producing irradiation) [178].

6.2. Diffusion to Dislocations and Irradiation Creep

An application, where the effect of stress on the diffusion is manifested at much more subtle level than in case of swelling, is irradiation creep. Generally, by creep one means long-term irreversible modification of material shape under the action of nonhydrostatic external loads, usually below the yield strength. Correspondingly, where the sample volume is simultaneously changing, it is a common practice to separate the total material strain into contributions from the volume change (swelling) and shape change (creep). The creep phenomenon is observed in metals even in the absence of irradiation. It has thermofluctuative nature and is usually quite pronounced at temperatures exceeding approximately half of the material melting temperature, T_m. However, irradiation creates in the material high levels of microscopic damage that can quite noticeably accelerate the matter transfer processes, resulting in the macroscopic strain accumulation. Hence, the creep (volume-conserving) strains are usually further separated into additive contributions from the irradiation-free mass transfer (thermal creep) and from that due to irradiation damage (irradiation creep).

6.2.1. A Simple Model of Irradiation Creep

It is experimentally established that creep in crystalline metals (both under irradiation and without it) is as a macroscopic manifestation of the defect microstructure rearrangement under the effect of external loading. As a rule, the shape change of material is related to dislocation system evolution (see, e.g., [179]). Let us recall, therefore, how the rate of macroscopic deformation is related to the dislocation motion parameters. As mentioned in preceding section, only edge dislocations (either network or loops) will be considered.

Let some Cartesian coordinate system (x_1, x_2, x_3) be associated with the material. In a general case, when the coordinate system is not related to any symmetry elements of material and external loading, the deformation rate of material is described by a second-order tensor, which will be denoted as $\dot{\varepsilon}^c_{ij}$ (where $i, j = 1, 2, 3$ and point over ε denotes time derivative). The first step in expressing this macroscopic strain rate in terms of microscopic parameters is to introduce some reasonable simplifications concerning the nature of the dislocation structure. A usual assumption is that network dislocations can be approximated by straight lines. Let us consider a dislocation line that moves with some velocity v (Fig. 15). The contribution of this dislocation segment to the macroscopic strain rate can be written down as [10]

$$\frac{d\varepsilon^c_{ij}}{dt} = V^{-1} e_{imn} \int v_m b_j \, dl_n \tag{332}$$

where integration is performed along the dislocation line, $\boldsymbol{b}$ is the Burgers vector of the dislocation where the considered segment belongs, V is the material volume, and e_{imn} is the

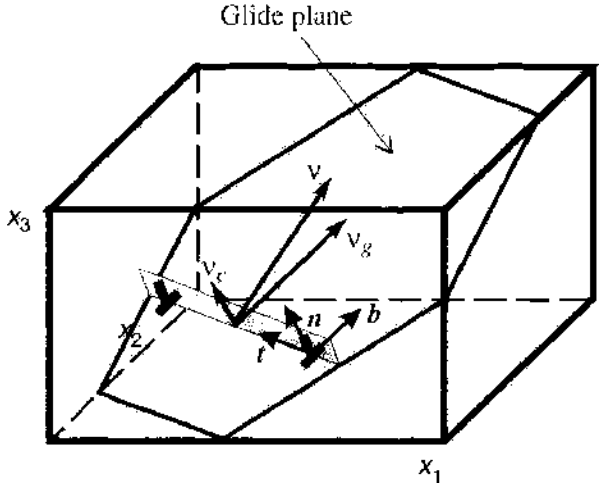

Figure 15. A sketch of dislocation movement geometry. The gray plane is the dislocation extra-plane. Vector notation is explained in the text.

asymmetric Kronecker's tensor. Here and below, the Einstein summation rule over repeated subscripts is implied.

It is usually safe to assume that the average velocity of a straight dislocation is the same over the whole dislocation line. This assumption is valid even in an externally loaded material, as long as the external stresses are uniform over the investigated sample (which is usually the case in creep experiments). However, irradiation creep implies anisotropy of external loading, and thus the dislocation velocity can depend on the dislocation orientation in the material. Usually, the number of possible dislocation orientations in a crystal is limited. Hence, in order to simplify the presentation below, we will assume that the total number of dislocation orientations, N^k, is finite. Under these assumptions, the dislocation network contribution to the total creep rate can be reduced to

$$\dot{\varepsilon}_{ij}^{v} = e_{imn}\rho_d\langle v_m t_n b_j\rangle \tag{333}$$

where $\boldsymbol{t}$ is a unit vector along a dislocation line and the angular brackets for an arbitrary function of dislocation orientation k ($1 < k < N^k$), F^k, mean its averaging,

$$\langle F\rangle = \sum_{k=1}^{N^k} f^k F^k \tag{334}$$

over dislocation orientations with the weight $f^k = \rho_d^k/\rho_d$, where ρ_d^k is the density of dislocations with orientation k.

From the physical point of view, it is convenient to be more specific about the dislocation velocity. Indeed, due to the symmetry reasons, the dislocation velocity is normal to the dislocation line direction $\boldsymbol{t}$. Having in mind that the Burgers vector of an edge dislocation is also normal to $\boldsymbol{t}$, we can write down $\boldsymbol{v}$ as a sum of two vectors, corresponding to two physically different types of dislocation motion (see Fig. 15):

$$v^k = -v_c^k n^k + v_g^k \hat{b}^k \tag{335}$$

where $\hat{b}^k = b^k/b$, $n^k = [\hat{b}^k \times \hat{t}^k]$, b is the absolute value of dislocation Burgers vector (assumed for simplicity to be independent of dislocation orientation) v_g^k is the velocity of dislocation parallel to the dislocation Burgers vector, and v_c^k is the velocity of dislocation in the direction of its extra plane. The movement in the direction of the Burgers vector (called "slide" or "glide") involves only shift of dislocation extra-plane and occurs under the action of local shear stresses. On the contrary, the movement in the direction normal to the Burgers vector (usually referred to as dislocation climb) requires the dissolution or buildup of the extra plane. Dislocation climb is possible only when some diffusional mechanisms of mass

transport are operative and is influenced by the external loads only indirectly, through their effect on the diffusing particle currents to the dislocation. The signs before the terms in the r.h.s. of Eq. (335) are chosen so that $v_c > 0$, when the dislocation climbs by extra plane build-up, while $v_g > 0$, when the dislocation glides in the direction of the Burgers vector.

Substituting (335) into (333), one obtains

$$\dot{\varepsilon}_{ij}^{D} = \rho b \langle \hat{b}_i \hat{b}_j v_c \rangle + \frac{1}{2} \rho b \left\langle \left(\hat{b}_i n_j + n_i \hat{b}_j \right) v_g \right\rangle \tag{336}$$

Note that up to this point, we were not concerned about the reasons for dislocation movement, and this relation is valid for both thermal and irradiation creep.

According to Eq. (336), one can formally consider contributions to creep rate from dislocation climb and glide as additive. This does not mean, however, that climb and glide of dislocations occur completely independently. On the contrary, when the external strains are below the yield strength, the average dislocation glide velocity in real materials is pronouncedly different (normally, much less) as compared to the glide velocity in a perfect crystal, because the glide is hindered by various barriers (point defects, impurity atoms, secondary phases, other dislocations, etc.). The barriers can be overcome either thermofluctuatively or by the climb of a pinned dislocation segment to another glide plane, where the barrier is no more operative. The temperatures relevant for the dominance of irradiation creep are usually too low for thermal fluctuations, and thus the dislocation climb limits both the average glide velocity and the second term in the r.h.s. of Eq. (336). Hence, in what follows, we restrict our consideration entirely to the dislocation climb based contribution.

The dislocation climb contribution to the creep rate is determined by the climb velocity v_c^k, which can be expressed in terms of point defect currents per unit dislocation length, $J_\alpha (\alpha = V$ for vacancies and $\alpha = I$ for interstitials) as

$$v_c^k = b^{-1} (J_I^k - J_V^k) \tag{337}$$

In order to calculate the point defect currents to dislocations, one has to solve an appropriate diffusion problem for point defects in the matrix, assuming that thermally equilibrium concentrations of point defects, $C_{\alpha d}^k$, are maintained at the jogs on the dislocation lines, where the point defect absorption occurs. Note that in externally loaded material, this equilibrium concentration can depend on dislocation orientation with respect to the stress orientation. According to the general rate theory formulation, the point defect current to a dislocation is proportional, first of all, to the difference between the average point defect concentration in the matrix $C_{0\alpha}$ and the equilibrium concentration near the dislocation, $C_{\alpha, \mathrm{th}}^k$, and, second, to the point defect diffusion coefficient $D_{0\alpha}$,

$$J_\alpha^k = Z_\alpha^k D_{0\alpha} (C_{0\alpha} - C_{\alpha, \mathrm{th}}^k) \tag{338}$$

where the bias factors, Z_α^k, are explicitly shown as dependent on dislocation orientation in space. Correspondingly, a simple (quasi-)steady-state balance equation has the form

$$K - \rho d \langle J_\alpha \rangle = 0 \tag{339}$$

Solving the set of Eqs. (339) and (338), one obtains the climb-controlled rate of material creep, $\dot{\varepsilon}_{ij}^c$, as

$$\dot{\varepsilon}_{ij}^c = \dot{\varepsilon}_{ij}^I + \dot{\varepsilon}_{ij}^T \tag{340}$$

that is, the creep rate consists of two contributions, one describing irradiation creep,

$$\dot{\varepsilon}_{ij}^I = \left(\frac{\langle \hat{b}_i \hat{b}_j Z_I \rangle}{\langle Z_I \rangle} - \frac{\langle \hat{b}_i \hat{b}_j Z_V \rangle}{\langle Z_V \rangle} \right) K \tag{341}$$

and another, the thermal one (which corresponds, in fact, to the Nabarro creep mechanism [180])

$$\dot{\varepsilon}_{ij}^{T} = D_{V}\left(\langle \hat{b}_i \hat{b}_j Z_V C_{V,\mathrm{th}}\rangle - \frac{\langle \hat{b}_i \hat{b}_j Z_V\rangle \langle Z_V C_{V,\mathrm{th}}\rangle}{\langle Z_V\rangle}\right) \tag{342}$$

The most important feature of these equations is the dependence of the climb rate on dislocation bias factors for vacancies and interstitials. Indeed, it is seen that irradiation causes dislocation climb acceleration only provided the external load leads in some way to the "double" asymmetry of point defect absorption by dislocations. First of all, dislocation bias factors should depend on dislocation orientation with respect to external loads and, second, this dependence should be different for vacancies and interstitials.

Let's consider now a particular loading scheme, namely, uniaxial external loading by stress σ. More complicated loading schemes can be reduced to it using the so-called Soderberg relations [181]. In order to be specific, we assume that the load is applied along axis 1 of the global coordinate system. When the load σ does not exceed some limiting value σ^*, the bias factors Z_α can be expanded to the first order in σ (or, more conveniently, in dimensionless parameter σ/μ):

$$Z_\alpha^k = Z_\alpha^0\left(1 + \delta_\alpha^k \frac{\sigma}{\mu}\right) \tag{343}$$

where Z_α^0 is the stress-free value of corresponding bias factor and

$$\delta_\alpha^k = \mu\left(\frac{\partial \ln Z_\alpha}{\partial \sigma}\right)_{\sigma=0} \tag{344}$$

The equilibrium concentration of vacancies at a dislocation is defined by the relation [121]:

$$C_{V,\mathrm{th}}^k = C_{V,\mathrm{th}} \exp\left(\frac{g^k \sigma \omega}{k_B T}\right) \tag{345}$$

where $g^k = \hat{b}_i^k \hat{b}_j^k \tilde{\sigma}_{ij}/\sigma$ and $\tilde{\sigma}_{ij}$ is the deviatoric component of the stress tensor. In the case of uniaxial loading, $g^k = (\hat{\mathbf{b}}^k \mathbf{s})^2 - (1/3)$, where $\mathbf{s}$ is the unit vector in the direction of applied load.

Substitution of (343) and (345) into (340) gives

$$\dot{\varepsilon}_{ij}^{DC} = B_{ij}\frac{\sigma}{\mu}K + S_{ij}^{T} Z_V^0 D_{0V} C_{V,\mathrm{th}} \rho d \frac{\sigma\omega}{k_B T} \tag{346}$$

where B_{ij} is the creep compliance, defined as

$$B_{ij} = \langle \hat{b}_i \hat{b}_j (\delta_I - \delta_V - \langle \delta_I - \delta_V\rangle)\rangle \tag{347}$$

and $S_{ij}^T = \langle \hat{b}_i \hat{b}_j (g - \langle g\rangle)\rangle$ is the structure factor of the thermal creep rate. Thus, at $\sigma < \sigma^*$, the creep rate dependence on the generation rate K and the stress value σ has universal character, excellently correlating with experimental observations, irrespective of the mechanism ensuring anisotropy of point defect absorption by dislocations. At the same time, the value of σ^* depends on the particular mechanism.

Historically, the first mechanism answering the necessary requirements of double anisotropy of dislocation biases was based on the effect, which is of the second order in strains and accounts for the stress-induced elastic moduli anisotropy caused by the interaction of point defects with dislocations [123, 141, 160, 182, 183]. Usually in the literature, this mechanism is referred to as stress-induced preferred absorption (SIPA), though in a more comprehensive sense the term SIPA implies any stress-induced anisotropy of point defect absorption.

The basic idea behind this mechanism is that any point defects can be modeled as spherical inclusions (isotropic centers of a dilatation) with elastic constants distinct from those of

surrounding matrix. Then the energy of interaction of a k-type dislocation with point defects has the form of Eq. (189), but the R_α^k is the characteristic radius of dislocation interaction with point defects, which equals to [160]:

$$R_\alpha^k = \frac{\mu\omega b}{\pi k_B T}\left(e_\alpha^0 + p_\alpha^K \frac{\sigma}{E} + p_\alpha^\mu q^k \frac{\sigma}{\mu}\right) \tag{348}$$

Here, E and μ are, respectively, the Young modulus and the shear modulus of material. e_α^0 is the effective dilatation of a point defect, p_α^K and p_α^μ are the factors expressed, respectively, in terms of either the bulk moduli (B, B_α) and shear moduli (μ, μ_α) of the matrix and the point defects of type α [160], or in terms of elastic polarizabilities of point defects P_α^K and P_α^μ [141]:

$$p_\alpha^K = \frac{(1-2\nu_E)(1+\nu_E)(B-B_\alpha)}{2(1-2\nu_E)B + (1+\nu_E)B_\alpha} = \frac{(1-2\nu_E)(1+\nu_E)}{3(1-\nu_E)}\frac{P_\alpha^K}{3B\Omega} \tag{349}$$

$$p_\alpha^\mu = -\frac{5(\mu-\mu_\alpha)}{2[(7-5\nu_E)\mu + 2(4-5\nu_E)\mu_\alpha]} = -\frac{1}{6(1-\nu_E)}\frac{P_\alpha^\mu}{\mu\Omega} \tag{350}$$

(in the original treatment, all values are taken for equilibrium positions and not for the saddle points of diffusion jumps).

The dependence of the interaction energy on the dislocation orientation is given by factor q^k [184]:

$$q^k = 3\nu(\boldsymbol{t}^k\boldsymbol{s})^2 + 3(\hat{\boldsymbol{b}}^k\boldsymbol{s})^2 - (1+\nu_E) \tag{351}$$

As follows from relation (348), the anisotropy of dislocation interaction energy with point defects is determined by differences of shear moduli of point defects and of the matrix. Experimental estimates [185] and results of computer modeling [186] indicate that $\Delta\mu_\alpha = \mu - \mu_\alpha > 0$ for both types of point defects. For vacancies, which occupy the sites of the crystal lattice, the difference between μ and μ_V is usually insignificant. For example, computer simulation of vacancy formation in α-Fe under the combined action of external and dislocation stress fields [187] indicated no dependence of the vacancy formation energy on the stress direction. On the contrary, for interstitial atoms having a dumbbell configuration and easily rotating on-site under the action of shear loads [185], $\mu_I \ll \mu$. For theoretical estimates, they usually accept $\Delta\mu_V = 0$, $\Delta\mu_I = \mu$ [183], which gives (at $\nu_E = 1/3$) $P_I^\mu \approx 0.5$ and $P_V^\mu = 0$. The estimates of p_I^μ and p_V^μ using the values for point defect polarizabilities in Al [188] also indicate that $P_I^\mu \gg P_V^\mu$, though the values of P_I^μ are predicted to be an order of magnitude higher.

The estimates of R_α^k show that at the experimentally relevant temperatures there holds the relation $r_0 \ll R_\alpha^k \ll R_d$, where r_0 is the radius of a dislocation core and $R_d \approx (\pi\rho_d)^{-1/2}$ is the average distance between dislocations. In such an approximation, one can use the zeroth order approximation for the dislocation bias factors , which gives:

$$Z_\alpha^k = \frac{2\pi}{\ln(2R_d/R_\alpha^k)} \approx Z_\alpha^0\left(1 + \frac{Z_\alpha^0 p_\alpha^\mu}{2\pi e_\alpha^0} q^k \frac{\sigma}{\mu}\right) \tag{352}$$

where Z_α^0 is the bias factor value in a stress-free matrix. As can be seen, Z_α^k depends, indeed, on both the type of point defects, and the dislocation orientation. When substituted into Eq. (347), the mechanism of elastic moduli anisotropy leads to the following expression for the irradiation creep compliance B_{ij}:

$$B_{ij} = S_{ij}^{\mathrm{EMA}}\left(\frac{Z_I^0 p_I^\mu}{2\pi e_I^0} - \frac{Z_V^0 p_V^\mu}{2\pi e_V^0}\right) \tag{353}$$

where S_{ij}^{EMA} is the structure factor determined by dislocation orientation distribution with respect to the applied load.

$$S_{ij}^{\mathrm{EMA}} = 3\nu_E\langle\hat{b}_i\hat{b}_j((\boldsymbol{ts})^2 - \langle(\boldsymbol{ts})^2\rangle)\rangle + 3\langle\hat{b}_i\hat{b}_j((\hat{\boldsymbol{b}}\boldsymbol{s})^2 - \langle(\hat{\boldsymbol{b}}\boldsymbol{s})^2\rangle)\rangle$$

Using the estimates $P_l^{\mu} \approx 0.5$, $P_l^{\mu} = 0$, $Z_l^{(l)} \approx 3$, $e_l^{(l)} \approx 1.5$, we get

$$B_{ij} \approx S_{ij}^{\mathrm{EMA}}$$

that is, the creep compliance is of the order of unity. This sounds very similar to the values commonly reported in experimental publications for the majority of reactor structural materials, steels in particular, which has been considered for some time in favor of the elastic moduli anisotropy as the basic mechanism of stress-induced preferred absorption of point defects by dislocations. However, later on it became clear that standard estimates of the point defect generation rate by fast neutrons exaggerate it by nearly an order of magnitude, and thus the analytical prediction of the creep compliance value should be at least an order of magnitude higher in order to fit experimental observations. So high an increase cannot be achieved by variation of parameters entering (353) within any reasonable limits. An additional inconsistency with the experimental data has more fundamental nature. Indeed, for the elastic modulus anisotropy mechanism, the limiting stress σ^* is of the order of the elastic moduli of material, $\sigma^* \sim \mu$, so that linear dependence of the creep rate on stress is retained at any reasonable load, which is in contrast to experimental observations that σ^* is of the order of (irradiation-modified) yield stress. For these reasons, the elastic modulus anisotropy mechanism is interesting rather from the historical point of view.

Much better description of irradiation creep was achieved when the stress-induced anisotropy of point defect diffusion was taken into account. This model was proposed in [99, 189] and has received rather wide development and justification later on [101, 102, 143, 190]. In a case when the external stress is sufficiently low ($\sigma\Omega/k_BT \ll 1$) and the crystalline lattice is cubic, the bias factors can be presented as [102]

$$Z_{\alpha}^{k} = Z_{\alpha}^{(0)}\left(1 - \frac{(1+\nu_E)}{2(1-2\nu_E)} e_{\alpha}^{s} q^{k} \frac{\sigma\Omega}{k_B T}\right) \tag{354}$$

where e_{α}^{s} is the point defect dilatation in the saddle point of diffusion jump, $Z_{\alpha}^{(0)}$ is the bias factor of dislocation in unloaded material, and the orientation factor q^k is defined by the relative orientations of the unit vector of dislocation orientation, $\boldsymbol{t}^k$, the unit vector $\boldsymbol{s}$ in the direction of applied stress, and the basis vectors $\boldsymbol{e}_p (p = 1, 2, 3)$ of the crystalline lattice,

$$q^{k} = d_{\alpha}^{(2)}(\boldsymbol{s}\boldsymbol{t}^{k})^{2} + d_{\alpha}^{(3)} \sum_{p=1}^{3} (\boldsymbol{s}\boldsymbol{e}_p)^{2} (\boldsymbol{t}^{k}\boldsymbol{e}_p)^{2} \tag{355}$$

where $d^{(2)}$ and $d^{(3)}$ are the same as in Eq. (325). As can be seen, the stress-induced modification of dislocation bias depends on the dislocation orientation with respect not only to the applied stress, but to the crystal lattice as well. Hence, let us first consider the case of creep in a monocrystal. In this case, the creep compliance has the form

$$B_{ij}^{DA} = \frac{3B\Omega}{4k_B T}\left[(e_l^s d_l^{(2)} - e_v^s d_v^{(2)}) S_{ij}^{(2)} + (e_l^s d_l^{(3)} - e_v^s d_v^{(3)}) S_{ij}^{(3)}\right] \tag{356}$$

where $S_{ij}^{(2)}$ and $S_{ij}^{(3)}$ are structure factors, defined as

$$S_{ij}^{(2)} = \langle \hat{b}_i \hat{b}_l \rangle \langle (\boldsymbol{t}\boldsymbol{s})^2 \rangle - \langle \hat{b}_i \hat{b}_j (\boldsymbol{t}\boldsymbol{s})^2 \rangle \tag{357}$$

and

$$S_{ij}^{(3)} = \sum_{r=1}^{3} (\boldsymbol{e}_r \boldsymbol{s})^2 \left\{ \langle \hat{b}_i \hat{b}_j \rangle \langle (\boldsymbol{e}_r \boldsymbol{t})^2 \rangle - \langle \hat{b}_i \hat{b}_j (\boldsymbol{e}_r \boldsymbol{t})^2 \rangle \right\} \tag{358}$$

An estimate of the creep compliance at $T = 300°C$ using the point defect polarization data from [82] gives for copper,

$$B_{ij}^{DA} \approx 20 S_{ij}^{(2)} + 7 S_{ij}^{(3)}$$

and for α-iron,

$$B_{ij}^{D4} \approx 70(S_{ij}^{(2)} - S_{ij}^{(3)})$$

Note that the identical coefficients before structure factors constitute a general feature of bcc metals, where $d_n^{(2)} = -d_n^{(3)}$ due to the specific point defect symmetry in the saddle points of diffusion jumps.

One of the most interesting features of Eq. (358) is the prediction of the creep compliance dependence on load orientation with respect to the crystal axes, this effect being the most pronounced in bcc materials [102]. This dependence provides a direct way to the experimental check for the validity of the elastodiffusion mechanism of irradiation creep. Moreover, if this is the case, the values of creep compliance can be used to estimate the parameters of anisotropic point defect diffusion in particular materials. But, to our knowledge, nobody tried to use this possibility up to now.

In polycrystalline materials, the expression for creep compliance should be additionally averaged over different grain orientations [i.e., over $\boldsymbol{e}_p$ in (358)]. Assuming full isotropy of grain orientations, one gets

$$S_{ij}^{(3)} = \frac{2}{5} S_{ij}^{(2)}$$

so that the dependence of $S_{ij}^{(3)}$ on lattice orientation is completely lost.

Because at temperatures up to 1000°C the relation $\mu\Omega/k_BT \gg 1$ holds, the value of creep compliance for the mechanism of diffusion anisotropy is at least one to two orders of magnitude higher than for the moduli anisotropy mechanism and thus much better correlates to experimental predictions, making elastodiffusion one of the most probable mechanisms for SIPA-type irradiation creep.

6.3. Alignment of Dislocation Loops in Irradiated Strained Materials

In this section, we discuss an interesting physical effect, which is essentially enabled by the effect of stress on the efficiency of diffusional capture by very similar microstructural features, such as network dislocations and dislocation loops.

Nucleation and growth of interstitial dislocation loops in the region of primary irradiation damage is one of the most typical features of irradiation effect on the microstructure of crystalline materials. Depending on the irradiation intensity and dose, the loop concentration can reach 10^{15}–10^{16} cm^{-3}. This fact is very well-known, but the question why the dislocation loops are able to grow stably under irradiation is not always trivial. Indeed, because point defects are always created as Frenkel pairs, a stable growth of interstitial loops implies that the excess vacancies are absorbed by alternative sinks. As a rule, the most efficient growth of dislocation loops occurs in the very beginning of irradiation, so practically the only alternative sinks for vacancies are network dislocations. Hence, one meets the question, what is the reason for different sink strength of such similar components of microstructure as network dislocations and dislocation loops? One of the most straightforward explanations is related to the combined effect of lattice symmetry and sink strain fields on the point defect diffusion in the vicinity of sinks. It is interesting that even in cubic lattices, the evolution of dislocation loop structure can occur astoundingly differently. For example, in copper (fcc), dislocation loops nucleate and grow easily (see, e.g., [191]), whereas in bcc α-iron, nucleation and growth of small interstitial loops is observed only in immediate vicinity of network dislocations [191, 192], where a prominent misbalance between interstitial and vacancy concentrations is possible due to the elastic interaction of point defects with dislocations. The same effect was observed also in vanadium [192] and is, probably, typical for bcc metals.

As described in the previous section, the sink strengths of dislocations are dependent on their orientation with respect to the lattice symmetry axes. This difference can be manifested directly, in particular, in the fact that the competition between dislocation loops with different orientations results in the survival of dislocation loops that are not always the most favorable from the energy gain point of view (e.g., in α-iron, the biggest part of dislocation loop population consists of dislocation loops of type $a\langle 100\rangle$ [191–194], which are less

energetically favorable than $(a/2)\langle 100\rangle$ loops). An additional source of diffusion anisotropy appears when the metal is subject to nonhydrostatic external loads. Such external strains can modify dislocation loop bias factors and lead to different kinetics even for dislocation loops lying on crystallographically equivalent atomic planes. As a result, an interesting effect can be possible under special conditions, namely the re-solution of interstitial dislocation loops in irradiated materials subjected to high tension strains, as predicted in [195] and experimentally observed by Jitsukawa et al. [196].

Let us consider in more detail the kinetics of dislocation loops in the case, where metal irradiation occurs under the action of external uniaxial load σ. The formation of interstitial dislocation loop population requires normally very short irradiation doses, so we can assume that from the very beginning the material contains very small dislocation loops. In addition to them, the material inevitably contains network dislocations (with the dislocation density ρ_d), and here we assume that they are the only alternative sinks of point defects. Let the number of orientations of dislocation loop Burgers vectors equal M, while the partial loop number density for loop orientation $m (m = 1, \ldots, M)$ are equal to N_m. If the loops were nucleated in an unstressed isotropic (or cubically symmetric) material, one would expect $N_m = N_L/M$, where N_L is the total number density of dislocation loops. However, when loops are formed in a material subjected to the action of external stress, the number densities of different loop orientations can depend on the stress, for example, as [197, 198]

$$N_m = \frac{N_L}{M} \exp\left(\frac{\Lambda \tilde{\sigma}_{nn} \Omega}{k_B T}\right) \tag{359}$$

where $\Lambda \approx 2$ to 3 is the number of interstitials in the loop nucleus, and $\tilde{\sigma}_{nn}$ is the component of the deviatoric stress tensor normal to the loop extra-plane.

The rate of radius change of a loop with orientation m is given by the relation

$$\frac{dR_m}{dt} = \frac{1}{b}(\eta_I D_I \Delta_I - \eta_V D_V \Delta_V) \tag{360}$$

where b is the Burgers vector value of the dislocation loop, D_α are the stress-free diffusion coefficients for point defects of type α, $\eta_{\alpha m}$ are the bias factors of mth type dislocation loops for point defect of type α, and $\Delta_\alpha = C_{0\alpha} - C_{\alpha, \text{th}}$ are the average point defect supersaturations that are defined by the balance equations

$$K - (Z_\alpha \rho_d + \eta_\alpha \rho_L) D_\alpha \Delta_\alpha = 0 \tag{361}$$

where Z_α are the bias factors of dislocations for point defect of type α (averaged over the dislocation orientations), $\rho_L = 2\pi N_L \langle R \rangle$, $\eta_\alpha = \langle \eta_{\alpha} \rangle$, and the angular brackets $\langle \ldots \rangle$ denote throughout this section the averaging of corresponding values over the loop orientations, for example,

$$\langle \eta_\alpha \rangle = \frac{1}{N_L} \sum_{m=1}^{M} N_m \eta_{\alpha m}$$

After simple transformations, one reduces Eq. (360) to

$$\frac{dR_m}{dt} = \frac{A_m \rho_d + B_m \rho_L}{(Z_I \rho_d + \eta_I \rho_L)(Z_V \rho_d + \eta_V \rho_L)} K \tag{362}$$

where

$$A_m = \eta_{Im} Z_V - \eta_{Vm} Z_I \quad \text{and} \quad B_m = \eta_{Im} \frac{\langle \eta_V R \rangle}{\langle R \rangle} - \eta_{Vm} \frac{\langle \eta_I R \rangle}{\langle R \rangle}$$

Let us estimate the order of magnitude values of the factors A_m and B_m. Even in the absence of external stress, the values of A_m are nonvanishing and the estimates can be done using stress-free values of dislocation and loop bias factors, $\eta_\alpha^{(0)}$ and $Z_\alpha^{(0)}$, respectively. The difference of dislocation biases for interstitials and vacancies is then expressed by Eq. (322),

while the loop bias in the absence of stress can be estimated using the explicit expression for the bias factors of sufficiently large loops [138]

$$\frac{\eta_I^{(0)} - \eta_V^{(0)}}{\eta_I^{(0)}} = \frac{\ln(\overline{P}_I^s/|\overline{P}_V^s|)}{\ln(\zeta R/|R_{sV}|)} \tag{363}$$

where ζ is a numerical factor of the order of unity. For typical values of $\overline{P}_I^s/|\overline{P}_V^s| \approx 5$, $R = 10$ nm, and $\rho_d = 10^8$ to 10^{10} cm^{-2}, we obtain $A^{(0)} = A_m\,(\sigma = 0) \approx 0.1$. The term proportional to $A^{(0)}$ in Eq. (362) describes the growth of all loops due to the preferential absorption of interstitials with respect to network dislocations.

In contrast to A_m, the values of B_m vanish in the absence of external loads, because in this case the loop bias factors are independent of the loop orientation in space. In order to estimate the angular dependence of loop bias factors due to uniaxial external loading, we can, similar to straight dislocations, approximate $\eta_{\alpha m}$ as

$$\eta_{\alpha m} = \eta_\alpha^{(0)}\left(1 + q_\alpha^m \frac{\sigma}{\mu}\right) \tag{364}$$

where q_α^m is the factor defined by the point defect force tensor (i.e., is a property of defect) and by the relative orientation of the loading axis and the loop Burgers vector. In particular, when the main reason for the bias factors is the elastodiffusion, the values q_α^m can be estimated by averaging Eq. (355) over all dislocation orientations, which are allowed for a fixed orientation of the loop Burgers vector,

$$q_\alpha = \frac{(1+\nu_E)}{4(1-2\nu_E)} e_\alpha^s \frac{\mu\Omega}{k_B T}\left[(d_\alpha^{(2)} + d_\alpha^{(3)}) - d_\alpha^{(2)}(\boldsymbol{s}\hat{\boldsymbol{b}}^m)^2 - d_\alpha^{(3)}\sum_{p=1}^{3}(\boldsymbol{s}\boldsymbol{e}_p)^2(\hat{\boldsymbol{b}}^m\boldsymbol{e}_p)^2\right]$$

where $\hat{\boldsymbol{b}}$ is the unit vector directed along the loop Burgers vector. Correspondingly, B_m is directly proportional to the stress applied,

$$B_m \approx \eta_I^{(0)}\eta_V^{(0)}(q_I^m - q_V^m - \langle q_I - q_V\rangle)\frac{\sigma}{\mu} \tag{365}$$

and can be either positive or negative depending on the loop orientation with respect to the applied stress. The term proportional to B_m in (362) corresponds to matter redistribution between differently oriented loops under the effect of external load and stipulates the differences in loop growth rates.

Thus, the kinetics of growth of loops is determined by two, generally competing, mechanisms, namely, (i) the growth of all types of loop owing to the preferential absorption of interstitials as compared to network dislocations, and (ii) the redistribution of matter between differently oriented loops. At the initial stage of loop growth, while $A^{(0)}\rho_d \gg B_m\rho_L$, all the loops grow due to preferential absorption of interstitials as compared to dislocations. However, with the increase of the loop average size, the transfer of matter between differently oriented loops becomes the dominant effect. As a result of this process, some loop orientations can disappear, leading to the creation of pronounced anisotropic distribution of dislocations with a definite orientation of Burgers vector, as it has been observed experimentally in [199, 200].

In order to demonstrate the qualitative behavior of the loop system, let's start with the simplest case of only two loop orientations, namely those with the Burgers vectors aligned along the external uniaxial stress (type 1) and those with the Burgers vectors normal to the stress direction. As can easily be shown, the radii of different loop types are related via

$$\frac{dR_2}{dt} = \frac{A^{(0)}\rho_d + 2\pi B N_1 R_1}{A^{(0)}\rho_d - 2\pi B N_2 R_2}\frac{dR_1}{dt} \tag{366}$$

where $B = \eta_{I1}\eta_{V2} - \eta_{V1}\eta_{I2}$. Introducing here dimensionless quantities $r_1 = R_1/R_{\max}$ and $r_2 = R_2/R_{\max}$, where $R_{\max} = A^{(0)}\rho_d/2\pi BN_1$, and integrating (366) with respect to time, we obtain

$$r_1^2 + pr_2^2 + 2(r_2 - r_1) = 0 \tag{367}$$

where $p = N_2/N_1$, and we have assumed that at the initial moment of time the loop sizes are negligible. In what follows, we neglect the dependence of loop nucleation on stresses and assume $p = 2$.

When the loops are sufficiently small ($r_1, r_2 \ll 1$), Eq. (366) predicts

$$R_2 \approx R_1 \approx R_c\left[\left(1 + \frac{t}{t_c}\right)^{1/3} - 1\right] \tag{368}$$

where

$$R_c = \frac{Z_{I'}\rho_d}{6\pi\eta_{I1}N_1} \quad \text{and} \quad t_c = \frac{b\rho_d^2\eta_{I1}Z_V^3}{18\pi N_1 K A^{(0)}\eta_{I1}^3}$$

The characteristic radius R_c corresponds to the dislocation loop size, where the sink strength of dislocation loops becomes the same as that of network dislocations, while t_c is the characteristic time for this process. At the cited values of the parameters and $K = 10^{-6}$ to 10^{-3} dpa/s, we get $R_c \approx 1$ to 10 nm and $t_c \approx 0.1$ to 1000 s.

The loop size kinetics at arbitrary times can be conveniently expressed in terms of a unique variable y, related to the dimensionless loop radii as

$$r_1 = 1 + \sqrt{\frac{3}{2}}y \quad \text{and} \quad r_2 = -\frac{1}{2} + \sqrt{\frac{3}{2}}(1 - y)$$

Note that these relations predict the maximum possible size of nonaligned loops $R_{2\max} \approx 0.37R_{\max}$.

The time variation of y is easily obtained by solution of equation set (362) and (367), being given by implicit dependence:

$$F(y) = \tau_0 + \tau \tag{369}$$

where

$$F(y) = (1 + \beta_I\beta_V)\arcsin y + (\beta_I + \beta_V)y^2 + (\beta_I\beta_V - 1)y\sqrt{1 - y^2} \tag{370}$$

$\tau = t/t_m$, $\tau_0 = F(-\sqrt{2/3}) \approx 1.45$, $\beta_\alpha = \sqrt{2}\eta_{\alpha 2}/\eta_{\alpha 1}$, and

$$t_m = \frac{3(A^{(0)}\rho_d)^2\eta_{I1}\eta_{V1}b}{4\sqrt{2}N_1 K B^3}$$

The plot of the loop radii r_1 and r_2 as a function of dimensionless time τ is presented in Fig. 16a. As can be seen, the aligned loops monotonically grow, whereas the nonaligned loop size reaches the maximum value and then decreases until at the time $t_r \sim 6.7t_m$, the nonaligned loops completely dissolve.

The characteristic time of the loop resolution is very sensitive to material parameters and irradiation conditions. At high irradiation fluxes, $K = 10^{-3}$ dpa/s, which can be reached only by irradiation in MV electron microscopes, and at high external loads, $\sigma/\mu \sim 5 \times 10^{-3}$, one gets $t_r \sim 10^3$ s in a well-annealed metal ($\rho_d \sim 10^8$ cm^{-2} and $N_1 \sim 10^{15}$ cm^{-3}). On the contrary, in cold-worked materials, this time can reach many years. In other words, in the normal operation conditions of nuclear reactors, such resolution will be practically unobservable over any reasonable time. Moreover, if the maximum possible size of the nonaligned loops exceeds the average distance between network dislocations, all the loops will incorporate into the dislocation network prior to the onset of the re-solution. In order to observe experimentally the effect of dislocation loop resolution, one should use highly efficient damage production conditions (e.g., irradiation in high-voltage electron microscope)

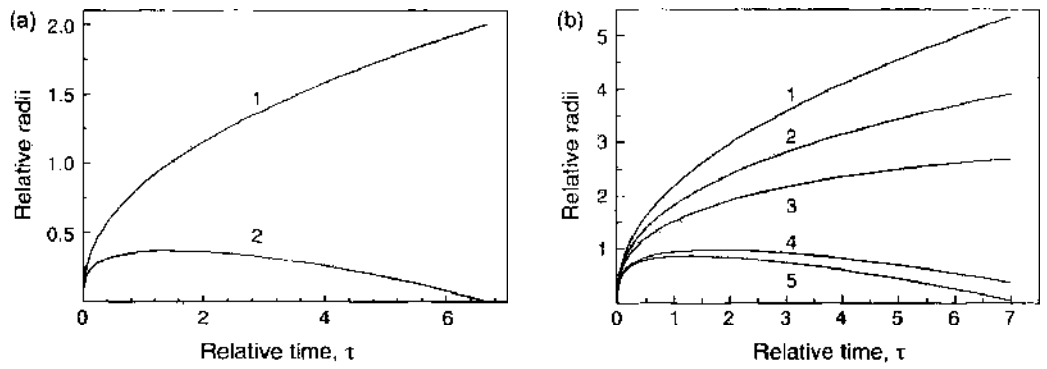

Figure 16. The dependence of dimensionless radii of the dislocation loops on dimensionless time τ. (a) The case of two loop orientations (curve numbering according to the loop type, as described in text). (b) The case of six loop orientations, as indicated by numbers at curves: 1-[110], 2-[$\bar{1}$01], 3-[0$\bar{1}$1], 4-[101], 5-[011] and [1$\bar{1}$0].

and high external loads. Additionally, in order to avoid the incorporation of nonaligned loops into the dislocation network, the condition $R_{\max} \ll (\pi\rho_d)^{-1/2}$ should be fulfilled, which is equivalent to the requirement (assuming $A^{(0)} \approx 0.1$ and $B \approx 3\sigma/\mu$):

$$\frac{\sigma}{\mu} \gg 0.1\frac{\rho_d^{3/2}}{N_1}$$

If this criterion is fulfilled, the nonaligned loops can completely disappear, while the aligned loops reach the size of $R_1 = 2R_{\max}$. At higher times, they grow approximately proportional to $(Kt)^{1/3}$, independent of the external load. Indeed, after the dissolution of nonaligned loops there remains no competition between loops, and the remaining loops grow at the expense of the preferential absorption of interstitials by loops as compared to network dislocations. The loop growth continues until the loops become sufficiently large to be incorporated into the dislocation network.

In contrast to many theoretical predictions that remain at the level of qualitative speculations, the effect of dislocation loop resolution has really been observed in annealed Ni samples, irradiated in the column of electron microscope [196]. It was found that the loops with the Burgers vector orientation [110] (nearly along the direction [43$\bar{2}$] of uniaxial load) grow steadily, the loops with Burgers vectors [$\bar{1}$01] (inclined with respect to the loading direction) grow noticeably slower, while loops with Burgers vectors [011] (i.e., nearly normal to the load direction) first grow and then dissolve. In other words, the loop behavior is in qualitative agreement with the simple model predictions.

It can easily be checked that the combination of experimental parameters met in [196] satisfies all the requirements, allowing observation of dislocation loop redistribution. The damage rate reached 2×10^{-3} dpa/s and loads were as high as 50 MPa (corresponding to $\sigma/\mu \sim 6 \times 10^{-3}$). Though the number densities of dislocation loops were not directly cited, a rough estimate based on the TEM micrographs presented in [196] gives $N_L \sim 10^{15}$ cm^{-3}. However, the real situation is more complicated than in the simple model, as the symmetry of fcc crystals allows six orientations of dislocation loops of the type $\langle 110 \rangle$, and all of them were observed in the experiment. In order to better represent the experiment, it is possible to solve numerically six equations of the form (362) with appropriate loop orientations. A typical dependence of loop radii on the relative time is demonstrated in Fig. 16b. Distribution between loop orientations was assumed to be uniform ($N_{in} = N_L/6$), while the stress was assumed to be applied along [43$\bar{2}$] direction. The predicted behavior is in excellent qualitative agreement with experimental observations of [196].

7. CONCLUSION

The level of qualitative understanding of diffusion at different length and time scales, both in stress-free and strained crystalline solids, is quite formidable, but the accumulation of reliable quantitative data characterizing atomic jumps in particular materials remains a major task.

The importance of such a database cannot be underestimated, because the diffusion in solids at the macroscopic length scales, where continuum equations are used to describe the diffusional mass transport, cannot be treated quantitatively without the knowledge of diffusion coefficients for all the particles that participate in the game. Unfortunately, except for simple crystalline lattices, it is not easy to measure experimentally the energies and other parameters of formation and migration of individual particles, especially at comparatively low temperatures,[2] where diffusion is relatively slow. Moreover, very often many different processes at the atomic level contribute to the diffusion transport of different atomic species, which makes interpretation of experimental results uncertain. For this reason, computer experiment remains the major source of diffusion parameters, and it is quite common even to interpret experimental observations using parameter values predicted in computer experiments. Still, regardless of the undoubtedly high power of modern computational tools, one should be cautious in assigning too much confidence to calculated parameters.

As can be seen from the presentation above, the majority of diffusion parameters are obtained using various versions of molecular statics approach. The ideological basis of this approach is, however, unreliable. Certainly, one can expect that such modeling is able to reproduce qualitative features of atomic system behavior, such as the relation between the heights of different diffusion barriers, but particular numbers can hardly be considered more than an order of magnitude estimate, even if the interatomic potentials used in simulations were exact. Unfortunately, the reliability of empirical interatomic potentials is unknown, at least as long as diffusion jumps are concerned. Indeed, standard procedures of empirical potential verification include fitting of potential parameters to the near-equilibrium properties of corresponding materials, such as elastic moduli, phonon spectra, cohesion energies (in compounds), and sometimes to the experimentally measured energies of simple defects, such as vacancies or stacking faults. This means that the empirical potentials are reliable mainly in the region of interatomic distances more or less close to the potential minimum position. Correspondingly, different potentials give similar results only for systems not much different from an ideal lattice. In far-from-equilibrium atomic configurations, the predictions very often become potential-sensitive. A nice example demonstrating how big a difference in predictions of different potentials may be is given by the simulation of vacancy binding to an edge dislocation in α–iron: for different potentials, the binding energy varied in the range of 0.45 to 1.3 eV [201]. For the modeling of diffusion jumps, the situation is even worse: in the saddle point of a diffusion jump, the jumping particle often interacts with its neighbors in the strong repulsion range of interatomic potential, where interaction energy varies sharply in response to small changes in interatomic distances. For this reason, the only reliable interaction energies may be expected from simulations based on *ab initio* methods. In the last decade there appeared quite a number of first-principles calculations of equilibrium energies of self defects and impurities in various kinds of solids: metals, semiconductors and insulators. Defect migration energies are addressed by this technique noticeably less, but in the last time the number of such calculations increases, especially when one tries to investigate diffusion-promoted kinetics of defect microstructure in the framework of multiscale treatment, including simultaneous application of several simulation techniques (e.g., kinetic Monte-Carlo defect annealing with defect energies provided by *ab initio* [202, 203]). The most seldom reported are first-principles calculations of defect force tensors [204–206], but even these can now be performed on a regular basis in some most widespread *ab-initio* packages, such as AIMPRO (e.g., [205]). However, these methods require extremely powerful computational means, which precludes at present their extensive use. One should also have in mind that the sizes of *ab initio* computation cells are currently limited to at best half a thousand atoms, which is often insufficient to eliminate the influence of boundary conditions on the simulation predictions, especially for defects that cause pronounced relaxation of surrounding lattice.

Much more reliable information about the atom migration kinetics can be obtained, in principle, by dynamic modeling performed in the framework of molecular dynamics. Modern

[2] It should be kept in mind that "comparatively low" temperatures can be quite high from the everyday life point of view, reaching hundreds of degrees Celsius.

computers allow one to study sufficiently big atomic systems (up to several millions of atoms), but the typical "physical time" of tens of nanonseconds, as reached in practical computations, is quite short as compared to typical times of diffusion movements. However, the main problem of modern MD simulations is that they only seldom try to cooperate with analytical understanding of diffusion jump kinetics reached by dynamic theories, which potentially can give correlation between atomic jump frequencies and the intensities of appropriate vibration modes in the crystal phonon spectrum (see, e.g., [207, 208]). Not much attention is paid to the investigation of individual jump geometries, which can be quite different from the paths that are tested in molecular statics approach (see, e.g., [208]). And certainly, there remains the problem of appropriate potentials. Possibly, the best computational tool for investigation of diffusion would *be ab initio* molecular dynamics—but for the crystal sizes appropriate for diffusion studies, this is definitely a matter of future.

It should be also kept in mind that the knowledge of appropriate formation and migration energies of diffusing particles is only the first step in the treatment of diffusion. As we have demonstrated, only in simple (usually, monatomic) crystals, the diffusion coefficients are straightforwardly expressed in terms of individual atomic jump parameters. In more complicated systems, it is quite a nontrivial task to correlate the rate of mass transfer with parameters of elementary diffusion events. Two examples of this kind (diffusion on fcc and diamond lattices) were considered in this chapter. More complicated situations, like diffusion in ordered compounds, or self-diffusion via competing mediators (e.g., vacancies and interstitials in silicon) remain the topics of modern research. A very helpful method here may be lattice kinetic Monte Carlo, but only provided it is used in conjunction with other computational techniques that provide appropriate input parameters for the relative jump frequencies of different diffusing particles. The advantage of this technique is the possibility to model simultaneously diffusion and clustering of particles on length scales of the order hundreds of nanometers and timescales of microseconds to seconds (see, e.g., [209]), which makes LKMC a link between the purely atomistic techniques and macroscopic analytical models. However, such simulations are extremely demanding to computational resources, especially for strained systems.

Finally, in the field of continuum modeling of diffusion, in practically interesting systems purely analytical methods are inevitably restricted to investigation of simplified models and are used in order to reach qualitative understanding of trends in material behavior. More detailed quantitative answers require numerical solution of appropriate diffusion equations. Technically this is seldom a problem, because the numerical techniques for solving diffusion equations are currently well developed and can be found in many textbooks and general-purpose computational packages, such as Maple or MathCad. The drawback of numerical approach to continuum modeling is also well-known: being restricted to a particular set of input parameters, it usually gives answer exclusively for the studied task and is completely useless in predicting trends of system behavior outside the investigated parameter range.

Summing up, regardless of the achieved level of understanding of diffusion in crystals, there remain a lot of tasks that require investigation by both analytical and numerical methods. This is even truer for the effect of stress on diffusion, which will certainly attract more attention with the development of technologies that use strains for monitoring the behavior of advanced modern materials.

REFERENCES

1. J. R. Manning, "Diffusion Kinetics for Atoms in Crystals," van Nostrand, Princeton, 1968.
2. C. P. Flynn, "Point Defects and Diffusion," Clarendon, Oxford, 1972.
3. B. S. Bokshtein, S. Z. Bokshtein, and A. A. Zhukhovitskii, "Thermodynamics and Kinetics of Diffusion in Solids," Metallurgia, Moscow, 1974. (in Russian).
4. P. Shewmon, "Diffusion in Solids," 2nd Edn. TMS, Warrendale, PA, 1989.
5. J. Philibert, "Atom Movements. Diffusion and Mass Transport in Solids," Les Editions des Physique, Les Ulis, 1991.
6. M. G. Ganchenkova and A. V. Nazarov, *Comp. Mater. Science*, 17, 319 (2000).
7. M. J. Aziz, *Appl. Phys. Lett.* 70, 2810 (1997).
8. A. Antonelli and J. Bernholc, *Phys. Rev. B* 40, 10643 (1989).

9. N. E. B. Cowern, P. C. Zalm, P. van der Sluis, D. J. Gravesteijn, and W. B. de Boer. *Phys. Rev. Lett.* 72, 2585 (1994).
10. J. P. Hirth and J. Lothe, "Theory of Dislocations." McGraw-Hill, New York, 1968.
11. P. M. Fahey, P. B. Griffin, and J. D. Plummer, *Rev. Mod. Phys.* 61, 289 (1989).
12. E. M. Lifshitz and L. P. Pitaevskii, "Physical Kinetics. Course of Theoretical Physics," Vol. 10. Pergamon, Oxford, 1981.
13. L. D. Landau and E. M. Lifshitz, "Statistical Physics Part I, Course of Theoretical Physics," Vol. 5. Pergamon, Oxford, 1980.
14. P. H. Dederichs and K. Schroeder, *Phys. Rev. B* 17, 2524 (1978).
15. V. A. Borodin, A. I. Ryazanov, and C. Abromeit, *J. Nucl. Mater.* 207, 242 (1993).
16. C. Zener, in "Imperfections in Nearly Perfect Crystals," p. 289. J. Wiley & Sons, New York, 1952.
17. L. A. Girifalco, "Statistical Physics of Materials." Wiley Interscience, New York, 1973.
18. H. B. Huntington, *Phys. Rev. B* 61, 325 (1942); H. B. Huntington and F. Seitz, *Phys. Rev. B* 76, 1728 (1949); H. B. Huntington, *Phys. Rev. B* 91, 1092 (1953).
19. D. Lazarus, in "Diffusion in Metals and Alloys, DIMETA-82" (F. J. Kedves and P. L. Beke, Eds.) p. 134. TransTech Publications, Zurich, 1983.
20. W. H. Press, S. A. Teukolsky, W. T. Vetterling, and B. P. Flannery, "Numerical Recipes In C: The Art of Scientific Computing." Cambridge University Press, Cambridge, 2002.
21. C. J. Cerjan and W. H. Miller, *J. Chem. Phys.* 75, 2800 (1981).
22. M. C. Payne, M. P. Teter, D. C. Allan, T. A. Arias, and J. D. Joannopoulos, *Rev. Mod. Phys.* 64, 1045 (1992).
23. R. Fletcher and C. M. Reeves, *Computer J.* 7, 149 (1964).
24. E. Polak, "Computational Methods in Optimization." Academic, New York, 1971.
25. K. W. Brodlie, in "The State of the Art in Numerical Analysis" (D. A. H. Jacobs, Ed.), ch. III.1.7. Academic, London, 1977.
26. M. P. Teter, M. C. Payne, and D. C. Allan, *Phys. Rev. B* 40, 12255 (1989).
27. A. R. Leach, "Molecular Modeling: Principles and Applications," 2nd Edn. Pearson Education Ltd., Dorset, 2001.
28. R. Johnson and J. Beeler, in "Interatomic Potentials and Crystalline Defects" (J. K. Lee, Ed.), p. 165. The Metallurgical Society of AIME, Warrendale, PA, 1981.
29. H. Jonsson, G. Mills, and K. W. Jacobsen, in "Classical and Quantum Dynamics in Condensed Phase Simulations" (B. J. Berne, G. Ciccotti, and D. F. Coker, Eds.), p. 385. World Scientific, Singapore, 1998.
30. G. M. Crippen and H. A. Scheraga, *Arch. Biochem. Biophys.* 144, 462 (1971).
31. R. L. Hilderbrandt, *Comp. Chem.* 1, 179 (1977).
32. J. Simons, P. Jørgensen, H. Taylor, and J. Ozment, *J. Chem. Phys.* 87, 2745 (1983).
33. D. J. Wales, *J. Chem. Phys.* 101, 3750 (1994).
34. L. J. Munro and D. J. Wales, *Phys. Rev. B* 56, 3969 (1999).
35. G. Henkelman and H. Jonsson, *J. Chem. Phys.* 113, 9978 (2000).
36. G. Kresse and J. Hafner, *Phys. Rev. B* 47, 558 (1993); G. Kresse and J. Furthmüller, *Phys. Rev. B* 54, 11169 (1996).
37. G. T. Barkema and N. Mousseau, *Phys. Rev. Lett.* 77, 4358 (1996).
38. O. S. Trushin, P. Salo, T. Ala-Nissila, and S. C. Yang, *Phys. Rev. B* 69, 033405 (2004).
39. A. F. Voter, F. Montalenti, and T. C. Germann, *Annu. Rev. Mater. Res.* 32, 321 (2002).
40. M. M. Steiner, P. A. Genilloud, and J. W. Wilkins, *Phys. Rev. B* 57, 10236 (1998).
41. G. H. Vineyard, *J. Phys. Chem. Sol.* 3, 121 (1957).
42. S. A. Rice, *Phys. Rev.* 112, 804 (1958).
43. O. P. Manley and S. A. Rice, *Phys. Rev.* 116, 632 (1960).
44. H. R. Glyde, *Rev. Mod. Phys.* 39, 373 (1967).
45. C. P. Flynn, *Phys. Rev.* 171, 682 (1968).
46. M. Toller, J. Jacucci, G. DeLorenzi, and C. P. Flynn, *Phys. Rev. B* 32, 2082 (1985).
47. R. Car and M. Parrinello, *Phys. Rev. Lett.* 55, 2471 (1985).
48. Yu. N. Osetsky, *Def. Diff. Forum* 188, 71 (2001).
49. H. J. C. Berendsen and W. F. van Gunsteren, in "Molecular Dynamics Simulation of Statistical-Mechanical Systems" (G. Ciccotti and W. G. Hoover, Eds.), p. 43. North-Holland, Amsterdam, 1986.
50. M. P. Allen and D. J. Tildesley, "Computer Simulation of Liquids." Clarendon, Oxford, 1987.
51. J. M. Haile, "Molecular Dynamics Simulation." John Wiley & Sons, New York, 1992.
52. H. C. Andersen, *J. Chem. Phys.* 72, 2384 (1980).
53. M. Parrinello and A. Rahman, *Phys. Rev. Lett.* 45, 1196 (1980); *J. Appl. Phys.* 52, 7158 (1981); M. Parrinello, in "Molecular Dynamics Simulation of Statistical-Mechanical Systems" (G. Ciccotti and W. G. Hoover, Eds.), p. 204. North-Holland, Amsterdam, 1986.
54. S. Nosé, *Molec. Phys.* 52, 255 (1984).
55. W. G. Hoover, *Phys. Rev. A* 31, 1695 (1985).
56. H. Ullmaier and W. Schilling, in "Physics of Modern Materials," p. 301. IAEA, Vienna, 1980.
57. G. Leibfried and N. Breuer, "Point Defects in Metals I: Introduction to the Theory." Springer, Berlin, 1978.
58. H. J. Kanzaki, *J. Phys. Chem. Sol.* 2, 24 (1957).
59. M. Werner, H. Mehrer, and H. D. Hochheimer, *Phys. Rev. B* 32, 3930 (1985).
60. F. J. Kedves and G. Erdelyi, *Def. Diff. Forum* 66, 175 (1989).
61. H. Wollenberger, in "Physical Metallurgy," 3rd Edn., Vol. 3, p. 1140. North-Holland, Amsterdam, 1983.

62. P. Ehrhart, in "Dimensional Stability and Mechanical Behaviour of Irradiated Metals and Alloys," p. 101. BNES, London, 1983.
63. R. W. Keys, *J. Chem. Phys.* 29, 467 (1958).
64. A. W. Lawson, *J. Phys. Chem. Sol.* 3, 250 (1957); A. W. Lawson, S. A. Rice, R. D. Corneliussen, and N. H. Nachtrieb, *J. Chem. Phys.* 32, 447 (1960).
65. R. E. Hanneman and H. C. Gatos, *J. Appl. Phys.* 36, 1794 (1965).
66. S. N. Vaidya, *J. Phys. Chem. Sol.* 42, 621 (1981).
67. M. Ganchenkova, A. Nazarov, and A. Kuznetzov, *Nucl. Inst. Meth. Phys. Res. B* 202, 107 (2003).
68. L. Tewordt, *Phys. Rev.* 109, 61 (1958).
69. K. H. Bennemann, *Phys. Rev.* 124, 669 (1961).
70. J. B. Gibbson, A. N. Goland, M. Milgram, and G. H. Vineyard, *Phys. Rev.* 120,1229 (1960).
71. R. A. Johnson, *Phys. Rev.* 134, A1329 (1964).
72. J. D. Eshelby, in "Solid State Physics," Vol. 3, p. 79. Academic, New York, 1956.
73. R. Johnson and W. D. Wilson, in "Interatomic Potentials and Simulation of Lattice Defects," p. 301. Battelle Inst., Seattle, 1971.
74. F. D. Murnaghan, *Proc. Natl. Acad. Sci. U. S. A.* 30, 244 (1944).
75. J. R. Hardy, *J. Phys. Chem. Sol.* 15, 39 (1960).
76. J. R. Hardy, *J. Phys. Chem. Sol.* 29, 2009 (1968).
77. P. T. Heald and K. M. Miller, *J. Nucl. Mater.* 66, 107 (1977).
78. H. R. Schober and K. W. Ingle, *J. Phys. F* 10, 575 (1980).
79. K. M. Miller and P. D. Bristowe, *Phys. Stat. Sol. (b)* 86, 93 (1978).
80. C. N. Tome and E. J. Savino, *Mater. Sci. Eng.* 24, 109 (1976); C. N. Tome, H. A. Ceratto, and E. J. Savino, *Phys. Rev. B* 25, 7428 (1982).
81. A. G. Crocker, M. Doneghan, and K. W. Ingle, *Philos. Mag. A* 41, 21 (1980).
82. H. R. Schober, *J. Nucl. Mater.* 126, 220 (1984).
83. A. V. Nazarov and A. A. Mikheev, *Def. Diff. Forum*, 143, 177 (1997).
84. A. V. Nazarov, M. G. Ganchenkova, and A. A. Mikheev, *Def. Diff. Forum*, 194, 49 (2001).
85. M. J. Gillan, *Philos. Mag. A* 48, 903 (1983).
86. M. J. Gillan, *J. Phys. C* 17, 1473 (1984).
87. M. P. Puls and C. H. Woo, *J. Nucl. Mater.* 139, 48 (1986).
88. V. A. Borodin, Yu. R. Kevorkyan, V. V. Kolomytkin, and A. I. Ryazanov, *J. Nucl. Mater.* 187, 131 (1992).
89. P. H. Dederichs, C. Lehmann, H. R. Schober, A. Scholz, and R. Zeller, *J. Nucl. Mater.* 69, 176 (1978).
90. M. S. Daw, W. Windl, N. N. Carlson, M. Laudon, and M. P. Masquelier, *Phys. Rev. B* 64, 045205 (2001).
91. G. D. Watkins, J. R. Troxell, and A. P. Chatterjee, in "Defects and Radiation Defects in Semiconductors" (J. H. Albany, Ed.), p. 16. IOP Conference Proceeding No. 46. Institute of Physics, Bristol, 1978.
92. M. J. Puska, S. Pöykkö, M. Pesola, and R. M. Nieminen, *Phys. Rev. B* 58, 1318 (1998).
93. W. G. Wolfer and M. Ashkin, *J. Appl. Phys.* 46, 547 (1974).
94. W. G. Wolfer, in "Fundamental Aspects of Radiation Damage in Metals," Vol. 2, p. 812. US ERDA CONF-751 006, 1975.
95. J. J. Sniegowski and W. G. Wolfer, in "Proceedings of Topical Conference on Ferritic Alloys for Use in Nuclear Energy Technologies" (J. W. Davis and D. J. Michel, Eds.), p. 579. The Metallurgical Society of AIME, Warrendale, 1984.
96. V. A. Borodin, V. M. Manichev, and A. I. Ryazanov, *Fiz. Met. Metalloved.* 63, 435 (1987).
97. F. S. Ham, *J. Appl. Phys.* 30, 915 (1959).
98. I. G. Margvelashvili and Z. K. Saralidze, *Fizika Tverdogo Tela* 15, 266 (1973).
99. E. J. Savino, *Philos. Mag.* 36, 323 (1977).
100. I. W. Chen, *J. Nucl. Mater.* 125, 52 (1984).
101. B. C. Skinner and C. H. Woo, *Phys. Rev. B* 30, 3084 (1984).
102. V. A. Borodin and A. I. Ryazanov, *J. Nucl. Mater.* 210, 258 (1994).
103. A. V. Nazarov, A. A. Mikheev, and M. G. Ganchenkova, in "Scientific Session MEPhI-2003," Vol. 9, p. 187. Moscow Engineering Physics Institute, Moscow, 2003.
104. J. F. Ziegler, J. P. Biersack, and U. Littmark, "The Stopping and Range of Ions in Solids." Pergamon, New York, 1999.
105. N. N. Lebedev, "Special Functions and Their Applications." Fizmatgiz, Moscow, 1963, (in Russian).
106. M. E. J. Newman, and G. T. Barkema, "Monte Carlo Methods in Statistical Physics." Clarendon, Oxford, 1999.
107. R. J. Elliot, J. A. Krumhansl, P. L. Leath, *Rev. Mod. Phys.* 46, 465 (1974).
108. A. D. Brailsford and R. Bullough, *J. Nucl. Mater.* 44, 121 (1972).
109. A. D. Brailsford, R. Bullough, and M. R. Hayns, *J. Nucl. Mater.* 60, 246 (1976).
110. R. Balescu, "Equilibrium and Non-Equilibrium Statistical Mechanics." Wiley-Interscience, New York, 1975.
111. A. D. Brailsford, *J. Nucl. Mater.* 60, 257 (1976).
112. B. U. Felderhof and J. M. Deutch, *J. Chem. Phys.* 64, 4551 (1976).
113. H. Gurol, *Trans. ANS* 28, 196 (1978).
114. A. D. Brailsford and R. Bullough, *Phil. Trans. Roy. Soc. London* 302, 78 (1981).
115. J. A. Marqusee and J. Ross, *J. Chem. Phys.* 80, 536 (1984).
116. V. A. Borodin, *Physica A* 211, 279 (1994).
117. S. Reiss and K.-H. Heinig, *Nucl. Instr. Meth. B* 84, 229 (1994); *Nucl. Instr. Meth. B* 102, 256 (1995); *Nucl. Instr. Meth. B* 112, 223 (1996).

118. K. Krishan, *Rad. Effects* 66, 121 (1982).
119. A. M. Kosevich, Z. K. Saralidze, and V. V. Slezov, *Fizika Tverdogo Tela* 9, 895 (1967).
120. H. Wiedersich, *Rad. Effects* 12, 111 (1972).
121. V. V. Slyozov and P. A. Bereznhyak, in "Physics of Radiation Effects in Crystals," p. 575. Elsevier Science, Amsterdam, 1986.
122. V. V. Slyozov, *Fizika Tverdogo Tela* 31, 20 (1989).
123. P. T. Heald and M. V. Speight, *Acta Metall.* 23, 1389 (1975).
124. J. C. Maxwell, "A Treatise on Electricity and Magnetism," 3rd Edn., Vol. 1. Clarendon, Oxford, 1892.
125. K. Mattern and B. U. Felderhof, *Physica* 135, 505 (1986).
126. V. A. Borodin, K.-H. Heinig, and S. Reiss, *Phys. Rev. B* 56, 5332 (1997).
127. L. A. Maximov, A. I. Ryazanov, and V. L. Tsymbalenko, *Sov. Phys.-JETP* 83, 199 (1996).
128. R. de Wit, *J. Res. Nat. Bur. Stand.* 77A, 49 (1973).
129. C. Cawthorne and E. J. Fulton, *Nature*, 216, 576 (1967).
130. L. K. Mansur, *Nucl. Techn.* 40, 5 (1978).
131. V. F. Zelenskyi, I. M. Neklyudov, and T. P. Chernyaeva, "Radiation Defects and Swelling of Metals." Naukova Dumka, Kiev, 1988. (in Russian).
132. F. A. Garner, in "Materials Science and Technology. A Comprehensive Treatment," Vol. 10A, p. 419. VCH, Weinheim, 1994.
133. V. A. Borodin, A. I. Ryazanov, and D. G. Sherstennikov, *J. Nucl. Mater.* 202, 169 (1993).
134. G. P. Pells, *J. Nucl. Mater.* 122, 1338 (1984).
135. F. A. Nichols, in "Annual Review of Material Science," Vol. 2, p. 463. Annual Reviews Press, Palo Alto, CA, 1972.
136. A. N. Orlov, G. N. Samsonidze, and Yu. V. Trushin, *Zh. Tech. Fiz.* 56, 1311 (1986).
137. A. I. Ryazanov and D. G. Sherstennikov, *J. Nucl. Mater.* 186, 33 (1991).
138. L. A. Maksimov and A. I. Ryazanov, *Rad. Effects* 33, 7 (1977).
139. G. Z. Gorbatov, *Fiz. Met. Metalloved.* 48, 100 (1979).
140. R. Bullough, M. R. Hayns, and C. H. Woo, *J. Nucl. Mater.* 84, 93 (1979).
141. W. G. Wolfer and M. Ashkin, *J. Appl. Phys.* 47, 791 (1976).
142. R. Bullough and T. M. Quigley, *J. Nucl. Mater.* 104, 1397 (1981).
143. C. H. Woo, *J. Nucl.Mater.* 120, 55 (1984).
144. S. I. Golubov, *Fiz. Met. Metalloved.* 67, 36 (1989).
145. A. H. King and D. A. Smith, *Rad. Effects* 54, 169 (1981).
146. R. J. White, S. B. Fisher, and K. M. Miller, *Rad. Effects* 41, 17 (1979).
147. R. Bullough, M. R. Hayns, and M. H. Wood, *J. Nucl. Mater.* 90, 44 (1980).
148. R. W. Balluffi, *Phys. Stat. Sol.* 31, 443 (1969).
149. A. D. Brailsford and R. Bullough, in "Vacancies'76," p. 108. Metals Society, London, 1976.
150. L. A. Maximov and A. I. Ryazanov, *Rad. Effects* 51, 197 (1980); *Rad. Effects* 52, 175 (1980).
151. A. I. Ryazanov and V. A. Borodin, *Rad. Effects* 55, 157 (1981).
152. V. V. Ivanov and V. M. Chernov, *Atomnaya Energiya* 61, 622 (1986); *Atomnaya Energiya* 61, 628 (1986).
153. H. Kamiyama, H. Rafii-Tabar, Y. Kawazoe, and H. Matsui, *J. Nucl. Mater.* 212, 231 (1994).
154. S. I. Golubov, *Metallofizika* 11, 10 (1989).
155. A. J. E. Foreman, C. A. English, and W. J. Phytian, *Philos. Mag. A* 66, 655 (1992); A. J. E. Foreman, W. J. Phytian, and C. A. English, *Philos. Mag. A* 66, 671 (1992).
156. Yu. N. Osetsky and D. J. Bacon, *Nucl. Instr. Meth. Phys. Res. B* 202 31 (2003).
157. H. Trinkaus, B. N. Singh, and A. J. E. Foreman, *J. Nucl. Mater.* 199, 1 (1992); *J. Nucl. Mater.* 206, 200 (1993).
158. V. A. Borodin, *Physica A* 260, 467 (1999).
159. A. V. Barashev, S. I. Golubov, and H. Trinkaus, *Philos. Mag. A* 81, 2515 (2001).
160. R. Bullough and J. R. Willis, *Philos. Mag.* 31, 855 (1975).
161. P. T. Heald, *Philos. Mag.* 31, 551 (1975).
162. H. Matsui, D. S. Gelles, and Y. Kohno, in "Effects of Radiation on Materials," 15th Int. Symp., ASTM STP 1125 (R. E. Stoller, A. S. Kumar, and D. S. Gelles, Eds.), p. 928. ASTM, Philadelphia, 1992.
163. H. Nakojima, S. Yoshida, Y. Kohno, and H. Matsui, *J. Nucl. Mater.* 191, 952 (1992).
164. F. A. Garner, D. S. Gelles, H. Takahashi, S. Ohnuki, H. Kinoshita, and B. A. Loomis, *J. Nucl. Mater.* 191, 948 (1992).
165. Yu. V. Konobeev, V. A. Pechenkin, and S. I. Rudnev, *J. Nucl. Mater.* 233, 1070 (1996).
166. A. J. E. Foreman and B. N. Singh, in "Irradiation Behaviour of Metallic Materials for Fast Reactor Core Components," p. 113. CEA-DMECN, Gif-sur-Yvette, 1979.
167. T. Takeyama, H. Takahashi, and S. Ohnuki, *J. Nucl. Mater.* 108, 465 (1982).
168. D. Blasl, H. Tsunakawa, K. Miyahara, and N. Igata, *J. Nucl. Mater.* 133, 517 (1985).
169. V. I. Dubinko, *J. Nucl. Mater.* 223, 1 (1995).
170. R. M. Thomson and R. W. Balluffi, *J. Appl. Phys.* 33, 803 (1962).
171. J. L. Katz and H. Wiedersich, *J. Chem. Phys.* 55, 1414 (1971).
172. K. C. Russel, *Acta Metall.* 26, 1615 (1978).
173. W. G. Wolfer, L. K. Mansur, and J. A. Sprague, in "Radiation Effects in Breeder Reactor Structural Material" (H. L. Bleiberg and J. W. Bennett, Eds.), p. 841. The Metallurgical Society of AIME, Warrendale, 1978.
174. D. Kashchiev, "Nucleation: Basic Theory with Applications." Butterworth-Heinemann, Oxford, 2000.

175. C. W. Gardiner, "Handbook of Stochastic Methods." Springer Series in Synergetics, Vol. 13. Springer-Verlag, Berlin, 1983.
176. V. A. Borodin, A. E. Volkov, and A. I. Ryazanov, *J. Nucl. Mater.* 307, 862 (2002).
177. E. H. Lee and L. K. Mansur, *Met. Trans. A.* 21A, 1021 (1990).
178. B. N. Singh and J. H. Evans, *J. Nucl. Mater.* 226, 277 (1995).
179. T. Atkins and R. J. McElroy, in "Effects of Radiation on Materials." 11th Conference. ASTM STP 782 (H. R. Brager and J. S. Perrin, Eds.), p. 841. ASTM, Philadelphia, 1982.
180. F. R. Nabarro, *Philos. Mag.* 16, 231 (1967).
181. E. Kroner, "Physik der Kondensierten Materie," Vol. 2, p. 262. Springer-Verlag, Berlin, 1964.
182. P. T. Heald and M. V. Speight, *Philos. Mag.* 29, 1075 (1974).
183. R. Bullough and M. R. Hayns, *J. Nucl. Mater.* 57, 348 (1975).
184. C. H. Woo, Report AECL-6791 (1980).
185. J. Holder, A. V. Granato and L. E. Rehn, *Phys. Rev. B* 10, 363 (1974).
186. P. H. Dederichs, C. Lehmann, and A. Scholz, *Phys. Rev. Lett.* 31, 1130 (1973).
187. E. Kuramoto, *J. Nucl. Mater.* 122, 422 (1984).
188. H. Wenzl, in "Vacancies and Interstitials in Metals" (A. Seeger et al., Eds.), p. 363. North-Holland, Amsterdam, 1970.
189. Z. K. Saralidze, *Fizika Tverdogo Tela* 20, 2716 (1978).
190. C. H. Woo and U. Gösele, *J. Nucl. Mater.* 119, 219 (1983).
191. C. A. English, *J. Nucl. Mater.* 108, 104 (1982).
192. L. L. Horton, J. Bentley, and K. Farrell, *J. Nucl. Mater.* 108, 222 (1982).
193. R. Bullough, M. H. Wood, and E. A. Little, in "Effects of Radiation on Materials." 10th Conference. ASTM STP 725 (D. Kramer, Ed.), p. 593. ASTM, Philadelphia, 1981.
194. D. S. Gelles, in "Effects of Radiation on Materials," 14th International Symposium, ASTM STP 1046 (N. H. Packan, R. E. Stoller, and A. S. Kumar, Eds.), Vol. I, p. 73. ASTM, Philadelphia, 1989.
195. A. I. Ryazanov and V. A. Borodin, *Rad. Effects* 59, 13 (1981).
196. S. Jitsukawa, Y. Katano, K. Shiraishi, and F. A. Garner, in "Effects of Radiation on Materials," 15th International Symposium, ASTM STP 1125 (R. E. Stoller, A. S. Kumar, and D. S. Gelles, Eds.), p. 1034. ASTM, Philadelphia, 1992.
197. R. V. Hesketh, *Philos. Mag.* 7, 1417 (1962).
198. G. W. Lewthwaite, *J. Nucl. Mater.* 46, 324 (1973).
199. F. A. Garner and W. G. Wolfer, *Trans. ANS* 28, 144 (1978).
200. F. A. Garner, W. G. Wolfer, and H. R. Brager, in "Effects of Radiation on Structural Materials," ASTM STP 683 (J. A. Sprague and D. Kramer, Eds.), p. 160. ASTM, Philadelphia, 1979.
201. K. W. Ingle and A. G. Crocker, *Acta Metall.* 26, 1462 (1978).
202. M. G. Ganchenkova, V. A. Borodin, and R. M. Nieminen, *Nucl. Instr. Meth. Phys. Res. B* 228, 218 (2005).
203. C.-C. Fu, J. Dalla Torre, F. Willaime, J.-L. Bocquet, and A. Barbu, *Nature Mater.* 4, 68 (2005).
204. J. P. Goss, R. Jones, and P. R. Briddon, *Physica B* 308–310, 604 (2001).
205. R. Jones, B. J. Coomer, and P. R. Briddon, *J. Phys.: Condens. Matter.* 16, S2643 (2004).
206. H. Üstünel, D. Roundy, and T. A. Arias, *Phys. Rev. Lett.* 94, 025503 (2005).
207. G. Vogl and W. Petry, *Phys. Blätter*, 50, 925 (1994).
208. A. G. Mikhin and Yu. N. Osetsky, *J. Phys: Condens. Matter.* 5, 9121 (1993).
209. T. Müller, K.-H. Heinig and W. Möller, *Appl. Phys. Lett.* 81, 3049 (2002).

CHAPTER 9

Adsorption at Nanostructured Surfaces

Axel Groß[1,*]

[1] *Physik-Department T30, Technische Universität München, Garching, Germany*

CONTENTS

1. INTRODUCTION

There is a strong current interest in the adsorption of atoms and molecules at nanostructured surfaces. This interest is fueled by the general attention that nanoscience and nanotechnology has received in recent years. Systems with reduced dimensions can exhibit surprising chemical, mechanical, vibrational, electronic, magnetic, or optical properties that are distinctly different from those of extended systems. Consequently, also the adsorption properties of molecules can be significantly modified by nanostructuring a substrate.

However, as far as the interaction with molecules is concerned, surfaces with structures at the nanometer scale have already played a significant technological role for many years, long before the advent of nanotechnology, in particular in the field of heterogeneous catalysis. One of the most prominent examples is the car exhaust catalyst, where small metal particles on an oxide support are the catalytically active species [1–4]. In fact, the activity of many real catalysts is often assumed to be dominated by so-called active sites, that is, sites with a specific geometric configuration on the nanometer scale that modifies their electronic and chemical properties. However, experimentally it is almost impossible to deduce the exact nature of these active sites.

Ideally, one would like to have a systematic microscopic understanding of the relationship between the geometric and electronic structure of a substrate and its adsorption properties

* Current address: Abteilung Theoretische Chemie, Universität Ulm, Germany.

ISBN: 1-58883-047-0

Handbook of Theoretical and Computational Nanotechnology
Edited by Michael Rieth and Wolfram Schommers
Volume 5: Pages (557–602)

and reactivity. This would allow the systematic tailoring of its activity but requires a detailed atomistic knowledge about the investigated nanostructures. The development of the scanning tunneling microscope (STM) [5] was an experimental milestone allowing the imaging of structures and processes on surfaces with atomic resolution. Still, one has to keep in mind that the STM does not directly yield the atomic structure but rather images the electronic density of states [6]. Therefore, sometimes it is not easy to identify the atomic structure underlying a particular STM image. Furthermore, nanostructured surfaces with a strong corrugation are hard to image because the finite size of the STM tip leads to a limited lateral resolution [7]. Therefore the size and shape of, for example, supported clusters are often not really known. It is true that the deposition of size-selected clusters together with soft-landing techniques allows the preparation of a monodisperse distribution of supported clusters [8]. Yet, the exact structure of the soft-landed clusters is also not known either.

Theoretical studies, on the other hand, have the advantage that they deal with well-defined systems. This means that the microscopic structure of the studied systems is of course predetermined by the theorist performing the calculations. Because of the tremendous progress in the computer power and the development of efficient electronic structure algorithms, a very fruitful and close collaboration between theory and experiment for the investigation of the interaction of atoms and molecules with surfaces and nanostructures has become possible [9, 10]. In the early days of theoretical surface science, quantum chemistry methods [11] based on representations of the electronic many-body wave function had prevailed. Unfortunately, wave function–based methods are limited to rather small systems because of their unfavorable scaling with the size of the treated systems. Nowadays, the *ab initio* treatment of surfaces and nanostructures is dominated by total energy calculations based on density functional theory (DFT) [12–15], which combines numerical efficiency with a satisfactory reliability and accuracy.

A broad variety of surface properties can now be described from first principles, that is, without invoking any empirical parameters [16]. First of all, *ab initio* total-energy calculations allow the determination of the equilibrium structure of a specific system. However, these calculations offer even more. They also yield the electronic structure underlying a particular optimum geometry. The analysis of the electron structure and its interpretation within a conceptual framework can lead to a general understanding of the principles underlying adsorbates structures, chemical trends, and the relation between reactivity and structure. In order to make such an understanding possible, it is very important to establish reactivity concepts. These allow one to categorize the immense variety of possible structures and reactions.

In this review, I will mainly focus on two types of nanostructured surfaces: stepped surfaces and supported clusters. It is true, however, that the nanostructures that can be addressed currently by electronic structure calculations are still very limited in size. For example, the separation of the steps treated in theoretical studies is often smaller than the corresponding separation of steps studied in experiments [17], and typically supported clusters with less than 10 atoms are treated in the calculations, whereas the clusters studied in experiments often contain more than 1000 atoms [18]. Hence, there is still a gap between the nanostructure sizes dealt with in theory and in experiment.

Nevertheless, it is still possible to extract qualitative trends from theoretical studies, for example as far as the role of low-coordinated sites at the nanostructures is concerned. Furthermore, modern experimental cluster sources together with soft-landing techniques allow the deposition of clusters with basically any desired number of atoms well below 100. In addition, the improvement in computer power and the efficiency of the computer codes will make it possible to address larger and larger systems. Thus, we will certainly see an ongoing closing of the gap between experiment and theory in the future. It should also be emphasized that the application of large-scale electronic structure calculations to surfaces and nanostructures is a relatively young field. Although the first detailed *ab initio* calculations of the interaction of molecules with low-index surfaces started in the early 1990s [19–22], the treatment of nanostructured surfaces became only possible in the new millenium except for a few studies that were carried out on supercomputers in the 1990s [8, 23].

The topic of this review is the adsorption of atoms and molecules on nanostructured surfaces. However, adsorption studies are often performed in order to understand the reactivity of a particular nanostructure. Hence studies of adsorption and reactions on nanostructures are often closely related. Therefore, I will also briefly discuss the chemical reactions that are promoted by specific nanostructures. Furthermore, I will not only address adsorbates on nanostructured surfaces but also nanostructuring by adsorbates, mainly by organic molecules, which might be useful for sensing, catalysis, or molecular electronics.

Instead of giving a comprehensive overview of many systems, I will focus on particular well-studied systems that allow manifestation of qualitative trends for the interaction of atoms and molecules with nanostructured surfaces. In particular, as far as the adsorption on supported clusters is concerned, I will mainly discuss the Au/TiO_2 system [18, 24, 25], which has become *the* model system for the understanding of the chemical reactivity of supported nanoparticles. This system is of particular interest because bulk Au is chemically inert in contrast to the Au nanoparticles, so that its study allows the identification of the geometric and electronic factors underlying the enhanced reactivity of nanoparticles.

This chapter is structured as follows. In the next section, a brief introduction into the theoretical concepts needed for the first-principles description of adsorption on nanostructured surfaces will be given. The third section is devoted to the adsorption on stepped surfaces, and the fourth section covers the adsorption on supported nanoparticles. Then there will be a brief introduction into the nanostructuring of surfaces by organic templates. Finally, some conclusions and an outlook will be given, where possible directions of further research will be sketched.

2. THEORETICAL CONCEPTS

In the realm of chemistry and solid-state physics, only the kinetic energy and the electrostatic interaction enter the basic expression for the total energy of a physical system. Because of their light mass, the electrons have to be treated quantum mechanically. Thus, a theoretical analysis "just" requires the solution of the appropriate quantum many-body Schrödinger equation. Unfortunately, the exact analytical solution of the Schrödinger equation for any realistic many-body system is not possible. Consequently, only approximate numerical solutions can be obtained, but they should be as reliable and as accurate as possible, and at the same time they should not be computationally too demanding so that the calculations can be carried out within a reasonable time.

The first calculations of surface structures were based on quantum chemistry methods [11, 26, 27] in which the Schrödinger equation is solved using necessarily finite basis sets for the wave functions. The theoretical tools used by quantum chemists are designed to describe finite systems such as molecules. In the quantum chemistry approach, surfaces are regarded as big molecules and modeled by a finite cluster. This ansatz is guided by the idea that bonding on surfaces is a local process. These methods significantly contributed to our understanding of processes at surfaces (see, e.g., [28, 29]). However, these calculations become prohibitively expensive for larger systems because of their unfavorable scaling with the system size. Nowadays, predominantly electronic structure calculations using density functional theory (DFT) [12, 13] are performed. They offer a good compromise between computational efficiency and sufficient accuracy for many systems. Still, there are important exceptions where present-day DFT methods are not accurate enough [30, 31].

Here I will only give a brief sketch of the fundamentals of DFT, which are important for a general understanding. Historically, the first attempts to relate the electronic density and the total energy were made within the framework of the Thomas-Fermi theory [32], which is only valid in the limit of slowly varying electron density. Hohenberg and Kohn extended this relation also to inhomogeneous situations [12]. The Hohenberg-Kohn theorem states that the exact ground-state density and energy can be determined by the minimization of the energy functional $E[n]$,

$$E_{\text{tot}} = \min_{n(\vec{r})} E[n] = \min_{n(\vec{r})}(T[n] + V_{\text{ext}}[n] + V_{\text{H}}[n] + E_{\text{xc}}[n]) \tag{1}$$

which means that there is a one-to-one correspondence between the electron ground-state density $n(\vec{r})$ and the total energy. In Eq. (1), $V_{ext}[n]$ and $V_H[n]$ are the functionals of the external potential and of the classical electrostatic interaction energy, respectively, and $T[n]$ is the kinetic energy functional for non-interacting electrons. These three terms do not contain any quantum mechanical many-body effects that are all lumped together in the so-called exchange-correlation functional $E^{xc}[n]$ that is, unfortunately, not known in general.

It had turned out that the Hohenberg-Kohn theorem is not useful for a direct implementation of the DFT, mainly because the kinetic energy functional $T[n]$ is not precisely known for inhomogeneous situations. One rather replaces the many-body Schrödinger equation by a set of coupled effective one-particle equations, the so-called Kohn-Sham equations [13]

$$\left\{ -\frac{\hbar^2}{2m}\nabla^2 + v_{ext}(\vec{r}) + v_H(\vec{r}) \; + \; v_{xc}(\vec{r}) \right\} \psi_i(\vec{r}) = \varepsilon_i \, \psi_i(\vec{r}) \tag{2}$$

where v_{ext} is the external potential and the *Hartree potential* v_H is given by

$$v_H(\vec{r}) = \int d^3\vec{r}\, n(\vec{r}) \frac{e^2}{|\vec{r} - \vec{r}'|} \tag{3}$$

The exchange-correlation potential $v_{xc}(\vec{r})$ is the functional derivative of the exchange-correlation functional $E_{xc}[n]$

$$v_{xc}(\vec{r}) = \frac{\delta E_{xc}[n]}{\delta n} \tag{4}$$

The electron density $n(\mathbf{r})$ that minimizes the total energy is then given by the sum over single-particle Kohn-Sham states

$$n(\vec{r}) = \sum_{i=1}^{N} |\psi_i(\vec{r})|^2 \tag{5}$$

The ground-state energy can now be expressed as

$$E = \sum_{i=1}^{N} \varepsilon_i + E_{xc}[n] - \int v_{xc}(\vec{r}) n(\vec{r}) \, d^3\vec{r} - V_H \tag{6}$$

The first term in the total-energy expression (6) is also called the band structure term E_{bs}, as it corresponds to the sum over the single-particle energies.

There is one complication as far as the solution of the Kohn-Sham equations is concerned. The electron density $n(\vec{r})$, which is derived from the Kohn-Sham states, actually enters the effective one-particle Hamiltonians, that is, the exact Hamiltonians are not known *a priori*. In such a situation, the solutions can be obtained within an iterative self-consistency scheme. Initially, the electron density has to be guessed, for example as a superposition of atomic densities. The Kohn-Sham equations are then solved, and the resulting density is compared to the initial guess. If the difference is larger than some prespecified value, the new density enters the Kohn-Sham equations (often using some mixing scheme), and the cycle is repeated so often until the iterations no longer modify the solutions, that is, until self-consistency is reached.

In principle, DFT is exact, but as already mentioned, the correct form of the nonlocal exchange-correlation functional is not known. This also applies to the exchange-correlation potential v_{xc}. Hence approximative expressions are needed. In the local density approximation (LDA), at any position $\vec{r}$ the exchange-correlation potential of the homogeneous electron gas with the corresponding electron density is used. This means that nonlocal effects in the exchange and correlation are entirely neglected. Although this is a rather crude approximation, the LDA has been surprisingly successful for many properties of bulk materials. However, for chemical reactions at surface, LDA is not sufficiently accurate [20]. Satisfactory accuracy is obtained within the so-called generalized gradient approximation (GGA) [33], which takes the gradient of the density also into account in the

exchange-correlation functional, but in such a way that important electronic sum rules are obeyed. GGA represents the state of the art for large-scale DFT calculations of surfaces and nanostructures.

There are quite a number of different GGA functionals available. Although quantum chemists using DFT prefer exchange-correlation functionals that are fitted to a number of reference reactions in the gas phase [34, 35], physicists rather rely on functionals that are derived without any adjustment of parameters [33, 36]. It should be mentioned that GGA calculations do not achieve *chemical accuracy* (error below ~0.1 eV) for all systems and that there can be quite significant quantitative discrepancies between the results of DFT calculations using different GGA functionals.

For example, there are two versions of the popular GGA functional developed by Perdew, Burke, and Ernzerhof, called the PBE functional [36] and the revised PBE, RPBE [30]. Both versions differ only by one interpolation function, which is not specified in the construction scheme for the functional. Hence there is no way to tell *a priori* which is the more correct functional. Still, for certain systems there are differences of up to 0.5 eV between the results using these two functionals, in particular as far as the adsorption energies of O_2, NO, or CO on metal surfaces are concerned [30]. Fortunately, often this only leads to quantitative but not qualitative differences or errors. Nevertheless, there are also systems where all present GGA functionals yield wrong qualitative results, for example for the adsorption site of CO on Pt(111) [31]. In most cases, DFT-GGA calculations are actually reliable, but one still should always be cautious and compare the DFT results with available experimental data.

Hence, the search for more accurate exchange-correlation functionals is an active research field [37, 38]. However, the problem in the development of more accurate exchange-correlation functionals is that they still represent in principle an uncontrolled approximation, that is, there is no systematic way of improving the functionals as there is no expansion in some small, controllable parameter.

As far as the practical implementation of DFT algorithms is concerned, it is numerically very efficient to use a plane-wave expansion of the Kohn-Sham single-particle states. However, such an approach usually requires a three-dimensional periodicity of the considered system. In the so-called supercell approach, surfaces are modeled by periodically repeated slabs with a sufficient vacuum layer between them in order to avoid any interaction between the slabs. A typical supercell describing the adsorption of atoms at the step sites of a nanostructured fcc(410) surface in a (2×1) geometry is shown in Fig. 1. The slabs have to be thick enough to reproduce the correct electronic structure of the substrate. One advantage of the slab approach is that the substrates are infinitely extended in lateral directions, which yields a correct description of the delocalized nature of the electronic states of metals, a feature that is not present when the substrates are modeled by finite clusters [29].

On the basis of total-energy calculations, adsorption energies and reaction barrier heights are determined as the differences of the total energies of the appropriate systems. For example, the adsorption energy E_{ads} of a molecule can be determined via

$$E_{\mathrm{ads}} = (E_{\mathrm{slab}} + E_{\mathrm{mol}}) - E_{\mathrm{slab+mol}} \tag{7}$$

where E_{slab}, E_{mol}, and $E_{\mathrm{slab+mol}}$ are the total energies per unit cell of the isolated slab, the isolated molecule, and the interacting system, respectively. Using this definition, the exothermic adsorption of molecules is represented by positive energies, as will be done throughout this chapter. However, often the sign convention is chosen to be the other way around.

In any implementation of DFT, the computational effort is directly linked to the number of electrons that have to be taken into account. Now most chemical and materials properties are governed almost entirely by the valence electrons while the influence of the core electrons on these properties is negligible. This fact is used in the pseudopotential concept [39] in which the influence of the core electrons on the other electrons is represented by an effective potential, the pseudopotential. Because this significantly reduces the number of electrons that have to be taken into account, the use of pseudopotentials leads to enormous savings of computer time.

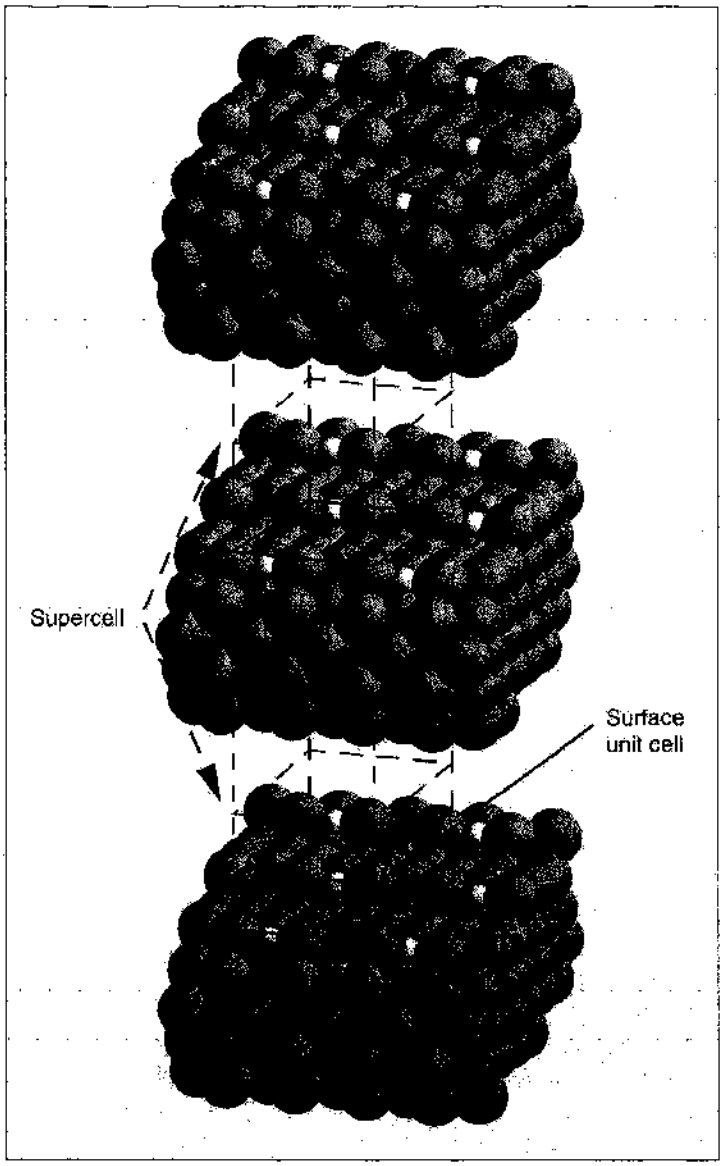

Figure 1. Illustration of the supercell approach. A substrate of a fcc crystal with a (410) surface termination and an adsorbed periodic atomic layer in a (2 × 2) geometry is represented by an infinite array of slabs. The supercell and the surface unit cell are indicated in the figure.

A further significant improvement has been the formulation of the projected augmented-wave (PAW) method [40] and the development of *ultrasoft* pseudopotentials [41]. Both methods are indeed closely related [42]. They introduce augmentation charges in the core region in order to create smooth potentials, which results in a dramatic reduction in the necessary size of the basis set in plane-wave calculations.

Almost all modern DFT studies presented in this chapter employ the pseudopotential concept, and many large-scale computations would be impossible without the use of pseudopotentials. Using the supercell technique in combination with the pseudopotential or PAW concept, modern efficient DFT algorithms [43–45] can treat up to several hundreds or even thousands of atoms per supercell (see, e.g., [46]).

DFT calculations not only yield total energies but also information about the electronic structure. First of all, plots of the total charge density are useful in order to get an idea of the nature of the chemical binding. However, even more instructive is the analysis of charge density difference plots, for example of the adsorption induced charge density difference

$$n_{\mathrm{diff}}(\vec{r}) = n_{\mathrm{total}}(\vec{r}) - n_{\mathrm{adsorbate}}(\vec{r}) - n_{\mathrm{substrate}}(\vec{r}) \tag{8}$$

These charge density difference plots illustrate the charge redistribution and the rehybridization due to the interaction of the reactants. Hence they allow the determination of charge transfer processes, and even the nature and symmetry of the involved orbitals can be deduced from the spatial patterns.

However, not only the electronic structure in real space but also in momentum and energy space yields valuable information. In particular, the determination of changes in the local density of states (LDOS), which is defined by

$$n(\vec{r}, \varepsilon) = \sum_i |\phi_i(\vec{r})|^2 \delta(\varepsilon - \varepsilon_i) \tag{9}$$

adds additional information about the electronic orbitals and bands that are involved in the adsorption process.

Still, for a deeper understanding of, for example, chemical trends qualitative concepts are needed that allow a fundamental analysis and interpretation of the electronic structure. A rather simple but still very useful reactivity concept was derived by Hammer and Nørskov [47, 48], the so-called *d*-band model. This scheme is closely related to the frontier orbital concept developed for gas-phase reactions [49, 50]. In the *d*-band model, the whole *d*-band is replaced by an effective level located at the center of the *d*-band ε_d. This level plays the role of the substrate frontier orbitals, that is, of the highest occupied molecular orbital (HOMO) and the lowest unoccupied molecular orbital (LUMO).

The principles underlying the *d*-band model are illustrated in Fig. 2. Let us first consider the interaction of an atomic level with a transition metal surface. This interaction is formally split into a contribution arising from the *s* and *p* states of the metal and a second contribution coming from the *d*-band. The *s* and *p* states lead to a broadening and a shift of the atomic level to lower energies. This broadening and shift is called *renormalization* of the energy level and can be modeled by the interaction with a jellium surface.

This renormalized level then splits due to the strong hybridization with the metal *d*-states in a bonding and an antibonding contribution. Both the strength of the interaction as well as the position of the center of the *d*-band ε_d determine whether the interaction is attractive or repulsive. The stronger the interaction, the more the two levels are split. A very strong interaction shifts the bonding orbital to lower energies. Furthermore, it pushes the antibonding contribution above the Fermi energy. Both effects lead to an effective attractive interaction.

As Fig. 2 illustrates, the position of the center of the *d*-band ε_d determines the occupation of the bonding and the antibonding contribution. The higher the *d*-band center, the smaller the occupation of the antibonding level and the more attractive the interaction. Therefore, transition metals are rather reactive because the Fermi energy is rather close to the *d*-band

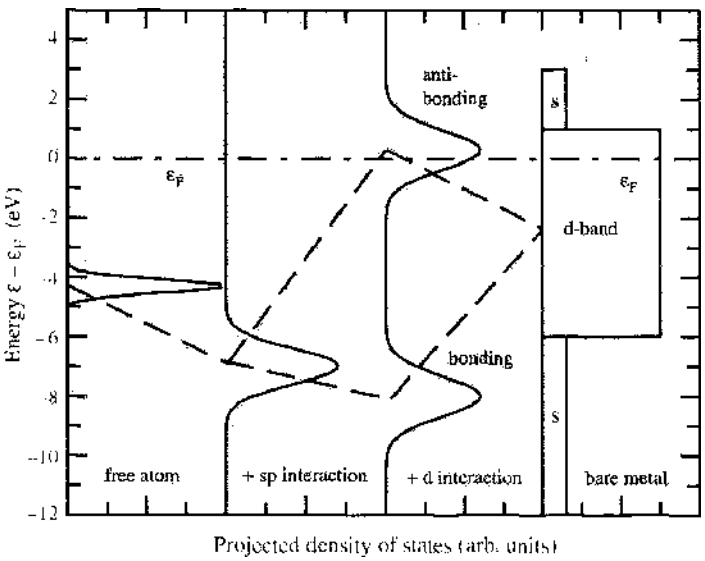

Figure 2. Schematic drawing of the interaction of an atomic level with a transition metal surface according to the *d*-band model [47].

center because of the only partially filled d-band. For a noble metal, on the other hand, the d-band center is so low that both the bonding *and* the antibonding state of adsorbate–substrate interaction are occupied, making this interaction repulsive. This is the reason why noble metals are noble, that is, less reactive than transition metals [48].

The d-band model is particularly useful for comparing the reactivity of relatively similar systems that only differ in the position of the d-band center. Then there is a linear relationship between the d-band center shift and the change in the chemisorption strength ΔE_d [51, 52],

$$\delta E_d = -\frac{V^2}{|\epsilon_d - \epsilon_a|^2}\delta\epsilon_d \tag{10}$$

which means that there is a stronger interaction or larger energy gain upon an upshift of the d-band.

This concept provides an intuitive picture for the enhanced reactivity of nanostructured surfaces which is illustrated in Fig. 3. Consider a typical transition metal with a more than half-filled d-band (Fig. 3a). At a step atom or at some other low-coordinated site, the local d-band density of states will be changed. In a simple tight-binding picture, the width of a band is directly related to the coordination and the overlap of the orbitals. At a low-coordinated site, the d-band will therefore become narrower (see Fig. 3b, the same is also true for pseudomorphic overlayers under tensile strain, which reduces the overlap between the electronic orbitals [53–55]). Now if the d-band is more than half-filled but not completely filled and the d-band center is kept fixed, the number of d-states below the Fermi energy will increase. This would lead to an higher occupation of the d-band. However, the number of d-electrons is conserved. In order to obey charge conservation, the narrower d-band has to shift up (Fig. 3c) so that the number of occupied states remains unchanged. Thus also the d-band center will move up. According to the d-band model, this results in a higher reactivity of the structured system.

That the simple concept of the d-band upshift due to the band narrowing is indeed true is illustrated in Fig. 4, where the layer-resolved, local d-band density of states (LDOS) of the stepped Pd(210) surface determined by GGA-DFT calculations [56] is plotted. The LDOS of the third layer is still rather close to the Pd bulk density of states. This is a consequence of the good screening properties of metals [57], which leads to a rapid recovery of bulk properties in the vicinity of imperfections such as surfaces. However, the width of the d-band of the second and first layer are significantly reduced, and this reduction in band width is accompanied by an upshift of the d-band centers indicated by the vertical dashed lines. The consequences of this upshift on the interaction strength with adsorbates will be discussed in the next section. Furthermore, it should also be remembered that density of states effect are only related to the band-structure energy. This is, however, only one term in the sum yielding the Kohn-Sham total energy. There are many systems where electrostatic effects or even exchange-correlation effects contribute to the chemical reactivity and interaction strengths.

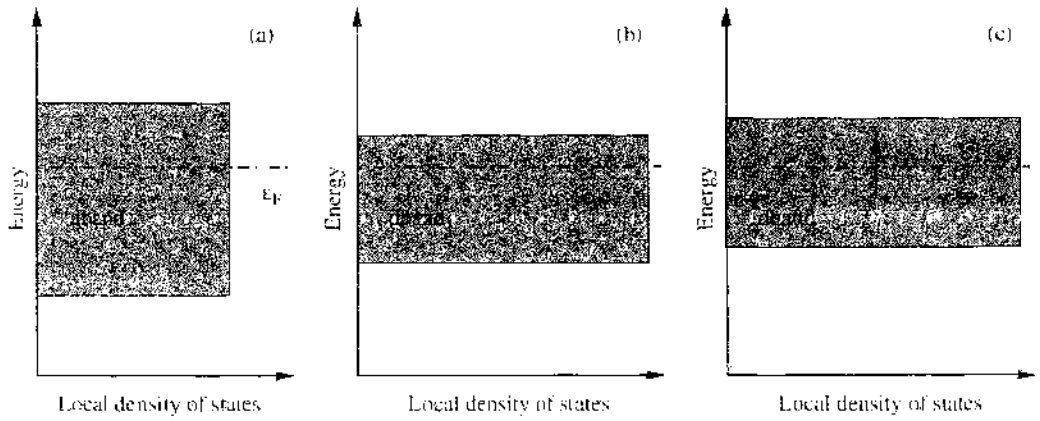

Figure 3. Illustration of the effect of a lower coordination or smaller atomic overlap on the width and position of a d-band. (a) d-band of a transition metal; (b) reduced width of the d-band due to a lower coordination or smaller overlap; (c) upshift of the d-band because of charge conservation.

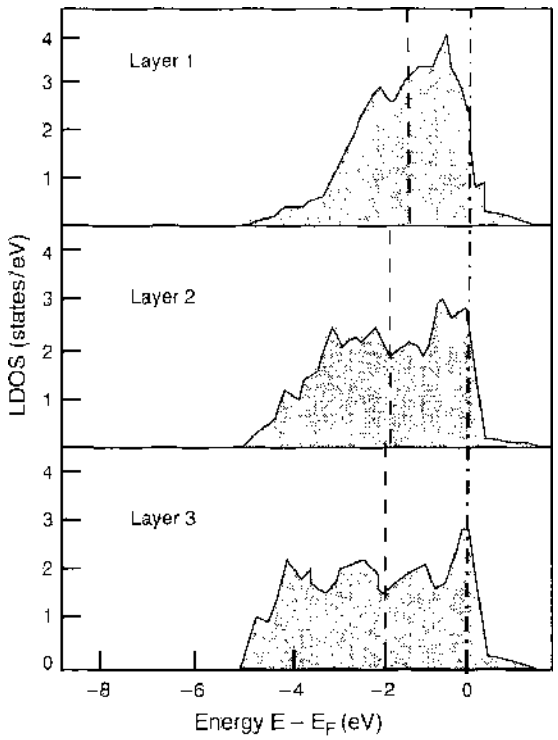

Figure 4. Layer-resolved, local *d*-band density of states of Pd(210) determined by GGA-DFT calculations. The Fermi level and the center of the *d*-band are indicated by vertical dash-dot and dashed lines, respectively. The third-layer LDOS is already very close to the bulk density of states of palladium (after [56]).

3. ADSORPTION ON STEPPED SURFACES

Nanostructures at surfaces often exhibit a broad variety of possible adsorption sites because of their open defect-rich structure. This makes a microscopic identification of the relation between the geometric and electronic structure and its reactivity toward adsorption rather complicated. Similarly, the activity of realistic, nanostructured catalysts is often assumed to be dominated by so-called active sites, that is, sites with a specific geometric configuration that modifies their electronic and chemical properties. However, the exact microscopic structure of these active sites is often unknown.

In order to systematically investigate the properties of nanostructures, it is desirable to prepare surface structures with one well-defined defect structure so that its influence can be isolated from that of all other possible structures. *Vicinal surfaces* are particularly well-suited for this purpose. These are surfaces that are only slightly misaligned from a low index plane. A vicinal surface is structured as a periodic array of terraces of a low-index orientation separated by monoatomic steps. By studying vicinal surfaces, the influence of steps on, for example, adsorption properties or reactions on surfaces can be studied in a systematic way. They allow one to determine the role of steps in the interaction of atoms and molecules with surfaces, they can be relatively easily prepared in the experiment, and they are accessible to electronic structure calculations.

In Fig. 5, a (755) surface is shown illustrating the structure of a vicinal surface. The high-index (755) surface consists of 6 atomic rows of (111) orientation separated by a step with a (100) ledge, that is, the ledge represents (100) microfacets. The misalignment from the [111] direction is 9.5°. In fact, in order to make the structure of a vicinal surfaces immediately obvious, they are often denoted by $n(hkl) \times (h'k'l')$ [58] where (hkl) and $(h'k'l')$ are the Miller indices of the terraces and of the ledges, and n gives the width of the terraces in number of atomic rows parallel to the ledges. Thus a (755) surface is represented by $6(111) \times (100)$. Another example is the $(911) = 5(100) \times (111)$ surface that is rotated by 9.5° from the [100] direction.

Experimentally, it is well-known that many adsorbates bind preferentially to step sites [17, 59]. This has of course motivated electronic structure calculations. A particularly

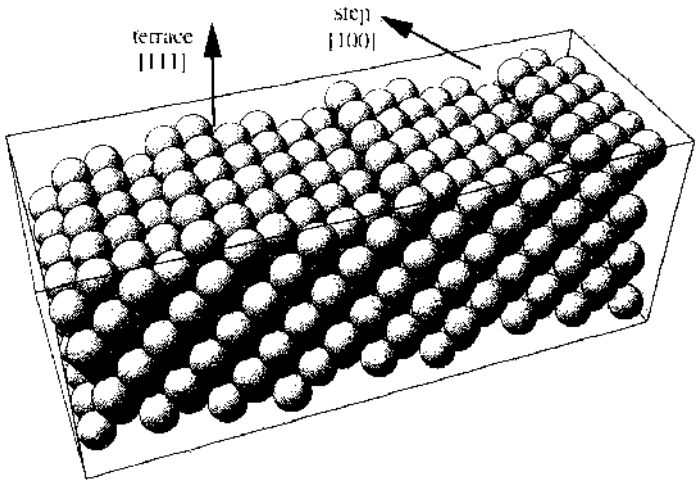

Figure 5. A stepped (755) = 6(111) × (100) vicinal surface. Steps with ledges of (100) orientations separate (111) terraces that are 6 atom rows wide.

well-studied system is the adsorption of CO on Pt surfaces. Interestingly enough, DFT calculations using present-day functional for the description of the exchange-correlation effects fail in predicting the correct adsorption site for CO/Pt(111) [31]. According to the DFT calculations, the threefold hollow site is energetically preferred by about 0.25 eV with respect to the top site although it is experimentally well-established that CO adsorbs on the top sites of Pt(111). The reasons for this failure are still debated. Some authors claim that the consideration of relativistic effects leads to the correct site preference. Others claim that the so-called CO/Pt(111) puzzle is caused by the incorrect position of the CO $2\pi^*$ orbital. By correcting its energetic location in a so-called GGA+U approach [60], the true site preference is recovered [61].

However, the system CO/Pt demonstrates that DFT calculations can still be useful and yield important insight into certain aspects of an adsorbate system even if other aspects are not well-described. This is due to the error cancellation in the comparison of similar structures. The binding energies of CO at the on-top sites of several flat, stepped, kinked, and reconstructed Pt surfaces have been investigated by DFT-GGA calculations [51]. These calculations have revealed a strong structure sensitivity of the binding strength with variations of 1 eV in the CO adsorption energies.

As far as stepped surfaces are concerned, the Pt(211) and Pt(11 7 5) surfaces have been considered. Both surfaces have (111) terraces of similar width, but while the (11 7 5) surface has an open kinked structure along the steps (see Fig. 6), the (211) surface is close-packed along the steps (see Fig. 7). And indeed, the lowest coordinated Pt atoms, which are the

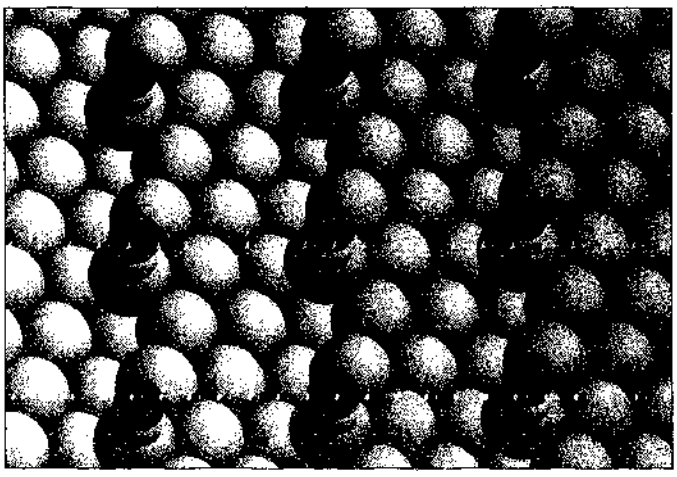

Figure 6. CO adsorption on top of the kink sites at the steps of a Pt(11 7 5) surface. CO binds with the C end down.

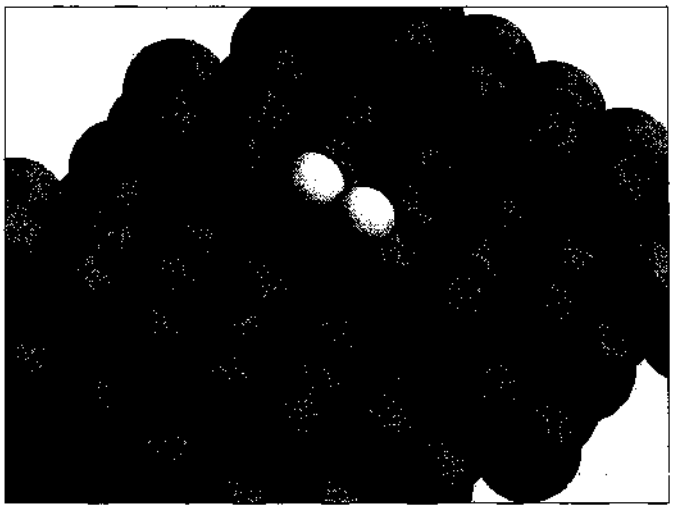

Figure 7. Molecular O_2 adsorption site at the steps of a Pt(211) surface determined by DFT calculations [17]. For the sake of clarity, the O_2 coverage in the figure does not correspond to the one used in the calculations.

kink atoms of the (11 7 5) surface, show the strongest binding to CO with bonding energies that are about 0.7 eV stronger than on the flat Pt(111) terrace. These findings have again been rationalized using the *d*-band model [51]. The lower the coordination, the larger the *d*-band shift and consequently the higher the adsorption energy.

In this context, it should be mentioned that the Pt(100) surface in equilibrium exhibits a Pt(100)-hex reconstruction that is an otherwise flat (100) surface covered by a hexagonally packed, buckled Pt overlayer. This overlayer is buckled because the Pt density in the overlayer is 4% higher than in the Pt(111) surface. This larger density has the same effect as a higher coordination. Because of the increased overlap the *d*-band broadens and shifts to lower energies making it less reactive. This is exactly what has been found for the binding of CO on the Pt(100)-hex(1 × 5) surface, which is weaker by 0.1 eV compared to the Pt(111) surface.

Apart from the CO/Pt system, the interaction of molecular oxygen with Pt surfaces represents one of the best studied systems in surface science, both experimentally [62–67] as well as theoretically [68–70]. This interest, as for CO/Pt, was also motivated by the technological relevance of the adsorption of O_2 on Pt as a crucial microscopic reaction step occuring in the car-exhaust catalyst. O_2 can adsorb both molecularly and dissociatively on Pt. At surface temperatures below 160 K, O_2 only adsorbs molecularly because of steric hindrances [70], even if the molecules impinge on the surface with high kinetic energies [64].

Experimentally, it has been found that the O_2 dissociation is strongly favored at step sites [17]. The local reactivity of the Pt step sites is reduced significantly when the step sites are decorated by Ag atoms. In the experiment, two vicinal surfaces were studied, Pt[9(111) × (111)] and Pt[8(111) × (100)], which have both (111) terraces that are nine and eight atom rows wide, separated by {111} and {100} monoatomic steps, respectively. In order to understand the enhanced reactivity of the Pt steps, GGA-DFT calculations have been performed [17, 71]. In the calculations, O_2 adsorption and dissociation on Pt(211) = Pt[3(111) × (100)] were addressed. The terraces of this surface are only three atom rows wide. Still, the steps of the (211) are far enough from each other to make the calculations relevant for the understanding of the reactivity of the vicinal surfaces studied in the experiments.

In the calculations, the O_2 molecular adsorption state and its energy E_{mol} and the energy of the transition state to dissociation E_{TS} were determined for the step site and a "near step" (NS) site one row away from the steps of the clean Pt(211) surface and for the Pt(211) surface with the steps decorated by a monoatomic row of silver atoms. The energetically most favorable molecular adsorption state of O_2 on Pt(211), which is shown in Fig. 7, is indeed at the Pt step atoms. The same is true for oxygen atoms, which also preferentially adsorb at the Pt step atoms [23]. In passing, I note that in order to illustrate both the surface geometry and the adsorbate location, in Fig. 7, as in many of the following figures, only a single adsorbed molecule has been plotted. However, one has to keep in mind that the coverages used in the calculations within the supercell approach are usually much higher.

The stronger binding to the steps can again be understood within the *d*-band model. In Fig. 8, the O_2 adsorption and transition state energies are compared to the corresponding ones for the Pt(111) surface as a function of the local *d*-band center ε_d. These energies were determined using both the RPBE and the PW91 functional, but only the PW91 results are plotted in Fig. 8 because the qualitative consequences do not depend on the functional. The correlation between the energies and the position of ε_d is obvious. At the step sites, the low coordination leads to a upshift of the *d*-band center, which results in a stronger interaction.

Interestingly enough, the local barrier for dissociation $E_a = E_{TS} - E_{mol}$ is not lowered at the steps. There, it is even higher than on the flat Pt(111) surface. Thus it seems to be surprising that there is a higher rate for dissociation at the steps. However, not only the height of the local dissociation barrier but also the absolute energetic position of the transition state with respect to the O_2 molecule in the gas phase are important. At the flat Pt(111) surface, the transition state energy approximately coincides with the energy of O_2 in the gas phase, which means that the energetic heights of the dissociation barrier and the desorption barrier are similar. Hence, in a thermally activated situation, a large fraction of adsorbed oxygen molecules will rather desorb than dissociate. At the steps, where the transition state energy is well below the O_2 gas phase energy, the branching ratio between dissociation and desorption is strongly shifted toward dissociation, although the absolute value of the barrier is higher at the steps. Hence, it is the stabilization of the molecular adsorption state that leads to an enhanced dissociation at steps.

Steps do not only provide sites for preferential adsorption, they could also lead to the lowering of reaction barriers. One important example is the N_2 dissociation on the Ru(0001) surface, which has been shown experimentally to be totally dominated by steps [72, 73]. This system is of particular importance, as the N_2 dissociation represents the first and rate-limiting step in the ammonia synthesis [74, 75]. The experimentalists have again used the fact that Au atoms deposited on a Ru(0001) surface will preferentially decorate the steps, thus blocking these sites [59]. The Ru(0001) surface used in the experiments had a step density of less than 1%. By depositing less than 2% of a monolayer of gold, the N_2 dissociation rate was suppressed significantly. From the experimentally measured rates, it was estimated that the dissociation rate at the steps is at least nine orders of magnitude higher than on the terraces at 500 K [72, 73].

Theoretically, the N_2 dissociation on Ru(0001) surface was described within a (2 × 2) surface unit cell [72, 76]. The step was modeled by using a (2 × 4) unit cell and removing two rows of Ru atoms (see inset of Fig. 9). The energetics along the reaction path from the molecular N_2 precursor state to atomic nitrogen on the surface is also shown in Fig. 9. It is

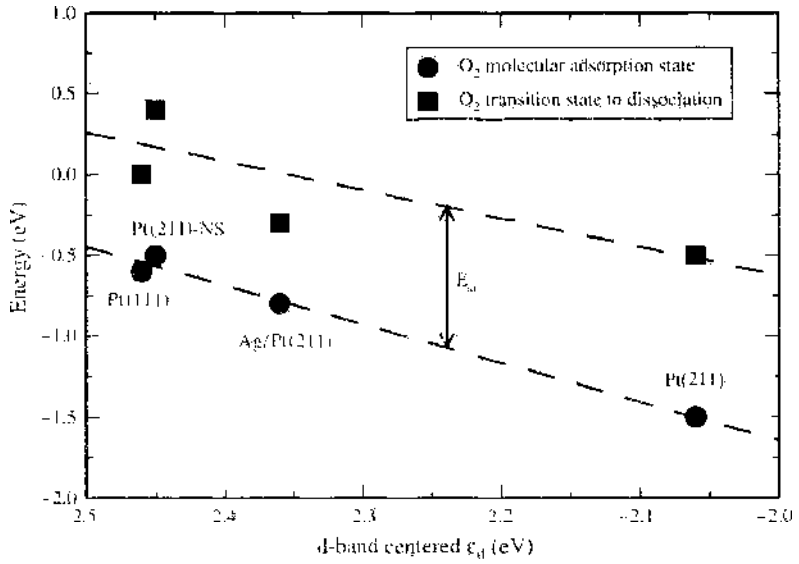

Figure 8. O_2 molecular adsorption energy and transition state energies determined using the GGA-PW91 functional as a function of the local *d*-band center ε_d [71]. The dashed lines are included as a guide to the eye.

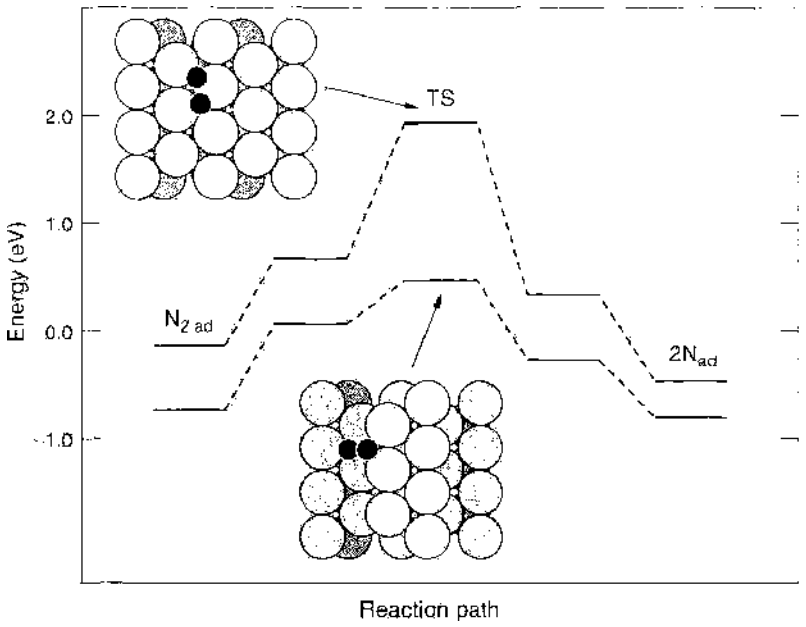

Figure 9. Energetics of the N_2 dissociaton on a terrace and a step of Ru(0001) as determined by DFT calculations [72]. The insets show the corresponding configurations at the transition state (TS) for dissociation. The energy zero is chosen to be the energy of the N_2 molecule in the gas phase.

obvious that the barrier for the dissociative adsorption of N_2 is significantly lowered from 1.9 eV at the terraces to 0.4 eV at the steps, in agreement with the experiment. Although the N_2 molecular precursor is also strongly stabilized at the steps, the difference in the binding energies of atomic nitrogen at the steps and the terraces is much smaller. For the N_2 dissociation, this is important because it means that the nitrogen atoms after dissociation do not block the step sites so that they can act as a low barrier channel for populating the terraces.

At first sight, the transition state configurations on the terrace and at the step are not too different. In both cases, one nitrogen atom is close to the most stable hcp site, whereas the other is located at a bridge position. However, at the step, the two N atoms do not share any Ru atoms as nearest neighbors. This reduces the indirect repulsive interactions that lead to the high N_2 dissociation barrier on the terrace [77]. Hence it is the modified geometrical arrangement of the steps that contributes significantly to the higher reactivity. In a subsequent theoretical study, it was shown that also for the ammonia synthesis over a Ru surface, the reactions mainly take place at the step sites [76].

Furthermore, a dramatic lowering of the dissociation barrier at stepped ruthenium surfaces does not only occur for N_2, but also for NO. DFT calculations found that this barrier is reduced from 1.28 eV at the flat Ru(0001) surface to 0.17 eV at a stepped Ru surface [78]. These results agree with the experimental findings of a STM study that NO dissociation only occurs at the steps of a vicinal Ru surface [79]. This strong reduction is caused by so-called final state effects. First, the reaction products, atomic nitrogen and oxygen, are more strongly bound at the steps than on the terrace, and second, at the steps, the reaction products share less nearest neighbor surface atoms, as in the case of N_2 dissociation. This again shows that the modified structural arrangement at the steps plays a very important role for their reactivity.

Stepped surfaces do not only lead to a stronger interaction with adsorbates because of the lower coordination of the step atoms, but they can also induce unusual adsorption structures, such as the stabilization of a molecular state by the presence of atomic adsorbates. Hydrogen molecules usually adsorbs dissociatively at metal surfaces [80], not molecularly. Molecularly chemisorbed H_2 species have only been found at stepped metal surfaces. On Ni(510), a molecular adsorption state at surface temperatures up to 125 K has been observed at the step sites, but only after the surface was passivated with a dense atomic hydrogen layer [81]. On Cu(510), a weakly bound species has been observed at low temperatures on the clean surface [82, 83].

On Pd(210), experiments have found the coexistence of chemisorbed hydrogen atoms and molecules on Pd(210), which was deduced from isotope exchange experiments [84]. The microscopic nature of the adsorbate states, however, could not be clarified from the experimental information. On the low-index Pd surfaces, it is well-accepted that hydrogen only adsorbs dissociatively [85, 86].

The hydrogen/palladium system has in fact been a model system for the study of the interaction of hydrogen with metal surfaces [87], which was also caused by the potential role of palladium as a hydrogen storage material. In order to identify the microscopic nature of the molecular H_2 adsorption state on Pd(210), DFT-GGA calculations have been performed [56, 84] using the Perdew-Wang functional (PW91) [33]. The geometry of the (210) surface plus the surface unit cell is shown in Fig. 10a in a top view. In addition, possible adsorption sites are labeled. The (210) surface can be regarded as a stepped surface with a high density of steps [88]. Vicinal fcc(n10) surfaces have (100) terraces with steps running along the [001] direction. These steps are forming open (110)-like microfacets.

The calculated hydrogen binding energies on Pd(210) are listed in Table 1. The long-bridge position between two Pd step atoms (site B) corresponds in fact to the most favorable adsorption site for atomic hydrogen, as indicated in Fig. 10b, although usually hydrogen prefers highly coordinated adsorption sites at metal surfaces [80]. This preferential adsorption on the low-coordinated step sites can be traced back to the upshift of the local d-band center at these first layer atoms (see Fig. 4). However, the long-bridge position is practically degenerate with the quasi-threefold position C' on the level of accuracy of the DFT calculations, as Table 1 indicates. In spite of the fact that there is mutual repulsion between the adsorption hydrogen atoms on Pd(210), still two additional hydrogen atoms can be adsorbed within the (210) surface unit cell at terrace sites A and C [56, 84].

On the clean Pd(210) surface, H_2 dissociates spontaneously without any hindering adsorption barrier, like on the low-index palladium surfaces [85, 90, 91]. However, once the long-bridge sites at the steps are occupied by hydrogen atoms, a barrier for the dissociative adsorption builds up, although hydrogen adsorption is still exothermic. This hydrogen precoverage leads to a metastable H_2 molecular chemisorption state above the Pd step atoms with a binding energy of 0.27 eV [56, 84]. This molecular state is also illustrated in Fig. 10. The preadsorbed atomic hydrogen does not significantly disturb the interaction of the H_2 molecules with the step Pd atoms but hinders the H_2 dissociation on Pd(210). In fact, the molecular adsorption state corresponds locally to the stable PdH_2 complex found in the gas phase [92, 93]. This unique feature of a nanostructured surfaces might be useful for catalyzing certain reactions in which, for example, relatively weakly bound hydrogen molecules are required.

Palladium is known to be able to absorb large amounts of hydrogen, which is important in the context of hydrogen storage and technology [94]. Therefore, the subsurface absorption

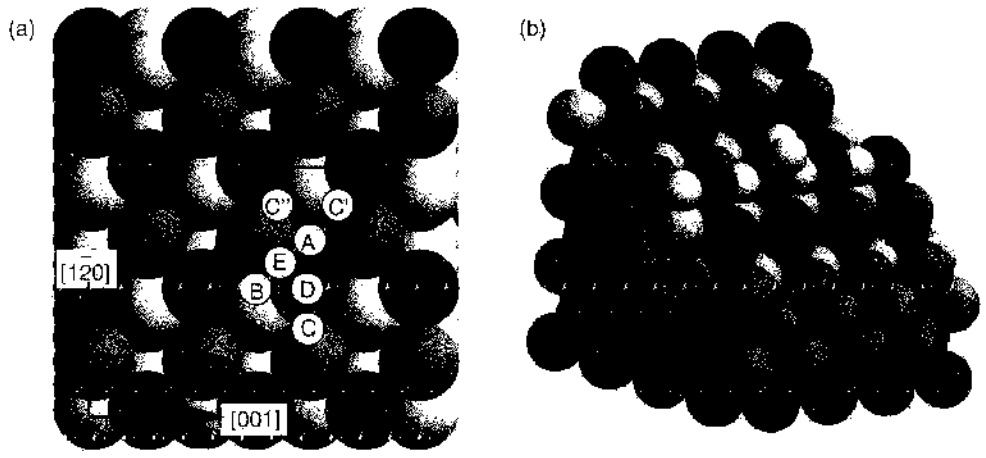

Figure 10. Structure of the Pd(210) surface. (a) Top view of the (210) surface together with the surface unit cell and CO and H adsorption sites; (b) one row of adsorbed hydrogen atoms at the open (110)-like microfacets is shown. Once these bridge sites are occupied by hydrogen atoms, a H_2 molecular chemisorption state becomes stabilized above the Pd step atoms [56, 84].

Table 1. Atomic hydrogen binding energies in eV/atom and CO binding energies in eV/molecule on clean Pd(210) for fixed and relaxed slabs.

		E_{ad} (eV)	
CO-pos	H-pos	Fixed slab	Relaxed slab
—	A	—	0.45
—	B	—	0.52
—	C'	—	0.51
—	O_h	—	0.21
E	—	1.83	1.88
C	—	1.76	1.86
B	—	1.73	1.77
E	A	0.09	0.12
E	C'	0.22	0.31
E	C''	0.19	0.27
C	A	0.13	0.22
C	B	0.24	0.30

For the site assignment, see Fig. 10a. For hydrogen, also the octahedral subsurface site O_h has been considered. For the coadsorption system, the listed binding energies correspond to atomic H adsorption on the CO-precovered Pd(210) surface. The coverage corresponds to one H atom and one CO molecule per (210) surface unit cell [56, 89].

as the first step for the hydrogen dissolution into the bulk is also of particular interest. The binding energy of hydrogen in the octahedral subsurface site is 0.21 eV (see Table 1), that is, significantly lower than on the surface. This means that hydrogen prefers to stay on the surface. Only if the surface is fully covered with hydrogen, absorption into the bulk starts [84]. Furthermore, the hydrogen subsurface binding energies at the open Pd(210) surface and at the low-index Pd(111), Pd(100) and Pd(110) surfaces are basically the same. The open structure of the steps does apparently not play a significant role in the subsurface absorption. Because of the small size of the hydrogen atom, the substrate relaxations induced by the hydrogen subsurface absorption are only relatively small and limited to the first layer [56].

In addition, the CO adsorption on Pd(210) was addressed by DFT calculations [89]. Interestingly, CO does not preferentially bind to the step sites B, as Table 1 shows, but rather to the bridge sites E and B, which are energetically degenerate according to the DFT calculations. The local bonding geometry of CO at these sites is shown in Fig. 11. These results can be understood considering the fact that CO is known to occupy bridge sites on Pd(100) [95, 96] and near-bridge sites on Pd(110) [97–99]: site E corresponds to a bridge position on the (100) terrace, site C to a bridge position on a (110) facet. It is furthermore obvious from Table 1 that relaxation effects of the substrate are indeed not negligible for the adsorption at the open Pd(210) surface.

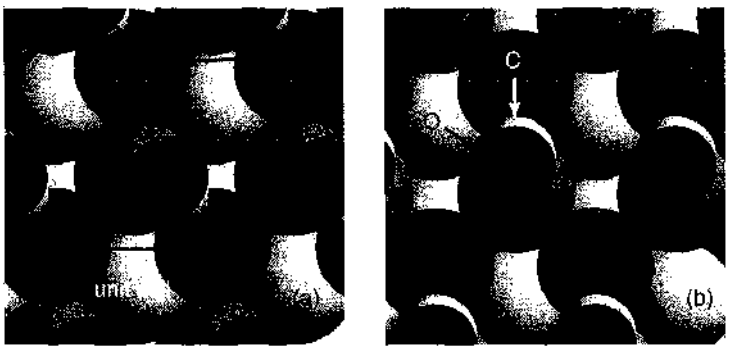

Figure 11. Adsorption geometries for CO on Pd(210), (a) at site E, and (b) at site B. O is drawn in black, C in white, and the Pd atoms are shaded in gray. In both cases, the bridge-bonded, inclined CO geometry is clearly visible.

As far as the CO adsorption site is concerned, the DFT calculations are in agreement with electron stimulated desorption ion angular distribution (ESDIAD) measurements [100] at low coverages up to $\theta = 1$, which suggests CO adsorbs in a bridge-bonded position at site E, inclined away from the surface normal. Thermal desorption results yield an initial adsorption energy of 1.52 eV [101] or 1.45 eV per CO molecule [102]. Thus the calculated CO binding energies on Pd(210) seem to be overestimated. This is a well-known phenomenon; GGA calculations using the PW91 exchange-correlation functional tend to overestimate the CO adsorption on a wide range of metal surfaces [103].

On Pd(100), the CO adsorption energy is 1.91 eV at the bridge position for the $c(2\sqrt{2} \times \sqrt{2})$ CO superstructure, in good agreement with other calculations using a slightly different setup [96]. However, this means that the adsorption energy of CO on Pd(210) is slightly lower than on Pd(100). Experimental TDS results, too, suggest a slightly higher adsorption energy on Pd(100) than on Pd(210) [101]. Considering the low coordination of the top Pd atom and thus its high reactivity, it might have been anticipated that CO would actually be more strongly bound to the stepped Pd(210) surface. For example, on stepped Pd(211) and Pd(311)-missing-row surfaces, the CO binding energies are larger than on Pd(100) and Pd(111) according to DFT calculations [104]. For the on-top site of Pd(210), this is indeed true: adsorption at site D gives a binding energy of 1.50 eV, whereas on-top adsorption on Pd(100) gives 1.44 eV [96].

The reduced binding energy of CO at the bridge sites of Pd(210) can be understood if the local bonding geometry is considered. Adsorption in both bridge-bonded sites results in rather strong relaxations. Furthermore, a tendency to minimize the CO inclination has been found. This indicates that the CO molecule is repelled by the protruding Pd atom at the next "step." Adsorption is thus not as favorable as on a flat (100) surface where there is no adjacent repelling Pd atom. In addition, the variations in the CO adsorption energy from site to site are comparably small. Hence, a rather small energy gain due to a more reactive bonding partner might just be overcompensated by the enforced, but unfavorable inclination of the molecule.

Furthermore, the coadsorption of CO and hydrogen on Pd(210) was studied by the DFT calculations [89]. Experiments of CO and H_2 adsorption showed a strong inhibition of hydrogen adsorption in the presence of CO on Pd(210) [102]. Coadsorption studies involving CO are of great technological relevance, as CO is known as a rather unwanted catalytic poison. Because it binds rather strongly ($\approx$ 1 to 2 eV) to many metal surfaces, it is able to passivate an otherwise reactive surface by just blocking the sites at which the wanted reaction would occur [105]. However, coadsorption studies are not only of interest in the context of the poisoning of a catalyst. In general, any heterogeneously catalyzed reaction requires the coadsorption of the reactants, thus confirming the importance of a fundamental insight into the interaction between two adsorbed species.

The computed atomic hydrogen adsorption energies for one hydrogen atom per surface unit cell in the presence of CO at different sites are also listed in Table 1. The overall trend is a significant reduction of atomic hydrogen adsorption energies at all sites due to the presence of CO on Pd(210), in agreement with the experimental results [102]. This reduction might be caused by a direct mutual electrostatic repulsion. Both atomic hydrogen and CO lead to an increase of the work function upon adsorption which means that they should experience a mutual dipole–dipole repulsion when they are coadsorbed. However, the increase of the work function upon atomic hydrogen adsorption is rather small, about 0.2 eV [84]. Furthermore, atomic hydrogen is adsorbed much closer to the surface than CO. Both facts indicate that the dipole–dipole interaction between adsorbed CO and H should be small.

Apart from the direct interaction between the coadsorbates, the CO-induced modification of the substrate density of states can also lead to significant changes in the hydrogen adsorption energies, as for example found in the case of the poisoning of hydrogen dissociation at Pd(100) by adsorbed sulfur [22, 106]. Upon CO adsorption, the local d-band center at the top Pd atom is shifted down significantly from $\varepsilon_d = -1.26$ eV at the clean surface to $\varepsilon_d = -1.82$ eV. This considerable downshift is caused by the strong interaction of CO with Pd and is much larger than the corresponding value for H adsorption on Pd(210). As mentioned

above, an energetic downshift of the position of the local d-band center leads to smaller chemical binding at the particular surface according to the d-band model [47]. This explains the rather large decrease in the hydrogen binding energies on the CO-covered surface.

The adsorption on (n10) surfaces was also the subject of a number of experimental and theoretical studies for the O/Ag system. Using molecular beam techniques and high-resolution electron energy loss spectroscopy (HREELS), Rocca and coworkers found that the steps of the Ag(210) and Ag(410) surface represent the active sites for the dissociative adsorption of O_2 while the oxygen atoms adsorb at different sites [107–109].

Motivated by these experimental investigations, the identification of the most stable atomic oxygen adsorption sites on Ag(210) and Ag(410) was addressed in a DFT study [110]. The results with respect to the binding energies of the oxygen atoms at step (S) and terrace (T) sites are summarized in Table 2. The given coverage θ_O is related to the number of oxygen atoms per surface unit cell. At the Ag(210) surface, the adsorption at the step sites is preferred compared to the terrace sites, as for H/Pd(210) [56], while on Ag(410) the adsorption energies are very similar at the step and the terrace sites. The subsurface incorporation of oxygen at the octahedral site of Ag(210) is energetically much less favorable than oxygen adsorption on the surface, again similar to H/Pd(210), but here it is mainly caused by the strong lattice distortion upon oxygen subsurface absorption [111].

The most peculiar result, however, is the increased stability of the oxygen atoms when they fully decorate the steps in a (1×1) geometry. This is in fact surprising because the negatively charged oxygen atoms experience a electrostatic repulsive interaction. For example, on Pt(211) where oxygen atoms also bind preferentially to the step sites, the (2×1) structure is more stable by 0.48 eV/adatom compared to the (1×1) structure [23] where every other step site is occupied.

The structure of oxygen atoms adsorbed in a (2 × 1) and a (1 × 1) structure at the step sites of a Ag(410) surface is illustrated in Fig. 12. First of all, it is obvious that the oxygen atoms are almost at the same height as the adjacent Ag atoms, which means that they are effectively screened from each other by the Ag step atoms. However, this alone can not explain the higher stability of the fully decorated steps. In fact, the authors of the computational study [110] do not have a waterproof explanation for this phenomenon. They believe that the mechanism causing this stability could be related to the arrangement of the O adatoms in O–Ag–O chains at the upper sides of the (110) steps. Such chains are for example also found in the added-row reconstruction of Ag(110) upon oxygen adsorption [112].

As far as the oxygen positions in the (2 × 1) and the (1 × 1) structures are concerned, for the high coverage the oxygen atoms are even closer to the surface than for the low coverage. Thus, the Ag and O are almost aligned at the same height. Although there is some hybridization between the oxygen and the silver electronic states, there is a significant charge transfer only from the silver atoms at the steps to the oxygen atoms, leading to a electrostatically stable chain of atoms with alternating charges in the (1 × 1) structures. Interestingly enough, in the (2 × 1) structure the charge transfer from the terrace atom to the oxygen atom is very similar to the transfer from the step atoms. Hence, the electrostatic rearrangement is not restricted to the step atoms. Certainly, the stability of the oxygen-decorated Ag steps deserves further investigation.

The molecules treated in the studies discussed above were relatively simple. However, the interaction of organic molecules with nanostructured surfaces is of course also very relevant in the field of heterogeneous catalysis [114]. In a DFT study, it was shown that there is also a

Table 2. Binding energy of oxygen atoms in eV/atom on Ag(210) and Ag(410) at step (S) and terrace (T) sites [110] and at the octahedral subsurface site O_s [111]. The coverage θ is related to the number of oxygen atoms per surface unit cell.

	E_{ad}(eV)				
Surface	S, $\theta_O = 1/2$	T, $\theta_O = 1/2$	S, $\theta_O = 1$	T, $\theta_O = 1$	O_s, $\theta_O = 1/2$
Ag(210)	0.68	0.49	0.80	0.42	0.07
Ag(410)	0.75	0.80	0.86	0.79	—

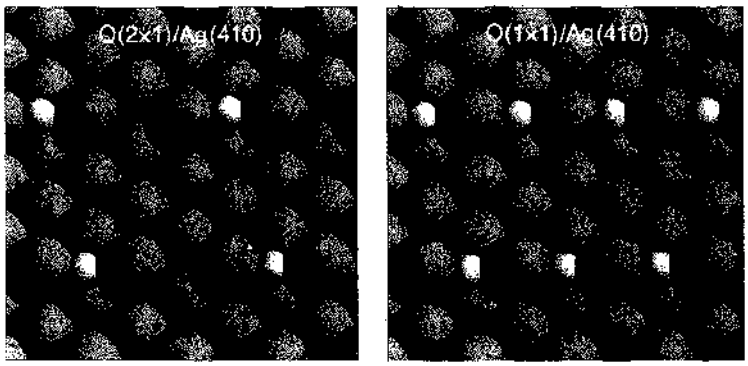

Figure 12. Optimized geometries of oxygen atoms adsorbed in a (2×1) and a (1×1) structure at the step sites of a Ag(410) surface [110].

considerable influence of steps on the adsorption of benzene on nickel [113]. Several adsorption positions of the benzene molecule, which corresponds to an aromatic π electron system, with respect to the step edge have been considered. The most stable adsorption position of benzene is illustrated in Fig. 13. The center of mass of the carbon rings is situated 1.0 Å away from the step edge. At this site, the binding energy of benzene, $E_b = 1.37$ eV, is enhanced by about 0.3 eV with respect to the value for the flat surface, $E_b = 1.05$ eV, and also with respect to the one for the center of mass of the benzene directly above the step edge.

Benzene binds to the nickel surface by forming bonds between the carbon and the metal atoms. The hydrogen atoms are rotated slightly upwards indicating a repulsive interaction between the hydrogen and the nickel substrate. This interpretation is supported by the fact that the binding energy of benzene to Ni(221) is further decreased by another 0.3 eV if the benzene molecule is shifted close to the step edge from below so that the hydrogen atoms interact with the Ni step atoms. The energetically most favorable adsorption position near the step allows the creation of strong bonds between the carbon ring and several nickel atoms. However, a shift of the molecule parallel to the surface hardly affects the binding energies. This seems to indicate that it is not the local bonding configuration at the step but rather the specific electronic properties of the step that cause its higher reactivity. And indeed, an analysis of the electronic structure shows that the polarization effects are larger at the steps, which leads to a larger charge transfer from the Ni atoms to the bonding region and thus to stronger bonds [113].

A similar enhancement of the binding energies at the steps of a metallic surface has also been found in DFT calculations addressing the adsorption of ethylene, C_2H_4, on Ag surfaces [115, 116]. Although ethylene hardly binds at the flat Ag(001) surfaces, the binding energy at the step sites of Ag(410) is 0.25 eV. This stronger binding, however, has been attributed to the enhanced hybridization between the silver d and the ethylene π^* states at the steps.

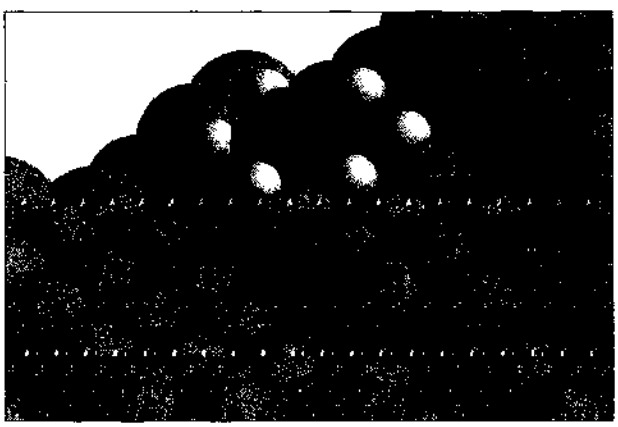

Figure 13. Optimized structure of benzene, C_6H_6, adsorbed above a stepped Ni(221) surface according to DFT calculations [113]. The center of mass of the benzene molecule is shifted by about 1.0 Å from the step edge.

The issue of chirality and so-called stereoselectivity of organic molecules on stepped surfaces had been addressed in a very ambitious DFT study [117]. High-index surfaces of fcc crystals with kink sites at the steps lack symmetry apart from translational symmetry when the step lengths or step faces on the two sides of the kink are not equal [118]. Two such surfaces that are created by reflection cannot be superimposed on each other, and the kink sites are either left- or right-handed, that is, they are chiral. One example of such a surface is the (643) surface, another one is the (17 1 1 9) surface, which is illustrated in Fig. 14. In fact, in Fig. 14 the $(17\,1\,1\,9)^S = (\bar{1}7\,1\,1\,9)$ surface is shown, whereas the $(17\,1\,1\,9)^R = (17\,1\,1\,9)$ is its enantiomorph that possesses the opposite chirality.

The chirality of organic molecules is actually rather important for molecular recognition and interaction. And the existence of chirality in kinked single crystal metal surfaces suggests that the adsorption and reaction probabilities of chiral molecules on these surfaces should be stereoselective, that is, they should depend on the chirality of the molecules. Indeed, such a selectivity has been found, for example, in the interaction of glucose with Pt(643) [119].

The first DFT study of the adsorption of a chiral molecule on a chiral surface was performed for the S and R enantiomers of 2-amino-3-(dimethylphosphino)-1-propanethiol (APPT, $HSCH_2CHNH_2CH_2P(CH_3)_2$) on $Au(17\,1\,1\,9)^S$ [120]. This particular molecule was chosen because in previous studies it was shown that its thiolate, phosphino, and amino groups are all able to bind to gold surfaces [121, 122]. The two most stable adsorption sites of the S and R enantiomers of APPT on $Au(17\,1\,1\,9)^S$ are shown in Fig. 14. Their binding energies are 0.9 eV and 0.8 eV, respectively, that is, there is an enantiospecifity in their binding. A closer analysis shows that in the enenergetically most favorable configurations APPT binds indeed with its thiolate, phosphino, and amino groups to the gold atoms. By performing model calculations for the three groups alone it was shown that the binding of APPT to $Au(17\,1\,1\,9)^S$ can be understood in terms of these three local bonds plus the deformation energies of the molecule and the surface, respectively.

In the most favorable binding configurations, the molecular deformation is rather small. The enantiospecific binding rather results from the ability or inability to simultaneously optimize three local bonds. Although the S-enantiomer of APPT is able to find such an optimal adsorption configuration, the R-enantiomer is less favored, as it is not capable of optimizing either the thiolate-gold or the amino-gold bonds. This fits into the picture that chiral recognition might be in general driven by the formation of three-point contacts [123], which represent the smallest number of contact points able to discriminate between two different enantiomers.

Interestingly enough, for two other related chiral molecules, the naturally occuring amino acid cysteine ($HSCH_2CHNH_2COOH$) and 2,3-diamino-1-propanethiol (DAPT, $HSCH_2CHNH_2CH_2NH_2$), no enantiospecific binding was found. For cysteine, the lack of stereoselectivity in the adsorption on $Au(17\,1\,1\,9)^S$ is caused by the fact that it only binds on $Au(17\,1\,1\,9)^S$ through two groups, its thiolate and amino groups. DAPT, however, has three groups that all form bonds with the surface, but two of them, the amino groups, are equal. Thus, it is apparently important for the chiral behavior that all three molecule–surface bonds

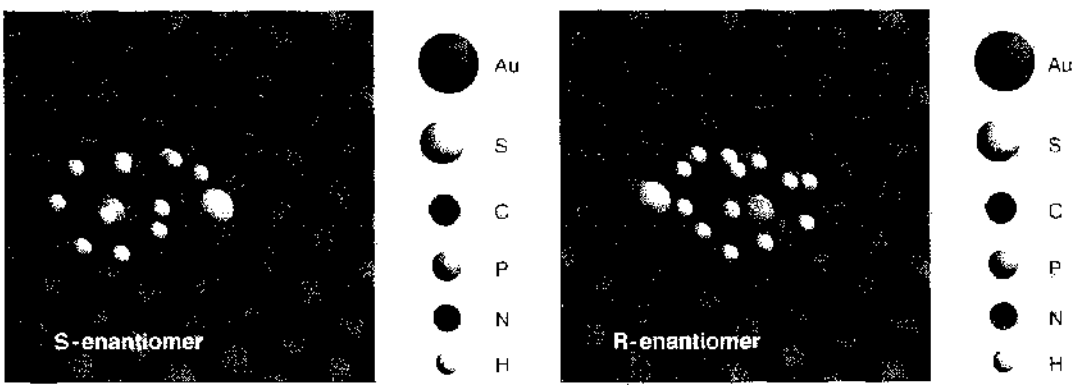

Figure 14. Most stable adsorption configurations for the S-enantiomer and the R-enantiomer of APPT on $Au(17\,1\,1\,9)^S$ as determined in DFT-GGA calculations (after [117]).

are different. This suggests that the character of the functional group mediating the binding is crucial for enantiospecific behavior.

So far, we have exclusively considered the adsorption of atoms and molecules on stepped *metal* surfaces. However, semiconductor surfaces are also of considerable technological importance, in particular Si surfaces, in the context of information technology. Especially the H_2/Si system has attracted a lot of attention [124] because hydrogen adsorption leads to a passivation of the surface. Furthermore, hydrogen desorption is the rate determining step in the growth of silicon wafers from the chemical vapour deposition (CVD) of silane.

On the flat Si(100) surface, the dissociative adsorption of H_2 is hindered by a barrier of the order of 0.4 eV according to DFT slab calculations [125, 126], although the exact value of this barrier is still debated [127]. However, it was found experimentally that the hydrogen sticking coefficient at steps of vicinal Si(100) surfaces is up to six orders of magnitude higher than on the flat terraces [128].

As far as stepped semiconductor surfaces are concerned, it is important to realize that the termination of semiconductor surfaces is usually much more complicated than those of metal surface. This is caused by the covalent nature of the interaction, which strongly favors directional bonding and leads to extended reconstruction patterns [16]. At the conditions of the experiment, vicinal Si(100) surfaces have steps with a double-atomic height, the so-called rebonded D_B steps, which have additional coordinated Si atoms attached to the steps [129]. To model the vicinal substrate, a Si(117) surface was used in the calculations [128, 130]. Its structure is shown in Fig. 15 where the rebonded Si atoms are shown in white. These calculations found that hydrogen atoms preferentially adsorb at the steps of the silicon surface. These sites are favored by about 0.1 eV with respect to the terrace sites, which is in fact also true for a Si surface with so-called rebonded single atomic height S_A and S_B steps [130].

However, the influence of the steps on the H_2 dissociation barrier is much more dramatic. Although this barrier is 0.40 eV and 0.54 eV at the terrace sites T_1 and T_2, respectively, there is no barrier for dissociation for the H_2 molecule approaching with an orientation parallel to the steps and the two H atoms dissociating toward the Si rebonded atoms [128]. The dissociation process, however, involves some relaxation of the Si atoms with the asymmetry of two adjacent rebonded Si atoms caused by a Jahn-Teller–like like splitting being lifted.

The high reactivity of the steps with respect to H_2 dissociation has been explained by the modification of the electronic structure at the steps. On the flat Si(100) surface, there are two surface bands formed from the dangling bonds located at the Si dimer atoms, which are split by approximately 1 eV due to a Jahn-Teller mechanism [131, 132]. The same splitting is observed for the rebonded Si atoms at the steps, as just mentioned above. However, when the rebonded Si atoms are forced to the same geometric height, the splitting is reduced to 0.4 eV, and the surface states can interact efficiently with the molecular orbitals of the H_2 molecules. At the flat Si(001) surface, the π interaction of the dangling bonds prevents the two surface bands from coming closer to each other, which makes the terrace sites less capable of breaking the H–H bond.

Interestingly enough, adsorbates can have a similar effect on the dissociation probability on Si as steps, as the electronic structure of the dangling bonds is perturbed in a similar way by both steps and adsorbates [133]. Recent scanning tunneling microscope (STM)

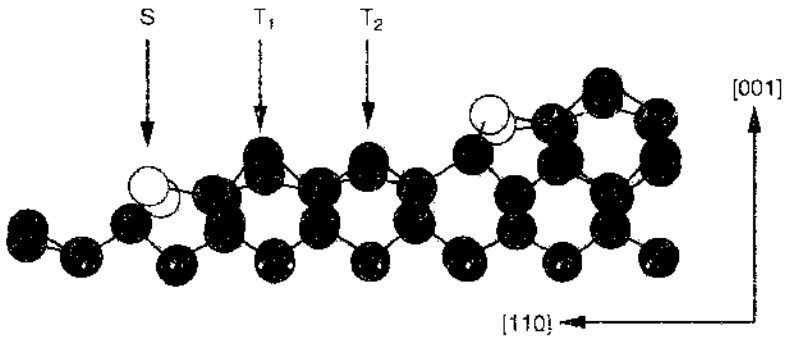

Figure 15. Relaxed structure of the Si(117) surface with rebonded D_B steps. The rebonded Si atoms are shown in white (after [128]). The step and terrace atoms are denoted by S and T, respectively.

experiments demonstrated that predosing the Si(100) surface by *atomic* hydrogen creates active sites at which the H_2 adsorption is considerably facilitated [134, 135]. This confirms that it is often the modified electronic structure that is crucial for the understanding of the chemical properties of nanostructured surfaces. Furthermore, these findings have finally resolved the so-called barrier puzzle for the H_2/Si system [126, 136]: Although the sticking coefficient of molecular hydrogen on Si surfaces is very small [137, 138] indicating a high barrier to adsorption, the low mean kinetic energy of desorbed molecules [139] suggests a small adsorption barrier. This puzzle arises from the fact that adsorption experiments are usually performed in the low-coverage regime while desorption experiments are carried out in the high-coverage regime, and for the system H_2/Si the hydrogen coverage has a crucial influence on the adsorption barrier heights.

4. ADSORPTION ON SUPPORTED CLUSTERS

Clusters are particles with sizes typically between a few and several thousands of atoms. They are characterized by the reduced dimension of the particle, a large surface to volume ratio, and a large number of low-coordinated atoms at edge sites. The properties of clusters lie usually between those of single atoms or molecules and those of bulk material. However, often small particles or clusters in the nanometer range show surprisingly strongly modified electronical, optical and chemical properties that can be characterized by saying that small is different [140]. Yet, it is often not clear whether the specific properties are caused by the reduced dimension of the particles ("quantum size effects") or by the large surface area of the nanocluster where many low-coordinated atoms or defects are present.

Free clusters are usually studied in molecular beam apparatuses. For technological applications, free clusters are in general not very useful; they rather have to be fixed in space, either in a bulk matrix as for example the so-called nanodots or quantum dots in semiconductor technology, or on a surface. For these embedded or supported clusters, the interaction with the environment has to be taken into account. In fact, for metal clusters on surfaces the so-called strong metal support interaction (SMSI) has been discussed intensively [141, 142] which significantly influences the catalytic properties of group VIII metals such as Fe, Ni, Rh, Pt, Pd, and Ir supported on metal oxides.

In recent years, supported gold clusters have become the prototype system for the study and understanding of the modified chemical properties of nanoscale structures. Although gold as a bulk material is chemically inert, mainly due to its energetically low-lying, completely filled *d* band [48], small Au clusters show a surprisingly high catalytic activity, especially for the low-temperature oxidation of CO [18, 24], but also for NO oxidation, the partial oxidation of proprene, and the partial hydrogenation of acetylene. The size dependence of the CO oxidation turn over frequency is shown in Fig. 16, which is the reaction rate per surface Au site per second. Clearly visible is the non-monotonous behavior as a function of the particle size. The turnover frequency is strongly peaked at about 3 nm, which corresponds to ~300 atoms per cluster. It should be noted that these cluster are rather flat with a height of only about two to three atomic layers. Additional scanning tunneling microscopy/spectroscopy experiments showed that the catalytic activity is related to size effects with respect to the thickness of the gold islands with two-layer-thick islands being most effective for the CO oxidation. At this cluster size also a band gap opens up with decreasing cluster size, that is, a metal-to-nonmetal transition occurs [18].

Still the reasons for the large difference in the properties between bulk material and supported clusters is far from being fully understood. Several factors have been discussed so far that could be responsible for the difference: particle roughness, size dependence of the band gap, finite size effects or charge transfer phenomena.

Of course, these open questions have raised the interest of theoreticians in the properties of supported gold clusters [143]. The theoretical treatment of nanosize particles by electronic structure theory methods still represents a great computational challenge. Due to the large number of symmetrically different atoms in nanostructures, the numerical effort required to treat these structures is enormous. On the other hand, there is definitely a need for the microscopic description of nanoparticles because the knowledge of the underlying mechanism

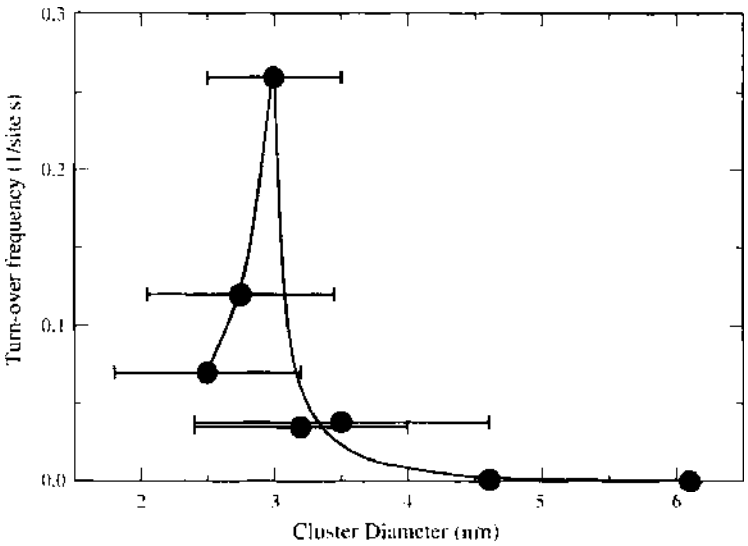

Figure 16. Measured CO oxidation turnover frequencies at 300 K as a function of the average size of Au clusters supported on a high surface TiO_2 support. The solid line is meant as a guide to the eye (after [18]).

leading to the modified nature of the particles is still rather limited. In this chapter, I will show the recent progress that has been made in the microscopic theoretical description of supported clusters. Usually the clusters treated in the theoretical studies are much smaller than the ones studied in experiments. Still some important qualitative aspects about cluster–adsorbate interaction can be learned from the theoretical studies as will be shown below.

In a fundamental study, Mills et al. studied the adsorption of O_2 on small free Au_n and supported Au_n/Au(111) clusters by DFT-GGA calculations [144]. They particularly focused on the role of the surface structure, the electron confinement, excess electrons and the band structure. The results of these calculations are summarized in Table 3. The calculations have been performed both for neutral as well as for negatively charged systems. The slab calculations for the supported clusters were performed within a 3 × 4 surface periodicity. The effect of the excess charges was also studied for the Au_n/Au(111) systems by adding one electron per unit cell, which was then compensated by a homogeneous positive charge background. It should be noted that for the free Au_n clusters with $n \leq 3$ the calculations were checked by state-of-the-art quantum chemistry calculations [145], and significant differences were found, which were attributed to the inaccurate description of oxygen in DFT. For the current discussion, however, these quantitative differences are not essential.

The adsorption geometries for O_2 on Au_5, Au/Au(111), and Au_3/Au(111) are shown in Fig. 17. All considered free Au_n clusters with $n \leq 6$ prefer a planar geometry, as for example the Au_5 cluster shown in Fig. 17a. In fact, there is no satisfactory explanation yet why these Au clusters are flat and do not condensate in a more compact structure. The O_2 bonding geometries on Au_n/Au(111) are in most cases similar to the corresponding bonding geometries on the free Au_n clusters, which demonstrates that the O_2 adsorption is a rather

Table 3. Binding energies of O_2 in eV on neutral and negatively charged Au(111), free Au_n clusters, and supported Au_n/Au(111) clusters calculated by DFT calculations [144] [$n = 0$ corresponds to the flat Au(111) surface in the case of Au_n/Au(111)].

	E_b(eV)			
n	Au_n	Au_n^-	Au_n/Au(111)	Au_n/Au(111)$^-$
0	—	—	0.09	0.20
1	0.54	0.50	0.38	0.65
2	0.49	1.40	0.63	0.96
3	0.90	0.37	0.30	0.45
4	0.47	1.19	--	--
5	1.08	0.76	--	--

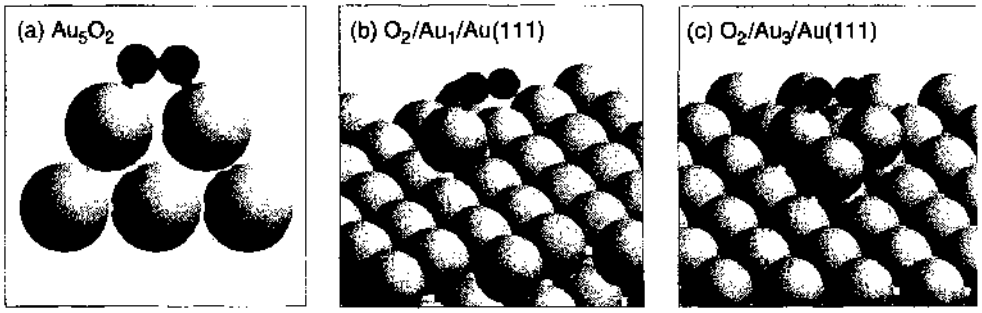

Figure 17. Calculated optimal adsorption geometries of O_2 on Au_5, Au/Au(111), and Au_3/Au(111), (after [144]).

local process. Indeed, an analysis of the electron density of the Au(111) slabs shows that the perturbation of the electronic structure due to the adsorption of O_2 is very efficiently screened by the metal electrons.

There is furthermore one common feature for all O_2 adsorption sites: O_2 does not bind on high-coordinated sites but rather at the edges of the clusters (see Fig. 17). At these edges, there are small regions with a high electron density. Such a configuration is favorable for electron transfer to the electronegative O_2 molecule, which leads to bonding. On the other hand, on the flat Au(111) surface, the electron distribution is rather smeared out without any regions of enhanced electron density. Consequently, the binding of O_2 on the flat Au(111) surface is very weak. However, there is also a complementary explanation in terms of the *d*-band model: low-coordinated sites have higher lying *d* states that interact more strongly with the adsorbate states [146]. Both views are appropriate and highlight different aspects of the bonding.

In addition, according to Table 3, O_2 binds stronger to the free Au_n cluster than to the corresponding supported Au_n/Au(111) with a single exception, neutral Au_2/Au(111). The supported clusters are strongly interacting with the underlying support. This removes electron density that could otherwise be used for binding O_2 at the low-coordinated sites of the clusters.

Nonetheless, low-coordination alone can sometimes not explain the reactivity. For example, at the Au_5 cluster the O_2 molecule does not bind to the twofold coordinated corner atoms but rather to the two threefold Au atoms in the upper part of Fig. 17a. This can be understood if the structure of the highest occupied molecular orbital of the cluster that interacts most strongly with the π^* orbital of O_2 is considered. Because Au_5 has an odd number of electrons, this orbital is in fact a singly occupied molecular orbital (SOMO [147]). The spatial distribution of this orbital is illustrated in Fig. 18. It is evident that the region in space where the SOMO of the *free* Au_5 cluster is mainly located coincides with the binding site of the oxygen molecule. At the twofold coordinated corner atoms, there is only little weight of the SOMO.

However, it should be noted that these results for the O_2 adsorption on Au_5 are in conflict with the results of a similar study of oxygen molecular and dissociative adsorption on Au_n clusters [148]. In this study, the energetically most favorable O_2 molecular adsorption position on the Au_5 cluster was determined to be at the twofold corner atoms. On the other hand, the important effect of the spatial distribution of the frontier orbitals for the energetically most favorable binding site has also been found in the adsorption of propene, C_3H_6, on small gold clusters and on Au(111) [147]. Thus the local electronic configuration at the low-coordinated sites has to be taken into account for a complete understanding of the binding properties.

The O_2 binding energy to the Au_n and Au_n^- gas-phase clusters is not correlated with the charge state of the clusters but rather with the parity of the number of electrons. The valence electrons of a single Au atom have a $5d^{10}6s^1$ configuration, that is, their number is odd. Au cluster with an odd number of electrons bind O_2 strongly; if there is an even number of electrons, O_2 is only weakly bound [149]. This means that paired electrons are apparently relatively inert, as far as the binding of O_2 is concerned. No such trend is obvious for the supported Au_n/Au(111) clusters, and the variation in the O_2 binding energies with the number *n* of atoms in the clusters is much less pronounced than for the free Au_n clusters.

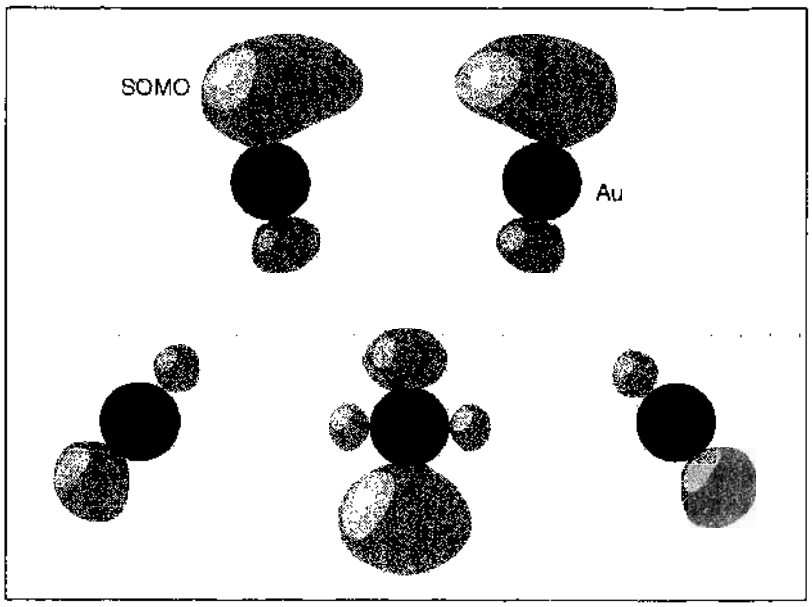

Figure 18. Illustration of the spatial distribution of the singly occupied molecular orbital (SOMO) of Au_5 (after [144]).

There is, however, one clear trend: the O_2 binding energies to the Au_n/Au(111) clusters increases significantly when an extra electron is added to the unit cell. This additional electron ends up in the LUMO of the uncharged system, which is localized at the site where the O_2 binds and thus contributes to the molecule–cluster interaction [144]. Thus both the low coordination as well the charging of the Au substrate lead to a strong O_2 binding.

The effect of the electron density in a nanostructure on the chemical reactivity was confirmed experimentally for a SnO_2 nanowire that was configured as a field-effect transistor [150]. By changing the electron density inside the nanowire through the applied gate voltage, the rate of oxygen adsorption and desorption and of CO_2 formation on the surface of the SnO_2 nanowire can be modified significantly.

The important role of the coordination of the Au atoms for the binding strength of oxygen has also been stressed by Nørskov and coworkers [146, 151, 152]. They calculated the adsorption energies of O and O_2 on a free Au_{10} cluster by DFT-GGA calculations and compared it to the corresponding adsorption energies on Au(211) and Au(111). (It should be noted that the adsorption energies of different groups differ due to technical details such as the exchange-correlation functional or the choice of the pseudopotential.) The Au_{10} cluster did not correspond to an energy minimum structure; rather a disklike geometry was chosen with seven atoms in the lower layer and three in the top layer (this structure is shown in Fig. 28) in order to mimic a Au cluster on a oxide support. On the cluster, the oxygen atom and molecule adsorb at the edges of the cluster. For example, the O_2 molecule binds to the lower plane in a geometry similar to the one shown in Fig. 17a. The O and O_2 binding energies are plotted as a function of the coordination number of the Au atoms in Fig. 19. It is obvious that there is a very strong dependence of the adsorption energies on the coordination number. Analogous trends have been also found in DFT calculations for CO adsorption on stepped Au surfaces and an Au adatom on Au(111) [153]. This confirms that low-coordinated atoms in nanostructures can act as preferential sites for atomic and molecular adsorption.

However, Fig. 19 also shows that the O_2 binding to Au(111) is stronger than to Au(211), although the coordination number of the Au atoms in the (111) surface is higher. Similarly, Liu et al. [154] have found that O atoms bind stronger to a Au(211) surface (coordination number 7) than to a kinked Au(211) surface (coordination number 6). For an oxygen atom on a Au adatom on Au(111) [Au/Au(111), coordination number 3], they even found that the atom is not stable with respect to the associative desorption of O_2 into the gas phase, which is surprising because the adsorbed O_2 molecule is stable (see Table 3). Apparently, the coordination number is an important parameter in order to understand the interaction

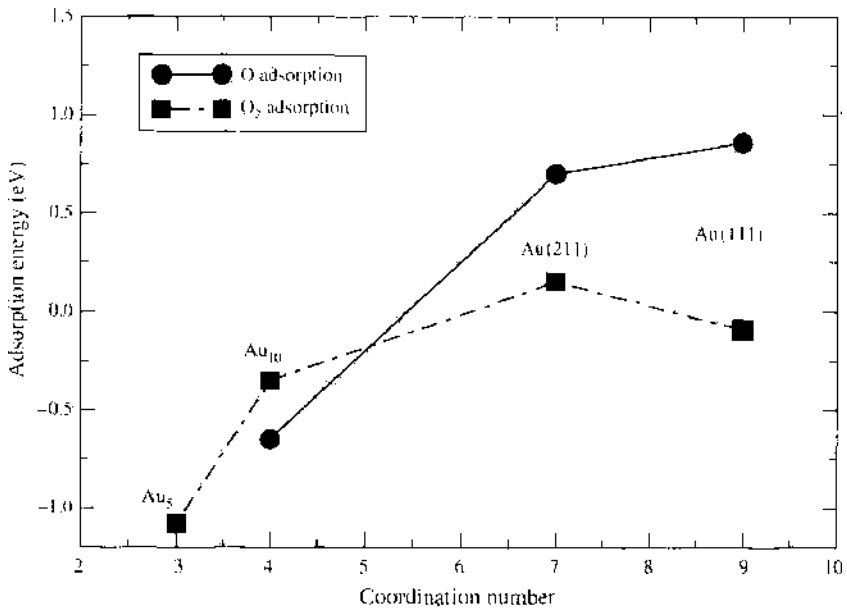

Figure 19. Adsorption energies of O and O_2 on a Au_{10} cluster, on Au(211), and Au(111) plotted as a function of the coordination number of the Au atoms (after [146]). In addition, the results for the O_2/Au_5 and $O_2/Au(111)$ by Mills et al. [144] are included. All the results have been obtained by DFT calculations using the PW91 functional [33].

of atoms and molecules with specific sites, but there are other parameters such as the nature of the orbitals involved in the bonding [144] that are crucial for a complete understanding.

In order to make closer contact with the experiments of Au clusters supported by oxide substrates, the adhesion and shape of Au atoms and clusters on oxide surfaces has been addressed by several authors from a theoretical point of view [155–159]. These studies indicated the importance of defect sites for the adsorption of Au clusters. As far as single atoms are concerned, the binding of Au to an oxygen vacancy site on TiO_2 is substantially stronger than to the stoichiometric (110) rutile surface, as was found in a periodic DFT study [155].

Similar results were also found in DFT calculations for Au_n particles with $n = 1$ to 3 on the TiO_2 anatase (101) surface [156]. Although the binding energies E_b of the Au_n particles on the stochiometric surface are typically between 0.3 eV and 0.8 eV (with the exception of Au_3 adsorbed in a bent geometry, $E_b = 1.9$ eV), the binding energies of these clusters on the reduced anatase surface with an oxygen vacancy are between 1.8 eV and 3.6 eV [156]. The strong binding is accompanied by a relatively large charge transfer to the gold atoms. Interestingly enough, CO interacts much more strongly with clusters adsorbed on the stochiometric surface than with clusters adsorbed on vacancies. This has been associated with the negative charge of the gold atoms which implies an unfavorable interaction with the dipole moment of the CO molecule [156]. However, it might also well be that the electrons involved in the strong bonding of the Au_n particles to the reduced surface are not available for the additional bonding of an adsorbate which then leads to the weak interaction.

It was furthermore found that the interaction between a monolayer of gold and a perfect rutile $TiO_2(110)$ surface is negligibly small [157]. On the other hand, if there are oxygen vacancies present, the interaction energy corresponds to -1.6 eV/defect. Thus it was concluded that the adhesion of gold to TiO_2 requires the presence of oxygen defects or possibly step and adatoms. The size and shape of supported particles can be derived from the Wulff construction [16] which is illustrated in Fig. 20: the particle is truncated in all directions at distances proportional to the interface or surface free energy of the crystal plane in that direction. This construction does not account for the formation energies for edge and corner atoms and is therefore only valid in the limit of large macroscopic crystals where the total formation energy of the edges is negligible compared to the total surface energies of the facets.

In order to account for defect and edge effects, Lopez et al. also included defect and edge energies estimated from calculations of slabs containing one to four gold layers [157]. Thus they found that Au particles with a diameter of 3–4 nm, such as the ones studied in the

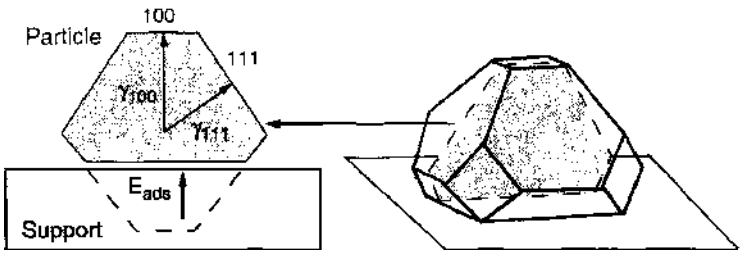

Figure 20. Schematic illustration of a truncated Wulff polyhedron on a support. The left panel corresponds to a two-dimensional cut through the three-dimensional polyhedron in the right panel (after [158]).

experiments [18] shown in Fig. 16, are three to four layers thick. This means that the Au particles are in fact rather flat, in good agreement with the experiment.

Already rather large Au nanoparticles on TiO_2 were addressed in DFT calculations by Molina et al. [159] using the RPBE functional. Since the nanosized Au clusters typically studied in the experiments are too large to be explicitly treated in DFT calculations, the authors chose just to model the interface between the nanoclusters and the substrate. They did so by replacing the nanoparticle with one-dimensional rods. One side of the rod was modeled according to the local bonding situation of the Au atoms at the edge of a nanoparticle while the other side of the rod only served the correct boundary conditions toward the interior of the supported clusters.

The general geometry of the one-dimensional rod model is illustrated in Fig. 21a, while Fig. 21b shows a side-view of the relaxed atomic structure of the Au rod on TiO_2 together with the optimal O_2 adsorption position. The adsorption studies are performed for $p(N \times 2)$, $N = 2, 3$ surface unit cells using four trilayer TiO_2 slabs (in Fig. 21 only the two uppermost trilayers are shown). Four trilayers are necessary in order to account for the strong relaxation effects upon adsorption. The structure shown in Fig. 21 has been chosen to model a sharp Au particle termination. Another rod with a more rounded termination has also been considered in the study (see Fig. 22).

On clean, stochiometric $TiO_2(110)$, O_2 does not bind [161]. The interesting point is that the adsorption of O_2 on top of a Ti trough atoms (see Fig. 21) is strongly stabilized by the presence of a Au cluster with its edge above the adjacent bridging O atoms of the $TiO_2(110)$ surface. An analysis of the charge density distribution shows that there is considerable charge transfer from the supported Au particle to the O_2 molecule mediated by the surface through electronic polarization. The O_2 molecule that is bound by 0.45 eV has a bond length of 1.41 Å indicating a charge state of the O_2 molecule close to the peroxo O_2^{-2} species. The O_2 adsorption is accompanied by a strong relaxation of the TiO_2 substrate with the Ti trough atom below the oxygen molecule pulled up by 0.8 Å. Furthermore, there is another weakly bound O_2 species (0.1 eV) within a leaning configuration connecting the Ti trough atom with the Au edge (see Fig. 22).

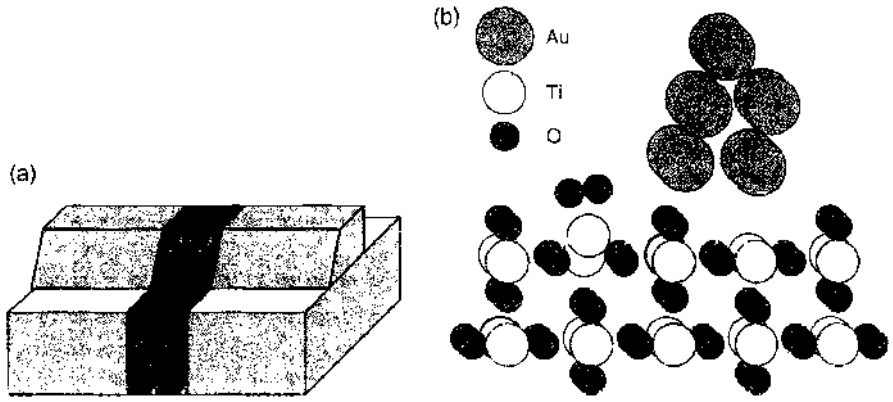

Figure 21. Illustration of the one-dimensional rod model for the adsorption of O_2 on Au/TiO_2 nanoparticles used in GGA-DFT calculations. (a) Schematic representation of the rod geometry. The dark-shaded area corresponds to the unit cell. (b) Relaxed structure of O_2 binding at the Ti trough close to a supported one-dimensional Au rod with a sharp Au edge (after [159, 160]).

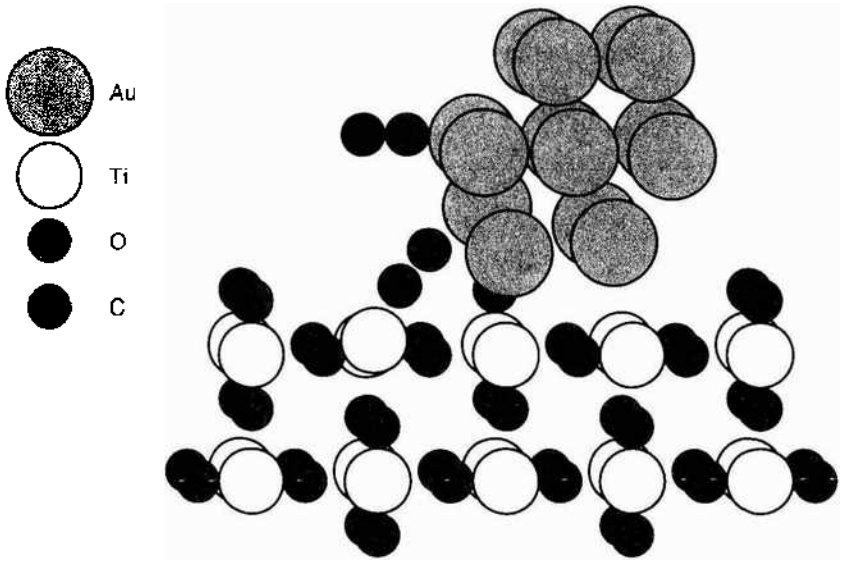

Figure 22. Minimum energy structure of a leaning O_2 molecule and a CO molecule bound to an Au rod on TiO_2 with rounded shape and the oxygen vacancy situated below the nanoparticle edge (after [159]).

Because TiO_2 is a reducible oxide, a TiO_2 substrate with a bridging oxygen vacancy in the $p(3 \times 2)$ surface unit cell was also considered in the calculations. On the clean reduced TiO_2 surface, a O_2 molecule on the adjacent Ti trough atom becomes strongly bound by more than 1 eV. There is a significant charge transfer from the O vacancy to the O_2 molecule leading again to a peroxo O_2^{-2} species. The O_2 binding energy is even further increased to 1.65 eV if the edge of the Au rod is located above the O vacancy. This suggests that the Au rod provides additional charge for the binding of the O_2 molecule. The Au rod does in fact only weakly interact with the O vacancy so that the adsorption configuration is very similar to the one for the stochiometric TiO_2 surface. This is different if a single Au atom is located at the vacancy site. Then the O_2 binding energy is reduced to 0.64 eV because of the competition between the O_2 molecule and the low-coordinated, reactive Au atom for the electrons of the vacancy [159].

As far as the CO oxidation is concerned, it turned out that the Au rod with the sharp edge binds CO very weakly. This is caused by the unfavorable orientation of the CO molecule with respect to the edge because of the presence of the substrate. On the other hand, at the Au rod with the rounded edge the CO molecule can bind rather strongly (~0.5 eV) to the low-coordinated Au atoms of the second layer, as illustrated in Fig. 22. This binding is only weakly influenced by the presence of O_2 on the substrate.

The structure shown in Fig. 22 with a leaning O_2 molecule and the CO bound to the second layer of the Au rod represents a favorable initial configuration for the CO oxidation because of the small binding energy of the O_2 molecule. The O_2 molecule can approach the CO molecule and react with the CO to CO_2 rather easily. The CO_2 formation according to a Langmuir-Hinshelwood mechanism is only hindered by a barrier of 0.15 eV with the remaining O atom bound on top of a Ti trough atom.

However, the fact that oxygen vacancies are required for the adhesion of gold on titania seems to be at variance with recent experimental findings that gold monolayers and bilayers can completely wet, that is, cover the titania support [162]. In this particular study, it was also found that the gold bilayer structure is significantly more active with respect to CO oxidation than the monolayer structure. This also means that the O_2 molecule involved in the CO_2 formation cannot bind to the TiO_2 substrate. In spite of the detailed investigations already performed for the Au/TiO_2 system, certainly further experimental and theoretical studies are needed to fully understand the exceptional activity of Au nanostructures supported on oxide substrates.

On the other hand, the important role of oxide defects for the catalytic activity of supported Au particles was verified both in experiment as well as in theory [8] for another oxide support material, namely MgO(100). In a combined experimental and theoretical study, the

CO oxidation catalyzed by size-selected Au_n clusters with $n \leq 20$ supported on defect-poor and defect rich MgO(100) films was investigated [8]. These experiments are different from the ones reported for Au/TiO_2 insofar as, first, the clusters used are much smaller, and second, the cluster were size-selected before deposition so that a monodisperse distribution of Au clusters was deposited on MgO(100). The experiments revealed that the gold clusters deposited on defect-rich MgO-films have a dramatically increased activity compared to clusters deposited on defect-poor films at temperatures between 200 and 350 K. The smallest catalytically active particle was found to be the Au_8 cluster.

In order to detect the microscopic mechanisms underlying the observed behavior, LDA-DFT calculations have been performed describing the oxide substrate in a finite setup [8]. Between 27 and 107 substrate atoms have been embedded into a lattice of about 2000 ± 2 e point charges at the positions of the MgO lattice. As a defect, an oxygen-vacancy F-center was introduced at the MgO(100) surface. The equilibrium shape of a Au_8 cluster adsorbed on the defect-free MgO surface and on the F-center was determined, and the energetically most favorable adsorption sites for O_2 and CO and the reaction paths of the CO oxidation catalyzed by the Au_8 cluster were explored. A side view of the Au_8 cluster located above the F-center is shown in Fig. 23. The structure of the Au_8 cluster corresponds to a deformed close-packed stacking.

In addition, in Fig. 23 the energetically most favorable adsorption position of O_2 on the Au_8 cluster is illustrated. This position corresponds to an edge-top configuration on the triangular top-facet of the Au_8 cluster. At this site, the O_2 adsorption energy is $E_a = 1.22$ eV, which is rather large compared to the values for the free Au_n and the supported $Au_n/Au(111)$ clusters (see Table 3, however, the adsorption energy might well be overestimated because of the notorious overbinding occuring in LDA calculations [16]). This high adsorption energy is believed to be caused by the partial electron transfer of 0.5 e from the MgO(100) surface to the gold octamer, according to the analysis of the electronic structure of the cluster [8]. On a Au_8 cluster supported on the stochiometric MgO(100) surface, the O_2 binding energy is much lower, only about 0.5 eV [163]. O_2 can also adsorb at other sites on the Au_8 cluster, for example in an edge configuration of the top-facet ($E_a = 0.88$ eV) or even at the interface of the Au_8 cluster periphery with the MgO substrate. At all these adsorption sites, the oxygen molecule

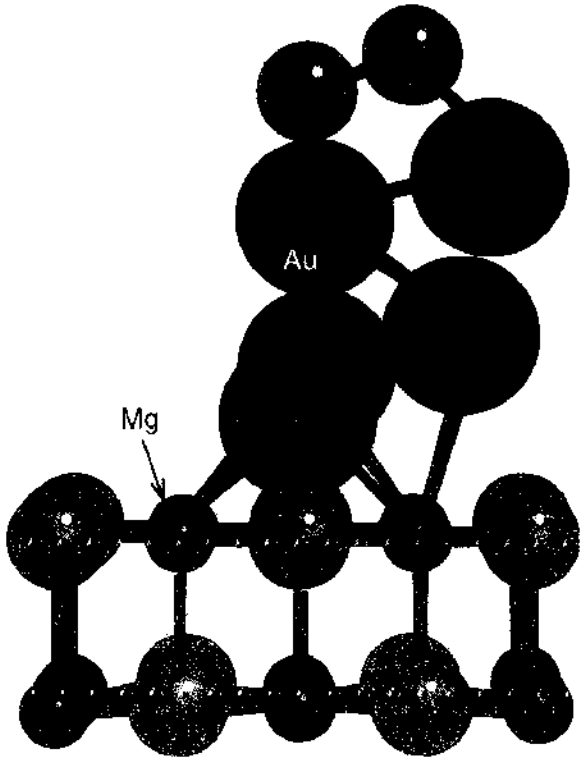

Figure 23. Most favorable O_2 adsorption site on an Au_8 cluster adsorbed on a MgO(100) surface containing an oxygen-vacancy F-center. Due to the perspective, not all Au atoms are visible (after [8]).

is found to be in a peroxo, that is, O_2^{2-}, state with a weakened highly stretched intramolecular bond (d_{O-O} = 1.41 to 1.46 Å) compared to that of the free molecule (d_{O-O} = 1.24 Å).

Another important aspect for the reactivity of small supported clusters is their dynamic structural fluxionality [163]. They are able to adapt their structure in order to provide energetically favorable adsorption sites. For the Au_8 cluster supported on the stochiometric MgO(100) surface, it was indeed found that constraining the cluster to its original geometry prevents the adsorption and activation of O_2 [163].

The adsorption configuration shown in Fig. 23 acts as a favorable initial configuration for the CO oxidation. A CO molecule approaching this adsorbed O_2 molecule can react spontaneously with the oxygen molecule to form a weakly bound (~ 0.2 eV) CO_2 molecule that can directly desorb plus an adsorbed oxygen atom. Such a mechanism is called an abstraction or so-called *Eley-Rideal mechanism*. Recall that although the CO oxidation is strongly exothermic, it is hindered by a large activation barrier in the gas phase. Another reaction pathway that has been found is of the Langmuir-Hinshelwood type, which means that the two reactants are initially coadsorbed on the top-facet of the Au_8 cluster. This CO oxidation path has a similarly small barrier. Through these reaction channels, the low-temperature CO oxidation down to 90 K can proceed. As far as the higher temperature oxidation is concerned, further channels have been identified at the periphery of the gold cluster. Their barriers are much smaller at the Au_8 cluster adsorbed above the F-center than on the perfect surface giving an explanation for the enhanced activity of the clusters on the defect-rich substrate. A similar effect has been found in a combined experimental and theoretical study addressing the reactivity of nano-assembled Pd catalysts on MgO thin films [164] where, however, the Pd catalysts were just modeled by single atoms in the calculations.

The CO oxidation at MgO supported gold aggregates was also addressed in a DFT study by Molina and Hammer [158, 160] who particularly focused on the role of the oxide support for the CO oxidation. As a first step, the shape of adsorbed gold particles was determined using the Wulff construction, which is illustrated for a two-dimensional cut in the left panel of Fig. 20. According to the calculated surface energies of Au low-index faces and the Au–MgO adhesion energies, the Au clusters assume a partial wetting shape as shown in the right panel of Fig. 20, in agreement with the experiment [165].

However, as already mentioned above, the Wulff construction does not account for the formation energies for edge and corner atoms and is therefore only valid in the limit of macroscopic crystals where the edge and corner energies do not play any role. For smaller clusters, the assumption of negligible total edge and corner energies is no longer justified. And indeed, Molina and Hammer found that the energetically most stable structure of a Au_{34} cluster on MgO does not look like the one shown in Fig. 20. The supported Au_{34} cluster rather shows a increasing degree of partial wetting, that is, the cluster assumes a flat shape with a enlarged interface area between support and cluster.

In a second step, the adsorption of CO, O_2 and the CO oxidation at the MgO supported gold aggregates were studied. Again, like in the study by Molina et al. of TiO_2 supported Au nanoparticles [159], the nanoparticles where replaced by an one-dimensional rod within a MgO(100)-(5×2) geometry. One of the considered rod structures is depicted in Fig. 24. CO and O_2 are found to adsorb on these rods at low-coordinates sites in the "equatorial plane." The O_2 binding energies, however, are much smaller (~0.2 eV using the PW91-functional) than on the small Au_n clusters with $n \leq 10$ [144, 146]. The O–O bond length is extended from the gas-phase value of 1.24 Å to 1.35 Å corresponding to a superoxo O_2 species. Atomic oxygen binds to the low-coordinated sites of the Au rods with adsorption energies that are much larger than on the flat Au(111) and Au(100) surfaces. Furthermore, the O_2 dissociation barriers are rather large (~1 eV) so that they were excluded as possible routes in the low-temperature CO oxidation. Instead, relatively stable peroxolike $CO{\cdot}O_2$ reaction intermediates with total binding energies of about 1 eV were identified in the DFT calculations. The most stable of the $CO{\cdot}O_2$ complexes is shown in Fig. 24.

This complex is in fact more stable by about 0.1 eV than the separate adsorption of CO and O_2. In order to understand this stabilization, the substrate-induced charge redistribution has been analyzed in detail. As Fig. 25 shows, there is an induced charge accumulation between a Mg atom and the terminal peroxo oxygen atom while there is charge depletion

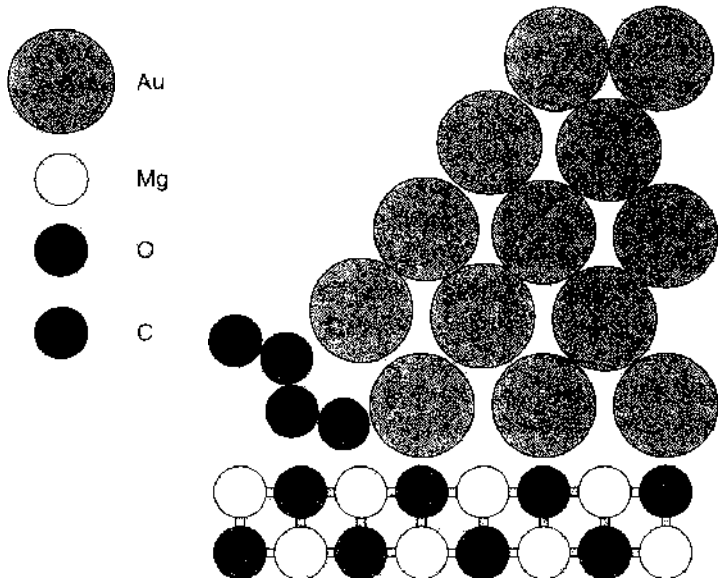

Figure 24. Schematic drawing of the $CO + O_2$ binding configuration at an Au–MgO interfacial structure modeled by a one-dimensional rod structure in GGA-DFT calculations (after [158]).

at the oxide. Thus, the stabilization is mediated by a charge transfer that leads to an additional attractive interaction. The energy barriers associated with the CO_2 formation from the CO-O_2 complexes are rather low (~0.3 eV), which means that the CO oxidation can readily occur already at room temperature, which is in agreement with experiments for the Au/MgO system [166].

This shows that the MgO support plays an active role in the bonding and activation of adsorbates bound to supported gold particles. However, it should be emphasized that this role is much less dramatic than for TiO_2 [159] where the reduced substrate not only provides charge for the binding of the O_2 molecule but actually binds the O_2 molecule.

As already discussed in the previous section, the promoting or poisoning effect of coadsorbates is an important issue in heterogeneous catalysis. The most well-known example for poisoning is the reduction of the activity of the platinum-based car-exhaust catalyst by lead present in the gasoline. Two studies have addressed the influence of coadsorbates on the catalytic performance of the MgO-supported Au nanoparticles. Häkkinen et al. considered the Au_n cluster shown in Fig. 23 to which the electron donor strontium was added [163]. This choice was motivated by the fact that the electron transfer to the Au_8 cluster seemed to be crucial for the understanding of the enhanced catalytic activity of the nanoparticle. And indeed, experiments revealed that pure MgO-supported Au_n clusters with $n \leq 7$ are catalytically inert as far the CO_2 production rate per deposited cluster is concerned, whereas supported Au_nSr clusters are catalytically active already for $n \geq 3$.

DFT calculations have confirmed the enhanced adsorption and activation of O_2 on the Sr-doped systems. Exchanging one Au atom by Sr of a MgO-supported Au_4 cluster modifies the adsorption properties significantly. The oxygen molecule bonds mainly to the strontium

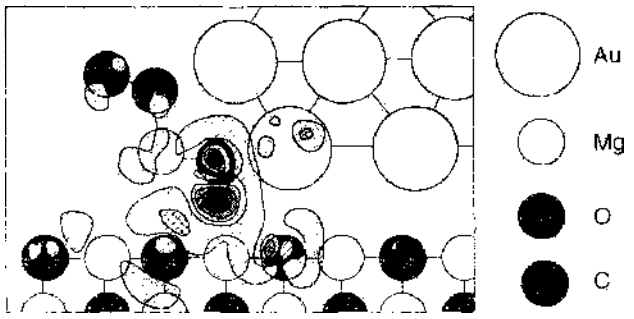

Figure 25. Charge density difference plot of the MgO-induced charge redistribution derived from DFT calculations. Shaded areas correspond to charge accumulation, and hatched areas denote charge depletion (after [159]).

atom of the Au_3Sr cluster with a considerably higher adsorption energy of 1.94 eV compared to 0.18 eV on the supported Au_4 cluster. The stronger interaction is caused by additional electron transfer to the O_2 molecules made possible by the charge provided by the Sr atom. This results in a superoxo-like state of the adsorbate which is reflected in an increased O–O bond length of 1.37 Å [163].

The coadsorption of both a single electron donor (Na) and a single electron acceptor (Cl) were considered in a *ab initio* study by Broqvist et al. [167] using the approach illustrated in Fig. 24 to replace the supported nanoparticle by an one-dimensional rod. In the coadsorption study, however, a smaller rod was used consisting only of the first three Au layers as shown in Fig. 26. The most favorable adsorption positions for both Na and Cl are at Au bridge sites of the second layer, that is, at the Au layer sticking out into the vacuum. As expected, Na adsorbs as a positively charge ion and Cl as a negatively charged ion, that is, there is significant charge transfer to and from the Au rod, respectively. However, the Na adsorption position is only metastable with respect to exchanging its position with a Au atom. Although Na prefers the low-coordinated site *in adsorption*, it rather absorbs into the Au rod forming a NaAu alloy.

The effects of the Na and Cl adsorption on the interaction of the rods with O_2, O, CO, and the $CO{\cdot}O_2$ complex are summarized in Table 4. At the Na-decorated Au edge, the O_2 binding is increased by 0.2 eV with respect to the clean Au edge. This increase is caused by the formation of a chemical bond between Na and O together with the higher capability of the Au rod to donate electrons to oxygen because of the additional electron provided by the Na atom. This stable adsorption configuration is illustrated in Fig. 26. Also, the adsorption energy of atomic oxygen is strongly enhanced. Interestingly, CO binds less strongly to the Na-decorated edge; its binding energy is reduced by 0.2 eV compared to the undecorated Au edge. It was suggested that the reduced binding is a consequence of the Na-induced downshift of 0.09 eV of the local *d*-band center at the Au edge [167]. However, this downshift seems to be too small to explain such a large reduction in the CO binding energy.

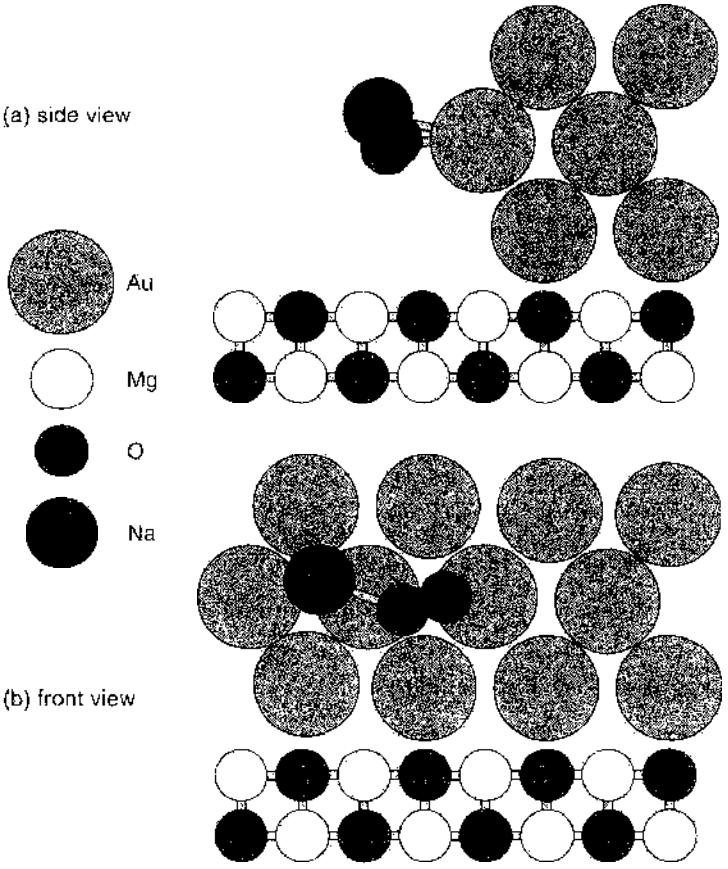

Figure 26. Side and front view of the stable adsorption configuration of O_2 at a Na-decorated edge of a Au rod deposited on MgO according to DFT-GGA calculations (after [167]).

Table 4. Calculated binding energies of O_2, O, CO, and the $CO{\cdot}O_2$ complex in eV on Au/MgO models with a clean, a Na-decorated, and a Cl-decorated Au edge [167], respectively. A negative binding energy corresponds to unstable adsorption.

	E_b(eV)		
	Au/MgO	Na/MgO/Au	Cl/Au/MgO
O_2	0.13	0.33	−0.20
O	0.13	0.84	0.03
O	0.75	0.52	0.60
$CO{\cdot}O_2$	0.98	1.62	0.49

On the other hand, the adsorption of the $CO{\cdot}O_2$ complex shown in Fig. 24 is again strongly promoted by the presence of Na atoms at the Au edge. The binding energy of the $CO{\cdot}O_2$ complex at the Na-decorated edge is 1.6 eV, which is almost twice its binding energy at the clean Au edge. The reason for this increased stability is again the formation of a Na-O_2 bond. Hence, Na acts as a promoter on the Au nanoparticles but its promotive character is related to the formation of strong Na–O bonds.

In contrast to Na, Cl has a poisoning effect when it is adsorbed at the Au edge. Its presence makes the O_2 adsorption unstable and reduces the O and CO binding energy. Furthermore, it makes the $CO{\cdot}O_2$ complex less stable by 0.5 eV. The poisoning effect of Cl is caused by an electrostatic repulsive interaction with the negatively charged adsorbates. Even for larger distances between the Cl atoms and the adsorbates, this repulsive interaction is still present due to the long-range character of the Coulomb interaction. The promoting effect of Na, on the other hand, is short-ranged because of the local nature of the attractive Na–O bonds.

Not only Au clusters deposited on MgO have been considered in *ab initio* electronic structure calculations. The adsorption properties of Ni_4 and Ni_8 clusters supported on regular and defect sites of the MgO(001) surface were studied in a DFT study, in which the oxide substrate was modeled by a $Mg_{13}O_{13}$ cluster embedded in two layers of 16 × 16 point charges each (PC=2e) in order to reproduce the correct Madelung potential at the adsorption site under study [168]. The structure of the supported Ni_4 and Ni_8 cluster was optimized under the constraint of the C_{4v} symmetry, that is, a fourfold symmetry was deliberately imposed on the clusters. Thus, the cluster does not necessarily correspond to minimum energy structures. The study was not meant to give quantitative results, but rather qualitative trends with respect to the size and the MgO adsorption site of the supported cluster.

Atomic oxygen and sodium have been used as adsorbates in the calculations to probe the reactivity of the clusters. The optimized structure of atomic oxygen on the supported Ni_8 cluster is shown in Fig. 27. It is obvious that the Ni_8 cluster is much less distorted than the Au_8 cluster on MgO(001) (see Fig. 23), probably because of the symmetry constraints used in this Ni/MgO study. The optimized structure of the supported Ni_4 cluster corresponds basically to the first layer of the Ni_8 cluster. The Ni cluster was also positioned above a neutral and positive oxygen vacancy, a F_s or F_s^+ center, respectively. Furthermore, the oxygen and sodium adsorption energies were also determined for free, unsupported Ni clusters.

First of all, the DFT calculations have confirmed that the metal clusters are much more strongly bound to the oxygen vacancy sites than to the stochiometric MgO surface [169]. Almost independent of the charge state, the binding energies are enhanced by more than 1.5 eV. The larger cluster interacts more strongly with all considered MgO surfaces, which can be explained by its higher polarizability [168].

For atomic oxygen, the adsorption energies on the supported clusters are in fact larger than on the free Ni cluster. The interaction of the electronegative oxygen with metal surfaces and clusters is characterized by a significant charge transfer to the oxygen atom. For the supported cluster, the oxygen anions of the surface act as an additional source of electrons increasing the charge transfer to the oxygen atom and thus its binding energy. For the cluster above the oxygen vacancies, the binding is further enhanced because the F centers represent an additional source of charge transfer. In the case of the F_s^+ center, there is also

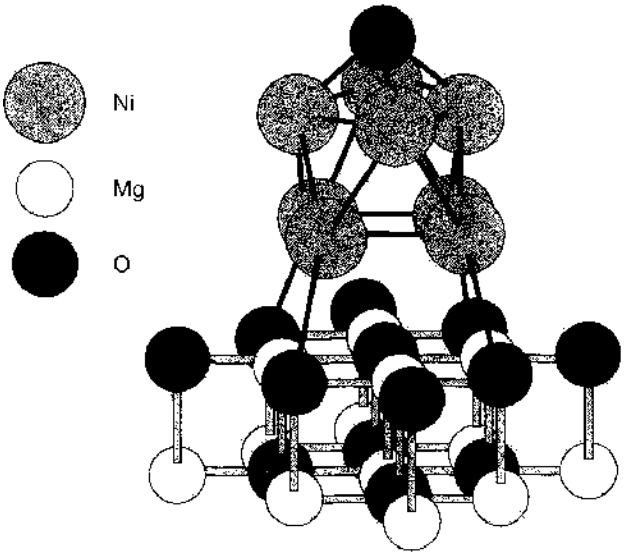

Figure 27. Optimized structure of an oxygen atom adsorbed on a Ni_8 cluster supported on Mgo(001). The oxide substrate is modeled by a $Mg_{13}O_{13}$ cluster embedded in two layers of 16 × 16 point charges each (PC=2e) [168].

the electrostatic attraction between the negatively charged adsorbed oxygen atom and the positively charged vacancy.

The effect of the vacancies on the atomic oxygen adsorption energies is particularly pronounced for the planar Ni_4 cluster where it leads to an increase of about 1 eV. For the three-dimensional Ni_8 cluster, however, the atomic oxygen adsorption energies are basically independent of the presence or absence of defects in the MgO substrate. This indicates that for the Ni/MgO system, the influence of the vacancies on the electronic structure of the supported clusters is restricted to the first layer, obviously in contrast to the Au/MgO system [8].

The electropositive sodium atom binds much weaker to the Ni clusters than the more electronegative oxygen atom. On the Ni clusters deposited on both the stochiometric MgO surface and the positively charged oxygen vacancy, sodium adsorbs as an anion, as an analysis of the dipole moment as a function of the vertical displacement shows [168]. Above the neutral oxygen vacancy, however, sodium is only partially charged because the electrons donated from the vacancy to the Ni cluster prohibit the charge transfer from the sodium to the metal atoms. In spite of these different bonding characteristic, the Na bonding energies are only very weakly dependent on the cluster size and MgO adsorption site, which is rather surprising. It has been speculated that this might be due to the cancellation of opposing effects [168].

So far, we have shown that the high density of low-coordinated sites at oxide-supported metal nanoparticle leads to a stronger interaction with adsorbates. Even the oxide support can act as a promoter for the bonding and activation of adsorbates on the metal particles. However, there is another effect that can counterbalance the promoting effect of the low coordination of the nanoparticles, namely the interatomic relaxation of the small particles. This leads to reduced interatomic distances, which, together with a strong cluster-support interaction, can cause a weaker interaction with adsorbates.

The important influence of the interatomic distances on the adsorption properties has been found in DFT calculations for small Pd_n cluster ($n = 3, 7, 10$) on Au(111) [170]. Transition metal cluster supported on inert noble metals are of particular interest in the field of electrochemistry [171] because the substrate has to be conductive so that supported nanostructures can act as electrodes. Furthermore, the electrochemical STM can be used for the nanostructuring of electrode surfaces. Based on the *jump-to-contact* between STM tip and sample, highly ordered arrays of metal clusters containing of the order of only 100 atoms can be generated [171–173]. These nanofabricated clusters exhibit an unusual electrochemical stability. It has been speculated that this stability might be caused by quantum size effects in the metal particles [171]. Furthermore, it has been shown that the catalytic activity of Pd

clusters supported on a gold surface toward electrochemical hydrogen evolution is enhanced by more than two orders of magnitude when the diameter of the palladium particles parallel to the support surface is decreased from 200 to 6 nm [174, 175].

In order to understand the chemical properties of the Pd/Au particles, in a first step the binding energies of hydrogen and CO on pseudomorphic Pd/Au overlayers has been evaluated by DFT calculations [54, 55]. These calculations have demonstrated that both the expansion of the pseudomorphic overlayers by 5% as well as the relative weak interaction of the Pd overlayer with the gold substrate lead to a stronger interaction with the adsorbates compared to a bulk Pd substrate. Both effects, which can again be understood within the *d* band model, enhance the adsorption energies on Pd/Au(111) by a similar amount, which is about 0.10–0.15 eV.

The adsorption energies of CO located at different sites of Pd_{10} clusters supported by Au(111) are shown in Fig. 28. Interestingly enough, all the CO binding energies are lower than those on pseudomorphic Pd/Au(111) overlayers. This means that for this system, CO binds less strongly to low-coordinated cluster atoms than to high-coordinated atoms in pseudomorphic overlayers. The same results have also been found for atomic hydrogen adsorption energies.

In order to understand these results, it is important to analyze the nearest neighbor Pd–Pd distances. The calculated value for Pd bulk is 2.80 Å; for Au bulk 2.95 Å. This means that the pseudomorphic Pd films on Au are expanded by 5%. Figure 28 also shows the Pd–Pd nearest neighbor distances of the supported Pd_n clusters. Although these clusters are supported by a gold substrate, their nearest neighbor distances of 2.76 Å are even below the Pd bulk value. These reduced distances are a consequence of the low coordination of the cluster atoms, which makes the single Pd–Pd bonds stronger than in a bulk situation where every Pd atom is 12-fold coordinated. At the second layer of the Pd_{10} cluster, the Pd–Pd distances are even further reduced to 2.65 Å. Note that for the free relaxed planar Pd_3 and Pd_7 cluster, the nearest neighbor distances are 2.50 Å and 2.64 Å, respectively.

The reduction in the interatomic distances results in a larger overlap of the *d* orbitals, which leads to a broader local *d*-band and a down-shift of the local *d*-band center because of charge conservation, as confirmed by the DFT calculations for the Pd_{10} clusters supported on Au(111) [170]. This is the opposite process of the one illustrated in Fig. 3 where a smaller overlap between the *d*-band metal atoms had been considered. Thus the reduced binding energies on the Pd atoms can be understood within the *d*-band model.

In Fig. 28, the CO adsorption energies on free Pd_{10} clusters in exactly the same configuration as the supported clusters are also given by the numbers in parentheses. These binding energies are in fact larger than on the supported clusters and also on flat [86] and stepped Pd surfaces [89]. This shows that in spite of their compression free clusters can still be much more reactive than surfaces because of their low coordination. Thus it is the interaction of the Pd clusters with the Au support that contributes to the low binding energies on the metal-supported clusters.

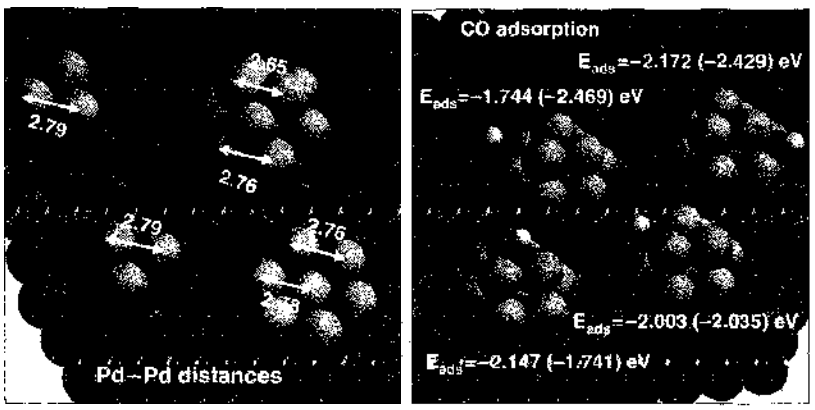

Figure 28. Calculated nearest neighbor Pd–Pd distances in Å of Pd_n cluster supported by Au(111) and CO adsorption positions and energies on the Pd_{10}/Au(111) cluster. The energies in parentheses correspond to the adsorption energies on free Pd_{10} clusters in exactly the same configuration as the supported clusters (after [170]).

Interestingly enough, at the top layer adsorption site of the Pd_{10} cluster, the CO binding energies on the free cluster are smaller than on the supported cluster. This surprising result is caused by the reactivity of the unsaturated hexagonal bottom layer of the free Pd_{10} cluster. It binds the three topmost Pd atoms so strongly that the top layer becomes less reactive, as an analysis of the energetics and the electronic structure of the free cluster confirms [170].

The coupling of the Pd clusters to the underlying Au substrate can also be revealed by analyzing the electronic structure of the system. In Fig. 29, the orbital resolved *d*-band local density of states (LDOS) for Pd_3 clusters deposited on Au(111) and on Pd(111) and for a free Pd_3 cluster is plotted. The free cluster exhibits a discrete structure of electronic levels, as is expected for a finite system. As far as the Pd_3 cluster supported on Au is concerned, all *d*-band orbitals that are confined within the cluster layer, that is, the d_{xy} and the $d_{x^2-y^2}$ orbitals, also show a rather discrete structure. This means that these orbitals are localized within the cluster. The LDOS of the other three orbitals that have a component along the vertical *z*-direction is rather broad. This indicates that these states are already delocalized because of their significant coupling to the electronic states of the Au support. For the Pd_3/Pd(111), *all d* states in the cluster are considerably broadened (see Fig. 29), demonstrating an even stronger coupling between the cluster and the substrate.

As alredy mentioned, it has been speculated that the unusual electrochemical stabibility of nanofabricated supported metal clusters [172] could be caused by quantum confinement effects [176] that would lead to a discrete electronic spectrum in the clusters. However, the DFT calculations yield a continuous spectrum already for small supported Pd_3 clusters.

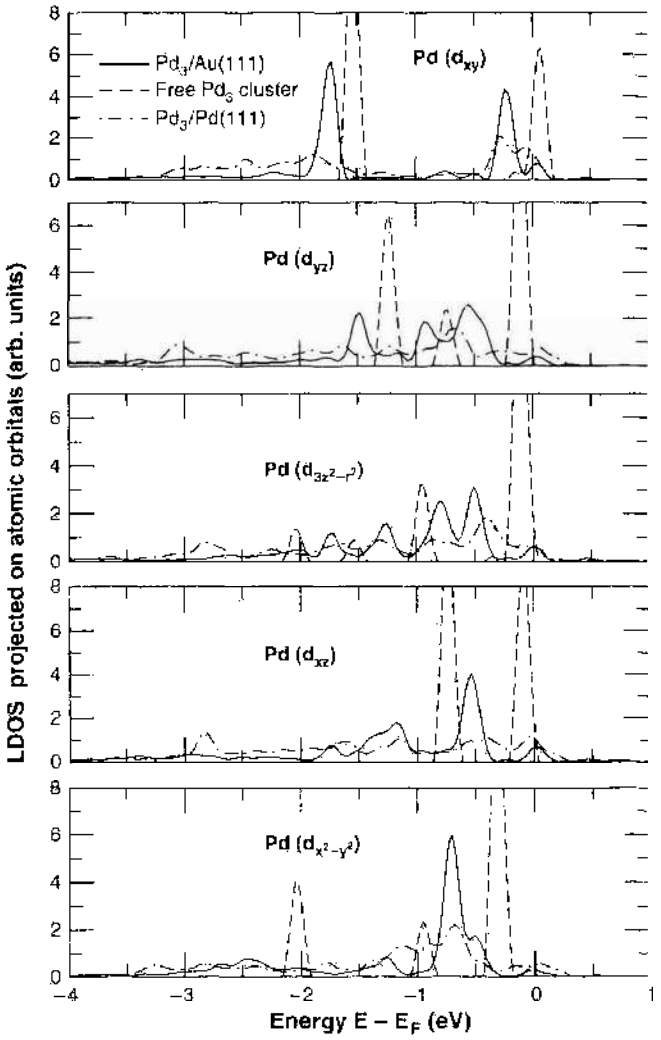

Figure 29. Orbital resolved *d*-band local density of states (LDOS) of the supported Pd_3/Au(111) and Pd_3/Pd(111) clusters and the free Pd_3 clusters determined by DFT calculations (after [170]).

For larger clusters, any quantum confinement effects would even be smaller. Thus these calculations do not support the speculation of [176].

As an alternative explanation it has been proposed [177, 178] that the electrochemical nanofabrication of the clusters by the jump-to-contact leads to an alloying of the clusters that causes their high electrochemical stability. The deposition of the clusters has been simulated using classical molecular dynamics with the interatomic interaction described within the empirical embedded-atom-method (EAM) [179, 180]. The stability of the deposited clusters was then analyzed by grand-canonical Monte Carlo simulations that took the electrochemical potential into account [181]. The simulations indicate that electrochemically stable clusters occur only in those cases where the two metals that are involved form stable alloys. In fact, DFT calculations also indicate that the Pd_{10} clusters on Au(111) [170] are stabilized by 0.1 eV if one of the Pd atoms at the base of the cluster is exchanged with an Au atom of the underlying substrate [182].

The possibility of intermixing or alloying is always an important issue in the case of bimetallic systems [183]. Recently, the electronic and chemical properties of Mo nanoparticles on Au(111) were studied experimentally [184]. This study was motivated by the fact that the nanoparticles can act as precursors for the preparation of molybdenum sulfide and molybdenum oxide aggregates [185, 186], which are widely used catalyst materials in the chemical industry [114]. The Mo particles were deposited by dosing $Mo(CO)_6$ at temperatures high enough so that $Mo(CO)_6$ decomposes thus creating Mo on the surfaces. DFT calculations of the $Mo(CO)_6$ defragmentation process indicate that the decomposition is an activated process which might be facilitated by the presence of defects on the surface [187].

Furthermore, the experiments indicated that CO does not adsorb on the Mo/Au(111) surface [184]. However, the exact structure of the Mo nanoparticles on Au(111) could not be determined experimentally. Therefore, DFT calculations were performed in order to study the structure and chemical properties of Mo nanoparticles on Au(111) [188]. Several structural models of the Mo/Au(111) system were investigated within a (2×2) surface unit cell. Two of them are shown in Fig. 30. The difference between the two structures is that the open Mo structure in Fig. 30a has been filled up with Au atoms in Fig. 30b, yielding a flat (111) surface.

The stability of the surface structures has been determined with respect to bulk Au and bulk Mo, that is, it was assumed that the formation energy of both bulk Au and bulk Mo is equal to zero. It turns out that Mo actually prefers to be embedded in the gold surface [187, 188]. The structure shown in Fig. 30b is by 0.3 eV/atom more stable than the one of

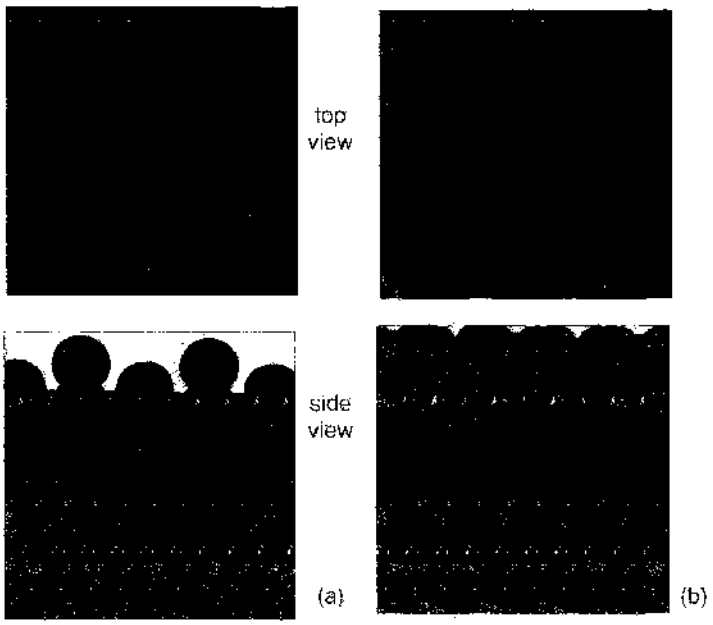

Figure 30. Top and side views of two Mo/Au(111) structures studied by DFT calculations [188]. The light and dark balls represent Au an Mo, respectively.

Fig. 30a. One gains even another 0.01 eV/atom if the surface is fully covered by Au atoms, that is, if a Au–Mo–Au sandwich structure is formed.

In order to analyze the reactivity of the Mo/Au(111) surface structures, the adsorption of CO, oxygen, and sulfur has been used as a probe. The adsorption of CO on both structures shown in Fig. 30 is exothermic, the CO binding energies are 2.22 eV and 1.03 eV for the structures a and b, respectively, using the RPBE functional. Interestingly enough, the binding energy of CO on one Mo monolayer on Au(111) is even larger, 2.79 eV. In this respect the Mo/Au system behaves like the Pd/Au system [170]: The nearest neighbor distances in Mo are 5% smaller than in Au so that the pseudomorphic Mo overlayer on Au is significantly expanded. This results in a significant upshift of the *d*-band center and consequently in stronger interaction energies with adsorbates.

The experimental findings that CO interacts very weakly with the Mo/Au(111) system can only be reconciled with the experimental results by assuming that they are caused by Mo–Au site exchange and Au segregation to the surface. This means that Mo nanostructures on Au are not stable, so that this system does also not exhibit any special chemical properties related to the limited size of the Mo particles, but rather behaves like a pure Au(111) surface.

In the case of the adsorption of oxygen and sulfur on the Mo/Au(111) system, the same qualitative trends have been found as for CO adsorption. Furthermore, two other admetals, Ni and Ru, were considered in the DFT calculations [188] in order to check whether they show a similar behavior as Mo on Au(111). And indeed, Ni and Ru also tend to mix with a Au substrate. In addition, the qualititative trends in the adsorption properties of the systems Ni/Au(111) and the Ru/Au(111) resemble the ones found in the Mo/Au(111) system. Thus, once the metal nanoparticles are embedded in the Au matrix, these bimetallic systems only exhibit properties of gold.

5. NANOSTRUCTURING OF SURFACES BY ORGANIC TEMPLATES

So far, we have only dealt with atomic and molecular adsorption *on* nanostructured surfaces. However, ordered arrays of adsorbed molecules can in fact lead to a nanostructuring of otherwise flat surfaces. In particular, *organic* adsorbates can induce a nano-patterning in the form of ordered overlayers or molecular wires. This phenomenon is often also discussed in the context of self-organization and self-assembly on surfaces [189]. It has been suggested that the spontaneous self-assembly of DNA-base molecules on mineral template surfaces may play an essential role for the origin of life under prebiotic conditions [190, 191]. These layers could act as a template for the assembly of higher ordered polymers. Furthermore, these structure might also be technologically relevant in the context of sensing, catalysis, or molecular electronics. These aspects have therefore motivated STM studies of DNA-bases self-assemblied as two-dimensional crystalline films [192, 193].

As a substrate for organic overlayers, often highly ordered pyrolytic graphite (HOPG) [192–194] or noble metals substrates [122, 195, 196] are used because these substrates are relatively inert so that the organic molecules are not significantly perturbed by the presence of the surface. The substrate might just serve as a template to fix the molecules in space, but in general the resulting self-assemblied supramolecular structures are a consequence of a subtle balance between molecule–molecule and molecule–substrate interactions. Only in the case of a sufficiently strong adsorbate–surface interaction, surface rearrangement induced by the adsorption might occur.

Several experimental studies addressing self-assemblied organic overlayers have focused on the purine base adenine (6-aminopurine, $C_5H_5N_5$) whose molecular structure is shown in Fig. 31. Yet, STM and atomic force microscopy (AFM) experiments of adenine adsorbed on graphite did not yield any atomic resolution [192, 197]. In the STM images, some ordered structure is visible, however, no microscopic adsorption configuration can be deduced. Combining the information from the STM with reciprocal space data from low-energy electron diffraction (LEED) experiments, a unit cell of rectangular shape with dimension 22 Å × 8.5 Å was proposed [198]. Although also the symmetry of the molecular structure within the surface unit cell could be specified, the relative positions of the adenine molecules could not

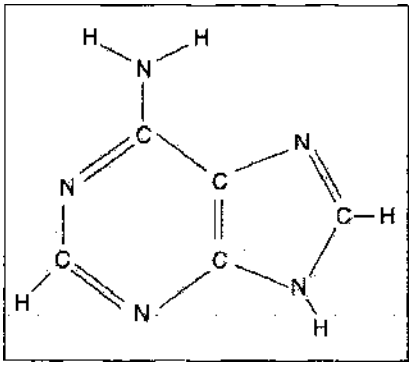

Figure 31. Molecular structure of the purine base adenine (6-aminopurine, $C_5H_5N_5$).

be determined. Still, the symmetry constraints on the adsorbate positions suggested that the adenine layer assembled in the form of centrosymmetrical hydrogen-bonded dimers.

It is true that it is possible to calculate the energetically most favorable structure by classical force field techniques [199, 200], however, these calculations do not yield any information about the electronic structure of the adsorbed molecules. They are useful in order to estimate the stability of possible adsorbate structures, but it is not really possible to assess whether their results are in agreement with STM experiments that do not have any atomic resolution. Thus, the force field techniques cannot be used as a tool to analyse and interprete the STM images. However, for a complete understanding of the organic layers the effect of directed molecular bonds on the self-assembly and the STM-imaging process should be clarified. There is an additional problem in the STM imaging process, namely that the contrast in the STM images can depend on the scanning direction in the experiments [193]. This effect has not been appropriately investigated by first-principles calculations so far.

With DFT methods, it has become possible to address self-assemblied organic overlayers on surfaces [196, 201]. In particular, the DFT calculations also yield information on the electronic structure of the systems, which makes it possible to simulate STM images. Within the Tersoff-Hamann picture [6], the tunneling current is simply proportional to the local density of states *of the surface* close to the Fermi energy at the position of the tip. There are more sophisticated DFT-based approaches to simulate STM images that also take into account the orbitals of the surface and the STM tip [202], but usually the simple Tersoff-Hamann picture is surprisingly successful and accurate.

A simulated STM image based on DFT calculations is shown in Fig. 32. The configuration space of possible adsorbate arrangements is immense. Therefore, the DFT structure optimization has been done using the results of force-field calculations as an initial guess.

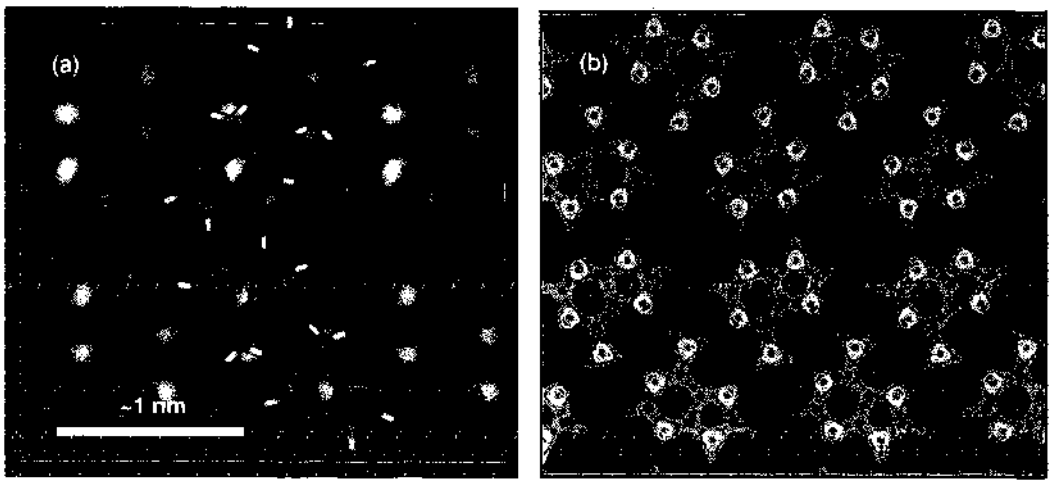

Figure 32. Calculated structure of adsorbed adenine. (a) simulated STM image according to the Tersoff-Hamann picture, that is, the LDOS of the HOMO band is plotted. In addition, the structure of adsorbed adenine molecules is indicated; (b) total charge density (courtesy of T. Markert).

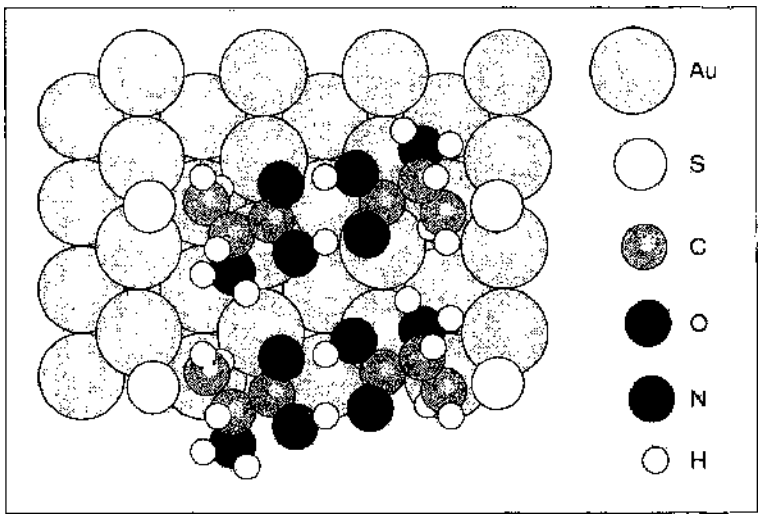

Figure 33. The energetically most stable configuration of the amino acid cysteine on Au(110) calculated by DFT calculations [195]. It corresponds to two units of the double-row structure of D-cysteine.

It turned out that the optimized structures of the DFT and the force-field calculations are rather similar. However, it should be emphasized again that the force-field calculations do not yield any information on the electronic structure. What is plotted in Fig. 32a is the local density of states of the HOMO band at some distance from the surface. In addition, the molecular structure of the adenine molecules is shown indicating the hydrogen-bonded dimer structure. It is obvious that from the STM simulation alone the molecular structure could not have been deduced because there is no one-to-one correspondence between regions of high local density of states and the atomic arrangement. In Fig. 32b, the total charge density is plotted. The comparison between both panels shows that the regions of high local density of states of the HOMO band do also not necessarily coincide with maxima in the *total* charge density. This again confirms that indeed the realistic simulation of STM images is needed in order to deduce the atomistic structure of organic layers from STM experiments.

The adsorption of cysteine ($HS\text{-}CH_2\text{-}CH(NH_2)\text{-}COOH$), a naturally occuring amino acid that has been briefly mentioned in the previous section, on the missing-row reconstructed Au(110) surface has been investigated by both STM experiments and DFT calculations [122, 195]. Cysteine exists in two different so-called enantiomeric forms, L-cysteine and D-cysteine, that is, two forms that are each others' mirror image with different chirality. In the STM experiments, both extended unidirectional molecular double rows as well as isolated dimers have been found. As far as the dimers are concerned, the DFT calculations have found that they are stabilized by forming double hydrogen bonds between their carboxylic group, as can be seen in Fig. 33. The STM experiments have found a high stereoselectivity in the dimerization of adsorbed cysteine molecules on the Au(110) surface, that is, only either LL pairs or DD pairs have been identified.

According to DFT calculations, cysteine, like other thiols [203], binds rather strongly via the formation of S–Au bonds. As far as the dimers are concerned, their structure is also stabilized by amino–gold and carboxylic–carboxylic bonds. The presence of sulfur causes the formation of four vacancies on the gold rows of the (110) surface upon the adsorption of the dimers because of the tendency of sulfur to bind to low-coordinated atoms. Now in any possible LD dimer adsorption structure, at least one of these bonds is lost, which makes the LD dimer energetically unfavorable. This explains why only LL or DD pairs have been observed in the STM experiments.

As for the double rows of cysteine on Au(110), their energetically most stable structure is shown in Fig. 33. In fact, the adsorption of cysteine leads to the lifting of the (2×1) missing-row reconstruction of the Au(110) surface. However, there are no strong covalent or hydrogen bonds between the repeat units of the double rows. Also the dipole–dipole interactions between two adjacent units are fairly small.

Instead, it is the molecule-induced surface rearrangement that is the driving force for the formation of the extended molecular rows [195]. The formation of a four-adatom vacancy

on Au(110) in order to nucleate the first repeat unit of the double row is energetically rather costly, 0.9 eV. However, the energetic cost is only 0.4 eV for expanding a double row already formed. This is so because the formation of a Au vacancy adjacent to an existing vacancy requires much less energy than the formation of an isolated vacancy. Hence, once a first double-row unit has been formed, it is energetically favorable for additional cysteine dimers to attach to the existing dimer instead of forming isolated adsorbates. Thus unidirectional, self-assembled molecular nanowires can be formed even in the absence of any significant direct adsorbate–adsorbate interaction along the growth direction.

6. CONCLUSIONS AND OUTLOOK

In this chapter, theoretical studies of the adsorption of atoms and molecules at nanostructured surfaces using first-principles electronic structure methods have been reviewed. Such studies have only become possible in the past 10 years because of their high computational demand. Although the size of the nanostructures treated in these studies is still limited [149, 164, 170], important qualitative concepts can be derived from these calculations. This is mainly due to the microscopic resolution of the calculations as far as both the geometric as well as the electronic structure of the studied systems is concerned.

Nanostructured surface often exhibit an enhanced interaction with adsorbates and a higher activity for certain reactions. An important aspect for the explanation of this high reactivity is the large number of low-coordinated atoms in nanostructures [146]. Many theoretical studies have shown that their is indeed a correlation between the low coordination of substrate atoms and a strong interaction with adsorbates. However, low coordination alone is often not sufficient for a strong interaction [147]. There are counterexamples of low-coordinated sites at nanostructured surfaces that do not bind adsorbates particularly well. Low-coordinated sites can lead to an enhanced electron density, but it is obviously also the nature of the orbitals localized at the low-coordinated sites that is important for the bonding of adsorbates.

In the future, first-principles electronic structure calculations will be able to address larger and larger systems due to the ongoing improvement in the computer power and the development of more efficient algorithms. This will certainly lead to further progress, as far as the microscopic analysis and understanding of nanostructures on surfaces and their reactivity is concerned. As already mentioned, the description of nanostructured surfaces by *ab initio* electronic structure calculations is a relatively new field. The first applications reviewed in this contribution have concentrated on a small number of particularly interesting systems such as Au cluster supported by oxide surfaces because of their strongly modified properties compared to bulk substrates. Still, systematic studies, for example of the role of the support on the reactivity of metallic clusters, are missing. Furthermore, a fundamental understanding of the size dependence of the adsorption properties and the reactivity of supported clusters is lacking [1].

A subject that has not at all been addressed so far in theoretical studies is the dynamics and kinetics of the adsorption at nanostructured surfaces based on *ab initio*–derived interaction potentials [204, 205]. Due to the complexity of the nanostructures, this certainly requires an high-computational effort, but there are important issues that need to be resolved. Nanostructures often offer the energetically most favorable sites for adsorption. However, the adsorbates have to get to these sites before they can bind. Does this occur via diffusion, or are the adsorbates directly steered [206] towards these sites? Furthermore, atomic and molecular adsorption require the dissipation of the energy gained upon binding to the substrate [207]. The question is still open whether nanostructures on surfaces represent an efficient sink for energy transfer.

There are also important kinetic aspects of the adsorption and reaction of molecules on nanoparticles to be studied. For example, it has been suggested that the activity of a catalyst particle can be significantly enhanced because of kinetic effects related to the interplay of different facets [208], but it is not clear yet how general this mechanism is. Kinetic rates can be estimated from electronic structure calculations using efficient transition state search routines [209, 210] in combination with transition state theory [211]. Although computational

demanding, only kinetic simulations would allow a true comparison between theory and experiments in which reaction rates are measured.

It will probably take some time before supported clusters with thousands of atoms can be handled by *ab initio* total-energy calculations. In order to be able to address larger system with first-principles electronic structure calculations, one can either wait for faster computers or try to improve the algorithms. One example of a very successful improvement is the already mentioned development of ultrasoft pseudopotentials [41], which made it possible to use much smaller plane-wave basis sets in the supercell calculations.

Another possibility to make the calculations faster is to run them in a massively parallel fashion on many processors. The computational bottleneck in massively parallel implementations is usually the communication, that is, the exchange of data between different processor. This problem could in principle be avoided by so-called O(N) (order N) methods [212]. These methods take advantage of the localization properties of the fundamental interactions in materials [213]. Thus, they are able to exhibit linear scaling with respect to the size of the system, i.e., their computational effort rises linearly with the number N of considered electrons or atoms in the calculations.

Due to the locality of the algorithm, only little communication is needed between the processors that treat each some localized region of the system. This makes O(N) methods very suitable for massively parallel implementations. However, O(N) applications so far have been mainly based on tight-binding [214] or semiempirical descriptions. This is due to the fact that there are still problems as far as the implementation of linear-scaling methods in DFT codes is concerned [212].

However, it is questionable whether large-scale *ab initio* total-energy calculations are really neccessary for a deeper understanding of nanostructured surfaces. The more complex a system is, the harder it is to analyze its basic properties and to derive general principles. The important role of special sites and configurations of nanostructures, for example, can already be investigated using smaller systems, as illustrated in this review, and other aspects of the nanostructures might be treated by more efficient, approximate methods such as multiscale methods.

In the multiscale approach, different aspects of a certain system are treated within different levels of microscopic accuracy [10, 215]. For example, in the theoretical description of large biomolecular systems so-called QM/MM (quantum mechanics/molecular mechanics) hybrid methods [216] have been successfully used for, for example, the simulation of enzymatic systems [217]. These methods are based on a mixed quantum-classical embedding scheme in which the active center treated by first-principles electronic structure methods is embedded in a classical potential of the remaining atoms at the periphery.

Progress is also needed as far as the exchange-correlation functionals used in DFT calculations are concerned. GGA-DFT calculations are still not reliable for certain systems [45]. There are attempts to improve the accuracy of the functionals, for example by constructing so-called meta-GGAs [37]. However, they require a second-order gradient expansion, which makes them computationally less efficient. Consequently, they have not found a widespread recognition. Another approach is to include the so-called exact exchange in the DFT calculations by evaluating the corresponding exchange integral [218, 219]. This is again computationally rather demanding, and some progress in the efficient implementation is needed before this ansatz will experience a widespread use.

Another problem of current exchange-correlation functionals is that the van der Waals and hydrogen bond interaction are not properly described. This is closely related to the fact that in the LDA and the GGA the exchange-correlation hole is still localized. Therefore, the effective electron potential outside of a metal falls off exponentially and not proportional to $1/z$. Although the van der Waals interaction is relatively weak, it is of relevance in the adsorption of large organic molecules that do not form any covalent bonds with the substrate. Thus, a proper description of the van der Waals interaction is of importance for the *ab initio* description of the nanostructuring of surfaces by organic templates. There have been attempts to include the van der Waals interaction in density functional theory [220, 221]. However, these approaches require the introduction of an explicit van der Waals

density functional. This leads to an increased computational effort which has prevented its implementation in standard DFT codes.

In spite of the technical obstacles, there will certainly be a growing number of first-principles studies addressing the adsorption on nanostructured surfaces, as the interest in nanostructured surfaces and their technological applications will still increase. Although there is also significant progress in the experimental techniques, theoretical studies will remain to be an indispensable tool for the interpretation and analysis of structures and processes on the nano-scale. We will even see closer and closer collaborations between theory and experiment in the future. The theoretical investigation of adsorption on nanostructured surfaces is certainly a challenging and demanding research field, but at the same time it is an exciting and rewarding area that will prosper in the years to come.

ACKNOWLEDGMENTS

It is a pleasure to acknowledge all the coworkers and friends whom I have worked with and who have contributed to my work. For the particular subject covered in this chapter, I have greatly benefited from the insights shared with me by Wilhelm Brenig, Andreas Eichler, Jürgen Hafner, Peter Jakob, Bjørk Hammer, Wolfgang Heckl, Ulrich Höfer, Peter Kratzer, Georg Kresse, Eckhard Pehlke, Matthias Scheffler, and Ulrich Stimming. I also want to thank my coworkers in my research group at the Technical University of Munich who carried out research projects in the field of adsorption at nanostructured surfaces: Markus Lischka, Christian Mosch, and Ata Roudgar. They all did a great job.

A significant fraction of this review has been written during my stay in the group of Prof. Horia Metiu at the Chemistry Department of the University of California at Santa Barbara. I thank him for his hospitality and for many fruitful discussions.

REFERENCES

1. C. R. Henry, *Surf. Sci. Rep.* 31, 235 (1998).
2. K. H. Hansen, S. Stempel, E. Lægsgaard, M. Bäumer, and H.-J. Freund, *Phys. Rev. Lett.* 83, 4120 (1999).
3. H.-J. Freund, *Surf. Sci.* 500, 271 (2002).
4. A. T. Bell, *Science* 299, 1688 (2003).
5. G. Binnig, H. Rohrer, C. Gerber, and E. Weibel, *Phys. Rev. Lett.* 49, 57 (1982).
6. J. Tersoff and D. R. Hamann, *Phys. Rev. Lett.* 50, 1998 (1983).
7. Y. L. Wang, H. J. Gao, H. M. Guo, H. W. Liu, I. G. Batyrev, W. E. McMahon, and S. B. Zhang, *Phys. Rev. B* 70, 073312 (2004).
8. A. Sanchez, S. Abbet, U. Heiz, W.-D. Schneider, H. Häkkinen, R. N. Barnett, and U. Landman, *J. Phys. Chem. A* 103, 9573 (1999).
9. A. Groß, *Surf. Sci.* 500, 347 (2002).
10. C. Stampfl, M. V. Ganduglia-Pirovano, K. Reuter, and M. Scheffler, *Surf. Sci.* 500, 368 (2002).
11. A. Szabo and N. S. Ostlund, "Modern Quantum Chemistry: Introduction to Advanced Electronic Structure Theory," McGraw-Hill, New York, 1989.
12. P. Hohenberg and W. Kohn, *Phys. Rev.* 136, B864 (1964).
13. W. Kohn and L. Sham, *Phys. Rev.* 140, A1133 (1965).
14. W. Kohn, *Rev. Mod. Phys.* 71, 1253 (1999).
15. R. M. Dreizler and E. K. U. Gross, "Density Functional Theory: An Approach to the Quantum Many-Body Problem," Springer, Berlin, 1990.
16. A. Groß, "Theoretical Surface Science—A Microscopic Perspective," Springer, Berlin, 2002.
17. P. Gambardella, Ž. Šljivančanin, B. Hammer, M. Blanc, K. Kuhnke, and K. Kern, *Phys. Rev. Lett.* 87, 056103 (2001).
18. M. Valden, X. Lai, and D. W. Goodman, *Science* 281, 1647 (1998).
19. B. Hammer, K. Jacobsen, and J. Nørskov, *Phys. Rev. Lett.* 69, 1971 (1992).
20. B. Hammer, M. Scheffler, K. Jacobsen, and J. Nørskov, *Phys. Rev. Lett.* 73, 1400 (1994).
21. J. A. White, D. M. Bird, M. C. Payne, and I. Stich, *Phys. Rev. Lett.* 73, 1404 (1994).
22. S. Wilke and M. Scheffler, *Surf. Sci.* 329, L605 (1995).
23. P. J. Feibelman, S. Esch, and T. Michely, *Phys. Rev. Lett.* 77, 2257 (1996).
24. M. Haruta, *Catal. Today* 36, 153 (1997).
25. M. Haruta, *CatTech* 6, 102 (2002).
26. K. Raghavachari and J. Anderson, *J. Phys. Chem.* 100, 12960 (1996).
27. J. A. Pople, *Rev. Mod. Phys.* 71, 1267 (1999).
28. G. W. Trucks, K. Raghavachari, G. S. Higashi, and Y. J. Chabal, *Phys. Rev. Lett.* 65, 504 (1990).

29. J. L. Whitten and H. Yang, *Surf. Sci. Rep.* 24, 55 (1996).
30. B. Hammer, L. B. Hansen, and J. K. Nørskov, *Phys. Rev. B* 59, 7413 (1999).
31. P. J. Feibelman, B. Hammer, J. K. Nørskov, F. Wagner, M. Scheffler, R. Stumpf, R. Watwe, and J. Dumesic, *J. Phys. Chem. B* 105, 4018 (2001).
32. E. H. Lieb, *Rev. Mod. Phys.* 53, 603 (1981).
33. J. P. Perdew, J. A. Chevary, S. H. Vosko, K. A. Jackson, M. R. Pederson, D. J. Singh, and C. Fiolhais, *Phys. Rev. B* 46, 6671 (1992).
34. A. D. Becke, *Phys. Rev. A* 38, 3098 (1988).
35. C. Lee, W. Yang, and R. Parr, *Phys. Rev. B* 37, 785 (1988).
36. J. P. Perdew, K. Burke, and M. Ernzerhof, *Phys. Rev. Lett.* 77, 3865 (1996).
37. J. P. Perdew, S. Kurth, A. Zupan, and P. Blaha, *Phys. Rev. Lett.* 82, 2544 (1999).
38. J. Tao, J. P. Perdew, V. N. Staroverov, and G. E. Scuseria, *Phys. Rev. Lett.* 91, 146401 (2003).
39. M. Fuchs and M. Scheffler, *Comput. Phys. Commun.* 119, 67 (1999).
40. P. E. Blöchl, *Phys. Rev. B* 50, 17953 (1994).
41. D. Vanderbilt, *Phys. Rev. B* 41, 7892 (1990).
42. G. Kresse and D. Joubert, *Phys. Rev. B* 59, 1758 (1999).
43. G. Kresse and J. Furthmüller, *Phys. Rev. B* 54, 11169 (1996).
44. M. Bockstedte, A. Kley, J. Neugebauer, and M. Scheffler, *Comput. Phys. Commun.* 107, 187 (1997).
45. B. Hammer, L. B. Hansen, and J. K. Nørskov, *Phys. Rev. B* 59, 7413 (1999).
46. A. Bogicevic, S. Ovesson, P. Hyldgaard, B. I. Lundqvist, H. Brune, and D. R. Jennison, *Phys. Rev. Lett.* 85, 1910 (2000).
47. B. Hammer and J. K. Nørskov, *Surf. Sci.* 343, 211 (1995).
48. B. Hammer and J. K. Nørskov, *Nature* 376, 238 (1995).
49. K. Fukui, *Science* 218, 747 (1982).
50. R. Hoffmann, *Rev. Mod. Phys.* 60, 601 (1988).
51. B. Hammer, O. H. Nielsen, and J. K. Nørskov, *Catal. Lett.* 46, 31 (1997).
52. V. Pallassana, M. Neurock, L. B. Hansen, B. Hammer, and J. K. Nørskov, *Phys. Rev. B* 60, 6146 (1999).
53. M. Mavrikakis, B. Hammer, and J. K. Nørskov, *Phys. Rev. Lett.* 81, 2819 (1998).
54. A. Roudgar and A. Groß, *Phys. Rev. B* 67, 033409 (2003).
55. A. Roudgar and A. Groß, *J. Electroanal. Chem.* 548, 121 (2003).
56. M. Lischka and A. Groß, *Phys. Rev. B* 65, 075420 (2002).
57. N. W. Ashcroft and N. D. Mermin, "Solid State Physics." Saunders College, Philadelphia, 1976.
58. B. Lang, R. W. Joyner, and G. A. Somorjai, *Surf. Sci* 30, 440 (1972).
59. R. Q. Hwang, J. Schröder, C. Günther, and R. J. Behm, *Phys. Rev. Lett.* 67, 3279 (1991).
60. V. I. Anisimov, F. Aryasetiawan, and A. I. Lichtenstein, *J. Phys.: Condens. Matter* 9, 767 (1997).
61. G. Kresse, A. Gil, and P. Sautet, *Phys. Rev. B* 68, 073401 (2003).
62. A. C. Luntz, M. D. Williams, and D. S. Bethune, *J. Chem. Phys.* 89, 4381 (1988).
63. W. Wurth, J. Stöhr, P. Feulner, X. Pan, K. R. Bauchspiess, Y. Baba, E. Hudel, G. Rocker, and D. Menzel, *Phys. Rev. Lett.* 65, 2426 (1990).
64. C. T. Rettner and C. B. Mullins, *J. Chem. Phys.* 94, 1626 (1991).
65. J. Wintterlin, R. Schuster, and G. Ertl, *Phys. Rev. Lett.* 77, 123 (1996).
66. B. C. Stipe, M. A. Rezaei, W. Ho, S. Gao, M. Persson, and B. I. Lundqvist, *Phys. Rev. Lett.* 78, 4410 (1997).
67. P. D. Nolan, B. R. Lutz, P. L. Tanaka, J. E. Davis, and C. B. Mullins, *J. Chem. Phys.* 111, 3696 (1999).
68. A. Eichler and J. Hafner, *Phys. Rev. Lett.* 79, 4481 (1997).
69. A. Eichler, F. Mittendorfer, and J. Hafner, *Phys. Rev. B* 62, 4744 (2000).
70. A. Groß, A. Eichler, J. Hafner, M. J. Mehl, and D. A. Papaconstantopoulos, *Surf. Sci.* 539, L542 (2003).
71. Ž. Šljivančanin and B. Hammer, *Surf. Sci.* 515, 235 (2002).
72. S. Dahl, A. Logadottir, R. C. Egeberg, J. H. Larsen, I. Chorkendorff, E. Törnqvist, and J. K. Nørskov, *Phys. Rev. Lett.* 83, 1814 (1999).
73. S. Dahl, E. Törnqvist, and I. Chorkendorff, *J. Catal.* 192, 381 (2000).
74. K. Jacobi, H. Dietrich, and G. Ertl, *Appl. Surf. Sci.* 121/122, 558 (1997).
75. S. Dahl, P. A. Taylor, E. Törnqvist, and I. Chorkendorff, *J. Catal.* 178, 679 (1998).
76. A. Logadottir and J. K. Nørskov, *J. Catal.* 220, 273 (2003).
77. J. J. Mortensen, B. Hammer, and J. Nørskov, *Phys. Rev. Lett.* 80, 4333 (1998).
78. B. Hammer, *Phys. Rev. Lett* 83, 3681 (1999).
79. T. Zambelli, J. Wintterlin, J. Trost, and G. Ertl, *Science* 273, 1688 (1996).
80. K. Christmann, *Surf. Sci. Rep.* 9, 1 (1988).
81. A.-S. Mårtensson, C. Nyberg, and S. Andersson, *Phys. Rev. Lett.* 57, 2045 (1986).
82. K. Svensson, L. Bengtsson, J. Bellman, M. Hassel, M. Persson, and S. Andersson, *Phys. Rev. Lett.* 83, 124 (1999).
83. L. Bengtsson, K. Svensson, M. Hassel, J. Bellman, M. Persson, and S. Andersson, *Phys. Rev. B* 61, 16921 (2000).
84. P. K. Schmidt, K. Christmann, G. Kresse, J. Hafner, M. Lischka, and A. Groß, *Phys. Rev. Lett.* 87, 096103 (2001).
85. S. Wilke and M. Scheffler, *Phys. Rev. B* 53, 4926 (1996).
86. W. Dong, V. Ledentu, P. Sautet, A. Eichler, and J. Hafner, *Surf. Sci.* 411, 123 (1998).
87. A. Groß, *Appl. Phys. A* 67, 627 (1998).

88. X.-G. Zhang, M. A. Van Hove, G. A. Somorjai, P. J. Rous, D. Tobin, A. Gonis, J. M. Mac Laren, K. Heinz, M. Michl, H. Lindner, K. Müller, M. Ehsasi, and J. H. Block, *Phys. Rev. Lett.* 67, 1298 (1991).
89. M. Lischka, C. Mosch, and A. Groß, *Surf. Sci.* 570, 227 (2004).
90. W. Dong and J. Hafner, *Phys. Rev. B* 56, 15396 (1997).
91. V. Ledentu, W. Dong, and P. Sautet, *Surf. Sci.* 412, 518 (1998).
92. A. Dedieu, *Chem. Rev.* 100, 543 (2000).
93. M. Lischka and A. Groß, in "Recent Developments in Vacuum Science and Technology," (J. Dabrowski, Ed.), p. 111. Research Signpost, Kerala (India), 2003.
94. R. F. Service, *Science* 305, 958 (2004).
95. R. J. Behm, K. Christmann, G. Ertl, and M. A. Van Hove, *J. Chem. Phys.* 73, 2984 (1980).
96. A. Eichler and J. Hafner, *Phys. Rev. B* 57, 10110 (1998).
97. P. Hu, D. A. King, M.-H. Lee, and M. C. Payne, *Chem. Phys. Lett.* 246, 73 (1995).
98. M. Kittel, R. Terborg, M. Polcik, A. M. Bradshaw, R. L. Toomes, D. P. Woodruff, and E. Rotenberg, *Surf. Sci.* 511, 34 (2002).
99. H. S. Kato, H. Okuyama, J. Yoshinobo, and M. Kawai, *Surf. Sci.* 513, 239 (2002).
100. T. E. Madey, J. T. Yates, Jr., A. M. Bradshaw, and F. M. Hoffmann, *Surf. Sci.* 89, 370 (1979).
101. H. Conrad, G. Ertl, J. Koch, and E. E. Latta, *Surf. Sci.* 43, 462 (1974).
102. P. K. Schmidt, "Wechselwirkung von Wasserstoff mit einer Pd(210)- und Ni(210)-Oberfläche," PhD thesis, Freie Universität Berlin, 2002.
103. E. Christoffersen, P. Stoltze, and J. K. Nørskov, *Surf. Sci.* 505, 200 (2002).
104. B. Hammer, *J. Catal.* 199, 171 (2001).
105. E. Christoffersen, P. Liu, A. Ruban, H. L. Skriver, and J. K. Nørskov, *J. Catal.* 199, 123 (2001).
106. C. M. Wei, A. Groß, and M. Scheffler, *Phys. Rev. B* 57, 15572 (1998).
107. L. Savio, L. Vattuone, and M. Rocca, *Phys. Rev. Lett.* 87, 276101 (2001).
108. L. Savio, L. Vattuone, and M. Rocca, *J. Phys.: Condens. Matter* 14, 6065 (2002).
109. L. Vattuone, L. Savio, and M. Rocca, *Phys. Rev. Lett.* 90, 228302 (2003).
110. N. Bonini, A. Kokalj, A. Dal Corso, S. de Gironcoli, and S. Baroni, *Phys. Rev. B* 69, 195401 (2004).
111. A. Kokalj, N. Bonini, A. Dal Corso, S. de Gironcoli, and S. Baroni, *Surf. Sci.* 566, 1107 (2004).
112. T. Schimizu and M. Tsukada, *Surf. Sci.* 295, L1017 (1993).
113. L. Delle Site and D. Sebastiani, *Phys. Rev. B* 70, 115401 (2004).
114. J. M. Thomas and W. J. Thomas, "Principles and Practice of Heterogeneous Catalysis," VCH-Wiley, Weinheim, 1997.
115. A. Kokalj, A. Dal Corso, S. de Gironcoli, and S. Baroni, *J. Phys. Chem. B* 106, 9839 (2002).
116. A. Kokalj, A. Dal Corso, S. de Gironcoli, and S. Baroni, *Surf. Sci.* 566, 1018 (2004).
117. Ž. Šljivančanin, K. V. Gothelf, and B. Hammer, *J. Am. Chem. Soc.* 124, 14789 (2002).
118. C. F. McFadden, P. S. Cremer, and A. J. Gellman, *Langmuir* 12, 2483 (1996).
119. G. A. Attard, *J. Phys. Chem. B* 105, 3158 (2001).
120. Ž. Šljivančanin and B. Hammer, *Phys. Rev. B* 65, 085414 (2002).
121. C. D. Bain, J. Evall, and G. M. Whitesides, *J. Am. Chem. Soc.* 111, 7155 (1989).
122. A. Kühnle, T. R. Linderoth, B. Hammer, and F. Besenbacher, *Nature* 415, 891 (2002).
123. T. D. Booth, D. Wahnon, and I. Wainer, *Chirality* 9, 96 (1997).
124. G. S. Higashi, Y. J. Chabal, G. W. Trucks, and K. Raghavachari, *Appl. Phys. Lett.* 56, 656 (1990).
125. E. Pehlke and M. Scheffler, *Phys. Rev. Lett.* 74, 952 (1995).
126. A. Groß, M. Bockstedte, and M. Scheffler, *Phys. Rev. Lett.* 79, 701 (1997).
127. C. Filippi, S. B. Healy, P. Kratzer, E. Pehlke, and M. Scheffler, *Phys. Rev. Lett.* 89, 166102 (2002).
128. P. Kratzer, E. Pehlke, M. Scheffler, M. B. Raschke, and U. Höfer, *Phys. Rev. Lett.* 81, 5596 (1998).
129. E. Pehlke and J. Tersoff, *Phys. Rev. Lett.* 67, 1290 (1991).
130. E. Pehlke and P. Kratzer, *Phys. Rev. B* 59, 2790 (1999).
131. P. Krüger and J. Pollmann, *Phys. Rev. Lett.* 74, 1155 (1995).
132. M. Rohlfing, P. Krüger, and J. Pollmann, *Phys. Rev. B* 52, 1905 (1995).
133. E. Pehlke, *Phys. Rev. B* 62, 12932 (2000).
134. A. Biedermann, E. Knoesel, Z. Hu, and T. F. Heinz, *Phys. Rev. Lett.* 83, 1810 (1999).
135. M. Dürr, Z. Hu, A. Biedermann, U. Höfer, and T. F. Heinz, *Phys. Rev. Lett.* 88, 046104 (2002).
136. W. Brenig and M. F. Hilf, *J. Phys.: Condens. Matter* 13, R61 (2001).
137. K. W. Kolasinski, W. Nessler, K.-H. Bornscheuer, and E. Hasselbrink, *J. Chem. Phys.* 101, 7082 (1994).
138. P. Bratu, K. L. Kompa, and U. Höfer, *Chem. Phys. Lett.* 251, 1 (1996).
139. K. W. Kolasinski, W. Nessler, A. de Meijere, and E. Hasselbrink, *Phys. Rev. Lett.* 72, 1356 (1994).
140. C. Landman and L. WD, *Faraday Disc.* 125, 1 (2004).
141. S. J. Tauster, S. C. Fung, and R. L. Garten, *J. Am. Chem. Soc.* 100, 170 (1978).
142. D. R. Jennison, O. Dulub, W. Hebenstreit, and U. Diebold, *Surf. Sci.* 106, L677 (2001).
143. P. Pyykko, *Angew. Chem. Int. Ed.* 43, 4412 (2004).
144. G. Mills, M. S. Gordon, and H. Metiu, *J. Chem. Phys.* 118, 4198 (2003).
145. S. A. Varganov, R. M. Olson, M. S. Gordon, and H. Metiu, *J. Chem. Phys.* 119, 2531 (2003).
146. N. Lopez and J. K. Norskov, *J. Am. Chem. Soc.* 124, 11262 (2002).
147. S. Chrétien, M. S. Gordon, and H. Metiu, *J. Chem. Phys.* 121, 3756 (2004).
148. B. Yoon, H. Häkkinen, and U. Landman, *J. Phys. Chem. A* 107, 4066 (2003).
149. G. Mills, M. S. Gordon, and H. Metiu, *Chem. Phys. Lett.* 359, 493 (2002).

150. Y. Zhang, A. Kolmakov, S. Chretien, H. Metiu, and M. Moskovits, *Nano Lett.* 4, 403 (2004).
151. M. Mavrikakis, P. Stoltz, and J. K. Nørskov, *Catal. Lett.* 64, 101 (2000).
152. N. Lopez, T. V. W. Janssens, B. S. Clausen, Y. Xu, M. Mavrikakis, T. Bligaard, and J. K. Nørskov, *J. Catal.* 223, 232 (2004).
153. L. Piccolo, D. Loffreda, F. J. C. S. Aires, C. Deranlot, Y. Jugnet, P. Sautet, and J. C. Bertolini, *Surf. Sci.* 566, 995 (2004).
154. Z.-P. Liu, P. Hu, and A. Alavi, *J. Am. Chem. Soc.* 124, 11262 (2002).
155. Y. Wang and G. S. Hwang, *Surf. Sci.* 542, 72 (2003).
156. A. Vittadini and A. Selloni, *J. Chem. Phys.* 117, 353 (2002).
157. N. Lopez, J. K. Nørskov, T. V. W. Janssens, A. Carlsson, A. Puig-Molina, B. S. Clausen, and J. D. Grunwaldt, *J. Catal.* 225, 86 (2004).
158. L. M. Molina and B. Hammer, *Phys. Rev. Lett.* 90, 206102 (2003).
159. L. M. Molina, M. D. Rasmussen, and B. Hammer, *J. Chem. Phys.* 120, 7673 (2004).
160. L. M. Molina and B. Hammer, *Phys. Rev. B* 69, 155424 (2004).
161. M. D. Rasmussen, L. M. Molina, and B. Hammer, *J. Chem. Phys.* 120, 988 (2004).
162. M. S. Chen and D. W. Goodman, *Science* 306, 252 (2004).
163. H. Häkkinen, S. Abbet, A. Sanchez, U. Heiz, and U. Landman, *Angew. Chem. Int. Ed.* 42, 1297 (2003).
164. S. Abbet, U. Heiz, A. M. Ferrari, L. Giordano, C. Di Valentin, and G. Pacchioni, *Thin Solid Films* 400, 37 (2001).
165. P. M. Ajayan and L. D. Marks, *Nature* 338, 139 (1989).
166. R. J. H. Grisel and B. E. Nieuwenhuys, *J. Catal.* 199, 48 (2001).
167. P. Broqvist, L. M. Molina, H. Grönbeck, and H. B., *J. Catal.* 227, 217 (2004).
168. L. Giordano, G. Pacchioni, F. Illas, and R. N., *Surf. Sci.* 499, 73 (2002).
169. L. Giordano, G. Pacchioni, A. M. Ferrari, F. Illas, and R. N., *Surf. Sci.* 473, 213 (2001).
170. A. Roudgar and A. Groß, *Surf. Sci.* 559, L180 (2004).
171. D. M. Kolb, *Surf. Sci.* 500, 722 (2002).
172. D. M. Kolb, R. Ullmann, and T. Will, *Science* 275, 1097 (1997).
173. G. E. Engelmann, J. C. Ziegler, and D. M. Kolb, *J. Electrochem. Soc.* 145, L33 (1998).
174. J. Meier, K. A. Friedrich, and U. Stimming, *Faraday Disc.* 121, 365 (2002).
175. J. Meier, J. Schiotz, P. Liu, J. K. Nørskov, and U. Stimming, *Chem. Phys. Lett.* 390, 440 (2004).
176. D. M. Kolb, G. E. Engelmann, and J. C. Ziegler, *Angew. Chem. Int. Ed.* 39, 1123 (2000).
177. M. G. Del Popolo, E. P. M. Leiva, H. Kleine, J. Meier, U. Stimming, M. Mariscal, and W. Schmickler, *Appl. Phys. Lett.* 81, 2635 (2002).
178. M. G. Del Popolo, E. P. M. Leiva, H. Kleine, J. Meier, U. Stimming, M. Mariscal, and W. Schmickler, *Electrochim. Acta* 48, 1287 (2003).
179. S. M. Foiles, M. I. Baskes, and M. S. Daw, *Phys. Rev. B* 33, 7983 (1986).
180. M. S. Daw, S. M. Foiles, and M. I. Baskes, *Mater. Sci. Rep.* 9, 252 (1993).
181. M. G. Del Popolo, E. P. M. Leiva, M. Mariscal, and W. Schmickler, *Nanotechnology* 14, 1009 (2003).
182. A. Roudgar, *private communication.*
183. J. A. Rodriguez, *Surf. Sci. Rep.* 24, 223 (1996).
184. J. A. Rodriguez, J. Dvorak, T. Jirsak, and J. Hrbek, *Surf. Sci.* 315, 315 (2001).
185. Z. P. Chang, Z. Song, G. Liu, J. A. Rodriguez, and J. Hrbek, *Surf. Sci.* 512, L353 (2002).
186. S. Helveg, J. V. Lauritsen, E. Lægsgaard, I. Stensgaard, J. K. Nørskov, B. S. Clausen, H. Topsøe, and F. Besenbacher, *Phys. Rev. Lett.* 84, 951 (2000).
187. P. Liu, J. A. Rodriguez, J. T. Muckerman, and J. Hrbek, *Surf. Sci.* 530, L313 (2003).
188. P. Liu, J. A. Rodriguez, J. T. Muckerman, and J. Hrbek, *Phys. Rev. B* 67, 155416 (2003).
189. F. Rosei, M. Schunack, Y. Naitoh, P. Jiang, A. Gourdon, E. Lægsgaard, I. Stensgaard, C. Joachim, and F. Besenbacher, *Prog. Surf. Sci.* 71, 95 (2003).
190. S. J. Sowerby, W. M. Heckl, and G. B. Petersen, *J. Mol. Evol.* 43, 419 (1996).
191. W. M. Heckl, in "Astrobiology, The Quest for the Conditions of Life" (G. Horneck and C. Baumstark-Khan, Eds.). Springer, Berlin, 2002.
192. S. J. Sowerby, M. Edelwirth, and W. M. Heckl, J. Phys. Chem. 102, 5914 (1998).
193. S. J. Sowerby, M. Edelwirth, M. Reiter, and W. M. Heckl, *Langmuir* 14, 5915 (1998).
194. U. Ziener, J.-M. Lehn, A. Mourran, and M. Möller, *Chem. Eur. J.* 8, 951 (2002).
195. A. Kühnle, L. M. Molina, T. R. Linderoth, B. Hammer, and F. Besenbacher, *Phys. Rev. Lett.* 93, 086101 (2004).
196. S. Clair, S. Pons, A. P. Seitsonen, H. Brune, K. Kern, and J. V. Barth, *J. Phys. Chem. B* 108, 14585 (2004).
197. N. J. Tao and Z. Shi, *J. Phys. Chem.* 98, 1464 (1994).
198. J. Freund, M. Edelwirth, P. Kröbel, and W. M. Heckl, *Phys. Rev. B* 55, 5394 (1997).
199. M. Edelwirth, J. E. Freund, S. J. Sowerby, and W. M. Heckl, *Surf. Sci.* 417, 201 (1998).
200. K. Shinoda, W. Shinoda, C. C. Liew, S. Tsuzuki, Y. Morikawa, and M. Mikami, *Surf. Sci.* 556, 109 (2004).
201. T. H. Rod and J. K. Nørskov, *Surf. Sci.* 500, 678 (2002).
202. W. A. Hofer, A. S. Foster, and A. Shluger, *Rev. Mod. Phys.* 75, 1287 (2003).
203. L. M. Molina and B. Hammer, *Chem. Phys. Lett.* 360, 264 (2002).
204. A. Groß, *Surf. Sci. Rep.* 32, 291 (1998).
205. D. Marx and J. Hutter, in "Modern Methods and Algorithms of Quantum Chemistry" (J. Grotendorst, Ed.), Vol. 3 of NIC series, p. 329. John von Neumann-Institute for Computing, Jülich, 2000.
206. A. Groß, S. Wilke, and M. Scheffler, *Phys. Rev. Lett.* 75, 2718 (1995).

207. A. Groß, in "The Chemical Physics of Solid Surfaces" (D. P. Woodruff, Ed.), Vol. 11, Chap. 1. Elsevier, Amsterdam, 2003.
208. V. P. Zhdanov and B. Kasemo, *Cat. Lett.* 81, 141 (2002).
209. G. Henkelman and H. Jónsson, *J. Chem. Phys.* 111, 7010 (1999).
210. G. Henkelman, B. P. Uberuaga, and H. Jónsson, *J. Chem. Phys.* 113, 9901 (2000).
211. P. Hänngi, P. Talkner, and M. Borkovec, *Rev. Mod. Phys.* 62, 251 (1990).
212. S. Goedecker, *Rev. Mod. Phys.* 71, 1085 (1999).
213. W. Kohn, *Phys. Rev. Lett.* 76, 3168 (1996).
214. S. Goedecker and L. Colombo, *Phys. Rev. Lett.* 73, 122 (1994).
215. F. Starrost and E. A. Carter, *Surf. Sci.* 500, 323 (2002).
216. M. Eichinger, P. Tavan, J. Hutter, and M. Parrinello, *J. Chem. Phys.* 110, 10452 (1999).
217. P. Carloni and U. Röthlisberger, in "Theoretical Biochemistry—Processes and Properties of Biological Systems" (L. Eriksson, Ed.), p. 215. Elsevier, Amsterdam, 2001.
218. M. Stadele, J. A. Majewski, P. Vogl, and A. Görling, *Phys. Rev. Lett.* 79, 2089 (1997).
219. F. Della Sala and A. Görling, *J. Chem. Phys.* 118, 10439 (2003).
220. W. Kohn, Y. Meir, and D. Makarov, *Phys. Rev. Lett.* 80, 4153 (1998).
221. E. Hult, H. Rydberg, B. Lundqvist, and D. Langreth, *Phys. Rev. B* 59, 4708 (1999).

CHAPTER 10

Computational Methods for Atomistic Modeling of Nanoporous Materials and Their Properties

Muhammad Sahimi, Theodore T. Tsotsis

Department of Chemical Engineering, University of Southern California, Los Angeles, California 90089, USA

CONTENTS

ISBN: 1-58883-047-0

Handbook of Theoretical and Computational Nanotechnology
Edited by Michael Rieth and Wolfram Schommers
Volume 5: Pages (603–689)

1. INTRODUCTION

In a lecture entitled, "There is Plenty of Room at the Bottom," and delivered at the American Physical Society meeting in 1959 [1], Richard P. Feynman, the (future) Nobel Laureate in physics, spoke about his vision for the future. In his presentation, considered at that time to be a futuristic lecture, Feynman boldly predicted that in the future, one could fit the entire *Encyclopædia Britannica* onto the head of a pin and use ions focused through a microscope lens in reverse to etch away silica in order to generate patterns on sub-micrometer scale. To achieve these lofty goals, he proposed a top-down approach by which one builds the smallest pair of hands possible, which he called the *magic hands*, to be used in building even smaller features down to the limit of lithography. We now know, in retrospect, that Feynman's predictions were amazingly accurate: What he was envisioning was materials at the meso- and nanoscales that have now been synthesized. In fact, fabrication, characterization, and modeling of materials (and, of course, their applications) with characteristic feature sizes that are at or near nanometer scale—the length scales that Richard Feynman was talking about in his lecture—are of great current interest, not only due to the fact that they have given rise to a set of fundamental unsolved problems but also for their potential for revolutionizing the current technologies. This field of research is currently undergoing rapid development, and the impetus for its advancement is twofold:

(i) Understanding the behavior of such materials under a wide range of conditions that are encountered in applications should ultimately lead to precise control over their properties, hence making it possible to tailor their effective properties.
(ii) As our ability for synthesizing materials and fabricating structures at the nanoscale improves, more and more applications for such materials and systems will also arise.

Of central importance to the research field of nanoscale materials are the development and application of effective experimental techniques for characterization of the morphology and electronic, magnetic, mechanical, and optical properties of such materials. At the same time, development of accurate and efficient computational techniques for modeling of such materials, and investigating the effect of factors that affect their properties, are of great importance.

In this chapter, we consider theoretical approaches to, and computational modeling of, a particular class of nanoscale materials, namely, nanoporous materials, that are currently of great scientific interest [2–4]. Examples of such materials include membranes, catalysts, and adsorbents that are used for reaction, separation and purification processes, as well as skin and biological tissues. In addition, nanoporous materials have many applications as low-dielectric constant materials, optical coatings, sensors, and insulating films.

At the most basic level, a nanoporous material may consist of a single nanopore or nanotube. For example, a new form of carbon, namely, buckministerfullerene C_{60}, was discovered by Smalley, Kroto, and coworkers [5], which led to a Nobel Prize for chemistry in 1997. This material is similar to a soccer ball and is made of pure carbon atoms that are bonded together in hexagon and pentagon configurations. Another form of quasi-one-dimensional material is carbon nanotube, which is also made of carbon atoms. These two classes of materials have a common feature, namely, their atoms are distributed on curved surfaces. However, whereas the atomic surfaces of fullerene are curved in 3D, the nanotubes generally exhibit 2D curvature. Carbon nanotubes are usually thought of as graphene sheets rolled into seamless tubes. Such materials are usually referred to as *single-wall nanotubes* and were discovered by Iijima and Ichihashi [6] and Bethune et al. [7]. If the tubes are concentrically stacked, one obtains a *multiwall carbon nanotube*, which was discovered by Iijima [8], who announced their discovery in carbon-soot made by an arc-discharge method.

More complex forms of nanoporous materials are prepared when the nanopores form networks. For example, carbon nanotubes can form a bundle in which the tubes are essentially parallel and form an array. In many of the theoretical and computational modeling of such

nanotube arrays, it is assumed that the tubes are chemically and structurally "perfect," hence forming a periodic array. This assumption simplifies greatly the theoretical analysis of such materials but can be a gross oversimplification. On the other hand, the nanopores can form an interconnected network, which can be nearly two-dimensional (as in thin nanoporous films), or fully three-dimensional (as in most membranes, catalysts, and similar materials). As an example, consider silica aerogels that are nanoporous materials with highly unusual properties. These materials are the subject of much current research, especially in the area of microelectronic interconnects. Their tunable porosity—typically 40–80%—and nanometer pore sizes allow their use as a low-dielectric constant material suitable for small feature–size integrated circuits. For ultralarge-scale integration devices, problems with the resistance–capacitance (RC) interconnection delay hinders device performance. Improvement of this RC delay requires replacement of conventional SiO_2, which has a dielectric constant $k \simeq 4$ with a material with lower k. Silica aerogels, with $k \simeq 2$ or lower, represent a leading candidate for this purpose.

Exact theoretical analysis of nanoporous materials and their various properties is extremely difficult, if not impossible. Hence, one must resort to approximate analysis and/or large-scale computer simulations in order to gain a better understanding of the properties of such nanoporous materials. Such theoretical analyses and computational modelings are the focus of this chapter. However, it would be very difficult to describe all the theoretical and computational approaches that have been developed for modeling of all nanoporous materials. Therefore, we restrict our attention to three classes of such materials, namely, nanopores and nanotubes, low-dielectric constant nanoporous materials, and membranes. Each of these materials have very important and broad practical applications. At the same time, the variation in the structure of these three classes of materials is broad enough that describing the theoretical and computational approaches to their modeling should provide the reader with a reasonable understanding of the complexities that are involved in such problems.

To organize our discussions, we divide into two groups the theoretical and computational approaches to modeling of nanoporous materials and their properties:

(i) In the first group are those that are used for modeling the nanoporous materials themselves. A wide variety of molecules and compounds are used for the synthesis and preparation of nanoporous materials, and, therefore, accurate modeling of these materials and the morphology of their pore space is essential for any realistic modeling of any phenomenon that may take place either throughout the matrix or in their pore space. For example, some of the problems that are important in modeling of carbon nanotubes are (1) classification of the tubes as either metals or semiconductors and, more generally, their electronic structure; (2) hybridization of the σ^* and π^* states of the graphene network and their effect on metallicity of the tubes, and several other important issues that will be discussed below.

(ii) In the second group are those approaches that are used for modeling the phenomena that take place either through the materials' matrix or in their pore space. Some of the phenomena that take place through a nanoporous material's matrix include (1) conduction; (2) deformation of the matrix under an external force and, in particular, the temperature-dependence of the materials' shape, and several other important phenomena. Some of the phenomena that occur in the pore space of nanoporous materials include (1) adsorption of gases; (2) flow and transport of fluids; (3) separation of a mixture of fluids, and several other phenomena.

Among the aforementioned phenomena, transport and adsorption of fluids in the pore space of a nanoporous material are of particular importance. Their significance is twofold:

(i) For such nanoporous materials as membranes, nanotubes, catalysts, and adsorbents, it is important to understand how transport and adsorption of fluids takes place in their pore space, so that their morphology can be optimized for such applications as separation, purification, and storage of gases in the pore space.

(ii) For low-dielectric constant nanoporous materials and similar composites, it is important to be able to characterize their pore space, which in turn greatly influences their

dielectric constant, resistance, and optical properties. Several methods of characterizing a pore space involve sending probe molecules into the pore space of the material that diffuse and flow inside the pores and adsorb on their internal surface.

Due to the exceedingly small sizes of the pores of nanoporous materials, the behavior of fluids and their mixtures in their pore space is typically different from that observed in the bulk. For example, because the average pore size of many membranes and nanotubes is typically of the order a few angstroms, the traditional continuum approach [2–4] cannot, *a priori*, be used for modeling flow and transport of fluids and other related phenomena in their pore space. This is due to the fact that the pores' small sizes imply that the molecular interactions between the diffusing and/or flowing fluids themselves, and between them and the pores' walls, are important and cannot be ignored. Hence, one must resort to atomistic modeling of such phenomena. Such modeling techniques are the focus of this chapter.

This chapter is organized as follows. In the next section, we briefly describe the main properties of the three classes of nanoporous materials that we consider in this chapter. In Section 3, we describe computational methods for atomistic modeling of nanoporous materials, including energy minimization techniques, and molecular-mechanical and quantum-mechanical methods. The main molecular-mechanical method that we describe is the classical molecular dynamics (MD) simulation technique, while the quantum-mechanical methods that we consider include the density-functional theory and its variants and quantum MD methods. Section 4 presents a discussion of efficient computational strategies for carrying out the classical and quantum MD simulations, including vectorized and massively-parallel techniques. Various protocols for generating models of nanoporous materials, using the techniques described in Sections 3 and 4, are described in Section 5. Some important equilibrium and nonequilibrium phenomena that occur in nanoporous materials, and their atomistic simulations, are described in Section 6.

2. THREE CLASSES OF NANOPOROUS MATERIALS

In what follows, we describe and discuss the main properties of the nanoporous materials that we consider in this chapter. Because our focus is the theoretical and computational approaches to modeling of such materials and their properties, we only describe briefly their essential properties.

2.1. Carbon Nanotubes

Single-wall nanotubes (SWNTs) are essentially a graphene sheet of carbon atoms that is rolled-over to form a cylindrical tube; see Fig. 1. The typical diameter of SWNTs is around 1 nm. They are essentially molecular wires with their structure characterized by integers: If one folds a graphene sheet into a cylindrical tube, such that the head and tail of a (m, n) lattice vector (with m and n being integers) in the sheet join together, one obtains what is usually referred to as a (m, n) nanotube. They are also sometimes called *armchair* tubes, as the carbon atoms that are around the circumference are in an armchair pattern. This is shown in Fig. 2. Clearly, the diameter of a nanotube is fixed once m and n are specified. As mentioned above, a multiwall nanotube (MWNT) is formed if one stacks concentric cylinders (SWNTs) with an interlayer spacing of 3.4 Å. The typical diameter of a MWNT is 10–20 nm. The length of SWNTs and MWNTs can be up to several centimeters but is typically a few hundred micrometers.

The structure of a nanotube is uniquely defined by the chiral vector, $\mathbf{C}_h = m\mathbf{a}_1 + n\mathbf{a}_2$, which connects crystalographically equivalent points of the graphene sheet that are folded back onto one another in the wrapping process. Here, $\mathbf{a}_1$ and $\mathbf{a}_2$ are the graphene lattice unit vectors (see Fig. 1). When $n = 0$, one obtains the *zigzag* nanotube. When the rows of hexagons spiral along the nanotube axis, one obtains the *chiral* nanotube. These are also shown in Fig. 2. The composition of SWNTs can be delineated by, for example, absorption spectroscopy, from the ultraviolet to the near infrared region [9].

One reason for the great current interest in nanotubes is their unusual mechanical strength. The tensile strength of a nanotube is more than 100 times higher than that of

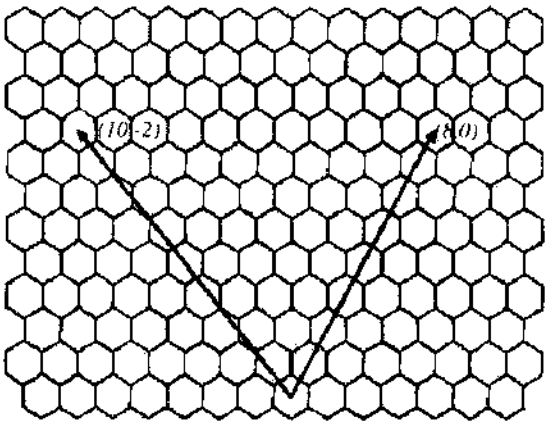

Figure 1. Hexagonal lattice structure of a graphene sheet in which the carbon atoms are at the sites of the lattice. Two examples of the lattice vectors are also shown (after Dai [35]).

steel. These materials are ductile and can tolerate large strains without breaking, unless the strain becomes too large [10]. Moreover, a fundamental question is the relation between the mechanical properties of nanotubes and their electrical properties, as nanotubes can behave as a metal, a semiconducting material, or a small-gap semiconductor. The conducting state of a nanotube depends sensitively on the parameters (m, n) and, hence, on its diameter and chirality [11].

To understand the conduction properties of nanotubes, one must recognize that, in a graphene sheet, the conduction and valence bands touch each other at the six corner points of the first Brillouin zone, filled with electrons at Fermi (highest) energy level. Therefore, in general, the sheet behaves as a semimetallic material with a zero band gap. If a nanotube is infinitely long, its electronic states will be parallel lines in the Fourier space. The lines are quantized along the circumference but continuous along the axis of the tube. Nanotubes can also behave as metallic materials if $m = n$, as in this case there are always electronic lines (states) that cross the corner points of the first Brillouin zone. Moreover, if $m - n$ is not a multiple of 3, the electronic states will not pass through the corner points, in which case the nanotubes act as semiconducting materials. If, on the other hand, $m - n$ is a multiple of 3, certain electronic states of the nanotubes cross the corner points of the first Brillouin zone, which means that the tubes should be semimetallic. However, curvature-induced orbital

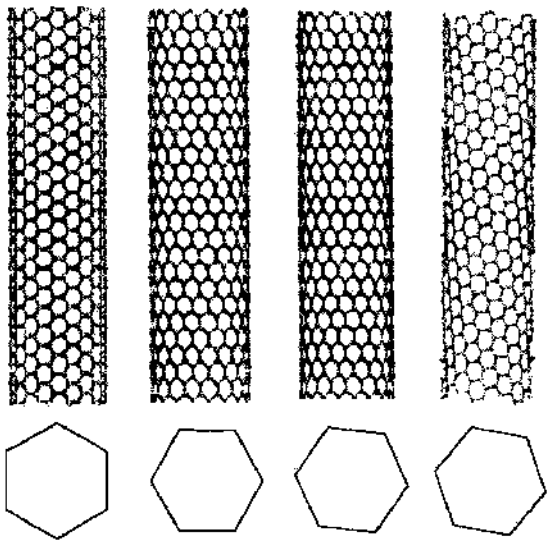

Figure 2. Four examples of single-wall nanotubes. Shown, from left to right, are, a (10, 10) armchair tube; a (12, 0) zigzag tube; a (14, 0) tube, and a (7, 16) tube. In each case, the hexagon at the bottom shows the first Brillouin zone of the graphene sheet in reciprocal space, and vertical lines crossing the hexagons (not shown) would represent the electronic state of the nanotube. Thus, the two right-most tubes are semiconducting because the vertical lines would miss the corner points of the hexagons, and the two left-most tubes are conducting (after Dai [35]).

rehybridization [12, 13] forces the nanotube to act as a semiconducting material. Therefore, the conduction properties of nanotubes depend very sensitively on the structural parameters (m, n). Controlling these parameters to synthesize a nanotube with a particular electronic property is a major challenge. In addition, it has been reported [14, 15] that the electronic properties of carbon nanotubes depend extremely sensitively on the chemical environment and, in particular, oxygen.

Nanotubes have many important potential applications. They have been used, either individually or as an ensemble, as scanning probes [16, 17], electron field emission source [18], electrochemical actuators [19], composite materials with improved mechanical properties [10], and nanoelectronic devices [20]. Nanotube molecular wires have been suggested as chemical sensors [15]. In addition, Dillon et al. [21] showed that soots that contain SWNTs can absorb large quantities of hydrogen molecules, although this remains a controversial subject. This phenomenon not only has an important practical application in hydrogen fuel cells, but also, from a fundamental point of view, may provide physical realization of a 1D matter. Since this discovery, the storage capacity of carbon nanotubes for hydrogen and other gases has been measured extensively [22–33]. Later in this chapter, we will describe computational modeling of gas adsorption in carbon nanotubes. Many aspects of preparation of SWNTs and MWNTs and their properties are described by Dresselhaus et al. [34] and Dai [35].

2.2. Low-Dielectric Constant Nanoporous Materials

Improving the performance of microprocessors involves a reduction in the size of the device used in the microprocessors, which would increase its speed and allow for a higher packing density of the device. However, the problem is not merely reducing the size of the device, but also the fact that higher device packing densities imply a very large increase in the number of the interconnects and, therefore, much more wiring. In addition, a higher device packing density would also necessitate a reduction in the wiring pitch, which is the sum of the metal line width and the spacing between the metal lines [36–39]. At the same time, if the device size becomes less than the transistor gate length, such problems as propagation delay, crosstalk noise, and power dissipation caused by resistance–capacitance (RC) coupling also arise due to the increase in wiring capacitance. Therefore, although one may increase the speed of the device by reducing its size, the interconnect delay would represent a very significant fraction of the total delay, hence limiting improvement in the device performance. To address these problems, one must not only design new architectures to replace the current Al(Cu) and SiO_2 interconnects but also use new materials as metal lines and interlayer dielectrics. In particular, the new architectures require materials with low-dielectric constants, $k < 3$.

To understand better the importance of the interlayer dielectric on the interconnect time delay τ_d, recall that τ_d depends on the resistance of the metallic interconnections as well as the capacitance of the dielectric medium. Figure 3 presents [40] schematics of a typical multilevel interconnect system. The thickness T of the metal and that of the dielectric material above and below the interconnect are equal. A simple first-order model [40] can estimate the interconnect RC delay. If ℓ and ρ are, respectively, the length of the interconnection and its resistivity, its total resistance is $R = 2\rho\ell/p_m T$, where p_m is the metal pitch (see Fig. 3). Therefore, if C_L and C_V are, respectively, the lateral line-to-line vertical and layer-to-layer capacitances, and assuming that the line-to-ground capacitance $C_{LG} = C_V$, and that the effects of fringing fields and finite electrode thickness can be neglected, then, the total parallel-plate capacitance is given by $C = 2k\epsilon_0(2\ell T/p_m + \ell p_m/2T)$, where k is the relative dielectric constant, and ϵ_0 the permittivity of the free space. The RC delay is then given by $\tau_d = 2\rho k\epsilon_0(4\ell^2/p_m^2 + \ell^2/T^2)$. Thus, use of high conductivity metals (such as Cu) and low-k dielectrics can significantly reduce τ_d. For example, replacing Al by Cu and SiO_2 ($k = 4$) by air ($k = 1$) will reduce the RC delay by, respectively, 35% and 75%.

Figure 4 shows the dependence of the delay time on the integrated-circuit (IC) feature size [41, 42]. As can be seen, the gate delay becomes important only when the feature size is larger than 1 μm. In contrast, the RC delay is dominant when the feature size is less than 0.5 μm. Figure 5 presents the interconnect capacitance *versus* the feature size. Because $C \propto k$, reducing k lowers C and the RC delay τ_d. If the interconnect space is less than

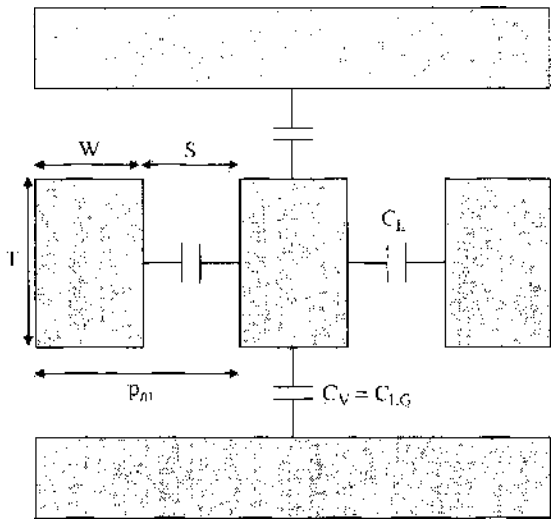

Figure 3. Schematics of an interconnect system (after Lee and Ho [40]).

0.3 μm, then the interconnect capacitances C_{LG} and C_V are both very small compared with C. Under this condition, C is dominated by the line-to-line capacitance C_L, which contributes close to 90% of C at feature sizes < 0.25 μm.

Given such considerations, preparation of low-dielectric constant materials, especially those that are porous (as the dielectric constant of air is very low), is a subject of much current interest and intensive research. Among such materials, organic fluorinated polymers, such as polytetrafluoroethylene (with $k = 1.8$ to 3.0), and nanoporous silica (with $k = 1$ to 2.8) are of particular interest. Porous silica can be in the form of xerogel (dried by solvent evaporation) or aerogel (dried by removing the solvent at a temperature above its critical temperature, i.e., under *supercritical* conditions). The ultralow dielectric constant of these nanoporous materials is due to their high porosity. Figure 6 presents the dependence of the dielectric constant of a silica-based nanoporous material on its porosity. Also shown are simple theoretical estimates (based on the assumption that the pores are either in series or in parallel), together with experimental data measured at high frequencies (1–40 GHz) [43, 44], indicating that at a porosity of 0.9 (which can be achieved with, e.g., aerogels) the dielectric constant is only 1.3.

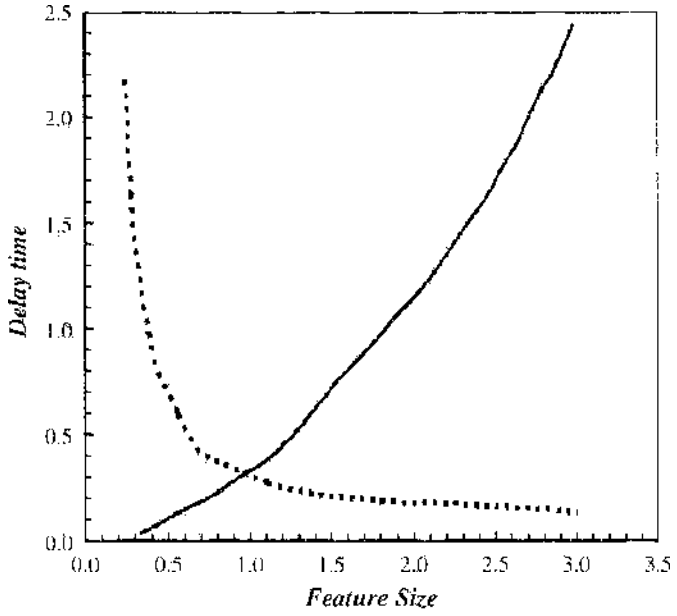

Figure 4. Dependence of the delay time ($\times 10^{-9}$ s) on the feature size (in μm). The continuous and dotted curves show, respectively, the intrinsic gate delay and the interconnect delay (RC) (after [41, 42]).

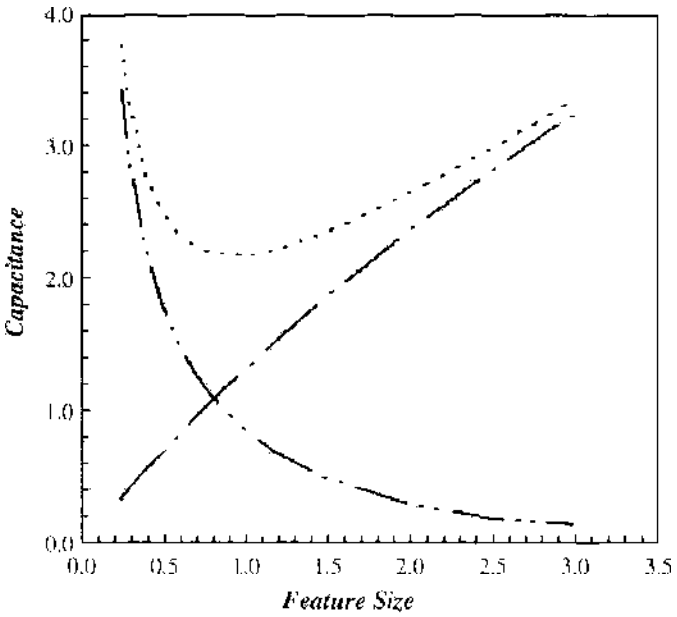

Figure 5. The capacitances ($\times 10^{-15}$ Farad/μm) *versus* feature size (in μm). The dotted curve shows the total capacitance, the single-dotted curve the capacitance C_{fg}, and the double-dotted curve the capacitance C_f (after Lee and Ho [40]).

It is, of course, possible to prepare many porous materials that have low dielectric constants. For example, in one extreme limit, one might employ air gaps (unit porosity!) with $k = 1$ (in practice, the effective k will be larger because of the liner). However, air gaps are not very strong and suffer from low breakdown voltage and low thermal conductivity. Therefore, low values of k is only part of the story. The best low-k nanoporous material has two important properties: (1) It is very strong even when its porosity is high, and (2) the size of its pores is much smaller than that of the microelectronic features.

In addition to possessing these two important properties, nanoporous silica materials have several other advantages over other low-k materials, some of which are (1) thermal stability at high temperatures (up to 900°C); (2) both the precursor (tetraethyorthosilicate) and the

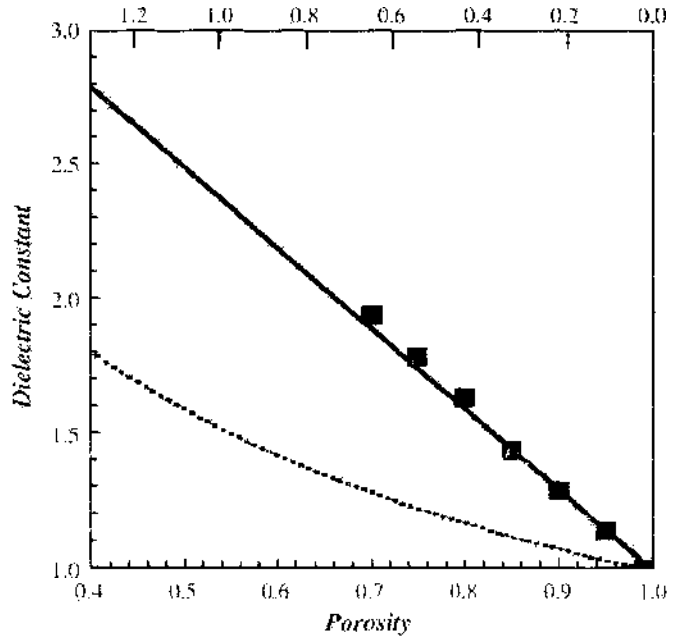

Figure 6. Dependence of the dielectric constant of a silica-based nanoporous material on its porosity. The continuous and dotted curves show, respectively, the predictions if the pores are assumed to be parallel or in series. The squares show the experimental data [43, 44] (after Jin et al. [44]).

material (silica) are widely used in the semiconductor industry; (3) their deposition tools are conventional, and (4) their dielectric constant can effectively be tuned over a wide range. In addition, from an economic view point, nanoporous silica materials offer a distinct advantage over other low-k materials in that one can use the same material, equipment, and integration schemes for multiple technologies. Note that as heat removal in microprocessors is an important problem, one may question the use of aerogels, which are excellent insulators. However, one of the key parameters is the density of the nanoporous material (which controls its pore size, thermal conductivity, and mechanical strength). For the application that we are discussing here, the appropriate density of aerogels is such that their thermal conductivity is actually larger than that of polymeric dielectric materials. Their thermal resistance is very high only at such low densities that are not of interest to the semiconductor industry.

2.3. Nanoporous Membranes

The third important class of porous materials that we focus on in this chapter consists of nanoporous membranes that are used for the separation of fluid mixtures into their constituent components. These materials, depending on their pore space morphology, contain a range of pore sizes, from nano- to meso- to micropores. However, the main resistance to any transport process in the pore space of these materials is offered mainly by the interconnected nano- and mesopores. Thus, studies of flow and transport processes in such materials have focused on this range of pore sizes.

A synthetic membrane (as opposed to natural biological membranes) is a permeable or semi-permeable material, typically in the form of a thin film and prepared from a variety of materials, ranging from various polymers to inorganic solids, such as metals and ceramics. As shown in Fig. 7, the main task of a membrane is to act as a barrier, controlling the rate of exchange of compounds between two adjacent fluid phases, hence helping to separate different species either by molecular sieving (separation based on molecular sizes) or by controlling the rate of their transport (diffusion and/or convection). The transport processes across a membrane are typically driven by an external potential gradient, such as a concentration, pressure, or an electrical potential gradient.

The effectiveness of a membrane is measured by two of its characteristics, which are its *permeability* and *selectivity*. The permeability to a fluid is defined as the ratio of its flux and the potential gradient imposed on the membrane. Often, the true thickness of the membrane is not known, in which case the membrane's *permeance*—its permeability per unit thickness—is used for characterizing its flow property. The selectivity of a membrane measures its ability for separating two fluids from each other, and is usually defined as the ratio of the two fluids' fluxes.

Membranes are classified by whether their permselective layer is porous or dense (having a very low permeability), and by the type of materials their thin film is made of. The type of materials used for preparing membranes, and the structure of their permselective layer (porous *vs.* dense), depend on the particular application for which they are intended. For example, if a membrane is to operate at high temperatures, polymers will not be suitable as the base or precursor materials. In addition, the degree of separation and the purity of

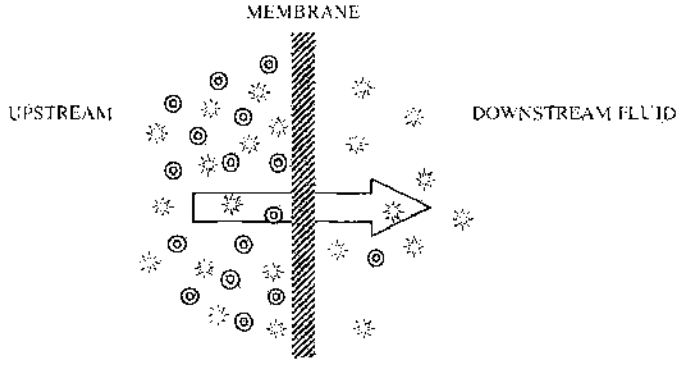

Figure 7. The basic principles in the operation of a membrane.

the fluid stream leaving a membrane are fundamental factors for selecting the materials for preparing the membrane. Moreover, if a membrane is to operate in a chemical reactor, it must be stable under reactive conditions [45].

Membranes are also classified by the symmetry of their morphology. Symmetric membranes (sometimes referred to as homogeneous membranes) are those that are made of materials that, due to their high mechanical strength, are self-supporting. In many cases, however, a membrane's thin permselective layer is not strong enough to be self-supporting, in which case the layer is deposited on a porous support. If the support is made of a material different from what is used to make the membrane's permselective layer, one has an asymmetric membrane. The geometry of membranes varies widely, ranging anywhere from flat, tubular, and multitubular shapes to hollow-fiber and spiral-wound membranes. Generally speaking, a membrane's geometry depends on the material that the membrane is made of. For example, the geometry of ceramic membranes is usually tubular, multitubular, or flat, whereas polymeric membranes are typically spiral-wound or hollow-fiber.

Porous membranes are made of various types of polymers, ceramics, and microporous carbons. The polymers used include perfluoropolymers, polyimides, and polyamides. For sieving to be an effective mechanism of separation by porous membranes, the molecular sizes of the species to be separated must be taken into account, and the pore size distribution of the membrane must be such that a significant fraction of its pore cannot accomodate one or more of fluids in a mixture that are to be separated. Dense polymeric and organic membranes are used for molecular-scale separation processes involving gas mixtures. In addition to polymers, metals and solid oxides are also used for preparing dense membranes. Metallic membranes include those that are made of precious metals, such as platinum, palladium, and silver, as well as various alloys containing at least one of these metals. Such membranes have been used for hydrogen (Pt, Pd, and their alloys) and oxygen (Ag) separation. Membranes that are made of dense solid oxide materials are also used for oxygen and hydrogen separation and are prepared by various types of ionic conducting materials, such as modified zirconia and perovskites.

3. MODELING OF NANOPOROUS MATERIALS

Before one can model any phenomenon of interest, such as diffusion, flow, adsorption, and separation of fluid mixtures, in a nanoporous material, or conduction through, and deformation of, its matrix, one must develop a realistic model for the material itself. Therefore, we describe in this section models of nanoporous materials, and Section 6 will take up the problem of modeling various phenomena in such materials.

As discussed by Sahimi [2, 3, 46], one can divide models of porous materials into two large classes. In one class are what we refer to as the *continuum models*, which are those in which a porous material is represented by its effective macroscopic properties, such as its effective permeability. Such models ignore the details of a material's morphology at the nano- and mesoscales. The material's effective properties are either measured experimentally or else predicted by (usually) oversimplified models that envision the material as a bundle of pores that are either in parallel or series. As mentioned earlier, however, due to the exceedingly small sizes of the pores of a nanoporous material, which are comparable with the molecular sizes of the fluids that pass through its pore space, the interatomic interactions between the fluids' molecules themselves, as well as those between the fluids and the pores' walls, cannot be neglected. Therefore, such classical laws of transport of molecules, such as Fick's law of diffusion, which are valid at the continuum scale cannot, *a priori*, be used for modeling transport of fluids through a nanoporous material. The validity of such continuum-scale transport laws must first be ascertained by careful molecular-scale modeling and simulations. This gives rise to the second class of models of materials, namely, the *discrete models*, in which the material is modeled by a collection of atoms and molecules that are connected to one another and follow the basic physical laws governing the interatomic interactions between them. The advent of very fast computers and development of vectorized and massively parallel computational strategies have made it feasible to carry out large-scale calculations at

the molecular level, and in this endeavor discrete models at the atomic scales have become indispensable tools for predicting the properties of materials at such length scales.

Prediction of electronic properties and morphology of a material requires, in principle, quantum-mechanical computation of the total energy of the system and minimization of this energy with respect to the electronic and nuclear coordinates. To carry out such computations, one must start with the Hamiltonian of the system, which, for a system of N electrons and N' nuclei with charges Z_n, is given by

$$\mathcal{H} = \sum_{i=1}^{N} \frac{p_i^2}{2m} + \sum_{n=1}^{N'} \frac{P_n^2}{2M_n} + \frac{1}{2}\frac{1}{4\pi\varepsilon_0} \sum_{i=1, i\neq j}^{N} \sum_{j=1}^{N} \frac{e}{|\mathbf{r}_i - \mathbf{r}_j|} - \frac{1}{4\pi\varepsilon_0} \sum_{n=1}^{N'} \sum_{i=1}^{N} \frac{Z_n e^2}{|\mathbf{r}_i - \mathbf{R}_n|} + \frac{1}{2}\frac{1}{4\pi\varepsilon_0} \sum_{n=1, n\neq n'}^{N'} \sum_{n'}^{N'} \frac{Z_n Z_{n'} e^2}{|\mathbf{R}_n - \mathbf{R}_{n'}|} \tag{1}$$

where p_i and P_n are the momenta of the ith electron and the nth nucleus, respectively (subscript i refers to the electrons and n to the nuclei), $\mathbf{r}_i$ and $\mathbf{R}_n$ are their position vectors, m is the electron mass, M_n is the mass of the nth nucleus, e is the electron charge, and ϵ_0 is the permittivity. The first two terms of Eq. (1) represent the kinetic energy of the electrons and nuclei, respectively, while the third and fourth terms are the result of Coulomb repulsion between the electrons and Coulomb attraction between electrons and nuclei. Equation (1) is too complex for use in exact computations, especially when one must deal with a large system and, therefore, reasonable approximations must be made in order to make the computations feasible.

One obvious simplification can be made by taking advantage of the fact that there is a large difference in mass between the electrons and nuclei, while the forces on the particles are the same. Therefore, the electrons respond essentially instantaneously to the motion of the nuclei. As a result, electronic and nuclear coordinates in the many-body wave function can be separated, and the nuclei can be treated adiabatically. This separation is the well-known *Born-Oppenheimer approximation*, which reduces the solution of the above many-body problem to that of the dynamics of the electrons in some frozen-in configurations of the nuclei. Thus, the Hamiltonian of the system in the Born-Oppenheimer approximation is given by

$$\mathcal{H} = \sum_{i=1}^{N} \frac{p_i^2}{2m} + \frac{1}{2}\frac{1}{4\pi\varepsilon_0} \sum_{i=1, i\neq j}^{N} \sum_{j=1}^{N} \frac{e^2}{|\mathbf{r}_i - \mathbf{r}_j|} - \frac{1}{4\pi\varepsilon_0} \sum_{n=1}^{N'} \sum_{i=1}^{N} \frac{Z_n e^2}{|\mathbf{r}_i - \mathbf{R}_n|} \tag{2}$$

Based on such simplifications, other approximate schemes have been suggested, a well-known example of which is the Hartree-Fock theory. Suppose that

$$\mathcal{F}\{\Psi_k\} = \epsilon_k \Psi_k \tag{3}$$

where $\mathcal{F}$ is called the *Fock operator* defined below, ϵ_k is the eigenvalue of the operator, and $\Psi_k(\mathbf{x})$ is the spin-orbital (electronic state or wave function), a function that depends on the spatial position $\mathbf{x}$ and spin coordinates of *one* electron. The Fock operator is defined by

$$\mathcal{F}\{\Psi_k\} = \left[-\frac{1}{2}\nabla^2 - \sum_n \frac{Z_n}{|\mathbf{r}_n - \mathbf{R}_n|}\right]\Psi_k(\mathbf{x}) + \sum_{l=1}^{N} \int |\Psi_l(\mathbf{x}')|^2 \frac{1}{|\mathbf{r} - \mathbf{r}'|}\Psi_k(\mathbf{x})\, dx' - \sum_{l=1}^{N} \int \Psi_l^*(\mathbf{x}')\frac{1}{|\mathbf{r} - \mathbf{r}'|}\Psi_k(\mathbf{x}')\Psi_l(\mathbf{x})\, dx' \tag{4}$$

where $*$ denotes a complex conjugate, and the following notation convention has been used: $\int dx' = \sum_{s'} \int d^3\mathbf{r}'$; that is, $\int dx'$ denotes a sum over the spin s' and an integral over the spatial coordinate $\mathbf{r}'$. Here, we have used the standard atomic units (using the Bohr radius, and the electron mass and charge as the basic units) so that, for example, instead of having the usual factor $\hbar^2/(2m)\nabla^2$, we have $1/2\nabla^2$. We use this convention throughout this chapter. Equations (3) and (4) constitute the well-known Hartree-Fock theory, also known as the

self-consistent field theory. Note that the fourth term of Eq. (4) is a *nonlocal* term because, although the operator acts on Ψ_k, its value at $\mathbf{r}$ is determined by the value assumed by Ψ_k at *all* the possible positions $\mathbf{r}'$. Note also that the ground state electron density $\rho(\mathbf{r})$ is given by

$$\rho(\mathbf{r}) = \sum_i |\Psi_i(\mathbf{r})|^2 \tag{5}$$

The Hartree-Fock equation has been a pillar of computation of the electronic structures of atoms and molecules. It is a nonlinear equation that is solved numerically by a sort of self-consistent iterative procedure, the essence of which is as follows. Because solving Eq. (4) yields an infinite spectrum, to obtain the ground state, one must take the lowest N eigenvalues of the spectrum as the electronic states (spin-orbitals of the electrons). These constitute the first approximate solution of Eq. (4) which are then used for constructing the next iteration of the Fock operator. The operator is then diagonalized again to obtain the next approximate solution to the electronic states. The procedure is repeated until convergence has been achieved.

However, computation of properties of solid materials based on the Hartree-Fock equation is an extremely difficult problem and, therefore, over the past several decades, other alternatives have been developed. Notable among them is the density functional theory (DFT) developed by Hohenberg and Kohn [47] and Kohn and Sham [48], which is now widely used for predicting the electronic properties of hard materials. (In recognition of his contributions to this research field, Walter Kohn received the 1998 Nobel Prize for chemistry.) The DFT allows one, in principle, to map *exactly* the problem of a strongly interacting electron gas, in the presence of nuclei, onto that of a *single particle* moving in an effective *nonlocal* potential, and provides an expression for the total energy of the system. The effective potential is not known exactly, but often, for reasons that are not completely understood yet, local approximations (see below) to the nonlocal potential are highly accurate. One can then minimize the total energy of the system that is provided by the DFT, often referred to as the Kohn-Sham total-energy functional, in order to determine its various properties. Beginning in the mid 1970s, the DFT was revitalized because extensive computations indicated that local approximations to the effective nonlocal potential can predict a variety of ground-state properties of materials that are within a few percent of experimental data [49].

Such a computational strategy, which requires only a specification of the ions present (by their atomic numbers), is usually referred to as an *ab initio* method. Although nearly two decades ago most *ab initio* methods, including the DFT, were capable only of modeling systems of a few atoms, they can now model systems with a large number of atoms. Of all the *ab initio* methods, the total-energy pseudopotential technique (see below) based on the DFT, stands alone. This technique, combined with a method developed by Car and Parrinello [50] (to be described below) or a direct method of minimization of the total energy, such as the conjugate-gradient technique (see below), have transformed the way in which people view quantum-mechanical *ab initio* computations and, hence, total-energy pseudopotential calculations because, in addition to their remarkable efficiency, they allow *ab initio* quantum-mechanical computations at *nonzero* temperatures.

Computation of materials' properties based on the DFT involves quantum-mechanical calculations. Over the past two decades, molecular dynamics (MD) simulations, in which atoms and molecules are treated as classical particles and quantum-mechanical effects are neglected, have also become an important tool for investigating and predicting various static as well as dynamical properties of materials. We refer to this method as the classical MD simulation. The increasing popularity of the classical MD methods is due to the fact that, over the past decade, highly efficient simulation techniques, based on massively parallel or vectorized computations (see below), have been developed that allow one to carry out MD simulations with *billions* of atoms [51]. In addition, emerging MD techniques may allow us to simulate a process of interest over much longer times than what was thought to be feasible only a decade ago.

In order to increase the efficiency of *ab initio* computations, one can combine quantum electronic structures with a MD simulation to not only calculate the nuclear positions, but also the electronic charge cloud. This method, pioneered by Car and Parrinello [50], is what

we refer to as the quantum molecular-dynamic (QMD) method. This technique describes a system in which the electronic structure does not, in general, completely relax to the true ground state, but follows it rather closely. The method has been proven to be highly successful for describing many properties of materials. We will describe this method later in this chapter.

Therefore, we wish to provide in this section an overview of the essential concepts and ideas of the *ab initio* quantum-mechanical computations, MD and QMD simulation, and related techniques, such as direct methods of minimizing the total energy of a system, and svectorized and parallelized algorithms for MD simulations. These methods are all used for modeling a (porous or nonporous) material and predicting its effective properties. Our goal is to describe the most recent advances that have been made in these areas. Our discussion is not, and cannot be, exhaustive as comprehensive description of all aspects of each technique would require a book by itself. For example, the review by Abraham [52], and books by Allen and Tildesley [53], Rapaport [54], and Frenkel and Smit [55] describe the classical MD simulations in detail. Instead, we set for ourselves the more modest goal of outlining the most recent advancements in these computational tools, which should enable the interested reader to pursue them further. In what follows, we first describe the classical methods, such as MD simulations, and then describe quantum-mechanical techniques.

3.1. Energy Minimization Techniques

One of the most essential steps in developing molecular models of materials is determining the minimum energy surface of a molecule that consists of many atoms, as the most stable configuration of the molecule corresponds to such an energy state. The difficulty in determining the minimum energy surface lies in the fact that there may be a large number of *local* minima on the energy surface, whereas one is interested in determining the true *global* minimum state. At the same time, studying the behavior of a molecule as its configuration varies from one local minimum energy state to another can shed light on its properties.

Generally speaking, the problem can be stated as follows: Given a function $f(x_1, x_2, \cdots)$, we are interested in determining its true global minimum at which $\partial f/\partial x_i = 0$ and $\partial^2 f/\partial x_i^2 > 0$ for $i = 1, 2, \cdots, n$, with n being the total number of independent variables. In molecular modeling of materials, the function $f(\mathbf{x})$ is the quantum-mechanical or molecular-mechanical energy, with x_i being the Cartesian or the internal states of the atoms in the molecules. The minimization is usually done in Cartesian coordinates, if molecular-mechanical methods, such as MD simulations, are used. If quantum-mechanical methods are used to model a material, then *internal coordinates* are often used in which the position of each atom is described relative to other atoms in the molecule. Internal coordinates are usually written as a Z-matrix that contains one line for each atom. Each line contains information (distances and angles) for each atom in the molecules with respect to other atoms. All the minimization techniques can be classified into two groups:

(i) In the first group are those that use the derivatives of the energy with respect to the coordinates. The derivatives are, of course, useful in the sense that they provide insight into the shape of the energy surface of a molecule. Used properly, the derivatives can also contribute to the efficiency of locating the true global minimum of the energy surface. The derivatives may be computed analytically or numerically, with the former being more accurate and more efficient. Considerable effort has gone into devising efficient methods for computing the first and second derivatives of energy with respect to the coordinates. For quantum-mechanical modeling of materials, the time to compute the derivatives is comparable to that required for the calculation of the total energy [56]. Analytical expressions for the derivatives of many terms that are commonly used in many force fields are also available [57].

(ii) Methods that do not use the derivatives of the energy to locate its global minimum are in the second group. These techniques include the *simplex method* and the *sequential univariate method*.

A geometrical figure with $N + 1$ interconnected vertices is called a simplex [56, 58], where N is the dimensionality of the energy function. For example, a triangular simplex is for a

function of two variables, whereas a tetrahedral simplex (which is not necessarily regular) is associated with an energy function of three variables. Therefore, an energy function of $3N$ Cartesian coordinates has a simplex with $3N + 1$ vertices. However, if internal coordinates are used, then the simplex will have $3N - 5$ vertices. The simplex algorithm requires one vertex more than the total number of degrees of freedom N in order to be able to explore the entire energy surface. The easiest way to see this is to consider an energy function of two variables, $N = 2$. With only two vertices, only the points that are on a straight line can be explored, which does not obviously constitute the entire energy surface.

To use the simplex method, one first generates the vertices of the initial simplex, where the initial configuration of the molecule corresponds to one of these vertices. The remaining points are obtained by simply adding a constant value to each coordinate in turn. Then, the energy of the system is computed at the new point, which gives the relevant vertex its function value. The simplex algorithm determines the location of a minimum by moving on the surface energy, using three basic moves [56]. In order to generate a new point with a lower energy, the method makes its most common move, which is reflecting the vertex with the highest value through the opposite face of the simplex. If this results in a point with an energy lower than any other point in the simplex, then the method performs a *reflection and expansion* move. However, if a local minimum is reached, reflection will not be able to generate a point with a lower energy, in which case the algorithm contracts along one dimension from the highest point. If this move also fails to produce a point with a lower energy, then the simplex contracts in *all* directions, hence pulling around the lowest point. The method is not very efficient as it must perform a very large number of function evaluation. However, if the problem at hand does not require very intensive computations, then the method may work very efficiently. It usually works most efficiently when the initial energy of the system is very high.

The sequential univariate method uses fewer function evaluations than the simplex method and, therefore, it is usually more efficient. In this method, for each coordinate x_i two new structures at $x_i + \delta x_i$ and $x_i + 2\delta x_i$ are generated and their energies are computed. A parabola is then fitted through the three points that correspond to the initial configuration (at x_i) and the two new structures generated from it. The coordinate is then moved to the minimum of the parabola. The algorithm is considered to have converged to the true minimum when the changes in all the coordinates are sufficiently small.

In practice, most simulators that aim to develop a molecular model of a given material use an energy minimization technique that uses the first two derivatives of the energy functions. In addition to making the energy minimization technique more efficient, the two derivatives provide insight into the shape of the energy surface. Because the energy function for almost all practical cases is not quadratic in $\mathbf{x}$, the implication is that, far from the minimum where the harmonic approximation may be valid, many energy minimization techniques fail, even if they work well near the minimum point. This points to the importance of carefully selecting the energy minimization technique. Moreover, every problem requires its own special considerations, implying that there is not a single universal minimization technique for all the problems.

Energy minimization methods that use the derivatives of the energy function can be classified according to the order of the derivatives that they use. Thus, for example, the simplex method can be thought of as a zeroth-order technique. Two first-order techniques that are very popular are the steepest-descent and the conjugate-gradient methods, while the Newton-Raphson method is the simplest second-order method. What follows is a brief description of each of these methods.

3.1.1. The Steepest-Descent Method

One of the best known methods for minimizing a function $f(\mathbf{x})$ of a 2D or 3D variable $\mathbf{x}$ is the *steepest-descent* method, which is the oldest and most straightforward minimization technique. The algorithm proceeds by making an initial guess $\mathbf{x}_1$ and then improving it by

moving in the direction where the functional $f(\mathbf{x})$ appears to change most rapidly. The steepest-descent direction is aligned with the vector

$$\mathbf{v}_1 = -\nabla f(\mathbf{x} = \mathbf{x}_1) \tag{6}$$

To reduce the value of $f(\mathbf{x})$, one travels in the direction of $\mathbf{v}_1$ from $\mathbf{x}_1$ to $\mathbf{x} = \mathbf{x}_1 + b\mathbf{v}_1$ (where b is a scalar parameter), where the function is minimum. Thus, one can, for example, sample $f(\mathbf{x})$ at a number of points along $\mathbf{x}_1 + b\mathbf{v}_1$ in order to determine that value of b that minimizes $f(\mathbf{x})$. This procedure minimizes only the value of the function along a particular line, and thus finds a *local* minimum. To find the global minimum of $f(\mathbf{x})$, one carries out a series of such line minimizations by using $\mathbf{x}_1 + b\mathbf{v}_1$ as the starting point for the next iteration and obtaining $\mathbf{x}_2$. Thus, a series of such vectors $\mathbf{x}_i$ is obtained such that the value of $f(\mathbf{x}_i)$ decreases with increasing i, the interation number.

The steepest-descent method can be made more efficient by taking a step of arbitrary length along the gradient unit vector $\mathbf{a}_i$. Thus, one writes, $\mathbf{x}_{i+1} = \mathbf{x}_i + b_i\mathbf{a}_i$, where b_i is the step size for the ith iteration. In practice, the initial step size has a predetermined value. Then, if the first iteration reduces the total energy, the step size is increased by a factor >1 for the second iteration. The step size in the subsequent iterations is increased by the same manner so long as it results in decreasing the energy. However, if after any iteration the energy increases, it indicates that the algorithm has "jumped" across the "valley" that contains the minimum, in which case the step size is reduced.

Because the direction of the gradient is determined by the largest interatomic forces, the steepest-descent method relieves efficiently the highest energy features in the initial configuration of the system. The method is generally robust even far from the true minimum of the system. However, although this method is *guaranteed* to converge to the true minimum, the rate of convergence can be prohibitively slow. For example, if $f(\mathbf{x})$ has narrow valleys, successive approximations bounce off opposite sides, slowly approaching the bottom. Moreover, after a minimization is performed along a given gradient direction, a subsequent minimization along the new gradient reintroduces errors that are proportional to the previous gradient.

3.1.2. The Conjugate-Gradient Method

Consider now the following symmetric and positive-definite functional form,

$$f(\mathbf{x}) = \frac{1}{2}\mathbf{x} \cdot \nabla \cdot \mathbf{x} \tag{7}$$

Suppose that we wish to minimize $f(\mathbf{x})$ along a direction $\mathbf{d}_1$, starting from $\mathbf{x}_1$. The minimum will be at a point $\mathbf{x}_2 = \mathbf{x}_1 + b_1\mathbf{d}_1$, where b_1 satisfies the following equation

$$(\mathbf{x}_1 + b_1\mathbf{d}_1) \cdot \nabla \cdot \mathbf{d}_1 = 0 \tag{8}$$

A subsequent minimization along a direction $\mathbf{d}_2$ yields $\mathbf{x}_3 = \mathbf{x}_2 + b_2\mathbf{d}_2$, with b_2 satisfying

$$(\mathbf{x}_1 + b_1\mathbf{d}_1 + b_2\mathbf{d}_2) \cdot \nabla \cdot \mathbf{d}_2 = 0 \tag{9}$$

The best choice of b_1 and b_2 for minimizing $f(\mathbf{x})$ along $\mathbf{d}_1$ and $\mathbf{d}_2$ is obtained by differentiating Eq. (7) with respect to b_1 and b_2 and evaluating the result at $\mathbf{x}_3$. This procedure yields two equations,

$$(\mathbf{x}_1 + b_1\mathbf{d}_1 + b_2\mathbf{d}_2) \cdot \nabla \cdot \mathbf{d}_1 = 0 \tag{10}$$

$$(\mathbf{x}_1 + b_1\mathbf{d}_1 + b_2\mathbf{d}_2) \cdot \nabla \cdot \mathbf{d}_2 = 0 \tag{11}$$

However, in order for Eqs. (8) and (9) to be consistent with (10) and (11), one must have

$$\mathbf{d}_1 \cdot \nabla \cdot \mathbf{d}_2 = \mathbf{d}_2 \cdot \nabla \cdot \mathbf{d}_1 = 0 \tag{12}$$

implying that the directions $\mathbf{d}_1$ and $\mathbf{d}_2$ must be conjugate to each other, hence the name conjugate-gradient (CG) method. More generally, the directions $\mathbf{d}_i$ and $\mathbf{d}_j$ must be such that

$$\mathbf{d}_i \cdot \nabla \cdot \mathbf{d}_j = 0, \qquad i \neq j \tag{13}$$

Hence, in the CG method one takes the initial direction to be $-\nabla f(\mathbf{x}_1)$, and the subsequent directions are constructed from a linear combination of the new gradient and the previous direction that minimized $f(\mathbf{x})$. In practice, the new direction $\mathbf{d}_i$ in the ith iteration is obtained from

$$\mathbf{d}_i = \mathbf{v}_i + \omega_i \mathbf{d}_{i-1} \tag{14}$$

where

$$\omega_i = \frac{\mathbf{v}_i \cdot \mathbf{v}_i}{\mathbf{v}_{i-1} \cdot \mathbf{v}_{i-1}} \tag{15}$$

and $\omega_1 = 0$; note that, $\mathbf{v}_i = -\nabla f(\mathbf{x}_i)$. It has also been observed that in some cases a better estimate of ω_i is given by

$$\omega_i = \frac{(\mathbf{v}_i - \mathbf{v}_{i-1}) \cdot \mathbf{v}_i}{\mathbf{v}_{i-1} \cdot \mathbf{v}_{i-1}} \tag{16}$$

Other formulas for the parameter ω_i have also been suggested, such as those due to Powell [59] (which is available in the IMSL library), Shanno and Phua [60] (which is available in the NAG library), and Gilbert and Nocedal [61]; see Adams and Nazareth [62] for a comprehensive discussion.

In the CG method, locating the true global minimum of a function is *guaranteed*. The reason is that because minimization along the conjugate directions are independent, each iteration reduces the dimensionality of the vector space by 1. Thus, one reaches the point at which the dimensionality of the function space is zero, that is, there are no new directions left along which one can minimize the function and, therefore, the trial vector must be at the position of the true minimum. The number of the iterations needed to reach the true minimum is, therefore, *at most* equal to the dimensionality of the vector space, although in practice it usually takes far fewer iterations to converge to the true solution.

3.1.3. The Newton-Raphson Method and Its Variants

In the Newton-Raphson (NR) method, one writes down a Taylor series expansion for the function, $f'(\mathbf{x}) = f'(\mathbf{x}_i) + (\mathbf{x} - \mathbf{x}_i)f''(\mathbf{x}_i) + \cdots$. Because at the true minimum, $f'(\mathbf{x}) = 0$, one obtains the well-known iterative scheme,

$$\mathbf{x}_{i+1} = \mathbf{x}_i - f'(\mathbf{x}_i) \cdot [f''(\mathbf{x}_i)]^{-1} \tag{17}$$

so that both the first-order and second-order derivatives of the energy function must be calculated. The Hessian matrix $f''(\mathbf{x}_i)$, usually denoted by $\mathbf{H}(\mathbf{x}_i)$, must be positive definite. Computing the inverse of $\mathbf{H}(\mathbf{x}_i)$ for a molecule with a large number of atoms is costly, as the computation time grows as N^3 if the matrix is dense. In addition, if the energy function has many local minima or maxima, the Hessian may become *ill-conditioned*, that is, have large maximal-to-minimal eigenvalue ratio, or *singular*, having a zero eigenvalue. For this reason, the NR method is usually most efficient for relatively small molecules.

To address the aforementioned problems with the NR method, a few other methods have been developed. For example, in the *quasi-Newton* (QN) method [63–68], one avoids using the actual Hessian and, instead, builds-up curvature information as the algorithm proceeds. To see how the QN method works, we first generalize the above NR method by expanding $f(\mathbf{x})$ locally along a search vector $\mathbf{s}$, $f(\mathbf{x}_i + \mathbf{s}_i) = f(\mathbf{x}_i) + \mathbf{g}(\mathbf{x}_i)^{\mathrm{T}}\mathbf{s}_i + 1/2\mathbf{s}_i^{\mathrm{T}}\mathbf{H}(\mathbf{x}_i)\mathbf{s}_i + \cdots$, where T denotes the transpose operation. Minimizing the right-side of this equation leads to the solution of a set of linear equations, similar to Eq. (17), with $\mathbf{H}_i\mathbf{s}_i = -\mathbf{g}_i$, and, $\mathbf{x}_{i+1} = \mathbf{x}_i - \mathbf{H}_i^{-1}\mathbf{g}_i$, so that a search vector, $\mathbf{s}_i = -\mathbf{H}_i^{-1}\mathbf{g}_i$, is used. If, $\mathbf{A} = \mathbf{H}^{-1}$, then the QN approximations to $\mathbf{A}$ are derived. In addition, for large systems $\mathbf{A}$ (an $N \times N$ matrix) can be very large, so that it is formulated through many vector operations, avoiding explicit storage of the entire matrix.

The QN method specifies the property that the new approximation $\mathbf{A}_{i+1}$ must satisfy: $\mathbf{A}_{i+1}\mathbf{p}_i = \mathbf{y}_i$, with, $\mathbf{p}_i = \mathbf{x}_{i+1} - \mathbf{x}_i$, and, $\mathbf{y}_i = \mathbf{g}_{i+1} - \mathbf{g}_i$. Then, one updates the matrix $\mathbf{A}$ by a formula that is written as $\mathbf{A}_{i+1} = \mathbf{A}_i + \mathbf{U}_i(\mathbf{p}_i, \mathbf{y}_i, \mathbf{A}_i)$. Various formulas have been proposed for $\mathbf{U}_i$ [63–68]. One of the most successful ones is due to Broyden, Fletcher, Goldfarb, and Shanno [69]:

$$\mathbf{A}_{i+1} = \mathbf{A}_i - \frac{\mathbf{B}_i\mathbf{p}_i\mathbf{p}_i^{\mathrm{T}}\mathbf{A}_i^{\mathrm{T}}}{\mathbf{p}_i^{\mathrm{T}}\mathbf{A}_i\mathbf{p}_i} + \frac{\mathbf{y}_i\mathbf{y}_i^{\mathrm{T}}}{\mathbf{y}_i^{\mathrm{T}}\mathbf{p}_i} \tag{18}$$

In addition, effective matrix/vector products have been developed to minimize memory requirements, needing only $O(N)$ memory to store the successive pairs of update vectors $\mathbf{p}_i$ and $\mathbf{y}_i$, hence making them very effective for large-scale multivariate minimization [70]. This method has also been extended to constrained optimization [71–73].

In addition to the QN method, one may also use the so-called *truncated-Newton* (TN) method [74]. The idea behind this method is that for a very large minimization problem, one does not have to have a very accurate solution of Eq. (17). That is, one can allow for a *nonzero* residual, $r_i = |\mathbf{x}_{i+1} - \mathbf{x}_i|$, as, far from the true minimum, even an approximate (but not very accurate) solution allows the algorithm to proceed toward the true minimum. It is only in the vicinity of the true minimum that the solution must be very accurate. Thus, as the minimization process advances toward the true minimum, one can impose smaller and smaller residuals on the system. To accelerate the convergence of the method, one may use [75, 76] *preconditioning*, which modifies the equation, $\mathbf{H}_i\mathbf{s}_i = -\mathbf{g}_i$, derived above by multiplying both sides by the inverse of a closely related matrix, $\mathbf{M}_i$, called the *preconditioner*. The matrix $\mathbf{M}$ is typically a sparse symmetric matrix that can rapidly be assembled. If the eigenvalues of $\mathbf{M}_i^{-1}\mathbf{H}_i$ are clustered, or if this matrix is approximately an identity matrix, then the convergence of the method improves.

Once the global minimum energy of a molecule has been determined, the corresponding molecular configuration is combined with a MD method in order to enter into the modeling the pressure and temperature of the system. Therefore, we now describe the basic concepts and ideas of MD simulations and the most recent advances in this important area. Energy minimization is also an important part of quantum-mechanical methods, to be described below.

3.2. Classical Molecular Dynamics Simulation

Historically, the first true MD simulation seems to have been carried out by Alder and Wainwright [77], who studied a system with only a few hundreds of hard-sphere particles and discovered a fluid–solid phase transition. At the same time, Wood and Parker [78] investigated the properties of simple fluids using the Monte Carlo method. Rahman [79] was apparently the first to carry out MD simulations using the Lennard-Jones potential (see below for a description of this potential). Unlike Alder and Wainwright, Rahman's work was the first to involve particles with smoothly varying potentials. He computed the diffusion coefficient and pair-correlation function for liquid argon and showed them to be in very good agreement with the experimental data. These pioneering works opened the way for simulation, and hence understanding, of many-body systems. Later work by Verlet [80], whose method helped MD simulations to become much more efficient (see below), by Alder and Wainwright [81], who discovered, unexpectedly, an algebraic long-time tail in the velocity autocorrelation functions of hard sphere (a discovery that intensified further the interest in MD simulations), and by Rahman and Stillinger [82], who addressed simulations of such complex molecules as liquid water, firmly established the classical MD simulations as an everyday tool of studying fluids and materials.

The 1970s witnessed further improvements in methodologies and algorithms for MD simulations. For example, Evans and Murad [83] succeeded in developing an algorithm for computing molecular rotations (Ciccotto et al. [84] made further improvement to this method), and Bennett [85] and Torrie and Valleau [86] developed efficient methods for measuring the free energies (see also Frenkel and Ladd [87]), and so on. Much more progress was made in the 1980s when Andersen [88] and Parinello and Rahman [89] developed methods for

carrying out MD simulations under constant pressure and constant temperature, and Nosé [90] developed equations for simulating constant-temperature MD simulations by introducing additional degrees of freedom (his equations were simplified by Hoover [91]; see below). At the same time, the advent of vector computers further motivated the search for methods that could take advantage of vectorization techniques, especially those that could be used with the Verlet algorithm. All of these advances took MD simulations to a stage where, by mid 1980s, they could be used for studying *nonequilibrium* systems. Abraham et al. [92] studied, using MD simulations, the incommensurate phase of Krypton on graphite using more than 160,000 atoms (a "revolution" for its time), and Car and Parinello [50] succeedded in combining MD simulations and electronic structure calculations (see below). The first million-particle MD simulations were carried out by Swope and Andersen [93] who studied homogeneous nucleation of crystals in a supercooled (i.e., below the freezing point) atomic liquid. Their study was important not only because of the large number of atoms that had been used, but also because it showed that certain physical phenomena can be reproduced in the MD simulations only when the system's size is large enough.

Generally speaking, two types of classical MD simulations can be carried out. Equilibrium MD simulations are suited for systems that can, in principle, be treated by statistical mechanics. This type of MD simulation can yield equilibrium properties of materials. Nonequilibrium MD techniques are appropriate for systems that are under the influence of an external driving force, and are most suitable for computing the transport properties of a system. We first describe and discuss general concepts and ideas of MD simulations that are applicable to both the equilibrium and nonequilibrium methods. Later in this chapter we will describe those aspects of nonequilibrium MD technique that are different from the equilibrium methods.

3.2.1. Basic Principles

So far as nanoporous materials are concerned, the goal in any MD simulation is twofold.

(i) One would like to describe by MD simulations the material and the phenomena that occur in it, the practical consequences of which are at *macroscopic* length scales, whereas the MD method considers the system at *atomic* scales.

(ii) One aims to demonstrate that, despite the disparity between the length scales at which MD simulations can be carried out and the practical length scales of interest, not only do the simulation results provide insights into the phenomena of interest, but also that the results are, in fact, in agreement with the experimental measurements.

The fundamental problem facing MD simulation and, more generally, atomistic description of *any* phenomenon in nanoporous materials, is one of length and time scales. Consider, as an example, silicon, a material with tremendous technological significance, not only to the semiconductor industry, but also to preparing nanoporous membranes for separation and purification processes. Silicon's single crystals with a variety of orientations are inexpensive, thus making numerical predictions amenable to experimental verification. Silicon is also very brittle, its crystal structure is well-known, and considerable effort has been expended in developing classical interatomic potentials suitable for use in its modeling by the MD method; we will describe many of such potentials later in this chapter. Therefore, silicon provides an ideal testing ground for the MD simulation of a material and direct comparison of its results with the experimental measurements. Suppose, for example, that we wish to consider a silicon sample with a length and width that are a few centimeters each and a thickness of only one millimeter (the typical dimensions of a nanoporous membrane). Such a sample contains of the order 10^{22} atoms. The duration of an actual experiment may range anywhere from a few microseconds to several minutes, whereas the largest simulations that are currently feasible allow one to follow what happens to a sample of about 10^8 atoms for about 10^{-9} seconds! Therefore, direct MD simulations of such a sample would require *eighteen* orders of magnitude increase in computer power over what is currently available, a truly daunting task.

Therefore, the question is, how does one compare the simulation results with the experimental observations and measurements? An appealing approach for doing this would be

to merge atomistic simulations with continuum modelling [3, 94–98]. For example, one may use an atomistic description of that area in the system where most, if not, all the interesting phenomena take place, and combine that with the continuum models for describing the system everywhere else. This approach can potentially solve the problem of length scales, but not that of the timescales. We describe below what has been accomplished so far without using such a *multiscale approach*.

Given the enormity of the problem of computer simulation of many phenomena of interest in nanoporous materials at the atomic scale, the goal in the MD simulations should *not* be performing the largest simulation possible, but constructing the *smallest* one that would be capable of providing insightful answers to specific physical questions. In fact, certain features of many phenomena in nanoporous materials may profitably be studied by relatively small simulations, involving only thousands or tens of thousands of atoms.

Another important point about many phenomena that occur in nanoporous materials is their severely nonequilibrium nature. The question, then, is whether it is possible that no classical interatomic potential can provide a realistic description of the material that is investigated by the MD simulations. If this possibility does exist, then, it is entirely possible that even the DFT would fail as well. Therefore, only a detailed and patient comparison of theory and experiment may be able to settle such issues. This also implies that one should not expect MD simulations to provide "easy" (i.e., without much effort, patience, and efficient computational strategy) predictions for nanoporous materials.

Molecular dynamics simulation of any phenomenon consists of integration of Newton's equation of motion for a system of N particles that represent the material or the system under study. Therefore, the MD method is a way of simulating the behavior of a system as it evolves with time because, unlike the Monte Carlo (MC) method, in the MD simulations the system moves along its physical trajectory. The main advantage of the MD method over the MC technique is that, not only does it provide a method for computing the static properties of a system but it also allows one to calculate and study the dynamical properties of many nanoporous materials that are of interest to us in this chapter.

We consider a collection of N particles in a $L_x \times L_y \times L_z$ simulation cell. The particles interact with each other, and for simplicity we assume for now that the interaction force can be written as a sum over pair forces $\mathbf{F}(r)$, the magnitude of which depends only on r, the distance between the particle pairs. Thus, the force acting on any particle i is given by

$$\mathbf{F}_i(\mathbf{r}^N) = \sum_{j=1, j\neq i}^{N} F(|\mathbf{r}_i - \mathbf{r}_j|)\hat{\mathbf{r}}_{ij} \tag{19}$$

where $\mathbf{r}^N = \{\mathbf{r}_1, \mathbf{r}_2 \cdots, \mathbf{r}_N\}$ is the position coordinates of all the particles, and $\hat{\mathbf{r}}_{ij}$ is a unit vector along $\mathbf{r}_j - \mathbf{r}_i$, pointing from particle i to j. Then, the equation of motion for particle i is given by

$$m_i \frac{d^2\mathbf{r}_i(t)}{dt^2} = \mathbf{F}_i(\mathbf{r}^N) + \mathbf{F}_e \tag{20}$$

where m_i is the atomic mass of particle i, and $\mathbf{F}_e$ represents all the external forces that are imposed on the system, either by nature (for example, the gravitational force) or by the experimentalist (e.g., an external pressure gradient applied to the system). Molecular dynamics consists of writing Eq. (20) for all the N particles of the system and integrating them numerically and simultaneously (as the equations are coupled through the force $\mathbf{F}_i$). The solution of this set of equations describes the time evolution of the system. If the forces between the particles depend only on their relative positions, then the system's energy and momentum are *automatically* conserved. To check whether the system has reached a steady state, if one exists, quantities such as the kinetic energy are computed and their variations with the time are monitored. When these quantities no longer vary appreciably with the time, then attainment of the steady state has been confirmed. The time to reach a steady state depends on the initial state of the system and how far it is from its steady state.

Although the MD approach is, in principle, a rigorous method, in practice (and similar to almost all computational strategies for studying a phenomenon), it is only an approximate

technique. Thus, it should be used with considerable care. Some of the problems that one must pay particular attention to are as follows.

(i) The exact interaction potentials between the particles are not, in almost all cases, known and, therefore, one must use approximate expressions for describing these potentials. In principle, quantum-mechanical calculations can be used for determining these forces, but such computations can be subject to errors. Typically, the interaction potentials or forces are written in terms of several parameters that are determined either by *ab initio* computations or by fitting the results to experimental data (see below).

At atomic scale, the interactions are either of intramolecular or intermolecular type. We will discuss the intramolecular interactions separately and, for now, briefly describe the intermolecular interactions. In many MD simulations, the interaction potential between a pair of particles, the centers of which are a distance r apart, is represented by the classical Lennard-Jones (LJ) potential, given by

$$U(r) = 4\epsilon\left[\left(\frac{\sigma}{r}\right)^{12} - \left(\frac{\sigma}{r}\right)^{6}\right] \tag{21}$$

where ϵ is the energy parameter of the potential (the maximum energy of attraction between a pair of molecules), or the LJ well depth, and σ is the size parameter (or the distance at which the LJ potential passes through zero), also called the *collision diameter*. Note that σ is not the same as molecular diameter of the molecules, although the two quantities are usually close to each other. In Eq. (21), the r^{-12} term represents a hard-core or repulsive potential, whereas the r^{-6} term is the attractive part. Although the attractive part of the LJ potential can be derived by quantum-mechanical considerations, the form of the repulsive part has been selected only for computational convenience. The force $\mathbf{F}(r)$ between the particles is then given by $\mathbf{F}(r) = -\nabla U(r)$.

The steep form of the repulsive part of $U(r)$ has a quantum origin in the interaction of the electron clouds with each other. The Pauli exclusion principle affects this, and this effect is also combined with the internuclear repulsions. On the other hand, London or dispersion force is responsible for the weak bonding attraction that, in quantum mechanics, corresponds to electron correlation contributions. In other words, large fluctuations of the electron density distribution around a nucleus generate a transient dipole moment and induce charge reorientation, which are London forces. One should also note that as $r \to \infty$, the potential $U(r)$ vanishes rapidly, so that the van der Waals (vdW) force is short-ranged. Hence, for computational convenience, vdW energies and forces are computed for pairs of atoms only within some *cutoff radius* r_c; for $r > r_c$, the forces are assumed to be zero.

If the system contains solid walls, then the interactions between the atoms in the system and those of the walls must also be taken into account. A well-known potential due to Steele [99] has been used in many simulations (although Steel's potential represents a kind of a mean-field approximation, as it assumes that the wall is smooth and structureless):

$$U_w = 2\pi\rho_w\epsilon_{sw}\sigma_{sw}^2\Delta\left[\frac{2}{5}\left(\frac{\sigma_{sw}}{z}\right)^{10} - \left(\frac{\sigma_{sw}}{z}\right)^{4} - \frac{\sigma_{sw}^4}{3\Delta(z+0.61\Delta)^3}\right] \tag{22}$$

where ϵ_{sw} and σ_{sw} are the energy and size parameters that characterize the interactions between the atoms in the system and those of the walls, z is the vertical distance from the wall, ρ_w is the density of the wall's atoms, and Δ is the distance between the atomic layers within the wall.

The accuracy of the MD method depends to a large extent on the accuracy of the interaction potentials used in the simulation. Lennard-Jones type potentials, as given by Eq. (21), are too simple to represent complex atoms and molecules. To remedy the situation, one can write the LJ potential in a more general form, $U(r) = -A/r^6 + B/r^{12}$, and fit the parameters A and B such that certain results of the MD simulations reproduce the experimental data. This procedure has been reasonably accurate for relatively simple molecules and might, in some cases, provide qualitative insight into the behavior of materials. More accurate fits

over broader ranges of the parameters can be obtained through the Buckingham potential [100, 101]:

$$U(r) = -\frac{A}{r^6} + B\exp(-Cr) \tag{23}$$

Note that the parameters A, B, and C must be determined separately for *each pair* of atoms.

There are several methods for fitting the parameters. In one approach, the coefficients are determined by requiring that an energy minimum E_{ij} should occur at a certain distance r_{ij}^0, taken to be the sum of the vdW radii of atoms i and j. For example, for the LJ potential, one obtains, $A_{ij} = 2(r_{ij}^0)^6 E_{ij}$ and $B_{ij} = (r_{ij}^0)^{12} E_{ij}$. The vdW radii can actually be estimated from the measured x-ray contact distances, quantities that reflect the distance of closest approach in the crystal and are smaller than the sum of the vdW radii of the atoms involved [102]. The parameters E_{ij} and r_{ij}^0 are then set as (the Lorentz-Berthelot rule), $E_{ij} = \sqrt{\epsilon_i \epsilon_j}$ and $r_{ij}^0 = \frac{1}{2}(r_i + r_j)$.

The second fitting procedure is based on the Slater-Kirkwood equation. The coefficient A_{ij} is determined as [103–105]:

$$A_{ij} = \frac{365\alpha_i\alpha_j}{(\alpha_i/N_{ei})^{1/2} + (\alpha_j/N_{ej})^{1/2}} \tag{24}$$

where α_i and N_{ei} are, respectively, the measured polarizability and the number of outer-shell electrons of atom i. Given the above estimate for A_{ij}, the coefficient B_{ij} is given by, $B_{ij} = \frac{1}{2}A_{ij}(r_{ij}^0)^6$. In addition, a more complex potential,

$$U(r_{ij}) = -\frac{A_{ij}}{(r_{ij} + c_1 r_{ij}^0)^7} + \frac{B_{ij}}{(r_{ij} + c_1 r_{ij}^0)^7[r_{ij}^7 + c_2(r_{ij}^0)^7]} \tag{25}$$

has also been used [106], where c_1 and c_2 are two constants.

However, many materials of technological interest have strong and specific chemical interactions that cannot be described by simple, pairwise additive potentials, such as the LJ- or Buckingham-type potentials. Thus, more sophisticated computations must be undertaken for determining the interaction potentials. We will come back to this issue later in this chapter.

(ii) Molecular dynamics suffers from the same problem that every computer simulation of a physical system suffers from, namely, while the intention is to simulate a real system that, at least in atomic units, is very large, the simulated system is of finite size. The finite-size effect can be particularly severe if there are correlations in the system (as is the case with almost any physical system). If the correlation length is much smaller than the linear size of the system, finite-size effects do not pose any significant problem. If the correlation length is much larger than the linear size of the system, then one can use finite-size scaling for extrapolating the results for a system of finite size to one with an infinite size (although finite-size scaling is usually used for second-order phase transitions, and the MD methods are not used very often for studying such transitions, as the computations would be very intensive). The intermediate case, in which the correlation length is not too large or too small, is usually addressed by using the periodic boundary conditions, as the finiteness of the system is manifested through its boundaries (an infinite system does not have any boundary!). Using periodic boundary conditions means that the finite simulation cell is embedded in an infinite system such that it is surrounded by replicas of itself on all sides. In that case,

$$\mathbf{F}(\mathbf{r}_i - \mathbf{r}_j) = \sum_{\mathbf{n}} \mathbf{F}\left(\left|\mathbf{r}_i - \mathbf{r}_j + \sum_{k=1}^{3} \mathbf{V}_k n_k\right|\right) \tag{26}$$

where $\mathbf{V}_k$ are vectors along the edges of the rectangular simulation cell. The first sum on the right-hand side of Eq. (26) is over all vectors $\mathbf{n} = (n_1, \cdots, n_k)$. The force $\mathbf{F}$ is along the line connecting particle i and the image particle $\mathbf{r}_j - \sum_{k=1}^{3} \mathbf{V}_k n_k$. In principle, calculating terms of this inifinite sum until it converges to a well-defined value is a difficult task, but methods have been developed for computing such sums. Use of periodic boundary conditions

also has a negative side effect: In a periodic system the angular momentum is *not* conserved, as the periodic boundary conditions break the spherical symmetry of the interactions.

(iii) When time-averaged properties are calculated, the averaging is clearly carried out over a finite-time period. There is, however, a limitation in time as a result of the finite number of integration steps that one can carry out. Finite size of the system also limits the time, especially if the particles (in, e.g., simulation of liquids or gases) travel more than half the linear size of the simulation cell.

(iv) In any MD simulation, there is always a competition between the speed of the computations and their accuracy. Normally, as the size of the time step increases, so also does the inaccuracy in the simulation results. Therefore, for any MD simulation, there is an optimal choice of the time step.

(v) The MD method is based on deterministic mechanics—Newton's second law of motion. In addition to the usual limitations of deterministic mechanics, only the nuclear motion of a molecule and its interaction with the surrounding are followed in a MD simulation, and electronic motion and quantum effects are neglected. Hence, in the strict sense, MD simulation is only an approximation that, however, is an excellent one for a wide range of materials. It is not, however, suitable if there are reactions in the system that involve rearrangements, such as bond formation, fracture, polarization, and chemical bonding of metal ions. In addition, MD simulations are not suitable for systems that are at low temperatures, where the energy gaps among the discrete levels of energy that are dictated by quantum mechanics are much larger than thermal energy available to the system. Under such conditions, the system is confined to a few low-energy states.

Using a harmonic approximation, one can obtain estimates for the characteristic motions for which the classical MD (i.e., deterministic Newtonian mechanics) is applicable. Because the quantized energies are separated by $\hbar\nu$, where $\hbar$ is the Planck's constant and ν is the vibrational frequency, the classical MD approach will be inappropriate at relatively high frequencies with $\nu \gg k_B T/\hbar$ or $\hbar\nu/(k_B T) \gg 1$, where k_B is the Boltzmann's constant. The critical frequency ν_c for which $\hbar\nu/(k_B T) \simeq 1$ is about, $\nu_c \simeq 6.0 \times 10^{12}$ s^{-1}, or 6 ps^{-1}. Thus, vibrational modes with characteristic timescales that are of the order picosecond or larger can be treated by the classical MD simulations.

From the computational viewpoint, the most intensive part of any MD simulation is calculation of the forces between the particles, which accounts for 70–90% of the total time. Periodic boundary conditions create a problem for evaluation of the forces between the particles, as in a periodic system not only does a particle interact with other particles in the simulation cell but also with those in the images of the system that surround it, and thus, in principle, one must sum over an infinite number of interactions. However, in many cases the force between two particles decays rapidly as the distance between them increases and, therefore, the particles that are far from any given particle, whether they are in the simulation cell or in its images, do not contribute significantly. If the force between two particles can be ignored for distances that are larger than half the system's linear size, then one can use the *minimum image convention* according to which, for each particle in the system, one takes into account only the interactions with the nearest copy of each of the remaining particles, implying that each infinite sum over all the images is replaced by a single term. The potential will, of course, no longer be analytic, but the discontinuities will not be important if the potential is small for distances that are larger than half the system's linear size.

In practice, what is done in most cases is cutting the interactions off at a distance r_c. Typically, r_c is set to be a multiple of the effective molecular diameter of the largest atom in the simulations and, therefore, it is usually smaller than half the system's linear size. If this approach is taken, then at every step of the integration one must check, for any particle i, the distances of all other particles from i to see whether they are at a distance larger or smaller than r_c. This search constitutes one of the three important tasks in any MD simulation (the other two being computing the forces and integrating the equations of motion). There are efficient methods of doing this that we will discuss below. We must point out, however, that cutting off the interaction potentials violates energy conservation, although if r_c is selected

carefully, the effect will be small. Moreover, by shifting the interaction potentials one can avoid violation of energy conservation altogether by writing

$$U(r) = \begin{cases} U_o(r) - U_o(r_c) & \text{if } r \le r_c \\ 0 & \text{if } r > r_c \end{cases} \tag{27}$$

where $U_o(r)$ represents the original interaction potential to be used. However, this shift does not affect the force resulting from the shifted potential; it remains discontinuous at r_c. In order to make the force also continuous at the cutoff point, we write

$$U(r) = \begin{cases} U_o(r) - U_o(r_c) - (r - r_c)\left[\dfrac{dU_o(r)}{dr}\right]_{r=r_c} & \text{if } r \le r_c \\ 0 & \text{if } r > r_c \end{cases} \tag{28}$$

This algorithm was first suggested by Stoddard and Ford [107]. The actual number of interacting particles (i.e., those that are within a sphere of radius r_c centered at the center of a given particle) is a function of the molecular density. For example, in the simulation of a typical liquid state using the LJ potential, the computation of a single pair-interaction requires about 30–40 floating-point operations. Therefore, a complete force calculation requires of the order 2000 floating-point operations per particle, still computationally intensive, but much more efficient than a full N-body calculation. Let us point out that the cut-and-shift procedure cannot be used if electric and gravitational forces are operative in the system, as they decay only as $1/r$. Such cases must be treated separately (see below).

If the LJ potential is used, then the sites of the FCC lattice are usually used as the initial positions of the atoms, as the FCC lattice represents the ground state of the LJ potential, although any other initial positions can also be used. The initial velocities v are drawn from a Maxwell-Boltzmann distribution with the specified temperature T:

$$f(v_x, v_y, v_z) = \left(\frac{m}{2\pi k_B T}\right)^{3/2} \exp(-mv^2/2k_B T) \tag{29}$$

where $v^2 = v_x^2 + v_y^2 + v_z^2$. This is done by drawing the x, y, and z velocity components for each particle from a Gaussian distribution. After generating the initial momenta, the average momentum per particle $\langle \mathbf{p} \rangle$ is computed and subtracted from the individual momentum $\mathbf{p}_i$ of each particle. This ensures that the total initial momentum of the system is zero.

Given the initial configuration of the molecular system and the velocities, an initial *equilibration* simulation is carried out before the quantities of interest are actually computed. In the initial simulations, the kinetic and potential energies fluctuate and an exchange takes place between them. If both of these energies, as well as the total energy, converge, the system can be considered as stable. On the other hand, it is well-known that the individual MD trajectories are *chaotic*, with the chaos being characterized by a *Lyapunov exponent*. This chaotic motion is, in fact, an *initial* period of exponential growth in the root-mean-square coordinate deviation of the atoms and represents a *local* instability. The theory of chaotic systems tells us that the trajectory error of compact systems (those with a finite phase space) reaches saturation where the magnitude of the deviations corresponds to a value that is system-dependent, hence helping the MD simulations reach a stable behavior.

3.2.2. The Verlet Algorithm and Its Variants

Once the initial configuration of the system has been prepared, the integration of Newton's equation of motion begins. In a typical MD simulation, the time that the computer program spends for integrating the equations of motion is about 2–3% of the total time. However, accurate integration of the equations of motion is the most important part of the computations. Various methods have been proposed for achieving this goal, a detailed discussion of which can by itself be the subject of a minireview. One frequently used procedure is due to Verlet [80]. The basic method was first proposed by Störmer [108] in 1907, but was

adapted 60 years later by Verlet! In Verlet's method, the algorithm for integrating the equation of motion for a single particle, which is subjected to a force **F** that depends only on the particle's position, is given by

$$\mathbf{r}(t+\Delta t) = 2\mathbf{r}(t) - \mathbf{r}(t-\Delta t) + \frac{\Delta t^2}{m^2}\,\mathbf{F}(\mathbf{r}) \tag{30}$$

where $\mathbf{r}(t)$ is the position of the particle at time t, and Δt is the integration time step (note that $t = n\Delta t$, where n is an integer). This is a two-step method, as one needs both $\mathbf{r}(t)$ and $\mathbf{r}(t-\Delta t)$ in order to compute $\mathbf{r}(t+\Delta t)$. A one-step method that, from a computer storage view point, may be preferable can also be devised (see below). The error per time step is usually $O(\Delta t^4)$, but in some cases can be as large as $O(\Delta t^2)$, which is still very accurate. To begin the integration, the positions at $t = \Delta t$ are first computed from

$$\mathbf{r}(\Delta t) = \mathbf{r}(0) + \Delta t\mathbf{v}(0) + \frac{1}{2m}\Delta t^2\,\mathbf{F}[\mathbf{r}(0)] + O(\Delta t^3) \tag{31}$$

which, together with the initial positions, provide us with the two previous positions that we need. The particles' velocities at any time t are calculated from

$$\mathbf{v}(t) = \frac{\mathbf{r}(t+\Delta t) - \mathbf{r}(t-\Delta t)}{2\Delta t} + O(\Delta t^2) \tag{32}$$

which is a standard finite-difference approximation to **v**. If periodic boundary conditions are used, then one must check whether any particle has left the simulation cell in the last integration step, in which case the particle must be translated back over a lattice vector $\mathbf{V}_k$ to keep it inside the cell. Clearly, the velocity evaluation step must be carried out *before* such a translation.

The Verlet algorithm, in its original form, is sometimes susceptible to error. A modified algorithm that is the exact arithmetic equivalent of the original Verlet algorithm, but is far less susceptible to numerical errors, is the *leapfrog* algorithm [109] by which one computes the velocity of a particle at midpoint between t and $t + \Delta t$,

$$\mathbf{v}\left(t+\frac{1}{2}\Delta t\right) = \mathbf{v}\left(t-\frac{1}{2}\Delta t\right) + \frac{\Delta t}{m}\,\mathbf{F}[\mathbf{r}(t)] \tag{33}$$

from which the position of the particle is calculated,

$$\mathbf{r}(t+\Delta t) = \mathbf{r}(t) + \Delta t\,\mathbf{v}\left(t+\frac{1}{2}\Delta t\right) \tag{34}$$

In another modification of the Verlet algorithm, the so-called *velocity-Verlet* algorithm [110], one calculates the position and velocity of a particle from

$$\mathbf{r}(t+\Delta t) = \mathbf{r}(t) + \Delta t\mathbf{v}(t) + \frac{\Delta t^2}{2m}\,\mathbf{F}[\mathbf{r}(t)] \tag{35}$$

$$\mathbf{v}(t+\Delta t) = \mathbf{v}(t) + \frac{\Delta t}{2m}\{\mathbf{F}[\mathbf{r}(t+\Delta t)] + \mathbf{F}[\mathbf{r}(t)]\} \tag{36}$$

This algorithm is most stable with respect to the finite precision arithmetic and requires no additional computations in order to calculate the velocities. Finally, in the *position-Verlet* algorithm [111–113], one has

$$\mathbf{r}(t+\Delta t) = \mathbf{r}(t) + \Delta t\mathbf{v}(t) + \frac{\Delta t^2}{2m}\mathbf{F}\left(t+\frac{1}{2}\Delta t\right) \tag{37}$$

$$\mathbf{v}(t+\Delta t) = \mathbf{v}(t) + \frac{\Delta t}{m}\mathbf{F}\left(t+\frac{1}{2}\Delta t\right) \tag{38}$$

An important property of the Verlet algorithm and its leapfrog modification is that the energy that one calculates when using these integration methods does not exhibit any drift

in the total energy. This important and desirable stability is due to the fact that the Verlet algorithm is time-reversible and, therefore, does not permit steady increase or decrease of the energy for periodic systems. An important time scale in the simulations is the so-called *Poincaré timescale*, which is the time after which a system that starts out with a random configuration returns to its initial configuration. The total time that one can integrate in any MD simulation is, however, much smaller than the Poincaré time, and, therefore, there is the possibility of having an increasing error in the calculated energy as the equations of motion are integrated for larger times. However, the Verlet algorithm has an additional property called *symplecticity*. This property gives rise to conserved quantities, and in particular Sanz-Serna [114] showed that, with this property present in the integration procedure, the discrete analogue of the total energy (in numerical integrations one can compute only discrete analogues of the properties of interest) is *rigorously* conserved and that the discrete analogue of the total energy deviates from its continuum (i.e., actual) counterpart by an amount that is of the order $O(\Delta t^k)$, where k is some relatively large integer. Therefore, the Verlet algorithm and its leapfrog version hold the deviations of the energy bounded. In addition, the position-Verlet algorithm has been shown to be preferable in large time-step computations [112, 113, 115]. Such desirable properties are the main reason for the popularity of the Verlet algorithm and its modifications.

3.2.3. Resonance, Efficient Simulation, and Multiple Time-Step Algorithms

In practice, every effort must be made to make MD simulations as efficient as possible. For example, introduction of a cutoff distance r_c described earlier increases the efficiency, as do updating the nonbonded pair list infrequently and reducing the number of degrees of freedom by constraining certain molecular regions in the system. However, the most important factor in determining the efficiency of MD simulations is perhaps the size of the time step Δt used in the integration of the equations of motion. The stability and desired accuracy of the simulation are the deciding factors in setting Δt. If Δt is too large, instability, manifested by uncontrolled growth of the atoms' positions and energies, will develop. One must, however, keep in mind that the instability emerges only over hundreds of thousands of picoseconds or longer periods of time.

Additional complication may arise due to resonance artifacts. Nonphysical resonance—an artifact of a symplectic integrator (e.g., the Verlet algorithm)—can occur for a periodic motion with natural frequency ω, where ω is related by integers m and n to the forcing frequency $(2\pi/\Delta t)$ by [69], $n\omega/m = 2\pi/\Delta t$, where n is the resonance order, and m and n are relatively prime. The Verlet algorithm preserves a time step-dependent effective frequency ω_e given by [116], $\omega_e = 2\sin(\omega\Delta t/2)/\Delta t$, and, therefore, $\Delta t_{n:m}^{\text{Verlet}} = 2\omega_e^{-1}\sin(m\pi/n)$, where n:m represents the *order* of the resonance [69]. Therefore, because the limiting time steps $\Delta t_{n:1}$ for resonance orders $n > 2$ are *smaller* than the linear stability limit $\Delta_{2:1}$, resonance limits the time step to values *smaller* than the classical stability. Because the third-order resonance leads to instability and the fourth-order resonance *often* causes instability [69], we must have $\Delta t < \Delta t_{4:1}$. This condition implies that for the Verlet algorithm one must have $\Delta t < \sqrt{2}\omega_e^{-1}$, which is due to the second-order resonance or linear stability. Note that for nonlinear systems, the forcing or effective frequency ω_e for the Verlet algorithm is not known. However, if the values of the energy are relatively small, one may approximate [69] ω_e by expressions known for harmonic oscillators, as discussed below.

To speed up MD computations, multiple time-step (MTS) methods have been introduced [117, 118]. The simulations will be more efficient if the forces that are long-ranged are held constant (i.e., not evaluated as frequently) over larger intervals than the short-range forces. If this is to be done, the slowly varying forces should be incorporated into the integration algorithm as piecewise constant functions using extrapolation. Suppose that F_f, F_m, and F_s denote the fast, medium, and slow forces, with the corresponding time steps being, Δt_f, Δt_m, and Δt_s. We then define $r_1 = \Delta t_m/\Delta t_f$ and $r_2 = \Delta t_s/\Delta t_m$. Thus, a Verlet-based, force-splitting approach using extrapolation can be developed using the position-Verlet method, Eqs. (37) and (38), because the fast and medium forces are evaluated at the middle of the corresponding interval, rather than at the beginning and the end. In this scheme, the slow

forces are evaluated *once*, the medium forces are evaluated r_2 *times*, and the fast forces are evaluated $r_1 r_2$ *times* at a corresponding midpoint. Thus, if calculation of the slow forces takes the majority of the computations time, the MTS method will result in very significant savings in the time.

Although the original MTS algorithms [117, 118] suffered from their non-symplectiveness, symplectic and time-reversible MTS algorithms have been developed [111, 119]. In these methods, the application of the slow forces results in an *impulse*, rather than extrapolation: The velocities are modified only at the onset and at the end of a sweep covering Δt_s by a term proportional to $r_1 r_2 \Delta t_s$. In other words, one has [69]

$$m\frac{d\mathbf{x}}{dt} = \Delta t_f \sum_i \delta(t - i\Delta t_f)\{F_f[\mathbf{x}(t)]\} + \Delta t_s \sum_j \delta(t - j\Delta t_s)\{F_s[\mathbf{x}(t)]\} \tag{39}$$

which should be compared with Eqs. (30)–(38), in which a single time-step Δt has been used. Recent works [120, 121] indicate that these methods are generally stable at the integer multiples of half the period of the fastest motion. The severity of the instability *worsens* with the time step. This should be compared with the extrapolative methods that are generally unstable, but the instability is bounded for large time steps.

3.2.4. Simulations with Constant Ensembles

Because a MD simulation conserves the number N of the particles and the system volume V, then, if the energy E and momentum are also conserved, the time averages of any physical property computed from this type of simulation will be equal to the averages in the micro-canonical, or the NVE ensemble. Let us describe how such MD simulations are carried out. One first specifies the number of particles and the interaction potentials between them and assigns them their initial positions and momenta. Because the temperature can be measured, and because one is usually interested in carrying out the simulations at a specified temperature rather than at a specified energy, one must "push" the system toward the desired temperature. However, in MD simulations it is often very difficult to fix the temperature of the system at the very outset. Because the temperature of an infinite system is proportional to the average kinetic energy per degree of freedom, with a proportionality constant $\frac{1}{2}k_B$, this quantity is used in MD simulations (of finite systems) to fix the temperature.

One procedure for obtaining a fixed temperature T_f is to calculate a rescaling factor α given by

$$\alpha = \left[\frac{3k_B T_f (N-1)}{\sum_{i=1}^{N} m_i v_i^2}\right]^{1/2} \tag{40}$$

where m_i and v_i are the mass and magnitude of velocity of particle i, respectively. The velocity $\mathbf{v}_i$ of each particle i is then rescaled by α, that is, $\mathbf{v}_i(t) \rightarrow \alpha\mathbf{v}_i(t)$. The rescaling of the velocity also necessitates rescaling of the time t, which will be discussed shortly. Each time this rescaling is done, the actual temperature of the system changes and gradually approaches the given fixed temperature T_f. This method can actually be derived by imposing a constant kinetic energy through a Lagrange multiplier term added to the Lagrangian of the isolated system [122]. So far as nanoporous materials are concerned, if the pores are slit-like channels, then the velocity rerscaling method is effective and efficient. However, if one must model cylindrical pores or those with more complex shapes, then the above velocity rescaling method may not be very accurate. At the same time, although the rescaling procedure can be derived, due to certain assumptions used in the derivation, it still represents some type of an *ad hoc* method.

This has motivated the development of more systematic methods for achieving a given temperature and, thus, being able to perform MD simulations at constant temperature. One particularly effective method is based on introducing an extra force acting on the particles. The force is frictional in nature, is assumed to be proportional to the velocity of the particles

and therefore, affects the kinetic energy of the system (and hence the system's temperature) in a direct way. Thus, the equation of motion for the ith particle is written as [123]

$$m\frac{d^2\mathbf{r}_i}{dt^2} = F_i(\mathbf{R}) - C_f\left(R, \frac{dR}{dt}\right)\frac{d\mathbf{r}_i}{dt} \tag{41}$$

where the friction parameter $C_f(R, dR/dt)$ is assumed to be the same for all the particles. The sign of C_f depends on whether heat is added to or extracted from the system; in the former case $C_f < 0$, while in the latter case $C_f > 0$. Various equations have been suggested for C_f. The best known equation was proposed by Nosé [90] and simplified by Hoover [91], according to which

$$\frac{dC_f}{dt} = \frac{\sum_i m_i v_i^2 - 3Nk_BT_f}{f} \tag{42}$$

where f is a parameter that must be selected carefully. In effect, in order to reach the desired temperature, the system is connected to a heat bath to exchange energy with it so that it can reach the intended temperature. The parameter f represents a coupling between the system and the heat bath. The Nosé-Hoover method yields precise canonical distribution for the particles' positions and momenta.

Despite many desirable features, the Nosé-Hoover method does have some shortcomings, the most serious of which is that the coupling parameter f must be chosen. Moreover, although Cho and Joannopoulos [124] showed that, for LJ fluids at high temperatures, the canonical distribution is reproduced correctly, Holian et al. [125] demonstrated that if the temperature is lowered, it begins to oscillate with an amplitude that is much larger than the standard deviations expected in the canonical ensemble. This method can also lead to artifacts as simple velocity scaling [126].

Many modifications of the Nosé-Hoover algorithm have been proposed. Chief among them is an approach proposed by Jellinek and Berry [127] who suggested a generalization of the Nosé Hamiltonian involving multiplicative scaling of coordinates, momenta, and time. They showed that there are *infinitely many distinct* Hamiltonians (i.e., distinct dynamics) that possess *all* the properties of the Hamiltonian dynamics of Nosé-Hoover algorithm. Their model was analyzed in detail by Brańka and Wojciechowsky [128].

In addition to temperature, it is often desirable to be able to carry out MD simulations at a constant pressure [the (NPT) ensemble]. This is achieved by uniform isotropic volume changes caused by rescaling the atomic coordinates. Andersen [88] proposed incorporating the volume V of the system into the equation of motion by rescaling the coordinates as

$$\mathbf{r}_i = \mathbf{r}_i' V^{-1/3} \tag{43}$$

where $\mathbf{r}_i'$ denotes the coordinates of the particles in the rescaled system. Furthermore, the momentum of the particle is also rescaled according to

$$\mathbf{p}_i = \mathbf{p}_i'(sV^{1/3}) \tag{44}$$

where s is a new dynamical variable that is equivalent to rescaling the real time, $dt = s(t')\,dt'$. In effect, the system is connected to a "piston" that can contract or expand it. The Hamiltonian of the system is given by

$$\mathcal{H} = \frac{1}{2}\sum_i \frac{\mathbf{p}_i^2}{ms^2V^{2/3}} + \frac{1}{2}\sum_{(i,\,i\neq j)} E_p(\mathbf{r}_{ij}V^{1/3}) + \frac{p_b^2}{2f} + PV + \frac{p_p^2}{2m_p} + (3N+1)k_BT\ln s \tag{45}$$

where p_p and m_p are the "momentum" and "mass" of the "piston," respectively, E_p is the potential energy, and $(3N + 1)$ represents the total number of independent momentum degrees of freedom of the system. The term involving p_b represents the coupling to the heat bath (so that the temperature is also held fixed), while PV and $p_p^2/2m_p$ represent the work

and kinetic energy arising from the connection of the system to the "piston." The governing equation for the dynamical variable $s(t)$ is simply

$$\frac{ds}{dt} = \frac{p_h}{f} = \frac{\partial \mathcal{H}'}{\partial p_h} \tag{46}$$

Note that if in Eq. (45) we do not rescale the lengths and momenta and delete the "piston" terms, then the modified equation also describes the system for the case in which only the temperature is held fixed, implying that in that case too, the time must be rescaled in the same way as in the current case.

Martyna et al. [129] suggested a Hamiltonian slightly different from Eq. (45) and also equations of motion that differed from those used in the above method, in order to remove a minor problem from the above formulation, namely, the fact that the trajectories of the particles produced by the above method depend on the choice of the basis lattice vector. See also Feller et al. [130] for an improved constant-pressure MD simulation method, and Martyna et al. [131] and Berendsen et al. [123] for extensions to anisotropic systems, and for allowing changes in the cell shape in addition to its size.

3.2.5. Constrained Dynamics and Simulation of Rigid Molecules

Accurate molecular simulations depend largely on realistic representation of the molecules. Although representing atoms or molecules as simple LJ hard spheres may be adequate for predicting many qualitative features of experimental data, more sophisticated and realistic representation of them is necessary if MD simulations are to provide quantitative predictions. As a relatively simple but important example, consider molecular modeling of CO_2, an important gas in the practical applications of nanoporous membranes. A molecular model of CO_2, which is much more realistic than a simple LJ hard sphere with effective parameters σ and ε, was developed by Murthy et al. [132] and further refined by Hammonds et al. [133]. In their model, CO_2 is represented by a rigid linear molecule with quadrupole moments and three LJ sites. Three partial charges, q_O, q_C, and q_O, are used on the O–C–O sites, chosen so to preserve the quadrupole moments of the molecule. The nonelectrostatic interactions are still modeled as site–site LJ potentials, where the interaction sites are located on the three atoms. To fit the interaction parameters, three states of CO_2 (namely, solid, liquid, and gas) are used. The LJ parameters are fitted to the phonon frequencies and lattice energy of the solid, the thermodynamic properties of the liquid, and the second virial coefficient of the gas. All the parameters are given in Table 1, where σ_{OO}, σ_{CO} and σ_{CC} are the LJ size parameters, ε_{OO}, ε_{CO}, and ε_{CC} are the LJ energy parameters between O–O, C–O, and C–C atoms in a CO_2 molecule, respectively, ℓ_{OC} is the distance between the O and C atoms, and $\mathcal{M}$ is the quadrupole moment. If the MD simulation involves CO_2 and other molecules, then the interaction potential between molecules i and j is expressed as

$$U(r_{ij}) = \sum_{m=1}^{3}\sum_{n=1}^{3}\left[U_{LJ}(r_{im,jn}) + U_C(r_{im,jn})\right] \tag{47}$$

where $r_{im,jn}$ is the distance between the interacting pairs (site m in molecule i and site n in molecule j), $U_{LJ}(r)$ is the-cut-and-shifted LJ potential described above, and $U_C(r)$ is the Coulomb potential given by

$$U_C(r) = \frac{q_{im}q_{jn}}{r} \tag{48}$$

Table 1. The interaction parameters for CO_2.

σ_{OO}(Å)	3.027	ε_{OO}/k_B (K)	74.8
σ_{CO}(Å)	2.922	ε_{CO}/k_B (K)	44.8
σ_{CC}(Å)	2.824	ε_{CC}/k_B (K)	26.2
$q_O(e)$	0.332	$q_C(e)$	+0.664
$\mathcal{M}$(cm^2)	-14.4×10^{-40}	ℓ_{OC}(Å)	2.324

During the MD simulations, one must keep track of the coordinates of CO_2 molecules. They can be represented by the vector $\mathbf{V}_j$, with $j = 1, 2, \ldots, N_{CO_2}$, where N_{CO_2} is the total number of CO_2 molecules. The vector $\mathbf{V}_j$ contains three Cartesian coordinates, (r_x, r_y, r_z), determining the position of the molecule's center, and two coordinates determining its orientation. The orientation of CO_2 can be determined by a unit vector $\mathbf{e} = (e_x, e_y, e_z)$, directed along the axis of the molecule (where only e_x and e_y are independent, as $e_z = 1 - e_x - e_y$) and the angle that it makes with the surface of the system's walls.

We now describe how MD simulations of more complex materials, such as rigid or semi-rigid molecules, are performed. So far as nanoporous materials are concerned, accurate representation of such molecules are very important, with their significance being twofold:

(i) Many nanoporous materials are prepared from either (1) polymeric precursors or (2) are themselves polymeric or macromolecular structures. Examples of the first type include various carbon molecular-sieve materials, usually prepared from polyetherimide or other types of polymers [134–136]. Hence, it is important to be able to generate accurate molecular structure of such polymers to be used in MD simulations in order to understand the effect of their morphology on the phenomena of interest that occur in the polymers themselves (when they are used on their own merit for separation processes) or in the nanoporous materials that are prepared using such polymers. Examples of the second type include xerogels and aerogels that are macromolecular structures, usually prepared by a sol-gel process, and have been suggested as low-dielectric constant materials (see above).

(ii) Nanoporous membranes are commonly used in the chemical, petrochemical, and pharmaceutical industries for separation of fluid mixtures that contain large polymer-like molecules, such as proteins and *n*-alkanes. Therefore, accurate molecular representation of polymeric macromolecules is crucial to successful modeling such phenomena.

The motion of a rigid molecule consists of translations of the center of mass and rotations around this point. The force acting between two such molecules consists of atomic pair interactions between atoms that belong to the two different rigid molecules. One can also consider off-center interactions, but we neglect them here. There are several methods for treating rigid molecules, and we describe one of them which is based on imposing constraints on the system that depend on the spatial positions, but are independent of the velocities. Consider the Lagrangian of the system,

$$\mathscr{L}_0 = \int_{t_1}^{t_2} \left[\frac{1}{2} \sum_i m_i \left(\frac{d\mathbf{r}_i}{dt} \right)^2 - \frac{1}{2} \sum_{i \neq j} E_p(\mathbf{r}_i - \mathbf{r}_j) \right] dt \tag{49}$$

where subscript 0 indicates that constraints have not been imposed yet. A constraint is imposed on the system through a Lagrange multiplier $\lambda(t)$, which is a function of time, as the constraint should hold for all times. For example, for a rigid molecule that consists of two atoms, we impose the constraint that the distance ℓ between the two particles is always fixed. When such a constraint, which is often called the *bond constraint*, is imposed on the system, then the Lagrangian $\mathscr{L}$ of the new system (with the constraint) is given by

$$\mathscr{L} = \mathscr{L}_0 - \int_{t_1}^{t_2} \lambda(t) \left\{ [\mathbf{r}_1(t) - \mathbf{r}_2(t)]^2 - \ell^2 \right\} dt \tag{50}$$

$\lambda(t)$ is determined by requiring that the solution must satisfy the constraint. We discuss this shortly.

Some of the material's atoms form its backbone and are fixed by the bond constraints discussed above, while the remaining atoms are fixed by *linear constraints* that we discuss shortly. A good example is provided by a branched polymer in which the backbone is made of the multiply connected atoms. To identify the backbone of any molecular structure, some rules of thumb may be useful. For a planar molecular structure, one can consider three noncolinear atoms as a backbone, as they satisfy the bond constraint, while the rest of the atoms in the structure are constrained linearly. In a 3D molecular structure, four backbone atoms are subjected to six bond constraints with the remaining ones to a linear vector constraint

each. A good example is provided by the linear molecule CS_2 [137], the motion of which is described by five positional degrees of freedom, two of which define the orientations of the molecules and the remaining three define the position of its center of mass. Without any constraint, the three atoms have nine degrees of freedom, but three of them are eliminated by the bond constraints, implying that we still have six degrees of freedom, instead of the required five. The inclusion of the unneeded degree of freedom adds to the computations and makes them inefficient. A better procedure is to fix only the distance between the two sulphur atoms by requiring that $|\mathbf{r}_{S(1)} - \mathbf{r}_{S(2)}|^2 = \ell^2$ and to fix the position of the carbon atom by a linear vector constraint which reads

$$\mathbf{r}_C = \frac{1}{2}[\mathbf{r}_{S(1)} + \mathbf{r}_{S(2)}] \tag{51}$$

which adds up to the four required constraints.

Therefore, let us denote by $\boldsymbol{\mu}$ the linear vector constraint. Then, from the extended Lagrangian, the equations of motion for the three atoms are given by

$$m_S \frac{d^2\mathbf{r}_{S(1)}}{dt^2} = \mathbf{F}_1 - 2\lambda(t)[\mathbf{r}_{S(1)} - \mathbf{r}_{S(2)}] - \frac{1}{2}\boldsymbol{\mu} \tag{52}$$

$$m_S \frac{d^2\mathbf{r}_{S(2)}}{dt^2} = \mathbf{F}_2 + 2\lambda(t)[\mathbf{r}_{S(1)} - \mathbf{r}_{S(2)}] - \frac{1}{2}\boldsymbol{\mu} \tag{53}$$

$$m_C \frac{d^2\mathbf{r}_C}{dt^2} = \mathbf{F}_C + \boldsymbol{\mu} \tag{54}$$

where m_S and m_C denote the mass of the sulphur and carbon atoms. If we now twice differentiate Eq. (51) with respect to time and use Eqs. (52)–(54), we obtain

$$\mathbf{F}_C + \boldsymbol{\mu} = \frac{m_C}{2m_S}(\mathbf{F}_1 + \mathbf{F}_2 - \boldsymbol{\mu}) \tag{55}$$

which helps us eliminate $\boldsymbol{\mu}$ and rewrite the equations of motion for the sulphur atoms as

$$m_S \frac{d^2\mathbf{r}_{S(1)}}{dt^2} = \left[1 - \frac{m_C}{2(2m_S + m_C)}\right]\mathbf{F}_1 + \frac{m_C}{2(2m_S + m_C)}\mathbf{F}_2 + \frac{m_S}{2m_S + m_C}\mathbf{F}_C - 2\lambda(t)[\mathbf{r}_{S(1)} - \mathbf{r}_{S(2)}] \tag{56}$$

$$m_S \frac{d^2\mathbf{r}_{S(2)}}{dt^2} = \left[1 - \frac{m_C}{2(2m_S + m_C)}\right]\mathbf{F}_2 + \frac{m_C}{2(2m_S + m_C)}\mathbf{F}_1 + \frac{m_S}{2m_S + m_C}\mathbf{F}_C + 2\lambda(t)[\mathbf{r}_{S(1)} - \mathbf{r}_{S(2)}] \tag{57}$$

Equations (56) and (57) govern the motion of the sulfhur atoms. The position of the carbon atom is, of course, fixed by the linear constraint that we have imposed on the system.

We still have one unknown, $\lambda(t)$, that must be determined. Because the bond constraint is quadratic, elimination of $\lambda(t)$ is not as easy as eliminating $\boldsymbol{\mu}$. Therefore, $\lambda(t)$ is determined at each time step by using the constraint equation, that is, by solving the equations of motion iteratively until their solutions satisfy the bond constraint. Thus, if, for example, we use the Verlet algorithm, we can write

$$\mathbf{r}_{S(1)}(t + \Delta t) = 2\mathbf{r}_{S(1)}(t) - \mathbf{r}_{S(1)}(t - \Delta t) + \Delta t^2 \left(1 - \frac{m_C}{2m_S + m_C}\right)\mathbf{F}_1(t) + \Delta t^2 \frac{m_S}{2m_S + m_C}\mathbf{F}_C(t) - 2\Delta t^2 \lambda(t)[\mathbf{r}_{S(1)}(t) - \mathbf{r}_{S(2)}(t)] \tag{58}$$

$$\mathbf{r}_{S(2)}(t + \Delta t) = 2\mathbf{r}_{S(2)}(t) - \mathbf{r}_{S(2)}(t - \Delta t) + \Delta t^2 \left(1 - \frac{m_C}{2m_S + m_C}\right)\mathbf{F}_2(t) + \Delta t^2 \frac{m_S}{2m_S + m_C}\mathbf{F}_C(t) + 2\Delta t^2 \lambda(t)[\mathbf{r}_{S(1)} - \mathbf{r}_{S(2)}] \tag{59}$$

It can be shown that the error in the numerical values of $\lambda(t)$ so obtained is of the order $O(\Delta t^4)$.

Our discussion so far has been restricted to totally rigid molecules. We now consider partially rigid molecules that consist of rigid clusters that can move with respect to one another. For this purpose, we describe the algorithm due to Ryckaert et al. [138], Ciccotti et al. [84], and Ryckaert [139]. Their algorithm, which is known as SHAKE (the authors do not know why this name was given to this algorithm), is formulated based on the notion that the forces that particles experience are the physical and constraint forces. If M is the number of the constraints, then the constraints are written as, $\mathscr{C}_k(R) = 0$, with $k = 1, 2, \ldots, M$, where $\mathscr{C}_k$ expresses the functional form of the constraint, for example, the restriction that the distance between two particles is always fixed. The constraint forces are given by,

$$\mathbf{F}_c = \sum_{k=1}^{M} \lambda_k \nabla_i \mathscr{C}_k \tag{60}$$

where λ_k is the Lagrange multiplier to be determined, and subscript i signifies the fact that the gradient of constraint $\mathscr{C}_k$ must be taken with respect to i. Because we use the Verlet algorithm for integrating the equations of motion, we have the particles' positions at times $t - \Delta t$ and t, which satisfy the constraints imposed on the system. Thus, an intermediate position $\tilde{\mathbf{r}}_i$ is first calculated for particle i,

$$\tilde{\mathbf{r}}_i(t + \Delta t) = 2\mathbf{r}_i(t) - \mathbf{r}_i(t - \Delta t) + \Delta t^2 \mathbf{F}_i[\mathbf{r}_i(t)] \tag{61}$$

where $\mathbf{F}_i$ represents all the physical forces that the particle experiences. The true position is then computed from

$$\mathbf{r}_i(t + \Delta t) = \tilde{\mathbf{r}}_i(t + \Delta t) - \sum_{k=1}^{M} \lambda_k \nabla_i \mathscr{C}_k(\mathbf{r}^N) \tag{62}$$

where, as usual, $\mathbf{r}^N = \{\mathbf{r}_1, \mathbf{r}_2, \ldots, \mathbf{r}_N\}$ represents the position coordinates of all the particles. The Lagrange multipliers are determined by an iterative process. For the jth iteration, a loop over the constraints is carried out, in each step of which the particles' positions and the Lagrange multipliers are updated. The positions are updated according to the following iterative scheme,

$$\mathbf{r}_i^{(n)} = \mathbf{r}_i^{(o)} - \Delta t^2 \lambda_k^{(j)} \nabla_i \mathscr{C}_k(\mathbf{r}^N) \tag{63}$$

where superscripts n and o denote the new and old values, respectively. To calculate the Lagrange multipliers $\lambda_k^{(j)}$, a first-order expansion of $\mathscr{C}_k(\mathbf{r}^N)$ is carried out, which is then required to vanish. Therefore,

$$\mathscr{C}_k(\mathbf{r}^N)^{(n)} = \mathscr{C}_k(\mathbf{r}^N)^{(o)} - \Delta t^2 \lambda_k^{(j)} \sum_i \left\{ \nabla_i \mathscr{C}_k(\mathbf{r}^N)^{(o)} \cdot \nabla_i \mathscr{C}_k[\mathbf{r}^N(t)] \right\} + \cdots = 0 \tag{64}$$

where the sum is over all the particles. The final expression for $\lambda_k^{(j)}$ is given by

$$\lambda_k^{(j)} = \frac{\mathscr{C}_k(\mathbf{r}^N)^{(o)}}{\Delta t^2 \{\sum_i \nabla_i \mathscr{C}_k(\mathbf{r}^N)^{(o)} \cdot \nabla_i \mathscr{C}_k[\mathbf{r}^N(t)]\}} \tag{65}$$

The iteration continues until the constraints are satisfied numerically to within a fixed acceptable error. This algorithm, which is obviously *semiexplicit*, has turned out to be highly efficient and accurate.

The SHAKE algorithm can easily accommodate angles constraints by recognizing that an angle constraint is equivalent to an additional distance constraint. Therefore, one can, for example, maintain the angle in a triatomic molecule at the desired value by requiring the distance between the two end atoms to take on the appropriate value. This is the method by which small molecules, such as water, are modeled by a rigid geometry. For example, the simple point charge model of H_2O uses three distance constraints. At the same time,

one must recognize that angle constraining in the MD simulation of molecules that are conformationally flexible may have a deleterious effect on the efficiency with which the system samples the configurational space, as many conformational transitions involve some angle change as well as rotations about bonds. The most common use of the SHAKE algorithm is for constraining bonds with hydrogen atoms.

Andersen [140] introduced a variant of SHAKE, usually referred to as the RATTLE, which uses the velocity-Verlet algorithm described earlier. Tobias and Brooks [141] proposed a similar technique for other internal degrees of freedom. Miyamoto and Kollman [142] proposed an algorithm, called SETTLE, for rigid H_2O molecules. Leimkuhler and Skeel [143] showed that the RATTLE algorithm is symplectic and that SHAKE, although technically not symplectic, yields solutions identical to those of RATTLE for the positions and only slightly different velocities.

Nanoporous materials are used extensively in the chemical and petrochemical industries for separation of mixtures that contain *n*-alkanes. These are complex molecules and, therefore, an efficient method for generating their molecular structures is essential to MD simulations of transport and adsorption of such mixtures in a nanoporous material. An efficient method for generation of *n*-alkanes is the configurational-bias Monte Carlo technique [144–151] to grow the alkane molecules. The atom-by-atom growth of the molecules is done in such a way that regions of favorable energy are identified, and overlap with other molecules are avoided, hence speeding up the computations greatly. More specifically, we consider the potential energy of an atom as the sum of two contributions, namely, the internal energy E^{int}, which includes parts of the intramolecular interactions, and the external energy E^{ext}, which contains the intermolecular interactions and those intramolecular interactions that are not part of the internal energy. The division is, of course, to some extent arbitrary and depends on the details of the model. The procedure to grow an *n*-alkane atom by atom consists of the following steps.

(i) One inserts the first atom at a random position and computes the energy $E_1(n)$ along with a quantity $w_1 = \exp[-\beta E_1(n)]$, where $\beta = (k_B T)^{-1}$, where n indicates the new state in which the system is in.

(ii) k trial orientations, denoted by $\{\mathbf{b}_k\} = \mathbf{b}_1, \mathbf{b}_2, \ldots, \mathbf{b}_k$ are then generated with a probability $p_i^{\text{int}}(\mathbf{b}_i)$, given by

$$p_i^{\text{int}}(\mathbf{b}_i) = \frac{1}{C} \exp[-\beta E_i^{\text{int}}(\mathbf{b}_i)] \tag{66}$$

in order to insert the next atom i, where C is a normalization factor. For each trial orientation, the *external energy* $E_i^{\text{ext}}(\mathbf{b}_i)$ is also computed, along with the quantity, $w_i(n) = \sum_{j=1}^{k} \exp[-\beta E_i^{\text{ext}}(\mathbf{b}_j)]$. One orientation, out of the k trial positions, is then selected with the probability

$$p_i^{\text{ext}}(\mathbf{b}_i) = \frac{1}{w_i(n)} \exp[-\beta E_i^{\text{ext}}(\mathbf{b}_i)] \tag{67}$$

Typically, a few trial orientations suffice.

(iii) Step (ii) is repeated $M - 1$ times until the entire alkane molecule is grown, and the Rosenbluth factor [152], $W(n) = \prod_{i=1}^{M} w_i(n)$, is computed. A molecular conformation is generated with a probability given by

$$P(n) = \prod_{i=2}^{M} p_i^{\text{int}}(n) p_i^{\text{ext}}(n) = \frac{1}{C^{M-1} W(n)} \exp[-\beta E(n)] \tag{68}$$

with $E = \sum_{i=1}^{M} E_i = \sum_{i=1}^{M} (E_i^{\text{int}} + E_i^{\text{ext}})$.

3.2.6. Ion–Ion and Long-Range Interactions

Coulombic (and van der Waals) forces represent nonbond, long-range interactions and are described by a pair-potential that is proportional to $\ln r$ in 2D and r^{-1} in 3D, hence decaying very slowly with the distance r. Their presence in MD simulations represents a computational bottleneck; the direct evaluation of all pairs of atoms scales with the number N of the atoms as $O(N^2)$, which should be compared with the bonded terms (such as stretching, bond-bending, and tortional forces) that have an $O(N)$ computational complexity. Hence, development of fast algorithms that reduce the computational cost of evaluating such interaction forces for all pairs of atoms has been a very active area of research.

Such issues are directly relevant to molecular modeling of nanoporous materials and the phenomena that occur in them. Many nanoporous materials, such as zeolites and pillared clays, that are used both as membranes and catalysts, contain a quenched distribution of local charges. At the same time, these materials are used in a variety of applications that involve transport of ions in them, implying that one must tackle a problem in which there are long-range interactions, not only between the mobile ions, but also between the ions and the local charge centers in the pore space of the material.

To treat such forces in MD simulations, three different approaches have been developed, which we now describe.

3.2.6.1. Cutoff Techniques In this approach, the distance-dependent nonbond potential is set to zero beyond a certain distance $r = r_c$. The cutoff methods are easy to implement in any MD simulations and are also computationally cheap [$O(N)$]. So far as MD simulations are concerned, any cutoff technique that is used in the simulations must not (1) introduce large, artificial forces around the cutoff region; (2) must alter the functions in a way that conserves energy, at least in an approximate manner; (3) must change the energies smoothly and gradually, so to avoid generating artificial minima on the energy surface of the system; and (4) change short-range forces and energies by values that are as small as possible. In general, there are three cutoff techniques:

(i) Truncation methods, in which for $r < r_c$, the values of the forces are directly computed from the nonbond potential and are abruptly set to zero for $r > r_c$. These methods satisfy the fourth criterion listed above but violate the other three.

(ii) Switch techniques, in which the values of the forces are directly computed for $r < r_1$, are changed for $r_1 < r < r_c$, and are set to zero for $r > r_c$. These techniques can violate criteria (1) and (3) listed above. In addition, they can have difficulty satisfying the second criterion when polar groups of atoms are involved near the cutoff region. One defines a switch function $S(r)$ that, for the truncation methods, is simple: $S(r) = 1$ for $r < r_c$, and $S(r) = 0$ otherwise. But, the switch function is usually a polynomial that alters the nonbond energy gradually in the buffer zone $[r_1, r_c]$, so that the energy vanishes at $r = r_c$, but leaves the energy unaltered in the region $r < r_1$. Typically, a sixth-order polynomial is used as the switch function.

(iii) Shift formulations, in which one uses a shift function to change the values of the forces more gradually for all $r < r_c$. Using large values of r_c, these formulations are often used in large-scale MD simulations. The shift function typically used is either $S_g(r) = [1 - (r/r_c)^2]^2$ or $S_a(r) = (1 - r/r_c)^2$ for $r \leq r_c$. Note that $S_a(r)$ augments the true Coulombic forces by a constant r_c^{-2} and is often referred to as the *force shift* (which is, however, somewhat misleading, as this shift function is applied to the potential not the force).

The question of the choice of a cutoff technique depends on the force field and the system under study. Norberg and Nilsson [153] discuss this issue in detail. Another most important task in using any cutoff technique is selecting the thresholds r_1 and r_c.

One can use the same techniques to evaluate the energies as well. One may also use these techniques for a group of atoms, rather than single atoms, in which case the thresholds r_1 and r_c are applied to the distance between the groups' *centers*. The charges associated with entire residues are better maintained when one uses group-based thresholds, hence avoiding possible instabilities in the forces or energies that arise when only a subset of atoms of

a particular residue is altered. In practical applications and in commercial softwares, the switch function $S_g(r)$ is used for group-based potential shift, while $S_a(r)$ is utilized for the atom-based shifting.

We note that, in case of a system with local electrical charges, even the overall neutrality of the system does not guarantee that the screening length is finite, since in most cases of practical interest the screening length is larger than the linear size of the system and, therefore, use of a finite cutoff distance r_c is not justified.

3.2.6.2. The Ewald-Summation Method If the system of interest is represented by a lattice with periodic boundary conditions, the Ewald-summation method (ESM) is used for calculating its electrostatic energy. In addition to d-dimensional simple-cubic lattices, one may use in the simulations other periodic structures, such as face-centered cubic lattice, truncated octahedron, and hexagonal prism, as the unit cell. The choice of the cell's geometry depends on the molecular structure to be studied by the MD simulations, as it affects the total number of pairwise interactions to be computed. Techniques for optimizing the structure of the unit cell have been developed [154, 155] for simulation of biomaterials, and can presumably be used for other types of macromolecules. It is clear that one only needs to record the coordinates of the unit cell; the rest of the coordinates are obtained using the periodicity of the system. In practice, one uses the convention that each atom i interacts with only the closest periodic image of the other $N - 1$ particles, and a spherical cutoff (see above) is also used to restrict further this interaction.

A problem that arises when periodic boundary conditions are used in simulation of a system with a distribution of local charges is that the sums over the image charges in the periodic images of the system do not converge *absolutely* but only *conditionally*. This problem can be addressed by subtracting an offset from the potential (as adding or subtracting a constant to the potential does not change the resulting force, as the force is the gradient of the potential), leading to the following expression for the total configurational energy of the system for a set of N particles with charges q_i,

$$E = \sum_{\mathbf{R}} \sum_{i<j}^{N} \sum_{j}^{N} \frac{q_i q_j}{|\mathbf{r}_i - \mathbf{r}_j + \mathbf{R}|} - \sum_{i=j} \sum_{j} q_i q_j \sum_{\mathbf{R}\neq\mathbf{0}} \frac{1}{\mathbf{R}} \tag{69}$$

The sum over $1/\mathbf{R}$ is over the locations $\mathbf{R}$ of the periodic replicas of the system. However, this is easier said than done, and the ESM is used to address this problem.

If we consider only the first term of the right-side of Eq. (69) and refer to it as E_{Coulomb}, then, as mentioned above, the sum is not absolutely convergent. Ewald noted that the convergence problem can be addressed by converting the sum into a sum of two absolutely and rapidly convergent series in direct and reciprocal space. The reciprocal lattice (used in the simulations) is an orthogonal system related to the orthogonal system associated with the atoms in the unit cell, which is called the real-space lattice. Splitting of the sum into the two sums is done by representing each point charge as a Gaussian charge density, which produces an exponentially decaying function. The Gaussian transformation is then counteracted by an analogue subtraction, as the net result must be an effective point charge. The width of the Gaussian distribution is an important parameter. As the width increases, the sum for the real space converges more rapidly, whereas that of the reciprocal space converges more slowly.

However, the above splitting trick is, strictly speaking, valid only if the system has an infinite dielectric constant, or for a unit cell with zero dipole moment. The correction term E_c for a nonuniform field associated with a macroscopic crystal in a dielectric medium with an external dielectric constant k was derived by De Leeuw et al. [156], and is given by

$$E_c = E_{\text{Coulomb}}(k = 1) - E_{\text{Coulomb}}(k = \infty) = \frac{2\pi}{3L^3} \left| \sum_{i=1}^{N} q_i \mathbf{x}_i \right|^2 \tag{70}$$

Because the long-range reciprocal-space summation (usually done by Fourier transformation) requires $O(N^2)$ computations, the above algorithm, though accurate, is still computationally intensive. To address this problem, methods were proposed [157, 158] for optimizing

the width of the Gaussian charge density distribution in order to balance the intensities of the computations for the real and reciprocal spaces (i.e., making one of them extremely fast to compensate for the slowness of the other one), resulting in an $O(N^{3/2})$ algorithm [158]. But, the most important breakthrough occured when it was realized [109] that the trigonometric values in the Fourier series for the computations in the reciprocal space can actually be evaluated by a smooth interpolation of the potential over a regular computational grid, which reduces the computational cost to $O(N \log N)$. The smoothing is done either by Lagrange [159] or B-spline interpolation [160]. The developments on the use of the ESM have been reviewed by Toukmaji and Board [161]; see also Luty et al. [162, 163] for implementation of these ideas in MD simulations.

3.2.6.3. The Multipole-Expansion Method Multipole-expansion (MPE) method is a highly accurate and efficient algorithm that has been proposed [164–167] as a powerful alternative to the Ewald-summation method, with applications in several branches of science and engineering. The method was probably first proposed by Appel [168] for astrophysical problems and was further refined and accelerated by Barnes and Hut [169] and independently by Rokhlin [170] to an $O(N \log N)$ algorithm. However, it was the seminal work of Greengard and Rokhlin [164–167] that turned this algorithm into a powerful computational technique. At an elementary level, it is easy to understand this technique. Consider the electrostatic potential $U(\mathbf{x}^N)$, where, $\mathbf{x}^N = \{\mathbf{x}_1, \mathbf{x}_2, \ldots, \mathbf{x}_N\}$. We can write this potential as,

$$U(\mathbf{x}^N) = \frac{1}{2}\sum_i \sum_j \frac{q_i q_j}{\mathbf{r}_{ij}} = \frac{1}{2}\sum_j q_j \Phi(\mathbf{x}_j) \tag{71}$$

where $\Phi(\mathbf{x}_j) = \sum_{i \neq j} q_j/|\mathbf{r}_{ij}|$, which can be expanded as

$$\Phi(\mathbf{x}_j) = \Phi(\mathbf{0}) + \nabla\Phi^{\mathrm{T}}\mathbf{x} + \frac{1}{2}\mathbf{x}^{\mathrm{T}}\mathbf{H}\mathbf{x} + \cdots \tag{72}$$

where H is the Hessian evaluated at $\mathbf{x} = \mathbf{0}$, and T denotes the transpose operation. Thus, expansion (72) produces expressions for $\Phi(\mathbf{0})$ in terms of the zero power of the moment $\mathcal{M}$, $\Phi(\mathbf{0}) = \mathcal{M}^0/|\mathbf{x}_j|$, for $\nabla\Phi(\mathbf{x})$ in terms of the dipole moment and for components of the Hessian in terms of the quadrupole moments, hence the name multipole-expansion.

To discuss the MPE method in detail, we consider a concrete example—transport of ions in a nanoporous material, such as a zeolite catalyst with a quenched distribution of charge centers—although in addition to transport in nanoporous materials, this problem is relevant to many other important phenomena, such as dynamic response of non-metallic materials (e.g., ionic glasses and polymeric and glassy conductors) and highly defected crystals. Although this problem has been studied extensively, until recently no consensus regarding the nature of the transport process had emerged. In particular, if $\langle R^2(t)\rangle$ is the mean square displacement of the mobile ions at time t, one expects to have

$$\langle R^2(t)\rangle \sim t^{\alpha} \tag{73}$$

where $\alpha = 1$ for diffusive transport. However, the precise value of α was a controversial subject with some researchers claiming that $\alpha > 1$, representing fast transport, but others believing that $\alpha \leq 1$, in which case the transport process is slow and anomalous. This controversy also prevented correct interpretation of the experimental data for diffusion of ions in disordered nanoporous media with a distribution of charge centers. For example, it has been observed during diffusion of ions through zeolites, which are nanoporous catalytic materials with a distribution of ions and cations, that, upon changing the charge on the diffusing particles (i.e., making the disorder stronger), the diffusivity decreases *by orders of magnitude*. Despite its great practical importance, no efficient and reliable computer simulation of this problem was carried out for many years because (1) of the long-range nature of Coulombic interactions and (2) the fact that the charge centers give rise to deep potential wells that may capture the mobile particles for long periods of time and slow down their motion.

Let us now describe how MD simulations of this problem can be carried and, in particular, how the effect of long-range Coulombic interactions can be taken into account by an

efficient and reliable algorithm developed by Mehrabi and Sahimi [171]. They used both a continuum and a lattice representation of the system. The continuum representation was used when the fixed charge centers were distributed randomly in the medium. The lattice, which was simple-cubic, was used when a potential–potential correlation function, defined below, was used for generating the potentials due to the fixed charge centers. At time $t = 0$, the charged mobile particles are distributed randomly in the system, but as they move correlations develop between them. In addition to the Coulombic interaction, a short-range, r^{-12} repulsive interaction was also used to prevent capture of a mobile charged particle by an immobile one with the opposite charge.

The charge centers are either distributed explicitly throughout the medium or are represented by their potential distribution generated by the potential–potential correlation function. To make the system neutral, equal numbers of the centers with opposite charges are inserted in the system and similarly for the mobile particles. The Coulomb potential U_i acting on the ith mobile particle is written as,

$$U_i = U_i^{(\mathrm{fm})} + U_i^{(\mathrm{mm})} \tag{74}$$

where $U_i^{(\mathrm{fm})}$ is due to the interaction between the mobile particle and the fixed centers, whereas $U_i^{(\mathrm{mm})}$ is contributed by the interaction between the mobile particles themselves. $U_i^{(\mathrm{fm})}$ can be calculated by two different methods (yielding idential results). In one method, $U_i^{(\mathrm{fm})}$ [and also $U_i^{(\mathrm{mm})}$] is computed by the MPE method described in detail below. In the second method, one can use the fact that diffusion of charged particles in a disordered medium can be viewed as a transport process in an external potential field generated by the quenched disorder that represents the fixed charge centers. Thus, instead of directly distributing the charge centers with a given density $\rho(\mathbf{r})$, $U_i^{(\mathrm{fm})}$ is formally represented by the solution of the Poisson's equation, which in 3D is given by

$$U_i^{(\mathrm{fm})}(\mathbf{r}) = -\frac{q_f q_m}{4\pi\varepsilon_0} \int \frac{\rho(\mathbf{r}')}{|\mathbf{r} - \mathbf{r}'|}\, d\mathbf{r}' \tag{75}$$

where q_f and q_m are the charges for the fixed and mobile particles, respectively, and ε_0 is the permittivity. The charge density $\rho(\mathbf{r})$ is represented by its correlation function $\chi_{\rho\rho}(\mathbf{r})$ which, in the case of Debye-Hückel statistics, is given by

$$\chi_{\rho\rho}(\mathbf{r}) = \rho_0 \delta(\mathbf{r}) - \frac{\rho_0 \kappa^2 \mathrm{e}^{-\kappa|\mathbf{r}|}}{4\pi|\mathbf{r}|} \tag{76}$$

where $\rho_0 = \langle \rho(\mathbf{r}) \rangle$, and κ^{-1} is the spatial correlation or the screening length. The depth of the potential wells in which the mobile particles are captured by the immobile ones, and thus the radius of influence of the traps, is controlled by κ^{-1}. The larger κ^{-1} is, the deeper is the potential well and, thus, the larger the times spent in such traps. In the limit $\kappa^{-1} \to \infty$, the trapping times become infinitely large and, therefore, the effective diffusivity is *zero*. The power spectrum $\hat{\chi}_{\phi\phi}(\omega)$ for the potential is calculated from that of the charge density $\hat{\chi}_{\rho\rho}(\omega)$, as Eq. (75) is a convolution integral of the charge density and the Green function for the potential generated by a single charge particle and, therefore, in 3D

$$\hat{\chi}_{\phi\phi}(\omega) = \left(\frac{q_f q_m}{\varepsilon_0} \right)^2 \frac{\rho_0}{\omega^2(\omega^2 + \kappa^2)} \tag{77}$$

Note that the 1D version of Eq. (77) is given by $\hat{\chi}_{\phi\phi} = \rho_0 (q_f q_m / \varepsilon_0)^2 / (\omega^2 + \kappa^2)$. Hence, a realization of the potential field is generated as follows. Random numbers, distributed uniformly in $[-\sqrt{3}, \sqrt{3})$ (factor $\sqrt{3}$ ensures that the power spectrum is 1, as it should be), are assigned to the sites of the system. The resulting array is then Fourier transformed and multiplied by $\sqrt{\hat{\chi}_{\phi\phi}(\omega)}$, and then inverse Fourier transformed.

$U_i^{(\mathrm{fm})}$ and $U_i^{(\mathrm{mm})}$ can also be calculated by the MPE method [164–167, 171, 172]. In this method, a particle i interacts with the nearby particles through the usual Coulomb potential, and with the far away particles through their *precalculated* multipole expansions of the potential. The total potential $U(\mathbf{r}) = \sum_j^N U_j(\mathbf{r})$ produced by a group of N charges is

$$U(\mathbf{r}) = \frac{q}{r} - \mathbf{P}\cdot\boldsymbol{\nabla}\left(\frac{1}{r}\right) + \frac{1}{2}\mathbf{Q}:\boldsymbol{\nabla}\boldsymbol{\nabla}\left(\frac{1}{r}\right) - \frac{1}{6}\mathbf{O}\vdots\boldsymbol{\nabla}\boldsymbol{\nabla}\boldsymbol{\nabla}\left(\frac{1}{r}\right) + \cdots \tag{78}$$

where q, $\mathbf{P}$, $\mathbf{Q}$, and $\mathbf{O}$ are, respectively, the monopole, dipole, quadrupole, and octapole moments of the group of charges around the origin. In practice, we write

$$U(r) = \frac{q}{r} + \frac{1}{r^3}\sum_\alpha P_\alpha r_\alpha + \frac{1}{2r^5}\left(\sum_\alpha Q_{\alpha\alpha} r_\alpha r_\alpha + \sum_\alpha\sum_\beta Q_{\alpha\beta} r_\alpha r_\beta - r^2 Q\right) + \frac{1}{6r^7}\left[15\left(\sum_\alpha O_{\alpha\alpha\alpha} r_\alpha r_\alpha r_\alpha + \sum_\alpha\sum_\beta O_{\alpha\alpha\beta} r_\alpha r_\alpha r_\beta + \sum_\alpha\sum_\beta\sum_\gamma O_{\alpha\beta\gamma} r_\alpha r_\beta r_\gamma\right) - 9r^2\left(\sum_\alpha O_\alpha\right)\right] + \cdots \tag{79}$$

with

$$q = \sum_i q_i \tag{80}$$

$$P_\alpha = \sum_i q_i R_{i\alpha} \tag{81}$$

$$Q_{\alpha\alpha} = \sum_i q_i R_{i\alpha}^2, \quad Q_{\alpha\beta} = \sum_i q_i R_{i\alpha} R_{i\beta}, \quad Q = \sum_i q_i R_i^2 \tag{82}$$

$$O_\alpha = \sum_i q_i R_i^2 R_{i\alpha}, \quad O_{\alpha\alpha\alpha} = \sum_i q_i R_{i\alpha}^3, \quad O_{\alpha\alpha\beta} = \sum_i q_i R_{i\alpha}^2 R_{i\beta}, \quad O_{\alpha\beta\gamma} = \sum_i q_i R_{i\alpha} R_{i\beta} R_{i\gamma}, \tag{83}$$

where $r = |\mathbf{r}|$, $\mathbf{R}_i$ is the position vector of the ith charge, α, β, and γ stand for the coordinates x, y, and z, and q_i is the charge of the ith (fixed or mobile) particle.

A highly efficient simulation technique is fundamental to this study. Hence, in addition to taking advantage of the multipole expansion, the 3D simulation cell is divided into 8 smaller equal boxes, called *children* of the original box [164–167]. Each child box is a *parent* to 8 smaller boxes, with the division continuing up to a certain level that is called the maximum level (maxlevel) of division. The data needed for each particle, that is, its position and type (mobile or fixed), are stored in a *particle object*. A *cell object* contains a list of its *current* particles. Each particle is also "connected" to the next and previous particle in the list. After setting up the entire data structure, the multipoles of each cell around its center at the maxlevel are calculated using the above expressions. Then, the multipoles of the parent cells are computed by translating and adding the multipoles of their children by a displacement vector $\boldsymbol{\ell} = (\ell_x, \ell_y, \ell_z)$. In terms of the old quantities, the new (primed) translated quantities are given by,

$$P'_\alpha = P_\alpha - q\ell_\alpha \tag{84}$$

$$Q'_{\alpha\alpha} = Q_{\alpha\alpha} - 2\ell_\alpha P_\alpha + q\ell_\alpha^2 \tag{85}$$

$$Q'_{\alpha\beta} = Q_{\alpha\beta} - \ell_\beta P_\alpha - \ell_\alpha P_\beta + q\ell_\alpha\ell_\beta \tag{86}$$

$$Q' = Q'_{\alpha\alpha} + Q'_{\beta\beta} + Q'_{\gamma\gamma} \tag{87}$$

$$O'_{\alpha\alpha\alpha} = O_{\alpha\alpha\alpha} - 3\ell_\alpha + 2\ell_\alpha^2 - q\ell_\alpha^3 \tag{88}$$

$$O'_{\alpha\alpha\beta} = O_{\alpha\alpha\beta} - \ell_\beta O_{\alpha\alpha} + \ell_\alpha[-2Q_{\alpha\beta} + 2\ell_\beta P_\alpha + \ell_\alpha(P_\beta - q\ell_\beta)] \tag{89}$$

$$O'_{\alpha\beta\gamma} = O_{\alpha\beta\gamma} + \ell_\gamma(\ell_\beta P_\alpha - Q_{\alpha\beta}) + \ell_\beta(\ell_\alpha P_\gamma - Q_{\alpha\gamma}) + \ell_\alpha(\ell_\gamma P_\beta - Q_{\beta\gamma}) - q\ell_\alpha\ell_\beta\ell_\gamma \tag{90}$$

Each particle's potential energy is divided into U_i^{near} and U_i^{far}. A particle in a cell at the maxlevel interacts with all other particles in the same cell and in the neighboring cells by the usual Coulomb potential, thus yielding U_i^{near}. The same particle also interacts with its

parent's neighbors' children through the corresponding multipole expansions. Computations continue up to the entire simulation cell, hence yielding U_i^{far}. In this way, the number of the cells that interact with each particle is drastically reduced as one moves away from the particle. For example, in 3D with four levels of division, the number of the interacting cells is only 415, rather than the original 4069 cells. This method is highly efficient for taking into account the effect of Coulomb and other long-range potentials.

However, even with such an efficient algorithm, MD simulation of this problem requires intensive computations. If the simulations are not carried out for long enough times, one may not be able to obtain the true asymptotic (long time) behavior of the system. As an example, consider the problem in a 1D system, such as a highly anisotropic material so that the motion of the mobile particles is restricted essentially to one direction. In this case, the mobile particles can only travel in the space *between* themselves, as they cannot "jump" over each other. There are many relatively fast diffusive jumps in the trajectory of the particles after certain periods of time. In between the jumps, one has a slow motion that causes the *overall* transport to be anomalous [i.e., $\alpha < 1$ in Eq. (73)], not only in 1D but also in 2D and 3D. The mobile particles can be trapped in the potential wells (traps) that the quenched distribution of the charge centers creates. The traps have a finite sphere of influence, such that for any particle i within the sphere the potential difference ΔU_i for a displacement that can take i out of the sphere is very large, and thus the probability of an appreciable jump is small. However, after some time, the particles are close to the boundary of the traps and escape with a displacement that takes them out of the traps. They then resume their diffusive motion until they are captured by another trap, and so on.

Let us mention that, in addition to the basic fast Ewald-summation method and the MPE technique described above, their variants and also other methods have also been developed. For example, Brandt and Lubrecht [173] developed an efficient summation technique based on multigrid method, which has been extended [174, 175] to electrostatic potential computations. In addition, a variable-order version of the Appel's algorithm [168] has been developed [176, 177]. Moreover, massively parallel versions of the MPE algorithm have also been developed and reported [178].

3.3. Force Fields and Interatomic Interaction Potentials

Classical MD simulations are a valuable tool for studying various properties of materials using millions of atoms. However, as discussed earlier, accurate interaction potentials are crucial to the success of MD computations. Although simple interaction forces, such as those derived from the LJ potentials, have provided us with much qualitative insight into the properties of various materials, quantitative predictions require much more realistic representation of the interactions between the atoms. Moreover, only for noble gases can one represent the interactions between atoms by *density-independent*, pairwise-additive forces, whereas the repulsive and attractive forces are due to spherical electron clouds that are close to the nuclei. The alternative to the LJ and similar potentials are semiempirical expressions designed for accurately describing small distortions from the ground state in more complex molecular systems. Although such potentials, which can be viewed as a kind of Taylor series expansions of the energy about its minimum, are useful for describing phonons and elastic deformations, they are incapable of describing the energy of states that differ significantly from tetrahedral ground state or when one must deal with large deformations.

The complexity of a force field depends on the chemical and geometrical structure of the molecules for which the force field is intended. Molecular vibrational spectra of molecules are used for deriving various force constants, internuclear distances, and other properties that are used in contructing a force field. Vibrations of a molecule are described as a superposition of the fundamental oscillations for that molecule, usually referred to as the normal modes. A molecules of N atoms has $3N - 6$ normal modes, which is the result of three degrees of freedom for each atom (hence yielding $3N$), minus three translational and three rotational degrees of freedom. In a force field for a complex molecule, such as a polymer, one usually includes forces that correspond to stretching, in-plane and out-of-plane bending, and tortional forces. In-plane deformation of an $A - B - C$ sequence forces A and

C closer together, usually referred to as *scissoring*, whereas another in-plane deformation, usually called *rocking*, moves A and C in the same direction while keeping their distance more or less the same. The out-of-plane deformation is also of two types. In one, usually referred to as *wagging*, the atoms move in the same direction with respect to the reference plane, whereas in the second type, called *twisting*, one atom moves in one direction while the other two move in the opposite direction. The potentials or force fields can be divided into two groups.

(i) In one group are those that are intended for bonded atoms. Examples include bond-length potentials that represent strain terms and model small deformations about a reference or equilibrium values. The reference values can be obtained from experimental x-ray crystal structures. Alternatively, they can be obtained from *ab initio* computations (see below). If the deformations are not too small, a Morse potential (see below) is used. Also included in this group are bond-angle potentials, as well as torsional potentials. The latter are included because, for example, one may have internal rotations of groups within a molecule. It must, however, be pointed out that the origin of the barrier to internal rotation has not been resolved. Most of these potentials are typically quadratic in either displacements (bond-length potentials) or angles and their cosines (bending), although higher order terms are also frequently used. Torsional potentials are more complex. If θ_i is the torsion angle, then the energy corresponding to it is usually represented by $E = \sum_{i=1}^{n} \frac{1}{2} V_i[1 + \cos(i\theta_i - \theta_0)]$, where a typical value of n is 3 or 4, and V_i is the barrier height.

(ii) In the second group are nonbond potentials, such as van der Waals and Coulomb potentials. These were already described.

It should, therefore, be clear that development of a realistic force field for representing all the important interatomic forces in a molecule is a difficult task. For this reason, developing accurate representation of the interaction forces between various atoms has been, for many years, an active research field. We summarize in this section some of the most significant results that have emerged over the last two decades.

3.3.1. The Embedded-Atom Model

The embedded-atom (EA) model, which was originally intended for metals, was developed by Daw and Baskes [179, 180] but has since been used for other types of materials. So far as nanoporous materials are concerned, the EA model is relevant to modeling of metallic membranes (see above).

In metals, electrons are not all localized around the nuclei, rather the valence electrons are often shared among many ions, similar to a nearly free-electron gas. This implies that the energy depends on the local electron density, resulting in many-body, rather than pairwise, forces between ions, hence allowing one to represent the interactions between ions in metals by a relatively simple approximate functional form, commonly referred to as the EA potential. In this approximation, the total potential energy E of N ions in an arbitrary volume V is given by

$$E = \sum_{i=1}^{n} \left[\frac{1}{2} \sum_{j \neq i} U_{ij}(r_{ij}) + E_i^e(\rho_i) \right] \tag{91}$$

where $U(r_{ij})$ is a *density-independent*, pairwise-additive, and short-range interaction potential that depends only on distance r_{ij} between particles i and j, and E_i^e is the embedding energy that depends on the local embedding density ρ_i at atom i. In effect, each atom is viewed as an impurity embedded in a host consisting of all other atoms, such that the embedding energy depends on the electron density. In this sense, the basic idea of the EA model is, on one hand, similar to a mean-field approximation and, on the other hand, similar to the DFT described later in this chapter. If one makes a further simplification by assuming that the density ρ_i can be approximated by

$$\rho_i = \sum_{j \neq i} \rho_j^a(r_{ij}) \tag{92}$$

where $q_i(r)$ is the effective charge of atom i. Note that $Z_i(r)$ must be positive and decrease monotonically with increasing r. A particularly simple, yet accurate, expression is given by

$$q(r) = Z_o(1 + a_1 r^{a_2}) \exp(-a_3 r) \tag{102}$$

where Z_o is the number of the outer electrons in the atom (e.g., $Z_o = 10$ for Ni, Pd, and Pt, and $Z_o = 11$ for Cu, Ag, and Au). The parameters a_1, a_2 and a_3 must be determined empirically, although $a_2 = 1$ is accurate for Ni, Pd, and Pt, while $a_2 = 2$ leads to accurate elastic constants for Cu, Ag, and Au. Using these observations and properties, Daw and Baskes [180] and Foiles et al. [181] obtained very accurate empirical correlations for the embedding energy and the effective charges for a variety of metals, from which they computed their various properties, such as their elastic constants and surface energy; see also Johnson [182], who used the EA model to study FCC metals.

Holian et al. [183] developed the following EA model for use in MD simulations of deformation of materials under high stresses. The local embedding density ρ_i was assumed to be given by a pairwise sum over all neighboring particles, weighted by a spherical localization function $w(r_{ij})$, such that

$$\rho_i = \sum_{j \neq i} w(r_{ij}) \tag{103}$$

with

$$w(r) = \frac{1}{ed(d+1)} \left(\frac{r_c^2 - r^2}{r_c^2 - r_e^2} \right)^2 \tag{104}$$

where d is the dimensionality of the system, $e = \exp(1)$, r_c is a cutoff distance, and r_e is the equilibrium nearest-neighbor distance. The pairwise interaction potential $U(r)$ was taken to be,

$$U(r) = \begin{cases} 4\chi\varepsilon \left[\left(\dfrac{\sigma}{r} \right)^{12} - \left(\dfrac{\sigma}{r} \right)^{6} \right], & r < r_i \\ -a_1(r_c^2 - r^2)^2 + a_2(r_c^2 - r^2)^3, & r_i \leq r \leq r_c \\ 0, & r > r_c \end{cases} \tag{105}$$

where χ is the fractional pair-potential contribution to the total cohesive energy ($\chi = 1/3$ is a reasonable value for many metals), and a_1 and a_2 two parameters that are given in terms of r_i, r_c, and the derivative of the LJ potential of $U(r)$, evaluated at r_i. Finally, the embedding energy E_i^e was taken to be

$$E_i^e(\rho_i) = \frac{1}{2} e\varepsilon d(d+1)(1-\chi)\rho_i \ln \rho_i \tag{106}$$

One can also replace the LJ potential by the more flexible Morse-like potential,

$$U_{\text{Morse}} = \varepsilon\{\exp[-\alpha(r/r_e - 1)] - 1\}^2 - \varepsilon \tag{107}$$

where α, the steepness of the repulsive well, is related to V_0, the volume of the undeformed system, and the bulk modulus of the system at equilibrium. The Morse potential [184] was originally suggested for modeling bond deformations that exceed very small fluctuations about equilibrium states and has proven accurate for reproducing certain features of small molecules.

However, the atomic densities can also be computed by the Hartree-Fock approximation, and the embedding energy and the pair potentials can be calculated by an *ab initio* method. The *ab initio* electronic structure calculations can be used in order to generate an accurate database for configurational energies, which are then used for determining the necessary parameters of the EA model [185] and take advantage of analytical functional forms obtained from the theoretical analysis. The *ab initio* electronic structure calculations are formulated in the context of the quantum mechanical DFT described later in this chapter.

Baskes et al. [186] proposed a potential based on the EA model by introducing an angular dependence in the host electron energy, which could then adequately account for the bond-bending forces in such materials as diamond. The potential could fit the energies of the high-density polymorphs, with the goodness of the fit being comparable with those of the other potentials described below. It could also describe exactly the static properties of cubic diamonds, and provide a relatively accurate description of bulk defects and vacancies. However, it provides high values for the energy of the intrinsic stacking faults in silicon. Most recently, Web and Grest [187] used a variant of the EA model to compute the surface tension of liquid–vapor interface of metals. The agreement between the predicted values and the experimental data was very good, hence indicating that the EA model can also describe fluid interface properties of materials.

3.3.2. The Stillinger-Weber Potential

Stillinger and Weber [188] proposed a semiempirical potential for silicon which appears to be relatively accurate. In their model, the total interatomic potential involves two- and three-body contributions and is written as

$$E = \sum_{i<j} U_2(r_{ij}) + \sum_{i,j<k} U_3(\mathbf{r}_{ij}, \mathbf{r}_{ik}) \tag{108}$$

where U_2—the two-body term—can include such effects as the steric repulsion, charge transfer between atoms, charge-dipole and van der Waals interactions. Therefore,

$$U_2(r_{ij}) = \frac{H_{ij}}{r_{ij}^{n_{ij}}} + \frac{q_i q_j}{r_{ij}} \exp\left(-\frac{r_{ij}}{a}\right) - \frac{D_{ij}}{r_{ij}^4} \exp\left(-\frac{r_{ij}}{b}\right) - \frac{W_{ij}}{r_{ij}^6} \tag{109}$$

The first term of Eq. (109) represents a two-parameter representation of the steric repulsion; the second term is the Coulombic interaction due to charge transfer and contains the effective atomic charges q_i and q_j; the third term takes into account the charge–dipole interaction due to the large polarizability of negative ions, while the last term corresponds to the induced dipole–dipole interactions. Covalent effects are taken into account through three-body bond-bending and bond-stretching terms and includes the Si–C as well as C–Si–C bond angles. The corresponding potential is given by

$$U_3(\mathbf{r}_{ij}, \mathbf{r}_{ik}) = B_{ijk} \exp\left(\frac{\gamma}{r_{ij} - r_0} - \frac{\gamma}{r_{ik} - r_0}\right) \frac{(\cos\theta_{jik} - \cos\bar{\theta}_{jik})^2}{1 + C(\cos\theta_{jik} - \cos\bar{\theta}_{jik})^2} \Theta(r_0 - r_{ij}) \Theta(r_0 - r_{ik}) \tag{110}$$

Here, B_{jik} is the strength of the interaction, $\Theta(r_0 - r_{ij})$ is the step function, θ_{jik} is the angle formed by $\mathbf{r}_{ij}$ and $\mathbf{r}_{ik}$, and $\bar{\theta}_{jik}$ is a constant. The constant C plays an important role if the material undergoes structural transformation. In the original Stillinger-Weber formulation, $\cos\bar{\theta}_{jik}$ was assumed to have a value of $-1/3$, but, more generally, one can treat this term as an adjustable parameter. Note that the "ideal" tetrahedral angle θ is such that $\cos\theta = -1/3$, so that the trigonometric part of Eq. (110) clearly discriminates in favor of pairs of bonds emanating from i with the desired geometry. It is clear that the Stillinger-Weber potential contains many parameters that must be estimated by fitting the predictions obtained with the potential to certain properties of the material. Shimojo et al. [189] employed this potential in their MD simulations of cubic SiC under isothermal-isobaric conditions, using only 1728 atoms. Table 2 compares the predictions of the MD simulations with the experimental data, indicating excellent agreement between the two sets. In addition, the volume-pressure relation was computed for SiC in the zinc-blende structure (that is, in a configuration with fourfold coordination), and was found to be in excellent agreement with the experimental data.

As far as nanoporous materials are concerned, silicon carbide, which has a wide range of applications, from optoelectric devices to engineering materials for various applications, also has an important use as the basic substrate for preparing nanoporous membranes that must operate at high-temperature, high-pressure conditions [190]. The reason for the SiC

Table 2. Comparison of the MD predictions of the properties of cubic SiC in zinc-blende structure, obtained by using the Stillinger-Weber potential, with the experimental data.

Property	MD	Experiment
Lattice constant (Å)	4.36	4.36
C_{11}	390	390
C_{12}	144	142
C_{44}	179	150–256
Bulk modulus	225	225
Melting temperature (°C)	3000	2830

The elastic constants are in GPa.

popularity is that it has excellent chemical stability, good electronic properties, and high stiffness and hardness.

The Stillinger-Weber potential is, by far, the most widely used potential. It has been used in the study of clusters, lattice dynamics, bulk point defects, the liquid and amorphous states, surface diffusion and reconstructions, Si(100) stepped surfaces, the liquid–vapor and crystal–melt interfaces, pulsed melting of surfaces, epitaxial growth from the vapor, liquid-phase epitaxy, and growth of amorphous films via atom deposition, as well as calculation of mechanical properties that was mentioned above. It has also been extended to Ge, sulfur, fluorine, and Si–F materials.

Mistriotis et al. [191] modified the Stillinger-Weber potential in order to describe correctly clusters with more than 6 atoms. The angular dependence of the three-body term was modified, and a four-body term was also added.

3.3.3. The Tersoff Potentials

It can be shown by simple quantum-mechanical arguments that the larger the number of neighbors that an atom has, the weaker the bond to each neighbor is. In general, the bond strength, or bond order, depends in a complex way on the geometry of the material. For example, even-membered rings might be favored over odd ones. However, the most important single variable is the coordination number—the number of neighbors close enough to form bonds. If the energy per bond decreases sufficiently rapidly with increasing coordination, then the diatomic molecule will be the most stable arrangement of atoms. Low coordination numbers are common for atoms at the far right of the Periodic Table (especially near the top). However, if the bond order depends only weakly on the coordination number, then, close-packed structures form so to maximize the number of bonds. This limit corresponds, roughly speaking, to metallic rather than covalent bonding, and is found for atoms at the left and bottom of the Periodic Table, with a trend in between from low coordination numbers at the upper right to high coordination numbers at the lower left. Thus, bond order is a monotonically decreasing function of the coordination number, and a trade-off between this property and number of bonds determines the equilibrium conditions.

Silicon, aside from its technological importance, is a remarkable material because, even with modest changes of pressure, it can take on structures with a large range of coordination. This is due to the fact that a decrease in bond strength with increasing coordination number essentially cancels the increase in the number of bonds over a large range of coordination number. As such, silicon provides a stringent test of our ability for describing the dependence of bonding upon coordination number and, hence, our ability for developing potentials that can accurately describe its structure.

In an important paper, Tersoff [192] suggested such a potential for silicon. Because of the crucial role of bond order and its dependence upon local geometry, one must include an environment-dependent bond order in the potential. Thus, in Tersoff's formulation the total interatomic potential energy is taken to be

$$E = \sum_i E_i = \frac{1}{2} \sum_i \sum_{j \neq i} E_{ij} \tag{111}$$

where

$$E_{ij} = U_c(r_{ij})[a_{ij}U_r(r_{ij}) + b_{ij}U_a(r_{ij})] \tag{112}$$

Here, E_i and E_{ij} are, respectively, a site and a bond energy, the sums are over the atoms of the system, and r_{ij} is the distance between (the centers of) the atoms i and j. The function U_r represents a repulsive pair potential, which includes the orthogonalization energy when atomic wave functions overlap (see below), whereas U_a is the attractive pair potential associated with bonding. As already emphasized throughout this chapter, in many applications short-ranged functions allow a tremendous reduction in computational effort, and, therefore, a cutoff function U_c has been introduced to limit the range of the potential. The *function* b_{ij} is a measure of the bond order, and is assumed to be a monotonically decreasing function of the coordination of atoms i and j. In addition, terms that act to limit the range of interaction to the first neighbor shell are included in b_{ij}, and the function a_{ij} consists solely of such range-limiting terms.

Ferrante et al. [193] showed that a large number of calculated binding energies for solid cohesion and chemisorption can be mapped onto a single dimensionless function using a three-parameter scaling, and Abell [194] showed that this universal behavior can be well-explained by use of a Morse or Morse-like pair potential, Eq. (107). Therefore, Tersoff [192] proposed the following expressions for U_r and U_a:

$$U_r(r) = A\exp(-\lambda_1 r) \tag{113}$$

$$U_a(r) = -B\exp(-\lambda_2 r) \tag{114}$$

whereas the cutoff function U_c was taken to be

$$U_c(r) = \begin{cases} 1, & r < R - D \\ \dfrac{1}{2} - \dfrac{1}{2}\sin\left[\dfrac{\pi(r-R)}{(2D)}\right], & R - d < r < R + D \\ 0, & r > R + D \end{cases} \tag{115}$$

The cutoff function (and its derivative) is continuous for all r, and varies between 0 and 1 in a small range around R, which is selected so as to include only the first-neighbor shell for most structures. In effect, the potential has the form of a Morse pair potential, ignoring the three-body and higher order effects, but with a bond-order parameter b_{ij} that depends on the local environment. The function b_{ij} is given by

$$b_{ij} = (1 + \beta\zeta_{ij}^n)^{-1/2n} \tag{116}$$

with

$$\zeta_{ij} = \sum_{k\neq i,\,j} U_c(r_{ik})g(\theta_{ijk})\exp[\lambda_3^3(r_{ij} - r_{ik})^3] \tag{117}$$

$$g(\theta) = 1 + c^2\{d^{-2} - [d^2 + (h - \cos\theta)^2]^{-1}\} \tag{118}$$

where θ_{ijk} is the angle between bonds ij and ik. The function $\cos\theta_{ijk}$ is used to ensure the proper analytic behavior for the dependence of b_{ij} on θ_{ijk}. Note that $b_{ij} \neq b_{ji}$, which, however, does not have any significant consequence. If, however, one insists on a more symmetric form, the sum over pairs of atoms in Eq. (112) can be replaced with a sum over bonds ($i > j$), with b_{ij} replaced by a symmetric function, $\bar{b}_{ij} = \frac{1}{2}(b_{ij} + b_{ji})$. Tersoff [192] also proposed the following equation for the function a_{ij}.

$$a_{ij} = (1 + \alpha^n\eta_{ij}^n)^{-1/2n} \tag{119}$$

$$\eta_{ij} = \sum_{k\neq i,\,j} U_c(r_{ik})\exp[\lambda_3^3(r_{ij} - r_{ik})^3] \tag{120}$$

where α is typically small enough that $a_{ij} \simeq 1$ unless, of course, η_{ij} is exponentially large.

Subsequently, Tersoff [195] modified his proposed potential in order to describe multicomponent mixtures, and more specifically C–Si and Si–Ge mixtures. In his generalization, Eqs. (111) and (112) remain the same, but the remaining expressions are modified to account for the multicomponent nature of the system. Thus,

$$U_r(r_{ij}) = A_{ij}\exp(-\lambda_{ij}r_{ij}) \tag{121}$$

$$U_a(r_{ij}) = -B_{ij}\exp(-\mu_{ij}r_{ij}) \tag{122}$$

$$U_c(r_{ij}) = \begin{cases} 1, & r_{ij} < R_{ij} \\ \dfrac{1}{2} + \dfrac{1}{2}\cos\left[\dfrac{\pi(r_{ij} - R_{ij})}{(S_{ij} - R_{ij})}\right], & R_{ij} < r_{ij} < S_{ij} \\ 0, & r_{ij} > S_{ij} \end{cases} \tag{123}$$

where the various parameters are given by

$$b_{ij} = \chi_{ij}(1 + \beta_i^{n_i}\zeta_{ij}^{n_i})^{-1/2n_i} \tag{124}$$

$$\zeta_{ij} = \sum_{k\neq i,j} U_c(r_{ik})\omega_{ik}g(\theta_{ijk}) \tag{125}$$

$$g(\theta_{ijk}) = 1 + c_i^2\{d_i^{-2} - [d_i^2 + (h_i - \cos\theta_{ijk})^2]^{-1}\} \tag{126}$$

$$\lambda_{ij} = \frac{1}{2}(\lambda_i + \lambda_j), \quad \mu_{ij} = \frac{1}{2}(\mu_i + \mu_j) \tag{127}$$

$$A_{ij} = \sqrt{A_i A_j}, \quad B_{ij} = \sqrt{B_i B_j} \tag{128}$$

$$R_{ij} = \sqrt{R_i R_j}, \quad S_{ij} = \sqrt{S_i S_j} \tag{129}$$

Note that the parameter χ_{ij} strengthens or weakens the heteropolar bonds and, therefore, represents in some sense the chemistry of the mixture. Note also that $\chi_{ii} = 1$ and $\chi_{ij} = \chi_{ji}$, and that $\omega_{ii} = 1$, although experience has indicated that $\omega_{ij} = 1$ is also a reasonable estimate. Compared with the case of a pure component, the potential for mixtures is somewhat simpler, as the parameter D of Eq. (115) has been eliminated. All the parameters of these potentials have been estimated by fitting them to the heat of formation and the properties of the respective elements. For Si the parameter D is about 0.15 Å. The rest of the parameters are listed in Table 3.

Table 3. Estimates of the parameters for carbon, silicon, and germanium to be used in the Tersoff potential. Except for R and S, all the parameters have been optimized (adapted from Tersoff [195]).

Parameter	C	Si	Ge
A (eV)	1393.6	1830.8	1769.0
B (eV)	346.7	471.18	419.23
R (Å)	1.8	2.7	2.8
S (Å)	2.1	3.0	3.1
c	38049.0	100390.0	106430.0
d	4.384	16.217	15.652
h	−0.57058	−0.59825	−0.43884
n	0.72751	0.78734	0.75627
β	1.5724×10^{-7}	1.1000×10^{-6}	9.0166×10^{-7}
λ (Å^{-1})	3.4879	2.4799	2.4451
μ (Å^{-1})	2.2119	1.7322	1.7047
		$\chi_{C\text{-}Si} = 0.9776$	$\chi_{Si\text{-}Ge} = 1.00061$

Mura et al. [196] studied the properties of $Si_{1-x}C_x$ compounds in the range $0.125 \leq x < 0.875$ by *ab initio* QMD method of Car and Parrinello [50] (see below) and by MD simulations using the Tersoff potentials and found very good agreement between the predictions of the two methods. However, because of the large difference in bonding characteristics between hydrogen and carbon (recall that H is monovalent whereas C has a valency of up to 4), a set of parameters cannot be found that can adequately describe bond energies for a large number of hydrocarbons. Furthermore, the Tersoff potentials cannot describe radicals and nonconjugated double bonds. These deficiencies motivated the development of several modified Tersoff potentials which we now briefly mention.

Chelikowsky et al. [197] developed an interatomic potential similar in form to Tersoff's, which was intended for describing the metallic to covalent transition that occurs in clusters when their size reaches a critical size. To describe the transition, an angular-dependent bond-bending force was incorporated in the potential. The resulting potential provides very accurate description of perfect diamond structure, as well as the high-density polymorphs of silicon. To model clusters, a so-called dangling-bond vector was introduced that describes the transfer of bond strength from a dangling bond to a backbone bond. The energies of Si_n clusters with $n < 10$ are, however, underestimated by their potential. Moreover, the ground-state structures for such values of n are also not well-described. The potential was not intended for bulk point defects and for surfaces.

Following Tersoff, Kohr and Das Sarma [198] developed a series of interatomic potentials for tetrahedrally bonded semiconductors. The bond-bending term was modified to deal with the larger angular distortions from the tetrahedral angle encountered on the various (111) surfaces. Moreover, because the bonds of a given atom can be of different nature, the value of the effective coordination number was fixed in an *ad hoc* way. The potential provides accurate description of various (111) surfaces.

Bolding and Andersen [199] generalized Tersoff's potential by expressing the attractive term of the potential as a sum of $\sigma-$ and $\pi-$bonding terms. The functional form is complex, and the potential contains over 30 parameters. Bolding and Andersen used a very large data base for fitting the parameters, including the static properties of the cubic diamond phase, the fact that the first pressure-induced phase transformation from cubic diamond is the β-tin phase, and the energies and geometries of global and local minima for clusters of 2–10 atoms. For small clusters, the Bolding-Andersen potential generates a surface that has most of the local and global minima predicted by *ab initio* computations. Moreover, its predictions for the ground-state structures and energies are in excellent agreement with those predicted by quantum-mechanical computations. The static properties of cubic diamond silicon are also well described by the potential.

3.3.4. The Brenner Potentials

In addition to the shortcomings of the Tersoff potentials for certain materials, there is another impetus for developing more sophisticated empirical or semiempirical potentials. Chemical vapor deposition (CVD) of diamond films is a process of tremendous technological importance. It is, however, a complex process in which diamond grows under apparently metastable conditions. Various factors, such as addition to the surface of such species as acetylene, methyl radicals, or a mixture of hydrocarbon molecules, the substrate temperature, and initiation of defects, all may play important roles. In order to obtain a better understanding of this complex process, atomic-scale simulations of this phenomenon are, of course, desirable. However, its QMD simulation is still too costly (in terms of the computation time) and, thus, the classical MD computations with an accurate interatomic potential are desirable. The potential developed by Brenner [200] is intended for this purpose. Its main use is for hydrocarbons, and it can take into account the effect of intramolecular chemical bonding (which the Tersoff potentials are incapable of doing) in many small hydrocarbon molecules, as well as graphite and diamond lattices.

In its spirit, Brenner's formulation is similar to Tersoff's. The binding energy E_b for the hydrocarbon potential is given by

$$E_b = \sum_i \sum_{j>i} [U_r(r_{ij}) - \bar{b}_{ij} U_a(r_{ij})] \tag{130}$$

where, similar to the Tersoff potentials, U_a and U_r are the attractive and repulsive part of the energy, and are given by

$$U_a(r_{ij}) = f_{ij}(r_{ij})\frac{D_{ij}^e S_{ij}}{S_{ij}-1}\exp\left[-\sqrt{\frac{2}{S_{ij}}}\beta_{ij}\left(r_{ij}-R_{ij}^e\right)\right] \tag{131}$$

$$U_r(r_{ij}) = f_{ij}(r_{ij})\frac{D_{ij}^e S_{ij}}{S_{ij}-1}\exp\left[-\sqrt{2S_{ij}}\beta_{ij}\left(r_{ij}-R_{ij}^e\right)\right] \tag{132}$$

where D_{ij}^e is the well depth, and R_{ij}^e is the equilibrium distance, the value of which is the same as r_e in the Morse potential, Eq. (107). In fact, for $S_{ij} = 2$ the attractive and replusive potentials are essentially identical with the Morse potential. The functions $f_{ij}(r_{ij})$ are cutoff functions given by

$$f_{ij}(r) = \begin{cases} 1, & r \le R_{ij}^{(1)} \\ \frac{1}{2} + \frac{1}{2}\cos\left[\dfrac{\pi(r - R_{ij}^{(1)})}{(R_{ij}^{(2)} - R_{ij}^{(1)})}\right], & R_{ij}^{(1)} < r < R_{ij}^{(2)} \\ 0, & r \ge R_{ij}^{(2)} \end{cases} \tag{133}$$

It should be clear that the cutoff functions explicitly restrict the interactions to nearest neighbors. The function $\bar{b}_{ij}$ is given by

$$\bar{b}_{ij} = \frac{1}{2}(b_{ij} + b_{ji}) + F_{ij}[N_i^{(t)}, N_j^{(t)}, N_{ij}^{\text{conj}}] \tag{134}$$

implying that, similar to the Tersoff potentials, $\bar{b}_{ij}$ depends on the environment around atoms i and j and implicitly contains many-body information. The function F_{ij} is a correction term which is used only for carbon-carbon bonds, and

$$b_{ij} = \left\{1 + \sum_{k\neq i,j} g(\theta_{ijk}) f_{ik}(r_{ik}) \exp\left(\alpha_{ijk}[(r_{ij} - R_{ij}^e) - (r_{ik} - R_{ik}^e)]\right) + H_{ij}[N_i^{(\mathrm{H})}, N_i^{(\mathrm{C})}]\right\}^{\delta_i} \tag{135}$$

Here, $N_i^{(\mathrm{C})}$ and $N_i^{(\mathrm{H})}$ are the number of carbon and hydrogen atoms bonded to atom i, $N_i^{(t)} = N_i^{(\mathrm{C})} + N_i^{(\mathrm{H})}$, N_{ij}^{conj} depends on whether a bond between carbon atoms i and j is part of a conjugated system, and θ_{ijk} is the angle between bonds ij and ik. Similar to F_{ij}, the function H_{ij} is a correction term, and both functions are used only for hydrocarbons.

The cutoff functions $f_{ij}(r)$ are used for defining the various quantities. One has

$$N_i^{(\mathrm{H})} = \sum_{j=\{\mathrm{H}\}} f_{ij}(r_{ij}) \tag{136}$$

$$N_i^{(\mathrm{C})} = \sum_{j=\{\mathrm{C}\}} f_{ij}(r_{ij}) \tag{137}$$

where, for example, $\{\mathrm{C}\}$ denotes the set of the carbon atoms. Values of $N_i^{(t)}$ for neighbors of two carbon atoms involved in a bond are used for determining whether the bond is part of a conjugated system. For example, if the neighbors are carbon atoms that have a coordination number of less than four (i.e., $N_i^{(t)} < 4$), the bond is defined as part of a conjugated system. For a bond between carbon atoms i and j,

$$N_{ij}^{\text{conj}} = 1 + \sum_{k(\neq i,j)=\{\mathrm{C}\}} f_{ik}(r_{ik}) F(x_{ik}) + \sum_{l(\neq i,j)=\{\mathrm{C}\}} f_{jl}(r_{jl}) F(x_{jl}) \tag{138}$$

with

$$F(x_{ik}) = \begin{cases} 1, & x_{ik} \leq 2 \\ \frac{1}{2} + \frac{1}{2}\cos[\pi(x_{ik} - 2)], & 2 < x_{ik} < 3 \\ 1, & x_{ik} \geq 3 \end{cases} \tag{139}$$

and

$$x_{ik} = N_k^{(i)} - f_{ik}(r_{ik}) \tag{140}$$

The function $F(x_{ik})$ yields a continuous value of N_{ij}^{conj} as bonds form and break and as second-neighbor coordinations change. If $N_{ij}^{\text{conj}} = 1$, a bond is not part of a conjugated system and the function yields appropriate values, while for $N_{ij}^{\text{conj}} \geq 2$ the bond is part of a conjugated system and the parameters fitted to conjugated bonds are used. Finally, to make the potential continuous, 2D and 3D cubic splines are used for interpolating, respectively, the functions H_{ij} and F_{ij} between values at discrete numbers of neighbors. The function $g(\theta)$ is very similar to that in the Tersoff potentials, Eqs. (118) and (126). For example, for carbon one has

$$g_C(\theta) = a_0\left[1 + \frac{c_0^2}{d_0^2} - \frac{c_0^2}{d_0^2 + (1 + \cos\theta)^2}\right] \tag{141}$$

The Brenner potential has a large number of parameters that must be fitted to experimental data. The procedure for doing this is to first fit to systems consisting of only carbons and hydrogen. Parameters are then selected for the mixed hydrocarbon system that produce additive bond energies. Because the pair terms are first fitted to solid-state carbon structures, the equilibrium carbon–carbon distances and the stretching force constants for hydrocarbons are completely determined by fitting to bond energies. To determine appropriate energies for hydrocarbons with carbon–carbon bonds, additive bond energies for single, double, conjugated double and triple carbon–carbon bonds, and carbon–hydrogen bonds are deterimined from molecular atomization energies. Values of the parameter δ_i of Eq. (135) for carbon and hydrogen turn out to be identical and equal to 0.80469. Values of the other parameters are listed by Brenner [200], a list too long to be given here. The Brenner potential has been used successfully in studying many phenomena, including reaction of hydrocarbon species on diamond surfaces, mechanical properties of graphite sheet and nanotubes, and CVD of diamond films. Moreover, excellent agreement was found [201] between the predictions of MD simulations of energetics of nanoscale graphitic tubules using the Brenner potential, and those of first-principle electronic structure calculations using local-density functional described later in this chapter.

Despite its success, the Brenner potential does have certain limitations. For example, it does not include the resonance effect of aromatics. Most importantly, the long-range van der Waals and Coulombic interactions are not included explicitly in the model, although such interactions play an important role in many materials. Che et al. [202] modified the Brenner potential to take such effects into account. In their formulation, the total energy of the system is written as

$$E = \sum_i \sum_{j>i} \left[U_{ij}^{\text{V}}(r_{ij}) + P_{ij}(r_{ij}) U_{ij}^{\text{NB}}(r_{ij})\right] \tag{142}$$

Here, superscript V denotes the valence short-range terms (for example, those in the Brenner potential), NB indicates the long-range non-bond part of the energy (e.g., the contribution of van der Waals or Coulombic forces), and $P_{ij} = P_{ji}$ is a screening function that properly weights the NB contributions to the total energy, and is given by

$$P_{ij} = f(U_{ij}^{\text{V}}, U_{ji}^{\text{V}}) \prod_{k \neq i,j} f(U_{ik}^{\text{V}}, U_{ki}^{\text{V}}) \tag{143}$$

with

$$f(x,y)=\begin{cases}\exp(-x^2y^2), & \text{if } x<0 \text{ and } y<0\\ 1, & \text{otherwise}\end{cases} \tag{144}$$

As pointed out by Che et al. [202], the screening function eliminates NB interactions between two atoms i and j when they are directly bonded (i.e., $U_{ij}^{\mathrm{V}}<0$) or when they are both bonded to a common atom k (i.e., $U_{ik}^{\mathrm{V}}<0$ and $U_{kj}^{\mathrm{V}}<0$). In both cases, the screening function P_{ij} is negligibly small and, therefore, the NB interactions do not make improper contribution to the total energy. Using the relation, $F_{\alpha\beta}=-\partial E/\partial r_{\alpha\beta}$, it is now straightforward to show that the force $F_{\alpha\beta}$ between atoms α and β is given by

$$F_{\alpha\beta}=F_{\alpha\beta}^{\mathrm{V}}+P_{\alpha\beta}F_{\alpha\beta}^{\mathrm{NB}}-4\sum_{i>j}P_{ij}U_{ij}^{\mathrm{VDW}}(U_{ij}^{\mathrm{V}})^3F_{ij,\alpha\beta}^{\mathrm{V}}-\sum_{ijk}U_{ik}^{\mathrm{V}}U_{kj}^{\mathrm{V}}P_{ij}U_{ij}^{\mathrm{VDW}}\left(U_{ik}^{\mathrm{V}}F_{kj,\alpha\beta}^{\mathrm{V}}+U_{kj}^{\mathrm{V}}F_{ik,\alpha\beta}^{\mathrm{V}}\right) \tag{145}$$

with

$$F_{ij,\alpha\beta}^{\mathrm{V}}=-\frac{\partial U_{ij}^{\mathrm{V}}}{\partial r_{\alpha\beta}},\quad F_{\alpha\beta}^{\mathrm{NB}}=\frac{\partial U_{\alpha\beta}^{\mathrm{NB}}}{\partial r_{\alpha\beta}} \tag{146}$$

In Eq. (145), $F_{\alpha\beta}^{\mathrm{V}}$ represents the valence forces, such as bond stretching, bending, and torsion, and is contributed by the Brenner-type potential. The second term represents the NB forces between two properly screened atoms. The third and fourth terms are due to forces arising from correlations between screened bonds that, in most cases, are negligible. Therefore, if atoms i and j do not form a valence bond and a bond with the same atom k, then usually $F_{ij,\alpha\beta}^{\mathrm{V}}=0$, and either $U_{ik}^{\mathrm{V}}=0$ or $U_{kj}^{\mathrm{V}}=0$, leading to zero contribution. However, even if both atoms i and j bind to a common atom k, or if they form a valence bond directly, these terms will still make a negligible contribution to the total energy due to the exponential screening factor, Eq. (144), as in this case either $U_{i\alpha}^{\mathrm{V}}<0$ or $U_{j\beta}^{\mathrm{V}}<0$. Note that there is no restriction on this formulation. That is, the specifics of the NB terms do not alter the general formulation of this potential. Che et al. [202] used this generalized interatomic potentials to study the energetics and structures of a variety of materials, including graphite and molecular crystals and bucky tubes, while Lim et al. [203] used it for generating nanoporous amorphous carbon structure, and investigating transport, chemisorption and separation of gases in such materials.

3.3.5. Force Fields for Organic and Polymeric Materials

In addition to the above force fields and potentials, over the past 15 years or so many other force fields have been developed, and some have even been commercialized, for simulating large organic and polymeric molecules, as well as small inorganic molecules. So far as application to nanoporous materials is concerned, such force fields are important to accurate modeling of polymeric materials, both when they are used as membranes and as precursor materials for preparing other types of nanoporous membranes.

Sun [204] reviewed and discussed many of such force fields. As he pointed out, such force fields can be classified in three different classes:

(i) In the first class are those force fields that were intended to be very generic and, therefore, applicable to a wide variety of materials. For example, the force field UFF [205] was developed to model molecules of any combination of elements of the Periodic Table. However, due to their generic nature, such force fields are expected to yield only reasonable predictions for the molecular structure of a material.

(ii) Force fields that have been designed for a specific class of molecules, mostly in biochemical applications, are in the second group. Great efforts have been made to improve the quality of the predictions of such force fields. The force fields AMBER [206, 207], CHARMM [208], and OPLS/AMBER [209–211] are in this group. These force fields, and also the UFF, use simple functional forms for the diagonal terms of the force-constant matrix.

(iii) Force fields that not only can model a broad class of materials but also can yield accurate predictions for many of their properties are in the third set of the force fields. Such force fields employ very complex functional forms, including off-diagonal entries of the force-constant matrix representing cross-coupling terms, and cubic and quartic forms for the force constants (see above). They contain a large number of parameters that must be estimated accurately. These parameters have been estimated using high-quality experimental data. The parameters of the force fields MM3 [212] and MM4 [213] were estimated by this method. Alternatively, quantum-mechanical *ab initio* computations (see below) can be used for estimating the force field's parameters. This method has been used for estimating the parameters of CFF93 [214] and MMFF [215] force fields. Such force fields, although complex, have been shown to yield very accurate predictions for many properties of a variety of polymeric as well as other types of materials.

The force fields mentioned above were developed mainly for biological molecules, which are mostly *natural* polymers. Attempts have also been made to develop force fields for synthetic (man-made) polymers. The well-known polymer-consistent force field (PCFF) [216–221] is an example. Here, we describe a more sophisticated force field for synthetic polymers and organic materials, which is called COMPASS (condensed-phase optimized molecular potentials for atomistic simulation studies) [204, 222–224], following Sun [204]. We use his notation, which might somewhat deviate from our notation in the rest of this chapter, in order to enable the reader to check the original sources without any confusion.

The functional form of the potential used in COMPASS is given by

$$
\begin{aligned}
U = {} & \sum_b [k_2(b-b_0)^2 + k_3(b-b_0)^3 + k_4(b-b_0)^4] + \sum_\theta [k_2(\theta-\theta_0)^2 + k_3(\theta-\theta_0)^3 + k_4(\theta-\theta_0)^4] \\
& + \sum_\phi [k_1(1-\cos\phi) + k_2(1-\cos 2\phi) + k_3(1-\cos 3\phi)] \\
& + \sum_\chi k_2\chi^2 + \sum_b \sum_{b'} k(b-b_0)(b'-b_0') + \sum_\theta \sum_{\theta'} k(\theta-\theta_0)(\theta'-\theta_0') + \sum_b \sum_\theta k(b-b_0)(\theta-\theta_0) \\
& + \sum_b \sum_\phi (b-b_0)(k_1\cos\phi + k_2\cos 2\phi + k_3\cos 3\phi) \\
& + \sum_\theta \sum_\phi (\theta-\theta_0)[k_1\cos\phi + k_2\cos 2\phi + k_3\cos 3\phi] \\
& + \sum_\theta \sum_{\theta'} \sum_\phi k(\theta-\theta_0)(\theta'-\theta_0')\cos\phi + \sum_i \sum_j \frac{q_i q_j}{r_{ij}} + \sum_i \sum_j \epsilon_{ij} \left[2\left(\frac{r_{ij}^0}{r_{ij}}\right)^9 - 3\left(\frac{r_{ij}^0}{r_{ij}}\right)^6 \right]
\end{aligned}
\tag{147}
$$

Generally speaking, the potential given by Eq. (146) is the sum of two major parts: the bonded (or what Sun [204] refers to as valence) terms, and the nonbond contributions. Here, b represents internal coordinates of a bond, θ is the angle (between two bonds joined at a common atom), ϕ is the torsional angle, while χ represents the out-of-plane angle. The coupling terms between these four quantities have been included, as they are important to predicting vibration frequencies and structural changes associated with conformational changes of the molecules.

The nonbonded terms of Eq. (147) represent the van der Waals (vdW) and Coulombic interactions. These are used for representing the interactions between two atoms that are separated by two or more atoms (so that they cannot be bonded). Note that while the vdW interaction potential that is used in Eq. (147) is similar to a LJ potential, the exponents 9 and 6 are not the same as those in the original 6-12 LJ potential. The reason is that the repulsive (r^{-12}) part of the original LJ potential is considered too hard, whereas the modified form (r^{-9}), which is somewhat "softer," represents better the repulsive interactions between two atoms that are relatively far from each other.

The mixing rules for the r_{ij}^0 and ϵ_{ij}, representing a pair of atoms, are given by,

$$r_{ij}^0 = \left[\frac{(r_i^0)^6 + (r_j^0)^6}{2}\right]^{1/6} \tag{148}$$

$$\epsilon_{ij} = 2\frac{\sqrt{\epsilon_i \epsilon_j}}{(r_i^0)^3 (r_j^0)^3} \tag{149}$$

The Coulombic interaction is represented by atomic partial charges. A parameter δ_{ij} is used, which represents the charge separation between two bonded atoms i and j, in order to make the charge parameters transferable. Hence, one writes,

$$q_i = \sum_j \delta_{ij} \tag{150}$$

where the sum is over all atoms j that are bonded to atom i. In addition, for simulation of liquids and crystals in the condensed phase, a cutoff distance r_c (typically taken to be about 10 Å) is used to truncate the nonbonded interactions. For computing energies and pressures, however, the long-range interactions are considered. This is done by computing the nonbonded contributions up to r_c, calculating the corrections to them due to distances $r > r_c$, and using spline functions to smoothen the transition from the region $r \leq r_c$ to $r > r_c$. For the vdW interactions, if we consider a system of N_n different nonbonded atoms interacting with pair potential $U_{ij}(r)$, the corrections to the total energy and pressure are given by [204],

$$U_c = \frac{1}{2}\sum_{i=1}^{N_n} N_i \sum_{j=1}^{N_n} 4\pi\rho_j \int_{r_c}^{\infty} g_{ij}(r) U_{ij}(r) r^2 dr \tag{151}$$

$$P_c = \frac{1}{6}\sum_{i=1}^{N_n} \rho_i \sum_{j=1}^{N_n} 4\pi\rho_j \int_{r_c}^{\infty} g_{ij}(r) [rU'(r)] r^2 dr \tag{152}$$

Here, $g_{ij}(r)$ is the pair radial distribution function, ρ_i is the density, and N_i is the number of atoms of type i. Because the vdW potential and its derivative are very flat for large values of r, one usually uses $g_{ij}(r) = 1$ for large r. For long-range interactions between two charge-neutral groups, the multipole-expansion method described earlier is used.

The COMPASS force field has a large number of parameters. They have been estimated using a very large amount of accurate experimental data, as well as *ab initio* quantum-mechanical computations. The resulting force field is capable of providing accurate predictions for many properties of polymeric and other organic molecules. Sun [204] provides a detailed comparison between the calculated properties and the reference data.

Development of empirical or semiempirical potentials for use in MD simulations remains an active research field. It is neither possible nor necessary to list all the interaction potentials that have been proposed in the past. Several such empirical potentials, in addition to those described here, are discussed by Günes et al. [225].

3.4. Quantum-Mechanical Modeling

In this section, we describe quantum-mechanical computational techniques for modeling nanoporous materials. These are fundamental methods that are based on the solution of the Schrödinger equation and compute the properties of interest based on fundamental principles, namely, the electronic and nuclear structures of atoms. Although, due to the highly complex computations that must be carried out, these methods, when they were first developed, could not be used for computing the properties of molecules with a large number of atoms, but the advent of fast computers, together with the development of highly efficient computational strategies, have gradually converted these methods into powerful tools for modeling various materials and their properties. These methods have been advanced to the

point that they can now be used even for proteins [226], molecules that were thought to be too complex for quantum-mechanical modeling.

So far as nanoporous materials are concerned, quantum-mechanical techniques can be (and have been) used for their modeling and estimating their properties. The application of these methods to nanoporous materials includes the following:

(i) Beginning, perhaps, with the work of Mintmire et al. [227], first-principle quantum-mechanical computations have been used for studying several properties of carbon nanotubes, fullerene tubules, and similar materials. Such applications include electronic structure calculations of fullerene tubules [227] and of carbon microtubules [12, 13, 201, 228, 229] and the study of the mechanical [230–232], adsorption [233, 234], oxidation [235], scattering [236], and thermal and vibrational [237] properties of carbon nanotubes.

(ii) One of the first applications of such methods has been to study silicon and silicon carbide, important materials not only for the semiconductor industry but also for preparing nanoporous membranes that can be effective under harsh operating conditions, such as high temperatures and/or high pressures, and in the presence of steam [190].

(iii) In addition, as pointed out earlier, *ab initio* quantum-mechanical computations have been used for estimating some of the parameters of the various force fields that have been developed for polymeric materials. In addition to the fact that polymeric materials can, on their own, be used as membranes for separations, they are often used as precursors for preparing several types of nanoporous membranes, such as carbon-molecular sieve membranes [134–136].

In what follows, we describe the main quantum-mechanical computational methods for modeling materials, including nanoporous materials, and studying their properties.

3.4.1. Density Functional Theory

Comprehensive reviews of the density functional theory (DFT) and its applications are given by Jones and Gunnarsson [238], Payne et al. [239], and Parr and Yang [240]. Some of our discussions in this section closely follow these reviews.

The original fundamental theoreoms for the DFT were developed by Hohenberg and Kohn [47]. Motivated by these theorems, Kohn and Sham [48] developed a set of accurate one-electron self-consistent eigenvalue equations that have provided a practical means of realistic electronic structure calculations on a large array of atoms, molecules and materials [238, 240, 241]. In addition, an integral formulation of the electronic structure has also been developed in which the one-electron density is obtained directly without the introduction of orbitals [242], although to our knowledge this theory, despite its promise, has not been used extensively in numerical studies.

The electron density $\rho(\mathbf{r})$ is subject to the constraint that

$$\int \rho(\mathbf{r})\, d^3r = N \tag{153}$$

where N is the total number of electrons in the system. The Hamiltonian of a many-electron system is given by

$$H = \sum_i \left[-\frac{1}{2}\nabla_i^2 + U_e(\mathbf{r}_i) \right] + \frac{1}{2} \sum_{i,i\neq j} \sum_j \frac{1}{|\mathbf{r}_i - \mathbf{r}_j|} \tag{154}$$

where $U_e(\mathbf{r})$ is an external potential representing the Coulomb attraction by the frozen-in nuclei. The ground state can be determined by a variational approach which is carried out in two steps.

(i) One minimizes, for a given electron density, the energy functional with respect to the wave functions that are consistent with the given density. In practice, this is done numerically. Methods for direct energy minimization, such as the conjugate-gradient method, were already described above. For the present problem, several "tricks" are used in order the minimize the total energy in a highly efficient manner [3, 238–240].

(ii) The result,

$$E[\rho(\mathbf{r})] = \min_{\Psi}\langle\Psi|\mathscr{H}|\Psi\rangle \tag{155}$$

is then minimized with respect to ρ, subjected to the constraint imposed by Eq. (153). If we now separate the Hamiltonian, $\mathscr{H} = \mathscr{H}_0 + U_e(\mathbf{r})$, where $\mathscr{H}_0$ represents the Hamiltonian without the external potential (i.e., the Hamiltonian of a homogeneous electron gas), then

$$E(\rho) = \min_{\Psi}[\langle\Psi|\mathscr{H}_0|\Psi\rangle] + \int U_e(\mathbf{r})\rho(\mathbf{r})\,d^3r = E'(\rho) + \int U_e(\mathbf{r})\,d^3r \tag{156}$$

where $E'(\rho) = \min_{\Psi}[\langle\Psi|\mathscr{H}_0|\Psi\rangle]$ does not depend on the external potential U_e.

The main problem lies in the fact that $E(\rho)$ is not known for both interacting and noninteracting electron systems. We know, however, that in the noninteracting case $E(\rho)$ can be written as

$$E(\rho) = E_k(\rho) + \int U_e(\mathbf{r})\rho(\mathbf{r})\,d^3r \tag{157}$$

where $E_k(\rho)$ is the kinetic contribution to $E(\rho)$. Variation of E with respect to ρ yields the following equation

$$\frac{\delta E_k(\rho)}{\delta\rho(\mathbf{r})} + U_e(\mathbf{r}) = \lambda\rho(\mathbf{r}) \tag{158}$$

where λ is the Lagrange multiplier associated with the constraint (153). The exact form of $E_k(\rho)$ is, of course, unknown, but we know that the ground state density is given by Eq. (5), and that the spin-orbitals satisfy the single-particle Schrödinger equation:

$$\left[-\frac{1}{2}\nabla^2 + U_e(\mathbf{r})\right]\Psi_k(\mathbf{r}) = \epsilon_k\Psi_k(\mathbf{r}) \tag{159}$$

where ϵ_k are the associated eigenvalues. The spin-orbitals Ψ_k must be normalized in order for the constraint (153) to be satisfied. It is clear that if $E_k(\rho)$ can be used in place of $E'(\rho)$, then it must also be assumed that E_k is independent of the external potential $U_e(\mathbf{r})$ (just as E' is independent of U_e). We now write down the energy functional for a many-electron system with electronic interactions included:

$$E(\rho) = E_k(\rho) + \int U_e(\mathbf{r})\rho(\mathbf{r})\,d^3r + \frac{1}{2}\int d^3r\int\rho(\mathbf{r}')\frac{1}{|\mathbf{r}-\mathbf{r}'|}\rho(\mathbf{r})\,d^3r' + E_{Xc}(\rho) \tag{160}$$

The first three terms of Eq. (160) represent the contribution to $E(\rho)$ by the noninteracting electron gas, whereas $E_{Xc}(\rho)$, which is called the *exchange-correlation energy*, represents all other contributions to $E(\rho)$ that are not accounted for by the first three terms. Equation (160) has the advantage that it contains no approximation, and that all the unknown contributions have been lumped in $E_{Xc}(\rho)$. Varying Eq. (160) with respect to ρ, we obtain

$$\frac{\delta E_k(\rho)}{\delta\rho(\mathbf{r})} + U_e(\mathbf{r}) + \int\frac{1}{|\mathbf{r}-\mathbf{r}'|}\rho(\mathbf{r}')\,d^3r' + \frac{\delta E_{Xc}(\rho)}{\delta\rho(\mathbf{r})} = \lambda\rho(\mathbf{r}) \tag{161}$$

In essence, we have an *effective potential* given by

$$U_{\text{eff}}(\mathbf{r}) = U_e(\mathbf{r}) + \int\frac{1}{|\mathbf{r}-\mathbf{r}'|}\rho(\mathbf{r}')d^3r' + \frac{\delta E_{Xc}(\rho)}{\delta\rho(\mathbf{r})} \tag{162}$$

Therefore, one may write

$$\left[-\frac{1}{2}\nabla^2 + U_{\text{eff}}(\mathbf{r})\right]\Psi_k(\mathbf{r}) = \epsilon_k\Psi_k(\mathbf{r}) \tag{163}$$

Putting everything together, we finally obtain

$$E = \sum_{i=1}^{N} \epsilon_i - \frac{1}{2} \int d^3r \int \rho(\mathbf{r}) \frac{1}{|\mathbf{r} - \mathbf{r}'|} \rho(\mathbf{r}')\, d^3r' - \int \frac{\delta E_{ex}(\mathbf{r})}{\delta \rho(\mathbf{r})} \rho(\mathbf{r})\, d^3r + E_{Xc}(\rho) \qquad (164)$$

Equations (5) and (162)–(164) constitute the DFT.

As Eqs. (162)–(164) indicate, the Kohn-Sham equations map the interacting many-electron system onto a system of noninteracting electrons moving in the effective potential U_{eff} generated by all the other electrons. If the exchange-correlation energy functional E_{Xc} were known exactly, then taking the functional derivative with respect to the density would produce an exchange-correlation potential that includes the effects of correlation and exchange *exactly*. However, E_{Xc} is not known exactly, and thus the main task is developing an accurate approximation for it. Once this approximation has been decided upon, the bulk of the work involves finding the solution of the eigenvalue problem described by Eq. (163). Note that the main difference between the Hartree-Fock and DFT approximations is that, the latter replaces the Hartree-Fock exchange term by the exchange-correlation energy. A particularly powerful method for developing accurate approximations for E_{Xc} is the so-called local-density approximation, which we will discuss shortly.

Thus, minimization of the total energy functional can be carried out directly using the Kohn-Sham model, Eqs. (163) and (164), subjected to the constraint (153), using various minimization techniques, such as those described above. Usually, the eigenvalues ϵ_k are interpreted as the excitation energy. When such interpretation has been used for predicting many properties of various atoms and molecules, the predictions have been found to be in excellent agreement with the experimental data.

The DFT has been extended to time-dependent problems [243]. Time-dependent DFT (TDDFT) makes it possible to apply the technique to excited states of many-body systems. In this scheme, one must define a dynamic exchange-correlation energy $E_{Xc}(\rho, \mathbf{r}, t)$, which must somehow be calculated. It has been shown that substantial improvements of excitation energies with respect to the original Kohn-Sham eigenvalues are obtained with the TDDFT. However, even within this extension, certain problems in solids persisted for some time, such as the wrong Kohn-Sham band gap, regardless of the type of approximation used for E_{Xc}. Tokatly and Pankratov [244] showed that, at excitation frequencies, $E_{Xc}(\mathbf{r}, \mathbf{r}')$ exhibits a highly non-local behavior with a range that is as large as the system itself, and, hence, it diverges as the system's size becomes very large. They developed a perturbation technique which maintains a correct electron density in every order of the perturbation theory and, therefore, removed this unphysical feature of the TDDFT.

However, in general, the DFT has been designed for predicting the *ground-state* properties, and the Kohn-Sham eigenvalues are actually the derivatives of the total energy with respect to the occupation numbers of these states. Therefore, it may be appropriate to interpret ϵ_k and Ψ_k as only auxiliary variables that are used for constructing the ground-state energy and density, because there are many materials for which interpretation of ϵ_k as the excitation energy is wrong and leads to erroneous results. Alternatively, one can use an indirect method for carrying out the minimization of the total energy functional. Among the most successful such indirect methods is the quantum molecular dynamics (QMD) method of Car and Parrinello [50], to be described shortly.

3.4.2. Local-Density Approximation

The local-density approximation assumes that the exchange-correlation energy functional is purely local. In an inhomogeneous material, the exchange-correlation potential at any point $\mathbf{r}$ depends not only on the electron density at that point, but also on its variations in the vicinity of $\mathbf{r}$. Thus, one may develop a gradient expansion in which E_{Xc} depends on $\rho(\mathbf{r})$, $\nabla\rho(\mathbf{r})$, $\nabla[\nabla\rho(\mathbf{r})]$, ... However, if such an expansion is used in the DFT, the required computations will be very difficult to carry out in a reasonable amount of time. In addition, simple gradient expansions behave rather badly and, therefore, one must be careful in using a gradient expansion, an issue that will be discussed in the next section. Such difficulties provided the prime motivation for developing the local-density approximation which ignores

all corrections to the exchange-correlation energy at any point $\mathbf{r}$ due to heterogeneities in its vicinity. Instead, one makes the *ansatz* that

$$E_{Xc}[\rho(\mathbf{r})] = \int \epsilon_{Xc}[\rho(\mathbf{r})]\rho(\mathbf{r})\, d^3r \tag{165}$$

where $\epsilon_{Xc}[\rho(\mathbf{r})]$ is the exchange-correlation energy per particle of a homogeneous electron gas at density $\rho(\mathbf{r})$. In other words, if the exchange-correlation potential is assumed to be a local *function*, as opposed to being a *functional*, of the density with the same value as for a uniform electron gas, one obtains the local-density approximation. The nonuniform gas at $\mathbf{r}$ is treated as if it were part of a uniform electron gas of constant density.

The local-density approximation is very accurate if $\rho(\mathbf{r})$ does not vary too rapidly, but is also surprisingly accurate when the distribution of electrons is strongly inhomogeneous, such as at surfaces and in molecules. To calculate ϵ_{Xc}, the exchange effects are separated out from the dynamic correlations effects that are due to the Coulomb interaction between the electrons. The exchange part, commonly denoted by ϵ_x, is given by

$$\epsilon_x[\rho(\mathbf{r})] \sim -c\rho^{1/3}(\mathbf{r}) \tag{166}$$

where c is a constant. Equation (166) can be derived based on calculations for a homogeneous electron gas. For open shell systems, the spin-up and -down densities $\rho_\uparrow$ and $\rho_\downarrow$ are usually taken into account as two independent densities in the exchange-correlation energy. In this version of the local-density approximation, which is called the *local spin-density approximation*, E_x, the exchange part of the energy, is given by

$$E_x(\rho_\uparrow, \rho_\downarrow) = -\frac{3}{(3/4\pi)^{1/3}} \int [\rho_\uparrow^{4/3}(\mathbf{r}) + \rho_\downarrow^{4/3}(\mathbf{r})]\, d^3r \tag{167}$$

which is obtained by inserting (166) into (165). Various schemes have also been proposed for taking into account the effect of the dynamic correlations [245, 246].

In general, the local-density approximation gives a single well-defined global minimum for the energy of a non–spin-polarized system of electrons in a fixed ionic potential, implying that any energy minimization scheme will locate the global energy minimum of the electronic system. If a material has more than one local minimum in the electronic energy, performing total-energy calculations will be very difficult because the global energy minimum can be found only by sampling the energy functional over a large region of phase space.

3.4.3. Generalized Gradient Approximation

Another popular approximation to the exchange-correlation energy that is now widely used is the generalized gradient approximation according to which

$$E_{Xc}[\rho(\mathbf{r})] = \int f(\rho, \nabla\rho) d^3r \tag{168}$$

where f is an analytic parameterized function that is fitted in such a way that E_{Xc} satisfies several exact requirements. Many functional forms for f have been suggested, a list of which is too long to be given here. Here, we only describe a relatively simple one due to Perdew et al. [247]. To begin with, the total electron density ρ is written as the sum of up and down spin densities, $\rho(\mathbf{r}) = \rho(\mathbf{r})_\downarrow + \rho(\mathbf{r})_\uparrow$, $E_{Xc} = E_X + E_c$, and $\epsilon_{Xc} = \epsilon_X + \epsilon_c$. Perdew et al. [247] proposed that

$$E_c(\rho) = \int \rho(\mathbf{r})[\epsilon_c(r_s, \zeta) + H(r_s, \zeta, t)] d^3r \tag{169}$$

where r_s is called the Seitz radius (such that $\rho = 3/4\pi r_s^3$), $\zeta = (\rho_\uparrow - \rho_\downarrow)/\rho$, and $t = |\nabla\rho|/(2k_s\phi\rho)$ is a dimensionless density gradient. Here, $\phi(\zeta) = \frac{1}{2}[(1+\zeta)^{2/3} + (1-\zeta)^{2/3}]$, and k_s is the Thomas-Fermi screening wave number. Moreover, $\epsilon_c(r_s, \zeta) = (e^2/a_0)\phi^3[\gamma \ln(r_s/a_0) - \omega]$, with $\gamma = (1 - \ln 2)/\pi^2 \simeq 0.031091$ and $\omega \simeq 0.046644$.

The function H is selected in such a way that E_{Xc} satisfies several rigorous constraints. The proposed form for H is given by

$$H = \gamma\phi^3 \left(\frac{e^2}{a_0}\right) \ln\left[1 + \frac{\beta}{\gamma} t^2 \left(\frac{1 + At^2}{1 + At^2 + A^2 t^4}\right)\right] \tag{170}$$

with

$$A = \frac{\beta}{\gamma}\left[\exp\left(-\frac{a_0 \epsilon_c}{\gamma \phi^3 e^2}\right) - 1\right]^{-1} \tag{171}$$

In these equations, e is the electron charge, $a_0 = \hbar^2/me^2$, and $\beta \simeq 0.066725$. The E_X portion of E_{Xc} is written as

$$E_X = \int \rho(\mathbf{r}) \epsilon_x(\rho) F_X(s)\, d^3r \tag{172}$$

where $\epsilon_X(\rho) = -3e^2(3\pi^2\rho)^{1/3}/(4\pi)$, and $s = (r_s/a_0)^{1/2}\phi t/c$ is, similar to t, a dimensionless density with $c \simeq 1.2277$. The function $F_X(s)$ is given by

$$F_X(s) = 1 + \kappa - \frac{\kappa}{1 + \mu s^2/\kappa} \tag{173}$$

with $\kappa = 0.804$ and $\mu = \beta\pi^2/3 \simeq 0.21951$. Let us emphasize that, although we only provide here the numerical values of the constants that appear in these equations, they are in fact related to fundamental physical constants and do not represent numerical fits to some experimental data. The above equations are widely used in the DFT computations of various materials in general, and of nanotubes and nanopores in particular.

3.4.4. Computation of NonPeriodic Systems

Although the DFT computations are carried out most conveniently for periodic systems, they run into difficulty when the system contains some sort of a defect. Such systems have attracted wide attention, especially when they contain a large number of atoms, in which case they are referred to as *mesoscopic systems*. Examples of such systems are abundant and include such materials as quantum dots and wires and biological macromolecules. To study them with the DFT, a periodic *supercell* is used. The supercell contains the defect that is surrounded by a region of bulk crystal. Periodic boundary conditions are applied to the supercell, so that it is replicated throughout space. Thus, due to periodicity, one actually computes the energy per unit cell of a crystal containing an array of defects, rather than the energy of a crystal containing a single defect. To prevent the defects in the neighboring cells to interact appreciably with each other, one must include enough bulk solid in the supercell.

Another case for which a supercell must be used in the computations is when a surface is only partially periodic. For example, it may have periodicity in its own plane but not in the direction perpendicular to its plane. The supercell for such systems contains a crystal slab and a vacuum region and is repeated over all space, so that the total energy of an array of crystal slabs is calculated. In order to ensure that the results of the computations are true representative of an isolated surface, the vacuum region must be wide enough that faces of adjacent crystal slabs do not interact across the vacuum. The crystal slab must also be thick enough that the two surfaces of each crystal slab do not interact through the bulk crystal. Even molecules can be studied in this fashion [248].

3.4.5. PseudoPotential Approximation

To simplify the computation for periodic systems, one takes advantage of Bloch's theorem, according to which in a periodic solid material each electronic wave function can be written as the product of a cell-periodic part and a wavelike part:

$$\Psi_i(\mathbf{r}) = \exp(i\mathbf{k} \cdot \mathbf{r}) f_i(\mathbf{r}) \tag{174}$$

The cell-periodic part of Ψ_i can be expanded using a basis set that consists of a discrete set of plane waves with wave vectors that are reciprocal lattice vectors of the crystal. Therefore,

$$f_i(\mathbf{r}) = \sum_{\mathbf{G}} c_{i,\mathbf{G}} \exp(i\mathbf{G} \cdot \mathbf{r}) \tag{175}$$

where the reciprocal lattice vectors $\mathbf{l}$ are defined by, $\mathbf{G} \cdot \mathbf{l} = 2\pi m$ for all $\mathbf{l}$, with $\mathbf{l}$ being a lattice vector of the crystal and m an integer. Therefore,

$$\Psi_i(\mathbf{r}) = \sum_{\mathbf{G}} c_{i,\mathbf{k}+\mathbf{G}} \exp[i(\mathbf{k} + \mathbf{G}) \cdot \mathbf{r}] \tag{176}$$

In practice, this series is truncated to include only plane waves that have kinetic energies less than a cutoff energy, resulting in some error that, however, decreases with increasing energy cutoff. A suitable value of the energy cutoff can be selected by an optimization technique [249], as the value of the cutoff is not included in the theory itself. Substitution of Eq. (176) in (163) converts the Kohn-Sham equations into a relatively simple set of equations for the coefficients $c_{i,\mathbf{k}+\mathbf{G}}$ and the eigenvalues ϵ_k in which the kinetic energy is diagonal. Even for systems that contain aperiodicity, such as those with defects, use of a supercell makes the system amenable to this type of analysis. In any event, the solution of the Kohn-Sham equations, when written in terms of the eigenvalues of the coefficients $c_{i,\mathbf{k}+\mathbf{G}}$, can be obtained by diagonalization of the associated matrix. The size of the matrix is dictated by the choice of the cutoff energy and can be prohibitively large if the system contains both valence and core electrons. The problem can be overcome by use of the *pseudopotential approximation*, which we now describe.

It is well-known that many properties of solid materials depend on the valence electrons much more strongly than on the core electrons. This fact is exploited in the pseudo-potential approximation by which one removes the core electrons and replaces them and the strong ionic potential by a weaker *pseudopotential* that acts on a set of *pseudo–wave functions*, rather than the true valence wave functions [250]. The valence wave functions oscillate strongly in the region occupied by the core electrons, due to the strong ionic potential in this region. Ideally, the pseudopotential must be constructed in such a way that its scattering properties for the pseudo–wave functions are identical to those of the ion and the core electrons for the valence wave functions. But, this must be done in a way that the pseudo-wave functions have no radial nodes in the core region, where the total phase shift produced by the ion and the core electrons will be greater by π, for each node that the valence functions had in the core region, than the phase shift produced by the ion and the valence electrons. The phase shift generated by the ion core is different for each angular momentum component of the valence wave function and, therefore, the scattering from the pseudopotential must depend on angular momentum. Outside the core region, the two potentials and their scatterings are identical. The most general form for a pseudopotential is then given by

$$U_{ps} = \sum_{lm} |lm\rangle u_l \langle lm| \tag{177}$$

where $|lm\rangle$ are the spherical harmonics, and u_l is the pseudopotential for angular momentum l. Acting on the electronic wave function with this operator decomposes the wave function into spherical harmonics, each of which is then multiplied by the relevant pseudopotential u_l.

A pseudopotential that does not depend on the angular momentum components of the wave function is called a *local pseudopotential*, which is a function only of the distance from the nucleus. Although it is possible to generate arbitrary, predetermined phase shifts for each angular momentum state with a local potential, there are, in practice, limits to the amount that the phase shifts can be adjusted for the different angular momentum states, as one must preserve the smoothness and weakness of the pseudopotential, without which it becomes difficult to expand the wave functions using a reasonable number of plane-wave basis states.

In order for the exchange-correlation energy to be represented accurately, the pseudo- and the true wave functions must be identical outside the core region. If one adjusts the pseudopotential to ensure that the integrals of the squared amplitudes of the true and pseudo–wave functions *inside* the core region are idential, the equality of the pseudo- and true wave functions outside the core region is guaranteed. Pseudopotentials that possess this property were first constructed by Starkloff and Joannopoulos [251], and have been shown to be highly accurate for heavy atoms. Moreover, Hamann et al. [252] pointed out that, a match of the pesudo- and real wave functions outside the core region also ensures that the first-order energy dependence of the scattering from the ion core is correct, so that the scattering is accurately described over a wide range of energy. A technique for constructing pseudopotentials that corrects even the higher order energy dependence of the scattering was introduced by Shirley et al. [253]. In the best-case scenario, one should develop nonlocal pseudopotentials that use a different potential for each angular momentum component of the wave function, and efforts in this direction [253] have also been fruitful.

The following procedure is typically used for constructing an ionic pseudopotential. The computations are carried out with a periodic unit cell (for nonperiodic systems, see above). All-electron computations are carried out for an isolated atom in its ground state and also some excited states, using a given equation for the exchange-correlation density functional, which result in valence electron eigenvalues and valence electron wave functions for the atom. A pseudopotential with a few parameters is then selected, and the parameters are adjusted in such a way that a pseudo-atom calculation using the same form for exchange-correlation as in the case of the all-electron atom yields both pseudo–wave functions that match the valence wave functions beyond some cutoff radius r_c and pseudo-eigenvalues that are equal to the valence eigenvalues. The ionic pseudopotential so obtained is then used, without further modifications, for any environment of the atom. The electronic density in any new environment of the atom is then determined using both the ionic pseudopotential obtained in this way and the same form of exchange-correlation functional employed in the construction of the ionic pseudo-potential.

One advantage of pseudopotential method is that, by replacing the true ionic potential by a weaker pseudopotential, one expands the electronic wave functions using far fewer plane-wave basis states that would be necessary if the full ionic potential were to be used. Moreover, the rapid oscillations of the valence wave functions in the cores of the atoms are removed, and the small core electron states are no longer present. Another advantage of the pseudopotential approximation is that fewer electronic wave functions must be calculated.

Total-energy pseudopotential computations require significant amounts of computer time, even when the number of atoms in the unit periodic cell is small. Moreover, the computations' time always increases with the number of atoms in the unit cell and, therefore, use of the most efficient computational method is crucial to the success of this method. The QMD method devised by Car and Parrinello [50] has improved dramatically the efficiency of these computations, hence allowing one to simulate systems with a large number of atoms.

3.4.6. Quantum Molecular-Dynamics Simulation

The seminal paper of Car and Parrinello [50] in which a MD technique was used for minimizing the total energy functional and allowed one to use, with a very high degree of efficiency, local and nonlocal pseudopotentials, opened the way for QMD computations. The key idea of Car and Parrinello was to treat the electronic wave functions Ψ_i as dynamical variables and to define a Lagrangian for the electronic system that is given by

$$\mathcal{L} = \sum_i m_\psi \langle \dot{\Psi}_i | \dot{\Psi}_i \rangle - E[\{\Psi_i\}, \{\mathbf{R}_I\}, \{\ell_\alpha\}] \tag{178}$$

Here, m_ψ is a *fictitious* mass associated with the electronic wave functions, giving rise to the kinetic energy term of the Lagrangian that arises due to the fictitious dynamics of the electronic degrees of freedom. E is the Kohn-Sham energy functional described earlier which plays the role of the potential energy, $\mathbf{R}_I$ is the position of the ion I. ℓ_α defines the size and shape of the periodic unit cell, and $\dot{\Psi}_i = d\Psi_i/dt$. As Eq. (178) suggests, the details

of the kinetic energy do not matter. What is more important is that the mass m_Ψ should be much smaller than the nuclear masses that would prevent transfer of energy from the classical to the quantum degrees of freedom over long periods of the numerical simulations. The electronic wave functions are subjected to the orthonormality constraints:

$$\int \Psi_i^*(\mathbf{r})\Psi_j(\mathbf{r})\, d^3r = \delta_{ij} \tag{179}$$

where δ_{ij} is the Kronecker delta. To incorporate these constraints, Lagrange multipliers are introduced, so that the Lagrangian of the system is rewritten as

$$\mathscr{L} = \sum_i m_\Psi \langle \dot{\Psi}_i | \dot{\Psi}_i \rangle - E[\{\Psi_i\}, \{\mathbf{R}_I\}, \{\ell_n\}] + \sum_i \sum_j \lambda_{ij} \left\{ \left[\int \Psi_i^*(\mathbf{r})\Psi_j(\mathbf{r})\, d^3r \right] - \delta_{ij} \right\} \tag{180}$$

Mathematically, the Lagrange multipliers λ_{ij} ensure that the wave functions remain normalized, while λ_{ij} (with $i \neq j$) guarantee that the wave functions remain orthogonal. Physically, the Lagrange multipliers can be thought of as providing additional forces acting on the wave functions, ensuring that they remain orthogonal at any given time t as they propagate along their MD paths. The Lagrange multipliers are symmetric, $\lambda_{ij} = \lambda_{ji}$, and represent $\frac{1}{2}N(N+1)$ independent values that are determined by the $\frac{1}{2}N(N+1)$ orthonormality conditions. The iterative algorithm SHAKE (or one of its modifications), described earlier, can be used for determining the Lagrange multipliers [50].

Given the Lagrangian of the system, the equations of motion for the electronic states are derived from

$$\frac{d}{dt}\left(\frac{\partial \mathscr{L}}{\partial \dot{\Psi}_i^*}\right) = \frac{\partial \mathscr{L}}{\partial \Psi_i^*} \tag{181}$$

which yield the following equations of motion

$$m_\Psi \frac{d^2\Psi_i}{dt^2} = -\mathscr{H}\Psi_i + \sum_j \lambda_{ij}\Psi_j \tag{182}$$

where $\mathscr{H}$ is the Kohn-Sham Hamiltonian. The similarity between Eq. (182) and Eq. (20), the equations of motion for a classical many-particle material solved by the MD method, is now apparent. To ensure that at any given time during the MD integration the wave functions remain orthonormal, the Lagrange multipliers must vary continuously with the time, and, therefore, they must be estimated continuously at *infinitely small* time separations. However, doing so would make the computations intractable. To make the computations tractable, it is usually assumed that the Lagrange multipliers remain constant in each time step Δt during which the equations of motion are integrated. Although this approximation makes the computations tractable, it also creates a new problem: At the end of each time step, the wave functions will not *exactly* be orthonormal, so that a separate orthonormalization must also be carried out at the end of each time step (see below).

However, as a separate orthonormalization step must be carried out at the end of each time step, one may remove the orthogonality constraints from the equations of motion and use *partially* constrained equations of motion. After these equations have been integrated, the orthogonality constraints are imposed again, and the Lagrange multipliers λ_{ij} for the normalization constraints are approximated by the expectation values of the energies of the states given by

$$\lambda_i = \langle \Psi_i | \mathscr{H} | \Psi_i \rangle \tag{183}$$

With this approximation, the equations of motion for the wave functions are given by

$$m_\Psi \frac{d^2\Psi_i}{dt^2} = -(\mathscr{H} - \lambda_i)\Psi_i \tag{184}$$

which ensures that the accelerated state of an electronic state is always orthogonal to that state, and that the acceleration vanishes when the wave function is an exact eigenstate. More generally, however, one can start from the estimate

$$\lambda_{ij} = 2\langle \Psi_i | \mathscr{H} | \Psi_j \rangle - m_\Psi \langle \dot{\Psi}_i | \dot{\Psi}_j \rangle \tag{185}$$

and proceed with integration of Eq. (182). The difference between Eqs. (183) and (185), aside from the approximate nature of (185), is that the latter depends on m_Ψ, which itself must somehow be selected carefully. Equations (184) are now integrated by a Verlet algorithm describe earlier. Thus, one write,

$$\Psi_i(t + \Delta t) = 2\Psi_i(t) - \Psi_i(t - \Delta t) - \frac{\Delta t^2}{m_\Psi}(\mathscr{H} - \lambda_i)\Psi_i(t) \tag{186}$$

Note that if a pseudopotential approximation is made, the coefficients $c_{i,\mathbf{k}+\mathbf{G}}$ of the expansion must be time-dependent, and the Verlet algorithm integrates the governing equations for these coefficients. It can be shown [239] that for these QMD simulations, the largest possible value of the time step Δt used in the Verlet algorithm is approximately given by

$$\Delta t \simeq 2\sqrt{\frac{m_\Psi}{\epsilon_M - \epsilon_m}} \tag{187}$$

where ϵ_M and ϵ_m are, respectively, the largest and smallest eigenvalues of the problem. Use of any Δt that is significantly larger than the estimate (187) will lead to instability and large errors in the numerical solution of the equations of motion. Note that if the cutoff energy is increased, the time step used in the Verlet algorithm must decrease. Moreover, the maximum allowed value of Δt decreases as the size of the system increases, limiting the maximum system size that can be simulated by this algorithm.

We also note that, in our discussion of the integration algorithm, we have tacitly assumed that the Kohn-Sham Hamiltonian $\mathscr{H}$ is constant during the time evolution of the system. However, in addition to the instabilities that are caused by using a too large value of the time step Δt, another type of instability arises if $\mathscr{H}$ is not allowed to vary when it must. Because the wave functions evolve under the MD scheme, the contribution of the exchange-correlation potential to the Kohn-Sham Hamiltonian also varies with the time, leading to a new Hamiltonian. Thus, at the end of each time step, the Kohn-Sham Hamiltonian is updated with the new electronic density, so that the final time step leads to a self-consistent solution of the Kohn-Sham Hamiltonian and the determination of the minimum in the total energy.

3.4.6.1. Eigenstates and Orthogonalization of the Wave Functions Because the wave functions that are obtained from integrating the partially constrained equations of motion are not orthogonal, an orthogonalization procedure must be used. The correct application of the constraints of orthogonality and normalization is actually essential for the success of the Car-Parrinello method, which uses an iterative method to orthogonalize the wave functions by using the following equation

$$\Psi_i^{(n)} = \Psi_i^{(o)} - \frac{1}{2}\sum_{j \neq i}\langle \Psi_j^{(o)} | \Psi_i^{(o)} \rangle \Psi_j^{(o)} \tag{188}$$

where the superscripts n and o refer to the new and old estimates of the wave functions, respectively. If Eq. (188) is applied repeatedly to the old estimates, then the electronic wave functions can be made orthogonal to any desired accuracy. Moreover, if the estimates of the wave functions are orthonormal up to order Δt^4 (the accuracy of the Verlet algorithm), then, over a given time step, algorithm (188) changes them to an extent within the same order. In general, the number of times that algorithm (188) must be applied depends on the number of the wave functions to be computed and their initial departure from orthogonality. However, algorithm (188) does not preserve normalization of the wave functions, and, therefore, they must be normalized after each application of the algorithm.

The Kohn-Sham energy functional is minimized by *any* set of wave functions that are a linear combination of its lowest energy eigenstates. Under the MD scheme, the wave functions that are obtained after orthogonalization will be stationary, implying that in the MD method, each wave function will converge to a linear combination of the lowest energy Kohn-Sham eigenstates, which creates severe problems for simulating certain materials [254]. The actual Kohn-Sham eigenvalues can be found by either diagonalization of the matrix $\mathbf{A} = (A_{ij})$, the entries of which are given by

$$A_{ij} = \langle \Psi_i | \mathcal{H} | \Psi_j \rangle \tag{189}$$

or by the Gram-Schmidt algorithm which is similar to Eq. (188) but without the factor 1/2 in front of the sum. Thus, instead of using algorithm (188), one can use the Gram-Schmidt method, which results in orthogonal wave functions in such a way that all of the higher energy wave functions are *forced* to be orthogonal to the lowest energy wave functions.

So far, we have assumed that the ionic positions and the shape of the unit cell remain fixed, which, in practice, represent additional degrees of freedom that have their own dynamics and, therefore, must be considered. The QMD technique of Car and Parrinello allows one to include in the computations the positions of the ions and the coordinates that define the size and shape of the unit cell, which requires writing down a new Lagrangian, commonly referred to as the Car-Parrinello Lagrangian, given by

$$\mathcal{L} = \sum_i m_\Psi \langle \dot{\Psi}_i | \dot{\Psi}_i \rangle + \sum_I \frac{1}{2} m_I \left(\frac{dR_I}{dt} \right)^2 + \sum_n \frac{1}{2} m_\ell \left(\frac{d\ell_n}{dt} \right)^2 - E[\{\Psi_i\}, \{\mathbf{R}_I\}, \{\ell_n\}] \tag{190}$$

which should be compared with Eq. (178) that was for a system in which the positions of the ions and the shape and size of the unit cell were fixed. Here, m_ℓ, similar to m_Ψ, is a fictitious mass associated with the dynamics of the coordinates that define the unit cell, namely, $\{\ell_n\}$, and m_I is the mass of the ions. The rest of the notations is the same as those for Eq. (178). Given Lagrangian (190), one can derive two new sets of equations of motion, one for the ions,

$$m_I \frac{d^2 \mathbf{R}_I}{dt^2} = -\frac{\partial E}{\partial \mathbf{R}_I} \tag{191}$$

and a second one for the coordinates of the unit cell,

$$m_\ell \frac{d^2 \ell_n}{dt^2} = -\frac{\partial E}{\partial \ell_n} \tag{192}$$

Although Eqs. (191) and (192) can be integrated at the same time that the equations of motion for the electronic states are integrated, the matter is not as straightforward as it may seem. The reason for this is that *physical* ground-state forces acting on the ions, and integrated stresses acting on the unit cell, cannot be calculated for *arbitrary* electronic configurations. Recall that the force $\mathbf{F}_I$ acting on an ion is given by

$$\mathbf{F}_I = -\frac{dE}{d\mathbf{R}_I} \tag{193}$$

As ions change their positions, the wave functions must change to self-consistent Kohn-Sham eigenstates corresponding to the new positions of the ions. These changes contribute to $\mathbf{F}_I$, as

$$\mathbf{F}_I = -\frac{\partial E}{\partial \mathbf{R}_I} - \sum_i \frac{\partial E}{\partial \Psi_i} \frac{d\Psi_i}{d\mathbf{R}_I} - \sum_i \frac{\partial E}{\partial \Psi_i^*} \frac{d\Psi_i^*}{d\mathbf{R}_I} \tag{194}$$

which should be compared with Eq. (191), which implies that, $\mathbf{F}_I = -\partial E / \partial \mathbf{R}_I$. This apparent contradiction is due to the fact that in Eq. (121), the force acting on the ions is not a physical force, rather it is a force that the ions experience from a particular electronic configuration. However, it is not difficult to show that when the electronic wave functions are

the eigenstates of the Hamiltonian, then the second and third terms of Eq. (194) vanish, and, therefore, in this case, $\partial E/\partial \mathbf{R}_I$ yields the true *physical force* on the ions. This important result is known as the *Hellmann-Feynman theorem* [255, 256] and in fact holds for *any* derivative of the total energy. It greatly simplifies the task of computing the physical forces acting on the ions and the integrated stresses that are exerted on the unit cell, as it allows one to compute these quantities only when the wave functions are very close to exact eigenstates.

Thus, the ions are moved along the directions of the Hellmann-Feynman forces until the residual forces (i.e., the deviations from $\partial E/\partial \mathbf{R}_I$) on all the atoms are smaller than a given value (but never zero). If the system is to approach its minimum energy state, the magnitudes of the errors in the Hellmann-Feynman forces must be reduced as the ionic configuration approaches the local energy minimum.

We also note that Eq. (124) does not contain the term $\partial\phi/\partial \mathbf{R}_I$, the derivative of the basis set $\{\phi\}$ with respect to the ionic positions, which is called the Pulay force [257]. If a plane-wave basis set is used for representing the wave functions, then, the Pulay forces will be exactly zero, in which case the Hellmann-Feynman forces are exactly equal to $\partial E/\partial \mathbf{R}_I$, provided that the electronic wave functions are Kohn-Sham eigenstates. If the Pulay forces do not vanish and are not computed either, then the calculated Hellmann-Feynman forces will be in error, with the error being independent of how close is the electronic configuration to its ground state, which means that a local energy minimum of the ionic system cannot be computed by calculating only the Hellmann-Feynman forces acting on the ions.

In practice, most pseudopotential computations are carried out with a cutoff energy at which energy differences have converged but at which the total energies have not converged, in which case the diagonal components of the Pulay stresses acting on the unit cell will have nonzero values. It can be shown [239] that the change in the total energy *per atom* is independent of the details of the ionic configuration, provided that the cutoff energy for the basis set is large enough for the energy differences to have converged. This facilitates computation of the Pulay stresses, as they can be calculated once and for all from the change in the total energy of a small unit cell as the cutoff energy is varied.

3.4.6.2. Computational Algorithm We may now summarize the QMD method [50]:

(i) One starts with an initial set of trial wave functions from which the Hartree potential and the exchange-correlation energy are computed. The choice of a reasonable initial set of trial wave functions is crucial to the efficiency and success of the computations [238–240].

(ii) The Hamiltonian matrices for each of the points included in the computations are constructed.

(iii) The equations of motion for the electronic states are integrated using the Verlet algorithm, and the resulting wave functions are orthogonalized, either by algorithm (188) or by the Gram-Schmidt method; the wave functions are also normalized. There are several "tricks" that can speed up these computations [3, 238–240].

(iv) The electronic density generated by the new set of the wave functions is then calculated, and the corresponding new Hamiltonian is constructed.

(v) A new set of the wave functions is obtained by integrating the equations of motion and orthonormalization of the results. The iterations are repeated until the resultant wave functions are stationary.

(vi) The Kohn-Sham energy functional is minimized; its value gives the total energy of the system. If the plane-wave basis set is used (which is always the case if pseudopotential approximation is used), convergence tests must be performed to ensure that the calculated total energy has converged both as a function of the number of terms included in the set and the value of the cutoff energy that has been used for truncating the set after a finite number of terms.

(vii) Integration of the equations of motion for the ionic positions and the coordinates of the unit cell is also done along the QMD computations for the electronic configurations. It is sensible in the QMD methods to treat the electronic and ionic systems independently when relaxing the ions to their equilibrium positions, and, therefore, it is also possible to use different time steps for the two systems. As the integration

proceeds, the time step for the ionic system must progressively be reduced as the ionic configuration approaches the local energy minimum. Such a procedure allows the electronic configuration to relax closer to its instantaneous ground-state configuration as the ions approach their equilibrium positions, hence ensuring that the errors in the Hellmann-Feynman forces are always less than the actual forces acting on the ions. The QMD technique allows one to search large regions of configuration space and locate the deeper energy minima in a very efficient manner. Because the QMD combines a MD method with the DFT, it makes it possible to study temperature-dependent effects by a method that is free of the common assumptions about the nature of the interatomic forces.

Let us mention two different and successful applications of the QMD and pseudopotential methods that we just described, which are relevant to nanoporous materials that are of interest in this chapter, but represent only a sample of a very large number of computations that have been reported so far. Marks et al. [258] reported the results of *ab initio* simulations of tetrahedral amorphous carbon based on the Car-Parrinello method. The simulated structure was in good agreement with the experimental data. Simulation and modeling of amorphous carbon is important to modeling of carbon molecular-sieve membranes, an important class of nanoporous membranes for separation processes. These membrane possess a solid matrix that consists typically of about 90% amorphous carbon. Yoon et al. [232] employed *ab initio* pseudopotential DFT with a linear combination of atomic orbits and an exchange-correlation functional in the generalized gradient approximation to study structural deformation and intertube conductance of crossed carbon nanotube junctions. They reported good agreement between the results of their simulations and the experimental data.

3.4.6.3. Linear System-Size Scaling The QMD method becomes increasingly less efficient as the size of the system increases, which is, of course, the problem with all molecular modelling methods. If the size of the system becomes too large, then the choice of an appropriate time step becomes very crucial as the charge density starts to fluctuate strongly. The fluctuations are the result of instabilities in the Kohn-Sham energy Hamiltonian, and reducing or eliminating them may require time steps that are too small, hence making the computations intractable. Thus, for very large systems one must use a highly efficient method.

The standard methods for solution of the electronic structure problems scale as $O(N^3)$ for large systems, where N is the number of atoms in a cluster or supercell. This scaling holds for both iterative as well as standard eigensolution methods because, as described above, one must keep the occupied wave functions orthonormal. Thus, a considerable amount of effort has been devoted to development of methods that can, in principle, provide $O(N)$ scaling for the computations. We mention two of such methods that seem to achieve linear scaling. In the variational method proposed by Li et al. [259], one takes advantage of the locality of the density matrix in real space to achieve $O(N)$ scaling. There is only one approximation that is controlled by the real-space radius R_c that is used to truncate off-diagonal elements of the density matrix. The method is, of course, exact when $R_c \to \infty$. The solution of the variational problem is obtained by an *unconstrained* minimization, which can be incorporated into the Car-Parrinello method. In another method [260, 261], an energy functional is used that possesses a global minimum for which (1) the electronic wave functions are orthonormal and (2) the correct electronic ground-state energy is obtained. Linear scaling is then achieved by introducing a spatially truncated Wannier-like representation for the electronic states.

3.4.6.4. Extensions The QMD simulation method that was described above has become an almost everyday tool of studying properties of materials. However, despite all of its success, the Car-Parrinello method has certain limitations. For example, it has the same shortcoming of the classical MD methods, namely, that the atomic nuclei are propagated according to the laws of *classical* mechanics on a single potential energy surface. In addition, because nuclear forces are obtained from the standard DFT, only the electronic ground state can be accessed.

Over the past few years, several extensions of the Car-Parrinello QMD have been proposed that have made the method an even more powerful technique. For example, one can

incorporate the nuclear quantum effects in the method through the use of path integrals [262]. In addition, a QMD has been developed [263] that allows efficient simulations of electronically nonadiabatic processes, by coupling the restricted Kohn-Sham excited state to the ground state using a surface hopping scheme. Evaluation of the nonadiabatic coupling is achieved by an efficient method that exploits the available derivatives of the wave function.

4. VECTORIZED AND MASSIVELY PARALLEL ALGORITHMS

A typical MD or QMD simulation does not usually need large amounts of computer memory, because one must record only the vectors that contain information about the atoms. The simulation becomes very intensive and large scale when one wishes to use a large number of atoms and study the behavior of the system over "long" periods of time. Such large-scale simulations are necessitated by the fact that because the effective size of atoms is typically several angstroms, to approach even sub-micrometer length scales, one must use millions of atoms in the simulations. Moreover, the typical time steps that are used in the MD simulations are of the order of femtoseconds, and, therefore, the equations of motion must be integrated over hundreds of thousands of time steps in order to simulate picoseconds of real time. Such length and time scale constraints conspire together to make large-scale MD simulations very time consuming. They also provide the impetus for developing efficient algorithms that are optimized for vector supercomputers [264–266] and for designing special-purpose computers (i.e., computers with a special architecture that simulate a specific phenomenon for which the architecture is optmized) for carrying out MD computations [267, 268].

Likewise, the electronic structure calculations and QMD computations also benefit tremendously from parallelization. In particular, parallel QMD can be a powerful method for computing realistic interaction potentials for use in the classical MD simulations [269]. Let us first briefly discuss the vectorized and parallelized algorithms.

4.1. Vectorized Algorithms

As pointed out earlier, if the interatomic forces are short-ranged, one usually uses a cutoff distance r_c such that any two particles that are apart a distance $r > r_c$ do not interact with each other. Thus, the key to efficient MD simulations with short-range forces is minimizing the number of neighboring atoms that must be checked for possible interactions. An efficient algorithm for doing so was already suggested by Verlet [80], which is commonly referred to as the *neighbor lists* method. In this algorithm, a list is constructed for every atom in the simulation cell that contains the nearby atoms that are at an extended distance $r_e = r_c + \delta$. Relative to r_c, the value of δ is small, but its optimal value depends on such parameters as the temperature and particle density. These lists are updated after every few integration steps, before any atom has moved from a distance $r > r_e$ to $r < r_e$.

Hockney et al. [270] proposed another method, usually referred to as the *link-cell* method. In their algorithm, at every time step, all the atoms are binned into 3D cells of linear size l with $l = r_c$ or slightly larger. Therefore, for every atom one must check only 27 bins—the bin the atom is in plus the 26 bins that surround it. A very efficient algorithm results when one combines the two methods such that the atoms are binned only every few time steps in order to construct (or update) the neighbor lists. The size of the cells is $l > r_c$. At intermediate time steps the neighbor lists are used in the usual way in order to identify neighbors within a distance r_c of each atom. The combined algorithm is made even more efficient by taking advantage of Newton's third law, which allows one to compute *once* a force for each *pair* of atoms, instead of once for each atom in the pair. This reduces the necessary searches to only half the surrounding bins of each atom to form its neighbor list.

The efficiency of a vectorized MD algorithm can greatly be increased if it contains careful data and loop structures, without which the computer program cannot completely be vectorized. Toward achieving such efficiency, Grest et al. [264] combined neighbor list/link-cell methods to create long lists of pairs of neighboring atoms. At each time step, they updated the lists to keep only those particle pairs that were within the cutoff distance r_c. They also

organized the lists into packets in order to prevent any atom from appearing twice in the lists, hence vectorizing the force computations for each packet and obtaining an algorithm that was about one order of magnitude faster than algorithms without such data structures.

4.2. Massively Parallel Algorithms

Molecular dynamics simulations with short-range forces benefit greatly from parallel computational algorithms. The reason is that calculations of the forces and updating of the atoms' positions can be done *simultaneously* for *all* the atoms. Thus, the main goal in developing any parallel algorithm is dividing the force computations evenly among the processors, so to achieve maximum parallelism. Such algorithms [51, 271–282] were developed for either single-instructor/multiple-data (SIMD) parallel machines or for multiple-instruction/multiple-data (MIMD) parallel computers. The latter machines, with several thousands of processors, possess the computational power that is comparable with the fastest vector computers. Here, we briefly desribe three such algorithms that were developed by Plimpton [281], whose algorithms and their variants have been used in large-scale simulations of materials. They are for systems in which the forces acting on the molecules are short-ranged. For MD simulations with short-range forces, the computational effort per time step scales as N, the number of atoms used in the simulations. Another feature of these algorithms is that the atoms can undergo large displacements over the duration of the simulation. Finally, the performance of these algorithms is optimal with respect to both the number N of the atoms and N_p of the processors. As such, they are very flexible and efficient.

4.2.1. Atom-Decomposition Algorithms

In this algorithm, at the beginning of the simulations, each of the N_p processors is assigned N/N_p atoms (N is usually taken to be a multiple of N_p). Atoms in a group do not have to have any special relation with each other. Throughout the simulations, each processor computes the forces on its designated N/N_p atoms and updates their positions and velocities, *regardless* of where they move in the physical space. The $N \times N$ force matrix $\mathbf{F}$ (where F_{ij} represents the force on atom i due to atom j) is sparse, and, due to Newton's third law, $F_{ij} = -F_{ji}$. Suppose that $\mathbf{r}$ and $\mathbf{f}$ are vectors of length N that store the position and total force on each atom, with $\mathbf{r}_i$ storing the three coordinates of atom i. The AD algorithm assigns each processor a subblock of $\mathbf{F}$ consisting of N/N_p rows of the matrix. If the processors are numbered from 0 to $N_p - 1$, processor P_m (with $m = 0, 1, \ldots, N_p - 1$) computes the matrix entries in the $\mathbf{F}_m$ subblock of rows and is also assigned the corresponding subvectors $\mathbf{r}_m$ and $\mathbf{f}_m$, each of length N/N_p.

A most important aspect of parallel computations is the communication between the processors, as each processor needs the positions of many atoms that belong to *other* processors, giving rise to *all-to-all* communication, an operation that, at every time step, supplies the updated positions of the particles to all the processors. Various algorithms have been developed for performing this operation efficiently [283]. The AD algorithm can be implemented in two different ways. In the first one—the AD1 algorithm—one assumes that at the beginning of each time step, every processor has an updated copy of the vector $\mathbf{r}$ and thus "knows" the positions of all the N atoms. Then, the algorithm first constructs the neighbor lists for all the pairwise interactions that must be computed in block $\mathbf{f}_m$. The lists are then used for calculating the nonzero entries of $\mathbf{F}_m$. Because each pairwise interaction force is calculated and the force components are summed into $\mathbf{f}_m$, $\mathbf{F}_m$ is never actually stored as a matrix, hence saving a lot of computer memory. The results are then used to update the positions and velocities of the particles (by using them in the equations of motion and integrating them over one time step) and then sharing the updated positions of the atoms among all the N_p processors.

The AD1 algorithm does not take advantage of Newton's third law. Algorithm AD2 does use this law and, thus, reduces the time of the computations by decreasing the cost of communications between the processors.

4.2.2. Force-Decomposition Algorithms

The force-decomposition (FD) algorithm is based on a block-decomposition of the force matrix $\mathbf{F}$, rather than a row-wise decomposition used in the AD algorithm. We assume, for the sake of ease of exposition, that N_p is a power of 2 and that N is a multiple of N_p, although the algorithm is general. Subblocks of the force matrix $\mathbf{F}$ are assigned to the processors, giving rise to a permuted force matrix $\mathbf{F}'$, formed by rearranging the columns of $\mathbf{F}$ in a particular way. If we arrange the $\mathbf{r}_\alpha$ pieces in row-order (where $\alpha = 1, 2, \ldots, \sqrt{N_p} - 1$), they form the usual position vector $\mathbf{r}$. One spans the columns with a permuted position vector $\mathbf{r}'_\beta$ (where $\beta = 1, 2, \ldots, \sqrt{N_p} - 1$). The size of subblock $\mathbf{F}'_m$ is $(N/\sqrt{N_p}) \times (N/\sqrt{N_p})$. Thus, to compute the entries of $\mathbf{F}'_m$, processor P_m must know $\mathbf{r}_\alpha$ and $\mathbf{r}'_\beta$ of the $\mathbf{r}$ and $\mathbf{r}'$ vectors, each with a length $N/\sqrt{N_p}$. These elements are computed and accumulated into corresponding force subvectors $\mathbf{f}_\alpha$ and $\mathbf{f}'_\beta$.

The algorithm can be implemented in two different ways. Algorithm FD1 first constructs the neighbor lists. For large N, the $N/\sqrt{N_p}$ atoms in $\mathbf{r}'_\beta$ are binned, and the 27 surrounding bins of each atom in $\mathbf{r}_\alpha$ are checked. The neighbor lists are used for computing the entries of $\mathbf{F}'_m$. As they are computed, the entries are summed into a local copy of $\mathbf{f}_\alpha$, and, therefore, $\mathbf{F}'_m$ does not have to be stored in matrix form. Each processor P_m then obtains the total force $\mathbf{f}_m$ acting on its $N/\sqrt{N_p}$ atoms and uses it to update the positions of the N/N_p atoms in $\mathbf{r}_m$. Finally, the processors in row α obtain the entire $\mathbf{r}_\alpha$, and similarly for the processors in each column β. This algorithm does not take advantage of Newton's third law and, therefore, calculates each pairwise interaction force twice. In algorithm FD2, this is avoided by taking advantage of Newton's third law of motion.

4.2.3. Spatial-Decomposition Algorithms

In this algorithm, the simulation cell is divided into small 3D boxes, with each box assigned to one processor that, at each time step, computes forces on and updates the positions and velocities of all atoms that it contains. The atoms that are assigned to the processors can change; they are assigned as they move through the simulation cell. To compute the forces acting on its atoms, a processor only needs to know the positions of atoms in the nearby boxes and, therefore, unlike the AD and FD algorithms, the communication in the SD algorithm is localized. The size and shape of the boxes depend on N, N_p, and the aspect ratio of the simulation cell (assumed to be a 3D rectangular parellelepiped). The number of the processors in each dimension is selected to make the boxes as close to a cubic structure as possible, as for large N such configurations minimize the cost of communications, which is proportional to the boxes' surface. The linear size of the boxes can be larger or smaller than the cutoff distances r_c and r_e defined above. Each processor maintains two data sets, one for the N/N_p atoms that have been assigned to it, and one for the atoms in the nearby boxes. One data set stores all the information, such as the positions, velocities, neighbor lists, and so forth. These data are stored in a linked list to allow insertions and deletions as the atoms move to new boxes. The second data structure maintains and updates, through communication with other processors, only the atoms' positions. More details are given in the original reference [281].

It must be pointed out that the above algorithms have their optimal efficiency only if there is *load-balance*, which means that each processor must have an equal amount of work to perform. For the AD algorithms, this will be the case if each $\mathbf{F}_m$ block has roughly the same number of nonzero entries, which will be the case if the atom density is uniform across the simulation cell. Typically, nonuniformities do arise, but they will not pose any problem if the atoms ordering at the beginning of the simulations is randomly permuted. There will be load-balance for the FD algorithms only if $\mathbf{F}'_m$, and a closely related matrix $\mathbf{G}'_m$ [281], are *uniformly* sparse. Thus, if the atoms are ordered geometrically, the matrices $\mathbf{F}'_m$ and $\mathbf{G}'_m$ will not be uniformly sparse, as geometrical ordering generates a force matrix with diagonal bands of nonzero entries. The way to achieve uniform sparsity is to randomly permute the atoms ordering. Finally, the SD algorithms will be load-balanced only if there is roughly the same number of atoms both in the boxes and in their surroundings. This will not be the case if there is nonuniformity in the density of the particles, or if the physical domain is not a rectangular parallelepiped. Hendrickson and Leland [284] developed a method for load-balancing

the SD algorithms by partitioning an irregular domain or a system with nonuniformly distributed clusters of atoms, although such algorithms add to the computational cost of the MD simulations.

5. PROTOCOLS FOR GENERATING MODELS OF NANOPOROUS MATERIALS

Now that we have equipped ourselves with an arsenal of computational methods, we can begin considering the question of how to generate a molecular model of a nanoporous material, using the "weapons" in our arsenal. We describe separately models of the three classes of nanoporous materials that we are considering in this chapter.

5.1. Carbon Nanotubes

Generating an atomistic model of carbon nanotubes is relatively straightforward, as the tubes have a well-defined and relatively well-understood structure with the position of the atoms in the structure being known. Thus, the initial configuration of the model nanotube is constructed based on the experimental data. The model is then relaxed using an energy minimization technique of the type that were described earlier. This can be done in two different ways.

(i) The first method is based on first-principle QMD method that was described above [238–241, 285, 286]. For example, Tada et al. [287] generated a model of a single-walled carbon nanotube in order to study hydrogen adsorption in the tubes. In their model, eight carbon atoms are located on the side opposite to the H_2 adsorption sites. These atoms were fixed in the model, while the positions of the rest of the atoms were relaxed by structural optimization. They used the first-principle QMD method with the generalized gradient approximation, together with the results of Perdew et al. [288] and Hammer et al. [289] for the exchange-correlation potential. The so-called NCPS97 norm-conserving pseudopotential [290, 291] was used, and the electronic wave functions were expanded in plane waves with a suitably selected energy cutoff. These techniques and concepts were all described earlier in this chapter. Others [12, 13, 201, 227–237, 292–299] have used similar techniques for studying many properties of carbon nanotubes, ranging from their mechanical [230–232] to thermal and vibrational [237] properties. Let us mention that commercial softwares, such as GAUSSIAN 98, are now available that can perform such calculations very efficiently.

(ii) The second method is based on the classical MD simulation described above. In this case, a model of the material itself can be generated in two different ways. (1) In one method, one combines the classical MD with an energy minimization technique in order to develop a molecular model of a carbon nanotube. (2) In the second method, one generates a single-walled carbon nanotube by simply rolling a graphite sheet, and specifying the interatomic interaction potential between the atoms. This relatively simple method has been used by many research groups [32, 300–321] in order to study adsorption of various gases, such as N_2 and H_2, diffusion of these and other gases [322–326], as well as fluid flow in carbon nanotubes [327–329]. In addition, using the MD simulations, Kwon et al. [330] studied deformation of carbon nanotubes as a result of increasing the temperature, and the resulting change in their volume, using the Nosé-Hoover algorithm described earlier. These computation and modeling efforts use a wide degree of sophistication, varying anywhere from models in which the atoms interact with each other through simple potentials, to those in which quite sophisticated molecular structural models and interaction potentials are employed.

5.2. Low-Dielectric Constant Nanoporous Materials

As we discussed earlier in this chapter, many newly proposed low-dielectric constant materials are nanoporous. Prominent among these are aerogels and xerogels, new materials with many unusual properties that were described earlier. In particular, aerogels are light

nanoporous materials that possess a fractal structure. That is, the mean density of the material is a scale-dependent quantity that *decreases* with the length scale L as

$$\rho \sim L^{D_f - d}, \qquad \text{or} \qquad \rho \sim M^{(D_f - d)/D_f} \tag{195}$$

where D_f is called the fractal dimension of the material, d is the Euclidean dimensionality of the space in which the material is embedded (with $D_f < d$), and M is the material's mass. Equation (195) indicates that the mean density of the material decreases with increasing length scale L.

Theoretically, a model that closely matches the properties of aerogels is [331] the diffusion-limited cluster–cluster (DLCC) aggregation [332, 333]. In this model, one starts with an empty lattice. At time $t = 0$, lattice sites are selected at random and occupied by particles, until a small fraction p_0 of the sites are occupied by the particles. Each occupied site can contain only one particle. A randomly selected cluster of occupied sites (a cluster is defined as a set of particles that are nearest neighbors to each other on the sites of the lattice), including a single site (considered to be a cluster of size 1), is selected and moved (allowed to diffuse) in a randomly chosen direction. Then, the perimeter sites of the cluster—the set of sites that are adjacent to the cluster—are examined to see whether they are occupied by other particles or clusters. If so, the perimeter particles or clusters are added (attached) to the cluster that was moved to form a larger cluster. Once a larger cluster is formed, it is not allowed to break up again. Another randomly selected cluster is moved again, its perimeter is examined for possible formation of a larger cluster, and so on. Figure 8 shows three stages of this process in 2D. The fractal dimension D_f of the DLCC aggregates are $D_f \simeq 1.45 \pm 0.05$ and 1.8 ± 0.05 in 2D and 3D, respectively. Note that in this model, it is assumed that the diffusivity $\mathcal{D}$ of a cluster is independent of its molecular weight M. In practice, one expects to have $\mathcal{D} \sim M^{-1/D_f}$ (as the radius of the cluster is proportional to M^{1/D_f}), or more generally, $\mathcal{D} \sim M^{\zeta}$, where ζ is an exponent that may depend on the type of the solution in which the aggregation takes place. Computer simulations [334] indicate that D_f is almost completely independent of ζ, provided that $\mathcal{D}$ decreases with increasing M. Note also that the model does not have to be defined on a lattice, but can be simulated in a continuum.

Three-dimensional molecular simulation of the DLCC aggregation, on a time and length scale that can be compared with the experimental data, is very difficult. Significant progress has, however, recently been made. Thus, in principle, one can generate a model of these materials by one of the two following methods:

(i) In one method, one uses MD simulations to generate a model of the aggregates. The initial stages of the aggregation formation is dominated by the interaction energies and the initial conditions of the aggregating particles. Among such interactions, van der Waals forces play a particularly important role in the formation of the aggregates, and, therefore, their inclusion in the MD simulations is crucial. Arunachalam et al. [335]

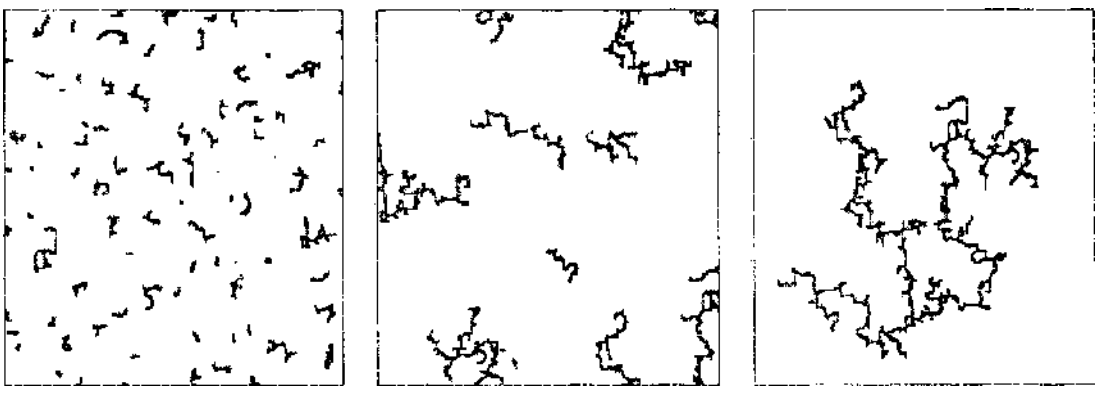

Figure 8. Three stages of formation of a diffusion-limited cluster–cluster aggregate

developed a MD method for so doing. If r is the surface-to-surface distance between two particles, then, the vdW is approximated by the potential [335]

$$U(r) = \frac{1 + a_1 r + \cdots + a_{n-1} r^{n-1}}{b_1 + b_2 r + \cdots + b_{n+7} r^{n-6}} \tag{196}$$

where the coefficients a_i and b_i depend on the size of the particles and are listed by Arunachalam et al. [335] for a few particle sizes. Note that Eq. (195), in the limit $r = 0$, yields $U(r) \to r^{-7}$, as opposed to the usual $U(r) \propto r^{-6}$ used in the LJ and similar potentials. The reason is the effect of the retardation on the long-range vdW forces. In addition to vdW forces, one must account for the effect of "reaction" between the diffusing particles (i.e., the rate by which the particles join the growing aggregate). The appropriate reaction rate is one for a second-order reaction:

$$\mathcal{R}(A, B) = R_s(A, B) C_A C_B \tag{197}$$

where R_s is the rate constant, and C_A and C_B are, respectively, the concentrations of A and B particles. The "reaction" between the particles is of *sticking* type, and, therefore, one can use the kinetic theory to write,

$$R_s(A, B) = \left(\frac{8 k_B T}{m\pi}\right)^{1/2} \sigma_s(A, B) \tag{198}$$

where m is the reduced mass, and σ_s is given by

$$\sigma_s = 2\pi \int_{\|}^{\infty} db \int_0^{\infty} dE_{\text{coll}} \int_{\infty}^{\infty} dp_A b \frac{E_{\text{coll}} \exp[-E_{\text{coll}}/(k_B T_{\text{coll}})]}{(k_B T_{\text{coll}})^2} \frac{\exp[-E_{\text{rot}}/(k_B T_A)]}{Z_{\text{rot}}}$$
$$\times P_s(b, E_{\text{coll}}, E_{\text{rot}}, p_A, \varphi_A, \psi_A, \theta_A) \frac{d\varphi_A}{2\pi} \frac{d\psi_A}{2\pi} \left(\frac{1}{2} \sin\theta_A \, d\theta_A\right) \tag{199}$$

Here, T_{coll} and E_{coll} are, respectively, the mean collision temperature and initial collision energy, E_{rot} and p_A are the rotational energy and momenta of the rigid aggregate, Z_{rot} the rotational partition function of the aggregate, and φ_A, ψ_A and θ_A are the angles that define the relative orientation of cluster A with respect to the axis that passes through its center of mass along which the collision occurs. The normalized probability density function for the sticking (reaction) is represented by P_s, which can be suitably approximated by relatively simply expressions, or else the integral in (198) can be estimated by a Monte Carlo method [336]. The Verlet algorithm is then used for integrating the equation of motion. An important result of these simulations is that, in the absence of vdW forces, the resulting aggregates have a compact structure with very low porosity, whereas the presence of the vdW forces causes the aggregates to take on a fractal and open structure with a large porosity, which is in agreement with the experimental observations [334].

A different molecular modeling approach for aerogels and xerogels has been proposed based on optimization techniques. For example, in the atomistic model of Stachs et al. [337], one starts with a given configuration of the atoms' of the material distributed in a simulation cell. The atoms are then moved according to a reasonable algorithm to obtain a new molecular configuration of the material. A property of the material, which can also be directly measured, is then computed and compared with the measurement. Then, a new molecular configuration is generated and the same procedure is repeated. If the difference between the computed and measured property is smaller than what was obtained in the previous iteration, the new configuration is accepted, and the search for finding configurations that further reduce the difference continues. If the difference is larger than what was obtained in the previous iteration, then the new configuration is rejected. One may impose additional constraints on this type of simulations in order to better match the structure of the real material with the simulated one. Clearly, the same idea may be used in the context of an energy minimization technique.

(ii) In the second method, one may either generate the aggregates using the standard aggregation model [334], and then use the resulting structure for simulation and study of their various properties, or use a hybrid method in which the primary clusters of the aggregates are generated by MD simulations, and then use the standard aggregation algorithm for generating the large-scale aggregate.

An example of the former approach is the work of Hamsy et al. [338], who studied gas transport in the pore space of the material. An example of the latter approach is the work of Rahmani et al. [339], who developed a hybrid MD simulation technique for modeling silica aerogels, represented by DLCC aggregates. They assumed that the primary particles (clusters) of the aggregates consist of vitreous SiO_2, which they generated by MD simulations [340]. The interaction potential between two particles was represented by a sum of Coulombic and the Buckingham [Eq. (23)] potentials [100, 101, 341]. They showed that vibrational spectra of the resulting aggregates are in agreement with the experimental data and, therefore, the generated aggregate is a reliable model for studying other properties of interest.

Other recent theoretical studies of low-dielectric constant materials include the work of Sodolski and Kozlowski [342], who studied the DC conductivity of silica aerogels and found that a suitable mobility theory can explain the experimental data. Fang and Tsui [343] studied electrical conductivity and dielectric constant of nanoporous carbon-doped oxide, which has been proposed as a low-dielectric constant material, and proposed a model for their experimental data. A somewhat similar study was carried out by Costescu et al. [344], who studied thermal conductivity of hydrogen-silsesquioxane, another potential candidate for a low-dielectric constant material. Pilla et al. [345] studied the dynamical structure factor (which is proportional to the scattering intensity) of model systems for aerogels and xerogels, stating that one can neglect the contribution of the elementary units of the materials' networks, and reproduce the dynamical properties of such materials based only on the dynamics of the networks.

5.3. Nanoporous Membranes

Models that have been developed for nanoporous membranes can be divided into two groups.

(i) In one group, the membrane is represented by a single nanosize pore. The motivation for doing so is the fact that in some membranes, the pores are more or less parallel to each other, and, therefore, studying the phenomena of interest in a single pore may suffice for understanding them in a nanoporous membrane. Many pore shapes have been used, ranging from cylindrical and slit pores to much more complex shapes [346]. The literature in this area is huge; reviewing and discussing all the works that have been carried out would require a review by itself. The interested reader should consult Gelb et al. [347] for extensive discussion of such works.

(ii) In the second class are those that model the nanoporous membrane by a 2D or 3D network of interconnected pores. Many different types of such molecular pore networks have been developed, which we now describe.

In one group, the pore network is generated based on geometrical and topological considerations, without any regard for the physicochemical process that generates the nanoporous membrane, and, therefore, the chemical and energetic details of creating the nanopores are ignored. As an example, consider pillared clays (PCs), nanoporous materials that were originally developed as a new class of catalytic materials, although it is currently believed that their greatest potential use may be as membrane materials for separation processes, especially separating CO_2 from a mixture of gases. Hence, in recent years a number of investigators have studied gas adsorption in PCs [348].

The synthesis of PCs was originally suggested by Barrer and McLeod [349]. They inserted molecules into clay minerals to prop apart the aluminosilicate sheets, thereby producing pores larger than those commonly found in native clays, or even in zeolites, another class of nanoporous materials that is used heavily in the chemical industry. However, the resulting

porous materials did not have the thermal stability that zeolites usually possess. Pillars of hydroxyaluminum and other cations are capable of being dehydrated to oxide pillars and withstand temperatures of up to 500°C without structural collapse under catalytic cracking conditions. They are relatively new and were first reported by Brindley and coworkers [350, 351] and, independently, by Lahav et al. [352] and Vaughan and Lussier [353].

In general, pillared montmorillomites are 2:1 dioctahedral clay minerals consisting of layers of silica in tetrahedral coordination, holding in between them a layer of alumina in octahedral coordination. Substituting Si^{4+} with Al^{3-}, or Al^{3-} with Mg^{2+} gives the silicate layer a negative net charge, which is normally compensated by Na^{+}, Ca^{2-} and Mg^{2+} ions [354]. By exchanging the charge compensating cations with large cationic oxyaluminum polymers, one can synthesize molecular sieve-type materials. Upon heating, these inorganic polymers form pillars which prop open the clay layer structure and form permanent PCs. The location and size of the pillars can, in general, vary, depending on such parameters as the type of the pillaring agent and the preparation conditions. As mentioned above, these materials are flexible enough to be used in separation processes [355], because access to their interior pore volume can be controlled by the distance between the silicate layers and the distance between the pillars. One or both can be adjusted to suit a particular separation application.

The first molecular models of such nanoporous materials were developed by Sahimi and co-workers [356–360]. In their model, the tetrahedral silicate layers, which we call the solid walls, were represented by the (100) face of a face-centered-cubic solid with specified surface number density. The pillars were represented by rigid chains consisting of a given number of LJ spheres separated by their size parameter. They were intercalated vertically in the space between the solid walls and were distributed uniformly between the solid walls such that the centers of the pillars were placed at the nodes of an imaginary square lattice attached to the walls. In the original model [356–359], the pillars were represented by rigid chains. X-ray diffraction and other experimental techniques indicated, however, that the structure of the pillars are far more complex than simple chains. Thus, a better model was developed [360] in which the structure of the pillars and the arrangement of the atoms, based on the experimental data, were taken into account. However, in both models only the spacial distribution of the pillars between the walls were considered, without much considerations for the energetics of the material.

As a second example, consider carbon molecular-sieve membranes (CMSMs) described earlier in this chapter. These membranes are prepared by pyrolysis of a polymeric precursor. If the pyrolysis of the polymeric precursor is done at high enough temperatures, the resulting solid matrix of the porous material will have a structure similar to graphite. Thus, one begins the molecular simulations of these materials with a 3D cell of carbon atoms with a structure corresponding to graphite. One then tessellates the graphite cell by inserting in it a given number of Poisson points, each of which is used for constructing a 3D Voronoi polyhedron, such that every point inside each polyhedron is closer to its own Poisson point than to any other Poisson point. The pore space is then generated by fixing its desired porosity and selecting a number of the polyhedra in such a way that their total volume fraction equals the desired porosity. The polyhedra, so chosen, are then designated as the membrane's pores by removing the carbon atoms inside them, as well as those that are connected to only one neighboring carbon atom (the dangling atoms), as it is impossible to actually have such atoms connected to the surface of the pores. The remaining carbon atoms constitute the membrane's solid matrix, while the pore space consists of interconnected pores of various shapes and sizes [359, 361–363].

We point out that once some of the carbon atoms are removed from the simulation cell, one should, in principle, allow the new system to relax to its minimum energy configuration. This procedure is necessary when one deals with such materials as polymers and polymeric membranes that have flexible structures, and hence their minimum energy configuration may differ significantly from any other configuration that they may take on. However, in the current problem we deal with a rigid structure, namely, the solid matrix of a pore space, and, therefore, very small changes, if any, might occur in the structure of the pore space if the system is driven toward its minimum energy configuration; in fact, the system is already at or very close to its minimum energy state.

In principle, the pore space can be generated by at least two different methods. If the pore polyhedra are selected at random, then, assuming that the size of the simulation cell is large enough, the size distribution will always be Gaussian, regardless of the porosity of the pore space or even the size of the initial graphite cell. In practice, however, the membranes that are used do *not* possess a Gaussian pore size distribution (PSD) [134–136]. Hence, in the second method, one designates the pore polyhedra in such a way that the resulting PSD would mimic, as much as possible, that of a real membrane, which is typically skewed, by first sorting and listing the polyhedra in the cell according to their sizes, from the smallest to the largest (or *vice versa*). The size of each polyhedron is taken to be the radius of a sphere that has the same volume as the polyhedron. The polyhedra are then designated as the pores according to their sizes, starting from the smallest (or the largest) ones in the list.

The PSDs and their averages that are generated with a bias toward the smallest (or largest) pores are, of course, dependent upon the porosity and resemble the experimental PSDs [134–136]. In addition, the average pore size can be fixed at any desired value by varying the number of the Poisson points inside the initial graphite cell. Clearly, the larger the number of the Poisson points, the smaller will be the average pore size. Note that, unlike the traditional pore networks that are used in the simulation of flow and transport in microporous media [46], the pore space generated by the models described here is a *molecular* pore network, hence allowing the interaction of the fluids' molecules with *all* the atoms in it to be taken into account.

One may also generate such molecular pore networks by a random packing of spheres [2–4, 364–366] or by lattice models in which selected sites of the lattice may be adsorption sites [367–372]. Off-lattice models of nanoporous materials, for example, for aerogels [364–366], have also been developed.

In practice, carbonization of the polymeric precursor of CMSMs may not be done at such high temperatures that the solid matrix of the final nanoporous material will have a structure similar to graphite; rather the pyrolysis of the polymeric precursors at lower temperatures will result in a matrix that is made of mainly of amorphous carbon. For this reason, another model has been developed [203, 363] that generates amorphous carbon that, when combined with a suitable method of generating the pores, will result in a molecular pore network with a solid matrix that consists mainly of amorphous carbon. In this method, one begins with a crystalline diamond structure (four-coordinated carbon atoms), based on a face-centered-cubic lattice, which consists of a large number of carbon atom. The Brenner potential [200], described earlier, is used to represent the interaction potentials between the atoms and describe the bonding properties, although one may also use an *ab initio* method [258] or a tight-binding formulation [373] to generate amorphous carbon. The amorphous carbon is then generated by melting the crystalline material using MD simulations in an (NVT) ensemble at very high temperatures (e.g., 6000 K) and then quenching it back to room temperature with an appropriate cooling rate. Then, the material is equilibrated (its energy is minimized) at room temperature. To speed up the computations, one may use a massively parallel computational strategy [281], based on the force-decomposition algorithm described above. One can, of course, use the same type of approach for generating a molecular model of silicon carbide nanoporous membrane [190], as atomistic models of SiC have now been developed [374, 375].

The resulting amorphous carbon (or SiC) can then be combined with an algorithm for creating the nanopores in order to generate a 3D molecular pore network. This can be done by at least two different methods. (1) In the first method, one may use the Voronoi algorithm described above in order to generate a nanoporous space. That is, instead of starting with a simulation cell of graphitic material, one can begin with a cell of amorphous carbon. The rest of the algorithm is similar to what we described above. (2) In the second method, one removes the carbon atoms during the melting process, which, physically, is what happens. The breaking of the bonds and the removal of the carbon atoms are based on the energies that are needed for breaking the atomic bonds. In this way, a nanoporous space with a solid amorphous carbon matrix is generated. The distinct advantage of this method is that it takes into account the chemistry and energetics of the material.

6. EQUILIBRIUM AND NONEQUILIBRIUM PHENOMENA IN NANOPOROUS MATERIALS

Now that we have learned how to generate an atomistic model of a nanoporous material, we can begin considering various phenomena that take place in such materials, either through their matrix or in their pore space. Although the set of such phenomena is rather large (some of which were already mentioned above), we consider here a few important phenomena that occur in the pores of a nanoporous material, two of which, adsorption of a single gas or a mixture of gases (an equilibrium phenomenon) and flow and transport of fluids in the pore space under the influence of an external potential gradient (a nonequilibrium phenomenon), have been studied extensively using molecular modeling. In what follows, we describe atomistic modeling of both types of phenomena.

6.1. Equilibrium Phenomena

One of the most important equilibrium phenomena that can occur in the pore space of a nanoporous material is adsorption of gases. There are several computational techniques for molecular modeling of adsorption phenomena in the pore space of such materials. One can naturally use the equilibrium MD method (described earlier) for simulating adsorption [362]. Such simulations are typically done in the *microcanonical ensemble*, that is, one in which the total number of particles, N, the total volume of the system, V, and its energy, E, are held fixed [which is why it is usually referred to as the NVE ensemble].

Because the adsorption isotherms are typically presented in terms of the number of the moles adsorbed *versus* the pressure, the chemical potentials of the components (in a multicomponent mixture of gases) are also computed, as direct calculation of the pressure (or the partial pressures) is very difficult (the pressure is, however, related to the chemical potentials through well-known thermodynamic relations). The chemical potentials are usually computed through the *test particle method*, originally devised by Widom [376, 377]; see also Deitrick et al. [378] for more recent developments. If the particle density in the system is high, then the algorithm due to Shing and Gubbins [379, 380] can be used. These methods are based on Widom's original observation that the chemical potential of a fluid is related to the ease with which a test particle can be inserted in the system.

At the beginning of the molecular simulations, one divides the simulation cell into a large number of small subcells, and a test particle is assigned to each subcell. The interaction energies (and their first two or three derivatives) between the test particles and the pores' solid walls, associated with each subcell, are then computed and recorded. The test particles with interaction energies less than a certain value are then considered as "active," while the rest are considered as "idle" as they make essentially no contribution to the chemical potential,

$$\beta\mu_i = \ln(\rho x_i) - \ln\langle \exp[-\beta E_{pi}(\mathbf{r})]\rangle \tag{200}$$

Here, $\beta = (k_B T)^{-1}$, ρ is the total density, x_i is the mole fraction of component i (in a multicomponent mixture of gases), E_{pi} is the potential energy of a test particle of type i, μ_i is the configurational chemical potential of component i, and $\langle\cdot\rangle$ denotes an average over time and active test particles.

6.1.1. Grand-Canonical Monte Carlo Method

In a grand-canonical ensemble, both the energy and density are allowed to fluctuate, hence making a grand-canonical Monte Carlo (GCMC) method a suitable technique for computing equilibrium properties of single- and multicomponent mixtures. In particular, it has been used extensively for computing the adsorption isotherms of gases and their mixtures in models of various types of nanoporous materials [356–360, 381–396]. The method was first used in studies of bulk fluids [397, 398], and was then extended to adsorbed systems [399, 400].

The GCMC method is based on using a Markov chain for generating a series of molecular configurations. In the GC ensemble, the probability $p(s)$ of any given state s of a system is given by,

$$p(s) = C\exp[-\beta(U - N\mu) - \ln N! - 3N\ln\Lambda + N\ln V] \tag{201}$$

where U is the total intermolecular potential energy of the system, Λ is the de Broglie wavelength, and C is a normalization constant. The rest of the notation is as before. In most simulations, the method due to Norman and Filinov [397] is used for generating the Markov chain. In their method, at each step of the simulations, the current molecular configuration is modified in order to generate the subsequent Markov chain. The modification is done by one of three ways, each of which is called a *move*: (1) inserting a new molecule into the system at a random position; (2) removing an existing molecule from the system; or (3) displacing one of the existing molecule by a random vector. The third move is rarely used. Each move is accepted or rejected according to a probability. The probability of inserting a particle of component i is given by

$$p_i^+ = \min\left\{\frac{Z_i V_i}{N_i + 1}\exp(-\beta\Delta E), 1\right\} \tag{202}$$

where $Z_i = \exp(\beta\mu_i)/\Lambda^3$ is the absolute activity at temperature T, ΔE the energy change resulting from inserting (or removing) a particle, and V_i and N_i the volume and number of atoms of component i, respectively. The probability of deleting a particle is given by

$$p_i = \min\left\{\frac{N_i}{Z_i V_i}\exp(-\beta\Delta E), 1\right\} \tag{203}$$

Finally, a displacement move is accepted with the probability,

$$p_i^{(d)} = \min\{\exp(-\beta\Delta E), 1\} \tag{204}$$

All the quantities of interest are computed by averaging their microscopic counterparts over a large number of molecular configurations of the system.

The thermodynamic potential suitable for the GC ensemble is the grand free energy F, given by

$$F = H - \langle N\rangle\mu \tag{205}$$

where H is the Helmholtz free energy ($H = U - TS$), and $\langle N\rangle$ is the average number of molecules. In case of a mixture, $\langle N\rangle\mu$ is replaced by $\sum_i \langle N_i\rangle\mu_i$. For a pore of any shape, one has

$$dF = -SdT - P_0 dV - \langle N\rangle d\mu + \sigma dA \tag{206}$$

where S is the entropy, P_0 is the bulk phase pressure, σ is the solid–fluid interfacial tension, and A is the pore's surface area. For example, for a slit pore, frequently used in the simulation of adsorption, one has,

$$dF = -SdT - P_0 dV - \langle N\rangle d\mu + 2\sigma dA - Afdh \tag{207}$$

where A should be interpreted as the surface area of one of the walls, h is the pore's width (which can vary), and f is called the *solvation* force given by $f = P_h - P_0$, with P_h being the pressure exerted on the pore walls by the adsorbate. The Gibbs adsorption isotherm is then given by,

$$\left(\frac{dF}{d\mu}\right)_{T,V,A,h} = -\langle N\rangle \tag{208}$$

One may also compute the desorption isotherm. This is done in three steps.

(i) A supercritical (and, therefore, reversible) adsorption isotherm is computed.

(ii) An integration along a path of decreasing temperature at constant μ is carried out, using the expression,

$$\left[\frac{\partial(F/T)}{\partial(1/T)}\right]_{V,A} = U - \langle N\rangle\mu \tag{209}$$

(iii) The desorption isotherm is integrated using Eq. (208).

One may also refine this method to study capillary condensation. An integration method is used in the refined method for precisely locating the thermodynamic condensation pressure in the pore [392]. The free energy F is integrated along the adsorption isotherm using Eq. (208), where the lower limit of the integration is taken to be an ideal gas state for which the grand potential can be computed directly from the external potential [401].

A method somewhat related to the GCMC technique is the semigrand MC method [402] which consists of molecular simulations at constant $(N, T, \mu_1 - \mu_2)$ for a binary mixture, and includes moves that attempt to convert molecules of type 1 into type 2, and *vice versa*. But, the method offers little advantage over the GCMC method. In addition, the Gibbs ensemble MC method [403, 404] can also be used for studying various equilibrium phenomena in a pore. Although this method allows computation of the chemical potentials at no extra cost, it has the drawback that the pore shape must be simple with smooth walls.

As mentioned earlier, nanoporous membranes are used extensively in the chemical and petrochemical industries for separating mixtures that involve n-alkanes. We already described the configurational-biased Monte Carlo (CBMC) method for efficient generation of molecular models of n-alkanes. Because adsorption is an important mechanism of separation of fluid mixtures in a nanoporous membrane, one also needs an efficient method for simulating this phenomenon, an important aspect of which is inserting the complex molecular structure of n-alkanes into the system. To do this, one combines the CBMC method described earlier with a GCMC method, which is referred to as the CBGCMC technique [405]. This is a method for computing the sorption thermodynamics of linear-chain molecules when the sorbates are represented with a united-atom (UA) force field [406]. In this model, the CH_2 and CH_3 groups are considered as single interaction centers with their own effective potentials. The atoms and the UA centers are connected by harmonic potentials. The intramolecular interactions consist of the contributions by bond-bending forces represented by [407],

$$U_{\mathrm{BB}}(\theta) = \frac{1}{2} k_\theta (\theta - \theta_0)^2 \tag{210}$$

where θ is the angle between the atomic bonds, and torsional forces for which the potential is given by [408],

$$U_{\mathrm{tor}}(\phi) = \sum_{i=1}^{5} c_i \cos^i(\phi) \tag{211}$$

where ϕ is the dihedral angle. Numerical values of the constants k_θ and c_i are listed by the original references.

The CBGCMC method consists of two steps. First, it generates the chain configurations, one atom at a time, by the CBMC method described earlier. Second, as the chain molecule is generated, the Rosenbluth weight W [152] is accumulated and used in the acceptance rule of the GCMC method for insertion of the molecules into the system. The probability of adding a single chain to a system of N_i chains is given by [409]

$$p^+ = \min\left[1, \frac{\exp(\beta\mu_i)V}{\Lambda_i^3(N_i + 1)} W(n)\right] \tag{212}$$

where μ_i is the chemical potential of chain i, V is the volume of the system, and Λ_i is the thermal de Broglie wavelength of component i. Equation (212) is completely similar to Eq. (202), the probability of inserting a molecule into a system in a standard GCMC computations with the main difference being the inclusion of the Rosenbluth weight W. For a deletion move, the Rosenbluth weight is evaluated by *pretending* to grow the alkane chain into its current position. To accomplish this, the quantities, $w_1(o) = \exp[-\beta u_1(o)]$, $w_l(o) = \sum_{j=1}^{k} \exp[-\beta u_l^{\mathrm{ext}}(\mathbf{b}'_j)]$, and $W(o) = \prod_{l=1}^{M} w_l(o)$ are computed, using $k - 1$ trial orientations, together with the actual current position of the atom l, which form the set $\{\mathbf{b}'_k\}$ [see Eqs. (66) and (67)], where o indicates the old state of the molecules. The probability of deletion of a chain from the system is then given by [409]

$$p^- = \min\left[1, \frac{N_i \Lambda_i^3}{\exp(\beta\mu_i)V} \frac{1}{W(o)}\right] \tag{213}$$

which, aside from the Rosenbluth weight, is similar to Eq. (203) for the standard GCMC computations.

Finally, there are systems in which in some parts of the phase diagram quantum effects may be important. An example is provided by liquid hydrogen (within or without a pore), as this fluid exhibits strongly quantum behavior that cannot be analyzed by a first- or second-order perturbation treatment. Using Feynman's observation [410] that there is an isomorphism between a quantum system and a classical one consisting of polymer rings, or "necklaces," of particles, one may develop a *path integral* GCMC method [411–417]. In this method, the probabilities for the displacement, insertion, and deletion of particles are very similar to those described above for the classical GCMC method.

6.1.2. Density Functional Theory

In the density functional theory (DFT), not to be confused with the DFT that was described earlier for quantum-mechanical computations, the equilibrium density $\rho(r)$ of the fluid is obtained by minimizing a free-energy functional [418]. Thus, if a pore is in equilibrium with a bulk phase, we write

$$F[\rho(r)] = H[\rho(r)] - \int \rho(r)[\mu - U_e(r)]\, dr \tag{214}$$

where U_e is an external potential field due to the pore material, and H is the Helmholtz free energy of the fluid *in the absence* of U_e. For fluids that can be described by the LJ and similar potentials, $H(r)$ is given by a first-order perturbation around the hard-sphere fluid. In that case, the attractive part of the fluid–fluid potential interactions is approximated by a mean-field theory:

$$H[\rho(r)] = H_h[\rho(r)] + \frac{1}{2}\iint \rho(r)\rho(r')U_{\text{att}}(|r - r'|)\, dr'dr \tag{215}$$

where H_h is the hard-sphere contribution, and U_{att} is the attractive portion of the fluid–fluid interaction potential, which is usually taken to be what Weeks et al. [419] suggested for the LJ potential. Then, H_h is written as the sum of an ideal and an excess part (with the ideal part being trivial). Several methods have been suggested for deriving an expression for the excess part. Notable among them are,

(i) *Weighted density approximation*, due to Tarazona and coworkers [420, 421], in which the excess hard-sphere free energy is given by

$$H_h^{\text{excess}}[\rho(r)] = \int \rho(r)h^{\text{excess}}[\bar{\rho}(r)]\, dr \tag{216}$$

where $\bar{\rho}(r)$ is a weighted average over the original density profile of the fluid, and h^{excess} is the excess free energy per molecule of the bulk hard-sphere fluid, which can be determined once an equation of state is specified for the fluid. The weighting functions are selected such that the direct correlation functions of the bulk fluid are reproduced accurately and are themselves functions of the weighted density.

(ii) *Local density approximation*, according to which

$$H_h^{\text{excess}}[\rho(r)] = \int \rho(r)h^{\text{excess}}[\rho(r)]\, dr \tag{217}$$

Because this approximation cannot take into account the effect of even short-range correlations in the fluid, it is not accurate for fluids inside nanopores.

(iii) Weighted density approximation due to Kierlik and Rosinberg [422, 423], which is similar to that of Tarazona and coworkers, but it is simpler. Moreover, this version of the weighted density approximation is more accurate for nanopores than that of Tarazona and coworkers.

6.2. Flow and Transport

As mentioned earlier, equilibrium MD (EMD) simulations are applicable to systems that, at least in principle, are amenable to treatment by statistical mechanics. Although, as our discussions so far should have made it clear, many assumptions must be made and several approximations must be used, their main purpose is to make the computations tractable. However, if we are to compute the effective flow and transport properties of fluids in nanoporous materials, such as the permeability, diffusivity, shear viscosity, and thermal conductivity, then EMD is not an effective tool. For example, as is well-known, by calculating the velocity correlation functions for every distinct pair of species in the system, one can obtain information about the microscopic motion of the molecules. However, as the velocity correlation function decays as the size of the system increases, use of EMD is not feasible for estimating the transport properties of a mixture of molecules in a system which is under the influence of an external potential gradient—a situation which is encountered in a very large number of practical problems. One can use the velocity autocorrelation function, but this quantity can only be used for predicting the *tracer* or *self-diffusivity* D_s of a species (i.e., when the system is very dilute) via the Green-Kubo equation:

$$D_s = \frac{1}{3N} \int_0^\infty \left\langle \sum_{i=1}^{N} [\mathbf{v}_i(t) \cdot \mathbf{v}_i(0)] \right\rangle dt \tag{218}$$

where $\mathbf{v}_i$ is the velocity of particle i. The self-diffusivity is, however, completely different from the *transport* diffusivity, because tracer diffusion ignores the effect of the collective motion of other molecules, especially in systems with a moderate or high density. As such, EMD is not suitable for investigation of a transport process in a system on which an external potential (pressure, voltage, chemical potential, concentration, etc.) gradient has been imposed.

Nonequilibrium MD (NEMD) simulation represents a practical alternative to EMD for those systems for which the velocity correlation function is difficult, or meaningless, to measure. It is particularly ideal for the practical situation in which an external driving force is applied to the system. Several such modeling efforts have been reported. Notable among them are the grand-canonical molecular dynamics (GCMD) method [424–426] in which MC and MD simulations are combined (see below), and a dual control-volume GCMD technique (DCV-GCMD) [323, 327, 328, 361, 405, 427–443]. We describe here the DCV-GCMD method that has become an effective tool for studying systems that are under the influence of an external potential gradient.

To describe this method, we consider a concrete example, namely, transport of binary gas mixture in a carbon nanopore or nanotube, a problem of considerable importance in separation and purification processes. The same method is applicable to transport of a one-component fluid in the pore that is under the influence of an external potential gradient. For simplicity, we consider a slit pore, a schematic representation of which is shown in Fig. 9 in which the origin of the coordinates is at the center. The external driving force is either a chemical potential (or, equivalently, pressure) or a concentration gradient applied in the x-direction. The system is divided into three regions. The h- and ℓ-regions at the two ends represent two control volumes (CVs) exposed to the bulk fluid at high and low chemical potential, pressure, or concentration, respectively, and the middle region represents the pore in which transport occurs. The pore's length is nL with n being an integer. Periodic boundary conditions are employed in the y-direction. The two carbon walls are located at the top and bottom of the xy planes. We consider transport of a binary gas mixture in a slit pore.

The DCV-GCMD method combines integration of the equations of motion with GCMC insertions and deletions of the gas molecules in the two CVs. It is essential to maintain the densities of each gas component in the two CVs at some fixed values, which are in equilibrium with two bulk phases, each at a fixed gas pressure and concentration. The densities, or the corresponding chemical potentials of each component in the CVs, are maintained by carrying out a sufficient number of GCMC insertions and deletions of the particles.

When a particle is inserted in a CV, it is assigned a thermal velocity selected from the Maxwell-Boltzmann distribution, Eq. (29), at the given T. An important parameter of

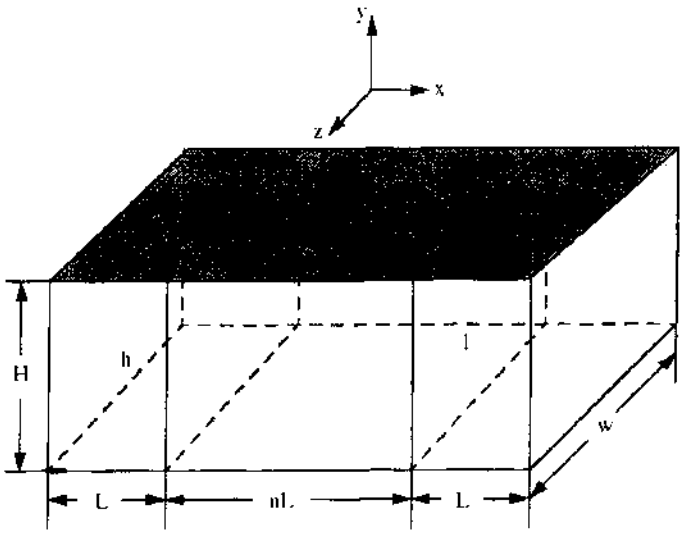

Figure 9. The slit-pore system used in the simulation of transport and adsorption in a nanopore. The left and right chambers show the two control volumes at high and low pressures, and the middle part is the pore system.

NEMD simulations is the ratio $\mathcal{R}$ of the number of GCMC insertions and deletions in each CV to the number of MD integration steps between successive GCMC steps. This ratio must be selected appropriately in order to maintain the correct density and chemical potentials in the CVs and also reasonable transport rates at the boundaries between the CVs and the transport region. Its typical value varies anywhere from 50:1 to 400:1. During the MD calculations particles crossing the outer boundaries of the CVs must be removed (the fraction of such particles is, however, very small). In addition, one should allow for a nonzero streaming velocity (the ratio of the flux to the concentration of each component) in the entire transport region of each component, consistent with the presence of bulk pressure/chemical potential gradients along the flow direction. Otherwise, a zero streaming velocity in the transport region will lead to severely underestimated fluxes. Because the two CVs are assumed to be well mixed and in equilibrium with the two bulk phases that are in direct contact with them, there should be no *overall* nonzero streaming velocity in these regions. However, to reduce the numerical instability caused by the discontinuity of the streaming velocities at

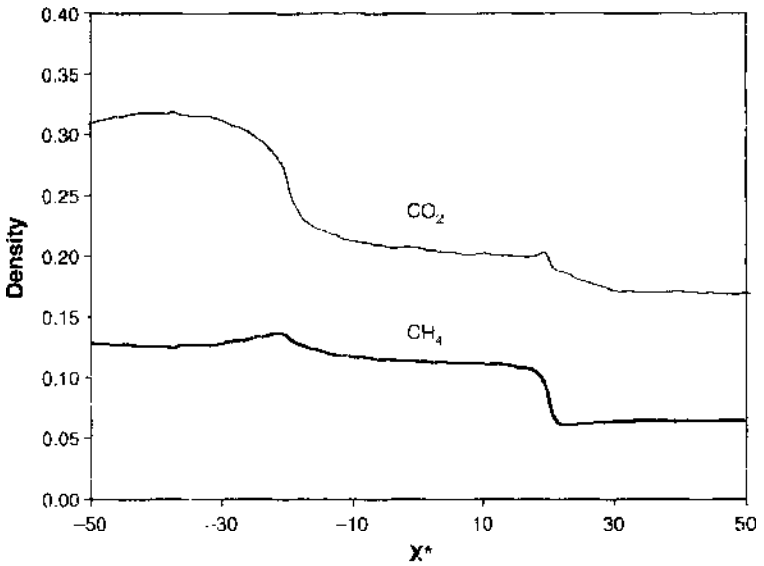

Figure 10. Density profiles for an equimolar mixture of CO_2 and CH_4 inside the slit-pore of Fig. 9. The profiles represent averaged values over the cross section of the system in the direction of the macroscopic transport. The upstream and downstream pressures are, respectively, 120 atm and 20 atm. The results were obtained after 3,500,000 time steps, using the DCV-GCMD simulations (courtesy of Mahnaz Firouzi).

the boundaries between the CVs and the transport region, a small streaming velocity can be added to the thermal velocity of all the newly inserted molecules within each CV that are located within a distance $0.5\sigma_1$ from the boundaries (the effect of this addition on the overall properties of the system has been shown [444, 445]) to be negligible, where σ_1 is the LJ size parameter (or the effective molecular size) of the lightest of the two gases. The streaming velocity of each component in the transport region is obtained by linearly interpolating between its two values in the two CVs. After a few thousands of integration steps, this procedure generates a potential gradient along the pore, an example of which is shown in Fig. 10. To study the transport of a mixture in a potential gradient, the temperature of the system must be held constant in order to eliminate any contribution of the temperature gradient to the transport; hence special care must be taken to achieve this. All the quantities of interest are calculated from such simulations. Its predictions for some properties of interest are in good quantitative agreement with experimental data [362, 443]. Massively parallel algorithms have also been developed [436, 437] for the DCV-GCMD method. Other NEMD methods have been described by Rapaport [54].

7. CONCLUSION

A large set of computational techniques has been developed that can not only model the morphology of nanoporous materials at the molecular scale but also be used for studying various phenomena in such materials. As techniques for studying materials at the atomic scale, molecular dynamics and Monte Carlo simulation, together with energy minimization techniques, have been used for several decades. However, development of vector computers and parallel machines, and hence vectorized and parallelized computational algorithms, together with the development of accurate interatomic potentials, have made these techniques powerful tools for studying materials at atomic scales using millions of atoms and molecules.

Ab initio quantum mechanical computations based on the density functional theory in the local density approximation, together with plane-wave pseudopotential formulation, offers an efficient and rigorous method for computing materials properties. The quantum MD simulation method of Car and Parrinello [50] did not change the essentials of such computations, but offered an enormous increase in the efficiency of the method, hence making much larger pieces of materials accessible to such computations.

These computational strategies have enabled us to investigate and accurately predict various properties of nanoporous materials. We believe that when these methods are joined with the multiscale approach [3, 94–98], the possibilities for accurate and efficient optimal design of nanoporous materials with specific properties may be limitless.

ACKNOWLEDGMENTS

We are grateful to the National Science Foundation, the Department of Energy, the Petroleum Research Fund (administered by the American Chemical Society), the California Energy Commission, and our industrial partners, and in particular Media and Process Technology, Inc., for supporting our work in this area. We would also like to thank our past and present collaborators in these problems, especially Mahnaz Firouzi, Jaleh Ghassemzadeh, Seong S. Lim, Ali Reza Mehrabi, Katherine S. Shing, Lifang Xu, and Xiaohua Yi.

REFERENCES

1. R. P. Feynman, paper presented at the Annual Meeting of the American Physical Society (1959).
2. M. Sahimi, "Heterogeneous Materials I: Linear Transport and Optical Properties," Springer, New York, 2003.
3. M. Sahimi, "Heterogeneous Materials II: Nonlinear and Breakdown Properties and Atomistic Modeling," Springer, New York, 2003.
4. S. Torquato, "Random Heterogeneous Materials," Springer, New York, 2002.
5. H. W. Kroto, J. R. Heath, S. C. O'Brien, R. F. Curl, and R. E. Smalley, *Nature* 318, 162 (1985).
6. S. Iijima and T. Ichihashi, *Nature* 363, 603 (1993).
7. D. S. Bethune, C. H. Kiang, M. S. de Vries, G. Gorman, R. Savoy, J. Vazquez, and R. Beyers, *Nature* 363, 605 (1993).

8. S. Iijima, *Nature* 354, 56 (1991).
9. A. Hagen and T. Hertel, *Nano Lett.* 3, 383 (2003).
10. A. B. Dalton, S. Collins, E. Muñoz, J. M. Razal, V. H. Ebron, J. P. Ferraris, J. N. Coleman, B. G. Kim, and R. H. Baughman, *Nature* 423, 703 (2003).
11. M. S. Dresselhaus, G. Dresselhaus, and P. C. Eklund, "Science of Fullerenes and Carbon Nanotubes." Academic Press, San Diego, 1996.
12. N. Hamada, S.-I. Sawada, and A. Oshiyama, *Phys. Rev. Lett.* 68, 1579 (1992).
13. X. Blase, L. X. Benedict, E. L. Shirley, and S. G. Louie, *Phys. Rev. Lett.* 72, 1878 (1994).
14. P. G. Collins, K. Bradley, M. Ishigami, and A. Zett, *Science* 287, 1801 (2000).
15. J. Kong, N. R. Franklin, C. Zhou, M. G. Chapline, S. Peng, K. Cho, and H. Dai, *Science* 287, 622 (2000).
16. H. Dai, J. H. Hafner, A. G. Rinzler, D. T. Colbert, and R. E. Smalley, *Nature* 384, 147 (1996).
17. S. Wong, E. Joselevich, A. Woolley, C. Cheung, and C. Lieber, *Nature* 394, 52 (1998).
18. W. A. de Heer, A. Chatelain, and D. Ugarte, *Science* 270, 1179 (1995).
19. R. H. Baughman, C. Cui, A. A. Zakhidov, Z. Iqbal, J. N. Barisci, G. M. Spinks, G. G. Wallas, A. Mazzoldi, D. De Rossi, A. G. Rinzler, O. Jaschinski, S. Roth, and M. Kertesz, *Science* 284, 1340 (1999).
20. S. Tans, A. Verschuren, and C. Dekker, *Nature* 393, 49 (1998).
21. A. C. Dillon, K. M. Jones, T. A. Bekkedahl, C. H. Klang, D. S. Bethune, and M. J. Heben, *Nature* 386, 377 (1997).
22. C. Nutzenadel, A. Zuttel, D. Chartouni, and L. Schlapbach, *Electrochem. Solid State Lett.* 2, 30 (1999).
23. C. Liu, Y. Y. Fan, M. Liu, H. T. Cong, H. M. Cheng, and M. S. Dresselhaus, *Science* 286, 1127 (1999).
24. P. Chen, X. Wu, J. Lin, and K. L. Tan, *Science* 285, 91 (1999).
25. M. S. Desselhaus, K. A. Williams, and P. C. Eklund, *MRS Bull.* 24, 45 (1999).
26. W. Teizer, R. B. Hallock, E. Dujardin, and W. T. Ebbesen, *Phys. Rev. Lett.* 82, 5305 (1999); 84, 1844(E) (2000).
27. A. Kuznetsova, J. T. Yates, J. Liu, and R. E. Smalley, *J. Chem. Phys.* 112, 9590 (2000).
28. A. Kuznetsova, D. B. Mawhinney, V. Naumenko, J. T. Yates, J. Liu, and R. E. Smalley, *Chem. Phys. Lett.* 321, 292 (2000).
29. S. E. Weber, S. Talapatra, C. Journet, A. J. Zambano, and A. D. Migone, *Phys. Rev. B* 61, 13150 (2000).
30. S. Talapatra, A. J. Zambano, S. E. Weber, and A. D. Migone, *Phys. Rev. Lett.* 85, 138 (2000).
31. M. Muris, N. Dufau, M. Bienfait, N. Dupont-Pavlosky, Y. Grillet, and J. P. Palmari, *Langmuir* 16, 7019 (2000).
32. K. A. Williams and P. C. Eklund, *Chem. Phys. Lett.* 320, 352 (2000).
33. R. T. Yang, *Carbon* 38, 623 (2000).
34. M. S. Dresselhaus, G. Dresselhaus, and P. Avouris, Eds., "Carbon Nanotubes." Springer, Berlin, 2001.
35. H. Dai, *Surface Sci.* 500, 218 (2002).
36. S. R. Wilson and C. J. Tracy, Eds., "Handbook of Multilevel Metallization for Integrated Circuits." Noyes Publications, Park Ridge, NY, 1993.
37. D. C. Edelstein, G. A. Sai-Halasz, and Y.-J. Mii, *IBM J. Res. Dev.* 39, 383 (1995).
38. J. G. Ryan, R. M. Geffken, N. R. Poulin, and J. R. Paraszczak, *IBM J. Res. Dev.* 39, 371 (1995).
39. M. T. Buhr, in "Advanced Metallization and Interconnect Systems for ULSI Applications in 1996," (R. Havemann, J. Schmitz, H. Komiyama, and K. Tsubouchi, Eds.), p. 3. Materials Research Society Symposium Proceedings, Pittsburgh, 1996.
40. W. W. Lee and P. S. Ho, *MRS Bull.* 22(10), 19 (1997).
41. S.-P. Jeng, P. Havemann, and M. Chang, in "Advanced Metallization for Devices and Circuits—Science, Technology, and Manufacturability" (S. P. Murarka, A. Katz, K. N. Tu, and K. Maex, Eds.), p. 25. Materials Research Society Symposium Proceedings, Pittsburgh, 1994.
42. S.-P. Jeng, M. Chang, T. Kroger, P. McAnally, and R. Havemann, *VLSI Tech. Symp. Tech. Dig.* (1994), p. 73.
43. L. W. Hrubesh, L. E. Keene, and V. R. Latorre, *J. Mater. Res.* 8, 1736 (1993).
44. C. Jin, J. D. Luttmer, D. M. Smith, and T. A. Ramos, *MRS Bull.* 22(10), 39 (1997).
45. J. G. Sanchez Marcano and T. T. Tsotsis, "Catalytic Membranes and Membrane Reactors." Wiley-VCH, Weinheim, 2002.
46. M. Sahimi, "Flow and Transport Through Porous Media and Fractured Rock." VCH, Weinheim, 1995.
47. P. Hohenberg and W. Kohn, *Phys. Rev.* 136, B864 (1964).
48. W. Kohn and L. J. Sham, *Phys. Rev.* 140, A1133 (1965).
49. R. M. Dreizler and E. K. U. Gross, "Density-Functional Theory." Springer, Berlin, 1990.
50. R. Car and M. Parrinello, *Phys. Rev. Lett.* 55, 2471 (1985).
51. J. Roth, F. Gähler, and H.-R. Trebin, *Int. J. Mod. Phys. C* 11, 317 (2000).
52. F. F. Abraham, *Adv. Phys.* 35, 1 (1986).
53. M. P. Allen and D. J. Tildesley, "Computer Simulation of Liquids." Oxford University Press, London, 1987.
54. D. C. Rapaport, "The Art of Molecular Dynamics." Cambridge University Press, London, 1985.
55. D. Frenkel and B. Smit, "Understanding Molecular Simulation," 2nd Edn. Academic Press, San Diego, 2002.
56. A. R. Leach, "Molecular Modelling. Principles and Applications." Addison Wesley Longman, Essex, 1996.
57. S. R. Niketic and K. Rasmussen, "The Consistent Force Field: A Documentation." Springer, Berlin, 1977.
58. W. H. Press, S. A. Teukolsky, W. T. Vetterling, and B. P. Flannery, "Numerical Recipes," 2nd Edn. Cambridge University press, New York, 1992.
59. M. J. D. Powell, *Math. Prog.* 12, 241 (1977).
60. D. F. Shanno and K. H. Phua, *ACM Trans. Math. Softw.* 6, 618 (1980).
61. J. C. Gilbert and J. Nocedal, Technical Report 1268, Institut National de Recherche en Informatique et en Automatique, 1991.

62. L. Adams and J. L. Nazareth, Eds., "Linear and Nonlinear Conjugate Gradient-Related Methods," SIAM, Philadelphia, 1996.
63. J. Nocedal and S. Wright, "Numerical Optimization," Springer, Berlin, 1999.
64. P. E. Gill and M. W. Leonard, *SIAM J. Optim.* 12, 209 (2001).
65. J. Nocedal, *Mathematics of Computation* 35, 773 (1980).
66. D. C. Liu and J. Nocedal, *Math. Prog. B* 45, 503 (1989).
67. J. C. Gilbert and C. Lemarechal, *Math. Prog. B* 45, 407 (1989).
68. J. Nocedal, in "The State of Art in Numerical Analysis" (A. Watson and I. Duff, Eds.), p. 311, Oxford University Press, London, 1997.
69. T. Schlick, "Molecular Modeling and Simulation," Springer, New York, 2002.
70. S. G. Nash and J. Nocedal, *SIAM J. Optim.* 1, 358 (1991).
71. R. H. Byrd, J. Nocedal, and R. B. Schnabel, *Math. Prog.* 63, 129 (1994).
72. R. H. Byrd, P. Lu, and J. Nocedal, *SIAN J. Sci. Stat. Comput.* 16, 1190 (1995).
73. C. Zhu, R. H. Byrd, P. Lu, and J. Nocedal, *ACM Trans. Math. Softw.* 23, 550 (1997).
74. R. S. Dembo and T. Steihaug, *Math. Prog.* 26, 190 (1983).
75. P. Derreumaux, G. Zhang, B. Brooks, and T. Schlick, *J. Comput. Chem.* 15, 532 (1994).
76. D. Xie and T. Schlick, *SIAM J. Optim.* 10, 132 (1999).
77. B. J. Alder and T. E. Wainwright, *J. Chem. Phys.* 27, 1208 (1957).
78. W. W. Wood and F. R. Parker, *J. Chem. Phys.* 27, 720 (1957).
79. A. Rahman, *Phys. Rev.* 136, A405 (1964).
80. L. Verlet, *Phys. Rev.* 159, 98 (1967).
81. B. J. Alder and T. E. Wainwright, *Phys. Rev. A.* 1, 18 (1969).
82. A. Rahman and F. H. Stillinger, *J. Chem. Phys.* 55, 3336 (1971).
83. D. J. Evans and S. Murad, *Mol. Phys.* 34, 327 (1977).
84. G. Ciccotti, M. Ferrario, and J.-P. Ryckaert, *Mol. Phys.* 47, 1253 (1982).
85. C. H. Bennett, *J. Comput. Phys.* 22, 245 (1976).
86. G. M. Torrie and J. P. Valleau, *J. Comput. Phys.* 23, 157 (1977).
87. D. Frenkel and A. J. L. Ladd, *J. Chem. Phys.* 81, 3188 (1984).
88. H. C. Andersen, *J. Chem. Phys.* 72, 2384 (1980).
89. M. Parrinello and A. Rahman, *J. Apply. Phys.* 52, 7182 (1981).
90. S. Nosé, *J. Chem. Phys.* 81, 511 (1984).
91. W. G. Hoover, *Phys. Rev. A* 31, 1695 (1985).
92. F. F. Abraham, W. E. Rudge, D. J. Auerbach, and S. W. Koch, *Phys. Rev. Lett.* 52, 445 (1984).
93. W. C. Swope and H. C. Andersen, *Phys. Rev. B* 41, 7042 (1990).
94. R. Phillips, "Crystals, Defects and Microstructures," Cambridge University Press, London, 2001.
95. J. Q. Broughton, F. F. Abraham, N. Bernstein, and E. Kaxiras, *Phys. Rev. B* 60, 2391 (1999).
96. E. B. Tadmor, M. Ortiz, and R. Phillips, *Philos. Mag. A* 73, 1529 (1996).
97. E. B. Tadmor, R. Miller, R. Phillips, and M. Ortiz, *J. Mater. Res.* 14, 2233 (1999).
98. M. Dadvar and M. Sahimi, *Chem. Eng. Sci.* 58, 4935 (2003).
99. W. A. Steele, *Surf. Sci.* 36, 317 (1973).
100. S. Lifson and A. Warshel, *J. Chem. Phys.* 49, 5116 (1968).
101. N. L. Allinger, Y. H. Yuh, and J.-H. Lii, *J. Am. Chem. Soc.* 111, 8551 (1989).
102. N. L. Allinger, M. A. Miller, F. A. VanCatledge, and J. A. Hirsch, *J. Am. Chem. Soc.* 89, 4345 (1967).
103. L. Pauling, "The Nature of the Chemical Bond," Cornell University Press, New York, 1960.
104. A. Larshminarayanan and V. Sasisekharan, *Biopolymers* 8, 475 (1969).
105. G. Némethy, M. S. Pottle, and H. A. Scheraga, *J. Phys. Chem.* 87, 1883 (1983).
106. T. A. Halgren, *J. Comput. Chem.* 17, 520 (1996).
107. S. D. Stoddards and J. Ford, *Phys. Rev. A* 8, 1504 (1973).
108. C. Störmer, *Arch. Sci. Physique Natur.* 24, 5–18, 113–158, 221–247 (1907) (see also pp. 190, 277, 415, and 501 of the 1911 volume and p. 51 of the 1912 volume).
109. R. W. Hockney and J. W. Eastwood, "Computer Simulation Using Particles," McGraw-Hill, New York, 1981.
110. W. C. Swope, H. C. Andersen, P. H. Berens, and K. R. Wilson, *J. Chem. Phys.* 76, 637 (1982).
111. M. E. Tukerman, B. J. Berne, and G. J. Martyna, *J. Chem. Phys.* 97, 1990 (1992).
112. B. Earth and T. Schlick, *J. Chem. Phys.* 109, 1617 (1998).
113. P. Batcho and T. Schlick, *J. Chem. Phys.* 115, 4019 (2001).
114. J. M. Sanz-Serna, *Acta Numerica* 1, 243 (1992).
115. P. Batcho, D. A. Case, and T. Schlick, *J. Chem. Phys.* 115, 4003 (2001).
116. M. Mandziuk and T. Schlick, *Chem. Phys. Lett.* 237, 525 (1995).
117. W. B. Strutt, D. J. Tildesley, and G. Saville, *Mol. Phys.* 35, 639 (1978).
118. R. D. Swindoll and J. M. Haile, *J. Chem. Phys.* 53, 289 (1984).
119. H. Grubmüller, H. Heller, A. Windemuth, and K. Schulter, *Mol. Simul.* 6, 121 (1991).
120. A. Sandu and T. Schlick, *J. Comput. Phys.* 151, 74 (1999).
121. E. Barth and T. Schlick, *J. Chem. Phys.* 109, 1632 (1998).
122. J. M. Haile and S. Gupta, *J. Chem. Phys.* 79, 3067 (1983).
123. H. J. C. Berendsen, J. P. M. Postma, W. F. van Gunsteren, A. DiNola, and J. R. Haak, *J. Chem. Phys.* 81, 3684 (1984).
124. K. Cho and J. D. Joannopoulos, *Phys. Rev. A* 45, 7089 (1992).

125. B. L. Holian, A. F. Voter, and R. Ravelo, *Phys. Rev. E* 52, 2338 (1995).
126. S. C. Harvey, R. K.-Z. Tan, and T. E. Cheatham, *J. Comput. Chem.* 19, 726 (1998).
127. J. Jellinek and R. S. Berry, *Phys. Rev. A* 38, 3069 (1988).
128. A. C. Brańka and K. W. Wojciechowski, *Phys. Rev. E* 62, 3281 (2000).
129. G. J. Martyna, M. L. Klein, and M. E. Tuckerman, *J. Chem. Phys.* 97, 2635 (1992).
130. S. E. Feller, Y. Zhang, R. W. Pastor, and B. R. Brooks, *J. Chem. Phys.* 103, 4613 (1995).
131. G. J. Martyna, A. Hughes, and M. E. Tuckerman, *J. Chem. Phys.* 110, 3275 (1999).
132. C. S. Murthy, S. F. O'Shea, and I. R. McDonald, *Mol. Phys.* 50, 531 (1983).
133. K. D. Hammonds, I. R. McDonald, and D. J. Tildesley, *Mol. Phys.* 70, 175 (1990).
134. M. G. Sedigh, W. J. Onstot, L. Xu, W. L. Peng, T. T. Tsotsis, and M. Sahimi, *J. Phys. Chem. A* 102, 8580 (1998).
135. M. G. Sedigh, L. Xu, T. T. Tsotsis, and M. Sahimi, *Ind. Eng. Chem. Res.* 38, 3367 (1999).
136. M. G. Sedigh, M. Jahangiri, P. K. T. Liu, M. Sahimi, and T. T. Tsotsis, *AIChE J.* 46, 2256 (2000).
137. J. M. Thijssen, "Computational Physics," Cambridge University Press, Cambridge, 1999.
138. J.-P. Ryckaert, G. Ciccotti, and H. J. C. Berendsen, *J. Comput. Phys.* 23, 327 (1977).
139. J.-P. Ryckaert, *Mol. Phys.* 55, 549 (1985).
140. H. C. Andersen, *J. Comput. Phys.* 52, 24 (1983).
141. D. J. Tobias and C. L. Brooks, III, *J. Chem. Phys.* 89, 5115 (1988).
142. S. Miyamoto and P. A. Kollman, *J. Comput. Chem.* 13, 952 (1992).
143. B. Leimkuhler and R. D. Skeel, *J. Comput. Chem.* 112, 117 (1994).
144. J. Harris and S. A. Rice, *J. Chem. Phys.* 88, 1298 (1988).
145. G. C. A. M. Mooij, D. Frenkel, and B. Smit, *J. Phys.: Condens. Matter* 4, L255 (1992).
146. M. Laso, J. J. dePablo, and U. W. Suter, *J. Chem. Phys.* 97, 2817 (1992).
147. J. I. Siepmann and D. Frenkel, *Mol. Phys.* 75, 59 (1992).
148. J. J. dePablo, M. Bonnin, and J. M. Prausnitz, *Fluid Phase Equil.* 73, 187 (1992).
149. D. Frenkel, G. C. A. M. Mooij, and B. Smit, *J. Phys.: Condens. Matter* 4, 3053 (1992).
150. B. Smit, S. Karaborni, and J. I. Siepmann, *J. Chem. Phys.* 102, 2126 (1995).
151. M. D. Macedonia and E. J. Maginn, *Mol. Phys.* 96, 1375 (1999).
152. M. N. Rosenbluth and A. W. Rosenbluth, *J. Chem. Phys.* 23, 356 (1955).
153. J. Norberg and L. Nilsson, *Biophys. J.* 79, 1537 (2000).
154. M. Mezei, *J. Comput. Chem.* 18, 812 (1997).
155. X. Qian, D. Strahs, and T. Schlick, *J. Comput. Chem.* 22, 1843 (2001).
156. S. W. De Leeuw, J. W. Perram, and E. R. Smith, *Proc. Roy. Soc. London A* 373, 27 (1980).
157. D. Fincham, *Mol. Simul.* 13, 1 (1994).
158. J. W. Perram, H. G. Petersen, and S. W. De Leeuw, *Mol. Phys.* 65, 875 (1988).
159. T. Darden, D. York, and L. Pedersen, *J. Chem. Phys.* 98, 10089 (1993).
160. U. Essmann, L. Perera, M. L. Berkowitz, T. Darden, H. Lee, and L. G. Pedersen, *J. Chem. Phys.* 103, 8577 (1995).
161. A. Y. Toukmaji and J. A. Board, Jr., *Comput. Phys. Commun.* 95, 73 (1996).
162. B. A. Luty, M. E. David, I. G. Tironi, and W. F. Van Gunsteren, *Mol. Simul.* 14, 11 (1994).
163. B. A. Luty, I. G. Tironi, and W. F. Van Gunsteren, *J. Chem. Phys.* 103, 3014 (1995).
164. L. Greengard and V. I. Rokhlin, *J. Comput. Phys.* 73, 325 (1987).
165. L. Greengard and V. I. Rokhlin, *Chemica Scripta* 29A, 139 (1989).
166. L. Greengard, *Science* 265, 909 (1994).
167. L. Greengard and V. I. Rokhlin, *Acta Numerica* 6, 229 (1997).
168. A. W. Appel, *SIAM J. Sci. Stat. Comput.* 6, 85 (1985).
169. J. Barnes and P. Hut, *Nature* 324, 446 (196).
170. V. I. Rokhlin, *J. Comput. Phys.* 60, 187 (1985).
171. A. R. Mehrabi and M. Sahimi, *Phys. Rev. Lett.* 82, 735 (1999).
172. H.-Q. Ding, N. Karasawa, and W. A. Goddard III, *J. Chem. Phys.* 97, 4309 (1992).
173. A. Brandt and A. A. Lubrecht, *J. Comput. Phys.* 90, 348 (1990).
174. B. Sandak, *J. Comput. Chem.* 22, 717 (2001).
175. R. D. Skeel, I. Tezcan, and D. J. Hardy, *J. Comput. Chem.* 23, 673 (2002).
176. Z.-H. Duan and R. Krasny, *J. Chem. Phys.* 113, 3492 (2000).
177. Z.-H. Duan and R. Krasny, *J. Comput. Chem.* 22, 184 (2001).
178. J. Board, A. John, C. W. Humphres, C. G. Lambert, W. T. Rankin, and A. Y. Toukmaji, "Eighth SIAM Conference on Parallel Processing for Scientific Computing," SIAM CD-ROM, Philadelphia, 1997.
179. M. S. Daw and M. I. Baskes, *Phys. Rev. Lett.* 50, 1285 (1983).
180. M. S. Daw and M. I. Baskes, *Phys. Rev. B* 29, 6443 (1984).
181. S. M. Foiles, M. I. Baskes, and M. S. Daw, *Phys. Rev. B* 33, 7983 (1986).
182. R. A. Johnson, *Phys. Rev. B* 37, 3924 (1988).
183. B. L. Holian, A. F. Voter, N. J. Wagner, R. J. Ravelo, S. P. Chen, W. G. Hoover, C. G. Hoover, J. E. Hammerberg, and T. D. Dontje, *Phys. Rev. A* 43, 2655 (1991).
184. P. M. Morse, *Phys. Rev.* 34, 57 (1929).
185. N. J. Wagner, B. L. Holian, and A. F. Voter, *Phys. Rev. A* 45, 8457 (1992).
186. M. I. Baskes, J. S. Nelson, and A. F. Wright, *Phys. Rev. B* 40, 6085 (1989).
187. E. B. Webb, III and G. S. Grest, *Phys. Rev. Lett.* 86, 2066 (2001).
188. F. H. Stillinger and T. A. Weber, *Phys. Rev. B* 31, 5262 (1985).

189. F. Shimojo, I. Ebbsjö, R. K. Kalia, A. Nakano, J. P. Rino, and P. Vashishta, *Phys. Rev. Lett.* 84, 3338 (2000).
190. V. Swaminathanond, E. Goo, P. K. T. Liu, G. Johnson, M. Sahimi, and T. T. Tsotsis, *Ind. Eng. Chem. Res.* 39, 3264 (2000).
191. A. E. Mistriotis, N. Flytzanis, and S. C. Farantos, *Phys. Rev. B* 39, 1212 (1989).
192. J. Tersoff, *Phys. Rev. B* 37, 6991 (1988).
193. J. Ferrante, J. R. Smith, and J. H. Rose, *Phys. Rev. Lett.* 50, 1385 (1983).
194. G. C. Abell, *Phys. Rev. B* 31, 6184 (1985).
195. J. Tersoff, *Phys. Rev. B* 39, 5566 (1989).
196. D. Mura, L. Colombo, R. Bertoncini, and G. Mula, *Phys. Rev. B* 58, 10357 (1998).
197. J. R. Chelikowsky, J. C. Phillips, M. Kamal, and M. Strauss, *Phys. Rev. Lett.* 62, 292 (1989).
198. K. E. Kohr and S. Das Sarma, *Phys. Rev. B* 40, 1319 (1989).
199. B. C. Bolding and H. C. Andersen, *Phys. Rev. B* 41, 10568 (1989).
200. D. W. Brenner, *Phys. Rev. B* 42, 9458 (1990).
201. D. H. Robertson, D. W. Brenner, and J. W. Mintmire, *Phys. Rev. B* 45, 12592 (1992).
202. J. Che, T. Cagin, and W. A. Goddard III, *Theor. Chem. Acc.* 102, 346 (1999).
203. S. Lin, T. T. Tsotsis, and M. Sahimi, *J. Chem. Phys.* (2005, in press).
204. H. Sun, *J. Phys. Chem. B* 102, 7338 (1998).
205. A. K. Rappé, C. J. Casewit, K. S. Colwell, W. A. Goddard, and W. M. Skiff, *J. Am. Chem. Soc.* 114, 10024 (1992).
206. W. D. Cornell, P. Cieplak, C. I. Bayly, I. R. Gould, K. M. Merz, D. M. Ferguson, D. C. Spellmeyer, T. Fox, J. W. Caldwell, and P. A. Kollman, *J. Am. Chem. Soc.* 117, 5179 (1995).
207. W. D. Cornell, P. Cieplak, C. I. Bayly, I. R. Gould, K. M. Merz, D. M. Ferguson, D. C. Spellmeyer, T. Fox, J. W. Caldwell, P. A. Kollman, *J. Am. Chem. Soc.* 118, 2309 (1996).
208. A. D. Mackerell, J. Wiorkiewiczkuczera, and M. Karplus, *J. Am. Chem. Soc.* 117, 11946 (1995).
209. W. L. Jorgensen, J. D. Madura, and C. J. Swenson, *J. Am. Chem. Soc.* 106, 6638 (1984).
210. W. L. Jorgensen and J. Tirado-Rives, *J. Am. Chem. Soc.* 110, 1657 (1988).
211. W. L. Jorgensen, D. S. Maxwell, and J. Tirado-Rives, *J. Am. Chem. Soc.* 118, 11225 (1996).
212. W. L. Cui, F. B. Li, and N. L. Allinger, *J. Am. Chem. Soc.* 115, 2943 (1993), where references to the earlier work of this group can also be found.
213. N. Nevins, J. H. Lii, and N. L. Allinger, *J. Comput. Chem.* 17, 695 (1996), where references to the earlier work of this group can also be found.
214. Z. W. Peng, C. S. Ewing, M. J. Hwang, M. Waldman, and A. T. Hagler, *J. Phys. Chem. A* 101, 7243 (1997), where references to the earlier work of this group can also be found.
215. T. A. Halgren and R. B. Nachbar, *J. Comput. Chem.* 17, 587 (1996), where references to the earlier work of this group can also be found.
216. H. Sun, *J. Comput. Chem.* 15, 752 (1994).
217. H. Sun, S. J. Mumby, J. R. Maple, and A. T. Hagler, *J. Am. Chem. Soc.* 116, 2978 (1994).
218. H. Sun, *Macromolecules* 26, 5924 (1994).
219. H. Sun, *Macromolecules* 28, 701 (1995).
220. H. Sun, S. J. Mumby, J. R. Maple, and A. T. Hagler, *J. Phys. Chem.* 99, 5873 (1995).
221. S. Lin, T. T. Tsotsis, and M. Sahimi, *J. Chem. Phys.* 119, 496 (2003).
222. H. Sun and D. Rigby, *Spectrochim. Acta A* 53, 1301 (1997).
223. D. Rigby, H. Sun, and B. Eichinger, *Polym. Int.* 44, 311 (1997).
224. H. Sun, J. R. Fried, and P. Ren, *Comput. Theor. Polym. Sci.* 8, 229 (1998).
225. P. Günes, S. Simsek, and S. Erkoc, *Int. J. Mod. Phys. C* 11, 451 (2000).
226. V. Gogonea, D. Suárez, A. van der Vaart, and K. M. Merz, *Curr. Opin. Struct. Biol.* 11, 217 (2001).
227. J. W. Mintmire, B. I. Dunlap, and C. T. White, *Phys. Rev. Lett.* 68, 631 (1992).
228. J.-C. Charlier and Ph. Lambin, *Phys. Rev. B* 57, R15037 (1998).
229. Y.-K. Kwon, S. Saito, and D. Tománek, *Phys. Rev. B* 58, R13314 (1998).
230. J. Tersoff and R. S. Ruoff, *Phys. Rev. Lett.* 73, 676 (1994).
231. M. B. Nardelli, B. I. Yakobson, and J. Bernholc, *Phys. Rev. B* 57, R4277 (1998).
232. Y.-G. Yoon, M. S. C. Mazzoni, H. J. Choi, J. Ihm, and S. G. Louie, *Phys. Rev. Lett.* 86, 688 (2001).
233. M. K. Kostov, M. W. Cole, J. C. Lewis, P. Diep, and J. K. Johnson, *Chem. Phys. Lett.* 332, 26 (2000).
234. X. Yang and J. Ni, *Phys. Rev. B* 67, 195403 (2003).
235. D. J. Mann and W. L. Hase, *Phys. Chem. Chem. Phys.* 3, 4376 (2001).
236. A. M. Vidales, V. H. Crespi, and M. W. Cole, *Phys. Rev. B* 58, R13426 (1998).
237. A. Mayer, N. M. Miskovsky, and P. H. Cutler, *Phys. Rev. B* 65, 155420 (2002).
238. R. O. Jones and O. Gunnarsson, *Rev. Mod. Phys.* 61, 689 (1989).
239. M. C. Payne, M. P. Teter, D. Allen, T. A. Arias, and J. D. Joannopoulos, *Rev. Mod. Phys.* 64, 1045 (1992).
240. R. G. Parr and W. Yang, *Ann. Rev. Phys. Chem.* 46, 701 (1995).
241. R. G. Parr and W. Yang, "Density Functional Theory of Atoms and Molecules." Oxford University Press, New York, 1989.
242. R. A. Harris and L. R. Pratt, *J. Chem. Phys.* 82, 856 (1985).
243. E. Runge and E. K. U. Gross, *Phys. Rev. Lett.* 52, 997 (1984).
244. I. V. Tokatly and O. Pankratov, *Phys. Rev. Lett.* 86, 2078 (2001).
245. D. M. Ceperley, *Phys. Rev. B* 18, 3126 (1978).
246. J. P. Perdew and A. Zunger, *Phys. Rev. B* 23, 5048 (1981).

247. J. P. Perdew, K. Burke, and M. Ernzerhof, *Phys. Rev. Lett.* 77, 3865 (1996).
248. J. D. Joannopoulos, P. Bash, and A. Rappe, Chemical Design Automation News 6 (No. 8), 6 (1991).
249. A. Rappe and J. D. Joannopoulos, in "Computer Simulation in Materials Science" (M. Meyer and V. Pontikis, Eds.), p. 409, NATO ASI, Vol. 205, Kluwer, Amsterdam (1991).
250. D. Vanderbilt, *Phys. Rev. B* 41, 7892 (1990).
251. T. Starkloff and J. D. Joannopoulos, *Phys. Rev. B* 16, 5212 (1977).
252. D. R. Hamann, M. Schlüter, and C. Chiang, *Phys. Rev. Lett.* 43, 1494 (1979).
253. E. L. Shirley, D. C. Allan, R. M. Martin, and J. D. Joannopoulos, *Phys. Rev. B* 40, 3652 (1989).
254. M. R. Pederson and K. A. Jackson, *Phys. Rev. B* 43, 7312 (1991).
255. H. Hellmann, "Einführung in die Quantumchemie." Deuticke, Leipzig, 1937.
256. R. P. Feynman, *Phys. Rev.* 56, 340 (1939).
257. P. Pulay, *Mol. Phys.* 17, 197 (1969).
258. N. A. Marks, D. R. McKenzie, B. A. Pailthorpe, M. Bernasconi, and M. Parrinello, *Phys. Rev. B* 54, 9703 (1996).
259. X.-P. Li, R. W. Nunes, and D. Vanderbilt, *Phys. Rev. B* 47, 10891 (1993).
260. F. Mauri, G. Galli, and R. Car, *Phys. Rev. B* 47, 9973 (1993).
261. P. Ordejón, D. A. Drabold, R. M. Martin, and M. P. Grumbach, *Phys. Rev. B* 51, 1456 (1995).
262. D. Marx, M. E. Tukerman, and G. J. Martyna, *Comp. Phys. Comm.* 118, 166 (1999).
263. N. L. Doltsinis and D. Marx, *Phys. Rev. Lett.* 88, 166402 (2002).
264. G. S. Grest, B. Dünweg, and K. Kremer, *Comp. Phys. Comm.* 70, 243 (1989).
265. M. Schöen, *Comp. Phys. Comm.* 52, 175 (1989).
266. J. J. Morales and M. J. Nuevo, *Comp. Phys. Comm.* 69, 223 (1992).
267. D. J. Auerbach, W. Paul, A. F. Bakker, C. Lutz, W. E. Rudge, and F. F. Abraham, *J. Phys. Chem.* 91, 4881 (1987).
268. A. F. Bakker, G. H. Gilmer, M. H. Grabow, and K. Thompson, *J. Comput. Phys.* 90, 313 (1990).
269. L. J. Clarke, I. Stich, and M. C. Payne, *Comp. Phys. Comm.* 72, 14 (1992).
270. R. W. Hockney, S. P. Goel, and J. W. Eastwood, *J. Comput. Phys.* 14, 48 (1974).
271. A. R. C. Raine, D. Fincham, and W. Smith, *Comp. Phys. Comm.* 55, 13 (1989).
272. F. Bruge and S. L. Fornili, *Comp. Phys. Comm.* 60, 39 (1990).
273. A. I. Mel'cuk, R. C. Giles, and H. Gould, *Computers in Physics* 11, 311 (1991).
274. S. L. Lin, J. Mellor-Crummey, B. M. Pettitt, and G. N. Phillips, Jr., *J. Comput. Phys.* 13, 1022 (1992).
275. K. Essenlink, B. Smit, and P. A. J. Hilbers, *J. Comput. Phys.* 106, 101 (1993).
276. W. Form, N. Ito, and G. A. Kohring, *Int. J. Mod. Phys. C* 4, 1075 (1993).
277. D. C. Rapaport, *Comp. Phys. Comm.* 76, 301 (1993).
278. P. S. Lomdahl, D. M. Beazley, P. Tamayo, and N. Grønbech-Jensen, *Int. J. Mod. Phys. C* 4, 1074 (1993).
279. D. M. Beazley and P. S. Lomdahl, *Parallel Computing* 20, 173 (1994).
280. W. Smith and T. R. Forester, *Comp. Phys. Comm.* 79, 63 (1994).
281. S. Plimpton, *J. Comput. Phys.* 117, 1 (1995).
282. J. Stadler, R. Mikulla, and H.-R. Trebin, *Int. J. Mod. Phys. C* 8, 1131 (1997).
283. G. C. Fox, M. A. Johnson, G. A. Lyzenga, S. W. Otto, J. K. Salmon, and D. W. Walker, "Solving Problems on Coeurrent Processors," Vol. 1, Prentice Hall, Englewood Cliffs, NJ, 1988.
284. B. Hendrickson and R. Leland, *SIAM J. Sci. Stat. Comput.* 16, 452 (1995).
285. G. Kresse and J. Furthmüller, *Phys. Rev. B* 54, 11169 (1996).
286. D. W. Oxtoby, *Annu. Rev. Mater. Res.* 32, 39 (2002).
287. K. Tada, S. Furuya, and K. Watanabe, *Phys. Rev. B* 63, 155405 (2002).
288. J. P. Perdew, J. A. Chevary, S. H. Vosko, K. A. Jackson, M. R. Pederson, D. J. Singh, and C. Fiolhais, *Phys. Rev. B* 46, 6671 (1992).
289. B. Hammer, L. B. Hansen, and J. K. Nørskov, *Phys. Rev. B* 59, 7413 (1999).
290. K. Kobayashi, *Comput. Mater. Sci.* 14, 72 (1997).
291. N. Troullier and J. L. Martins, *Phys. Rev. B* 43, 1993 (1991).
292. H. Tanaka, M. El-Merraoui, W. A. Steele, and K. Kaneko, *Chem. Phys. Lett.* 352, 334 (2002).
293. E.-C. Lee, Y.-S. Kim, Y.-G. Jin, and K. J. Chang, *Phys. Rev. B* 66, 073415 (2002).
294. P. A. Gordon and R. B. Saeger, *Ind. Eng. Chem. Res.* 38, 4647 (1999).
295. A. Ricca and J. A. Drocco, *Chem. Phys. Lett.* 362, 217 (2002).
296. A. Siber and H. Buljan, *Phys. Rev. B* 66, 075415 (2002).
297. Y. Akai and S. Saito, *Jpn. J. Appl. Phys.* 42, 640 (2003).
298. P. Giannozzi, R. Car, and G. Scoles, *J. Chem. Phys.* 118, 1003 (2003).
299. L. G. Zhou and S. Q. Shi, *Carbon* 41, 579 (2003).
300. T. Ohba, K. Murata, K. Kaneko, W. A. Steele, F. Kokai, T. Takahashi, D. Kasuya, M. Yudasaka, and S. Iijima, *Nano Lett.* 7, 371 (2001).
301. G. Gao, T. Cagin, and W. A. Goddard, III, *Phys. Rev. Lett.* 80, 5556 (1998).
302. K. G. Ayappa, *Chem. Phys. Lett.* 282, 59 (1998).
303. I. Ali Khan and K. G. Ayappa, *J. Chem. Phys.* 109, 4576 (1998).
304. G. Stan, V. H. Crespi, M. W. Cole, and M. Boninsegni, *J. Low Temp. Phys.* 113, 447 (1998).
305. G. Stan and M. W. Cole, *Surface Sci.* 395, 280 (1998).
306. G. Stan, M. J. Bojan, S. Curtarolo, S. M. Gatica, and M. W. Cole, *Phys. Rev. B* 62, 2173 (2000).
307. S. M. Gatica, M. J. Bojan, G. Stan, and M. W. Cole, *J. Chem. Phys.* 114, 3765 (2001).

308. M. M. Calbi, S. M. Gatica, M. J. Bojan, and M. W. Cole, *J. Chem. Phys.* 115, 9975 (2001).
309. M. M. Calbi and M. W. Cole, *Phys. Rev. B* 66, 115413 (2002).
310. M. M. Calbi, M. W. Cole, S. M. Gatica, M. J. Bojan, and G. Stan, *Rev. Mod. Phys.* 73, 857 (2001).
311. M. Rzepka, P. Lamp, and M. A.de la Casa-Lillo, *J. Phys. Chem. B* 102, 10894 (1998).
312. F. Darkrim and D. Levesque, *J. Chem. Phys.* 109, 4981 (1998),
313. F. Darkrim, A. Aoufi, and D. Levesque, *Mol. Simul.* 24, 51 (2000).
314. Q. Wang and J. K. Johnson, *J. Chem. Phys.* 110, 577 (1999).
315. Q. Wang and J. K. Johnson, *J. Phys. Chem. B* 103, 277 (1999).
316. Q. Wang, S. R. Challa, D. S. Sholl, and J. K. Johnson, *Phys. Rev. Lett.* 82, 956 (1999).
317. V. V. Simonyan, P. Diep, and J. K. Johnson, *J. Chem. Phys.* 111, 9778 (1999).
318. V. V. Simonyan, J. K. Johnson, A. Kuznetsova, J. T. Yates, Jr., *J. Chem. Phys.* 114, 4180 (2001).
319. F. Alain, Y. F. Yin, T. J. Mays, and B. McEnaney, *Stud. Surf. Sci. Catal.* 128, 313 (2000).
320. U. Bünger and W. Zittel, *Apply. Phys. A* 72, 147 (2001).
321. P. Dubot and P. Cenedese, *Phys. Rev. B* 63, 241402 (2001).
322. Z. Mao and S. B. Sinnott, *J. Phys. Chem. B* 104, 4618 (2000).
323. T. Düren, F. J. Keil, and N. A. Seaton, *Chem. Eng. Sci.* 57, 1343 (2002).
324. S. B. Sinnott, Z. Mao, and K.-H. Lee, *CMES* 3, 575 (2002).
325. A. I. Skoulidas, D. M. Ackerman, J. K. Johnson, and D. S. Sholl, *Phys. Rev. Lett.* 89, 185901 (2002).
326. D. M. Ackerman, A. I. Skoulidas, D. S. Sholl, and J. K. Johnson, *Mol. Simul.* 29, 677 (2003).
327. V. P. Sokhan, D. Nicholson, and N. Quirke, *J. Chem. Phys.* 117, 8531 (2002).
328. S. Supple and N. Quirke, *Phys. Rev. Lett.* 90, 214501 (2003).
329. R. Qiao and N. R. Aluru, *Nano Lett.* 3, 1013 (2003).
330. Y.-K. Kwon, S. Berber, and D. Tománek, *Phys. Rev. Lett.* 92, 015901 (2004).
331. A. Hamsy, M. Foret, F. Anglaret, J. Pelous, R. Vacher, and R. Jullien, *J. Non-Cryst. Solids* 186, 118 (1995).
332. P. Meakin, *Phys. Rev. Lett.* 51, 1119 (1983).
333. M. Kolb, R. Botet, and R. Jullien, *Phys. Rev. Lett.* 51, 1123 (1983).
334. P. Meakin, "Fractals, Scaling and Growth far from Equilibrium." Cambridge University Press, Cambridge, 1998.
335. V. Arunchalam, R. R. Lucchese, and W. H. Marlow, *Phys. Rev. E* 60, 2051 (1999).
336. R. N. Porter and L. M. Raff, in "Dynamics of Molecular Collisions" (W. H. Miller, Ed.), p. 1, Modern Theoretical Chemistry, Part B. Plenum, New York, 1973.
337. O. Stachs, Th. Gerber, and V. Petkov, *J. Non-Cryst. Solids* 210, 14 (1997).
338. A. Hamsy, N. Olivi-Tran, and R. Jullien, *J. Phys.: Condens. Matter* 10, 4947 (1998).
339. A. Rahmani, P. Judd, C. Benoit, and R. Jullien, *J. Phys.: Condens. Matter* 13, 5413 (2001).
340. P. Judd and R. Jullien, *Philos. Mag. A* 79, 1223 (1999).
341. B. W. Van Beest, G. J. Kramer, and R. A. van Santen, *Phys. Rev. Lett.* 64, 1955 (1990).
342. H. Sodolski and M. Kozlowski, *J. Non-Cryst. Solids* 194, 241 (1996).
343. K.-L. Fang and B.-Y. Tsui, *J. Appl. Phys.* 93, 5546 (2003).
344. R. M. Costescu, A. J. Bullen, G. Matamis, K. E. O'Hara, and D. C. Cahill, *Phys. Rev. B* 65, 094205 (2002).
345. O. Pilla, A. Fontana, and G. Viliani, *J. Non-Cryst. Solids* 280, 164 (2001).
346. T. Düren, S. Jakobtorweihen, F. J. Keil, and N. A. Seaton, *Phys. Chem. Chem. Phys.* 5, 369 (2003).
347. L. D. Gelb, K. E. Gubbins, R. Radhakrishnan, and M. Sliwinska-Bartkowiak, *Rep. Prog. Phys.* 62, 1573 (1999).
348. J. T. Kloprogge, "Faculteit Aardwestenschappen der Rijksuniversiteit." Utreeht, 1992.
349. R. M. Barrer and D. M. MacLeod, *Trans. Faraday Soc.* 51, 1290 (1977).
350. G. W. Brindley and R. E. Sempels, *Clay Minerals* 12, 229 (1977).
351. S. Yamanaka and G. W. Brindley, *Clays Clay Miner.* 26, 21 (1978).
352. H. Lahav, V. Shani, and J. Shabtai, *Clays Clay Miner.* 26, 107 (1978).
353. D. E. W. Vaughan and R. J. Lussier, Proc. Int. Conf. Zeolites, Naples, Italy, 1980.
354. F. Figueras, *Cat. Rev.-Sci. Eng.* 30, 457 (1988).
355. L. S. Cheng and R. T. Yang, *Ind. Eng. Chem. Res.* 34, 2021 (1995).
356. X. Yi, K. S. Shing, and M. Sahimi, *AIChE J.* 41, 456 (1995).
357. X. Yi, K. S. Shing, and M. Sahimi, *Chem. Eng. Sci.* 51, 3409 (1996).
358. X. Yi, J. Ghassemzadeh, K. S. Shing, and M. Sahimi, *J. Chem. Phys.* 108, 2178 (1998).
359. J. Ghassemzadeh, L. Xu, T. T. Tsotsis, and M. Sahimi, *J. Phys. Chem. B* 104, 3892 (2000).
360. J. Ghassemzadeh and M. Sahimi, *Mol. Phys.* 102, 1447 (2004).
361. L. Xu, T. T. Tsotsis, and M. Sahimi, *Phys. Rev. E* 62, 6942 (2000).
362. L. Xu, T. T. Tsotsis, and M. Sahimi, *J. Chem. Phys.* 114, 7196 (2001).
363. M. Sahimi and T. T. Tsotsis, *Physica B* 338, 291 (2003).
364. R. D. Kaminsky and P. A. Monson, *J. Chem. Phys.* 95, 2936 (1991).
365. K. S. Page and P. A. Monson, *Phys. Rev. E* 54, R29 (1996).
366. K. S. Page and P. A. Monson, *Phys. Rev. E* 54, 6557 (1996).
367. D. Stauffer and R. B. Pandey, *J. Phys. A* 25, L1079 (1992).
368. E. Pitard, M. L. Rosinberg, G. Stell, and G. Tarjus, *Phys. Rev. Lett.* 74, 4361 (1995).
369. E. Kierlik, M. L. Rosinberg, G. Tarjus, and E. Pitard, *Mol. Phys.* 95, 341 (1998).
370. T. MacFarland, G. T. Barkema, and J. F. Marko, *Phys. Rev. B* 53, 148 (1996).
371. R. Salazar, R. Toral, and A. Chakrabarti, *J. Sol-Gel Sci. Technol.* 15, 175 (1999).
372. L. Sarkisov and P. A. Monson, *Phys. Rev. E* 65, 011202 (2001).

373. R. Haerle, A. Balderschi, and G. Galli, *J. Non-Cryst. Solids* 266-269, 740 (2000).
374. F. Finocchi, G. Galli, M. Parrinello, and C. M. Bertoni, *Phys. Rev. Lett.* 68, 3044 (1992).
375. J. L. Mercer, *Phys. Rev. B* 54, 4650 (1996).
376. B. Widom, *J. Chem. Phys.* 39, 2808 (1963).
377. B. Widom, *J. Phys. Chem.* 86, 869 (1963).
378. G. L. Deitrick, L. E. Scriven, and H. T. Davis, *J. Chem. Phys.* 90, 2370 (1989).
379. K. S. Shing and K. E. Gubbins, *Mol. Phys.* 43, 717 (1981).
380. K. S. Shing and K. E. Gubbins, *Mol. Phys.* 46, 1109 (1982).
381. R. F. Cracknell and K. E. Gubbins, *Langmuir* 9, 824 (1993).
382. R. F. Cracknell and D. Nicholson, *J. Chem. Soc. Faraday Trans.* 90, 885 (1993).
383. R. F. Cracknell and D. Nicholson, *J. Chem. Soc. Faraday Trans.* 91, 1487 (1994).
384. R. F. Cracknell, D. Nicholson, and K. E. Gubbins, *J. Chem. Soc. Faraday Trans.* 91, 1377 (1995).
385. J. D. Gale, A. K. Cheetham, R. A. Jackson, C. Richards, A. Catlow, and J. M. Thomas, *Adv. Mater.* 2, 487 (1990).
386. R. L. June, A. T. Bell, and D. Theodorou, *J. Phys. Chem.* 94, 8232 (1990).
387. R. L. June, A. T. Bell, and D. Theodorou, *J. Phys. Chem.* 96, 1051 (1992).
388. J. L. Keldsen, J. B. Nicholas, K. A. Carrado, and R. E. Winans, *J. Phys. Chem.* 98, 279 (1994).
389. M. W. Maddox and K. E. Gubbins, *Int. J. Thermophys.* 15, 1115 (1994).
390. M. Mezei, *Mol. Phys.* 40, 901 (1980).
391. G. W. Miller, K. S. Knaebel, and K. G. Ikels, *AIChE J.* 33, 194 (1987).
392. J. K. Percus, *Chem. Phys. Lett.* 123, 311 (1986).
393. B. K. Peterson and K. E. Gubbins, *Mol. Phys.* 62, 215 (1987).
394. D. Plee, F. Borg, L. Gatineau, and J. J. Fripiat, *J. Am. Chem. Soc.* 107, 2362 (1985).
395. N. T. Skipper, K. Pefson, and J. D. C. McConnell, *Clay Minerals* 24, 411 (1989).
396. S. Yamanaka, in "Materials Science Forum" (J. Rouxel and M. Tournoux, Eds.), p. 123. Materials Research Society, Pittsburgh, 1994.
397. G. E. Norman and V. S. Filinov, *High Temp. (USSR)* 7, 216 (1969).
398. D. J. Adams, *Mol. Phys.* 29, 307 (1975).
399. W. Van Megen and I. K. Snook, *Mol. Phys.* 45, 629 (1982).
400. W. Van Megen and I. K. Snook, *Mol. Phys.* 54, 741 (1985).
401. K. E. Gubbins, M. Sliwinska-Bartkowiak, and S.-H. Suh, *Mol. Simul.* 17, 333 (1996).
402. D. A. Kofke and E. D. Glandt, *Mol. Phys.* 64, 1105 (1988).
403. A. Z. Panagiotopoulos, *Mol. Phys.* 61, 813 (1987).
404. A. Z. Panagiotopoulos, N. Quirke, M. Stapleton, and D. J. Tildesley, *Mol. Phys.* 63, 527 (1988).
405. M. Firouzi, Kh. Molaai Nezhad, T. T. Tsotsis, and M. Sahimi, *J. Chem. Phys.* 120, 8172 (2004).
406. J.-P. Rykaert and A. Bellemans, *Faraday Discuss. Chem. Soc.* 66, 95 (1978).
407. P. van der Ploeg and H. J. C. Berendsen, *J. Chem. Phys.* 76, 3271 (1982).
408. J.-P. Rykaert and A. Bellemans, *Chem. Phys. Lett.* 30, 123 (1975).
409. M. D. Macedonia and E. J. Maggin, *Mol. Phys.* 96, 1375 (1999).
410. R. P. Feynman and A. R. Hibbs, "Quantum Mechanics and Path Integrals." McGraw-Hill, New York, 1965.
411. T. L. Beck, *J. Chem. Phys.* 96, 7175 (1992).
412. M. E. Tukerman, B. J. Berne, G. J. Martyna, and M. L. Klein, *J. Chem. Phys.* 99, 2796 (1993).
413. A. Liu and T. L. Beck, *Mol. Phys.* 86, 225 (1995).
414. Q. Wang, J. K. Johnson, and J. Q. Broughton, *Mol. Phys.* 89, 1105 (1996).
415. Q. Wang and J. K. Johnson, *J. Chem. Phys.* 107, 5108 (1997).
416. Q. Wang and J. K. Johnson, *Mol. Phys.* 95, 299 (1998).
417. P. Diep and J. K. Johnson, *J. Chem. Phys.* 112, 4465 (2000).
418. R. Evans, *Adv. Phys.* 28, 143 (1979).
419. J. D. Weeks, D. Chander, and H. C. Andersen, *J. Chem. Phys.* 54, 5237 (1971).
420. P. Tarazona, *Phys. Rev. A* 31, 2672 (1985).
421. P. Tarazona, U. Marini Bettolo Marconi, and R. Evans, *Mol. Phys.* 60, 573 (1987).
422. E. Kierlik and M. Rosinberg, *Phys. Rev. A* 42, 3382 (1990).
423. E. Kierlik and M. Rosinberg, *Phys. Rev. A* 44, 5025 (1991).
424. T. Cagin and B. M. Pettitt, *Mol. Simul.* 6, 5 (1991).
425. M. Sun and C. Ebner, *Phys. Rev. A* 46, 4813 (1992).
426. M. Lupkowski and F. van Swol, *J. Chem. Phys.* 95, 1995 (1995).
427. E. J. Maginn, A. T. Bell, and D. N. Theodorou, *J. Phys. Chem.* 97, 4173 (1993).
428. G. S. Heffelfinger and F. van Swol, *J. Chem. Phys.* 100, 7548 (1994).
429. J. M. D. MacElroy, *J. Chem. Phys.* 101, 5274 (1994).
430. R. F. Cracknell, D. Nicholson, and N. Quirke, *Phys. Rev. Lett.* 74, 2463 (1995).
431. D. M. Ford and E. D. Glandt, *J. Phys. Chem.* 99, 11543 (1995).
432. D. Nicholson, R. F. Cracknell, and N. Quirke, *Langmuir* 12, 4050 (1996).
433. S. K. Kjelstrup and B. Hafskjold, *Ind. Eng. Chem. Res.* 35, 4203 (1996).
434. S. Sunderrajan, C. K. Hall, and B. D. Freeman, *J. Chem. Phys.* 105, 1621 (1996).
435. S. Furukawa, K. Hayashi, and T. Nitta, *J. Chem. Eng. Japan* 30, 1107 (1997).
436. G. S. Heffelfinger and D. M. Ford, *Mol. Phys.* 94, 659 (1998).
437. D. M. Ford and G. S. Heffelfinger, *Mol. Phys.* 94, 673 (1998).

438. A. P. Thompson, D. M. Ford, and G. S. Heffelfinger, *J. Chem. Phys.* 109, 6406 (1998).
439. P. I. Pohl and G. S. Heffelfinger, *J. Memb. Sci.* 155, 1 (1999).
440. L. Xu, M. G. Sedigh, M. Sahimi, and T. T. Tsotsis, *Phys. Rev. Lett.* 80, 3511 (1998).
441. L. Xu, T. T. Tsotsis, and M. Sahimi, *J. Chem. Phys.* 111, 3252 (1999).
442. L. Xu, M. G. Sedigh, T. T. Tsotsis, and M. Sahimi, *J. Chem. Phys.* 112, 910 (2000).
443. M. Firouzi, T. T. Tsotsis, and M. Sahimi, *J. Chem. Phys.* 119, 6810 (2003).
444. M. G. Martin, A. P. Thompson, and T. M. Nenoff, *J. Chem. Phys.* 114, 7174 (2001).
445. G. Arya, H.-C. Chang, and E. J. Maggin, *J. Chem. Phys.* 115, 8112 (2001).

CHAPTER 11

Modeling of Electrocatalytic Surface Reactions

S. J. Mitchell, M. T. M. Koper

Schuit Institute for Catalysis and Department of Chemical Engineering, Eindhoven University of Technology, Eindhoven, The Netherlands

CONTENTS

1. INTRODUCTION

Heterogeneously catalyzed reactions take place at the interface between a solid phase, often a metal or an oxide (the catalyst), and a gas or liquid phase. In order to maximize the contact between the solid phase and the reactant molecules in the gas or liquid phase, the catalyst is commonly dispersed as nanometer-sized particles on a conducting or nonconducting support. In fact, heterogeneous catalysis may well be the field with oldest existing applications of nanoparticles.

ISBN: 1-58883-047-0

Handbook of Theoretical and Computational Nanotechnology
Edited by Michael Rieth and Wolfram Schommers
Volume 5: Pages (691–716)

Our understanding of heterogeneously catalyzed reactions has, in the past few decades, profited enormously from developments in computational chemistry. Applications of density functional theory–based quantum-chemical calculations and kinetic modeling based on Monte Carlo approaches are now carried out rather routinely, often by groups that typically focus on experimental methods. This illustrates the level of acceptance of computational methods by the catalysis community at large. Of course, most computational studies tend to focus on understanding surface science experiments involving single-crystal substrates, rather than more industrially realistic catalysts. To the extent that the activity of catalytic nanoparticles may be interpreted as stemming from the activity of the different single-crystal facets and their interaction, the insight obtained from such single-crystal studies may have direct consequences for real catalytic systems.

In this chapter, we will give a brief review of the modeling of a particular type of catalytic reactions, namely electrocatalytic reactions. This choice is entirely based on our own expertise. Nevertheless, the methods described herein are entirely transferable to modeling catalytic reactions at the solid–gas interface. Electrocatalytic reactions are of importance in many applications, notably fuel cells and batteries, but also for heterogeneously catalyzed reactions taking place at the solid–liquid interface. We focus primarily on the statistical–mechanical aspects of modeling reactions at the electrode–electrolyte interface, as the quantum-chemical aspects of (electro)catalytic reactions have recently been discussed in detail elsewhere [1–4]. Our discussion of the density functional theory (DFT) is restricted to explaining how such DFT calculations may be employed to provide the energetic input parameters for the statistical–mechanical Monte Carlo (MC) simulations, including both equilibrium and kinetic MC models. Additional background can be found in [5].

In Section 2, some necessary theoretical background is discussed. Next, Section 3 treats the main ideas of Monte Carlo simulation methods. In Section 4, we discuss two examples of Monte Carlo simulations in electrochemistry, bromide adsorption on silver and gold electrodes and carbon monoxide oxidation on platinum–ruthenium surfaces. Whereas the first two examples illustrate the importance of phase transitions, lateral interaction energies and the appropriateness or inappropriateness of the lattice-gas approximation, the second example provides a case in which the importance of surface diffusion in understanding catalytic reactivity is clearly demonstrated.

2. THEORETICAL BACKGROUND

In this section, we discuss theoretical material necessary for understanding the modeling of catalytic surface reactions. This material covers concepts and methods used throughout atomic scale physical chemistry and surface science, including a discussion of reaction rates, steady states, thermal equilibrium, and basic computational and simulation techniques such as Monte Carlo simulations and density functional theory calculations. Because many of the examples given later in this work involve statistical simulation methods like Monte Carlo, much of this section is devoted to a basic discussion of the foundations of statistical physics and statistical simulation methods. Additional material can be found in [5] and references therein.

Unfortunately, an in-depth discussion of all theoretical background material is not possible within the scope of the current work, and much consideration has been given as to the best approach for the presentation of the material. Whenever possible, we have attempted to present the material in a way and with a vocabulary common to both chemists and physicists. Inevitably, some confusion may arise, as some terms may have very specific meanings in one field but may have dual or less precise meanings in the other field. For instance, physicists often use the word "equilibrium" to indicate thermal (thermodynamic) equilibrium defined by the Boltzmann distribution, but chemists sometimes use the word to indicate a quasi-equilibrium reaction within an overall series of reactions, which are not in thermodynamic equilibrium.[1] Additionally, in chemistry the word "bond" has the precise meaning of

[1] "Quasi-equilibrium" implies that the concentrations in the associated reactions are well approximated by their thermal equilibrium values.

a chemical or ionic bond, but physicists sometimes use the word to indicate both a chemical bond and an interacting pair of atoms, where such interactions may even be repulsive. Therefore, we have chosen to present the material in a way that attempts to avoid any confusion of terminology, giving preference, whenever possible, to the more precise use of the various terms.

2.1. Reaction Rates

Let us consider a simple chemical reaction in which two reactants, A and B, react to give product C,

$$A + B \Rightarrow C \tag{1}$$

Each side of the equation can then be thought of as representing the same set of atoms or molecules in two different states, unreacted on the left-hand side and reacted on the right-hand side. We also refer to the unreacted state as the initial state, or state I, and to the reacted state as the final state, or state F. In general, the back reaction is also possible,

$$A + B \Leftarrow C \tag{2}$$

and for simplicity, the initial or unreacted state still refers to A + B, and the final or reacted state still refers to C.

Consider a volume of space, V, into which we place N_I reacting pairs A + B and N_F products C. We can consider this volume to represent $N = N_I + N_F$ two-state systems. The reaction and back reaction can then be viewed as possible transitions between these two states, $I \rightarrow F$ and $F \rightarrow I$, respectively. The forward reaction rate, $R_{I \rightarrow F}$, is then defined as the probability per unit time that two reactants in the volume will react to form C. We define the back reaction rate, $R_{F \rightarrow I}$, in a similar way as the probability per unit time that a single product C in the volume will dissociate into A + B. In general, these reaction rates will depend on a number of factors such as the density N/V, the energy of each state, the interactions between the species, and the temperature; however, for now, we simply assume that these effects are either negligible or have been taken into account in an average way.

Often, the average or macroscopic reaction rates can be determined from the microscopic probabilistic reaction rates, such as with the mean-field models, but as this article is concerned primarily with microscopic modeling of such systems, we will not discuss macroscopic models in any significant detail. Suffice it to say, macroscopic models often work well for well-mixed systems, like in solution or gas chemistry, but the introduction of catalysts and catalytic surfaces usually adds sufficient complication that such macroscopic models are often either unreliable or provide little insight into the mechanisms of the reaction behavior. Mean-field methods are, however, a useful tool to investigate general behaviors of surfaces under certain circumstances, and this category of macroscopic or analytic methods will be discussed in brief in Section 3.

2.2. Thermal Equilibrium and Statistical Ensembles

Consider the simple reaction in Eqs. (1) and (2), and consider also a volume, V, into which we place either a single pair of reactants or a single product. In addition to the reaction state (I or F), each atom or molecule has a position within the volume, an orientation, and a velocity. When taken as a whole, these parameters are called the degrees of freedom of the system, and the space of all possible values for the degrees of freedom is called the configuration space or state space. An ensemble is then a collection of noninteracting volumes taken from the configuration space.

Figure 1 shows a schematic representation of a typical ensemble where the volume of the system is held fixed. This is often referred to as a fixed-volume ensemble. There are many different possible ensembles, but the most common are the micro-canonical ensemble, where the volume, total energy, and number of particles are held fixed; the canonical ensemble, where the volume, temperature, and number of particles are held fixed; and the grand-canonical ensemble, where the volume, temperature, and chemical potential are held fixed.

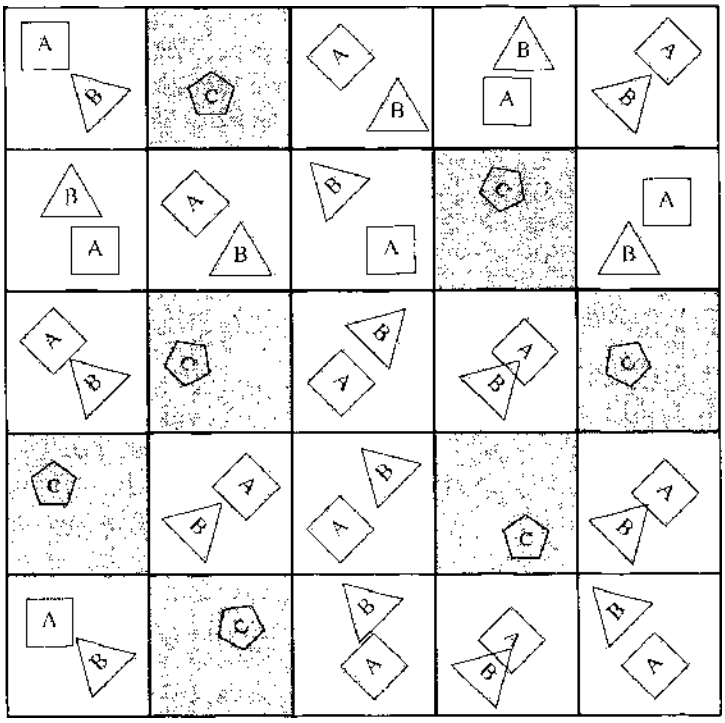

Figure 1. Schematic diagram of a fixed-volume ensemble. The positions, orientations, and reaction state are varied.

Strictly speaking, it is incorrect to speak of temperature if the total energy is held fixed. Instead, one should speak of the energy per particle or per degree of freedom. Likewise, one cannot speak of pressure if the volume is held fixed or speak of chemical potentials if the number of particles is held fixed. Here, we will be interested only in the canonical and grand-canonical ensembles where temperature is defined and thus a true thermal equilibrium exists.

Suppose that we have an experimental system equivalent to that described in Eq. (1), Eq. (2), and Fig. 1. What would be the probability of finding the experimental system in a particular configuration? In a canonical ensemble, the probability of observing a particular configuration for the degrees of freedom follows the well-known Boltzmann distribution,

$$P_i = \frac{e^{-E_i/k_B T}}{\mathcal{Z}} \tag{3}$$

where i indicates a particular point in configuration space or a particular set of values for the degrees of freedom, E_i is the total energy of the state i, k_B is the well-known Boltzmann's constant, and T is the temperature in degrees Kelvin. The value of $k_B T$ is often called the thermal energy, and at room temperature, $k_B T \approx 25$ meV.

The normalization constant in Eq. (3), $\mathcal{Z}$, is usually referred to as the canonical partition function and is given by

$$\mathcal{Z} = \sum_i e^{-E_i/k_B T} \tag{4}$$

where $\sum_i$ indicates a sum or integral over all possible configurations i in the ensemble.

Most experimentally observable quantities are averages over the possible states of the system. Such averages are often referred to as thermal averages or ensemble averages. Typical average quantities are the average energy, average number of reactions products, and so forth. In principle, the average total energy can be calculated by

$$\langle E \rangle = \sum_i E_i \frac{e^{-E_i/k_B T}}{\mathcal{Z}} \tag{5}$$

where $\langle \cdots \rangle$ indicates a thermal or ensemble average and $\sum_i$ indicates the same summation or integration used to determine $\mathcal{Z}$.

For systems with interactions between the different atoms or molecules, it is not possible, in general, to calculate analytically the ensemble averages. In such cases, computer simulations must be performed to sample the configuration space. This will be discussed in greater detail in Section 3. There is, however, one useful class of analytic approximations known as mean-field models that can be calculated analytically. Mean-field methods will also be discussed in brief in Section 3.

2.3. Steady States, Thermal Equilibrium, and Detailed Balance

From Eq. (3), we know the probability to observe a particular configuration of the system, but what is the probability that the configuration of the system will change, and how does this relate to the probabilistic reaction rates ($R_{I\to F}$ and $R_{F\to I}$)? The key to answering this question lies in a basic understanding of the statistical principle of detailed balance.

Imagine that we have a very simple system that has only two states. The entire configuration space is then composed of only these two states. For simplicity, let us call these states the initial state, I, and the final state, F, and they might indicate an unreacted and reacted system, or they might indicate some other simple difference between the two states, like an up and down orientation.

The canonical partition function is

$$\mathcal{Z} = e^{-E_I/k_B T} + e^{-E_F/k_B T} \tag{6}$$

and if the system is in equilibrium, the probability of observing the system in one of the two state states is simply given by $P_I = \exp(-E_I/k_B T)/\mathcal{Z}$ and $P_F = \exp(-E_F/k_B T)/\mathcal{Z}$. Experimentally, these probabilities would be relevant only by repeated measurement of either independent and identical systems, such as in an ensemble of experimental systems, or by repeated measurement of the same system but at different times.

Suppose that we have only a single copy of the experimental system with which to work, or equivalently, suppose that we have a large number of copies of the system, but all of the copies are prepared in such a way that they are all in the same configuration, say state I. If we perform repeated measurements of the system over a short period of time, we will most likely get the same result, namely that the system is in state I. The natural and naive conclusion would be that the system is always in state I, but if we measure over a long enough period of time, we should observe both states with probabilities given by the Boltzmann distribution.

Such short-time deviations from the Boltzmann distribution are referred to as out-of-equilibrium behavior. If the system is to eventually reach thermal equilibrium, that is if the probability distribution of the various states is to reach to Boltzmann distribution as $t \to \infty$, then the probabilistic transition rates must satisfy detailed balance, which is sometimes also referred to as microscopic reversibility,

$$P_I R_{I\to F} = P_F R_{F\to I} \tag{7}$$

Under the transition rates $R_{I\to F}$ and $R_{F\to I}$, a steady state will always be reached. This steady state will have the property

$$\frac{P_I}{P_F} = \frac{R_{F\to I}}{R_{I\to F}} \tag{8}$$

which follows directly from Eq. (7), but this steady state will be equivalent to thermal equilibrium only if P_I and P_F satisfy the Boltzmann distribution. It follows from Eqs. (3) and (8) that for thermal equilibrium to be reached, the transition rates must satisfy the special relation

$$\frac{e^{-E_I/k_B T}}{e^{-E_F/k_B T}} = \frac{R_{F\to I}}{R_{I\to F}} \tag{9}$$

There are an infinite number of transition rates that will satisfy this equation; however, some rates are more convenient or realistic than others. Some common transition rates are the Metropolis rate [6] and the Glauber rate [7], both of which are common for equilibrium Monte Carlo simulations. Barrier hopping rates are commonly used for dynamic simulations, which we discuss in detail in the next subsection.

2.4. Transition State Theory and Energy Surfaces

Any transition rates that satisfy Eq. (9) will lead to a steady state that is identical to thermal equilibrium, but not all such rates necessarily represent physically realistic transition rates. Typically, the energy (or free energy) landscape of a system has many local minima. These minima represent easily identifiable states that are relatively long lived and are stable or metastable.

Figure 2 shows a schematic representation of the energy landscape for a two-state system. For most problems of interest, the energy landscape is actually a very complex multidimensional space, but this greatly simplified schematic does show the most interesting features that are also found in more realistic energy landscapes. Out of the continuum of possible states, represented by the abstract reaction coordinate axis, three more general states are labeled. The two minima, which represent the two most easily observable stable states, are labeled I and F. Between these two states is a third state, T, which has a higher energy and represents an unstable intermediate transition state, corresponding to a saddle point or local maximum in the free energy between states I and F. Whereas the two minima represent stable or metastable states, the transition state is much shorter lived and is very difficult to see in any measurement. However, because any transition between states I and F must pass through state T, the effect of T can be seen in the transition rates between I and F.

In its simplest form, transition state theory suggests that the transition rate between I and F is given by [5]

$$R_{\mathrm{I}\to\mathrm{F}} = \nu e^{-(E_{\mathrm{T}}-E_{\mathrm{I}})/k_{\mathrm{B}}T} \tag{10}$$

where ν is the attempt frequency that determines the overall timescale for the transition and is typically of the order a phonon frequency. The reverse transition, similarly, is given by

$$R_{\mathrm{F}\to\mathrm{I}} = \nu e^{-(E_{\mathrm{T}}-E_{\mathrm{F}})/k_{\mathrm{B}}T} \tag{11}$$

and these transitions easily satisfy Eq. (9), as both the attempt frequency and the energy of the transition state cancel in the division.

This approximation for the transition rates becomes more accurate as the energy of the transition state becomes higher [8], but the exact value of the transition state energy depends very much on the specific nature of the problem and on the specific details of the type of transition in question. One commonly used approximation for the transition state energy is

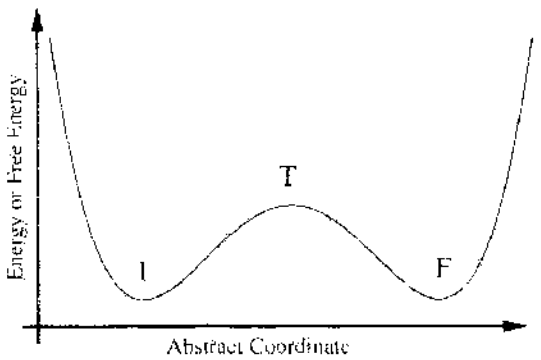

Figure 2. Schematic representation of a two-state system. The states I and F represent easily observable states and T represents a transition state intermediate between the two.

referred to as the symmetric Butler-Volmer approximation and involves the energies of both the initial and final states as well as an energy barrier parameter [5],

$$E_T = \frac{(E_I + E_F)}{2 + \Delta} \tag{12}$$

where Δ is the barrier for the transition process in question. Typically, there will be a different barrier for each type of diffusion process and different barriers for all of the different chemical reactions. This will become more apparent in Section 4 when we discuss models of specific systems.

As one final note, we point out that thermal equilibrium between the states I and F is determined entirely by the energies of those two states and not by the energy of state T. The barrier between states I and F serves only to determine the timescale of transitions between these two states. Thus, in an experiment represented by a canonical or grand-canonical ensemble, changing the barrier of a process or reaction, such as by introducing a catalyst, will not alter the equilibrium between the two end states, I and F. Of course, in industrial processes, the system is rarely allowed to reach thermal equilibrium, as the desired reaction products are usually carried away by some irreversible process.

2.5. *Ab Initio* Quantum Calculations and Total Energies

Much of the formalism of the previous subsections has depended on the knowledge of the energies of the various states; however, there is no simple analytic formula for finding such energies. For many problems, simplified formulas are often used to describe the interactions between the various atoms and molecules. Such formulas may reflect electrostatic interactions, like $1/r^2$ potentials for simple ions or $1/r^3$ interactions for simple dipoles, or the formulas may represent a combination of interactions such as a short-range repulsion caused by overlapping orbitals combined with a longer range interaction.

In general, the exact functional form of the energies can be very difficult to describe, but in recent years, quantum total energy calculations have emerged as a reliable way to calculate the energy of a combination of atoms or molecules from basic quantum-mechanical principles. From the user perspective, all that should be input into the calculation are the positions of the atomic nuclei, the atomic number of the nuclei, and the total number of electrons. From this information, the total energy of the configuration can be calculated, within certain approximations, and the various properties of the energy landscape can be explored by varying the positions of the nuclei.

Such quantum methods, especially those based on density functional theory, can typically treat up to a few hundred atoms and come in a variety of forms, ranging widely in speed and accuracy. In the broadest sense, *ab initio* quantum methods attempt to solve the many-body Schrödinger wave equation for the wave functions of the electrons with a given configuration of atomic nuclear positions, but such a complete solution is extremely difficult and, for most problems, is well beyond the scope of current computer technology. However, for DFT calculations, no direct attempt is made to solve the many-electron Schrödinger equation, but instead, the many-electron problem is replaced with a simpler problem in which only the electron density is used. For DFT, the Kohn-Sham equation [9], similar to the Schrödinger equation, is solved for the local density of electrons.

Solving the Kohn-Sham equations is physically equivalent to solving the many-electron Schrödinger equation, provided that the electron exchange correlation functional is known [9]. Unfortunately, this exchange correlation functional is not known, in general, but two approximations are commonly used, the local density approximation (LDA), which assumes that the correlation energy is a function of the local electron density, and the generalized gradient approximation (GGA), which assumes that the correlation energy is a function of the local electron density and its gradient. Both approximations are commonly used in DFT calculations, and the choice of which to use depends very much on the specific problem being studied.

The reader should also be aware of several other common approximations and formulations of DFT calculations. Usually, to speed up the calculation, only the valence electrons

are considered. In this case, the ordinary electric potential from the positive nuclear core is replaced by an approximate pseudo-potential to improve the speed of the calculations. Also, there are two main forms of DFT calculations, periodic calculations and cluster calculations. Cluster calculations assume that the atoms are isolated in space, and periodic calculations assume that the atoms are repeated in a supercrystal in all directions.

A more complete discussion of DFT can be found in [9]. We assume that the interested reader can consult these or other sources when attempting to perform actual DFT calculations, as there is much important information that is specific to the particular needs and necessities of the user but is beyond the scope of the current work. Useful applications of DFT techniques will become more clear in the following sections.

3. SIMULATION METHODS

There are essentially three broad categories of simulation and calculation techniques. Each method has its own particular benefits and drawbacks, and the methods are often combined to give a more complete picture of the system of interest. Molecular dynamics simulations attempt to solve the classical equations of motion and typically involve thousands or tens of thousands of atoms and molecules and can simulate timescales of the order nanoseconds. Density functional theory calculations attempt to solve the quantum mechanical state equations in a simplified form and can provide useful information about the interatomic interaction potentials and energy landscapes. Density functional theory simulations typically include about 100 atoms or less, and when combined with molecular dynamics, density functional theory simulations can typically simulate timescales of the order picoseconds, but simulations of this length usually require the use of a parallel supercomputer.

Monte Carlo simulations make up the third category of simulation methods. This method is rather abstract and uses statistical principles to calculate ensemble averages or to calculate the approach to equilibrium. Much of Section 2 was directed toward an understanding of this technique, and Monte Carlo simulations can be extremely efficient, often simulating tens of thousands of atoms over simulation timescales of seconds and beyond with the use of only a single PC.

Of course, all three of these simulation methods are extremely useful, and no single technique should be considered to the exclusion of the others; however, because Monte Carlo methods are so powerful and provide such useful insights into the cooperative mechanisms of catalytic surface reactions, we focus our discussion in this section on equilibrium and dynamic Monte Carlo simulations. The reader should, nevertheless, keep in mind that density functional theory is often used to determine the parameters necessary for a Monte Carlo model, and *ab initio* molecular dynamics calculations are often used to determine vibrational spectra, which are invaluable in identifying the chemical species present in many catalytic reaction experiments.

3.1. Sampling the Boltzmann Distribution

Suppose that we have a very simple system with only a single continuous degree of freedom, say the x position of a single atom in the potential energy landscape of Fig. 2. From Eq. (3), we can analytically calculate a probability function that tells us the probability of finding the atom at position x (see Fig. 3).[2] The calculation of ensemble averages is now simple and straightforward, but is this necessarily the case for more realistic systems?

Let us consider a general form for the total energy of a generic grand-canonical model of a catalytic surface, which is also called the Hamiltonian,

$$\mathcal{H} = E_{\text{pot}} + E_{\text{kin}} - \sum_i \mu_i N_i \tag{13}$$

where E_{pot} is the total potential energy of the system, E_{kin} is the total kinetic energy of the system, μ_i is the chemical potential of species i, N_i is the number of species i in the

[2] Note that strictly speaking, for continuous variables, we should speak of probability densities, and we should speak of ordinary probabilities only for discrete variables. However, for simplicity, we refer to both as probabilities.

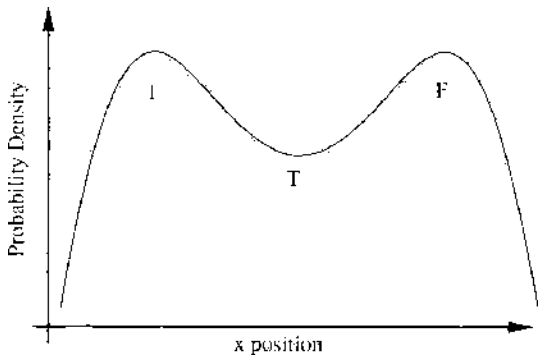

Figure 3. The Boltzmann distribution for the potential energy landscape of Fig. 2.

system volume, and $\sum_i$ denotes a summation over all of the possible species in the model. The inclusion of the chemical potential terms in Eq. (13) is a common way of treating a grand-canonical ensemble (variable number of atoms or molecules). Strictly speaking, the chemical potential terms do not represent real energies but rather represent free energies. However, when the chemical potential terms are included in the total energy and the number of particles is treated as just another degree of freedom of the problem, the Boltzmann distribution for a grand-canonical ensemble has the same simple form as that in Eq. (3).

As one might imagine, the number of degrees of freedom in Eq. (13) is generally quite large, and even for very small and simple systems, the state space quickly becomes too large and complex to calculate ensemble averages by direct integration of the Boltzmann distribution. We must therefore calculate ensemble averages, not by integrating the Boltzmann distribution over the entire state space, but by calculating the Boltzmann weight for only a select number of configurations.

One might, at first, consider a random sampling of the configuration space, but generally, most configurations will have very large energies and thus will not contribute greatly to an ensemble average, as states with large energies have a lower probability. For this reason, Monte Carlo methods normally make use of importance sampling [10], which weights the sampling procedure to improve efficiency. The importance sampling procedure begins with the system in some configuration, I, and a series of random changes are made to generate a series of sample configurations taken from the Boltzmann distribution. These samples can then be used to calculate ensemble averages. The importance sampling algorithm is as follows:

1. Randomly choose one of the degrees of freedom of the system.
2. Make a small random change to the chosen degree of freedom, resulting in a new configuration, F.
3. Calculate the probability to accept F as the next configuration in the sample sequence, $R_{I\to F}$.
4. Generate a random number, r, uniformly distributed on the interval (0, 1).
5. If $r < R_{I\to F}$, then F is the next configuration in the sample sequence, if not, then the configuration F is rejected, and I is the next configuration in the sample sequence.
6. Go to 1.

The importance sampling procedure results in a long sequence of configurations, and as long as $R_{I\to F}$ satisfies Eq. (9), the samples will represent the Boltzmann distribution as the length of the sample sequence tends to infinity. The most common form for the importance sampling transition rate is the Metropolis form, $R_{I\to F} = \min\{1, \exp[-(E_F - E_I)/k_B T]\}$ [6]. When this form is used, the importance sampling procedure is often called the Metropolis method.

Ensemble averages are calculated by simply averaging the quantity of interest over the sample sequence, such as $\langle E\rangle = \sum_{i=1}^{n} E_i/n$, where i indexes the sample configurations in the sequence. As $n \to \infty$, the average obtained from the sample sequence approaches the value of the true ensemble average, but practically, the sample sequence usually converges

to thermal equilibrium within a few thousand samples, and the beginning of the sequence is normally discarded to improve the convergence of the average.

In conventional importance sampling, which is also called equilibrium Monte Carlo, like the Metropolis method, the order of the sample sequence has no resemblance to time; however, when the random changes between configurations correspond to physically realistic transitions between states, the order of the sample sequence may correspond to a real time. When this occurs, the importance sampling process is referred to as dynamic or kinetic Monte Carlo (DMC) [5]. For dynamic Monte Carlo simulations to be valid, transition state theory must hold, as discussed in Section 2.4, and this is summarized by two requirements necessary for dynamic Monte Carlo to be valid.

1. The energy or free-energy landscape of the system must be well described by a collection of well-defined local minima, which implies that the local minima are separated by relatively high transition states.
2. The barrier hopping transition rates must satisfy Eq. (9).

For catalytic surfaces, both of these criteria are usually met, and the collection of local minima is normally described by the lattice-gas approximation.

3.2. The Corrugation Potential and the Lattice-Gas Approximation

Most adsorbates have preferential binding sites on catalytic surfaces. Exactly which site is preferred depends very much on the type of adsorbate and on the type of surface. For instance, Br atoms preferentially adsorb at the fourfold hollow site on the Ag(100) surface [11] but adsorb at the bridge site on the Au(100) surface [12]. Preferential adsorption is clearly seen in the corrugation potential, which is the binding energy as a function of the (x, y) position on the surface.

Figure 4 shows a typical corrugation potential. One can clearly see that the energy landscape has many local minima corresponding, in the case of this example, to the fourfold hollow sites. One can also see that the transition states separating the local minima correspond to the bridge sites. In the case of Br adsorption on Ag(100), the corrugation potential at the bridge site is approximately 100 meV higher than at the hollow site, according to DFT calculations. Therefore, at room temperature, the transition state energy is about four times larger than the thermal energy. This is sufficiently high that an adsorbate will remain near the fourfold hollow position nearly all of the time, suggesting that a lattice-gas approximation for the adlayer is appropriate.

A lattice-gas approximation assumes that the adsorbates are located at discrete positions on a lattice of adsorption sites. Thus, the surface of Fig. 4 would be represented by a square grid or lattice, with each cell in the grid representing one hollow site. A grid cell

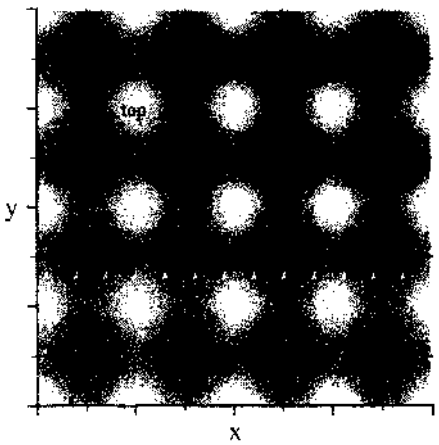

Figure 4. A typical corrugation potential for a surface with a square arrangement of surface atoms. Br adsorbed on Ag(100). The grayscale indicates the binding energy, where lighter shades indicate less favorable binding. The circles indicate the location of the catalytic surface atoms. Reprinted with permission from [8], S. J. Mitchell et al., *Faraday Disc.* 121, 53 (2002). © 2002, Royal Society of Chemistry.

is usually referred to as a lattice site, and a lattice site may be either empty or occupied. By this approximation, a complex state space of continuous degrees of freedom is reduced to a simple discrete space, where transitions are manifested simply as a change in the site occupation variables. For adsorption and desorption transitions, lattice occupation variables change from unoccupied to occupied, and *vice versa*. For reactive transitions, the occupation variables change from denoting one species to denoting another, and for diffusion transitions, an occupied site variable is exchanged with a neighboring unoccupied variable.

In addition to simplifying the particle positions, lattice-gas models normally neglect the kinetic energy. The reason for this is twofold. First, in the absence of velocity-dependent forces, which is usually the case, velocities are distributed according to the Gaussian distribution, and therefore, the velocity distributions do not need to be calculated. Second, for dynamic Monte Carlo simulations, the barrier must be high compared to the thermal energy, and thus, over the timescales necessary to hop the barrier, the velocity of the particle should have changed many times, due to interactions with the surrounding atoms and molecules. This process of changes in the velocity is sometimes referred to as thermalization and represents essentially the same noise phenomenon underlying Brownian motion.

3.3. The Mean-Field Approximation

In addition to the computational approaches discussed thus far, mean-field analytic methods represent an important and often useful class of methods, and although mean-field models are not capable of correctly reproducing phase transitions in the adlayer, for well-mixed systems, they are often quite effective in describing the general behavior of the adlayer.

Consider the simple Hamiltonian for a nearest-neighbor interacting model on a 2D square lattice

$$\mathcal{H} = -\sum_{\langle ij \rangle} \phi c_i c_j - \bar{\mu} \sum_{i=1}^{N} c_i \tag{14}$$

where c_i and c_j represent the occupation variables for the adsorption sites i and j, respectively, and may have values equal to 0 (empty) or 1 (occupied), ϕ represents the interaction energy for the nearest-neighbor pair i, j, $\bar{\mu}$ represents the electrochemical potential, the sums $\sum_{i=1}^{N}$ runs over all N sites on the surface, and $\sum_{\langle ij \rangle}$ runs over all nearest-neighbor pairs on the surface.

The partition function for such a system is

$$\mathcal{Z} = \sum_{c_1} \sum_{c_2} \cdots \sum_{c_N} \exp\left[\frac{\{-\sum_{\langle ij \rangle} \phi c_i c_j - \bar{\mu} \sum_{i=1}^{N} c_i\}}{k_B T} \right] \tag{15}$$

which, in general, will be quite difficult, if not impossible, to solve analytically. In such cases, a complete and accurate solution will require a computational approach such as Monte Carlo simulation. However, if we simply wish to find a rather general behavior for the adlayer, we may employ the simple mean-field approximation to generate an analytic solution, where we estimate the interactions, not with the actual site occupation variables, but with the average site occupation. In this case, each site is said to interact with the mean field generated by all the other sites on the surface.

The coverage is defined as $\Theta = \sum_{i=1}^{N} c_i / N$, and we consider a simple expansion of the first interaction term as

$$\begin{aligned} c_i c_j &= (c_i - \Theta + \Theta)(c_j - \Theta + \Theta) \\ &= \{(c_i - \Theta) + \Theta\}\{(c_j - \Theta) + \Theta\} \\ &= \Theta^2 + \Theta(c_i - \Theta) + \Theta(c_j - \Theta) + (c_i - \Theta)(c_j - \Theta) \end{aligned} \tag{16}$$

Under the mean-field approximation, we neglect the spatial fluctuations within the system, and thus we neglect the last term in this equation. This leads us to the mean-field Hamiltonian

$$\begin{aligned}\mathcal{H}_{\mathrm{MF}} &= -\sum_{\langle ij\rangle}\phi\{-\Theta^2+\Theta c_i+\Theta c_j\}-\bar{\mu}\sum_{i=1}^{N}c_i\\ &= nN\Theta^2\phi-2\phi\Theta\sum_{\langle ij\rangle}c_i-\bar{\mu}\sum_{i=1}^{N}c_i\\ &= nN\Theta^2\phi-2n\phi\Theta\sum_{i}^{N}c_i-\bar{\mu}\sum_{i=1}^{N}c_i\\ &= n\phi N\Theta^2-(2n\phi\Theta+\bar{\mu})\sum_{i}^{N}c_i\\ &= 2\phi N\Theta^2-(4\phi\Theta+\bar{\mu})\sum_{i}^{N}c_i\end{aligned} \tag{17}$$

where $n = 2$ is the number of "bonds" per adsorbate on a 2D square lattice with nearest-neighbor interactions, as considered here.

From this Hamiltonian, we may conclude that the partition function for a single site is

$$\mathcal{Z} = \exp\left\{-\frac{2\phi\Theta^2}{k_BT}\right\}\left[1+\exp\left\{\frac{(4\phi\Theta+\bar{\mu})}{k_BT}\right\}\right] \tag{18}$$

and as each site is treated identically in a mean-field model, the average site occupation, $\langle c_i\rangle = \langle\Theta\rangle = \Theta$. Thus, we have the mean-field model for this system,

$$\ln\left\{\Theta^{-1}-1\right\}+\frac{4\Theta\phi}{k_BT} = -\frac{\bar{\mu}}{k_BT} \tag{19}$$

which is a specific example of the Frumkin isotherm.

In the next section, we will see more specific examples of mean-field theories. In particular, we will see dynamic mean-field theories applied to understand specific electrocatalytic systems.

4. EXAMPLES

In this section, we present a variety of examples that are typical studies of electrocatalytic surface reactions. Note that not all of the examples involve actual chemical reactions. The nonreactive examples have been included to illustrate some simple concepts of catalytic surface modeling without the need to discuss the complications of reactions. The concepts illustrated in these examples include phase transitions, lattice-gas models, the importance of the corrugation potential, the use of DFT methods to extract reasonable values for the model parameters, and the importance of surface diffusion and the practical application of equilibrium and dynamic Monte Carlo simulation methods.

4.1. Br/Ag(100)

The electrosorption of simple halide anions onto single-crystal surfaces provides an excellent quantitative example of how to construct reasonable surface models and how to use simulation methods to provide insight and make predictions of surface behavior. Bromide adsorption on a (100) single-crystal surface of silver is one of the best studied examples in electrochemistry and has been studied experimentally by both classical electrochemical methods [11, 13–15] and by *in situ* techniques such as surface x-ray scattering (SXS) [11, 14] and x-ray absorption fine structure (XAFS) [15] methods. There have also been a wide variety of theoretical studies ranging from simple equilibrium and dynamic lattice-gas models [16–19] to more advanced off-lattice methods [8].

Cyclic voltammetry (CV) experiments for this system show what is often called a butterfly curve with a broad pre-wave in the negative-potential region and a sharp peak at more positive potentials [11, 13–15]. SXS experiments [11] have shown that the sharp peak corresponds to a second order or continuous phase transition in the Br adlayer between a disordered adlayer at low Br coverages to a $c(2 \times 2)$ ordered phase at higher coverages. The pre-wave structure is also associated with phase transitions [19]; however, these phase transitions are not observable at room temperature, and the pre-wave can only be understood as the shadow of a phase-transition that would exist in the system, if the system could be cooled well below the freezing point of water [19].

4.1.1. Equilibrium Lattice-Gas Model

Much success has been made by modeling the bromide adlayer as a simply lattice-gas model. Figure 4 shows the corrugation potential for Br/Ag(100) as obtained from DFT calculations. As discussed in Section 3.2, the amplitude of this corrugation potential is sufficiently high to allow for a lattice-gas treatment of the adlayer. For a more elaborate off-lattice treatment of the adlayer, see [8].

The lattice-gas model consists of an $L \times L$ square array of Br adsorption sites, each site corresponding to the fourfold hollow sites on the Ag(100) surface. The configurational energy of the Br adlayer is given by the grand-canonical lattice-gas Hamiltonian or energy functional, [19]

$$\mathcal{H} = -\sum_{i<j} \phi_{ij} c_i c_j - \bar{\mu} \sum_{i=1}^{L^2} c_i \tag{20}$$

Here, i and j denote adsorption sites, c_i is the occupation at site i, which is either 0 (empty) or 1 (occupied), $\sum_{i<j}$ is a sum over all pairs of sites, being careful to avoid double counting, ϕ_{ij} is the lateral interaction energy of the pair (i, j), and $\bar{\mu}$ is the electrochemical potential. The sign conventions are that $\phi_{ij} < 0$ denotes a repulsive interaction, and $\bar{\mu} > 0$ favors adsorption. Both ϕ_{ij} and $\bar{\mu}$ are measured in units of meV/pair and meV/particle, respectively. For simplicity, both are written as meV. To reduce finite-size effects, it is common to use periodic or wrap-around boundary conditions, which was also done here.

In the weak-solution approximation, $\bar{\mu}$ is related to the electrode potential by [5]

$$\bar{\mu} = \bar{\mu}_0 + k_B T \ln \frac{[C]}{[C_0]} - e\gamma E \tag{21}$$

where $\bar{\mu}_0$ is an arbitrary reference level, k_B is Boltzmann's constant, T is the absolute temperature, e is the elementary charge unit, $[C]$ is the concentration of Br^- in solution, $[C_0]$ is an arbitrary reference concentration, γ is the electrosorption valency, and E is the electrode potential in mV. Note that this form for the relationship between the electrode potential and the electrochemical potential assumes that the electrosorption valency does not depend explicitly or implicitly on either coverage or potential [20].

It was shown in [21] that a short-range nearest-neighbor excluded volume interaction and a longer range dipole–dipole repulsion are sufficient to reproduce the shape of the experimental CV and coverage curves. Thus, within a simplified dipolar interaction model, the long-range part of the interaction energy is $\phi(r) = 2^{3/2}\phi_{nnn} r^{-3}$ for $r \geq \sqrt{2}$, where r is the separation of an interacting Br pair, measured in units of the Ag(100) lattice spacing ($a = 2.889$ Å [11]), and ϕ_{nnn} (which is negative) is the lateral dipole–dipole repulsion between next-nearest neighbors. For $r < \sqrt{2}$ (nearest neighbor distances), the interactions are infinitely repulsive, indicating a large overlap energy due to the large size of the Br adsorbates compared to the Ag(100) lattice spacing. To simplify the calculations, the interactions are truncated for $r > 5$. This interaction scheme is slightly different from that found in [21]; however, no noticeable differences have been seen between the results of the scheme in [21] and the simpler interactions given here, which are taken from [17].

In general, the values for the model parameters can be found by fitting the results of the model in equilibrium to known experimental results, such as by fitting the coverage isotherm

or the CV curve. For more complex models, such fitting procedures can become quite complex [22], and in such cases, DFT results can sometimes be used to find approximate values for the parameters. For Br/Ag(100), the parameter values can be found rather simply by a nonlinear fit [18] of the equilibrium Monte Carlo results to experimental results for the coverage. The resulting values are $\phi_{min} = -26 \pm 2$ meV and $\gamma = -0.73 \pm 0.03$ [17, 19].

The short-range exclusion gives rise to two different possible $c(2 \times 2)$ configurations, one corresponding to the black squares on a chessboard being occupied with Br whereas the white squares are empty, and the other configuration is the reverse, with the white squares being filled with Br whereas the black squares are empty. Each color on the chessboard is then referred to as a sublattice, with say the white-colored squares being labeled as sublattice A, and the black squares being labeled as sublattice B. For a fully ordered $c(2 \times 2)$ phase, either all of the white squares will be occupied or all of the black sites will be occupied. The extent of the ordering can be quantified by the so-called order parameter, which in this case is sometimes called the staggered coverage and can be expressed as $\Theta_S = |\Theta_A - \Theta_B|$, where Θ_A and Θ_B represent the coverages of the two sublattices and each run between 0 and 1.

In the disordered phase, the coverage on the two sublattices should, on average, be equal. Thus, in the disordered phase, the staggered coverage will be close to zero, but in the $c(2 \times 2)$ ordered phase, the symmetry between the two sublattices is spontaneously broken, and the staggered coverage takes on values close to one. The staggered coverage can be measured experimentally by observing the intensity in the half-order diffraction peaks that correspond to the c(2 × 2) phase in SXS experiments [11].

4.1.2. Equilibrium Monte Carlo Method and Results

In equilibrium, the Monte Carlo procedure is greatly simplified over that of dynamic Monte Carlo methods, as the method need only satisfy detailed balance, and there is no need for the Monte Carlo procedure to mimic a physical dynamic. Although dynamic Monte Carlo procedures can, in principle, also be used to find equilibrium results, it is usually far more effective to use a method specifically designed for equilibrium, as such methods usually reach equilibrium in less computational time.

For Br/Ag(100), the simplest equilibrium Monte Carlo procedure is as follows:

1. Calculate the energy of the system using Eq. (20). Call this E_I.
2. Pick a site at random. Call this site i.
3. If $c_i = 1$, change to $c_i = 0$, or if $c_i = 0$, change to $c_i = 1$.
4. Calculate the energy of the system using Eq. (20). Call this E_F.
5. Calculate the transition rate using the Metropolis rate [6], $R = \min\{1, \exp[-(E_F - E_I)/k_B T]\}$.
6. Generate a random number, $r \in (0, 1)$.
7. If $r > R$, then reset c_i back to it's value at step 1.
8. Go to 1.

The Monte Carlo sample series is then the series of system configurations after step 7, and after the initial relaxation to equilibrium, average values, such as the average coverage, can be calculated by simply averaging the values of that quantity, say the coverage, from each of the configurations in the sequence.

The coverage and staggered coverage results for Br/Ag(100) are shown in Fig. 5. The phase transition is easily observed in both the system configurations and in the order parameter, the staggered coverage. These results also fit extremely well to experimental values [19], thus justifying the model.

4.1.3. Dynamic Monte Carlo Model and Results

Dynamic simulations have the same Hamiltonian as the equilibrium simulations, but the transitions between configurations are somewhat different. For Br/Ag(100), we must consider the dynamic processes of adsorption/desorption (represented in the equilibrium procedure as a change in the occupation variable of a single site) as well as the processes of lateral

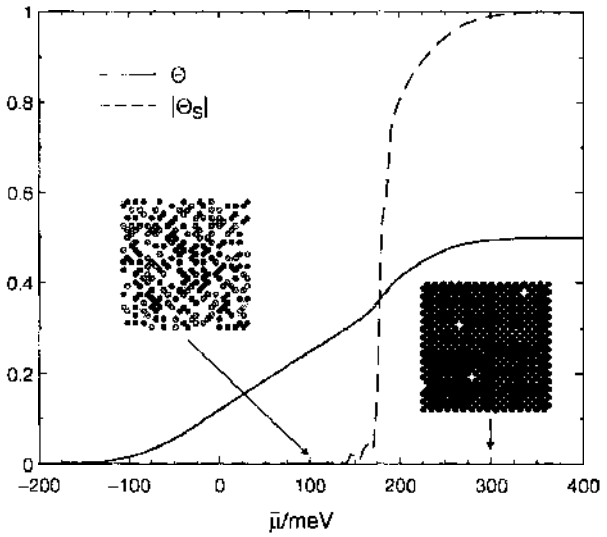

Figure 5. Equilibrium coverage and staggered coverage for a simple lattice-gas model for Br/Ag(100), at room temperature with $L = 32$. The insets show typical adlayer configurations for two different values of the overpotential, $\bar{\mu} = 100$ meV (disordered) and $\bar{\mu} = 300$ meV (ordered). The differently shaded circles indicate adsorbed bromine on each of the two different sublattices. See [19]. Reprinted with permission from [19], S. J. Mitchell et al., *Surf. Sci.* 471, 125 (2001). © 2001, Elsevier.

diffusion within the adlayer. The timescale for each of these processes is set by the height of a barrier, with a different barrier being used for adsorption/desorption and lateral diffusion processes, and a prefactor [see Eq. (10)]. Time is measured in Monte Carlo steps per site (MCSS), and the exact relationship between MCSS and time in more physical units, such as seconds, is not generally known but can sometimes be estimated, given the appropriate experimental data [19].

The dynamic simulation proceeds with a simple algorithm, in which a new configuration is randomly chosen from a weighted list of possible microscopic moves. First, a lattice site is chosen at random. The configuration can only be changed through adsorption, desorption, or lateral diffusion processes that include the chosen site. If the site is empty, only adsorption may be attempted. If the site is occupied, then either desorption or lateral diffusion may be attempted, and if any of the nearest-neighbor sites are occupied in the final state, the transition rate will be zero. A list is then kept of all the possible moves, and the final state is chosen from this list, weighted by the rates calculated using Eqs. (10) and (12). To maintain detailed balance, the movement list must also include the null move, where the probability to remain in the initial state is $R(I|I) = 1 - \sum_{F \neq I} R(F|I)$. Further details on the simulation algorithm and its implementation are given in [5, 18, 19].

The free-energy barriers associated with the different simulation moves are Δ_{nn} for nearest-neighbor diffusion, Δ_{nnn} for next-nearest neighbor diffusion, and Δ_a for adsorption/desorption. The rough estimates used here, $\Delta_{nn} = 100$ meV and $\Delta_{nnn} = 200$ meV, are based on DFT calculations in vacuum [23, 24]. Estimates of Δ_a depend on the reorganization of water when the adsorbate enters or leaves the adlayer, and the necessary calculations required for an accurate DFT estimation of this barrier would be extremely difficult and time consuming; however, from calculations of the potential of mean force for halide ions in water near a Cu(100) surface [25], we can conclude that reasonable values for the adsorption/desorption barrier are between 200 and 500 meV. Therefore a choice of $\Delta_a = 300$ meV, as used in [18, 19], is not unreasonable, but a more accurate estimation of the adsorption/desorption barrier is not possible at this time.[3]

This dynamic Monte Carlo algorithm can be used to simulate a wide range of dynamic surface responses, such as simulating the results of a potential step experiment [19] or the results of a CV experiment [18]. Because a full discussion of the dynamic Br/Ag(100) simulation studies is beyond the scope of the current work, we will leave the reader with the

[3] For a discussion of how a more accurate value for this parameter might be found from a series of simulations and a series of experiments, see [19].

results of only two simple examples: a simulated potential step experiment to study the phase-ordering behavior and a simulated CV scan to study the hysteresis-like response of the system.

For the simple potential step simulation, the electrochemical potential is stepped from the disordered phase, at a point where the coverage is near zero, to a point deep inside of the ordered phase ($\tilde{\mu} = 600$ meV), where the adlayer is fully ordered into a $c(2 \times 2)$ phase. The results of such a potential step simulation are discussed in detail in [19]. Figure 6 shows two typical system configurations following such a potential step. One can easily see that the length scale of the domains increases with time, and this follows the well-known dynamical growth law known as model A, or phase separation with nonconserved order parameter [19].

For the simulated CV scans, the electrochemical potential is changed continuously as a function of time with a sawtooth function, and the change in coverage, which is proportional to the CV current response, is observed. Figure 7 shows the results of such a simulations, which are discussed in more detail in [18]. Such simulations require a large amount of computational time and are difficult to implement in a parallel computational format, but the comparison of such simulations with experimental results could provide useful insights into the microscopic timescales of the different atomic scale dynamic processes, such as diffusion and adsorption/desorption.

4.2. Br/Au(100)

Although chemically, one would expect that the behavior of Br/Au(100) should be similar to that of Br/Ag(100), the coverage isotherm and ordered phases are actually quite different. The primary reason for this difference is that the corrugation potential for Br/Au(100) differs in both amplitude and symmetry from that of Br/Ag(100) [26]. This in turn, leads to two different ordered phases, one commensurate phase with coverage one-half and a second incommensurate phase with coverage greater than one-half [12].

The fact that this system displays an incommensurate ordered phase suggests the states are not well-localized, implying that a lattice-gas treatment of the adlayer will not be valid. Thus, equilibrium Monte Carlo simulations must employ an off-lattice simulation method [8] and not a lattice-gas approximation. Furthermore, the lack of well-localized states means that a dynamic Monte Carlo treatment is not possible, and any dynamic simulations must use less efficient molecular dynamics-like methods [8].

To construct an off-lattice model for the surface, we not only need to know the lateral interactions between adsorbates, as was also needed for a lattice-gas treatment of the adlayer, but the off-lattice method also requires a knowledge of the corrugation potential. In the following subsections, we will explain how to use the results of DFT calculations to obtain

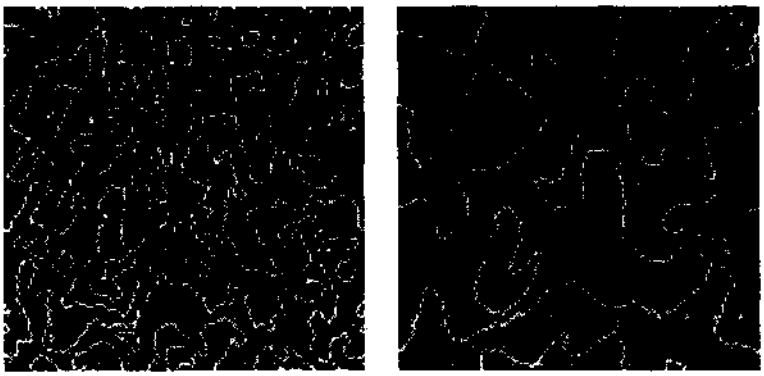

(a) t = 1000 MCSS (b) t = 5000 MCSS

Figure 6. Typical system configurations following a simulated potential step experiment from a potential where $\Theta \approx 0$ to $\tilde{\mu} = 600$ meV, deep inside of the $c(2 \times 2)$ ordered phase. The two different shades of gray indicate $c(2 \times 2)$ phases on each of the two different sublattices, and the white areas indicate the empty domain boundaries between the two degenerate $c(2 \times 2)$ phases. The characteristic length scale of the domains grows as $t^{1/2}$ as expected for models of phase separation with nonconserved order parameter. All results are given for room temperature. See [19]. Reprinted with permission from [19], S. J. Mitchell et al., *Surf. Sci.* 471, 125 (2001). © 2001, Elsevier.

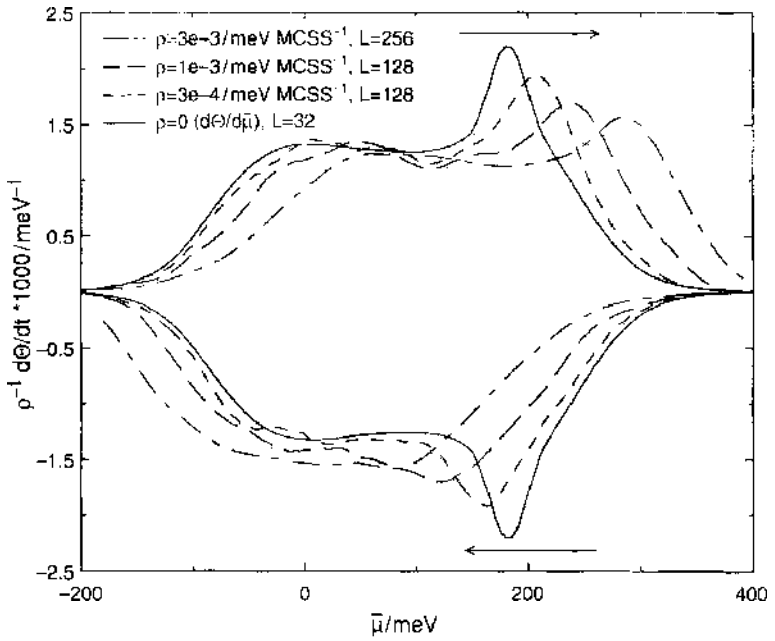

Figure 7. Simulated CV experiments using dynamic Monte Carlo simulations. The slope of the sawtooth linear scan or the CV scan rate is given by ρ in units of meV/MCSS. The results for $\rho = 0$ are taken from equilibrium Monte Carlo results and are included as a reference. All results are given for room temperature. The vertical axis represents the response current. The results for the different scan rates have been scaled in the vertical direction to aid comparison, as indicated on the vertical axis. Reprinted with permission from [18], S. J. Mitchell et al., in "Computer Simulation Studies in Condensed-Matter Physics XIII" (D. P Landau, S. P. Lewis, and H.-B. Schüttler, Eds.). Springer, Berlin, 2001. © 2001, Springer.

accurate values of the parameters necessary to construct an off-lattice model for Br/Au(100). It should be noted that the use of DFT to estimate model parameters is still somewhat new and unproven for electrochemical systems; however, for Br/Au(100), DFT methods do seem to give quite accurate, although imperfect results [26]. DFT calculations may be more or may be less accurate for other systems. For surface reactions taking place at the interface in vacuum, DFT methods seem to have reached semiquantitative accuracy and predictive power.

4.2.1. DFT Calculations

As was discussed in [27], one should be very careful when using DFT calculations to predict binding sites, and thus corrugation potentials, for halides on noble metal surfaces. The calculations can be quite sensitive to the symmetry of the calculations, and the cluster methods should, in general, be avoided for these purposes. Instead, it is more reliable to use the DFT supercell or slab methods, using a plane-wave basis set for the electronic wave functions, as they seem to reproduce more accurately the delocalization effects of the electrons in the vicinity of a metallic surface.

Figure 8 shows a typical DFT supercell used to study Br/Au(100) [26]. This figure shows a so-called slab configuration, in which the supercell contains several metallic layers separated by a vacuum region in the z direction.

The accuracy of the calculations depends on a number of factors that can be separated into two general categories, the method-specific parameters and the geometric parameters. The method-specific parameters include basis set parameters, such as the cutoff energy, k-point sampling, and other electronic parameters such as the type of pseudopotentials used and the type of approximation used for the exchange correlation energy (LDA or GGA). The geometric parameters include the overall size of the DFT cell, the number of slab layers, the size of the vacuum region gap, and the type of geometric relaxations performed. To obtain accurate and reasonable results, each DFT calculation must consider the accuracy as it depends on both classes of parameters, and there is no universally accepted set of parameters for all problems.

For the results discussed here, which are taken from [26], DFT results were calculated using the periodic slab geometry with a periodic plane-wave basis set with the Vienna

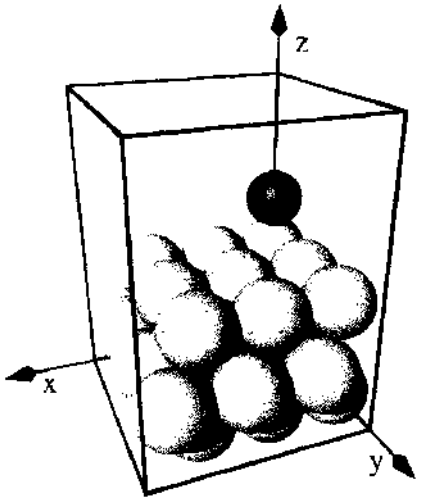

Figure 8. A typical DFT supercell configuration for the study of Br/Au(100). The lighter shaded spheres indicate the Au substrate atoms, and the darker shaded sphere represents an adsorbed Br atom. The contents of the box are then repeated infinitely in the x, y, and z directions. Reprinted with permission from [26], S. J. Mitchell and M. T. M. Koper, Unpublished.

ab Initio Simulation Package (VASP) [28–30]. The generalized gradient-corrected exchange-correlation functional (GGA) [31] was used with the Vanderbilt ultrasoft pseudopotentials [32] and a cutoff energy of 400 eV. Each slab contained three metal layers separated by six vacuum layers, each vacuum layer being the equivalent thickness of a metal layer. Additionally, two different-sized supercells were used to examine possible coverage dependence, a $2(2.97) \times 2(2.97) \times 12.6$ Å cell (denoted as 2×2), containing 4 surface Au atoms, and a $3(2.97) \times 3(2.97) \times 12.6$ Å cell (denoted as 3×3), containing 9 surface Au atoms. The k-point mesh was generated automatically using the Monkhorst method with a $7 \times 7 \times 1$ grid for the 2×2 cells and a $5 \times 5 \times 1$ grid for the 3×3 cells. Initial convergence tests suggested that these parameters are sufficient for the accuracy desired, as justified by Fig. 12.

4.2.2. Corrugation Potential

The corrugation potential was calculated by placing a single Br atom at a specific (x, y) location above the 3×3 Au(100) surface, and the z position of the adsorbate was varied until the total energy of the system was minimized. This process was repeated for a number of different lateral positions, until an understanding of the corrugation potential was reached.

Of course, such calculations only tell us information about specific locations on the surface, and any simulation needs the corrugation potential, $U(x, y)$, to be defined for all (x, y) positions on the surface. Thus, we must construct an analytic approximation to the results found from DFT calculations [26],

$$U(x, y) = \Delta_1 \frac{[\cos(2\pi x/a)\cos(2\pi y/a) + 1]}{2} + \Delta_2 \frac{[\cos(2\pi x/a) + \cos(2\pi y/a)]}{2} \tag{22}$$

where $\Delta_1 = 274$ meV and $\Delta_2 = 234$ meV. This approximation reproduces the DFT results in the region near the preferred bridge binding sites.

Figure 9 shows a plot of Eq. (22). The bridge site can clearly be seen as the most energetically favorable site for adsorption. This is also confirmed by both experiments [12] and previous DFT studies [27]. Cluster calculations predict fourfold binding for Br/Au(100) [33], which is not correct.

4.2.3. Lateral Interactions

In addition to the corrugation potential, the construction of an off-lattice model also requires knowledge of the lateral interactions between adsorbates. In principle, the interactions can be found by analyzing the total energy for different configurations of the adlayer; however, this is not always the most accurate method, as the DFT total energy results can depend

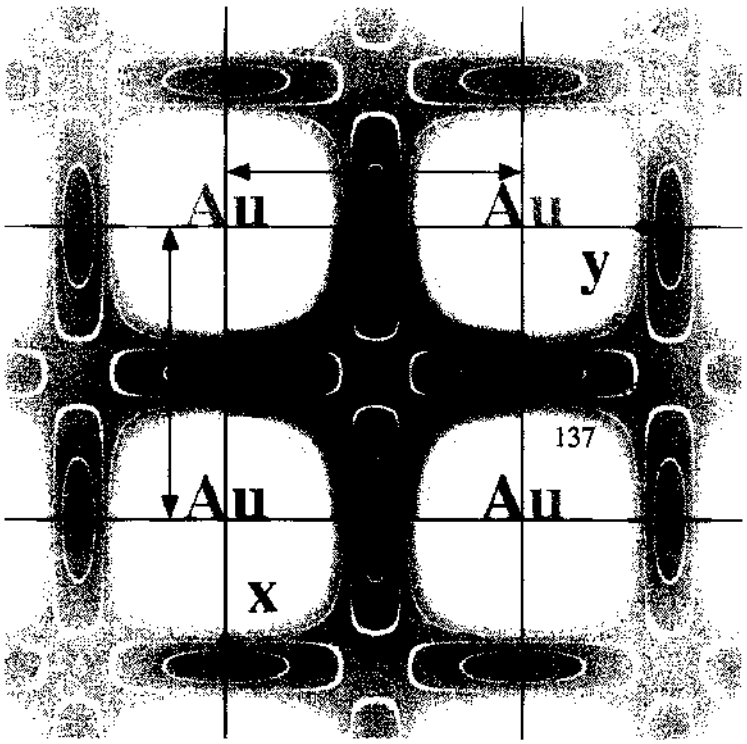

Figure 9. The corrugation potential for Br/Au(100) as derived from DFT results and the approximation of Eq. (22). The grayscale indicates the value of the corrugation potential, and the white lines indicate contour lines with values as labeled. One can clearly see that the bridge sites are the most preferred locations for binding, as known from experiments [12] and previous DFT calculations [27]. Reprinted with permission from [26], S. J. Mitchell and M. T. M. Koper, Unpublished.

rather strongly and anomalously on the local symmetries of the adlayer [26]. Instead, when the interactions are believed to be dominated by electrostatics, as was the case with the dipolar interactions of Br/Ag(100) and is also the case with Br/Au(100), an analysis of the electron density can be performed.[4]

Unfortunately, a simple plot of the full electron density is difficult to interpret; however, when the "background" charge is removed, the dipolar character of the surface to adsorbate bond is clearly seen. We therefore define the charge transfer function, so-called because it clearly shows where charge has been transferred as a result of the formation of the surface bond, as follows [26]:

$$\Delta\rho(\vec{x}) = \frac{\left\{\rho(\vec{x})_{N\mathrm{Br-Au(100)}} - \sum_i \rho_i(\vec{x})_{\mathrm{Br}} - \rho(\vec{x})_{\mathrm{Au(100)}}\right\}}{N} = -\frac{\left\{\rho_e(\vec{x})_{N\mathrm{Br-Au(100)}} - \sum_i \rho_{ei}(\vec{x})_{\mathrm{Br}} - \rho_e(\vec{x})_{\mathrm{Au(100)}}\right\}}{N} \tag{23}$$

where $\rho(\vec{x})_{N\mathrm{Br-Au(100)}}$ is the full charge density of the adlayer and substrate system with N Br in the cell, $\rho_i(\vec{x})_{\mathrm{Br}}$ is the charge density of a single Br atom at the same position as that in the Br–Au bonded system, i indexes the N adsorbed Br, $\rho(\vec{x})_{\mathrm{Au(100)}}$ is the charge density of the Au(100) slab with all atoms at the same positions as in the Br–Au bonded system, and the subscripts "e" denote electron-only densities, having the sign convention that positive indicates greater electron density. Note that the charge transfer function is calculated using only charge densities for the same size cells.

Figure 10 shows the charge transfer function for DFT cells representing different coverages. The fact that each curve overlaps the other indicates that there is no noticeable direct dependence of the dipole moment on the coverage itself. A simple integration of the charge transfer function yields a dipole moment of $s = 0.3$ eÅ [26], regardless of coverage, provided

[4] In addition to obtaining the total energy of an atomic configuration, DFT calculations also produce the local electron density, since this is one of the vital quantities of the DFT method.

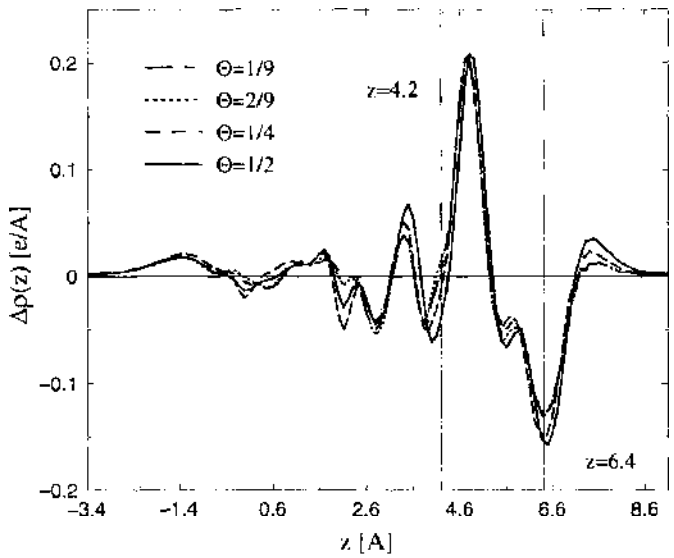

Figure 10. The charge transfer function for various coverages of Br/Au(100) for bridge-site binding. No noticeable differences can be seen. The vertical lines indicate the top Au(100) slab surface at 4.2 Å and the Br adlayer at 6.4 Å. Reprinted with permission from [26], S. J. Mitchell and M. T. M. Koper, Unpublished.

that all adsorbates remain at the bridge site. Note that a determination of the dipole moment by examination of the total DFT energy for the different coverage configurations is not effective, as the energy changes are very small.

In addition to the long-range interactions, there is a short-range excluded volume interaction that is not electrostatic but steric in character. Therefore, the total DFT energy must be used to obtain the interactions at this length scale. Because the repulsive interactions at short range should be very large, a determination of the short-range repulsion from the DFT coverage dependence should be possible by examining the total energy for adlayer configurations with bridge-site binding for $\Theta = 2, 1, 1/2, 1/4, 2/9$, and $1/9$. Each adlayer configuration had a square geometry of adsorbed Br [26].

The lateral interaction energy can be determined from the DFT total energy calculations as [26]

$$\Phi = E_{\text{tot}} - E_{\text{slab}} - NE_{\text{Br}} - N\mathscr{B} \tag{24}$$

where E_{tot} is the DFT total energy of the Br–Au bonded system, E_{slab} is the DFT energy of the Au(100) slab, N is the number of Br within the cell, E_{Br} is the DFT energy of a single Br atom in the cell, and $\mathscr{B}$ is the binding energy of Br to the Au(100) surface. Figure 11

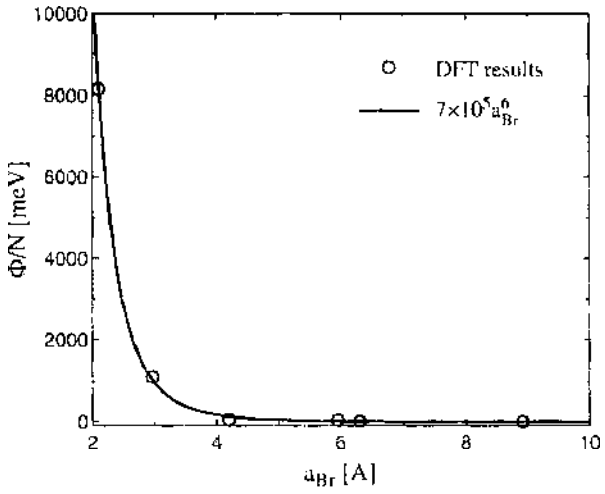

Figure 11. The lateral interactions from DFT total energy calculations. The plot represents the reformulation of results for calculations with $\Theta = 2, 1, 1/2, 1/4, 2/9$, and $1/9$. Reprinted with permission from [26], S. J. Mitchell and M. T. M. Koper, Unpublished.

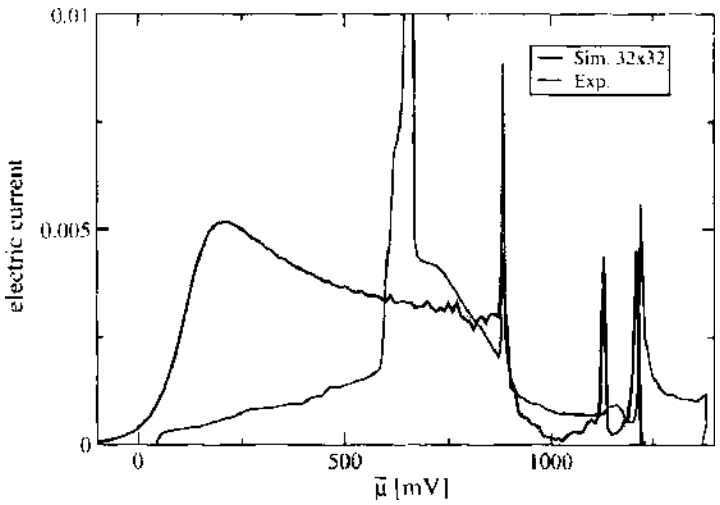

Figure 12. The results of an off-lattice model for Br/Au(100) using the parameters as determined by DFT. The experimental CV current is taken from [12] and is reproduced with permission of the author. Simulation data taken from [26]. Reprinted with permission from [26], S. J. Mitchell and M. T. M. Koper, Unpublished.

summarizes the results for the total interaction energy per particle, represented in a way that indicates a short-range repulsive $1/r^6$ potential, where a_{Br} is the separation between nearest Br in the adlayer.

From both the charge density analysis and the DFT interaction energy analysis, we can conclude that Br within the adlayer interact in two ways. On short length scales, there is the expected $1/r^6$ repulsive interaction, caused by an excluded volume interaction. On longer length scales, there is a $1/r^3$ dipolar interaction, caused by the electrostatic interactions between the polar Br–Au bonds.

4.2.4. Off-Lattice Monte Carlo Results

Once the corrugation potential and lateral interactions are known, an off-lattice Monte Carlo simulation can be performed. Such a simulation is far more complex than the simple lattice-gas method, and as such, we refer the interested to [8] for a discussion on off-lattice Monte Carlo simulation. The results of such a simulation can be found in Fig. 12 along with the experimental data from [12].

From left to right in the experimental data, the first peak represents a transition from the reconstructed Au surface to the 1 × 1 Au surface at higher potentials. The second peak in the experimental curve represents a disorder/order transition of the Br adlayer to a commensurate ordered phase, and the third and final peak in the experimental data indicates a transition between the commensurate ordered adlayer phase to a uniaxially incommensurate ordered phase [12]. The simulations show similar results with several major differences. First, the simulation model is not intended to reproduce any changes in the substrate itself, and thus the lifting of the reconstruction is not reproduced by the simulation. Second, the simulation shows two different incommensurate phases, and the reason for this is not currently understood. The second incommensurate ordered phase may indicate some small inaccuracies in the model parameters,[5] or it may indicate that the simulation size was too small, $L = 32$.

4.3. CO Oxidation on Pt–Ru Alloys

One issue that is particularly well suited to a dynamic Monte Carlo (DMC) simulation study is the influence of CO surface diffusion on the electrochemical oxidation kinetics of a CO layer that is adsorbed on the catalytic surface. This has been a subject of considerable interest

[5] Off-lattice models are extremely sensitive to values of the parameters, and even rather small changes in one parameter, such as the strength of the short-range repulsion, can cause rather large changes in the predictions of the model.

in many recent experimental studies of CO oxidation, and it is of obvious importance for understanding CO oxidation on bimetallic catalysts (as will be illustrated below). Bimetallic catalysts are the catalysts of choice for CO tolerant anodes in low-temperature fuel cells.

CO oxidation on a Pt electrode is generally assumed to take place by a Langmuir-Hinshelwood mechanism between adsorbed CO and an oxygen-containing species that is formed from water, usually assumed to be adsorbed OH. The OH is formed on a free site, denoted "*", by the dissociative adsorption of water, and then reacts with a CO adsorbed on a neighboring site leaving behind two free sites:

$$H_2O + * \leftrightarrow OH_{ads} + H^+ + e \tag{25}$$

$$CO_{ads} + OH_{ads} \rightarrow CO_2 + H^+ + e + 2* \tag{26}$$

This mechanism, when considered in the mean-field approximation, can explain quite a few experimental observations. It reproduces, for instance, the shape of the chronoamperometric transient in a stripping experiment [34, 35], the negative reaction order in the CO bulk concentration in a continuous oxidation experiment [35], and the hysteresis and S-shaped form of the polarization curve for continuous CO oxidation experiments [36].

Dynamic Monte Carlo simulations have been carried out to assess the influence of a finite CO surface mobility on the stripping voltammetry and the chronoamperometric oxidation transient [37]. The surface was modeled as a square lattice of surface sites. The site is either empty or occupied by OH or CO. The surface hydroxyl is formed by the reaction in Eq. (26), and as we are considering a CO stripping experiment, CO is pre-adsorbed up to a certain maximum coverage. Typically, 99% percent of the surface is initially covered with CO to model a saturated CO adlayer.

The reaction in Eq. (26) can take place with a certain potential-dependent reaction probability when CO and OH are adsorbed on neighboring sites. The overall reaction rate, and hence electric current, will depend on the degree of mixing, which is primarily influenced by the CO diffusion rate, as OH formation can take place reversibly on any part of the surface. CO diffusion is modeled as a CO exchange between two neighboring sites, where one site is occupied by a CO and the other site is empty. The rate of this process is D s^{-1}, which corresponds to a surface diffusion coefficient of approximately $D \times 10^{-15} cm^2 s^{-1}$.

Figure 13 compares the stripping voltammetry for various initial coverages of CO and various CO diffusion rates D with the mean-field predictions. The rate constants were chosen such that, qualitatively, the voltammetry on platinum is mimicked. It was observed that the Monte Carlo voltammogram approaches the mean-field prediction for high diffusion rate D and low initial coverages of CO. A high diffusion coefficient implies a thorough mixing of CO and OH, when the CO coverage is low, providing a sufficient number of empty sites around individual CO adsorbates where OH can adsorb. The diffusion of OH is less important as it can be formed reversibly at any site on the surface. It is also seen in Fig. 13 that the shape of the voltammogram changes as D increases. At low D, the stripping peak is broad and of relatively low current. In this case, the system can be modeled adequately by a nucleation-and-growth description, in which OH adsorbs in the holes ("nucleation centers") of the CO adlayer, and the reaction with CO takes place at the perimeter of these growing holes. At high D, the stripping gets much sharper and the mean-field description works well.

It is of interest to note that in the simulations, the potential dependence of the overall reaction, as evaluated from a Tafel plot, is not very sensitive to the diffusion rate D. The Tafel slope (in stripping experiments usually evaluated by plotting the potential of the current peak *versus* the logarithm of the scan rate) depends primarily on the rate-determining reaction and much less on the type of nucleation-and-growth mode, as has been suggested in chronoamperometric experiments of CO oxidation [38].

These simulations have been extended to CO stripping from randomly mixed Pt–Ru alloy electrodes [39]. The primary goal of these simulations was to investigate what factors should be incorporated into the model in order that they reproduce, qualitatively, the stripping experiments of Gasteiger et al. [40]. These authors prepared well-characterized Pt–Ru alloys in vacuum before their transfer to the electrochemical cell. The surface consisted of a random mixture of Pt and Ru sites, onto which a saturated monolayer of CO was adsorbed.

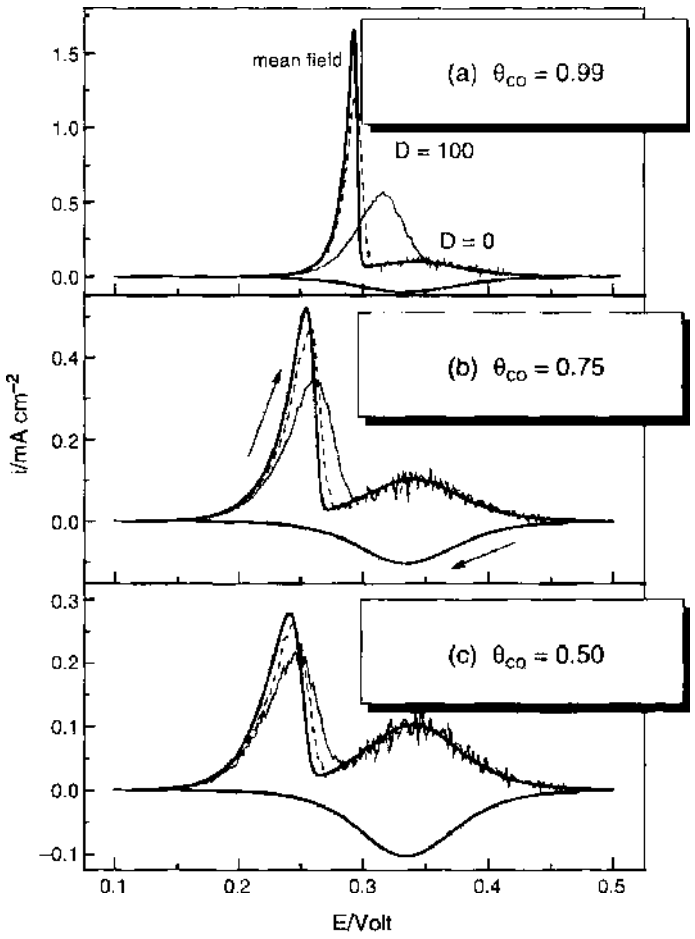

Figure 13. CO stripping voltammetry at three initial coverages of CO, as indicated in the figure. Sweep rate is 50 mV/s. The thick solid line indicates the mean-field results, the thin dashed line indicates $D = 100$, and the thin solid line indicates $D = 0$, or no diffusion. Reprinted with permission from [37], M. T. M. Koper et al., *J. Chem. Phys.* 109, 6051 (1998). © 1998, American Institute of Physics.

The monolayer was oxidized in a CO-free electrolyte by stripping voltammetry, and the catalytic activity of the Pt–Ru alloy was studied as a function of the fraction of Ru sites on the surface, x_{Ru}. The lower the potential needed to oxidize the CO layer, the higher the catalytic activity of the surface.

The important reactions taken into account in the model reflect the generally accepted bifunctional model, in which the OH with which CO is supposed to react is preferentially formed on the Ru surface sites:

$$H_2O + *_{Ru} \leftrightarrow OH_{Ru} + H^+ + e^- \tag{27}$$

$$CO_{Ru} + OH_{Ru} \leftrightarrow CO_2 + H^+ + 2\,*_{Ru} + e^- \tag{28}$$

$$CO_{Pt} + OH_{Ru} \leftrightarrow CO_2 + H^+ + *_{Pt} + *_{Ru} + e \tag{29}$$

In our DMC simulations, we prepared a randomly mixed Pt–Ru lattice, which was initially filled with CO up to 99%, with no preference for either site. The CO adlayer was oxidized on a series of Pt–Ru surfaces with varying Ru content. The resulting stripping voltammetry for high diffusion rates D is shown in Fig. 14, and the dependence of the peak potential, at which the oxidation current reaches a maximum, as a function of Ru fraction and diffusion rate in Fig. 15. (The motivation for the choice for the exact numerical values of the other rate constants can be found in the original paper.) It is clearly observed from Fig. 15 that a relatively fast diffusion rate is necessary for the surface to show a significant catalytic enhancement. For fast diffusion, the optimum catalytic activity is observed for a surface with about 50% Ru, in agreement with experiment. This optimum can be understood

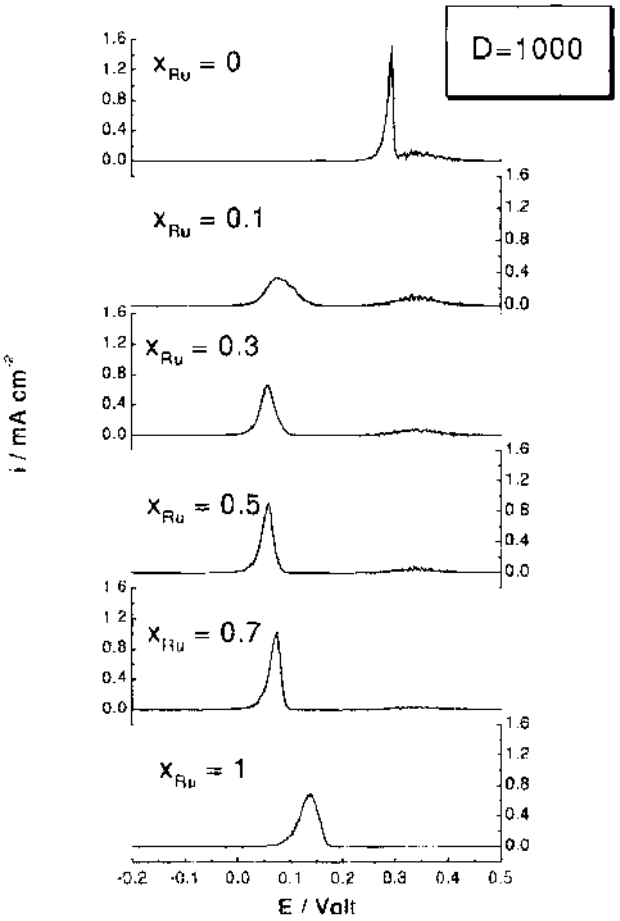

Figure 14. CO stripping voltammetry from dynamic Monte Carlo simulations, for pure Pt($x_{Ru} = 0$), various Pt-Ru alloy surfaces, and pure Ru. Details of the kinetic rate constants can be found in the original publication. CO surface diffusion is very fast, hopping rate D from site to site of 1000 s^{-1}. Reprinted with permission from [39], M. T. M. Koper et al., *J. Phys. Chem. B* 103, 5522 (1999). © 1999, American Chemical Society.

as being the result of a maximization of the number of Pt–Ru neighbors. More importantly, the DMC simulations for fast diffusion show that only a small fraction of Ru is needed to observe a major negative shift (~200 mV) in peak potential. This fact is in excellent agreement with the stripping experiments of Gasteiger et al. [40]. Moreover, the shape of the stripping voltammetry shown in Fig. 14, from relatively broad at low x_{Ru}, narrower at intermediate x_{Ru}, and broader again at the highest x_{Ru}, agrees very well with the experimental results. These results clearly suggest the importance of CO surface mobility in explaining the electrocatalytic activity of well-mixed Pt–Ru alloys.

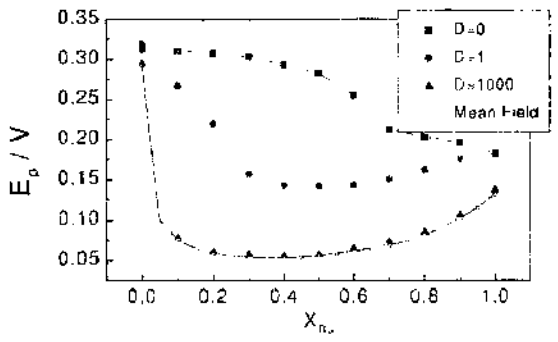

Figure 15. CO stripping peak potential, E_p, from dynamic Monte Carlo simulations as a function of Ru fraction on the Pt-Ru surface for three different surface diffusion rates $D = 0$, 1, and 1000 s^{-1} and for a mean-field model. Reprinted with permission from [39], M. T. M. Koper et al., *J. Phys. Chem. B* 103, 5522 (1999). © 1999, American Chemical Society.

More recently, we have extended these simulations by taking into account the varying CO binding energies on the Pt–Ru surface [41], as evaluated from the DFT-GGA calculations [42]. These studies were motivated by the experimental studies of CO stripping from Ru-island covered Pt(111) electrodes by the groups of Baltruschat [43] and Wieckowski [44]. These authors consistently observe two stripping peaks in the voltammetry: one at low potentials supposedly related to the oxidation of CO from Ru islands and neighboring Pt sites, and one at higher potentials related to CO oxidation from Pt(111) sites. Two stripping peaks were indeed predicted on Pt–Ru surfaces with an island structure with the DMC model described in the previous paragraph, but only for very low diffusion rates or very large distances between islands. Because CO is known to be very mobile on Pt(111), and the average island distance in the experiments is such that effects of slow diffusion are not expected, an apparent paradox arises. The paradox can be resolved by realizing that on Pt sites that coordinate to Ru surface atoms, DFT calculations show that the CO binding energy is much weaker than on pure Pt [42]. Farther away from the Ru island, on pure Pt(111), the binding is ~0.4–0.5 eV stronger. This causes an unfavorable binding energy difference against which CO on the bulk Pt surface has to diffuse to be oxidized at the Ru islands. This effect may lead to an apparently slow CO diffusion rate and may explain many of the experimental trends observed on Ru-modified Pt(111) electrodes.

REFERENCES

1. B. Hammer and J. K. Nrksov, *Adv. Catal.* 45, 71 (2001).
2. J. Greeley, J. K. Nrksov, and M. Mavrikakis, *Annu. Rev. Phys. Chem.* 53, 319 (2002).
3. M. T. M. Koper, R. A. van Santen, and M. Neurock, in "Catalysis and Electrocatalysis at Nanoparticle Surfaces" (E. R. Savinova, C. G. Vayenas, and A. Wieckowski, Eds.). Marcel Dekker, New York, 2003.
4. M. T. M. Koper, in "Modern Aspects of Electrochemistry" (C. G. Vayenas, B. E. Conway, and R. E. White, Eds.), Vol. 36. Kluwer Academic/Plenum Press, New York, 2003.
5. G. Brown, P. A. Rikvold, S. J. Mitchell, and M. A. Novotny, in "Interfacial Electrochemistry: Theory, Experiment, and Application" (A. Wieckowski, Ed.). Marcel Dekker, New York, 1999.
6. N. Metropolis, A. W. Rosenbluth, M. N. Rosenbluth, A. H. Teller, and E. Teller, *J. Chem. Phys.* 21, 1087 (1953).
7. R. J. Glauber, *J. Math. Phys.* 4, 294 (1963).
8. S. J. Mitchell, S. Wang, and P. A. Rikvold, *Faraday Disc.* 121, 53 (2002).
9. W. Kohn, A. D. Becke, and R. G. Parr, *J. Phys. Chem.* 100, 12974 (1996), and references therein.
10. K. Binder and D. W. Heermann, "Monte Carlo Simulation in Statistical Physics. An Introduction," 2nd Edn. Springer, Berlin, 1992.
11. B. M. Ocko, J. X. Wang, and T. Wandlowski, *Phys. Rev. Lett.* 79, 1511 (1997).
12. T. Wandlowski, J. X. Wang, O. M. Magnussen, and B. M. Ocko, *J. Phys. Chem.* 100, 10277 (1996).
13. G. Valette, A. Hamelin, and R. Parsons, *Zeitshrift fur Physikalishe Chemie Neue Folge* 113, 71 (1978).
14. J. X. Wang and T. Wandlowski, in "Proceedings of the Symposium on The Electrochemical Double Layer." Vol. 97-17, p. 293. The Electrochemical Society, New Jersey, 1997.
15. O. Endo, M. Kiguchi, T. Yokoyama, M. Ito, and T. Ohta, *J. Electroanal. Chem.* 473, 19 (1999).
16. M. T. M. Koper, *J. Electroanal. Chem.* 450, 189 (1998).
17. S. J. Mitchell, G. Brown, and P. A. Rikvold, *J. Electroanal. Chem.* 493, 68 (2000).
18. S. J. Mitchell, P. A. Rikvold, and G. Brown, in "Computer Simulation Studies in Condensed-Matter Physics XIII" (D. P Landau, S. P. Lewis, and H.-B. Schüttler, Eds.). Springer, Berlin, 2001.
19. S. J. Mitchell, G. Brown, and P. A. Rikvold, *Surf. Sci.* 471, 125 (2001).
20. I. Abou Hamad and S. J. Mitchell, unpublished.
21. Marc T. M. Koper, *J. Electroanal. Chem.* 450, 189 (1998).
22. G. Brown, P. A. Rikvold, M. A. Novotny, and A. Wieckowski, *J. Electrochem. Soc.* 146, 1035 (1999).
23. A. Ignaczak and J. A. N. F. Gnomes, *J. Electroanal. Chem.* 420, 71 (1997).
24. S. J. Mitchell, Sanwu Wang, P. A. Rikvold, and G. Brown, in "Computer Simulation Studies in Condensed Matter Physics XIV" (D. P. Landau, S. P. Lewis, and H. B. Schuttler, Eds.). Springer, Berlin, 2001.
25. A. Ignaczak, J. A. N. F. Gomes, and S. Romanowski, *J. Electroanal. Chem.* 450, 715 (1998).
26. S. J. Mitchell and M. T. M. Koper, submitted.
27. Sanwu Wang and P. A. Rikvold, *Phys. Rev. B* 64 (2002).
28. G. Kresse and J. Hafner, *Phys. Rev. B* 47, 558 (1993).
29. G. Kresse and J. Hafner, *Phys. Rev. B*, 49, 14251 (1994).
30. G. Kresse and J. Furthmuller, *Comput. Mater. Sci.* 6, 15 (1996).
31. J. P. Perdew, J. A. Chevary, S. H. Vosko, K. A. Jackson, D. J. Pederson, M. R. and Singh, and C. Fiolhais, *Phys. Rev. B* 46, 6671 (1992).
32. D. Vanderbilt, *Phys. Rev. B* 41, 7892 (1990).
33. A. Ignaczak and J. A. N. F. Gomes, *J. Electroanal. Chem.* 420, 71 (1997).

34. N. P. Lebedeva, M. T. M. Koper, J. M. Feliu, and R. A. van Santen, *J. Electroanal. Chem.* 524, 242 (2002).
35. H. A. Gasteiger, N. M. Markovic, and P. N. Ross, Jr., *J. Phys. Chem.* 99, 8290 (1995).
36. M. T. M. Koper, T. J. Schmidt, N. M. Markovic, and P. N. Ross, *J. Phys. Chem. B* 105, 8361 (2001).
37. M. T. M. Koper, A. P. J. Jansen, R. A. van Santen, J. J. Lukkien, and P. A. J. Hilbers, *J. Chem. Phys.* 109, 6051 (1998).
38. B. Love and J. Lipkowski, *ACS Symp. Ser.* 378, 484 (1988).
39. M. T. M. Koper, J. J. Lukkien, A. P. J. Jansen, and R. A. van Santen, *J. Phys. Chem. B* 103, 5522 (1999).
40. H. A. Gasteiger, N. M. Markovic, P. N. Ross, and E. J. Cairns, *J. Phys. Chem.* 98, 617 (1994).
41. M. T. M. Koper, N. P. Lebedeva, and C. G. M. Hermse, *Faraday Disc.* 121, 301 (2002).
42. M. T. M. Koper, T. E. Shubina, and R. A. van Santen, *J. Phys. Chem. B* 106, 686 (2002).
43. H. Massong, H. Wang, G. Samjesk, and H. Baltruschat, *Electrochim. Acta.* 46, 701 (2000).
44. G.-Q. Lu, P. Waszczuk, A. Wieckowski, *J. Electroanal. Chem.* 532, 49 (2002).

CHAPTER 12

Radiation-Induced Modifications in Nanomaterials

M. Chipara

Radiation Effects Research Program, Indiana University Cyclotron Facility, Bloomington, Indiana, USA

D. Hui

University of New Orleans, Department of Mechanical Engineering, New Orleans, Louisiana, USA

CONTENTS

ISBN: 1-58883-047-0

Handbook of Theoretical and Computational Nanotechnology
Edited by Michael Rieth and Wolfram Schommers
Volume 5: Pages (717–806)

1. INTRODUCTION

The radiation-induced modification of materials is an intricate multiscale process and crosses various disciplines such as physics, chemistry, and biology. The interaction of radiation with materials starts with excitations, ionizations, spin-spin interactions, and knockout collisions at sub-nanometer scale and extremely short timescales (of the order 10^{-15} s or shorters see Figs. 1 and 2). The energy deposited by the incident radiation within the target is further dissipated over larger distances. The transfer of the deposited energy to vibrational modes (thermal effects) starts after 10^{-14} s. If the energy deposited locally by the incident radiation is sufficiently large, collective defects such as spurs, blobs, and tracks are generated

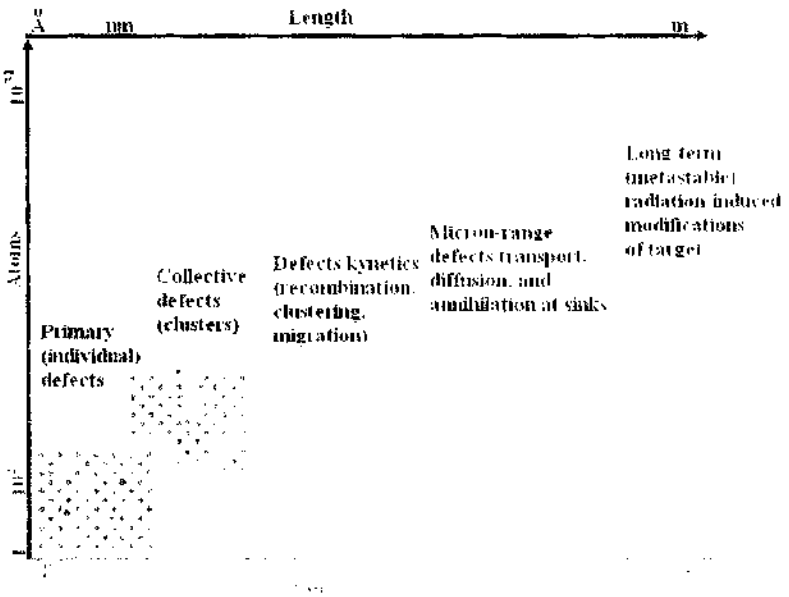

Figure 1. A qualitative picture of the time-length scale of the radiation effects in materials

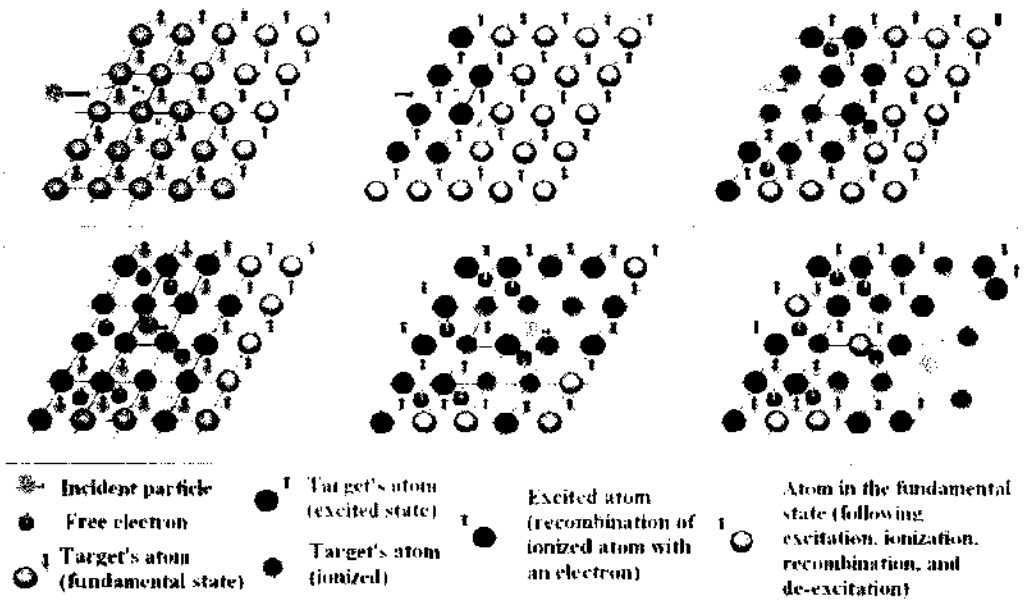

Figure 2. The interaction of an incident charged particle with a two-dimensional crystal.

by the incident radiation. Defect diffusion eventually accompanied by chemical reactions contributes to the spreading of the energy deposited by the incident particle within the target. Discontinuous collective defects named spurs are produced within the target subjected to electron beams, if the energy deposited by the incident electron is ranging between 10 eV and 10^2 eV [1–3]. In isotropic targets, the distribution of the deposited energy in sections of spurs perpendicular on the incident particle trajectory show cylindrical symmetry [1–5]. Further increase of the deposited energy in the range 100 eV to about 500 eV results in the formation of another type of collective defects (blobs) [1]. At higher deposited energies (in the range 500 eV to 5000 eV), a continuous collection of defects named latent track (short latent track) [1–3] is produced within the target along the incident particle trajectory. The diameter of latent tracks is ranging between 1 and 10^2 nm [1,2]. Eventually, these nanometer-sized structures coalesce into micrometer-sized modifications of the target [1–9]. These collective defects produce significant changes of the physical and chemical properties of the target. Under certain conditions [1–8], the target may be vaporized (partially or completely) by the impinging radiation. Element transmutation may be induced by nuclear collisions [1–4]. This process will not be considered.

Chemical reactions may compete with ionization processes. In polymeric targets subjected to ionizing radiation, scissions, and cross-linking reactions produce low molecular compounds (gases such as H_2, CO, CO_2), which are released from the target [1–10]. The ionization process of polymers results eventually in the generation of free radicals due to chain ionization or to the scission of macromolecular chains [2–7]. Depending on the average distance between free radicals and on the effectivness of the diffusion process these free radicals will eventually recombine through cross-linking reactions. During the irradiation of polymers both scissions and cross-linking reactions are competing [1–8]. If radicals are not able to recombine, scissions reactions will be dominant resulting in the decrease of the average molecular mass [1–10]. As the radical states are carried by polymeric fragments, cross-linking reactions have a low probability at low temperatures. At higher temperatures (usually above the glass transition temperature, T_G) the radical moiety of the macromolecular sweeps over a sphere with a radius of the order of the statistic (Kuhn) segment. This enhances dramatically the probability of cross-linking reactions.

In most cases, at the end of the irradiation, the target is left in an excited state [1–10]. A slow decay of its physical and chemical properties to some equilibrium values has been reported [1–10]. The timescale of these relaxation processes (see Fig. 1) is ranging from 10^{-6} s up to 10^9 s (in some irradiated polymers) [1–6]. In certain cases, the equilibrium (stable or long-time) state of the irradiated material differs from the initial one [1–9]. This feature has been exploited to obtain new materials with enhanced properties.

Some materials such as polymers, biopolymers, and biological systems are extremely sensitive to irradiation [1–10]. In order to protect the polymeric chain and to increase its lifetime low molecular compounds such as antioxidants, UV stabilizers, and fillers are dispersed within commercially available polymers [4–9]. In such polymers, the degradation processes are retarded as long as the stabilizers and/or the antioxidants are not exhausted. A detailed knowledge of degradation processes in pristine and stabilized polymers and of the procedures necessary for the accurate estimation of their lifetime is required to asses the functionality of polymeric materials in different environments. The radiation environment triggers and/or amplifies degradation processes in polymers. A classical example is Teflon (polytetrafluoroethylene, or PTFE), which exhibits an outstanding thermal stability in air [4–10]. Teflon is sensitive to incoming radiation, which ionizes the macromolecular chain and produces free radicals [4–10]. If the irradiation of Teflon is carried out in air or oxygen atmosphere, the radiation-induced radicals initiate an autoaccelerated oxidation of the macromolecular chain that results in a catastrophic destruction [4–10]. In this case, the radiation triggers the oxidative degradation process. Frequently, polymeric materials are subjected to several competing degradation processes induced by radiation, temperature, mechanical stresses, and oxygen. In thick samples of Teflon irradiated in air, at room temperature with gamma rays, an inhomogeneous degradation process has been reported [4–10]. This has been proved by electron spin resonance (ESR). The external shell of the irradiated cylindrical sample is responsible for a slightly asymmetric ESR spectrum, due to peroxy radicals, while the core of the sample presents a weak peroxy-like signal superimposed over a resonance spectrum with an incompletely resolved hyperfine splitting assigned to the primary radical [10]. The computer simulation of the resonance spectrum is consistent with the appearance of $\bullet CF_2$-radicals, indicating the high lability to radiation of the C—C bond in fluorinated polymers see Fig. 3 [10].

The oxygen affects significantly the behavior of polymeric materials subjected to irradiation. Oxygen itself is capable of reacting with the polymeric chain producing labile compounds as hydroperoxides (ROOH) and with primary radicals ($\bullet R$), shifting the equilibrium between cross-linking and scission reactions towards scission reactions [4–10]. The competition between oxidative degradation and radiation-induced degradation of polymers presents frequent deviations from a simple addition of effects [4–8]. Nonlinear effects are induced by the inhomogeneous degradation of bulk polymers subjected to both irradiation and oxygen attack, at low temperatures [6–8]. This effect is due to the low mobility of the macromolecular chains, which hinders the oxygen diffusion. In such cases, the diffusion process—which is the slowest step—controls the overall degradation process. Raising the polymer temperature

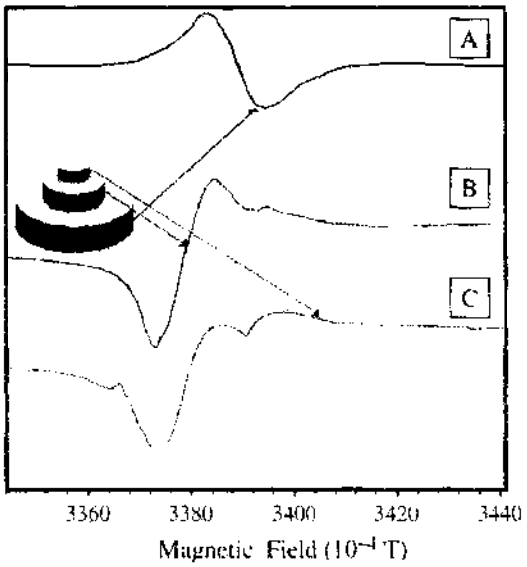

Figure 3. The inhomogeneous degradation of Teflon, as revealed by electron spin resonance. It is observed that the resonance spectrum of the core of the sample shows an incompletely resolved hyperfine structure due to the interaction of the uncoupled electronic spin with the nuclear spin of fluorine.

above T_G, the segmental motions are activated, resulting in an increase of the oxygen diffusion constant with several orders of magnitude. This converts the inhomogeneous oxidation of the sample into an homogeneous oxidation. The behavior of polymers subjected to radiation is complex. Under the effect of the incident ionizing radiation, the average molecular weight of the pristine polymer is changed [4–8]. This triggers a change of most physical properties (glass transition temperature, melting temperature, mechanical properties, electrical conductivity, and thermal conductivity) [11–14]. This "new polymer" obtained after an infinitesimal irradiation of the target has a different behavior to ionizing radiation. Accordingly, the subsequent irradiation will induce slightly different chemical and physical modification. To conclude, it is possible to imagine the polymer subjected to ionizing radiation as a small and extremely simple living cell (see Fig. 4.); the physical and chemical properties of the polymer are continuously modified by the incoming radiation and as a feedback to this stimulus the extend of radiation-induced damage within the polymer is continuously adjusted.

Radiation-induced modifications of materials are mixing several ideal (pure) types of irradiation. There are four theoretical limits for a material subjected to irradiation, namely:

1. The electronic limit, which describes a pure electronic irradiation.
2. The nuclear limit, which describes the modifications induced by direct interactions (collisions) with the nuclei of the target.
3. The spin-spin limit controlled by the interactions between the spins of incoming particles and the spin of the target.
4. The electromagnetic limit that describes the behavior of the target subjected to electromagnetic radiation (as long as ionizing processes are assumed negligible).

In certain cases, the irradiation of the target produces a significant increase of the sample temperature that may enhance the radiation-induced degradation of the target. For charged impinging particles, the radiation-induced modifications of the target are controlled by the electronic and nuclear limits. At high incoming velocities, the interaction between incident charged particles and target is dominated by the electronic limit, while at low kinetic energies (near the end of the projected trajectory within the target) the nuclear limit may represent an important contribution (even the largest one for heavy incident particles). The rapid development of spintronics requires a careful investigation of the consequences of spin-spin interaction, mainly due to the neutron background at the earth level.

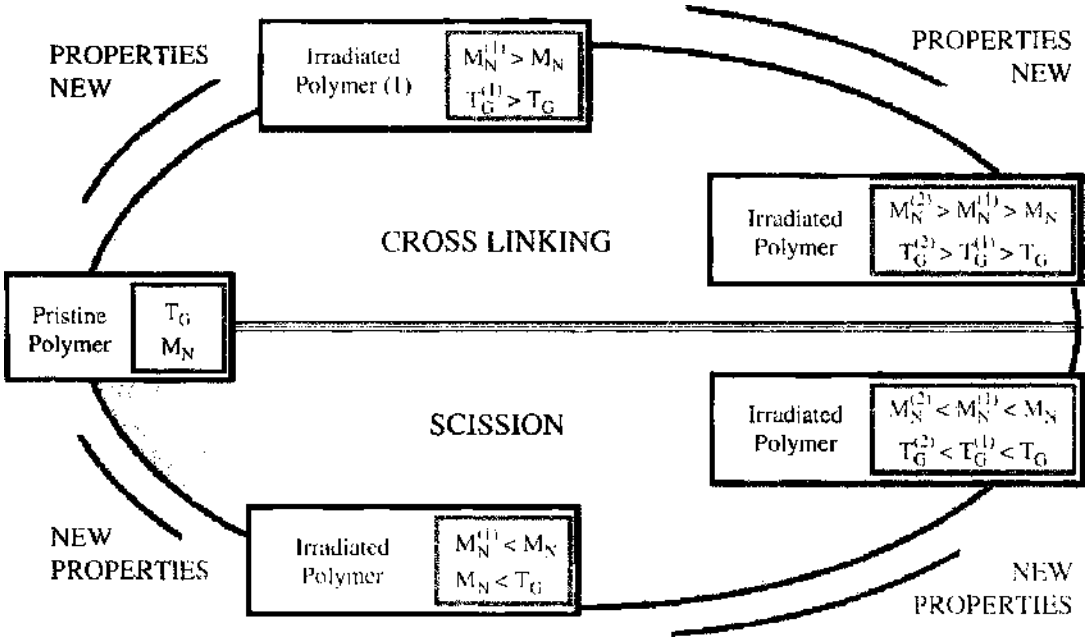

Figure 4. The continuous modifications induced by the incident radiation in polymers suggests an analogy with a living cell.

The recent discovery of nanomaterials and nanocomposites pushed further the studies of radiation-induced modifications of materials. Although the interaction between the incident radiation and the atoms of the nanomaterials are rather well understood and known, new aspects triggered from the nanometer-sized confinement are expected. Among them, the most important one is the general expectation that nanomaterials are more sensitive to radiation than bulk materials [15]. This is explained by the effect of the nanometer size confinement on the electronic properties of the nanomaterial. The simplest effect of electrons confinement is the shift of their energy levels as the size of the confinement is reduced at nanometer scale [16–18].

The goal of this review is to define the rudiments required to understand the interaction of the radiation with the matter and to analyze the state of arts in the theoretical and experimental study of the interaction between nanomaterials and radiation.

1.1. The Interaction of Radiation with Condensed Matter: Introductory Remarks

In the general case, the term *radiation* includes both accelerated particles and electromagnetic radiation. Some accelerated particles such as electrons, protons, and ions are charged. In most cases, the electrons of incoming ions are striped (partially or completely). Certain incident particles possess a spin (such as neutrons, protons, and electrons), whereas others have no spins. For simplicity, the term charged particle will specify a completely ionized (all electrons removed) atom with no nuclear spin. The interaction of the radiation with condensed targets results in modifications of the physical and chemical properties of the target. Hereafter the term target will identify a condensed material. The modifications induced by the incident radiation are a direct consequence of the energy deposited by the incident radiation within the target. As it is shown in Figs. 1. and 2, the deposition of the energy within the target starts with the excitation and ionization of target's atoms or molecules. The modification of the physical and chemical properties of the target results from two main contributions:

1. Primary radiation effects, that is, the physical and chemical modifications produced within the target by the energy deposited solely by the impinging radiation.
2. Secondary effects, which include physical and chemical modifications resulting from the energy deposited within the target by the radiation (either particles or electromagnetic radiation), resulted from the interaction of the incident radiation with the target. This self-irradiation of the target due to highly energetic incident radiation may have a significant contribution to the overall radiation-induced degradation. An important result of secondary effects consists in the delocalization of the energy deposited by the incoming radiation within the target (reduced the energy density). The most known contribution is represented by secondary electrons (or δ electrons) [1–3].

The impinging radiation may produce within targets two main types of defects:

1. Localized defects, that is, defects confined at sub-nanometer scale such as vacancies, interstitials, color centers, or free radicals [1–10].
2. Cooperative (or extended) defects such as cascades or latent tracks [1–3]. In certain cases, such defects are observed and nanometer and micron scales.

The incident particle interacts with the target through three main modes, direct collisions, electromagnetic interactions, and spin interactions. The fast deceleration of the impinging particles within the target may be responsible for an additional Bremsstrahlung contribution.

1.2. One-Dimensional Two-Particle Collision

The interaction between an incoming particle and the target may be modeled as a collision between the incident particle and the atoms of the target. During the collision between two particles, both the momentum and angular momentum are conserved [19–20]. The angular momentum conservation is important solely if at least one of the particles involved in the collision has a finite size. The analysis of the collision process will be done assuming that the

interacting particles may be assimilated with dimensionless points (no angular momentum conservation is required for such collisions). The energy of the ensemble of interacting particles is conserved (before and after collision) solely in elastic collisions. The simplest collision process is the one-dimensional collision of two particles. For simplicity, this process will be shortly analyzed supposing that the two particles are two points to which the masses M_1 and M_2 have been attached. The one-dimensional character of the collision forces all collisions to be head-on collisions.

1.2.1. The Elastic One-Dimensional Collision

The direct scattering of an incident particle with the atoms (nuclei) of a target may be easily understood within the classical mechanics framework. The elastic collision of two particles characterized by the masses M_1, M_2, and the speeds V_1, V_2 relative to a coordinates system imposes the conservation of both momentum and kinetic energy (see Fig. 5).

$$\begin{aligned} M_1\vec{V}_1^{\,\mathrm{IN}} + M_2\vec{V}_2^{\,\mathrm{IN}} &= M_1\vec{V}_1^{\,\mathrm{OUT}} + M_2\vec{V}_2^{\,\mathrm{OUT}} \\ \frac{M_1(\vec{V}_1^{\,\mathrm{IN}})^2}{2} + \frac{M_2(\vec{V}_2^{\,\mathrm{IN}})^2}{2} &= \frac{M_1(\vec{V}_1^{\,\mathrm{OUT}})^2}{2} + \frac{M_2(\vec{V}_2^{\,\mathrm{OUT}})^2}{2} \end{aligned} \tag{1}$$

where the superscripts IN and OUT denote incoming and out coming velocities, respectively. For simplicity, it is assumed that the second particle is at rest before the collision with the incoming particle 1. The energy $\Delta E_K^{(\mathrm{El})}$ transferred from the impinging particle during the elastic collision is

$$\Delta E_K^{(\mathrm{El})} = \frac{2M_1^2M_2}{(M_1+M_2)^2}(\vec{V}_1^{\,\mathrm{IN}})^2 \tag{2}$$

The fraction of free energy transferred from incoming particle in an elastic one-dimensional collision is

$$\frac{\Delta E_K^{(\mathrm{El})}}{E_K^{\mathrm{IN}}} = \frac{4M_1M_2}{(M_1+M_2)^2} = 4\mu \tag{3}$$

where μ is the reduced mass of the two-particles system.

From Eq. (3) it is observed that $\Delta E_K^{(\mathrm{El})}/E_K^{\mathrm{IN}}$ depends only on the mass of the interacting particles and not on the speed of the incoming particles. This conclusion is fair at relatively low velocity. The classical description of the collision between two particles is oversimplified. A real collision develops in a three dimensional space and the finite non-zero size of the interacting particles requires additionally the angular momentum conservation (before and after the collision).

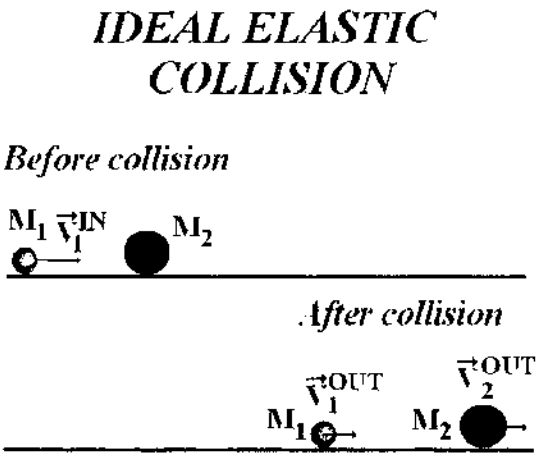

Figure 5. The ideal one-dimensional elastic collision of two particles.

The relativistic analysis of such a collision results in a more complex expression of the energy transfer that contains the dependence of the fraction of the transferred energy on the speed of the incoming particle [21].

$$\Delta E_K^{(\mathrm{EL})\mathrm{REL}} = \frac{2(1-(V/c)^2)M_2V^2}{1+(M_1/M_2)^2+2(M_1/M_2)\sqrt{(1-(V/c)^2)}} \tag{4}$$

where V is the velocity of the incoming particle 1 while the second particle is assumed fixed.

1.2.2. The Plastic One-Dimensional Collision

In inelastic collisions, only the momentum of the particles involved in the collision is conserved. The extreme case of an inelastic collision is represented by the plastic collision. After such a collision, the two particles coalesce into a single particle (see Fig. 6.) and $V_1^{\mathrm{OUT}} = V_2^{\mathrm{OUT}} = V^{\mathrm{OUT}}$. A part of the kinetic energy of the incoming particle is converted into heat. The energy transferred from the impinging particle M_1 during a plastic collision, $\Delta E_K^{(\mathrm{PI})}$ is

$$\Delta E_K^{(\mathrm{PI})} = \frac{M_1M_2}{(M_1+M_2)^2}(M_2+2M_1)(\vec{V}_1^{\mathrm{IN}})^2 \tag{5}$$

The fraction of the incoming particle energy that is transferred either as kinetic energy of the second particle or to various heating processes during a plastic collision is

$$\frac{\Delta E_K^{(\mathrm{PI})}}{E_K^{\mathrm{IN}}} = \frac{2M_2(M_2+2M_1)}{(M_1+M_2)^2} = 4\mu_r + 2\left(\frac{M_2}{M_1+M_2}\right)^2 \tag{6}$$

As expected, in the plastic collision a larger amount of energy is transferred from the incoming particle than in an elastic collision [compare Eqs. (3) and (6)]. The fraction of kinetic energy transferred from the incident particle depends solely on the mass of the two interacting particles and not on the speed of the incoming particle. This simple classical description depicts qualitatively what is happening during the interaction of a particle with a target. In the real case, the actual interaction between the incoming particle and the target is well described by theoretical models based on quantum mechanics [17, 18, 22–24].

1.3. Two-Dimensional Two-Particle Collision

In order to derive the classical expression of the cross-scattering, the two-dimensional collision between two particles will be analyzed. For simplicity, only head-on collisions will be considered. The collision process may be described within different frames (reference systems). The most important are the laboratory and the center of mass frames.

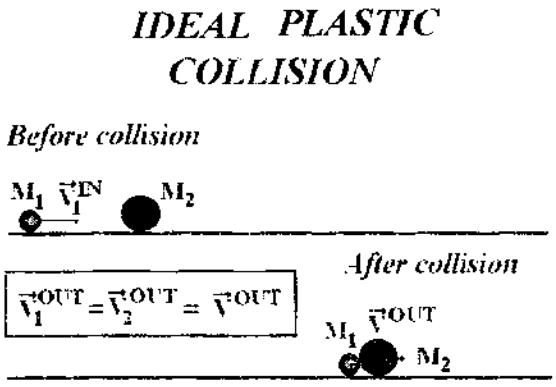

Figure 6. The ideal one-dimensional plastic collision of two particles.

1.3.1. The Laboratory Frame

The collision between two particles of masses M_1 and M_2 is shown in Fig. 7. In the laboratory frame, the particle 1 is directed toward the second particle, which is assumed fixed. After collision, the incoming particle will be scattered at an angle φ_2 relative to its initial direction, while the particle M_1 will be ejected at an angle φ_1 relative to the initial direction of the incoming particle. In the laboratory frame V_1^{IN} and V_2^{IN} are the velocities of the particles 1 and 2 before collision and V_1^{OUT} and V_2^{OUT} are the velocities of the two particles after collision. In the laboratory frame $V_2^{IN} = 0$ (see Fig. 7).

1.3.2. The Center of Mass Frame

The position of the center of mass R_{CM}, for an ensemble of two particles of masses M_1 and M_2 described by the position vectors R_1 and R_2 is defined by [19–21, 25]:

$$\vec{R}_{CM} = \frac{M_1\vec{R}_1 + M_2\vec{R}_2}{M_1 + M_2} \tag{7}$$

The internal and external forces acting on each particle, F_j^{INT} and F_j^{EXT} $(j = 1, 2)$ are connected with the time evolution of the position vectors of the two particles according to the second law of dynamics

$$\frac{d^2\vec{R}_1}{dt^2} - \frac{d^2\vec{R}_2}{dt} = \frac{\vec{F}_1^{EXT} + \vec{F}_1^{INT}}{M_1} - \frac{\vec{F}_2^{EXT} + \vec{F}_2^{INT}}{M_2} \tag{8}$$

where d^2R_1/dt^2 and d^2R_2/dt^2 define the acceleration of the first and second particle, respectively. The (internal) forces that are acting on the first particle come for the second particle

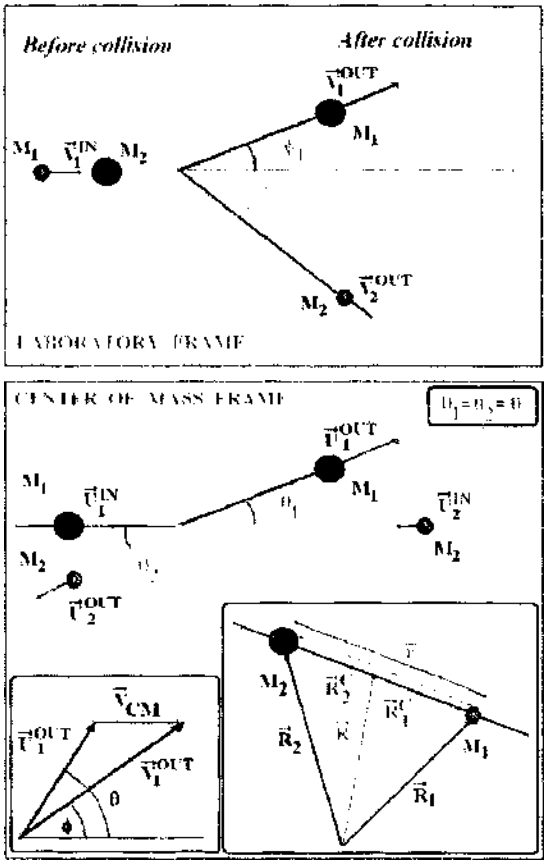

Figure 7. The two-dimensional collision of two particles. The upper panel describes the collision in the laboratory frame, andthe bottom panel depicts the collision in the center of mass frame.

($F_1^{INT} = -F_2^{INT} = F$), and $R_1 - R_2 = r$. Assuming the absence of external forces is obtained,

$$\frac{d^2\vec{r}}{dt^2} = \frac{\vec{F}}{M_1} + \frac{\vec{F}}{M_2} = \mu\vec{a} \tag{9}$$

where a is the acceleration in the center of mass system and μ is the reduced mass [see Eq. (9)]. In the center of mass frame, the velocities U_1 and U_2 of the two particles are defined by the first derivative of the position vectors R_1^C and R_2^C. From Fig. 7. (or from the relationship $r = R_1^C - R_2^C$ and the center of mass definition) is obtained:

$$\begin{aligned} \vec{R}_1^C &= \frac{\mu}{M_1}\vec{r} \\ \vec{R}_2^C &= -\frac{\mu}{M_2}\vec{r} \end{aligned} \tag{10}$$

The velocities of the two particles relative to the center of mass are obtained by the derivation of Eq. (10) with respect to the time

$$\begin{aligned} \vec{U}_1 &= \frac{d\vec{R}_1^C}{dt} = \frac{\mu}{M_1}\vec{V}_{CM} \\ \vec{U}_2 &= -\frac{d\vec{R}_2^C}{dt} = -\frac{\mu}{M_2}\vec{V}_{CM} \end{aligned} \tag{11}$$

In the center of mass frame, the initial velocities of the incoming particles are U_1^{IN} and U_2^{IN}, and the final velocities (after collision) of the out coming particles are U_1^{OUT} and U_2^{OUT}. The center of mass frame has a drift motion relative to the laboratory system with a velocity equal to V_{CM}. The relation between the velocity of each particle in the laboratory and center of mass frame is:

$$\begin{aligned} \vec{U}_1^{OUT} &= \vec{V}_1^{OUT} + \vec{V}_{CM} \\ \vec{U}_2^{OUT} &= \vec{V}_2^{OUT} + \vec{V}_{CM} \end{aligned} \tag{12}$$

where V_1^{OUT} and V_2^{OUT} are the velocities of the two particles in the laboratory frame. The relationship between the two reference frames is shown in Fig. 7. In the center of mass frame due to the momentum conservation law, the particle of mass μ is moving freely with the same speed before and after collision. Actually, the velocities for the two-particle system are given by Eq. (12). Projecting the speed of the particle 1 after collision on two orthogonal axes is obtained (see Fig. 7)

$$\begin{aligned} V_1^{OUT}\sin\phi_1 &= U_1^{OUT}\sin\theta \\ V_1^{OUT}\cos\phi_1 &= U_1^{OUT}\cos\theta + V_{CM} \end{aligned} \tag{13}$$

Owing to the law of momentum conservation, the momentum of the two particle systems before collision $M_1V_1^{IN}$ should be the same as the momentum of the two particles after collision (assuming that the two particles are moving as a single body of mass μ, with the speed V_{CM})

$$V_{CM} = \frac{M_1}{M_1 + M_2}\vec{V}_1^{IN} \tag{14}$$

The center of mass frame allows the reduction of a collision between two particles to the evolution of a single particle projected over a potential $V(r)$. The mass of this equivalent particle is equal to the reduced mass. The physics in the center of mass frame is simpler as the momentum conservation implies a free motion of the equivalent particle.

1.3.3. The Classical Expression of the Cross Section

Let us assume two hard spherical particles of masses M_1 and M_2 and of radius r_1 and r_2. If the particle M_2 is directed toward M_1, in order to have a collision between the two particles it is necessary that the perpendicular distance b between these particles to be smaller than

the sum of the radii of the two particles (see Fig. 8). The parameter b that describes the collision is named impact parameter. Each pair incident particle-target particle will generate a circular area S_C.

$$S_C = \pi(r_1 + r_2)^2 \tag{15}$$

The collision probability for an incident particle that is directed toward a target of area S is equal with the ratio between S_C and S. In the hard sphere approximation, the parameter $(r_1 + r_2)$ is named collision parameter (see the top panel in Fig. 8). It is important to mention that neither the parameter b nor the radii r_1 and r_2 represent the actual size of colliding particles. In the interaction between two particles of the same charge, even if point-like particles are considered, the electrostatic interaction will prevent the contact of the two particles. In this case, the parameter b is the smallest distance between the two particles.

The impact parameter may be used to define the angular momentum of the incoming particle, L^{INC}:

$$|\vec{L}^{INC}| = L^{INC} = mV_1^{IN}b \tag{16}$$

Within the classical mechanics approximation, L^{INC} may be expressed as [19–21]

$$L^{INC} = b\sqrt{2M_1E} \tag{17}$$

where E is the kinetic energy of the incoming particle. The angular momentum is conserved during the collision, that is,

$$L^{INC} = L^{OUT} \tag{18}$$

To conclude, the cross section is a hit area; any particle that hits the cross section is subjected to a collision while if the incident particle is not hitting this area no collision occurs. In the general case, there are several incoming particles, N_P, directed toward the target. The probability of a scattering event is defined as the ratio between the number of particles that hit the cross section (are scattered by the target), dN_P, and the total number of incoming particles. This probability is equal to the ratio between the area of the cross section and the total area of the incoming beam. If the target consists of n atoms per unit volume and has a thickness x, the total cross section for collision will be obtained by multiplying the cross section defined for a single target atom with the total number of scattering centers (atoms). Hence, the scattering probability P_S may be expressed as [19–21, 25]

$$P_S = -\frac{dN_P}{N_P} = \frac{(nS\,dx)\sigma}{S} = n\sigma\,dx \tag{19}$$

where S is the area of the target. The total number of scattered particles, N_{SC}, is

$$N_{SC} = N_P(1 - e^{-n\sigma x}) \tag{20}$$

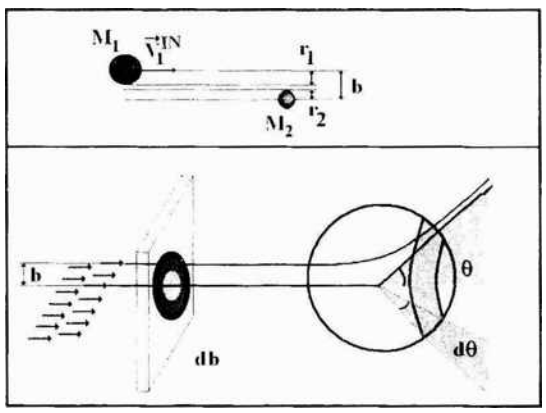

Figure 8. An oversimplified definition of the impact parameter (top panel). The relationship between the impact parameter of the incident particle and its deflection angle is shown in the bottom panel.

If the target consists of k different atoms of isotopes $n_1, n_2, \ldots n_k$, each of them characterized by the cross sections $\sigma_1, \sigma_2, \ldots \sigma_k$, the total cross section of the target, σ_T will be [21, 25]

$$\sigma = \frac{\sum_{i=1}^{n} \sigma_i n_i}{\sum_{i=1}^{n} n_i} \tag{21}$$

The cross section is an area that expresses how many incident particles are colliding with the atoms of the target. Usually it is a rather small number of the order 10^{-25} to 10^{-30} m^2. The cross section in atomic and nuclear physics is frequently expressed in barns (1 barn = 10^{-28} m^2).

In three dimensions, the number N of particles that are scattered in a solid angle $d\Omega = \sin\theta\, d\theta\, d\varphi$ around the direction defined by the angles θ and φ, per unit time is [19–25]:

$$dN = J\sigma(\theta, \varphi)d\Omega \tag{22}$$

where θ is the angle between the direction of the scattered particle and the incidence direction (scattering angle) and J is the flux of impinging particles (intensity of the incoming particles, that is, the number of particles that are crossing a surface normal to the incident beam directions, of unit area, in a second). In conclusion,

$$\sigma(\theta, \varphi) = \frac{1}{J}\frac{dN}{d\Omega} \tag{23}$$

The total cross section σ_T is obtained by integrating the cross section over all angles (θ and φ)

$$N^{\text{TOTAL}} = J \int \sigma(\theta, \varphi)d\Omega \equiv J\sigma_T \tag{24}$$

The total cross section defines the total number of particles scattered per time unit. There is a strong relationship between the cross section and the impact parameter because the fraction of incoming particles scattered within a solid angle $d\Omega$ defined between θ and $\theta + d\theta$ has to be equal to the number of particles with the impact parameter ranging between b and $b + db$ (see the bottom panel of Fig. 8).

For nonpolarized beams and targets, this is expressed by the relationship

$$dN = JdA = 2\pi Jb|db| = 2\pi J\frac{b}{\sin\theta}\left|\frac{db(\theta)}{d\theta}\right|d\Omega \tag{25}$$

If the target contains K scattering (atomic or nuclear centers) the expression (25) becomes

$$dN = JKdA = 2\pi KJb|db| = 2\pi KJ\frac{b}{\sin\theta}\left|\frac{db(\theta)}{d\theta}\right|d\Omega \tag{26}$$

For simplicity it is assumed that $K = 1$. This leads to the following alternative expression for the cross section [19–21, 25]

$$\sigma(\theta) = \frac{b}{\sin\theta}\left|\frac{db}{d\theta}\right| \tag{27}$$

The differential cross section $d\sigma(\Omega)/d\Omega$ defines the total number of incoming particles that scattered per unit solid angle Ω. The relationship between the (total) cross section and the differential cross section is [25]

$$\sigma = \int_0^{2\pi} d\phi \int_0^{\pi} \frac{d\sigma(\theta, \phi)}{d\Omega} \sin\theta\, d\theta \tag{28}$$

When the target and the incident beam are not polarized, the differential section is independent of φ (all directions are equivalent)

$$\sigma = 2\pi \int_0^{2\pi} \frac{d\sigma(\theta)}{d\Omega} \sin\theta\, d\theta \tag{29}$$

The parameter b hides the details of the potential. This will be discussed in the next section for a Coulomb scattering. The differential cross section as defined within this paragraph is the differential angular cross section. It is also possible to define a differential energy cross section, which reflects the probability of collisions that transfers energies ranging between E and $E + dE$.

1.3.4. The Rutherford Model

One of the simplest collision processes in classical mechanics is represented by the interaction between an incoming particle of mass M, and velocity V^{IN} with a heavy particle. Such a process has been analyzed by Rutherford, in connection with a simple model of atom. In this case, the target is represented by a fixed particle of charge $Z_1 e$ while Ze is the charge of the incoming particle. At large distances from the collision center, the collision is characterized by the impact parameter b. The two particles (incident particle and nucleus) interact through electrostatic (Coulomb) forces

$$F = \frac{Z_1 Z e^2}{4\pi\varepsilon_0 r^2} \tag{30}$$

where ε_0 is the vacuum permittivity and r is the distance between the target and the incident particle. Before and after the collision, at far distances from the collision center ($r \to \pm\infty$), the force exerted on the incoming particles becomes almost zero and the particle moves (freely) with a constant velocity. Assuming that the collision is elastic and that the nucleus is fixed before and after collision, the energy conservation law requires

$$\frac{M(V^{IN})^2}{2} = \frac{M(V^{OUT})^2}{2} \tag{31}$$

The angular momentum conservation before and after collision imposes

$$MV^{IN}b^{IN} = MV^{OUT}b^{OUT} \tag{32}$$

where b^{IN} is the impact parameter associated to the trajectory of the incoming particle and b^{OUT} is the impact parameter of the particle after collision. It is observed that such an elastic collision implies $V^{IN} = V^{OUT}$ and $b^{IN} = b^{OUT} = b$. According to Newton's law, the time evolution of the impinging particle is described by [19–21]

$$\frac{ZZ_1 e^2}{4\pi\varepsilon_0 r^2} = M\left[\left(\frac{d^2\vec{r}}{dt^2}\right) - r\left(\frac{d\phi}{dt}\right)^2\right] \tag{33}$$

The first term in the bracket represents the change in the speed of the trajectory along the radius (radial linear acceleration), while the second one is responsible for the curvature of the trajectory representing the centripetal force acting on the particle. By making the substitution $w = r^{-1}$, the equation that describes the time evolution of the impinging particle becomes

$$\frac{d^2w}{d\varphi^2} + w + \frac{ZZ_1 e^2 MV^2}{16\pi\varepsilon_0 b^2} = 0 \tag{34}$$

To estimate the constants included in the solution of this equation it is necessary to analyze the initial conditions. For Coulomb scattering the collision angle ϕ before collision is almost zero. This results in the following relation [19, 20]

$$\frac{1}{r} = \frac{1}{b}\sin\phi + \frac{ZZ_1 e^2 MV^2}{16\pi\varepsilon_0 b^2}(\cos\phi - 1) \tag{35}$$

The scattering angle θ is defined by [19].

$$\theta = \pi - \phi \tag{36}$$

The expressions of the impact parameter b for a Coulomb scattering and for a classical collision are

$$b = \begin{cases} \dfrac{Z_1 Z e^2}{16\pi\varepsilon_0^2 (MV^2/2)} \cot(\theta/2) & \text{for } U \propto \dfrac{Z_1 Z_2}{r} \\ \dfrac{K}{\mu V_{CM}^2} \cot(\theta/2) & \text{for } U \propto \dfrac{k}{r} \end{cases} \tag{37}$$

The cross section for the interaction between an incoming particle of energy $E = MV^2/2$, charge Z_1 and the target ionic moieties characterized by the electric charge Z_2 is

$$\frac{d\sigma(\theta)}{d\Omega} = \left(\frac{Z_1 Z e^2}{8\pi\varepsilon_0 MV^2}\right)^2 \frac{1}{\sin^4(\theta/2)} \tag{38}$$

This defines mathematically the Rutherford formula for Coulomb-like potentials. If the nucleus is not fixed and its mass (M_2) is not very large in comparison with the mass of the impinging particle M_1, the expression becomes [19, 20]

$$\frac{d\sigma(\theta)}{d\Omega} = \left(\frac{Z_1 Z e^2}{8\pi\varepsilon_0 M_1 V^2}\right)^2 \left(\frac{M_1 + M_2}{M_2}\right) \frac{1}{\sin^4(\theta/2)} \tag{39}$$

The Coulomb cross section depends on the charge and mass of the incident particle and of the target. It decreases as the speed of the incoming particle is increased. The Coulomb cross section depends on the reduced mass of the incoming particle-target atom system.

1.3.5. Rudiments of Quantum Collision Theory

In quantum mechanics, the evolution of a free particle is described by its wave function. For a given Hamiltonian, there are some characteristics wave functions and energy levels. In the simple case of a plane wave function, $\psi(\psi = C_1 e^{iKr}$, where C_1 is a constant, K is the wave vector and r the distance), the normalization condition imposes [16–18, 23–25]

$$P(r, t) = \int_{V_C} \psi^* \psi \, d\vec{r} = |C_1^2| \leq 1 \tag{40}$$

Such a wave function has an unit density, and C_1^2 represents the probability to find the particle confined within a volume V_C. The time evolution of the probability to find a quantum particle within this volume is [16]

$$\frac{\partial P(r, t)}{\partial t} = \int_{V_C} \left(\frac{\partial \psi^*}{\partial t}\psi + \psi^* \frac{\partial \psi}{\partial t}\right) d\vec{r} \tag{41}$$

By using the Green theorem, we obtain

$$\frac{\partial P(r, t)}{\partial t} = \frac{i\hbar}{2m} \int_A [\psi^* \nabla\psi - (\Delta\psi^*)\psi]_N \, dA \tag{42}$$

where A is the bounding area of the integration volume V_C and N identifies the direction of components between brackets (normal outward to the surface element A). In conclusion, if no particles are generated or destroyed within V_C, then the flow of particles through this volume is described by

$$\frac{\partial P(r, t)}{\partial t} + \vec{\nabla}\vec{S}(r, t) = 0 \tag{43}$$

with

$$S(r, t) = \frac{i\hbar}{2m}[\psi^* \nabla\psi - (\Delta\psi^*)\psi] = \mathrm{Re}\, \psi^* \left[\frac{\hbar}{im}(\psi^* \nabla\psi)\right] \tag{44}$$

$S(r, t)$ defines the probability current density, that is, the probability that a particle will crosses the area A in one second. For a plane wave $[\psi = C_1 \exp(ikr)]$, the expression of the probability current density is [16–18, 22–25]

$$S(r, t) = \frac{i\hbar}{2m}[\psi^* \nabla\psi - (\Delta\psi^*)\psi] = \frac{k\hbar}{m}|C|^2 \tag{45}$$

From the quantum mechanical point of view, the collision process is described within the center of mass frame, by the scattering of a particle characterized by the mass μ and velocity $\mathbf{V}_{CM}$ on a potential $U(r)$. The corresponding quantum mechanical problem is defined in a first approximation by the time independent Schrödinger equation:

$$-\frac{\hbar^2}{2\mu}\frac{\partial^2\psi_K(\vec{r})}{\partial r^2} + U(\vec{r})\psi_K(\vec{r}) = E\psi_K(\vec{r}) \tag{46}$$

The incoming particle has the energy E, the momentum $\boldsymbol{p} = m\boldsymbol{V} = \hbar\boldsymbol{k}$. Its evolution is described by the wave function ψ.

1.3.5.1. The One-Dimensional Collision The one-dimensional collision of a particle with a potential barrier $U(x)$ is a simple quantum mechanical problem capable of showing the most important elements of the collision process. The incoming particle moves freely (no accelerate) along the OX axis and interacts with the potential barrier placed in the origin of the reference frame (see Fig. 9.). The Schrödinger equation associated to this problem is a simplified version of the Eq. (46)

$$-\frac{\hbar^2}{2\mu}\frac{\partial^2\psi_K(x)}{\partial x^2} + U(x)\psi_K(x) = E\psi_K(x) \tag{47}$$

For the potential shown in Fig. 9. the expression (45) becomes

$$\begin{aligned}
-\frac{\hbar^2}{2\mu}\frac{\partial^2\psi_K(x)}{\partial x^2} &= E\psi_K(x) \quad \text{for } x \le 0 \\
-\frac{\hbar^2}{2\mu}\frac{\partial^2\psi_K(x)}{\partial x^2} &= (E-U)\psi_K(x) \quad \text{for } 0 \le x \le a \\
-\frac{\hbar^2}{2\mu}\frac{\partial^2\psi_K(x)}{\partial x^2} &= E\psi_K(x) \quad \text{for } x \ge a
\end{aligned} \tag{48}$$

where U is the height of the potential barrier and a the width of the potential barrier. The general expression of the wave function of the incident particle, assuming that the potential barrier U is higher than the kinetic energy of the incoming particle, E, is

$$\psi_K(x) = Ae^{ikx} + Be^{-ikx} \tag{49}$$

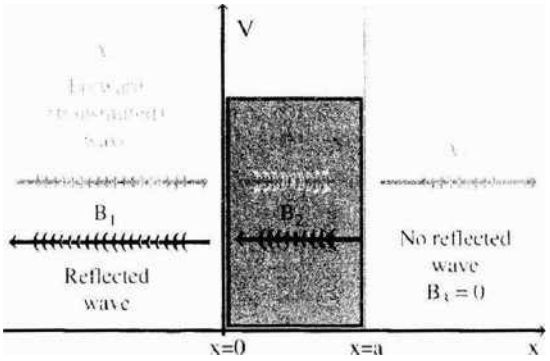

Figure 9. The one-dimensional collision of two particles in the center of mass frame, within the nonrelativistic, time-independent quantum mechanical approximation.

where k is the momentum of the particle, Ae^{ikx} describes the wave assigned to the out coming particle (that is moving in the positive x direction) and Be^{-ikx} the wave that defines the reflected particle (that is moving in the negative x direction. By introducing the solution into the Schrödinger equation, we obtain

$$\begin{aligned}
&\frac{\hbar^2}{2\mu}(A_1e^{ik_1x} + B_1e^{-ik_1x})k_1^2 = E(A_1e^{ik_1x} + B_1e^{-ik_1x}) \quad \text{for } x \le 0\\
&\frac{\hbar^2}{2\mu}(A_2e^{ik_2x} + B_2e^{-ik_2x})k_2^2 = (E - V)(A_2e^{ik_2x} + B_2e^{-ik_2x}) \quad \text{for } 0 \le x \le a\\
&\frac{\hbar^2}{2\mu}(A_3e^{ik_3x} + B_3e^{-ik_3x})k_3^2 = E(A_3e^{ik_3x} + B_3e^{-ik_3x}) \quad \text{for } x \ge a
\end{aligned} \tag{50}$$

where indices 1, 2, and 3 define the three domains shown in Fig. 9. The values of the momentum k in the three regions are

$$\begin{aligned}
k_1 &= \frac{\sqrt{2\mu E}}{\hbar} \quad \text{for } x \le 0\\
k_2 &= \frac{\sqrt{2\mu(U - E)}}{\hbar} \quad \text{for } 0 \le x \le a\\
k_3 &= \frac{\sqrt{2\mu E}}{\hbar} \quad \text{for } x \ge a
\end{aligned} \tag{51}$$

To estimate the values of the coefficients A_1, A_2, A_3, B_1, B_2, and B_3, it is necessary to impose the continuity condition for the wave function ψ and its derivative $d\psi/dx$ in the points of coordinates $x = 0$ and $x = a$.

$$\begin{aligned}
A_1e^{ik_1x} + B_1e^{-ik_1x} &= A_2e^{ik_2x} + B_2e^{-ik_2x} \quad \text{for } x = 0\\
ik_1A_1e^{ik_1x} - ik_1B_1e^{-ik_1x} &= ik_2A_2e^{ik_2x} - ik_2B_2e^{-ik_2x} \quad \text{for } x = 0\\
A_2e^{ik_2x} + B_2e^{-ik_2x} &= A_3e^{ik_3x} + B_3e^{-ik_3x} \quad \text{for } x = a\\
ik_2A_2e^{ik_2x} - ik_2B_2e^{-ik_2x} &= ik_3A_3e^{ik_3x} - ik_3B_3e^{-ik_3x} \quad \text{for } x = a
\end{aligned} \tag{52}$$

This equation may be further simplified by observing that in the third region, characterized by $x > a$ there is no reflected wave. This implies $B_3 = 0$

$$\begin{aligned}
A_1 + B_1 &= A_2 + B_2\\
k_1A_1 - k_1B_1 &= k_2A_2 - k_2B_2\\
A_2e^{ik_2a} + B_2e^{-ik_2a} &= A_3e^{ik_3a}\\
k_2A_2e^{ik_2a} - k_2B_2e^{-ik_2a} &= k_3A_3e^{ik_3a}
\end{aligned} \tag{53}$$

For $x < 0$, the probability current density, J_1^{IN}, for the incident wave is

$$J_1^{IN} = \frac{\hbar K_1}{\mu}(A_1A_1^*) \tag{54}$$

For the reflected wave, the probability current density, J_1^R, is

$$J_1^R = \frac{\hbar K_1}{\mu}(B_1B_1^*) \tag{55}$$

The net probability current density in the domain 1, J_1, is

$$J_1 = J_1^{IN} - J_1^R = \frac{\hbar K_1}{\mu}(A_1A_1^* - B_1B_1^*) \tag{56}$$

For $x > 0$, the probability current density, J_3, for the emerging wave is

$$J_3 = \frac{\hbar K_3}{\mu}(A_3 A_3^*) \tag{57}$$

The scattering of the incident particle is described by the transmission of the current probability density through the potential barrier, T [16–18, 22–24]:

$$T = \left(\frac{J_3}{J_1^{\text{IN}}}\right)^2 = \frac{1}{1 + V^2[\sinh(a\sqrt{2\mu(U-E)}/\hbar)]/4E(U-E)} \tag{58}$$

It is observed that the transmission coefficient of the barrier contains only the probability current densities in the asymptotic regions. For $E > U$, the expression of the transmission coefficient through the barrier is [16–18, 22–24]

$$T = \frac{1}{1 + V^2[\sin(a\sqrt{2\mu(E-U)}/\hbar)]/4E(E-U)} \tag{59}$$

1.3.5.2. The Three-Dimensional Collision The one-dimensional discussion of the scattering process revealed that the incoming and outcoming particles may be represented by wave functions, or in the general case as a packet of wave functions. Hence, the wave packet assigned to the incident particle is scattered by the atoms of the target and is further transmitted as a wave packet with different characteristics. The wave packets are represented by wave functions of the form (constant) × (exp**ikr**). The quantum problem of a three dimensional collision is described by the Schrödinger equation [22–24]

$$-\frac{\hbar^2}{2\mu}\frac{\partial^2 \psi_K(\vec{r})}{\partial r^2} + V(\vec{r})\psi_K(\vec{r}) = E\psi_K(\vec{r}) \tag{60}$$

In order to solve the time independent Schrödinger equation at large distance from the collision center it is necessary to have an asymptotic wave function that represents a transmitted (not scattered) wave function (of the form exp i**kr**) and an additional term that represents the incoming particle moving radially outward after the collision, of the form $\mathbf{r}^{-1}$exp**ikr**. As this last term reflects the collision process it will be a function of the angles θ and φ (see Fig. 10). The plane wave component of the solution describes a particle moving in the positive direction with the wave vector K. The second term includes a radial contribution, which will ensure that the radial flux is falling off as the inverse square of the distance from the collision point. The energy E is the energy in the center of mass system. As in the case of classical collisions, E is the energy of a fictive particle of mass equal to the reduced mass μ traveling with a velocity equal to the transport (relative velocity) of the center of mass frame relative to the laboratory frame, V_{CM}. This reflects the fact that the quantum mechanics problem of the collision between two particles is analyzed as a single particle evolution in a potential U.

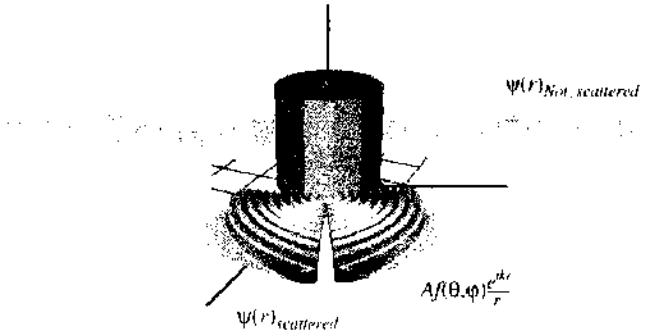

Figure 10. The three-dimensional collision of two particles in the center of mass frame, within the nonrelativistic, time-independent quantum mechanical approximation.

To conclude, the asymptotic form of the out coming wave function after a three-dimensional collision is

$$\psi(r) = A(e^{ikr} + f(\theta,\varphi)\frac{e^{ikr}}{r} \equiv \psi(r)_{\text{Not\_scattered}} + \psi(r)_{\text{scattered}} \tag{61}$$

The flux of incoming particles, J_{Inc}, and the flux of scattered particles are

$$J_{\text{Inc}} = \mu\left[A^* e^{-iKr}\left(\frac{d}{dr}Ae^{iKr}\right) - Ae^{iKr}\left(\frac{d}{dr}A^* e^{-iKr}\right)\right] = \frac{\hbar K}{m}|A|^2 \tag{62}$$

$$J_{\text{Sc}} = \frac{\hbar}{2\mu i}\left[A^* f^*(\theta,\varphi)\frac{e^{-iKr}}{r}\left(\frac{d}{dr}A^* f^*(\theta,\varphi)\frac{e^{-iKr}}{r}\right) - A^* f^*(\theta,\varphi)\frac{e^{-iKr}}{r}\left(\frac{d}{dr}Af(\theta,\varphi)\frac{e^{iKr}}{r}\right)\right]$$
$$= \frac{\hbar k}{\mu r^2}|f(\theta,\varphi)|^2|A|^2 \tag{63}$$

The number of particles scattered through an area dS subtended by the solid angle $d\Omega$ per unit time is [16–18]

$$dN = J_{\text{sc}}dS = J_{\text{Sc}}r^2\,d\Omega \tag{64}$$

This leads to a quantum mechanical definition of the cross section (assuming that $|A| = 1$)

$$\sigma(\theta,\varphi) = \frac{1}{J_{\text{Sc}}}\frac{dN}{d\Omega} = |f(\theta,\varphi)|^2 \tag{65}$$

The quantity $f(\theta, \phi)$ is named *scattering amplitude* and plays a central role in the analysis of the collision process. The calculation of the scattering amplitude is a central goal of the quantum theory of collisions. Excepting some very simple cases, there is not an exact solution of the Schrödinger equation associated to the collision process. Hence, approximate techniques are required for the solution of the Schrödinger equation. Two techniques are frequently used to estimate the scattering amplitude, namely the partial wave analysis and the perturbation technique proposed by Bohr.

1.3.5.2. The Partial Wave Analysis The quantum mechanical problem associated to a particle in a three-dimensional field characterized by the potential energy $U(r)$, in spherical coordinates, may be written as follows:

$$-\frac{\hbar^2}{2\mu}\left[\frac{1}{r^2}\frac{\partial}{\partial r}\left(r^2\frac{\partial}{\partial r}\right) + \frac{1}{r^2\sin\theta}\frac{\partial}{\partial\theta}\left(\sin\theta\frac{\partial}{\partial\theta}\right) + \frac{1}{r^2\sin^2\theta}\frac{\partial^2}{\partial\varphi^2}\right]\psi(r,\theta,\phi) = [E - U(r)]\psi(r,\theta,\phi) \tag{66}$$

The radial and angular components of this equation are easily separated by writing the wave function of the system as a product of two wave functions one that contains only the radial dependence and the other that contains only the angular components:

$$\psi(r,\theta,\varphi) = R(r)Y(\theta,\varphi) \tag{67}$$

After the separation of the two wave functions is obtained:

$$\frac{1}{R}\frac{d}{dr}\left(r^2\frac{dR}{dr}\right) + \frac{2\mu r^2}{\hbar^2}[E - V(r)] = -\frac{1}{Y}\left[\frac{1}{\sin\theta}\frac{\partial}{\partial\theta}\left(\sin\theta\frac{\partial Y}{\partial\theta}\right) + \frac{1}{\sin^2\theta}\frac{\partial^2 Y}{\partial\varphi^2}\right] = \lambda = l(l+1) \tag{68}$$

where λ, and l are constants. The radial equation may be rewritten by using the substitution

$$R(r) = \frac{\chi(r)}{r} \tag{69}$$

The corresponding Schrödinger equation will be

$$-\frac{\hbar^2}{2\mu}\frac{d^2\chi}{dr^2} + \left[V(r) + \frac{l(l+1)\hbar^2}{2\mu r^2}\right]\chi = E\chi \tag{70}$$

Hence, for the radial component, the evolution of a particle in a three-dimensional potential, U, is analogous to the evolution of the same particle in a one-dimensional potential U_1, where [22–24, 31]

$$U_1(r) = U(r) + \frac{l(l+1)\hbar^2}{2\mu r^2} \tag{71}$$

The additional potential reflects the centrifugal force F_C exerted on the particle of mass μ in the center of mass system during the collision process:

$$F_C = \mu\omega^2 r = \frac{L^2}{\mu r^3} \tag{72}$$

This force is equivalent with an additional potential energy U_C:

$$U_C = \frac{L^2\hbar^2}{2\mu r^2} \equiv \frac{l(l+1)\hbar^2}{2\mu r^2} \tag{73}$$

At large distances from the collision center as well as for $l = 0$, the Schrödinger equation (60) describes the evolution of a free particle in a potential $V(r)$. The corresponding wave function may be written as follows [17, 18, 23–25]:

$$\chi(r)|_{r\ll 0} = A_1 \sin(K_1 r) + B_1 \cos(K_1 r) \tag{74}$$

and

$$\chi(r)|_{r\gg a} = A_3 \sin(K_3 r) + B_3 \cos(K_3 r) \tag{75}$$

with

$$K_1 = K_3 = \frac{\sqrt{2\mu(E - U(r))}}{h} \approx \frac{\sqrt{2\mu E}}{\hbar} = K \tag{76}$$

The expression of the radial function will be

$$R(r) = A_1 \frac{\sin(Kr)}{r} + B_1 \frac{\cos(Kr)}{r} \tag{77}$$

The most important step is to derive the wave function near the collision center and to match the wave function inside and far away from the collision center in such a way that both the wave function and its derivatives are continuous. The wave function (77) cannot be used near the collision center due to the divergence introduced by the term in B_1. To overcome this, it is supposed that $B_1 = 0$.

The partial wave analysis exploits the fact that in an ideal collision the angular momentum is conserved. Hence, the wave function may be expressed in term of angular momentum states, by using Legendre polynomials, assuming that the wave vector $\boldsymbol{K}$ defines a symmetry axis and supposing not polarized beams (the scattering amplitude is not a function of φ). The incident plane wave Ae^{iKr} may be expanded in terms of Legendre polynomials, $P_l(\cos\theta)$, where l identifies the order of the polynomial [22–25].

$$\psi(r, \theta) = \sum_{l=0}^{\infty} i^l (2l+1) P_l(\cos\theta) \frac{\chi_l(r)}{r} \tag{78}$$

At large distances from the scattering center, the wave function associated to incoming particle should have the form

$$R_l(r) \propto \frac{\sin(Kr - l\pi/2)}{Kr} \tag{79}$$

Far away from the collision center, the incoming and out coming wave functions should be alike. Assuming that no particles are generated or destroyed within the collision center, the

only possible difference between incident and emergent waves is a phase constant, δ_l. Hence the asymptotic solution will have the general form, $R_l^{(A)}$:

$$R_l^{(A)}(r) \propto \frac{\sin(Kr + \delta_l - l\pi/2)}{Kr} \tag{80}$$

The actual wave function will be a superposition of such asymptotic wave functions, $\Gamma_K(\theta, \phi)$

$$\Gamma_K(\theta,\varphi) = \sum_{l=0} C_l \frac{\sin(Kr+\delta_l - l\pi/2)}{Kr} P_l(\cos\theta) = \sum_{l=0} 2(l+1) i^l A_l \frac{\sin(Kr+\delta_l - l\pi/2)}{Kr} P_l(\cos\theta) \tag{81}$$

where C_l and A_l are constants. The l component of the sum identifies the lth partial wave, and δ_l is the phase shift of this partial wave. Introducing (78) and (81) into (61), for $|A| = 1$ is obtained

$$\sum_{l=0} 2(l+1) i^l A_l \frac{\sin(Kr + \delta_l - l\pi/2)}{Kr} P_l(\cos\theta) = \sum_{l=0}^{\infty} i^l (2l+1) P_l(\cos\theta) \frac{\sin(Kr - l\pi/2)}{Kr} + f(\theta,\phi)\frac{e^{iKr}}{r} \tag{82}$$

Developing the function f in Legendre polynomials results [22–24]

$$f(\theta) = \sum_{l=0}^{\infty} C_l P_l(\cos\theta) \tag{83}$$

Observing that $A_l = e^{i\delta l}$, the following is obtained:

$$\sum_{l=0} C_l f(\theta,\phi) P_l(\cos\theta)\frac{e^{iKr}}{r} = \sum_{l=0} 2(l+1) i^l P_l(\cos\theta)\left[e^{i\delta_l}\frac{\sin(Kr+\delta_l - l\pi/2)}{Kr} - \frac{\sin(Kr - l\pi/2)}{Kr}\right] \tag{84}$$

Finally, the expression of the function f in terms of Legendre polynomials is

$$f(\theta) = \frac{1}{K}(2l+1) e^{i\delta_l} \sin\delta_l P_l \cos(\theta) \tag{85}$$

Taking into account the relationship between $f(\theta)$ and the cross section, we obtain

$$\sigma(\theta) = \frac{1}{K^2}\left|\sum_{l=0}(2l+1)(e^{2i\delta_l} - 1) P_l(\cos\theta)\right|^2 \tag{86}$$

The total cross section, σ_T of the collision process is

$$\sigma_T = \int_0^{2\pi}\left(\int_0^{\pi} \sigma(\theta)\sin\theta d\theta\right) d\varphi = \frac{4\pi}{K^2}\sum_{l=0}(2l+1)\sin^2\delta_l \tag{87}$$

The orthogonality property of Legendre polynomials was used in the estimation of the integral. Finally, the total cross section may be expressed as a function of $f(0)$:

$$\sigma = \frac{4\pi}{K} IM[f(0)] \tag{88}$$

Equation (88) defines the optical theorem. It shows that the scattering process is described by the removal of a number of particles (proportional to the total cross section) from the incident beam. This reduces the intensity of the beam behind the collision center relative to the beam intensity in front of the collision center.

1.3.5.3. Scattering by a Hard Sphere Potential The hard sphere potential is defined by

$$U(r) = \begin{cases} \infty & r < a \\ 0 & r > a \end{cases} \tag{89}$$

The general solution of the radial equation is

$$R_l(r) = B_l[j_l(Kr) - \eta_l(Kr)\tan\delta_l] \tag{90}$$

The incident particle is not capable of penetrating into the region with $r < a$, and this implies

$$\tan\delta_l = \frac{j_l(ka)}{\eta_l(ka)} \tag{91}$$

In the low energy limit, for $ka \ll 1$ the s wave is dominating the collision process. In this case:

$$j_0(Kr) = \frac{\sin(Kr)}{Kr} \quad \text{and} \quad \eta_0(Kr) = -\frac{\cos(Kr)}{Kr} \tag{92}$$

In conclusion, $\delta_0 = -Ka$ and the total cross section will be

$$\sigma_T = 4\pi a^2 \tag{93}$$

1.4. Radiation Concepts, Measures, and Units

The effects of the interaction between radiation and targets are analyzed within the dosimetry framework using an energy-based approach. The following main radiation measures and units have been accepted by the International Commission for Radiation Units.

1.4.1. Dose, D

The most important measure in radiation dosimetry [25–30] is the dose, D. The actual concept of dose means absorbed dose and it is defined by the ratio between the energy imparted to the target by the incident radiation, ΔE, and the mass of the target, m.

$$D = \frac{\Delta E}{m} \tag{94}$$

The units for the dose are J/kg or Gray (Gy) [25–30]. An older unit still in use is the rad (100 rad = 1 Gy). A detailed discussion of the dose concept will be provided in the next paragraphs.

1.4.2. Dose Rate, D_R

The dose rate characterizes the amount of energy transfer to a target of unit mass in the time unit [25–30].

$$D_R = \frac{\Delta E}{mt} = \frac{D}{t} \tag{95}$$

1.4.3. Dose Equivalent

For biological and medical purposes, another dose concept (equivalent dose concept) was introduced. This concept allows comparing in a quantitative fashion the biological effectiveness of different kinds of radiation and expresses the dose required to reach the same degree of damage inside a target. The dose equivalent is defined by the product between the actual dose (absorbed dose) and a quality factor Q, which depends on the stopping power of the impinging radiation.

1.4.4. Kerma, K (or Simple Kerma)

Kerma (kinetic energy released in matter) [25], K, is defined by the ratio between the sum of all kinetic energies of all charged particles produced by uncharged ionizing particles (ΔE_K) and the mass of the target, m.

$$K = \frac{\Delta E_K}{m} \tag{96}$$

Kerma accounts the contribution of indirectly ionizing particles characterizing the interaction of uncharged particles with the target. Kerma is measured in the same units as the dose. In the subsequent analysis, the contribution of Kerma to the modifications induced within the target by the incident radiation will be neglected. In a real irradiation experiment, the weight of this contribution relative to other possible mechanisms capable to induce damages in the structure and physical properties of the target has to be accurately estimated.

1.4.5. Exposure, ϵ

The exposure characterizes ionizing electromagnetic radiation (gamma and x-rays) and reflects the amount of ionization produced in air [23, 24, 29, 30]. However, it is also used to characterize the amount of ionization produced in different targets. It is generally assumed that the electrical neutrality of the target (in this case air) is preserved during the irradiation. Under these circumstances, the exposure is equal to the ratio between the number of all charges of a given sign produced when all electrons generated by the incident radiation on a target of mass m are stopped. The exposure is currently defined for the interaction of electromagnetic radiation with various targets. The unit for exposure is roentgen, $R(1R = 2.58 \times 10^{-4}$ C/kg). The definition is somehow confusing as it is possible to imagine the case of a small target, from which some electrons are eventually ejected. The relationship between the exposure and the dose (taking into account that the energy required to produce an ion pair in air is about 34 J/C) is $1R = 0.0088$ Gy (air). For a soft tissue $1R = 0.0095$ Gy.

1.4.6. The Incident Particle Fluence, F

The incident particle fluence, F, is defined as the number of particles flowing through a sphere of a projected area dS centered at a given point r [25–30]

$$F = \frac{dN(r)}{dS} \tag{97}$$

The fluence can be interpreted as the track length density [29]

$$F = \frac{dL(r)}{dV} \tag{98}$$

where $L(r)$ is the sum of the track lengths of all particles hitting the volume V centered around the point r.

1.4.7. The Incident Particle Flux, Φ

The incident particle flux is defined as the flow of particles through a sphere of unit area projected about a point in space. If the attenuation is neglected the energy flux at a distance r, $\Phi(r, E)$, from a point source of strength I_0 is

$$\Phi(r, E) = \frac{I_0}{S} = \frac{I_0}{4\pi r^2} \tag{99}$$

The unit for particle flux is $m^{-2} s^{-1}$.

1.4.8. The Differential Flux Energy, $\varphi(E)\,dE$

The differential flux energy is the number of particles, with the energy between E and $E + dE$ crossing an unit sphere in a second. The relation between Φ and $\varphi(E)\,dE$ is

$$\Phi = \int_0^\infty \phi(E)\,dE \tag{100}$$

1.4.9. The Incident Particle Intensity, I

The incident particle intensity is defined as the number N of incident particle that are crossing an unit area normal to the incident beam direction in a second (time unit).

$$F = \frac{N}{St} \tag{101}$$

The intensity of particles has the same units as the flux of particles. The intensity of particles is defined for a collection of particles moving in the same direction (with parallel trajectories), while the flux is defined from particles originating from a source (point source to be accurate).

1.4.10. The Stopping Power

The stopping power, S, is the energy deposited by the incoming particles within the target per unit length traveled by the particle inside the target [25–30].

$$S = -\frac{dE}{dx} \tag{102}$$

There is a very subtle difference between the stopping power and the linear energy transfer or linear rate of loss of energy. The stopping power defines the energy lost by the incident particle while the linear energy transfer determines the energy transferred to the target. The stopping power concept requires a somewhat well defined trajectory within the target. It is well applied to impinging charged particles. While some authors [26] criticize its use for neutron irradiation, it is important to notice that in some materials the neutrons have a well defined trajectory and hence it is possible to use the stopping power concept. Generally, the stopping power concept is not used to describe the interaction of electromagnetic radiation with the target. The stopping power concept should be used with caution if bremsstrahlung is an important mode of energy transfer from the incident particle to the atoms and molecules of the target. The mass stopping power, S_M, is defined by

$$S_M = -\frac{dE}{d\xi} = -\frac{S}{\rho} \quad \text{with} \quad \xi = \rho x \tag{103}$$

where ρ is the density of the target and x is the length of the particle path within the target.

As the most frequent mechanism of energy transfer between an impinging charged particle and a target is the interaction between the incoming particle and the electrons of the target, an electronic stopping power, S_E, defined as the stopping power per electron, is frequently used.

$$S_E = -\frac{A}{N_0 Z \rho}\frac{dE}{ds} = \frac{A}{N_0 Z \rho}S \tag{104}$$

For a target consisting of a single element, N_0 is Avogadro's number, A is the atomic number, and Z is the charge of the target.

1.4.11. The Specific Ionization

The specific ionization defines the number of ions produced by the incident particle per unit path length [25, 26, 28–30]. With a fair accuracy, the specific ionization is equal to the stopping power divided by the energy necessary to produce an ion pair.

1.4.12. Range

The range is the length of the path traveled by the incident particle within the target. It is approximately equal to the mean free path [25–30]. The total range is related to the stopping power by

$$R_{TOT} = \int_0^R dx = \int_0^{E_{MAX}} \frac{dE}{(dE/dx)} \tag{105}$$

Where E_{MAX} is the initial kinetic energy of the incoming particle.

The projected range R_P is the component of the total range along the incident particle trajectory. In the general case, there are two main contributions to the stopping power, one due to Coulomb interactions between the incident particle and the electron of the sample defined as electronic stopping power and the other due to the interaction with the nuclei of the target, named nuclear stopping power. The electronic stopping power dominates and high velocities of incident particles while the nuclear one dominates at low velocities. This allows the definition of a critical energy E_C that separates the two regimes and leads to a better definition of the range.

$$R_{TOT} = \int_{E_C}^{E_{MAX}} \frac{dE}{(dE/dx)_E} + \int_{0}^{E_C} \frac{dE}{(dE/dx)_N} \tag{106}$$

where the subscripts E and N identify the electronic and the nuclear stopping powers, respectively.

1.4.13. The Stopping Time

The stopping time is the time required to stop a particle within a target. Assuming that the impinging particle has a low velocity (the relativistic corrections are not required), and that it travels within the target with an average speed $\langle V \rangle$, the stopping time, t_S, is defined by

$$t_S = \frac{R}{\langle V \rangle} \tag{107}$$

Where R is the particle range.

1.5. The Interaction of Electromagnetic Radiation with Condensed Targets

The electromagnetic radiation may interact through elastic and inelastic scattering processes with the atoms and the electrons of the target. The elastic interactions (Thomson and Rayleigh) are not able to transfer efficiently the energy of the incoming radiation to the target and are usually neglected. The most important processes that control the transfer of energy from the incoming radiation to the target are the photoelectric effect, the Compton effect, and the electron-positron pair generation.

Qualitatively, the electromagnetic radiation is absorbed by the matter. This is phenomenologically described by a surface approach reminiscent to the total cross section concept [25]:

$$I = I_0 \exp -\mu x \tag{108}$$

where I is the intensity of the electromagnetic radiation (defined as the rate of energy flow of the radiation across an unit area) after traveling through a target material over a given length x, I_0 is the intensity of the incoming radiation, and μ is the absorption coefficient of the target (material constant). Several absorption coefficients are used to describe the decay of electromagnetic radiation within targets. The most important are [25, 26]:

- The linear absorption coefficient, μ_L, measured in m^{-1}.
- The mass absorption coefficient μ_M, measured in $m^2\ kg^{-1}$.
- The atomic absorption coefficient, μ_A, measured in m^2/atom.
- The electronic absorption coefficient μ_e, measured in m^2/electron.

The relations between these coefficients are

$$\mu_L = \frac{\mu_M}{\rho} = \frac{\mu_A A}{\rho N} = \frac{\mu_e A}{\rho N Z} \tag{109}$$

where ρ is target's density, N is Avogadro's number. A is target's atomic weight, and Z is target's atomic number. For an estimation of the penetration capability of the electromagnetic radiation, the half value layer absorption, $x_{1/2}$, that is, the thickness of the target

that will reduce the intensity of the incoming electromagnetic radiation by one half has a particular importance.

$$x_{1/2} = \frac{\ln 2}{\mu_L} = \frac{0.693}{\mu_L} \tag{110}$$

1.5.1. Elastic Scattering of the Electromagnetic Radiation on Targets

1.5.1.1. Thomson Scattering The Thomson scattering is an elastic scattering of the electromagnetic radiation with free electrons. Virtually, the Thomson scattering is not transferring any energy to the target as the free electron, irradiated with an electromagnetic radiation is emitting an electromagnetic radiation of the same frequency. The fraction of the incident electromagnetic energy that is scattered by one electron of the target into an unit solid angle Ω, at an angle ϕ relative to the direction of the incoming beam, $d\sigma/d\Omega$ is [21, 25]:

$$\frac{d\sigma}{d\Omega} = \frac{e^4}{2m_e^2c^2}(1+\cos^2\phi) \tag{111}$$

This process is important as it transfers the energy away from the incident particle track within within the target.

1.5.1.2. Rayleigh Scattering The Rayleigh scattering is also an elastic interaction that involves an incoming electromagnetic radiation and an atom of the target. The scattering angle is very small, and the electromagnetic radiation is re-emitted with a very small change of the incoming direction. In a Rayleigh scattering the wavelength of the electromagnetic radiation is larger than the size of the atoms or molecules excited by the impinging radiation. A bound electron of an atom that absorbs the incoming electromagnetic radiation quanta of energy $h\nu$ is raised on an excited energy level and it is de-excited by a transition to the initial energetic state accompanied by the emission of an electromagnetic quantum of the same energy ($h\nu$). The energy deposited within the target by the ideal Rayleigh scattering is zero. The main difference between Thomson and Rayleigh scattering originates from the fact that the Rayleigh scattering involves a bound electron.

1.5.2. Inelastic Scattering of the Electromagnetic Radiation on Targets

Various inelastic processes are competing to the modification of the physical and chemical properties of solid targets subjected to electromagnetic radiation. Among them, the most important ones the photoelectric effect, Compton effect, and the electron-positron pair generation. Several other processes such as Bremstrahlung are capable to generate electromagnetic radiation within the solid target.

1.5.2.1. Photoelectric Effect The photoelectric effect consists in the ejection of electrons from metallic surfaces, because of the interaction between the incoming radiation and the free electrons of the target (see Fig. 11). The energy of the incoming photon ($h\nu$) should

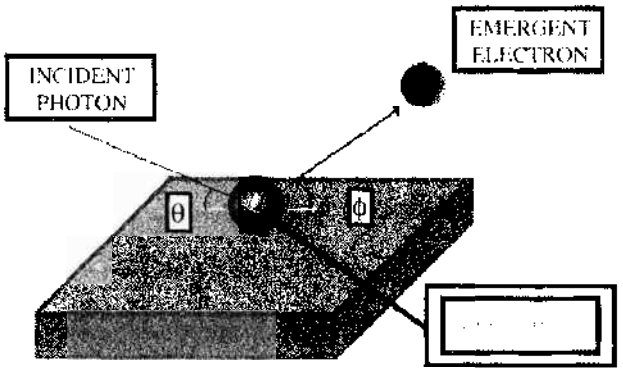

Figure 11. The photoelectric effect.

be higher that the work necessary to extract the electron from the metal (E_W). The kinetic energy of ejected electrons, E_K^{PH} is [16, 18, 21–26]

$$E_K^{PH} = h\nu - E_W = \frac{m_e v_e^2}{2} \tag{112}$$

where m_e is the electron mass and v_e its speed. There is a minimum frequency (threshold frequency) at which the electrons are still emitted (equal to E_W/h). E_W is a material constant for metallic targets.

1.5.2.2. Compton Effect The Compton effect describes the interaction of the electromagnetic radiation with a weakly bound or free electron (see Fig. 12). The electron of the target will appear to be a free electron for the incoming electromagnetic radiation if the energy of the incoming quanta is significantly larger than the binding energy of the electron. Because of this interaction the electrons is recoiled with energy E_e at a certain angle φ and the photon is scattered at an angle θ with a different kinetic energy. The angles are measured relative to the initial direction of the incoming electromagnetic radiation. The shift in the frequency of the incident photon due to a Compton interaction is independent on the frequency of the incident photon and depends only on the angle between the incident photon and the emitted photon. For the Compton effect, it is important to consider the relativistic energy momentum conservation relation.

In the analysis of the Compton effect before the collision, the energy of the system electron—electromagnetic radiation consists of the incoming photon energy $h\nu$ and relativistic electron energy $m_e c^2$, where c is the light speed. After the collision, the scattered (emerging) photon energy will be $h\nu'$ and the electron will be ejected with an energy E and a momentum p [16, 21, 25]. The energy and momentum conservation laws will result in the following system of equations that describe the Compton effect (see Fig. 12).

$$\begin{aligned} h\nu + m_0 c^2 &= h\nu' + E \\ \frac{h\nu}{c} &= \frac{h\nu'}{c}\cos\phi + p\cos\theta \\ \frac{h\nu'}{c}\sin\phi &= p\sin\theta \end{aligned} \tag{113}$$

In real targets, the radiation scattered by one electron may interfere with the radiation scattered from other electrons. Such contributions are important when the fluence of electromagnetic quanta is large. A particular case is represented by targets with a regular distribution of atoms (crystals) as the radiation scattered in certain directions may be very intense.

1.5.2.3. Pair Production An incoming photon of energy E higher or at leas equal to 1.02 MeV may interact with a nucleus and result in the emission of a electron-positron pair of equal energies, E_{e-} and E_{e+}. The energy conservation law implies [25]:

$$h\nu - 2m_0 c^2 = E_{e-} + E_{e+} \tag{114}$$

where $2m_0 c^2$ is the critical energy for pair production (1.02 MeV).

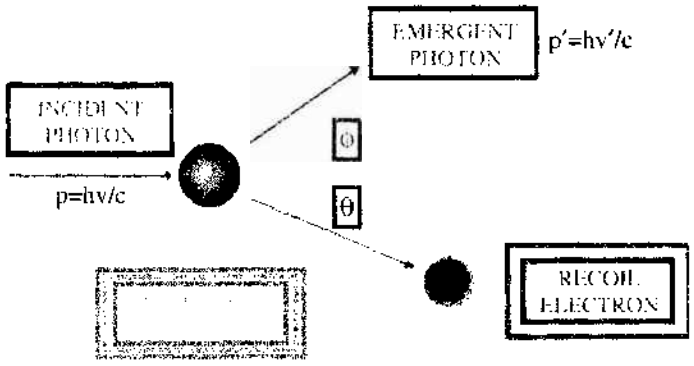

Figure 12. The Compton effect.

In the general case, the energy deposited within a target by the incoming electromagnetic radiation will be a sum of all contributions mentioned above. The total mass absorption, μ_M^T, coefficient is usually defined by [25]

$$\mu_M^T = \frac{\mu_L^T}{\rho} = \frac{\mu_L^{Ph}}{\rho} + \frac{\mu_L^C}{\rho} + \frac{\mu_L^{PP}}{\rho} \tag{115}$$

where μ_L^T is the total liner absorption coefficient, μ_L^{Ph} is the linear absorption coefficient for the photoelectric effect, μ_L^C is the linear absorption coefficient for the Compton effect, and μ_L^{PP} is the linear absorption coefficient for pair production.

1.5.2.4. Bremsstrahlung Rapidly accelerated or decelerated particles are emitting an electromagnetic radiation when passing through the field of atomic nuclei of the target (external bremsstrahlung). The emitted radiation is proportional to m^{-2}, where m is the mass of the decelerating particles. This shows that actually the *bremsstrahlung* radiation is important for electrons and becomes negligible in the case of accelerated heavy ions.

1.6. The Interaction of Accelerated Particles with Condensed Target

The charged particle directed onto a target interacts both with the electrons of the target and with its nuclei or ionic moieties via electrostatic interactions. Due to the large mass of the nucleus relative to the electron mass, electrons are more susceptible to be affected by the electrostatic interaction with the impinging particle.

1.6.1. Coulomb Interaction (Charged Particles)

One of the most simple and elegant model to calculate the energy deposited by an incident charged particle per unit trajectory (named linear energy transfer, LET, or stopping power) in a condensed target has been proposed by Bohr [21, 25–33]. The model considers that the most important mechanism for energy transfer from the impinging particle to the target is the electrostatic interaction. It is assumed that the incoming particle has the mass M, charge Ze (where Z is the atomic number and e the electronic charge), and speed v. and that the target has a crystalline cubic structure, characterized by a spacing, a. between the adjacent atoms. The following expression for the total momentum imparted to the electrons of the target has been derived (see Fig. 13).

$$p = \frac{ZZ_2e^2}{4\pi\varepsilon_0}\int \frac{\cos\theta}{r}\,dt \tag{116}$$

The energy transferred by the incident particle to a target electron is (total linear rate of energy loss) is [21, 25–29]

$$-\frac{dE}{dx} = \frac{16n\pi^2Z^2Z_2^2e^4}{mV^2}\ln\frac{b_{max}}{b_{min}} \tag{117}$$

where Z_2 is the charge of the target nuclei, n is the density of electrons per unit volume (assumed constant), m is the mass of the electron, and b_{max} and b_{min} are supposed to be constants (impact parameters).

During the interaction of a charged (ionized) particle with composite materials, there are two main routes available to transfer the energy from the incoming particle to targets. The first one is represented by the interaction between the incident charged particle and the electronic cloud of the sample. It is named electronic stopping power or electronic LET. There is also a nuclear electrostatic interaction between the impinging particle and the nuclei of the polymeric matrix, named nuclear LET. The total stopping power is the sum of these contributions:

$$\left(\frac{dE}{dx}\right)_{TOTAL} = \left(\frac{dE}{dx}\right)_e + \left(\frac{dE}{dx}\right)_N \tag{118}$$

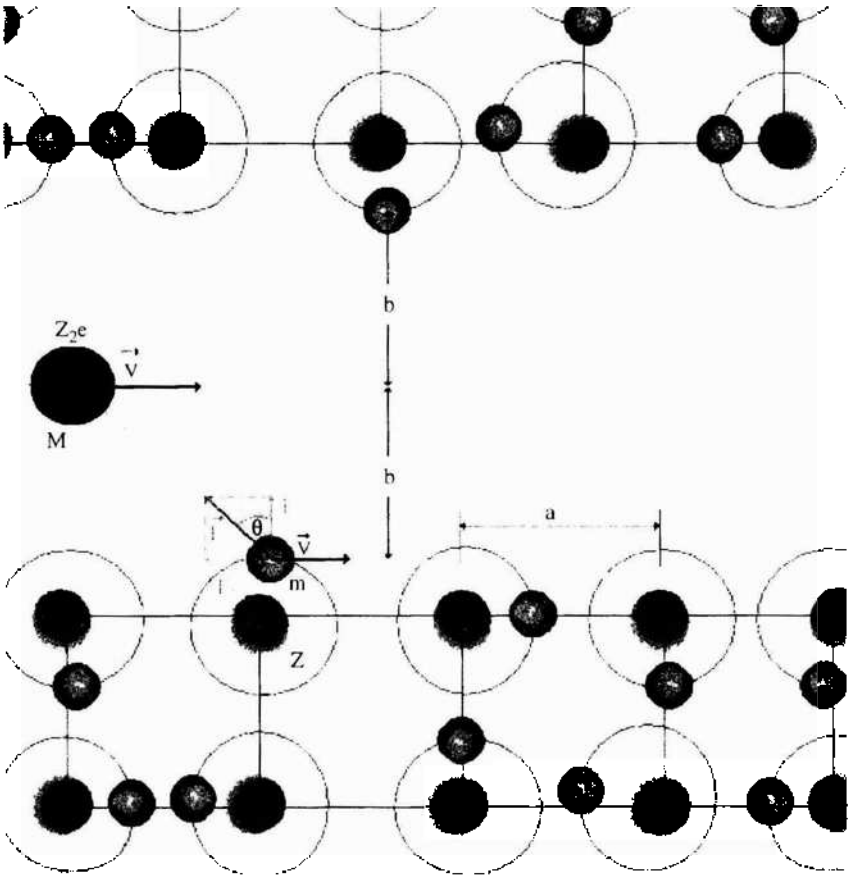

Figure 13. The interaction of a charged particle with the electrons of a crystalline target.

The dependence of the stopping power on the penetration depth for protons accelerated up to 1 MeV and directed towards the target is shown in Fig. 14. It is noticed that the nuclear stopping power is smaller than the electronic one. The weight of the nuclear stopping power (relative to the electronic one) increases as the charge of the incoming particle is increased (compare Fig. 14. and 15).

The stopping power has been also estimated within the relativistic quantum mechanics. The following refined expression has been derived by Bethe [25–30]

$$-\frac{dE}{dx} = \frac{4n\pi^2 k_0^2 Z^2 e^4}{m_e V^2}\left[\ln\frac{2m_e V^2}{I(1-V^2/c^2)} - \left(\frac{V}{c}\right)^2\right] \tag{119}$$

where k_0 is a constant and I represents the mean excitation energy of the target.

In the simple theory of the stopping power that includes the relativistic correction, the stopping power and the ionization of the target due to incoming charged particles increase as the energy of the incoming particle is increased. In order to improve the calculation of the energy deposited inside the target by the incoming charged particle, it is necessary to calculate a restricted energy loss, for kinetic energies smaller or equal to a threshold value of the kinetic energy, $E_K^{(0)}$ [31]

$$\left(\frac{dE}{dx}\right)_{E_K \le E_K^{(0)}} = -A\left(\frac{V}{c}\right)^2\left(2C + \left(\frac{V}{c}\right)^2 + \ln\frac{2mV^2}{I^2(Z)\sqrt{1-(V/c)^2}}\right) \tag{120}$$

where A is a constant. This expression is valid for a single charged incident particle (not electron). C represents the density effect correction. Another contribution to the energy loss

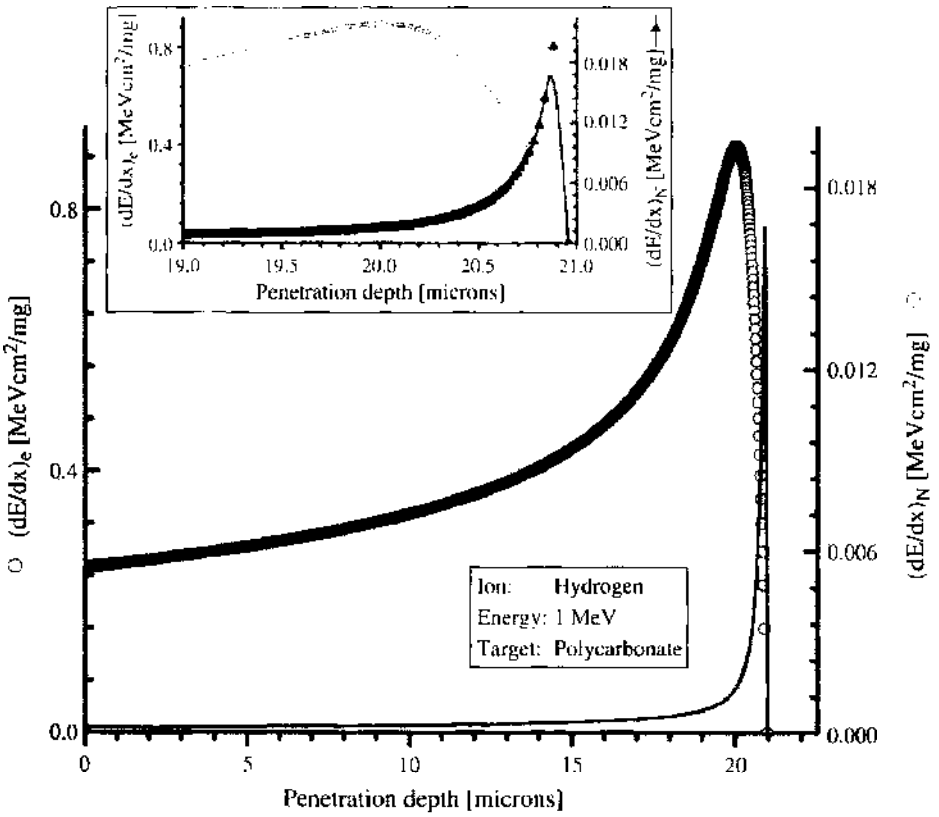

Figure 14. The dependence of the stopping power of a charged particle on the penetration depth, for a light incoming particle (proton). The Bragg peak near the end of the particle trajectory in the target is shown.

of impinging particles is due to the *bremsstrahlung* or electromagnetic radiation emission of the decelerated impinging particle. The stopping power for this process is [30, 31]

$$\left(\frac{dE}{dx}\right)_B = -\frac{NEZ(Z+1)e^4}{137m_0^2c^4}\left(4\ln\frac{2E}{m_0c^2} - \frac{4}{3}\right) \tag{121}$$

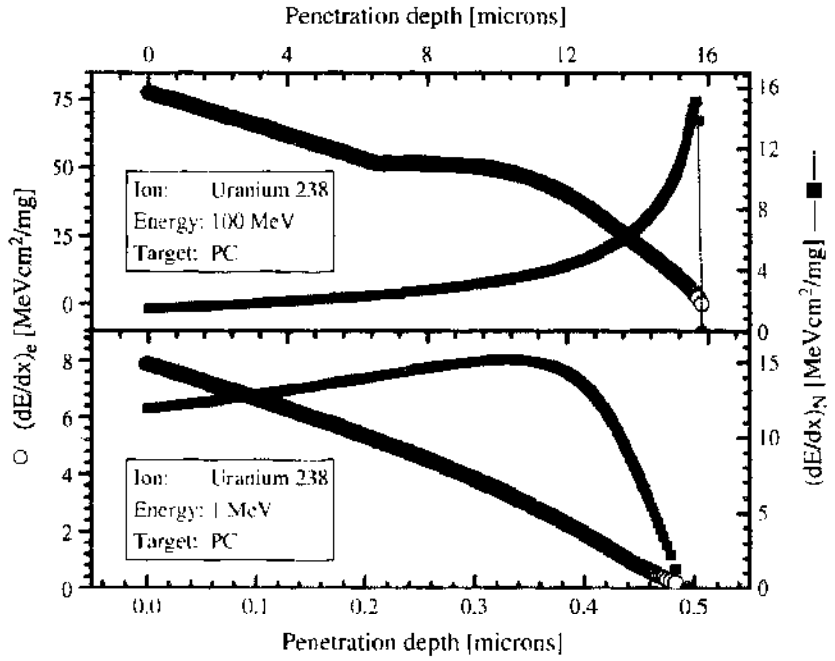

Figure 15. The dependence of the stopping power of a charged particle on the penetration depth for a heavy incoming particle. The Bragg peak near the end of the particle trajectory in the target is shown.

The stopping power is large for incident beams of high energies E and for target materials with large Z. The amount of energy transferred from the incident particle to the target depends on the speed (kinetic energy) of the incoming particle and on its charge. This dependence is expressed with a fair accuracy by Eq. (122), which correlates the stopping power of an ion at the speed V with the stopping power of the proton at the same energy [32].

$$\left[\left(\frac{dE}{dx}\right)\right]_V^{\text{ION}} = \left(Z^*\left(\frac{V}{c}\right)\right)^2\left[\left(\frac{dE}{dx}\right)\right]_V^{\text{PROTON}} \tag{122}$$

where Z^* is the effective charge of the incoming ion.

For complex materials, it is generally assumed that atomic stopping cross section, Ξ_{AT} are additive and the molecular stopping cross section is rather well describe by the sum of atomic contributions [25–32].

$$\Xi_{\text{MOL}}^{\text{XnYm}} = n\Xi_{\text{AT}}^{X} + m\Xi_{\text{AT}}^{Y} \tag{123}$$

The stopping power of a proton in a target consisting of 2 atoms X and Y is [32]

$$\left(\frac{dE}{dx}\right)_{\text{PROTON}} = -N\Xi_{\text{MOL}}^{\text{XnYm}} \tag{124}$$

where N is the total number of molecules per gram in the target.

1.6.1.1. The Bragg Peak The Bethe formula of the stopping power presents no extreme point, and hence the stopping power is expected to increase monotonously as the speed of the particle within the target is decreased. Experimentally, a maximum of the energy transferred from the impinging particle to the target's atom is observed near the end of the particle's trajectory in the target (i.e., at very low traveling velocities). In order to explain the Bragg curve, it is necessary to derive a more accurate expression for the stopping power. The stopping power including the shell correction factor, C, which includes the contribution of L shell electrons is

$$-\frac{dE}{dx} = \frac{4n\pi^2k_0^2Z^2e^4}{m_eV^2}\left[\ln\frac{2m_eV^2}{I(1-V^2/c^2)} - \left(\frac{V}{c}\right)^2 - \frac{C}{Z}\right] \tag{125}$$

The density correction proposed by Fano [1] takes into account the fact that the incident particle is not interacting with a single atom of the target. The correction takes into account the plasma screening of target electrons. Although this correction is negligible for particles with velocities smaller than 0.9c (c is the light velocity), it is interesting to point out that the expression of the corrected stopping power as a function of the incident particle velocity has two extreme points, one located at $V = c$ and the other at $V = 0$.

$$-\frac{dE}{dx} = \frac{4n\pi^2k_0^2Z^2e^4}{m_eV^2}\left[\ln\frac{2m_eV^2}{I(1-V^2/c^2)} - \left(\frac{V}{c}\right)^2 - \frac{C}{Z} - \ln\left(\frac{\hbar^2\omega_P^2}{I^2(1-(V/C)^2)}\right)\right] \tag{126}$$

where ω_P is the plasma frequency.

1.6.1.2. The Range The range of a charged particle $R(E_K)$ inside a solid target is the distance traveled by the impinging particle within the target. The range depends on the kinetic energy of the incoming particle and it is correlated to the stopping power of the incoming particle in the target [1, 21, 25–30]

$$R(E_K) = -\int_0^{E_K}\frac{dE}{(dE/dx)}\,dE \tag{127}$$

where E is the energy of the incident particle inside the target.

Although this definition of the range is found in most textbooks, it has to be corrected for the so-called Lewis effect that includes two contributions [33]. The first one reflects that the mean path per unit energy loss has been incorrectly identified with the reciprocal of the

stopping power and the second reflects the implicit assumption that the stopping power is independent on the mass of the incoming particle [33].

$$R^*(E_K) = \frac{M}{Z^2}\left[-\int_0^{E_K} \frac{dE}{(dE/dx)}\,dE\right]_{\text{PROTON}} + MZ^{3/2}C\left(\frac{V}{cZ}\right) \quad \text{with}$$
$$C\left(\frac{V}{cZ}\right) = \frac{\left[-\int_0^{E_K}(dE/(dE/dx))\,dE\right]_{\text{ION}}}{MZ^{3/2}} \tag{128}$$

The refined expression of the range $R^*(E_K)$ of an incoming charged particles with a kinetic energy E_K, as a function of the range of a proton with the same kinetic energy is given by the expression (128) [33], where M is the mass of the incoming particle, V its speed, and Z its charge (the proton's mass and charge are assumed to be 1).

1.6.1.3. The Range Straggling Due to the inherent statistical character of the irradiation process, identical particles will be stopped after different penetration depths within the same target (suppose to be homogeneous and uniform). The length of all these trajectories of identical particles, with the same incident kinetic energy will present a Gaussian distribution centered on an average value, which is the actual range of the particle. The magnitude of the range straggling, σ_R^2 is defined by the width of this distribution and it is given by [25–30, 33]

$$\sigma_R^2 = \langle R^2(E_K)\rangle - \langle R(E_K)\rangle^2 = 4\pi n_0 Z^2 e^4 \int_0^{E_K} \frac{dE}{(dE/dx)^3}\,dE \tag{129}$$

where "⟨⟩" denotes the average of the particle range in the target, n_e is the electron density of the target, Z is the charge of the incoming particle and e the electronic charge. In the general case it is possible to define [33] the straggling of the momentum of incident particle, a distortion straggling, a heterogeneity straggling, and a fluence straggling.

1.6.2. Spin-Spin Interactions

The spin-spin (hyperfine) interaction between the spin of the incident particle and the electronic spin of target atoms affects both the linear energy transfer of energy from the incident particle to target atoms as well as the differential cross section $d\sigma$. The Born approximation for various impinging particles, characterized by different spins leads to the following expressions for the differential cross section [26]

$$\frac{d\sigma}{d\theta} = \frac{\pi Z_{in}^2 Z^2}{2}\left(\frac{e^2}{m_0c^2}\right)^2\left(\frac{m_0c^2}{\beta p}\right)\frac{\sin\theta}{\sin^4(\theta/2)} \quad \text{Spin } 0$$
$$\frac{d\sigma}{d\theta} = \frac{\pi Z_{in}^2 Z^2}{2}\left(\frac{e^2}{m_0c^2}\right)^2\left(\frac{m_0c^2}{\beta p}\right)\frac{(1-\beta^2\sin^2(\theta/2))\sin\theta}{\sin^4(\theta/2)} \quad \text{Spin } 1/2 \tag{130}$$
$$\frac{d\sigma}{d\theta} = \frac{\pi Z_{in}^2 Z^2}{2}\left(\frac{e^2}{m_0c^2}\right)^2\left(\frac{m_0c^2}{\beta p}\right)\frac{(1+1/6(p\beta/m_0c^2)^2\sin^2\theta)\sin\theta}{\sin^4(\theta/2)} \quad \text{Spin } 1$$

where θ is the deflection angle, $p^2c^2 = E^2 - M^2c^2$, E is the total energy of the particle of mass M, Z is the nucleus charge (for target atoms). Z_{in} is the charge of the incoming beam, m_0 is the electron mass (rest), and e is the electron's charge. It is observed that the spin contribution increases as the deflection angle is increased. The transmitted beam is not affected by the spin-spin interaction.

1.7. The Structure of Solid Targets: Rudiments

In this section, the main properties of the condensed matter will briefly be reviewed. They will allow a better understanding of the physical and chemical modifications induced by radiation in nanostructures and materials confined at nanometer scale.

1.7.1. Crystalline and Amorphous Solids

Due to the difficulties to solve the Schrödinger equation for a large number of atoms, approximate solution and techniques have been developed [16–18, 22–24, 34–37]. Crystalline solids are characterized by a regular distribution of atoms in space. This provides a simple and efficient route to solve the Schrödinger equation. By definition, a crystal consists of a lattice (defined as an ensemble of points in space regularly distributed named nodes) and a base of atoms (identifying the atoms or molecules that occupy the lattice nodes) [34].

$$\text{CRYSTAL} = \text{LATTICE} + \text{BASE} + \text{additional\_term(s)} \tag{131}$$

The definition of the crystalline state—see Eq. (131)—contains a third term defined as additional term(s). Its role will be discussed later. In Fig. 16 is shown a simple crystal obtained by assigning a single type of atoms to the nodes of a two-dimensional lattice. This structure is invariant to a translation of the lattice by R_X, R_Y, or any linear combination of R_X and R_Y (with integer coefficients). If each atom of this crystal characterized by the position vector **R** is described by a wave function $\psi(\mathbf{R})$, then

$$\psi(\vec{R}) = \psi(\vec{R} + \vec{R}_L) = \psi(\vec{R} + nR_X + mR_Y) \tag{132}$$

where n and m are integers. The same symmetry should be imposed to the potential $V(\mathbf{R})$,

$$V(\vec{R}) = V(\vec{R} + \vec{R}_L) = V(\vec{R} + nR_X + mR_Y) \tag{133}$$

The electrons associated to these atoms are placed in a symmetric potential. The symmetry requirements impose that the square of their wave function in a point of coordinates **R** to be equal to the square of the wave function at the point $\mathbf{R} + \mathbf{R}_L$. This implies that the wave functions located in **R** and $\mathbf{R} + \mathbf{R}_L$ may differ at most by a phase factor (this is not changing the modulus of the wave functions) [34],

$$\psi(\vec{R}) = \psi(\vec{R} + \vec{R}_L) = \psi(\vec{R} + nR_X + mR_Y) = e^{i\vec{k}\vec{R}_L}\psi(\vec{R}) = e^{i(nK_XR_X + mK_YR_Y)}\psi(\vec{R}) \tag{134}$$

Equation (134) defines the Bloch wave function in two-dimensional crystal. The archetypal amorphous material is characterized by the absence of the lattice, (i.e., by an almost random distribution of atoms in space). An amorphous material that shows a lattice disorder is shown in Fig. 17.

A more complex crystalline structure is obtained by distributing several types of atoms on the nodes of a crystalline lattice (see an example for a base consisting of two atoms in Fig. 18). In this case, the crystalline structure requires a regular distribution of base atoms. If the base atoms are randomly distributed, the resulting solid will be amorphous even if the lattice is not distorted. This situation is schematically depicted in Fig. 19. The amorphous features of such a material are triggered solely by the random distribution of base atoms.

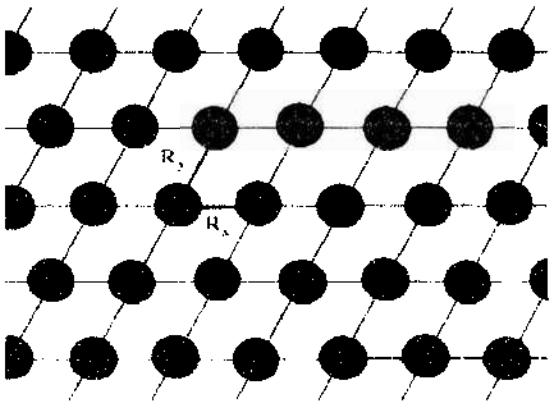

Figure 16. An ideal two-dimensional crystal. The associated base consists of a single type of atom.

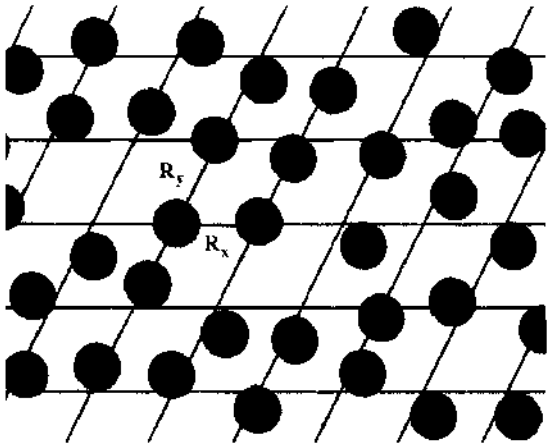

Figure 17. A two-dimensional amorphous material. The associated base consists of a single type of atom, and the disorder is induced by the modulation of distance between atoms (lattice disorder).

Complex materials such as liquid crystals and polymeric liquid crystals consist of asymmetric molecules. This may result in the appearance of exotic amorphous states determined by the random orientation of these molecules (see Fig. 20). Depending on the actual definition of the crystalline phase, the additional terms in Eq. (131) will reflect an order in the orientation of dipole moments, molecules, spins, or magnetic moments.

Some condensed materials such as most polymers are neither amorphous nor crystalline [14] (see Fig. 21). They consist of crystalline domains embedded in an amorphous ocean and they are currently characterized by a degree of crystallinity defined as the ratio between the volume of crystalline domains and the volume of the sample. The crystalline domains are formed by a close packing of polymeric chains while the amorphous regions contain preferentially chain ends or bulky lateral groups.

1.7.2. Metals, Semiconductors, and Insulators

In condensed materials, the energy levels are collapsed in bands, due to the small distance between adjacent atoms (of the order 10^{-10} m). The structure of energy bands in materials, allows their classification in insulators, semiconductors, and metals. In the general case, there is a low energy band with allowed states, named valence band, V_B, and a high-energy band named conduction band, C_B, with allowed states spaced by an energy gap, E_G (see Fig. 22) [34]. An ideal insulator has all states in V_B filled, all states in C_B empty, and an energy gap larger than 3 eV [34].

In an ideal semiconductor, the forbidden gap is less than 3 eV. This allows the thermal excitation of an electron from the valence band to the conduction band and triggers the electrical conductivity. The place of the electron left unoccupied in the valence band is also contributing to the electrical conductivity (holes conductivity). The probability to find a state

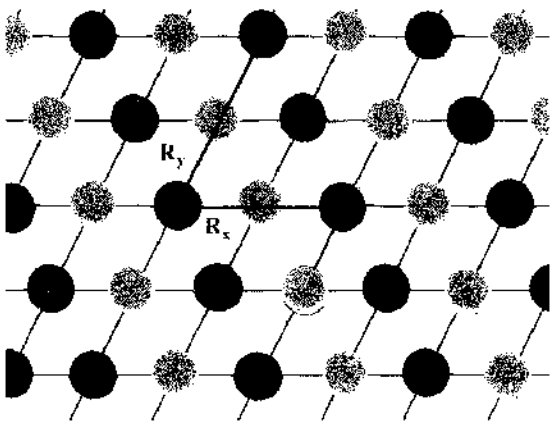

Figure 18. A two-dimensional crystal. The associated base consists of two types of atom.

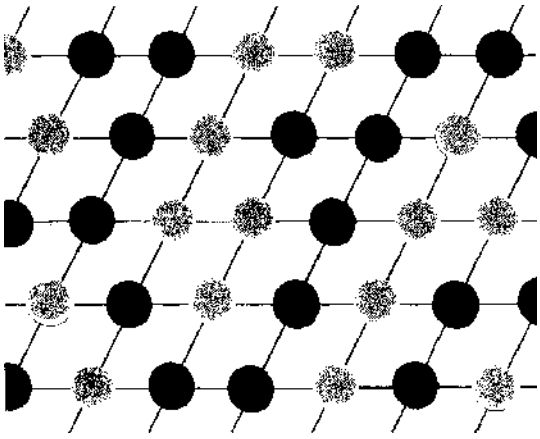

Figure 19. A two-dimensional amorphous material with two atoms in the base. The disorder is triggered by the random distribution of base atoms on the lattice nods (base disorder). The crystalline lattice structure is fully preserved.

characterized by the wave vector K and by the energy E_K, occupied (at thermal equilibrium) in degenerates semiconductors and metals is [34]

$$f(E_K) = \frac{1}{e^{(E_K - E_F/K_B T)} + 1} \tag{135}$$

where E_F is named Fermi level (or chemical potential) and represents the highest occupied level in solids at 0 K. In all semiconductors, the Fermi energy lies between the valence band and the conduction band. At 0 K this distribution has a rectangular shape. By increasing the temperature, the shape of $f(E_K)$ is modified. This shows the possibility to activate thermally the conductivity of semiconductors. Most semiconductors are extrinsic, that is, contain additional impurities that are able to release electrons (donors) or to accept electrons (acceptors). In such semiconductors, the most important electronic transitions are the band-to-band excitation (injection of an electron from the valence band into the conduction band), acceptor-donor compensation, acceptor, and donor ionization. The semiconductors that contain a large number of states occupied or that are heavily doped are named degenerated semiconductors. For such semiconductors, the Fermi-Dirac statistics defines with a good accuracy the electron distribution. In metals, V_B and C_B are overlapping. Nondegenerate semiconductors are characterized by $\exp[(E_K - E_F)/K_B T] \gg 1$. The DC electric conductivity σ of a semiconductor is [34]

$$\sigma = q(n_e \mu_e + n_h \mu_h) \tag{136}$$

where n_e is the concentration of electrons, n_h is the concentration of holes, μ_e is the electron mobility, μ_h is the hole mobility, and q is the electron charge.

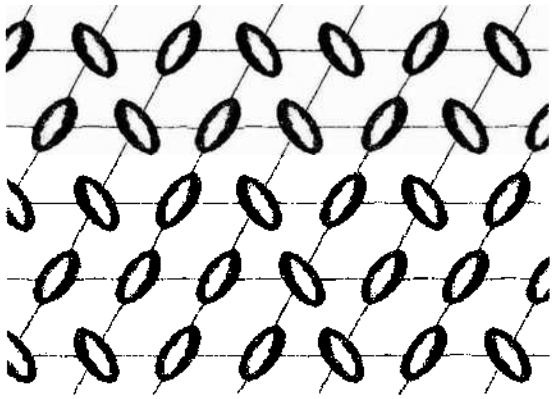

Figure 20. A two-dimensional amorphous material consisting of a single type of base atom. The disorder is due to the random orientation of the symmetry axes of molecules (orientational disorder).

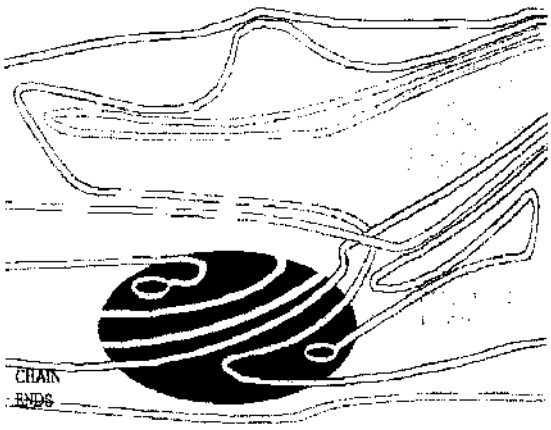

Figure 21. A typical structure of a solid polymer showing crystalline and amorphous domains.

The ideal semimetal is characterized (at 0 K) by a completely filled C_B, a completely empty V_B and a zero energy gap. Such a material is insulator at 0 K but is semiconductor or even conductor at high temperatures due to the excitation of the electrons from the V_B into the C_B.

The electrons in ideal metals behave just like a gas of electrons. This explains why it is not necessary any activation energy to trigger the electric conductivity in metals. In this case, the distribution function of electrons is approximated by a Boltzmann distribution

$$f(E_K)\Big|_{\frac{E_K - E_F}{K_B T} \gg 1} \approx e^{-(E_K - E_F/K_B T)} \tag{137}$$

The temperature dependence of the conductivity in an ideal metal has three domains. At low temperatures, the temperature dependence of the conductivity is described by Matthiessen law [34]

$$\sigma^{-1} = \sigma_0^{-1} + \sigma_1^{-1}\left(\frac{T}{T_D}\right)^5 \tag{138}$$

where $\rho_0 = \sigma_0^{-1}$ is the residual resistivity and T_D is Debye temperature. At high temperatures, the temperature dependence of the conductivity is

$$\sigma^{-1} = \sigma_2^{-1}\left(\frac{T}{T_D}\right) \tag{139}$$

Theoretically, there is an intermediate range of temperatures where $E_F \gg K_B T$. This case is characterized by a temperature independent conductivity.

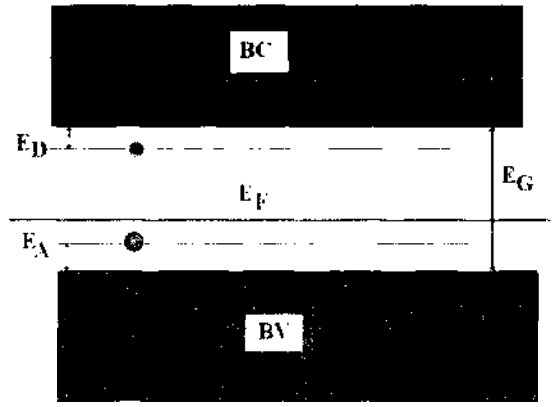

Figure 22. The electronic (band) structure of semiconductors.

1.7.3. Magnetic Materials

The magnetic properties of the matter are resulting from the movement of charged particles, either free or not. As no isolated magnetic poles were observed, it was assumed that magnetic poles occur in pairs named *dipoles* characterized by magnetic moments μ [34–37],

$$\vec{\mu} = m\vec{d} \tag{140}$$

where **d** is a vector pointing from the negative to the positive pole, whose magnitude is proportional to the distance between poles. By default, the magnetism was assigned to electrons. Two possible sources were identified for poles one is the motion of electrons around the nucleus (defined by the orbital angular momentum) and the other is the rotation of the electrons about its own axis (spin angular momentum). The second source of magnetism suggests that the electron is not the only possible responsible for magnetism. Other particles that carry a spin angular momentum (such as various nuclei or neutrons) would be capable to exhibit magnetic properties. Nevertheless, the spin angular momentum triggered magnetism of nuclei is significantly weaker than the electron induced magnetism and its contribution is usually neglected.

The magnetization **M** is defined as the total magnetic moment of the material per unit volume [34–37]

$$\vec{M} = \frac{1}{V}\sum_i \vec{\mu}_i \tag{141}$$

where V is the volume of the sample and the sum is over all magnetic moments confined within the volume V. The magnetization of materials is modified in the presence of external magnetic field. For isotropic samples, the magnetic susceptibility χ describes this modification

$$\chi = \left(\frac{d\vec{M}}{d\vec{H}}\right)_{H=0} \tag{142}$$

where H is the intensity of the external magnetic field. The magnetic susceptibility allows the classifications of materials as diamagnetic, paramagnetic, and magnetic.

1.7.3.1. Diamagnetic Materials The diamagnetic materials are characterized by $\chi < 0$, as the magnetization is oriented antiparallel to the external magnetic field H. The classical example of diamagnetism is the Langevin diamagnetism originating from the motion of the electron on a closed orbit around the nucleus, with the Larmor pulsation ω_L [34–36]

$$\omega_L = \frac{eH}{2m_e c} \tag{143}$$

If each atom has a single electron, this motion produces a current of intensity I

$$I = -\frac{e}{T} = -\frac{e^2 H}{4\pi mc} \tag{144}$$

This closed current is equivalent with a magnetic moment with the absolute value m

$$m = \frac{IS}{c} \qquad S = \pi\langle x_i^2 + y_i^2\rangle \tag{145}$$

S represents the averaged area of the projection of the electron orbit on a plane normal to the external applied electric field, and "⟨⟩" denotes an average of the square of the coordinates of all electrons. The expression of the magnetization for an ensemble of n magnetic ions per unit volume, if Z is the number of electrons of each ion, is

$$M = -\frac{Ze^2 n}{4mc^2}\sum_i \langle x_i^2 + y_i^2\rangle H \approx -\frac{Ze^2 n}{6mc^2}\langle r^2\rangle H \tag{146}$$

Hence, the susceptibility of a diamagnetic material depends on the average of the square radius of the electron. As this value is always positive, the susceptibility of diamagnetic materials is negative. Conduction electrons are also responsible for a diamagnetic behavior.

1.7.3.2. Paramagnetic Materials The energy of a magnetic moment in an external magnetic field, E_m, is [34–37]

$$E_m = -\vec{\mu}\vec{H} = -g\mu_B m_j H \tag{147}$$

Where g is the spectroscopic factor, μ_B the electron's magneton (Bohr), and m is the magnetic quantum number. The electron in its closed orbit is characterized by two operators associated to the angular momentum, L, and to the magnetic quantum momentum (spin), S. The magnetic quantum number is an integer that takes $2l + 1$ values between $-l$ and $+l$ and is frequently associated with the orientation of the electron orbit relative to the atom. The eigenvalues of the spin operator are $+1/2$ and $-1/2$. The operator of the total momentum of electrons, $J(J = L + S)$, controls the magnetic properties of solids. The associated eigenvalue, mj, takes $2j + 1$ values between $-j$ and $+j$. The magnetization of a collection of N atoms placed in an external magnetic field is

$$M = Ng\mu_B \frac{\sum_{-j}^{j} m_j g\mu_B e^{(m_j g\mu_B H/K_B T)}}{\sum_{-j}^{j} e^{(m_j g\mu_B H/K_B T)}} = Ng\mu_B j B_j\left(\frac{g\mu_B m_j H}{K_B T}\right) \tag{148}$$

where B represents the Brillouin function defined by

$$B_j\left(\frac{g\mu_B m_j H}{K_B T}\right) = \frac{2j+1}{2j} cth\left(\frac{2j+1}{2j}\frac{g\mu_B m_j H}{K_B T}\right) - \frac{1}{2j} cth\left(\frac{1}{2j}\frac{g\mu_B m_j H}{K_B T}\right) \tag{149}$$

Hence, the susceptibility of this collection is

$$\chi = \frac{Ng^2\mu_B^2 j(j+1)}{3K_B T} = \frac{Ng^2}{3K_B T}(\mu_B^2 p_{\text{eff}}^2) \tag{150}$$

where p_{eff} is the effective number of Bohr's magnetons. The particular expression of p_{eff} depends on the details of the coupling between the spins and the angular motion.

1.7.3.3. Ferromagnetic Materials The diamagnetic and paramagnetic properties of the matter are triggered by the angular momentum of electrons. The magnetic momentum of electrons is responsible for several types of magnetic order such as ferromagnetism, ferrimagnetism, and antiferromagnetism (see Fig. 23). In contrast with the previous types of magnetism, the electronic spin generated magnetism is responsible for the spontaneous ordering of electronic spins.

1.7.3.3.a. The Exchange Interaction The helium atom provides the simplest quantum mechanical problem that contains the main features of the exchange interaction. In this case the nucleus (or the ionic moiety) has the charge Ze and the mass M_N. Two electrons of identical mass m_E, characterized by the position vectors r_1 and r_2, are orbiting around the nucleus. The corresponding Hamiltonian is [16–18, 22–24, 34, 37]

$$\aleph = -\frac{\hbar^2}{2M_N}\nabla_N^2 - \frac{\hbar^2}{2m_E}\nabla_{E1}^2 - \frac{\hbar^2}{2m_E}\nabla_{E2}^2 - \frac{Ze^2}{4\pi\varepsilon_0 r_1} - \frac{Ze^2}{4\pi\varepsilon_0 r_2} + \frac{e^2}{4\pi\varepsilon_0|r_1 - r_2|} \tag{151}$$

The subscripts N and E identify the electrons and the nucleus. The total wave function of this time independent Schrödinger equation, Φ may be expresses as a product of electronic wave functions, Ψ with nuclear wave functions, ζ. As magnetism is by excellence an electronic property solely the electronic part of the Schrödinger equation is important.

$$\aleph = -\frac{\hbar^2}{2m_E}\nabla_{E1}^2 - \frac{\hbar^2}{2m_E}\nabla_{E2}^2 - \frac{Ze^2}{4\pi\varepsilon_0 r_1} - \frac{Ze^2}{4\pi\varepsilon_0 r_2} + \frac{e^2}{4\pi\varepsilon_0|r_1 - r_2|} \tag{152}$$

This Hamiltonian may be rewrite to include one-electron Hamiltonians such as

$$\aleph_i = -\frac{\hbar^2}{2m_E}\nabla_{Ei}^2 - \frac{Ze^2}{4\pi\varepsilon_0 r_i} \qquad i = 1, 2 \tag{153}$$

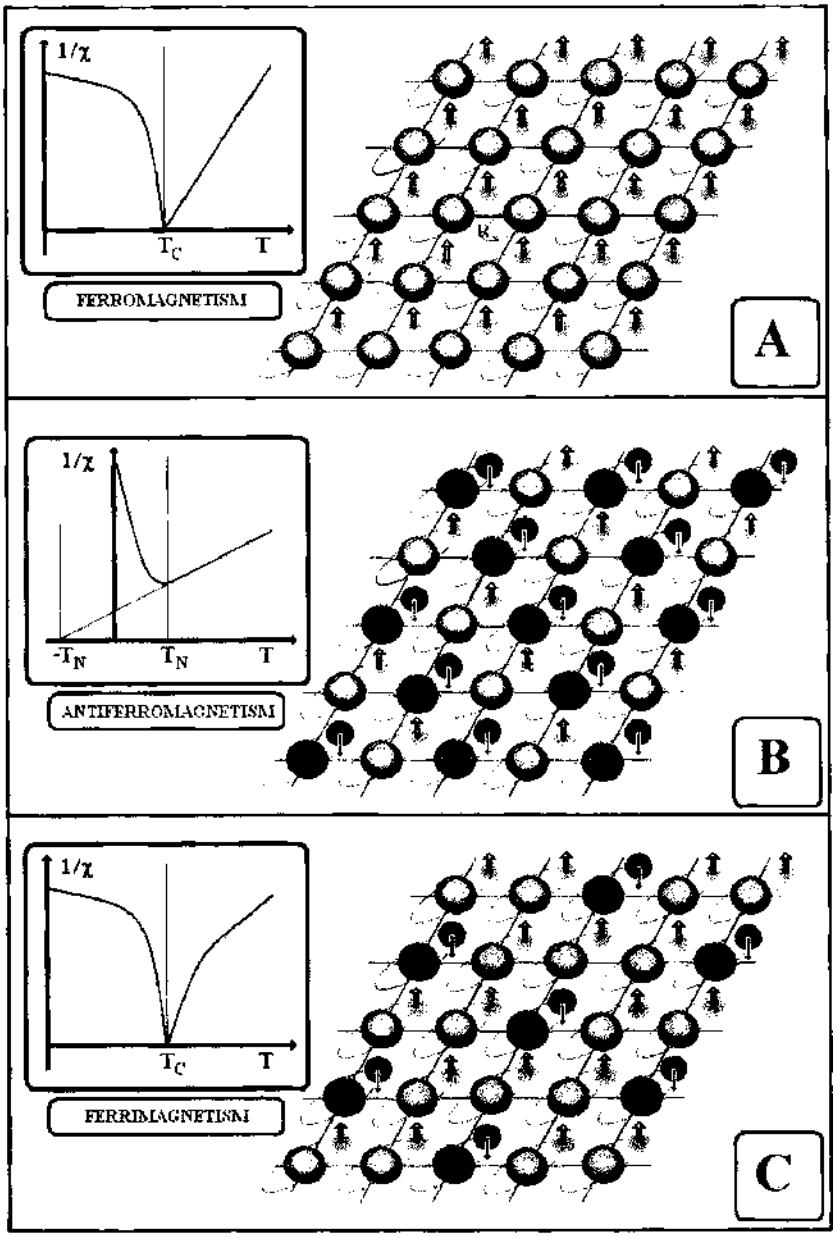

Figure 23. Various magnetic structures: (A) ferromagnetism, (B) antiferromagnetism, (C) ferrimagnetism.

with

$$\aleph = \aleph_1 + \aleph_2 + \frac{e^2}{4\pi\varepsilon_0|r_1 - r_2|} \tag{154}$$

Hence, the total Hamiltonian contains two one-electron Hamiltonians corresponding to the two electrons and an additional term that describes the Coulomb interaction among the electrons. According to Pauli principle, up to two electrons with antiparallel spins may be located in the same orbital. The one-electron wave functions $\varphi_a(ri) = \varphi_a(i)$ and $\varphi_a(r_i) = \varphi_b(i)$, with $i = 1$ and 2 satisfies the time independent Schrödinger equations for one-electron Hamiltonians

$$\begin{aligned} \aleph_i\varphi_a(i) &= E_a\varphi_a(i) \\ \aleph_i\varphi_b(i) &= E_b\varphi_b(i) \end{aligned} \tag{155}$$

The two Hamiltonians are identical. To analyze this system it is possible to start from a very simple Hamiltonian equal to the sum of one-electron Hamiltonians

$$\aleph_0 = \aleph_1 + \aleph_2 \tag{156}$$

The wave function of this system is a product of one-electron wave functions $\phi_a$and ϕ_b and should include also the effect of the electronic spin orientation introduced by the spin wave functions $\alpha(\sigma)$ and $\beta(\sigma)$ reflected the spin up and spin down orientations, respectively. The total wave function has to be antisymmetric. It will be expressed by Slater determinants [37]

$$\begin{aligned}
\Psi_1(r_1,\sigma_1,r_2,\sigma_2) &= \frac{1}{\sqrt{2}}\begin{vmatrix}\varphi_a(r_1)\alpha(\sigma_1) & \varphi_a(r_2)\alpha(\sigma_2)\\ \varphi_a(r_1)\alpha(\sigma_1) & \varphi_a(r_2)\alpha(\sigma_2)\end{vmatrix}\\
\Psi_2(r_1,\sigma_1,r_2,\sigma_2) &= \frac{1}{\sqrt{2}}\begin{vmatrix}\varphi_a(r_1)\beta(\sigma_1) & \varphi_a(r_2)\beta(\sigma_2)\\ \varphi_a(r_1)\alpha(\sigma_1) & \varphi_a(r_2)\alpha(\sigma_2)\end{vmatrix}\\
\Psi_3(r_1,\sigma_1,r_2,\sigma_2) &= \frac{1}{\sqrt{2}}\begin{vmatrix}\varphi_a(r_1)\alpha(\sigma_1) & \varphi_a(r_2)\alpha(\sigma_2)\\ \varphi_a(r_1)\beta(\sigma_1) & \varphi_a(r_2)\beta(\sigma_2)\end{vmatrix}\\
\Psi_3(r_1,\sigma_1,r_2,\sigma_2) &= \frac{1}{\sqrt{2}}\begin{vmatrix}\varphi_a(r_1)\beta(\sigma_1) & \varphi_a(r_2)\beta(\sigma_2)\\ \varphi_a(r_1)\beta(\sigma_1) & \varphi_a(r_2)\beta(\sigma_2)\end{vmatrix}
\end{aligned} \tag{157}$$

The factor $1/\sqrt{2}$ has been introduced to normalize the wave functions Ψ (the wave functions φ_a si φ_b are normalized). The energy levels for this simple system are:

$$\begin{aligned}
E_T &= E_A + E_B + K_{AB} - J_{AB}\\
E_S &= E_A + E_B + K_{AB} + J_{AB}
\end{aligned} \tag{158}$$

where K_{AB} describes the Coulomb interaction between the two electrons A and B and J_{AB} the exchange interaction between these electrons, defined by

$$\begin{aligned}
K_{AB} &= \iint\left(\frac{e^2}{4\pi\varepsilon_0|r_1-r_2|}\right)|\varphi_A(r_1)|^2|\varphi_B(r_2)|^2\,dr_1\,dr_2\\
J_{AB} &= \iint\varphi_A^*(r_1)\varphi_B^*(r_2)\left(\frac{e^2}{4\pi\varepsilon_0|r_1-r_2|}\right)\varphi_A(r_2)\varphi_B(r_1)\,dr_1\,dr_2
\end{aligned} \tag{159}$$

By inspecting the energy levels it is observed that the exchange interactions splits the energy levels into a singlet state and a triplet state and that for $J_{AB} > 0$ the triplet state is the lowest state. If the exchange integral is positive, the minimum energy of the system corresponds to the triplet state with all spins aligned parallel, while if the exchange integral is negative the minimum energy state will correspond to antiparallel electronic spins.

Heisenberg and Dirac used for the exchange interactions a simplified Hamiltonian [34–37]

$$\Xi_S = A + B\vec{S}_1\vec{S}_2 \tag{160}$$

In the general case, the exchange interaction may be expressed, up to an additive constant, by the following Hamiltonian

$$\Xi_S = -\frac{1}{2}\sum_{\substack{A,B\\A\neq B}} J_{AB}\vec{S}_A\vec{S}_B \tag{161}$$

For an ensemble of electronic spins, if the exchange integral is positive, the minimum energy will impose the parallel orientation of all electronic spins resulting in a ferromagnetic order.

1.7.3.3.b. The Molecular Field Approximation The Heisenberg Hamiltonian that describes the exchange interaction for an ensemble of atoms located in a crystalline lattice (with a quenched orbital momentum) specified by the position vectors R_A and by the total electronic spin S_A is [34–37]

$$\Xi = \Xi_0 - \left(\frac{1}{2}\right)\sum_{\substack{A,B\\A\neq B}} J_{AB}\vec{S}_A\vec{S}_B \tag{162}$$

In the molecular field approximation, the atomic total spin, S_A, is interacting with the average spin $\langle S_B \rangle$ of nearest atoms. Hence,

$$\Xi = \Xi_0 - \left(\frac{1}{2}\right) \sum_{A \neq B} \left(\sum_B J_{AB} \langle \vec{S}_B \rangle \right) \vec{S}_A = \Xi_0 - \sum_{A \neq B} \left(\sum_B \frac{J_{AB} \langle \vec{S}_B \rangle}{2g\mu_B} \right) g\mu_B \vec{S}_A \tag{163}$$

It is observed that this Hamiltonian describes an electron of spin S_A placed in an effective magnetic field H_{eff}^A

$$\Xi_H^A = -\sum g\mu_B \vec{H}_{\text{eff}}^A \vec{S}_A \tag{164}$$

This allows the identification of the effective field if all electronic spins

$$\vec{H}_{\text{eff}}^A = \frac{\sum_B J_{AB} \vec{S}_{AB}}{2g\mu_B} \tag{165}$$

If all electronic spins are identical, the effective magnetic field acting on the S_A spin is

$$\vec{H}_{\text{eff}}^A = \frac{zJ_A \vec{M}}{2g^2 n\mu_B} \tag{166}$$

where z is the number of nearest neighbors, **M** the magnetization due to the z nearest neighbor spins, and n is the density of nearest electrons

$$\vec{M} = -2\mu_B \frac{\sum g\vec{S}}{V} = -ng\mu_B S \tag{167}$$

The exchange interaction has a strong distance dependence decreasing drastically as the distance between the electronic spins is increased. Hence, the effect of remote spins on the spin S_A may be neglected, as the distance to these electronic spins is large. To conclude, it is possible to identify H_{eff}^A with the molecular (in a first-order approximation). Within the Weiss description of the molecular field [34], the magnetic energy, E_{WEISS}, is

$$E_{\text{WEISS}} = -\lambda_W g\mu_B \vec{M}\vec{S} \tag{168}$$

Accordingly, the relationship between the Weiss molecular field constant λ_{WEISS} and the exchange integral is

$$\lambda_{\text{WEISS}} = \frac{zJ}{2ng^2\mu_B} \tag{169}$$

The model allows the estimation of the Curie temperature, T_C, which is the temperature at which the spin orientation is shuffled (by increasing the temperature from low temperatures above the Curie temperature a transition form the ferromagnetic state into the paramagnetic state is predicted at Curie temperature) [34, 37].

$$T_C = \frac{zS(S+1)}{6K_B} J \tag{170}$$

The molecular field approximation explains of the magnetization curves [34–37]

$$\frac{M(T,H)}{M_S(T)} = B_j\left(\frac{g\mu_B m_j (H \pm H_{\text{MOL}})}{K_B T}\right) = \frac{2j+1}{2j} cth\left(\frac{2j+1}{2j} \frac{g\mu_B m_j (H \pm H_{\text{MOL}})}{K_B T}\right) - \frac{1}{2j} cth\left(\frac{1}{2j} \frac{g\mu_B m_j (H \pm H_{\text{MOL}})}{K_B T}\right) \tag{171}$$

where M_S is the magnetization at saturation and T is a temperature.

The existence of a molecular field explains the organization of a bulk ferromagnetic sample in domains. Refined theoretical calculations showed that the domain structure of ferromagnetic materials results from the minimum of the energy of the ferromagnetic material. The

domains are separated by very thin walls. Within these walls, the orientation of electronic spins is changed. Placed in an external magnetic field, the domains are reoriented and only at sufficiently high magnetic fields the spin reorientation process will also occur in the wall resulting in an homogeneous magnetic state at saturation.

The dependence of the magnetization of ferromagnetic materials on the applied external field has a typical shape, defined as hysteresis loop (see Fig. 24) [35, 36]. Increasing the external magnetic field, the magnetization of the sample is increased toward an asymptotic value, named magnetization at saturation. In this state, in an ideal ferromagnetic bulk sample, all electronic spins will be oriented along the direction of the external magnetic field. Changing the field orientation the magnetization is decreased. At zero external magnetic fields, a residual magnetization named magnetization at saturation is observed (M_R^-). Further increase of the magnetic field in the opposite direction would result in the quenching of the magnetization at an external magnetic field named coercive field (H_C^-), and further to a saturation value of the magnetization, M_S^-. Increasing the field back to the high values new remanent magnetization (M_R^-), coercive field (H_C^+), and magnetization at saturation (M_S^+) will be observed. In an ideal ferromagnetic sample, the following relations are satisfied (see Fig. 24)

$$\begin{aligned} H_C^+ &= H_C^- = H_C \\ M_S^+ &= M_S^- = M_S \\ M_R^+ &= M_R^- = M_R \end{aligned} \tag{172}$$

1.7.3.4. Ferrimagnetic and Antiferromagnetic Materials There are several types of magnetic ordering related to different kinds of correlations between the electronic spins [34–37] (see Fig. 23). The most important ones are the ferromagnetic and the antiferromagnetic order. The antiferromagnetic order has been observed [34–37] in materials that present two sublattices. The magnetization of each sublattice M_A and M_B is identical but each is pointing in opposite directions. The temperature dependence of the magnetic susceptibility of antiferromagnetic materials is (see panel *B* of Fig. 23)

$$\chi = \frac{C}{T + T_N} \tag{173}$$

where C is a constant and T_N is the Neel temperature, which characterizes the transition from antiferromagnetism to paramagnetism.

The ferrimagnetic order may be assimilated with a ferromagnetic order (see panel *C* of Fig. 23). A ferromagnetic material consisting of two sublattices has different magnetization pointing in opposite directions on each sublattice. The temperature dependence of the

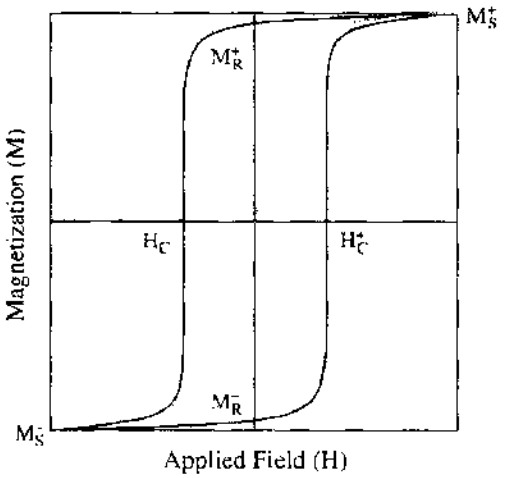

Figure 24. The hysteresis loop.

susceptibility for magnetic materials consisting of two magnetic sublattices is described by the magnetization of each sublattice, $\mathbf{M}_1$ and $\mathbf{M}_2$:

$$\begin{aligned}\vec{M}_1 &= \frac{C_1}{T}(\vec{H} + \lambda_{12}\vec{M}_2)\\ \vec{M}_2 &= \frac{C_2}{T}(\vec{H} + \lambda_{21}\vec{M}_1)\end{aligned} \tag{174}$$

The temperature dependence of the susceptibility for such a material is

$$\begin{aligned}\chi &= (C_1 + C_2)\frac{T - T_A}{T^2 - T_N^2}\\ T_A &= -\frac{C_1 C_2}{C_1 + C_2}(\lambda_{12} + \lambda_{21})\\ T_N &= \sqrt{C_1 C_2 \lambda_1 \lambda_2}\end{aligned} \tag{175}$$

Several effects occur when one-dimensional magnetic nanostructures (thin films) are sandwiched together in a multilayer structure. If two thin films, one ferromagnetic is deposited over an antiferromagnetic film, and enhancement of the coercive field usually assigned to interfacial spins is obtained. If the film is deposited in an external magnetic film or the bilayer is heated above the Neel temperature of the antiferromagnetic film (which is lower than the Curie point of the ferromagnetic layer), an exchange bias phenomenon that consists in de displacement of the coercive field (in this case $H_C^+ \neq H_C^-$) is observed.

2. THE INTERACTION OF IONIZING RADIATION WITH MATERIALS (AT NANOMETER SCALE)

The interaction of radiation with targets is a multiscale process occurring in the time-space domain. Shortly after the interaction of the incident radiation with the atoms and/or electrons of the target, localized excitations and ionization processes are observed [1–3]. The deposited energy is delocalized over larger domains by various processes. The most important elements and feature of the interaction between radiation and condensed matter will be briefly discussed in this section.

2.1. Excitation and Ionization Processes of Atoms and Molecules

The interaction between the incoming particles and the target's atoms or molecules results locally and at extremely short times in the excitation and eventually in the ionization of target's atoms. These are the elementary processes triggered by the energy deposited within the target by impinging charged particles. Several routes for the excitation and ionization of the target atoms are possible. The most important are:

2.1.1. The Simple Electronic Capture

In this case, the (target) molecule AB captures a low energy electron generating an excited molecule ion. An atom, a molecule, a radical molecule, or an ion molecule may initiate the capture. This process is described by

$$AB + e^- \Rightarrow (AB^-)^* \tag{176}$$

The dissociating electronic capture is a two-step process: the first one is represented by a classical electronic capture while in the second step the excited molecule is rapidly dissociated. This process is favoured over the simple electron capture if the kinetic energy of the electron is high.

2.1.2. The Dissociation of Excited Molecules

An excited molecule may dissociate into two or more molecules or atoms. The excited molecule eventually releases an electromagnetic quantum of frequency, ν. The dissociating molecule may be neutral, ion, radical, and radical ion. The resulting molecules or atoms may

be also in excited states. The resulting molecules (or atoms) may be neutral molecules, ions, or radicals, or radical ions.

$$(AB)^* \Rightarrow (A)^* + (B)^* + h\nu \tag{177}$$

where h is the Planck constant.

2.1.3. Transfer Reactions

Two main transfer reactions, namely charge transfer reactions and energy transfer reactions, are usually triggered by the energy deposited within the target by the impinging radiation. The resonant transfer reaction occur between identical ions and molecules (but in different ionization states in the case of charge transfer reactions)
Charge transfer reactions:

$$(A^+) + (B) \Rightarrow (B^+) + (A) \tag{178}$$

$$(A^-) + (B) \Rightarrow (B^-) + (A) \tag{179}$$

Resonant charge transfer reactions:

$$(A^+) + (A) \Rightarrow (A^+) + (A) \tag{180}$$

$$(A^-) + (A) \Rightarrow (A^-) + (A) \tag{181}$$

Excitation transfer:

$$(A)^* + (B) \Rightarrow (B)^* + (A) \tag{182}$$

2.1.4. Recombination Reactions

Ionized molecules and atoms as well as radical ion molecules exhibit usually a high chemical reactivity. They may recombine leading to the formation of neutral molecules that are eventually in an excited state. The typical recombination reaction is represented by

$$(A^+)^* + (B^-)^* \Rightarrow (AB)^* \tag{183}$$

The generation of excited states such as ion pairs is quantitatively defined by the ionization yield, G, that measures the number of ion pairs produced by 100 eV of energy deposited within the target. In a gas, the mean energy necessary to generate a ion pair is greater than the lowest ionization potential of the molecule [1]. This indicates that a lot of energy is wasted solely to excite the molecules of the target. For example, the lowest ionization potential for oxygen is about 12.1 eV, while $W = 30.8$ eV [38]. The mean energy, W, required to produce a ion pair when an incoming particle of kinetic energy E is completely stopped within a gas is

$$W = \frac{E}{N} \tag{184}$$

where N is the number of ion pairs produced by the incident radiation. G and W are related by the relationship

$$G = \frac{100}{W} \tag{185}$$

This definition of G takes into account solely the production of primary radicals.

2.2. Quantum Excitation and Ionization of Molecules: Rudiments

For a better understanding of the excitation and ionization processes in molecules, the case of the diatomic molecule will briefly be analyzed. The time independent Schrödinger equation for this simple quantum problem is [17, 18, 22–24, 38]

$$-\frac{\hbar^2}{2M_A}\nabla^2\Psi(r_A, r_B) - \frac{\hbar^2}{2M_A}\nabla^2\Psi(r_A, r_B) - \frac{\hbar^2}{2m_e}\sum_i \nabla_i^2\Psi(r_A, r_B) = (E - E_i + V)\Psi(r_A, r_B) \tag{186}$$

where M_A and M_B is the mass of the ion A and B, respectively, m_e is the mass of the electron, V is the potential energy of the system, E_t its total energy, and Ψ is the wave function of the molecule. In the center of mass system is obtained:

$$-\frac{\hbar^2}{2M_A}\nabla_0^2\psi(r_0, r) - \frac{\hbar^2}{2M_A}\nabla^2\psi(r_0, r) - \frac{\hbar^2}{2m_e}\sum_i \nabla_i^2\psi(r_0, r) = (E + V)\psi(r_0, r) \quad (187)$$

where $M = M_A + M_B$ is the total mass, $\mu = M_A M_B/(M_A + M_B)$ is the reduced mass, and $r_0 = (M_A r_A + M_B r_B)/(M_A + M_B)$ defines the center of mass position. The wave function of the hydrogen atoms may be written as a product between the wave function in the fix (center of mass) system ξ_0 and a wave function ζ,

$$\Psi = \xi_0\zeta \quad (188)$$

Hence, the Schrödinger equation (187) is deconvoluted into two equations:

$$-\frac{\hbar^2}{2M_A}\nabla_0^2\xi_0 = E_\xi\xi_0 \quad (189)$$

$$-\frac{\hbar^2}{2M_A}\nabla^2\zeta(r_0, r) - \frac{\hbar^2}{2m_e}\sum_i \nabla_i^2\zeta(r_0, r) = (E - E_\zeta - V)\zeta(r_0, r) \quad (190)$$

The equation (189) is the time-independent Schrödinger equation for a free particle with the kinetic energy, E_ξ. The expression (190) contains both the nuclear and electronic motions. The nuclear and electronic motions may be decoupled by writing the wave function ζ as the product of two wave functions associated with the nuclear, ζ_N, and electronic, ζ_e, movements, respectively. The Born-Oppenheimer approximation [18, 22, 24, 34] is based on the assumption that it is possible to suppose that the nuclei motions are frozen in comparison with the electronic ones. This allows a further deconvolution of the Schrödinger equation (189) into two Schrödinger equations:

$$-\frac{\hbar^2}{2M_A}\nabla^2\zeta_e = (E_\zeta - V_e)\zeta_e \quad (191)$$

$$-\frac{\hbar^2}{2m_e}\sum_i \nabla_i^2\zeta(r_0, r) = (E_t - E_\zeta - V)\zeta(r_0, r) \quad (192)$$

where V_e is the potential energy of the electronic system with the frozen nuclei, and V is the potential energy of the system. As observed from Fig. 25, the potential energy $V(r)$ has a minimum corresponding to a bond state of the molecule. The minimum is observed both in fundamental and excited states. If the potential energy $V(r)$ has a monotonous dependence on distance, r, the system is labile and its state corresponds to an antibonding orbital (see Fig. 25).

The excitation of molecules in condensed state involves also the lattice, which receives a fraction of the energy of the incident particle. In these cases, the energy is migrating incoherently from the high-energy particles produced by the interaction of the incident particle with the target to the lattice and it is finally dissipated over a large volume around the incident particle trajectory within the target. Eventually, these excited states are trapped by capture centers within the target [1–3, 38]. The ionization and dissociation are the extreme cases of excitations. By assuming that the molecule of the target are initially in the ground state, characterized by $v = 0$, the interaction with the impinging radiation will excite some of these molecules to a new energy level described by $v' = 1$. The subsequent transfer of energy from the excited molecule AB_i to a ground state molecule AB_j is schematically depicted by the equation

$$AB_i^{v'=1} + AB_j^{v=0} \Rightarrow AB_i^{v=0} + AB_j^{v'=1} \quad (193)$$

where the inferior index characterizes the molecules and the superior one its vibrational state (0 for ground and 1 for excited). The theoretical description of molecular excitations

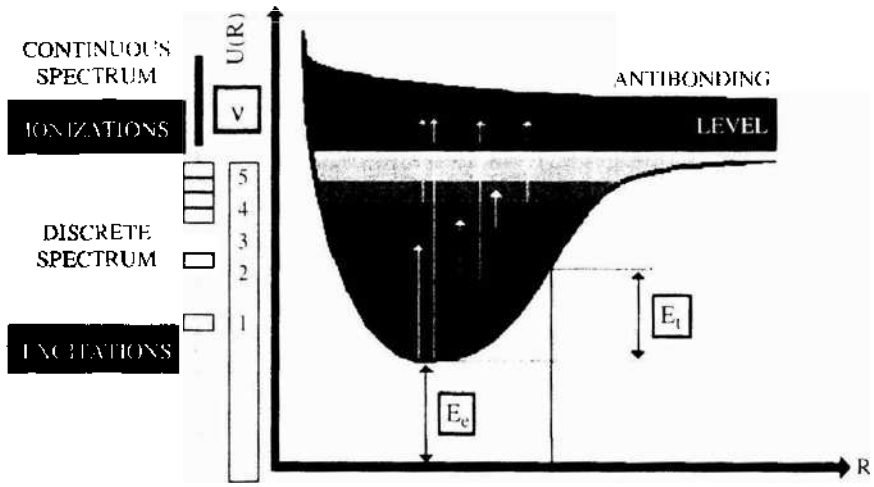

Figure 25. The excitation and ionization of a molecule.

is based on the assumption that the time required for electrons to jump from the ground level to an excited state is very short and accordingly it is fair to neglect the modifications in the nuclear configuration of molecules during such transitions (see Fig. 26).

2.2.1. Frank-Condon Principle

The Frank-Condon principle exploits the fact that the electronic motions are much faster than the nuclear ones. Hence, with an acceptable accuracy the configuration of nuclei may be supposed frozen during electronic transitions. Few important consequences are derived from this principle [39]:

1. In the energy position representation, (see Figs. 25 and 26) all electronic transitions (emission and absorption) are vertical transitions.
2. If both the initial and final states have the same (nuclear) equilibrium configuration (i.e., the same R_e; see Figs. 25 and 26), there are no restrictions for the excitation of the molecule.
3. If the equilibrium position of the initial state is not identical to the equilibrium position of the final state, not all transitions from the ground state to the excited state are possible (see Fig. 26).

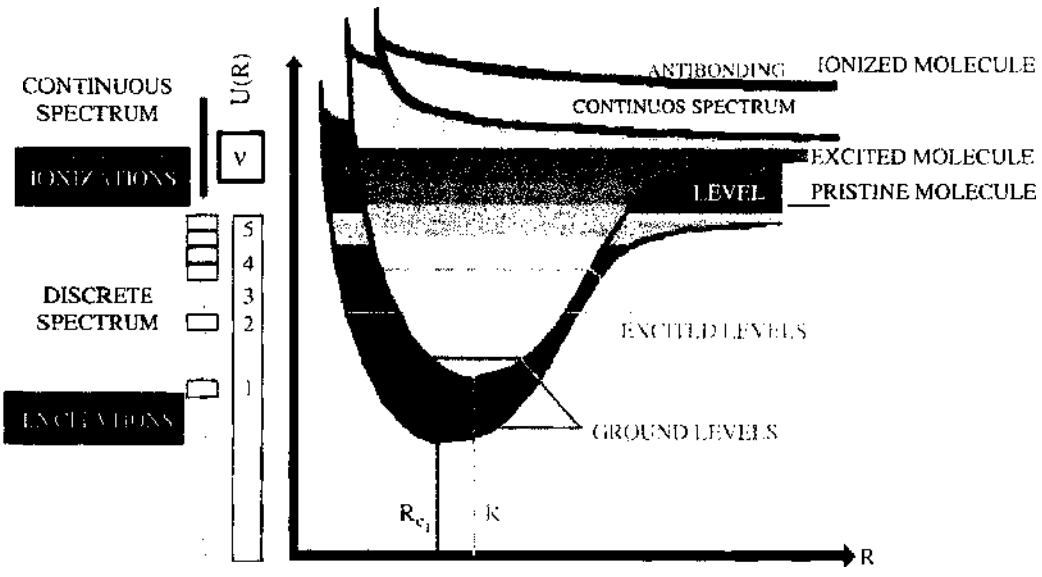

Figure 26. Energy transfer in molecules.

2.3. Latent Tracks, Spurs, and Blobs

The incident radiation excites and ionizes the atoms or the molecules of the target. If the energy deposited within the target is small up to 10^2 eV, only few atoms or molecules of the target will be ionized. Such a cluster of few ions is defining a spur. The size of the spur is between 0.1 nm to about 1 nm [1]. By increasing the energy of the incident particle, isolated spurs along the incident particle trajectory within the target will be produced. Higher incident kinetic energies lead to the formation of blobs or spurs distributed like a string of beads along the incident particle trajectory. For energies larger than 10^3 eV, the energy deposited within the target by the impinging particle is able to produce short tracks, which are in fact an overlapping collection of spurs along the incident particle trajectory in the target. The blob is supposed to represent a knock-on electron that has no sufficient energy to overcome the attraction of its sibling hole [1].

Further increase of the energy deposited within the target by the impinging radiation leads to the appearance of a collective modification within the target, named *latent track*. The latent track is represented by a continuous, collective degradation of target material. In isotropic targets, the latent track has a conical shape. For very thin targets, the shape of the latent track may be supposed to be cylindrical. The radius of the core of the track is frequently ranging between few nanometers and hundreds of nanometers, depending on the charge, mass, and kinetic energy of the incoming particle.

Although the elemental defect induced by the incident particle inside the target is the spur, its reduced size and the limited sensitivity of instruments prevented a thorough analysis of spurs. Further increase of the energy deposited within the target by the incoming particle will increase the size (diameter) of the spur and eventually will produce branched spurs or/and a collection of spurs that will eventually degenerate into a quasi-continuous modification (latent track).

3. DOSIMETRY, MICRODOSIMETRY, AND NANODOSIMETRY

The most important quantities of dosimetry were defined in Section 2.3. These definitions will be critically reviewed in this section together with a brief introduction of the main quantities in microdosimetry. The limits of these definitions at nanometer scale will be analyzed in detail.

3.1. The Dose Definition

Macrodosimetry is a theoretical limit of dosimetry at large scales. It is instructive to start from this point in order to locate the main limits of dosimetry, at different scales. The most important parameter describing the radiation-induced modifications quantifies the energy, ΔE, deposited by the incident radiation within a target characterized by the mass M. In macrodosimetry, the universe is divided into two halves, one filled with the target and the other one empty. The impinging radiation is coming from the empty side of the universe and is interacting with the target. The ideal solid target is a perfect single crystal that covers half of the universe and presents a high thermal conductivity. The most important parameter in dosimetry is the dose, D_M, defined by the ratio between the energy deposited by the radiation within the target and the mass of the target, [21, 25–30] M:

$$D_M = \frac{\Delta E}{M} = \frac{E_{INC}}{M} \tag{194}$$

where E_{INC} is the energy of the incident beam. Within the ideal conducting crystal approximation, the excitations produced by the energy deposited within the target by the incident radiation will be dissipated over the whole crystal. By neglecting possible reflections at the interface between the empty half of the universe and the ideal crystalline half of the universe, the full energy of the impinging radiation will be transferred to the target and delocalized over the entire filled half of the universe. The main problem is that in macrodosimetry the dose will be almost zero due to the large value of M and to the hypothesis that the deposited energy is delocalized over the whole target.

To overcome this difficulty, a local deposited dose, D_L^M, may be defined within the macrodosimetry approximation

$$D_L^M = \frac{\Delta E_{\text{LOC}}}{\Delta M_{\text{LOC}}} = \frac{E_{\text{INC}}^{(V)} - E_{\text{TRANS}}^{(V)}}{\Delta M_{\text{LOC}}} \tag{195}$$

where ΔE_{LOC} is the energy deposited by the incident beam within the small volume characterized by the mass ΔM_{LOC} (which now it is a finite number). As there are no boundaries, there are no reflections at the edges of the volume V. Accordingly, the energy deposited by the incident radiation within this volume is defined as the difference between the energy incident on the volume, $E_{\text{INC}}^{(V)}$, and the energy transmitted through this volume, $E_{\text{TRANS}}^{(V)}$. The ideal characteristics of the target ensure that $D_M = D_L^M$. The dose is expressed in Gray, Gy (1 Gy = 1 J/kg).

To conclude, in macrodosimetry it is accepted that the whole energy of the incident beam is delocalized over the whole target. The dose is the simple ratio between the energy of the incoming radiation and the mass of the target. The local dose and the dose are equal. In macrodosimetry, both M and M_L are constants. By default, in macroscopic dosimetry it is assumed that no radiation or particles are leaving the target. This was an important source of errors in the estimation of the energy deposited within the target by the incident radiation.

3.1.1. Dose in the Dosimetry of Real and/or Finite Size Targets

If the crystalline half of the universe is an insulator, the phonon excitations of the lattice due to the energy deposited by the incident radiation within the target are damped and eventually after a penetration depth, L, no more energy is transferred from the incident particle to the target. Hence, the energy of the incident radiation is dissipated only within a restricted mass M' rather than over the all-crystalline half of the universe. Under these circumstances, the definition of the dose as given by Eq. (194) is no more valid and has to be replaced by

$$D = \frac{\Delta E}{M'} \tag{196}$$

This example shows the actual difficulties in an accurate estimation of the dose for finite size samples. In the general case, it will be necessary to estimate accurately the energy of the incident beam E_{INC}, the energy of the reflected beam $E_{\text{REFLECTED}}$, and the energy of the transmitted beam, $E_{\text{TRANSMITTED}}$. For an accurate estimation of the energy deposited within the target by the incident radiation, ΔE, has to be replaced by $E_{\text{INC}} - (E_{\text{REFLECTED}} + E_{\text{TRANSMITTED}})$. The exact estimation of M' is a little trickier, as it will be necessary to estimate accurately only the volume that was affected by the energy deposited by the incident radiation and to multiply it with the initial density of the target. In dosimetry, the difficulty to estimate accurately M' has rather a technical character as this mass is still supposed to be constant during irradiation.

As in the case of macrodosimetry, the local dose, D_L, is defined by an analogous expression.

$$D_L = \frac{\Delta E_{\text{LOC}}}{\Delta M'_{\text{LOC}}}; \quad \Delta M'_{\text{LOC}} \leq M_{\text{LOC}} \tag{197}$$

The condition imposed to $\Delta M'_{\text{LOC}}$ is equivalent with the condition to have the local volume corresponding to $\Delta M'_{\text{LOC}}$ completely embedded in the volume over which the energy of the incident radiation is dissipated (which defines M'). As in the case of macrodosimetry, for most samples it is still possible to assume that the local dose and the dose are equal, as long as cautions are taken in the proper definition of the mass. The big lesson of dose in the dosimetry of real and finite size targets is that the dose in itself is not relevant. The significant quantity is the absorbed dose. This requires a proper definition of the mass M. For simplification, throughout this paper the term *dose* will refer to absorbed dose. The difficulties reached in the accurate definition of M increase as the size of the target is reduced.

3.1.2. Dose in Microdosimetry

The dose definition in microdosimetry, D_μ, is a natural refinement of the local dose definition in dosimetry, and may be easily obtained by shrinking the mass of the target [26–30].

$$D_\mu = \lim \frac{\Delta E}{\Delta M'}\bigg|_{\Delta M' \to 0} \tag{198}$$

The specific energy, z, is a principal microdosimetry quantity analogous to the absorbed dose and defined by the expression

$$z = \frac{\Delta E'}{\Delta M'} \tag{199}$$

where $\Delta E'$ is the energy imparted to target atoms confined within the volume $\Delta V'$ and characterized by the mass $\Delta M'$. The energy of the incident radiation is delocalized over the whole volume $\Delta V'$.

The microdosimetry dose is somehow related to the local dose in dosimetry. Nevertheless, the average dose in microdosimetry should be equal to the dosimetry dose as long as the mass of the target is properly defined. In the microdosimetry definition of dose, the mass is still supposed to be constant (i.e., not affected by the incoming radiation). The huge number of atoms and molecules contained in a solid at micron scale justifies this assumption. The eventual changes in the local density of the target due to the energy deposited by the incident radiation are in most cases associated with the displacement of a relatively reduced fraction of atoms over small distances. Hence the number of atoms contained in the volume defined by $\Delta M'$ is not significantly modified. Nevertheless, severe irradiation would eventually result in modifications at micron scale that are at variance with these assumptions.

3.1.3. Dose in Nanodosimetry

The definition of the dose in microdosimetry survived due to the huge number of atoms at micron scale. The nanometer scale is associated with a reduced number of atoms. A crystalline gold cube with the edge of 1 nm contains about 100 atoms. If such a small feature is hit by an incident particle, the effects of the energy deposited by this particle within the target—at nanometer scale—are dramatic. As shown in Figs. 27A to 27D, the crystalline structure is locally destroyed, and the atom displacements would make impossible a proper definition of the mass. This is because at this scale the mass is no more a constant. As it is observed from Fig. 27D, the local density of the target is changed after the interaction with the incident beam. The only parameter that would be invariant is the volume. In the case of the gold cube (with the edge of one nanometer), few atom displacements may reduce the mass of the atoms confined in a given volume (invariant to irradiation) by few percents. A micrometer-sized gold cube would contain about 10^{11} atoms, and hence the displacement

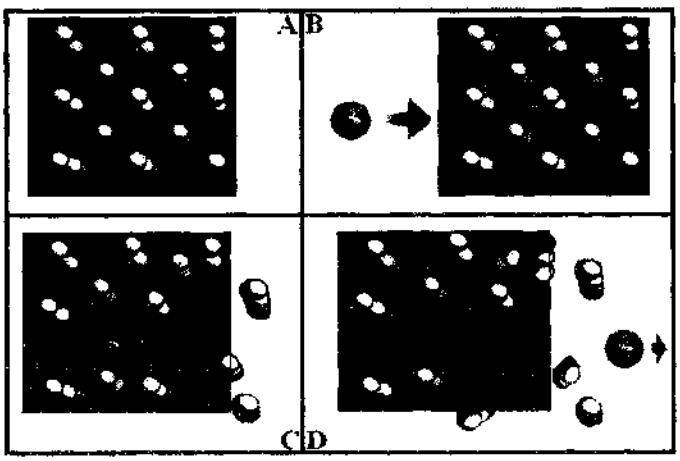

Figure 27. The interaction of a particle with a nanocrystalline cluster.

of few atoms will produce no significant changes in the mass of the target. Amorphization is one of the first effects of radiation at nanometer scale that reflects the effect of atomic displacements [40–42].

Although the difficulties encountered by a proper definition of the dose were not obvious in microdosimetry, the development of microdosimetry was associated with important advances in the understanding of the interactions between incident particles and solid targets, at micrometer scale. Various quantities have been defined and their correspondence and significance to dosimetry were carefully investigated. The interactions between the impinging ionizing radiation and the condensed matter—at nanometer scale—required a new classification of track interactions. Assuming a nanometer sized sphere within the target, various trajectories have been defined [29] (see Fig. 28). The crossed defines a particle that is mowing through the sphere, the stopper a particle stopped within the sphere, the starter a new particle (electron) that is emerging from the sphere, and the insider a particle (electron) that was generated and stopped within the sphere. A passer or a toucher is a secondary electron, produced inside the sphere by a ionizing radiation whose trajectory is not intersecting the sphere.

3.2. The Linear Energy Transfer (Stopping Power) in Nanodosimetry

The linear energy transfer, LET, represents the energy lost by an incident particle across its trajectory within a solid target [25–30]. Within the ideal macrodosimetry model, if the particle is channeling along the crystal and it is stopped at infinity the linear energy transfer L_M is zero.

$$L_M = \frac{E}{l} \tag{200}$$

Although the particle is traveling through the target, several kinds of interaction are responsible for the transfer of the energy from the incident particle to the target. The most important interactions are (1) the electric interaction between the electrons and the ionic cores (nuclei) amd the incident charged particle and (2) the direct collision between the incident particle amd the nuclei of the target. In the ideal crystalline solid, the channeling allows the incident particle to travel without a direct hit with the ionic cores (nuclei). Hence, its energy will be gradually decreased due to the interaction between the incident particle and the electrons of the target. The trajectory of the particle would be linear, and regularly distributed interaction points between the target and the incident particle are expected. In real experiments, small local inhomogeneities randomizes the space distribution if interaction points.

As in the previous case, it is possible to define a local linear energy transfer, L_{loc}:

$$L_{\text{loc}} = \frac{\Delta E}{\Delta l} \tag{201}$$

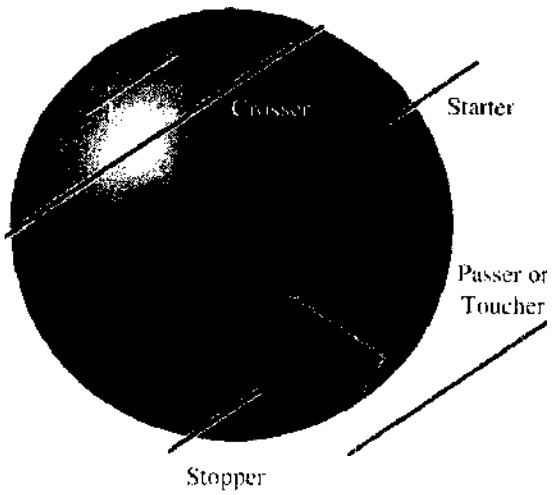

Figure 28. A classification of the interactions between an ionizing particle and a nanosphere.

where ΔE is the energy lost by the particle along its trajectory, over a length, l, while L_M is zero or extremely low (the particles is stopped at infinity), and L_{loc} is a finite quantity. In finite targets, the incident particle may leave the target with a reduced kinetic energy. By exposing real targets to accelerated charged particles, the nuclear collisions and the electrical interactions between target's nuclei and incident particles will compete with the energy transfer via electric interaction between the incident particle and the electrons of the target. At moderate and low energy, the contribution of both electric interactions (electronic and nuclear) to LET have to be considered.

$$L_{\text{loc}} = L_{\text{loc}}^{\text{electronic}} + L_{\text{loc}}^{\text{nuclear}} = \left(\frac{\Delta E}{\Delta l}\right)_{\text{electronic}} + \left(\frac{\Delta E}{\Delta l}\right)_{\text{nuclear}} = \frac{\Delta E}{\Delta l} \tag{202}$$

Leaving the ideal model of particle channeling, the trajectory of the incident particles within target is no more linear. The distance traveled by the particle within the target along the incidence direction l_{target} is no more equal to the length of the particle trajectory within the sample, $l_{\text{trajectory}}$, which is a sum of individual trajectories $l_{\text{trajectory}}^{(i)}$:

$$l_{\text{trajectory}} = \sum_{i=1}^{N} l_{\text{trajectory}}^{(i)} \geq l_{\text{target}} \tag{203}$$

As may be inferred from Fig. 29, there is a difference between the thickness of the target (l_{target}) and the total trajectory of a particle in a finite target. In the real case, the charged particle changes its direction within the target due to N interactions with the target. This makes the total trajectory larger than the length of the target (see Fig. 30). The total LET, L_T, may be defined as a sum of N local LETs that contain both electronic and nuclear contributions

$$L_T = \sum_{i=1}^{N} L_{\text{loc}}^{(i)} = \sum_{i=1}^{N} \frac{\Delta E_i}{l_{\text{trajectory}}^{(i)}} \tag{204}$$

where ΔE_i is the energy deposited by the particle after the ith collision event (i.e., along the ith trajectory). In the general case the positions where the incident particle interacts (collides) with the nuclei or with the electrons of the matrix are randomly distributed. The number of interaction points is also random, in the sense that an identical particle passing through an identical crystal will have neither the same number of interaction points nor the same position of the interacting points as the first particle. The statistical nature of the interaction between an identical charged particle and a target is depicted in Figure 29, where two identical particles are traveling within the same target. The right panel shows the lateral straggling of the incident particle (in this case even for a normal incidence the positions of the point where the particle hit the target and of the point where the particle left the target are not identical).

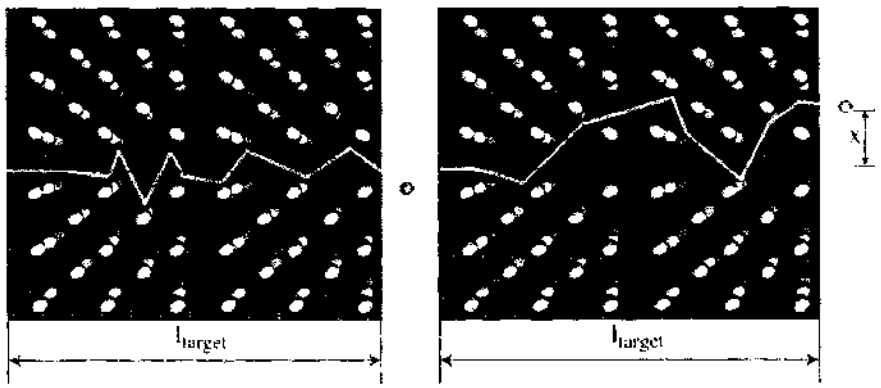

Figure 29. The trajectory of an ionizing particle within a nanocrystal. The lateral straggling of the incident particle is shown.

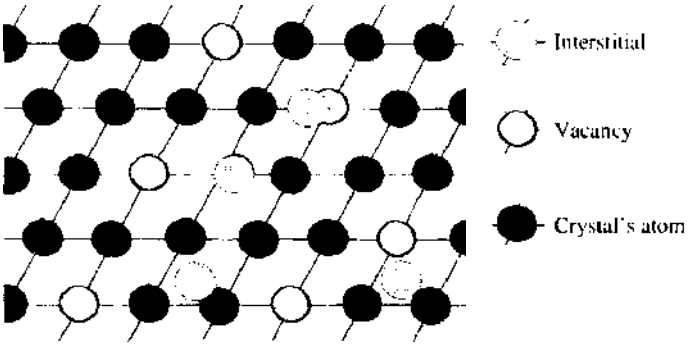

Figure 30. The primary defects produced by ionizing radiation in crystals (vacancies and interstitials).

In dosimetry, LET decreases as the particle penetrates within the target. The formal definition of LET in dosimetry is expressed by

$$L_M = \frac{dE}{dx} \tag{205}$$

LET is an important quantity in both dosimetry and microdosimetry. To understand properly this concept, a detailed analysis of the electrostatic interaction between the incident particle and the electrons of the target will be presented.

The analysis of the electromagnetic interactions between the incident charged particle and the electronic cloud of the target revealed that the actual models proposed for the description of the interaction between incident charged particles and solid targets were developed at sub-nanometer scale (see Fig. 13). Accordingly, these approximations are fair at nanometer scale and they cannot account for eventual deviations from the theoretical predictions.

A subtle difference arises between the stopping power and the linear energy transfer. The linear energy transfer defines the energy lost by the incident particle due to its electrostatic interactions with the electrons (and the ions) of the target. At least theoretically, this quantity may be estimated with an acceptable accuracy. The stopping power is the energy deposited within the target by the incident particles. While in microdosimetry and macrodosimetry it was tacitly assumed that the linear energy transfer is equal to the stopping power, this simplified hypothesis cannot hold at nanometer scale. Several processes are building a gap between the linear energy transfer and the stopping power. Among them the most important are:

- A fraction of the incident energy will be transmitted through the nanometer-sized target or reflected by the nanometer-sized target. This problem was addressed in microdosimetry by introducing a detailed energy balance. The same procedure may be used at nanometer scale.
- The target mass is no more a constant. Eventually it is possible to define an imaginary volume, with a size and shape not affected by irradiation. In this case, the mass of the sample after irradiation will be the mass of all particles still residing within this volume. Hence, the mass of the target has to be renormalized and the energy balance equation has to be modified to include this effect.
- The interaction of ionizing radiation with targets has been described in dosimetry and microdosimetry as a statistical process. At nanometer scale, the number of individual interactions is too small to have a representative statistical ensemble, and hence to have well defined averaged quantities. If the irradiation experiment involves a large ensemble of identical nanometer-sized features, or a huge number of interactions acts (high fluence), then the statistical analysis of the experimental data would result in accurate estimations. However, in the last case, attention should be paid to nonlinear processes triggered by multiple collisions.
- The interaction of ionizing radiation with a single nanometer-sized target—at the low fluence limit—may be modeled through molecular simulations.
- The nanometer-sized confinement of atoms and molecules affects some relevant quantum-mechanical features such as excitations and ionizations energies. These modifications have to be considered and introduced in the model that describes the effect of

ionizing radiation within nanodosimetry. If the interaction between the incident radiation and the nanometer-sized target is changing the details of atoms and molecules confinement, a renormalization step will be required to take into account such contributions.

4. RADIATION-INDUCED MODIFICATIONS AT NANOMETER SCALE

The interactions between radiation and target left the target in an excited state. After irradiation, the target relaxes toward an equilibrium state, which in the general case is not identical with the state of the target before irradiation. These physical and chemical modifications are extended at different scales. In this section, the most frequent modifications induced by the incident radiation in target are briefly presented. The actual models assumed that the radiation-induced modifications of the target are controlled by the stopping power. Some experimental data suggest that this is solely an approximation. The ratio between the secondary electron yield of carbon targets irradiated with accelerated protons and the stopping power was found to depend solely on the stopping power. In the case of heavy ions, this ratio was found to increase with the speed of the impinging ions (above the Bragg peak). In the Bragg peak region, at constant stopping power, secondary electrons generation is lower for high speed particles than for low speed particles. This reflects the possibility to have damage mechanisms that are not fully controlled by the stopping power [43].

4.1. Single Crystals

Several kinds of defects are generated by the interaction between incident particles and crystalline targets [25–30, 34]. At low kinetic energies (of incident particles), nuclear processes become important relative to the electronic ones. The direct collision between the impinging particles and the nuclei of the target may remove the atoms (or ionic moieties) from their position in the crystal leaving an empty space in the crystalline lattice named vacancy (see Fig. 3). This process is named *atom displacement* and occurs at sub-nanometer scale. In most cases, the atoms removed from their positions in the crystal lattice are not ejected from the crystal. Due to eventual minima of the potential energy these atoms may be accommodated by the crystalline lattice (see Fig. 31). They will occupy nonlattice sites in the crystal (interstitials). If the number of vacancies generated by the incident radiation is large enough, an atom removed from its position in the lattice may reach another lattice position in an adjacent vacancy. Such atom cannot be identified as a displaced atom by usual techniques. The lack of ability to distinguish fully which atom has been displaced at nanometer scale makes difficult a precise counting of atoms displacements induced by radiation in amorphous targets. These point defects may undergo clustering reactions, increasing their size to

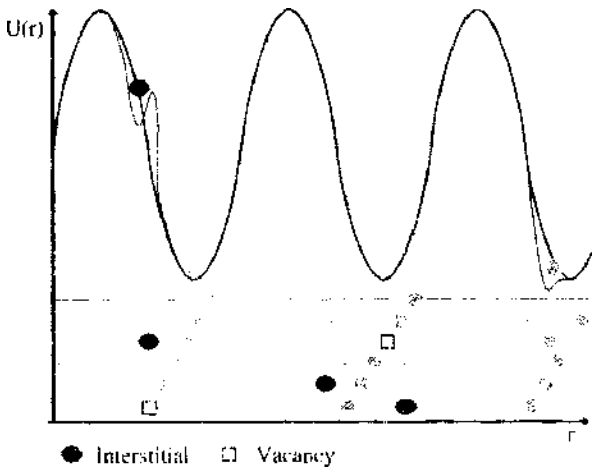

Figure 31. Radiation-induced interstitials in a crystal (the role of local imperfections in the energy structure of the crystal).

the micrometer scale. Recombination (annihilation) reactions between vacancies and interstitials are also possible. The clustering reactions depend on the binding energies between various species, diffusion coefficients, and temperature. It was recently reported [42] that the irradiation of crystalline nanoparticles (ZrO_2) with Xe ions accelerated up to about 1 MeV resulted in the amorphization of the target, although a not significant increase in the target temperature was measured.

Some of these defects are known as color centers [24, 34, 43, 44]. The structure of some simple color centers is depicted in Figs. 32–34. Figure 32 shows the structure of the F center, which is the simplest point defect in a crystal consisting of an electron trapped at a negative ion vacancy [34, 44, 45]. Figure 33 shows the F_2 center, which consists of two adjacent F centers. In general, the clusterization of F centers leads to the formation of F_N centers [45]. The F center is paramagnetic (has an uncoupled electronic spin). In Fig. 34 is shown the structure of M center [34, 44], which essentially consists of two F centers and has diamagnetic features (zero total spin). The point defects are studied by optical spectroscopy (UV spectra) and ESR spectroscopy (if the electronic spins are not coupled). The concentration of F centers, N_F, depends on the fluence Φ of impinging particles [34, 44, 45]

$$n_F = n_F^S\left(1 - e^{-\pi R_F^2 \Phi}\right) \tag{206}$$

where n_F^S is the saturation value of F centers concentration and R_F is the F center radius.

4.2. Insulators and Polymers

It is generally assumed that the distinct behavior of insulators subjected to ionizing radiation comes from the reduced thermal conductivity of insulators. Hence, the energy deposited within the insulator target by the impinging particle cannot be efficiently delocalized, resulting in a significant increase of the local temperature.

4.2.1. Excitation and Ionization of the Macromolecular Chain; Free-Radicals Generation

The energy deposited by the incident radiation results in the excitation of the macromolecular chain followed rapidly by its ionization, and free radicals generation. Such modifications were observed by various spectroscopic techniques such as Fourier transform infrared spectroscopy (FTIR) [46], x-ray photoelectron spectroscopy (XPS) [47, 48], electron spin

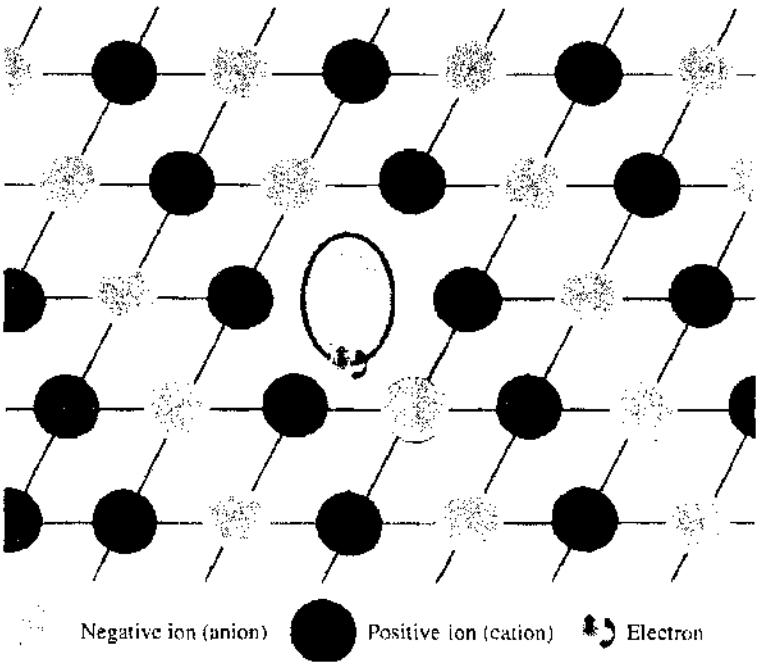

Figure 32. Radiation-induced defects in crystal: the paramagnetic F center.

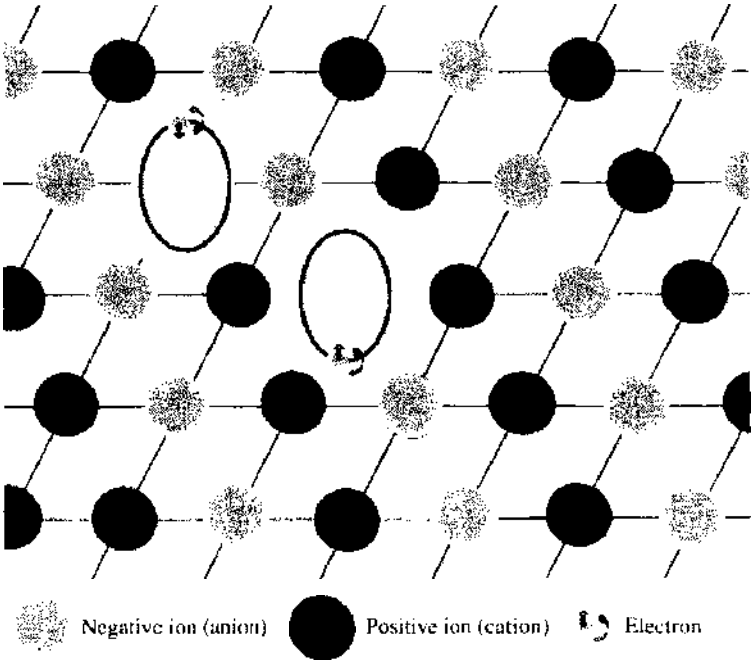

Figure 33. Radiation-induced defects in crystal: the F_2 center (the simplest cooperative defect).

resonance (ESR) [49–51], nuclear magnetic resonance (NMR) [52], and ultraviolet-visible (UV-vis) spectroscopy [46, 49]. The free-radical generation may result either from the subtraction of an electron from the polymeric chain or from the macromolecular chain scissions. A preferential reorientation of polymeric chain and of paramagnetic defects produced by the interaction with the incoming accelerated particles was observed by polarized spectroscopy [53] and ESR [54]. The orientation of the macromolecular chain depends on the incident beam fluence. At relatively low fluences, as long as the tracks are not overlapping significantly the polymeric chains are oriented along the incident particle trajectory. At high fluence, due to the overlapping of latent tracks the effect was no more observed [55]. The track

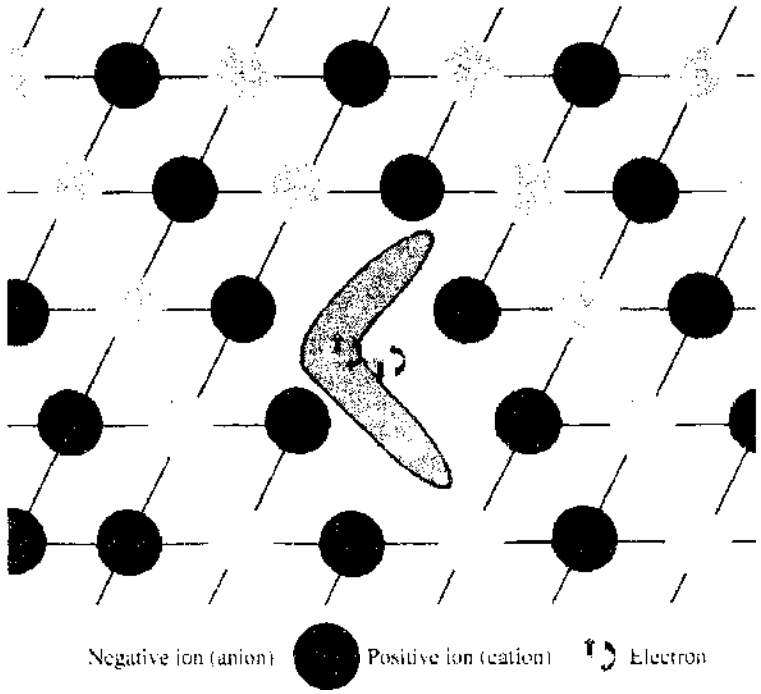

Figure 34. Radiation-induced defects in crystal: the M center.

overlapping probabilities are [55]

$$\begin{aligned} P_O^{(1)} &= C_{01} e^{-4\pi R^2 \Phi} \\ P_O^{(2)} &= 4\pi R^2 \Phi C_{02} e^{-4.7\pi R^2 \Phi} \\ P_O^{(n>2)} &= 1 - C_{01} e^{-4\pi R^2 \Phi} - 4\pi R^2 \Phi C_{02} e^{-4.7\pi R^2 \Phi} \end{aligned} \tag{207}$$

where C_{01} and C_{02} are constants and the superscript of P_0 identifies 1, 2 or more tracks.

Assuming that the hitting probability, $P^{(k)}(\pi\Phi R^2)$, is described by a Poisson distribution, the probabilities for no hit ($k = 0$), one hits ($k = 1$), and two or more hits ($n \geq 2$) are

$$\begin{aligned} P^{(0)}(\pi\Phi R^2) &= e^{-\pi\Phi R^2} \\ P^{(1)}(\pi\Phi R^2) &= (\pi\Phi R^2) e^{-\pi\Phi R^2} \\ P^{(n>2)}(\pi\Phi R^2) &= 1 - e^{-\pi\Phi R^2} - \pi R^2 \Phi e^{-\pi\Phi R^2} \end{aligned} \tag{208}$$

If P_0, P_1, and P_N are the permeability of the no hit, one hit, and more than two hits regions, the total permeability of the polymer subjected to accelerated beams will be [56]

$$P = P_0 e^{-\pi\Phi R^2} + \pi\Phi R^2 P_1 e^{-\pi\Phi R^2} + P_{n(N\geq 2)}(1 - e^{-\pi\Phi R^2} - \pi\Phi R^2 P_1 e^{-\pi\Phi R^2}) \tag{209}$$

In general, the permeability (and the diffusion constant) of the irradiated film is depressed by irradiation and there is not a direct correlation between the energy loss and the permeability of the irradiated film [56].

Several models have been proposed to describe the effect of the interaction between radiation and polymeric targets. As long as the main mechanism for the energy deposition within the target is the interaction of the incident radiation with the target's electrons, the cross section for thermal generation of tracks σ_T depends on the electronic stopping power as σ_T = constant S_e^2, while the original hit model is consistent with a dependence σ_T = constant S_e [57]. In the general case, the ratio between the property E_0 of the polymer before irradiation and its new values after irradiation E_{IR} may be expressed by [57]

$$\frac{E_0}{E_{IR}} \propto (\Phi S_e^n)^k \tag{210}$$

where Φ is the fluence of the incident radiation. For different physical parameters (conductivity, spin concentration, amplitude of various IR and UV bands, energy gap, and mechanical properties) different values for the exponents n and k were obtained [57]. This explains the difficulties in analyzing radiation-induced modifications in polymeric materials.

There is an important difference between the irradiation of a simple solid and the irradiation of a polymer. In solid materials, at low velocities of impinging charged particles, the energy is deposited within the target mainly by nuclear interactions. Hence, atoms displacement is the main consequence. In polymers and biopolymers, at low incoming velocities, some nuclei will receive a huge amount of energy. If the energy is sufficient, the nucleus will leave the polymeric chain. In contrast with simple solids, it will not be captured as an interstitial but it will be released as a volatile. The macromolecular chain will either be left ionized or will be converted into a macroradical. This indicates that there is not such a big (and qualitative) difference between the effects of nuclear and electron stopping powers in polymers, and biopolymers as in the case of simple solids (especially single crystals). It is important to notice that chain scission is the very first step in the radiation-induced degradation of polymers. Two main types of radicals may be produced in polymers by ionization processes; the in-chain radical (see the top panel of Fig. 35) and the end-chain radical (see the bottom panel of Fig. 35). These free radicals are represented in Fig. 35 for the simplest polymeric chain (polyethylene).

The generation of free radicals and the role of scissions and cross-linking reactions of radicals have been proved by ESR experiments on polymers irradiated at low temperature

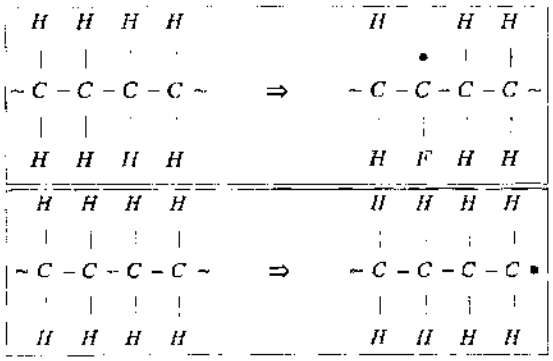

Figure 35. Primary radiation-induced defects in polymers; the in-chain radical (top panel) and the end-chain radical (bottom panel).

(77 K or lower temperatures). As the macromolecular chains are frozen at such low temperatures, ESR spectroscopy was able to sense the presence of radical pairs, i.e. of two radicals situated at distances smaller than 1 nm. From the analysis of the resonance line two kinds of radical-pairs where reported (see Fig. 36); the intrachain radical pair (both radicals belong to the same macromolecular chain) and the inter-chain radical pair (each radical belong to a different polymer chain). Both the intra-chain and the inter-chain radical pairs are characterized by an effective spin electronic $S = 1$ and present a resonance signal located at about $g = 4.00$ [51]. These processes, which are confined at sub-nanometer scale, occur very fast. Even in a simple polymer such as polyethylene there is a debate regarding the formation of radiation-induced free radicals. The simultaneous removal of two hydrogen atoms would result in a chemical modification of the polymeric chain that has no uncoupled electronic spins and hence is not radical (see the top panel of Fig. 37). The nonradical mechanism [58] implies the formation of a double bond. It requires a high amount of energy deposited in a small volume in order to abstract simultaneously two hydrogen atoms from the macromolecular chain. The reaction may be decomposed into a simple in-chain radical generation reaction, a subsequent in-chain radical generation, and a final reorganization of electrons. The formation of free radicals that present a double bond in polyethylene irradiated by high dose radiation has been proved by ESR spectroscopy by the identification

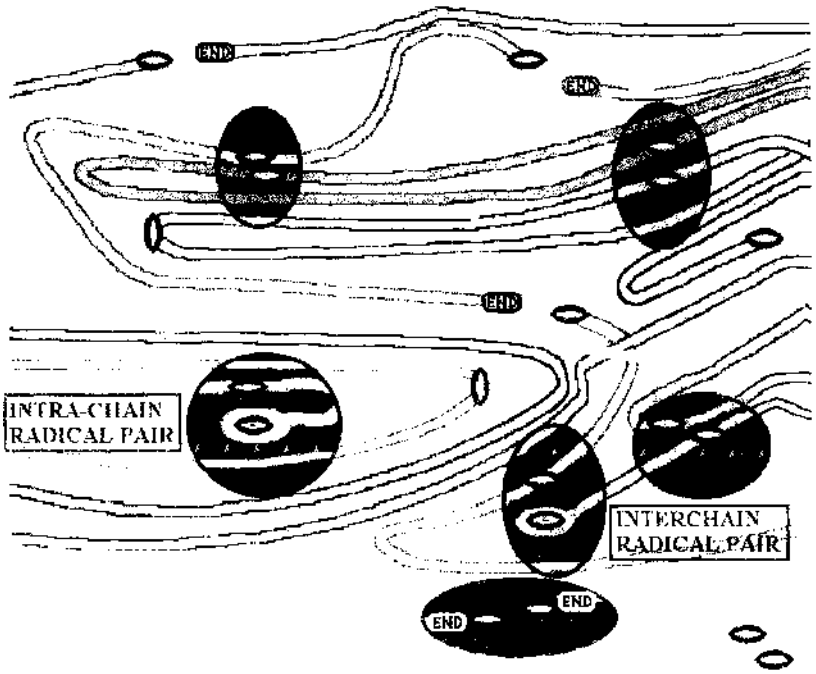

Figure 36. Radiation-induced modifications in polymers (free-radical generation).

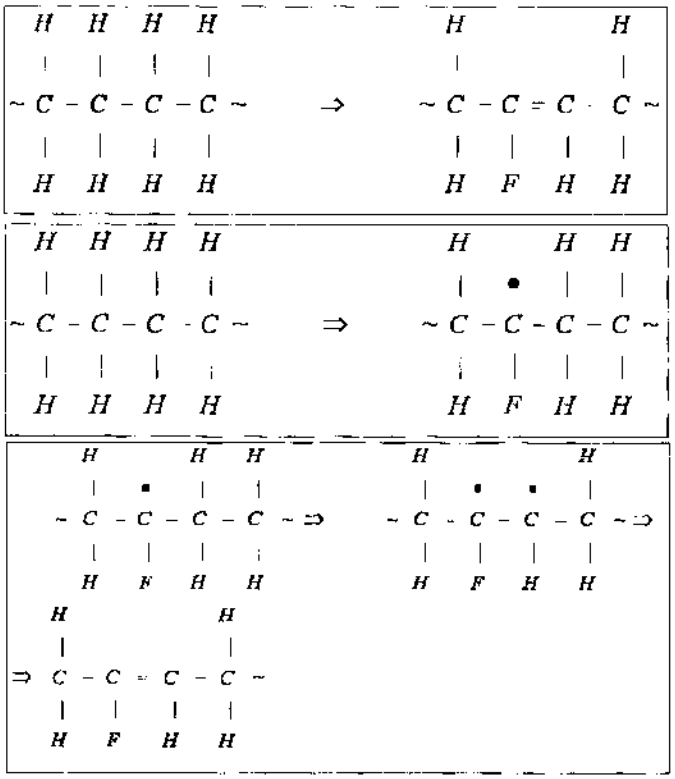

Figure 37. The nonradical mechanism proposed for the radiation-induced degradation of polyethylene (top panel). The next panels shows a two-step radicalar mechanism that would produce the same chemical modification.

of allyl (-CH=CH-CH$^{\bullet}$-CH$_2$-) and polyenil radicals (-CH=CH-CH$^{\bullet}$-CH=CH-) [58]. Free radicals are chemically reactive due to the uncoupled electronic spins. In time, free radicals disappear through recombination reactions. The position and the parameters of absorption lines and bands in UV-Vis, FTIR, and Raman spectroscopy are affected by the irradiation of polymeric targets. For example, UV-Vis spectroscopy revealed changes in the amplitude, width, and position of these lines. The amplitude reflects the light absorbance in UV and it is determined by the absorption coefficient α_{UV} [59]

$$\alpha_{UV} = \frac{8\pi^2 e^2 N}{n\lambda\mu_E} \frac{\omega\gamma}{(\omega - \omega_0)^2 + \gamma^2\omega^2} \tag{211}$$

where N is the electron (defect) density, n the refractive index, μ_E the effective mass of the electron, ω_0 the frequency of the oscillator, γ is the oscillator damping, and λ the wavelength. The difference between the absorption of the irradiated and pristine sample ΔA is proportional to the absorption cross section of defects, σ_{DUV}:

$$\Delta A = N\sigma_{DUV}l = \alpha l \tag{212}$$

where l is the target thickness. It was reported that in ion-beam irradiated polystyrene the defect concentration scales linearly with the energy density [59].

The irradiation of polymers with charged particles produces significant modifications in the UV-Vis spectrum of the target. As most polymers are insulators, their electrical features are described by the band theory of solids by observing that the gap between the top of the valence band and the bottom of the conduction band is large (frequently equal or larger than 5 eV). During the irradiation, the electrical resistivity of polymers is drastically depressed. This is associated with a reduction in the value of the band gap. The UV-Vis absorption curves are calculated by measuring the transmittance of the specimen relative to an identical not-irradiated polymer. The absorption coefficient α is calculated by using the equation [39]

$$\ln T = -x\alpha \tag{213}$$

where T is the measured transmission and x is the thickness of the target. The dependence of $(\alpha h\nu)^{1/2}$ on the energy of UV quanta is expected to be linear, with a slope that defines the constant B and an ordinate equal to the optical gap [39]

$$\sqrt{h\nu\alpha} = B(h\nu - E_{\text{Gap}}) \tag{214}$$

where h is the Planck constant and ν the frequency of the photon.

The modifications induced by high-energy charged particles are dominated by the electronic stopping while at low impact energies the contribution of nuclear interactions cannot be neglected. The alkyne production is considered a typical result of ion-beam irradiation of polymers in the track-overlapping regime [60]. The irradiation process is essentially a chain of excitations and ionizations processes that that involves the incident particle and some atoms or/and molecules of the target. Apparently, no dose effects and no differences between a continuous and a pulse irradiation are expected. This observation is fair at relatively low fluxes. At high incoming particles fluxes, if it is required to deposit the same amount of energy in the same time (which is significantly larger than the duration of the pulse) the energy deposited during the radiation pulse into the materials is higher than the energy deposited in the same time by a continuous irradiation. Usually this is achieved by increasing the number of incident particles during the irradiation pulse. If the flux is sufficiently high, it is possible to imagine that some atoms interact (at higher fluxes) with two or more incident particles. These atoms will receive energy from different incoming particles and they will be ionized even if during the very first interaction solely an excitation process occurred. The main requirement for the appearance of dose rate effects or of discrepancies between the continuous and pulsed irradiation is to exceed a certain critical value for the flux of incoming particles (in order to trigger nonlinear processes of energy deposition within the material). Such effects were noticed during the continuous/pulsed irradiation of polyethylene with accelerated ions [61].

Results that are more complicated are expected if the target is subjected to complex irradiation. For example, in polyethyleneterephtalate, the post–UV irradiation destroys the cross-linked regions within the latent track [62]. The intricate interactions between the incident particle and the target at nanometer scale is reveled by the "guiding effect" of low energy ions, incident on a polymeric membranes with capillaries of 100-nm diameter and 10-μm length [63]. A self-organizing charge-up process has been claimed to explain the experimental data.

4.2.2. The Effect of Radiation on the Average Molecular Mass of Polymers

Not all polymers are degraded by irradiation. Some polymers, irradiated above a certain critical temperature (frequently close to the glass transition temperature, T_G) show an increase of the average molecular mass upon irradiation (see Table 1). This is because the primary radicals generated by the incident radiation are able to recombine each with other. There are three main reactions; initiation reactions, propagation reactions, and recombination reactions. There are three main kinds of recombination reactions for free radicals; end free radical–end free radical recombination (see panel A of Fig. 38), in chain free radical–in chain free radical recombination (see panel B of Fig. 38), and end radical–in chain free radical (see panel C of Fig. 38). In order to recombine, the radicals have to be close to each other. This is accomplished by the temperature-controlled diffusion of free radicals, justifying the existence of a critical temperature. Below this temperature, no more cross-links are possible. These processes are occurring at nanometer scale, as the radius of gyration of macromolecular chains is typically ranging between 10^1 and 10^2 nm. In irradiated polymers, the average molecular mass of the pristine polymeric target is shifted by the competition between chain cross-linking and scission reactions.

In a polymer sample, each chain may have a different length. For simple polymers build up of a single monomer the length of the polymeric chain is equal to the number of monomers N_M multiply by the length of the monomer l_M. The distribution of polymeric chains upon their lengths shows usually a single mode. This distribution is rather well described by a

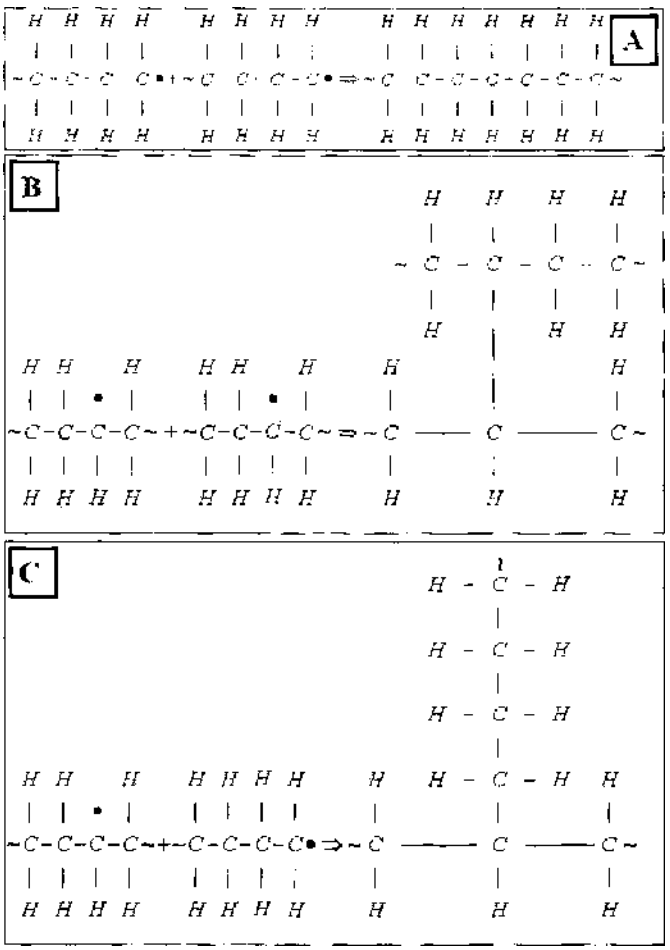

Figure 38. Main chemical recombination reactions between free radicals.

simple Gaussian distribution. Due to these features, the polymers are characterized by their average molecular masses. Several types of averages are frequently used in polymer physics. The numerical average molecular mass $\langle M_N \rangle$ is

$$\langle M_N \rangle = \frac{\sum_i M_i N_i}{\sum_i N_i} \tag{215}$$

Table 1. The dominant radiation-induced degradation process for polymers irradiated under inert atmosphere, at room temperature and normal pressure.

Polymer	Main Degradation Process	Ref.
Polyethylene	Cross-linking reactions are dominant	[58, 68]
Natural rubber	Cross-linking reactions are dominant	[58]
Polystyrene	Cross-linking reactions are dominant	[58, 68]
Polymethacrylate	Cross-linking reactions are dominant	[58]
Polyvinyl chloride	Cross-linking reactions are dominant	[58]
Polyether-ether ketone (PEEK)	Cross-linking reactions are dominant	[193]
Polydimethylsiloxane (PDMS)	Cross-linking reactions are dominant	[70]
Polyvinylidene fluoride	Cross-linking reactions are dominant	[68]
Polytetrafluorethylene (Teflon)	Scissions reactions are dominant	[67]
Polycarbonate	Scissions reactions are dominant	[69]
Poly isobutylene	Scissions reactions are dominant	[68]
Polyethyleneterephtalate	Scissions reactions are dominant	[47, 60]
Polyimide	Scissions reactions are dominant	[69]
Polymethyl methacrylate	Scissions reactions are dominant	[58]
Poly-α-methyl styrene	Scissions reactions are dominant	[58]
Poly-vinylidene chloride	Scissions reactions are dominant	[58]

where N_i represents the number of chains characterized by the mass M_i (or equivalently by the length $l_i = il_M$). The weight average molecular mass $\langle M_W \rangle$ is defined by

$$\langle M_N \rangle = \frac{\sum_i M_i^2 N_i}{\sum_i M_i N_i} \tag{216}$$

The heterogeneity factor (or polydispersity index) I, is defined by

$$I = \frac{\langle M_W \rangle}{\langle M_N \rangle} \tag{217}$$

The estimation of the change in the average molecular mass of polymers during or after irradiation is important in the understanding of the physical and chemical modifications induced by irradiation. There are several experimental techniques available for the measurement of the averaged molecular mass such as viscosimetry, light scattering, and chromatography techniques. For polymers that undergo dominant cross-linking reactions, these techniques cannot be used. The increase of chain cross-linking is usually monitored by the gel fraction or swelling equilibrium. The gel fraction is a rather qualitative measurement that estimates the ratio between the soluble and the insoluble (cross-linked) components of the irradiated polymer. The effect of the stopping power on the heterogeneity index has been investigated in the case of PMMA irradiated with protons, accelerated C ions and gamma rays (Co^{60}) [64]. After a sharp decrease from $I = 3$ to $I = 2$, the heterogeneity index showed no dependence on the stopping power ranging from 0.1 eV/nm to 100 eV/nm [64]. The reported value of $I(I = 2)$ is typical for random scissions. The formation of cross-links (gel) in PMMA irradiated with He ions at fluencies higher than 10^{13} ions cm^{-2}, and the increase of I up to about 3.0 has been reported [65].

The degree of swelling at equilibrium is

$$V_R^{5/2} = \frac{M_C V_S (1 - 2(M_C/M))(1/2 - \zeta_{PS})}{V_M} \tag{218}$$

where V_R is the ratio between the volume of the swollen polymer and the volume of the dry polymer, V_S is the specific volume of the polymer, M_C is the average molecular weight between cross-links, M is the average molecular weight of the pristine polymer, and ζ_{PS} is a constant that characterizes the interaction between the polymer and the solvent. If both scission and cross-linking reactions are competing during polymer degradation, the radiation dose required to obtain an incipient gelation, D_{G0} is [2, 3, 66]

$$D_{G0} = \frac{1}{(1/E_C - 1/2E_S)} N_A \langle M_W \rangle \tag{219}$$

where N_A is the Avogadro number, $\langle M_W \rangle$ is the average weight molecular mass of the pristine polymer, E_C is the energy absorbed by polymer by cross-link, and E_S is the energy absorbed by the polymer per scission.

Charlesby [66] studied radiation-induced cross-linking in polymers assuming that the termination probability of the chain at any step i is small ($i \ll 1$) and that the number of double bonds N_{DB} is large. The value of gel dose, D_{G0} is

$$D_{G0} = \frac{i^2 N_{DB}}{2.08 \times 10^{-6}(1 - i)(N_{DB} - 1) G \langle M_W \rangle} \tag{220}$$

where G is the radical yield defined by the number of radicals resulted from each 100 eV absorbed by the polymer from the incident radiation.

The competition between scission and cross-linking reactions results in the shift of the average molecular masses and eventually in the distortion of the distribution of molecular masses. If the scission reactions are dominant, the average molecular masses of the polymeric target are depressed during irradiation, while if the cross-linking reactions are dominant the average molecular masses are increased during the irradiation of the polymeric samples.

Eventually, at sufficiently large irradiation doses the sample becomes insoluble. Most experimental studies were focused on the changes of the average molecular masses; almost no attention was paid to the radiation-induced modification of the molecular mass distribution shape (see Fig. 39).

It is important to notice that the presence of oxygen or the irradiation at different temperatures is capable of modifying the dominant degradation mechanisms in polymers subjected to radiation. For example, in irradiated polytetrafluorethylene (Teflon), at low and moderate temperatures chain-scission reactions are dominant, while cross-linking reactions were noticed near the melting temperature [67]. At large doses, due to the high concentration of free radicals cross-linking reactions may become dominant even if the main degradation process at low doses is the chain scission mechanism. Such effects were reported in irradiated polymethylmethacrylate (PMMA) and polycarbonate (PC). The nature of the dominant degradation process depends also on the incident particle. For example [68] in PMMA the yield for scission reactions initiated by gamma irradiation or electrons is 0.003 while for cross-linking reactions the yield is 0.004. In ion-beam irradiated PMMA the yield of scissions is 1.2 while the cross-linking yield is 1.0 [68]. Radiation-sensitive polymers are frequently used as resists. The polymers that are dominantly cross-linked by radiation are named positive resists and the polymers in which the radiation triggers dominant cross-linking reactions are named negative resists.

Chain scissions reactions are dominant in polycarbonate (Makrofol *N*) and polyimide irradiated with protons ions accelerated at 62 MeV, at different integral doses ranging from 10 kGy to 80 kGy [69]. In ion-beam-irradiated polydimethylsiloxane the cross-linking process is dominant; the observation of gel strings by AFM is a simple elegant proof [70].

4.2.3. The Effect of the Changes in the Average Molecular Masses on the Physical Properties of Polymers

4.2.3.1. Glass and Melting Transition Temperatures One of the first consequences of the interaction between ionizing radiation and polymeric targets is the modification of the average molecular masses. The change of the average molecular mass determines a shift in the glass and melting transitions temperatures of polymers. These shifts were measured by several experimental techniques such as differential scanning calorimetry, dynamical mechanical analysis, and dielectric spectroscopy. For linear polymers, the relationship between the average numerical mass of the polymer M_N and its glass transition temperature T_G^N is given

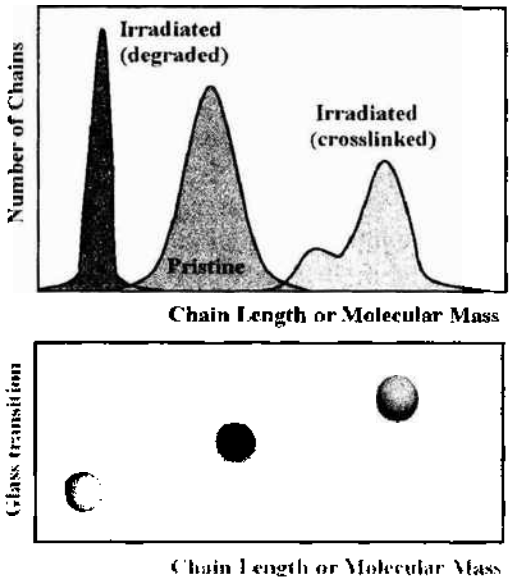

Figure 39. The effect of ionizing radiation of the average molecular mass of polymers.

by Fox-Flory equation [11–14]

$$T_G^N = T_G^\infty - \frac{K}{M_N}$$
$$K = 2\frac{N_A V_E T_G^\infty}{f_G V_G^\infty \ln V_G} \tag{221}$$

T_G^∞ is the glass transition temperature of the infinite polymeric chain, K is a constant (specific to the polymer), V_E is the average free volume of chain ends, f_G is the free volume fraction at the glass transition temperature, and V is the volume fraction. This expression may be used if the dominant radiation-induced degradation process is the chain-scission. For linear polymers, there is a simple relationship between the glass transition temperature and the melting transition temperature, T_M[12]

$$T_G = \zeta_{GM} T_M \tag{222}$$

where ς_{GM} is a constant ranging between 0.5 and 0.8.

If chain cross-linking reactions are dominant, the shifted glass transition temperature of the cross-linked polymer, T_G^C is given by the Fox-Lockashek [13] equation,

$$T_G^C = T_G^0 + \frac{N_A}{C_C \rho_C} \tag{223}$$

T_G^0 is the glass transition temperature of the pristine polymer, C_C is a constant, and ρ_C is the cross-links density.

In the general case, due to the competition between scissions and cross-linking processes, the glass and melting transition temperatures may show a different dependence on the absorbed dose.

4.2.3.2. The Effect of Radiation on the Degree of Crystallinity of Polymers Several processes are competing to modify the degree of crystallinity of polymers subjected to ionizing radiation. The reduction of the degree of crystallinity in some ethylene-glycol based polymers was associated with a conformational transition of ethylene glycol residues from the *trans* configuration into the *cis* one. The reduction of the degree of crystallinity due to the formation of branches was reported in CR 39 irradiated with neutrons, accelerated at energies ranging between 6 MeV and 20 MeV [71]. The amorphization of PET subjected to ion-beam bombardment has been confirmed by spectroscopic measurements [60]. Above certain critical ion fluence, the polymeric target becomes completely amorphous [68].

The complex modifications occurring at nanometer scale affect significantly all physical properties of such materials (mechanic, electric, thermal, and optic). An ample reorganization of macromolecular chains has been reported [72] by x-ray in irradiated polyethyleneterephtalate. Low LET irradiations (such as γ irradiation) and high LET irradiations (such as accelerated ions) are inducing in ethylene-*co*-tetrafluorethylene (-CH_2-CH_2-CF_2-CF_2-) a decrease of the crystallinity and an increase of the modulus and yield strength. These modifications are enhanced by increasing the irradiation temperature [73]. The role of irradiation temperature on the radiation-induced defects in polymers was confirmed by FTIR data. It was reported that the generation of alkyne and vinyl depends on both total dose and irradiation temperature. By increasing the total dose (irradiation time), the concentration of radiation-induced alkyne groups is increased towards a stationary value [73]. It was reported [74] that the absorption bands are shifted towards longer wavelengths as the temperature is increased. The decrease of the sample temperature increases the concentration of alkynes as the defects are frozen and the recombination reactions are no more efficient [74]. The concentration of vinyl groups decreases as the LET of the incident particle is decreased [74]. Radiation-induced cross-linking of polyethylene decreases the crystallinity degree of the pristine polymer [75].

4.2.3.3. The Effect of Radiation on the Mechanical Properties of Polymers For small cross-linking densities the changes of mechanical properties of amorphous polymers (in melt) are rather well described by the expression [58]

$$\tau = \frac{RT(1 - 2\langle M_C\rangle/\langle M_W\rangle)(\alpha - \alpha^{-2})}{\langle M_C\rangle\langle V_{SP}\rangle} \tag{224}$$

where τ is the tensile stress per unit cross sectional area of the pristine polymer, R is the perfect gas constant, T is the temperature, V_{SP} is the specific volume of the polymer, M is the molecular weight of the polymer, M_C is the molecular weight of the polymer between cross-links, α is the ratio of the extended length to the initial length, and "$\langle\rangle$" indicates an average. This equation is valid for relatively small elongations (α not much larger than 2).

It was reported that in cross-linked polymers, the elastic modulus increases by cross-linking while the elongation at break decreases as the polymer is cross-linked [61]. The Flory theory leads to the following relationship between the elastic modulus and the cross-linking density [76]

$$\rho_C = \frac{E_C}{6RT} - \rho_C^0 \tag{225}$$

where ρ_C^0 is the initial density of cross-links and ρ_C is the final cross-links density. This formula is derived assuming that the temperature dependence of the Young modulus of the amorphous cross-linked polymer is well described by the rubber elasticity theory

$$E = \frac{n\rho RT}{\langle M_C\rangle} \tag{226}$$

where n is a constant (theoretically equal to 3). This expression describes with an acceptable accuracy the evolution of the mechanical properties of polyethylene during irradiation [77].

Studies [78] on radiation-induced modifications in several polymers (PET, PEN, PP, and PC) showed a continuous decrease of the tensile strength as the dose is increased.

4.2.3.4. The Release of Volatiles During Polymer Degradation: Polymer Erosion The interaction between ionizing radiation and polymer is associated with the generation of volatile gases [79, 80]. High erosion rates were reported in proton-irradiated polymethylmethacrylate [80]. The release of volatiles during polymer irradiation was confirmed by mass spectroscopy measurements [79]. It was found that the total ejected mass per ion depends as a power law (with $n = 2$) on the velocity of impinging ions, and shows a saturation at high velocities [81].

4.2.3.5. The Electric Properties of Irradiated Polymers The irradiation of polymers increases usually the electric conductivity of the targets. This is due to radiation-induced formation of impurity levels in the forbidden gap. The irradiation of low density polyethylene by nitrogen ions accelerated up to 20 keV resulted in the decrease of the energy gap from about 2.5 eV for the pristine material down to about 0.5 eV for the sample irradiated up to a total fluence of 10^{16} nitrogen atoms/cm^2 [61].

At large doses, the impurity level collapses into an impurity band and the irradiated target becomes conducting. In the case of neutron-irradiated polycarbonate (CR 39) the thermal activation of the charge conductivity was found to have a complex dependence on the total dose. An analogous result was found for the refraction index. The DC electrical resistance of polyvinylidene chloride and polyethylene was decreased by irradiation [82], due to the production of free electrons followed by their eventual trapping in sites that corresponds to impurity energy states in the forbidden gap.

In some irradiated insulating polymers as well as in irradiated semiconducting and conducting polymer, the electrical conductivity is rather well described by the Variable Range Hopping (VRH) [83] model. Poorly conducting samples with σ_{RT} of the order of or less

than 1 S/cm are similar to amorphous semiconductors; their DC conductivity is strongly dependent on temperature and its best fit is given by a "1D Mott's law" [83]:

$$\sigma = \sigma_0 \exp -\left(\frac{T_0}{T}\right)^{1/2} \tag{227}$$

The temperature T_0 is related to the density of states at the Fermi level and to the localization length L_{loc} by

$$T_0 \cong \frac{16}{K_B N(\varepsilon_F) L_{loc}^3} \tag{228}$$

An analogous temperature dependence of the DC conductivity, for 1D systems, has been derived within the percolation model, charging energy limited tunneling, hopping with a Coulomb gap, and the granular metal approach. This discussion is intimately related to the nature of the metallic state and of the transport process (hopping *versus* phonon-assisted tunneling). The validity of this expression for the 1D case is still under debate (some authors found an Arrhenius-like dependence for charge transport in one-dimensional systems [84, 85]).

The average hopping radius, R_S, the characteristic temperature, T_0, and the localization length, L_{loc}, are related by:

$$\frac{R_s}{L_{loc}} = \frac{3}{8}\left(\frac{T_0}{T}\right)^{1/4} \qquad R_s = \frac{1}{4} K_B T \left(\frac{T_0}{T}\right)^{1/4} \tag{229}$$

Even if the conduction in the pristine polymers and blends may be described by a one dimensional variable range hopping, the polymer doping increases probability of electronic jump on the nearest chains, leading to an increase in the dimensionality of the conduction process. Accordingly, the relation (227) has been generalized [83]:

$$\sigma = \sigma_0 \exp -\left(\frac{T_0}{T}\right)^{1/(d+1)} \qquad \text{(d DIMENSIONAL VRH)} \tag{230}$$

where d is the dimensionality of the charge transport. For $d = 1$, most electronic jumps are along the macromolecular chain and the probability of an electronic jump across the macromolecular chain is negligible, whereas for $d = 3$ the jump probabilities in all directions are almost equal. It was suggested [85] that during ion-beam bombardment of polymers an one-dimensional conductivity should be superimposed on the DC conductivity of the pristine polymer. The one-dimensional character is imposed by the latent track produced within the target by the impinging particles. ESR spectroscopy is an important technique that may provide additional details regarding the nature of the conducting particle and the transport mechanism [86, 87]. Conductometry is another simple technique used to estimate the radius of the latent track produced by incident ions in polymeric materials [81].

4.2.3.6. Radiation-Induced Chemical Modifications of Polymers The main chemical reactions triggered by the incident radiation within polymeric targets may be classified as initiation reactions, propagation reactions, and recombination reactions:

Initiation reactions:

$$(RH)_N \rightarrow (RH)_{N-1}R\bullet + \left(\frac{1}{2}\right)H_2 \tag{231}$$

$$(RH)_N \rightarrow (RH)_{N-M-1}R\bullet + \left(\frac{1}{2}\right)H_2 + (RH)_M \tag{232}$$

$$(RH)_N \rightarrow (RH)_{N-M-1}R\bullet + H_2 + (RH)_{M-1}R\bullet \tag{233}$$

Propagation reactions:

$$(RH)_{N-M-1}R\bullet + (RH)_N \rightarrow (RH)_{N-M} + (RH)_{N-1}R\bullet \tag{234}$$

$$(RH)_{N-M-1}R\bullet \rightarrow (RH)_{N-M-K-1}R\bullet\bullet + (RH)_K \tag{235}$$

Recombination reactions:

$$(RH)_{L-1}R\bullet + (RH)_{K-1}R\bullet \rightarrow (RH)_{K+L} \tag{236}$$

RH identifies the monomer and N is the polymerization degree. It is observed that the propagation reaction is a transfer reaction and that hydrogen is produced during initiation reactions.

Real polymers contain various low molecular compounds such as stabilizers, antioxidants, inhibitors, and fillers. Hence, in the real case, the polymer degradation under the effect of ionizing radiation will be an intricate competition between the radiation-induced degradation of all these components. Labeling these low molecular weight fillers by AH the main radiation-induced chemical reactions assigned to their degradation are:

Initiation reactions:

$$AH \rightarrow A\bullet + \left(\frac{1}{2}\right)H_2 \tag{237}$$

Transfer reactions:

$$(RH)_{N-1}R\bullet + AH \rightarrow (RH)_N + A\bullet \tag{238}$$

$$A\bullet + (RH)_N \rightarrow AH + (RH)_{N-1}R\bullet \tag{239}$$

Recombination reactions:

$$A\bullet + R\bullet \rightarrow AR \tag{240}$$

$$A\bullet + A\bullet \rightarrow A - A \tag{241}$$

The degradation of commercial polymers shows several stages. In the very first stage, the radiation behaviour of the polymer is controlled by the presence of inhibitors and stabilizers. After the exhaustion of inhibitors and stabilizers, the polymer is left unprotected and the radiation-induced degradation of the polymer is close to that of a pure polymer (that contains no low molecular compounds). This reveals the complexity of radiation-induced degradation processes in commercial polymers.

4.2.3.7. The Effect of Oxygen on Irradiated Polymers The oxygen is affecting significantly the stability of polymeric materials to radiation. Oxidation reactions shift the overall polymer degradation toward a scission-like degradation. In the general case, the irradiated polymer will be subjected to a competition between an oxidative degradation and a radiation-induced degradation. The main chemical reactions occurring during polymer irradiation in air are:

Initiation reactions:

$$(RH)_N \rightarrow (RN)_{N-1}R\bullet + \left(\frac{1}{2}\right)H_2 \tag{242}$$

$$(RH)_N + O_2 \rightarrow (RH)_{N-1}ROOH \tag{243}$$

$$(RH)_{N-1}R\bullet + O_2 \rightarrow (RH)_{N-1}ROO\bullet \tag{244}$$

$$2(RH)_N + O_2 \rightarrow 2(RH)_{N-1}ROH \tag{245}$$

Propagation reactions:

$$(RH)_{N-1}R\bullet + (RH)_N \rightarrow (RH)_N + (RH)_{N-1}R\bullet \tag{246}$$

$$(RH)_{N-1}ROO\bullet + (RH)_N \rightarrow (RH)_{N-1}ROOH + (RH)_{N-1}R\bullet \tag{247}$$

$$(RH)_{N-1}ROOH + (RH)_N \rightarrow (RH)_{N-1}R\bullet + (RH)_{N-1}RO\bullet + H_2O \tag{248}$$

$$(RH)_{N-1}RO\bullet + (RH)_N \rightarrow (RH)_{N-1}ROH + (RH)_{N-1}R\bullet \tag{249}$$

$$(RH)_{N-1}ROOH \rightarrow (RH)_N - 1RO\bullet + \bullet OH \tag{250}$$

$$\bullet OH + (RH)_N \rightarrow (RH)_{N-1}R\bullet + H_2O \tag{251}$$

Termination reactions:

$$(RH)_{N-1}R\bullet + (RH)_N - 1R\bullet \rightarrow (RH)_{N-1}R - R(RH)_{N-1} \quad (252)$$

$$(RH)_{N-1}R\bullet + (RH)_{N-1}ROO\bullet \rightarrow (RH)_{N-1}ROOR(RH)_{N-1} \quad (253)$$

$$(RH)_{N-1}ROO\bullet + (RH)_{N-1}ROO\bullet \rightarrow (RH)_{N-1}ROOOO(RH)_{N-1} \quad (254)$$

If the polymer contains low molecular weight molecules (IH and AH) as antioxidants, stabilizers, inhibitors, and fillers, these molecules are capable of adding to the previous chain of chemical reactions or their own radiation-induced and oxidative degradation.

$$(RH)_{N-1}ROOH + IH \rightarrow (RH)_{N-1}RO\bullet + I\bullet + H_2O \quad (255)$$

$$AH + O_2 \rightarrow AOOH \quad (256)$$

$$(RH)_{N-1}ROO\bullet + AH \rightarrow (RH)_{N-1}ROOH + A\bullet \quad (257)$$

$$(RH)_{N-1}RO\bullet + AH \rightarrow (RH)_{N-1}ROH + A\bullet \quad (258)$$

$$(RH)_{N-1}R\bullet + AH \rightarrow (RH)_{N-1}ROH + A\bullet \quad (259)$$

$$A\bullet + (RH)_N \rightarrow AH + (RH)_{N-1}R\bullet \quad (260)$$

$$A\bullet + (RH)_{N-1}R\bullet \rightarrow AR(RH)_{N-1} \quad (261)$$

$$A\bullet + (RH)_{N-1}RO\bullet \rightarrow AOR(RH)_{N-1} \quad (262)$$

$$A\bullet + (RH)_{N-1}ROO\bullet \rightarrow (RH)_{N-1}ROOA \quad (263)$$

$$I\bullet + (RH)_{N-1}R\bullet \rightarrow IR(RH)_{N-1} \quad (264)$$

$$I\bullet + (RH)_{N-1}RO\bullet \rightarrow IOR(RH)_{N-1} \quad (265)$$

$$I\bullet + (RH)_{N-1}ROO_2\bullet \rightarrow IOOR(RH)_{N-1} \quad (266)$$

The presence of oxygen modifies the radiation stability of polymers through different mechanisms. In real polymers, there is a certain amount of oxygen dissolved within polymers. These molecules are able to attack the polymeric chain and to produce hydroperoxides. Catalysts residues are able to participate in the production of hydroperoxides. Due to their high lability, hydroperoxides are easily converted into peroxy radicals.

In bulk samples, the presence of oxygen is capable of inducing a complicate degradation mechanism, if the polymer is irradiated at temperatures lower than the glass transition temperature. At low temperatures, the oxygen diffusion within bulk samples is difficult as the segmental motions are frozen. Hence, the irradiation will exhaust in the first step the oxygen diffused within the polymer. After that, the degradation of the bulk polymeric target will be inhomogeneous. A thin external shell of the target will be dominantly degraded to peroxy like radicals due to the presence of a high concentration of oxygen while the core of the polymer will be subjected to a "vacuum like radiation-induced chemical degradation." Such an inhomogeneous degradation is depicted in Fig. 40.

The diffusion constant of oxygen through polymers increases by several orders of magnitude as the temperature is raised above the glass transition temperature of the polymer. Segmental motions help the oxygen diffusion within the polymer. Hence, the radiation-induced degradation of the polymeric target will be homogeneous or quasi-homogeneous. The behavior of polymers subjected to radiation is complicated by the charging of polymeric targets [88]. Under the effect of the incident radiation, free electrons are released within the polymeric material. Under certain conditions some of these electrons are emitted from the target. The subsequent charging of the target is capable of damaging the polymeric target [89].

The possibility to cross-link different polymers by irradiation and to obtain new materials by radiation initiated grafting of polymers has been investigated [7, 90]. Various irradiations such as gamma irradiations [9, 90, 91], accelerated particles (protons [7, 90] or heavy ions [92]) irradiation were used. The radiation-induced graft polymerization initiated by swift ion irradiation was explained within the target theory [90]. Radiation-induced grafting polymerization on nanoclays was used to further improve the physical properties of nanocomposites [93, 94].

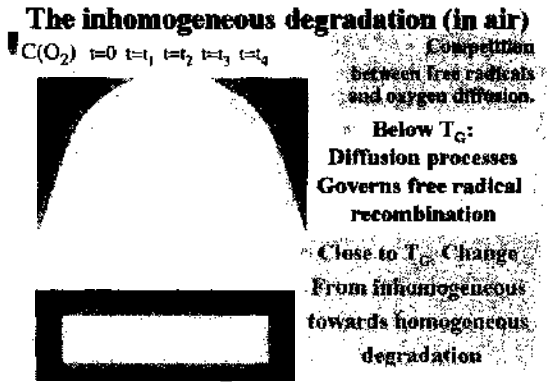

Figure 40. The inhomogeneous degradation of polymers.

4.3. Semiconductors

A huge number of papers focused on local and nanometer-sized modifications in semiconductors have been published elsewhere [34, 95–102]. Some of them are focused on radiation-induced generation and evolution of point defects or defect clusters [98, 100, 101]. Radiation-induced defects segregate by increasing the total dose. In most cases, the irradiation affects the electrical characteristics of semiconductors, as these defects are represented by states localized within the forbidden gap [34]. Increasing the energy deposited within the target by the incident radiation the impurity level(s) corresponding to point defects are converted into impurity band(s). This reflects the strong interactions among radiation-induced defects. At high fluence or stopping power the irradiation adds a conduction channel and eventually affects the proper function of devices based on semiconductors. The latent track formation and characteristics in semiconductors have many analogies to latent track formation and characteristics in polymers (for broad gap semiconductors) or in metals (for narrow gap or degenerate semiconductors).

4.4. Metals

Radiation effects in metals and alloys start at sub-nanometer scale with the same interactions between the incident particle and the target. The electronic stopping power dominates the energy transfer to the target, at relatively high velocities of the incident particle. This behavior was also noticed in insulating targets. As most metals and alloys are conductors, the electrons behave just like a gas [34]. There is a close analogy between sub-nanometer scale radiation-induced defects in insulators, semiconductors, and metals. In all these cases, the interaction between the incident radiation and the target produces atomic displacements [104]. These are responsible for the generation of vacancies (V) and interstitials (I). Additional microstructural details of the target such as cavities, gases, grains, and associated grain boundaries affect the mechanisms for the relaxation and delocalization of the energy deposited by the incident radiation within the target. The crystalline structure, typical to many metals and alloys, will allow a more precise analysis of atom displacement and point defects. Diffusion processes are responsible for the growth of the point defects through clustering reactions

$$\begin{aligned} V + V &\Rightarrow V_2 \\ V_N + V &\Rightarrow V_{N+1} \\ V_N + V_M &\Rightarrow V_{N+M} \\ I + I &\Rightarrow I_2 \\ I_N + I &\Rightarrow I_{N+1} \\ I_N + I_M &\Rightarrow I_{N+M} \end{aligned} \tag{267}$$

These reactions are analogous to a polymerization reaction. A cluster of N individual point defects (V_N and I_N) growths by adding one more defect of the same type at each step. Usually, this process requires an activation energy, which is received from the impinging particle during the irradiation. The diffusion of a vacancy, D_V, through a solid is related to the activation energy for vacancy diffusion E^V through

$$D_V \propto \frac{d^2 \upsilon z}{6} e^{-(E_V/K_B T)+(\Delta S_M/T)} \tag{268}$$

where d is the jump distance, υ is the jump frequency, z is the number of nearest neighbors, and ΔS_M is the entropy of mixing (of vacancies within the target).

Under certain conditions, cluster coalescence reactions are possible. The development of radiation-induced modification from nanometer-scale to the micrometer-scale is carried out by such processes. Nevertheless, the extend of cluster is limited by recombination reactions

$$\begin{aligned} V + I &= O \\ V_N + I &\Rightarrow V_{N-1} \\ I_N + V &\Rightarrow I_{N-1} \end{aligned} \tag{269}$$

where O indicates no defect. The cluster recombination is a rare event, as it requires a huge amount of energy. Formally, it is possible to decompose such an event into a chain of single step point defect recombination processes. The cluster of vacancies reflects the appearance of radiation-induced voids in the target. The interstitials clusters are responsible for the formation of dislocations and loop growth.

4.4.1. Collective Defects Produced by the Impinging Radiation in Metallic Targets: Atomic Cascades

The most important features of point defects generation in metals are identical to those described previously in the section focused on crystalline targets. In the study of radiation-induced defects in materials, it is important to separate the electronic processes from the nuclear ones. At high energy of the incoming particle, the electronic stopping power dominates, whereas at low energy the nuclear stopping power is the most important contribution. Qualitatively, it is possible to introduce a critical energy, E_C, which separates the two behaviors, that is,

$$\begin{aligned} E > E_C &\Rightarrow S_e > S_N \\ E < E_C &\Rightarrow S_e < S_N \end{aligned} \tag{270}$$

The energy loss for high incident energies incoming particles (ranging from E to E_C) (stopping power) is controlled by electronic processes, and a negligible amount of displacements are expected. At low energies (of incoming particles), the nuclear processes are dominant and accordingly the number of atom displacements, N_D, is

$$N_D = \frac{E}{2E_D} \tag{271}$$

where E_D is the energy required to displace the atom in the lattice.

The incident particle, characterized by the kinetic energy $E^{(0)}$, struck an atom of the metallic target. During this collision, the energy $E^{(1)}$ will be transferred from the incident particle to the atom (i) of the target, while the incident particle will be scattered with a reduced energy $E^{(01)}$. If the energy $E^{(1)}$ is smaller than the energy required to displace (permanently) the atom within the lattice, E_D, no displacement of lattice's atoms will be observed. If the energy transferred $E^{(1)}$ is larger than E_D (E_D for metallic targets is typically in the range 25 eV to 50 eV), then the struck atom will be displaced. Such an event requires $E_D \leq E^{(1)} \leq 2E_D$. If after this collision the energy of the scattered particle is sufficiently high (i.e., $E^{(1)} > 2E_D$), assuming head-on perfectly elastic collisions, each individual collision will reduce the energy of the incident particle with the same amount. The cascade ceases when the average energy ($2E_D$) is proportional to $(E/2)N$, where N is the number of collisions. During this process, the number of displaced atoms is 2^N.

4.4.1.1. Radiation Focusing At the end of a collision cascade, a low recoil energy process known as *focusing* may occur. This may easily be imagined by observing that if the atoms in the lattice are replaced by ideal elastic head-on collision the process will continue indefinitely. Actually, the first collisions are not perfectly head-on and hence some kinetic energy is lost. After several collisions, the energy loss is reduced and finally the collisions tend to be perfect head-on elastic collisions. In real crystals, the imperfections in atom distributions, the presence of impurities, local or extended defects, and grain boundaries have an important contribution to the decay of the energy transferred to the next atom. Such defects prevent the focusing of the incident ionizing radiation through the sample.

4.4.1.2. Radiation Channeling An analogous phenomenon was observed during the irradiation of crystals with accelerated particles. The channeling of the incident particle within a crystal has been observed mainly in thin metallic foils but is not restricted to metals. Recent data proved the ion channeling in insulating ionic crystals and in nanometer sized pores produced in polymeric membranes. The critical energy for particle channeling, E_{CH}, requires that the wavelength of the incoming particle λ_{CH} to be at least equal to two atom spacing along the channel (see Fig. 41):

$$E_{CH} = \frac{k\lambda_{CH}^2}{\pi^2} \tag{272}$$

where k is the force constant of the channel potential $U(U = kr^2$, where r is the radial distance measured from the channel axis). A detailed analysis on charged particles channeling in crystals is presented in Ref. [95]. By excellence, channeling effects require a target with a large number of atoms, regularly distributed (crystal). Accordingly, such effects are not expected to be important in nanomaterials and nanostructures.

4.5. Radiation-Induced Modifications in Magnetic Materials

The energy deposited by the incident particle in a magnetic target leads to complex physical and chemical modifications [104–116]. Recent data on irradiated one-dimensional magnetic nanomaterials (Pt/Co/Pt trilayers) revealed their radiation sensitivity at low fluence He ions. The possibility to control by low fluence irradiations relevant magnetic properties such as coercivity, anisotropy, and Curie temperature, while preserving the surface and the planarity almost unmodified triggered the investigations of the radiation effects on magnetic multilayers. $(Pt/Co)_nPt$ multilayers have been patterned by irradiation with He ions, accelerated at different energies in the range 20 to 100 keV at fluencies of about 10^{15} to 10^{16} ions/cm^2 [104]. The displacement rate per incoming ion at the Pt/Co interface is about 1% and the average distance traveled by the atom is of the order of the atomic distance [109].

Three different irradiation-induced modifications with sharp transition between each were reported in Co/Pt multilayers irradiated with Ga ions accelerated at 30 keV [105]. For fluencies less than 5.3×10^{12} ions/cm^2, the irradiated region retains the perpendicular uniaxial anisotropy but the coercivity is decreased by irradiation. For fluencies between 5.3×10^{12}

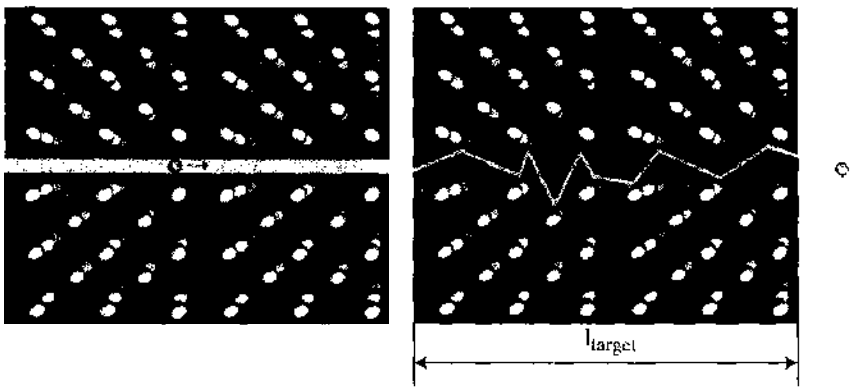

Figure 41. The channeling of a particle through a crystal.

and 1.3×10^{13} Ga ions/cm^2, a transition from perpendicular to in-plane magnetization was reported. Above this fluence, the magnetization remains confined in the plane of the film. A transition from ferromagnetism to paramagnetism was reported at fluencies around 1.3×10^{15} Ga ions/cm^2. For irradiation fluencies, up to about 1.3×10^{15} Ga ions/cm^2, both grain size and texture in the multilayer increase as the fluence is increased. Larger doses induce significant thinning of the multilayer. Analogous effects were noticed in Co/Pt films irradiated with He ions accelerated at 30 keV, at fluencies up to 10^{16} He$^+$/cm^2 [104]. At fluencies of the order 10^{16} He$^+$/cm^2, the Curie temperature of irradiated Co/Pt multilayers is depressed from about 365 K up to 280 K. Irradiation of Co/Ag multilayers with Si ions accelerated up to 1 MeV [106] revealed a continuous increase of the lattice parameter of Ag grains from 3.98 A to about 4.07 A (typical for bulk Ag) and a decrease in the magnetoresistance, as the fluence is increased from 10^{13} to 10^{17} Si/cm^2. It was reported that fluencies larger than 10^{17} Si/cm^2 enhance the coercive field up to about 100 Oe. At low ion fluencies, the irradiation induced a weak demixing of elements [106]. Increasing the fluence Co is progressively segregated from Ag and an incipient granular structure was noticed above 10^{16} Si/cm^2. Directional effects in Fe (3.8 nm)/Tb (1.9 nm) multilayers irradiated with ^{208}Pb ions, accelerated up to 6 GeV, at a fluence of 5×10^{12} ions/cm^2, have been discussed [107].

The irradiation of Fe_x-C_{1-x} nanocomposites film with Ar^+ ions accelerated up to 100 keV [107] increases the coercive field from 60 Oe to 410 Oe, the squareness of the hysteresis loop from 0.24 to 0.72, the blocking temperature from 23 K to 220 K, but reduces the magnetization at saturation from 830 to 540 emu/cm^3. The decrease in the magnetization at saturation was assigned to the formation of Fe-C solid solution (due to the thermal heating induced by thermal spikes followed by a rapid quenching). Above the blocking temperature, the samples are superparamagnetic. $(Pt/Co)_nPt$ multilayers have been irradiated with He ions, accelerated at different energies in the range 20 to 100 keV at fluencies of about 10^{15} to 10^{16} ions/cm^2. Directional effects induced by incoming accelerated heavy ions were reported [107]. In $Pt_{50}Mn_{50}$ or $Cr_{50}Mn_{50}$ antiferromagnetic bilayers the coercive magnetic field decreases as the fluence is increased. In helium irradiated bilayers containing $Fe_{50}Mn_{50}$ as antiferromagnetic layer, by increasing the fluence of incident ions (up to 3×10^{14} helium ions per cm^2), the coercive field is increased up to a maximum value higher by about 50% than the coercive field of the not-irradiated bilayer. A gradual decrease of the coercive field toward an asymptotic superparamagnetic state (characterized by a zero coercive field) as the ion fluence is further increased, was reported [110].

NdFeB magnets have a low Curie temperature (583 K), whereas the $SmCo_5$ have a high Curie temperature (997 K). Samples of $SmCo_5$ were irradiated by protons accelerated up to 19.5 MeV and fluencies ranging between 10^{13} and 10^{14} protons/cm^2, at different temperatures in the range 300 to 850 K. The experimental data indicated that the magnetization drops dramatically when irradiation temperature approaches Curie temperatures. It was estimated that the radius of the nucleation center is about 23 nm and the diameter of the resulting domain, D_g, is 1300 nm. The authors claimed [111] that the incident particle heats locally the sample causing the nucleation of domains magnetized in opposite directions [112].

A theoretical model for the radiation-induced flux loss in permanent magnets, based on the assumption that a large part of the energy of the incoming particle is transferred to the lattice by primary knock-on atom was suggested [112]. This model was tested on experimental results reported earlier on proton irradiated NdFeB permanent magnets, with a thickness of about 0.5 mm. The irradiation was carried out with protons with a fluence of about 10^{13} protons/cm^2, accelerated at different energies (14, 16, 18, and 20 MeV), and at various temperatures in the range 22 K to 295 K. The energy transferred to target's electrons is then dissipated within a larger volume (spherical), in which the local temperature raises above the Curie temperature. If the volume of this region exceeds a critical value V^*, the demagnetizing field flips the electronic spins, and the nucleation of a new magnetic domain with opposite spin direction is triggered. The model uses two parameters, the radius of the nucleation center R and the average diameter of the new domains (D_g). Thermal fluctuations preclude an exact estimation of R. For simplicity, it is assumed that the critical size of

the nucleation center is determined in the same way as the nucleation volume in magnetic viscosity experiments:

$$H_C = \frac{K\varepsilon_V}{V_a^{1/3} M_S} - 4\pi N_D M_S \tag{273}$$

H_C is the coercive field, ε_V the domain-wall energy density, K is a constant, M_S the magnetization at saturation, N_D the demagnetizing factor, and V_a the activation volume ($V_a \approx V^*$). The volume of the spherical nucleation center in air, in an external magnetic field is given by

$$-H_{ex} = \frac{K\varepsilon_V}{V_a^{1/3} M_S} - 4\pi(N_{DT} - N_{DS})M_S \tag{274}$$

where N_{DT} is the demagnetizing factor associated with the magnetic track and N_{DS} is the demagnetizing factor connected with the macroscopic shape of the sample. The diameter of the new domains was estimated to be of the order 1 μm, significantly smaller than in the pristine NdFeB magnets (where D_g is of the order of 10 μm) but compatible with the grain size in melt spun magnets. This indicates a rapid solidification of the magnetic material within these critical volumes.

Irradiation of ferrites with swift heavy ions (3.8 Gev of 129 Xe and 6.0 GeV of 208 Pb) [115] revealed also a change in the orientation of the magnetization, with a flipping along the track axis direction. The appearance of continuous and homogeneous cylindrical amorphous tracks was reported at an electronic stopping range of about 20 keV/nm [41].

Proton (2.25 MeV) and electron irradiation (1.25 MeV) effects on amorphous alloys of Fe-Ni-P-B have been reported [112, 113]. The increase of Curie temperature upon irradiation was reported. The proton implantation (0.25 MeV) resulted in an inhomogeneous sample with two-Curie temperatures; one characteristic of the as-quenched state and the other characteristic of the irradiation-induced structurally relaxed state. The region of enhanced Curie temperature is shown by electrochemical thinning to extend only to the end of range of the 0.25-MeV protons in the materials studied. Relative magnetic permeability measurements in the low-field region indicate an increase in permeability upon either proton irradiation or thermal annealing. The variation of the protons energy in the range 14 MeV to 20 MeV (total dose of 10^{13} protons) does not affect significantly the magnetic flux [112]. Irradiation of biotin with protons accelerated up to 3 MeV (2.4×10^{14} protons/cm^2) enhanced the magnetic features due to an oxidation reaction that converted Fe^{2+} ions into Fe^{3+} ions. This reaction was assigned to heating effects. Both the Curie temperature and the low temperature saturation magnetization are increased by irradiating $Fe_xNi_{80-x}P_{14}B_6$ ($20 < x < 34$) amorphous ferromagnets with proton fluence up to 10^{16} cm^{-2}. The magnetic features are constant at higher fluencies [114]. Proton bombardment at the same fluencies produces scattering centers (which may indicate incipient recrystallization, void formation, and phosphorous segregation) with a size of about 16–30 Å that are observed by small angle x-ray scattering. The concentration of scattering centers increases with proton fluence up to 10^{16} cm^{-2}, but remains constant thereafter.

The effect of surfaces (and in particular of surface roughness) and interfaces on the magnetic features is not fully understood. Irradiation is a straightforward modality to enhance in a controlled manner the roughness of surfaces and to generate new interfaces, because of cooperatively coupled defects. The role of structures in quenching the moments and frustrating spin alignments may be modeled by irradiating perfect ensembles of spins. In the case of proton irradiation, the changes in spin orientations may result also from the direct interaction between the spin of the proton and the electronic spins. Such interactions would shuffle the spin orientations within the latent track, affecting dramatically the magnetic state of the nanoparticle. The magnetic anisotropy is also connected to the structure of the magnetic nanomaterials although contains contributions due to small strains, stresses, texturing, surface, and interface. The proximity-induced effects (induced magnetism) are of particular importance in nanometer size materials, due to the reduced thickness of the boundaries.

5. COLLECTIVE RADIATION-INDUCED MODIFICATIONS AT NANOMETER SCALE

Low temperature conductivity measurements showed that the energy gap of irradiated C_{60} films decreases from about 1.97 eV to almost zero as the fluence of Ni ions is increased up to 10^{14} ions/cm^2 [117]. Radiation-induced amorphization in ion-beam irradiated fullerenes was reported [117, 118] along with the formation of a nanometer-sized graphitic material.

The irradiation of multiwalled carbon nanotubes by 1 keV Ar^{+1} ions produces the amorphization of the carbon nanotube. It is estimated that the sensitivity of carbon nanotubes is larger than expected; each incident ion produced 10^1 defects (driven-out atoms and vacancies) [117]. The charge motion within a carbon nanotubes has been investigated in connection with the possibility to use carbon nanotubes for beam bending. It was concluded that the charged particle channeling through a carbon nanotube is possible and that short carbon nanotubes may be used to bend the trajectory of relativistic proton beams [119]. The electron irradiation (at 300 keV) of a soot containing predominantly carbon nanotubes induced [120, 122] a change from nanotubes to a multiwalled fullerene-like structure (onion).

A recent study [121] on ion-beam irradiation effects on thin carbon films revealed important differences between the films rich in sp^2 and sp^3 carbons [121–123]. The hardness and the elastic modulus of sp^2-rich amorphous carbon films are enhanced by irradiation due to densification and crystallization. Carbon films rich in sp^3 showed the opposite modifications during ion-beam bombardment and remained amorphous after irradiation. The radiation-induced fusion of carbon nanotubes as well as the possibility to graft various polymers with carbon nanotubes [122] will eventually result in high strength materials.

The irradiation of polymers with swift accelerated heavy ions resulted in the formation of craters. It was reported that in PS irradiated with accelerated Au ions the length and the width of craters decrease as the molecular mass of the target is increased [124].

Ion-beam irradiation of nanometer sized particles (mean grain size of about 100 nm) SnO_2 produced cylindrical holes; their diameter was compared with the thermal spike approximation predictions. It was found that holes size corresponds to the region of the particle heated above the melting temperature [125].

5.1. Latent Tracks

The energy released by the impinging radiation in the target produces primary effects confined at sub nanometer scale. If the energy deposited within the target is sufficiently high, the concentration of these defects is sufficiently large to allow the interaction among them. Such collective defects are observed starting from relatively low values of the energy of incident particles. The local dose deposited around the incident particle trajectory within a solid has complex position dependence. The latent track is a continuous collection of defects, extended at nanometer scale. Within the latent track, two regions are commonly defined; an inner region named latent track core that corresponds to a highly degraded material and a penumbra region around the latent track core. For an isotropic target, both core and penumbra regions have a cylindrical symmetry in a plane normal to the incident particle trajectory within the target. The local energies, d_E, deposited within the core and the penumbra of such a track by an impinging particle as a function of the distance d from the incident particle trajectory in the target are [126]

$$\begin{aligned} d_E^{\text{core}} &= \frac{(dE/dx)}{2\pi d_C^2} + \frac{(dE/dx)}{4\pi d_C^2 \ln(\sqrt{e}(d_P/d_C))} \quad d \le d_C \\ d_E^{\text{pen}} &= \frac{(dE/dx)}{4\pi d^2 \ln(\sqrt{e}(d_P/d))} \quad d_C \le d \le d_P \end{aligned} \tag{275}$$

where d_C is the radius of the latent track core, and d_P is the radius of the latent track penumbra, defined as the maximum distance that the knock on electron is able to travel away from the incident particle trajectory. The superscripts core and pen indicate the latent track core and penumbra, respectively. The diameter of the latent track ranges from a few

nanometers to about 100 nm, and the length of latent tracks is controlled by the speed, mass, and charge of the incident particle as well as by the stopping power of the target.

5.1.1. Latent Tracks in Polymers and Insulators

The latent track in polymeric solid-state nuclear track detectors (SSNTD) is one of the most known modifications induced by ionizing radiation in insulators at nanometer scale. It has been exploited for several decades for the dosimetry of charged particles. The impinging particle deposits a relatively high amount of energy around its trajectory within the polymeric target. The density of the energy deposited by the incident beam is $\Phi(S_e + S_N)$, where S_e and S_N are the electronic and nuclear stopping powers, respectively, and Φ is the flux on incident particles. These experimental results suggest a huge local heating of the target due to the energy deposited by the ionizing radiation, as predicted by several theoretical approaches such as Coulomb explosion model [45, 80], thermal spike approximation [80], or the liquid drop model [127].

The appearance of latent tracks in insulating materials is intimately related to the stopping power of the incident charged particle within the target. If the stopping power is sufficiently low, the density of the energy deposited by the incoming particle within the target is eventually not sufficient to trigger the appearance of latent tracks. This explains the existence of a threshold value of the stopping power, for track formation. The structure and the size of latent tracks was proved by microscopy. Atomic force microscopy (AFM) studies on ion-beam irradiated polyethyleneterephtalate (PET) revealed the formation of cylindrical cavities in the samples irradiated with Xe ions holes with a diameter of about 7 nm and of hillocks with diameters ranging between 60 nm and 80 nm presenting central cylindrical cavities with a diameter of about 12 nm to 15 nm. These modifications describe the AFM picture of the latent track and the cylindrical hole represents the hard core of the track [126].

The morphology of latent tracks produced by accelerated particles in polymeric materials is complex. The cross-link of macromolecules within the latent tracks has been recently reported in polydimethylsiloxane, PDMS, irradiated with carbon ions accelerated up to 204 MeV. [118, 126]. In the case of gamma irradiated polymers the gel fraction, g, depends on the irradiation (absorbed) dose, D, according to

$$1 - g + \sqrt{1 - g} = \frac{G(s)}{2G(x)} + \frac{4800000}{G(X)DM_n} \tag{276}$$

where M_n is the numerical average molecular mass of the polymer, $G(s)$ and $G(c)$ is the number of scissions and cross-links per 100 eV of energy deposited by the incident particle(s), respectively. In gamma-irradiated PDMS, the gel fraction is zero if the absorbed dose is smaller than a critical dose. At higher absorbed doses, the gel fraction increases abruptly and approaches unity. In the case of ion-beam irradiated polymers, the gel fraction increases linearly with the dose [118–126]. This behavior has been assigned to the nonuniform distribution of the energy within the target.

There is no direct connection between the gel fraction and the radical yield in polymeric materials. At low doses, the radical yields is almost constant. By increasing the dose, the radical yield starts to decrease asymptotically toward zero [70]. The simulation was done by assuming that the dose distribution within the particle track in a polymer is analogous to the dose distribution within the latent track in water, as expressed by Eq. (275). In certain polymeric materials, the latent track has a complex structure. For example, in polyimides (PI) and polyethylene naphtalate (PEN) irradiated with heavy ions (Xe, Bi, Kr) accelerated at few MeV per nucleon, it was reported [128] that the latent track is characterized by a fast etching rate (relative to the pristine polymer) that indicates dominant scission reactions. The latent track core has an etchability lower than the unirradiated polymer, suggesting dominant cross-linking reactions. AFM studies revealed [129] a change in the morphology of latent track at a temperature identified as the glass transition temperature of the polymer. The minimum latent track diameter that still allows the detection of tracks in polymers irradiated with ions is ranging from 26 nm to 32 nm in polyimide and from 11 nm to 14 nm in polyethylene naphthalene [128]. The differential behavior of different macromolecular chains resulted

in radiation-induced chain segregation of block copolymers [130]. The chemical reactions triggered by the incident radiation release a certain amount of volatiles such as hydrogen. The gas evolution at nanometer scale in polymeric materials during irradiation was studied by several authors [131, 132]. As the irradiation starts, the hydrogen concentration in polymeric targets has a rapid increase followed by a very slow decay. This behavior was explained within the saturated core approximation [131] by assuming that the hydrogen-depleted regions (saturated cores) are no more able to sustain hydrogen production, resulting in a decrease of the amount of the hydrogen released during polymer irradiation. The number of hydrogen atoms created per incident ion, N, depends on the particle range, R, within the polymer and on the core cross section, σ_C [131]:

$$\frac{dN}{di} = -\sigma_C R(1 - P)(\rho_0 - \rho_f) \tag{277}$$

where ρ_0 is the initial hydrogen concentration in the target, ρ_f is the final hydrogen content within the target, and P reflects the core overlapping probability. The rate of hydrogen generation was related to the incident particle flux Φ

$$\frac{dN}{d\Phi} = \sigma\rho_f \mathrm{Re}^{-\sigma\Phi} = n_{SC} S e^{-\sigma\Phi} \tag{278}$$

where n_{SC} is the number of hydrogen atoms in a saturated core and S is the target area. This model predicts the release of atomic hydrogen. Such a process is associated with the appearance of free radicals in the early stages of the polymer irradiation. As free radicals generation was not confirmed by electron spin resonance, it was supposed that hydrogen atoms recombine locally producing hydrogen molecules. This is a second order reaction and accordingly the density of molecular hydrogen production within the latent track, ρ_{H2}, for each incident ion, i, is given by

$$\frac{d\rho_{H2}}{di} = K_2 \rho_{H2} \tag{279}$$

where K_2 is the constant rate for molecular hydrogen production. Finally, by adding this process the following expression for the generation of hydrogen molecules has been derived

$$\frac{d\rho_{H2}}{d\Phi} = \frac{\sigma(\rho_0^{-1} - \rho_f^{-1})e^{-\sigma\Phi}}{\left[\rho_f^{-1} + \sigma(\rho_0^{-1} - \rho_f^{-1})e^{-\sigma\Phi}\right]^2} \tag{280}$$

This expression describes the local yield of hydrogen molecules. To be released from the polymer, hydrogen molecules have to permeate through the polymer. The flux of hydrogen molecules released from the polymeric target by irradiation, Φ_{H2}, depends on the flux of hydrogen molecules generated within cores, Φ_{H2}^C, and on the diffusion coefficient of hydrogen within the polymer, D_{H2}:

$$\Phi_{H2} = (C_1 D_{H2} t + C_2 e^{-C_3 D_{H2} t} + C_4)\Phi_{H2}^C \tag{281}$$

where C_1, C_2, C_3, and C_4 are constants. Another approach to hydrogen release in ion-beam irradiated polymers was suggested by Jong et al. [133].

5.1.2. Latent Tracks in Metals

Under the effect of accelerated charged particles, the local modifications that define the latent track are observed in metallic targets as local changes of their resistivity [134–147]. For bulk metallic samples, no track formation is expected as the energy deposited by the incident particle is rapidly delocalized [138, 139]. Early experiments indicated that the appearance of tracks in polycrystalline metallic films depends on film resistivity and thickness [138]. The complex process of track formation in conducting samples reflects the balance between the thermal heating, due to the energy deposited within the target by the impinging particle, and the rate of energy delocalization. If the heat cannot be rapidly delocalized, the target is

locally melted. The high thermal conductivity of the sample results in a quick annealing to room temperature, that frozen in the local stresses and defines the metallic track [139].

If the energy of the incoming particle is sufficiently low, the target resistivity decreases as the fluence of the incoming radiation is increased [135]. Al higher fluencies the resistivity of the target decreases, as the fluence is increased [135]. In conducting metals such as Bi, Fe, and Ti [134, 127], the resistivity inside the track, ρ_T, is higher than the resistivity of the nonirradiated metal ρ_0. The modification of the resistivity of metals due to beams of accelerated particles has been modeled by Poisson's law [137]

$$\rho_T = \rho_0 + \rho_{00} \exp -(\pi \phi R_T^2) \tag{282}$$

where ρ_{00} is the saturation value of the resistivity of the irradiated metal, Φ is the fluence of incoming particles, and R_T is the track radius. The dependence of the track radius *versus* the electronic stopping power shows a threshold value for track creation, S_e^T. A lower threshold value for the electronic stopping power is associated with a high electron-phonon coupling. This allows the fast transfer of the energy transferred by the incident charge particles to the electrons of the target (with characteristic times of the order 10^{-14} to 10^{-15} s). Due to the fast energy transfer, the energy cannot be spread over a large volume of the materials and a local melting of the material is possible even at relatively low electronic stopping powers. For high electronic stopping power thresholds the electron-phonon coupling is weak, resulting in a slow transfer of the energy from the impinging particle to the electrons of the target (of the order 10^{-13} to 10^{-14} s in metals). This slower transfer of energy allows for a better delocalization of the energy; a larger area will be affected by the energy deposited by incoming particle, and consequently the energy density will be lower.

This approximation is not able to explain the ion-beam induced modifications of the electrical resistivity in Fe-B amorphous ribbons. The data where accurately fit within the two hit model [136], indicating the following dependence of the change in the sample resistivity ($\Delta\rho$) on fluence

$$\Delta\rho = \rho_0 D_0 \Phi_C \left[1 - \exp\left(-\frac{\Phi}{\Phi_C}\right)\right] \tag{283}$$

where Φ_C is a critical (incubation) fluence, and D_0 is the rate of resistivity increase at the beginning of the irradiation [136].

Although gold is an excellent thermal conductor, the anisotropic plastic deformation from spherical colloids into ellipsoidal colloids during the irradiation of Au nanoislands at 45° relative to the Si substrate was assigned to a thermal spike [142–144]. This films (of the order 1 nm) deposited on silica are easily converted in nanoislands by irradiation with Au^{2+} ions accelerated up to 1.5 MeV, at fluencies ranging from 10^{13} to 10^{15} ions. This is due to the radiation-induced melting of the Au film combined with the surface tension between liquid Au and Si (gold is not wetting Si). The formation of craters, islands, and hillocks is a direct expression of the fact that the energy deposited by the incident particle cannot be delocalized over the Au nanoislands due to the boundary conditions (the thermal conductivity of Si is poor in comparison with Au). In the isolated cluster model, the largest volume that can be evaporated from the target by an incident particle is [142–144]

$$V_{\text{Max}} = -\left(\frac{dE}{dx}\right)\frac{l}{E_S \rho} \tag{284}$$

where E_S is the sublimation energy of the target material and l the maximum length of the particle path within nanoparticles.

Ion-beam effects in NiTi titanium indicates that for electronic stopping powers larger than 46 keV/nm, latent tracks appeared solely in the martensitic phase and not in the austenitic one [145]. This indicated [145] that track formation in such alloys is not solely the result of thermal spikes but involves also a contribution that reflects local structure.

5.1.3. Latent Tracks in Magnetic Materials

Latent tracks or radiation-induced continuous collective magnetic defects at nanometer scale were observed in magnetic materials bombarded with accelerated particles. In this case, the "magnetic description" of the latent track is extremely important. In the case of swift heavy ions accelerated up to GeV, the electronic stopping power is larger than the nuclear one by three order of magnitude. The effects of heavy ions impinging in magnetic targets is well described by the stopping power of the target against the incident particle [148–151]. The track formation threshold depends on the target material. An average value for magnetic targets is about 10 keV/nm [149]. A transition from discontinuous to continuous tracks occurs at a threshold of about 15 keV/nm and finally a transition to homogeneous, continuous cylindrical tracks is observed at a threshold of about 20 keV/nm. In $Y_3Fe_5O_{12}$, for stopping powers less than 8 keV/nm, the latent tracks have a spherical shape. At larger stopping powers, long cylindrical defects were produced [149] by the bombardment with accelerated charged particles.

Sm_2Fe_{17} powder with a particle size of 20–65 μm was nitrided in a flowing mixed gas ($NH_3 + H_2$) system, mixed with epoxy resins (2:1 by weight) and irradiated by Pb^{56+} ions, accelerated up to 5 GeV, at fluencies ranging from 10^{11} to 10^{13} ions/cm^2. The irradiation produces a paramagnetic phase and not uniform magnetic defects. The fraction of the total damaged surface, $p(F, r)$ depends on the fluence F and on the latent track radius r [152, 153]

$$p(F, r) = 1 - e^{-4\pi r^2 F} \tag{285}$$

Mossbauer data were assigned to discontinuous tracks with a minimum diameter of about 1.5 nm. The study of the in-plane and out-of-plane coercivity indicated that the tracks have a cylinder-like shape. By increasing the fluence of impinging ions from 10^{10} ions/cm^2 to 10^{14} ions/cm^2, the coercive field ($\mu_0 H_C$) is raised from about 0.3 T to about 1.6 T. The initial depinning field is also increased by increasing the fluence.

In garnets films, coercivity has been induced by etching the latent tracks to create cylindrical voids [41]. Coarse grain powders (grain length larger than 10 μm) of $Sm_2Fe_{17}N_3$ showed a very small coercivity, probably due to the presence of Fe precipitates. Both the coercive field and the threshold field (the minimum field required to depin the domain walls from a radiation-induced defect) increase sharply beyond a threshold fluence of 2.5×10^{12} ions/cm^2. This fluence corresponds to an average distance between pinning centers of about 7 nm. In irradiated magnetic materials above the threshold for defects generation, the morphology is changed from a string of spherical defects to discontinuous cylindrical effects and finally to continuous defects as the energy loss, dE/dx, is enhanced.

The magnetic latent track has been studied by several authors. A simple theoretical model was suggested by [111, 112]. The minimum energy required to heat a sphere of radius R above a critical temperature T_{Cr} was estimated by assuming that the primary knock of atoms causes a thermal spike. The following differential equations were used to describe the energy diffusion to the lattice:

$$\frac{\partial T}{\partial t} = \alpha^2 \nabla^2 T \tag{286}$$

Assuming that the initial temperature has a delta distribution, it is obtained:

$$T(r, t) = (T_1 - T_0)\left(\frac{V^{2/3}}{4\pi\alpha^2 t}\right)^{3/2} e^{-(r^2/4\alpha^2 t)} + T_0 \tag{287}$$

where α is a constant, T_1 is the initial temperature of the primary knock on atom, T_0 is the initial temperature of the sample, and V is the volume of an atom. To estimate the maximum radius of the sphere, R, it is assumed that $T(r, t) = T_{Cr} = T_C$, where T_C is the Curie temperature.

$$T_C = (T_1 - T_0)\left(\frac{V^{2/3}}{4\pi\alpha^2 t}\right)^{3/2} e^{-(r^2/4\alpha^2 t)} + T_0 \tag{288}$$

Finally is obtained

$$T_1 = T_0 + (T_C - T_0)\left(\frac{2\pi R^2}{3V^{2/3}e^{-t}}\right)^{3/2} \tag{289}$$

Temperature T_1 is related with the kinetic energy of the primary knock on atom:

$$E_{\text{kin}} = \frac{3}{2}K_B(T_1 - T_0) \tag{290}$$

where

$$E_{\text{kin}} = E_{\text{inc}}\left(1 - \frac{(\cos\theta + (M_2/M_1 - \sin^2\theta)^{1/2})^2}{(M_2/M_1 + 1)^2}\right) \tag{291}$$

E_{inc} is the kinetic energy of the impinging particle, θ the scattering angle, m_1 the mass of the impinging atom, and m_2 is the mass of the target atom. The cross section can be obtained by integrating the Coulomb scattering cross section over angles larger than θ_{min}:

$$\sigma = \frac{z^2Z^2e^4}{8\pi\varepsilon_0^2 m^2 v_n^4}\left(\frac{1}{1 - \cos\theta_{\text{min}}} - \frac{1}{2}\right) \tag{292}$$

The relative change in the magnetization is

$$\frac{\Delta M}{M} = 2PN_P\frac{V_{\text{grain}}}{V_{\text{sample}}} \tag{293}$$

where N_P is the number of incoming particles, V_{grain} is the grain volume, V_{sample} is the sample volume, and P is given by the product between the total cross section of the sample and the thickness of the magnetic film, L, given by

$$P = n\sigma L \tag{294}$$

where n is the ion density of the sample.

5.1.4. Models for Latent Track Formation

5.1.4.1. Coulomb Explosion Model This model assumes that the dominant effect of the energy deposited at nanometer scale around the incident particle trajectory within the solid target consists of a high density of local excitations and ionizations. This cooperative region of ionizations around the incident particle track is not in equilibrium, and consequently atoms from the solid target are ejected into the nonexcited part of the target via Coulomb repulsion [155]. The Coulomb explosion is the result of the electrostatic interactions between the transiently ionized atoms of the target. Because of Coulomb explosion, the ionization track produced by the energy deposited by the impinging particle within the target is converted into an area of damaged material that defines the latent track.

5.1.4.2. Thermal Spike Description Thermal spike description is a thermodynamic model. It assumes that the interaction of charged particles with condensed target occurs in two steps; in the first step, the charged particle interacts with the electrons of the target and deposits within the target an energy that is proportional to the electronic stopping power [97, 147, 148, 153–161]. This increases the temperature of the free electrons gas up to a temperature T_E. In the second phase, the interactions between electrons and the lattice result in an energy transfer from the electronic gas to the target that enhances lattice vibrations, raising the temperature of the target. Frequently the role of electron-electron interactions in the energy transfer from the electronic gas to the lattice is neglected. An important parameter is the mean diffusion length. In insulators such as SiO_2 [97], the thermal extends up to about 10^1 nm from the incident particle trajectory within the target and last for 10^{-15} s to 10^{-10} s. At 0.5 nm from the incident particle track in SiO_2, the local temperature exceeds 5500 K while at 10 nm the local temperature is about 800 K [97, 159].

The differential equations that describe the thermal spikes are [147, 148]

$$\begin{aligned} C_S^E \frac{\partial T_E}{\partial t} &= \nabla(\kappa_E \nabla T_E) - g(T_E - T_L) + B(r,t) \\ \rho C^L(T_L) \frac{\partial T_L}{\partial t} &= \nabla(\kappa_L \nabla T_L) + g(T_E - T_L) \end{aligned} \tag{295}$$

where C_S^E is the electronic specific heat, C^L is the lattice specific heat, T_E is the temperature of the electronic gas, T_L is the lattice temperature, κ_E is the electronic thermal conductivity, κ_L is the lattice thermal conductivity, g represents the electron-phonon coupling constant, and $B(r, t)$ depends on beam characteristics. The parameter g is proportional to the reciprocal of the electron-phonon interaction mean time.

Taking into account the cylindrical symmetry of latent tracks results [159, 161]

$$\begin{aligned} C_S^E \frac{\partial T_E}{\partial t} &= \frac{1}{r}\frac{\partial}{\partial r}\left(r\kappa_E \frac{\partial T_E}{\partial r}\right) - g(T_E - T_L) + B(r,t) \\ \rho C^L(T_L) \frac{\partial T_L}{\partial t} &= \frac{1}{r}\frac{\partial}{\partial r}\left(r\kappa_L \frac{\partial T_L}{\partial r}\right) + g(T_E - T_L) \end{aligned} \tag{296}$$

where according to δ theory the function $B(r, t)$ representing the energy density per unit time may be written as a Gaussian distribution

$$B(r,t) = B_0 S_e e^{-F(r)/(t-t_0)^2/2\sigma_t^2)} \tag{297}$$

where t_0 is the mean flight time of secondary (δ) electrons perpendicular to the incident particle trajectory.

In a first-order approximation, the energy transfer from hot electrons to the lattice is proportional to the difference between the T_E and T_L, where T_L is the lattice temperature. Finally, the model correlates the electronic stopping power to the track radius. The thermal spikes have cylindrical symmetry. The temperature distribution, $T(r, t)$ defined as the temperature measured at a point situated at the distance r from the incident particle trajectory and at a time t, is

$$T(r,t) = T_S + \Delta T(r,t) \tag{298}$$

where T_S is the substrate temperature, and $\Delta T(r, t)$ measures the increase in the target temperature in the point characterized by the position r at the moment t. For simplicity, it was assumed [150, 154, 155] that the temperature profile has a Gaussian distribution

$$\Delta T(r,t) = \frac{Q}{\pi q^2(t)} \exp - \frac{r^2}{q^2(t)} \tag{299}$$

where $q(t)$ is a function that depends on the thermal diffusivity of the target, and Q is related to the energy released within the target by the impinging particle. Actually [150],

$$Q = \frac{gS_E - \pi L \rho R^2(t)}{\rho C_S} \tag{300}$$

where gS_e is the fraction of energy deposited by the incident beam into the track through electronic interactions between the incident particle and the electronic cloud of the target, R is the radius of the melted region, C_S is the specific heat of the target, ρ is the target density, and L is the latent heat of phase transformation (melting). For simplicity, it was assumed that the volume of the amorphous phase produced by the incident ion is proportional to the volume of the melted region. The maximum track radius is obtained from the condition $dr/dt = 0$ at $\Delta T = T_0 = T_M - T_S$.

The model predicts the following dependence of the effective track radius, R_e on the electronic stopping power of the target, S_e [150, 154, 160, 162]

$$R_e^2 = \begin{cases} q^2 \ln\left(\dfrac{S_E}{S_0}\right) & S_0 < S_e < 2.7S_0 \\ q^2\left(\dfrac{S_e}{2.7S_0}\right) & S_e > 2.7S_0 \end{cases} \tag{301}$$

with

$$S_0 = \pi C_S T_0 q^2 \frac{\rho}{g} \tag{302}$$

where T_0 is the maximum temperature of the phonon system, g is a fitting parameter defining the efficiency of energy transfer from the incident particle to the thermal spike, and $q(0)$ is the initial Gaussian width of the temperature distribution (at the highest temperature). In the thermal spike model, the energy-deposited profile is converted into a temperature profile and it is further delocalized over the target by thermal diffusion. The atoms within the latent tracks are displaced or ejected from the surface if their energy exceeds a barrier limit. Most simulations of latent tracks within the thermal spikes approximation are based on the assumption that the number of ions ejected from the target per incident ion depends on $(dE/dx)^2$. Recent simulations suggested the possibility of a process in which the atom yield, Y_A, depends linearly on the stopping power [155]

$$Y_A \approx C_S \frac{r_{SP}}{E_{COEH}}\left(\frac{dE}{dx}\right) \quad \text{for} \quad \left(\frac{dE}{dx}\right) \geq \pi r_{SP}^2 n E_{COEH} \tag{303}$$

where r_{SP} is spike's radius, E_{COEH} is the cohesion energy of the target, n is the density, and C_S is a constant of the order of 10^{-1}. This model assumes that as a result of the thermal spike, a region of the material is melted and a pressure wave is produced within the target. The energy transport is controlled by the competition between these factors. Molecular simulations suggested that the Coulomb explosions and thermal spikes in semiconductors refer to the early and late stage of the ionization track produced by an impinging particle.

The thermal spike model predicts a radiation-induced amorphization of the sample. This results from the fast cooling of the sample from a temperature far above the melting temperature to the substrate temperature. It is important to mention that tracks were noticed also in ionic crystals assumed non-amorphizable [159]. In materials such as Al_2O_3-SiO_2, such an amorphization process triggered by ion-beam bombardment has been reported [42]. The critical amorphization dose D is related to the irradiation temperature T via an activation energy E_{AA}

$$\ln\left(1 - \frac{D}{D_0}\right) = C - \frac{E_{AA}}{K_B T} \tag{304}$$

where C is a constant and D_0 is the amorphization dose extrapolated at 0 K. It is important to mention that ion-beam irradiation is able to produce not only the amorphization but also the crystallization of amorphous alloys. Such a modification has been recently observed in $Fe_{73.5}CuNb_3Si_{13.5}B_9$ irradiated with 5 GeV Pb ions at a fluence of 10^7 ions/m^2 [163]. Although the local rise of the temperature above 520°C is required to explain the crystallization of the amorphous alloy, the unexpected behavior comes from the fact that the rapid cooling to the substrate temperature was not able to disorder the material. It was concluded that the crystallization was due to local stress relaxations triggered by the incoming particle and not by the heating of the sample.

There is a debate regarding the applicability of the thermal spike description to radiation-induced modifications in polymers. A computer simulation [164] of the local heating of PET targets subjected to an ion-beam irradiation with ions accelerated at 1500 eV, at current intensities of 1.0 A/m^2 resulted in a rather modest heating of the target.

In insulating targets such as polymers, the local temperature decreases very fast as the radial distance from the incident particle trajectory is increased. For Au ions accelerated at

20 MeV projected onto PMMA targets, the local heating estimated at 20 nm from the center of the track is about 200°C and lasts for about 3×10^{-9} s. This time is short in comparison with the relaxation timescale for macromolecular chain, although [165] it is sufficient to affect the polymeric segments. Thermal spikes description has also been used to simulate the features of latent tracks in metallic targets [147, 148]. Many papers have focused on the appearance and parameters of tracks in irradiated condensed targets [166–172].

5.1.4.3. The Liquid Drop Model The liquid drop model is based on the thermal spike description [127, 156]. The radial dose distribution in samples irradiated with charged particles (for the cases in which the electronic stopping power is larger than the nuclear one) has been calculated [68, 173–175], assuming a decrease of the local deposited dose proportional to the square of the distance from the incident particle trajectory within the solid and an energy cutoff. In-depth studies of the interaction of charged particles with polymers revealed that the threshold for latent track appearance is neither the 1.7-nm critical dose (i.e., about 25 kGy for most polymers) nor the 66% mean energy loss density [156]. The experimental data were simulated by using a modified version of the Marlowe 12 code, adapted to include both elastic and inelastic collisions. A description of the local heating is obtained by solving in cylindrical coordinates the following differential equation [127]:

$$\frac{\partial Q}{\partial t} = \nabla\left(\frac{\kappa}{\rho c}\right)\nabla Q \tag{305}$$

where κ is the thermal conductivity, Q is the total energy transferred by the electrons to the lattice ($Q = E_{\text{elas}} + gE_{\text{incl}}$), g is a parameter that identifies the transfer of the inelastic energy transfer to the target, E is the elastic energy transfer to the matrix, and E_{incl} represents the inelastic energy transfer to the polymeric target.

If R_T is the theoretical radius of the track and R_{exp} the experimental one, the following relationship is observed:

$$R_{\text{exp}}[\text{nm}] = 16.5 \text{ nm} + 1.3R_T[\text{nm}] \tag{306}$$

The model predicts the existence of latent tracks even for electronic stopping power lower than the threshold value of 320 eV/nm, derived from Szenes criterion [176, 177] for Makrofol *E*. The liquid drop model allows for the appearance of latent tracks at lower stopping powers than other description, in agreement with experimental data [127]. Nevertheless, although the agreement between theoretical predictions and experimental data is improved by this model, there are still significant discrepancies.

In magnetic insulators, the damage efficiency, D_E is defined as the ratio between the latent track area and the stopping power [151]

$$D_E = \frac{\pi R_T^2}{(dE/dx)} \tag{307}$$

where R_T is the latent track radius. In the case of iron yttrium garnets, D_E does not have a linear dependence on the stopping power. For the low-velocity regime, a maximum of the inflicted damage in the target is observed at about 25 keV/nm. In the high-velocity regime, the damage efficiency increases as the stopping power is increased for 0 up to about 25 keV/nm. Larger stopping powers are no more capable of affecting the damage efficiency. A maximum in the diameter of the latent track diameter, equal to about 13 nm, was observed for impinging particles capable of transferring to the target about 30 keV/nm. The morphology of radiation-induced defects depends on the stopping power. At stopping powers smaller than 5 keV/nm, the defects are isolated and their estimated diameter is up to about 0.5 nm. The shape of these defects is almost spherical and the electronic stopping power is larger than the nuclear one.

5.1.4.4. Latent Track in Metallic Magnetic Materials as a Result of Point Defects Clusterization In crystalline metals, the incident radiation produces point defects. Frenkel defect is one of the simplest defects generated by irradiation. The concentration of point defects is dynamic, and the equilibrium value corresponds to the equilibrium between

generation reactions, recombination reactions, defect clusterization, and interaction with sinks [146]. Mobile defects are able to diffuse within the lattice of the target. This qualitative picture is described mathematically by the following set of equations (written for tracks with cylindrical symmetry):

$$\begin{aligned}
\frac{\partial n_{I,V}}{\partial t} &= \frac{1}{r}\frac{\partial}{\partial r}\left(rD_{I,V}\frac{\partial n_{I,V}}{\partial r}\right) - R_{I,V} + G_{I,V} \\
D_{V,I} &= D^0_{V,I}e^{-(Q^M_{V,I}/k_BT)} \\
G_{I,V} &= (N_a - n_V)\left(1 - \frac{n_I}{\alpha N_a}\right)\nu_D e^{-(Q^F_{FP}/2K_BT)} \\
R_{I,V} &= 2\nu_D\left(\frac{v_a(n_I + n_V)}{2N_a}\right)^{1/3}\left[n_V e^{-(Q^M_V/K_BT)} + \sum_{k=1}^{k_0} n_{I,k}e^{-(Q^M_{I,k}/K_BT)}\right]\eta
\end{aligned} \tag{308}$$

where superscripts M and F indicate migration and formation, and the subscripts I and V represent interstitials and vacancies. D_I and D_V are the diffusion coefficients of interstitials and vacancies, and D^0_I and D^0_V are the diffusion coefficients for interstitials and vacancies, extrapolated at very large temperatures. In Eq. (308), k identifies the substage of the stage (defined by I), k_0 represents the total number of stages, n is the concentration of point defects, G is the local electronic energy loss responsible for point-defect generation, and R_I is the recombination rate. Q are the activation energies for various defects at different stages, N_a is the atomic density, ν_D is the Debye phonon frequency, and α is the number of interstitial positions [146]. The temperature T is a function of the electronic stopping power and of the electron-phonon coupling factor. It depends also on the thermal properties of the target.

5.2. Ionization of Nanometer-Sized Metallic Clusters

The fate of the energy deposited within the target by the incident radiation is governed by the energy required to ionize the atoms and the molecule of the target. For a spherical metallic cluster, confined at nanometer scale, it is possible to consider the electrons as a gas of free electrons confined within a sphere of diameter D.

The one-dimensional model of the effect of confinement on the energy levels of the electrons in a metallic cluster is rather well described by the simple quantum well problem. Assuming that the potential outside the sphere is very large (at limit tending to infinity), the energy levels of confined electrons are [14–16, 22, 24]

$$E_n = \frac{h^2n^2}{8m_ea^2} \tag{309}$$

where n is an integer (quantum number), and h is Planck's constant. Hence, the ionization potential is expected to increase as the size of the confinement is depressed. Detailed experimental and theoretical studies confirmed the dependence of the ionization energy of a spherical cluster, E_I^R, on the radius of spherical clusters [178–182]

$$E_I^R = E_I + \frac{\alpha e^2}{R} + O(R^{-2}) \tag{310}$$

where E_I is the ionization energy of the macroscopic material, and α is a constant.

5.3. Photoelectric Effect of Nanometer-Sized Metallic Clusters

The classical theory of the photoelectric effect was discussed in a previous section. The classical quantum approach showed no correlations between the threshold frequency of the incoming electromagnetic radiation or the number of emitted photoelectrons and the size of the metallic target. Relatively recent data proved that this approximation fails for metallic targets confined at nanometer scale [183, 184]. The main reason for this change resides in the dependence of the energy necessary to remove the electron from the metallic surface (work function), which increases slightly as the size of the metallic particle is decreased.

The simple quantum well model shows that as the size of the confinement is reduced, the energy levels of the confined electron shift to higher values. This provides a qualitative basis for the understanding of the effect of confinement on the work function. A classical explanation for the size dependence of the work function was suggested by Wood [184]. From the effect of the surface shape on the image potential, he estimated the relation between the work function of an ideal plane E_W and the work function for a spherical metallic particle of radius R, E_W^R:

$$E_W^R = E_W + \frac{3e^2}{32\pi\varepsilon_0 R} \tag{311}$$

The yield of photoelectron generation, Y, is defined as the ration between the number of photo-emitted electrons and the number of incident photons. Near threshold, the Fowler-Nordheim law connects the yield of photoelectron generation to the energy of the incoming photon ($h\nu$) and the work function, E_W:

$$Y(\nu) = K(h\nu - E_W)^2 \tag{312}$$

where K is a constant. Experimental data [183, 184] revealed that the photoelectron yield is enhanced by up to two orders of magnitude in small metallic clusters relative to bulk macroscopic metallic surfaces. The changes in the photoelectric effect as the size of the metallic targets is shrunk to nanometer scale is a strong indication about size effects in the interaction between the radiation and targets confined at nanometer scale.

5.4. The Stopping Power of Nanometer-Sized Metallic Clusters

The stopping power of nanometer-sized metallic clusters to low-charge ions (typically singly charged ions) at fairly low incident kinetic energies was recently studied from both experimental and theoretical standpoints [182]. At low incoming energies, the charge of the impinging particle is shielded by the delocalization of the target's electrons located in the valence band, resulting in a perturbation in the electron density of the target. The unexpected result will be the dominancy of the electronic stopping power over the nuclear one (assigned to elastic interactions of the incident particle with the target). The experimental data showed a weak decrease of the loss energy as the number of atoms (in the cluster) is decreased.

5.5. The Effect of Irradiation on the Exchange Biased Field

An interesting consequence of the irradiation of magnetic nanoparticles consists in the capability to control, suppress, and even reverse by irradiation in external magnetic field the exchange bias [185–187]. The sensitivity of the exchange bias field in ferromagnetic/antiferromagnetic structures (sandwiches, bilayers, and multilayers) to interface exchange interaction, interface roughness, magnetization, and ferromagnetic layer thickness was confirmed by the strong effect of ionizing radiation on such structures [185–187]. It was reported [185] that it is possible to control the exchange bias field by irradiations with He ions accelerated up to 60 kV, at fluencies ranging between 10^{14} and 10^{17} He^+/cm^2.

Bilayers consisting of ferromagnetic 5-nm $Fe_{0.19}Ni_{0.81}$ film and 10-nm $Fe_{0.5}Mn_{0.5}$ antiferromagnetic film, grown on thermal oxidized Si substrates, heated (after deposition) below Neel temperature, and slowly cooled in an external magnetic field of about 500 Oe (to initiate exchange bias field) were irradiated. The irradiation was done with helium ions accelerated up to 10 keV at fluencies ranging from 10^{13} to 10^{16} helium ions/cm^2 [186]. During irradiation, a magnetic field of 1000 Oe was applied parallel or antiparallel to the exchange bias field. If the external magnetic field applied during irradiation is parallel to the exchange bias field, an enhancement of the exchange bias field was reported by increasing the fluence of helium ions up to about 3×10^{14} ions/cm^2. By increasing further the fluence, the exchange bias field is gradually decreased toward zero. If the external magnetic field applied during irradiation is antiparallel with respect to the exchange bias field, by increasing the fluence up to about 3×10^{14} ions/cm^2, the exchange bias field reaches a maximum negative value.

Larger fluencies would continuously reduce the bias exchange field to zero. The experimental data are discussed within a simplified model that assumes that the radiation-induced modifications of the exchange bias field are due to defects. The normalized concentration of defects in the bulk antiferromagnetic layer is N_V, whereas N_I is the total concentration of defects in the interface. If all atoms in the antiferromagnetic phase have been displaced, $N_V = 1$. It was assumed that the magnitude of the exchange bias effect is linearly proportional to the number of displaced atoms within the ferromagnetic layer. This hypothesis is supported by current models, which assume that exchange bias field, H_{eb}, is proportional to the number of domain walls. It was assumed that the defects generated at interfaces are dominated by mixing effects, which reduce the effective exchange coupling across ferromagnetic/antiferromagnetic interface. For simplicity, an exponential decay of exchange coupling as a function of N_I was considered. The final expression of the normalized exchange field is

$$\frac{H_{eb}(N)}{H_{eb}^{initial}} = (1 \pm apt N)e^{-\gamma bN} \tag{313}$$

where N is the total number of impinging ions, a is the efficiency of volume defects to modify H_{eb}, and b reflects the efficiency of interface defects to modify H_{eb}. The "+" sign indicates that the irradiation is carried out in a magnetic field parallel to the initial exchange bias field, and the minus reflects that the irradiation was carried out in a magnetic field antiparallel to the initial exchange bias field. The probability of displaced atoms per incoming ion and per unit length, estimated by TRIM simulations, is p, and t is the thickness of the antiferromagnetic layer. In deriving this expression, the following relations were considered:

$$\begin{aligned} \frac{dN_V}{dN} &= pt[1 - N_V(N)] \\ N_I(N) &= \gamma N \end{aligned} \tag{314}$$

where γ is a proportionality factor. The decrease in the exchange bias field is largely controlled by the interfacial mixing that reduces the exchange coupling whereas the creation of pinning sites in the antiferromagnetic layer, at low fluencies, is responsible for the enhancement of the exchange bias field.

Samples of a bilayer consisting of 5-nm ferromagnetic film of FeNi and a 10-nm antiferromagnetic layer of FeMn were irradiated by He ions, accelerated up to 60 keV, at fluxes of about 10^{15} ions/cm^{2}s and fluencies ranging between 10^{12} and 10^{17} ions/cm^2 [186]. It was reported that the exchange bias field is decreased by irradiation. Temperature effects have been excluded. For $Fe_{50}Mn_{50}$ antiferromagnetic bilayers irradiated in a parallel magnetic field the exchange bias field presents a sharp increase as the ions fluence is increased up to about 10^{14} helium ions/cm^2, followed by a weak decrease toward a zero exchange bias field at fluencies greater than 10^{15} ions/cm^2. If the external magnetic field is antiparallel with the exchange bias field, the exchange-biased field is reversed. Fluencies larger than 3×10^{14} helium ions per cm^2 decrease the exchange bias field toward zero. In the case of $Pt_{50}Mn_{50}$, the exchange bias field is decreased as the ion dose is increased, for both parallel and antiparallel orientations.

5.6. Ion-Beam Mixing of Magnetic Multilayers

The displacement of atoms due to nuclear interactions was speculated in thin magnetic multilayers to produce magnetic granular films with enhanced colossal magneto-resistance capabilities. Most studies were focused on the Fe-Co-Pt system. Ion-beam mixing of magnmetic multilayers, ion beam grafting, cross-linking and polymerization reactions, and nanopowder production by high-intensity short-pulse irradiation are the very first applications of ionizing radiation in nanomaterials. Radiation-induced fabrication of templates has been used for several decades to build various structures (such as nanowires) at nanometer scale.

5.7. Ion-Assisted Molecular-Beam Epitaxy

Ion-assisted molecular-beam epitaxy (IAMBE) is an emerging technique for the production of nanomaterials that exploits the benefits of ionizing radiation at nanometer scale. The

growth of the surface in IAMBE is typically a diffusion-like process [188]:

$$\frac{dN}{dt} = D\frac{d^2N}{dx^2} - V\frac{dN}{dx} + S \tag{315}$$

where N is the number of defects, V is the surface growth rate, x is the distance from the moving surface, D is the diffusion constant at the irradiation temperature, and S is the source function represented by the defect profile produced by the incident beam. Such a simple model results in values too low for the pre-exponential factor of the diffusion constant. For this reason, a cascade-assisted diffusion was considered. In this case, the impinging particle generates a cascade. The cascade recovery has two components: an athermal recovery and a thermal recovery. The thermal recovery reflects the local heating of the target by the energy deposited by the incident particle. For a target characterized by the thermal conductivity κ, heat capacity C_h, and density ρ, the temperature at the position x at the time T is

$$T(x,t) = T_S + \frac{F_d}{4\pi\kappa t}\exp\left[-\frac{\rho C_h x^2}{4\pi\kappa t}\right] \tag{316}$$

where T_S is the substrate temperature, and F_d represents the heat produced by the impinging beam per unit length. The thermal spike will affect the defect migration. The number of jumps per unit time for a defect with an activation energy E_{AS} and an attempting frequency f_s is

$$\eta = J_{INC} f_S \int_0^\infty 2\pi x\,dx \int_{t_0}^\infty \left\{\exp\left[-\frac{E_{AS}}{K_B T(x,t)}\right] - \exp\left[-\frac{E_{AS}}{K_B T_S}\right]\right\} \tag{317}$$

where J_{INC} is the flux of incident particles, and K_B is Boltzmann's constant. The parameter t_0 reflects the initial width of the spike, supposed to have a cylindrical symmetry. The effective diffusion coefficient was defined by using Eq. (317):

$$D = D_0\left[\frac{\eta}{f_S} + \exp\left(-\frac{E_{AS}}{K_B T_S}\right)\right] \tag{318}$$

There is a critical temperature for thermal species (TCTS). Below this temperature, the defect-diffusion is cascade-assisted, and above it the defect-diffusion is thermally activated. The critical temperature is defined by the expression

$$T_{CTS} = \frac{E_{AS}}{K_B \ln(f_S/\eta)} \tag{319}$$

5.8. Recent Advances in Radiation Dosimetry at Nanometer Scale

A great effort has been made to improve the actual radiation detectors up to the point where it will be possible to test and eventually to refine the predictions of nanodosimetry. Although such efforts [189–192] are beyond the goals of this contribution, it is worth mentioning briefly some of the most important achievements. Shchemelinin et al. [189, 191] suggested that a resolution (at tissue equivalent scale) of about 1 nm can be achieved by collecting and counting the positive ions produced during the interaction of the impinging radiation with the matter. An improved ion-counting nanodosimeter was recently proposed [190]. De Nardo et al. [190] focused their efforts toward a track detector designed as an ensemble of electrodes able to collect the electrons at a very small scale. Their aim was to measure the ionization cluster distribution at a given distance (at nanometer scale) from the track of a charged particle within a condensed target. The lateral extend of ionization events for a particle with an energy of about 1 MeV/amu is typically extending up to about 200 nm, from the incident particle trajectory within the target.

6. CONCLUSIONS

The main elements associated with the interaction between ionizing radiation and condensed targets were reviewed. Although it was recognized that the actual models are able to describe the interaction between charged incident particles and the electronic cloud of the target with a fair accuracy, the difficulties of projecting the dosimetry concepts at nanometer scale were critically reviewed.

The nature and the extent of the defects produced within condensed targets by the impinging radiation depend at a certain extend on the nature of the incident radiation. An incoming spinless charged particle will interact with the target through direct collisions and Coulomb interactions. If the energy of the incoming particle is sufficiently large, the *bremsstrahlung* contribution has to be added, and it will be necessary to analyze further if the trail of defects (produced by accelerated electrons, ions, or electromagnetic radiation) is not able to modify further the physical and chemical properties of the target. Even if the incoming radiation consists solely of charged particles, the primary interaction between impinging charged particles and the atoms of the target will result in atom excitations and eventually ionizations. These atoms are responsible for the emission of electromagnetic quanta and finally for an irradiation of the target with electromagnetic radiation. The energy deposited within the target by the Coulomb interaction between the incident charged particle and the electrons of the target is eventually responsible for a cloud of accelerated electrons (secondary or δ electrons) that are also irradiating the target. Eventually, some nuclei may be activated during the interaction of the target atoms in the incident particle and may further irradiate the target by radioactive decay. The detailed and precise estimation of the energy deposited within the target, required to properly estimated the dose, is not such a simple task. These difficulties were discussed in detail, aiming at the conceptual differences between dosimetry and nanodosimetry.

Historically, radiation-induced defects in condensed materials were divided into ionizing and non-ionizing effects. The ionizing (non-ionizing) radiation term was introduced to point to incident radiation (not) capable of producing ionizations within the target. The simplest criterion for an ionizing radiation would reflect its capability to transfer to an atom of the condensed target an amount of energy at least equal to the smallest ionization energy for a solid. The main weakness of this definition resides in the heating of the target during irradiation that will reduce the minimum ionization energy, in the possibility of nonlinear processes such as multiple quanta excitations and ionizations, and in the possibility of catalyzed (synergetic) ionizations assisted by neighboring atoms. As a result, ionization products may eventually be observed even in targets irradiated by the so-called non-ionizing radiation.

Thermal spikes description is based on the hypothesis that the interactions between the incident particles and the target results in huge local temperatures over short time periods. For example in polymers such as polyethylene irradiated with nitrogen ions accelerated up to 20 keV, the local temperature within the target (along the incident particle track) should be as high as 10^4 *K* for 10^{-10} to 10^{-9} s [61]. Spectroscopic investigations showed that the local temperature in irradiated polymers is significantly lower, reaching no more than 400 K in irradiated PE [61]. This is not in itself at variance with the thermal spike description. Such "heat pulses" should be extremely short, while the measured increase of the sample temperature was averaged over a huge time in comparison with the timescale of thermal spikes. Nevertheless, we may imagine an alternative picture for the delocalization of the energy deposited by the incident particle; First ionization processes will remove electrons from the target. Finally, the target will be surrounded by a conducting electron plasma that will allow the efficient delocalization of the energy deposited by the incident beam without a huge increase of the target temperature.

The reduced number of interactions between the incident particle and the nanotarget is another extreme, as the current dosimetry and microdosimetry approaches are based on statistical concepts. Hence, the description of the interaction between an incident charged particle and the nuclei of a nanofeature is associated with large fluctuations. The statistical character and the associated increase in the accuracy of theoretical predictions will be reached again solely in studies over a huge ensemble of isolated nanofeatures. In such cases,

the averaging over large ensembles of nanofeatures will result in a relatively good agreement between nanodosimetry and dosimetry predictions.

At this stage, the accumulated experimental data provide strong support for the future development of nanodosimetry. However, the main concepts of this development have to be better defined and empirically tested. The first problem of nanodosimetry is the "invariant." Macrodosimetry was built exploiting the invariance of the mass of the target. At nanometer scale, we proved that this approximation is too strong. Will the length of the nanofeature be the next invariant? This seems to be the most logical step. Dosimetry, including microdosimetry, represent basically nonrelativistic approaches. How important are the chemical bond strengths and the nuclear interactions in the energy balance necessary to estimate accurately the energy deposited or emitted by the nanometer-sized target? Is the Born-Oppenheimer approximation still valid in the case of the interaction of an incident particle with a nanostructure, and at what extent? Fundamental questions are waiting for answers. The recent data points toward LET/stopping power as nanometer-scale possible substitutes of dose. Local changes of the physical properties of the target (such as the shift of the glass temperature [193]) may be responsible for the evolution of nanotargets subjected to ionizing radiation.

The last section was focused on latent tracks, defined as a collection of local (nanometer-sized) chemical and physical modifications of the target due to the interaction with ionizing radiation. The diameter of latent tracks is usually in the range 1 nm to few hundreds of nanometers. Latent tracks, generated by a huge local heating, are probably the classical nanometer-scale effect of the interaction between an impinging particle and a bulk, macroscopic target. The main features of nanotubes are hidden in two contributions: the heat generation and the heat diffusion. As a first-order approximation, the heat generation will not be dramatically affected by the nanometer-sized confinement. It was shown in some simple cases (effect of confinement on the ionization potential [15]) that these contributions are easily embedded in the actual formalism. The real problem of nanodosimetry is the heat transfer. No "nano effects" will be observed unless the length(s) of the target is significantly smaller than the diameter of the latent track produced by the same particle in the same target. The nanodosimetry will describe what is happening when a particle hits a target with at least one linear dimension smaller or equal to the latent track diameter. The observed difference will result from the boundary conditions imposed to the heat flow (due to the finite size of the target). Huge local temperatures, at very short timescales, over extremely reduced volumes are expected to result from the interaction of the incident particle with the nanostructure.

To conclude, the interaction between solid target (either nanoconfined, nanostructure, or macroscopic) and the ionizing particles occurs at sub-nanometer scales, and it is accurately described by the theoretical models. This process results in physical and chemical modifications of the target at nanometer scale that are described with a fair accuracy by existing models. Although the difficulties of nanodosimetry have "apparently" a technical nature, it is significant to mention that the nanometer-size confinement is expected to bring new properties and results rather than the mechanism of interaction between the charged particle and the target in itself. More intriguing results are expected from the studies concerning the interaction of ionizing radiation with nanostructured materials, due to the interactions between nanofeatures. Many applications are expected to emerge. Some of them (ion-beam mixing of magnetic multilayers, ion-beam assisted molecular-beam epitaxy) were briefly discussed.

REFERENCES

1. A. Chatterjee, in "Radiation Chemistry" (Farhataziz and M. R. Rodgers, Eds.), p. 1. VCH Publishers, Weinheim, Germany, 1987.
2. J. L. Magee and A. Chatterjee, in "Radiation Chemistry" (Farhataziz and M. R. Rodgers, Eds.), VCH Publishers, Weinheim, Germany, 1987.
3. A. Chatterjee and J. L. Magee, in "Radiation Chemistry" (Farhataziz and M. R. Rodgers, Eds.), VCH Publishers, Weinheim, Germany, 1987.
4. A. Chapiro, "Radiation Chemistry of Polymeric Systems," Wiley-Interscience, New York, 1962.
5. A. Charlesby, "Atomic Radiation and Polymers," Pergamon Press, New York, 1962.
6. W. Schnabel, "Polymer Degradation: Principles and Applications," Hanser Gardner Publications, Berlin, 1981.
7. M. Dole, "The Radiation Chemistry of Macromolecules," Academic Press, New York, 1972.

8. R. L. Clough and A. Shalaby, Eds., "Irradiation of Polymers: Fundamentals and Technological Applications." Oxford University Press, Oxford, 1996.
9. R. L. Clough, *Nucl. Instrum. Methods Phys. Res. B* 185, 8 (2001).
10. M. D. Chipara and M. Chipara, *Polym. Degrad. Stab.* 37, 79 (1992).
11. P. J. Flory and T. G. Fox, *J. Appl. Phys.* 21, 587 (1950).
12. A. Tager, "Physical Chemistry of Polymers." MIR Publishers, Moscow, 1978.
13. T. G. Fox and S. Loshaeck, *J. Polymer Sci.* 15, 371 (1951).
14. F. Bueche, "Physical Properties of Polymers." John Wiley, New York, 1962.
15. M. Chipara, Nanomaterials in Space: Is the Future granted? World Space Congress, Houston, TX, 10, 2002.
16. E. Ikenberry, "Quantum Mechanics for Mathematicians and Physicist." Oxford University Press, New York, 1962.
17. R. L. Liboff, "Introductory Quantum Mechanics." Holden-Day Inc, Oakland, 1980.
18. L. I. Schiff, "Quantum Mechanics," 3rd Edn., McGraw-Hill Book Co., New York, 1968.
19. H. Goldstein, C. Poole, and J. Safko, "Classical Mechanics," 3rd Edn., pp. 106–121. Addison Wesley, San Francisco, 2002.
20. H. Y. C. Corben and P. Stehle, "Classical Mechanics," pp. 58–65. 2nd Edn., Robert E Krieger Publishing Co., Huntington, 1960.
21. J. E. Turner, "Atoms, Radiation, and Radiation Protection." John Wiley & Sons, New York, 1995.
22. A. Messiah, "Quantum Mechanics." North Holland Publishing Co., Amsterdam, 1961.
23. Ta You Wu and T. Ohmura, "Quantum Theory of Scattering." Prentice Hall Inc., Englewood, 1962.
24. C. Cohen-Tannoudji, F. Laloe, and B. Dui, "Quantum Mechanics," John Wiley, New York, 1996.
25. H. A. Enge, "Introduction to Nuclear Physics," p. 3–26. Addison Wesley, Reading, 1966.
26. J. J. Fitzgerald, G. L. Brownell, and F. J. Mahoney, "Mathematical Theory of Radiation Dosimetry." Gordon and Breach, New York, 1967.
27. M. Inokuti, Y. Itikawa, and J. E. Turner, *Rev. Mod. Phys.* 50, 23 (1971).
28. J. F. Ziegler, *J. Appl. Phys.* 85, 1249 (1999).
29. H. H. Tossi, M. Zaider, "Microdosimetry and Its Applications," Springer Verlag, Berlin, 1996.
30. G. F. Knoll, "Radiation Detection and Measurement," 2nd Edn., John Wiley & Sons, New York, 5, 1989.
31. C. A. Nicoletta, P. J. McNully, and P. L. Jain, *Phys. Rev.* 164, 1693 (1967).
32. R. L. Fleisher, P. B. Price, R. M. Walker, and E. L. Hubbard, *Phys. Rev.* 133, A1443 (1964).
33. W. H. Barkas, F. M. Smith, and W. Bienbaum, *Phys. Rev.* 98, 605 (1955).
34. Ch. Kittel, "Introduction to Solid State Physics." 7th Edn., Wiley, New York, 1996.
35. A. H. Morrish, "The Physical Principles of Magnetism." John Wiley & Sons, New York, 2001.
36. S. Chikazumi, "Physics of Ferromagnetism," 2nd Edn., Clarendon Press, Oxford, 1997.
37. S. V. Vonsovskii, "Magnetism." John Wiley & Sons, New York, 1974.
38. N. V. Klassen, in "Radiation Chemistry Principles and Applications" (Farhartazizi and M. A. J. Rodgers, Eds.), pp. 29–64. VCH Publishers, Weinheim, Germany, 1987.
39. H. H. Jaffe and M. Orchin, "Theory and Applications of Ultra Violet Spectroscopy," pp. 133–146. John Wiley, New York, 1962.
40. S. X. Wang, L. M. Wang, and R. C. Ewing, *J. Appl. Phys.* 81, 587 (1997).
41. M. Constantini, J. M. Desvignes, and M. Toulemonde, *J. Appl. Phys.* 87, 4164 (2000).
42. A. Meldrum, L. A. Boatner, and R. C. Ewing, *Phys. Rev. Lett.* 88, 025503 (2002).
43. R. Neugebauer, R. Wuensch, T. Jalowy, K. O. Groneveld, H. Rothard, A. Clouvas, and C. Potiriadis, *Phys. Rev. B* 50, 11113 (1999).
44. M. Ikeya, "New Applications of Electron Spin Resonance Dating, dosimetry, and Microscopy" (M. R. Zimmerman and N. Whitehead, Eds.), World Scientific, Singapore, 1993.
45. C. Trautmann, K. Schwartz, and T. Steckenreiter, *Nucl. Instrum. Methods Phys. Res. B* 156, 162 (1999).
46. Y. Wang, Y. Jin, Z. Zhu, C. Liu, Y. Sun, Z. Wang, M. Hou, X. Chen, C. Zhang, J. Liu, and B. Li, *Nucl. Instrum. Methods Phys. Res. B* 164, 420 (2000).
47. A. M. Ektessabi and K. Yamaguchi, *Thin Solid Films* 377, 793 (2000).
48. C. Liu, Y. Jin, Z. Zhu, Y. Sun, M. Hou, Z. Wang, Y. Wang, C. Zhang, X. Chen, J. Liu, and B. Li, *Nucl. Instrum. Methods Phys. Res. B* 169, 72 (2000).
49. C. Liu, Z. Zhu, Y. Jin, Y. Sun, M. Hou, Z. Wang, Y. Wang, C. Zhang, X. Chen, J. Liu, and B. Li, *Nucl. Instrum. Methods Phys. Res. B* 169, 78 (2000).
50. M. Chipara and J. Reyes-Romero, *Nucl. Instrum. Methods Phys. Res. B* 185, 77 (2001).
51. M. Chipara, *Nucl. Instrum. Methods Phys. Res. B* 131, 85, (1997).
52. M. J. Maryanski, R. J. Schulz, G. S. Ibbott, J. C. Gatenby, J. Xie, D. Horton, and J. C. Gore, *Phys. Med. Biol.* 39, 1437 (1994).
53. M. Esser and J. Fuhrmann, *Nucl. Instrum. Methods Phys. Res. B* 151, 118 (1999).
54. D. Barb, M. Chipara, V. Perelygin, M. Velter-Stefanescu, P. Yu Appel, and M. Rogalski, *Nuclear Tracks: Rad. Methods Instrum. Appl.* 16, 65 (1989).
55. M. Esser and J. Fuhrmann, *Nucl. Instrum. Methods Phys. Res. B* 146, 480 (1998).
56. G. U. Bacmeister and W. Enge, *Rad. Measurements* 28, 45 (1997).
57. R. Klett, D. Fink, A. Schmoldt, and L. T. Chadderton, *Rad. Measurements* 28, 55 (1997).
58. G. Adler, *Science, New Series*, 141, 321 (1963).
59. L. Calcagno, G. Compagnioni, and G. Foti, *Phys. Rev. B* 46, 10573 (1992).
60. T. Steckenreiter, E. Balanzat, H. Fuess, and C. Trautmann, *Nucl. Instrum. Methods Phys. Res. B* 131, 159 (1997).

61. A. Kondyurin, R. Khaybullin, N. Gavrilov, and V. Popok, *Vacuum* 68, 341 (2003).
62. A. I. Vilensky, D. L. Zagorski, V. Ya. Kabanov, and B. V. Mchedlishvili, *Rad. Measurements* 36, 131 (2003).
63. N. Stolterfoht, V. Hoffmann, R. Hellhammer, Z. D. Pesic, D. Fink, A. Petrov, and B. Sulik, *Nucl. Instrum. Methods Phys. Res. B* 203, 246 (2003).
64. T. Seguchi, H. Kudoh, M. Sugimoto, and Y. Hama, *Nucl. Instrum. Methods Phys. Res. B* 151, 154 (1999).
65. M. E. Fragala, A. Licciardello, and O. Puglisi, *Nucl. Instrum. Methods Phys. Res. B* 131, 103 (1997).
66. A. Charlesby, *Proc. R. Soc. London Ser. A* 241, 495 (1957).
67. P. Alegaonkar, V. N. Bhoraskara, P. Balaya, and P. S. Goyal, *Appl. Phys. Lett.* 80, 640 (2002).
68. L. Calcagno, *Nucl. Instrum. Methods Phys. Res. B* 105, 63 (1995).
69. S. P. Tripathy, R. Mishra, K. K. Dwivedi, D. T. Khathing, S. Ghosh, and D. Fink, *Rad. Measurements* 36, 107 (2003).
70. H. Koizumi, T. Ichikawa, M. Taguchi, Y. Kobayashi, and H. Namba, *Nucl. Instrum. Methods Phys. Res. B* 206, 1124 (2003).
71. S. A. Nouh, M. H. Abdel-Salam, and A. Ahmed Morsy, *Rad. Measurements* 37, 25 (2003).
72. M. Mujahid, P. Singh, D. S. Srivastava, S. Gupta, D. K. Avasthi, and D. Kanjil, *Rad. Measurements* 38, 197 (2004).
73. A. Oshima and M. Washio, *Nucl. Instrum. Methods Phys. Res. B* 208, 380 (2003).
74. M. Melot, Y. Ngono-Ravache, and E. Balanzat, *Nucl. Instrum. Methods Phys. Res. B* 209, 205 (2003).
75. A. Charlesby and M. Ross, *Proc. R. Soc. London Ser. A* 217, 122 (1953).
76. J. Davenas, I. Stevenson, N. Celette, S. Cambon, J. L. Gardette, A. Rivaton, and L. Vignoud, *Nucl. Instrum. Methods Phys. Res. B* 191, 653 (2002).
77. N. Charlesby and N. H. Hancock, *Proc. R. Soc. London Ser. A* 218, 245 (1953).
78. M. Buczkowski, B. Sartowska, D. Wawszczak, and W. Starosta, *Rad. Measurements* 34, 597 (2001).
79. T. Steckenreiter, E. Balanzat, H. Fuess, and C. Trautmann, *Nucl. Instrum. Methods Phys. Res. B* 151, 161 (1999).
80. G. M. Mladenov, M. Braun, and B. Emmoth, *J. Appl. Phys.* 58, 2534 (1985).
81. V. R. Oganessian, V. V. Tromov, J. Vetter, M. Danziger, B. Dorschel, and D. Hermsdorf, *Rad. Measurements* 37, 609 (2003).
82. A. L. Evelyn, D. Ila, R. L. Zimmerman, K. Bhat, D. B. Poker, and D. K. Hensley, *Nucl. Instrum. Methods Phys. Res. B* 141, 164 (1998).
83. N. F. Mott and E. A. Davis, "Electronic Processes in Non-Crystalline Materials." Clarendon Press, Oxford, 1979.
84. R. S. Kohlman, A. Zibold, D. B. Tanner, G. G. Ihas, T. Ishiguro, Y. G. Min, A. G. MacDiarmid, and A. J. Epstein, *Phys. Rev. Lett.* 78, 3915 (1997).
85. Y. Wang, L. Bridwell and R. E. Giedd, *J. Appl. Phys.* 73, 474, 1993.
86. M. Chipara, Gh. Aldica, D. Hui, M. Dimonie, K. T. Lau, L. Georgescu, I. Munteanu, and H. Marascoiu, *J. Optoelectron. Adv. Mater.* 6, 297 (2004).
87. R. Bonomo, O. Gueven, M. Chipara, C. S. Yang, G. Tabbi, and M. D. Chipara, "Irradiation effects on polypyrrole," 219th American Chemical Society Conference, PMSE Part 2, p. 147, 2000.
88. C. K. Ongy, Z. G. Songyx, and H. Gongz, *J. Phys.: Condens. Matter* 9, 9289 (1997).
89. J. Cazaux, *Polym. Int.* 50, 748 (2001).
90. R. O. Mazzei, E. Smolko, A. Torres, D. Tadey, C. Rocco, L. Gizzi, and S. Strangis, *Radiat. Phys. Chem.* 64, 149 (2002).
91. R. L. Clough, *Nucl. Instrum. Methods Phys. Res. B* 185, 8 (2001).
92. V. V. Shirkov, O. L. Orelovich, L. P. Chihacheva, S. V. Budris, A. M. Evtushenko, and V. P. Zubov, *Radiat. Measurements* 34, 61 (2001).
93. C. Lei Wu, M. Q. Zhang, M. Z. Rong, and K. Friedrich, *Composites Sci. Technol.* 62, 1327 (2002).
94. M. Z. Rong, M. Q. Zhang, Y. X. Zheng, H. M. Zeng, R. Walter, and K. Friedrich, *Polymer* 42, 167 (2001).
95. F. F. Komarov, *Phys. Uspekhi* 46, 1253 (2003).
96. P. Hazdra, K. Brand, and J. Vobecku, *Nucl. Instrum. Methods Phys. Res. B* 192, 291 (2002).
97. A. Meftah, F. Brisard, J. M. Constantini, E. Dooryhee, M. Hage-Ali, M. Hervieu, J. P. Stoquert, F. Studer, and M. Toulemonde, *Phys. Rev. B* 49, 12457 (1994).
98. R. Laiho, L. S. Vlasenko, M. P. Vlasenko, V. A. Kozlov, and V. V. Kozlovski, *Appl. Phys. Lett.* 74, 3948 (1999).
99. S. Klaumeunzer, *Nucl. Instrum. Methods Phys. Res. B* 225, 136 (2004).
100. M. C. Moore, N. Kalyanasundaram, J. B. Freund, and H. T. Johnson, *Nucl. Instrum. Methods Phys. Res. B* 225, 241 (2004).
101. W. Wesch, A. Kamarou, and E. Wendler, *Nucl. Instrum. Methods Phys. Res. B* 225, 111 (2004).
102. F. Komarov, P. Gaiduk, and A. Kamarou, *Vacuum* 63, 657 (2001).
103. V. I. Boiko, A. N. Valyaev, and A. D. Pogrebnyak, *Phys. Uspekhi*, 42, 1139 (1999).
104. T. Devolder, J. Ferré, C. Chappert, H. Bernas, J.-P. Jamet, and V. Mathet, *Phys. Rev. B* 64, 064415 (2001).
105. R. Hyndman, P. Warin, J. Gierak, J. Ferré, J. N. Chapman, J. P. Jamet, V. Mathet, and C. Chappert, *J. Appl. Phys.* 90, 3843 (2001).
106. T. Veres, M. Cai, S. Germain, M. Rouabhi, F. Schiettekatte, S. Roorda, and R. W. Cochrane, *J. Appl. Phys.* 87, 8513 (2000).
107. J. Juraszek, A. Fnidiki, J. Teillet, M. Toulemonde, A. Michel, and W. Keune, *Phys. Rev. B* 61, 12 (2000).
108. D. Babonneau, J. Briatico, F. Petroff, T. Cabioch, and A. Naudon, *J. Appl. Phys.* 87, 3432 (2000).
109. H. Bernas, T. Devolder, C. Chappert, J. Ferre, V. Kottler, Y. Chen, C. Vieu, J. P. Jamet, V. Mathet, E. Cambril, O. Kaitasov, S. Lemerle, F. Rousseaux, and H. Lenois, *Nucl. Instrum. Methods Phys. Res. B* 148, 872 (1999).

110. J. Juraszek, J. Fassbender, S. Poppe, T. Mewes, B. Hillebrands, D. Engel, A. Kronenberger, A. Ehresmann, and H. Schmoranzer, *J. Appl. Phys.* 91, 6896 (2002).
111. O.-P. Kahkonen, E. Kautto, M. Manninen, and M. Talvitie, *J. Appl. Phys.* 72, 2075 (1992).
112. O.-P. Kahkonen, M. Talvitie, E. Kautto, and M. Manninen, *Phys. Rev. B* 49, 6052 (1994).
113. D. G. Fisher, R. B. Murray, and C. P. Swann, *J. Appl. Phys.* 56, 1055 (1984).
114. W. T. Franz, G. Steck, J. J. Kramer, R. B. Murray, and D. G. Fisher, *J. Appl. Phys.* 52, 1883 (1981).
115. J. M. Constantini, F. Studer, and J. C. Peuzin, *J. Appl. Phys.* 90, 126 (2001).
116. H. H. Andersen, H. Knudsen, P. Møller Petersen, *J. Appl. Phys.* 49, 5638 (1978).
117. M. M. Brzhezinskaya, E. M. Baitinger, and V. V. Shnitov, *Physica B* 348, 95 (2004).
118. A. I. Vilensky, D. L. Zagorski, S. A. Bystrov, S. S. Michailova, R. V. Gainutdinov, and A. N. Nechaev, *Surf. Sci.* 507, 911 (2002).
119. A. A. Greenenko and N. F. Shulga, *Nucl. Instrum. Methods Phys. Res. B* 193, 133 (2002).
120. V. V. Kirsanov, *Vacuum*, 51, 305 (1998).
121. S. Logothetidis, C. Charitidis, and P. Patsalas, *Diamond Relat. Mater.* 11, 1095 (2002).
122. A. V. Krasheninnikov and K. Nordlund, *Nucl. Instrum. Methods Phys. Res. B* 216, 355 (2004).
123. A. Gonzalez-Berrios, D. Huang, N. M. Medina-Emmanuelli, K. E. Kristian, O. O. Ortiz, J. A. Gonzalez, J. De Jesus, I. M. Vargas, B. R. Weiner, and G. Morell, *Diamond Relat. Mater.* 13, 221 (2004).
124. L. S. Farenzena, R. P. Livi, M. A. de Araujo, G. Garcia Bermudez, and R. M. Papaleo, *Phys. Rev. B* 63, 104108 (2001).
125. A. Berthelot, F. Gourbilleau, C. Dufour, B. Domenges, and E. Paumier, *Nucl. Instrum. Methods Phys. Res. B*, 166, 927 (2000).
126. H. Koizumi, M. Taguchi, Y. Kobayashi, and T. Ichikawa, *Nucl. Instrum. Methods Phys. Res. B* 208, 161 (2003).
127. H. De Cicco, G. Saint-Martin, M. Alurralde, O. A. Bernaola, and A. Filevich, *Nucl. Instrum. Methods Phys. Res. B* 173, 455 (2001).
128. P. Yu. Appel, I. V. Blonskaya, V. R. Oganessian, O. L. Orelovitch, and C. Trautmann, *Nucl. Instrum. Methods Phys. Res. B* 185, 216 (2001).
129. R. M. Papaleo, *Nucl. Instrum. Methods Phys. Res. B* 191, 669 (2002).
130. S. Fan and T. Kyu, *Macromolecules* 33, 9568 (2000).
131. J. Davenas and P. Thevenard, *Nucl. Instrum. Methods Phys. Res. B* 208, 170 (2003).
132. S. K. Srivastava, D. K. Avasthi, and J. C. Pivin, *Nucl. Instrum. Methods Phys. Res. B* 191, 718 (2002).
133. M. P. de Jong A. J. H. Maas, L. J. van Ijzendoorn, S. S. Klein, and M. J. A. de Voigt, *J. Appl. Phys.* 82, 1058 (1997).
134. H. Dammak, A. Dunlop, and D. Lesueur, *Nucl. Instrum. Methods Phys. Res. B* 107, 204 (1996).
135. B. A. Gurovich, D. I. Dolgii, E. A. Kuloshova, E. P. Velikhov, E. D. Ol'Shanskii, A. G. Domantovskii, B. A. Aronzon, and E. Z. Melikhov, *Phys. Uspekhi* 44, 95 (2001).
136. A. Audouard, J. Dural, M. Toulemonde, A. Lovas, G. Szenes, and L. Thome, *Phys. Rev. B* 54, 15690 (1996).
137. V. Hnatowicz, *Nucl. Instrum. Methods Phys. Res. B* 20, 145 (2003).
138. J. L. Kelsch, A. N. Goland, and A. Paskin, *J. Phys. Chem. Solids* 26, 203 (1965).
139. V. A. Boronin, A. E. Volkov, and D. N. Kolev, *Nucl. Instrum. Methods Phys. Res. B* 209, 122 (2003).
140. S. G. Mayr, Y. Ashkenazy, and R. S. Averback, *Nucl. Instrum. Methods Phys. Res. B* 212, 246 (2003).
141. Yu. Yavlinskii, *Nucl. Instrum. Methods Phys. Res. B* 146, 142 (1998).
142. D. Ila, R. L. Zimmerman, C. I. Muntele, P. Thevenard, F. Orucevic, C. L. Santamaria, P. S. Guichard, S. Schiestel, C. A. Carosella, G. K. Hubler, D. B. Poker, and D. K. Hensley, *Nucl. Instrum. Methods Phys. Res. B* 191, 416 (2002).
143. P. V. Satyam, J. Kamilla, S. Mohapatra, B. Satpati, D. K. Goswami, B. N. Dev, R. E. Cook, L. Assoufid, J. Wang, and C. Mishra, *J. Appl. Phys.* 93, 6399 (2003).
144. H. H. Andersen, H. Knudsen, and P. Møller Petersen, *J. Appl. Phys.* 49, 5638 (1978).
145. A. Barbu, A. Dunlop, A. Hardouin Dupare, G. Jaskierowicz, and N. Lorenzelli, *Nucl. Instrum. Methods Phys. Res. B* 145, 354 (1998).
146. Z. G. Wang, Ch. Dufour, Y. F. Jin, M. D. Hou, G. M. Jin, and E. Paumier, *Nucl. Instrum. Methods Phys. Res. B* 146, 290 (1998).
147. Z. G. Wang, Ch. Dufour, E. Paumier, and M. Toulemonde, *Nucl. Instrum. Methods Phys. Res. B* 115, 577 (1996).
148. M. Toulemonde, J. M. Costantini, Ch. Dufour, A. Meftah, E. Paumier, and F. Studer, *Nucl. Instrum. Methods Phys. Res. B*, 116, 37 (1996).
149. M. Toulemonde, N. Enault, and J. Y. Fuan, *J. Appl. Phys.* 68, 1545 (1990).
150. G. Szenes, *Phys. Rev. B* 51, 13, 8026 (1995).
151. A. Meftah, F. Brisard, J. M. Constantini, M. Hage-Ali, J. P. Stoquert, F. Studer, and M. Toulemonde, *Phys. Rev. B* 48, 920 (1993).
152. N. M. Dempsey, X. L. Rao, J. M. D. Coey, J. P. Nozieres, M. Ghidini, and B. Gervais, *J. Appl. Phys.* 83, 6902 (1998).
153. N. M. Dempsey, M. Ghidini, J. P. Nozieres, P. A. I. Smith, B. Gervais, and J. M. D. Coey, *Phys. Rev. Lett.* 81, 5652 (1998).
154. G. Szenes, *Phys. Rev. B* 52, 6154 (1995).
155. R. M. Bringa and R. E. Johnson, *Phys. Rev. Lett.* 88, 165501 (2002).
156. H. de Cicco, G. Saint-Martin, M. Alurralde, and O. A. Barnaola, *Rad. Measurements* 31, 77 (1999).

157. G. Szenes, K. Havancsák, V. Skuratov, P. Hanák, L. Zsoldos, and T. Ungár, *Nucl. Instrum. Methods Phys. Res. B* 166, 933 (2000).
158. R. M. Papaléo, A. Hallén, B. U. R. Sundqvist, L. Farenzena, R. P. Livi, M. A. de Araujo, and R. E. Johnson, *Phys. Rev. B* 53, 2303 (1996).
159. M. Toulemonde, Ch. Dufour, A. Meftah, and E. Paumier, *Nucl. Instrum. Methods Phys. Res. B* 166, 903 (2000).
160. Y. Sun, Z. Zhu, Z. Wang, J. Liu, Y. Jin, M. Hou, Y. Wang, and J. Duan, *Nucl. Instrum. Methods Phys. Res. B* 212, 211 (2003).
161. N. Bajwa, K. Dharamvir, V. K. Jindal, A. Ingale, D. K. Avasthi, Ravi Kumar, and A. Tripathi, *J. Appl. Phys.* 94, 326 (2003).
162. G. Szenes, *Phys. Rev. B* 60, 3140 (1999).
163. A. Dunlop, G. Jaskiwrowicz, G. Rizza, and M. Kopcewicz, *Phys. Rev. Lett.* 90, 015503, (2003).
164. Ari Ide- Ektessabi and Y. Watanabe, *Rev. Sci. Instrum.* 73, 849 (2002).
165. R. M. Papaleo, L. D. Oliveira, L. S. Farenzana, and R. P. Livi, *Nucl. Instrum. Methods Phys. Res. B* 185, 55 (2001).
166. E. J. Kobetich, R. Katz, *Phys. Rev.* 170, 405 (1968).
167. A. I. Vilensky, D. L. Zagorski, P. Yu. Apel, N. V. Pervov, B. V. Mchedlishvili, V. N. Popok, and N. N. Mel'nik, *Nucl. Instrum. Methods Phys. Res. B* 218, 294 (2004).
168. W. H. Barkas, *Phys. Rev.* 124, 897 (1961).
169. M. Mélot, Y. Ngono-Ravache, and E. Balanzat, *Nucl. Instrum. Methods Phys. Res. B* 209, 205 (2003).
170. E. H. Lee, *Nucl. Instrum. Methods Phys. Res. B* 151, 29 (1999).
171. A. Adla, V. Buschmann, H. Fuess, and C. Trautmann, *Nucl. Instrum. Methods Phys. Res. B* 185, 210 (2001).
172. G. Szenes, *Nucl. Instrum. Methods Phys. Res. B* 155, 301 (1999).
173. R. Katz and E. J. Kobetich, *Phys. Rev.* 186, 344 (1969).
174. L. Calcagno, *Nucl. Instrum. Methods Phys. Res. B* 105, 63 (1995).
175. G. Compagnini, L. Calcagno, *Mater. Sci. Eng.* R13, 193 (1994).
176. G. Szenes, *Nucl. Instrum. Methods Phys. Res. B* 107, 146 (1996).
177. G. Szenes, *Nucl. Instrum. Methods Phys. Res. B*, 107, 150 (1996).
178. M. Seidl, J. Perdew, M. Brajczewska, and C. Fiolhais, *Phys. Rev. B* 55, 13288 (1997).
179. J. J. Zhao, M. Han, and G. H. Wang, *Phys. Rev. B* 48, 15297 (1993).
180. S. Yang and M. Knickelbein, *J. Chem. Phys.* 93, 1533 (1990).
181. O. D. Haberlen, S. C. Chung, M. Stener, and N. Rosch, *J. Chem. Phys.* 106, 5189 (1997).
182. T. Bergen, A. Brenac, F. Chandezon, C. Guet, H. Lebius, A. Pesnelle, and B. A. Huber, *Eur. Phys. J. D* 14, 317 (2001).
183. B. Schleicher, H. Burtscher, and H. G. Siegmann, *Appl. Phys. Lett.* 63, 9, 1191 (1993).
184. D. M. Wood, *Phys. Rev. Lett.* 46, 749 (1981).
185. T. Mewes, R. Lopusnik, J. Fassdbender, B. Hillebrands, M. Jung, D. Engel, A. Ehresmann, and H. Schmoranzer, *Appl. Phys. Lett.* 76, 1057 (2000).
186. A. Mougin, T. Mewes, M. Jung, D. Engel, A. Ehrsmann, H. Schmoranzer, J. Fassbender, B. Hillicbrands, *Phys. Rev. B* 63, 060409-R (2001).
187. J. Juraszek, J. Fassbender, S. Poppe, T. Mewes, B. Hillebrands, D. Engel, A. Kronenberger, A. Ehresmann, and H. Schmoranzer, *J. Appl. Phys.* 91, 6896 (2002).
188. C. J. Tsai, T. Vreeland, Jr., and H. A. Atwater, *Phys. Rev. B* 46, 7103 (1992).
189. S. Shchemelinin, A. Breskin, R. Chechik, A. Pansky, P. Colautti, V. Conte, L. De Nardo, and G. Tornielli, *Nucl. Instrum. Methods Phys. Res. A* 368, 859 (1996).
190. L. De Nardo, A. Alkaa, C. Khamphan, V. Conte, P. Colautti, P. Slegur, G. Tornielli, *Nucl. Instrum. Methods Phys. Res. A* 484, 312 (2002).
191. G. Garty, S. Shchemelinin, A. Breskin, R. Chechik, G. Assaf, I. Orion, V. Bashkirov, R. Schulte, and B. Grosswendt, *Nucl. Instrum. Methods Phys Res. A* 492, 212 (2002).
192. S. Shchemelinin, G. Garty, A. Breskin, R. Chechik, and R. W. M. Schulte, *Nucl. Instrum. Methods Phys. Res. A* 477, 527 (2002).
193. A. S. Vaughan and G. C. Stevens, *Polymer* 42, 8891 (2001).

Index

A

ISBN: 1-58883-047-0

Handbook of Theoretical and Computational Nanotechnology
Edited by Michael Rieth and Wolfram Schommers
Volume 5: Pages (807–833)

B

C

D

E

F

G

H

I

J

K

L

M

N

O

P

Q

R

S

T

U

V

W

X

Y

Z

Handbook of THEORETICAL and COMPUTATIONAL NANOTECHNOLOGY

Edited by **Michael Rieth** and **Wolfram Schommers**

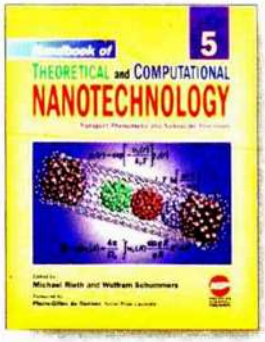

The future applications of nanotechnology in high-tech industries require deep understanding of the theoretical and computational aspects of all kinds of materials and devices on a nanometer scale. ***Handbook of Theoretical and Computational Nanotechnology*** is the first single reference source ever published in the field that offers such an unified approach, covering all of the major topics dealing with theory, modeling, design, and simulations of nanostructured materials and nanodevices, quantum computing, computational chemistry, physics, and biology, nanomechanics, nanomachines, nanoelectronics, nanoprocesses, nanomagnetism, nanooptics, nanomedicines, nanobiotechnology, etc. This 10-volume handbook provides the first ideal introduction and an up-to-date survey of the fascinating new developments and interdisciplinary activities in the whole field presented by scientists working in different subject areas of science, engineering, and medicine. This handbook is the most profound publication on this topic-the first treatment of computational nanotechnology. This outstanding handbook, presented by the world's leading scientists, is the most significant academic title ever published in this research field. This handbook has been divided into 10 thematic volumes by documenting computational treatment of nanomaterials and nanodevices.

Volume 1: Basic Concepts, Nanomachines, and Medical Nanodevices
Volume 2: Atomistic Simulations—Algorithms and Methods
Volume 3: Quantum and Molecular Computing, Quantum Simulations
Volume 4: Nanomechanics and Multiscale Modeling
Volume 5: Transport Phenomena and Nanoscale Processes
Volume 6: Bioinformatics, Nanomedicine, and Drug Design
Volume 7: Magnetic Nanostructures and Nanooptics
Volume 8: Functional Nanomaterials, Nanoparticles, and Polymer Design
Volume 9: Nanocomposites, Nano-Assemblies, and Nanosurfaces
Volume 10: Nanodevice Modeling and Nanoelectronics

KEY FEATURES

- The World's first handbook ever published in the field of theoretical and computational nanotechnology.
- The first comprehensive reference dedicated to all disciplines of science, engineering, and medicine.
- Most up-to-date reference source drawing on the past two decades of pioneering research.
- About 140 Review chapters written by world leading scientists familiar with the current trends of nanotechnology.
- Over 8,000 pages written by 265 authors from 30 countries, truly international.
- 26,000 references, 4124 figures, 374 tables, and thousands of mathematical equations and formula.
- Clearly written, self-contained, timely, authoritative, and most comprehensive contributions.
- Extensive cross-refereeing in each chapter provides reader with a broader range of knowledge.
- Multidisciplinary reference source for scientists, engineers, biologists, medical experts and related professionals.

READERSHIP

This handbook is an invaluable reference source for scientists, engineers, and biologists working in the field of theoretical and computational nanotechnology. The handbook is intended for a broad audience working in the fields of quantum chemistry, physics, biology, materials science, electrical and electronics engineering, mechanical engineering, optical science, ceramic and chemical engineering, device engineering, aerospace engineering, computer science and technology, information technology, bioinformatics, biotechnology, medical sciences, medicine, surface science, and polymer science and technology.

ISBN 1-58883-047-0
9 781588 830470 90000

ASP **AMERICAN SCIENTIFIC PUBLISHERS**
Los Angeles, California, USA

Printed in the United States of America